Bone Mechanics HANDBOOK

Second Edition

Edited by Stephen C. Cowin

Bone Mechanics HANDBOOK

Second Edition

Bone Mechanics HANDBOOK

Second Edition

Edited by
Stephen C. Cowin

CRC Press
Boca Raton London New York Washington, D.C.

Library of Congress Cataloging-in-Publication Data

Bone mechanics handbook / edited by Stephen C. Cowin.
p. cm.
Includes bibliographical references and index.
ISBN 0-8493-9117-2 (alk. paper)
1. Bones--Handbooks, manuals, etc. 2. Biomechanics--Handbooks, manuals, etc. I. Cowin, Stephen C. (Stephen Corteen), 1934-

QP88.2 .B5885 2001
612.7′5--dc21 00-051909
CIP

International Standard Book Number 0-8493-9117-2
Library of Congress Card Number 00-051909
Printed in the United States of America 1 2 3 4 5 6 7 8 9 0
Printed on acid-free paper

To Martha

Preface

The progress in bone mechanics in the last decade has been extraordinary. CRC Press published my previous edited book on this subject in 1989. It was entitled *Bone Mechanics* and it was a snapshot of the subject in the summer of 1988. The present book is a snapshot of the subject sometime in early 2000. The difference between these volumes reflects the extraordinary progress made in that decade between the publication of the two volumes. The first book covered the field in 12 chapters by 13 authors. This volume contains 36 chapters by 47 authors. The field has expanded in the number of people involved and in content. The flow of bone fluid, techniques to measure skeletal gene function and expression, bone transgenic effects, the mechanical testing of bone cells, and the design and manufacture of bone replacement scaffolds were not subjects mentioned in the 1989 volume. I believe that this decade and the next will be viewed as the decades of the most rapid accumulation of knowledge in bone mechanics research.

In the preparation of the current volume, I was struck not only by how much the field of bone mechanics had developed in the decade, but also by how many women are now working in the field. There was one woman among the 13 authors of the previous volume (7%), whereas there are 10 women authors among the 47 authors of this volume (21%), a factor of three increase. This outcome is not the result of a bias in favor of women. This volume represents a great deal of work by a number of different people, but these women carried more than a 21% share. Although they represented only a fifth of the authors, the women provided critical help at many stages. In particular, I very much appreciate the extra effort of Adele Boskey and my colleague Susannah Fritton in reviewing chapters. Further, I am deeply indebted to Catherine Ford, Eliana Lucchinetti, and Marta Villarraga for taking over development of chapters on not previously surveyed topics.

An editor learns the variety of problems that a chapter author can encounter. For example, traditionally, scholars writing chapters for volumes such as these are given credit by their institution and encouraged in this endeavor. However, government research administrators in several European countries have changed this policy in recent years. In these countries, the career evaluation systems for scholars have downgraded the value of writing chapters of the type that appear in this volume and the scholar-author is given no credit for this activity. Publication credit in these countries is based on impact, a measure of the circulation and prestige of the journal in which a publication occurs. These governments should consider the consequences of such a policy.

I should note that, as editor, I have not forced a uniform viewpoint on the authors, and the reader may find occasional contradictory statements. For example, the reader will find that my chapter on Bone Fluid Poroelasticity and Sol Pollack's chapter on Streaming Potentials in Bone are not consistent on the question of the anatomical location of streaming potentials in bone. Sol Pollack and I hope that the reader will not be frustrated by this inconsistency, but rather view the presentations as two sides of an unsettled question. It would be rewarding if the reader were inspired to seek or provide a resolution for such questions.

It was a pleasure working with all authors of the chapters of this volume. I thank each of them for their contribution. I hope that the reader will find the information gathered by these authors to be both accessible and useful. I also hope that readers of this book may, if they are not doing so already, be stimulated to work in this fascinating field.

Stephen C. Cowin

Manhattan, July 2000

Advisory Board

Webster S. S. Jee
University of Utah
Salt Lake City, Utah

Karl J. Jepsen
Mount Sinai School of Medicine
New York, New York

Jonathan J. Kaufman
The Mount Sinai Medical Center
and CyberLogic, Inc.
New York, New York

Tony M. Keaveny
University of California
Berkeley, California

Melissa L. Knothe Tate
University and Swiss Federal
Institute of Technology
Zurich, Switzerland
and AO Research Institute
Davos, Switzerland

Roderic Lakes
University of Wisconsin–
Madison
Madison, Wisconsin

Eliana Lucchinetti
Swiss Federal Institute of
Technology
Schlieren, Switzerland

Robert J. Majeska
Mount Sinai School of Medicine
New York, New York

R. Bruce Martin
University of California at
Davis Medical Center
Sacramento, California

Marjolein C. H. van der Meulen
Cornell University
Ithaca, New York

Melvin L. Moss
Columbia University
New York, New York

Elizabeth R. Myers
Weill Medical College of
Cornell University
and Hospital for Special
Surgery
New York, New York

Eric A. Nauman
Tulane University
New Orleans, Louisiana

Anders Odgaard
St. Mary's Hospital
London, England

Mark Otter
State University of New York
Stony Brook, New York

Solomon R. Pollack
University of Pennsylvania
Philadelphia, Pennsylvania

Patrick J. Prendergast
Trinity College Dublin
Dublin, Ireland

Bert van Rietbergen
Eindhoven University of
Technology
Eindhoven, The Netherlands

Clinton T. Rubin
State University of New York
Stony Brook, New York

Peter Rüegsegger
University of Zurich and ETH
Zurich, Switzerland

Mitchell B. Schaffler
Mount Sinai School of Medicine
New York, New York

Neil A. Sharkey
The Pennsylvania State
University
University Park, Pennsylvania

Robert S. Siffert
Mount Sinai School of Medicine
New York, New York

Charles H. Turner
Indiana University
Indianapolis, Indiana

Marta L. Villarraga
Exponent Failure Analysis
Associates
Philadelphia, Pennsylvania

Sheldon Weinbaum
The City College of New York
New York, New York

Howard Winet
Orthopaedic Hospital and
University of California at
Los Angeles
Los Angeles, California

Tianshun Xu
Glaxo-Wellcome, Inc.
Morrisville, North Carolina

Marian F. Young
National Institutes of Health
Bethesda, Maryland

Contents

Section I Basic Biology

Section II Techniques from Mechanics and Imaging

Section III Mechanical and Architectural Properties of Bone

Section IV Flow of Fluids in Bone

Section V Bone Adaptation

Section VI Clinically Related Issues

I

Basic Biology

1

Integrated Bone Tissue Physiology: Anatomy and Physiology

Webster S. S. Jee
University of Utah

1.1 Introduction

The skeletal system, important to the body both biomechanically and metabolically, is made up of individual bones and the connective tissue that joins them. Bone is the main constituent of the system and differs from the connective tissues in rigidity and hardness. These characteristics of bone result from inorganic salts impregnating the matrix, which consists of collagen fibers, a large variety of noncollagenous proteins, and mineral. The rigidity and hardness of bone enable the skeleton to maintain the shape of the body; to protect the soft tissues of the cranial, thoracic, and pelvic cavities; to supply the framework for the bone marrow; and to transmit the force of muscular contraction from one part of the body to another during movement. The mineral content of bone serves as a reservoir for ions, particularly calcium, and also contributes to the regulation of extracellular fluid composition, particularly ionized calcium concentration. In addition, bone is a self-repairing structural material, able to adapt its mass, shape, and properties to changes in mechanical requirements and endures voluntary physical activity for life without breaking or causing pain.

0-8493-9117-2/01/$0.00+$.50

TABLE 1.1 Subdivision of the Skeleton

Feature	Axial	Appendicular
Main bone tissue	Cancellous	Cortical
Adjacent soft tissue	Viscera	Muscle
Cortices	Thin	Thick
Marrow	Hematopoietic	Fatty
Turnover	High	Low
Main function:		
Cortical	Mechanical	Mechanical
Cancellous[a]	Metabolic	Mechanical

[a] Metabolic activity such as uptake and release of calcium occurs in all cancellous bone in red marrow sites throughout the skeleton.

Source: Bronner, F. and Worrell, R.V., Eds., *Orthopaedics, Principles of Basic and Clinical Science,* CRC Press, Boca Raton, FL, 1999. With permission.

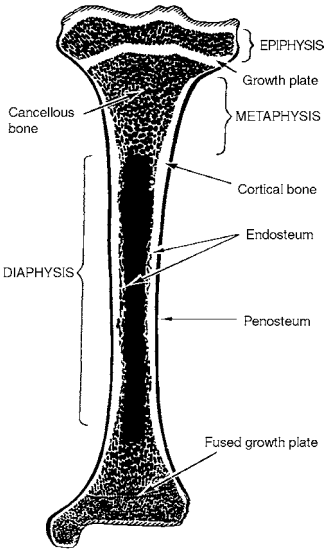

FIGURE 1.1 Schematic diagram of a tibia. The interior of a typical long bone showing the growing proximal end with a growth plate and a distal end with the epiphysis fused to the metaphysis. See text for further details. (From Weiss, L., Ed., *Cell and Tissue Biology, A Textbook of Histology*, Urban and Schwarzenberg, Baltimore, 1988. With permission.)

The skeleton has been divided into axial and appendicular subdivisions. This separation is important because composition and functions of the skeleton are divided differently between axial and appendicular components (Table 1.1).[1]

1.2 Morphology: Macroscopic and Microscopic Structures

The long bones (e.g., humerus, femur, and tibia) serve as the classical model for the macroscopic structure of bone (Fig. 1.1). A typical adult long bone consists of a central cylindrical shaft, or diaphysis, and two wider and rounded ends, the epiphyses. Conical regions called the metaphysis connect the diaphysis with each epiphysis. Most bone ends are wider than their central part because the ends have joints covered by articular cartilage and to carry equal loads indefinitely takes larger areas of articular cartilage than bone. Epiphyseal and metaphyseal bone supports the articular cartilage, which makes the epiphysis and metaphysis wider than the diaphysis.[1–3]

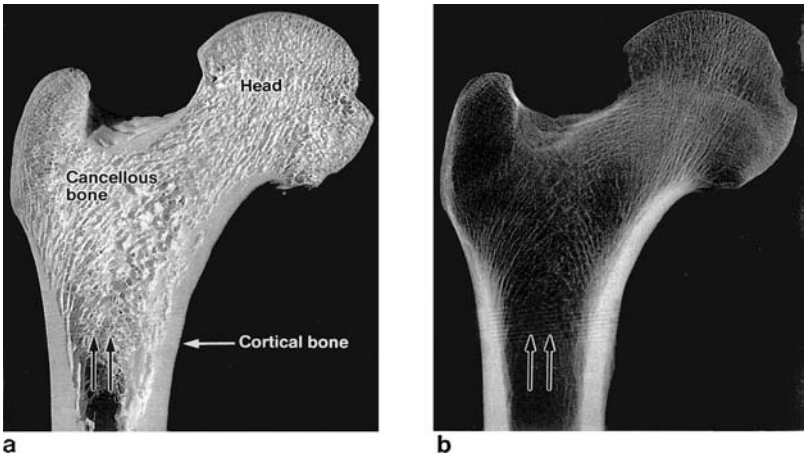

FIGURE 1.2 Bone section and radiograph of dried proximal end of femur. Original magnification × 0.5. (a) Photograph of 8-mm-thick proximal femur cut in a frontal plane. The head and greater trochanter are covered by a thin shell of cortical (compact) bone, whereas the shaft is covered by a thick cylinder of cortical bone. Note the arching pattern of trabeculae. (b) Radiograph of same bone section. The disappearance of the trabeculae is the basis of the Singh index for diagnosis of osteoporosis.[143] (From Weiss, L., Ed., *Cell and Tissue Biology, A Textbook of Histology,* Urban and Schwarzenberg, Baltimore, 1988. With permission.)

1.2.1 Cortical and Cancellous Bone

The diaphysis is composed mainly of cortical bone, while the epiphysis and metaphysis contain mostly cancellous bone with a thin shell of cortical bone (Figs. 1.1 and 1.2). In the growing animal, the epiphysis is separated from the metaphysis by a plate of hyaline cartilage known as the growth plate–metaphyseal complex, or the epiphyseal plate. The growth plate and the adjacent cancellous bone of the metaphysis constitute a region where cancellous bone production and elongation of the cortex occur. In the adult, the cartilaginous growth plate has been replaced by cancellous bone, which causes the epiphysis to become fused to the metaphysis. Obliteration of this cartilage by the fusion of the two cancellous bone masses is called the closure of the epiphysis and forms a synostosis. On the articulating (joint) surfaces at the ends of the long bone, or the ends of the epiphysis, the shell of subchondral bone is covered by a thin layer of specialized hyaline cartilage, the articular cartilage.[1–3]

The outer surface of most bone is covered by the periosteum, a sheet of fibrous connective tissue and an inner cellular or cambium layer of undifferentiated cells. The periosteum has the potential to form bone during growth and fracture healing. It is not present in areas where tendons or ligaments insert in bone, on bone ends that are lined with articular cartilage, on the surface of sesamoid bones, in subscapular areas, and in the neck of the femur. The marrow cavity of the diaphysis and the cavities of cortical and cancellous bone are lined with a thin cellular layer called the endosteum. The endosteum (an internal periosteum) is a membrane of bone surface cells (osteoclasts, osteoblasts, and bone lining cells).

Cortical bone is a dense, solid mass with only microscopic channels (Figs. 1.2, 1.4, and 1.5). Approximately 80% of the skeletal mass in the adult human skeleton is cortical bone, which forms the outer wall of all bones and is largely responsible for the supportive and protective function of the skeleton. The bulk of cortical bone is in the shaft of long bones of the appendicular skeleton. The remaining 20% of the bone mass is cancellous bone, a lattice of large plates and rods known as the trabecula, found in the inner parts of bones (Figs. 1.1 and 1.3). The distribution of cortical and cancellous bone varies greatly between individual bones. For example, the ulna is 92% cortical and only 8% cancellous bone, while a typical vertebra consists of 62% cortical and 38% cancellous bone. In addition, cortical and cancellous bone differ in their development, architecture, function, proximity to the bone marrow, blood supply, rapidity of turnover time, and magnitude of age-dependent changes and fractures (Table 1.2).[1–3]

TABLE 1.2 Differences in Cortical and Cancellous Bone

	Cortical	Cancellous
Skeletal mass	80%	20%
Bone surface	33%	67%
Surface/volume ratio (mm^2/mm^3)	20	2.5
Soft tissue	~10%	~75%
Adult tissue	Secondary osteon (Haversian systems) Interstitial lamellae Circumferential lamellae	Curved plates, rods (Hemiosteons) Interstitial lamellae
Porosity	Low	High
Marrow	Fatty	Hematopoietic
Main soft tissue	Viscera	Marrow
Developmental	Intramembranous ossification	Endochondral ossification
Turnover	Slow	Rapid
Function	Mainly biomechanical also supportive and protective	Mainly mineral homeostasis, also supportive

Source: Bronner, F. and Worrell, R.V., Eds., *Orthopaedics, Principles of Basic and Clinical Science,* CRC Press, Boca Raton, FL, 1999. With permission.

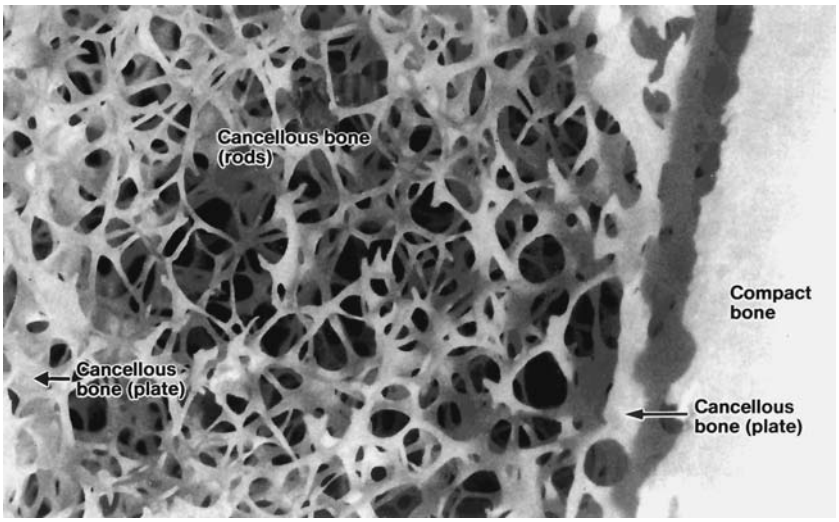

FIGURE 1.3 Photograph of a thick ground section of part of the proximal tibia showing the cortical (compact) bone and the trabecular (cancellous) bone. The trabecular bone consists of vertical trabecular plates with perforations and a network of trabecular rods or bars. In living specimens, bone marrow occupies the intertrabecular spaces. Original magnification × 4. (From Weiss, L., Ed., *Cell and Tissue Biology, A Textbook of Histology*, Urban and Schwarzenberg, Baltimore, 1988. With permission.)

1.2.2 Woven and Lamellar Bone

Mammalian cortical or cancellous bone is of two main types, woven or lamellar. Bone tissue in the developing embryo is the woven type. Cancellous woven bone is formed by endochondral and intramembranous ossification. In postfetal osteogenesis that occurs when fractures heal, or in ectopic ossification or osteosarcoma, new bone is deposited in woven form. Woven bone, a matrix of interwoven coarse collagen fibers with

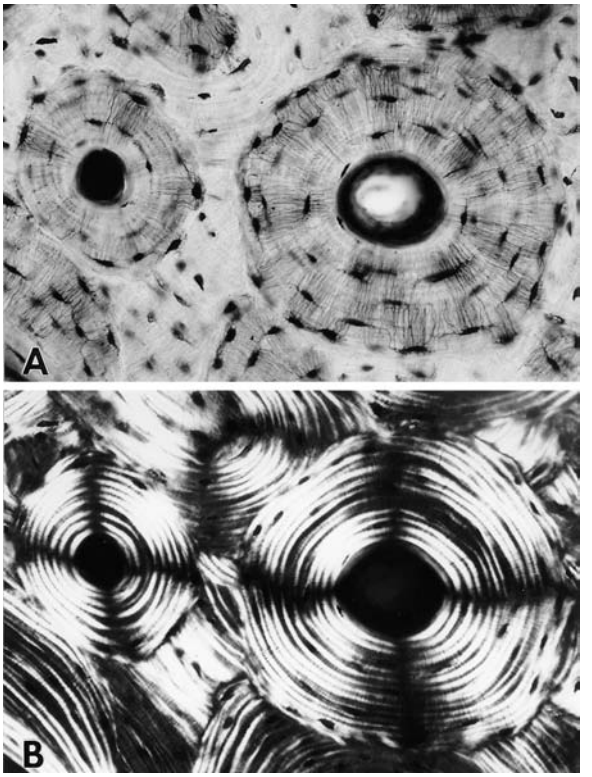

FIGURE 1.4 (A) Cross section of cortical bone showing osteon with its lacunae and canaliculi and Haversian canals. Note intervening interstitial lamellae between osteons. (B) Same section in polarized light. Note the osteons composed of numerous lamellae. (From Royce, P. M. and Steinmann, B., Eds., *Connective Tissue and Its Heritable Disorders, Molecular, Genetic and Mineral Aspects,* John Wiley & Sons, New York, 1993. With permission.)

osteocytes distributed more or less at random, is less organized and shorter-lived than lamellar bone.[1–8] It is provisional material that is eventually resorbed and replaced by lamellar bone. In human long bones, woven bone is replaced by lamellar bone at age 2 and 3 years. Lamellar bone is built up of unit layers (lamellae), like plywood. Each lamella is approximately 3 to 7 μm thick and contains fine fibers that run in approximately the same direction, but whose axes can differ by as much as 90° in adjacent units. In histological preparations, the laminations are best seen under polarized light. They appear as alternating light and dark layers, the result of differing orientations of collagen fibers within adjacent lamellae (Figs. 1.4 and 1.5).[1–8]

The lamellae of adult cortical bone appear in three major patterns: (1) circular rings of lamellae (concentric lamellae) surrounding a longitudinally vascular channel that together form a structural cone, the osteon or Haversian system; (2) several layers of lamellae extending uninterrupted around part or all of the circumference of the shaft to form what is known as the circumferential lamellae; and (3) angular fragments of what formerly were concentric or circumferential lamellae filling the gaps between the Haversian systems, known as the interstitial lamellae (Figs. 1.4 and 1.5). The spicules (trabeculae) of adult cancellous bone consist of two major types: trabecular packets or hemiosteon shaped like shallow crescents and interstitial lamellae (Fig. 1.6).[1–8]

Small cavities (lacunae) connected by their tubular canals (canaliculi) are found throughout woven and lamellar bone. Entrapped bone cells (osteocytes) and their long cytoplasmic processes occupy the lacunae and canaliculi, respectively. The cell processes communicate by gap junctions with the processes of osteocytes lying in adjacent lacunae, bone lining cells, progenitors, and the vasculature of bone marrow and Haversian canals. Canaliculi that open to the extracellular fluid and bone surfaces form an anastomosing network for the nutrition and metabolic activities of the osteocytes (Figs. 1.4, 1.5, and 1.7).[1–6,8–10]

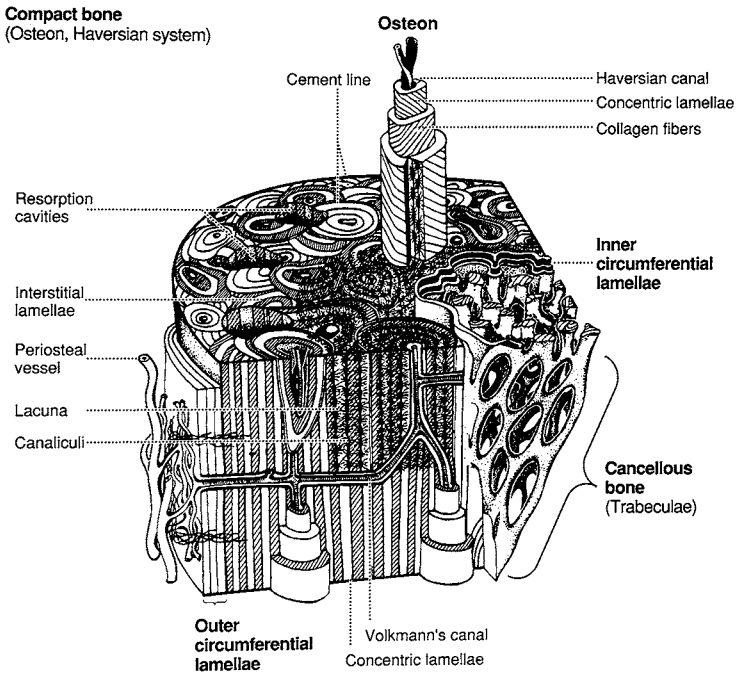

FIGURE 1.5 Diagram of a portion of a long bone shaft containing histological details of cortical bone. (From Weiss, L., Ed., *Cell and Tissue Biology, A Textbook of Histology,* Urban and Schwarzenberg, Baltimore, 1988. With permission.)

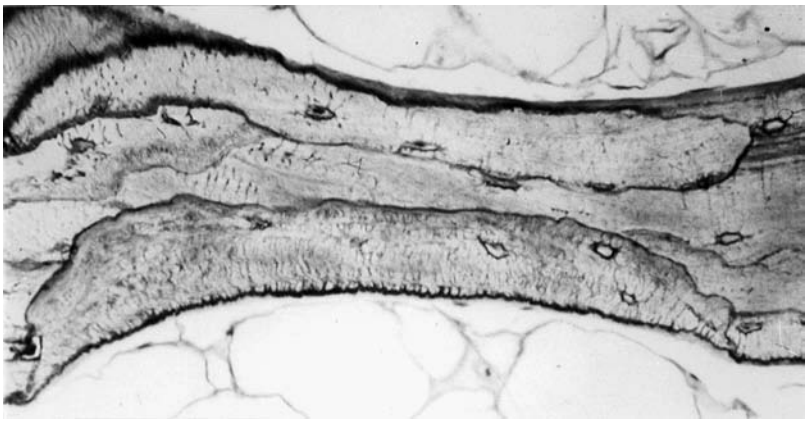

FIGURE 1.6 A part of a trabecula showing two packets (hemiosteons) separated by scalloped cement lines with the intervening interstitial lamellae. (From Fleisch, H., *Bisphosphonates in Bone Disease. From the Laboratory to the Patient,* Parthenon Publishing Group, New York, 1997. With permission.)

1.2.3 Composition of Bone

Bone consists of 65% mineral, 35% organic matrix, cells, and water. The bone mineral is in the form of small crystals in the shape of needles, plates, and rods located within and between collagen fibers. The mineral is largely impure hydroxyapatite, $Ca_{10}(PO_4)_6(OH)_2$, containing constituents such as carbonate, citrate, magnesium, fluoride, and strontium incorporated into the crystal lattice or absorbed onto the crystal surface. Foreign substances such as tetracyclines, polyphosphates, bisphosphonates, and bone-seeking radionuclides can also be incorporated with high affinity.[11,12] The organic matrix consists of 90% collagen and

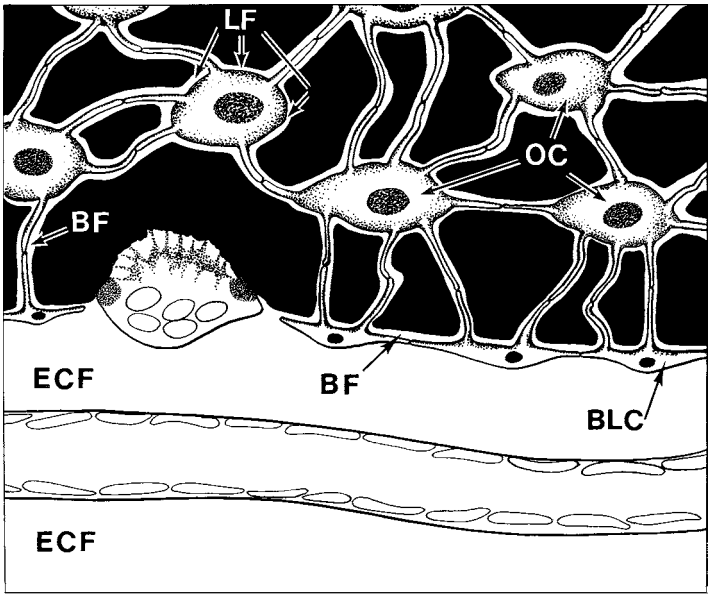

FIGURE 1.7 Diagrammatic representation of the bone fluid compartment (BFC) and gap junction intercellular communication (GJIC) in the postulated control of plasma calcium and the role of fluid flow in the skeletal adaptation to mechanical usage. It is now postulated the bone fluid is continuously circulated through each subcompartment; extracellular fluid (ECF); bone-lining cell (BLC); bone fluid (BF); bone (black); lacuna fluid (LF); and osteocyte (OC). Calcium ions enter the bone fluid compartment through channels between cells that line the bone surface and are actively returned to extracellular fluid through lining cells on the surface of bone. The cells of the osteogenic lineage (stromal cells, preosteoblasts, osteoblasts, bone-lining cells, osteocytes), and vascular endothelium form a continuous protoplasmic network that extends from osteocytes to vascular endothelium and gap junctions. (From Weiss, L., Ed., *Cell and Tissue Biology, A Textbook of Histology,* Urban and Schwarzenberg, Baltimore, 1988. With permission.)

about 10% of various noncollagenous proteins.[11–13] The roles of noncollagenous proteins are unclear. The most abundant ones are osteocalcin, osteonectin, osteopontin, and bone sialoprotein. The urinary excretion and plasma or serum levels of some of the noncollagenous proteins unique to bone are used clinically to assess bone turnover.[11,12,14] (See osteoblast function in Section 1.2.7.2.4 for more details on this topic.)

1.2.4 Vascular and Nervous Supply[1,2,15]

The routing of blood is closely related to patterns of growth, modeling, and remodeling. Most of the blood supply to the cortex of the long bone shaft comes by way of medullary vessels (Fig. 1.8), which consist of the nutrient artery and the metaphyseal and epiphyseal arteries after the epiphyseal–metaphyseal growth plate has closed.

The nutrient artery enters the long bone, divides into ascending and descending arteries, and gives off branches into the endosteal surface of the cortex. The small arteries and arterioles are conducting vessels to the capillaries of the cortex, which are the exchange vessels of the tissues. At the ends of the long bones, periosteal arteries enter from the outside (toward the epiphyseal and metaphyseal system in adults) while, in the diaphysis, vessels supply circulation from within and are directed centrifugally.

Venous drainage from a long bone occurs via venous pathways that accompany the arterial supply. Small venules in the cortex drain periosteally and endosteally. Large emissary veins collect from the central medullary sinus and a periosteal venous system. The central medullary sinus drains the cortical bone and connects with veins exiting at either ends of the bone.

Periosteal conducting arteries are most abundant at muscle attachments. Periosteal veins drain venous blood from bone and proteins and other substances from the interstitial fluid system.[1,2,15]

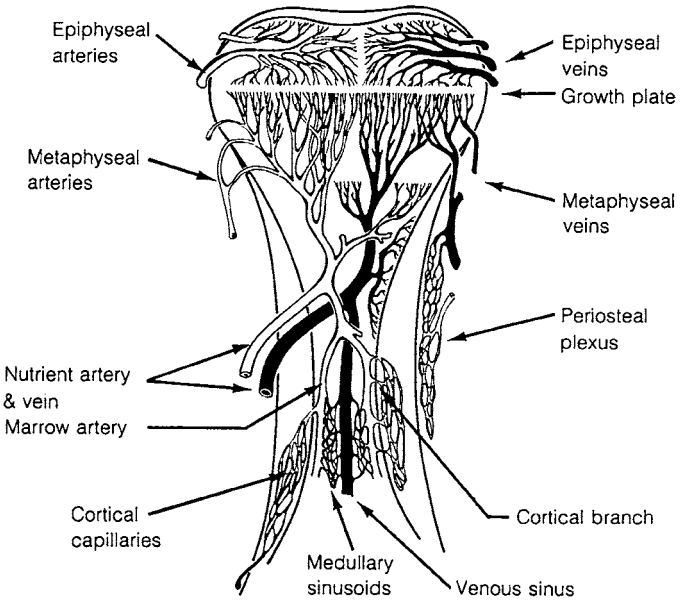

FIGURE 1.8 Diagram of longitudinal section of proximal portion of growing long bone illustrating bone vascularization. Several discrete points of arterial inflow (nutrient, metaphyseal and epiphyseal arteries, and periosteal plexus) supply regional capillary and sinusoidal networks within the bone and marrow. These drain into venous channels that exit at the bone surface. When growth is complete, the growth plate disappears and the trabecular bone circulation of the epiphysis and metaphysis join together. (From Weiss, L., Ed., *Cell and Tissue Biology, A Textbook of Histology,* Urban and Schwarzenberg, Baltimore, 1988. With permission.)

Capillary arcades are formed in marrow spaces between trabeculae in cancellous bone. Capillaries have a continuous endothelial layer and a continuous basement membrane surrounded by layers of endothelial cells. The capillary is the end of the vascular pathway and acts as a molecular sieve.

Bone growth, modeling, and remodeling have a dependency on the vascular system. All cells not only require oxygen, but the vascular system is a source of bone cells. The capillary is the only source for new preosteoclasts that originate in the bone marrow and leave the circulation at a specific location, in accordance to signals expressed by endothelial cells. The endothelial cells may also play a central role in the local coupling of formation to resorption. Furthermore, vascular pericytes and endothelial cells, present in small blood vessels except bone marrow sinusoids, are postulated as potential precursors of osteoblasts.[258] In addition, the capillary system makes available newly released mineral ions and carbonate to facilitate remodeling.

Little of the hemodynamics of the circulation in bone is known. It has been estimated from studies in laboratory animals that the rate of cortical blood flow is 3 to 8 ml/100 g bone/min and the rate for the diaphyseal marrow is 4 to 18 ml/100 g/min. The intravascular pressure is high at the endosteal surface about 60 mmHg and low at the periosteal surface, about 15 mmHg.

It has been demonstrated that there is a transient increase in bone blood flow following paraplegia, nerve section, ovariectomy, and orchiectomy and a decrease in blood flow following parathyroid hormone, prostaglandin E_2, and nitric oxide treatment.[16–20] Also marrow blood flow decreases with age.[21]

The nerve supply for bone, which might exert a controlling influence on local circulation, is largely unknown. Haversian canals, periosteum, and medullary vessels are innervated. Poorly myelinated nerve fibers are present in Haversian canals.

Adrenergic, but not vasoactive intestinal peptide (VIP)-immunoreactive, nerve fibers have been demonstrated in Haversian canals and bone marrow. VIP-immunoreactive nerve fibers of sympathetic origin were found in the periosteum of numerous species. Vasodilatation is probably not the primary action of VIP in bone and *in vitro* studies hypothesize that VIP may modulate bone resorption *in vivo*.[1,22,23]

Recent electron microscopy studies showed bone is rich in nerve fiber processes running along vessels adjacent to bone trabeculae.[24] Some of the nerve processes showed local dilatations in contact with bone cells. These studies found glutamate receptors in osteoclasts and osteoblasts as well as nerve processes in proximity to bone,[24–27] and since glutamate is a neuromediator of the central and peripheral nervous system it suggests a glutamateric inneration in bone.[28]

1.2.5 Bone Surfaces[1–3,5,8]

Unlike cartilage, which grows both interstitially and appositionally, bone is restricted to appositional growth because of the nonexpandable nature of mineralized bone tissue; thus, all bone activities occur at bone surfaces. Bone tissue has two major surfaces, periosteal and endosteal. The endosteal surface subdivides into the intracortical (Haversian or osteonal), endocortical, and cancellous or trabecular surfaces. Cancellous bone surface contributes more than 61% of the total bone surface because the mean trabecular surface-to-volume ratio is eight times greater in cancellous than in cortical bone (20 mm^2/mm^3 vs. 2.5 mm^2/mm^3; Tables 1.2 to 1.4).[1–3,5]

At any specific time the bone surfaces may be in one of three functional states: forming, resorbing, or quiescent. Bone-forming surfaces are characterized by osteoid and by a covering of osteoblasts. In contrast, resorbing surfaces contain scalloped concavities (Howship's lacunae) that frequently contain osteoclasts or have osteoclasts located nearby. Quiescent, or resting, bone surfaces are free of osteoclasts and osteoblasts. They are lined by bone-lining cells. An osteoid layer 1 μm thick exists between the lining cells and mineralized bone. Most bone surfaces in the human adult are in the quiescent state (Table 1.4).[1–3,5]

TABLE 1.3 Adult Bone Surfaces

Surface	Surface Area ($\times 10^6$ mm^2)	Total Surface (%)
Periosteal	0.5	4.4
Endocortical (cortical–endosteal)	0.5	4.4
Intracortical–Haversian or osteonal	3.5	30.4
Trabecular–endosteal	7.0	60.8
Total surface	11.5	100.0

Source: Weiss, L., Ed., *Cell and Tissue Biology, A Textbook of Histology,* Urban and Schwarzenberg, Baltimore, 1988. With permission.

TABLE 1.4 Comparison of Cortical and Trabecular Bone Volume and Bone Surface

Factors	Cortical	Trabecular
Fractional volume (mm^3/mm^3)	0.95	0.20
Surface/bone volume (mm^2/mm^3)	2.5	20
Total bone volume (mm^3)	1.40×10^6	0.35×10^6
Total internal surface (mm^2)	3.50×10^6	7.0×10^6
Forming (%)	3.0	6.0
Resorbing (%)	0.6	1.2
Quiescent (%)	96.6	92.8

Source: Recker, R.R., Ed., *Bone Histomorphometry: Techniques and Interpretation,* CRC Press, Boca Raton, FL, 1983. With permission.

TABLE 1.5 Comparison of Adult Cortical and Cancellous Bone Structural Units

Parameter	Cortical (Osteonal)	Cancellous (Trabecular Packet)
Length (mm)	2.5	1.0
Circumference (mm)	0.6	0.6
Wall thickness (mm)	0.075	0.040
Number/mm^3 bone volume	15	40
Total number in skeleton	21×10^6	14×10^6
Duration of resorption (days)	24	21
Duration of formation (days)	124	91
Remodeling period (days)	148	112
Bone turnover rate (%/year)	43	26

Source: Modified from Recker, R. R., Ed., *Bone Histomorphometry: Techniques and Interpretation,* CRC Press, Boca Raton, FL, 1983. With permission.

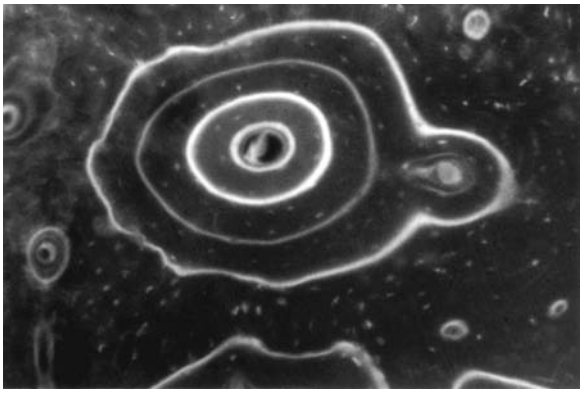

FIGURE 1.9 A Haversian system or secondary osteon labeled at four different intervals with four different fluorescent labels. (From Harris, W. H., *Nature,* 188, 1039, 1960. By permission of author and MacMillan and Co., Ltd., publisher.)

1.2.6 Bone Structural Unit[1–8]

In cortical bone the main structural unit is the osteon or Haversian system (Figs. 1.4, 1.5, and 1.9). Osteons form approximately two thirds of the cortical bone volume; the remaining one third is interstitial bone composed of the remnants of past generations of osteons and subperiosteal and subendosteal circumferential lamellae. A typical osteon is a cylinder about 200 or 250 μm in diameter; the canals are interconnected by transverse Volkmann's canals that divide to form a branching network. Within the central canal run blood vessels, lymphatics, nerves, and loose connective tissue that continue through the bone marrow and the periosteum. The total length of a single canal from periosteum to endosteum is about 1 cm with a mean distance between branch points of about 2.5 mm. The wall of the osteon is made up of 20 to 30 concentric lamellae approximately 70 to 100 μm thick. Surrounding the outer border of each osteon is a cement line, a 1- to 2-μm-thick layer of mineralized matrix deficient in collagen fibers. Two types of cement lines are apparent: reversal lines, which are irregular or scalloped, and arrest lines, which have a smooth contour.

In cancellous or trabecular bone the structural unit is the trabecular packet, a hemiosteon (see Figs. 1.6 and 1.23c). The ideal trabecular packet is shaped like a shallow crescent with a radius of 600 μm and is about 50 μm thick and 1 mm long. As with cortical bone, cement lines hold the trabecular packets together. Table 1.5 summarizes differences between basic multicellular units or bone structural units (BSU) in cortical and cancellous bone.[1,5]

1.2.7 Cells of Bone[1–8,12,29,35–39,44–57]

The major cellular elements of bone include osteoclasts, osteoblasts, osteocytes, bone-lining cells, the precursors of these specialized cells, cells of the marrow compartment, and an immune regulatory system that supplies the precursor cells and regulates bone growth and maintenance.

1.2.7.1 The Osteoclasts[1–8,29–35]

1.2.7.1.1 The Phenotype

Osteoclasts, the bone-resorbing cells, are multinucleated giant cells that contain from 1 to more than 50 nuclei and range in diameter from 20 to over 100 μm. Their role is to resorb bone. Actively resorbing osteoclasts are usually found in cavities on bone surfaces, called resorption cavities or Howship's lacunae. The cytoplasm of the osteoclasts tends to be foamy in appearance and is acidophilic in its staining characteristics (Figs. 1.10, 1.23A, 1.25, and 1.26). The surface of osteoclasts adjacent to bone surface has a striated appearance and a ruffled border, an area of extensive membrane enfolding. The ruffled border is surrounded by an ectoplasmic zone, devoid of organelles but containing many active filaments, called the clear or filamentous zone. Osteoclasts adhere to the bone surface at the clear zone, which acts as a permeable seal to maintain the microenvironment needed for bone resorption to occur. The ruffled border secretes products leading to bone destruction (Figs. 1.11 and 1.12).[29–36]

1.2.7.1.2 Origin and Fate

The osteoclast is derived from cells in the mononuclear/phagocytic lineage of the hematopoietic marrow, the granulocyte/macrophage colony-forming unit (GM-CFU). Although osteoclast differentiation occurs

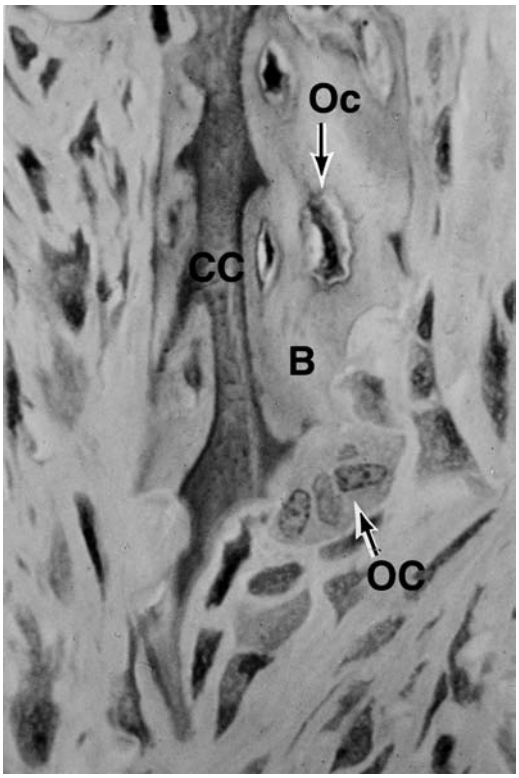

FIGURE 1.10 Light micrograph of osteoclasts (arrows). Typical multinucleated osteoclast nestled in its Howship's lacuna. Bone (B), calcified cartilage (CC). Decalcified, methylene blue, and azure II stained section. Original magnification × 800. (From Weiss, L., Ed., *Cell and Tissue Biology, A Textbook of Histology,* Urban and Schwarzenberg, Baltimore, 1988. With permission.)

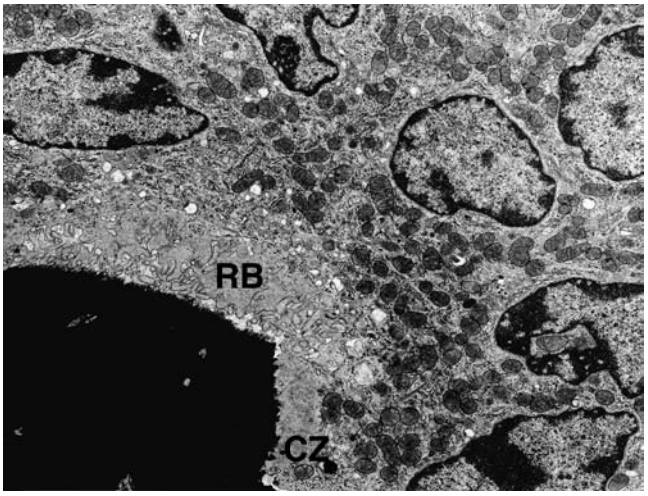

FIGURE 1.11 Electron micrograph of a part of an osteoclast. The osteoclast has multiple nuclei, numerous mitochondria, ruffled border (RB), and clear zone area (CZ); mineralized bone (black area). Original magnification × 6500. (From Miller, S. C. and Jee, W. S. S., *Anat. Rec.,* 193, 439, 1979. By permission of authors and Wiley-Liss, New York.)

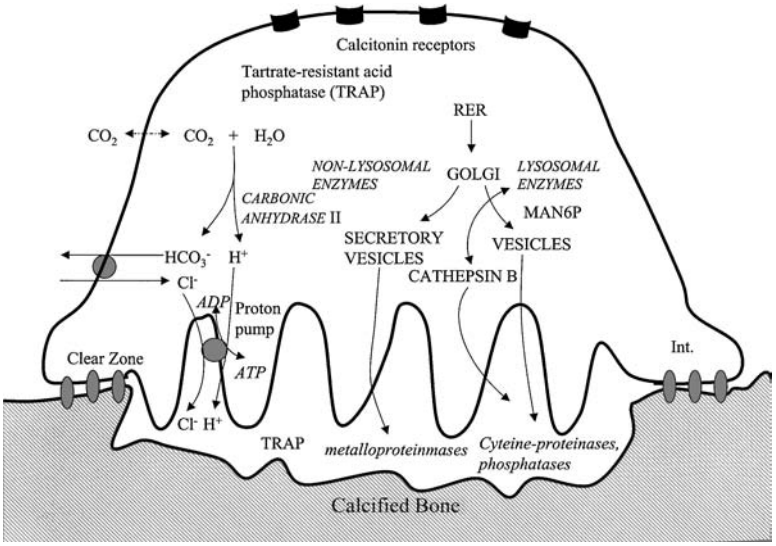

FIGURE 1.12 Model of osteoclast-mediated bone resorption. Schematic representation of enzyme secretion and ion transport polarity. The numerous nuclei and organelles are not shown. The plasma membrane of the facing bone is extensively folded and forms the ruffled border. RER = endoplasmic reticulum, INT = integrin receptors. (Adapted from Refs. 4, 29–32)

at the early promonocyte stage, already committed monocytes and macrophages might still be able to form osteoclasts under special circumstances.[263] Despite its mononuclear/phagocytic origin, the osteoclast expresses distinct markers: it is devoid of several receptors and markers in macrophages and expresses calcitonin and vitronectin (integrin $\alpha_v\beta 3$) receptors.[29] It is controversial whether osteoclasts express receptors for parathyroid hormones, estrogen, or vitamin D. There is little information concerning the life cycle of osteoclast cells *in vivo*. The life span of osteoclasts *in vivo* appears to be up to 7 weeks with a half-life of around 6 to 10 days. The life span of an osteoclast nucleus is believed to be about 10 days.

TABLE 1.6 Agents Acting on Osteoclast Regulation[a]

Stimulation		Inhibition
Parathyroid hormone (PTH)	Basic fibroblast growth factor	Calcitonin
PTH-related protein	Insulin growth factor 1	Gonadal steriods
1,25–Dihydroxy vitamin D_3[b]	Bone morphogenetic protein 2,4	Interluekin-4,18
Thyroid hormone	5-Lipoxygenase metabolite	Nitric oxide
Glucocorticoids[b]	Osteoprotegerin ligand (ODF, RANKL, TRANCE)	Interferon-γ
Retinoid (Vit A)	Fluoride	Bisphosphonate
Prostaglandin E_2[b]	Stem-cell factor	Osteoprotegerin (OPG, OCIF)[e]
		17β-Estadiol
		Bone morphogenetic protein 2
Interleukin-1,3,6,11	Erythropoietin	Calcium[f]
Macrophagecolony–stimulating factor	cFos and cSRC	
Colony-stimulating factor-1 (CSF)	PU 1[c]	
Granulocyte/macrophage CSF	NF_kB_1 (p50)[c,d]	
Transforming growth factor-α	NF_kB_2 (p52)[c,d]	
Transforming growth factor-β[b]	Caspace and adhesion molecules	
Tumor necrosis factor-α	Chaperonin	
Epidermal growth factor	Carbonic anhydrase	
Leukotrienes	Proton pump (H^3-ATPase)	

[a] Regulate genesis, growth, proliferation, function, fusion, attachment, polarization or bone resorption functions.

[b] Biphasic regulation.

[c] PU 1 myeloid and B lymphocyte transcription factor.

[d] NF_kB_1 or NF_kB_2 (the gene is termed p50 and p52)—lymphoid specific transcription factor involved with B lymphocyte maturation.

[e] OCIF = osteoclast inhibitory factor.

[f] Elevation of extracellular calcium concentration inhibits osteoclast resorptive activity via a negative feedback mechanism.

Source: Data obtained from Rodan and Rodan (1995),[29] Teitelbaum et al. (1996),[30] Suda et al. (1992),[31] Roodman (1996),[32] Baron et al. (1993),[33] Mundy (1999),[34] Puzas and Lewis (1999),[35] Pacifici (1999),[36] and Hofbauer et al. (2000).[158]

Cessation of bone resorption is associated with migration of osteoclasts from endosteal surfaces into adjacent marrow space where they undergo apoptosis.

1.2.7.1.3 Regulation

The osteoclasts are regulated by numerous factors (Table 1.6). Although many factors regulate various aspects of osteoclast formation, the final two effectors are osteoprotegerin ligand (OPG-L)/osteoclast differentiation factor (ODF) and osteoprotegerin (OPG)/osteoclastogenesis inhibiting factor (OCIF). Both are members of the tumor necrosis (TNF) receptor superfamily and secreted by osteoblastic lineage cells. OPG-L/ODF exerts its effect by binding to its receptor, osteoclast diffentiation, and activator receptor (ODAR)/receptor activator of NF_kB (RANK) on osteoclast lineage cells. OPG-L/ODF mRNA levels in osteoblastic lineage cells are increased by dexamethasome, 1α, 25$(OH)_2D_3$, IL-1β, IL-11, TNF-α, parathyroid hormone (PTH), and prostaglandin $E_2(PGE_2)$, while transforming growth factor β (TGF-β) supresses them. OPG-L/ODF stimulates osteoclast differentiation and mature osteoclast activity and inhibits osteoclast apoptosis. Macrophage colony–stimulatory factor (M-CSF) and OPG-L/ODF are both required for the initiation of differeniation by uncommitted osteoclast precursors. OPG/OCIF mRNA in osteoblastic lineage cells is upregulated by IL-1α, IL-1β, TNF-α, TNF-β, 1α25$(OH)_2D_3$, and bone morphogenetic protein-2, estrogen, and transforming growth factor-beta (TGF-β), while glucocorticoid, PGE_2, and estrogen receptor antagonists suppress them. The biological effects of OPG/OCIF are the opposite of that of OPG-L/ODF in inhibiting differentiation, fusion, and activation of committed precursors, decreasing mature osteoclastic activity and inducing apoptosis (Table 1.6); (Fig. 1.13).[158–164] Therefore, the activity of OPG-L/ODF is

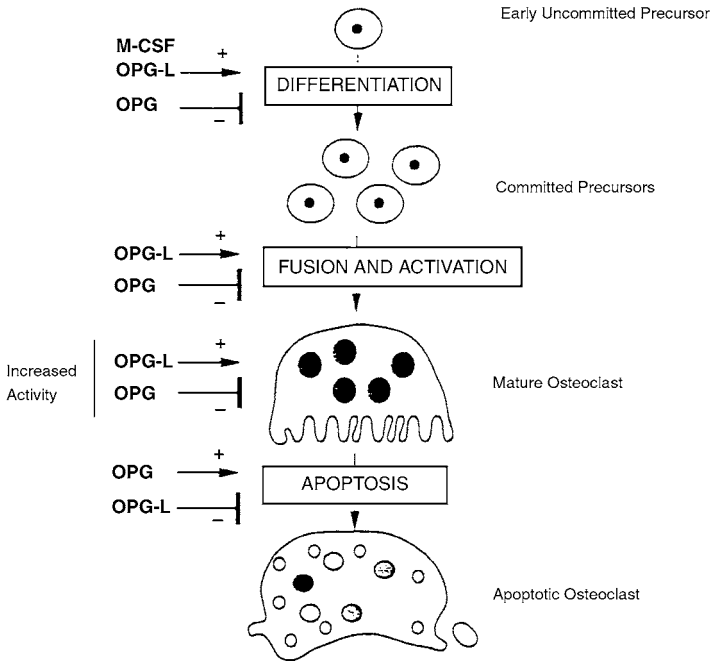

FIGURE 1.13 Regulation of osteoclast population by osteoclast differentiation factor (OPG-L/ODF) and osteoclastogenesis inhibitory factor (OPG/OCIF). M-CSF is required only for initiation of the differentiation by uncommitted osteoclast precursors in bone marrow. The addition of glucocorticoids, PTH and PGE_2, will increase OPG-L levels and glucocorticoids and PGE_2 will suppress OPG levels to enlarge pool size. The addition of TGF-β will lower OPG-L levels and 17β-estradiol and TGF-β will lower OPG levels to decrease osteoclast pool size. (From Hofbauer, L. C. et al., *J. Bone Miner. Res.,* 15, 2, 2000. With permission.)

neutralized by binding to OPG/OCIF. Thus, the osteoclast pool may be regulated by the ratio of OPG-L/ODF to OPG/OCIF in the bone marrow microenvironment. (Why the marrow environment? Because bone resorption occurs in regions adjacent to marrow!) The alteration in the ratio may be the cause of bone loss in many metabolic disorders.[58,59]

1.2.7.1.4 Function

The osteoclasts solubilize both the mineral and organic component of the matrix. Osteoclasts can be either active or inactive and, when active, they are polarized and exhibit ruffled borders. The signals for the selection of sites to be resorbed is unknown. Bone lining cells may contract and dissolve the protective osteoid layer to expose the mineral.[29,34,35] The mechanism of attachment of osteoclasts to the bone surface is not known (see Fig. 1.27). It is thought that cell membrane receptors ($\alpha_2\beta_1$ and $\alpha_v\beta_3$), which are called integrins expressed by osteoclasts and which interact with extracellular matrix protein, are involved; the $\alpha_2\beta_1$ interacts with collagen and $\alpha_v\beta_3$ associates with vitronectin, osteopontin, and bone sialoprotein through an arginine–glycine–aspartic acid (RGD) sequence.[29] Why the lining cell allows access to specific sites and how the osteoclast is activated are not clear. It has been suggested that the lining cell releases a soluble signal that activates the osteoclast, and the recently discovered RANKL ligand, receptor activator of NFkB ligand (ODF, OPG-l, TRANCE) is a likely factor.[29–35]

Bone resorption occurs at the ruffled border in a closed space where the pH is about 3.5 and the secretion of H^+ ions, which dissolve the bone mineral, originating from H_2CO_3 as a result of the action of carbonic anhydrase and are secreted by means of an electrogenic proton-pump ATPase. Also various proteolytic enzymes, especially metalloproteinases, cystiene-proteinases, phosphatase, cathepsin K, etc.,

digest the collagen and other proteins of bone matrix (Fig. 1.12).[4,29–35] In addition vascularity is involved because of the location of sinusoid preferentially adjacent to bone remodeling sites.

Besides its unique phenotype, the osteoclast possesses receptors for calcitonin and responds to parathyroid hormones, $1,25(OH)_2$ vitamin D_3 and calcitonin. Because osteoclasts lack PTH receptors, the current belief is that the response to PTH is mediated by cells of the osteoblast lineage, which exert their influence on the localization, induction, stimulation, and inhibition of osteoclastic resorption. Calcitonin inhibits resorption by the induction of cytoplasmic quiescence, whereas $1,25(OH)_2$ vitamin D_3 stimulates osteoclastic resorption by the induction of osteoclastic precursors to become osteoclasts.

Bisphosphonates, calcitonin, and estrogen are commonly used to inhibit resorption and are believed to act by inhibiting the formation and activity of osteoclasts and promoting osteoclast apoptosis.[57,108,144]

1.2.7.2 The Osteoblasts[1–8,12,29,35,37–39]

1.2.7.2.1 The Phenotype

Osteoblasts are bone-forming cells that synthesize and secrete unmineralized bone matrix (the osteoid), participate in the calcification and resorption of bone, and regulate the flux of calcium and phosphate in and out of bone. Osteoblasts occur as a layer of contiguous cells which in their active state are cuboidal (15 to 30 μm thick).[1–8,12,29,37]

The following properties belong to the active osteoblast phenotype: morphologically, active osteoblasts are cuboidal cells (that rarely undergo mitosis) with a large nucleus, cellular processes, gap junctions, abundant endoplasmic reticulum, enlarged Golgi, and collagen-containing secretory vesicles. Except for their location, polarization, and organization in layers, the osteoblasts resemble fibroblasts, but can be distinguished by their products (Figs. 1.14 through 1.16, 1.23B, and 1.26). (Table 1.7 lists known osteoblast markers of immature and mature osteoblasts.)[38] Osteoblasts produce all the constituents of the bone matrix. The only bone-specific proteins identified thus far are osteoclacin and bone sialoprotein; however, the combination of high alkaline phosphatase abundance, the secretion of type I collagen, and the synthesis of noncollagenous protein in addition to specific mechanical and nonmechanical responses are characteristic of the osteoblastic phenotype.

The active osteoblasts possess receptors to many bone agents, such as PTH, parathyroid hormone–related protein (PTHrP), prostaglandins, vitamin D metabolites, gonadal and adrenal steroids, and certain cytokines, lymphokines, etc. Major growth factors influencing bone formation and fracture repair are listed in Table 1.8.[39] Some responses by their receptors may allow the osteoblast to initiate osteoclastic bone resorption by secreting collagenase and other metalloproteinases and plasminogen activator to promote matrix access to the osteoclast.

The active osteoblasts are supplied with abundant alkaline phosphatase and secrete mainly type I collagen and bone matrix osteoid toward the mineralization front of the bone tissue. The osteoid width is approximately 10 μm and the adult mineral apposition rate is about 0.55 μm/day. The collagen fibers support mineralization. The cell–matrix and cell–cell interactions from signaling pathways assisted by integrin and cadherins play roles in osteoblast differentiation and mineralization of the osteoid matrix.

1.2.7.2.2 Origin and Fate

The osteoblasts are derived from mesenchymal progenitors. Osteoblast precursors are located near bone surfaces: the periosteum, the endosteum, and the adjacent marrow stroma (perivascular parenchymal cells). They arise from local, undifferentiated intraskeletal mesenchymal cells that are capable of mitosis. The identity of cell types that may transform into an osteoblast progenitor is not known. There is overwhelming evidence that postnatal marrow stroma, but not functioning hematopoietic tissue, can differentiate into osteoblasts. Also, there is a good possibility that precursors of osteoblasts are undifferentiated mesenchymal cells with a potential similar to that found in the early stages in the embryo. There is strong evidence, although inconclusive, that pericytes and endothelial cells are osteoblast precursors.[258] Gimble et al.[259] cited *in vivo* data suggesting that fully mature adipocytes retain function associated with the osteoblast phenotype and recently Maurin et al.[260] showed matured adipocytes inhibited ostoblast production *in vitro*. It is believed the active osteoblast becomes a flat bone lining cell (resting osteoblast), or an osteocyte, or

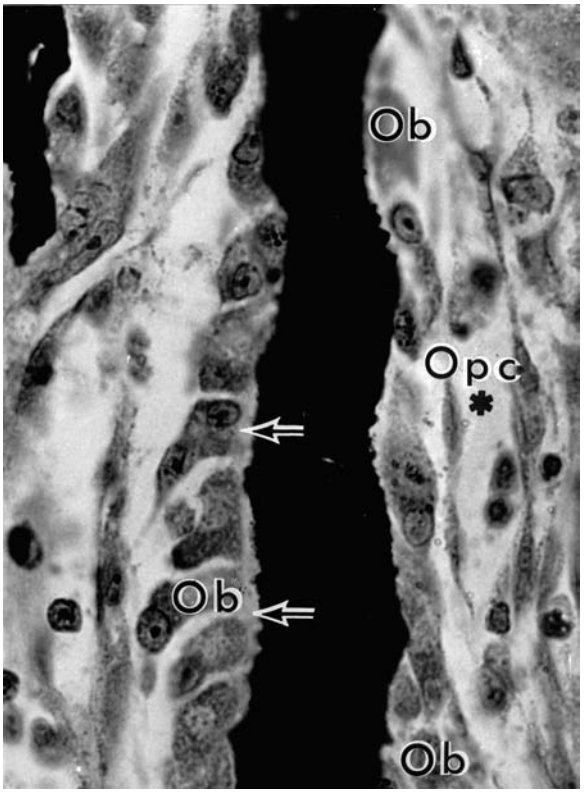

FIGURE 1.14 Light micrograph of osteoblasts. Spicule of calcified core lined with osteoblasts (Ob) and thin osteoid (arrows). Osteoprogenitor cells (Opc) are located between osteoblasts and blood vessel (*). Original magnification × 600, Von Kossa/methyl green-pyronine stain. (From Weiss, L., Ed., *Cell and Tissue Biology, A Textbook of Histology,* Urban and Schwarzenberg, Baltimore, 1988. With permission.)

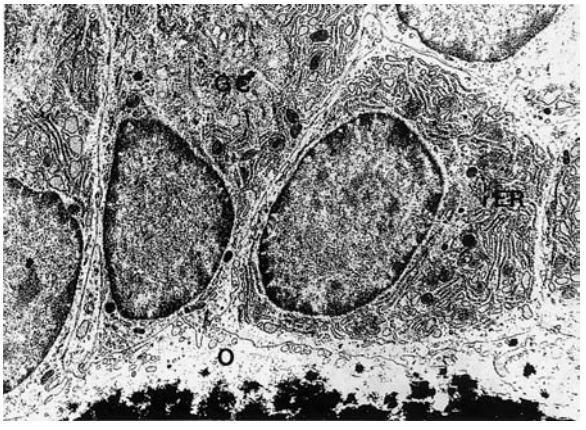

FIGURE 1.15 Electron micrograph of osteoblasts. Notice the prominent Golgi complex (GC) and extensive rough endoplasmic reticulum (rER). Adjacent to the osteoblasts are the unmineralized matrix or osteoid seam (O) and the mineralized matrix. The mineralized matrix is black because of the electron scattering of the hydroxyapatite crystals. Original magnification × 5500 (preparation by S. C. Miller). (From Weiss, L., Ed., *Cell and Tissue Biology, A Textbook of Histology,* Urban and Schwarzenberg, Baltimore, 1988. With permission.)

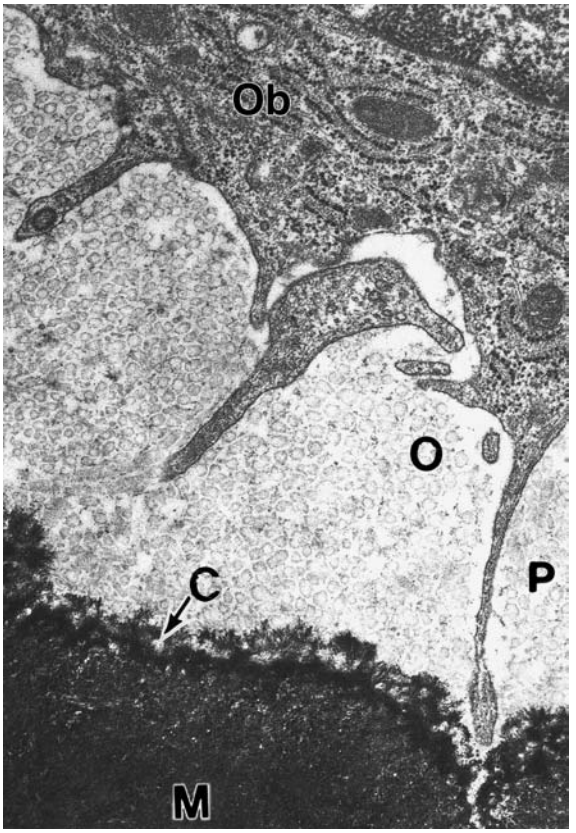

FIGURE 1.16 Electron micrograph of an osteoid seam. A region of osteoid (O) between edge of an osteoblast (Ob) and mineralized matrix (M). The osteoblast contains mitochondria and rough endoplasmic reticulum with three cytoplasmic processes (P) extending into the osteoid. Note cement line (C) separating old bone from new bone. Original magnification × 3000. (Courtesy of R. Baron and A. Vignery.) (From Weiss, L., Ed., *Cell and Tissue Biology, A Textbook of Histology,* Urban and Schwarzenberg, Baltimore, 1988. With permission.)

undergoes apoptosis.[56,57,155] Recently, it has been shown PTH and PGE_2 have antiapoptotic effect on mature osteoblasts.[261,262]

1.2.7.2.3 Regulation

The sequence of events characterizing the differentiation process leading the stem cell to differentiate in osteoblasts is not well understood. Osteoblast differentiation is believed to be under the control of the transcription factor, core-binding factor-α1 (Cbfa1). It performs a dominant and nonredundant role in osteoblast differentiation and controls bone formation after osteoblast differentiation is achieved.[166] Osteoblasts are derived from mesenchymal stem cells in the mesenchyme or in the marrow stroma. Once committed to the osteoblast lineage, osteoblast precursor cells proliferate and then differentiate into preosteoblasts and then into mature osteoblasts.[38,39] The cessation of cell growth leads to the matrix maturation stage, which induces expression of alkaline phosphatase and specialized bone proteins that render the osteoid competent for mineral deposition. The expression of osteocalcin and bone sialoprotien may function in regulating the ordered deposition of mineral (Table 1.7).[38] The bone alkaline phosphatase, osteocalcin markers along with bone collagen degradation (C-terminal propeptides of type I collagen, PICP, and N-terminal propeptides of type I collagen, PINP) can be monitored in serum as useful biochemical markers of bone formation.[14]

TABLE 1.7 Phenotypic Osteoblast Markers in Human Osteoblastic Cells

Markers	Immature Cell	Mature Osteoblast
	General	
ALP	±	±
Stro-1	+	−
	Matrix Proteins	
Col-III	−	−
Col-1	+	++
OP	++	+
ON	+	+
OC	−	+
BSP	−	+
Thrombospondin	nd	+
Biglycan	nd	±
Decorin	nd	±
	Local Factors/Receptors	
PTHrP	++	+
PTH/PTHrP-R	+	++
FGF-2	+	nd
FGFR-1	+	nd
FGFR-2	+	nd
LIF	nd	±
TNFα	nd	±
IL-6	nd	++
GM-CSF	nd	+

ALP, alkaline phosphatase; Stro-1, an antibody that recognizes osteoprogenitor stem cells of the colony-forming-unit-fibroblastic; Col, collagen; OP osteopontin; ON, osteonectin; OC osteocalcin; BSP, bone sialoprotein; PTHrP, parathroid hormone receptor protein; R, receptor; FGF, fibroblast growth factor; LIF, leukemia inhibitory factor; TNFα, tumor necrosis factor-α; IL-6, interleukin-6; GM-CSF, granulocyte/macrophage colony-stimulating factor. ±, +, ++: weak, clear, marked expression, respectively; nd: not determined.

Source: Marie, P. J., *Histol. Histopathol.,* 14, 528, 1999. With permission.

1.2.7.2.4 Function

The osteoblasts synthesize and secrete the unmineralized bone matrix or ground substance of bone. The bone matrix consists of 90% collagen and about 10% noncollagenous protein.

Bone formation occurs in two stages: matrix formation and mineralization. Matrix formation, which precedes mineralization by about 15 days, occurs at the interface between osteoblasts and osteoid. Preosteoblasts have been present for 9 days before matrix synthesis occurs. During the period of bone formation, the height of an average osteoblast nucleus declines from about 7 to 1 μm at the end of bone formation. Extracellular mineralization occurs at the junction of osteoid and newly formed bone; this region is known as the mineralization front. Because mineralization occurs some time after matrix production, a layer of unmineralized matrix called the osteoid seam remains (Fig. 1.16). The mineralization lag time is normally 10 days in the adult, resulting in an osteoid seam of 8 to 10 μm. In contrast to adult bone, embryonic or woven bone formation has a very short mineralization lag time; as a result, the osteoid seam is either absent or very thin.

The rate of bone formation can be readily determined in humans and animals by administering tetracycline or other types of fluorescent bone markers. Tetracycline is an antibiotic that localizes at the mineralization front, thereby causing the newly deposited bone to appear as a tetracycline-labeled band. A labeled bone fluoresces under ultraviolet light and thus marks the location of bone formation at the time of tetracycline administration (Figs. 1.9 and 1.17).[1,2,5–7,40–43,145]

TABLE 1.8 Major Growth Factors in Bone Formation and Fracture Repair

Source of Factor	Cellular Response
Bone Morphogenetic Protein (BMP-2, -3, -4, and -7)	
Bone extracellular matrix	Activation of cortical osteoblast
Osteoblasts and osteoprogenitors	Initiates differentiation of osteoprogenitor cells into osteoblasts
Fibroblast Growth Factor (FGF-1 and -2)	
Inflammatory cells (macrophages)	Mitogenic effects on mesenchymal cells and osteoblasts
Mesenchymal cells	Angiogenic actions
Chondrocytes	Mesoderm induction
Osteoblasts	TGF-β production
Bone extracellular matrix	
Insulin Growth Factors (IGF-1 and -2, GFBP 3/5)	
Liver	Stimulating stem cell differentiation
Osteoblasts	Increase bone turnover
Bone extracellular matrix	Mitogenic to osteoblast stimulates type I collagen production
Platelet-Derived Growth Factor (PDGF-AA, -AB, -BB)	
Degranulating platelets	Macrophage chemotaxis
Monocytes and macrophages	Mesenchymal cell chemotaxis
Hypertrophic chondrocytes (PDGF-α)	Mesenchymal cell proliferation
Osteoblasts (PDGF-β)	Angiogenic action
Bone extracellular matrix	Stimulates osteoblast proliferation
Transforming Growth Factor-β (TGF-β-1 and -2)	
Degranulating platelets	Pleiotropic factor
Bone extracellular matrix	Osteoprogenitor cell proliferation
Inflammatory cells	Stimulates undifferentiated mesenchymal cell proliferation
Chondrocytes	Stimulates extracellular matrix production
Osteoblasts	Mitogenic effects on osteoblast stimulates alkaline phosphatase production stimulates collagen synthesis

Note: Several other growth factors that stimulate osteoblasts *in vitro*: Epidermal growth factor (EGF) and vascular endothelial growth factor (VEGF) that could play a role in bone formation.

Source: Modified from Barnes, G. L., Kostenuik, P. J., Gerstenfeld, L. C., and Einhorn, T. A., *J. Bone Miner. Res.,* 14, 1807, 1999. With permission.

Bone consists predominately of type I collagen with traces of type III, V, and X collagen. These trace amounts may be present during certain stages of bone formation and may regulate collagen fibril diameter (Table 1.9).[12] Collagen fibers constitute the shape-forming structural framework of bone in which the hydroxyapatite is inserted. The collagen molecules making up the fiber are aligned in a quarter-staggered, end-overlap fashion and calcification is initiated by the formation of hydroxyapatite plates within the gap regions (hole) of the fiber. The hydroxyapatite confers rigidity on the collagen framework. Bone collagen is stabilized by trivalent pyrodinoline and pyrroles cross-links linking the molecules end to end. The pyrroles and pyridinolones may form interfibrillar cross-links and have been shown to correlate with the mechanical properties of bone. [12,37]

The noncollagenous proteins include glycoaminoglycan-containing proteins, glycoproteins, gamma carboxyglutamic acid (GLA)–containing proteins and other proteins. The role of the noncollagenous proteins is not yet well understood. A detailed listing of the numerous bone proteins and their probable functions is presented in Table 1.10.[12] These NCPs are thought to play an important role in the calcification

TABLE 1.9 Collagen-Related Proteins and Their Functions

Protein	Abundance	Function
Type I	90%	Serves as scaffolding; may be nucleator of mineral deposition
Type X	Trace	Matrix organization and template for type I collagen
Type III	Trace	May regulate collagen fibril diameter
Type V	Trace	Their paucity in bone may explain the large diameter size of bone collagen fibrils

Source: Modified from Favus, M. J., *Primer of Metabolic Bone Diseases and Disorders of Mineral Metabolism,* 4th ed., Lippincott/Williams & Wilkins, Philadelphia, 1999, chap. 3. With permission.

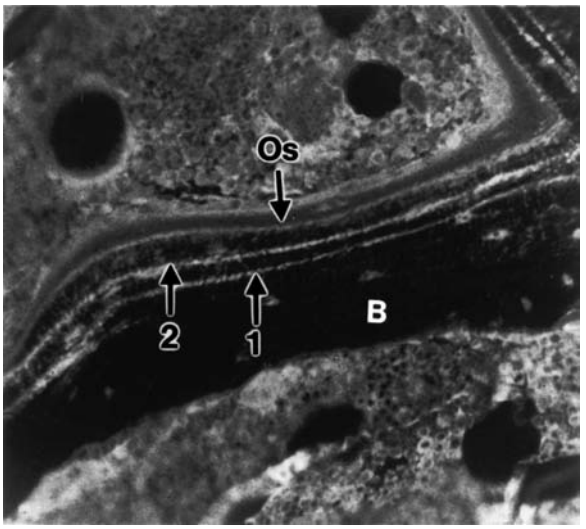

FIGURE 1.17 Double tetracycline labeling of part of a trabecula. The first label was given 10 days before the second and the dog was killed 72 h later. B = trabecular bone; Os = osteoid. Ground section Villanueva stain. Original magnification × 200. (From Weiss, L., Ed., *Cell and Tissue Biology, A Textbook of Histology,* Urban and Schwarzenberg, Baltimore, 1988. With permission.)

process and the fixation of the hydroxyapatite crystals to the collagen. The most abundant ones are osteonectin, osteocalcin, and bone sialoprotein.[11–13,37]

Several cytokines (IL-1, IL-6, and CSFs) and growth factors (TGF-Mβ family of polypeptides), platelet-derived growth factors (PDGFs), fibroblast growth factors (FGFs), insulin-like growth factors (IGFs), and insulin-like growth factor binding proteins (IGFBPs) are present in bone matrix and can be released to exert their biological effects. The status of the organic matrix of bone can be assessed in blood and urine by measuring its breakdown products, which include hydroxyproline and collagen cross-links.[14]

Control of bone mineral crystal growth and proliferation is governed by the spatial limitation of the collagen fibrils, as well as by the absorption of matrix proteins. Such matrix proteins often are also apatite nucleators, but, because of their affinity for specific crystal faces, can retard or block apatite growth. Mineral formation and growth are regulated by ionic concentrations, the removal of inhibitors, and the exposure of nucleation (See Chapter 5 by Boskey on factors controlling bone mineralization).

The growth of bone mineral crystals is governed in part by the constraints of the collagen matrix on which the mineral is deposited and species introduced through the diet, given therapeutically. Many impurities thus introduced tend to make crystals smaller, more imperfect, and more soluble. Bisphosphonate, a type of antiremodeling agent used in the treatment of osteoporosis, binds to the surface of apatite crystals and thereby

TABLE 1.10 Noncollagenous Proteins and Their Functions

	Function
	Glycoprotein
Alkaline phosphatase	A phosphotransferase; potential Ca^{2+} carrier; hydrolyzes inhibitors of mineral deposition such as pyrophosphates
Osteonectin	May mediate deposition of hydroxyapatite; binds to growth factors; may influence cell-cycle antiadhesive protein
Tetranectin	Binds to plasminogen; may regulate matrix mineralization
Tenascin-C	Unknown
	Glycoaminoglycan
Versican	May capture space destined to be bone
Decorin	Binds to collagen and may regulate fibril diameter Binds to TGF-β, may inhibit cell attachment to fibronectin
Biglycan	May bind to collagen and TGF-β
Fibromodulin	Binds to collagen and TGF-β, may regulate fibril diameter
Osteoadherin	May mediate cell attachment
Hyaluronan	May capture spaces destined to be bone
	Gamma-Carboxyl Glutamic Acid
Matrix gla protein	May function in cartilage metabolism, may inhibit mineralization
Osteocalcin (bone gla protein, BGP)	May regulate activity of osteoclasts and their precursors; may mark turning point between bone resorption and formation; regulate mineral maturation
Protein S	Protein S deficiency may result in osteopenia
	RGD-Containing Glycoprotein
Thrombospondin	Cell attachment, binds to heparin, platelets, type I and C collagen, thrombin, fibrogen, laminin, plasminogen, and plasminogen activator inhibitor
Fibronectin	Binds to cells, fibrin, heparin, gelatin, collagen
Vitronectin	Cell attachment protein, binds to collagen, plasminogin and plasminogen activator inhibitor, and to heparin
Osteopontin	Binds to cell, inhibits mineralization and nitric oxide synthase; may regulate proliferation, tissue repair, and initiate mineralization
Bone sialoprotein	Binds to cell, binds Ca^{2+}; may initiate mineralization
	Serum Protein
Albumin	Transports proteins; inhibits hydroxyapatite crystal growth
α_{-2} HS glycoprotein	Mineralization inhibitor

Source: Modified from Favus, M. J., *Primer of Metabolic Bone Diseases and Disorders of Mineral Metabolism,* 4th ed., Lippincott/Williams & Wilkins, Philadelphia, 1999, chap. 3. With permission.

is believed to be one of its mechanisms of action in blocking dissolution.[146–148] Although bisphosphonate-treated crystals are not altered in size, they tend to increase the bone mineral content (BMC).[29]

Cellular activity can influence mineral properties such as in hypophosphatemic rickets (retarded deposition), osteopetrosis (small crystal persists), osteoporosis (larger crystal persists), and fluorosis (larger crystals formed). The size and distribution of mineral crystals may influence bone mechanical properties. Although the bone strength has been correlated with bone mineral density, a technique like quantitative computed tomography, which describes the amount of bone in a given volume instead of area and gives information on architecture that allows one to derive a bone strength index that is more useful. Meaningful studies relating bone strength to mineral characteristics are lacking.

1.2.7.2.5 Linkage of Osteoblast and Osteoclast Development

The development of osteoblast and osteoclast are inseparably linked because both are derived from precursors originating in bone marrow (osteoblasts from multipotent mesenchymal stem cells and osteoclasts from hematopoietic cells of the monocyte/macrophage lineage) and osteoblast differentiation is a prequisite

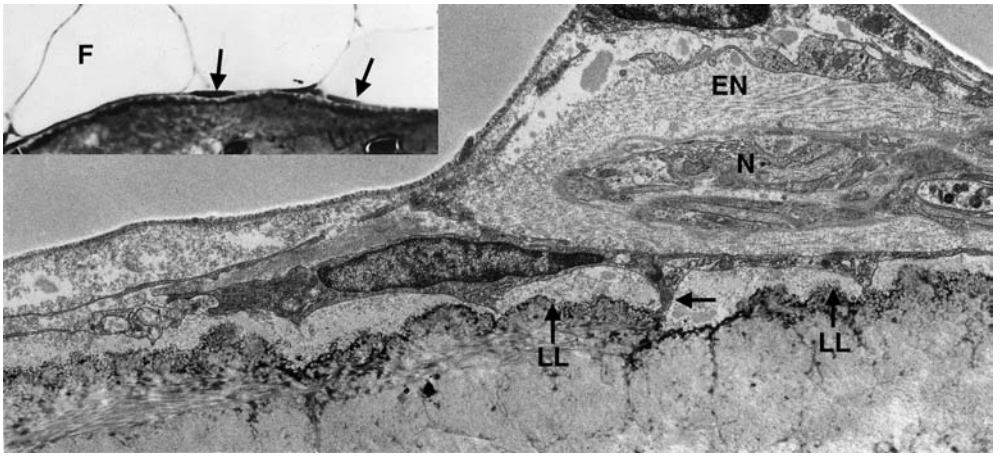

FIGURE 1.18 Electron micrograph of a bone-lining cell with several cell processes extending into the canalicular channels in the bone matrix (arrows) and a gap junction between bone-lining cell processes and an adjacent nerve (N) with surrounding endoneurim (EN). Lamina limitans (LL), original magnification × 8900. The insert is a light micrograph of bone-lining cells (arrows) in region of fatty marrow (F). Undecalcified, toluidine blue O stained; original magnification × 600. (From Miller, S. C. and Jee, W. S. S., *Anat. Rec.*, 198, 163, 1980. By permission of authors and Wiley-Liss, New York.)

for osteoclast development. Mesenchymal cell differentiation toward the osteoblast phenotype is initiated by bone morphogenetic proteins (BMPs) and TGF-β.[12,38,165] BMPs stimulate expression of osteoblast transcription regulator Cbfa1/Osf2[166] in stromal/osteoblast progenitor cells, which activate osteoblast-specific genes and osteoclast function factors. The latter are osteoclast differentiation factor (ODF/OPG-L) and osteoclast inhibitory factor (OCIF/OPG), and the binding of these factors to hematopoietic osteoclast progenitors controls osteoclastic differentiation, fusion, activation, and apoptosis. Thus, the BMP → Cbfa1 → ODF/OPG-L and OCIF/OP6 gene expression casade consitutes the molecular basis of osteoblast and osteoclast linkage.[164]

1.2.7.3 The Bone-Lining Cells[1–6,8–10,29,44–52,148]

1.2.7.3.1 The Phenotype

When the osteoblasts are not in the process of forming bone, they are flattened, elongated cells covering quiescent bone surfaces and are called resting osteoblasts or bone-lining cells. The bone-lining cell has a distinct morphological phenotype: direct apposition to the bone surface, a thin, flat nuclear profile with attenuated (1 μm thick and up to 12 μm long) cytoplasm extending along the bone surface. Gap junctions are seen between adjacent bone-lining cells and between bone-lining cells and osteocytes (Figs. 1.7 and 1.18). The surface density of bone-lining cells is about 19 cells/mm bone surface perimeter in fatty marrow sites of young adult dogs, and decreases somewhat with age. Their density seems greater in hemopoietic marrow.[44,48]

1.2.7.3.2 Origin and Fate

Bone-lining cells are believed to be derived from osteoblasts that have become inactive or osteoblast precursors that have ceased activity or differentiated and flattened out on bone surfaces. They occupy the majority of the adult bone surface. Little is known of their history. They do become active osteoblasts but their fate is not known. They may return to the stem cell or preosteoblast pool and/or apoptose. Both the prolific capacity and differentiation potential of bone-lining cells under normal physiological condition is poorly understood.

1.2.7.3.3 Function

The bone-lining cells are capable of forming bone,[44] without prior bone resorption (formation drift) in response to bone anabolic agents[46,47] and may regulate mineral homeostasis with the complex of osteoblasts and osteocytes.[44,48–50,150] Bone-lining cells, like osteocytes, may be influenced by functional strain within bone tissue that influences adaptive changes.[51,52] Thus, bone-lining cells may be involved in homeostatic, morphogenetic, and restructuring processes that constitute regulation of bone mineral, mass, and architecture as well as the hematopoietic process.

Bone-lining cells serve as an ion barrier separating fluids percolating through the osteocyte and lacunar canalicular system from the interstitial fluids. This membrane barrier around bone may have a role in mineral homeostasis by regulating the fluxes of calcium and phosphate in and out of bone fluids (Fig. 1.7) as well as in controlling the growth of bone crystals by maintaining a suitable microenvironment.[44,48–50] In addition, bone-lining cells are involved in osteoclastic bone resorption. They digest the surface osteoid by neutral proteases and contract themselves to allow osteoclast access to mineralized tissue.[29,34,35,159] Furthermore, the three-dimensional networks of bone-lining cells and osteocytes making junctional communication with each other have been postulated to sense the shape of bone and its reaction to stress and strain and to transmit these sensations as signals to the bone surface, where new bone formation/resorption is possible.[4,5,32,128]

1.2.7.4 The Osteocytes[1–6,8–10,12,51–57]

1.2.7.4.1 The Phenotype

Osteocytes are the most abundant cell type in mature bone with about ten times more osteocytes than osteoblasts in normal human bone. During bone formation some osteoblasts are left behind in the newly formed osteoid as osteocytes when the bone formation moves on. The embedded osteoblasts in lacunae differentiate into osteocytes by losing much of their organelles but acquiring long, slender processes encased in the lacunar–canulicular network that allow contact with earlier incorporated osteocytes and with osteoblasts and bone lining and periosteal cells lining the bone surface and the vasculature (Figs. 1.7, 1.10, and 1.19). The osteocytes are the cells best placed to sense the magnitude and distribution of strains. They are strategically placed both to respond to changes in mechanical

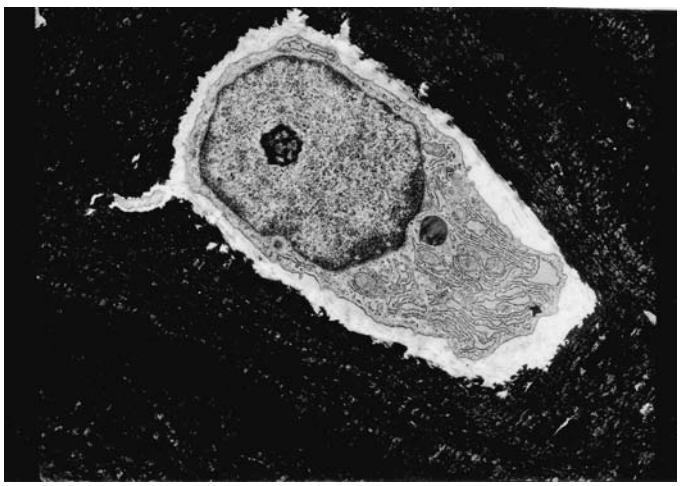

FIGURE 1.19 Electron micrograph of a young osteocyte. The cell still has some Golgi membrane and numerous rough endoplasmic reticulum. Notice that it does not completely fill its lacuna. The clear space around the cell is occupied by an unmineralized matrix in which collagen fibers are partially visible. At the left, a cell process is seen entering into a canaliculus. Original magnification × 4000. (Courtesy of S. C. Miller.) (From Weiss, L., Ed., *Cell and Tissue Biology, A Textbook of Histology,* Urban and Schwarzenberg, Baltimore, 1988. With permission.)

strain and to disseminate fluid flow to transduce information to surface cells of the osteoblastic lineage via their network of canalicular processes and communicating gap junctions.[255–257] Gap junctions are transmembrane channels, which connect the cytoplasm of two adjacent cells that permits molecules with molecular weights of less than [1 kDa] such as small ions and intracellular signaling molecules (i.e., calcium, cAMP, inosital triphosphate) to pass through. Gap junction channels are formed by a family of proteins known as connexins (Cx). Connexin 43 is the major connexin identified in bone.[53] The gap junction channels in osteoblasts are regulated by such factors such as ions, hormones, and mechanical loading.

1.2.7.4.2 Origin and Fate

It is well established that the origin of osteocytes is osteoblasts embedded in its own matrix and some that eventually will have died (apoptosis).[152] Aging, loss of estrogen, loading, and chronic glucocorticoid administration is known to increase osteocyte apoptosis,[56,57,152,155–157] while estrogen saves osteocytes in the rat ovariectomy model[156] and loading decreases the proportion of apoptotic osteocytes in cortical bone in rats.[157] Empty and hypermineralization lacunae of cortical bone have been consistently observed in aged individuals and old dogs.[152] The loss of osteocytes has been postulated to be the result of increased mean age of cortical bone and vascular degeneration or vascular disease leading to osteonecrosis. Also, it has been proposed that the death of an osteocyte by apoptosis provides the bone removal cue under a number of conditions including matrix microdamage.[54,55,161] Prevention of osteocyte apoptosis has been reported with PTH treatment.[261]

1.2.7.4.3 Function

The osteocytes may (1) stabilize bone mineral by maintaining an appropriate local ionic milieu, in collaboration with the bone-lining cells (the bone-lining–osteocyte complex or gap junction intercellular communication) that controls the efflux of calcium ions[44,48–50]; (2) detect microdamage[51,52,54,55]; and (3) respond to the amount and distribution of strain within bone tissue that influence adaptive modeling and remodeling behavior through cell–cell interaction.[51,52] Thus, osteocytes play a key role in homeostatic, morphogenetic, and restructuring processes of bone mass that constitute regulation of mineral and architecture.

1.3 Skeletal Development[1,2]

Skeletal development begins as mesenchymal condensations that appear early in the fetal period. These condensations ossify to form membrane (dermal) bones through intramembranous ossification and cartilage bones through endochondral ossification. The latter become chondrified and form hyaline cartilage in the shape of future bones. However, in both types of ossification, bone formation is similar, beginning with an increase in the number of cells and fibers. The cells differentiate into osteoblasts, which lay down an unmineralized matrix, the osteoid that mineralizes almost immediately. Some osteoblasts are trapped in the matrix around them and become osteocytes. The shape and manner of growth of this new bony tissue depend on the individual bone and are genetically determined. Embryonic bone formation involves woven bone formation and fine-bundled lamellar bone that replaces woven bone through bone remodeling is not formed until after birth.

1.3.1 Intramembranous Ossification[1–4]

Intramembranous ossification or membrane bone formation forms the bulk of the future cortical bone shell. This forms most of the bones of the vault of the skull, many of the bones of the sense organs and of the facial skeleton, and parts of the clavicle and mandible. Fibrocellular condensations during the embryonic period constitute the first indication of membrane bones. Then the primary center of ossification of each bone appears as an increase in cells and fibers, and then bone is apposed. Loose spicules or trabeculae are formed by osteoblasts and interconnect to form the primary cancellous bone (spongiosa). Trabeculae continue to increase in thickness and enlarge by addition to their free ends. Compact bone is formed when the spaces between the primary spongiosa are filled in by the primary osteons or Haversian systems (compaction). This bone is then gradually replaced by secondary Haversian systems or osteons.

TABLE 1.11 Comparison of Modeling and Remodeling

	Remodeling	Modeling
Location	Spatially related	Different surfaces
Coupling	A → R → F	A → F; A → R
Timing	Cyclical	Continuous
Extent	Small (<20%)[a]	Large (>90%)
Apposition rate	Slow (0.3–1.0 μm/day)	Fast (2–10 μm/day)
Cement line	Scalloped	Smooth
Balance	No change or net loss	Net gain
Occurrence	Throughout life span	Prominent during growth; ineffective in adults
MES threshold[b]	<200 microstrain	>1500 microstrain

[a] Of available surface.

[b] MES = minimum effective strain; A = activation; R = resorption; F = formation.

Modified from Parfitt, A. M., in *Bone Histomorphometry: Techniques and Interpretation,* R. R. Recker, Ed., CRC Press, Boca Raton, FL, 1982. With permission.

1.3.2 Endochondral Ossification[1–4]

Endochondral ossification or cartilage bone formation forms the bulk of the future cancellous bone. It forms most of the bones at the base of the skull, the vertebral column, the pelvis, and the extremities. A cartilage bone begins as a mesenchymal condensation or blastema, which usually appears during the embryonic period. Cartilage cells (chondrocytes) proliferate and deposit matrix until a cartilage model of the future bone is formed. The cartilage cells mature, grow, and its matrix subsequently calcifies. Unresorbed calcified cartilage cores form the substrate in which osteoblasts appose woven bone to form the primary spongiosa. The spicules in the primary spongiosa are composed of mosaic pieces of calcified cores surrounded by woven bone tissue. This is later lost to be either replaced by bone marrow or replaced with a lamellar trabecular packet or hemiosteon as the secondary spongiosa, i.e., the future adult spongiosa.

1.3.3 Growth[1–4,7]

It is the combination of genetic and circulating systemic factors that controls general growth, while systemic and regional factors, especially mechanical usage, can modulate it locally. Longitudinal bone growth adds new spongiosa to preexisting spongiosa and new length of cortical bone to preexisting cortex, whereas radial or periosteal bone growth adds new width by apposing subperiosteal bone to the cortex.

Animal and human studies show that the skeleton is most receptive to mechanical stimulation during growth (see Table 1.17).[139]

1.3.4 Modeling[1–5,7,8,58–67]

Growth and modeling go hand in hand.[1–4,60] Local influences modulate growth to produce functionally and mechanically purposeful architecture. Modeling involves resorption drifts and formation drifts that remove or add bone over wide regions of bone surfaces. (See Table 1.11 for the attributes of modeling.) During growth, formation drifts add periosteal bone faster than resorption drifts remove endosteal bone. Modeling controls the growth, shape, size, strength, and anatomy of bones and joints. Collectively, modeling leads to increasing the outside cortex and marrow cavity diameters, shaping the ends of long bones (Figs. 1.20 and 1.21), drifting of trabeculae and cortices, enlarging the cranial vault and changing the cranial vault curvature.

Modeling allows not only the development of normal architecture during growth, but also the modulation of this architecture and mass when the mechanical condition changes. When bone strains exceed a "modeling threshold," window, or range, the minimum effective strain (MES_m) centered near 1000 microstrain in young adults, modeling in the formation mode (formation drift) is turned on to

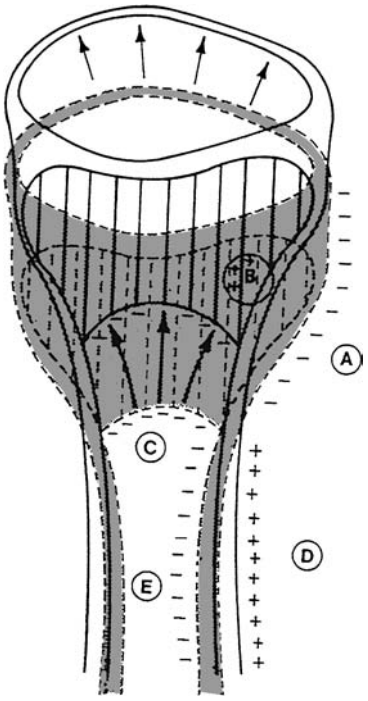

FIGURE 1.20 Diagram of the modeling occurring during growth of proximal end of the tibia. Frontal section of original proximal tibia is indicated as stippled area. The situation after a growth period of 21 days is superimposed. (A) Reduction of metaphyseal funnel into a narrower shaft by osteoclastic bone resorption (resorption drift) along periosteal surface of metaphysis (−). (B) Thickening of cortex by osteoblastic bone formation (formation drift) along cortical endosteal surface of metaphysis (+). (C) Enlargement of marrow cavity by osteoclastic resorption of metaphyseal trabecular and subendocortical bone (−). (D) Increase of the diameter of the shaft by periosteal bone formation drift (+). (E) Enlargement of the marrow cavity by cortical endosteal bone resorption (−). (From Weiss, L., Ed., *Cell and Tissue Biology, A Textbook of Histology,* Urban and Schwarzenberg, Baltimore, 1988. With permission.)

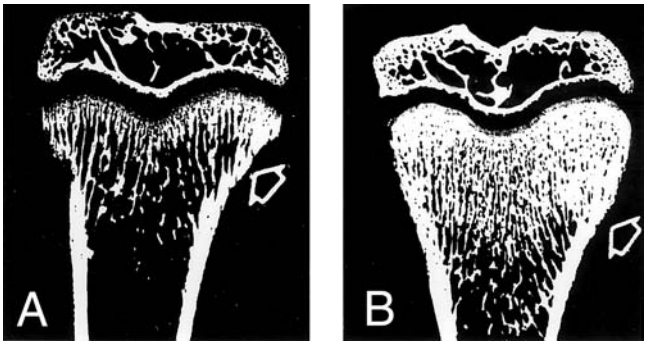

FIGURE 1.21 Microradiograph of proximal tibia from control and bisphosphonate (a bone resorption depressor or antimodeling or antiremodeling agent) treated growing rats. (A) Control rat with concave-shaped periosteal metaphysis (arrow). (B) Treated rat with convex-shaped periosteal metaphysis (arrow) and increased metaphyseal and epiphyseal bone mass due to inhibition of resorption drift. Original magnification × 4. (From Miller, S. C. and Jee, W. S. S., *Anat. Rec.,* 193, 439, 1979. By permission of authors and Wiley-Liss, New York.)

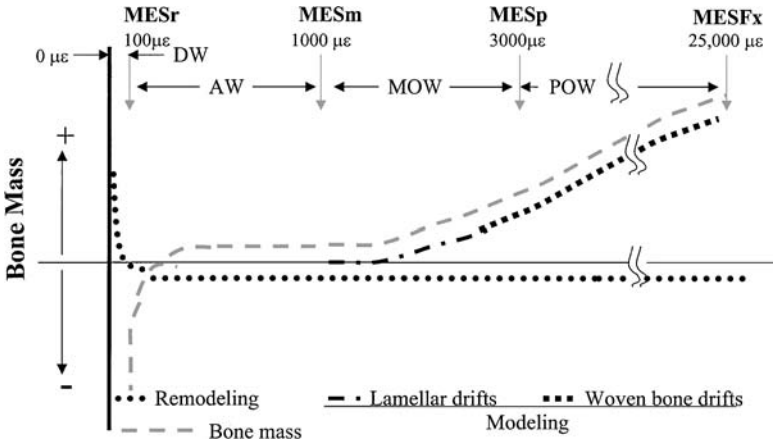

FIGURE 1.22 Mechanical usage window, thresholds, or set points according to the mechanostat. MES = minimum effective strain, r = remodeling, m = modeling, p = pathologic, Fx = fracture, $\mu\varepsilon$ = microstrain. (Adapted from Frost, H. M., *J. Bone Miner. Res.,* 12, 1539, 1997.)

increase bone mass and strength and lower its strains toward the bottom of the window. When strains remain below the modeling threshold, mechanically controlled formation drifts stay inactive. As the forces on bones increases 20 times in size between birth and maturity, modeling in the formation mode keeps making bones strong enough to keep their strains from exceeding the modeling threshold and therefore from reaching the microdamage threshold (MES_{FX}) (Fig. 1.22).[8,59–67]

Anabolic agents like PTH, PGEs, and NaF and rigorous activity can stimulate early bone gain by activating formation drifts. The mechanism is postulated to be by lowering the modeling set point of the mechanostat.[47,66,89–92,185]

1.3.5 Remodeling[1–8,34,40,68,69]

Bone remodeling produces and maintains bone that is biomechanically and metabolically competent. Immature (woven) bone formed at the metaphyses is structurally inferior to mature bone. Moreover, the quality of adult bone deteriorates with time. Therefore, bone must replace or renew itself. The replacement of immature (primary) and old bone occurs by resorption, followed by formation of new lamellar bone, a process called remodeling (see Table 1.11 for the comparison of modeling and remodeling characteristics). The products of bone remodeling are reversal (scalloped) cement lines, secondary osteons or Haversian systems, trabecular packets or hemiosteons, and interstitial lamellae (surviving fragments of bone units that have been partially resorbed by continual bone remodeling).

In humans, after 2 to 3 years of age, the immature (primary) bone during infancy is resorbed and replaced by secondary bone. A drastic reduction in the amount of bone occurs during the conversion of primary to secondary spongiosa (remodeling-dependent bone loss). Changes in architecture of bone trabeculae during the conversion of primary to secondary spongiosa are dramatic. Remodeling does not end with the replacement of primary bone, but continues throughout life. The secondary bone is continuously destroyed and replaced by new generations of bone. Assuming normal rates of adult bone turnover, cortical bone has a mean age of 20 years and cancellous bone 1 to 4 years.[5] The periodic replacement of bone (bone turnover) helps to maintain load bearing and the capacity of the skeleton to regulate calcium homeostasis and hematopoiesis and to repair structural damage.

Remodeling has positive and negative effects on bone quality on the tissue level. It serves to remove microdamage, replace dead and hypermineralized bone, and adapt microarchitecture to local stresses. Remodeling of trabecular bone may perforate and remove trabeculae, and remodeling of cortical bone increases cortical porosity, decreases cortical width, and possibly reduces bone strength.

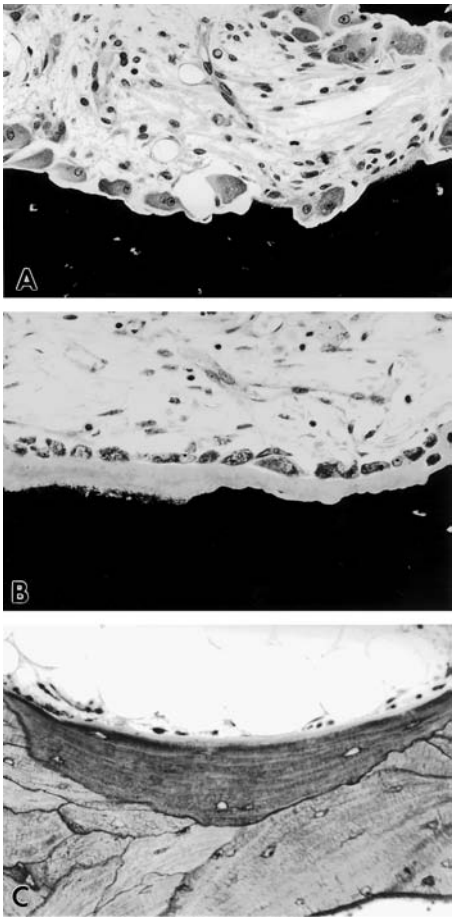

FIGURE 1.23 Cancellous bone remodeling to form a trabecular packet or hemiosteon. (A) The resorption phase—osteoclasts eroding a parcel of bone (black); (B) formation phase with osteoblasts and osteoid seam; and (C) completed trabecular packet or hemiosteon showing bone lining cells and scalloped cement line. (From Royce, P. M. and Steinmann, B., Eds., *Connective Tissue and Its Heritable Disorders, Molecular, Genetic and Mineral Aspects,* Wiley-Liss, New York, 1993. With permission.)

1.3.6 Basic Multicellular Unit or Bone Remodeling Unit[1–8,34,35,40,151]

The operational group of bone cells that accomplishes one quantum of bone turnover—removal and replacement of preexisting bone with a new structural unit (the osteon or hemiosteon)—is referred to as a bone remodeling unit (BRU) or basic multicellular unit (BMU) (Figs. 1.23 to 1.27). The life cycle of the unit includes six consecutive stages of resting, activation, resorption, reversal (coupling), formation, mineralization, and back to resting.

1.3.6.1 Resting

In large adult animals, including humans, about 80% of the cancellous and cortical bone surfaces (periosteal and endosteal) and about 95% of the intracortical surface are inactive with respect to bone remodeling at any given time (see Table 1.4). These inactive surfaces are in the resting stage. They are covered by bone-lining cells that may function as osteogenic precursor cells and an endosteal membrane, a thin 0.1 to 0.5 μm layer of unmineralized connective tissue with fewer collagen fibers and less amorphous ground substance than found in bone.[44]

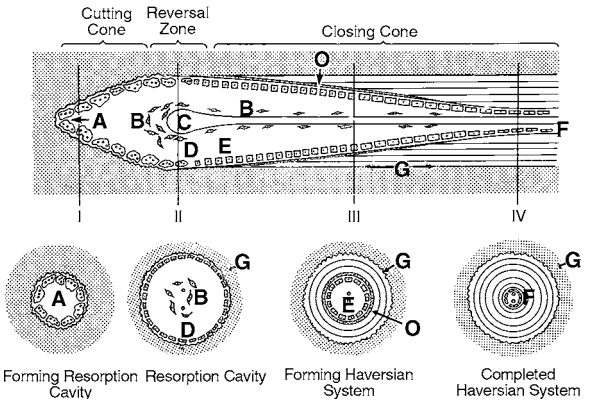

FIGURE 1.24 Diagram showing a longitudinal section through a cortical remodeling unit with corresponding transverse sections below. (A) Multinucleated osteoclasts in Howship's lacunae advancing longitudinally from right to left and radially to enlarge a resorption cavity. (B) Perivascular spindle-shaped precursor cells. (C) Capillary loop delivering osteoclast precursors and pericytes. (D) Mononuclear cells (osteoblast progenitors) lining reversal zone. (E) Osteoblasts apposing bone centripetally in radial closure and its perivascular precursor cells. (F) Flattened cells lining Haversian canal of completed Haversian system or osteon. Transverse sections at different stages of development: (I) resorption cavities lined with osteoclasts; (II) completed resorption cavities line by mononuclear cells, the reversal zone; (III) forming Haversian system or osteons lined with osteoblasts that had recently apposed three lamellae; and (IV) completed Haversian system or osteon with flattened bone cells lining canal. Cement line (G); osteoid (stippled) between osteoblast (O), and mineralized bone. (From Parfitt, A. M., *Metabolism,* 25, 909, 1976. With permission of author and Grune and Stratton, Inc., publisher.)

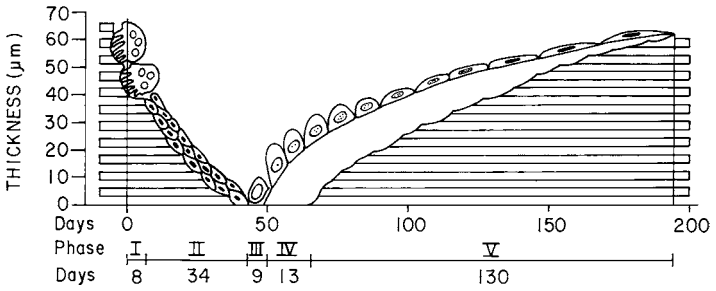

FIGURE 1.25 Cancellous bone remodeling. The total remodeling period in 20 normal individuals (19 to 60 years of age). The remodeling period is subdivided into osteoclastic resorption phase (I, 8 days), mononuclear cell resorption phase (II, 34 days), preosteoblastic or reversal phase (III, 9 days), initial mineralization lag time (IV, 13 days), and mineralization phase (V, 130 days). Total remodeling period of 196 days. Osteoclast depth, 19 $\pm$ 4.9 μm; mononuclear cells depth, 49.1 $\pm$ 10.2 μm; and preosteoblasts, 62.6 $\pm$ 12.5 μm. (Modified from Eriksen, E. F. et al., *Metab. Bone Dis. Relat. Res.,* 5, 243, 1984. With permission of authors, Pergamon Press, and Société Nouvelle de Publications Medicales et Dentaires.)

1.3.6.2 Activation

The conversion of the quiescent bone surface to resorption activity is referred to as activation. The factor that initiates this process is unknown, but activation is believed to occur partly in response to local structural or biomechanical requirements. The remodeling cycle requires the recruitment of osteoclasts and the means for them to gain access to the bone surface (neoangiogenesis, attraction, and attachment; Fig. 1.28).[1] Briefly, growth of capillary is required and bone-lining cells are believed to digest the endosteal membrane and to retract, thereby exposing the mineralized bone surface, which is chemotactic for

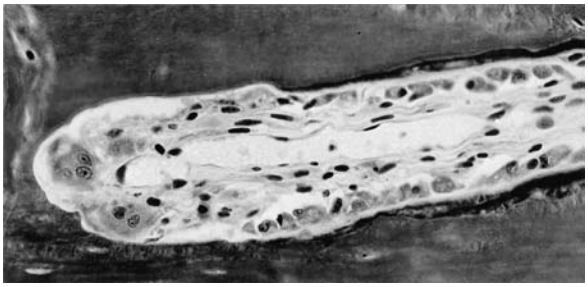

FIGURE 1.26 Cortical bone remodeling. Osteoclasts resorbing a tunnel and osteoblasts filling it. (From Royce, P. M. and Steinmann, B., Eds., *Connective Tissue and Its Heritable Disorders, Molecular, Genetic and Mineral Aspects,* Wiley-Liss, New York, 1993. With permission.)

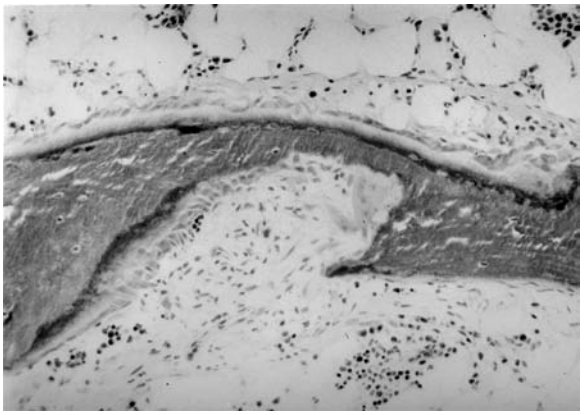

FIGURE 1.27 A cancellous bone remodeling or metabolic unit (BMU) in a renal osteodystrophy patient. The osteoclastic resorption is abnormally deep and may sever the trabecula. (From Weiss, L., Ed., *Cell and Tissue Biology, A Textbook of Histology,* Urban and Schwarzenberg, Baltimore, 1988. With permission.)

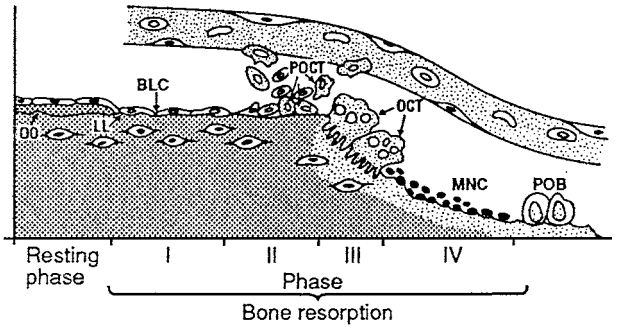

FIGURE 1.28 Diagrammatic representation of working hypothesis of bone resorption. A typical resting bone surface is lined by a thin unmineralized layer (OO), a lamina lamitans (LL), and flat bone-lining cells (BLC). Signals (morphogenetic or physical) received directly or indirectly by bone-lining cells shift these cells from resting (neutral) to an osteoid destruction state (secretion of collagenase, change in shape followed by detachment from bone surface, and attraction of osteoclasts) and thus help initiate osteoclastic bone resorption through mineral exposure. Note the homing of preosteoclasts to a designated bone site needing replacement by blood vessels. POCT, preosteoclast; OCT, osteoclast; MNC, mononuclear cell; POB, preosteoblast. (From Weiss, L., Ed., *Cell and Tissue Biology, A Textbook of Histology,* Urban and Schwarzenberg, Baltimore, 1988. With permission.)

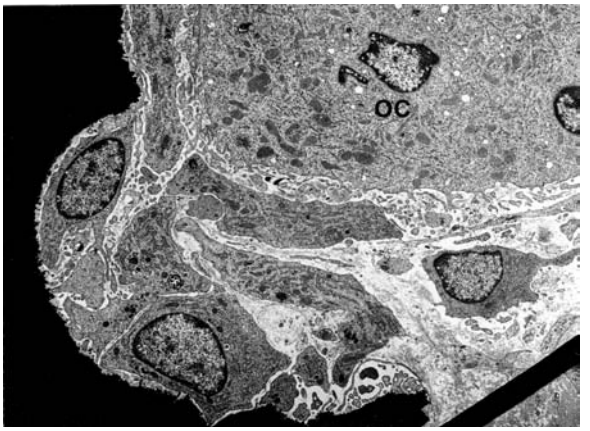

FIGURE 1.29 Electron micrograph of a typical reversal zone of a bone remodeling unit. At the upper right corner is an inactive osteoclast (OC) off bone surface. Within the well-defined Howship's lacuna, adjacent to bone that appears black, are mononuclear phagocytes with numerous cytoplasmic extensions and lysosomes. Original magnification × 3000. (From Baron, R. and Vignery, A., in *Bone Histomorphometry,* W. S. S. Jee and A. M. Parfitt, Eds., Elsevier Science, Paris, 1981. With permission.)

osteoclast precursor cells.[29,34,35,159] This insulated behavior of osteoblast-lineage cells may explain why receptors of many of the known bone-resorbing agents are found in osteoblasts and not in osteoclasts.

1.3.6.3 Resorption

Where osteoclasts come in contact with the surface of bone, they begin to erode the bone, forming cavities referred to as Howship's lacunae, in cancellous bone, and as cutting cones or resorption cavities, in cortical bone (Figs. 1.23A, 1.26, and 1.27). In the cortical bone of dogs, the osteoclasts in the cutting cone travel in a direction roughly parallel to the long axis of the bone at a speed of about 20 to 40 μm/day and radially about 5 to 10 μm/day. The mean depth of erosion is about 60 μm in trabecular bone and about 100 μm in cortical bone.[160] This phase takes about 1 to 3 weeks.

1.3.6.4 Reversal (Coupling)

This term refers to a 1- to 2-week interval between the completion of resorption and the commencement of formation. The histological counterpart of the reversal period is the point in time when the Howship's lacunae and the cutting cones lack osteoclasts, but contain mononuclear cells of unknown origin and function (Fig. 1.29).[149]

In physiological circumstances, the "coupling" of bone formation to bone resorption occurs. The cellular and hormonal mechanisms involved in coupling are unclear. One suggestion is the growth factor concept of coupling in which osteoblast-stimulating factors (IGF I and II, TGF-β, and FGFs) are released from bone matrix and stimulate osteoblast activity for new bone formation. Another is that bone surfaces other than resorbing surfaces are populated by osteoblast-lineage cells because of cell-surface molecules.[29,34,89]

1.3.6.5 Formation and Mineralization

Bone formation occurs in two stages: matrix synthesis followed by extracellular mineralization. Soon after the deposition of cement substance (the scalloped, reversal line), the new osteoblasts begin to deposit a layer of bone matrix referred to as the osteoid seam. The osteoid seam will reach a level of approximately 70% of its final mineralization after about 5 to 10 days. Complete mineralization takes about 3 to 6 months in both cortical and trabecular bone. (See Table 1.11 for the static and dynamic histomorphometric parameters of the cortical (osteonal) and cancellous (hemiosteonal) BMU.)[1,2,7,40,41]

In the adult skeleton, the usual BMU resorbs 20 parts of bone but replaces 19, creating a negative bone balance. This has led to the term *bone remodeling-dependent bone loss*. Increased mechanical usage

(MU) depresses the number of new remodeling packets. It may also cause each completed packet to become less negative, thus conserving trabecular and endocortical bone next to marrow. Remodeling increases as a result of disuse. This accelerates trabecular and endocortical bone loss, with the spongiosa becoming osteopenic and the marrow cavity enlarging.[1,8,59,88]

1.3.6.6 Bone Turnover[1,5,7]

Bone turnover depends on the surface-restricted activation frequency and on the surface-to-volume ratio. Activation frequency is the intensity of remodeling, the reciprocal of the average time interval between the start of consecutive cycles of remodeling at the same site. The surface-to-volume ratio of typical cancellous and cortical bone differs about five- to tenfold (see Tables 1.2 and 1.4). Site measurements of turnover in the human skeleton have been limited to the rib and ilium. Cortical bone turnover in the rib is about 4%/year. In the ilium, activation frequency is about the same on cancellous, endocortical, and intracortical subdivisions of the endosteal surfaces, so the difference in bone turnover at this site is related entirely to the difference in surface-to-volume ratio. At other sites, differences in mechanical loading can further modify activation frequencies.[5,8,51,52]

1.3.6.7 Remodeling Space[2]

The remodeling space consists of the hole made by the remodeling process. Each BMU makes a temporary evacuation in compacta or on a trabecular surface. Accordingly, increasing the number of evacuations, or bone turnover, increases the transient bone loss, the remodeling space. Usually the remodeling space equals 2 to 8% of bone volume but can exceed 20% and more in spongiosa because of its large surface to volume. Increased turnover of BMU creations and prolonged remodeling periods increase this space while decreased bone turnover and shortened remodeling periods decrease it. Estrogen, calcitonin, and bisphosphonates decrease BMU creations and let the existing remodeling space fill with bone. This causes an increase in areal bone "density" that plateaus. Remodeling rate is dominated by mechanical usage and modulated by parathyroid hormone, thyroxin, growth hormone, 1,25 $(OH)_2$ vitamin D and microdamage. Accordingly, an increase in the number of BMUs and in the time required to fill the hole will increase remodeling space.[2,37,59]

1.3.6.8 Remodeling Map

There are a few studies showing the location of bone remodeling sites known as a "remodeling map."[70,71] These maps show BMU-based turnover or remodeling does differ in different parts of the skeleton and different parts of a given bone at any moment. The reason for many of those differences is not known. Possible reasons are as follows: (1) In the region where microdamage occurs BMU-based remodeling increases to try to repair it. Such regions are usually highly loaded sites like the compacta and epiphyseal spongiosa.[72] (2) In one's life span, especially during growth, parts of the skeleton exist in relative or partial disuse due to the accumulation of unneeded bone that increase remodeling-dependent bone loss.[73] For example, the longitudinal growth creates more spongiosa than needed for mechanical usage. (3) Adult remodeling provides a mechanism for the skeleton to adapt to its mechanical environment (inactivity or hypervigorous activity). All these phenomena are due to targeted biomechanical-driven remodeling. On the other hand, some believe there is genetically driven remodeling or stochastic remodeling that prevents fatigue damage ("fatigue damage prevention"). The latter hypothesis is highly disputed.[72,73]

Direct measurements of turnover in axial and appendicular cancellous bone in the adult beagle dog and their relationship to hematopoietic (red) and fatty (yellow) marrow showing higher bone turnover rates at red marrow sites are listed in Table 1.12.[74,75]

1.3.6.9 Conservation and Disuse Mode Remodeling

Remodeling can take place usually in either the conservation or disuse mode. In conservation remodeling, resorption equals formation. In the disuse mode, remodeling BMUs make less bone than they resorb, a net loss of bone next to marrow. The latter mode is the usual condition with disuse and aging (remodeling-dependent bone loss). When strains with disuse are below remodeling threshold range or window (the MESr centering near 50 to 100 microstrain), disuse-mode remodeling (remodeling-dependent bone loss) is stimulated to remove bone next to marrow. This can result in osteopenia in which bones have less spongiosa, thinner

TABLE 1.12 Cancellous Bone Turnover in Adult Beagle Dogs

Site	Marrow	Turnover Rate (%/year)
Lumbar vertebra	Red	205
Proximal femur	Red	138
Ilium	Red	164
Distal radius	Yellow	85

Source: Data derived from Wronski, T. J., Smith, J. M., and Jee, W. S. S., *Radiat. Res.*, 83, 74, 1980; Wronski, T. J., Smith, J. M., and Jee, W. S. S., *Calcif. Tissue Int.*, 33, 583, 1981.

TABLE 1.13 Prostaglandin E_2 Induces Modeling and Remodeling Bone Gain

Units	Control	Treated[a]	% Change
Formation	32 ± 7[b]	67 ± 17	+109[c]
Modeling	8 ± 1	30 ± 7	+275[c]
Remodeling	19 ± 6	29 ± 7	+52
Uncertain	5 ± 2	8 ± 3	+60
Bone area (%)	13.5 ± 3	43.2 ± 1.4	+220[c]

[a] 3 mg PGE_2/kg/day for 30-day-to 20-month-old male Wistar rats; secondary spongiosa of proximal tibial metaphysis.

[b] ±SD.

[c] $p < 0.05$ vs. controls.

cortices, and large marrow cavities. When strains exceed the remodeling threshold range, as in normal and hypermechanical usage, remodeling is dampened back toward normal levels (see Fig. 1.22).[2,8,61,65,66,69]

1.3.6.10 Remodeling-Dependent Bone Gain

An exception to these usual modes of remodeling is the situation induced by bone anabolic agents such as PGE_2 in which there is remodeling-dependent bone gain (Table 1.13). Here, the BMUs make more bone than they resorb, usually in the form of woven bone.[47]

1.3.6.11 A Unifying Theory of Bone Remodeling

The current concept assumes that signals generated by osteocytes to mechanical loading stimulates bone-lining cells to activate remodeling. This concept could not resolve the inconsistencies that remodeling increases both when mechanical loading is exceedingly low and when it is exceedingly high. Therefore, Martin[161] recently developed a new theory that "lining cells are inclined to activate remodeling unless restrained by an inhibitory signal and that the mechanically provoked osteocyte signal serves this inhibitory function." For example, remodeling is elevated when signal production declines due to reduced loading or when signal production or transmission is disturbed by damage due to excessive loading or mineralization. The inhibitory signal proposed is similar to that of Marotti's[162,163] hypothesis that osteocytes send inhibitory signals to active osteoblasts to recruit additional osteocytes.

1.4 Development of a Typical Long Bone[1]

The sequence of growth and development in a long bone is outlined below. Briefly:

1. A hyaline cartilage model is laid down and grows by apposition from the perichondrium and by proliferation of the cells at the ends;
2. A subperiosteal ring of bone is laid down by intramembranous ossification;
3. The central portion of cartilage anlage calcifies and vascular mesenchyme enters to form the primary endochondral ossification center;
4. The zone of ossification spreads toward the ends of the bone;

5. Blood vessels and mesenchyme enter the superior and inferior epiphyseal ossification centers to form articular cartilage and growth plate;
6. The growth plate, responsible for bone elongation, consists of cartilage cells that multiply, hypertrophy, die, and calcify their matrix in the form of cell columns;
7. Blood vessels and osteogenic cells invade and selectively destroy about two thirds of the calcified cartilage matrix and deposit bone around the remaining deposits to form the primary spongiosa that subsequently is remodeled into secondary spongiosa and bone marrow;
8. The shaft of cortical bone increases in width, with periosteal bone formation exceeding endocortical bone resorption; and
9. Bone elongation stops when the growth plate ossifies (epiphyseal closure) to form the continuous bone marrow cavity.

A more-detailed description of this process can be found in any basic histology textbook.

1.5 Skeletal Mass and Its Changes[2,59]

A child's bone bank represents the difference between bone added by growth and by modeling-dependent bone gain, on the one hand, and bone removed by remodeling-dependent bone loss on the other. In adults, however, where growth no longer goes on and where modeling comes to a near standstill, remodeling-dependent bone loss controls most of the adult bone bank. This means the bone bank depends mostly on the activation frequency (a histological index of the intensity of bone remodeling), or the bone balance at a given moment on the bone mass accumulated during growth, i.e., the peak bone mass. In other words, accumulating bone mass and establishing the functional systems in bone in children depends on controlling longitudinal and circumferential bone growth, by endochondral and intramembranous ossifications, modeling, and remodeling (Table 1.14). Managing bone mass in adults depends upon the peak bone mass and how remodeling converts it thereafter.[1,2,59,76]

1.5.1 Skeletal Adaptation to Mechanical Usage[1,2,8,77–85]

Mechanical usage plays an important role in skeletal development and maintenance. Mechanical regulation of bone biology begins at about 5 to 7 weeks of prenatal life when most of the adult skeletal elements and soft tissue has formed. Intermittent skeletal tissue strains caused by muscular contraction modulate cartilage growth, ossification, bone modeling, and remodeling throughout the skeleton. After birth, growth and ossification of the skeleton are strongly influenced by externally applied forces.

TABLE 1.14 Functional Systems in Bone

	Structural				Ca Homeostasis	
	Endochondral Ossification	Intramembranous Ossification	Modeling	Remodeling	Error Correcting (min-h)	Blood–bone Equilibrium (days)
Function	Longitudinal growth	Circumferential growth	Shape	Turnover	Restore baseline plasma Ca	Determine steady-state level of Ca
	Production of cancellous bone	Production of cortical bone	Size			
Cells	Chondroblasts	Osteoclasts	Bone-lining cells	Bone-lining cell	Bone-lining cell	Bone-lining cell
	Chondroclasts Osteoblasts Osteoclasts	Osteoblasts	Osteoblasts	Osteoclasts Osteoblasts Osteocytes	Osteocytes Osteoclasts	Osteocytes

Source: Weiss, L., Ed., *Cell and Tissue Biology, A Textbook of Histology,* 6th ed., Urban and Schwarzenberg, Baltimore, 1988. With permission.

1.5.1.1 The Mechanostat

How mechanical usage regulates bone mass and architecture introduces another new concept of bone response to mechanical usage and can best be explained by Frost's mechanostat hypothesis.[2,8,65,66] The hypothesis helps explain many clinical and experimental observations that are poorly understood. Nevertheless, no matter how logical it is, it is still a hypothesis. Frost proposed the mechanostat as a name for the biologic mechanisms that fit skeletal mass and architecture to the needs of one's normal physical activities. It is well recognized that bone mass adapts to mechanical usage (MU) in a special way: The MU makes its biologic mechanisms correct errors between the mass and its MU. The mechanism would behave like a home thermostat in that it would turn "on" in response to error and "off" in its absence, so that is why it was named the mechanostat. The relationship can be encoded thus:

$$\text{MU} \rightarrow \text{bone} \rightarrow \text{mechanostat} \rightarrow \text{bone mass effect} \tag{1.1}$$

The mechanostat has been proposed to consist of at least these tissue-level biologic mechanisms: growth, modeling, and remodeling mechanisms, the MES mechanisms that control the latter two including their location and rates, plus the mechanical transducers (mechanical signals and relay stations) in bone that pass that information on to the biologic side of the MES mechanisms. That relation could be written thus:

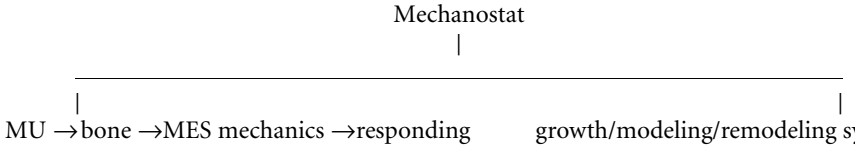

(1.2)

The mechanostat concept is based on the idea that there exists an effective strain (MES), set point, with a mechanical overload, a response will occur that increases muscle and bone mass and strength. If there is a persistent underload, as in hypogravity situations, muscle and bone mass will diminish to a level corresponding to the lower load. The set point is defined as a range of strain values that will produce no response. Strains above the set point (or set point range), i.e., beyond 1500 to 3000 microstrain will evoke a positive response leading to an increased bone mass. Strains below the physiological set point range, i.e., below 200 microstrain, will trigger a response that causes bone loss. Thus, modeling-dependent bone gain is stimulated at strain above 1500 microstrain and remodeling is stimulated with strains below about 200 microstain. For a given bone surface, modeling is "on," remodeling is "off," and vice versa, because modeling-dependent bone gain and remodeling-dependent bone loss take place within different strain ranges (see Fig. 1.22).[86] Nonmechanical agents can evoke changes or errors in the set point range, leading in turn to changes in modeling and remodeling activities, even though there has been no effective change in the strain environment (Table 1.15).[65,185]

Others are in agreement on these strain ranges. Cowin[62] proposed a similar range of effective strains, which he termed *banks of remodeling equilibrium strains*. Also, Carter[63,64] suggested a wide physiological range within which alteration of strain will produce no significant adaptive response.

The mechanostat system also contains the mechanical usage feedback loop, an important concept that limits the extent of the response to a given stimulus, as well as limiting the transient response to a given stimulus.[2,47] For example, a given dose level of an anabolic agent like PGE_2 will evoke an increase in bone for some 30 days (transient), which stabilizes at steady state thereafter with continual treatment. The increase in bone mass has kicked in the negative mechanical usage feedback loop opposing any further addition of bone because added bone will lessen the bone strain.[47] Another example of the negative feedback loop in action is the loss of bone gain by anabolic agents on discontinuation of treatment.[47]

The mechanostat system is similar to the temperature control system in a house. Let heat = bone mass and strength, let modeling = heating, let remodeling = cooling, and let two thermostats analogize the

TABLE 1.15 Proposed Effects of Mechanical Usage (MU), Disease, Drugs, and Hormones on the Set Point Range for Bone and Resulting Effects on Bone Mass

	Set Point	Annual Net Bone Loss, Global	Annual Remodeling
Mechanical usage, normal	O	N	N
Mechanical usage, deficient	I	I	I
Oophorectomy	I	I	I
Paralysis	I	I	I
Adrenal steroids	I	I	I
1^0 Hyperparathyroidism	I	I	I
Calcium deficiency	I	I	I
Mechanical usage, increased	D	D	D
Estrogen	D	D	D
Thyroidectomy	D	D	D
Calcitonin	D	D	D
Weight lifting	D	D	D

Key: O, no change; N, normal; D, decreased; I, increased; 1^0, primary.

Source: Bronner, F. and Worrell, R.V., Eds., *Orthopaedics, Principles of Basic and Clinical Science,* CRC Press, Boca Raton, FL, 1999. With permission.

strain thresholds. Then, one thermostat can signal the furnace to turn on to add heat when needed, but turns it off (the feedback loop) when there is enough. Another thermostat (remodeling threshold) can signal the air conditioning system to remove heat, but turn off (the feedback loop) when it cools to the desirable temperature. The settings of those thermostats would provide the criteria for heating and cooling.

1.5.1.2 The Utah Paradigm of Skeletal Physiology

Pondering how the mechanostat system functions in bone physiology led to Frost's development of the Utah paradigm of skeletal physiology.[59,60,86–88] For the skeleton (bones), the bold-face caps in Relation 1.3 identify the mechanically dedicated message traffic and feedback in the mechanostat, which is part of that paradigm. The paradigm considers the view only nonmechanical agents (hormones, calcium, vitamin D, cytokine, genes, genetic, etc.) control osteoblast and osteoclast activities that control changes in bone mass and strengths obsolete. First, mechanical factors play a major role in the control of the biologic mechanisms that change postnatal bone and mass; and, second, normally osteoblastic and osteoclastic activity are not independent and are not independently controlled. Instead, they are part of remodeling (BMUs) or of modeling drift (formation and resorption drifts). Modeling increases bone strength and mass and strength. Remodeling repairs microdamage and conserves or removes unneeded bone adjacent to marrow.

Nonmechanical agents, such as growth hormones, androgens, calcium, and vitamin D, act directly to influence biologic mechanisms, but also affect muscles and thus indirectly affect the bone loads and strains that help to control the biologic mechanisms[59,86,126,128–132,154] (Relation 1.3).

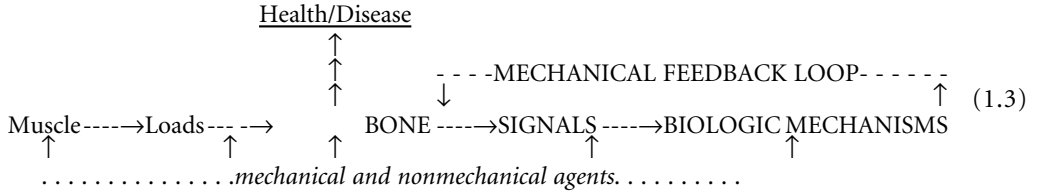

(1.3)

The Utah paradigm of bone physiology suggest four conditions:

1. The biologic mechanisms that determine skeletal health and disease need effector cells and nonmechanical agents in order to work;

2. Mechanical factors guide those mechanisms in time and space;
3. After birth, neuromotor physiology and anatomy dominate control of those biologic mechanisms; and
4. Most nonmechanical factors can directly or indirectly help or hinder the mechanical control.[5]

Nonmechanical agents influence the mechanical regulation and have a direct influence on bone cells and their precursors involved with biologic mechanisms that are independent of the mechanical stimuli. In addition, there are interactions between mechanical and nonmechanical factors. Such additive or synergistic influences have shown that mechanical stimuli for bone hypertrophy or atrophy can be altered by nonmechanical agents.[47,92–100] If one maintains the view that mechanical factors dominate bone regulation, one can consider nonmechanical factors as agents that effectively alter the level of mechanical stimulus. Frost and others support this viewpoint.[62] Frost[65,90,91,185] has proposed that some nonmechanical factor may alter the mechanical "set point," while Carter and co-workers[63,82] view is that nonmechanical factors will cause variation in the attractor stress stimulus, ∅AS, which regulates the mechanically related bone remodeling stimulus. Table 1.15 lists the proposed effects of mechanical usage and nonmechanical agents on the set point and the resulting effects on bone mass. Recently, it has been shown that mechanical and nonmechanical factors are both important and that the effect of mechanical stimulus is dependent on the nonmechanical environment in that the combination showed additive or synergistic anabolic effects.[47,93–100]

1.5.1.3 Animal Models of Skeletal Underloading (Immobilization)

Methods to reduce skeletal loading include local or systemic immobilization.[193,194] The local disuse models, usually in one limb, include nerve,[181,190,216,206,222,226,231] spinal cord,[206,207] or tendon[209,217,225,230] resections, casting,[190–192,222,223] bandaging of one limb,[78,188,189,198,199] or suspension of both hindlimbs[182,200] in rats. Systemic or whole body immobilization involves body casting (restraint)[177,178,186,187,195,205,228,229] and space flight.[200–202] The whole-body casting and restraint models are cumbersome and expensive, resulting in very few studies with meager observations and few published reports and will not be discussed here. Space flight studies are too numerous to be discussed here.

The most frequently employed disuse models are the tail suspension, limb taping, nerve resections, tendon resection, and casting of one limb in rats (Table 1.16). All these models elicit similar responses with the major endpoint being site specific bone loss. They differ only in the speed of bone loss depending upon whether there is a regional acceleratory phenomenon (RAP) response from surgery. The RAP constitutes a considerable acceleration of all normal tissue turnover processes initiated by an irritative phenomenon like surgery.[184] Because the RAP increases regional bone remodeling, it usually increases bone loss next to marrow.

The classical immobilization-induced bone loss response can best be described from the studies of the one hindlimb immobilization models in rats and dogs.[78,191,192,198,199,223] The rate of bone loss is related to the level of normal stress and strain to the bone. More bone loss is seen in the weight-bearing lower extremities than the non-weight-bearing upper extremities or, in the case of tetrapods, the distal part of the limbs[192] (Fig. 1.30). In addition, it has been shown that the cancellous bone in caudal vertebrae loses less bone than weight-bearing bones with immobilization. Animals with lower peak bone mass lose less bone than those with higher bone mass. In addition, trabecular bone loss is much faster than that in cortical bone. This is due in part to the difference in surface-to-volume ratio and more surfaces adjacent to marrow. The immobilization or unloading evokes a rapid, transient (acute) remodeling-dependent bone loss associated with an increase in resorption and a decrease in bone formation (focal imbalance), which reduces bone adjacent to marrow.[78,198,199] This response occurs in cancellous bone as early as 3 h post-tenotomy.[43] Other models avoiding surgery and the RAP response occur slightly more slowly. At steady (chronic) state, the bone loss has plateaued with cellular activities back to near control levels (Figs. 1.31 to 1.34). In the rat one hindlimb immobilized (IM) by bandaging model, the steady state plateaued between 10 and 18 weeks in cancellous bone and more than 26 weeks post-IM in cortical bone (Fig. 1.32).[78] In the dog casted forelimb model, cancellous bone loss plateaued at 18 weeks and cortical bone loss at

TABLE 1.16 Models of Unloading (Immobilization) of the Rat Skeleton[a]

Attribute	Suspension[182]	Limb taping[78]	Nerve resection[222,231]	Tenotomy[207,217,225]	Limb casting[191,222]
Site	Hindlimb	One hindlimb	One hindlimb	Lower hindlimb; foot	One limb
Surgery	No	No	Yes (sciatic or femoral nerve)	Yes (knee calcaneal)	No
Hardware	Specialized cages; tail hardness	No (tape)	No	No	No (plaster cast)
Time frame	Short term <5 wks	Long term	Long term	Short term (tendon regrowth)	Long term
Responses					
Blood flow affected	Yes	Potential problem	Potential	?	↓ (?)
Cellular fluid shift	Yes	No	No	No	No
Muscle function	Yes	Restricted	No	Mildly affected	No
Nerve function	Yes	Yes	No	No	Yes
Cancellous bone loss	No	↓ (50)	↓ (50) (72)[222]	↓ (50)	↓ (60)[191](68)[222]
Tb Formation	↓ (66)	↓ (35)	↓ (50)	↓ (45)	↓
Tb Resorption	No	↑ (50)	↑ (150)	↑ (125)	↑
Cortical bone loss	No	↓ (10)	↓ (4)	—	↓ (50)[191] (14)[190*]
Formation (Ps)	↓ (85)	↓ (90)	↓ (40)	—	↓
Resorption (Ec)	No	↑ (19)	↑ (100)	—	↑
Muscle weight	↓ (48)	↓ (55)	↓ (70)	—	↓
Convenience	Daily care	Daily care	Minor care	Excellent	Weekly care
Recovery possible	Yes	Yes	No	Possible; unpredictable	Yes

[a] Findings only from older rats studies are sited; Ps = periosteal; Ec = endocortical; Tb = trabecular; ↑ increase (%); ↓ decrease (%); — = no data; * = cortical width.
Source: Data adapted from Refs. 78, 182, 190, 191, 209, 217, 225, 231.

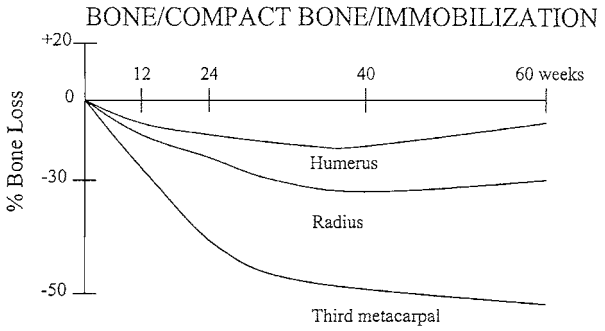

FIGURE 1.30 Plot of net immobilization-induced bone loss in select forelimb bones (humerus, radius, and third metacarpal) of adult beagle dogs expressed as percentage of control. The more distal loaded bones showed more bone loss. (Adapted from Refs. 191, 192, 223.)

FIGURE 1.31 Microradiographs of rat proximal tibia from: (a) 9-month-old basal control, (b) 15-month-old aging control, (c) 15-month-old after 26 weeks of underloading, and (d) 15-month-old after 26 weeks of overloading. Fewer but thicker trabeculae are seen in the 15-month-old than the 9-month-old metaphysis (b vs. a), the underloaded tibia lost cancellous bone (fewer and thinner trabeculae; c vs. a,b). The overloaded tibia added bone by conserving and thickening trabeculae (d vs. all others). (From Jee, W. S. S. et al., *Cells Mater.,* 1, Suppl., 131, 1991. With permission.)

more than 60 weeks.[86] All the rat one limb IM models resulted in about 60% cancellous and less than 10% cortical bone loss (Table 1.16). Possibly there would be more cortical bone loss if the rat studies were carried out longer because Jaworksi and Uhthoff[191] reported that the metacarpal in the dog lost up to 50% of the cortical bone after 60 weeks of forelimb casting. Both transient elevated trabecular bone resorption and depressed bone formation occur to accelerate the cancellous bone loss. In contrast, in cortical bone there was an immediate near cessation of periosteal bone formation (modeling in the formation mode) and a significant increase in endocortical resorption that evoked the slow loss of compacta and a nonsignificant enlargement of the marrow cavity at 26 weeks (Figs. 1.33, 1.34). More laborious, longer-term studies are needed to determine whether the rat will react like the dog in immobilization-induced cortical bone loss. Regardless, the important observations in cortical bone loss are the stimulation of endocortical bone resorption and the immediate depression in periosteal bone formation. Furthermore, there are profound architectural changes in the loss of trabecular connectivity and the conversion of trabecular plates to rods. In addition, immobilized limb cancellous bone mechanical properties were 28 to 74% of control values and cortical bone mechanical properties were 71 to 98% of control values in adult mongrel dogs immobilized for 16 weeks.[232]

Most of the responses from the IM models in Table 1.16 are in agreement with the general responses described above except for those seen in 6-month-old rats with hindlimb suspension.[182] In the latter model, only periosteal and trabecular bone formation were depressed with no impact on either cancellous

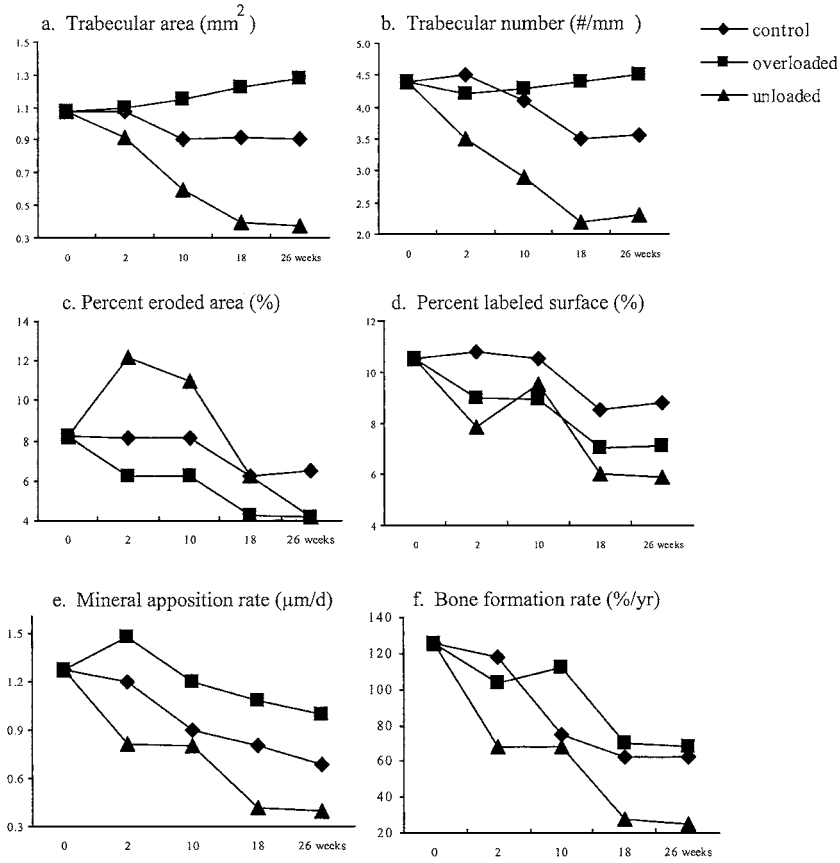

FIGURE 1.32 Time course of select static and dynamic histomorphometry changes of the proximal tibial metaphyseal cancellous bone in control, underloaded, and overloaded limbs. See text for explanation. (From Jee, W. S. S. et al., *Cells Mater.,* 1, Suppl., 131, 1991. With permission.)

and cortical bone mass. A careful inspection of the remaining models listed in Table 1.16 suggests the one hindlimb taping or casting to be the recommended model for IM-induced bone loss. The model is readily reproducible, needs no surgery that sets off the RAP, and static and dynamic histomorphometric data and time course data from slowly growing rats (e.g., from 9 months or older) and adult bone sites (e.g., distal tibial metaphyses) are available and recovery studies can be studied. Nevertheless, the current literature on IM models leaves much to be desired. There is very little data generated from skeletally mature bone sites in rats and no data on the effects of immobilization in the vertebrae and proximal femur (e.g., femoral neck) sites at risk to osteoporosis-induced bone fracture. None of the current models can be readily employed to study the vertebral response. There is one article concerning the vertebra. It deals with caudal vertebra neurectomy.[181] It caused a reduction in cancellous bone formation rate and a trend toward increased bone resorption. The effects were similar to the effect of mechanical disuse in weight-bearing bones. The authors concluded that strains associated with normal mechanical usage in caudal vertebrae exert a significant influence on bone formation rate in caudal vertebrae. Furthermore, the one-hindlimb IM taping or casting or possibly nerve resection can be used to explore the proximal femur response. Last, it is puzzling why the distal tibia IM response has not been studied. The distal tibia is an adult bone site in rats more than 3 months of age. Its growth plate closes at 3 months[169] with trabecular and dynamic histomorphometric profiles similar to humans.[233,234]

In summary, immobilization or disuse sets off an early (i.e., acute-stage) cancellous bone loss that shuts down modeling-dependent bone gain (e.g., inhibits periosteal bone formation) and increases bone

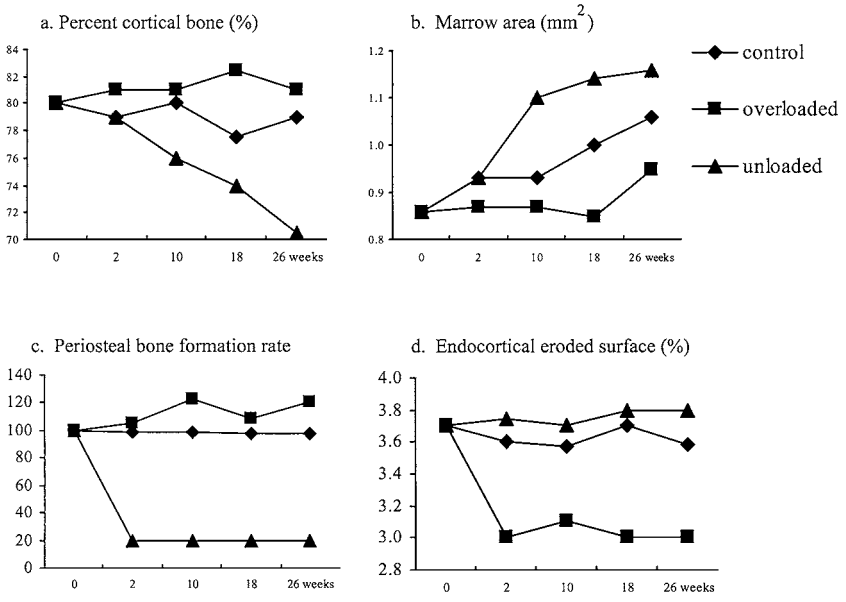

FIGURE 1.33 Time course of static and dynamic histomorphometry changes of the tibial shaft in control, underloaded, and overloaded limbs. See text for explanation. (From Jee, W. S. S. et al., *Cells Mater.,* 1, Suppl., 131, 1991. With permission.)

remodeling-dependent bone loss (e.g., BMU creations increase and completed BMUs make less bone than normal) so that trabecular and endocortical bone turnover and net losses increase. The early cancellous bone loss levels off despite continual immobilization (the final or steady state stage) and bone turnover decreases to near normal with permanently reduced bone mass as bone mass and reduced mechanical demand equilibrate. It is reasonable to assume the same acute and steady state also occurs in cortical bone sites but much slower. These tissue-level responses are in accordance with the predictions of Frost's mechanostat theory that when bone strains fall and stay below the remodeling threshold in disuse or immobilization, remodeling functions in its disuse bone loss mode (increase bone turnover and loss) and mechanically controlled modeling stays off and no microdamage or RAP arise.[65–67]

1.5.1.4 Animal Models of Skeletal Loading

This brief survey of overloaded animals is restricted to the rat, an animal whose skeletal biology is exceptionally well characterized and where the bulk of the literature resides. Animal models of increased loading of the rat skeleton include whole-body models in which individuals are trained to run, jump, or swim so as to induce strain in the bones that are not the same as those commonly used. These models include the popular running on the treadmill[203,204,215,227,235,236–238] and isolated studies involving voluntary wheel running,[239–241] jumping,[224] and swimming[242,243] models. The overloading of the contralateral limb of the one hindlimb immobilization among the whole-body loading models have also been included even though increased loading occurred only to the contralateral[78] limb (Table 1.17). These models have not been used to study the effect of specific measured strains in bones, because it was difficult to measure local strain in the rat. Regardless, the exercise studies in rats have contributed to better understanding of principles of responses to increased loading (e.g., the aging effects and the bone histomorphometry and strength change in select cortical and cancellous bone sites).

1.5.1.4.1 Aging and Exercise

The bulk of the aging data was generated from the treadmill running model[203,204,215,226,235,236,238] (Table 1.17). Rats ranging from 1 to 13 months and the aging effects on rapidly growing (1-month-old rats) and slower

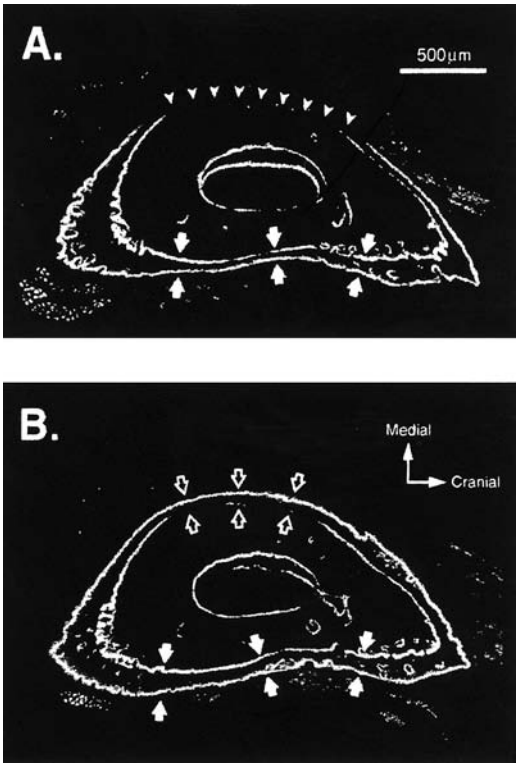

FIGURE 1.34 Fluorescent images of cross sections through the distal ulna of rat from high-strain rate loading-induced bone modeling. (A) Control nonloaded ulna with medial-to-lateral modeling drift. There is periosteal resorption on the medial surface (arrowheads) and deposition of bone laterally (solid arrows). (B) Contralateral loaded ulna with complete reversal of resorption to active formation on medial surface (open arrows) and the conversion of resorption to formation on the lateral surface (solid arrows). (From Mosley, J. R. and Lanyon, L. E., *Bone,* 23, 313, 1998. With permission.)

growing (13-month-old) proximal tibial spongiosa (PTM), distal femoral metaphyses (DFM), and tibial shaft (TX), and the different responses in the more rapidly growing PTM vs. the slowly growing lumbar vertebral body (LVB) were studied. These studies found that rapidly growing bones have a greater capacity to add new cancellous but not cortical bone than the slowly growing bones. Even with the wide range of ages in the rat life span, the cortical bone response in aged TX was equal and may be greater than in younger animals. Nevertheless, these aging studies would be more meaningful if skeletally immature bone sites were compared with skeletally mature sites for exercise-induced bone gain because the PTM of a 13-month-old rat is still growing and possesses the bone histomorphometric profile of juvenile bone sites.

1.5.1.4.2 Site-Specific Cancellous Bone Response in Growing Rats

Iwanoto et al.[235] studied the capacity of the DTM, PTM, and LVB to maximize bone mass between 1 and 5 months of age by treadmill running. They repeated the stimulation of more cancellous bone volume (almost by a factor of 2), labeled perimeter, mineral appositional rate, and bone formation rate than at the proximal tibial metaphysis. In addtion, the exercise had no significant effect on cancellous bone mass and formation in the vertebral body, only the cortical periosteal bone formation rate was increased. Their findings suggest that cancellous bone adaptation to treadmill exercise is site specific and the effect may be influenced by factors such as mechanical loading and metaphyseal bone histomorphometry and architecture in the growing rat.

TABLE 1.17 Skeletal Responses to Exercise in Rats

Bone	Sites	Attribute	Treadmill		Wheel Running	Jumping	Overloading	Swimming
Cortical bone (TX/FX)	Y	Bone mass	↑5[224]	—[204]	↑9[235]	↑17[224]		↑11[243]
		Marrow cavity	→	—				
		Ps-MAR	→	—				
		Ps-BFR	↑50	↑35				
		Ec-BFR	→	↑45				
		Ec-BR	↘ 15	—				
	O	Bone mass	↑9[238]	↑10[227]	↑15[66] ↑18[67]		↑2[78]	↘15[242]
		Marrow cavity	→	→	↓11		↓10	→
		Ps-MAR	↗45	↗33	↑8		↑13	—
		Ps-BFR	↑200	↑145	↑70		↗25	↓41
		Ec-BFR	—	↑200	→		—	—
		Ec-BR	↘ 10	↘8	—		↘16	↓16
Cancellous bone (PTM/DFM)	Y	Bone mass	↑23[235]					
		Tb.N	→					
		MAR	↑50					
		BFR	↑50					
		BR	—					
	O	Bone mass	↗8[204]	↗34[236]			↑45[78]	
		Tb.N	—	↗25			↑32	
		MAR	—	↗19			↑38	
		BFR	↑100	↗42			↑23	
		BR	↘10	↓28			↓18	
Cancellous bone (LVB)	Y	Bone mass	→[204]	↑18[203]				↓25[242]
		Tb.N	—					→
		MAR	→					—
		BFR	↗10					↓37
		BR	—					↓20
	O	Bone mass	↗17[236]	→[227]	↑[241]			
		Tb.N	↗17	→				
		MAR	↗6	↘36				
		BFR	↗26	↘56				
		BR	↓28	↘7				
FN (Cn)	Y	Bone mass	↑23[215]					

Y = young; 1–3 months of age; O = old; 9–14 months of age; ↑ increase (%); ↓ decrease (%); —, no data; ↗ nonsignificant increase, %; ↘ nonsignificant decrease, %; TX, tibial shaft; FX, femoral shaft; PTM, proximal tibial metaphysis; DFM, distal femur metaphysis; LVB, lumbar vertebral body; FN, femoral neck; Ps, periosteal; Ec, endocortical; Tb.N, trabecular number; MAR, mineral appositon rate; BFR, bone formation rate; BR, bone resorption; Cn, cancellous.

Source: Data adapted from Refs. 78, 203, 204, 215, 224, 235, 236, 238, 242, 243.

1.5.1.4.3 Time Course Study of the Exercise Response

A time course study of the effect of exercise is a prerequisite to a better understanding of the response to exercise. Unfortunately, time course studies are spotty even with employing the popular treadmill exercise model. One time course study exists for the overloading model, the overloading of the contralateral immobilized limb.[78] Overloading the proximal tibial metaphysis at first increased cancellous bone mass by 44% over that of controls and then stabilized after week 26 (Figs. 1.31 and 1.32). This positive bone balance was accompanied by three changes: a significant increase in osteoblastic activity (mineral appositional rate) at 26 weeks, and a significant increased bone formation rate at 10 and 18 weeks (Fig. 1.32). Overloading was effective in preventing age-related cortical bone loss, but not effective in adding bone. It creates a slight, positive cortical bone balance after 18 weeks by an insignificant increase in periosteal bone formation and a decrease in endocortical eroded surface (Figs. 1.33, 1.34). They concluded that overloading tends to stimulate formation-associated bone modeling and depresses the

TABLE 1.18 Effects of Exercises on Bone Strength in Rats

Bone	Sites	Attribute	Treadmill	Wheel Running	Jumping	Swimming
Femur	Y	Maximum force	→[75,76]	↑11[28]	↑16[52]	
		Stress	→	→	↑14	
		Strain	↗20	→	↑13	
		Stiffness	→	→		
	O	Maximum force	→[75,77] ↑23[78]	↑20[79]		
		Stress	→ →	↑15		
		Strain		→		
		Stiffness	→ →			
Humerus	Y	Maximum force	↗19 [75] →[80]			↑13[69]
		Stress	↗10			
		Strain	↗14			
		Stiffness	↑50 →			
Tibia	Y	Maximum force				
		Stress	↗13[76]			
		Strain				
		Stiffness	↑55			
Lumbar vertebra	Y	Maximum force		↑7[28]		
		Stress		→		
		Strain		→		
		Stiffness		↑19		
	O	Maximum force		↑20[79]		
		Stress		↑15		
		Strain				
		Stiffness		→		
Femoral neck	Y	Maximum force	↑18[41] →[80]			
		Stress	→			
		Strain	↑34 ↗9			
	O	Maximum force		→[79]		
		Stress				
		Strain				
		Stiffness		→		

Y = young; 1 to 3 months of age; O = old; 9 to 14 months of age; ↑ increase (%); ↓ decrease (%); blank space, no data; ↗ nonsignificant increase, %; ↘ nonsignificant decrease.

Source: Data adapted from Refs. 28, 41, 52, 69, 75–80.

activation of resorption associated remodeling and shortens the resorption period during bone remodeling in accordance with the predictions of Frost's mechanostat theory.[65,66]

1.5.1.4.4 Exercise and Bone Strength

In most rat studies, not only the mass but also the biomechanical properties of the loaded bone have been shown to improve as a consequence of increased exercise by various methods (Table 1.18). Most of the results were generated from treadmill running, which proved to be quite varied and gave little insight into whether loading of rapidly growing (young) bones between 1 and 3 months old leads to better results than in slowing growing bones with ages between 8 and 15 months.[215,249–252,254] The two studies of voluntary wheel running[203,204] showed this treatment improved biomechanical properties at multiple sites more than the treadmill model. It may be premature, but the limited biomechanical properties data suggest that the voluntary wheel running model is more productive and should be employed more often than treadmill running when studying the principal effects of exercise.

1.5.1.4.5 In Vivo *Loading Models*

There is a need for more time course and site-specific studies as well as better experimental design and more thorough analysis of cell and tissue level changes with exercise. Time course change studies are needed to determine the timing and the characteristics of the transient or acute and steady-state or

chronic phases. The above information allows one to design better protocols to analyze the tissue and cellular responses in the future. Site-specific studies are needed to involve adult bone sites and fracture sites at risk in osteoporotic individuals. It is apparent from Table 1.17 even 15-month-old rats do not assure one is studying a skeletally mature site; besides training an adequate number of 13- to 15-month-old rats to exercise may be impossible and time-consuming. Involving the distal tibial metaphysis site of animals older than 3 months will allow one an adult bone site in 4-month-old animals, which are more trainable. Table 1.17 shows that the cancellous bone of the slowly growing LVB does not respond well to typical exercise. This is not surprising because strain changes by exercise are concentrated in long bone and minimally in the spine. Recently, a raised cage model has been employed that exercises the spine when the rat stands on its two hindlimbs to reach for food and water. The hope is that it will mimic the strains on the spine in humans.

Proper experimental design is a prerequisite to the harvesting of well-controlled data and their interpretation. For example, in Table 1.17 one of the swimming studies[242] reported bone loss from swimming, but instead it is more reasonable to postulate that an inhibition of bone growth occurred with swimming. To determine whether it is inhibition of bone growth or bone loss, they must add to their protocol a basal or beginning control group. A baseline control group is needed especially when dealing with growing animals. Furthermore, the claim of the lack of osteoblastic and osteoclastic response to exercise is reported because one is studying the chronic stage or steady-state phase when the cellular dynamics have returned to near normal. Last, more thorough bone histomorphometry analysis should be performed on exercise studies since these studies are unique and expensive, expensive because they are so time-consuming. Therefore, one should collaborate with others to utilize the valuable material.

Since animal exercise models have not generally been used to study the effect of specific measured strains on changes at identified sites in bone, they offer less opportunity to dissect the mechanism of strain-related changes than models in which loads are applied to bone artificially. In the late 1970s, Lanyon and co-workers[247] adapted the osteotomy models of Sedillott[244] and Wermel[245] to study the way bone adapts in response to an increased load in growing pigs. After osteotomy, they found the peak strains on the overloaded radius increased from 800 to 1000 microstrain associated with immediate deposition of woven bone on the periosteal surface of the intact radius. After 3 months, the ulnar cross-sectional area was equal to the combined areas of the ulna and the radius in the intact limb.[246]

Lanyon and colleagues[247] then studied the effects of ulnar osteotomy in skeletally mature sheep to eliminate the effects of growth and modeling. They found that most new bone formation occurred on the periosteal surface adjacent to the missing ulna.

To control the mechanical loading more carefully, Lanyon and Rubin[196,212,213,248] developed the isolated avian ulna model in the skeletally mature turkey in which the shaft of the ulna was isolated and loaded by pins surgically inserted through its ends. Since the animal had no other means for loading its limbs, the only strains on the ulna were imposed experimentally. Several studies were done to study the effect of strain magnitude, of daily number of cycles, of static and cyclic loading, and of strain rates. Histologically, they observed woven bone formation on periosteal and endosteal surfaces and increased intracortical porosity. The increased intracortical porosity may have been part of the RAP associated with the surgery.[184] Currently, the avian model has been abandoned because it is cumbersome, invasive, and nonmammalian.

Currently, there are only four *in vivo* loading models contributing to the literature:

1. The functional rat ulna model, which is valuable but not ideal;[83,218,257]
2. The rat tibial four-point bending model, which is considered flawed since load is applied through the periosteum, which in consequence elaborates woven bone at the points of pressure;[175,210,211,219–221]
3. The rat tail loading model, which is invasive, uses very high strains, and relates primarily to cancellous bone;[179,180,197] and
4. The isolate avian ulna and radius models, which now have been abandoned[212,213] (Table 1.19).

All the models have the drawback of being laborious, which leads to experiments with few animals.

TABLE 1.19 Skeleton Responses to *in-Vivo* Loading

Attribute	Tail Vertebrae Loading[179]	Axial Ulna Loading[218,257]	Four-Point Bending[95,219–221]	Compressive Loading[196,213]
Age/gender	13 mo/F; rats	43 d/M; rats	3–8 mo/F; rats	Skeleton mature turkey
Site	8th caudal vertebral body	Ulna (shaft)	Tibia (shaft)	Ulna/radius (shaft)
Loading				
Frequency	0.5 Hz	2 Hz/10 Hz	2 Hz	1Hz
Rate	360 cycles × 1 or 36 cycles × 9 d	0.08–0.1/s × 14 d[257] or 1200 cycles × 9 d[218]	20 cycles × 9 d[219 or] 1–108 cycles × 12[219,95] or 360 cycles × 3 d[196]	100 cycles
Magnitude	680 $\mu\varepsilon$	4000 $\mu\varepsilon$	2000–3500 $\mu\varepsilon$	3000 $\mu\varepsilon$
Responses				
Cancellous				
Formation	↑3000 or 1000			
Resorption	↓ 85			
Cortical				
Ps-lateral^{+}	↑ (woven bone)	↑↑ (new bone)	↑↑ (woven bone)	↑↑ (woven bone)
Ps-medial^{++}		↑$^{+++}$	↑	↑
Endosteal		→	→[219, 220] ↑[95, 220–221]	→
Intracortical				→

↑ Increase; ↓ decrease; F = female; M = male; + lateral surface in tension, ++ medial surface in compression, +++ conversion of resorption to active formation; Ps-lateral, periosteal surface of lateral face; Ps-medial, periosteal surface of medial face; Hz, hertz; $\mu\varepsilon$, microstrain.

Source: Data adapted from Refs. 95, 179, 213, 218–221, 257.

The tail vertebrae loading model dealt with cancellous bone while the others loaded cortical bone from ulna/radius or the tibia. Excepting with the tail loading models, the studies were carried out on rather young animals. All but the isolated avian ulna and radius models were performed on the rat, an animal whose skeletal biology is well characterized or can be readily characterized.

Despite their disadvantages, all these models have contributed to understanding of the osteoregulatory components of the strain waveform (such as strain magnitude, frequency, and strain rate). They show that bone modeling may be profoundly influenced by short periods of loading at daily intervals and that the osteogenic potential of the response is related to the peak strain magnitude, the maximum strain rate, the component frequencies of the strain waveform, and the mismatch between habitual strain distributions of the the bones and those to which they are currently exposed (loading errors or altered strain distribution) (Table 1.19).

1.5.1.4.6 Loading-Related Changes in Modeling

In the axial ulna loading in rats, the adaptive modeling was achieved by an increase in mineral apposition rate of lamellar bone on the lateral (tension) periosteal bone surface and an arrest of resorption with conversion to bone formation at the medial (compression) periosteal surface. The new bone was lamellar in form. The medial endosteal surface showed a slight reduction in bone formation, while that in the lateral endosteal surface (Fig. 1.34)[83] did not. These adaptive modeling responses are in accordance with the predictions of Frost's mechanostat theory.[65–67]

These external loading models have produced ample evidence that the bone cell response is immediate. After a single loading session the periosteum shows increases in glucose-6-phosphate dehydrogenase (G6PG) with 6 min, c-fos mRNA with 2 h, IGF-1 and TGF-β with 4 h, IGF-1 at 48 h with maximal expression at 72 h that return to normal at 5 days.[197,211,214,255–257] In addition, the periosteal cellular layer is transformed from a quiescent to an osteogenic cell layer forming woven bone and the length of periosteal surface covered with osteoblasts was increased as early as day 2, with a peak at day 3 and a return to nonloaded control level by day 9. Mineral appositional rate is highest between 5 and 8 days.[176,208] Besides the production of

TABLE 1.20 WHO Definitions of Osteoporosis

Classification	BMD T-Score
Normal	above −1
Low bone mass (osteopenia)	−1 to −2.5
Osteoporosis, no fracture	−2.5
Severe osteoporosis, with fracture	−2.5

Source: WHO Technical Services Report 843, 1994.[109] With permission.

growth factors, production of prostaglandin and nitric oxide is likely to mediate in the process of bone modeling and remodeling.[255–257]

1.5.2 Osteoporosis[1,2,59,87,88,91,101–110]

Osteoporosis is a skeletal disease characterized by a decrease in bone strength (a decrease in bone mass and a deterioration in bone microarchitecture), which leads to an enhanced fragility of the skeleton and consequently to a greater risk of fracture. The most common sites of fracture are spine, hip, and wrist (Colles' fracture).

1.5.2.1 Definition

The World Health Organization (WHO) recommends a definition of osteoporosis on T-scores—standard deviations (SD) from the mean for young adult Caucasian women. T-score changes reflect in fracture risk. Osteoporosis is present when areal bone mineral density (aBMD) or areal bone mineral content (aBMC) is over 2.5 SD below the mean (−2.5 T-score). If fractures are present, the condition is called "severe osteoporosis." An aBMD or aBMC with T-scores between −1.0 and −2.5 SD are classified as an osteopenia, a decrease in the absence of fracture. Patients with osteopenia do not have increased fracture risk but may be at risk of developing osteoporosis in the future (Table 1.20).[109]

Osteoporosis is a disorder that will increase with an increase of life expectancy. The incidence is much higher in women than in men. Of those affected 80% are women and it is estimated up to three to four women out of ten over the age of 50 will have an osteoporosis-related fracture (postmenopausal osteoporosis) in their lifetime. The disease also affects males—one in eight men will have an osteoporosis-related fracture in his lifetime. The hip fracture rate is two times higher in women than men. In general, osteoporotic fractures in men begin to increase several decades later than in women. It has been reported that over 90% of hip fractures in the elderly are associated with a fall. In contrast, in vertebral fractures, in one study, only 10% of fractures were associated with lifting of heavy objects, whereas nearly 40% were associated with falling.[108]

The main cause of osteoporosis is the continuous loss of bone during life, which is exacerbated in women after menopause (postmenopausal osteoporosis) and men with andropause. The second contributory factor is a lesser bone production during adolescence, a decrease peak bone mass.[76] Other osteoporosis risk factors are listed in Table 1.21. Recently, Frost[103] differed with the WHO definition of osteoporosis. He suggested classifying osteoporoses by their mechanical pathogenesis instead of low bone mass. Defining osteoporoses as some arbitrarily low bone mass is like defining all anemias as an arbitrarily low hemoglobin; for medical needs, that definition is insufficient. It is necessary to know the cause of the anemia or osteoporosis, since effective treatment depends on this. His definitions are an attempt to assign different names to osteopenias with different biomechanical causes.

1. "True osteoporosis," a condition in which bone fragility would increase with normal physical activity to cause spontaneous fracture and/or bone pain mainly to the spine. Also falls could cause extremity bone fractures.
2. "Physiological osteopenia," a condition of reduced bone strength and "mass" fitting with reduced physical activities and muscle strength so well that fracture would not occur without falls or injuries. These fractures would affect extremity bones more than spine.

TABLE 1.21 Osteoporosis Risk Factors

- Low bone strength (low peak bone mass, low bone BMU and BMC
- Age: each decade with 1.6-fold increased risk
- Gender: female > male
- Decreased gonadal steroids (late menarche, early menopause, oophorectomy, gonadal loss, glucocorticoid suppression)
- Nutrition (low Ca and vitamin D intake; excess phosphorus, sodium, thyroid hormones, protein, caffeine)
- Impaired renal function (secondary hyperparathyroidism)
- Heredity/genetic factors (race, gender, lean habitus: low weight-to-height ratio; longer hip axis length)
- Immobilization (spinal cord injury, strokes)
- Lifestyle factors (mainly inactivity, cigarettes, alcohol)
- Diseases (renal, gastrointestinal, cirrhosis, connective tissue, malignancy, diabetes, hypercortisolism, hyperthyroidism, etc.)
- Medications (anticonvulsants, thiazides, thyroid hormones, gluocorticoids, etc.)
- Physical characteristics (mass, size, geometry, microarchitecture, compostion)
- Falls

Note: Many of these are age-related bone loss factors.

Source: Modified from Favus, M. J., *Primer of Metabolic Bone Diseases and Disorders of Mineral Metabolism,* 4th ed., Lippincott/Williams & Wilkins, Philadelphia, 1999, chap. 46[107] and 49.[106] With permission.

3. "Combination of physiological osteopenia and true osteoporosis states," a condition combining variants of 1 and 2.
4. "Transient osteopenia," a condition of local low "bone mass" due to serious injuries that usually resolve without treatment; fractures occur only from injuries.

1.5.2.2 Prevention and Treatment

There are two indications for drug use in osteoporosis: treatment and prevention. Hormone replacement therapy with estrogen is the mainstay of the treatment and/or prevention of osteoporosis and fracture. However, the Food and Drug Administration (FDA) has approved several antiresorptive or antiremodeling drugs recently (calcitonin, bisphosphonates, and a selective estrogen receptor modulator). The FDA criterion for approval of new drugs for the treatment of osteoporosis is the ability to reduce fracture rates; such clinical trials are costly. Although newer, more powerful antiremodeling drugs are coming, there are recent efforts directed toward drugs that stimulate bone formation.[106,108,144]

Genetics to osteoporosis. A single gene such as that which produces cystic fibrosis is unlikely to play a large role in osteoporosis. A gene may play an important role in osteoporosis from a public health perspective if the high-risk variants of the gene are relatively common and if the gene is modifiable by diet, physical activity, and medications. If not modifiable, knowledge of one's risk should provide motivation for better decision making toward prevention. A polygenic model is more likely, in which multiple genes act in conjunction with environmental factors to produce disease.[110]

1.5.2.3 Animal Models for *in Vivo* Experimentation in Osteoporosis Research[167]

The FDA has established guidelines for using animals in preclinical testing of agents for the prevention and treatment of postmenopausal osteoporosis. It recommends use of animals that have become osteopenic following ovariectomy, because of the relationship of human osteoporosis to estrogen depletion.[167] The FDA requires data from both the rat and a larger species, usually a nonhuman primate.[171] Studies of all rats must be of 12 months duration, but those in other species must be of 16 months duration, ostensibly equivalent to 4 years of human treatment, and include histological evaluation, bone density, and biochemical markers of bone turnover; also bone strength by biomechanical testing, as surrogates for the development of fragility fractures. Currently, guidelines for testing of bone anabolic agents are lacking.

The FDA has made a wise choice in requiring rat experiments during osteoporosis research. The ovariectomized rat model has become the gold standard for preclinical testing of agents. It is an excellent model that emulates most of the important clinical features of the estrogen-deplete adult human skeleton. These similarities include:

1. The development of osteopenia, primarily in poorly loaded cancellous bone sites with a rapid phase of bone loss during the early stages of estrogen deficiency.
2. Increased bone turnover is associated with the initial, rapid phase of bone loss induced by estrogen deficiency.
3. Estrogen treatment prevents osteopenia by depressing bone turnover in estrogen-deficient rats and humans.
4. Treatment with bisphosphonate compounds depresses bone turnover and protects against osteopenia in the early estrogen-deficient state.

Despite these similarities, there are limitations:

1. Skeletal processes of modeling and longitudinal bone growth that occur in growing rat skeletons but are absent in the adult human skeleton.
2. The rat is a poor animal model to study the intracortical effect on cortical bone. It has a low level of Haversian remodeling and ovariectomy-induced bone loss is slow to develop.
3. The ovariectomized rat does not develop fragility fractures.

The limitation of modeling and longitudinal bone growth in the rat can be minimized or eliminated by the use of the 10-month-old female rat. Bone elongation slows and epiphyseal closure occurs at important sampling sites in female rats by age 6 to 9 months[168] and some sites like the distal tibia closes at 3 months.[169] Furthermore, Erben[170] has shown that almost all the trabecular bone surfaces of the lumbar vertebral body are remodeling in 6- and 12-month-old female rats. The rats' low levels of Haversian remodeling present no immediate problem when testing agents because the bulk of the cortical bone loss is originating from the endocortical surface in both rats and human. Moreover, ovarectomy-induced cortical bone loss can be accelerated by the combination with immobilization. The rat, not unlike other animal models of osteoporosis, has no fragility fractures associated with the osteopenia. This shortcoming can be overcome by mechanical testing of various bone sites.[168]

Currently, the choice of a larger species for the testing of agents to treat osteoporosis is the nonhuman primate. Data on estrogen-depleted adult nonhuman primates are scarce,[167,171,172] but they are the large animal of choice when Haversian remodeling effects are to be studied. Data about ovariectomized mice are accumulating and the induced bone loss appears to be similar to rats.[167,173,174] The high state of usage of the ovariectomized rat model suggests that developing an ovariectomized mouse model as an alternative is not urgent. Nevertheless, the mouse skeleton is useful in revealing genetic markers that affect bone mass and structure and in studying glucocorticoid-induced osteoporosis.[168]

1.5.3 Age-Related Bone Loss[1–3,36,113–118,127,128]

Human bone mass increases during growth, plateaus in young adult life, and after about 30.5 years it begins to decrease. At 70 years, less than 70% of the young adult mass can remain (Fig. 1.35).[107]

The loss of bone is an universal component of aging. Reviews of the subject in humans suggest:

1. With advancing age, bone is lost from all parts of the skeleton, but not in equal amounts.
2. If onset of osteopenia is before skeletal maturity, almost complete recovery is possible. In adult life, the deficit becomes permanent.
3. The loss of bone begins approximately 10 years earlier and proceeds approximately twice as fast in women as in men.
4. Both cortical and trabecular bone are thinned primarily by the removal of bone at the endosteal surfaces adjacent to marrow (Fig. 1.36). Cortical bone loss occurs predominantly at the cortical-endosteal surface and to a small degree from the enlargement of the Haversian canals. A small net

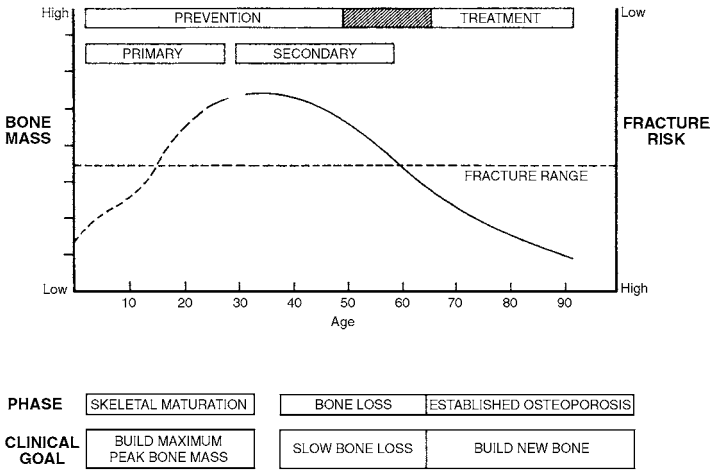

FIGURE 1.35 Diagram illustrating the course of bone gain and loss throughout life and fracture risk. Horizontal dotted line represents level below which structural failures or fractures are likely to occur. This level is reached earlier in women than in men because of the differences in the magnitude of the age-related bone loss. In both sexes, level is reached earlier in those who accumulate less bone (peak bone mass) during growth. (From Favus, M. J., *Primer on Metabolic Bone Diseases and Disorders of Mineral Metabolism,* 4th ed., Lippincott/Williams & Wilkins, Philadelphia, 1999, chap. 46. With permission.)

gain of bone at the periosteal surface[111,112] partially offsets this loss.[8,118] The net effect is the thinning of the cortex and expansion of the marrow cavity with enlargement of the bone circumference to a lesser degree.

5. Age-related cancellous bone loss is due to the imbalance of excess resorption relative to formation in bone remodeling (focal imbalance); the amount of bone replaced at the trabecular-endosteal remodeling sites appears to decrease with advancing age. The sequence of A $\rightarrow$R $\rightarrow$F is often uncoupled because trabecular plates are perforated or lost, thus reducing the available bone surface for bone formation. The net effect is loss of bone mass and architecture (reduced trabecular strength and connectivity) (Figures 1.36 and 1.37).
7. In many cases the reduction of bone mass in specific parts of the skeleton progresses to levels that are no longer sufficient to maintain mechanical support, a condition called "osteoporosis."

Bone quality changes with age. Other than the bone mass, such things as bone architecture and collagen cross-linkage and size and conformation of the calcium apatite crystals may be involved. Furthermore, there is disruption in bone cell signaling to activate osteoclastic and depress osteoblastic activities and the addition of periosteal surface with age. The overall effect is a loss of bone mass and strength. However, not all sites begin to change at the same time or rate.

1.5.4 Factors Influencing Age-Related Bone Loss and Fracture Risk[55–57,113–138,140–142]

Most fracture risk factors can fit into five major categories: age or age-related; genetics, environmental; endogenous hormones; chronic diseases; and physical characteristics of bone (Table 1.21).

The factors influencing age-related increase in bone loss and fracture risk are

1. Decrease in gonadal hormones;[57,88,116–118,154]
2. Decrease in calcium, vitamin D, and $1,25(OH)_2D_3$ and $1,25(OH)_2D_3$ resistance;[119–123]
3. Decrease in anabolic agents;[124]
4. Decrease in muscle mass (sarcopenia) and inactivity;[85,125–136]
5. Fatigue damage;[54,55,137]

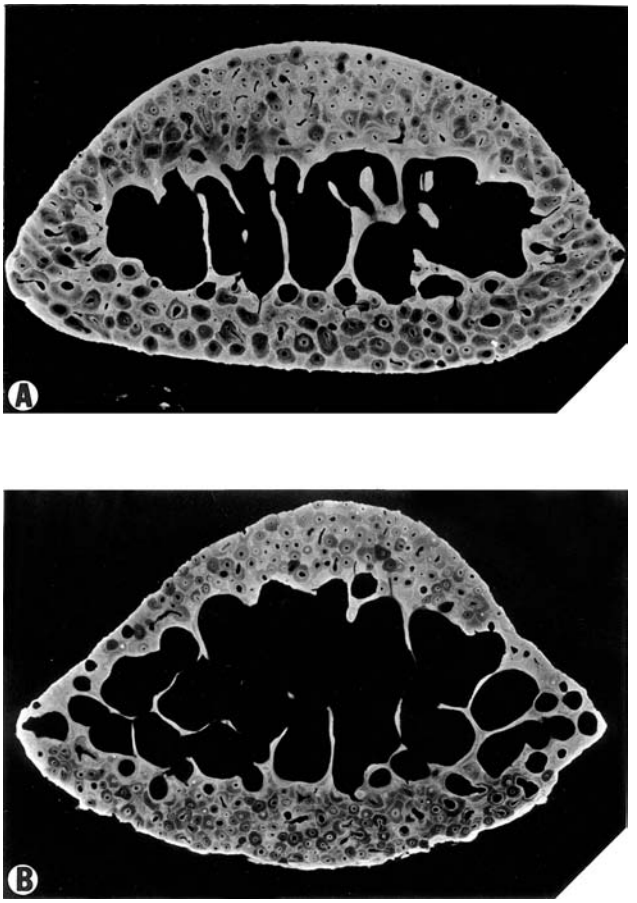

FIGURE 1.36 Changes in cortical bone as a function of age as seen in mocroradiograph of midshaft of rib from a 1.5–year-old (A) and a 15-year-old (B) female beagle dog. The thinning of the cortex and increase in intracortical porosity and thinning and loss of trabeculae are due to bone resorption initiated at bone surface adjacent to marrow. (From Weiss, L., Ed., *Cell and Tissue Biology, A Textbook of Histology,* Urban and Schwarzenberg, Baltimore, 1988. With permission.)

6. Osteocyte apoptosis and micropetrosis;[56,57,152,153,155]
7. Increased blood flow;[21] and
8. Decreased osteoblast cell lineage production due to adipocyte production, etc.[140,141]

These factors and others can contribute to decreased low bone mass and bone fragility and increased tendency to fall and this increased fracture risk (Fig. 1.38).

Estrogen deficiency has been recognized as a major cause of bone loss in the first decade after menopause. There is a strong relation of endogenous estrogen and bone mass in aged men and women. The potential pathways by which menopause lead to bone loss are summarized in Fig. 1.39.[117] Increased cytokine and tumor necrosis factor release that increased osteoclast recruitment and activity (some from reduced apoptosis), malfunction of vitamin D activation and calcium malabsorption due to falls in estrogen, and decreases in nitric oxide and TGF-β secretions are some of the causes for increased bone turnover. This along with the decrease in TGF-β, tumor necrosis factor (TNF-α) impairing osteoblast function resulting in remodeling-dependent bone loss are the cause of postmenopausal bone loss. The bone loss persists and results in high risk of fractures in those women whose peak bone mass was in the lower part of normal range.[57,88,116–118]

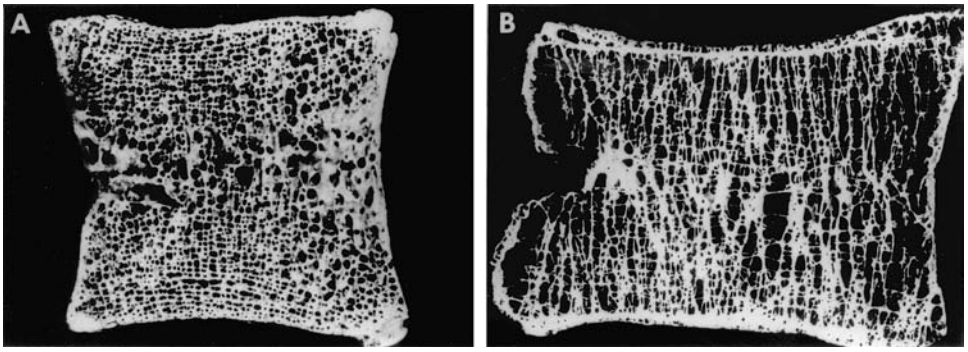

FIGURE 1.37 Photograph of a 2- to 3-mm-thick sagittal sections of the lumbar vertebral bodies from an 18-year-old male (A) and an 80-year-old female (B). (A) Horizontal elements consisting of perforated transverse plates (seen on edge) stabilize the closely spaced broad flat vertical plates. Note the broad platelike structure surrounding the basivertebral vein on the left and plate like structures on the right that form fuzzy triangles. The penetrated plates in the end zones are seen as continuous long transverse trabeculae. (B) An 80-year-old female with age-related bone loss. Note the thinned plates and rods, reduced number of horizontal intercommunicating elements, and the enlarged spacing between the vertical and horizontal elements. Original magnification × 2. (Courtesy of J. S. Arnold.) (From Weiss, L., Ed., *Cell and Tissue Biology, A Textbook of Histology*, Urban and Schwarzenberg, Baltimore, 1988. With permission.)

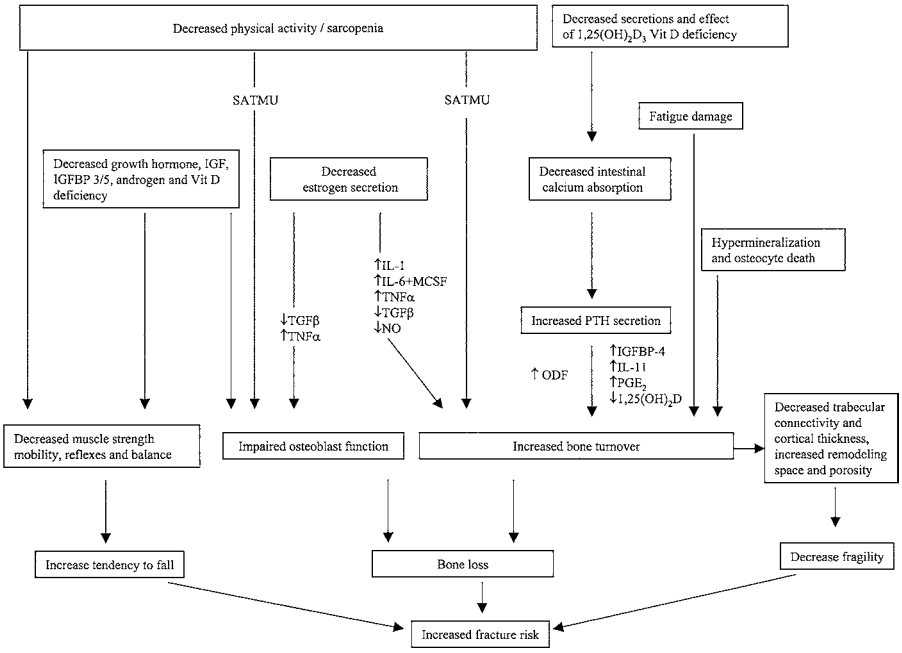

FIGURE 1.38 Factors influencing age-related bone loss and fracture risk. SATMU = skeletal adaptation to mechanical usage, IGF = insulin-like growth factors, IGFBF = insulin-like growth factor binding protein, IL = interleukin, MCSF = macrophage colony–stimulating factor, TNF = tumor necrosis factor, TGF = transforming growth factor, NO = nitric oxide, ODF = osteoclast diffferentiation factor, PGE_2 = prostaglandin E_2. See text for details.

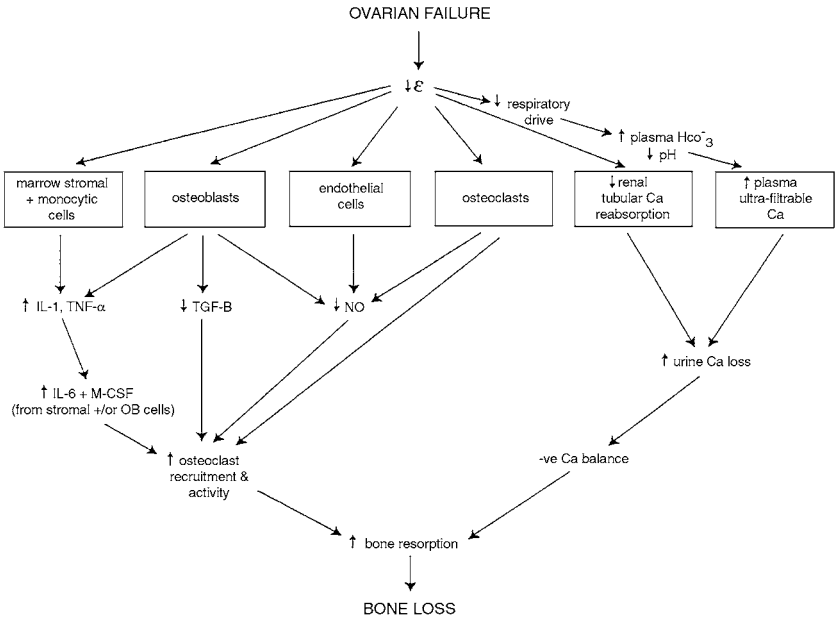

FIGURE 1.39 The potential pathways by which menopause (estrogen deficiency) leads to bone loss. E, estrogen; NO, nitric oxide; = ve, negative. (From Reid, I. R., in *Primer on the Metabolic Bone Diseases and Disorders of Mineral Metabolism,* 4th ed., Favus, M. J., Ed., Lippincott/Williams & Wilkins, 1999. With permission.)

Recent evidence indicates estrogen rather than testosterone levels may be needed for maintenance of bone mass in men suffering from age-related bone loss.[104] Serum estradiol levels in older men correlated closely with bone mass. Testosterone levels decline with age at a rate of about 1.2%/year. However, it is controversial whether male hormone levels are causally related to bone loss in elderly men. Nevertheless, reduced testosterone levels can increase fracture risk by directly decreasing muscle mass and indirectly affecting bone mass and increasing the tendency to fall.

The most common cause of increased bone resorption in the aged is calcium and vitamin D deficiency. Low calcium and vitamin D intake in elderly people will result in secondary hyperparathyroidism. Additionally, elderly people have low vitamin D intake, impaired renal conversion of 25(OH)D to $1,25(OH)_2D_3$, intestinal resistance to $1,25(OH)_2D_3$, or impaired binding of vitamin D to the vitamin D receptors. In addition, the reduced presence of cofactors of 1α-hydroxylase, namely, estrogen, testosterone, IGF, and their binding protein (IGFBP4 $\uparrow$, IGFBP 3/5 $\downarrow$) limits the synthesis of bone matrix proteins by osteoblasts. Elevated IGFBP4 secretion inhibits IGF I and II activity. Together, all these factors lead to reduced bone mass from an increase in PTH secretion (e.g., increased bone resorption) and reduced bone formation.[119–123] Furthermore, the lack of D hormone causes reduction in muscular strength, consequently increasing the tendency to fall and increase fracture risk.[120]

The hypothalmic–pituitary axis is affected by aging. Growth hormone (GH) secretion is reduced, resulting in lower levels of circulating IGFs than in younger people. These age differences are a function of an altered hypothalmic–pituitary set point due in part to changes in lifestyle and nutrition. GH has direct and indirect effects on bone and skeletal maturity. Indirectly, GH can enhance bone mass through its effect on muscle mass, ovary, testis, and calcium transport in gut and kidney (Fig. 1.40). In addition, GH can directly stimulate bone remodeling and increase endochondral growth through its action on osteoblasts. Both IGF I and II are mitogenic to bone cells and stimulate type I collagen synthesis, alkaline phosphatase, and osteocalcin. Large quantities of IGFs are stored in bone and released during active resorption, suggesting that the IGFs could couple formation to resorption. Although GH and IGF-I declines with age, several large cross-sectional studies failed to demonstrate an association

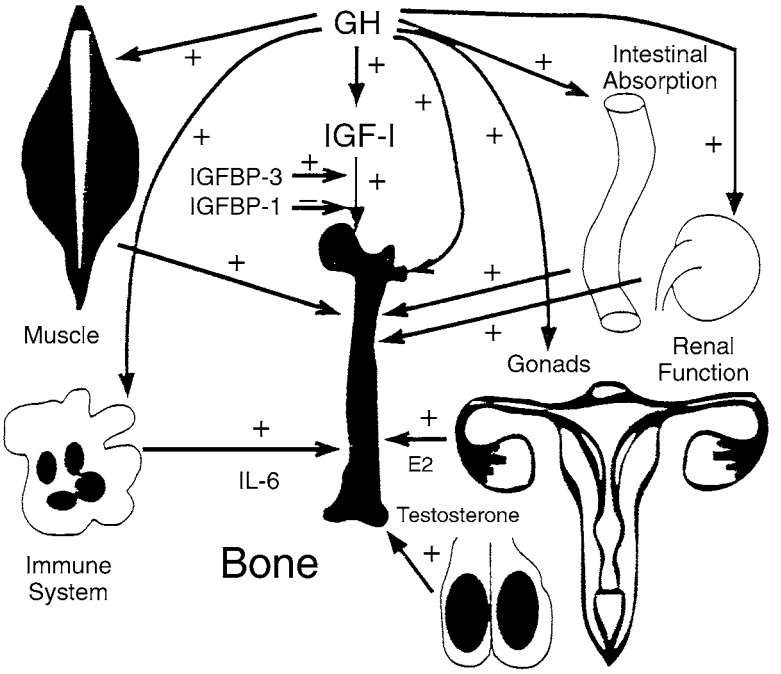

FIGURE 1.40 Summary of the effects of GH on various systems that influence directly or indirectly bone and calcium metabolism. (From Marcus, R. et al., Eds., *Osteoporosis,* Academic Press, San Diego, 1996. With permission.)

between IGF-I and age-related bone loss.[124] Nevertheless, reducing GH/IGF-I levels will directly decrease muscle mass and strength, indirectly decrease bone mass (strength), and increase the tendency to fall and increase fracture risk.

Muscle mass and strength increases during growth and plateaus in young adults and then usually declines so that at 80 years less than half the young adult muscle mass and strength remain, a sarcopenia. Since muscles apply the largest loads on bone and bones normally adapt their mass and strength to the largest load, the weak muscle forces on bone that had adapted to stronger young adult muscles should shift bone strains toward the remodeling threshold and cause slow bone loss. (See Section 1.5.1.) Thus, age-related changes in bone mass and strength lag and follow the age-related reduction in muscle mass and strength.[125–136] Additionally, loss of muscle mass and strength will increase the tendency to fall. The combined low bone mass and falls will increase fracture risk.

In inactive adults, decreasing muscle strength would follow and decrease the load on bones, placing such bone in partial disuse and shift their strains into the remodeling threshold region (MESr) to disuse mode remodeling to cause a slow loss of bone next to marrow where a typical disuse osteopenia would develop. (See Section 1.5.1.) "Vigorous" exercise in aged adults can raise strain above the remodeling threshold to activate conservation mode remodeling and stop further bone loss, but causing larger strain to reach the modeling threshold requires larger increases in muscle strength than most aged adults can achieve. Moreover, exercises that increase bone mass and strength in children and adolescents can reduce bone loss in aged adults. This difference is partially due to the numerous factors dampening age-related decrease in bone formation that makes bone seem unresponsive to physical exercise.[85,127]

Frost[137,138] originally proposed that remodeling occurs to repair microdamage in bone. He suggested that disruption of the canalicular connections occurred when microcracks traversed them and could provide the stimulus to initiate remodeling. Recent studies provide evidence this may in fact be true.[8,54,55] There is mounting support for the view that an intact gap junction intercellular communication (GJIC)

or osteocyte–canalicular system inhibits the activation of osteoclast resorption and that disruption of the system, like microcracks or osteocyte apoptosis, releases the inhibitions to resorption.[161] In support is the identification of an osteocyte-derived protein shown to inhibit osteoclastic resorption.[142]

There is growing evidence that osteocyte apoptosis is an important factor in interruping the osteocyte–canalicular transmission system (e.g., interrupting osteocyte inhibition of bone remodeling)[161] and activating remodeling sites. Recent studies show that

1. Osteocyte apoptosis is induced by bone fatigue,
2. The apoptotic response is localized in regions containing microcrack,
3. Osteoclastic resorption of bone after fatigue coincides with regions of osteocyte apoptosis,
4. Osteocyte apoptosis coincides with bone resorption in growing bones,
5. There is a positive correlation between osteocyte apoptosis and increased activation frequency found in postmenopausal osteoporosis, and
6. Osteocyte death by apoptosis occurs with reduced mechanical loading.[56,57,152,155–157]

The activation of bone resorption would produce the result of replacing dead bone with less new bone with viable osteocytes. Furthermore, gradual and diffuse osteocyte death has been reported with aging that would lead to increased remodeling and bone loss. Futhermore, osteocyte death and the consequence of perilacunar hypermineralization (or micropetrosis)[153] would make bones more brittle and susceptible to fatigue damage and subsequent bone remodeling–dependent bone loss.

This is an area of neglected research. There have been reports of decreased bone marrow blood flow in growing animals, but recent studies cannot be found for aged humans and animals. There are numerous papers on the increase in bone blood flow in paraplegia, ovariectomy, and orchiectomy-induced bone loss. The sinusoidal compartment is reduced, contributing partly to increased blood flow. On the contrary, vasodilatory factors such as PTH, PGE_2, NO, which are bone anabolic agents, reduce arterial blood pressure and bone blood flow.[16-21] Whether one can assume that aging causes an increased bone blood flow, a possible contributor to age-related bone loss needs more study.

The bone marrow stroma, the stromal system, represents the local reservoir of osteoblastic lineage cells that participate in bone formation. A unique feature of the system is its ability to convert to other phenotypes comprised in the system (e.g., bone, hematopoiesis, and adipocytes). With aging, there is a shift in balance from a stroma that activity supports osteogenesis and active hematopoieses to one that is primarily adipogenic and an altered form of hematopoieses. The cause of this shift is believed to be mediated by steroid and peptide hormones, members of the TGF-β superfamily cytokines and mechanical usage. Aged stromal cells lack self-renewal of the progenitor population, loss of plasticity, altered responsiveness to external signal through changes in receptor content, receptor activity, and intercellular pathways with age, which contribute to the decrease in bone formation.[140,141]

Nutritional factors may play a role in age-related bone loss. Malnutrition (reduced protein intake), vitamin K deficiency, dehydroepiandrosterone (DHEA) (known to decrease with age and are anabolic on lean mass), and intercurrent disease (affecting gastrointesterial tract and absorption, kidney, diabetes, connective tissue, and neoplastic disease causing tissue wasting) may contribute to increased risk. Environmental agents such as smoking, alcohol, glucocorticoids, and anticonvulsants may contribute to an excessive rate of bone loss in some elderly persons (Table 1.21).[2,106,107,113,114,164] A controversial issue is the hypothesis that genetic programming, when triggered, may lead to bone loss.

Dedication

Most appropriately, this chapter is dedicated to Rebecca Burggraaf Setterberg, a long-term research associate of the "Utah Bone Group," who has put in many uncompensated hours to help the author meet the promised deadline. No dedication to Becky can fail to note her tremendous contribution as "Mother" to the Sun Valley Hard Tissue Workshops.

Acknowledgments

The author wishes to acknowledge the contribution of Harold M. Frost, M.D., who has provided numerous discussions over many years, comments, and advice on matters discussed in this chapter. The author wishes to acknowledge Wei Yao, M.D., for her invaluable assistance in generating several of the figures and tables.

References

1. Jee, W. S. S., The skeletal tissues, in *Cell and Tissue Biology, A Textbook of Histology,* Weiss, L., Ed., Urban and Schwarzenberg, Baltimore, 1988, chap. 7.
2. Frost, H. M., *Introduction to a New Skeletal Physiology,* Vol. I and II, Pajaro Group, Pueblo, 1995.
3. Jee, W. S. S., Structure and function of bone tissue, in *Orthopaedics, Principles of Basic and Clinical Science,* Bronner, F. and Worrell, R. V., Eds., CRC Press, Boca Raton, FL, 1999, chap. 1.
4. Baron, R., Anatomy and ultrastructure of bone, in *Primer on the Metabolic Bone Disease and Disorder of Mineral Metabolism,* 4th ed., Favus, M. J., Ed., Lippincott/Williams & Wilkins, 1999, chap. 1.
5. Parfitt, A. M., The physiologic and clinical significance of bone histomorphometric data, in *Bone Histomorphometry: Techniques and Interpretation,* Recker, R. R., Ed., CRC Press, Boca Raton, FL, 1983, 143.
6. Schenk, R. K., Felix, R., and Hofstetter, W., Morphology of connective tissue: bone, in *Connective Tissue and Its Heritable Disorders: Molecular, Genetic and Medical Aspects,* Royce, P. M. and Steinmann, B., Eds., Wiley-Liss, New York, 1993, 85.
7. Ericksen, E. F., Axelrod, D. W., and Melsen, F., *Bone Histomorphology,* Raven Press, New York, 1994.
8. Martin, R. B. and Burr, D. B., Mechanical adaptation, in *Sructure, Function and Adaptation of Compact Bone,* Raven Press, New York, 1989, chaps. 2, 4, 7, and 8.
9. Marotti, G., Palazzini, S., Palumbo, D., and Ferretti, M., Ultrastructural evidence of the existence of a dentritic network throughout the cells of the osteogenic lineage: the novel concept of wiring- and volume-transmission in bone, *Bone,* 19, 151S, 1996.
10. Donahue, H. J., Gap junctional intercellular communication in bone: a cellular basis for mechanostat set point, *Calcif. Tissue Int.*, 62, 85, 1998.
11. Gehron-Robey, P. and Boskey, A. L., The biochemistry of bone, in *Osteoporosis,* Marcus, F., Feldman, D., and Kelsey, J., Eds., Academic Press, San Diego, 1996, chap. 4.
12. Lian, J. B., Stein, G. S., Canalis, E., Gehron-Robey, P., and Boskey, A. L., Bone formation: osteoblast lineage cells, growth factors, matrix proteins and the mineralization process, in *Primer on the Metabolic Bone Diseases and Disorders of Mineral Metabolism,* 4th ed., Favus, M. J., Ed., Lippincott/Williams & Wilkins, Philadelphia, 1999, chap. 3.
13. Gorski, J. P., Is all bone the same? Distinctive distributions and properties of non-collagenous matrix proteins in lamellar and woven bone imply the existence of different underlying osteogenic mechanisms, *Crit. Rev. Oral Biol.,* 9, 201, 1998.
14. Khosla, S. and Kleerekoper, M., Biochemical markers and bone turnover, in *Primer on the Metabolic Bone Diseases and Disorders of Mineral Metabolism,* 4th ed., Favus, M. J., Ed., Lippincott/Williams & Wilkins, 1999, chap. 22.
15. Kelly, P. J., Montgomery, R. J., and Bronk, J. T., Reaction of the circulatory system to injury and regeneration, *Clin. Orthop.,* 254, 275, 1990.
16. Verhas, M., Martinello, Y., Mone, M., Heilporn, A., Bergmann, P., Tricot, A., and Schoutens, A., Demineralization and pathological physiology of the skeleton in paraplegic rats, *Calcif. Tissue Int.,* 30, 83, 1980.

17. Schoutens, A., Verhas, M., L'Hermite, M., Tricot, A., Verschaeren, A., Dourov, N., and Heilporn, A., Increase of bone blood flow, an initial step of bone demineralization in the rat, *Calcif. Tissue Int.,* 36(Suppl. 2), S3, 1984.
18. Verhas, M., Schoutens, A., L'Hermite-Baleriaux, M., Dourov, N., Verschaeren, A., Mone, M., and Heilporn.A., The effect of orchiectomy on bone metabolism in aging rats, *Calcif. Tissue Int.,* 39, 74, 1986.
19. Kapitola, J., Kubickova, J., and Andrle, J., Blood flow and mineral content of the tibia of female and male rats: changes following castration and/or administration of estradiol or testosterone, *Bone,* 16, 69, 1995.
20. Cochrane, E. and McCarthy, I. D., Rapid effects of parathyroid hormone (1-34) and prostaglandin E_2 on bone blood flow and strontium clearance in the rat *in vivo, J. Endocrinol.,* 131, 359, 1991.
21. Kita, K., Kawai, K., and Hirohata, K., Changes in bone marrow blood flow with aging, *J. Orthop. Res.,* 5, 569, 1987.
22. Thurston, T. J., Distribution of nerves in long bones as shown by silver impregnation, *J. Anat.,* 134, 719, 1982.
23. Miller, M. R. and Kashara, M., Observations on the innervation of human long bones, *Anat. Rec.,* 145, 13, 1963.
24. Serre, C. M., Farlay, D., Delmas, P. D., and Chenu, C., Evidence for a dense and intimate innervation of the bone tissue, including glutamate-containing fibers, *Bone,* 25, 623, 1999.
25. Mason, D. J., Suva, L. J., Genever, P. G., Patton, A. J. Steuckle, S., Hillam, R. A., and Skerry, T. M., Mechanically regulated expression of a neural glutamate transporter in bone: a role for excitatory amino acids as osteotropic agents, *Bone,* 20, 199, 1997.
26. Chenu, C., Serre, C. M., Raynal, D., Burt-Pichet, B., and Delmas, P. D., Glutamate receptors are expressed by bone cells and are involved in bone resorption, *Bone,* 22, 295, 1998.
27. Patton, A. J., Genever, P. G., Birch, M. A., Suva, L. J., and Skerry, T. M., Expression of an *N*-methyl-*D*-aspartate-type receptor by human and rat osteoblasts and osteoclasts suggest a novel glutamate signaling pathway in bone, *Bone,* 22, 645, 1998.
28. Mayer, M. L. and Westbrook, G. L., The physiology of excitatory amino acids in the vertebrate central nervous system, *Prog. Neurobio.,* 28, 197, 1987.
29. Rodan, G. A. and Rodan, S. B., The cells of bone, in *Osteoporosis: Etiolology, Diagnosis and Management,* 2nd ed., Riggs, B. L. and Melton III, L. J., Eds., Lippincott-Raven, Philadelphia, 1995, chap. 1.
30. Teitelbaum, S. L., Tondravi, M. M., and Ross, F. P., Osteoclast Biology, in *Osteoporosis,* Marcus, R., Feldman, D., and Kelsey, J., Eds., Academic Press, San Diego, 1996, chap. 3.
31. Suda, T., Takahashi, N., and Martin, T. J., Modulation of osteoclast differentiation, *Endocrinol. Rev.,* 13, 66, 1992.
32. Roodman, G. D., Advances in bone biology: the osteoclast, *Endocrinol. Rev.,* 17, 308–332, 1996.
33. Baron, R., Chakraborty, M., Chatterjee, D., Horne, W., Lomri, A., and Ravesloot, J.-H., Biology of the osteoclast, in *Physiology and Pharmacology of Bone,* Mundy, G. R., and Martin, T. J., Eds., Springer-Verlag, New York, 1993, 111.
34. Mundy, F. R., Bone remodeling, in *Primer on the Metabolic Bone Diseases and Disorders of Mineral Metabolism,* 4th ed., Favus, M. J., Ed., Lippincott/Williams & Wilkins, 1999, chap. 4.
35. Puzas, E. J. and Lewis, G. D., Biology of osteoclasts and osteoblasts, in *Orthopaedics. Principles of Basic and Clinical Science,* Bronner, F., and Worrell, R. V., Eds., CRC Press, Boca Raton, FL, 1999, chap. 3.
36. Pacifici, R., Aging and cytokine production, *Calcif. Tissue Int.,* 65, 345, 1999.
37. Lian, J. B., and Stein, G. S., Osteoblast biology, in *Osteoporosis,* Marcus, R., Feldman, D., and Kelsey, J., Eds., Academic Press, San Diego, 1996, chap. 2.
38. Marie, P. J., Cellular and molecular alterations of osteoblasts in human disorders of bone formation, *Histol. Histopathol.,* 14, 525, 1999.

39. Barnes, G. L., Kostenuik, P. J., Gerstenfield, L. C., and Einhorn, T. A., Perspective, growth factor regulation of fracture repair, *J. Bone Mineral Res.,* 14, 1805, 1999.
40. Recker, R. R., Ed., *Bone Histomorphometry: Techniques and Interpretation,* CRC Press, Boca Raton, FL, 1983.
41. Parfitt, A. M., Drezner, M. K., Glorieux, F. H., Kanis, J. A., Malluche, H., Meunier, P. J., Ott, S. M., and Recker, R. R., Bone histomorphometry: standardization of nomenclature, symbols and units. Report of the ASBMR histomorphometry nomenclature committee, *J. Bone Mineral Res.,* 2, 595, 1987.
42. Frost, H. M., Tetracycline-based histological analysis of bone remodeling, *Calcif. Tissue Res.,* 3, 211, 1969.
43. Harris, W. H., Haywood, E. A., Lavorgna, J., and Hamblen, D. L., Spatial and temporal variations in cortical bone formation in dogs, *J. Bone Joint Surg.,* 50A, 118, 1968.
44. Miller, S. C. and Jee, W. S. S., The bone lining cell: a distinct phenotype? *Calcif. Tissue Int.,* 41, 1, 1992.
45. Merz, W. and Schenk, R., A quantitative histological study on bone formation in human cancellous bone, *Acta Anat.,* 76, 1, 1970.
46. Dobnig, H. and Turner, R., Evidence that intermittent treatment with parathyroid hormone increase bone formation in adult rats by activation of bone lining cells, *Endocrinology,* 136, 3632, 1995.
47. Jee, W. S. S. and Ma, Y. F., The *in vivo* anabolic actions of prostaglandins in bone, *Bone,* 21, 297, 1997.
48. Miller, S. C., Bowman, B. M., Smith, J. M., and Jee, W. S. S., Characterization of endosteal bone-lining cells from fatty marrow bone sites in adult beagles, *Anat. Rec.,* 198, 163, 1980.
49. Talmage, R. V., Calcium homeostasis-calcium transport-parathyroid action, *Clin. Orthop. Relat. Res.,* 67, 210, 1969.
50. Holtrop, M. E. and Weinger, J. M., Ultrastructural evidence for a transport system in bone, in *Calcium, Parathyroid Hormone and Calcitonins,* Talmage, R. V. and Munson, P. L., Eds., Excerpta Medica, Amsterdam, 1972, chap. 2.
51. Lanyon, L. E., Osteocytes, strain detection, bone modeling and remodeling, *Calcif. Tissue Int.,* 53 (Suppl.), 102, 1993.
52. Lanyon, L. E., Using functional loading to influence bone mass and architecture, *Bone,* 18, 375, 1996.
53. Schiller, P. C., Parmender Mehta, P., Roos, B. A., and Howard, G. A., Hormonal regulation of intercellular communication: parathyroid hormone increases connexin 43 gene expression and gap junctional communication in osteoblastic cells, *Mol. Endocrinol.,* 6, 1443, 1992.
54. Mori, S. and Burr, D. B., Increased intracortical remodeling following fatigue damage, *Bone,* 14, 103, 1993.
55. Bentolila, V., Boyce, T. M., Fyhrie, D. P., Drumb, R., Skerry, T. M., and Schaffler, M. B., Intracortical bone remodeling in adult rat long bones after fatigue loading, *Bone,* 23, 275, 1998.
56. Noble, B., Stevens, H., Loveridge, N., and Reeve, J., Identification of apoptotic changes in osteocytes in normal and pathological human bone, *Bone,* 20, 273, 1997.
57. Tomkinson, A., Reeve, J., Shaw, R. W., and Noble, B. S., The death of osteocyte by apoptosis in human bone is observed following estrogen withdrawal by GnRH analog, *J. Clin. Endocrinol. Metab.,* 82, 3128, 1997.
58. Frost, H. M., *Bone Modeling and Skeletal Modeling Errors,* Charles C Thomas, Springfield, 1973.
59. Frost, H. M., *Osteoporoses: New Concepts and Some Implications for Future Diagnosis, Treatment and Research* (based on insights from the Utah paradigm), Ernst Schering Research Foundation, Berlin, 1998, 7.
60. Frost, H. M., Bone development during childhood, a tutorial (some insights of a new paradigm), in *Paediatric Osteology,* Schönau, E., Ed., Elsevier, Amsterdam, 1996, 3.

61. Frost, H. M., A determinant of bone architecture: the minimum effective strain, *Clin. Orthop. Relat. Res.,* 175, 286, 1983.
62. Cowin, S. C., Mechanical modeling of the stress adaptation process in bone, *Calcif. Tissue Int.,* 36, 598, 1984.
63. Carter, D. R., Harris, W. H., Vasu, R., and Caler, W. E., The mechanical and biological response of cortical bone to *in vivo* strain histories, in *Mechanical Properties of Bone,* Cowin, S. C., Ed., ASME, New York, 1981, chap. 6.
64. Carter, D. R., The relationship between *in vivo* strains and cortical bone remodeling, *Criti. Rev. Biomed. Eng.,* 87, 1, 1982.
65. Frost, H. M., Bone "mass" and the "mechanostat," a proposal, *Anat. Rec.,* 219, 1, 1987.
66. Frost, H. M., The mechanostat: a proposed pathogenic mechanism of osteoporoses and the bone mass effects of mechanical and nonmechanical agents, *Bone Miner.,* 2, 73, 1987.
67. Frost, H. M., Structural adaptations to mechanical usage (SATMU): 1. Redefining Wolff's law: the bone modeling problem, *Anat. Rec.,* 226, 403, 1990.
68. Parfitt, A. M., The skeletal heterogeneity and the purposes of bone remodeling: implications for the understanding of osteoporosis, in *Osteoporosis,* Marcus, R., Feldman, D., and Kelsey, J., Eds., Academic Press, San Diego, 1996, chap. 12.
69. Frost, H. M., Structural adaptations to mechanical usage (SATMU): 2. Redefining Wolff's Law: The bone remodeling problem, *Anat. Rec.,* 226, 414, 1990.
70. Marotti, G., Map of bone formation rate values recorded throughout the skeleton of the dog, in *Proceedings of First Workshop on Bone Morphometry,* Jaworski, Z. F. G., Ed., University of Ottawa Press, Ottawa, 1976, 202.
71. Kimmel, D. B. and Jee, W. S. S., A quantitative histologic study of bone turnover in young adult beagles, *Anat. Rec.,* 203, 31, 1982.
72. Burr, D. B., Martin, R. B., Schaffler, M. B., and Radin, E. L., Bone remodeling in response to *in vivo* fatigue damage, *J. Biomech.,* 18, 189, 1985.
73. Frost, H. M. and Jee, W. S. S., Perspectives: a vital biomechanical mode of endochondral ossification mechanism, *Anat. Rec.,* 240, 435, 1994.
74. Wronski, T. J., Smith, J. M., and Jee, W. S. S., The microdistribution and retention of injected ^{239}Pu on trabecular bone surfaces of the beagle: implications for the induction of osteosarcoma, *Radiat. Res.,* 83, 74, 1980.
75. Wronski, T. J., Smith, J. M., and Jee, W. S. S., Variations in mineral apposition rate of trabecular bone within the beagle skeleton, *Calcif. Tissue Int.,* 33, 583, 1981.
76. Heaney, R. P. and Matkovic, V., Inadequate peak bone mass, in *Osteoporosis, Etiology, Diagnosis and Management,* 2nd ed., Riggs, B. L. and Melton III, L. J., Eds., Lippincott-Raven, Philadelphia, 1995, chap. 5.
77. O'Connor, J. A., Lanyon, L. E., and MacFie, H., The influence of strain rate on adaptive bone remodeling, *J. Biomech.,* 15, 767, 1982.
78. Jee, W. S. S., Li, X. J., and Ke, H. Z., The skeletal adaptation to mechanical usage in the rat, *Cells Mater.,* Suppl., 1, 131, 1991.
79. Jee, W. S. S. and Frost, H. M., Skeletal adaptations during growth, *Triangle,* 31, 77, 1992.
80. Forwood, M. R. and Turner, C. H., Skeletal adaptations to mechanical usage: results from tibial loading studies in rats, *Bone,* Suppl., 17, 197, 1995.
81. Kiratli, B. J., Immobilization osteopenia, in *Osteoporosis,* Marcus, R., Feldman, D., and Kelsey, J., Eds., Academic Press, San Diego, 1996, chap. 42.
82. Carter, D. R., van der Meulen, M. C. H., and Beaupre, G. S., Skeletal development: mechanical consequences of growth, aging and disease, in *Osteoporosis,* Marcus, R., Feldman, D., and Kelsey, J., Eds., Academic Press, San Diego, 1996, chap. 13.
83. Mosley, J. R. and Lanyon, L. E., Strain rate as a controlling influence on adaptive modeling in response to dynamic loading of the ulna in growing male rats, *Bone,* 23, 313, 1998.

84. Rubin, C. T. and Rubin, J., Biomechanics of bone, in *Primer on the Metabolic Bone Diseases and Disorders of Mineral Metabolism,* 4th ed., Favus, M. J., Ed., Lippincott/Williams & Wilkins, 1999, chap. 5.
85. Marcus, R., Physical activity and regulation of bone mass, in *Primer on the Metabolic Bone Diseases and Disorders of Mineral Metabolism,* 4th ed., Favus, M. J., Ed., Lippincott/Williams & Wilkins, 1999, chap. 48.
86. Frost, H. M., Perspective, on our age-related bone loss: insights from a new paradigm, *J. Bone Miner. Res.,* 12, 1539, 1997.
87. Frost, H. M., On defining osteopenias and osteoporoses: problems! Another view (with insights from a new paradigm), *Bone,* 20, 385, 1997.
88. Frost, H. M., On rho, a marrow mediator and estrogen: their roles in bone strength and "mass" in human females, osteopenias and osteoporoses (insights from a new paradigm), *J. Bone Miner. Metab.,* 16, 113, 1998.
89. Rodan, G. A., Mechanical loading, estrogen deficiency and the coupling of bone formation to bone resorption, *J. Bone Miner. Res.,* 6, 527, 1991.
90. Burr, D. B. and Martin R. B., Errors in bone remodeling: toward a unified theory of metabolic bone disease, *Am. J. Anat.,* 186, 186, 1989.
91. Frost, H. M., The pathomechanics of osteoporoses, *Clin. Orthop. Relat. Res.,* 200, 198, 1985.
92. Jee, W. S. S., Ma, Y. F., Li, M., Liang, X. Q., Lin, B. Y., Li, X. J., Ke, H. Z., Mori, S., Setterberg, R. B., and Kimmel, D. B., Sex steroids and prostaglandin in bone metabolism, in *Sex Steroids and Bone,* Ziegler, R., Pfeilschifter, J., and Brautigam, M., Eds., Springer, Berlin, 1994, 119.
93. Yeh, J. K., Aloia, J. F., and Chen, M., Growth hormone administration potentiates the effect of treadmill exercise on long bone formation but not on the vertebrae in middle-aged rats, *Calcif. Tissue Int.,* 54, 38, 1994.
94. Tam, C. S., Akhter, M. P., Johnston, E., Covey, M. A., Pearse, A., Ringer, L., and Recker, R. R., A new peptide for bone formation with its action related to exercise, *Bone,* 23, S613, 1998.
95. Tang, L. Y., Raab-Cullen, D. M., Yee, J. A., Jee, W. S. S., and Kimmel, D. B., Prostaglandin E2 increases the skeletal response to mechanical loading, *J. Bone Miner. Res.,* 12, 276, 1997.
96. Chow, J. W. M., Fox, S. W., Jagger C. J., and Chambers, T. J., Role for parathyroid hormone in mechanical responsiveness of rat bone, *Am. J. Physiol.,* 274, E146, 1998.
97. Mosekilde, L., Thomsen, J. S., Orhii, P. B., McCarter, R. J., Meya, W., and Kalu, D. N., Additive effect of voluntary exercise and growth hormone treatment on bone strength assessed at four different skeletal sites in an aged rat model, *Bone,* 244, 71, 1999.
98. Gasser, J. A., Quantitative assessment of bone mass and geometry by pQCT in rats *in vivo* and site specificity of changes at different skeletal sites, *J. Jpn Soc. Bone Morphometry,* 7; 107–114, 1997.
99. Gasser, J. A., Modulation of strain sensing: a new approach for the treatment of osteoporosis, in *Musculoskeletal Interactions,* Vol. 2, Lyritis, G. P., Ed., Hylonome Editions, Athens, 1999, 77.
100. Jee, W. S. S., Zhou, H., Yao, W., Cui, L., and Ma, Y. F., The interaction of mechanical loading and bone anabolic agents, in *Osteoporosis Update 1999, Proceedings, Third International Congress on Osteoporosis,* Xi'an, P.R. China, Beijing, China, 1999, 78.
101. Marcus, R., Feldman, D., and Kelsey, J., Eds., *J. Osteoporosis,* Academic Press, San Diego, 1996.
102. Eastell, R., Pathogenesis of postmenopausal osteoporosis, in *Primer on the Metabolic Bone Diseases and Disorders of Mineral Metabolism,* 4th ed., Favus, M. J., Ed., Lippincott/Williams & Wilkins, 1999, chap. 47.
103. Frost, H. M., "Osteoporosis": a rationale for further definitions? *Calcif. Tissue Int.,* 62, 89, 1998.
104. Orwell, E. S., Osteoporosis in men, in *Primer on the Metabolic Bone Diseases and Disorders of Mineral Metabolism,* 4th ed., Favus, M. J., Ed., Lippincott/Williams & Wilkins, 1999, chap. 54.
105. Lukert, B. P., Glucocorticoid-induced osteoporosis, in *Primer on the Metabolic Bone Diseases and Disorders of Mineral Metabolism,* 4th ed., Favus, M. J., Ed., Lippincott/Williams & Wilkins, 1999, chap. 55.

106. Lindsay, R., Prevention of osteoporosis, in *Primer on the Metabolic Bone Diseases and Disorders of Mineral Metabolism,* 4th ed., Favus, M. J., Ed., Lippincott/Williams & Wilkins, 1999, chap. 49.
107. Wasnich, R. D., Epideminology of osteoporosis, in *Primer on the Metabolic Bone Diseases and Disorders of Mineral Metabolism,* 4th ed., Favus, M. J., Ed., Lippincott/Williams & Wilkins, 1999, chap. 46.
108. Dawson-Hughes, B., Pharmocologic treatment of postmenopausal osteoporosis, in *Primer on the Metabolic Bone Diseases and Disorders of Mineral Metabolism,* 4th ed., Lippincott/Williams & Wilkins, Philadelphia, 1999, chap. 53.
109. WHO Study Group, Assessment of fracture risk and its applications to screening for postmenopausal osteoporosis, WHO Technical Report Series 843, WHO, Geneva, 1994.
110. Cooper, G. S., Editorial. Genetic studies of osteoporosis! What have we learned? *J. Bone Miner. Res.,* 14, 1646, 1999.
111. Garn, S. M., Rohmann, C. G., and Wagner, B., Bone loss, a general phenomenon in man, *Fed. Proc.,* 26, 1729, 1967.
112. Garn, S. M., Wagner, B., Rohmann, C. G., and Ascoli, W., Further evidence for continuing bone expansion, *Am. J. Physiol. Anthropol.,* 28, 219, 1968.
113. Blumshon, A. and Eastell, R., Age-related factors, in *Osteoporosis, Etiology, Diagnosis and Management,* 2nd ed., Riggs, B. L. and Melton III, L. J., Eds., Lippincott-Raven, Philadelphia, 1995, chap. 7.
114. Rosen, C. J. and Kiel, D. P., The aging skeleton, in *Primer on the Metabolic Bone Diseases and Disorders of Mineral Metabolism,* 4th ed., Favus, M. J., Ed., Lippincott/Williams & Wilkins, 1999, chap. 9.
115. Sherman, S., Heaney, R. P., Parfitt, A. M., Hadley, E. C., and Dutta, C., Eds., NIA Workshop on Aging and Bone Quality, *Calcif. Tissue Int.,* 53, Supplement 1, 1993.
116. Lindsay, R., Estrogen deficiency, in *Osteoporosis, Etiology, Diagnosis and Management,* 2nd ed., Riggs, B. L. and Melton III, L. J., Lippincott-Raven, Philadelphia, 1995, chap. 6.
117. Reid, I. R., Menopause, in *Primer on the Metabolic Bone Diseases and Disorders of Mineral Metabolism,* 4th ed., Favus, M. J., Ed., Lippincott/Williams & Wilkins, 1999, chap. 8.
118. Frost, H. M., On the estrogen-bone relationship and postmenopausal bone loss: a new model, *J. Bone Miner. Res.,* 14, 1473, 1999.
119. Peacock, M., Effects of calcium and vitamin D insufficiency on the skeleton, *Osteoporosis Int.,* 8, S45, 1998.
120. Schacht, E., Rationale for treatment of involutional osteoporosis in women and for prevention and treatment of corticosteroid-induced osteoporosis with alfacalcidol, *Calcif. Tissue Int.,* 65, 317, 1999.
121. Lau, K. H., and Baylink, D. J., Vitamin D therapy of osteoporosis: plain vitamin D therapy versus active vitamin D analog (D-hormone) therapy, *Calcif. Tissue Int.,* 65, 295, 1999.
122. Holick, M., Vitamin D: photodensity, metabolism mechanism of action and clinical applications, in *Primer on the Metabolic Bone Diseases and Disorders of Mineral Metabolism,* 4th ed., Favus, M. J., Ed., Lippincott/Williams & Wilkins, 1999, chap. 15.
123. Hollis, B. W., Clemens, T. L., and Adams, J. S., Vitamin D metabolites, in *Primer on the Metabolic Bone Diseases and Disorders of Mineral Metabolism,* 4th ed., Favus, M.J., Ed., Lippincott/Williams & Wilkins, 1999, chap. 21.
124. Rosen, C. and Wuster, C., Growth hormone, insulin-like growth factor. Potential applications and limitations in the management of osteoporosis, in *Osteoporosis,* Marcus, R., Feldman, D., and Kelsey, J., Eds., Academic Press, San Diego, 1996, chap. 69.
125. Buckwalter, J. A., Woo, S. L. Y., Goldberg, V. M., Hadley, E. C., Booth, R., Oregema, T. R., and Eyre, D. R., Soft tissue aging and musculoskeletal function, *J. Bone Joint. Surg.,* 75A, 1533, 1993.
126. Schönau, E., Westermann, F., Mokow, E., Scheidhauer, K., Werhahn, E., Stabrey, A., and Müller-Berghaus, J., The functional muscle-bone-unit in health and disease, in *Paediatric Osteology. Prevention of Osteoporosis—A Paediatric Task?* Schönau, E. and Matkovic V., Eds., Excerpta Medica, Amsterdam, 1998, 191.

127. Frost, H. M., Perspective, why do bone strength and "mass" in aging adults become unresponsive to vigorous exercise? Insights of the Utah paradigm, *J. Bone Miner. Metab.,* 17, 90, 1999.
128. Burr, D. B., Muscle strength, bone mass and age related bone loss, *J. Bone Miner. Res.,* 12, 1547, 1997.
129. Jee, W. S. S., The interactions of muscles and skeletal tissue, in *Musculoskeletal Interactions,* Vol. II, Lyritis, G. P., Ed., Hylonome Editions, Athens, 1999, 35.
130. Aniansson, A., Zetterberg, C., Hedberg, M., and Henriksson K., Impaired muscle function with aging: a background factor in the incidence of fractures of the proximal end of the femur, *Clin. Orthop.,* 191, 193, 1984.
131. Faulkner, J. A., Brooks, S. V., and Zerva, E., Skeletal muscle weakness and fatigue in old age: underlying mechanisms, in *Annual Review of Gerontology and Geriatrics,* Cristofalo, V. J. and Lawton, M.P., Eds., Springer-Verlag, New York, 1990, 147.
132. Kritz-Silverstein, M. and Barrett-Connor, E., Grip strength and bone mineral density in older women, *J. Bone Miner. Res.,* 9, 45, 1994.
133. McCarter, R., Age-related changes in skeletal muscle function, *Aging,* 2, 27, 1990.
134. Murray, M., Gardner, G., Mollinger, L., and Sepic, S., Strength of isometric and isokinetic contractions: knee muscles of men aged 20 to 86, *Phys. Therapy,* 60, 412, 1980.
135. Raloff, J., Vanishing flesh: muscle loss in the elderly finally gets some respect, *Sci. News,* 150, 90, 1996.
136. Sinaki, M., Musculoskeleal rehabilitation, in *Osteoporosis, Etiolology, Diagnosis and Management,* 2nd ed., Riggs, B. L. and Melton III, L. J., Eds., Lippincott-Raven, Philadelphia, 1995, chap. 20.
137. Frost, H. M., Presence of microscopic cracks in vivo in bone, *Bull. Henry Ford Hosp.,* 8, 25, 1960.
138. Frost, H. M., Bone microdamage: factors that impair its repair, in *Current Concepts in Bone Fragility,* Uhthoff, H. K., Ed., Springer, Berlin, 1985, 123.
139. Kannus, P., Haapasalo, H., Sankelo, M., Sievanen, H., Pasanen, M., Heinomem, A., Oja, P., and Vuori, I., Effect of starting age of physical activity on bone mass in the dominant arm of tennis and squash players, *Ann. Intern. Med.,* 123, 27, 1995.
140. Gehron-Robey, P. and Bianco, P., Cellular mechanisms of age-related bone loss, in *The Aging Skeleton,* Bilezikian, J. P., Rosen, C. J., and Glowacki, J., Eds., Academic Press, San Diego, 1999, 145.
141. Bergman, R. J., Gazit, D., Kahn, A. J., Gruber, H., McDougall, S., and Hahn, T. J., Age-related changes in osteogenic stem cells in mice, *J. Bone Miner. Res.,* 11, 568, 1996.
142. Owan, I., Burr, D. B., Turner, C. H., Qiu, J., Tu, Y., Onyia, J. E., and Duncan, R. L., Mechanotransduction in bone: osteoblasts are more responsive to fluid forces than mechanical strain, *Am. J. Physiol.,* 273, C810, 1997.
143. Singh, Y. M., Nagarth, A. R., and Maini, P. S., Changes in trabecular pattern of the upper end of the femur as an index of osteoporosis, *J. Bone Joint Surg.,* 52A, 457, 1970.
144. Fleisch, H., *Bisphosphonates in Bone Diseases. From the Laboratory to the Patient,* 3rd ed., Parthenon Publishing Group, New York, 1997, chap. 1.
145. Harris, W. H., A microscopic method for determining rates of bone growth, *Nature,* 188, 1038, 1960.
146. Miller, S. C. and Jee, W. S. S., The effect of dichloromethylene diphosphonate, a pyrophosphate analog, on bone and bone cell structure in the growing rat, *Anat. Rec.,* 193, 439, 1979.
147. Schenk, R., Merz., W. A., Muhlbauer, R., Russell, R. G. G., and Fleisch, H., Effect of ethane-1-hydroxy-1,1-diphosphonate (EHDP) and dichloromethylene diphosphonate (Cl2MDP) on the calcification and resorption of cartilage and bone in the tibial epiphysis and metaphysis of rats, *Calcif. Tissue Res.,* 11, 196, 1973.
148. Miller, S. C., Bowman, B. M., Smith, J. M., and Jee, W. S. S., Characterization of endosteal lining cells from fatty marrow bone sites in adult beagles, *Anat. Rec.,* 198, 163, 1980.
149. Baron, R., Vignery, A., and Tran Van, P., The significance of lacunar erosion without osteoclasts: Studies on the reversal phase of the remodeling sequence, in *Bone Histomorphometry,* Jee, W. S. S. and Parfitt, A. M., Eds., Pergamon Press/Societe-Nouvelle de Publications Medicales et Dentaires, Paris, 1981, 35.

150. Parfitt, A. M., The actions of parathyroid hormone on bone. Relation to bone remodeling and turnover, calcium homeostasis and metabolic bone disease. II. PTH and bone cells: bone turnover and plasma calcium regulation, *Metabolism,* 25, 909, 1976.
151. Ericksen, E. F., Gundersen, H. J. G., Melsen, F., and Mosekilde, L., Reconstruction of the formative site in iliac trabecular bone in 20 normal individuals employing a kinetic model for matrix and mineral apposition, *Metab. Bone Dis. Relat. Res.,* 5, 243, 1984.
152. Frost, H. M., In vivo osteocyte death, *J. Bone Joint Surg.,* 42A, 138, 1960.
153. Frost, H. M., Micropetrosis, *J. Bone Joint Surg.,* 42A, 144, 1960.
154. Schiessl, H., Frost H. M., and Jee, W. S. S., Estrogen and bone muscle strength and mass relationship, *Bone,* 22, 1, 1998.
155. Weinstein, R. S., Jilka, R. L., Parfitt, A. M., and Manolagas, S. C., Inhibition of osteoblastogenesis and promotion of apoptosis of osteoblasts and osteocytes by glucocorticoids, *J. Clin. Invest.,* 102, 274, 1998.
156. Tomkinson, A., Bevers, E. F., Wit, J. M., Reeve, J., and Noble, B. S., The role of estrogen in the control of rat osteocyte apoptosis, *J. Bone Miner. Res.,* 13, 1243, 1998.
157. Noble, B. S., Stevens, H., Mosley, J. R., Pitsillides, A. A., Reeve, J., and Lanyon, L., Bone loading changes the number and distribution of apoptotic osteocytes in cortical bone, *J. Bone Miner. Res.,* 12, 5111, 1997.
158. Hofbauer, L. C., Khosla, S., Dunstan, C. R., Lacey, D. L., Boyle, W. J., and Riggs, B. L., The role of osteoprotegerin and osteoprotegerin ligand in the paracrine regulation of bone resorption, *J. Bone Miner. Res.,* 15, 2, 2000.
159. Chambers, T. J., Revell, P. J., Fuller, K. et al., Resorption of bone by isolated osteoclasts, *J. Cell Sci.,* 66, 383, 1984.
160. Jaworski, Z. F. G., Lok, E., and Wellington, J. L., Impaired osteoclastic function and linear bone erosion rate in secondary hyperthyroidism associated with chronic renal failure, *Clin. Orthop.,* 107, 298, 1975.
161. Martin, R. B., Toward a unifying theory of bone remodeling, *Bone,* 26, 1, 2000.
162. Marotti, G., The structure of bone tissues and the cellular control of their deposition, *Ital. J. Anat. Embryol.,* 101, 25, 1996.
163. Marotti, G., Ferretti, M., Muglia, M. A., Palumbo, C., and Palazzini, S., A quantitative evaluation of osteoblast-osteocyte relationships on growing endosteal surface of rabbit tibiae, *Bone,* 13, 363, 1992.
164. Manolagas, S. C. and Weinstein, R. S., New developments in the pathogenesis and treatment of steroid-induced osteoporosis, *J. Bone Miner. Res.,* 14, 1061, 1999.
165. Abe, E., Yamamoto, M., Taguchi, Y., Lecka-Czernik, B., Economides A. N., Stahl, N., Jilka, R. L., and Manolagas, S. C., Requirement of BMPs2/4 for postnatal osteoblast and osteoclast formation: antagonism by noggin, *Bone,* 23, S242, 1998.
166. Ducy, P., Zhang, R., Geoffroy, V., Ridall, A. L., and Karsenty, G., Osf2/Cbfal: a transciptional activator of osteoblast differentiation; *Cell,* 89, 747, 1997.
167. Kimmel, D. B., Animal models for in vivo experimentation in osteoporosis reasearch, in *Osteoporosis,* Marcus, R., Feldman, D., and Kelsey, J., Eds., Academic Press, San Diego, 1996, chap. 33.
168. Kimmel, D. B., Quantitative histologic changes in the proximal tibial epiphyseal growth cartilage of aged female rats, *Cells Mater.,* 1 (Suppl.), 11, 1992.
169. Dawson, A. B., The age order of epiphyseal union in the long bones of the albino rat, *Anat. Rec.,* 31, 1, 1925.
170. Erben, R. G., Trabecular and endocortical bone surfaces in the rat: modeling and remodeling, *Anat. Rec.,* 246, 39, 1996.
171. Brommage, R., Hotchkiss, C. E., Lees, C. J., Stancill, M. W., Hock, J. M., and Jerome, C. P., Daily treatment with human recombinant parathyroid hormone-(1-34), LY333334, for one year increases bone mass in ovariectomized monkeys, *J. Clin. Endocrinol. Metab.,* 84, 3757, 1999.

172. Burr, D. B., Hirano, T., Turner, C. H., Hotchkiss, C. E., Brommage, R., and Hock, J. M., Intermittently administered hPTH (1-34) treatment increases intracortical bone turnover and porosity without reducing bone strength in the humerus of ovariectomized cynomolgus monkeys, *J. Bone Miner. Res.*, 15, 157, 2001.
173. Bain, S. D., Bailey, S. C., Celino, D. L., Lantry, M. M., and Edwards, M. W., High-dose estrogen inhibits bone resorption and stimulates bone formation in the ovariectomized mouse, *J. Bone Miner. Res.,* 8, 435, 1993.
174. Bain, S. D., Jensen, E., Celino, D. L., Bailey, M. C., Lantry, M. M., and Edwards, M. W., High-dose gestagens modulate bone resorption and formation and enhance estrogen-induced endosteal bone formation in ovariectomized mouse, *J. Bone Miner. Res.,* 8, 219, 1993.
175. Akhter, M. P., Raab, D. M., Turner, C. H., Kimmel, D. B., and Recker, R. R., Characterization of in vivo strain in the rat tibia during external application of four-point bending load, *J. Biomechs.,* 25, 1241, 1992.
176. Boppart, M. D., Kimmel, D. B., Yee, J. A., and Cullen, D. M., Time course of osteoblast appearance after in vivo mechanical loading, *Bone,* 23, 409, 1998.
177. Cann, C. E., Genant, H. K., and Young, D. R., Comparison of vertebral and peripheral mineral losses in disuse osteoporosis in monkeys, *Radiology,* 134, 525, 1980.
178. Cann, C. E. and Young, D. R., Bone formation rate in experimental disuse osteoporosis in monkeys (*M. nemestrina*), *Physiologist,* 19, 147, 1976.
179. Chambers, T. J., Evans, M., Gardner, T. N., Turner-Smith, A., and Chow, J. W. M., Induction of bone formation in rat tail vertebrae by mechanical loading, *Bone Miner.,* 20, 167, 1993.
180. Chow, J. W. M., Jagger, C. J., and Chambers, T. J., Characterization of osteogenic response to mechanical stimulation in cancellous bone of rat caudal vertebrae, *Am. J. Physiol.,* 265, E340, 1993.
181. Chow, J. W. M., Jagger, C. J., and Chambers, T. J., Reduction in dynamic indices of cancellous bone formation in rat tail vertebra after caudal neurectomy, *Calcif. Tissue Int.,* 59, 117, 1996.
182. Dehority, W., Halloran, B. P., Bikle, D. D., Curren, T., Kostenuik, P. J., Wronski, T. J., Shen, Y., Rabkin, B., Bouraoui, A., and Morey-Holten, E., Bone and hormonal changes induced by skeletal unloading in the mature male rat, *Am. J. Physiol.,* 276(1 Pt. 1), E62, 1999.
183. Forwood, M. R., Owan, I., Takano, Y., and Curner, C. H., Increased bone formation in rat tibiae after a single short period of dynamic loading in vivo, *Am. J. Physiol.,* 270, E419, 1996.
184. Frost, H. M., The regional acceleratory phenomenon. A review, *Henry Ford Hosp. Med. J.,* 31, 3, 1983.
185. Frost, H. M., Perspectives: the role of changes in mechanical usage set points in the pathogenesis of osteoporosis, *J. Bone Miner. Res.,* 7, 253, 992.
186. Gross, A. L., Roberrtson, K. T., and Krough, L. H., Jr., A study of calcium, phosphorus and nitrogen mobilization resulting from conditions of inactivity in Macaca irus monkeys, USAF School of Aerospace Medicine, Brooks AFB, SAM-TR-66-94, 1966.
187. Howard, W. H., Parcher, J. W., and Young, D. R., Primate restraint system for studies of metabolic responses during recumbency, *Lab. Anim. Sci.,* 21, 112, 1971.
188. Ijiri, K., Jee, W. S. S., Ma, Y. F., and Yuan, Z., Remobilization partially restored bone mass in a non-growing cancellous bone site following long term immobilization, *Bone,* 17(S), 213S, 1995.
189. Ijiri, K., Ma, Y. F., Jee, W. S. S., Akamine, T., and Liang, X., Adaptation of non-growing former epiphyses and metaphyseal bones to aging and immobilization in rat, *Bone,* 17, 207S, 1995.
190. Izawa, Y., Makita, T., Hino, S., Hashimoto, Y., Kushida, K., Inoue, T., and Orimo, H., Immobilization osteoporosis and active vitamin D: effect of active vitamin D analogs on the development of immobilization osteoporosis in rats, *Calcif. Tissue Int.,* 33, 623, 1981.
191. Jaworski, Z. F. G. and Uhthoff, H. K., Disuse osteoporosis: current status and problems, in *Current Concepts of Bone Fragility,* Uhthoff H. K., Ed., Springer-Verlag, New York, 1986, 181–194.
192. Jaworski, Z. F. G., Liskova-Kiar, M., and Uhthoff, H. K., Effect of long term immobilization on the pattern of bone loss in older dogs, *J. Bone Joint Surg.,* 62B, 104, 1980.

193. Jee, W. S. S., Ma, Y. F., and Li, X. J., The immobilized adult cancellous bone site in a growing rat as an animal model of human osteoporosis, *J. Histotechnol.,* 20, 201, 1997.
194. Jee, W. S. S. and Ma, Y. F., Animal models of immobilization osteopenia, *Morphologie,* 83, 25, 1999.
195. Kazarain, L. E. and Von Gierke, H. E., Bone loss as a result of immobilization and chelation. Preliminary result in Macaca mulatta, *Clin. Orthop. Relat. Res.,* 65, 67, 1969.
196. Lanyon, L. E. and Rubin, C. T., Static vs. dynamic loads as an influence on bone remodeling, *J. Biomech.,* 17, 897, 1984.
197. Lean, J. M., Jagger, C. J., Chambers, T. J., and Chow, J. W., Increased insulin-like growth factor 1 mRNA expression in rat osteocytes in response to mechanical stimulation, *Am. J. Physiol.,* 268, E318, 1995.
198. Li, X. J. and Jee, W. S. S., Adaptation of diaphyseal structure to aging and decreased mechanical loading in the adult rat: a densitometric and histomorphometric study, *Anat. Rec.,* 229, 291, 1991.
199. Li, X. J., Jee, W. S. S., Chow, S. Y., and Woodbury, D. M., Adaptation of cancellous bone to aging and immobilization in the rat: a single photon absorptiometry and histomorphometry study, *Anat. Rec.,* 227, 12, 1990.
200. Morey, E. R., Spaceflight and bone turnover: correlation with a new rat model of weightlessness, *BioScience*, 29(3), 168, 1979.
201. Morey, E. R. and Baylink, D. J., Inhibition of bone formation during space flight, *Science,* 201, 1138, 1978.
202. Rittweger, J., Gunga, H. C., Felsenberg, D., and Kirsch, K. A., Muscle and bone—aging and space, *J. Gravitational Physiol.,* 6, 133, 1999.
203. Mosekilde, L., Danielsen, C. C., Søgaard, C. H., and Thorling, E., The effect of long-term exercise on vertebral and femoral bone mass, dimensions, and strength-assessed in a rat model, *Bone,* 15, 292, 1994.
204. Myburgh, K. H., Noakes, T. D., Roodr, M., and Hough, F. S., Effects of exercise on the development of osteoporosis in adult rats, *J. Appl. Physiol.,* 66(1), 14, 1989.
205. Niklowitz, W. J., Bunch, T. E., and Young, D. R., The effects of immobilization on cortical bone in monkeys (*M. nemestrina*), *Physiologist,* 26, S115, 1983.
206. Okumura, H., Yamamuro, T., Kasai, R., Ichisaka, A., Hayashi, T., and Matsushita, M., The effects of immobilization on osteoporosis in rats, *Jpn J. Bone Miner. Metab.,* 1986, 4, 75, 1986.
207. Okumura, H., Yamamuro, T., Kasai, R., Hayashi, T., Tada, K., and Nishii Y., Effect of 1 α-hydroxy-vitamin D_3 on osteoporosis induced by immobilization combines with ovariectomy in rats, *Bone,* 8, 351, 1988.
208. Pead, M. J., Skerry, T. M., and Lanyon, L. E., Direct transformation from quiescence to bone formation in the adult periosteum following a single brief period of bone loading, *J. Bone Miner. Res.,* 3, 647, 1988.
209. Shaker, J. L., Fallon, M. D., Goldfarb, S., Farber, J., and Attie, M. F., WR-2721 reduces bone loss after hindlimb tenotomy in rats, *J. Bone Miner. Res.,* 4, 885, 1989.
210. Raab-Cullen, D. M., Akhter, M. P., Kimmel, D. B., and Recker, R. R., Bone response to alternate day mechanical loading of the rat tibia, *J. Bone Miner. Res.,* 9, 203, 1994.
211. Raab-Cullen, D. M., Thiede, M. A., Petersen, D. N., Kimmel, D. B., and Recker, R. R., Mechanical loading stimulates rapid changes in periosteal gene expression, *Calcif. Tissue Int.,* 55, 473, 1994.
212. Rubin, C. T. and Lanyon, L. E., Dynamic strain similarity in vertebrates: an alternative to allometric limb bone scaling, *J. Theore. Biol.*, 107, 321, 1984.
213. Rubin, C. T. and Lanyon, L. E., Regulation of bone mass by mechanical strain magnitude, *Calcif. Tissue Int.,* 37, 411, 1985.
214. Skerry, T. M., Bitensky, L., Chayen, J., and Lanyon, L. E., Early strain-related changes in enzyme activity in osteocytes following bone loading in vivo, *J. Bone Miner. Res.,* 4, 783, 1989.
215. Søgaard, C. H., Danielsen, C. C., Thorling, E. B., and Mosekilde, L., Long term exercise of young and adult female rats: Effect on femoral neck biomechanical competence and bone structure, *J. Bone Miner. Res.,* 9, 409, 1994.

216. Steinberg, M. E. and Trueta, J., Effects of activity on bone growth and development in the rat, *Clin. Orthop. Relat. Res.,* 156, 52, 1981.
217. Thompson, D. D. and Rodan, G. A., Effects of indomethacin on bone resorption produced by tenotomy, *J. Bone Miner. Res.,* 3, 409, 1988.
218. Torrance, A. G., Mosley, J. R., Suswillo, R. R. L., and Lanyon, L. E., Noninvasive loading of the rat ulna in vivo induces a strain-related modeling response uncomplicated by trauma or periosteal pressure, *Calcif. Tissue Int.,* 54, 241, 1994.
219. Turner, C. H., Akhter, M. P., Raab, D. M., Kimmel, D. B., and Recker, R. R., A non-invasive, in vivo model for studying strain adaptive bone modeling, *Bone,* 12, 73, 1991.
220. Turner, C. H., Forwood, M. R., Rho, J. Y., and Yoshikawa T., Mechanical loading thresholds for lamellar and woven bone formation, *J. Bone Miner. Res.,* 9, 87, 1994.
221. Turner, C. H., Owen, I., Alvey, T., Hulman, J., and Hock, J. M., Recruitment and proliferative responses of osteoblasts after mechanical loading in vivo determined using sustained release bromodeoxyuridine, *Bone,* 22, 463, 1998.
222. Tuukkanen, J., Wallmark, B., Jalovaara, P., Takala, T., Sjogren, S., and Vaananen, K., Changes induced in growing rat bone by immobilization and remobilization, *Bone,* 12, 113, 1991.
223. Uhthoff, J. K. and Jaworski, Z. F. G. Bone loss in response to long-term immobilization, *J. Bone Joint Surg.,* 60-B, 420, 1978.
224. Umemura, Y., Ishiko, T., Yamauchi, T., Kurono, M., and Mashiko S., Five jumps per day increase bone mass and breaking force in rats, *J. Bone Miner. Res.,* 9, 1480, 1997.
225. Weinreb, M., Rodan, G. A., and Thompson, D. D., Osteopenia in the immobilized rat hindlimb is associated with increased bone resorption and decreased bone formation, *Bone,* 10, 187, 1989.
226. Yeh, J. K., Liu, C. C., and Aloia, J. F., Effects of exercise and immobilization on bone formation and resorption in young rats, *Am. J. Physiol.,* E182, 1993.
227. Yeh, J. K., Aloia, J. F., Chen, M. M., Koo, H. C., and Millard, W. J., Effects of growth hormone administration and treadmill exercise on serum and skeletal IGF-1 in rats, *Am. J. Physiol.,* E129, 1994.
228. Young, D. R., Nikowitz, W. J., and Steele, C. R., Tibial changes in experimental disuse osteoporosis in the monkey, *Calcif. Tissue Int.,* 35, 304, 1983.
229. Young, D. R., Niklowitz, W. J., Brown, R. J., and Jee, W. S. S., Immobilization-associated osteoporosis in primates, *Bone,* 7, 109, 1986.
230. Zeng, Q. Q., Jee, W. S. S., Ke, H. Z., and Wechter W. J., S-Ketoprofen inhibits tenotomy-induced bone loss and dynamics in weanling rats, *Bone Miner.,* 21, 203, 1993.
231. Zeng, Q. Q., Jee, W. S. S., Bigornia, A. E., King, J. G., D'Souza, S. M., Li, X. J., Ma, Y. F., and Wechter, W. J., Time responses of cancellous and cortical bones to sciatic neurectomy in growing female rats, *Bone,* 19, 13, 1996.
232. Kaneps, A. J., Stover, S. M., and Lane, N. E., Changes in canine cortical and cancellous bone mechanical properties following immobilization and remobilization with exercise, *Bone,* 21, 419, 1987.
233. Ito, H., Ke, H. Z., Jee, W. S. S., and Sakou, T., Anabolic responses of an adult cancellous bone site to prostaglandin E2 in the rat, *Bone Miner.,* 21, 219, 1993.
234. Ke, H. Z., Jee, W. S. S., Ito, H., Setterberg, R. B., Li, M., Lin, B. Y., Liang, X. G., and Ma, Y. F., Greater bone formation induction occurred in aged than young cancellous bone sites, *Bone,* 14, 481, 1993.
235. Iwamoto, J., Yeh, J. K., and Aloia, J. F., Different effect of treadmill exercise on three cancellous bone sites in the young growing rats, *Bone,* 24, 163, 1999.
236. Yeh, J. K., Aloia, J. F., Chen, M. M., Tierney, J. M., and Sprintz, S., Influence of exercise on cancellous bone of aged female rats, *J. Bone Miner. Res.,* 9, 1117, 1993.
237. Yeh, J. K., Aloia, J. F., Chen, M. M., Koo, H. C., and Millard, W. J., Effects of growth hormone administration and treadmill exercise on serum and skeletal IGF-1 in rats, *Am. J. Physiol.,* E129, 1994.

238. Chen, M. M., Yeh, J. K., Aloia, J. F., Tierney, J. M., and Sprintz, S., Effect of treadmill exercise on tibial cortical bone in aged female rats: a histomorphometry and dual energy X-ray absorptiometry study, *Bone,* 15, 313, 1994.
239. Newhall, K. M., Rodnick, K. J., van der Meulen, M. C., Carter, D. R., and Marcus, R. T., Effects of voluntary exercise on bone mineral content in rats, *J. Bone Miner. Res.,* 6, 289, 1991.
240. Banu, M. J., Orhii, P. B., Wejia, W., McCarter, R. J. M., Mosekilde, L., Thomsen, J. S., and Kalu, D. N., Analysis of the effects of growth hormone, voluntary exercise, and food restriction on diaphyseal bone in female F344 rats, *Bone,* 25, 469, 1999.
241. Mosekilde, L., Thomsen, J. S., Orhii, P. B., McCarter, R. J., Mejia, W., and Kalu, D. N., Additive effect of voluntary exercise and growth hormone treatment on bone strength assessed at four different skeleton sites in an aged rat model, *Bone,* 24, 71, 1999.
242. Bourrin, S., Ghaemmaghami, F., Vico, L., Chappard, D., Gharib, C., and Alexandre, C., Effect of a five-week swimming program on rat bone: a histomorphometric study, *Calcif. Tissue Int.,* 51, 137, 1992.
243. Swissa-Sivan, A., Simkin, A., Leichter, I., Nyska, A., Nyska, M., Statter, M., Bivas, A., Menczel, J., and Samueloff, S., Effect of swimming on bone growth and development in young rats, *Bone Miner.,* 7, 91, 1989.
244. Sedillot, M. C., Des modification que subissent les membres reseques pendant leur periode de developpement, et en particulier du siege et des degres du raccourvissement oberve a la suite de la resection coxo-femorale, *C. R. Acad. Sci.,* 68, 1444, 1869.
245. Wermel, J., Untersuchungen uber die Kinetogenese und ihre Bedeutung in der onto- und phylogenetischen Entwicklung (Experimente und Vergleichungen an Wirbeltierextremitaten). Regeneration der Knochen und Gelenke, sowoe Newbuldung der Letzteren, *Morphol Jahrb.*, 75, 445, 1935.
246. Goodship, A. E., Lanyon, L. E., and McFie, H., Functional adaption of bone to increased stress, *J. Bone Joint Surg.,* 61A, 539, 1979.
247. Lanyon, L. E., Goodship, A. E., Pye, C. J., and MacFie, J. H., Mechanically adaptive bone remodeling, *J. Biomech.,* 15, 141, 1982.
248. Rubin, C. T. and Lanyon, L. E., Regulation of bone formation by applied dynamic loads, *J. Bone Joint Surg.,* 66A, 397, 1984.
249. Raab, D. M., Smith, E. L., Crenshaw, T. D., and Thomas, D. P., Bone mechanical properties after exercise training in young and old rats, *Am. J. Physiol.,* 68, 130, 1990.
250. Forwood, M. R. and Parker, A. W., Repetitive loading, in vivo of the tibiae and femora of rats: effects of repeated bouts of treadmill-running, *Bone Miner.,* 13, 35, 1991.
251. Oxlund, H., Andersen, N. B., Ørtoft, G., Ørskov, H., and Andreassen, T. T., Growth hormone and mild exercise in combination markedly enhance cortical bone formation and strength in old rats, *Endocrinology,* 139, 1899, 1998.
252. Barengolts, E. I., Curry, D. J., Bapna, M. S., and Kukreja S. C., Effects of endurance exercise on bone mass and mechanical properties in intact and ovariectomized rats, *J. Bone Miner. Res.,* 8, 937, 1993.
253. Mosekilde, L., Thomsen, J. S., Orhii, P. B., McCarter, R. J., Mejia, W., and Kalu, D. N., Additive effect of voluntary exercise and growth hormone treatment on bone strength assessed at four different skeleton sites in an aged rat model, *Bone,* 24, 71, 1999.
254. Peng, J., Tuukkanen, J., and Väänänen, H. K., Exercise can provide protection against bone loss and prevent the decrease in mechanical strength of femoral neck in ovariectomized rats, *J. Bone Miner. Res.,* 10, 1559, 1994.
255. Turner, C. H., Duncan, R. L., and Pavalko, F. M., Mechanotransduction: an inevitable process for skeletal maintenance, in *Novel Approaches to Treatment of Osteoporosis,* Russell, R. G. G., Skerry, T. M., and Kollenkirchen, U., Eds., Springer, Berlin, 1998, Ernst Schering Research Foundation Workshop, 25, chap. 7.

256. Skerry, T. M., The regulation of gene expression in bone by mechanical loading, in *Novel Approaches to Treatment of Osteoporosis,* Russell, R. G. G., Skerry, T. M., and Kollenkirchen, U., Eds., Springer, Berlin, 1998, Ernst Schering Research Foundation Workshop, 25, chap. 8.
257. Lanyon, L. E., Amplification of the osteogenic stimulus of load-bearing as a logical therapy for the treatment and prevention of osteoporosis, in N*ovel Approaches to Treatment of Osteoporosis,* Russell, R. G. G., Skerry, T. M., and Kollenkirchen, U., Eds., Springer, Berlin, 1998, Ernst Schering Research Foundation Workshop, 25, chap. 9.
258. Parfitt, A. M., The mechanism of coupling: a role for the vasculature, *Bone,* 26, 319, 2000.
259. Gimble, J. M., Robinson, C. E., Wu, X., and Kelly, K. A., The function of adipocytes in the bone marrow stroma: an update, *Bone,* 19, 421, 1996.
260. Maurin, A. C., Chavassieux, P. M., Frappart, L., Delmas, P. D., Serre, C. M., and Meunier, P. J., Influence of mature adipocytes on osteoblast proliferation in human primary co-cultures, *Bone,* 26, 485, 2000.
261. Jilka, R. L., Weinstein, R. S., Bellido, T., Roberson, P., Parfitt, A. M., and Manolagas, S., Increased bone formation by prevention of osteoblast apoptosis with parathyroid hormone, *J. Clin. Invest.,* 104, 439, 1999.
262. Machwate, M., Rodan, S. B., Rodan, G. A., and Harada, S. I., Sphingosine kinase mediates cyclic AMP suppression in rat periosteal cells, *Mol. Pharmacol.,* 64, 70, 1995.
263. Jee, W. S. S. and Nolan, P. D., Origin of osteoclasts from the fusion of phagocytes, *Nature,* 208, 225, 1963.

2

Cell Biology of Bone

Robert J. Majeska
Mount Sinai School of Medicine

2.1 Introduction

The unique physical and biological properties of bone are the direct results of actions by its constituent cells. The previous chapter introduced the cells of bone and their functions in skeletal physiology. This chapter will revisit those cells with a closer look at some of the fundamental cellular processes used in carrying out those functions—for example, proliferation, differentiation, migration/adhesion, synthesis and degradation of the extracellular matrix (ECM), and several modes of cell–cell communication. A final section discusses briefly some of the *in vitro* experimental systems currently used to study bone cells.

2.2 Bone Cells and Their Lineages

As described in the previous chapter, there are four major types of bone cells, readily identifiable *in vivo* by histological criteria: osteoblasts, osteoclasts, osteocytes, and bone-lining cells. Osteoblasts, osteocytes, and lining cells are closely related, and represent different stages in the maturation of a single cell type.[1] These cells and their progenitors are considered to comprise the "osteoblastic" cell lineage, a subset of the developmental lineage that includes connective tissue cells including muscle, fat, and cartilage cells. Osteoclasts, on the other hand, are part of the hematopoietic cell family that includes all of the circulating blood cells; they are an extension of the monocyte cell lineage and represent a terminal stage in the differentiation of these cells.[2]

At the outset, it may be useful to point out (or reiterate) that, while osteoblasts and osteoclasts have opposite functions and have different developmental origins, they exhibit several parallel features, particularly with respect to their life cycles. Both are temporary cells with relatively short life spans.[3] In bone lineages, differentiation of progenitor cells occurs at the sites where they are needed. Mature osteoblasts or osteoclasts do not migrate very far (although osteoclasts tunnel through bone), but progenitors may be recruited to specific sites from a distance. Proliferation of progenitors is required to prevent cellular depletion, since both osteoblasts and osteoclasts are destined to die or undergo a substantial phenotypic change.

0-8493-9117-2/01/$0.00+$.50

Thus, both bone formation and resorption necessitate mechanisms to control the proliferation of progenitors, their differentiation along specific pathways, and their eventual cessation of activity. Some of these mechanisms will be discussed further in Section 2.4.

2.3 Bone Cell Properties and Functions

2.3.1 Osteoblasts

The function of osteoblasts is to form bone. Like most instances of biological mineralization,[4] this process occurs in two stages. First, an organic matrix ("osteoid") is laid down, after which mineral salts are precipitated throughout that matrix from ions (principally calcium and phosphate) in the extracellular fluid. The osteoid serves as a template whose organization largely determines that of the subsequently formed mineral phase. Osteoblasts participate to varying degrees in all phases of the process. They synthesize and secrete the major structural elements of osteoid, regulate their assembly into an organized matrix, and finally facilitate mineral deposition.

2.3.1.1 Morphology

Osteoblast morphology (rounded shape, organelle-rich cytoplasm) reflects the principal function of the cell: synthesis and secretion of osteoid constituents; however, an additional feature of osteoblasts is a polar appearance (see Chapter 1). Osteoblast polarity may arise because these cells almost invariably reside in an asymmetric environment, e.g., at the interface between a newly forming bone surface and either another tissue (marrow, periosteum) or a resorption space. It may be an important factor in defining how osteoblasts organize the matrix they produce. Mechanisms for maintaining cell polarity have been extensively investigated in epithelial cell models, and a recent finding suggests that osteoblasts may share these mechanisms. Epithelial cells specifically target the VSV-G protein and influenza virus hemagglutinin to their apical and basolateral surfaces, respectively; cultured osteoblastic cells similarly targeted these molecules to opposing cell surfaces.[5]

Osteoblasts may sense the asymmetry of their environment through their cell surface receptors for extracellular matrix molecules (e.g., integrins);[6,7] in epithelial cells these receptors are differentially distributed between the apical and basolateral cell surfaces.[8]

2.3.1.2 Matrix Synthesis and Secretion

Osteoblasts secrete a large and diverse set of macromolecules, including all critical structural elements of osteoid. These are listed in Chapter 1 (Tables 1.9 and 1.10) and their properties and possible physiological functions are discussed in greater depth by Boskey (Chapter 5). An important point, however, is that most osteoid constituents are not bone specific; consequently, the uniqueness of bone matrix depends not so much on the presence of a unique structural element, but on the way a fairly common set of building blocks is organized. In addition, nearly all bone matrix molecules are proteins, or at least contain a protein component. As a result, cellular control over matrix composition and organization begins at the genetic level, since all proteins (even if only a minor component of the final molecule) are encoded within the genome. This feature offers some justification for assessing osteoblast function by matrix protein mRNA levels (but this approach has limits—see below). It also implies that these newly synthesized matrix molecules follow similar pathways through the cell, and may begin to interact with each other before they leave the osteoblast. Little information is available as yet about this possibility.

Most bone matrix proteins undergo one or more post-translational modifications. These include (1) covalent cross-linking (e.g., between amino acids of collagen chains);[9] (2) N- and O-linked glycosylations of amino acids to yield proteoglycans (e.g., biglycan, decorin) or other glycoprotein types (osteopontin, bone sialoprotein, BAG-75); (3) phosphorylation of amino acid residues (e.g., osteopontin, BAG-75); and (4) the vitamin K-dependent gamma-carboxylation of glutamate residues (osteocalcin). One consequence of these modifications is that many matrix constituents are polyfunctional and can interact simultaneously with other matrix macromolecules, with free ions, with bone mineral, or with cells. This clearly has potential implications for tissue organization. Furthermore, post-translational modification

offers a potential regulatory point where the function of matrix molecules could be modified independent of changes in gene expression. Few examples of such regulation at this level are known; however, Ref. 10 suggests a novel possibility.

Finally, many bone matrix proteins, like those in most ECMs, contain motifs specifically recognized by cellular receptors. For example, fibronectin, osteopontin, and bone sialoprotein, among others, contain the tripeptide sequence arg-gly-asp (RGD) required for binding by several members of the integrin adhesion receptor family.[6,7,11] Other molecules like osteonectin and thrombospondin can also support cell adhesion under some circumstances, but may also have antiadhesive actions suggesting possible roles in cellular migration.[12,13]

The pathways of protein synthesis and secretion in osteoblasts are the same as those found in fibroblasts and other connective tissue cells.[14,15] Messenger RNAs for each secretory protein are transcribed and processed in the nucleus, then transported to the cytoplasm where they direct protein synthesis on ribosomes associated with the endoplasmic reticulum (ER). As proteins are synthesized, they are packaged within the ER lumen, then moved sequentially through several membrane-bound compartments of the Golgi apparatus into secretory vesicles. These vesicles finally fuse with the plasma membrane and expel their contents to the extracellular space. During their transit through the intracellular membrane system, proteins fold into mature, three-dimensional conformations and undergo most of the post-translational processing and modification steps mentioned above (e.g., proteolytic cleavage or targeting or "leader" sequences, glycosylation, phosphorylation, gamma carboxylation). For each protein, information within the primary amino acid sequence identifies such details as the specific amino acids to be modified and the nature of the modification; however, the extent of modification is also determined by external factors like the activity of modifying enzymes and the availability of substrates. Assembly of multisubunit proteins (e.g., the triple helix of type I collagen) also begins during their transit through the ER/Golgi system prior to secretion. Assembly of larger units, e.g., the aggregation of mature collagen molecules into fibrils and the interaction of those fibrils with other ECM constituents, occurs primarily after the proteins have been secreted.[16,17]

Osteoblasts do not synthesize all bone matrix proteins uniformly; rather, the expression patterns of individual matrix proteins or their mRNAs vary spatially and temporally.[18–20] For example, proteins like fibronectin and osteonectin are expressed early in osteoblastic cell cultures undergoing mineralization *in vitro*, while osteocalcin is expressed only after the development of an established matrix.[20] In addition, changes in the antigenic properties of bone sialoprotein during osteoblast maturation suggest that either protein structure or its interaction with other matrix constituents could change with time.[21]

Once bone matrix constituents are secreted, they proceed to form an organized matrix. The details of this process are not well understood, but osteoblasts appear to exert some control over it. Fibroblastic cells initially assemble a pericellular matrix consisting largely of fibronectin, which binds both to collagen and to cell surface receptors including the integrins $\alpha 5\beta 1$ and $\alpha 4\beta 1$; formation of this matrix precedes and can regulate further matrix development.[22,23] Osteoblasts, particularly at the early stages of differentiation, similarly secrete fibronectin.[20,24,25] Moreover, disrupting the binding of fibronectin to integrins with competing RGD-containing peptides or by antibodies to fibronectin or to integrins that recognize fibronectin results in production of a disorganized matrix, diminished mineralization, and impaired differentiation of osteoblasts.[24,25]

2.3.1.3 Mineralization

How osteoblasts regulate the deposition of mineral within osteoid is still not fully understood. In addition to producing an appropriately organized matrix, osteoblasts express high levels of alkaline phosphatase (ALP), a cell-surface enzyme associated with the mineralization process almost since its discovery.[26] Although expressed in numerous tissues (e.g., kidney, liver), it is abundant in many cells producing mineralizable matrices (e.g., hypertrophic chondrocytes odontoblasts) and is considered a marker enzyme for cells with this function.[27] Interestingly, ALP expression rises very early in osteoblastic differentiation,[1,28] although its activity remains high in mature osteoblasts. Levels of ALP are also high in plasma-membrane-derived extracellular matrix vesicles where early mineral deposits in bone and calcifying cartilage have

been identified.[29] That ALP functions in mineralization is supported most strongly by the genetic disease hypophosphatasia, where a lack of functional ALP is linked to impaired mineralization of bone, cartilage, and teeth.[30] The precise function of ALP is not absolutely defined. At physiological pH levels its phosphatase activity is substantially lower than at its optimum; however, under those conditions it is able effectively to cleave pyrophosphate, a cellular metabolic product and inhibitor of mineralization.[31]

2.3.2 Osteocytes

Osteocytes are former osteoblasts that became buried in lacunae within the bone matrix. They have little synthetic activity, but may carry out low-level remodeling of their local environment, since they constitutively express mRNA for osteocalcin.[32,33] Osteocytic secretion of matrix proteins may be designed to prevent mineral from precipitating on lacunar surfaces. The ability of osteocalcin to bind to mineral crystal surfaces via its gamma-carboxyglutamate residues[34] suggests such a role. The loss of osteocytes with aging is associated with hypermineralization of lacunae (Chapter 1, this volume).

2.3.2.1 Morphology: Cell Connections and Gap Junctions

The most dramatic morphological feature of osteocytes is the extensive network of cellular processes that link them physically and functionally to each other and to cells at the bone surface.[35,36] The formation of stable cell–cell contacts between osteocytes may involve cadherins.[37–40] These adhesion molecules are discussed further in Section 2.5. More evident at the contact points between osteocyte processes are gap junctions, specialized membrane contacts that form channels permitting the passage of ions and other small molecules directly between the cytoplasms of the two cells. Gap junctions between cells are formed by the interaction of membrane proteins termed *connexins*, contributed by both partners; the properties of a gap junction, e.g., its permeability to selected ions, depend on the specific connexins that form it.[41,42] In osteoblastic cells, the principal connexin is Cx43, although others including Cx45 have also been identified.[43] The type of connexins and the extent of gap junctional communication between cells were shown to regulate gene expression and hormonal responsiveness.[44,45]

2.3.2.2 Function: Mechanosensation and Damage Recognition

Osteocytes and lining cells are believed to comprise a sensory network that monitors mechanical load and tissue damage, and triggers appropriate adaptive responses, either formation or resorption.[32] Mechanisms by which osteocytes could sense mechanical loads have been proposed, e.g., by fluid movements throughout the lacunar–canalicular system, with some combination of shear stresses and streaming potentials providing the proximate stimuli; these are discussed in greater detail elsewhere in this volume. However, experiments in other cellular systems have demonstrated that the continuum formed by extracellular matrix molecules, integrin adhesion receptors, and the cytoskeleton is capable of sensing and transducing mechanical stimuli.[46,47] The presence in osteocytes of integrins[6] and CD44, a receptor recognizing osteopontin and hyaluronan and also associated with the cytoskeleton,[48] makes these likely candidates to operate in osteocytes as well.

Osteocytes sense not only mechanical loading but also tissue damage. Microdamage due to fatigue was shown to stimulate local osteoclastic remodeling;[49] however, prior to the onset of bone resorption, osteocytes near the lesions underwent changes consistent with apoptosis (programmed cell death).[50] Apoptosis, in contrast to necrotic cellular death from injury, is a highly regulated process under the control of specific genes, sometimes triggered by receptor-mediated signaling, mediated by specific enzymes (caspases) and involving characteristic morphological and biochemical changes that include nuclear chromatin condensation, DNA fragmentation ("laddering"), and active membrane vesiculation.[51–53] Apoptosis is a common physiological, as opposed to pathological, process often associated with developmental processes.[54] Interestingly, osteocytes in rats also undergo apoptosis following estrogen deprivation, another stimulus to increased bone turnover.[55] This lends support to the notion that apoptosis may be part of a signaling pathway to initiate bone remodeling. The nature of the signal produced by these apoptotic cells is still unknown.

2.3.3 Bone-Lining Cells

Bone-lining cells cover resting bone surfaces. Some of their properties have been outlined in the previous chapter, but much remains to be clarified about their fundamental biology. Lining cells are interesting from a regulatory standpoint, since they reside at the point where both bone formation and resorption take place, and they participate in both processes. *In situ*, lining cells can be activated to an osteoblastic state (as described in Chapter 1), and while they do not divide, they may secrete growth factors that trigger proliferation of nearby osteoblast progenitor cells. On the other hand, lining cells are capable of proliferation under proper stimuli; they are probably the major source of "osteoblasts" or "osteoblast-like" cells that grow out from adult bone explants and proliferate in culture under the influence of serum-derived growth factors.[56] It is likely that some of the phenotypic traits attributed to "osteoblasts" or "osteoblast-like" cells from studies in cell culture may be expressed *in vivo* by lining cells rather than osteoblasts in the process of matrix formation.

Lining cells also participate in bone resorption, probably in several ways that include (1) identifying a site of incipient resorption and recruiting osteoclast precursors to that site from the circulation; (2) enhancing the differentiation of osteoclast precursors into active osteoclasts; and (3) preparing the bone surface for osteoclastic resorption. Evidence supporting these pathways has come in large part from studies of osteoblastic cells or in some cases organ cultures treated with bone resorption-stimulating agents like parathyroid hormone (PTH) or interleukin-1 (IL-1). Activated osteoblastic cells secrete several proteolytic enzymes including matrix metalloproteinases (collagenases, gelatinase) and their inhibitor TIMP (tissue inhibitor of metalloproteinases), as well as plasminogen activator.[57] Proteases of the type released by osteoblastic cells were shown to enhance osteoclastic resorption activity *in vitro*.[58]

The differentiation of osteoclasts from precursor cells requires the direct action of the stromal cell population (See Section 2.4.2). A crucial factor in this process was recently identified as RANK Logan (RANKL), an osteoblast product that stimulates osteoblastic differentiation via its co-receptor RANK, which is expressed on monocytes.[59] PTH was shown to stimulate RANKL expression by osteoblastic cells;[60] however, this mechanism also needs to be demonstrated for lining cells *in situ*.

Osteoblastic cells can regulate the activity of blood vessels as well as osteoclasts and their precursors. This may be important in facilitating passage of osteoclast precursors through the vessel walls to reach the bone surface. In addition to other growth factors with activities on multiple cell types (see Section 2.5), osteoblasts produce vascular endothelial growth factor (VEGF), a protein that stimulates endothelial cell proliferation, migration, and permeability.[61] PTH and prostaglandin E_2 (PGE_2)[62] also stimulate its production. Finally, osteoblastic cells must move away from the surface of bone to allow access of osteoclasts. PTH stimulates osteoblastic cells *in vitro* and on bone surfaces to undergo a retractile shape change.[63]

2.3.4 Osteoclasts

Osteoclasts are large, multinucleated cells completely specialized to resorb bone. Resorption, like formation, occurs in two steps: dissolution of mineral and enzymic digestion of organic macromolecules. Unlike formation, however, these two processes are essentially simultaneous.

2.3.4.1 Morphology

Osteoclasts have several distinctive morphological features, as described in the previous chapter. These are large-size, multiple nuclei, the "ruffled border" of plasma membrane at the resorbing surface, a surrounding "clear zone" where attachment to the bone occurs, and numerous lysosomes. A lysosomal enzyme, tartrate-resistant acid phosphatase (TRAP) is also used as a convenient histological marker for osteoclasts *in situ* or in cell culture.

2.3.4.2 Bone Mineral Dissolution

Osteoclasts dissolve the mineral phase of bone by secreting H^+ ions into the extracellular resorption space, lowering the pH within this limited environment. The H^+ ions neutralize negative charges on hydroxyl ions and PO_4^{3-} ions in the highly basic bone mineral hydroxyapatite, whose formal structure

is $Ca_{10}(PO_4)_6(OH)_2$); this leads to the release of Ca^{2+} and phosphate as HPO_4^{2-} and $H_2PO_4^-$. Transport of protons is accomplished by an electrogenic ATP-driven enzyme (vacuolar ATPase);[64] however, whether the protons are pumped directly into the resorption cavity or into cytoplasmic vesicles and released upon fusion with the ruffled border membrane is not clear. Additional enzymes and pumps, including carbonic anhydrase, a Cl^- pump and a bicarbonate exchange mechanism are probably involved in compensating for activity of the proton pump.[65]

2.3.4.3 Bone Matrix Degradation

Osteoclasts break down organic bone matrix constituents using an array of proteases and glycosidases. Among the proteolytic enzymes identified in osteoclasts are matrix metalloproteinases including MMP-1[66] and MMP9/gelatinase B[67] and several lysosomal cysteine protease of the cathepsin family.[68] The roles of these enzymes are still not completely understood. For instance, MMPs are active at neutral pH, so their effectiveness in the presumably acidic environment of a resorption space has been questioned. Recent data however, suggested that cathepsins may act prior to the MMPs.[69]

The importance of cathepsin K to osteoclastic resorption was illustrated recently by its identification as the deficient enzyme in pycnodysostosis, a genetic disease characterized by moderate skeletal deformity including dwarfism, and normal or elevated numbers of poorly functional osteoclasts.[70] Interestingly, the mild phenotype of this disease also demonstrates that cathepsin K is not absolutely essential for osteoclastic function. Mutations of several other genes lead to a much more severe phenotype of osteopetrosis where osteoclasts are either absent or completely nonfunctional. As a result, bone marrow cavities fail to form during bone development, and severe immunological defects can ensue. There are several forms of naturally occurring osteopetroses in animals (as well as humans) that result from impaired development of or function of osteoclasts.[71] Other osteopetroses have been generated by various gene "knockouts." These animal models have proved extremely valuable for gaining insight into these processes. One example of a knockout osteopetrosis arose by deletion of the c-src proto-oncogene; the c-src-null mice produce normal numbers of osteoclasts that fail to form ruffled borders and do not resorb bone.[72] Other examples of osteopetroses are discussed elsewhere in this chapter.

2.3.4.4 Osteoclast Integrins and Cytoskeleton

The adhesion receptor/cytoskeletal system plays a crucial role in many aspects of osteoclast function. The integrin $\alpha V\beta 3$ in particular has been implicated in osteoclast binding to bone, perhaps via osteopontin[73] and possibly transducing a signal to initiate resorption.[74] In addition, the actin cytoskeleton in osteoclasts is highly organized into ring structures co-localized with the adhesion receptors.[65,75] Interference with integrin–ligand interactions by the snake venom protein echistatin[76] or disruption of the osteoclast cytoskeleton by modifying the activities of rho GTP-binding proteins[77] abolishes resorption.

2.4 Bone Cell Life Cycles and Their Regulation

2.4.1 The Osteoblastic Lineage

2.4.1.1 Alternative Differentiation Pathways

Osteoblastic cells arise initially from a self-renewing population of pluripotential precursors (termed *mesenchymal stem cells*) that also gives rise to chondrocytes, myocytes, adipocytes, and fibroblasts.[28,78] Differentiation of these stem cells along the osteogenic pathway proceeds in several stages from committed osteoblast progenitors to preosteoblasts, to mature osteoblasts, and ultimately to either osteocytes or lining cells.[28] The characteristics of progenitor cells for osteoblasts, or other mesenchymal cell types are not very well defined. In part, this is because regardless of their developmental potential these cells are not readily distinguishable by routine morphological criteria; when isolated and cultured, all have a typically fibroblastic appearance. The identification of cell-surface molecules expressed on mesenchymal stem cells and on osteoprogenitor cell populations during the early stages of osteoblastic differentiation

(e.g., Thy-1,[79] Stro-1,[80] SB-10[81]) has begun to resolve these uncertainties. These tools have also proved useful in allowing the isolation of osteogenic subpopulations from mixed populations of bone marrow stromal cells.[82,83]

2.4.1.2 Osteoblast-Specific Genes

Commitment to differentiation along specific pathways often entails the expression of lineage-specific transcriptional regulators;[84] a classic example is MyoD, a helix-loop-helix protein that regulates expression of genes needed for subsequent myoblast differentiation.[85] The transcription factor cbfa1/osf2, identified as a regulator of osteocalcin gene expression, apparently is such an activator of osteoblast differentiation.[86] It is an essential gene; mice genetically lacking cbfa1 fail to produce bone or to exhibit functional osteoblasts, although they form cartilaginous tissues that are the precursors of bone.[87]

2.4.1.3 Induction of Osteoblastic Differentiation

Inducing mesenchymal stem cells to differentiate into osteoblasts is the role of the bone morphogenetic proteins (BMPs). BMPs comprise a family of closely related proteins that are members of the much larger transforming growth factor-beta (TGF-β) superfamily that also includes the activins and inhibins.[88] Although first identified as the bone and cartilage-inducing factor in demineralized bone matrix (hence the name),[89] various BMPs regulate tissue patterning at virtually all stages of development.[90,91] BMPs are also expressed during morphogenetic events in adult tissues, for example, in fracture healing.[92,93] Cells of osteoblastic lineage produce (at least) BMPs 2, 4, and 6,[94] which, like other growth factors, accumulate in the bone matrix.

At the cellular level, BMPs stimulate undifferentiated mesenchymal cells to differentiate along osteogenic and chondrogenic pathways and also enhance proliferation and phenotypic expression in osteoblastic cells.[95,96] In cells capable of differentiating along more than one pathway *in vitro*, BMPs only promote the expression of osteoblastic phenotypic traits but also suppress the expression of alternative (e.g., myogenic, adipogenic) pathways.[97,98] BMP receptors and intracellular signal transduction pathways are clearly distinct from, although highly similar to, those of the TGF-β family; their actions on target cell populations that share both receptor sets are likewise distinct[88] (see Section 2.5.2.2).

The activities of several BMPs (including BMPs 2, 4, and 6) are modulated by two natural antagonists, noggin and chordin, which bind specifically to the BMPs and block their function. Noggin has specifically been implicated in regulating skeletal development. It is expressed in developing embryonic cartilage and its genetic ablation in mice caused overproduction of cartilage and a failure to form joints.[99] This suggests that BMP actions in skeletal morphogenesis may need to be tightly controlled. More recently, BMPs as well as TGF-β were shown to induce noggin expression in osteoblastic cells,[100] indicating a possible mechanism for this regulation.

2.4.1.4 Control of Proliferation, Maturation, and Death

In vitro, cells of the osteoblastic lineage proliferate in response to the same mitogens that induce cell proliferation in other mesenchymal cells; these include the platelet-derived growth factor (PDGF), fibroblast growth factor (FGF), and insulin-like growth factor (IGF) families, as well as the BMPs. Osteoblastic cells also produce some or all isoforms from all of these families.[101–103] *In vivo*, however, cells in the osteoblastic lineage also proliferate, but this response is mostly restricted to progenitor populations; mature osteoblasts, osteocytes, and lining cells do not proliferate. An exception appears to occur in fracture healing, where new bone forms very rapidly by the differentiation of periosteal cells on either side of the fracture site.[104] Proliferation occurs throughout the periosteum and the newly forming hard callus; it probably includes cells that are simultaneously producing osteoid.[105]

The phenotypic maturation of osteoblastic cells is not well understood. Although some antigenic markers have been identified from developmental stages leading from stem cells to osteoblasts,[78–83] the signals that control the transitions between states are not yet clear. Interestingly, one of the antigenic markers, SB-10, was recently found to be a cell–cell adhesion molecule, implicating it as a possible participant in a signaling pathway.[106]

The transitions from active osteoblasts to osteocytes and lining cells are beginning to be investigated. What controls these transitions is not yet known, but it has become clear that apoptotic cell death is an alternative fate of the osteoblast. Osteoblast apoptosis has been observed at sites of bone formation, and the process appears to be regulated. Glucocorticoids, known to inhibit bone formation, were found to increase apoptosis,[107] while PTH, which has potent stimulatory effects on bone formation,[108] suppressed it.[109]

2.4.2 The Osteoclastic Lineage

2.4.2.1 Hematopoietic Stem Cells and Monocyte Precursors

Osteoclastic differentiation parallels that of osteoblasts in many respects. Pluripotential hematopoietic stem cells in sites like bone marrow differentiate into monocytes and all other blood cell types under the influence of colony-stimulating factors produced by both hematopoietic cells and stromal cells.[2,110] Since osteoclasts differentiate from the monocytic branch of this lineage, granulocyte macrophage-colony stimulating factor (GM-CSF) and macrophage colony–stimulating factor (MCSF) are of particular importance in regulating these stages of development.[110]

2.4.2.2 Differentiation of Monocytes into Osteoclasts: Interactions with Stromal/Osteoblastic Cells

The final stages of osteoclast differentiation (e.g., from circulating monocytes) occur only after the cells are recruited from the circulation or the marrow to sites of resorption. These stages involve several phenotypic changes; these include the *de novo* expression of $\alpha V\beta 3$ integrin adhesion receptors, synthesis of novel enzymes (e.g., tartrate-resistant acid phosphatase), fusion to form multinucleated cells, and finally development of the characteristic morphological elements of mature osteoclasts such as cellular polarity, a ruffled border, and a characteristic actin cytoskeleton.[2,73,75,110]

The formation of multinucleated, functional osteoclasts from monocytic precursors has been investigated extensively using *in vitro* assay systems.[111] From these studies it has become clear that the final stages of osteoclast differentiation require the direct interaction of monocytes with cells of the bone marrow stroma or of the osteoblast lineage. Numerous cytokines and growth factors that these cells produce, e.g., IL-1, tumor necrosis factor-α (TNFα), IL-6, PGE_2) are potent stimulators of osteoclastogenesis;[2] however, they could not replace the requirement for the supporting cells. This cellular interaction is mediated by a protein produced by stromal and osteoblastic cells termed ODF (osteoclast differentiation factor). ODF is known by several other names including TRANCE (tumor necrosis factor-related activation-induced cytokine) and RANKL (RANK ligand). ODF/TRANCE/RANKL activates a receptor on monocytes identified as RANK (receptor activator of NFκB).[59,110,112]

As is the case with other agonist/antagonist pairs like BMP and noggin or the MMPs and TIMPs, stromal and osteoblastic cells produce an antagonist to TRANCE/RANKL/ODF termed osteoprotegerin (OPG). OPG is a soluble protein that binds to RANKL and prevents it from interacting with RANK on monocytes. Thus, the balance of RANKL and OPG determine the ability of this regulatory system to promote osteoclastogenesis, and regulation of either one could affect that balance.[59,110,112] PTH, which stimulates osteoclastogenesis *in vitro* by action on osteoblastic cells,[2,111] was recently shown to decrease OPG expression as well as increase TRANCE.[60]

As differentiation of osteoblast progenitors into osteoblasts is dependent on cbfa-1, the differentiation of monocytes into osteoclasts appears to require the proto-oncogene and transcription factor c-fos. Unlike cbfa-1, however, c-fos does not have a limited tissue expression pattern; it is expressed by nearly all cell types and is considered an "immediate early" gene whose expression is rapidly stimulated by a wide variety of effectors including many mitogens.[113] Expression of c-fos has usually been associated with osteoblast function, and its overexpression with the development of bone and cartilage tumors.[114] On the other hand, the principal phenotypic manifestation in c-fos knockout mice is osteopetrosis associated with a complete absence of osteoclasts.[114] The deficiency was found

to reside in the monocytic cells, since stromal cells from c-fos$^{-/-}$ mice supported osteoclastogenesis by wild-type monocytes; the ability of c-fos$^{-/-}$ monocytes to differentiate into macrophages was not impaired.

2.4.2.3 Osteoclast Death

Osteoclasts undergo apoptosis, and this is a major determinant of the cell life span.[53] Studies testing the effects of factors known to stimulate or inhibit osteoclast activity found several consistent results with respect to aopotosis. Agents that stimulate bone turnover (IL-1, PTH, TNF, and 1,25-dihydroxyvitamin D_3) prevented apoptosis while those known to inhibit osteoclast activity, bisphosphonates, antagonists of adhesion (RGD peptides) and TGF-β, increased it. Estrogen was also found to increase osteoclast apoptosis, an effect possibly mediated by enhanced TGF-β production.[116] Intracellular control of osteoclast life span may involve the MAPK (mitogen-activated protein kinase) signal transduction pathway; constitutive activation of the pathway suppressed spontaneous apoptosis in osteoclasts but did not affect their resorptive activity. On the other hand, inhibition of NFκB (the intracellular target of RANK, activated when osteoclasts differentiate from monocytes) reduced osteoclast function without affecting survival.[117]

2.5 Regulators of Bone Cell Function

The need for coordinated cellular action in bone formation, modeling, remodeling, and repair necessitate multiple levels of regulation. As a result, bone cells of all types are regulated by a host of factors ranging from systemic hormones to local factors acting between different cell types (paracrine factors) or between cells of the same type (autocrine factors). Systemic hormones tend to regulate cell behavior based on global conditions, e.g., changes in plasma Ca levels, but some of their actions on target cells include regulating their production of local regulatory factors or their response to them. The local factors, on the other hand, are more responsible for fine-tuning and coordination of cellular activities within constrained spatial and temporal limits, e.g., within a bone modeling unit.

The local regulatory factors important to skeletal function tend to fall into two groups whose names sometimes reflect the history of their discovery as much as their functions. Growth factors were named for their ability to stimulate the proliferation of cultured cells usually of epithelial or mesenchymal origin. In bone, they often have this effect on mesenchymal cells of osteoblastic and nonosteoblastic lineage alike; however, they may have other actions as well. Cytokines were originally identified as products of activated immune cells, but many are also produced by mesenchymal cells, and act on both cell types. Still, many of the cytokines involved with bone cells act to promote inflammatory-type tissue responses (e.g., bone resorption). The following section summarizes some properties of these regulators, grouped according to the properties of their receptors (and thus their general mechanisms of action at the cellular level).

2.5.1 Systemic Factors

2.5.1.1 G Protein-Associated Receptors: Parathyroid Hormone and Calcitonin

The receptors for PTH and calcitonin (CT) belong to distinct subfamilies of the G protein-associated receptor superfamily;[118,119] however, both are both cell surface transmembrane proteins having external N-termini, cytoplasmic C-termini, and seven membrane-spanning domains. Both function via their interaction with cytoplasmic GTP-binding proteins (G proteins); ligand binding to the receptor leads to activation of the G proteins, which then stimulate or inhibit their respective target enzymes. The nature of a hormone response thus depends not only on the amount of receptor present, but also on the specific type and amount of the G proteins with which they interact.

The PTH and CT receptors are each capable of coupling to two intracellular signaling pathways: the cyclic AMP/protein kinase A pathway and the phosphoinositide/protein kinase C pathway. In the first, receptor binding activates adenylate cyclase, leading to cAMP formation and the activation of cAMP-dependent protein kinases; in the second, binding activates phospholipase C, which cleaves membrane

phosphatidylinositol to yield diacylglycerol (DAG) and inositol triphosphate (IP_3). The DAG then activates a distinct protein kinase family with its own target substrates (protein kinase C), while the IP_3 appears to facilitate Ca^{2+} fluxes through membranes.

PTH acts on bone and kidney to maintain plasma calcium levels. It acts on bone to stimulate bone remodeling. It is a potent stimulator of osteoclastic bone resorption,[120] although its primary target cells in bone are osteoblasts and certain cells (osteoblast progenitors?) in the marrow stroma.[121] Consequently, its effects on osteoclasts are mediated through them, by enhancing the production of cytokines (see below) and altering the balance of OPGL/OPG production. PTH also has strong anabolic (formative) actions on bone; low intermittent doses of PTH *in vivo* dramatically stimulate bone formation.[108]

At the cellular level, several PTH effects are consistent with bone resorption-stimulating activity. These include enhancement of osteoclast formation in marrow cultures,[111] increased expression of TRANCE/ODF and decreased expression of OPG,[60] stimulation of matrix metalloproteinase production,[122] and inhibition of type I collagen expression[123] in osteoblastic cells. Anabolic effects of PTH on osteoblasts include a suppression of apoptosis, suggested to account for increased life span of these cells and the resultant increases in bone formation the hormone can produce.[109] The complexity of these effects was pointed out by the demonstration that PTH actions on osteoblastic cells are dependent on the stage of osteoblastic differentiation.[124]

CT[125] acts physiologically to suppress bone resorption on a temporary basis. It acts on mature osteoclasts to inhibit their activity. These actions are well replicated *in vitro*, including its temporary nature; despite the continued presence of ligand, receptors become desensitized and resorption resumes. Interestingly, while CT causes retraction from cytoskeletal disruption, it was reported not to promote apoptosis like other inhibitors of osteoclast activity.[53]

2.5.1.2 Steroid/Retinoid Receptors: 1,25$(OH)_2D_3$, Glucocorticoids, Estrogens, Androgens

Steroid and retinoid receptors are nuclear receptors.[125–128] Their ligands are generally fat soluble and diffuse through membranes easily, but are brought to cells and to the nucleus via carrier proteins. Steroid hormone receptors are transcription factors with distinct binding domains for ligand and for specific DNA sequences (response elements). Ligand binding activates the receptors to bind the response elements in the promoter regions of their target genes and regulate transcriptional activity. These receptors act as dimers and in some cases are capable of heterodimerization; for example, the vitamin D receptor (VDR) acts as part of a dimeric complex with the "retinoid X receptor" (RXR). In addition, these receptors can interact with other transcriptional regulators as well, and may act as large multiprotein complexes.

The retinoids and thyroid hormone as well as steroids utilize receptors of this family, and have physiological effects on bone, some of which have been demonstrated in cell systems; however, these remain incompletely characterized and will not be discussed here.

2.5.1.3 1,25$(OH)_2$ vitamin D_3

The principal active metabolite of vitamin D, 1,25$(OH)_2D_3$ acts mainly on the intestine to stimulate Ca uptake.[127] Its target genes include specific Ca-binding proteins (calbindins), but the genes for several bone proteins (e.g., osteocalcin, osteopontin) also contain vitamin D response elements. 1,25$(OH)_2D_3$ has several PTH-like effects on bone cells including stimulation of osteoclastogenesis[2,73,111] and regulating the expression of osteoblastic genes.[128]

In addition to its receptor-mediated actions, 1,25$(OH)_2D_3$ also exerts a distinct set of nongenomic effects, including modulation of calcium fluxes through the plasma membrane.[10,129] One effect noted earlier is the suppression of osteopontin phosphorylation, leading to a secreted product with markedly different charge.[10]

2.5.1.4 Glucocorticoids

Glucocorticoids at chronic, high levels *in vivo* produce osteoporosis-depressing bone formation and increase the frequency of remodeling site activation.[130] Specific cellular effects on osteoblastic/stromal cells include promoting the differentiation of osteoblast progenitors in marrow stroma, an effect attributed to

increased production of BMP6.[95] In addition, glucocorticoids enhanced the actions of several hormones, both anabolic and catabolic, including PTH[131] and IGF-1.[132] On the other hand, most glucocorticoid effects on active osteoblasts are inhibitory. Glucocorticoids inhibited mineralization in rat calvarial organ cultures and caused marked disorganization of cellular and matrix architecture, probably by inhibiting expression of fibronectin and integrins by osteoblastic cells.[133,134] Glucocorticoids also caused apoptosis in osteoblastic cells both *in vivo* and *in vitro*.[107]

2.5.1.5 Estrogens and Androgens[125,126,135]

Estrogens promote the maintenance of bone mass, and *in vivo* appear to inhibit bone formation as well as resorption.[36] Androgens also promote bone growth during development, and its depletion also has been associated with osteoporosis.[137] Osteoblastic cells contain two isoforms of estrogen receptor (α and β) as well as androgen receptors.[138] The mechanism by which gonadal steroid depletion promotes increased bone turnover remains unclear. Estrogen reduction *in vivo* has been associated with increased production of resorption-stimulating cytokines, notably IL-1 and IL-6.[139] While estrogen was found to suppress production of such cytokines by osteoblastic/stromal cells in some systems,[140] others found that cytokine production was not regulated by gonadal steroids.[141] Estrogens also increase osteoclast apoptosis,[53] probably via stimulation of TGF-β production.[142]

Estrogens (and androgens) also regulate osteoblastic growth and phenotypic expression 143,144, and suppresses apoptosis in osteocytes.[55] Although the mechanism underlying this effect is unknown, it suggests a possible link between endocrine (estrogen depletion) and mechanical (microdamage) stimuli of bone remodeling.

2.5.2 Local Regulators: Growth Factors and Prostaglandins

2.5.2.1 G Protein-Associated Receptors: Prostaglandins

Prostaglandins are fatty acid derivatives formed by the action of prostaglandin G/H-synthase (PGHS) or cyclooxygenase (COX) on 20-carbon polyunsaturated fatty acids (arachidonic acid is the best known, it is the precursor of prostaglandin E_2, or PGE_2). There are two isoforms of COX, one constitutively expressed and not usually sensitive to regulation (COX1) and one expressed at very low levels but inducible (COX2).[145] Stimulators of bone resorption markedly activate Pt production by osteoblastic cells,[146] as does mechanical stimulation.[147] Many of these agents also regulate expression of COX2.[148]

The actions of PGs are very much like those of PTH; PGs activate adenylate cyclase in osteoblastic cells, and produce a similarly complex spectrum of responses. PGs are potent stimulators of bone resorption and osteoclastogenesis *in vitro*, effects that are mediated by osteoblastic/stromal cells.[145,146] Also like PTH, however, PGE_2 stimulates bone formation dramatically when administered exogenously.[149]

2.5.2.2 The TGF-β Superfamily: TGF-βs and BMPs

TGF-βs and BMPs have distinct functions, but belong to the same multigene family and so have homologous structures. They also utilize structurally similar receptors intracellular signal transduction components; some of the latter may be shared.[88]

The receptors for BMPs and TGF-βs are heterodimers (Type I and Type II subunits) with serine-threonine kinase activity. Ligand binding causes phosphorylation of the receptor itself plus its intracellular substrates, members of the SMAD protein family. BMP receptors activate SMADs I and 5, TGF-βs activate SMADs 2 and 3; SMAD 4 is common to both pathways. Two additional SMADs, 6 and 7, inhibit the actions of the others. Upon activation, SMADs translocate to the nucleus, where they interact with DNA and other transcriptional regulators. The spectrum of genes regulated by each pathway differs, consistent with the distinct functions of the initial effectors.

The inductive effects of BMPs on osteoblastic progenitors were noted previously (Section 2.4.1.3). TGF-βs can also promote the formation of new bone and cartilage *in vivo*, but only at skeletal sites, not by nonskeletal tissues.[150] Its overall effects at the cellular level are to inhibit proliferation of endothelial

and epithelial cells, promote chemotaxis of several cell types including hematopoietic cells and fibroblasts, and to stimulate matrix production by mesenchymal cells.[150,151] Transgenic mice with osteoblastic cells dramatically overexpressing TGF-β2 under control of the osteocalcin promoter (i.e., principally in osteoblastic cells) showed high turnover with features of an osteoporotic phenotype including spontaneous fractures.[152]

Both BMPs and TGF-βs are present in bone matrix. TGF-βs, however, are secreted as a latent, covalent complex that can be activated by a transient shift in pH[153] or by proteases. The complex may also be covalently linked (through the inactive portion, or latency-associated peptide) to a latent TGF-β binding protein (LTBP) that forms fibrillar structures in matrix.[156]

2.5.2.3 Receptor Tyrosine Kinases: Insulin-Like Growth Factors and Binding Proteins, Fibroblast Growth Factors, Platelet-Derived Growth Factors

These growth factors comprise a set of local regulators initially discovered and studied for their ability to promote cell proliferation *in vitro*. Their receptors are dimeric transmembrane proteins with tyrosine kinase activity activated by ligand binding. All can activate the intracellular MAP kinase pathway, leading to their mitogenic actions. Elements of this pathway also can engage in "cross talk" with other intracellular signaling pathways.

2.5.2.4 Fibroblast Growth Factors[102]

The FGFs include at least nine members, of which two (FGF-1 and FGF-2) are abundant and active in bone. There are four FGF receptors. FGFs are potent mitogens for all types of mesenchymal cells, but their effects *in vivo* are particularly evident in cartilage development.[155] FGFs also stimulate the proliferation of osteoblastic cells in culture, while suppressing phenotypic expression,[156] and stimulate bone resorption *in vitro* as well.[157] *In vivo*, FGF1 and FGF2 are both expressed actively in the fibrous tissues forming granulation tissue in fracture repair;[158] moreover, exogenous FGF promoted fracture healing in both normal and diabetic rats.[159]

2.5.2.5 Platelet-Derived Growth Factors[101]

The PDGFs are produced by many cell types other than platelets. The two forms (A and B) produce three active dimer combinations (AA, AB, BB). They also have three types of receptors ($\alpha\alpha$, $\alpha\beta$, and $\beta\beta$). PDGF was identified as a "competence factor" needed to permit cells to enter the G1 phase of the cell cycle, but unable by itself to support passage to the stage of DNA synthesis.[160] Osteoblastic cells produce only the B form of PDGF, but respond to all dimeric combinations. PDGF stimulates proliferation of osteoblastic cells, but does not enhance expression of differentiated traits.[161] *In vivo*, the function of PDGF is not clear, although both A and B forms are expressed in healing fractures, where their functions are similar to those in soft tissue wound healing.[162]

2.5.2.6 Insulin-Like Growth Factors and IGF-Binding Proteins[103]

The IGFs are also mitogenic, but were considered as "progression" rather than "competence" factors like PDGF.[160] In competent cells, they could support passage through G1 to the S phase. IGFs are produced by many mesenchymal cell types, including osteoblasts. There are two forms, IGF-I and IGF-II. IGF-I is the predominant form produced by murine osteoblasts; IGF-II is the major form made by human osteoblasts. In bone, IGFs stimulate the proliferation of osteoblast precursors and, in contrast to the other growth factors described above, independently promote matrix production by mature osteoblasts.[163] There are also two forms of IGF receptor. The Type I receptor is a tyrosine kinase that mediates its mitogenic activities; the second is identical to the mannose-6-phosphate receptor that regulates endocytic pathways and intracellular protein trafficking, sorting, and degradation.[103]

In addition to IGFs, osteoblasts and other cells produce a family of IGF binding proteins (IGFBPs). There are at least six IGFBPs. Some increase the effectiveness of IGFs; others inhibit their activity. In addition, IGFBPs are sensitive to degradation by several proteases, some of which are specific for various forms of IGFBP.

2.5.3 Local Regulators: Cytokines

2.5.3.1 Interleukin-1, Tumor Necrosis Factor[164]

Both IL-1 and TNF exist as two isoforms (α and β), but are structurally unrelated and act through completely disparate receptors and signal transduction pathways; however, they are produced under similar circumstances and cause almost the same set of effects on bone. In particular, both IL-1 and TNF are potent stimulators of bone resorption. Both IL-1, previously identified as "osteoclast activating factor," and TNF are produced by inflammatory cells, particularly activated macrophages, and also by mesenchymal cells. Both exert multiple effects on osteoblastic cells, most of which are consistent with increasing bone resorption and suppressing bone formation. These include increased synthesis and secretion of proteolytic enzymes, reduced collagen synthesis, and stimulated production of other local factors implicated as stimulators of bone resorption such as IL-6 and PGs. Increased production of IL-1 by macrophages and other cells has been suggested as a mechanism for the increased bone turnover at menopause.[165] An inactive homolog of IL-1, termed IL-1 receptor antagonist (IL-1RA), competes for binding of IL-1 receptors and thus antagonizes the cytokine's action.[166]

2.5.3.2 gp130-Associated Receptors: Interleukin-6, Leukemia Inhibitory Factor, Oncostatin-M, Interleukin-11, Ciliary Neurotrophic Factor[167]

In contrast to IL-1 and TNF, this family of cytokines is related by sequence homology and shares a common receptor element and signaling pathways. The shared receptor is a transmembrane protein, gp130, but each cytokine has an additional receptor element specific to itself. All form complexes comprised of ligand, gp130, and the additional receptor element. In addition, the specific receptor proteins for IL-6, IL-11, and ciliary neurotrophic factor (CNTF) can exist either in a transmembrane form or as a soluble form after proteolytic cleavage from cell membranes. The soluble forms are also capable of binding to their ligands and activating gp130.

gp130 is the signal-transducing element in these complexes. It has no intrinsic kinase activity, but upon ligand binding it interacts with and activates cytoplasmic Janus kinases (JAKs). These kinases subsequently phosphorylate other cytoplasmic molecules, the STATs (for signal transducers and activators of transcription). The STATs then translocate rapidly to the nucleus and regulate the transcription of their target genes.[168,169] The STAT family consists of several members, and the spectrum of STATs activated by a given ligand depends on the cell type and the effector. Since STATs act as dimers, and since other effectors (e.g., PDGF) can activate the STAT pathway as well,[170] there is considerable opportunity for cross talk between signaling systems and hence multiple levels of control.

Members of this cytokine family are produced by osteoblastic and stromal cells, among others. The most intensively studied with respect to the skeleton is IL-6. Its synthesis is stimulated by resorption-stimulating agents like IL-1, PTH, and FGF, as well as by members of its own family. IL-6 synthesis by marrow stromal cells and by osteoblasts is also suppressed by estrogen;[171] moreover, bone loss in mice following ovariectomy can be inhibited by treatment with anti-IL-6[172] and did not occur in IL-6-null knockout mice.[173] These findings led to the suggestion that IL-6 was a mediator of estrogen-deficiency bone loss.[167]

2.5.4 Local Regulators: Adhesion-Based Signaling

The ability of cells to communicate with each other by contact-mediated mechanisms, and to recognize and respond to changes in their extracellular matrix, have long been appreciated. It is becoming clear that bone cells also depend on these sorts of interactions to coordinate their activities. The following describes some properties of adhesion-based signaling systems that have been identified in bone cells.

2.5.4.1 Cell–Matrix Interactions: Integrins

A nearly universal mode of interaction between cells and ECM molecules involves the integrins.[174] Integrins are a diverse family of heterodimeric receptors comprised of an α and a β subunit. The specific combination of these subunits determines the ligand binding specificity. Among those already noted for important

actions on bone cell are the "fibronectin receptor" $\alpha 5\beta 1$ (in osteoblast adhesion) and the "vitronectin receptor" $\alpha V\beta 3$ (in osteoclast adhesion). Both α and β integrin subunits are transmembrane proteins; their external portions combine to form a ligand binding site and the internal domains interact with cytoplasmic proteins associated with the actin-based cytoskeleton (e.g., α-actinin, vinculin). Thus, integrins are directly linked to the intracellular systems involved in cell motility and the maintenance of cell shape. Changes in integrin occupancy by its ligands or application of mechanical force to integrin–Iigand complexes activates cytoplasmic signaling pathways that regulate gene expression, cell proliferation, and apoptosis.[46,175–177] Adhesion of cells to substrata activates a focal adhesion kinase (FAK) associated with the complexes between integrins and cytoskeletal proteins that form at sites where cells adhere.[47] This and/or other kinases are likely mediators of integrin-based signaling.

2.5.4.2 Cell–Cell Interactions: Cadherins[37,40]

Cadherins are transmembrane proteins whose extracellular domains mediate Ca^{2+}-dependent associations between cells, and whose intracellular portions interact with cytoplasmic α and β catenins. α-Catenin participates in linking the cadherins to cytoplasmic actin filaments; it is similar in structure to the protein vinculin, which links the cytoplasmic domains of integrins to the actin cytoskeleton.[47] These links indicate that receptors mediating cell–cell interactions (cadherins) and those regulating cell–matrix interactions (integrins) can cross talk in regulating cell shape and motility. β-Catenin is structurally distinct from α-catenin; it resembles plakoglobin, a constituent of desmosomes. When associated with cadherins, β-catenin remains in the cytoplasm; when released, it is capable of translocation to the nucleus where it participates in transcriptional regulation.[40] Several structural isoforms of cadherins are expressed in cells of the osteoblast lineage[38,39] and they have been suggested to help maintain cellular responsiveness to BMPs.

2.6 *In Vitro* Systems to Study Bone Cells[178–181]

Many of the recent advances in bone cell biology have come from *in vitro* studies using experimental systems that allowed investigators tremendous advantages over *in vivo* systems for manipulating and analyzing cellular behavior. These systems are, of course, limited approximations not only of *in vivo* tissue but even of each other—a fact that has frequently led to rather intense discussions and will undoubtedly continue to do so. On the other hand, having disparate data from several systems is often beneficial; it provides a sort of parallax that is often necessary to resolving difficult issues. The following section describes some general features and a few idiosyncracies of some *in vitro* systems currently used in bone research.

2.6.1 Cell Culture vs. Organ Culture

2.6.1.1 Organ Cultures[179,181]

In organ culture, tissue pieces (e.g., plugs of cartilage, bone chips, sheets of periosteum) or sometimes entire bones are cultured. Such systems are commonly used to study integrated processes like bone formation and resorption, or tissue morphogenesis, in the absence of systemic influences like hormonal fluctuations or mechanical stimuli. They have been especially useful in studying the effects of drugs or putative regulators on these processes. Often, fetal or newborn tissues are used because the tissues are actively growing and both formation and resorption rates are high. Furthermore, in developing tissues morphogenetic changes may occur in culture at rates comparable to those seen *in vivo*.

The twin goals of organ culture are to preserve both viability and local tissue architecture. Architecture is often maintained by preventing excessive growth (often by eliminating serum supplements from the medium). Viability, on the other hand, may depend on the same (or other) factors present in serum. For this reason, organ cultures usually have a limited life span. Another disadvantage is that it becomes difficult to assess the behavior or response of individual cell types. This disadvantage is lessened by the availability of techniques like *in situ* hybridization that allow evaluation of gene expression in individual cells of a tissue.

2.6.1.2 Cell Cultures[178,180]

Cell culture sacrifices most features of tissue architecture to gain greater access to individual cells. Two distinct approaches and philosophies govern the development of cell culture systems. The first focuses on cells freshly isolated from tissue or maintained through limited numbers of subcultures; this minimizes the phenotypic changes that occur over time in culture. The second seeks to establish permanent lines of cells (usually clonal, i.e., originating from a single selected cell), with unlimited proliferative potential and a more uniform phenotype than the heterogeneous populations usually isolated from tissues even with careful dissection. Both approaches have advantages and disadvantages, usually complementary; both have also been applied to bone biology with reasonable success.

Primary cultures include "osteoblast-enriched" or "osteoblast-like" cells. Fetal or newborn rodent calvaria have been popular cell sources, although it has been possible to culture these cells from essentially all species and all ages. Alternatively, bone marrow stromal cells (the adherent population of marrow) contain few mature osteoblasts, but rather progenitor cells that can be induced to form osteoblastic cells by appropriate stimuli. Freshly isolated mature osteoclasts are rare, although obtainable from tissues undergoing highly active resorption like medullary bone of hens. Osteoclastogenesis is usually studied in total marrow cultures (adherent plus nonadherent cells) or in combinations of nonadherent spleen cells (containing monocytes) with adherent osteoblastic or stromal populations.

Permanent cell lines of osteoblastic cell lines were originally established from bone tumors and subsequently by immortalization of normal bone cells in culture by transfection with viral genes like SV40 T antigen. Recently, the development of transgenic mice bearing various transforming genes, or lacking certain control elements in cell cycle, has allowed the culture of bone cells from phenotypically "normal" tissues, but having the ability to survive indefinitely in culture.

The phenotype of cultured bone cells has been defined largely by their more evident functional traits (i.e., those associated with resorption or formation, like the synthesis of matrix proteins or the expression of marker enzymes). This has been useful in modeling the activities of active osteoblasts or osteoclasts; however, it has been difficult to establish *in vitro* the properties of more "quiescent" populations like osteocytes or lining cells. Whether, for example, a culture of "osteoblastic" cells in a nondividing, confluent monolayer is a reasonable model for lining cells or osteocytes has yet to be evaluated systematically. The recent development of means to isolate and culture osteocytes[182] and the establishment of an osteocytic permanent cell line[183] has begun to offer experimental approaches to these and other questions.

References

1. Aubin, J.E. and Liu, F., The osteoblast lineage, in *Principles of Bone Biology,* Bilezikian, J.P., Raisz, L.G., and Rodan, G.A., Eds., Academic Press, San Diego, 1996, chap. 5.
2. Suda. T., Udagawa, N., and Takahashi, N., Cells of bone: osteoclast generation, in *Principles of Bone Biology,* Bilezikian, J.P., Raisz, L.G., and Rodan, G.A., Eds., Academic Press, San Diego, 1996, chap. 7.
3. Parfitt, A.M., Problems in the application of *in vitro* systems to the study of human bone remodeling. *Calcif. Tissue Int.* 56 (Suppl. 1), S5–S7, 1995.
4. Lowenstam, H. and Weiner, S., *On Biomineralization,* Oxford University Press, New York, 1989.
5. Ilvesaro, J., Metsikko, K., Vaananen, K., and Tuukkanen, J., Polarity of osteoblasts and osteoblast-like UMR-108 cells, *J. Bone Miner. Res.,* 14, 1338–1344, 1999.
6. Clover, J., Dodds, R.A., and Gowen, M., Integrin subunit expression by human osteoblasts and osteoclasts *in situ* and in culture, *J. Cell Sci.,* 103, 267–271, 1992.
7. Grzesik, W. and Gehron Robey, P., Bone matrix RGD glycoproteins: immunolocalization and interaction with human primary osteoblastic bone cells *in vitro., J. Bone Miner. Res.,* 9, 487–496, 1994.
8. Marchisio, P.C., Bondanza, S., Cremona, O., Cancedda, R., and DeLuca, M., Polarized expression of integrin receptors ($\alpha7\beta4$, $\alpha2\beta1$, $\alpha3\beta1$, and $\alpha v\beta5$) and their relationship with the cytoskeleton and basement membrane matrix in cultured human keratinocytes, *J. Cell Biol.,* 112, 761–773, 1991.

9. Eyre, D., Biochemical basis of collagen metabolites as bone turnover markers, in *Principles of Bone Biology,* Bilezikian, J.P., Raisz, L.G., and Rodan, G.A., Eds., Academic Press, San Diego, 1996, chap. 11.
10. Safran, J.B., Butler, W.T., and Farach-Carson, M.C., Modulation of osteopontin post-translational state by 1,25-$(OH)_2$-vitamin D_3. Dependence on Ca^{2+} influx, *J. Biol. Chem.,* 273, 29935–29941, 1998.
11. Horton, M.A., Townsend, P., and Nesbitt, S., in *Principles of Bone Biology,* Bilezikian, J.P., Raisz, L.G., and Rodan, G.A., Eds., Academic Press, San Diego, 1996, chap. 17.
12. Robey, P.G., Young, M.F., Fisher, L.W., and McClain, T.D., Thrombospondin is an osteoblast-derived component of mineralized extracellular matrix, *J. Cell Biol.,* 108, 719–727, 1989.
13. Lane, T.F. and Sage, E.H., The biology of SPARC, a protein that modulates cell-matrix interactions, *FASEB J.,* 8, 163–173, 1994.
14. Rothman, J.E., Mechanisms of intracellular protein transport, *Nature,* 372, 5–63, 1994.
15. Hammond, C. and Helenius, A., Quality control in the secretory pathway, *Curr. Opin. Cell Biol.,* 7, 523–529, 1995.
16. Prockop, D.J., Kivirikko, K.I., Tuderman, L., and Guzman, N.A., The biosynthesis of collagen and its disorders, *N. Engl. J. Med.,* 301, 13–23, 1979.
17. Rossert, J. and de Crombrugghe, B., Type I collagen: structure, synthesis and regulation, in *Principles of Bone Biology,* Bilezikian, J.P., Raisz, L.G., and Rodan, G.A., Eds., Academic Press, San Diego, 1996, chap. 10.
18. Weinreb, M., Shinar, D., and Rodan, G.A., Different pattern of alkaline phosphatase, osteopontin and osteocalcin expression in developing rat bone visualized by in situ hybridization, *J. Bone Miner. Res.,* 5, 831–842, 1990.
19. Bianco, P., Riminucci, M., Silvestrine, G., Bonucci, E., Termine, J.D., Fisher, L.W., and Robey, P.G., Localization of bone sialoprotein (BSP) to Golgi and post-Golgi secretory structures in osteoblasts and to discrete sites in early bone matrix. *J. Histochem. Cytochem.,* 41, 193–203, 1993.
20. Owen, T.A., Aronow, M., Shalhoub, V., Barone, L.M., Wilming, L., Tassinari, M.S., Kennedy, M.B., Pockwinse, S., Lian, J.B., and Stein, G.S., Progressive development of the rat osteoblast phenotype *in vitro*: reciprocal relationships in expression of genes associated with osteoblast proliferation and differentiation during formation of the bone extracellular matrix, *J. Cell. Physiol.,* 143, 420–430, 1990.
21. Bianco, P., Riminucci, M., Bonucci, E., Termine, J.D., and Robey, P.G., Bone sialoprotein (BSP) secretion and osteoblast differentiation: relationship to bromodeoxuridine incorporation, alkaline phosphatase, and matrix deposition, *J. Histochem. Cytochem.,* 41, 183–191, 1993.
22. Christopher, R.A., Kowalczyk, A.P., and McKeown-Longo, P.J., Localization of fibronectin matrix assembly sites on fibroblasts and endothelial cells, *J. Cell Sci.,* 110, 569–581, 1997.
23. Schwarzbauer, J.E. and Sechler, J.L., Fibronectin fibrillogenesis: a paradigm for extracellular matrix assembly, *Curr. Opin. Cell Biol.,* 11, 622–627, 1999.
24. Gronowicz, G. and DeRome, M., A synthetic peptide containing arg-gly-asp inhibits bone formation and resorption in a mineralizing organ culture system of fetal rat parietal bones *J. Bone Miner. Res.,* 9, 193–202, 1994.
25. Moursi, A.M., Damsky, C.H., Lull, J., Zimmerman, D., Doty, S.B., Aota, S., and Globus, R.K., Fibronectin regulates calvarial osteoblast differentiation. *J. Cell Sci.,* 109, 1369–1380, 1996.
26. Robison, R., Possible significance of hexosephosphoric esters in ossification, *Biochem. J.,* 17, 286–293, 1923.
27. Wuthier, R.E. and Register, T.C., Role of alkaline phosphatase, a polyfunctional enzyme, in mineralizing tissues, in *Chemistry and Biology of Mineralized Tissues*, Butler, W.T., Ed., Ebsco Media, Birmingham, 1984, 113.
28. Aubin, J.E. and Liu, F., The osteoblast lineage, in *Principles of Bone Biology,* Bilezikian, J.P., Raisz, L.G., and Rodan, G.A., Eds., Academic Press, San Diego, 1996, chap. 5.

29. Anderson, H.C., Calcium-accumulating vesicles in the intercellular matrix of bone, in *CIBA Foundation Symposium on Hard Tissue Growth Repair and Remineralization,* Elliot, K. and Fitzsimons, D.W., Eds., Elsevier, Amsterdam, 1973, 236.
30. Whyte, M.P., Hypophosphatasia and the role of alkaline phosphatase in skeletal mineralization, *Endocr. Rev.,* 15, 439–461, 1994.
31. Felix, R. and Fleisch, H., Pyrophosphatase and ATP-ase of isolated cartilage matrix vesicles, *Calcil. Tissue Res.,* 22, 1–7, 1976.
32. Nijweide, P.J., Burger, E.H., Klein-Nulend, J., and Van der Plas, A., The osteocyte, in *Principles of Bone Biology,* Bilezikian, J.P., Raisz, L.G., and Rodan, G.A., Eds., Academic Press, San Diego, 1996, chap. 9.
33. Mason, D.J., Hillam, R.A., and Skerry, T.M., Constitutive *in vivo* mRNA expression by osteocytes of b-actin, osteocalcin, connexin-43, c-fos and c-jun, but not TNF-α nor tartrate-resistant acid phosphatase, *J. Bone Mineral Res.,* 11, 350–357, 1996.
34. Hauschka, P.V. and Gallop, P.M., Purification and calcium-binding properties of osteocalcin, the gamma-carboxyglutamate-containing protein of bone, in *Calcium-Binding Proteins and Calcium Function,* Wasserman, R.H., Corradino, R.A., Carafoli, E., Kretsinger, R.H., Maclennan, D.H., and Siegel, F.L., Eds., Elsevier, Amsterdam, 1977, 338.
35. Doty, S.B., Morphological evidence of gap junctions between bone cells, *Calcif. Tissue Int.,* 33, 509–511, 1981.
36. Palumbo, C., Palazzini, S., and Marrotti, G., Morphological study of intercellular junctions during osteocyte differentiation, *Bone,* 11, 401–406, 1990.
37. Ranscht, B., Cadherins and catenins: interactions and functions in embryonic development, *Curr. Opin. Cell Biol.,* 6, 740–746, 1994.
38. Okazaki, M., Takeshita, S., Kawai, S., Kikuno, R., Tsujimura, A., Kudo, A., and Amann, E., Molecular cloning and characterization of OB-cadherin, a new member of cadherin family expressed in osteoblasts, *J. Biol. Chem.,* 269, 12092–12098, 1994.
39. Cheng, S.-L., Lecanda, F., Davidson, M.K., Warlow, P.M., Zhang, S.-F., Zhang, L., Suzuki, S., StJohn, T., and Civitelli, R., Human osteoblasts express a repertoire of cadherins which are critical for BMP-2-induced osteogenic differentiation. *J. Bone Miner. Res.,* 13, 633–644, 1998.
40. Bienz, M., APC: the plot thickens, *Curr. Opin. Genet. Devl.,* 9, 595–603, 1999.
41. Saez, J.C., Berthoud, V.M., Moreno, A.P., and Spray, D.C., Gap junctions: multiplicity of controls in differentiated and undifferentiated cells and possible functional implications. *Adv. Second Messenger Phosphoprotein Res.,* 27, 163–198, 1993.
42. Beyer, E.C., Paul, D.L., and Goodenough, D.E., Connexin family of the gap junction proteins, *J. Membr. Biol.,* 116, 187–194, 1990.
43. Minkoff, R., Rundus, V.R., Parker, S.B., Hertzberg, E.L., Laing, J.G., and Beyer, E.C., Gap junction proteins exhibit early and specific expression during intramembranous bone formation in the developing chick mandible, *Anat. Embryol.,* 190, 231–241, 1994.
44. Vander Molen, M.A., Rubin, C.T., McLeod, K.J., McKauley, L.K., and Donahue, H.J., Gap junctional intercellular communication contributes to hormonal responsiveness in osteoblastic networks, *J. Biol. Chem.,* 271, 12165–12171, 1996.
45. Lecanda, L., Towler, D.A., Ziambaras, K., Cheng, S.-L., Koval, M., Steinberg, T.H., and Civitelli, R., Gap junctional communication modulates gene expression in osteoblastic cells, *Mol. Biol. Cell,* 9, 2249–2258, 1998.
46. Chicurel, M.E., Chen, C.S., and Ingber, D.E., Cellular control lies in the balance of forces, *Curr. Opin. Cell Biol.,* 10, 232–239, 1998.
47. Clark, E.A. and Brugge, J.S., Integrins and signal transduction pathways: the road taken, *Science,* 268, 233–239, 1995.
48. Hughes, D.E., Salter, D.M., and Simpson, R., CD44 expression in human bone: a novel marker of osteocytic differentiation, *J. Bone Miner. Res.,* 9, 39, 1994.

49. Bentolila, V., Boyce, T.M., Fyhrie, D.P., Skerry, T.M., and Schaffler, M.B., Intracortical remodeling in adult rat long bones after fatigue loading, *Bone,* 23, 275–281, 1998.
50. Verborgt, O., Gibson, G.J., and Schaffler, M.B., Loss of osteocyte integrity in association with microdamage and bone remodeling after fatigue *in vivo, J. Bone Miner. Res.,* 15, 60–67, 2000.
51. Kerr, J.F.R. and Harmon, B.V., Definition and incidence of apoptosis, in *Apoptosis: The Molecular Basis of Cell Death,* Tomei, L.D. and Cope, F.O., Eds., Cold Spring Harbor Press, Cold Spring Harbor, NY, 1991, 5.
52. Buja, L.M., Eigenbrodt, M.L., and Eigenbrodt, E.H., Apoptosis and necrosis—basic types and mechanisms of cell death, *Arch. Pathol. Lab. Med.,* 117, 1208–1214, 1993.
53. Boyce, B.F., Role of apoptosis in local regulation, in *Principles of Bone Biology,* Bilezikian, J.P., Raisz, L.G., and Rodan, G.A., Eds., Academic Press, San Diego, 1996, chap. 53.
54. Raff, M.C., Barres, B.A., Burne, J.F., Coles, H.S., Ishizaki, Y., and Jacobson, M.D., Programmed cell death and control of cell survival—lessons from the nervous system, *Science,* 262, 695–700, 1993.
55. Tomkinson, A., Gevers, E.F., Wit, J.M., Reeve, J., and Noble, B.S., The role of estrogen in the control of rat osteoyte apoptosis, *J. Bone Miner. Res.,* 13, 1243–1250, 1998.
56. Robey, P.G. and Termine, J.D., Human bone cells *in vitro*, *Calcif. Tissue Int.,* 37, 453–460, 1985.
57. Partridge, N.C. and Winchester, S.K., Osteoblast proteinases, in *Principles of Bone Biology,* Bilezikian, J.P., Raisz, L.G., and Rodan, G.A., Eds., Academic Press, San Diego, 1996, chap. 16.
58. Holliday, L.S., Welgus, H.G., Fliszar, C.J., Veith, G.M., Jeffrey, J.J., and Gluck, S.L., Initiation of osteoclast bone resorption by interstitial collagenase, *J. Biol. Chem.,* 272, 22053–22058, 1997.
59. Lacey, D.L., Timms, E., Tan, H.-L., Kelley, M.J., Dunstan, C.R., Burgess, T., Elliott, R., Colombero, A., Elliot, G., Scully, S., Hsu, H., Sullivan, J., Hawkins, N., Davy, E., Capparelli, C., Eli, A., Qian,Y.-X., Kaufman, S., Sarosi, I., Shalhoub, V., Senaldi, G., Guo, J., Delaney, J., and Boyle, W.J., Osteoprotegerin ligand is a cytokine that regulates osteoclast differentiation and activation, *Cell,* 93, 165–176, 1998.
60. Lee, S.-K. and Lorenzo, J.A., Parathyroid hormone stimulates TRANCE and inhibits osteoprotegerin messenger ribonucleic acid expresison in murine bone marrow cultures: correlation with osteoclast-like cell formation, *Endocrinology.,* 140, 3552–3561, 1999.
61. Clemens, T.L., Vasoactive agents and bone metabolism, in *Principles of Bone Biology,* Bilezikian, J.P., Raisz, L.G., and Rodan, G.A., Eds., Academic Press, San Diego, 1996, chap. 42.
62. Harada, S., Nagy, J.A., Sullivan, K.A., Thomas, K.A., Endo, N., Rodan, G.A., and Rodan, S.B., Induction of vascular endothelial growth factor expression by prostaglandin E2 and E1 in osteoblasts, *J. Clin. Invest.,* 93, 2490–2496, 1994.
63. Murray, E.J., Tram, K.K., Spencer, M.J., Tidball, J.G., Murray, S.S., and Lee, D.B., PTH-mediated osteoblast retraction: possible participation of the calpain pathway, *Miner. Electrolyte Metab.,* 21, 184–188, 1995.
64. Bekker, P.J. and Gay, C.V., Biochemical characterization of an electrogenic vacuolar proton pump in purified chicken osteoclast plasma membrane vesicles, *J. Bone Miner. Res.,* 5, 569–579, 1990.
65. Vaananen, K., Osteoclast function: biology and mechanisms, in *Principles of Bone Biology,* Bilezikian, J.P., Raisz, L.G., and Rodan, G.A., Eds., Academic Press, San Diego, 1996, chap. 8.
66. Delaisse, J.M., Eeckhout, Y., Neff, L., Francois-Gillet, C., Henriet, P., Su,Y., Vaes, G., and Baron, R., (Pro)collagenase (matrix metalloproteinase-1) is present in rodent osteoclasts and in the underlying bone resorbing compartment, *J. Cell Sci.,* 106, 1071–1082, 1993.
67. Okada, Y., Naka, K., Kawamura, K., and Matsumoto, T., Localization of matrix metalloproteinase 9 (92-kilodalton gelatinase/type IV collagenase = gelatinase B) in osteoclasts: implications for bone resorption, *Lab. Invest.,* 72, 311, 1995.
68. Goto, T., Kiyoshima, T., Moroi, R., Tsukuba, T., Nishimura, Y., and Kato, K., Immunocytochemical localization of cathepsins B, D and L in the rat osteoclast, *Histochemistry.,* 99, 411–414, 1993.
69. Everts, V., Delaisse, J.-M., Korper, W., and Beertsen, W., Cysteine proteinases and matrix metalloproteinases play distinct roles in the subosteoclastic resorption zone, *J. Bone Miner. Res.,* 13, 1420–1430, 1998.

70. Gelb, B.D., Shi, G.-P., Chapman, H.A., and Desnick, R.J., Pycnodysostosis, a lysosomal disease caused by cathepsin K deficiency, *Science,* 273, 1236–1238, 1996.
71. Popoff, S.N. and Marksk S.C., Jr., The heterogeneity of the osteopetroses reflects the diversity of cellular influences during skeletal development, *Bone,* 17, 437–445, 1995.
72. Soriano, P., Montgomery, C., Geske, R., and Bradley, A., Targeted disruption of the c-src proto-oncogene leads to osteopetrosis in mice, *Cell,* 64, 693–702, 1991.
73. Mimura, H., Cao, X., Ross, F.P., Chiba, M., and Teitelbaum, S.L., 1,25-Dihydroxyvitamin D3 transcriptionally activates the beta 3-integrin subunit gene in avian osteoclast precursors, *Endocrinology.,* 134, 1061–1066, 1994.
74. Miyauchi, A., Alvarez, J., Greenfield, E.M., Teti, A., Grano, M., Colucci, S., Zambonin-Zallone, A., Ross, F.P., Teitelbaum, S.L., Cheresh, D., and Hruska, K.A., Recognition of osteopoontin and related peptides by an $\alpha V\beta 3$ integrin stimulates immediate cell signals in osteoclasts, *J. Biol. Chem.,* 266, 20369–20374, 1991.
75. Lakkakorpi, P.T., Helfrich, M.H., Horton, M.A., and Vaananen, H.K., Spatial organization of microfilaments and vitronectin receptor, alpha V beta 3 in osteoclasts. A study using confocal laser scanning microscopy, *J. Cell Sci.,* 104, 663–670, 1993.
76. Fisher, J.E., Caulfield, M.P., Sato, M., Quartuccio, H.A., Gould, R.J., Garsky, V.M., Rodan, G.A., and Rosenblatt, M., Inhibition of osteoclastic bone resorption *in vivo* by echistatin, an "arginyl-glycyl-aspartyl" (RGD)-containing protein, *Endocrinology,* 132, 1411–1413, 1993.
77. Zhang, D., Udagawa, N., Nakamura, I., Murakami, H., Saito, S., Yamasaki, K., Shibasaki, Y., Morii, N., Narumiya, S., Taakhashi, N., and Suda, T., The small GTP-binding protein, rho p21, is involved in bone resorption by regulating cytoskeletal organization in osteoclasts, *J. Cell Sci.,* 108, 2285–2292, 1995.
78. Triffit, J.T., The stem cell of the osteoblast, in *Principles of Bone Biology,* Bilezikian, J.P., Raisz, L.G., and Rodan, G.A., Eds., Academic Press, San Diego, 1996, chap. 4.
79. Chen, X.-D., Qian, H.-Y., Neff, L., Satomura, K., and Horowitz, M.C. Thy-1 antigen expression by cells in the osteoblastic lineage, *J. Bone Miner. Res.,* 14, 362–375, 1999.
80. Gronthos, S., Graves, S.E., Ohta, S., and Simmons, P.J., The STRO-1 fraction of adult human bone marrow contains the soteogenic precursors, *Blood,* 84, 4164–4173, 1994.
81. Bruder, S.P., Horowitz, M.C., Mosca, J.D., and Haynesworth, S.E., Monoclonal antibodies reactive with human osteogenic cell surface antigens, *Bone,* 21, 225–235, 1997.
82. Joyner, C.J., Bennett, A., and Triffitt, J.T., Identification and enrichment of human osteoprogenitor cells by using differentiation stage-specific monoclonal antibodies, *Bone,* 21, 1–6, 1997.
83. Oyajobi, B.O., Lomri, A., Hott, M., and Marie, P.J., Isolation and characterization of human clonogenic osteoblast progenitors immunoselected from fetal bone marrow stroma using STRO-1 monoclonal antibody, *J. Bone Miner. Res.,* 14, 351–361, 1999.
84. Rodan, G.A. and Harada, S., The missing bone, *Cell,* 89, 677–680, 1997.
85. Weintraub, H., The MyoD family and myogenesis: redundancy, networks and thresholds, *Cell,* 75, 1241–1244, 1983.
86. Ducy, P., Zhang, R., Geoffroy, V., Ridall, A.L., and Karsenty, G., Osf2/Cbfa1: a transcriptional activator of osteoblast differentiation, *Cell,* 89, 747–754, 1997.
87. Komori, T., Yagi, H., Nomura, S., Yamaguchi, A., Sasaki, K., Deguchi, K., Shimizu, Y., Bronson, R.T., Gao, Y.-H., Inada, M., Sato, M., Okamoto, R., Kitamura, Y., Yoshiki, S., and Kishimoto, T., Targeted disruption of cbfa1 results in a complete lack of bone formation owing to maturational arrest of osteoblasts, *Cell,* 89, 755–764, 1997.
88. Massague, J., TGF-β signal transduction, *Annu. Rev. Biochem.,* 67, 753–791, 1998.
89. Wozney, J.M., Rosen, V., Celeste, A.J., Mitsock, L.M., Whitters, M.J., Kriz, R.W., Hewick, R.M., and Wang, E.A., Novel regulators of bone formation: molecular clones and activities, *Science,* 242, 1528–1534, 1988.
90. Winnier, G., Blessing, M., Labosky, P.A., and Hogan, B.L.M., Bone morphogenetic protein-4 is required for mesoderm formation and patterning in the mouse, *Genes Dev.,* 9, 2105–2116, 1995.

91. Kingsley, D.M., Bland, A.E., Grubber, J.M., Marker, P.C., Russell, L.B., Copeland, N.G., and Jenkins, N.A., The mouse short-ear skeletal morphogenesis locus is associated with defects in a bone morphogenetic member of the TGFβ superfamily, *Cell,* 71, 399–410, 1992.
92. Bostrom, M.P.G., Lane, J.M., Berberian, W.S., Missri, A.A.E., Tomin, E., Weiland, A., Doty, S.B., Glaser, D., and Rosen, V.M., Immunolocalization and expression of bone morphogenetic proteins 2 and 4 in fracture healing, *J. Orthop. Res.,* 13, 357–367, 1995.
93. Bax, B.E., Wozney, J.M., and Ashhurst, D.E., Bone morphogenetic protein-2 increases the rate of callus formation after fracture of the rabbit tibia, *Calcif. Tissue Int.,* 65, 83–89, 1999.
94. Ghosh-Choudhury, N., Harris, M.A., Feng, J.Q., Mundy, G.R., and Harris, S.E., Expression of the BMP-2 gene during bone cell differentiation, *Crit. Rev. Eukaryot. Gene Expr.,* 4, 345–355, 1994.
95. Boden, S.D., Hair, G., Titus, L., Racine, M., MeKuaig, K., Wozney, J.M., and Nanes, M.S., Glucocorticoid-induced differentiation of fetal rat calvarial osteoblasts is mediated by bone morphogenetic protein-6, *Endocrinology.,* 138, 2820–2828, 1997.
96. Boden, S.D., Liu, Y., Hair, G.A., Helms, J.A., Hu, D., Racine, M., Nanes, M.S., and Titus, L., LMP-1, a LIM-domain protein, mediates BMP-6 effects on bone formation, *Endocrinology.,* 139, 125–134, 1998.
97. Yamaguchi, A., Katagiri, T., Ikeda, T., Wozney, J.M., Rosen, V., Wang, E.A., Kahn, A.J., Suda, T., and Yoshiki, S., Recombinant human bone morphogenetic protein-2 stimulates osteoblastic maturation and inhibits myogenic differentiation *in vitro*, *J. Cell Biol.,* 113, 681–687, 1991.
98. Gimble, J.M., Morgan, C., Kelly, K., Wu, X., Dandapani, V., Wang, C.-S., and Rosen, V., Bone morphogenetic proteins inhibit adipocyte differentiation by bone marrow stromal cells, *J. Cell. Biochem.,* 58, 393–402, 1995.
99. Brunet, L.J., McMahon, J.A., McMahon, A.P., and Harland, R.M., Noggin, cartilage morphogenesis and joint formation in the mammalian skeleton, *Science,* 280, 1455–1457, 1998.
100. Gazzerro, E., Gangji, V., and Canalis, E., Bone morphogenetic proteins induce the expression of noggin, which limits their activity in cultured rat osteoblasts, *J. Clin. Invest.,* 102, 2106–2114, 1998.
101. Canalis, E. and Ryzdiel, S., Platelet-derived growth factor and the skeleton, in *Principles of Bone Biology,* Bilezikian, J.P., Raisz, L.G., and Rodan, G.A., Eds., Academic Press, San Diego, 1996, chap. 44.
102. Hurley, M.M. and Florkiewicz, R.Z., Fibroblast growth factor and vascular endothelial cell growth factor families, in *Principles of Bone Biology,* Bilezikian, J.P., Raisz, L.G., and Rodan, G.A., Eds., Academic Press, San Diego, 1996, chap. 45.
103. Conover, C.A., The role of insulin-like growth factors and binding proteins in bone cell biology, in *Principles of Bone Biology,* Bilezikian, J.P., Raisz, L.G., and Rodan, G.A., Eds., Academic Press, San Diego, 1996, chap. 43.
104. McKibbin, B., The biology of fracture healing in long bones, *J. Bone Joint Surg.,* 60B,150–162, 1978.
105. Iwaki, A., Jingushi, S., Oda, Y., Izumi, T., Shida, J., Tsuneyoshi, M., and Sugioka, Y., Localization and quantification of proliferating cells during rat fracture repair: detection of proliferating cell nuclear antigen by immunohistochemistry, *J. Bone Mineral Res.,* 12, 96–102, 1997.
106. Bruder, S.P., Ricalton, N.S., Boynton, R.E. et al., Mesenchymal stem cell surface antigen SB-10 corresponds to activated leukocyte cell adhesion molecule and is involved in osteogenic differentiation, *J. Bone Miner. Res.,* 13, 655–663, 1998.
107. Weinstein, R.S., Jilka, R.L., Parfitt, A.M., and Manolagas, S.C., Inhibition of osteoblastogenesis and promotion of apoptosis of osteoblasts and osteocytes by glucocorticoids, *J. Clin. Invest.,* 102, 274–282, 1998.
108. Dempster, D.W., Cosman, F., Parisien, M., Shen, V., and Lindsay, R., Anabolic actions of parathyroid hormone on bone, *Endocr. Rev.,* 14, 690–708, 1993.
109. Jilka, R.L., Weinstein, R.S., Bellido, T., Roberson, P., Parfitt, A.M., and Manolagas, S.C., Increased bone formation by prevention of osteoblast apoptosis with parathyroid hormone, *J. Clin. Invest.,* 104, 439–446, 1999.
110. Roodman, G.D., Cell biology of the osteoclast, *Exp. Hematol.,* 27, 1229–1241, 1999.

111. Takahashi, N., Yamana, H., Yoshiki, S., Goodman, G.D., Mundy, G.R., Jones, S.J., Boyde, A., and Suda, T., Osteoclast-like cell formation and its regulation by osteotropic hormones in mouse bone marrow cultures, *Endocrinology,* 122, 1373–1382, 1988.
112. Yasuda, H., Shima, N., Nakagawa, N., Yamaguchi, K., Kinosaki, M., Mochizuki, S., Yomoyasu, A., Yano, K., Goto, M., Murakami, A., Tsuda, E., Morinaga, T. et al., Osteoclast differentiation factor is a ligand for osteoprotegerin/osteoclastogenesis-inhibitory factor and is identical to TRANCE/RANKL, *Proc. Natl. Acad. Sci. U.S.A.,* 95, 3597, 1998.
113. Grigoriadis, A.E., Wang, Z.-Q., and Wagner, E.F., Regulation of bone cell differentiation and bone remodelling by the c-fos/AP-1 transcription factor, in *Principles of Bone Biology,* Bilezikian, J.P., Raisz, L.G., and Rodan, G.A., Eds., Academic Press, San Diego, 1996, chap. 2.
114. Grigoriadis, A.E., Wang, Z.-Q., and Wagner, E.F., c-fos oncogene expression in cartilage and bone tissues of transgenic and chimeric mice; in *Cellular and Molecular Biology of the Bone,* Noda, M., Ed., Academic Press, San Diego, 1993, 497.
115. Grigoriadis, A.E., Wang, Z.-Q., Cecchini, M.G., Hofstetter, W., Felix, R., Fleisch, H.A., and Wagner, E.F., c-Fos: a key regulator of osteoclast-macrophage lineage determination and bone remodeling, *Science,* 266, 443–448, 1994.
116. Tau, K.R., Hefferan, T.E., Waters, K.M., Robinson, J.A., Subramaniam, M., Riggs, B.L., and Spelsberg, T.C., Estrogen regulation of a transforming growth factor-beta inducible early gene that inhibits deoxyribonucleic acid synthesis in human osteoblasts, *Endocrinology,* 139, 1346–1353, 1998.
117. Miyazaki, T., Katagiri, H., Kanegae, Y., Takayanagi, H., Sawada, Y., Yamamoto, A., Pando, M., Asano, T., Verma, I.M., Oda, H., Nakamura, K., and Tanaka, S., Reciprocal role of ERK and NFkB pathways in survival and activation of osteoclasts, *J. Cell Biol.,* 148, 333–342, 2000.
118. Segre, G.V., Receptors for parathyroid hormone and parathyroid hormone-related protein, in *Principles of Bone Biology,* Bilezikian, J.P., Raisz, L.G., and Rodan, G.A., Eds., Academic Press, San Diego, 1996, chap. 28.
119. Goldring, S.E., The structure and molecular biology of the calcitonin receptor, in *Principles of Bone Biology,* Bilezikian, J.P., Raisz, L.G., and Rodan, G.A., Eds., Academic Press, San Diego, 1996, chap. 33.
120. Fitzpatrick, L.A. and Bilezikian, J.P., Actions of Parathyroid Hormone, in *Principles of Bone Biology,* Bilezikian, J.P., Raisz, L.G., and Rodan, G.A., Eds., Academic Press, San Diego, 1996, chap. 25.
121. Rouleau, M.F., Mitchell, L., and Goltzman, D., *In vivo* distribution of parathyroid hormone receptors in bone: evidence that a predominant osseous target cell is not the mature osteoblast, *Endocrinology,* 123, 187–191, 1988.
122. Quinn, C.O., Scott, D.K., Brinckerhoff, C.E., Matrisian, L.M., Jeffrey, J.J., and Partridge, N.C., Rat collagenase: cloning, amino acid sequence comparison and parathyroid hormone regulation in osteoblastic cell, *J. Biol. Chem.,* 265, 22342–22347, 1990.
123. Kream, B.E., LaFrancis, D., Petersen, D.N., Woody, C., Clark, S., Rowe, D.W., and Lichtler, A.W., Parathyroid hormone represses a1(I) collagen promoter activity in cultured calvariae from neonatal transgenic mice, *Mol. Endocrinol.,* 7, 399–408, 1993.
124. Isogai, Y., Akatsu, T., Ishizuya, T., Yamaguchi, A., Hori, M., Takahashi, N., and Suda, T., Parathyroid hormone regulates osteoblast differentiation positively or negatively depending on the differentiation stages, *J. Bone Miner. Res.,* 11, 1384–1393, 1996.
125. Lauber, A., Sandhu, N.P., Schuchard, M., Subramaniam, M., and Spelsberg, T.C., Nuclear matrix acceptor binding sites for steroid hormone receptors: a candidate nuclear matrix acceptor protein, in *Int. Rev. Cytol.,* Berezney, R., Ed., Academic Press, San Diego, 1995, 337.
126. Harris, S.A., Tau, K.R., Turner, R.T., and Spelsberg, T.C., Estrogens and progestins, in *Principles of Bone Biology,* Bilezikian, J.P., Raisz, L.G., and Rodan, G.A., Eds., Academic Press, San Diego, 1996, chap. 36.
127. Christakos, S., Vitamin D gene regulation, in *Principles of Bone Biology,* Bilezikian, J.P., Raisz, L.G., and Rodan, G.A., Eds., Academic Press, San Diego, 1996, chap. 31.

128. Stein, G.S., Lian, J.B., Stein, J.L., van Wijnen, A.J., Frenkel, B., and Montecino, M., Mechanisms regulating osteoblast proliferation and differentiation, in *Principles of Bone Biology,* Bilezikian, J.P., Raisz, L.G., and Rodan, G.A., Eds., Academic Press, San Diego, 1996, chap. 6.
129. Norman, A.W. and Collins, E.D., Vitamin D receptor structure, expression and nongenomic effects. in *Principles of Bone Biology,* Bilezikian, J.P., Raisz, L.G., and Rodan, G.A., Eds., Academic Press, San Diego, 1996, chap. 30.
130. Lukert, B.P. and Kream, B.E., Clinical and basic aspects of glucocorticoids on bone, in *Principles of Bone Biology,* Bilezikian, J.P., Raisz, L.G., and Rodan, G.A., Eds., Academic Press, San Diego, 1996, chap. 38.
131. Kream, B.E., Petersen, D.N., and Raisz, L.G., Cortisol enhances the anabolic effects of insulin-like growth factor Ion collagen synthesis and procollagen messenger ribonucleic acid levels in cultured 21 day fetal rat calvariae, *Endocrinology,* 126, 1576–1583, 1990.
132. Rodan, S.B., Fischer, M.K., Egan, J.J., Epstein, P.M., and Rodan, G.A., The effect of dexamethasone on parathyroid hormone stimulation of adenylate cyclase in ROS 17/2.8 cells, *Endocrinology,* 115, 951–958, 1984.
133. Gronowicz, G.A., DeRome, M.E., and McCarthy, M.-B., Glucocorticoids inhibit fibronectin synthesis and messenger ribonucleic acid levels in cultured fetal rat parietal bones, *Endocrinology,* 128, 1107–1114, 1991.
134. Gronowicz, G.A. and McCarthy, M.-B., Glucocorticoids inhibit the attachment of osteoblasts to bone extracellular matrix proteins and decrease β1 integrin levels, *Endocrinology,* 136, 598–608, 1995.
135. Orwoll, E., Androgens, in *Principles of Bone Biology,* Bilezikian, J.P., Raisz, L.G., and Rodan, G.A., Eds., Academic Press, San Diego, 1996, chap. 40.
136. Turner, R.T., Riggs, B.L., and Spelsberg, T.C., Skeletal effects of estrogen, *Endocr. Rev.,* 15, 275–300, 1994.
137. Orwoll, E.S. and Klein, R.F., Osteoporosis in men, *Endocr. Rev.,* 16, 87–116, 1995.
138. Gruber, R., Czerwenka, K., Wolf, F., Ho, G.-M., Willheim, M., and Peterlik, M., Expression of the vitamin D receptor, of estrogen and thyroid hormon receptor α- and β-isoforms, and of the androgen receptor in cultures of native mouse bone marrow and stromal/osteoblastic cells, *Bone,* 24, 465–473, 1999.
139. Horowitz, M.C., Cytokines and estrogen in bone: anti-osteoporotic effects, *Science,* 260, 626–627, 1993.
140. Bismar, H., Diel, I., Ziegler, R., and Pfeilschifter, J., Increased cytokine secretion by human bone marrow cells after menopause or discontinuation of estrogen replacement, *J. Clin. Endocrinol. Metab.,* 80, 3351–3355, 1995.
141. Rifas, L., Kenney, J.S., Marcelli, M., Pacifici, R., Cheng, S.-L., Dawson, L.L., and Avioli, L.V., Production of interleukin-6 in human osteoblasts and human bone marrow stromal cells: evidence that induction by interleukin-1 and tumor necrosis factor is not regulated by ovarian steroids, *Endocrinology,* 136, 4056–4067, 1995.
142. Yang, N.N., Bryant, H.U., Hardikar, S., Sato, M., Galvin, R.J.S., Glasebrook, A.L., and Termine, J.D., Estrogen and raloxifene stimulate transforming growth factor-β3 gene expression in rat bone: a potential mechanism for estrogen- or raloxifene-mediated bone maintenance, *Endocrinology,* 137, 2075–2084, 1996.
143. Ernst, M., Heath, J.K., and Rodan, G.A., Estradiol effects on proliferation, messenger ribonucleic acid for collagen and insulin-like growth factor-I and parathyroid hormone-stimulated adenylate cyclase activity in osteoblastic cells from calvariae and long bones, *Endocrinology,* 125, 825–833, 1989.
144. Turner, R.T., Backup, P., Sherman, P.J., Hill, E., Evans, G.L., and Spelsberg, T.C., Mechanism of action of estrogen on intramembranous bone formation: regulation of osteoblast differentiation and activity, *Endocrinology,* 131, 883–889, 1992.

145. Pilbeam, C.C., Harrison, J.R., and Raisz, L.G., Prostaglandins and bone metabolism, in *Principles of Bone Biology,* Bilezikian, J.P., Raisz, L.G., and Rodan, G.A., Eds., Academic Press, San Diego, 1996, chap. 51.
146. Kawaguchi, H., Pilbeam, C.C., Harrison, J.R., and Raisz, L.G., The role of prostaglandins in the regulation of bone metabolism, *Clin. Orthop. Relat. Res.,* 313, 36–46, 1995.
147. Klein-Nulend, J., van der Plas, A., Semeins, C.M., Ajubi, N.E., Frangos, J.A., Nijweide, P.J., and Burger, E.H., Sensitivity of osteocytes to biomechanical stress *in vitro*, *FASEB J.,* 9, 441–445, 1995.
148. Kawaguchi, H., Raisz, L.G., Voznesensky, O.S., Alander, C.B., Hekeda, Y., and Pilbeam, C.C., Regulation of the two prostaglandin G/H synthases by parathyroid hormone, interleukin-1, cortisol and prostaglandin E2 in cultured neonatal mouse calvariae, *Endocrinology,* 135, 1157–1164, 1994.
149. Jee, W.S.S. and Ma, Y.F., The *in vivo* anabolic actions of prostaglandins in bone, *Bone,* 21, 297, 1997.
150. Bonewald, L.F., Transforming growth factor-β, in *Principles of Bone Biology,* Bilezikian, J.P., Raisz, L.G., and Rodan, G.A., Eds., Academic Press, San Diego, 1996, chap. 46.
151. Bottinger, E.P., Letterio, J.J., and Roberts, A.B., Biology of TGF-β in knockout and transgenic mouse models, *Kidney Int.,* 51, 1355–1360, 1997.
152. Erlebacher, A. and Derynck, R., Increased expression of TGFβ2 in osteoblasts results in an osteoporosis-like phenotype, *J. Cell Biol.,* 132, 195–210, 1996.
153. Gehron Robey, P.G., Young, M.F., Flanders, K.C., Dody, N.S., Kondaiah, P., Reddi, A.H., Termine, J.D., Sporn, M.D., and Roberts, A.B., Osteoblasts synthesize and respond to transforming growth factor type β (TGF-β) *in vitro, J. Cell Biol.,* 105, 457–463, 1987.
154. Dallas, S.L., Miyazono, K., Skerry, T.M., Mundy, G.R., and Bonewald, L.F., Dual role for the latent transforming growth factor beta binding protein (LTBP) in storage of latent TGFβ in the extracellular matrix and as a structural matrix protein, *J. Cell Biol.,* 131, 539–549, 1995.
155. Murakami, S., Kan, M., McKeehan, W.L., and de Crombrugghe, B., Up-regulation of the chondrogenic Sox9 gene by fibroblast growth factors is mediated by the mitogen-activated protein kinase pathway, *Proc. Natl. Acad. Sci. U.S.A.,* 97, 1113–1118, 2000.
156. McCarthy, T.L., Centrella, M., and Canalis, E., Effects of fibroblast growth factors on deoxyribonucleic acid and collagen synthesis in rat parietal bone cells, *Endocrinology,* 125, 2118–2126, 1989.
157. Simmons, H.A., Thomas, K.A., and Raisz, L.G., Effects of acidic and basic fibroblast growth factor and heparin on resorption of cultured fetal rat long bone, *J. Bone Miner. Res.,* 6, 1301–1305, 1991.
158. Scully, S.P., Joyce, M.E., Abidi, N., and Bolander, M.E., The use of polymerase chain reaction generated nucleotide sequences as probes for hybridization, *Mol. Cell. Probes,* 4, 485–495, 1990.
159. Kawaguchi, H., Kurokawa, T., Hanada, K., Hiyama, Y., Tamura, M., Ogata, E., and Matsumoto, T., Stimulation of fracture repair by recombinant human basic fibroblast growth factor in normal and streptozotocin-diabetic rats, *Endocrinology,* 135, 774–781, 1994.
160. Stiles, C.D., Capone, G.T., Scher, C.D., Antonaides, H.N., Van Wyk, J.J., and Pledger, W.J., Dual control of cell growth by somatomedins and platelet-derived growth factor, *Proc. Natl. Acad. Sci. U.S.A.,* 76, 1279–1283, 1979.
161. Hock, J.M. and Canalis, E., Platelet-derived growth factor enhances bone cell replication but not differentiated function of osteoblasts, *Endocrinology.,* 134, 1423–1428, 1994.
162. Andrew, J.G., Hoyland, J.A., Freemont, A.J., and Marsh, D.R., Platelet-derived growth factor expression in normally healing human fractures, *Bone,* 16, 455–460, 1995.
163. Hock, J.M., Centrella, M., and Canalis, E., Insulin-like growth factor I has independent effects on bone matrix formation and cell replication, *Endocrinology,* 122, 254–260, 1988.
164. Horowitz, M.C. and Lorenzo, J.A. Local regulators of bone: IL-1, TNF, lymphotoxin, interferon-γ, IL-8, IL=10, IL-4, the LIF/IL-6 family, and additional cytokines, in *Principles of Bone Biology,* Bilezikian, J.P., Raisz, L.G., and Rodan, G.A., Eds., Academic Press, San Diego, 1996, chap. 49.
165. Pacifici, R., Brown, C., Puscheck, E., Friedrich, E., Slatopolsky, E., Maggio, D., McCracken, R., and Avioli, L.V., Effect of surgical menopause and estrogen replacement on cytokine release from human blood mononuclear cells, *Proc. Natl. Acad. Sci. U.S.A.,* 88, 5134–5138, 1991.

166. Arend, W.P., Welgus, H.G., Thompson, R.C., and Eisenberg, S.P., Biological properties of recombinant human monocyte-derived interleukin 1 receptor antagonist, *J. Clin. Invest.,* 85, 1694–1697, 1990.
167. Manolagas, S.C., Jilka, R.L., Bellido, T., O'Brien, C.A., and Parfitt, A.M., Interleukin-6-type cytokines and their receptors, in *Principles of Bone Biology,* Bilezikian, J.P., Raisz, L.G., and Rodan, G.A., Eds., Academic Press, San Diego, 1996, chap. 50.
168. Sadowski, H.B., Shuai, K., Darnell, J.E., and Gillman, M.Z., A common nuclear signal transduction pathway activated by growth factor and cytokine receptors, *Science,* 261, 1739–1744, 1993.
169. Stahl, N., Farruggella, T.J., Boulton, T.G., Zhong, Z., Darnell, J.E., and Yancopoulos, G.D., Choice of stats and other substrates specified by molecular tyrosine-based motifs in cytokine receptors, *Science,* 267, 1349–1353, 1995.
170. Silvennoninen, O., Wittuhn, B., Quelle, F., Cleveland, J., Yi, T., and Ihle, J., Structure of the murine JAK2 protein-tyrosine kinase and its role in IL-3 signal transduction, *Proc. Natl. Acad. Sci. U.S.A.,* 90, 8429–8433, 1993.
171. Girasole, G., Jilka, R.L., Passeri, G., Boswell, S., Boder, G., Williams, D.C., and Manolagas, S.C., 17β estradiol inhibits interleukin-6 production by bone marrow-derived stromal cells and osteoblasts *in vitro*: a potential mechanism for the antiosteoporotic effect of estrogens, *J. Clin. Invest.,* 89, 883–891, 1992.
172. Jilka, R.L., Hangoc, G., Girasole, G., Passeri, G., Williams, D.C., Abrams, J.S., Boyce, B., Broxmeyer, H., and Manolagas, S.C., Increased osteoclast development after estrogen loss: mediation by interleukin-6, *Science,* 257, 88–91, 1992.
173. Poli, V., Balena, R., Fattori, E., Markatos, A., Yamamoto, M., Tanaka, H., Ciliberto, G., Rodan, G.A., and Costantini, F., Interleukin-6-deficient mice are protected from bone loss caused by estrogen depletion, *EMBO J.,* 13, 1189–1196, 1994.
174. Ruoslahti, E., Integrins, *J. Clin. Invest.,* 87, 1–5, 1991.
175. Ilic, D., Almeida, E.A., Schlaepfer, D.D., Dazin, P., Aizawa, S., and Damsky, C., Extracellular matrix survival signals transduced by focal adhesion kinase suppress p53-mediated apoptosis, *J. Cell Biol.,* 143, 547–560, 1998.
176. Werb, Z., Tremble, P.M., Behrendtsen, O., Crowley, E., and Damsky, C.H., Signal transduction through the fibronectin receptor induces collagenase and stromelysin gene expression, *J. Cell Biol.,* 109, 877–889, 1989.
177. Bottazzi, M.E., Zhu, X., Bohmer, R.M., and Assoian, R.K., Regulation of p21(cip1) expression by growth factors and the extracellular matrix reveals a role for transient ERK activity in G1 phase, *J. Cell Biol.,* 146, 1255–1264, 1999.
178. Hakeda, Y. and Kumegawa, M., The growth and culture of bone cells: osteoclastic, in *Principles of Bone Biology,* Bilezikian, J.P., Raisz, L.G., and Rodan, G.A., Eds., Academic Press, San Diego, 1996, chap. 88.
179. Murrills, R.J., *In vitro* bone resorption assays, in *Principles of Bone Biology,* Bilezikian, J.P., Raisz, L.G., and Rodan, G.A., Eds., Academic Press, San Diego, 1996, chap. 90.
180. Majeska, R.J., Culture of osteoblastic cells, in *Principles of Bone Biology,* Bilezikian, J.P., Raisz, L.G., and Rodan, G.A., Eds., Academic Press, San Diego, 1996, chap. 89.
181. Gronowicz, G. and Raisz, L.G., Bone formation assays, in *Principles of Bone Biology,* Bilezikian, J.P., Raisz, L.G., and Rodan, G.A., Eds., Academic Press, San Diego, 1996, chap. 91.
182. Van der Plas A., Aarden, E.M., Feyen, J.H.M., de Boer, A.H., Wiltink, A., Alblas, M.J., de Ley, L., and Nijweide, P.J., Characteristics and properties of osteocytes in culture, *J. Bone Miner. Res.,* 7, 389–396, 1994.
183. Kato, Y., Windle, J.J., Koop, B.A., Mundy, G.R., and Bonewald, L.F., Establishment of an osteocyte-like cell line, MLO-Y4, *J. Bone Miner. Res.,* 12, 2014–2023, 1997.

3

Molecular Biology Techniques to Measure Skeletal Gene Expression

Marian F. Young
National Institutes of Health

Suzanne C. Dieudonné
University of Nijmegen

3.1 Introduction

The goal of this chapter is to provide the biomechanical engineer with a description of the fundamental tools and procedures that are currently used to access the quality and quantity of genes made by specific tissues and cells. Genes can be controlled at many levels, as shown schematically in Fig. 3.1. The control of gene expression begins in the nucleus where a combination of DNA sequences (*cis* acting) and proteins (transcription factors, or *trans* acting) interact in the nucleus to make (transcribe) RNA, which then transits to the cytoplasm. By using the ribosome machinery (made of 18S and 28S RNA embedded in proteins) (see Fig. 3.2), the mRNA is translated into proteins that are either used within the cell or secreted and function outside the cell. This chapter will focus exclusively on the analysis of mRNA expression. The methods described are designed to compare the quantity (amount) and quality (specific type of gene) of mRNA activation in control and experimental situations. Thus, the techniques described are used to evaluate the response of a cell or tissue to environmental influences such as biomechanical stress specifically at the "mRNA level." By examining the nature of the RNA that is altered one can extrapolate the corresponding changes in protein expression and develop a framework for understanding the molecular

0-8493-9117-2/01/$0.00+$.50

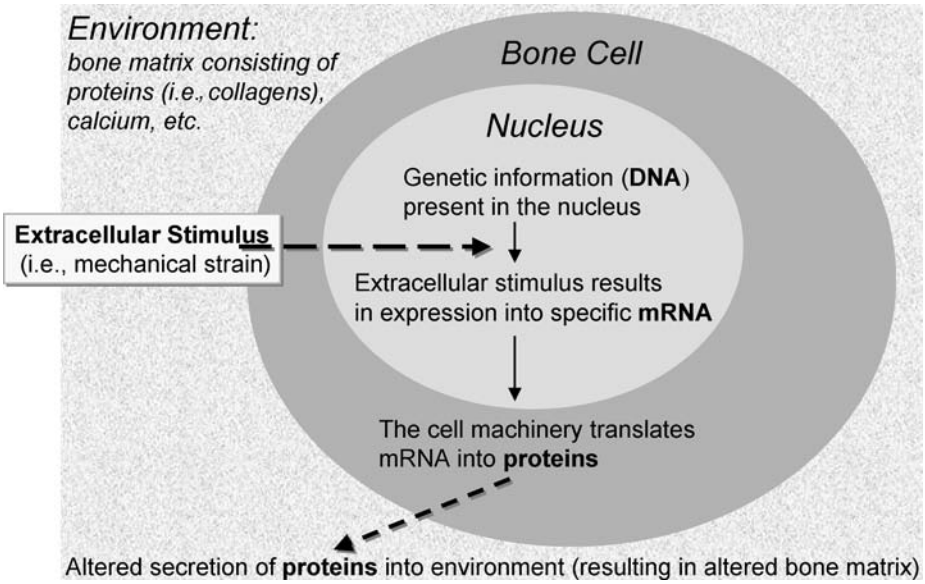

FIGURE 3.1 Schematic representation of gene expression response to extracellular stimuli. This diagram shows the pathway mRNA activation starting in the nucleus. Extracellular stimuli alter this process, leading to changes in the amount and quality of genes (mRNA) expressed. This in turn leads to changes in protein expression that results in an altered bone matrix.

events that accompany changes in skeletal structure and function. Altered protein production results in altered bone matrix composition that can, in turn, affect bone elasticity.

3.2 Examination of Known (Previously Identified) Genes

3.2.1 Northern Blotting

One of the earliest methods that was used to assess gene expression is Northern blotting (Fig. 3.2). In this procedure RNA is extracted from tissues or cultured cells (see Chapter 2) using denaturing agents such as guanidine isothiocyate. Proteins are removed from extracted mixture using organic reagents such as phenol and RNA is concentrated by precipitation with alcohol. In this modern era numerous "kits" are available for RNA isolation, which have all necessary reagents prepacked ready for use. For the "homemade" protocols, several excellent manuals have been written and should be referred to for details of this and other molecular procedures.[1,2] The quantity of RNA extracted is determined by its absorbence of ultraviolet (UV) light at Å260. The quality of RNA is tested by electrophoresis of the RNA through a denaturing agarose gel resulting in separation of the RNA that is expressed. By including a small quantity of ethidium bromide in the samples, the separated RNA can be visualized under shortwave UV light and appears as two bright bands representing the 28S and 18S ribosomal RNA species. The messenger RNA (mRNA or RNA that gets expressed into protein, which together with ribosomal RNA represents what is called total RNA) is not perceptible in the gel and needs further processing for visualization. For easier handling, RNA is transferred from the gel to a solid support or membrane that is made of nitrocellulose or nylon or a mixture of both. The "blotting" refers to the transfer technique; typically RNA is released from the gel by capillary action by placing it next to the membrane. After blotting the RNA is immobilized onto the membrane by UV cross-linking or by heating under a vacuum. The blot is then immersed in a solution that contains a specific gene fragment previously labeled with the isotope P^{32}; this is referred to as the probe. The basis for Northern blotting is that specific probes will hybridize to complementary RNA sequences on the membrane, thus locating any gene of interest (lock-key principle). After washing away unbound probe the blot is exposed to X-ray film and specific mRNA bands are visualized.

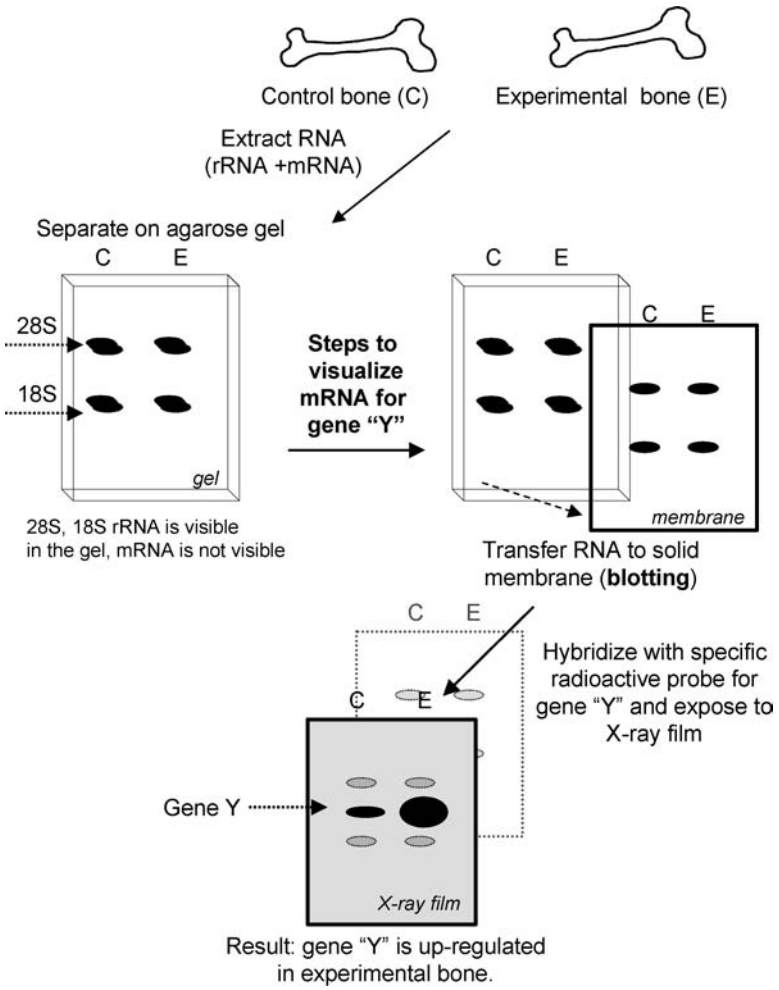

FIGURE 3.2 Northern blotting. In this technique RNA is separated by gel electrophoresis and transferred to a membrane for detection of specific mRNAs. This is done by labeling a specific gene (cDNA) using radioactive nucleotides (typically α-deoxy CTP^{32}) and "random priming." In this procedure short (six base pair) primers are added to the denatured cDNA (see Fig. 3.3) and through the action of the DNA polymerase (see Figs. 3.3 and 3.5) the radioactive nucleotide is incorporated into a new DNA strand thereby making the cDNA radioactive. The labeled cDNA is then used to detect a specific gene, resulting in a specific, quantitative analysis.

Each mRNA has a characteristic length that can be verified using known sized RNA markers on the gel. The intensity of the radioactive bands reveals the relative amount of the mRNA present (see Fig. 3.2). New imaging techniques allow direct quantitation of the mRNA expressed using metal screens coated with material that is sensitive to P^{32}. The exposed screen is then placed directly in an imaging device and the radioactivity present is quantitated using computer software programs.

Using the Northern blotting procedure numerous mRNAs were shown to be altered in the bones of animals subject to spaceflight,[3,4] mechanical unloading,[5,6] or unloading followed by reloading.[7]

3.2.2 Reverse Transcriptase-Polymerase Chain Reaction

One drawback to the Northern blotting procedure is that at least 1 to 20 μg of RNA (depending on the expression level of the gene of interest) is required for each analysis. To examine very low quantities of mRNA, a problem that often occurs in bone material, some investigators have turned to the powerful

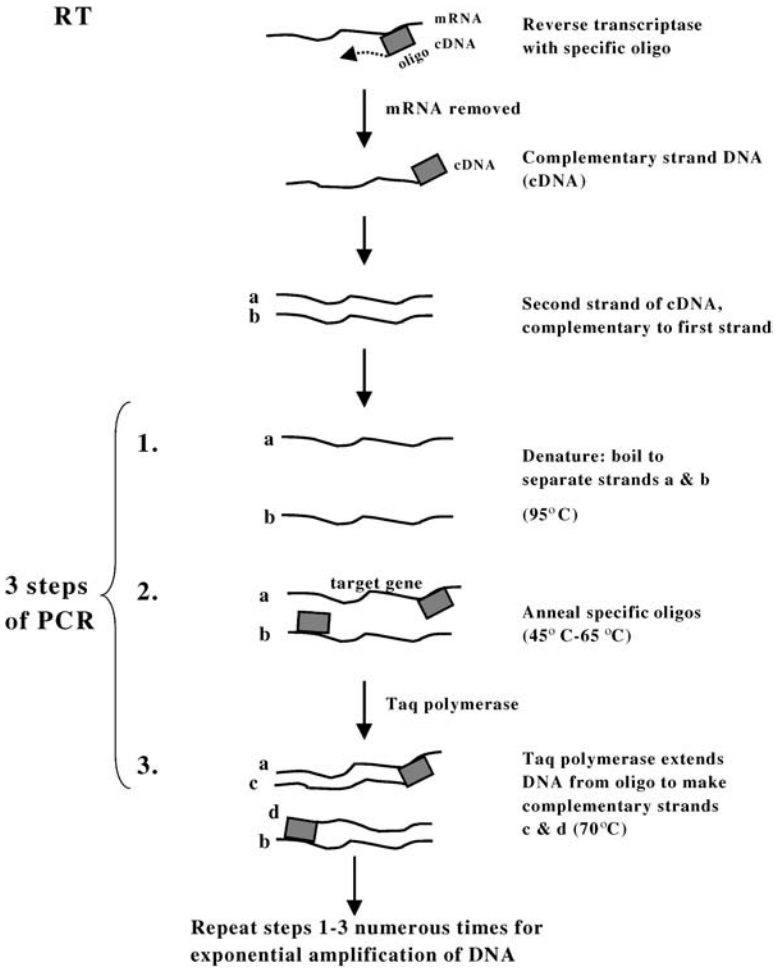

FIGURE 3.3 RT-PCR. This procedure has two parts: (1) a conversion of mRNA to cDNA through the action of RT and (2) amplification of the cDNA using the PCR. Products of the reaction are visualized after separation by gel electrophoresis.

new technique of PCR (polymerase chain reaction) (Fig 3.3). This procedure allows the amplification of minute amounts of material; there are reports of gene detection using a single cell.[8,9] In this method RNA must first be converted to DNA using the enzyme reverse transcriptase (RT). The resulting copy of RNA is called a cDNA and is used as a template for the PCR reaction. By using the enzyme polymerase that was originally isolated from bacteria that live at temperatures up to 70°C (*thermus aquaticus*), DNA can be amplified specifically and exponentially by repeated incubations at various extremes in temperatures. The specificity of the PCR reaction relies on the construction of two short pieces of DNA called oligonucleotides (oligos) that have complementary sequences in the target gene of interest. Different temperatures are used for the three following steps of the PCR process: (1) denaturing the DNA (>95°C); (2) annealing (binding) of the oligo to the target DNA (~45 to 65°C depending on sequence and length of oligos used); and (3) extending the DNA by the action of the polymerase (~70°C) (see Fig. 3.3). The PCR product usually can be visualized directly on agarose gels by staining with ethidium bromide. Every cell contains genomic DNA coding for all genes in the body. It is essential that RNA preparations are not contaminated with genomic DNA; if it is present, it can be amplified and will mask the intended target, which is the mRNA (see Fig. 3.1). DNA can be removed by either (1) treating the RNA preparation with DNase or

(2) designing oligonucleotides that "span an intron" (see Chapter 4). Introns are sequences in the genomic DNA that are not found in mRNA. If they are amplified by PCR, they are detected because they are much larger than the product predicted from the mRNA sequence. One way to "test the system" is to perform the RT-PCR reaction in the absence of RT; mRNA cannot be amplified unless it is first converted to cDNA and no products should be observed.

Many groups have been successful applying this mRNA analysis procedure. Using RT-PCR, changes in *c-fos* (a transcription factor) mRNA expression have been detected in osteoblasts subject to centrifugation in a manner that simulated a space shuttle launch ($3g$).[10] Similarly, when osteocytes were isolated and stretched using a special device that deformed a petri plate with 2000 to 4000 μE, a notable increase of *c-fos* and COX-2 (enzyme that makes prostaglandin) was detected as early as 15 min after treatment.[11]

Some mRNAs are expressed at very low amounts in the cell. For even greater sensitivity, the PCR product (sometimes called an amplicon) is transferred to a solid support or membrane and analyzed in a fashion that is similar to Northern blotting. The membrane containing the amplicon is hybridized to radioactively labeled probes corresponding to the amplified gene, and the amount of hybridization is measured using X-ray film or image screens described in the previous section (see Fig. 3.2).

One drawback to the RT-PCR procedure is that it is semiquantitative in nature. More quantitative procedures based on RT-PCR have been developed using "mimics." In this case, target genes of interest are modified so that when used as a template for RT-PCR they generate a product with a different size than the normal gene. By adding known amounts of the mimic to the PCR reaction, one can estimate the amount of material required to compete with the normal gene and obtain a more accurate estimate of the amount of a specific mRNA in a sample. This procedure was recently carried out using RNA extracted from MG-63 cells (human osteoblast-like cells) (see Chapter 2) and mimics to the bone matrix proteins type I collagen, alkaline phosphatase, and osteocalcin. All three matrix mRNAs were decreased in cells subject to microgravity.[12]

3.2.3 *In Situ* Hybridization

The aforementioned methods of measuring the type and amount of mRNA rely on extracting mRNA from tissues and cells prior to the analysis. One drawback to these methods is that, if a tissue is heterogeneous and composed of several cell types, there is no way to determine which part of the tissue has changes in gene expression. ISH (*in situ* hybridization) is a method that allows localization of specific mRNAs within a tissue (see Ref. 13 and 14 for detailed methodology). Tissues of interest are fixed in buffered 4% paraformaldehyde and, in general, demineralized prior to embedding for histology; some studies show that undecalcified bone sections can be used,[15] but this is not a commonly used approach. Tissue sections are then hybridized with specific RNA or DNA probes in a manner similar to that described for Northern blotting. Because the P^{32} signal has a low resolution, often P^{33} or S^{35} are substituted for labeling the probes. There is an increasing trend to use nonradioactive labeling protocols as well. The advantage here is that probes can be made well in advance and are not subject to half-life considerations.

In many cases investigators complement ISH with immunohistochemistry (*in situ* detection of the protein of interest). Recently, this combined approach was used to show the upregulation of tenascin-C mRNA and protein in bones exposed to mechanical stimulation.[16] In other cases, several methods of mRNA analysis are additionally combined to give greater confidence in the observed results. A good example is the recent discovery of *N*-methyl-D-aspartate-type receptor in osteoblasts and osteoclasts; a combined approach of RT-PCR, ISH, and immunohistochemistry was used to suggest a novel glutamate signaling pathway in bone.[17]

Recently, the RT-PCR was modified so that it could be performed *in situ* (directly on the tissue section). Specifically, in these studies RNA was reverse transcribed *in situ* and subject to PCR to measure mechanically mediated changes in gene expression in osteocytes. When a mechanical stimulus was applied to bones, elevated levels of collagen mRNA in a turkey model[18] and of β-actin, osteocalcin,

connexin-43, insulin-like growth factor-I (IGF-I), c-fos, and c-jun in a rat model[19] were observed. Even though these findings are a relative assessment of gene activity, this is an exciting new development that combines sensitivity with precise cell localization.

3.2.4 RNase Protection Assay

RNase protection assay (RPA) is a method that combines sensitivity with quantitation of extracted RNA. By using this technique, it is possible to examine multiple genes in a single reaction. A specific RNA probe is made, usually labeled with S^{35} or P^{33}, that has a distinct length. RNA is hybridized to the probe, which is complementary to it and therefore called "antisense." Incubation of the hybrid with RNase destroys single-stranded RNA not hybridized or "protected" by the probe (Fig. 3.4). The resulting material that is protected can be visualized after separation on denaturing acrylamide gels followed by autoradiography

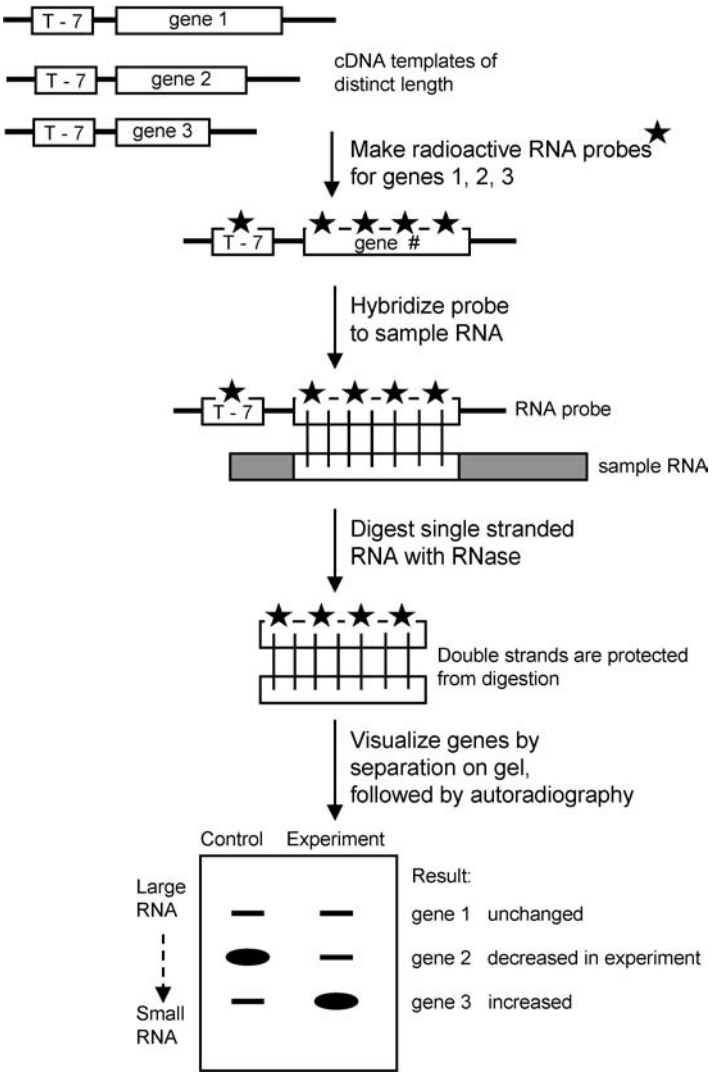

FIGURE 3.4 RPA. Isolated genes are used to make radioactive RNA probes using radiolabeled UTP[P33/S35]. Both sense (same sequence as the mRNA) and antisense (complementary sequence to the mRNA) are used. Only the antisense probe hybridizes and protects the mRNA from the action of added RNase. The protected fragments are visualized by electrophoresis using denaturing acrylamide gels and reveal the relative amount of mRNA present.

similar to Northern blotting. Each gene is identified based on length and quantitated based on its intensity. To date, most RPA kits are geared toward cytokine analysis, but one can generate custom templates using any purified gene of interest.

3.2.5 Array Technology

As more genes are cloned and identified there is a trend to try to examine the expression of numerous genes simultaneously. For this reason array technology was developed, where instead of a dozen genes being analyzed hundreds or even thousands of genes can be examined in a single experiment. The procedure is essentially a modification of the procedures already described. Previously identified genes are amplified and dotted onto membranes in a grid fashion. Instead of labeling specific probes, extracted mRNA is labeled (radioactive or nonradioactive) in an RT reaction (see RT-PCR) and the resulting cDNA is hybridized to the membrane. If an RNA is present in the mixture that corresponds to a gene on the membrane, it will hybridize to it. After washing away nonspecifically bound mRNA, the blot is analyzed as is done for a Northern blot or RPA. Figure 3.5 shows a simplified version of an "array" (i.e., "dot blot"). Current arrays contain hundreds of genes and can be obtained commercially. By using the array technology, analysis of RNA from cells with a nonfunctional estrogen receptor-alpha (ER-α) gene led to the discovery of at least two genes, transforming growth factor-beta (TGF-β) and c-fos, that may be affected by estrogen through ER-α-independent pathways.[20] It must be cautioned here that discovery of differential gene expression using arrays must be confirmed by alternative methods such as Northern, RNase protection, or competitive RT-PCR.

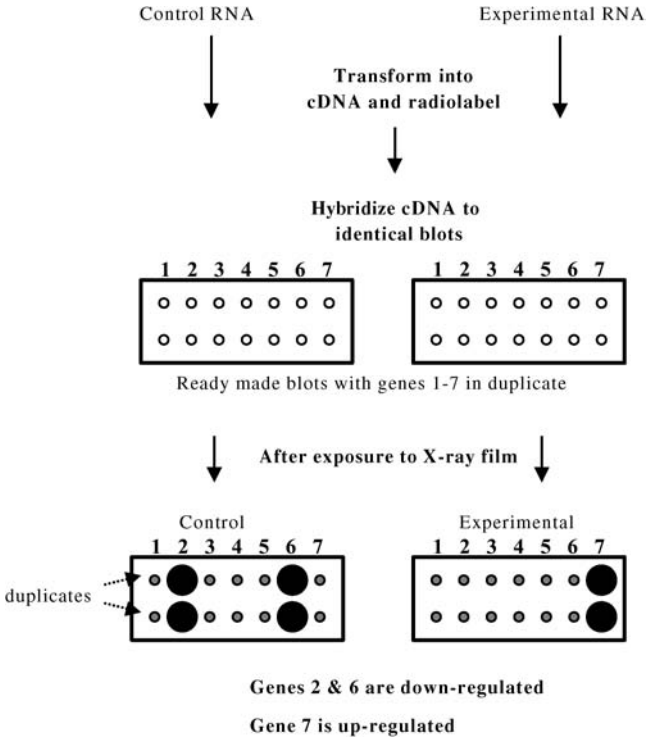

FIGURE 3.5 Arrays. Individual cDNA (genes) are isolated and "dotted" onto a membrane usually in duplicate. mRNA is isolated from control and experimental samples and labeled by incubation with RT, primers, and radioactive nucleotide that will be incorporated into a cDNA (copy DNA). mRNA can also be labeled directly by gentle NaOH digestion (to make it smaller lengths) followed by labeling with T4 kinase and a radioactive nucleotide that will "end label" it such as γ ATP.[32]

3.3 Gene Discovery

3.3.1 Differential Display (DD), Subtractive Hybridization, and Representational Difference Analysis (RDA)

In 1992, Liang and Pardee[21] described a modification of RT-PCR procedure to identify genes that were differentially expressed. In these experiments RNA is extracted and annealed to sets of different oligos (also called primers) that together cover all expressed genes. The oligos are first used to make cDNA using the enzyme RT and then for cDNA amplification using PCR (Fig. 3.6). By adding a radioactive nucleotide in the reaction the cDNA can later be traced or visualized. The resulting amplicons, which theoretically, based on the oligo pairs used, correspond to all genes expressed by the cells, are electrophoresed through thin denaturing acrylamide gels that allow the separation of fragments with a single

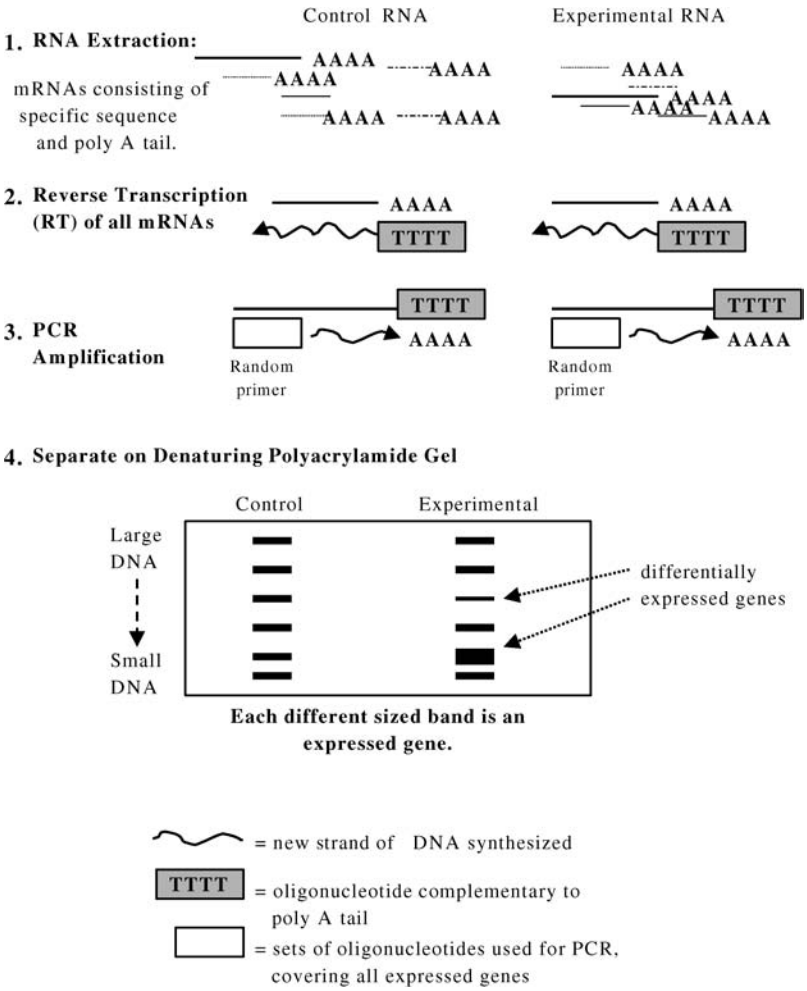

FIGURE 3.6 DD. A mixture of RNA from control and experimental material is subject to RT-PCR using random primers (short pieces of DNA) that can amplify all the genes expressed in a cell. A radioactive nucleotide is included (typically α ATP [S35]) so that the products of the reaction can be visualized after separation on acrylamide gels. The "bands" that show more or less intensity than the controls are, in theory, up- or downregulated, respectively. They are cut from the gel, reamplified, and used to (1) confirm their differential expression and (2) determine their DNA sequence to see if they are novel or previously reported to DNA databases such as GenBank.

base difference (DNA sequencing gels). By comparing the patterns of control and experimental samples, one can visualize distinct genes that are either upregulated (more intense) or downregulated (less intense) compared with control samples. For this reason, the method is called the "differential display" (DD). To identify the nature of the altered gene, the band is extracted from the gel, reamplified by PCR, and cloned for detailed sequence analysis. By consulting available public databases on the Internet (such as GenBank), one can determine if the gene is novel or, rather, previously isolated, characterized, and reported to the database. By using this approach several genes have been identified that are regulated by mechanical loading in rat bone, including osteopontin and myloperoxidase[22] and the glutamate/aspartate transporter.[23] This observation raises an interesting point about the technique: some findings are quite unexpected and lead to molecular pathways (in the latter case to the nervous system) that were probably not anticipated.

Other procedures can also be used to isolate genes that are differentially expressed in an experimental situation. One such alternative is "subtractive hybridization." There are many ways to carry out the method but all rely on the subtraction of genes common to the control and experimental mRNA. One recent report described the isolation of osteoclast-specific genes by subtracting cDNA, constructed from a rabbit osteoclast mRNA, with biotin-labeled mRNA previously isolated from rabbit spleen.[24] Thus, the cDNA in the osteoclast mRNA repertoire (called a library) that was also in the spleen was hybrized and subtracted out using a biotin-avidin method. The material that remained after subtraction was, in theory, osteoclast specific and is currently being analyzed.[24] By using the same procedure numerous genes were discovered that were differentially expressed in human cochlear (essential for hearing) mRNA compared with human brain mRNA. Some genes were previously identified such as collagens type I, II, and III while one was novel and termed Cock-5B2.[25] As with the differential display method, one must confirm that the gene is differentially regulated using Northern analysis, RPA, or quantitative RT-PCR. This confirmation eliminates "false positives" that appear to be differentially regulated in the first screen but really upon further analysis are not.

Still a third method for discovery of differentially expressed genes is called representational differences analysis (RDA). The procedure was originally designed[26] to measure the difference between two complex genomes (nuclear DNA) but was adapted so that genes could be isolated that encoded differentially expressed mRNA.[27] The method is PCR based and relies on a subtraction concept. In this procedure double-stranded DNA is made from the two RNA populations, and cut with a restriction enzyme so that it can be modified to contain specific DNA sequences at its terminus that can then be amplified using specific oligonucleotides. The DNA produced by the two different RNA preparations is referred to as "representative amplicons." The amplicon from the experimental sample is called the "tester" and the control material termed the "driver." By adding an excess of driver and oligos that can only amplify the tester to a mix of "driver and tester" the DNA common to the two samples forms a DNA duplex that cannot be amplified. Consequently, only tester DNA, not found in the driver, will be amplified and further characterized. The difference between this method and differential display (DD) is that in RDA only two samples can be compared (subtracted); in DD, numerous samples can be analyzed on a single gel. This is helpful for comparing patterns in different cell types or in one sample subject to different doses or time of treatment. In theory, DD, subtraction hybridization, and RDA will have the same outcome, namely, the isolation of genes differentially expressed between two samples. In this regard it is interesting to note that when the expression of genes was examined in rat livers treated with aflatoxin[28] using DD, RDA, and a subtraction procedure many genes were isolated that were differentially expressed; however, in each method different genes were obtained. No matter what method is selected, the isolated genes will need to be further characterized for functional capacity using the procedures outlined in later sections of this chapter (Sections 3.4 and 3.5) or in Chapter 4.

3.3.2 Serial Analysis of Gene Expression (SAGE)

In attempts to examine multitudes of genes simultaneously from a single sample, a nonradioactive modification of the DD procedure was devised.[29] The method relies on multiple amplification and cloning steps that result in the production of concatamers (many short pieces of DNA in tandem)

each corresponding to one molecule of RNA from the initial preparation. By extensive sequence analysis of the DNA, one can determine the occurrence (how many copies) and nature (known or unknown) of the most abundant genes in an mRNA sample. By using this gene discovery method,[29] numerous sets of identified and unidentified genes referred to as EST (expressed sequence tag) were submitted to gene databases that await further study to determine their structure and function. By analyzing over 300,000 transcripts derived from at least 45,000 different genes, Zhang et al.[30] discovered more than 500 genes that were expressed at different levels in normal and cancer cells. The advantage of this technique is that most of the equipment needed for the analysis would be found in a well-equipped molecular biology laboratory. Considering most of the analysis is based on DNA sequence comparison excellent computer software and hardware would additionally be required.

3.3.3 Microchip Technology (DNA Chip)

Along a similar rationale as the SAGE, the DNA chip was designed so that numerous genes could be analyzed simultaneously in a single RNA preparation.[31] The technique takes conventional arrays one step farther allowing the theoretical analysis of up to 10,000 genes in a single experiment. High throughput arrays use robots to spot the individual genes onto glass microscope slides resulting in the so-called cDNA chips. The mRNA extracted from the cells of interest is labeled with fluorescent dyes and is used as a probe. Special equipment has been developed that can detect and quantitate the intensity of hybridization results by measuring the intensity of the fluorescent signal. Two important points must be considered in this type of analysis, namely, (1) the characterization of the DNA that goes onto the chip and (2) the extensive "data mining" that follows. On the first point, before starting, one must have some knowledge about the composition of the DNA that will arrayed. For example, usually the array material is made by PCR of individual clones of a cDNA library (all the mRNAs converted into cDNA and packaged for biological expansion and immortalization). To avoid duplication of genes on the array, it is advantageous to have previously sequenced at least part of each DNA that will be used.[32] On the second point, copious amounts of data can be reamed from this microchip analysis. The difficult task, therefore, is to categorize the data in a meaningful fashion so that new hypotheses can be tested. Recently, the expression of 8600 distinct genes was examined in skin fibroblasts treated with serum. Interestingly, sets of genes were activated that previously have been linked to wound healing.[33] A good command of bioinformatics is required for this kind of analysis.

3.4 Gene Transfer

With the identification of genes involved in various genetic diseases, gene therapy is a new trend in the scientific medical field but is still in its experimental phase; for a review see Romano et al.[46] For example, in some diseases mutations of genes result in lack of protein production and theoretically the disease could be cured by transferring the normal gene into the diseased tissue.

From a more basic science point of view, once genes have been identified using the procedures described in the previous sections a critical next step is to determine the function of the gene. That is to say, if a gene is turned off, for example, by mechanical strain, it would be important to determine directly if an alteration in the expressed gene is in fact related to a functional consequence of the applied strain. One way to test the function of a target gene is to isolate the entire coding region (the part of the gene that will make a protein) and connect it to a regulatory DNA (promoter) that will force its expression or inactivation in a cell or tissue. Typical promoters that are used for such overexpression studies are derived from Simian Virus 40 (SV 40), cytomegalovirus (CMV), or rous sarcoma virus (RSV). The gene construct (transgene) is then transferred (transfected) into cultured cells (see Chapter 2) or used to make transgenic mice (see Chapter 4).

In both gene therapy and functional studies a critical step is the transfer of the gene of interest into the cells. Thus, the procedures discussed below are essential for (1) testing the function of a gene and (2) gene therapeutics.

3.4.1 Nonvirus-Based Gene Transfer

Numerous methods have been described for the transfer of genes into cells and tissues, and transfer efficiency depends on cell type, tissue origin, and species. Nonvirus-based methods may use basic polymers such as DEAE dextran[34] that have affinity for DNA or liposomes[35,36] that facilitate fusion and entry of the DNA through the cell membrane. Electroporation, on the other hand, relies on an electric field presumably to make small "holes" in the cell for DNA transfer.[37] Fine precipitates of $CaPO_4$ are also used and, in the authors' hands, are most successful for cultured bone cells.[38] Other novel procedures that might be suitable in the future for gene transfer, but are yet untested on skeletal tissue, include particle bombardment (gene gun)[39] and liposomes chemically tailored for mineralized tissue.[40] It should be pointed out that even "naked" DNA or DNA immersed in saline has also been successfully transferred into tissue. Recently, DNA encoding TGF-β1 was shown to suppress induced arthritis when injected intramuscularly into rodents.[41]

3.4.2 Adenovirus-Based Gene Transfer

Cells that are particularly resistant to gene transfer can often be successfully transfected using adenovirus-based methods. A major advantage of this method is that it is highly efficient and can be used on nondividing cells ranging from chick to human. One drawback is that the transgene expression is transient or temporary; the recombinant adenovirus is made replication deficient and, once infected into a cell, cannot make more of itself. Nevertheless this method is currently being explored for gene therapy in certain cases of arthritis.[42]

Recombinant adenovirus is made by genetically engineering the transgene into a plasmid DNA that is flanked with specific DNA sequences derived from the adenovirus. These virion sequences are complementary to sequences of a second larger piece of DNA that contains virion DNA that had these sequences removed (they are "missing"). By co-transfecting the two DNA types into 293 cells (these cells provide replication capacity) homologous recombination occurs in the cells (see Chapter 4) and the transgene is incorporated into the adenoviral genome providing the deleted virion with the "missing" material needed for viral production. In this way the transgene is recombined into the viral genome and can be propagated as virus particles. The presence of the transgene can be confirmed either by Northern, PCR, or by Western (protein) analysis using antibodies specific for the gene of interest and extracts from the infected cells (for details, see review by Becker et al.[43]). By growing virus in 293 cells, endless supplies can be produced to examine gene function in cultured cells and or injected tissues. Recently, the authors have tested a modification of this procedure that allows gene transfer without genetically engineering DNA into the adenoviral genome. Purified virus was covalently linked to polylysine and then incubated with the transgene. Efficient gene transfer was noted using either cultures of human bone marrow stroma (Fig. 3.7) and human trabecular bone[44] using this technique. A recent modification of the procedure has been devised[45] that substitutes polysine with polyethlyenimine (PEI) and may be an additional promising new adenovirus-based method that would also not require previous engineering of transgenes into the viral genome.

The adeno-associated virus (AAV) has, more recently, been of great interest for gene transfer;[46] it is distinct from adenovirus and has the advantage of integrating into the host genome. Because this virus requires a "helper" virus for replication, there are concerns that it could not be completely eliminated from viral preparations making it unsafe for clinical use. Nevertheless, as more becomes known about the vector system and viral life cycle, AAV holds promise for an alternative means of gene transfer and therapy in bone material.

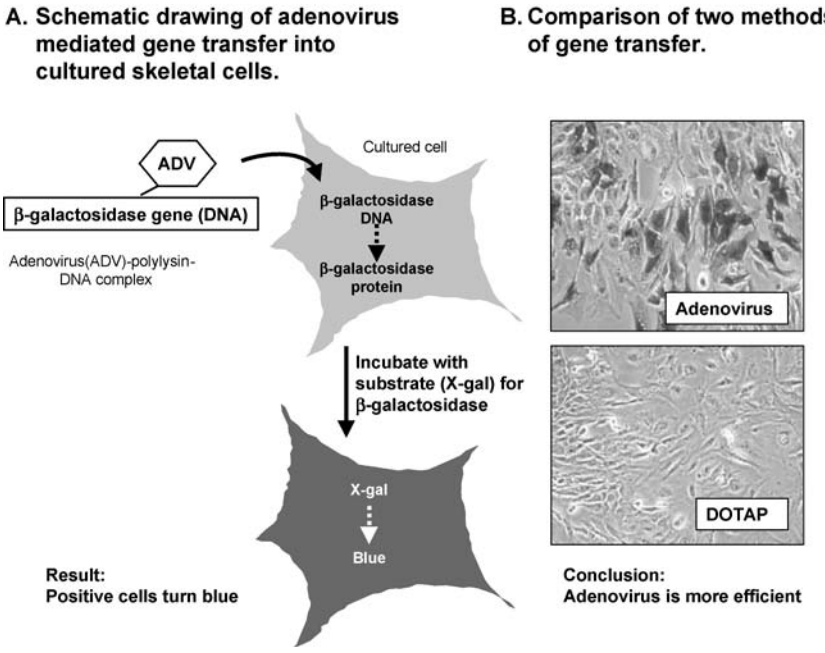

FIGURE 3.7 Gene transfer into cultured skeletal cells using two different methods. DNA for β-galactosidase is mixed with adenovirus previously covalently attached to polylysine (called a complex). The DNA (acidic) has affinity for the polylysine (basic). When DNA is added to the complex the adenovirus attaches to the cell membrane and carries the DNA into the cell like a "Trojan horse." β-Galactosidase mRNA is then transcribed from an attached promoter and the β-galactosidase mRNA translated into protein. Fixed cells incubated with the X-gal, which is a substrate for β-galactosidase, turn blue if it is present. The extent of the blue color is an indirect measure of the efficiency of gene transfer. The upper right panel shows the efficiency of gene transfer using the polylysine-adenovirus compared to DOTAP™ liposomes, which are shown on the lower right panel. The cultured cells receiving the DNA are marrow stromal fibroblasts derived from human bone.

3.4.3 Retrovirus-Based Gene Transfer

Retroviruses are RNA viruses that are constructed in a manner somewhat similar to adenoviruses.[47,48] Target genes are isolated and cloned into a vector that is flanked at each end by retrovirally derived long terminal repeats (LTR) that are essential for the life cycle of the virus. All other genes of the retrovirus have been previously removed to allow insertion of the foreign gene. To package the RNA inside a viral particle the DNA construct is transfected into special cells (usually NIH-3T3) that have been previously engineered to be able to package the foreign gene. Because gene transfer is often inefficient and many cells do not take up the transgene, a selectable marker such as neomycin resistance is included in the construct. In this way cells that do not take up the transgene and consequently the neomycin resistance gene are killed by treatment with neomycin. Surviving cells that produce the transgene, on the other hand, can be grown indefinitely and provide an endless source of packaged viral RNA. When recombinant retroviral particles are used to infect the tissue of interest, the transgene is converted to double-stranded DNA and incorporated into the host genome using the LTR sequences.[49] Thus, the major difference between the retrovirus and adenovirus is that the former is integrated in the host DNA and is therefore considered a "stable" transfection. The adenovirus transgene expression, while temporary or transient, does not require drug selection like the retrovirus. Retrovirus infection, on the other hand, requires cells that are undergoing cell division. Both methods suffer from the fact that the transgene, even when stably incorporated, is often not sustained. Nevertheless, for analysis of protein function either method could be used to examine fundamental parameters that occur within a reasonable time frame.

3.5 Inactivation of Specific Genes

3.5.1 Antisense: Oligonucleotides and Full-Length Constructs

One way to test for specific gene function is to ablate or inhibit the gene of interest and see what the ramifications are. This can be done by homologous recombination (see Chapter 4), which relies on double drug selection and vigorous cell division. Many bone cell types either do not divide well (the osteocyte) or do not respond well to drug treatment. For that reason, transient methods have been designed to interfere with RNA transcription from the promoter or with protein translation of the RNA. Small pieces of DNA are complementary to the target genes and are called antisense oligodeoxynucleotides (ODNS). In the first case, ODNS bind to the promoter and cause it to form a triplex structure that is no longer functional. In the second case, the ODNS bind to sequences in the mRNA, and through the action of RNase H present in the cell, the duplex is destroyed and can no longer function. In either case, both methods rely on efficient transfer of the ODNS into the target cells using the gene transfer methods described in Section 3.4 and reviewed in Ref.[50]

Antisense experiments have also been successful with full-length cDNA (the entire coding sequence) engineered in a gene construct in the reverse orientation. In this way a longer antisense stretch of DNA is made that binds to the complementary mRNA and makes it inactive. One drawback to the latter approach is that selection of the transgene is required so that new cell lines can be derived. This is done so that the entire population (i.e., clone) of cells contains and expresses the transgene. Nevertheless using this approach Vander Molen et al.[51] created ROS 17/2.8 cells (see Chapter 2) that were unable to make connexin-43 because of the presence of an antisense transgene. Interestingly, these cells showed deficiencies in cell-to-cell coupling, indicating the importance of this protein in the networking of bone cells.

3.5.2 Ribozymes

Ribozymes are RNA molecules that can bind a target RNA and enzymatically cleave or cut it so it is no longer functional.[52] These unique RNAs are referred to as "hammerhead" because of their structure; they are composed of a hairpin loop (i.e., a stem loop where the stem contains complementary RNA) and have the potential to bind to target DNA with great specificity. Binding occurs through the "arms" of the hammerhead that are attached to the stem. As with the previously described procedures, the ribozyme must first be introduced into the cells by gene transfer for either transient expression or stable integration. Hammerhead ribozymes have recently been described that can distinguish a single base-pair difference between normal and type I collagen mutants.[53] This method offers promising new possibilities for inactivating mutated RNA that has a "dominant-negative" deleterious effect on bone such as occurs in osteogenesis imperfecta[54] or McCune Albright syndrome.[55] This and all of the other gene transfer methods can be taken to further steps of sophistication. By changing the promoter that directs the production of the transgene, one can elicit cell-specific or inducible expression repertoires so that the time and place of expression within a cell type or organism can be regulated (see Chapter 4).

3.6 Summary

In summary, there are many ways to examine molecular events in bone tissue. Each has advantages and disadvantages (Tables 3.1 and 3.2 for summary). Many methods are used in combination for confirmation of the data or for practical reasons such as limitation in sample size. Now that the genome project is complete all human genes have been sequenced. One hopes that this vast amount of new information can be used to examine sets of genes that are activated or inactivated during development, aging, and in the pathology of skeletal tissues. The ultimate challenge will be to determine how multiple genes and proteins work in concert to control the function and structure of bone material under normal and stressed conditions.

TABLE 3.1 Summary of Methods to Examine Molecular Events of Known Genes in Bone Tissue

	Number of Genes Detected	Advantage	Disadvantage
Northern blotting	One gene	• Direct quantitative detection of RNA	• Relatively large amounts of RNA necessary
RT-PCR	One gene	• Small amounts of RNA necessary • Nonradioactive	• Semiquantitative
RNase protection	Multiple genes: ~10	• Direct detection of RNA	• Radioactive
Array technology	Numerous genes: ~100–1000	• Screen many genes in one single experiment	• Differential gene expression needs confirmation using one of the methods above

TABLE 3.2 Summary of Methods for Gene Discovery

	Description	Advantage	Disadvantage
Differential display	First method described to screen many known and novel genes simultaneously	• First steps easy • Many samples on a single gel (experiment)	• Analysis of clones is lengthy • False positives
SAGE	Nonradioactive method of screening many known and novel genes	• Nonradioactive • Screen many genes in one cloning step • Quantitation possible • Modification of the technique prevents nonspecific binding of linkers	• Extensive computer analysis required • Multiple cloning steps involved
RDA, subtractive hybridization	Subtract common genes by hybridization of control to experimental	• Differentially expressed genes obtained directly	• Only two samples can be compared at one time
Microchip technology	Fluroscence-based method of screening many known and novel genes	• Nonradioactive • Fluorescent quantitation	• Extensive characterization of cDNA library is needed prior to designing the chip • Extensive data mining

Acknowledgments

The authors wish to thank Jennifer Liang for assistance in preparation of the figures used for this chapter.

References

1. E. F. Fritsch and T. Maniatis, *Molecular Cloning: A Laboratory Manual,* 2nd ed., Cold Spring Harbor Press, Cold Spring Harbor, NY, 1989.
2. F. M. Ausubel, *Current Protocols in Molecular Biology,* John Wiley & Sons, New York, 1987.
3. D. D. Bikle, J. Harris, B. P. Halloran, and E. Morey-Holton, Altered skeletal pattern of gene expression in response to spaceflight and hindlimb elevation, *Am. J. Physiol.,* 267, E822–827, 1994.
4. P. Backup, K. Westerlind, S. Harris, T. Spelsberg, B. Kline, and R. Turner, Spaceflight results in reduced mRNA levels for tissue-specific proteins in the musculoskeletal system, *Am. J. Physiol.,* 266, E567–573, 1994.

5. D. M. Raab-Cullen, M. A. Thiede, D. N. Petersen, D. B. Kimmel, and R. R. Recker, Mechanical loading stimulates rapid changes in periosteal gene expression, *Calcif. Tissue Int.,* 55, 473–478, 1994.
6. T. Inaoka, J. M. Lean, T. Bessho, J. W. Chow, A. Mackay, T. Kokubo, and T. J. Chambers, Sequential analysis of gene expression after an osteogenic stimulus: c-fos expression is induced in osteocytes, *Biochem. Biophys. Res. Commun.,* 217, 264–270, 1995.
7. T. Matsumoto, K. Nakayama, Y. Kodama, H. Fuse, T. Nakamura, and S. Fukumoto, Effect of mechanical unloading and reloading on periosteal bone formation and gene expression in tail-suspended rapidly growing rats, *Bone,* 22, 89S–93S, 1998.
8. E. E. Karrer, J. E. Lincoln, S. Hogenhout, A. B. Bennett, R. M. Bostock, B. Martineau, W. J. Lucas, D. G. Gilchrist, and D. Alexander, *In situ* isolation of mRNA from individual plant cells: creation of cell-specific cDNA libraries, *Proc. Natl. Acad. Sci. U.S.A.,* 92, 3814–3818, 1995.
9. R. F. Bonner, M. Emmert-Buck, K. Cole, T. Pohida, R. Chuaqui, S. Goldstein, and L. A. Liotta, Laser, capture microdissection: molecular analysis of tissue, *Science,* 278, 1481–1483, 1997.
10. J. Fitzgerald and M. Hughes-Fulford, Gravitational loading of a simulated launch alters mRNA expression in osteoblasts, *Exp. Cell Res.,* 228, 168–171, 1996.
11. A. Kawata and Y. Mikuni-Takagaki, Mechanotransduction in stretched osteocytes—temporal expression of immediate early and other genes, *Biochem. Biophys. Res. Commun.,* 246, 404–408, 1998.
12. G. Carmeliet, G. Nys, I. Stockmans, and R. Bouillon, Gene expression related to the differentiation of osteoblastic cells is altered by microgravity, *Bone*, 22, 139S–143S, 1998.
13. D. G. Wilkinson and M. A. Nieto, Detection of messenger RNA by *in situ* hybridization to tissue sections and whole mounts, *Methods Enzymol.,* 225, 361–373, 1993.
14. R. A. Conlon and B. G. Herrmann, Detection of messenger RNA by *in situ* hybridization to postimplantation embryo whole mounts, *Methods Enzymol.*, 225, 373–383, 1993.
15. T. Ikeda, Y. Nagai, A. Yamaguchi, S. Yokose, and S. Yoshiki, Age-related reduction in bone matrix protein mRNA expression in rat bone tissues: application of histomorphometry to in situ hybridization, *Bone,* 16, 17–23, 1995.
16. C. M. Webb, G. Zaman, J. R. Mosley, R. P. Tucker, L. E. Lanyon, and E. J. Mackie, Expression of tenascin-C in bones responding to mechanical load, *J. Bone Miner. Res.,* 12, 52–58, 1997.
17. A. J. Patton, P. G. Genever, M. A. Birch, L. J. Suva, and T. M. Skerry, Expression of an N-methyl-D-aspartate-type receptor by human and rat osteoblasts and osteoclasts suggests a novel glutamate signaling pathway in bone, *Bone,* 22, 645–649, 1998.
18. Y. Q. Sun, K. J. McLeod, and C. T. Rubin, Mechanically induced periosteal bone formation is paralleled by the upregulation of collagen type one mRNA in osteocytes as measured by in situ reverse transcript-polymerase chain reaction, *Calcif. Tissue Int.,* 57, 456–462, 1995.
19. D. J. Mason, R. A. Hillam, and T. M. Skerry, Constitutive in vivo mRNA expression by osteocytes of beta-actin, osteocalcin, connexin-43, IGF-I, c-fos and c-jun, but not TNF-alpha nor tartrate-resistant acid phosphatase, *J. Bone Miner. Res.,* 11, 350–357, 1996.
20. S. C. Dieudonne, D. McBride, N. S. Fedarko, and M. F. Young, Use of HERKO (human estrogen receptor alpha knock out) cells to explore novel mechanisms of estrogen action, *Bone,* 23, S367, 1998.
21. P. Liang and A. B. Pardee, Differential display of eukaryotic messenger RNA by means of the polymerase chain reaction, *Science,* 257, 967–971, 1992.
22. R. R. Miles, C. H. Turner, R. Santerre, Y. Tu, P. McClelland, J. Argot, B. S. DeHoff, C. W. Mundy, P. R. Rosteck, Jr., J. Bidwell, J. P. Sluka, J. Hock, and J. E. Onyia, Analysis of differential gene expression in rat tibia after an osteogenic stimulus *in vivo*: mechanical loading regulates osteopontin and myeloperoxidase, *J. Cell Biochem.,* 68, 355–365, 1998.
23. D. J. Mason, L. J. Suva, P. G. Genever, A. J. Patton, S. Steuckle, R. A. Hillam, and T. M. Skerry, Mechanically regulated expression of a neural glutamate transporter in bone: a role for excitatory amino acids as osteotropic agents? *Bone,* 20, 199–205, 1997.
24. M. Kobori, Y. Ikeda, H. Nara, M. Kato, M. Kumegawa, H. Nojima, and H. Kawashima, Large scale isolation of osteoclast-specific genes by an improved method involving the preparation of a subtracted cDNA library, *Gene Cells,* 3, 459–475, 1998.

25. N. G. Robertson, U. Khetarpal, G. A. Gutierrez-Espeleta, F. R. Bieber, and C. C. Morton, Isolation of novel and known genes from a human fetal cochlear cDNA library using subtractive hybridization and differential screening, *Genomics,* 23, 42–50, 1994.
26. N. Lisitsyn and M. Wigler, Cloning the differences between two complex genomes, *Science,* 259, 946–951, 1993.
27. M. Hubank and D. G. Schatz, Identifying differences in mRNA expression by representational difference analysis of cDNA, *Nucl. Acids Res.,* 22, 5640–5648, 1994.
28. A. J. Harris, J. G. Shaddock, M. G. Manjanatha, J. A. Lisenbey, and D. A. Casciano, Identification of differentially expressed genes in aflatoxin B1-treated cultured primary rat hepatocytes and Fischer 344 rats, *Carcinogenesis,* 19, 1451–1458, 1998.
29. V. E. Velculescu, L. Zhang, B. Vogelstein, and K. W.Kinzler, Serial analysis of gene expression [see comments], *Science,* 270, 484–487, 1995.
30. L. Zhang, W. Zhou, V. E. Velculescu, S. E. Kern, R. H. Hruban, S. R. Hamilton, B. Vogelstein, and K.W. Kinzler, Gene expression profiles in normal and cancer cells, *Science,* 276, 1268–1272, 1997.
31. M. Schena, D. Shalon, R. W. Davis, and P. O. Brown, Quantitative monitoring of gene expression patterns with a complementary DNA microarray [see comments], *Science,* 270, 467–470, 1995.
32. L. Jia, D. Wilkin, L. King, M. Young, A. R. DeRubeis, J. Powell, L. Yang, G. Schuler, G. Lennon, R. Wilson, R. Hotchkiss, P. Gehron Robey, and C. Francomano, The skeletal genome anatomy project (SGAP): exploring gene expression in the genome of bone and related tissues, *Bone,* 23, S420, 1998.
33. V. R. Iyer, M. B. Eisen, D. T. Ross, G. Schuler, T. Moore, J. C. F. Lee, J. M. Trent, L. M. Staudt, J. Hudson, Jr., M. S. Boguski, D. Lashkari, D. Shalon, D. Botstein, and P. O. Brown, The transcriptional program in the response of human fibroblasts to serum [see comments], *Science,* 283, 83–87, 1999.
34. W. Holter, C. M. Fordis, and B. H. Howard, Efficient gene transfer by sequential treatment of mammalian cells with DEAE-dextran and deoxyribonucleic acid, *Exp. Cell Res.*, 184, 546–551, 1989.
35. P. L. Felgner, T. R. Gadek, M. Holm, R. Roman, H. W. Chan, M. Wenz, J. P. Northrop, G. M. Ringold, and M. Danielsen, Lipofection: a highly efficient, lipid-mediated DNA-transfection procedure, *Proc. Natl. Acad. Sci. U.S.A.,* 84, 7413–7417, 1987.
36. N. Zhu, D. Liggitt, Y. Liu, and R. Debs, Systemic gene expression after intravenous DNA delivery into adult mice, *Science,* 261, 209–211, 1993.
37. C. Baum, P. Forster, S. Hegewisch-Becker, and K. Harbers, An optimized electroporation protocol applicable to a wide range of cell lines, *Biotechniques,* 17, 1058–1062, 1994.
38. J. M. Kerr, D. R. Hiscock, W. Grzesik, P. G. Robey, and M. F. Young, The human bone sialoprotein gene contains an NF-E1/YY1 cis-acting sequence with putative regulatory activity, *Calcif. Tissue Int.,* 60, 276–282, 1997.
39. W. C. Heiser, Gene transfer into mammalian cells by particle bombardment, *Anal. Biochem.,* 217, 185–196, 1994.
40. N. S. Templeton, D. D. Lasic, P. M. Frederik, H. H. Strey, D. D. Roberts, and G. N. Pavlakis, Improved DNA: liposome complexes for increased systemic delivery and gene expression, *Nat. Biotechnol.,* 15, 647–652, 1997.
41. X. Y. Song, M. Gu, W. W. Jin, D. M. Klinman, and S. M. Wahl, Plasmid DNA encoding transforming growth factor-beta1 suppresses chronic disease in a streptococcal cell wall-induced arthritis model, *J. Clin. Invest.,* 101, 2615–2621, 1998.
42. S. C. Ghivizzani, E. R. Lechman, R. Kang, C. Tio, J. Kolls, C. H. Evans, and P. D. Robbins, Direct adenovirus-mediated gene transfer of interleukin 1 and tumor necrosis factor alpha soluble receptors to rabbit knees with experimental arthritis has local and distal anti-arthritic effects, *Proc. Natl. Acad. Sci. U.S.A.,* 95, 4613–4618, 1998.
43. T. C. Becker, R. J. C. Noel, W. A. M. Gomez-Foix, T. Alam, R. D. Gerard, and C. B. Newgard, Use of recombinant adenovirus for metabolic engineering of mammalian cells, in *Methods in Cell Biology,* Vol. 43, Academic Press, New York, 1994, 161–189.

44. B. Sommer, S. A. Kuznetsov, P. G. Robey, B. O'Connell, R. J. Cristiano, and M. F. Young, Efficient gene transfer into normal human skeletal cells using recombinant adenovirus and conjugated adenovirus-DNA complexes, *Calcif. Tissue Int.,* 64, 45–49, 1999.
45. A. Baker, M. Saltik, H. Lehrmann, I. Killisch, V. Mautner, G. Lamm, G. Christofori, and M. Cotten, Polyethylenimine (PEI) is a simple, inexpensive and effective reagent for condensing and linking plasmid DNA to adenovirus for gene delivery, *Gene Ther.,* 4, 773–782, 1997.
46. G. Romano, P. P. Claudio, H. E. Kaiser, and A. Giordano, Recent advances, prospects and problems in designing new strategies for oligonucleotide and gene delivery in therapy, *In Vivo,* 12, 59–67, 1998.
47. M. A. Eglitis and W. F. Anderson, Retroviral vectors for introduction of genes into mammalian cells, *Biotechniques,* 6, 608–614, 1988.
48. R. K. Naviaux and I. M. Verma, Retroviral vectors for persistent expression *in vivo*, *Curr. Opin. Biotechnol.,* 3, 540–547, 1992.
49. S. C. Ghivizzani, E. R. Lechman, C. Tio, K. M. Mule, S. Chada, J. E. McCormack, C. H. Evans, and P. D. Robbins, Direct retrovirus-mediated gene transfer to the synovium of the rabbit knee: implications for arthritis gene therapy, *Gene Ther.,* 4, 977–982, 1997.
50. A. M. Gewirtz, C. A. Stein, and P. M. Glazer, Facilitating oligonucleotide delivery: helping antisense deliver on its promise, *Proc. Natl. Acad. Sci. U.S.A.,* 93, 3161–3163, 1996.
51. M. A. Vander Molen, C. T. Rubin, K. J. McLeod, L. K. McCauley, and H. J. Donahue, Gap junctional intercellular communication contributes to hormonal responsiveness in osteoblastic networks, *J. Biol. Chem.,* 271, 12165–12171, 1996.
52. H. A. James and I. Gibson, The therapeutic potential of ribozymes, *Blood,* 91, 371–382, 1998.
53. G. Grassi, A. Forlino, and J. C. Marini, Cleavage of collagen RNA transcripts by hammerhead ribozymes *in vitro* is mutation-specific and shows competitive binding effects, *Nucl. Acids Res.,* 25, 3451–3458, 1997.
54. G. Grassi and J. C. Marini, Ribozymes: structure, function, and potential therapy for dominant genetic disorders, *Ann. Med.*, 28, 499–510, 1996.
55. P. Bianco, S. A. Kuznetsov, M. Riminucci, L. W. Fisher, A. M. Spiegel, and P. G. Robey, Reproduction of human fibrous dysplasia of bone in immunocompromised mice by transplanted mosaics of normal and Gsalpha-mutated skeletal progenitor cells, *J. Clin. Invest.,* 101, 1737–1744, 1998.

4

Creating Transgenic Mice to Study Skeletal Function

Marian F. Young
National Institutes of Health

Tianshun Xu
Glaxo-Wellcome, Inc.

4.1 Introduction

Rapid advances in the field of genetic engineering have led to a parallel "boom" in the number of transgenic mice generated. By combining new technologies in recombinant DNA with advances in cell and developmental biology, a host of novel animal models were developed that have specific skeletal defects. These models are useful for two majors reasons. First, many new models closely mimicking human diseases such as osteopetrosis or osteoporosis have been developed. Second, transgenic mice provide a critical test for the function of an individual gene *in vivo*. The results from these investigations have often been surprising, yet, have led to fascinating new discoveries about the role of individual proteins in the development and aging of bone tissue.

The first part of this chapter outlines methods that are typically used to generate transgenic mice. In describing these procedures, commentary is provided about the advantages and disadvantages of the two major types of transgenic mice that are currently produced, namely, "conventional" (in general results in a gain of function) or "knockout" (in general a loss of function). Variation and combinations of the two types of transgenics are also described (Section 4.6). Numerous examples of animal models generated using the procedures that have skeletal defects are listed in two tables according to the transgenic type

0-8493-9117-2/01/$0.00+$.50

they are. In some cases biomechanical defects have been documented for these mouse models either due to alterations in mineral content or composition (see Chapter 5) or from other imbalances the matrix or growth factor milieu. As transgenic methodology becomes more refined, it is reasonable to expect that many more mouse lines will be produced. They will, in turn, be important resources for the engineer interested in testing the biomechanical properties of bones with defined genetic and skeletal defects.

4.2 Construction of Conventional Transgenic Mice

Transgenic mice are designed to "overexpress" a specific gene over and above the normal patterns of genes expressed by an organism. This is done by genetic manipulation and insertion of transgenes into a host genome. Subsequently, the gene can be transmitted to its offspring. The first transgenic mouse line of this type was prepared by Brinster et al.[1] almost 20 years ago. In these early experiments foreign Xenopus (frog) ribosomal DNA was injected into the pronucleus of a fertilized mouse egg; transcripts of the foreign gene were detected indicating it was active. This work followed with a report of the successful insertion and expression of a gene coding for an enzyme[2] under the control of the regulatory apparatus (promoter) of a separate gene. The procedures described in these early studies are still currently used and are outlined in Fig. 4.1. It should be noted that several good technical manuals are available that describe in great detail the specifics of each step and are excellent guides for the novice embarking on creation of their own transgenics.[3] The material presented in this chapter is intended to provide the biomechanical engineer with a general guideline about how transgenics are produced and, further, how various mouse models differ genetically and functionally.

The first step to construct a transgenic mouse line is to isolate and characterize the gene of interest. The gene (either cDNA, which is the coding region of the gene, or total genomic DNA) is then connected (ligated) to a regulatory DNA that controls the transcription and final expression pattern of the transgene. Often, additional DNA elements are added to the transgene including intron sequences placed between the promoter and cDNA to enhance expression, and a poly-A attachment site to enhance stability of the transcribed gene (Fig. 4.1 and Ref. 4). In some cases "enhancer" sequences derived from introns or DNA distal from the promoter are added to facilitate tissue-specific gene expression.[5] The sum of these DNA parts is often referred to as a "construct." When attached to a vector or plasmid, it can be amplified in bacteria and then large quantities are purified for DNA sequence to confirm its integrity. Promoter attached to the transgene is then purified, and injected into the pronucleus of a fertilized egg. Several injected eggs are surgically transferred to a pseudopregnant mouse and the offspring born referred to as the F_0 generation. A few weeks after birth, a small piece of the tail is removed from the mice, DNA extracted, and then subject to either Southern blotting or polymerase chain reaction (PCR) for genotyping (see Chapter 3 for details). This is done to test for the presence of the transgene. Positive transgenic mice are then bred to wild-type animals and the next generation (F_1) is tested to assure that the transgene is passed on in the germline (see Fig. 4.1).

There are several categories of conventional transgenics that differ in the type (location) of trangene patterns they direct and the functional outcome (gain or loss). A description of each type and examples are listed below and in Table 4.1.

4.2.1 Ectopic Expression

In this category transgenes are placed behind a promoter that will direct their expression in tissues where they are not normally produced. This is done by specifically choosing a promoter that is active in tissues where the transgene is not made. One example in this category is a transgenic line where the myogenic (muscle)-determining gene was produced under the control of a ubiquitously expressed mouse sarcoma virus promoter. In this study, multinucleated striated myotubes (cells characteristic of muscle) were found in the brains of transgenic mice, indicating this transgene was operational *in vivo* at a site distant from where muscle is normally made.[6] In many cases, dramatic effects have been noted; overexpression of the homeobox HOXb-8 under the control of the retinoic acid β promoter resulted in animals that had mirror image duplications of their forelimbs.[7]

TABLE 4.1 Comparing Features of Various Transgenic Types

Category	Method	Result
"Conventional"		
a. Ectopic	Transgene driven by	a. Makes gene in ectopic site
b. Tissue specific	promoter that directs	b. Makes gene in specific tissues
c. Dominant-negative	expression above normal gene	c. Inactivates normal gene
Knockout	Gene targeting in embryonic stem cells	No expression from either allele; null throughout life-span
Knockin or subtle mutation	Gene targeting in embyonic stem cells	Exchange normal gene for a different or mutated gene
Cre-recombinase	Combines gene targeting of loxP with tissue-specific cre-recombinase	Tissue-specific knockout or mutation

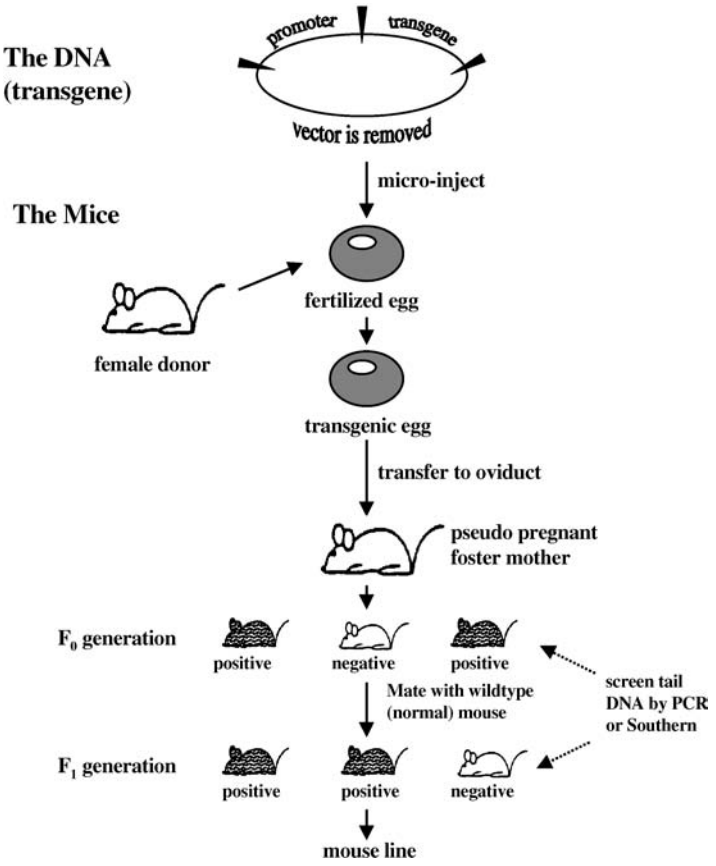

FIGURE 4.1 Construction of "conventional" gain of function mouse lines. A construct is prepared that contains a cDNA or genomic DNA attached to a promoter that regulates its tissue-specific expression. The promoter and transgene are injected into an isolated fertilized egg, which is then transferred to the oviduct of a pseudo-pregnant mouse that is the "foster mother" and host for the developing transgenic mouse. After birth, a small biopsy is taken usually from the tail and used to isolate DNA. PCR (see Chapter 3) is is then performed with the DNA to determine which offspring have the transgene. Transgenic animals are bred to each other or to other wild-type animals and their offspring analyzed for the presence of the transgene. Offspring (F_1) retaining the transgene are used for propagation of the mouse line.

4.2.2 Tissue-Specific Transgene Expression

Many proteins critical to the function of bone are, in fact, produced in numerous tissues beside bone. To study the effects of such factors specifically in skeletal tissue, promoters or DNA regulatory regions have been isolated and their temporal and spatial pattern of expression tested using markers such as β-galactosidase that can produce a blue color. By using such specific promoters, transgenic mice that overexpress transgenes in specific cells such as the osteoblast[8] or osteoclast[9] have been made. When the osteocalcin gene, which is exclusively produced in the osteoblast, was used to drive the bone-specific expression of human growth hormone, mice were generated that showed increased bone growth.[8] The osteocalcin promoter has also been used to drive growth factors; overexpression of transforming growth factor-β2 (TGF-β2) in the osteoblast led to the creation of a mouse line that had lower bone mass compared with its normal littermates.[10] Thus, by careful selection of a promoter (driving) DNA, mice can be created that express transgenes in any selected tissue. It should be noted that promoters are not available for all cell types. One promoter not yet available is for osteocyte-specific expression. Further characterization and cloning of the genes specifically made by osteocytes and other skeletal cells will be required for future advances in this area.

4.2.3 Dominant Negative Transgenics

By genetic engineering it is now possible to create genes that contain mutations that make them nonfunctional. By careful design, such mutations in addition render the normal gene nonfunctional. Due to this characteristic, they are termed "dominant." Because the gene of interest can no longer function, it is also termed "negative." A dominant negative mutation therefore overexpresses a mutant gene that makes the normal gene nonfunctional. One example in this category is a specific mutation in the TGF-β II receptor.[11] The receptor has a truncation in its cytoplasmic tail; it can bind TGF-β but cannot initiate further signaling cascades. Thus, it is possible to create mice with dominant negative mutations that are made ectopically or in a tissue-specific fashion.[12]

4.3 Construction of Gene-Targeted or Knockout Mice

The generation of mice with targeted deletions of specific genes is a more recent technology than conventional transgenics.[13] This method was developed to make cells and subsequently mouse lines that have a single gene mutation in the context or background of a normal mouse. This type of alteration differs from that discussed in Section 4.2 in that the knockout mice have no functional gene throughout their life span. To accomplish this, an additional step is added to the procedure that uses embryonic stem (ES) cells. ES cells are derived from the inner cell mass (ICM) of an early embryo and by themselves cannot easily develop into an embryo except in rare cases.[14] However, when placed into the cavity of a 3.5-day fertilized egg the ES cells can contribute to the tissues of the developing embryo. By culturing the cells *in vitro* (in a petri plate), specific gene deletions can be selected in culture using drug selections and subsequent stem cells used to generate mutated embryos. In a manner similar to that described for conventional transgenics, the chimeric mice (which are a mixture of normal and ES cells) can be bred and offspring tested for the presence of the mutated allele. The goal is to obtain transgenes that are inherited so that a mouse line can be developed with a null mutation in a single specific gene. Additional details about this procedure can be found in Ref. 15 with salient features outlined as follows.

4.3.1 DNA Preparation

To target a specific gene, it is necessary to isolate and characterize its DNA from a genomic library made from a strain of mice that is identical (isogenic) to the embryonic stem cell used. In general, this is from the 129/SVJ strain of mouse. DNA corresponding to the gene of interest is then characterized by restriction digestion and the intron (noncoding) and exon (coding) parts clearly identified. This is done so that a mutation can be designed that will inactivate the gene. Two selectable markers are then engineered into the

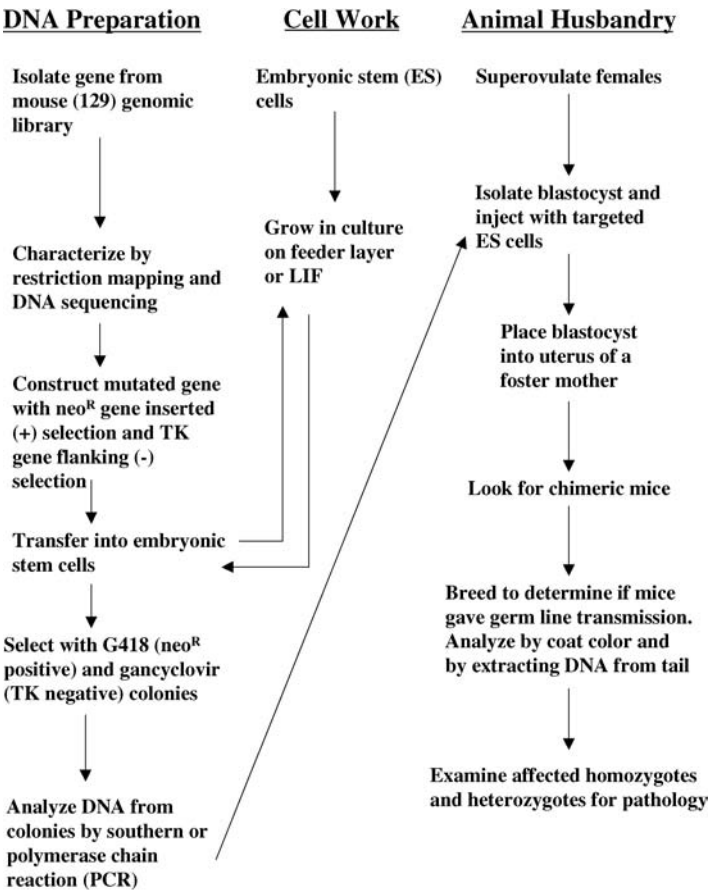

FIGURE 4.2 Outline of parallel procedures required to make a knockout mouse. Three separate lines of experimentation must be successfully performed to create a knockout mouse line. One part of the procedure involves isolation and extensive characterization of the gene that will be knocked out. A second part requires cultivation of embryonic stem cells, which are used to insert the transgene by homologous recombination (see Fig. 4.3). DNA prepared in step 1 is transferred to the ES cells, which are then treated with drugs to select for the presence of the gene at the correct gene locus. So called "targeted" ES cells are injected into a normal host blastocyst, which is then transferred to the uterus of a foster mother. ES cells incorporate into the tissues of the developing embryo and generate a "chimeric" mouse. By breeding the mouse and testing the offspring for the presence of the transgene, one determines if the targeted gene is in the "germline" and subsequently passed on to subsequent generations for the creation of a new mouse line.

isolated DNA (Figs. 4.2 and 4.3). A "positive" selection marker (i.e., neomycin or hygromycin resistance neo^R, hyg^R) is used to screen for mutant gene transfer into the ES cells. The second marker in the construct is for "negative" selection and is used to "enrich" (i.e., increase) the amount of ES cells having homologous gene transfer events (usually using thymidine kinase, TK). Genomic DNA contains repetitive elements that make up 5% of the genome, which can interfere with homologous recombination.[16] For this reason, they should be avoided when preparing a targeting construct. They can be identified by digesting the construct with restriction enzymes followed by hybridization with radiolabeled total genomic DNA.

4.3.2 Embryonic Stem Cells

While ES cells can be freshly prepared, most investigators use aliquots of cells prepared and frozen in batches for long-term storage.[17] These cells were originally isolated from the inner cell mass of very young mouse embryos (4 days old) and are characterized by rapid growth and pleuripotency (can develop into

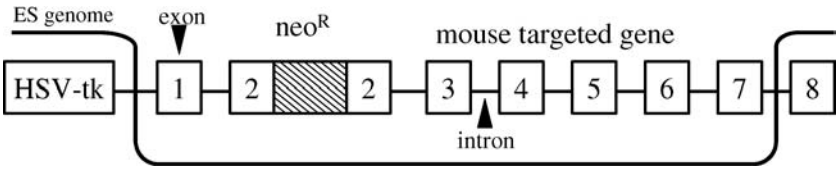

FIGURE 4.3 Details of typical targeting vector. The numbered boxes show the position of the exons, which are determined using a combination of restriction digestion (mapping) and DNA sequencing. The exons have sequences that match the mRNA while the introns do not. They are removed from the mRNA by "splicing" in the nucleus prior to exit into the cytoplasm (see Chapter 3). Using conventional techniques of genetic engineering, a "positive" selection marker is inserted within one of the exons. Shown here is one commonly used marker that codes for neomycin resistance (neo^R). It is used for selecting cells that have taken the transgene in their genome using the selection drug neomycin (G418). A negative marker is also engineered into the construct. Shown here is one such marker that codes for the TK gene. If a gene has recombined into the correct locus (see where the ES genome accepts mutant DNA by a double-crossing-over event) the TK is removed; cells that have not removed the TK are killed by treatment with gancyclovir (this is negative selection), thus enriching the population for cells that have "targeted" alleles. Cells are tested for this homologous recombination using a combination of Southern blotting and PCR (see Chapter 3). Both gene selection markers have their own promoters (usually PGK) that allow continuous (constitutive) expression if present in the cell.

many tissues of an organism). Details about the culture conditions required to keep the cells in a "undifferentiated state" are outlined in detail in Ref. 15. Briefly, the cells must be maintained either on a coating of gelatin or over a layer of embryonic fibrobasts that have been previously inactivated by mitomycin C or by irradiation so that they can no longer divide. To inhibit differentiation, the cells are passaged often and supplemented with the cytokine leukemia inhibition factor (LIF). DNA constructs are transferred (transfected) (see Chapter 3) into the ES cells and screened for the presence of the transgene using the drug G418. If the transgene is randomly integrated, the thymidine kinase gene will be present, and will kill the cells treated with gancylovir. This latter procedure is a negative selection that eliminates cells that have not undergone homologous recombination or gene targeting. Colonies resistant to the two drugs are isolated, expanded, and frozen for future growth. DNA is subject to restriction digestion and Southern blotting or PCR (see Chapter 4). DNA from transgenes with homologous recombination will have characteristic banding patterns when analyzed by electrophoresis.

4.3.3 Animal Husbandry

ES cells containing targeted transgenes are used for injection into host blastocystes. Usually 15 or more cells are used for each injection using finely drawn glass needles under a microscope. The procedure is similar to DNA injections into fertilized pronuclei (conventional transgenics), except the ES cells and blastocystes are much larger. Injected blastocystes are allowed to recover and are then transferred into a foster mother; mice that are born are chimeric. The extent of chimerism can be judged by the coat color; ES cells are from mice that are agouti, which has a light brown color (129) while the recipient host blastocyste is usually from mice with a black coat (C57). One strives to obtain a high percentage of contribution of ES cells (agouti color) to assure that the transgene will be in the germ cells that are used for inheritance. Chimeric mice are bred and offspring tested for the presence of the transgene as described above. If the F_1 generation has the transgene, then it is considered to be "germline transmission" and the line can be maintained indefinitely. In this first generation, the trangenic mice will be heterozygous with one mutated allele. By breeding heterozygous mice, new animals can eventually be generated that are normal (wild-type), heterozygous (one normal and one mutant allele), or total knockouts (two mutant alleles). Mice can be maintained on a mixed background (129/C57) or bred against different strains to change the background over time. This may be a critical feature in the manifestation of the phenotype; it may be more or less severe depending on the background of the mouse line. Recent studies showed that different strains of mice vary in bone mass as a result of intrinsic differences in rates of bone formation.[18]

One category of "loss-of-function-mice" that will not be discussed in detail relies on retrovirus insertion of DNA randomly into the genome to inactivate genes. Although some interesting models like the Mov 13 mouse have been described in this category,[19,20] the procedure is limited because it cannot control the site and subsequent type of gene that is inactivated. Similarly, several mouse models of skeletal disease have been created by spontaneous or induced mutation in unknown genes. Often, the phenotypes are very interesting but, again, they are limited because the primary gene defect is unknown. Nevertheless, by linkage analysis the causative gene in this latter case can, in theory, be identified using "reverse genetics."

4.4 Examples of Transgenic Mice with Skeletal Phenotypes

There are many transgenic mouse lines that show skeletal alterations due to either overexpression of the transgenes or expression of mutant proteins that inactivate the function(s) of the normal endogenous genes. They include growth factors, cytokines, receptors, and structural matrix genes (Table 4.2 and Ref. 21).[22–48] The expression of some transgenes was targeted to bone tissues through bone-specific promoters such as osteocalcin (osteoblast specific) or TRAP (osteoclast specific), and others were expressed in nonbone tissues. The phenotypes range from osteopetrosis (too much bone) to osteoporosis (not enough bone) resulting from impaired formation or to altered activities of the osteoblasts and osteoclasts. In other cases, skeletal abnormalities resulted from defects in cartilage and matrix structures. In most cases, the phenotypes were consistent with data drawn from *in vitro* studies; however, others were surprising or even contradictory to previously reported results. For example, interleukin-6 (IL-6) was long thought to be a bone resorption cytokine; however, overexpression of IL-6 in transgenic mice decreased osteoclast number and bone resorption.[38] Despite these sometimes paradoxical data that are reamed from these mice lines, they provide many new skeletal models that can be analyzed further to delineate pertubations in their molecular, cellular, or biomechanical integrity.

4.5 Examples of Knockout Mice with Skeletal Phenotypes

By gene targeting using homologous recombination, knockout mice have been generated with expected or predicable bone defects (Table 4.3 and Refs. 49 to 84). These include vitamin D receptor, alkaline phosphatse, calcitonin, and cathepsin K. On the other hand, additional functions were discovered from knockout mice. For example, deletion of 24-hydroxylase, which is thought to play a role in the degradation of vitamin D3, resulted in impaired vitamin D catabolism as well as intramembranous bone ossification. Further, targeted disruption of the widely expressed gene c-*src* led to defects primarily in bone tissues. Deletion of two structurally related bone-enriched matrix genes osteopontin[84] and bone sialoprotein (see Chapter 5) had no discernible phenotype *in vivo* possibly due to redundancy, while lack of a transcription factor cbfa-1 implicated to regulate their expression led to dramatic changes in the skeletal formation. Consistent results, on the other hand, were obtained from the separate deletion of osteoprotegrin (OPG)[49] and its ligand.[50] The results obtained were opposite to the phenotype in osteoprotegrin transgenic mice[21] and, taken together, strongly suggest that OPG is an inhibitor of osteoclast differentiation and activity. Therefore, they may be a potential therapeutic agent for the treatment of osteoporosis.

An important point to note is that only a fraction of all the mouse lines listed in Tables 4.1 and 4.2 have been tested for biomechanical integrity. An example of two knockouts that have been examined for biomechanical properties are osteocalcin[68] and biglycan,[69] both of which are extracellular matrix proteins. Both are expressed by the osteoblast but are structurally very different; osteocalcin is a small protein with a γ carboxylation post-translational modification, while biglycan is a small proteoglycan whose mass is composed primarily of carbohydrates. Mutations in these abundant structural genes showed no profound effects on the development of the bones (i.e., gross abnormalites in shape or number) but, rather, they had age-related effects on the accumulation of bone mass (see Fig. 4.4). Specifially, a disruption of the biglycan gene led to a decrease in bone formation and less bone mass, while osteocalcin mutant mice had

TABLE 4.2 Examples of Transgenic Mice with Skeletal Phenotye

Gene	Promoter	Phenotype	Ref.
		Overexpression (Gain of Function)	
Osteoprotegrin	Human ApoE	Osteopetrosis due to decreased osteoclast formation	21
IGF-I	Osteocalcin	No change in bone formation rate Increased bone density and osteocyte number	22
TRAP (tartrate-resistant acid phosphatase)	TRAP/SV40 enhancer	Increased bone resorption Decreased trabecular bone volume	23
Soluble tumor necrosis factor receptor	α1-anti-trypsin	Protected against bone loss caused by estrogen deficiency	24
Human osteoblast stimulating factor-1	Human osteocalcin	Increased bone density	25
Human TGF-β2	Rat osteocalcin	Progressive bone loss Increased bone matrix deposition and defective bone mineralization Hypoplasia of the clavicles	10
Interleukin 4	lck	Osteoprosis due to decreased osteoblast activity	26
Stretch-activated cation channel (α-rENaC)	Osteocalcin	Increased bone formation rate and bone density	27
Vitamin D receptor	GOSCAS	Increased bone formation rate Thicker and stronger bone	28
Human G-CSF	SRα	Osteoporosis due to increased bone resorption	29
c-fos	H-2Kb class I MHC	Osteosarcoma	30
Human BMP4	BMP4	Decreased body size Failure in the development of hair and whisker follicles, high incidence of neonatal death Increased apoptosis in cartilage and hair follicles	31
Human bFGF	Phosphoglycerate kinase	Shortening and flattening of long bones, moderate macrocephaly	32
Human TNF-α	Human TNF-α	Arthritis	33
Interferon γ	Mouse immunoglobin λ chain enhancer	Osteochondrodysplasia characterized by thin cortical bones, fractures, disruption of the epiphyseal plate and degeneration of articular cartilage	34
Ets2	Mouse metallothionein	Neurocranial, viserocranial, and cervical skeletal abnormalities similar to Down's syndrome	35
Human growth hormone	Rat osteocalcin	Longer femora and greater mid-diaphyseal cross-sectional geometry associated with impaired mechanical integrity due to lower ash content, presence of cartilage and woven bone and greater porosity in the mid-diaphysis	8, 36
HTLV-I tax	LTR	High bone turnover and myelofibrosis	37
Human IL-6	H-2Ld	Decreased osteoclast number and bone resorption	38
PTHrP	Collagen type II	Chondrodysplasia characterized by short-limbed dwarfism and a delay in endochondral ossification	40
Mutant PTH/PTHrP receptor (constitutively active)	Rat α 1 (II) collagen	Delayed mineralization, decelerated conversion of proliferative chondrocytes into hypertrophic cells and prolonged presence of hypertrophic chondrocytes	39
Natriuretic peptide	Human serum amyloid	Skeletal overgrowth	41
		Dominant-Negative Expression	
Mutant human α1 (I) collagen	Human α (I) collagen	Short bones, decreased collagen and mineral content, poor mechanical properties and spontaneous fractures	42

(*Continued*)

TABLE 4.2 Examples of Transgenic Mice with Skeletal Phenotye (Continued)

Gene	Promoter	Phenotype	Ref.
Mutant α1 (II) collagen	Mouse α (II) collagen	Short limbs, hypoplastic thorax, abnormal craniofacial development, disruption of the normal organization of growth plate with decreased proliferating zone and increased hypertrophic zone, defect in endochondral ossification	43
Mutant α1(IX) collagen	Rat collagen II	Osteoarthritis and mild chondrodysplasia	44
Truncated type X collagen	Chick type X	Compression of hypertrophic growth plate cartilage, decreased bone formation, leukocyte deficiency and lymphopenia	45
Mutant β-1 integrin	Osteocalcin	Thinner bone and increased osteoclast number and bone resorption in female mice	46
Truncated TGF-β type II receptor	Metallothionein	Osteoarthritis	47
Klotho	Gene interrupted by foreign transgene	Osteoprosis, infertility, short life span, arteriosclerosis, and skin atrophy	48

an increase in bone formation resulting in "thicker" bones. Similarly, both mice lines had biomechanical pertubations that were quite distinct. Biglycan-deficient mice had spontaneously decreased yield energy and failure load at 6 months of age[69] while osteocalcin mice showed increased bone strength only after ovarectomy.[68] As can be seen by the phenotypes listed in Tables 4.2 and 4.3 many of the trangenic lines have been well characterized at the tissue and cellular level and thus offer an immense resource for the biomechanical engineer interested in testing the relationship of a specific gene to biomechanical soundness.

4.6 New Frontiers: Designer Mice

4.6.1 Tissue-Specific Knockout Using Cre-recombinase

Some genes when knocked out from conception are lethal. Although these observations clearly show the importance of a protein, they limit examining its function later in life. For this reason, a technology has been developed where genes can be knocked out at a specific time and location. In this procedure promoters with the desired developmental expression regime are connected to the enzyme cre-recombinase (Fig. 4.5). The enzyme by itself has no effect on normal eukaryotic cells. It was originally isolated from λ phage (virus that infect bacteria) and has the ability to remove a stretch of DNA that has loxP DNA sequences attached to both ends. The short loxP sites are placed at the ends of (or flanking) a gene being tested using genetic engineering and homologous recombination (see previous section). Thus, two mice strains are created: one with a promoter connected to cre-recombinase so that it will be made in a specific place at a specific time during development. The second mouse strain contains loxP sites outside (flanking) the gene that is to be deleted. By crossing the two mouse strains, both genetic modifications can be incorporated into a single mouse that will, subsequently, have the gene with loxP sites deleted in tissues that express the cre-recombinase. This is referred to as a "conditional allele" in contrast to a total knockout, which is termed a *null* allele. The advantage of making the two types of mice separately is that the cre-recombinase transgenic lines can be used repeatedly to make additional mice defective in any gene with previously engineered loxP sites. An example of this procedure was recently described for the enzyme glucokinase, which is essential for glucose homeostasis. Using various promoters to drive the cre-recombinase, the gene was ablated either in the β cell of the pancreas or in the liver.[85] The differential knockout of the enzyme showed that pancreatic cell expression was more critical to hyperglycemia while the liver expression was important for glycogen synthesis and glucose turnover. Further, by careful placement of the loxP sites within the targeted gene, mice have been made with only a portion of the

TABLE 4.3 Examples of Knockout Mice with Skeletal Phenotype

Gene	Phenotype	Ref.
Osteoprotegrin	Osteoporosis due to impaired osteoclast formation, arterial calcification	49
Osteoprotegrin ligand	Toothless, osteopetrosis due to lack of osteoclasts, lack of lymph nodes, defect in thymocyte differentiation	50
Transcription factor PU.1	Osteopetrosis due to lack of osteoclasts	51
c-fos	Osteoporosis and absence of tooth eruption Hematopoietic defects	52, 53
c-sac	Osteopetrosis due to impaired osteoclast function	54
Tartrate-resistant acid phosphatase	Mild osteopetrosis due to impaired bone resorption	55
Calcitonin	Decreased bone density	56
Cathepsin K	Osteopetrosis due to impaired osteoclast function	57
β-3 Integrin	Osteoscelerosis Dysfunctional osteoclasts and osteblasts	58
Cbfa-1	Lack of bone formation due to maturational arrest of osteoblasts	59
PTHrP receptor	Accelerated chondrocyte differentiation	60
Vitamin D receptor	Hypocalcemia, hyperparathyroidism, rickets and osteomalacia, alopoecia, and infertility	61
24-hydroxylase	Impaired vitamin D3 catabolism, Impaired intramembranous bone ossification	62
Thyroid hormone receptors	Decreased bone growth, disorganized growth plate and delayed ossification, decreased bone mineral content and serum IGF-I level	63
BMP-3	Increased bone density	64
Alkaline phosphatase	Spontaneous fracture, defective mineralization Epileptic seizures and death before weaning	65
Connexin 43	Small dome-shaped skull Impaired intramembraneous bone formation Decreased ALPase activity in osteoblasts	66
β-Adrenergic receptor kinase	Decreased bone formation in heterozygous mice	67
Osteocalcin	Increased bone formation	68
Biglycan	Osteoporosis due to decreased bone formation	69
Osteonectin	Osteopenia	70
IL-6	Protection from bone loss caused by estrogen deficiency	71
IL-1 receptor	Prevention of ovariectomy-induced bone loss	72
Collagen II α1	Lack of extracellular fibrils in cartilage with disorganized chondrocytes, absence of endochondrial bone and growth plate in long bone	73
BMP7	Holes in the basisphenoid bone and xyphoid cartilage, retarded ossification of bones, fused ribs and vertebrae, a kinked tail, polydactyly of the hind limbs	74
LIF receptor	Severe osteopenia of perinatal bone associated with increased osteoclast number	75
FGF receptor 3	Deafness, kyphosis, scoliosis, crooked tails, curvature and overgrowth of long bones and vertebrae	76
Gli 2 and 3	Lack of trabecular bone, presence of calcified cartilage and absence of primary ossification center in the diaphysis	77
IGF-1	Delayed bone ossification	78
PTHrP	Abnormal endochondral bone formation and lethal skeletal displasia	79
TGF-β1	Decreased bone mineral content and longitudinal growth and elasticity, dental abnormalities	80, 81
NF-KB1 and NF-KB2	Osteopetrosis due to lack of osteoclast differentiation	82
GMCSF (OP/OP)	Osteopetrosis	83
Osteopontin	Altered osteoclast function *in vitro*	84

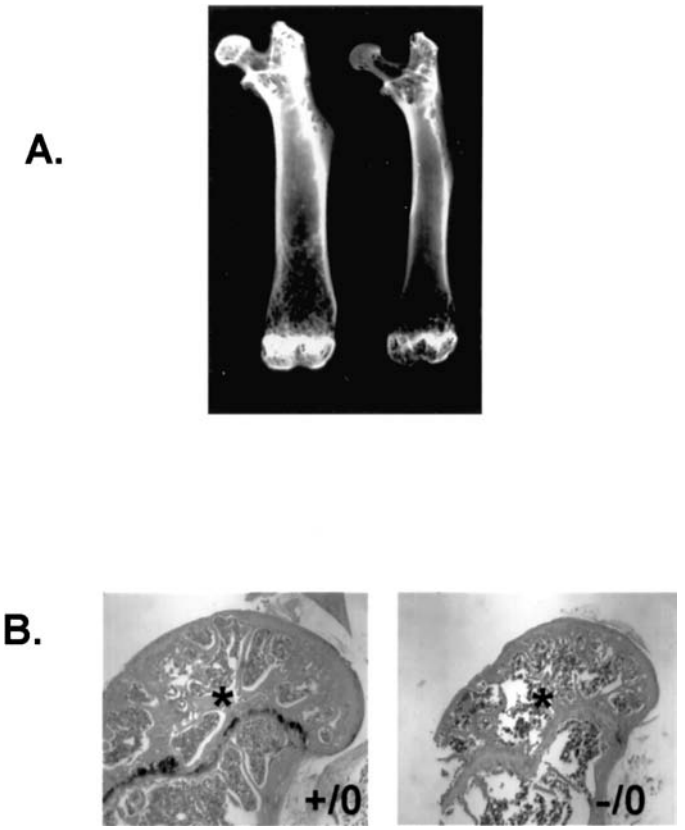

FIGURE 4.4 Femurs of transgenic mouse with knockout of biglycan gene. (A) Faxitron of femurs of 6-month-old normal (+/0) and biglycan (−/0) mice. The mice are designated with a second alelle "0" because biglycan is located on the X chromosome; male mice have no second biglycan allele. (B) Sections through the femoral head of the bones shown in panel A. Note the relative loss of trabecular volume designated by an* and thinning of the cortex in the mutant (0/−) compared with normal littermates (0/+).

targeted gene deleted also in a tissue-specific manner.[86] In the future, one can expect to see mice conditionally knocked-out or mutated in specific skeletal cells such as osteoblast and osteoclast or in any place where cell-specific promoters become available.

4.6.2 Point Mutations or Subtle Gene Alterations

In an attempt to refine the knockout technology, further new methods were developed to create small (not total knockout) changes in genes. This is an ideal way to study protein structure–function relationships *in vivo*. This strategy is referred to as "hit and run,"[87] "in out,"[88] "tag and exchange,"[89] or "double replacement."[90] Essentially, the technique uses two homologous recombination steps: one to insert selectable markers (sometimes called a cassette) for targeted gene uptake (the hit) and a second step to replace the normal gene with a mutated version (the run or replacement). This strategy was successfully used to create a "site-directed" mutation in the collagenase cleavage site of type I collagen. Animals with this mutation showed skin defects and altered osteocyte activities.[91]

4.6.3 From Knockout to Knockin

Variations of the gene targeting have also been used to replace one gene for another such that the inserted gene is under the control of the replaced gene. This is done to determine whether a structurally similar

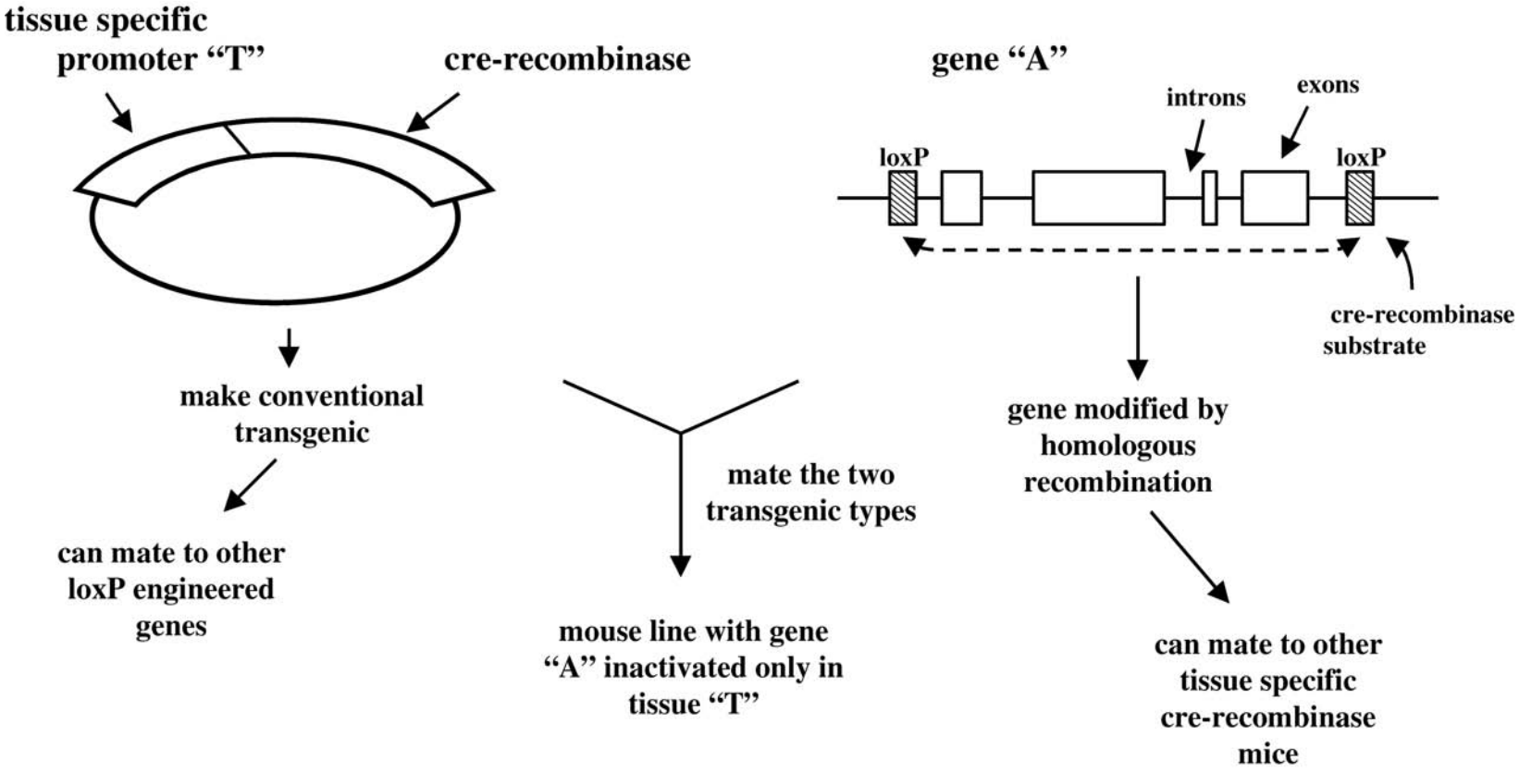

FIGURE 4.5 Construction of cre-recombinase tissue specific knockouts. This experiment uses a combination of conventional transgenic mice (described in Fig. 4.1) and targeted (homologously recombined) genes. In the first case a mouse line is made that expresses the enzyme cre-recombinase under the direction of a tissue-specific promoter. A second mouse line is made that has loxP sites engineered at either side of the gene being tested for function. LoxP sequences are removed in the presence of cre-recombinase. By breeding two mice lines, a third line is created that will inactivate the gene with the loxP sites only in a select tissue and are considered "conditionally" knocked out. The first two lines made by this approach can be bred to other mice in any number of combinations ultimately to create mice that have inactivated genes in any tissue for which specific promoters are available.

protein could "rescue" the ablated gene if expressed at the same time and place during development.[92] One could imagine testing, for example, whether the actions of the many isoforms of TGF-β are interchangeable in the context of a null background. In this case one could exchange TGF-β1 for TGF-β2 (under the control of TGF-β1 promoter) to determine if the second isoform could compensate for the action of the first. Undoubtedly, new phenotypes will continue to arise from these types of experiments creating even more models to test for bone structure and function.

4.6.4 Inducible Gain of Function: Timing Is Everything

To control the production of the transgene, new techniques were devised where genes can be induced or repressed in the live organism through the administration of a soluble agent. Two examples in this category use either ecdysone, which is a fly protein,[93] or tetracyline,[94] which represses or induces genes depending on the DNA used for construction. This latter procedure has been used in numerous studies using cultured cells and should be useful to examine the role of a gene at a specific window of time during the life span of the mouse.

4.6.5 Tissue-Specific Gene Inactivation: Combining Space and Time

By using the trangenic technologies described, it is now possible to destroy specific cell types by connecting a poison to a cell-specific promoter. This has been done using diphtheria toxin[95,96] or the TK gene. This latter approach, which relies on the subsequent application of gancylovir, has an advantage because the timing of cell destruction can be controlled. By creating trangenic mice that had the TK gene under the control of the osteocalcin[97] or type I collagen promoters,[98] the osteoblasts in the skeleton were inactivated leading to induced osteopenia. An advantage of this procedure is that it is reversible or "conditional"; withdrawal of the drug removes the toxic effects on the osteoblast and subsequently leads to a wave of new bone formation.

4.7 Summary

In summary, there are numerous ways to create trangenic mice and each method has advantages and disadvantages. With conventional transgenics the overexpressed gene must have effect over the endogenous one. Further, because the transgene is randomly integrated into the host chromosome, it is possible that it can become inactivated or expressed in an unusual pattern due to effects from nearby gene sequences. Integration of foreign DNA could also inactivate genes within the host.[48] If the overexpression of the gene is lethal, inducible methods are an alternative. Some methods differ genetically but have a similar outcome; a dominant-negative tissue-specific transgene is quite similar to a cre-recombinase tissue-specific knockout. In either case, the gene of interest would be inactive or not expressed in a specific tissue.

Due to the nature of the way knockout mice are made, they should not have DNA integration effects if screened properly. There is, however, the possibility of gene redundancy where no phenotype is detected because a second gene takes over the function of the ablated gene. Knowing the structure and abundance of related genes, one can create mice with "double knockouts." This is done by breeding two separate single knockouts with each other through two generations (the first generation is all heterozygote). Using this strategy, the authors have discovered that the small proteoglycan decorin partially compensates for biglycan in regulating bone mass.[99]

Having created a mutant mouse line, an evolving trend is to combine all aspects of basic biology in the analysis of the transgenic. For example, knowing that bone formation is affected in a particular mouse model (see Chapter 1) one might isolate bone-forming cells and study their activity in culture (see Chapter 2). Detailed molecular analysis could then be carried out using the procedures outlined in Chapter 3. Mineral character and composition would also be critical to examine either *in vivo* or *in vitro* (see Chapter 5). By mixing and matching the host of genetic features available, an "Alice's Restaurant" picture emerges: "You can get anything you want." In summary, anything is possible in creating transgenic mice; one is limited only by well-characterized genes and promoters and the proper analyses.

Acknowledgments

The authors wish to thank Ms. Jennifer Liang for preparation of the illustrations in the chapter.

References

1. R. L. Brinster, H. Y. Chen, and M. E. Trumbauer, Mouse oocytes transcribe injected Xenopus 5S RNA gene, *Science,* 211, 396–398, 1981.
2. R. L. Brinster, H. Y. Chen, M. Trumbauer, A. W. Senear, R. Warren, and R. D. Palmiter, Somatic expression of herpes thymidine kinase in mice following injection of a fusion gene into eggs, *Cell,* 27, 223–231, 1981.
3. G. Hogan, F. Costantini, and E. Lacy, *Manipulating the Mouse Embryo*. Cold Spring Harbor Laboratory, Cold Spring Harbor, NY, 1986.
4. K. Ibaraki-O'Connor, K. Nakata, and M. F. Young, Toward understanding the function of amelogenin using transgenic mice, *Adv. Dent. Res.,* 10, 208–214, 1996.
5. W. Horton, T. Miyashita, K. Kohno, J. R. Hassell, and Y. Yamada, Identification of a phenotype-specific enhancer in the first intron of the rat collagen II gene, *Proc. Natl. Acad. Sci. U.S.A.,* 84, 8864–8868, 1987.
6. R. F. Santerre, K. R. Bales, M. J. Janney, K. Hannon, L. F. Fisher, C. S. Bailey, J. Morris, R. Ivarie, and C. K. d. Smith, Expression of bovine myf5 induces ectopic skeletal muscle formation in transgenic mice, *Mol. Cell. Biol.,* 13, 6044–6051, 1993.
7. J. Charite, W. de Graaff, S. Shen, and J. Deschamps, Ectopic expression of Hoxb-8 causes duplication of the ZPA in the forelimb and homeotic transformation of axial structures, *Cell,* 78, 589–601, 1994.
8. A. R. Baker, P. G. Hollingshead, S. Pitts-Meek, S. Hansen, R. Taylor, and T. A. Stewart, Osteoblast-specific expression of growth hormone stimulates bone growth in transgenic mice, *Mol. Cell. Biol.,* 12, 5541–5547, 1992.
9. S. V. Reddy, T. Scarcez, J. J. Windle, R. J. Leach, J. E. Hundley, J. M. Chirgwin, J. Y. Chou, and G. D. Roodman, Cloning and characterization of the 5′-flanking region of the mouse tartrate-resistant acid phosphatase gene, *J. Bone Miner. Res.,* 8, 1263–1270, 1993.
10. A. Erlebacher and R. Derynck, Increased expression of TGF-β2 in osteoblasts results in an osteoporosis-like phenotype, *J. Cell Biol.,* 132, 195–210, 1996.
11. R. H. Chen, R. Ebner, and R. Derynck, Inactivation of the type II receptor reveals two receptor pathways for the diverse TGF-β activities, *Science,* 260, 1335–1338, 1993.
12. A. Erlebacher, E. H. Filvaroff, J. Q. Ye, and R. Derynck, Osteoblastic responses to TGF-β during bone remodeling, *Mol. Biol. Cell.,* 9, 1903–1918, 1998.
13. K. R. Thomas and M. R. Capecchi, Site-directed mutagenesis by gene targeting in mouse embryo-derived stem cells, *Cell,* 51, 503–512, 1987.
14. A. Nagy, J. Rossant, R. Nagy, W. Abramow-Newerly, and J. C. Roder, Derivation of completely cell culture-derived mice from early-passage embryonic stem cells, *Proc. Natl. Acad. Sci. U.S.A.,* 90, 8424–8428, 1993.
15. E. J. Robertson, *Teratocarcinomas and Embryonic Stem Cells: A Practical Approach*, IRL Press, Oxford, 1987.
16. S. Kobayashi, K. Yoshida, T. Ohshima, N. Esumi, V. M. Paralkar, G. J. Wistow, and A. B. Kulkarni, DNA sequence motifs are associated with abberrant homologous recombination in the mouse macrophage migration inhibitory factor (Mif) locus, *Gene,* 215, 85–92, 1998.
17. H. Gardner, J. Kreidberg, V. Koteliansky, and R. Jaenisch, Deletion of integrin α 1 by homologous recombination permits normal murine development but gives rise to a specific deficit in cell adhesion, *Dev. Biol.,* 175, 301–313, 1996.
18. H. M. Sheng, W. G. Beamer, L. R. Donahue, C. J. Rosen, D. J. Bayling, and J. E. Wergedal, The greater bone formation rate (BF) in the C3 (high bone density) mice compared to the B6 (low bone density) mice is due to a higher mineral apposition rate, *Bone,* 23, S276, 1998.

19. K. Harbers, M. Kuehn, H. Delius, and R. Jaenisch, Insertion of retrovirus into the first intron of alpha 1(I) collagen gene to embryonic lethal mutation in mice, *Proc. Natl. Acad. Sci. U.S.A.,* 81, 1504–1508, 1984.
20. K. J. Jepsen, M. B. Schaffler, J. L. Kuhn, R. W. Goulet, J. Bonadio, and S. A. Goldstein, Type I collagen mutation alters the strength and fatigue behavior of Mov13 cortical tissue, *J. Biomech.,* 30, 1141–1147, 1997.
21. W. S. Simonet, D. L. Lacey, C. R. Dunstan, M. Kelley, M. S. Chang, R. Luthy, H. Q. Nguyen, S. Wooden, L. Bennett, T. Boone, G. Shimamoto, M. DeRose, R. Elliott, A. Colombero, H. L. Tan, G. Trail, J. Sullivan, E. Davy, N. Bucay, L. Renshaw-Gegg, T. M. Hughes, D. Hill, W. Pattison, P. Campbell, W. J. Boyle, et al., Osteoprotegerin: a novel secreted protein involved in the regulation of bone density [see comments], *Cell,* 89, 309–319, 1997.
22. G. Zhao, M.-C. Faugere, H. Malluche, J. Wang, T. Nakayama, T. Pike, J. Fagin, and T. Clemens, Osteoblast-specific overexpression of IGF-I in transgenic mice increases cancellous bone volume, *Bone,* 23, S172, 1998.
23. A. I. Cassady, N. Z. Angel, M. M. Cahill, F. M. R., N. Walsh, M. C. Ostrowsik, and D. A. Hume, Transgenic mice overexpressing tartrate-resistant acid phosphatase exhibit an increased rate of bone turnover, *Bone,* 23, S225, 1998.
24. P. Ammann, R. Rizzoli, J. P. Bonjour, S. Bourrin, J. M. Meyer, P. Vassalli, and I. Garcia, Transgenic mice expressing soluble tumor necrosis factor-receptor are protected against bone loss caused by estrogen deficiency, *J. Clin. Invest.,* 99, 1699–1703, 1997.
25. H. Masuda, A. Tsujimura, M. Yoshioka, Y. Arai, Y. Kuboki, T. Mukai, T. Nakamura, H. Tsuji, M. Nakagawa, and T. Hashimoto-Gotoh, Bone mass loss due to estrogen deficiency is compensated in transgenic mice overexpressing human osteoblast stimulating factor-1, *Biochem. Biophys. Res. Commun.,* 238, 528–533, 1997.
26. D. B. Lewis, H. D. Liggitt, E. L. Effmann, S. T. Motley, S. L. Teitelbaum, K. J. Jepsen, S. A. Goldstein, J. Bonadio, J. Carpenter, and R. M. Perlmutter, Osteoporosis induced in mice by overproduction of interleukin 4, *Proc. Natl. Acad. Sci. U.S.A.,* 90, 11618–11622, 1993.
27. N. L. Kizer, T. L. Clemens, J. W. Pike, and K. A. Hruska, Overexpression of stretch-activated cation channels in osteoblasts of transgenic mice increases bone mineral density, *Bone,* 23, S200, 1998.
28. E. M. Gardiner, N. A. Sims, G. P. Thomas, P. A. Baldock, C. P. White, N. K. Henderson, K. L. Sunn, N. A. Morrison, W. R. Walsh, and J. A. Eisman, Elevated osteoblastic vitamin D receptor in transgenic mice yield stronger bones, *Bone,* 23, S176, 1998.
29. T. Takahashi, T. Wada, M. Mori, Y. Kokai, and S. Ishii, Overexpression of the granulocyte colony-stimulating factor gene leads to osteoporosis in mice, *Lab. Invest.,* 74, 827–834, 1996.
30. A. E. Grigoriadis, K. Schellander, Z. Q. Wang, and E. F. Wagner, Osteoblasts are target cells for transformation in c-fos transgenic mice, *J. Cell. Biol.,* 122, 685–701, 1993.
31. J. Q. Feng, X. Li, R. Dunn, J. Dai, B. L. M. Hogan, M. MacDougall, G. R. Mundy, and S. E. Harris, Overexpression of BMP4 driven by a −1135 to +258 BMP4 promoter fragment leads to decreased body size, hair, and whisker loss and tissue specific apoptosis, *Bone,* 23, S184, 1998.
32. J. D. Coffin, R. Z. Florkiewicz, J. Neumann, T. Mort-Hopkins, G. W. Dorn, II, P. Lightfoot, R. German, P. N. Howles, A. Kier, B. A. O'Toole, et al., Abnormal bone growth and selective translational regulation in basic fibroblast growth factor (FGF-2) transgenic mice, *Mol. Biol. Cell.,* 6, 1861–1873, 1995.
33. J. Keffer, L. Probert, H. Cazlaris, S. Georgopoulos, E. Kaslaris, D. Kioussis, and G. Kollias, Transgenic mice expressing human tumour necrosis factor: a predictive genetic model of arthritis, *EMBO. J.,* 10, 4025–4031, 1991.
34. A. Nii, D. A. Reynolds, H. A. Young, and J. M. Ward, Osteochondrodysplasia occurring in transgenic mice expressing interferon-γ, *Vet. Pathol.,* 34, 431–441, 1997.
35. S. H. Sumarsono, T. J. Wilson, M. J. Tymms, D. J. Venter, C. M. Corrick, R. Kola, M. H. Lahoud, T. S. Papas, A. Seth, and I. Kola, Down's syndrome-like skeletal abnormalities in Ets2 transgenic mice, *Nature,* 379, 534–537, 1996.

36. K. F. Tseng, J. F. Bonadio, T. A. Stewart, A. R. Baker, and S. A. Goldstein, Local expression of human growth hormone in bone results in impaired mechanical integrity in the skeletal tissue of transgenic mice, *J. Orthop. Res.,* 14, 598–604, 1996.
37. N. H. Ruddle, C. B. Li, W. C. Horne, P. Santiago, N. Troiano, G. Jay, M. Horowitz, and R. Baron, Mice transgenic for HTLV-I LTR-tax exhibit tax expression in bone, skeletal alterations, and high bone turnover, *Virology,* 197, 196–204, 1993.
38. H. Kitamura, H. Kawata, F. Takahashi, Y. Higuchi, T. Furuichi, and H. Ohkawa, Bone marrow neutrophilia and suppressed bone turnover in human interleukin-6 transgenic mice. A cellular relationship among hematopoietic cells, osteoblasts, and osteoclasts mediated by stromal cells in bone marrow, *Am. J. Pathol.,* 147, 1682–1692, 1995.
39. E. Schipani, B. Lanske, J. Hunzelman, A. Luz, C. S. Kovacs, K. Lee, A. Pirro, H. M. Kronenberg, and H. Juppner, Targeted expression of constitutively active receptors for parathyroid hormone and parathyroid hormone-related peptide delays endochondral bone formation and rescues mice that lack parathyroid hormone-related peptide, *Proc. Natl. Acad. Sci. U.S.A.,* 94, 13689–13694, 1997.
40. E. C. Weir, W. M. Philbrick, M. Amling, L. A. Neff, R. Baron, and A. E. Broadus, Targeted overexpression of parathyroid hormone-related peptide in chondrocytes causes chondrodysplasia and delayed endochondral bone formation, *Proc. Natl. Acad. Sci. U.S.A.,* 93, 10240–10245, 1996.
41. M. Suda, Y. Ogawa, K. Tanaka, N. Tamura, A. Yasoda, T. Takigawa, M. Uehira, H. Nishimoto, H. Itoh, Y. Saito, K. Shiota, and K. Nakao, Skeletal overgrowth in transgenic mice that overexpress brain natriuretic peptide, *Proc. Natl. Acad. Sci. U.S.A.,* 95, 2337–2342, 1998.
42. R. Pereira, J. S. Khillan, H. J. Helminen, E. L. Hume, and D. J. Prockop, Transgenic mice expressing a partially deleted gene for type I procollagen (COL1A1). A breeding line with a phenotype of spontaneous fractures and decreased bone collagen and mineral, *J. Clin. Invest.,* 91, 709–716, 1993.
43. M. Metsaranta, S. Garofalo, G. Decker, M. Rintala, B. de Crombrugghe, and E. Vuorio, Chondrodysplasia in transgenic mice harboring a 15-amino acid deletion in the triple helical domain of pro α 1(II) collagen chain, *J. Cell. Biol.,* 118, 203–212, 1992.
44. K. Nakata, K. Ono, J. Miyazaki, B. R. Olsen, Y. Muragaki, E. Adachi, K. Yamamura, and T. Kimura, Osteoarthritis associated with mild chondrodysplasia in transgenic mice expressing α 1(IX) collagen chains with a central deletion, *Proc. Natl. Acad. Sci. U.S.A.,* 90, 2870–2874, 1993.
45. O. Jacenko, P. A. LuValle, and B. R. Olsen, Spondylometaphyseal dysplasia in mice carrying a dominant negative mutation in a matrix protein specific for cartilage-to-bone transition, *Nature,* 365, 56–61, 1993.
46. D. L. Zimmerman, P. Leboy, and C. Damsky, Altered intergrin function in mature osteoblasts results in impaired bone formation, *Bone,* 23, S154, 1998.
47. R. Serra, M. Johnson, E. H. Filvaroff, J. LaBorde, D. M. Sheehan, R. Derynck, and H. L. Moses, Expression of a truncated, kinase-defective TGF-β type II receptor in mouse skeletal tissue promotes terminal chondrocyte differentiation and osteoarthritis, *J. Cell. Biol.,* 139, 541–552, 1997.
48. M. Kuro-o, Y. Matsumura, H. Aizawa, H. Kawaguchi, T. Suga, T. Utsugi, Y. Ohyama, M. Kurabayashi, T. Kaname, E. Kume, H. Iwasaki, A. Iida, T. Shiraki-Iida, S. Nishikawa, R. Nagai, and Y. I. Nabeshima, Mutation of the mouse klotho gene leads to a syndrome resembling ageing [see comments], *Nature,* 390, 45–51, 1997.
49. N. Bucay, I. Sarosi, C. R. Dunstan, S. Morony, J. Tarpley, C. Capparelli, S. Scully, H. L. Tan, W. Xu, D. L. Lacey, W. J. Boyle, and W. S. Simonet, Osteoprotegerin-deficient mice develop early onset osteoporosis and arterial calcification, *Genes Dev.,* 12, 1260–1268, 1998.
50. W. J. Boyle, Y. Kung, D. L. Lacey, I. Sarosi, C. R. Dunstan, E. Timms, H.-L. Tan, G. Elliott, M. J. Kelley, A. Colombero, R. Elliott, S. Scully, C. Capparelli, S. Morony, and J. Penninger, Osteoprotegerin ligand (OPGL) is required for murine osteoclastogenesis, *Bone,* 23, S189, 1998.

51. M. M. Tondravi, S. R. McKercher, K. Anderson, J. M. Erdmann, M. Quiroz, R. Maki, and S. L. Teitelbaum, Osteopetrosis in mice lacking haematopoietic transcription factor PU.1, *Nature,* 386, 81–84, 1997.
52. R. S. Johnson, B. M. Spiegelman, and V. Papaioannou, Pleiotropic effects of a null mutation in the c-fos proto-oncogene, *Cell,* 71, 577–586, 1992.
53. Z. Q. Wang, C. Ovitt, A. E. Grigoriadis, U. Mohle-Steinlein, U. Ruther, and E. F. Wagner, Bone and haematopoietic defects in mice lacking c-fos, *Nature,* 360, 741–745, 1992.
54. P. Soriano, C. Montgomery, R. Geske, and A. Bradley, Targeted disruption of the c-src proto-oncogene leads to osteopetrosis in mice, *Cell,* 64, 693–702, 1991.
55. A. R. Hayman, S. J. Jones, A. Boyde, D. Foster, W. H. Colledge, M. B. Carlton, M. J. Evans, and T. M. Cox, Mice lacking tartrate-resistant acid phosphatase (Acp 5) have disrupted endochondral ossification and mild osteopetrosis, *Development,* 122, 3151–3162, 1996.
56. A. O. Hoff, P. M. Thomas, G. J. Cote, H. Qiu, S. Bain, D. Puerner, M. Strachan, E. Loyer, G. Pinero, N. Ordonez, A. Bradley, and R. F. Gagel, Generation of a calcitonon knockout mouse model, *Bone,* 23, S164, 1998.
57. P. Saftig, E. Hunziker, O. Wehmeyer, S. Jones, A. Boyde, W. Rommerskirch, J. D. Moritz, P. Schu, and K. von Figura, Impaired osteoclastic bone resorption leads to osteopetrosis in cathepsin-K-deficient mice, *Proc. Natl. Acad. Sci. U.S.A.,* 95, 13453–13458, 1998.
58. K. P. McHugh, K. Hodivala-Dilke, S. L. Cheng, M. H. Zheng, L. V. Avioli, R. O. Hynes, F. P. Ross, and S. L. Teitelbaum, The β_3 integrin knockout mouse is osteoclerotic and has dysfunctional osteoblasts, *Bone,* 23, S190, 1998.
59. T. Komori, H. Yagi, S. Nomura, A. Yamaguchi, K. Sasaki, K. Deguchi, Y. Shimizu, R. T. Bronson, Y. H. Gao, M. Inada, M. Sato, R. Okamoto, Y. Kitamura, S. Yoshiki, and T. Kishimoto, Targeted disruption of Cbfa1 results in a complete lack of bone formation owing to maturational arrest of osteoblasts [see comments], *Cell,* 89, 755–764, 1997.
60. B. Lanske, A. C. Karaplis, K. Lee, A. Luz, A. Vortkamp, A. Pirro, M. Karperien, L. H. K. Defize, C. Ho, R. C. Mulligan, A. B. Abou-Samra, H. Juppner, G. V. Segre, and H. M. Kronenberg, PTH/PTHrP receptor in early development and Indian hedgehog-regulated bone growth [see comments], *Science,* 273, 663–666, 1996.
61. T. Yoshizawa, Y. Handa, Y. Uematsu, S. Takeda, K. Sekine, Y. Yoshihara, T. Kawakami, K. Arioka, H. Sato, Y. Uchiyama, S. Masushige, A. Fukamizu, T. Matsumoto, and S. Kato, Mice lacking the vitamin D receptor exhibit impaired bone formation, uterine hypoplasia and growth retardation after weaning, *Nat. Genet.,* 16, 391–396, 1997.
62. F. Barletta, C. Arrigo, G. A. Parker, M. Raval-Pandya, S. Christakos, and R. St. Arnaud, Administration of 1,25 dihydroxyvitamin D^3 to mice deficient in the 24-hydroxylase gene results in kidney pathology consistent with hypervitaminosis D and altered responsiveness of vitamin D dependent genes, *Bone,* 23, S185, 1998.
63. S. Gothe, C. Ohlsson, J. Nilsson, D. Forrest, and B. Vennstrom, Disturbed ossification in mice devoid of thyroid hormone receptors, *Bone,* 23, S177, 1998.
64. T. Engstrand, A. Daluiski, N. Wolffman, K. Thompson, R. Pederson, A. Nguyen, V. Rosen, and K. M. Lyons, Bone morphogenetic protein-3/osteogenin antagonizes BMP2-induced osteogenic differentiation and is a negative regulator of bone formation *in vivo, Bone,* 23, S173, 1998.
65. C. Wennberg, P. Lundberg, S. Narisawa, U. H. Lerner, and J. L. Millon, Functional studies on osteoblasts from alkaine phosphatase knock-out mice, *Bone,* 23, S153, 1998.
66. F. Lecanda, P. M. Warlow, L. R. Halstead, and T. H. Steinberg, Impaired intramembranous bone formation in connexin43 null mice, *Bone,* 23, S149, 1998.
67. M. Bliziotes, K. Wiren, M. Gunness, P. Turner, R. Nissenson, and M. Caron, Reduction of β-adrenergic receptor kinase activity results in impairment of osteoblast function, *Bone,* 23, S195, 1998.

68. P. Ducy, C. Desbois, B. Boyce, G. Pinero, B. Story, C. Dunstan, E. Smith, J. Bonadio, S. Goldstein, C. Gundberg, A. Bradley, and G. Karsenty, Increased bone formation in osteocalcin-deficient mice, *Nature,* 382, 448–452, 1996.
69. T. Xu, P. Bianco, L. W. Fisher, G. Longenecker, E. Smith, S. Goldstein, J. Bonadio, A. Boskey, A. M. Heegaard, B. Sommer, K. Satomura, P. Dominguez, C. Zhao, A. B. Kulkarni, P. G. Robey, and M. F. Young, Targeted disruption of the biglycan gene leads to an osteoporosis-like phenotype in mice, *Nat. Genet.,* 20, 78–82, 1998.
70. A. Delany, M. Amling, M. Priemel, G. Delling, C. Howe, R. Baron, and E. Canalis, Osteonectin-null mice develop severe osteopenia, *Bone,* 23, S199, 1998.
71. V. Poli, R. Balena, E. Fattori, A. Markatos, M. Yamamoto, H. Tanaka, G. Ciliberto, G. A. Rodan, and F. Costantini, Interleukin-6 deficient mice are protected from bone loss caused by estrogen depletion, *EMBO J.,* 13, 1189–1196, 1994.
72. J. A. Lorenzo, A. Naprta, Y. Rao, C. Alander, M. Glaccum, M. Widmer, G. Gronowicz, J. Kalinowski, and C. C. Pilbeam, Mice lacking the type I interleukin-1 receptor do not lose bone mass after ovariectomy [see comments], *Endocrinology,* 139, 3022–3025, 1998.
73. S. W. Li, D. J. Prockop, H. Helminen, R. Fassler, T. Lapvetelainen, K. Kiraly, A. Peltarri, J. Arokoski, H. Lui, M. Arita, et al., Transgenic mice with targeted inactivation of the Col2 α 1 gene for collagen II develop a skeleton with membranous and periosteal bone but no endochondral bone, *Genes Dev.,* 9, 2821–2830, 1995.
74. N. Jena, C. Martin-Seisdedos, P. McCue, and C. M. Croce, BMP7 null mutation in mice: developmental defects in skeleton, kidney, and eye, *Exp. Cell Res.,* 230, 28–37, 1997.
75. C. B. Ware, M. C. Horowitz, B. R. Renshaw, J. S. Hunt, D. Liggitt, S. A. Koblar, B. C. Gliniak, H. J. McKenna, T. Papayannopoulou, B. Thoma, et al., Targeted disruption of the low-affinity leukemia inhibitory factor receptor gene causes placental, skeletal, neural and metabolic defects and results in perinatal death, *Development,* 121, 1283–1299, 1995.
76. J. S. Colvin, B. A. Bohne, G. W. Harding, D. G. McEwen, and D. M. Ornitz, Skeletal overgrowth and deafness in mice lacking fibroblast growth factor receptor 3, *Nat. Genet.,* 12, 390–397, 1996.
77. S. A. Kawas, D. S. Wang, L. Cheng, L. Malynowsky, C.-C. Hui, D. Goltzman, and J. E. Henderson, Combined loss of function of Gli2 and Gli3 results in failure to develop trabecular bone in the tibiae of mutant mice, *Bone,* 23, S200, 1998.
78. J. Baker, J. P. Liu, E. J. Robertson, and A. Efstratiadis, Role of insulin-like growth factors in embryonic and postnatal growth, *Cell,* 75, 73–82, 1993.
79. A. C. Karaplis, A. Luz, J. Glowacki, R. T. Bronson, V. L. Tybulewicz, H. M. Kronenberg, and R. C. Mulligan, Lethal skeletal dysplasia from targeted disruption of the parathyroid hormone-related peptide gene, *Genes Dev.,* 8, 277–289, 1994.
80. A. G. Geiser, Q. Q. Zeng, M. Sato, L. M. Helvering, T. Hirano, and C. H. Turner, Decreased bone mass and bone elasticity in mice lacking the transforming growth factor-β1 gene, *Bone,* 23, 87–93, 1998.
81. R. N. D'Souza, A. Cavender, R. Sood, R. Tarnuzzer, D. P. Dickinson, A. Roberts, and J. Letterio, Dental abnormalities in mice lacking a functional transforming growth factor-beta1 (TGF-β1) gene indicate a role for TGF-β1 in biomineralization, *Int. J. Oral Biol.,* 23, 119–131, 1998.
82. V. Iotsova, J. Caamano, J. Loy, Y. Yang, A. Lewin, and R. Bravo, Osteopetrosis in mice lacking NF-κB1 and NF-κB2 [see comments], *Nat. Med.,* 3, 1285–1289, 1997.
83. W. Wiktor-Jedrzejczak, E. Urbanowska, and M. Szperl, Granulocyte-macrophage colony-stimulating factor corrects macrophage deficiencies, but not osteopetrosis, in the colony-stimulating factor-1-deficient op/op mouse, *Endocrinology,* 134, 1932–1935, 1994.
84. S. R. Rittling, H. N. Matsumoto, M. D. McKee, A. Nanci, X. R. An, K. E. Novick, A. J. Kowalski, M. Noda, and D. T. Denhardt, Mice lacking osteopontin show normal development and bone structure but display altered osteoclast formation *in vitro, J. Bone Miner. Res.,* 13, 1101–1111, 1998.

85. C. Postic, M. Shiota, K. D. Niswender, T. L. Jetton, Y. Chen, J. M. Moates, K. D. Shelton, J. Lindner, A. D. Cherrington, and M. A. Magnuson, Dual roles for glucokinase in glucose homeostasis as determined by liver and pancreatic beta cell-specific gene knock-outs using cre recombinase, *J. Biol. Chem.,* 274, 305–315, 1999.
86. C. Baudoin, M. J. Goumans, C. Mummery, and A. Sonnenberg, Knockout and knockin of the β1 exon D define distinct roles for integrin splice variants in heart function and embryonic development, *Genes Dev.,* 12, 1202–1216, 1998.
87. P. Hasty, R. Ramirez-Solis, R. Krumlauf, and A. Bradley, Introduction of a subtle mutation into the Hox-2.6 locus in embryonic stem cells, *Nature,* 350, 243–246, 1991.
88. V. Valancius and O. Smithies, Testing an "in-out" targeting procedure for making subtle genomic modifications in mouse embryonic stem cells, *Mol. Cell. Biol.,* 11, 1402–1408, 1991.
89. G. R. Askew, T. Doetschman, and J. B. Lingrel, Site-directed point mutations in embryonic stem cells: a gene-targeting tag-and-exchange strategy, *Mol. Cell. Biol.,* 13, 4115–4124, 1993.
90. H. Wu, X. Liu, and R. Jaenisch, Double replacement: strategy for efficient introduction of subtle mutations into the murine Col1a-1 gene by homologous recombination in embryonic stem cells, *Proc. Natl. Acad. Sci. U.S.A.,* 91, 2819–2823, 1994.
91. W. Zhao and S. Krane, Inability of collagenase to cleave type I collagen *in vivo* is associated with osteocyte apoptosis, *Bone,* 23, S185, 1998.
92. M. Hanks, W. Wurst, L. Anson-Cartwright, A. B. Auerbach, and A. L. Joyner, Rescue of the En-1 mutant phenotype by replacement of En-1 with En-2 [see comments], *Science,* 269, 679–682, 1995.
93. D. No, T. P. Yao, and R. M. Evans, Ecdysone-inducible gene expression in mammalian cells and transgenic mice, *Proc. Natl. Acad. Sci. U.S.A.,* 93, 3346–3351, 1996.
94. P. Shockett, M. Difilippantonio, N. Hellman, and D. G. Schatz, A modified tetracycline-regulated system provides autoregulatory, inducible gene expression in cultured cells and transgenic mice, *Proc. Natl. Acad. Sci. U.S.A.,* 92, 6522–6526, 1995.
95. L. A. Bruggeman, H. X. Xie, K. S. Brown, and Y. Yamada, Developmental regulation for collagen II gene expression in transgenic mice, *Teratology,* 44, 203–208, 1991.
96. P. Lee, G. Morley, Q. Huang, A. Fischer, S. Seiler, J. W. Horner, S. Factor, D. Vaidya, J. Jalife, and G. I. Fishman, Conditional lineage ablation to model human diseases, *Proc. Natl. Acad. Sci. U.S.A.,* 95, 11371–11376, 1998.
97. D. A. Corral, M. Amling, M. Priemel, E. Loyer, S. Fuchs, P. Ducy, R. Baron, and G. Karsenty, Dissociation between bone resorption and bone formation in osteopenic transgenic mice, *Proc. Natl. Acad. Sci. U.S.A.,* 95, 13835–13840, 1998.
98. I. K. Visnjie, A. Naprta, G. Gronowicz, S. H. Clark, and D. W. Rowe, Characterization of the Col12.3ΔTK transgenic mouse, *Bone,* 23, S181, 1998.
99. M. Young, T. Xu, B. Sommer, J. Liang, X.-D. Chen, P. Bianco, M. Mankani, L. Fisher, E. Eanes, R. Iozzo, K. Danialson, and P. Robey, The relationship of decorin and biglycan to bone mass as revealed by knockout and double knockout transgenic animals, *Bone,* 23, S200, 1998.

5

Bone Mineralization

Adele L. Boskey
Weill Medical College of Cornell University

5.1 Introduction

Bone is a composite material that consists of mineral deposited in an oriented fashion on a collagen backbone. Lesser amounts of noncollagenous proteins, lipids, and water are also present in the bone matrix. There are also cells (osteoblasts, osteocytes, and osteoclasts) reviewed by Majeska (Chapter 2) which determine the formation, metabolism, and the turnover of this dynamic composite material.

The importance of the mineral component for the mechanical integrity of the bone as discussed in detail throughout this book can be appreciated from the simple experiment of soaking a chicken bone (or a baby tooth) in dilute acid overnight. The acid dissolves the mineral, leaving an unmineralized matrix that is very flexible. The literature is full of detailed experiments in which acid extraction or extraction with a calcium-specific chelator caused a switch from a rigid material to a pliable one.[1–3]

The mineral contributes both to the mechanical strength of bone and to the ability of the skeleton to regulate mineral ion homeostasis. The body's pools of ionic calcium (Ca^{2+}) and magnesium (Mg^{2+}) are maintained at critical levels by the coupled actions of hormones such as parathyroid hormone, 1,25-dihydroxycholecalciferol (and related vitamin D metabolites), and calcitonin, *inter alia*. Because the mineral crystals of bone are extremely small, they are relatively soluble[4] and can be dissolved or reprecipitated in response to signals that reflect serum or even local cation concentrations. To understand how the mineral can perform these functions it is first necessary to examine what bone mineral is.

The mineral in bone is an analogue of the naturally occurring mineral hydroxyapatite, whose unit cell can be represented as $(Ca_{10}\ (PO_4)_6\ (OH)_2)$. The analogy to geologic apatite was first recognized in 1926 by de Jong[5] based on the X-ray diffraction pattern of ground bone. The broad diffraction pattern and the nonstoichiometric calcium-to-phosphorus ratio observed in chemical analyses of bone (range of molar ratios 1.3 to 2.3:1) led investigators to postulate that bone mineral contained other noncrystalline phases[6] and other calcium phosphate phases.[7–9] Suggestions have also been made that bone mineral is a calcium-deficient and hydroxide-deficient apatite.[6,10,11] Today, it is recognized that because bone mineral crystals are so small ($\sim 20 \times 40 \times 200$ Å), much of the unit cell is on the surface. This provides an

0-8493-9117-2/01/$0.00+$.50

opportunity for substitution by similarly sized abundant cations (Mg^{2+}, Sr^{2+}, Fe^{2+}, Pb^{2+}, Na^{+}, K^{+}) and anions (CO_3^{2-}, F^{-}, $HPO_4^{=}$, and $H_2PO_4^{-}$).[10] These adsorbed and incorporated impurities make the composition of bone mineral difficult to analyze, and difficult to summarize. Detailed analyses indicate that, in general, the initial description[5] of bone mineral composition was correct! Bone mineral is a poorly crystalline or crypto-crystalline (small), carbonate- and other substituent-containing analogue of geologic apatite. Substituents are found within the lattice and on the surface of the apatite crystals. If there is any other phase present, there is too little of it (<10%) to be detected by current methods of analysis.[10–12]

5.2 Analysis of Bone Mineral

The techniques used for characterizing bone mineral provide information above and beyond the chemical and crystalline composition of bone. They can be and are frequently used to indicate variations in bone composition with age and disease, to characterize mineral in cell and organ culture, and to study bone ingrowth into synthetic/implant materials. Mineral analyses have occasionally been used for forensic and archaeologic evaluations.[13–15] Since a variety of measures of mechanical strength have been correlated with mineral content (e.g., Refs. 16 to 19; Chapter 19 by Currey), techniques for assessing the amount of mineral present in bone and their limitations are of importance to those studying bone biomechanics.

5.2.1 Elemental Analysis

Bone mineral composition can be determined using classic analytic techniques (gravimetry, calorimetry, atomic absorption spectrophotometry) or more modern methods (flameless atomic absorption spectroscopy, ion-emission spectroscopy, electron spectroscopic chemical analysis, or ESCA, etc.). Examples of each of these abound in the literature.

5.2.1.1 Gravimetric Analysis

Gravimetric analyses are used to measure the water content, the mineral content, and the carbonate content of bone. Often, the bone is pulverized before analysis, and aliquots used to provide percent water, mineral, or carbonate per weight of bone. These analyses are most often based on the loss of water at 110°, the loss of organic matrix at 600°, and the loss of carbonate at 900°. Differential thermal gravimetric analysis (DTA) provides equivalent information. Carbonate content can be determined more precisely using quantitative analysis.[20] Data may also be expressed per whole bone, and in this case large differences may be observed when bones under consideration differ in size and shape.

The residue (ash) obtained when heating bone powder to constant weight at 600° may be analyzed for inorganic constituents using a variety of standard techniques.[21] Similar analyses have been performed on whole bone/whole bone powder; however, extensive hydrolysis is required to solubilize the bone. Typical values for the chemical composition of major components detected in a variety of bones are presented in Table 5.1. In addition to the major components, trace elements are often found within the bone mineral. The content of the minor substituents such as strontium, lead, fluoride, or aluminum can be used to reflect dietary history,[10,15] efficacy of therapy,[10,22] or disease status.[10,23,24] Differences in analytical and preparative techniques, as well as the heterogeneity of bone, contribute to the wide variation in the literature.

Mineral content sometimes is measured after lipids are extracted from bone, or after marrow is removed (a comparable exercise, as marrow is ~90% lipid). Bones contain from 1 to 7% by weight lipid,[25] thus, comparisons between delipidated and intact bones may appear significantly different, when they really are not. Ash weight occasionally is expressed per volume (ash density). For these measurements either a uniform measurable shape is cut out of the bone[26] or the volume is determined by water displacement.[27] Ash density is most closely related to bone mineral density as measured by dual-energy X-ray absorptiometry,[21] a two-dimensional parameter evaluated clinically. Nonetheless, the most commonly measured

TABLE 5.1 The Chemical Composition of Bone

	Bovine Cortical Bone (wt% of whole bone)	Range in Literature for Healthy Adult Whole Bone (wt% of ash)
Calcium	26.7 ± 0.15	32.6–39.5
Magnesium	0.436 ± 0.009	0.32–0.78
Sodium	0.731 ± 0.015	0.26–0.82
Potassium	0.055 ± 0.0009	—
Strontium	0.035	—
Phosphorus	12.47	13.1–18.0
Carbonate	3.48	3.2–13
Citrate	0.863	0.04–2.67
Chloride	0.077	—
Fluoride	0.072	0.02–0.207[a]

[a] Additional data from Zerwekh.[12]

Source: Modified from Driessens, F. C. M. and Verbeeck, R. H. M., *Biominerals*, CRC Press, Boca Raton, FL, 1990, tables 10.5 and 10.6. With permission.

parameter is ash weight. While this number does not take into account the porosity of the bone measured by ash density, it does provide a readily measurable parameter that varies reproducibly with age, tissue, tissue site, and species. These gravimetric measures provide reproducible quantitative information, but they do not provide information on the quality of the mineral, or on the presence of other mineral phases.

5.2.1.2 EDAX and Related Methods

Energy dispersive X-ray microanalysis (EDAX), neutron activation analysis, flame and flameless atomic absorption spectrometry (AAS), and instrumented neutron activation analysis provide comparable information on the chemical composition of bone.[28] The first three methods were compared to AAS in a study of skeletal muscle.[29] EDAX provided slightly lower values than the other methods; however, this was explained based on the sampling procedure. Of the three techniques, only EDAX looks at site-to-site variations, while each of the other methods involve examination of homogenized tissues. EDAX analysis of unmineralized osteoid as well as fully mineralized bone provides information on geographic distributions of calcium to phosphorus (Ca:P) ratios and on the presence of trace elements in bone when appropriate corrections and instrumental calibrations are included.[29] The limitations of EDAX are the need for appropriate standards and instrumental corrections, while the ability to detect trace elements, and to map the localization of these elements at different sites in the bone, makes EDAX a powerful technique for evaluating mineral composition. Ca:P ratios, however, are not indicative of phase or of mineral quality.

5.2.2 X-Ray Diffraction

Crystalline materials produce characteristic X-ray and election diffraction patterns, wherein the angular locations of the peaks are directly related to the spacing between the planes of atoms. It was this type of analysis that enabled bone mineral to be identified as an analogue of hydroxyapatite[5] and to show that no other crystalline phases were present.[11,12,30] The peaks in the bone X-ray diffraction pattern are broadened, as is characteristic of poorly crystalline materials in which the lattice planes are not perfectly in register, and/or where there are impurities (holes, substitutions, kinks) in the lattice positions. According to the Debye-Scherrer equation,[31] the line broadening, ß, of any unique peak measured at half maximum is inversely related to the size and crystal perfection in that lattice plane. The broadening associated with plane that cuts half-way thorough the c-axis of the apatite structure (the 002 plane) is often used to calculate the approximate c-axis size/perfection in bone samples.[32–48]

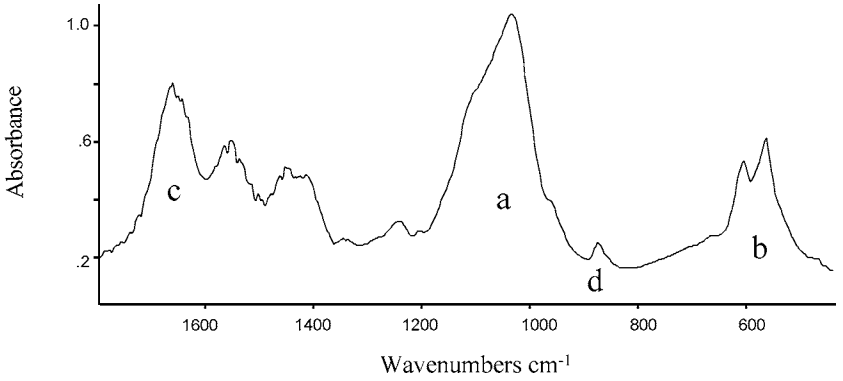

FIGURE 5.1 FTIR spectra of fetal calf bone. Regions of interest are a and b (phosphate absorptions), c (protein, Amide I), and d (carbonate).

The limitation of X-ray diffraction analysis of bone is the requirement for homogenizing the tissue prior to evaluation. Even if the bone is fractionated by density centrifugation,[35] spatial variation in mineral quality cannot be determined. X-ray diffraction is a powerful method for detecting the presence of noncrystalline phases,[35] and for assessing mineral quality.

5.2.3 Spectroscopic Methods

5.2.3.1 Infrared

Infrared (IR) spectra provide qualitative and quantitative information on all components that have IR active vibrations. In the case of bone this includes the protein, the mineral phosphate, lipids, and carbonate. Structural information relating to the mineral often is obtained by IR spectroscopy.[49–63] The features of the spectra are characteristics of the environment in which the IR absorbing bonds sit. The IR spectrum can be used to determine the nature of the calcium phosphate phase present,[50,51] the crystallinity of the apatite,[52–54] the presence of hydroxide,[60] and the carbonate content of the mineral.[55] A typical spectrum of ground fetal calf diaphyseal bone is presented in Fig. 5.1, with the relevant absorption peaks labeled.

IR spectra have been used extensively to assess mineral crystallinity in synthetic apatites[52] and normal and diseased bones.[14,56–58] The introduction of computerized Fourier transform (FT) IR spectrometers made calculation of spectra parameters easier, and there are now numerous papers that rely on FTIR for characterization of bone mineral.[36,44,59–63] Coupling an IR spectrometer to a light microscope allowed FTIR spectra to be recorded and mapped at anatomically distinct portions in bone,[54,64–72] as illustrated by the osteon, and its component spectra and spectral properties in Fig. 5.2. More recently, the use of an array detector has allowed IR images of the spectral features seen in Fig. 5.2 to be displayed in three dimensions.[73]

The advantage of FTIR microspectroscopy or imaging is that changes in mineral properties can be mapped at a spatial resolution of $\sim 20\mu$m. Thus, the variation in mineral quality and quantity across an osteon can be documented,[69] and changes across developing bones going from the periosteum to the endosteum or across the trabeculae can be noted (e.g., Refs. 70 and 71).

As seen in Fig. 5.1 the components that contribute to the observed bone IR spectra are from the protein, mineral phosphate, and carbonate. Amide I (1620 to 1680 cm^{-1}), amide II (1530 to 1560 cm^{-1}), and amide A (3200 to 3300 cm^{-1}, not shown) provide information on secondary structure (amide I and II) and hydrogen bonding (amide A). Phosphate absorptions at $\sim$960 cm^{-1} and 980 to 1200 cm^{-1} provide insight into the symmetry of the phosphate ion, while carbonate absorptions at 850 to 890 cm^{-1} can be analyzed to indicate the nature of carbonate substitution in the apatite lattice.[62] The ratio of the integrated areas of the phosphate to amide I peaks is highly correlated with ash weight[59] (Fig. 5.3).

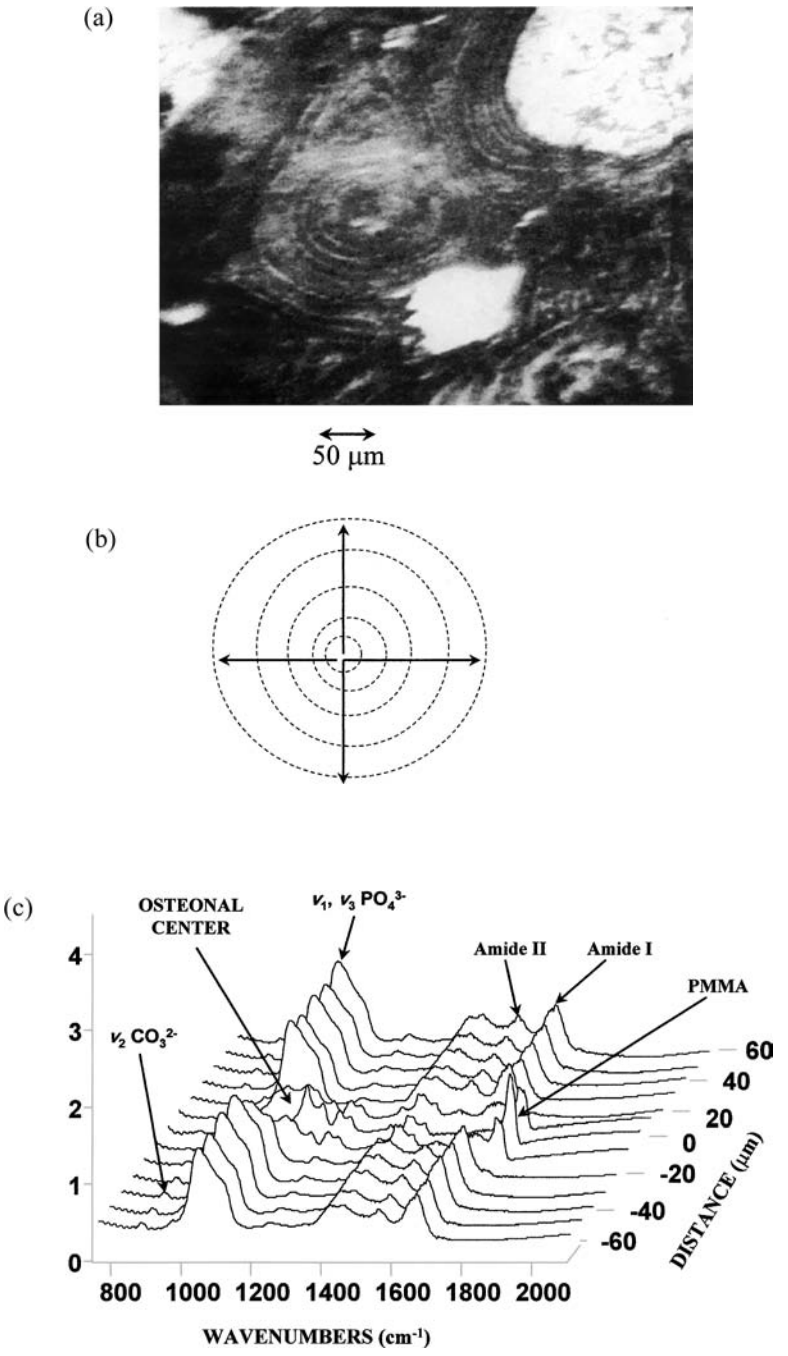

FIGURE 5.2 FTIR microspectroscopic analysis of normal human osteonal bone. (a) View of an osteon as viewed through the light microscope attached to the FTIR, (b) the directions of collection of spectra, (c) typical spectra at discrete distances from the center of the osteon. The bone used for analysis was embedded in polymethylmethacrylate (PMMA). The spectral regions attributed to the PMMA are noted. (d) Mineral:matrix ratio increases with increasing distance from the osteon center. (e) The 1020/1030 peak area ratio, which is inversly related to crystal size and perfection, decreases from the osteon center. (From Paschalis, E. P. et al., *Calcif. Tissue Int.*, 59, 480, 1996. With permission.)

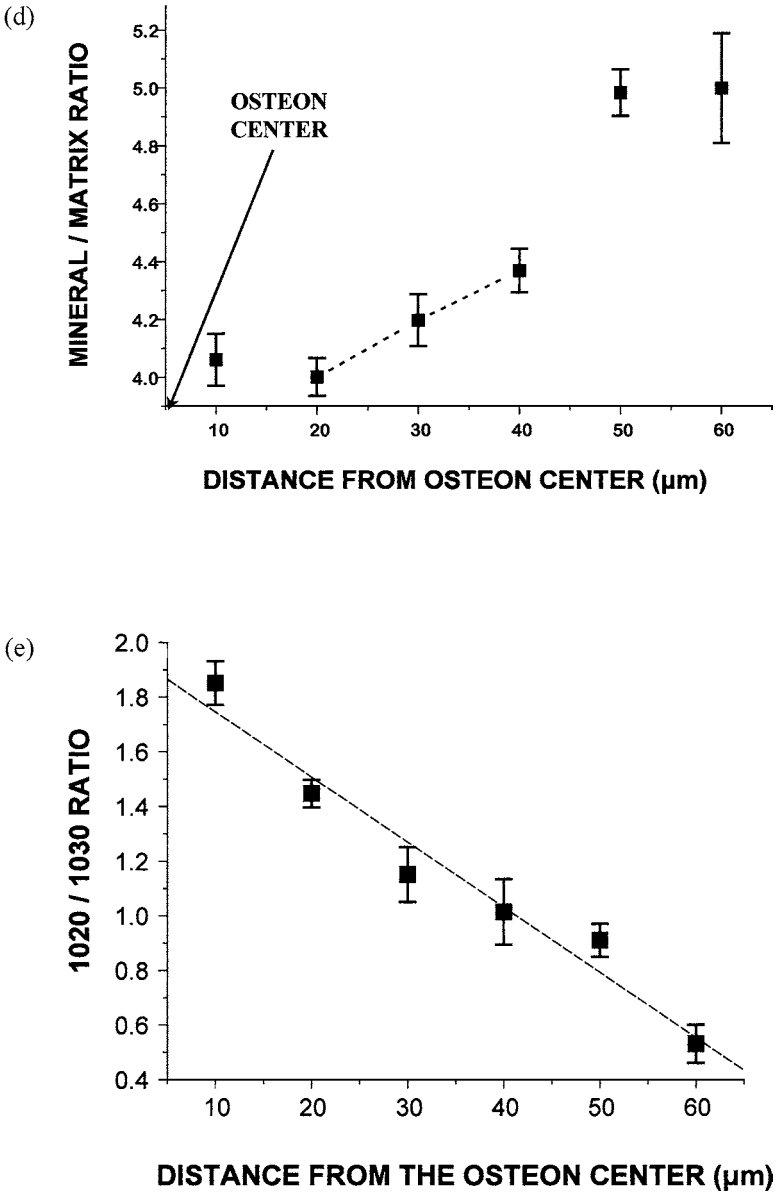

FIGURE 5.2 (continued).

The carbonate-to-phosphate ratio agrees well with the percent carbonate measured by other analytical techniques, although the IR data vary with mineral phosphate content, while gravimetric data are dependent only on carbonate content.

The broad bands in the FTIR spectra can be curve-fit to provide information on underlying components. The percent areas of the components of the phosphate band have been correlated with several measures of mineral crystallinity, carbonate, and acid phosphate substitution.[53,54,65,69] FTIR microspectroscopy and imaging are restricted to sectioned bones; thus, it is an invasive technique. When bones or bone biopsies are available, its unique ability to provide information on both protein and mineral properties at discrete sites makes it an optimal analytic tool.

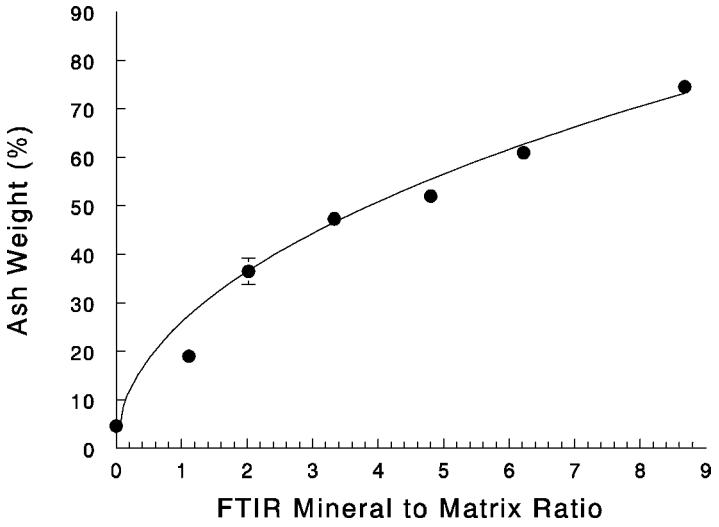

FIGURE 5.3 Mineral-to-matrix ratio as determined by FTIR is linearly related to the gravimetrically determined ash weight. Data points are synthetic mixtures of apatite and collagen.

5.2.3.2 Raman

Raman spectra for synthetic apatites were first published in 1974.[74] While absorbances occur at the same wavelengths as those in the IR, allowed vibrations in the IR are generally not observed by Raman, and vice versa. Raman microprobe spectroscopy has been used for analysis of normal and pathologically calcified tissues at the microscopic level.[75] The main disadvantage of this technique is the inherent interference from the fluorescent components of the organic matrix. Deproteinating the sample effectively removes the fluorescence interference,[76] but the effects of deproteinating are uncertain. With the introduction of more-sophisticated instruments, these deproteination methods have proved unnecessary.[77] In a typical Raman spectrum of intact bone, there is a strong peak at 952 cm^{-1}, which is characteristic of a poorly crystalline apatite. The line-broadening of the peak has been used to determine the extent of carbonate substitution in synthetic apatites.[78] Thus, in the future as Raman microspectroscopy and Raman imaging are developed, in the absence of background fluorescence, they should provide complementary information to that obtained by FTIR microspectroscopy and IR imaging.

5.2.3.3 NMR

Nuclear magnetic imagining and nuclear magnetic resonance (NMR) spectroscopy has provided supplemental information on bone mineral chemical composition. Wu et al.[79] demonstrated that the youngest bone mineral contained phosphate ions in an acid-phosphate-like environment. The presence of the acid-phospate-containing species brushite and octocalcium phosphate were excluded based on comparisons with these compounds. Although the same conclusion concerning an acid-phosphate-like environment in newly formed bone was made based on FTIR microscopic analysis of mineralizing turkey tendon,[80] the advantage of the NMR technique is that it can be applied *in situ*.

5.2.4 Backscatter Electron Imaging and Tomographic Methods

Backscatter electron imaging (BSE) provides detailed information on the distribution of mineral, similar to that which is produced by microradiography. The detail of BSE is much greater, and BSE images can be obtained more rapidly. BSE correlates with mineral content[81] and thus has been used to analyze changes in osteonal and trabecular bone mineral content when evaluating treatment methodologies.[82] BSE provides a two-dimensional image, which is reported to be highly correlated with ash weight but independent of compositional and crystal size variations.[81]

Tomography refers to the production of three-dimensional images. Classically, for the study of bone mineral, the term describes the presentation of X-ray images from which bone architecture can be visualized. More recently, computer assisted tomography (CT) and high-resolution micro-CT have provided structural models for the prediction of bone mechanical properties space[83–85] since quantitative (QCT) is highly correlated with ash density and radiographically determined bone mineral content.[21,84]

Information about bone mineral structure has come from a different type of tomography. High-resolution electron microscopic (EM) tomographs introduced by Landis and co-workers[86,87] provide insight into the mineral matrix interaction, the shape of mineral crystals, and the organization of mineral within the collagen fibrils. These studies, which compute three-dimensional reconstructions from high resolution, have shown that the mineral crystals develop as plates upon and within the collagen fibrils and that with maturation these plates coalesce. Specifically, these studies have demonstrated that the crystal widths in calcifying tendon, and probably by analogy in bone, vary from 30 to 45 nm, and the crystal thickness is approximately 6 nm. The lengths of turkey tendon crystals were as large as 170 nm. The size differences noted comparing tendon crystals (measured by EM tomography) and bone crystals (measured by X-ray diffraction line-broadening) may be attributable to many factors. As seen below, they may reflect real differences in the tissues, comparison of aggregates and "single" crystals, the influence of crystal perfection on the calculated X-ray diffraction values, or an underestimate of the constant in the Scherrer equation. A study in the 1970s[88] reported c-axis lengths in a variety of bones as $\sim$36 nm, noting they were in agreement with X-ray diffraction data. This suggests that the differences in the tomographic data may be due to crystal aggregation.

5.2.5 Other Techniques of Mineral Analyses

A variety of additional methods have been used to characterize the mineral in bone. The results provided by such methods agree with the information derived by the other analytical techniques previously discussed. Most, like ultrasound[89] and positron emission scanning,[90] confirm the bone density measurements made by other techniques. They do not provide information on mineral composition or quality.

In contrast, small-angle X-ray scattering (SAXS) does provide information on crystal size. SAXS was first used to examine the mineral crystal sizes within bone in the 1960s.[6] The method, which requires assumptions to be made about the shape (ellipticity) of the X-ray scatterer, was initially developed for determining sizes of large globular proteins and was later applied to fibrous proteins such as collagen.[31] More recently, Fratzl et al.[91–93] have applied a microversion of this technique to determine crystal thickness and orientation in animals of different species, age, and health status. The trends found comparing different bones are qualitatively in agreement with results of other methods, although the absolute values for mineral crystal size tend to be larger than those of X-ray diffraction and EM techniques because of the shape assumptions noted above.

5.3 Bone Mineral Is Not Always the Same

A limitation of trying to correlate mechanical properties with mineral content or density is that not all bone mineral is equivalent. Bone mineral varies in content, composition, and crystal size. In addition to the spatial variations, which reflect the age of the mineral at a specific site in the bone, there are also age-dependent changes when the same bone is considered. In general, mineral content varies with age; during periods of rapid growth bone tends to be hypomineralized, while during more senescent periods the bone tends to become hypermineralized.[94–96] There are also sex differences in bone mineral content and the way bone mineral content changes with age. Mineral content and mineralization rate also differ with ethnicity.[97] What is not known is at what age the mineral properties are optimal, or what the optimal mineral content, distribution, and composition should be.

TABLE 5.2 Bone Mineral Composition[a] Varies with Species, Age, and Tissue

	Ash (%)	Ca:P (molar)	Min:Mat	CO_3/PO_4	Size (Å)	Ref.
			Bovine			
Fetal diaphysis	51		4.23	0.011		np
Skull	50		4.23	0.011		np
1-d diaphysis	61		4.47	0.010		np
2-mo diaphysis	62 ± 2	1.65 ± 0.02		0.041%	91 ± 3	32
7-yr diaphysis	62 ± 2	1.69 ± 0.02		0.047%	206 ± 6	32
			Rat Diaphysis			
At birth	50 ± 2	1.51 ± 0.003		0.018%	97	32
4 wk	58 ± 1	1.31 ± 0.03		0.105	144	33
30 d	60 ± 1	1.61 ± 0.003		0.032%	133	32
8 wk	65 ± 2	1.37		0.129	156	33
14 wk	70 ± 1	1.40		0.140	162	33
18 wk					155	34
22 wk	72 ± 1	1.46		0.155	155	33
30 wk					156	34
1 yr	65 ± 1	1.65		0.047%	157	32
			Avian (chick)			
17–d periosteum	20.7	1.1			107	35
17–d diaphysis	48.9	1.41			143	35
4–wk diaphysis	62	1.67			161	36
5–wk diaphysis	61	1.70			170	36
10–wk diaphysis	64	1.70			163	36
12–wk diaphysis	58 ± 3		4.5 ± 2	0.014 ± 0.001	173	37
30–wk diaphysis	65	1.71			174	35
1–yr diaphysis	67	1.64			196	35
2–yr diaphysis	66	1.74			199	35

[a] Parameters: ash weight (ash %) as percent of non-defatted dry weight, Ca:P molar ratio by analysis of the ash, mineral:matrix ratio (Min:Mat), and carbonate-to-phosphate ratio determined by FTIR, carbonate listed as (%) determined by chemical analysis and expressed as percent of dry weight, size refers to the c-axis (002) length as determined by X-ray diffraction line-broadening analysis. np = not published.

5.3.1 Age and Sex Differences

Despite the variation with site and species, and the different analytical methods, there are several age-dependent generalizations that have been confirmed in studies with single species. Specifically, as seen in Table 5.2, the ash weight, mineral-to-matrix ratio which is linearly related to ash weight,[59] (see Fig. 5.3), and mineral crystal size along the c-axis increase rapidly during the earliest stages of development, and continue to increase but at a much slower rate with maturity. Handshin and Stein[98,99] studied over 100 human illiac crest biopsies of juveniles (0 to 25 years), younger adult (25 to 50 years), and older adult (50 to 90 years), in which the mineral content increased with age, and the crystal size in the younger groups also increased. A study in fetuses confirmed the same increase in mineralization rate during early development.[100] Parallel to these increases in mineral crystal size and mineral content, the carbonate content increases.[62]

Similar changes are noted within a single osteon (Fig. 5.2), going from the periosteal to the endosteal side of cortical bone, or going from the outer surface of the trabeculae into the center.[54,69] In each of these instances, the most recently deposited mineral has the smallest size, the least perfection, the lowest carbonate content, and the highest proportion of labile (surface) carbonate.

Mineral content and mineral composition appear to be sex dependent, with males increasing in bone density with age to a greater extent than females.[101] Additionally, in females, changes in bone mineral

content and bone mineral properties occur during pregnancy and lactation.[102,103] These changes have been correlated with hypoestrogenic conditions,[103] but clearly have an impact on the fragility of bone during pregnancy.[102]

There are variations in bone mineral composition as a function of exercise[17,104] and immobilization.[105] In pair-fed exercised rats, the greatest changes in the mineral composition were in the strontium-to-calcium ratio. This ratio increased with exercise;[104] however, this change has not yet been explained in terms of effects of loading (bone adaptation), changes in muscle mass, and changes in eating pattern.

5.3.2 Diet and Bone Mineral Properties

Malnutrition decreases bone mineral density and bone mineral content as do severe burns and acidosis.[106–108] These conditions also change the bone mineral composition and bone mineral crystal size. The bone serves as a "storehouse" of trace and other elements in the body. Thus, it is reasonable that the chemical composition of the skeleton reflects dietary history.[13–15] Diet thus has a direct effect on the bone mineral content and composition; dietary effects are also dependent on the age of the animal exposed to the diet. For example, in young animals, high-saturated-fat diets decrease calcium absorption, and thus have been postulated to contribute to osteoporosis in more mature animals.[109] But in mature animals, high-saturated-fat diets have no effect on mineral density of cortical bone. In contrast, bone mineral content was significantly higher in cancellous bones of young and old animals fed a low-fat diet.

Table 5.3 provides some typical examples of dietary supplements and deficiencies (Sr, Ga, Mg), that could substitute for calcium in the mineral lattice and vitamin deficiencies that impact mineral metabolism (vitamin D) and collagen synthesis (vitamin B_6). In magnesium deficiency, there is an increase in bone remodeling, as the smallest, most-soluble bone crystals are lost to provide the body's necessary magnesium ions.[42] This results in bones with larger mineral crystals than those in magnesium-replete animals. Magnesium excess causes a decrease in mineral formation and also increases crystal size of the existing mineral.[108]

Vitamin D deficiency (or alterations in body calcium and phosphate stores that are dependent on vitamin D) reduces mineral content, increases mineral crystal size, but in these osteomalacic/rachitic animals the calcium-to-phosphate ratios vary depending on the dietary history. Calcium deficiency by itself reduces bone mineral content, but increases Ca:P ratio.[110] Zinc deficiency synergistically increases the decrease in bone density associated with calcium deficiency,[111] and zinc deficiency by itself decreases bone density. The bones of animals with vitamin D-deficient osteomalacia in general are more brittle[112,113] than those of age-, sex-, or size-matched controls, stressing the importance of mineral size and content on bone properties.

Other dietary modifications also affect bone mineral content and composition. Vitamin A excess has marked effects on the skeleton;[114] however, there have been few reports of the specific alterations in bone mineral composition. Deficiencies of dietary antioxidants such as selenium and vitamin E also decrease bone mineral content, producing a condition resembling osteomalacia;[115] bone mineral properties were not evaluated in these animals.

Both gallium and strontium substitution (Table 5.3) decrease mineral content and crystal size.[40,41] Gallium is known to have a direct effect on bone cells and bone matrix synthesis,[41] whereas strontium is directly substituted into the mineral, but does affect calcium retention in other organs.[42] Aluminum also reduces bone mineral content, creating a condition known as aluminum (renal) osteomalacia.[23,24] These are but a few examples of dietary and environmental factors that can contribute to bone mineral properties.

One of the most interesting dietary supplements, from the point of view of understanding the contribution of bone mineral to the mechanical properties of the tissue, is the vitamin B_6-deficient chick. In these animals, given a slightly vitamin B_6-deficient diet after birth, the mineral content is not altered, neither is the crystal size nor other features of bone mineral composition, but the elastic properties of the bone are diminished because of alterations in the collagen structure.[37] This just serves as a reminder of the contribution of both the matrix and the mineral to the bone composite.

TABLE 5.3 Diet Alters Bone Mineral Composition[a]

Dietary Manipulation	Species/Site	Ash (%)	Ca:P(molar)	Size (Å)	Ref.
Excess calcium (normal vitamin D)					
Experimental	Chick diaphysis	61 ± 1	1.55 ± 0.2	173	36
Control		61.9 ± 0.3	1.67 ± 0.04	161	
Vitamin D deficiency (normal phosphate)					
Experimental	Chick diaphysis	45.9 ± 5	2.4 ± 0.5	193	36
Control (see above)					
Low phosphate diet (normal vitamin D)					
Experimental	Chick diaphysis	60.1 ± 0.6	1.78 ± 0.3	193	36
Control (see above)					
Calcium deficiency and vitamin D deficiency					
Experimental	Chick diaphysis	44.5 ± 1.3	1.90 ± 0.06	181	36
Control (see above)					
Vitamin D deficiency (+ low phosphate)					
Experimental	Rat metaphysis	40.3 ± 2		151	38
Control		54 ± 0.4		153	
Experimental	Rat diaphysis	54 ± 2		153	38
Control		65.2 ± 0.4		146	
Vitamin D deficiency (second generation)					
Experimental	Rat diaphysis	62 ± 1		144	39
Control		63 ± 1		135	
Vitamin B6 deficiency					
Experimental	Chick diaphysis	63 ± 6		169	37
Control		58 ± 3		173	
Trace element supplementation					
Strontium					
Experimental	Rat Metaphysis	55.5 ± 1.5		137	40
Control		60.0 ± 3.8		166	
Gallium					
Experimental	Rat Metaphysis	54.5 ± 0.5		138	41
Control		56.8 ± 0.8		144	
Mg deficiency					
Experimental	Rat Metaphysis	53 ± 4	1.50 ± 0.01	164 ± 11	42
Control		59 ± 4	1.59 ± 0.05	152 ± 7	
Experimental	Rat Diaphysis	66 ± 4	1.63 ± 0.01	152 ± 17	42
Control		67 ± 2	1.60 ± 0.06	147 ± 7	

[a] Parameters: ash weight (ash %) as percent of non-defatted dry weight, Ca:P molar ratio by analysis of the ash, size refers to the c-axis (002) length as determined by X-ray diffraction line-broadening analysis.

5.3.3 Bone Diseases and Their Therapies

Bone mineral content and mineral composition are affected by the health status of the organism. Table 5.4 presents some typical conditions, modeled in animals and studied in humans, in which there are detectable changes in crystal size and perfection, mineral distribution, and/or mineral composition. Included among those diseases that affect bone mineral are untreated diabetes in which crystal size and

TABLE 5.4 Mineral Variation[a] in Bones of Diseased Animals

Disease /Site		Age	Ash (%)	Ca:P	Min:Mat	CO_3/PO_4	Size (Å)	Ref.
				Hypophosphatemic (hyp) mouse				
Distal	hyp	35 d	41.4	1.64 ± 0.041	—	—	157	43
metaphysis	Control		60 ± 2	55 ± 0.1			151	
Proximal	hyp	35 d	46 ± 1	1.67 ± 0.07			173	43
metaphysis	Control		61 ± 5	1.55 ± 0.1			151	
Diaphysis	hyp	35 d	64 ± 6	1.71 ± 0.04			189	43
	Control		69.3 ± 0.8	1.5 ± 0.2			125	
	hyp	12 wk	56.1 ± 0.1		1.01 ± 0.27	0.0036	168	44
	Control		68.4 ± 0.6		3.57 ± 0.52	0.0019	168	
				Brachymorphic Mouse				
Diaphysi	bm/bm	10 wk	62			0.00353	178	45
	Control		60			0.00451	164	
				Osteopetrotic Rats				
Metaphysis	ia/ia	11 d	42 ± 1.2				144	46
	Control		36 ± 1.2				113	
	ia/ia	52 d	62 ± 1.2				149	46
	Control		46 ± 1.2				131	
Calvaria	ia/ia	11 d	42 ± 2				138	46
	Control		43 ± 5				131	
	ia/ia	52 d	62 ± 4				143	46
	Control		57 ± 1				143	
Diaphysis	tl/tl	6 wk	65	[b]				48
	Control		61					
				Diabetic Rat—Metaphysis				
	Experimental	Adult	67 ± 2	1.39 ± 0.07			173	47
	Control		64 ± 2	1.49 ± 0.09			185	
				Ovariectomized primates—Vertebra, Trabecular Bone				
	Experimental	Adult		1.7	5.9 ± 1[c]	0.0137	189	48[c]
	Control			1.8	6.8 ± 0.5	0.0095	202	

[a] Parameters: ash weight (ash %) as percent of non-defatted dry weight, Ca:P molar ratio by analysis of the ash, mineral:matrix ratio (Min: Mat) and carbonate-to-phosphate ratio determined by FTIR, carbonate listed as (%) determined by chemical analysis and expressed as percent of dry weight, size refers to the c-axis (002) length as determined by X-ray diffraction line-broadening analysis.

[b] Crytallinity of tl/tl estimated from EPR to be 30 to 50% wild type.

[c] S. Gadaletta, thesis, Department of Chemistry, Rutgers University, New Brunswick, NJ, 1997. With permission.

Ca:P ratio are decreased,[47,116,117] Paget's disease of bone in which the crystal size is decreased,[118] and osteopetrosis where crystal sizes and mineral content are increased.[46,119] Rarer diseases, such as osteogenesis imperfecta, will be discussed in Section 5.4.

In studies of patients and animal models with osteoporosis, there have been reports of increased crystal size, decreased crystal size, and an absence of detectable change.[14,56–58,69,120] Using FTIR microspectroscopy, Paschalis et al.[54] showed that the osteons in the osteoporotic individuals do not show the increase in mineral-to-matrix ratio, or the increase in crystal perfection seen in age matched controls.[54,66] On average, the osteonal mineral crystals were larger, and more perfect. This has also been noted in a variety of animal models.[48,95] Osteoporotic trabecular bone has been reported to have a decreased magnesium content,[56] and increased crystal size in agreement with the increase seen in magnesium-deficient animals.[42] In ovariectomized monkeys, Lundon et al.[48] demonstrated a slight, but not significant, proportion of bone

particles had low density as contrasted with age-matched controls. They found no significant difference in crystal size or mineral content. Gadaletta et al.[48a] performed FTIR microscopic analysis on vertebrae from a similar group of ovariectomized and intact monkey vertebrae. Because samples were not homogenized, the microscopic analysis demonstrated significantly increased carbonate-to-phosphate ratios and increased crystal size and perfection in the trabeculae of ovariectomized animals. Curve-fitting also demonstrated an increase in the crystallinity of the trabecular bone in the ovariectomized animals (Gadaletta, thesis, 1997). Distinctive differences in the number of trabeculae were noticed between ovariectomized and control animals and among animals in both groups.

Therapies for diseases such as osteoporosis also change bone mineral properties. Treating the osteoporotic individual with fluoride (and calcium and vitamin D) does not significantly modify the crystal size distribution; it does, however, make the mineral content more uniform[93] and alters the carbonate substitution, since fluoride substitutes for OH. Thus, the carbonate in the OH sites is reduced[90] (unpublished observations). Fluoride treatment in healthy bone increases crystal size[22] and, in patients with osteoporosis, increases connectivity.[121] Bisphosphonates, drugs that stabilize the apatite crystal structure and decrease osteoclastic activity,[122] tend to increase bone mineral crystal size and increase mineral content.[92,93,123]

Therapies for osteoporosis are often evaluated based on their effects on bone density and, in animal models, based on mechanical properties. Usually, histomorphometric measures are included, but only rarely are mineral analyses considered. Sometimes, such studies reveal no detectable differences in ash, mineral content, or crystal size, and perfection as measured by line-broadening.[124] The failure to detect differences in the face of alterations in mechanical properties may reflect alterations in porosity and architecture, localized alterations in mineral properties not detected when whole bones are homogenized, or the effect of the therapy on the matrix rather than the mineral.

5.4 Bone Mineral Formation

To understand why the bone mineral properties vary so extensively with age, sex, diet, and disease, an appreciation for the bone mineral formation process is required. In the following sections, emphasis will be placed on how the mineral forms, with less attention played to the roles of the cells in modeling the structure of bone, and remodeling the mineral in response to mechanical and hormonal stress.

5.4.1 A Digression: The Physical Chemistry of Crystal Formation

The chemistry of crystal formation describes events involved when an insoluble material with an organized repeat (lattice) structure is formed. These events include nucleation, crystal growth, and crystal proliferation. For an inorganic crystal such as hydroxyapatite, the crystal formation process generally starts with the collision, in solution, of the component lattice ions (calcium, phosphate, hydroxide) or clusters of these ions. When the colliding ions or ions clusters remain together in the orientation they will have in the final crystal lattice, a crystal nucleus is formed. This nucleation process requires the most energy of the crystal formation events. After a stable nucleus is formed, ions or ion clusters add to the existing nuclei during the crystal growth process. Crystal growth requires less energy than nucleation. As the crystal grow, new nuclei may form on their surfaces, providing growth sites for additional crystals (secondary nucleation). These crystals will continue to proliferate as long as there are sufficient concentrations of the component ions in solution, i.e., as long as the solution is supersaturated with respect to the precipitating phase. In other words, crystal growth and proliferation will continue as long as the ion activity product of the precipitating phase exceeds the solubility product of that phase. Crystals grow by adding on additional ions. They proliferate (increase in number) by the formation of additional nuclei. Often the crystals aggregate, resulting in an apparent increase in crystal size.

The nucleation process can be accelerated by increasing the concentration of the component ions, increasing their rates of collision (increasing temperature, decreasing viscosity), providing "nucleation sites" on foreign (heterogeneous) materials or on "epitatic" materials that resemble structural features of the crystal, or adding preformed crystals, bypassing the nucleation process. These preformed crystals can grow and

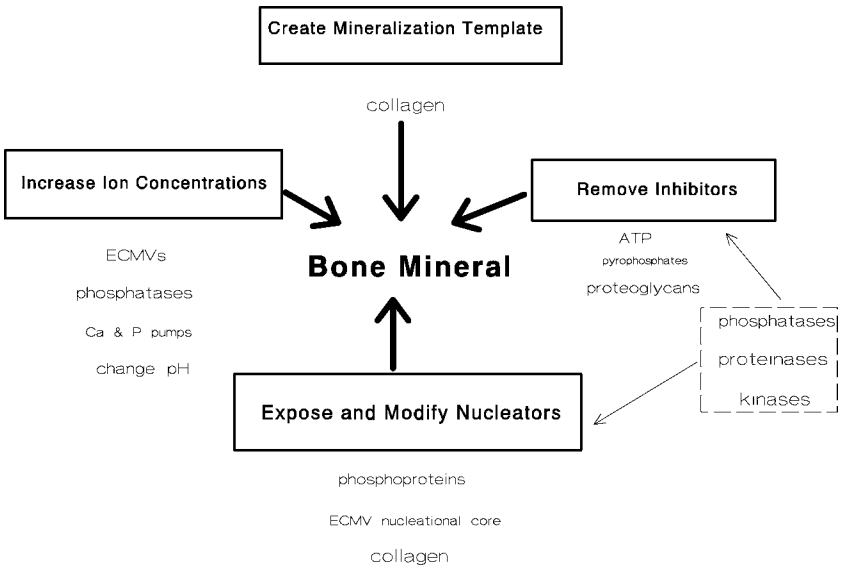

FIGURE 5.4 The mineralization process.

proliferate by the processes mentioned above. In solution studies, heterogeneous nuclei are often scratches on glass surfaces, while epitatic nucleators are selected because they mimic the crystal structure desired.

Crystal growth can be accelerated by decreasing the rate at which crystals are proliferating (lowering ionic concentrations, lowering temperatures), while aggregation may be accelerated by increasing temperatures. Crystal growth is often impeded if there are defects in the crystal lattice, or by the addition of "crystal poisons," which bind to the surface of the crystal and block further growth in one or more dimension. Similar, albeit more complex, events occur during the biomineralization process (Fig. 5.4).

5.4.2 Factors Controlling Initial Bone Mineral Deposition

Mineral deposits in bone at discrete sites. Although there is some debate whether these sites initially are external to or associated with the collagen fibrils,[11] it is quite apparent from numerous studies using the techniques described above that the majority of bone mineral crystals are associated with collagen fibrils.[125,126] Further, the mineral crystals are aligned with their long axis parallel to the collagen fibril axis. Thus, it was suggested[11,127] that collagen was the apatite nucleator in bone. But type I collagen similar to that found in bone also exists in tissues such as skin, ligaments, and tendons that do not normally become calcified. Increases in local ion concentrations, removal of inhibitors of apatite nucleation, growth, and proliferation, and the exposure of other nucleating matrix proteins associated with the collagen, are important in controlling the initial deposition of mineral. Additionally, in certain situations, e.g., in the calcifying cartilage of the growth plate and in tendons and ligaments, extracellular matrix vesicles, along with collagen, are important for initiating mineralization.[86,87,128–130]

Control of bone mineral crystal growth and proliferation is governed by the spatial limitations of the collagen fibrils,[11] as well as by the adsorption of matrix proteins. Such matrix proteins often are also apatite nucleators but, due to their affinity for specific apatite crystal faces, can retard or block apatite growth. Mineral formation and growth are regulated by ionic concentrations, the removal of inhibitors, and the exposure of nucleators.

5.4.2.1 Ion Concentrations

Increases in local concentrations of the ions in the apatite lattice are clearly important, as evidenced by the dystrophic formation of apatite[128,131] in conditions of elevated concentrations of calcium (e.g., milk alkali syndrome, vitamin D toxicity) or phosphate (tumoral calcinosis, vitamin D-resistant rickets). The loss of

water from cartilage in advanced stages of osteoarthritis, resulting in an increase in ion concentration, may be associated with the deposition of calcific nodules within the articular cartilage.[132] Increases in local ion concentrations may contribute to bone mineral deposition in remodeling bone, where, following osteoclastic removal of existing mineral, osteoblasts lay down a new matrix, and that matrix rapidly mineralizes.

Within the epiphyseal growth plate, membrane-bound bodies, known as extracellular matrix vesicles (ECMVs), provide a site for the accumulation of mineral ions. ECMVs, which on average have a diameter of about 70 nm, are the site of initial mineral deposition in calcifying cartilage, and in the earliest-forming (mantle) dentin.[128,129] In calcifying turkey tendon, ECMV and collagen-based mineralization occur concurrently.[86,87] ECMVs appear much less frequently in newly mineralizing osteoid.[133] This could be because the abundant mineral prevents their detection or because, in tissues where mineralization is already occurring, ECMVs are less necessary. During embryonic bone formation, when woven bone is first formed, ECMVs may be needed to assist in mineral ion accumulation; yet they are not often seen.

There are several questions debated through the literature concerning the significance of ECMVs in the mineralization process.[11,25,134] Whether these bodies are always the first site of mineral deposition? Whether ECMVs are essential for mineral deposition? How does mineral formed within the ECMVs relate to the mineral that is predominantly associated with the collagen? Of significance is the presence of similar membrane-bound bodies in the calcifying organs of lower species.[135] In addition to providing a protected environment in which mineral ions can collect, enzymes associated with matrix vesicles can degrade inhibitors of mineral nucleation and mineral growth and proliferation, and can increase local ion concentrations.[136] Metalloproteinases[137] associated with the ECMVs[138] degrade cartilage proteoglycans. ATPases, abundant in the ECMVs,[139] can hydrolyze nucleoside triphosphates (NTPs). Proteoglycans and NTPs are inhibitors of apatite formation and growth.[130] An important illustration of the inhibitory action of proteoglycans occurs in animals that lack MMP-9 (gelatinase B). Gelatinase B is a metalloproteinase that degrades proteoglycans. In the MMP-9-deficient animals the growth plate develops to eight times its normal length, and ossification is significantly retarded.[140] ATPases, neutral pyrophosphatase, and alkaline phosphatase, all associated with matrix vesicles,[139] also would increase the local phosphate concentration. During osteoid mineralization, in the presence or absence of ECMVs, alkaline phosphatase is important for increasing the local phosphate concentration. Animals with defective alkaline phosphatase expression develop hypophosphatasia, a disease characterized by significantly decreased bone mineralization,[141] related to that seen in hypophosphatemic rickets.[43,44] Similarly, calcium ion concentrations may be increased due to efflux of this ion from the cells and/or by the release of calcium from calcium-binding proteins in the matrix.

Similar to increases in calcium or phosphate concentrations, increases in pH (increases in OH concentration) also favor apatite deposition. Osteoclasts remove mineral by increasing the hydrogen ion concentration (decreasing pH),[142] but the optimal pH for osteoblast function is 7.2 to 7.8,[143] implying that the pH adjacent to the osteoblast is in this range. The anionic proteins of the matrix may help maintain this basic environment, indirectly facilitating apatite deposition.

5.4.2.2 Removal of Mineralization Inhibitors Facilitates Bone Mineral Deposition

Based on solution studies, several ionic species and macromolecules (Table 5.5) that could act as inhibitors of apatite formation and growth have been identified.[144–163] These include pyrophosphate,[144] pyrophosphate analogues such as the bisphosphonates[122] and the nucleoside triphosphates,[145] large aggregating proteoglycans,[146–149] and other anionic proteins and sugars.[150–163] It was postulated that collagenous tissues that did not normally mineralize were protected by the presence of these ions and molecules. When mineralization occurred, enzymes such as the metalloproteinases[137,140] and phosphatases and kinases[164] could modify these inhibitors, preparing the tissue for mineral deposition. No tissue-specific inhibitor was identified in bone, although osteopontin seemed a likely candidate, because of its ability to inhibit both bone apatite[154,158,159] and calcium oxalate deposition.[165]

The evaluation of the matrix-gla protein (MGP) knockout mouse[166] provided the first evidence that this protein was a tissue-specific mineralization inhibitor. MGP is expressed in highest quantities in

TABLE 5.5 Cell-Free Solution Studies Demonstrate Multifunctional Effects of Bone Matrix Proteins

Protein	System[a]	Observation	Ref.
Albumin[b]	Seeded growth-Const comp	Nucleator	np[c]
	Direct pptn	Inhibitor	1, 57, 153, 156
α-2HS glycoprotein (fetuin)	ACP/HA	Inhibitor	145, 152,
	Direct pptn		160
Biglycan	Gelatin gel	Nucleator/ inhibitor	162
Bone sialoprotein	Agar/gelatin gels	Nucleator	1, 61, 158, 159, 182
	Direct pptn	Inhibitor	159
	Seeded growth		163
Chondrocalcin	Gelatin gel	No effect	161
	Agarose gel	Inhibitor	
Decorin	Gelatin gel	No effect	162
Osteocalcin	Direct pptn	Inhibitor	150, 151, 161
	Direct pptn + beads	Nucleator	187
Osteonectin	Seeded growth	Inhibitor	151, 161
	Agarose gel		
	Denatured collagen	Promoter	173
Osteopontin	Gelatin gel	Inhibitor	154, 155
	Agarose gel		
	Direct pptn		
Milk-osteopontin	Gelatin gel	Promoter	np[d]
Proteoglycan aggregates	Gelatin gel	Inhibitor	148, 149
	Direct pptn		146
Type X collagen	Gelatin gel	No effect	180, 186
Type I collagen	Gelatin gel	Nucleator	172
		No effect	146
MV nucleational core (CPLX + proteins)	Direct pptn	Nucleator	96, 195 98, 197

[a] A variety of different methods have been used to study *in vitro* apatite formation. These include, but are not limited to, direct precipitation in which changes in Ca, PO_4, or OH are monitored (direct pptn); constant composition (const comp), in which the Ca, PO_4, and OH concentrations are maintained at a fixed level; conversion of amorphous calcium phosphate to apatite (ACP/HA) in a pH stat; growth of preformed apatite seed crystals (seeded growth) with one or more of the component ion concentrations being monitored, or gel diffusion in which the ions enter a gelatin, agar, or agarose medium. In some cases, proteins under investigation are immobilized on agarose beads (beads).

[b] Liver adsorbed, found in bone but not made by bone cells.

[c] np = personal communication, G.H. Nancollas.

[d] np = unpublished, Boskey.

cartilage and smooth muscle cells. The MGP knockout mice do not express any of this protein and have extensive calcification of their articular, growth plate, and tracheal cartilage, and their blood vessels.[166] The mineral phase present was a bonelike apatite (unpublished observation). Thus, a tissue-specific mineralization inhibitor was identified. This inhibitor is not abundant in bone or other normally calcifying tissues, suggesting that its function is to protect tissues from mineralization, not to regulate mineralization.

5.4.2.3 Collagen—The Template for Mineral Deposition

The importance of collagen for bone mineral deposition is apparent from electron micrographs in which the mineral crystals are aligned with the collagen fibril axis.[11,84,85] An even more convincing demonstration comes from animals and people in whom the collagen structure is disrupted. Osteogenesis imperfecta is a heterogenous set of diseases most of which are associated with quantitative changes in collagen production (less severe forms) and qualitative and quantitative abnormalities in type I collagen structure.[167] The disease, also known as "brittle bone disease," is typified by fragile bones and abnormal bone and skin

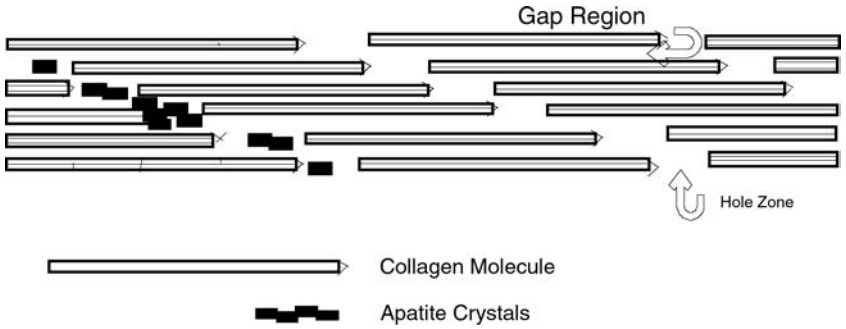

FIGURE 5.5 Schematic illustrating the way in which mineral crystals deposit initially in the hole regions of the collagen fibrils, and then spread to the gap regions.

architecture. In animal models of the disease and in humans, the mineral crystals tend to be smaller,[67,168,169] and, while the ash weight of homogenized tissues do not differ from age-matched controls,[168] the mineral-to-matrix ratio at discrete sites is significantly altered.[67] The mineral composition is also altered,[67] perhaps because of the delayed deposition of the mineral on the abnormal collagen fibrils. Mineral deposits are sometimes found away from the collagen fibrils,[170] indicating the importance of the collagen in providing a template for mineral deposition.

Mergenhagen et al.[171] showed that collagen could support apatite formation when implanted *in vivo*. In solution, collagen was reported to increase[172] the yield of mineral, or to have no effect on the extent of mineralization.[146] But collagen prepared for implant and solution studies has both noncollagenous proteins[173] and lipids[25] associated with it. Removing noncollagenous proteins from demineralized bone blocks its recalcification.[173] Furthermore, dephosphorylating collagen enzymatically reduces its ability to nucleate apatite from solution in a dose-dependent fashion.[174] Accordingly, while collagen is clearly the template upon which mineral is deposited, other proteins associated with the collagen seem to be directing the sites of initial mineralization. Since, as illustrated in Fig. 5.5, mineral first appears within the holes between quarter-stacked arrays of collagen fibrils,[11] nucleators were hypothesized to be localized there.[175]

Cross-links between and among collagen molecules also appear to be related in some way to mineralization. The cross-linking pattern in mineralized bone is very different from that in nonmineralized bone.[176] Whether the cross-links come first, and then direct mineralization, or whether they are formed in the nonmineralized osteoid later on is still under investigation. It is of interest to note, however, that blocking cross-link formation in a variety of models does decrease the extent of mineral deposition.[177,178]

5.4.2.4 Noncollagenous Proteins as Regulators of Mineral Deposition

Based on dry weight, the nonmineralized osteoid is about 95% collagen and 5% noncollagenous proteins.[173] Most of the noncollagenous proteins associated with the bone matrix are anionic and, as such, have the ability to chelate calcium and bind to bone mineral.[151,179] The noncollagenous proteins are thought to have a variety of functions, including, but not limited to, regulation of bone mineral deposition.[180] In terms of mineralization, these proteins may act as nucleators, may control the arrangement and orientation of other matrix proteins that are nucleators, and may regulate the growth and proliferation of mineral crystals. Many of the bone matrix molecules are capable of acting both as apatite nucleators and as apatite growth inhibitors, depending on solution conditions and concentration (Table 5.5).

5.4.2.4.1 Cell-Free Solution Studies

A protein that plays a role in the mineralization process must change in content, conformation, or concentration as mineral deposition commences. The phosphorylated sialoproteins (osteopontin and bone sialoprotein), osteocalcin, osteonectin, and the small bone proteoglycans meet this definition.[180,181]

Although *in situ* these proteins probably act in concert with other proteins, considerable insight into their effects on mineralization have been provided from *in vitro* studies of their effects on apatite formation and apatite growth. By using different cell-free *in vitro* systems, bone sialoprotein was shown to be an effective apatite nucleator.[159,182] The small bone proteoglycan, biglycan, is also an *in vitro* apatite nucleator.[162] Proteolipids (lipid–protein complexes),[25] and, according to preliminary data from the author's laboratory, highly phosphorylated osteopontin also can nucleate apatite in solution. One of the most likely *in situ* bone apatite nucleators is bone sialoprotein (BSP), a protein specific to bone,[183] which appears at the site of new mineralization in both endochondral and intramembranous bone formation.[184]

Through studies of native, dephosphorylated, recombinant, and rephosphorylated dentin matrix proteins, the author has obtained evidence that the extent of phosphorylation affects not only the proteins ability to bind calcium, but also its conformation and its ability to affect apatite nucleation and apatite growth,[185,186] (unpublished observations). These same studies have demonstrated that some of these phosphoproteins at low concentrations can act as nucleators, while when their concentrations increase they block crystal growth and proliferation.

When some matrix proteins are immobilized on agar beads[187] or on an agarose substrate,[161,182,188] they appear to be more effective nucleators than they are in solution. This is likely because a region of the protein needed for binding of calcium and/or stabilization of apatite nuclei is fixed in place.

Noncollagenous matrix proteins may self-associate,[189,190] associate with other matrix proteins,[191] and/or with collagen.[192–194] The nucleational core of extracellular matrix vesicles associates with a variety of extracellular matrix and cell membrane proteins.[195,196] This nucleational core consists predominantly of an acidic phospholipid complex, which itself is a hydroxyapatite nucleator,[197,198] and annexin V, a calcium-binding protein.[199] In solution, the nucleational core is an effective nucleator, and it appears that this intricate structure has a similar action *in situ*.

5.4.2.4.2 Cell Culture Studies

While cell-free solution studies can be used to determine the effects of such protein–protein and protein–lipid interactions on the abilities of matrix proteins to act as nucleators and inhibitors, more insight into their *in situ* function can be provided by cell culture studies. By using cell and organ cultures, mineralized matrices can be produced that by all the analytic criteria indicated above resemble the mature mineralized tissue from which these cells or organs were derived.[200–209] Such cultures are thus useful for evaluating the effects of matrix proteins and other matrix molecules on the mineralization process.

Several investigators have used cell and organ culture systems to determine which genes are expressed prior to mineralization. Gerstenfeld et al.[200] was the first to do such an analysis, identifying the importance of type I collagen, osteopontin, and BSP. Yao et al.[207] using marrow cell cultures, showed that mineralization was associated with an increase in levels of mRNA of collagen type I, osteonectin, alkaline phosphatase, osteopontin, BSP, and osteocalcin. Type I collagen, osteonectin, alkaline phosphate, and osteopontin were expressed whether or not minerlization occured; the expression of BSP and osteocalcin was unique to the bone-forming cultures. The pattern of expression of bone matrix proteins in culture was found by Cowles et al.[208] to be like that in the tissue. Recently, Gerstenfeld et al.[201] compared two osteoblast-like cell lines, one that did not mineralize and one that did. The mineralizing cell line had high levels of expression of type I collagen, BSP, and alkaline phosphatase. The nonmineralizing line did not. Osteocalcin expression was comparable in both. These cumulative cell culture data, although they conflict from system to system, strongly support a role for BSP along with type I collagen in the mineralization process.

To date, there have only been a limited number of studies directly examining the effects on mineralization of protein overexpression or underexpression, or the addition of exogenous protein to culture systems. Such studies can verify cell-free *in vitro* data. Studies of Kuboki et al.[209] demonstrate the types of collagen cross-links that form in culture prior to mineralization. Studying a model of the epiphyseal growth plate, the author's group[210,211] has demonstrated that blocking matrix protein phosphorylation decreases the extent of mineralization,[210] and that removing or modifying proteoglycans has the opposite

effect, increasing mineralization.[211] By using an osteoblast cell culture system, addition of α2-HS glycoprotein was shown to inhibit mineral deposition, as previously noted in solution.[160] Kresse's group[212] cultured osteoblasts from human nasal bone in the presence or absence of β-glycerophosphate and ascorbate. In the supplemented cultures, there was a reduced expression of the small proteoglycan decorin. In the mineralizing cultures, pulse-chase experiments demonstrated an increased turnover of both decorin and the other small bone proteoglycan, biglycan. Since in solution biglycan can act as a nucleator while decorin has no effect on apatite formation or growth,[162] these cell culture data support the role for biglycan noted in cell-free solution studies.

5.4.2.4.3 Studies of Animals with Genetic Defects

Confirmation that a particular protein, or class of proteins, can influence *in situ* bone mineralization has recently come from studies on animals in which these proteins are absent, because of naturally occurring, dietary-induced, or genetically introduced defects. Chapter 3 discusses the ways in which transgenic and knockout animals are generated, and thus they will only be mentioned here in light of the insight they provide into the mineralization process.

As noted above, the most insight into the role of collagen as a template for bone mineral deposition has come from studies of animals and humans with osteogenesis imperfecta. These animals include a naturally occurring cow model,[168] as well as naturally occurring and genetically engineered rodent models.[213–216] Since 70% of all body proteins are collagenous, it is obvious why an animal that fails to express type I collagen (null mutation or "knockout") would not be possible, although, because there are two different collagen molecules that are incorporated into the final triple helical molecule, it might be possible to engineer an α1-trimer, such as is found in the naturally occurring oim/oim model,[213] or an α2-trimer.

The most important lesson to date from the knockout animals involving bone matrix proteins (Table 5.6) is that, if not lethal, the changes observed in terms of mineralization are generally not profound. This is likely because the mineralization process is redundantly controlled, and there is more than one

TABLE 5.6 Mineral Analyses of Transgenic and Knockout Animals Reveal Functions of Bone Matrix Proteins in the Mineralization Process

Protein	Postulated Function	Modification	Observed Effect	Ref.
Collagen (type I)	Mineralization template	Transgenic	Brittle bones	214
			Smaller crystals	215
Collagen (type X)	Mineralization regulator	Transgenic	Altered pattern of mineral deposition	66, 68, 218
		Knockout	No effect	69, 219
Osteocalcin	Osteoclast recruiter	Knockout	Thickened bones, smaller crystals	70, 220
Biglycan	Nucleator/regulator	Knockout	Fewer, but larger crystals, thinner bones	71
Osteopontin	Inhibitor	Knockout	Larger crystals	226
Bone sialoprotein	Nucleator	Knockout	No reported phenotype or mineral defect	[a]
Osteonectin	Inhibitor	Knockout	Corneal defect, mineral not studied	230
Alkaline phosphatase	Increases local [Pi]	Knockout-bone specific enzyme only	Hypophosphatasia/ poorly mineralized bones	141
Matrix gla-protein	Inhibitor	Knockout	Cartilage and blood vessel calcification	165

[a] J. Aubin, personal communication.

protein that may act as a nucleator and regulator of crystal growth. The src knockout, generated to study the role of this protoconcogene in brain and vascular development, had osteopetrosis,[217] a disease characterized by thickened, hypermineralized bones. The details of the mineral properties in these animals have not been reported, but they are mentioned just to introduce the concept that when generating "knockout" animals one does not always find an effect in the system under investigation. However, when examined closely, using the analytical methods discussed at the start of this chapter, these models do provide new insights into the function of matrix proteins in regulating mineralization.

The type X collagen transgenic mouse[218] expressed an abnormal type X collagen that could not assemble properly into a triple helix. Young animals showed no obvious abnormalities, but as the transgenic mice aged, spinal curvature similar to that seen in humans with spondyloepiphyseal dysplasia developed. Mineral analyses demonstrated that the mineral was distributed differently from that in the wild-type controls.[68] Some slight differences in mineral crystal size and perfection were also noted based on FTIR microspectroscopy.[68] In contrast, the type X knockout animals, which had no type X collagen,[219] showed no such abnormalities.[66] These cumulative data were interpreted as demonstrating the function of type X collagen in forming a backbone for the start of endochondral ossification. In agreement with a variety of solution and cell culture data, no direct effect on mineralization was suggested.

The osteocalcin knockout[220] also had an unexpected bone mineral phenotype. Osteocalcin, one of the most abundant of the bone noncollagenous proteins, had been shown in solution to be an inhibitor of crystal growth[150,151] and in culture to be chemotactic for osteoclasts.[221–223] The osteocalcin knockout animals showed excessive bone formation that did not appear to be dependent on osteoclastic resorption,[220] implying that osteocalcin had an effect on bone formation. More detailed mineral analyses, based on FTIR microspectroscopy, revealed that the mineral in the widened bones was all of roughly the same size, and did not show the crystal maturation seen in the wild-type animals.[70] This indicated that osteocalcin was important for mineral maturation, perhaps via a defect in osteocyte- or osteoclast-mediated remodeling.

The biglycan knockout[71] had a phenotype that was more predictable from solution data. Biglycan is a small bone proteoglycan that associates with type I collagen. Similar to patients with Turner's syndrome who often have defective biglycan expression and tend to be short,[224,225] the biglycan-deficient animals were small and had thinner bones. FTIR microspectroscopic analyses of the mineral revealed a decreased mineral content, but the presence of larger mineral crystals. This was explained in terms of the absence of one of a group of bone mineral nucleators. With fewer crystal nuclei present, as discussed above, crystals would have a longer time to grow, and would tend to be larger.

Potentially most interesting of the bone matrix protein knockouts, the BSP knockout developed by Aubin's group (unpublished), was reported to have no bone phenotype, and no alteration in mechanical or crystallographic properties. Similarly, the osteopontin knockout[226] was said to have no mineralization defect, but defective osteoclast development *in vitro*. FTIR microscopic analyses indicate that the mineral crystals in the bones of these animals are smaller, but more abundant, reflecting an impaired ability to remodel these crystals.

Other interesting knockout and transgenic animals that should provide additional insights into the mineralization process include: a 24,25-vitamin D hydroxylase knockout in which intramembranous ossification is reported to be abnormal,[227] a bone morphogenetic protein knockout with impaired skeletal development,[228] a mutation in a new protein that causes premature skeletal aging,[229] and the osteonectin knockout.[230]

5.4.3 Regulation of Bone Mineral Crystal Size

The nucleators discussed above also can influence the size, shape, and composition of mineral crystals. Since not all mineral crystals are the same, and composition and size varies with diet, age, health and disease, and tissue site, it is important to consider the factors influencing the progress of mineralization. Consider the osteon (see Fig. 5.2). Here, mineral deposition occurs on the periphery of the vascular canal.

Viewed in cross section, rings of mineral of increasing density and mineral-to-matrix ratio are observed.[54] With time, in the healthy individual, the mineral matures, the crystallinity increases, and the total carbonate content increases. Parallel to that there is a decrease in the amount of labile (surface) carbonate and incorporated acid phosphate.[54] Similar changes are seen going from the periosteal surface of cortical bone to the endosteal surface,[70,71,73] or moving from the surface to the center of a single trabeculae.[70,71,73,231] There are several factors controlling these changes in mineral crystal properties.

A major part of the control of crystal size and perfection is physicochemical. As the crystals are resorbed by osteoclasts and reformed on newly deposited osteoid, the most-soluble crystals, i.e., the smallest crystals, are resorbed first. The larger crystals persist. Their ions may be incorporated onto the surfaces of the larger crystals, and as these crystals grow, dissolve, and reprecipitate, the lattice becomes more ordered. Carbonate in the environment is probably incorporated at a constant rate, but as the crystals become larger, there is less surface area exposed per individual crystal, and hence less surface (labile) carbonate.[62]

As noted previously, resorption and remodeling is controlled by the activity of the osteoclast and osteocyte, which in turn are controlled by cell signaling. Osteocalcin seems to be involved in the recruitment of osteoclasts.[232,233] A newly discovered protein, osteoprotegerin, seems to have a similar effect.[234] Additional proteins not yet identified may also be involved in osteoclast differentiation and recruitment.

Collagen limits the extent to which crystals can aggregate, and the length to which they can grow.[86,87,126] Other proteins associated with the collagen also can regulate the size and shape of the crystals. The extent to which they do this in the organism still remains to be determined, but some of the data from the knockout and transgenic animals suggests their involvement is real.

5.4.4 Bone Development

The description of bone development, from the first patterning molecules,[2] to the cellular regulation of gene expression, is beyond the scope of this chapter. Yet it is important to point out that mineral deposition is a key step in this process, and a key marker of bone development. Errors in patterning genes and signaling molecules, absence of differentiation markers, as well as abnormal expression of matrix molecules and collagen each leads to improper mineral deposition.[213–220,226–229,235–238] Abnormalities in bone development may also leads to changes in the way loads are applied to bone, which in turn can affect the properties of the bone mineral.

Likewise, bone adaptation, the way bones respond to load, may induce mineral deposition.[239,240] That mineral appears in quality to be like other newly formed mineral.[241] The cells responding are periosteal cells, and their gene expression is altered within the first hour.[240] Exactly what the mechanoreceptors are, and how they alter the way the matrix is deposited in response to stress, remains a mystery. Detailed analysis of the mineral and matrix as the bone responds to load should provide clues to this mystery.

References

1. Burstein, A. H., Zika, J. M., Heiple, K. G., and Klein. L., Contribution of collagen and mineral to the elastic-plastic properties of bone, *J. Bone Joint Surg. (Am. vol.),* 57, 956, 1975.
2. Sasaki, N. and Yoshikawa, M., Stress relaxation in native and EDTA-treated bone as a function of mineral content, *J. Biomech.,* 26, 77, 1993.
3. Hasegawa, K., Turner, C. H., and Burr, D. B., Contribution of collagen and mineral to the elastic anisotropy of bone, *Calcif. Tissue Int.,* 55, 381, 1994.
4. Neuman, M. W., Imai, K., Kawase, T., and Saito, S. J., The calcium-buffering phase of bone mineral: some clues to its form and formation, *Bone Miner. Res.,* 2, 171, 1987.
5. de Jong, W. F., La substance minérale dans le os, *Rec. Trav. Chim. Pays-Bas,* 45, 445, 1926.
6. Posner, A. S. and Beebe, R. A., The surface chemistry of bone mineral and related calcium phosphates, *Semin. Arthritis Rheum.,* 4, 267, 1975.

7. Roberts, J. E., Bonar, L. C., Griffin, R. G., and Glimcher, M. J., Characterization of very young mineral phases of bone by solid state^{31}phosphorus magic angle sample spinning nuclear magnetic resonance and X-ray diffraction, *Calcif. Tissue Int.,* 50, 42, 1992.
8. Münzenberg, K. J. and Gebhardt, M., Brushite, octocalcium phosphate and carbonate of mineral apatite in bone, *Clin. Orthop. Relat. Res.,* 90, 271, 1973.
9. Driessens, F. C. and Verbeeck, R. M., Evidence for intermediate metastable states during equilibration of bone and dental tissues, *Z. Naturforsch. [C],* 35, 262, 1980.
10. Driessens, F. C. and Verbeeck, R. M., *Biominerals,* CRC Press, Boca Raton, FL, 1990, chaps. 10 to 14.
11. Glimcher, M. J., The nature of the mineral phase in bone: biological and clinical implications, in *Metabolic Bone Disease and Clinically Related Disorders,* Avioli, L. V. and Krane, S. M., Eds., Academic Press, San Diego, 1998, chap. 2.
12. Holden, J. L., Clement, J. G., and Phakey, P. P., Age and temperature related changes to the ultrastructure and composition of human bone mineral, *J. Bone Miner. Res.,* 10, 1400, 1995.
13. Franc, S., Marzin, E., Boutillon, M. M., Lafont, R., Lechene de la Porte, P., and Herbage, D., Immunohistochemical and biochemical analyses of 20,000–25,000-year-old fossil cartilage. *Eur. J. Biochem.,* 234, 125, 1995.
14. Thompson, D. D., Posner, A. S., Laughlin, W. S., and Blumenthal, N. C., Comparison of bone apatite in osteoporotic and normal Eskimos, an infrared and x-ray diffraction study of osteoporotic and normal, archaeological Eskimo bones. *Calcif. Tissue Int.,* 35, 392, 1983.
15. Holden, J. L., Phakey, P. P., and Clement, J. G., Scanning electron microscope observations of heat-treated human bone, *Foren. Sci. Int.,* 74, 29, 1995.
16. Alho, A., Husby, T., and Hoiseth, A., Bone mineral content and mechanical strength. An ex vivo study on human femora at autopsy, *Clin. Orthop.,* 227, 292, 1988.
17. Gordon, K. R., Burns, P., and Keller, G., Experimental changes in mineral content of juvenile mouse femora, *Calcif. Tissue Int.,* 51, 229, 1992.
18. Van der Perre, G. and Lowet, G. Physical meaning of bone mineral content parameters and their relation to mechanical properties, *Clin. Rheumatol.,* 13, (Suppl. 1), 33, 1994.
19. Currey, J. D., Brear, K., and Zioupos, P., The effects of ageing and changes in mineral content in degrading the toughness of human femora, *J. Biomech.,* 29, 257, 1996.
20. Larsen, L. A., Teubner, E. J., and Burnell, J. M., Determination of CO_2 in biologic materials., *J. Appl. Physiol.,* 35, 82, 1977.
21. Louis, O., Van den Winkel, P., Covens, P., Schoutens, A., and Osteaux, M., Mineral content of vertebral trabecular bone: accuracy of dual energy quantitative computed tomography evaluated against neutron activation analysis and flame atomic absorption spectrometry, *Bone,* 15, 35, 1994.
22. Grynpas, M. D. and Rey, C., The effect of fluoride treatment on bone mineral crystals in the rat, *Bone,* 13, 423, 1992.
23. Jeffery, E. H., Abreo, K., Burgess, E., Cannata, J., and Greger, J. L., Systemic aluminum toxicity: effects on bone, hematopoietic tissue, and kidney, *J. Toxicol. Environ. Health,* 48, 649, 1996.
24. Velasquez Forero, F., Altamirano, E., and Ramos, P. T., High frequency of iron bone deposits in a Mexican population with renal osteodystrophy, *Nephrol. Dial. Transplant,* 13 (Suppl. 3), 46, 1998.
25. Goldberg, M. and Boskey, A. L., Lipids and biomineralizations, *Prog. Histochem. Cytochem.,* 31, 1, 1996.
26. Rimnac, C. M., Petko, A. A., Santner, T. J., and Wright, T. M., The effect of temperature, stress and microstructure on the creep of compact bovine bone, *J. Biomech.,* 26, 219, 1993.
27. Johanson, N. A., Charlson, M. E., Cutignola, L., Neves, M., DiCarlo, E. F., and Bullough, P. G., Femoral neck bone density. Direct measurement and histomorphometric validation, *J. Arthroplasty,* 8, 641, 1993.
28. Akesson, K., Grynpas, M. D., Hancock, R. G., Odselius, R., and Obrant K. J., Energy-dispersive X-ray microanalysis of the bone mineral content in human trabecular bone: a comparison with ICPES and neutron activation analysis, *Calcif. Tissue Int.,* 55, 236, 1994.

29. Wroblewski, R., Wroblewski, J., Lundstrom, H., Edstrom, L., and Jansson, E., Energy dispersive X-ray microanalysis, neutron activation analysis and atomic absorption spectrometry—comparison using biological specimens, *Scanning Microsc.,* 3, 467, 1989.
30. Bigi, A., Cojazzi, G., Panzavolta, S., Ripamonti, A., Roveri, N., Romanello, M., Noris Suarez, K., and Moro, L., Chemical and structural characterization of the mineral phase from cortical and trabecular bone, *J. Inorg. Biochem.,* 68, 45, 1997.
31. Cullity, B. D., *Elements of X-ray Diffraction.,* Addison Wesley, Reading, MA., 1967.
32. Legros, R., Balmain, N., and Bonel, G., Age-related changes in mineral of rat and bovine cortical bone, *Calcif. Tissue Int.,* 41, 137, 1987.
33. Burnell, J. M., Teubner, E. J., and Miller, A. G., Normal maturational changes in bone matrix, mineral, and crystal size in the rat, *Calcif. Tissue Res.,* 31, 13, 1980.
34. Ghezzo, C., Civitelli, R., Cadel, S., Borelli, G., Maiorino, M., Bufalino, L., and Bongrani, S., Ipriflavone does not alter bone apatite crystal structure in adult male rats, *Calcif. Tissue Int.,* 59, 496, 1996.
35. Bonar, L. C., Roufosse, A. H., Sabine, W. K., Grynpas, M. D., and Glimcher, M. J., X-ray diffraction studies of the crystallinity of bone mineral in newly synthesized and density fractionated bone, *Calcif. Tissue Int.,* 35, 202, 1983.
36. Boskey, A. L. and Dickson, I. R., Influence of vitamin D status on the content of complexed acidic phospholipids in chick diaphyseal bone, *Bone Miner.,* 4, 365, 1988.
37. Masse, P. G., Rimnac, C. M., Yamauchi, M., Coburn, S. P., Rucker, R. B., Howell, D. S., and Boskey, A. L., Pyridoxine deficiency affects biomechanical properties of chick tibial bone, *Bone,* 18, 567, 1996.
38. Boskey, A. L., Lipid changes in the bones of the healing vitamin D deficient, phosphate deficient rat, *Metab. Bone Dis. Relat. Res.,* 6, 173, 1985.
39. Boskey, A. L., DiCarlo, E. F., Gilder, H., Donnelly, R., and Wientroub, S., The effect of short-term treatment with vitamin D metabolites on bone lipid and mineral composition in healing vitamin D-deficient rats, *Bone,* 9, 309, 1988.
40. Neufeld, E. and Boskey, A. L., The effect of strontium on lipid-mediated calcification *in vitro* and *in situ, Bone,* 4, 425, 1994.
41. Donnelly, R., Bockman, R., DiCarlo, E., Betts, F., and Boskey, A., The effect of gallium nitrate on healing of vitamin D- and phosphate-deficient rickets in the immature rat, *Calcif. Tissue Int.,* 53, 400, 1993.
42. Boskey, A. L., Rimnac, C. M., Bansal, M., Federman, M., Lian, J., and Boyan, B. D., Effect of short-term hypomagnesemia on the chemical and mechanical properties of rat bone, *J. Orthop. Res.,* 10, 774, 1992.
43. Boskey, A. L., Gilder, H., Neufeld, E., Ecarot-Charrier, B., and Glorieux, F. H., Phospholipid changes in the bones of hypophosphatemic mouse, *Bone,* 12, 345, 1991.
44. Camacho, N. P., Rimnac, C. M., Meyer, R. A., Doty, S. B., and Boskey, A.L., Effect of abnormal mineralization on the mechanical behavior of x-linked hypophosphatemic mice femora, *Bone,* 17, 271, 1995.
45. Boskey, A. L., Maresca, M., and Hjerpe, A., Hydroxyapatite formation in the presence of proteoglycans of reduced sulfate content:studies in the brachymorphic mouse, *Calcif. Tissue Int.,* 49, 389, 1991.
46. Boskey, A. L. and Marks, S. C., Jr., Mineral and matrix alterations in the bones of incisors-absent (ia/ia) osteopetrotic rats., *Calcif. Tissue Int.,* 37, 287, 1985.
47. Einhorn, T. A., Boskey, A. L., Gundberg, C. M., Vigorita, V. J., and Beyer, M. M., The mineral and mechanical properties of bone in chronic experimental diabetes, *J. Orthop. Res.,* 6, 317, 1988.
48. Lundon, K., Dumitriu, M., and Grynpas, M., The long-term effect of ovariectomy on the quality and quantity of cancellous bone in young macaques, *Bone Miner.,* 24, 135, 1994.

48a. Gadeletta, S. J., Boskey, A. L., Paschalis, E., Carlson, C., Menschik, F., Baldini, T., Peterson, M., and Rimnac, C. M., A physical, chemical, and mechanical study of lumbar vertebrae from normal, ovariectomized, and nandrolone decanoate-treated cynomolgus monkeys, *Bone,* 27, 541, 2000.
49. Bailey, R. T. and Holt, C., Fourier transform infrared spectroscopy and characterisation of biological calcium phosphates, in *Calcified Tissue,* Hukins, D. W. L., Ed., Macmillan Press, Houndsmills, England, 1989, chap 5.
50. Baddiell, C. B. and Berry, E. E., Spectra structure correlations in hydroxy and fluoroapatite, *Spectrochim. Acta,* 22, 1407, 1966.
51. Fowler, B. O., Moreno, E. C., and Brown, W. E., Infra-red spectra of hydroxyapatite, octacalcium phosphate and pyrolysed octacalcium phosphate, *Arch. Oral Biol.,* 11, 477, 1966.
52. Blumenthal, N. C., Betts, F., and Posner, A. S., Effect of carbonate and biological macromolecules on formation and properties of hydroxyapatite, *Calcif. Tissue Res.,* 18, 81, 1975.
53. Gadaleta, S. J., Paschalis, E. P., Betts, F., Mendelsohn, R., and Boskey, A. L., Fourier transform infrared spectroscopy of the solution-mediated conversion of amorphous calcium phosphate to hydroxyapatite: new correlations between X-ray diffraction and infrared data, *Calcif. Tissue Int.,* 58, 9, 1996.
54. Paschalis, E. P., DiCarlo, E., Betts, F., Sherman, P., Mendelsohn, R., and Boskey, A. L., FTIR microscopic analysis of human osteonal bone, *Calcif. Tissue Int.,* 59, 480, 1996.
55. LeGeros, R. Z., Trautz, O. R., Le Geros, J. P., and Klein, E., Carbonate substitution in the apatitic structure, *Bull. Soc. Chim. Fr.,* 1712, 1968.
56. Cohen, L. and Kitzes, R., Infrared spectroscopy and magnesium content of bone mineral in osteoporotic women, *Isr. J. Med. Sci.,* 17, 1123, 1981.
57. Baud, C. A., Pouëzat, J. A., and Tochon-Danguy, H. J., Quantitative analysis of amorphous and crystalline bone tissue mineral in women with osteoporosis, *Calcif. Tissue Res.,* 21S, 452, 1976.
58. Baud, C. A., Very, J. M., and Courvoisier, B., Biophysical study of bone mineral in biopsies of osteoporotic patients before and after long-term treatment with fluoride, *Bone,* 9, 361, 1988.
59. Pienkowski, D., Doers, T. M., Monier-Faugere, M. C., Geng, Z., Camacho, N. P., Boskey, A. L., and Malluche, H. H., Calcitonin alters bone quality in beagle dogs, *J. Bone Miner. Res.,* 12, 1936, 1997.
60. Rey, C., Miquel, J. L., Facchini, L., Legrand, A. P., and Glimcher, M. J., Hydroxyl groups in bone mineral, *Bone,* 16, 583, 1995.
61. Rey, C., Shimizu, M., Collins, B., and Glimcher, M. J., Resolution-enhanced Fourier transform infrared spectroscopy study of the environment of phosphate ions in early deposits of a solid phase of calcium-phosphate in bone and enamel, and their evolution with age. I: Investigations in the v4 PO_4 domain, *Calcif. Tissue Int.,* 46, 384, 1990.
62. Rey, C., Renugopalakrishnan, V., Collins, B., and Glimcher, M. J., Fourier transform infrared spectroscopic study of the carbonate ions in bone mineral during aging, *Calcif. Tissue Int.,* 49, 251, 1991.
63. Kim, H. M., Rey, C., and Glimcher, M. J., Isolation of calcium-phosphate crystals of bone by non-aqueous methods at low temperature, *J. Bone Miner. Res.,* 10, 1589, 1995.
64. Mendelsohn, R., Hassenkhani, A., DiCarlo, E., and Boskey, A. L., FT-IR microscopy of endochondral ossification at 20μ spatial resolution, *Calcif. Tissue Int.,* 44, 20, 1989.
65. Boskey, A. L., Camacho, N. P., Gadaleta, S., Paschalis, E. P., and Mendelsohn, R., Applications of Fourier transform infrared microscopy to the study of biologic mineralization, *Fr. Eurobiol.,* 30, 259, 1996.
66. Paschalis, E. P., Jacenko, O., Olsen, B., Decrombugghe, B., and Boskey, A. L., The role of type X collagen in endochondral ossification as deducted by FT-IR microscopic analysis, *Connect. Tissue Res.,* 35, 371, 1996.
67. Camacho, N. P., Landis, W. J., and Boskey, A. L., Mineral changes in a mouse model of osteogenesis imperfecta detected by Fourier transform infrared microscopy, *Connect. Tissue Res.,* 35, 259, 1996.

68. Paschalis, E. P., Jacenko, O., Olsen, B., Mendelsohn, R., and Boskey, A. L., FT-IR microscopic analysis identified alterations in mineral properties in bones from mice transgenic for type X collagen, *Bone,* 18, 151, 1996.
69. Paschalis, E. P., Betts, F., DiCarlo, E., Mendelsohn, R., and Boskey, A. L., FTIR microspectroscopic analysis of human iliac crest biopsies from untreated osteoporotic bone, *Calcif. Tissue Int.,* 61, 487, 1997.
70. Boskey, A. L., Gadaleta, S., Gundberg, C., Doty, S. B., Ducy, P., and Karsenty, G., FTIR microspectroscopic analysis of bones of osteocalcin deficient mice provides insight into the function of osteocalcin, *Bone,* 23, 187, 1998.
71. Xu, T., Fisher, L., Bianco, P., Longnecker, G., Boskey, A. L., Smith, E., Bonadio, J., Goldsteins, S., Zhao, C., Dominguez, P., Heegaard, A. M., Satomura, K., Gehron-Robey, P., Kulkarni, A., Sommer, B., and Young, M., Targeted disruption of the biglycan gene leads to osteoporosis in mice, *Nat. Genet.,* 20, 78, 1998.
72. Bohic, S., Rohanizadeh, R., Touchais, S., Godard, A., Daculsi, G., and Heymann, D., Leukemia inhibitory factor and oncostatin M influence mineral phases formed in a murine heterotopic calcification model: a Fourier transform-infrared microspectroscopic study, *J. Bone Miner. Res.,* 13, 1619, 1998.
73. Marcott, C., Reeder, R. C., Paschalis, E., P., Tatakis, D. N., Boskey, A. L., and Mendelsohn, R., Infrared microspectroscopic imaging of biomineralized tissues using a mercury-cadmium-telluride focal-plane array detector, *Cell Mol. Biol.* (Noisy-le-grand), 44, 109, 1998.
74. O'Shea, D. C., Bartlett, M. L., and Young, R. A., Compositional analysis of apatites with laser-raman spectroscopy: (OH,F,Cl) apatites, *Arch. Oral Biol.,* 19, 995, 1974.
75. Casciani, F., Etz, E. S., Newbury, D. E., and Doty, S. B., Raman microprobe studies of two mineralizing tissues: enamel of the rat incisor and the embryonic chick tibia, *S.E.M.,* II, 383, 1979.
76. Walters, M. A., Leung, Y. C., Blumenthal, N. C., LeGeros, R. Z., and Konsker, K. A., A Raman and infrared spectroscopic investigation of biological hydroxyapatite, *J. Inorg. Biochem.,* 39, 193, 1990.
77. Rehman, I., Smith, R., Hench, L. L., and Bonfield, W., Structural evaluation of human and sheep bone and comparison with synthetic hydroxyapatite by FT-Raman spectroscopy, *J. Biomed. Mater. Res.,* 29, 1287, 1995.
78. deMul, F. F., Hottenhuis, M. J., Bouter, P., Greve, J., Arends, J., and ten Bosch, J. J., Micro-Raman line broadening in synthetic carbonated hydroxyapatite, *J. Dent. Res.,* 65, 437, 1986.
79. Wu, Y., Glimcher, M. J., Rey, C., and Ackerman, J. L., A unique protonated phosphate group in bone mineral not present in synthetic calcium phosphates. Identification by phosphorus-31 solid state NMR spectroscopy, *J. Mol. Biol.,* 244, 423, 1994.
80. Gadaleta, S. J., Camacho, N. P., Mendelsohn, R., and Boskey, A. L., Fourier transform infrared microscopy of calcified turkey leg tendon, *Calcif. Tissue Int.,* 58, 17, 1996.
81. Bloebaum, R. D., Skedros, J. G., Vajda, E. G., Bachus, K. N., and Constantz, B. R., Determining mineral content variations in bone using backscattered electron imaging, *Bone,* 20, 485, 1997.
82. Boyde, A., Compston, J. E., Reeve, J., Bell, K. L., Noble, B. S., Jones, S. J., and Loveridge, N., Effect of estrogen suppression on the mineralization density of iliac crest biopsies in young women as assessed by backscattered electron imaging, *Bone,* 22, 241, 1998.
83. Link, T. M., Majumdar, S., Lin, J. C., Augat, P., Gould, R. G., Newitt. D., Ouyang, X., Lang, T. F., Mathur, A., and Genant, H. K., Assessment of trabecular structure using high resolution CT images and texture analysis, *J. Comput. Assist. Tomogr.,* 22, 15, 1998.
84. Hvid, I., Bentzen, S. M., Linde, F., Mosekilde, L., and Pongsoipetch, B., X-ray quantitative computed tomography: the relations to physical properties of proximal tibial trabecular bone specimens, *J. Biomech.,* 22, 837, 1989.
85. Wong, F. S., Elliott, J. C., Anderson, P., and Davis, G. R., Mineral concentration gradients in rat femoral diaphyses measured by X-ray microtomography, *Calcif. Tissue Int.,* 56, 62, 1995.

86. Landis, W. J., Song, M. J., Leith, A., McEwen, L., and McEwen, B. F., Mineral and organic interaction in normally calcifying tendon visualized in three dimensions by high-voltage electron microscopic tomography and graphic image reconstruction, *J. Struct. Biol.,* 110, 39, 1993.
87. Landis, W. J., Hodgens, K. J., Song, M. J., Arena, J., Kiyonaga, S., Marko, M., Owen, C., and McEwen, B. F., Mineralization of collagen may occur on fibril surfaces: evidence from conventional and high-voltage electron microscopy and three-dimensional imaging, *J. Struct. Biol.,* 117, 24, 1996.
88. Jackson, S. A., Cartwright, A. G., and Lewis, D., The morphology of bone mineral crystals, *Calcif. Tissue Res.,* 25, 217, 1978.
89. Antich, P. P., Ultrasound study of bone in vitro, *Calcif. Tissue Int.,* 53, S157, 1993.
90. Ahmed, K., Inoue, T., Tomiyoshi, K., Sarwar, M., Oriuchi, N., Mizunuma, H., and Endo, K., Comparative study of positron emission tomography and quantitative digital radiography (QDR) in detecting effects of aging and diet on bone metabolism of guinea pig, *Radiat. Med.,* 16, 239, 1998.
91. Fratzl, P., Schreiber, S., and Klaushofer, K., Bone mineralization as studied by small-angle X-ray scattering, *Connect. Tissue Res.,* 34, 247, 1996.
92. Fratzl, P., Schreiber, S., Roschger, P., Lafage, M. H., Rodan, G., and Klaushofer, K., Effects of sodium fluoride and alendronate on the bone mineral in minipigs: a small-angle X-ray scattering and backscattered electron imaging study, *J. Bone Miner. Res.,* 11, 248, 1996.
93. Roschger, P., Fratzl, P., Klaushofer, K., and Rodan, G., Mineralization of cancellous bone after alendronate and sodium fluoride treatment: a quantitative backscattered electron imaging study on minipig ribs, *Bone,* 20, 393, 1997.
94. Matsushima, N. and Hikichi, K., Age changes in the crystallinity of bone mineral and in the disorder of its crystal, *Biochim. Biophys. Acta,* 992, 155, 1989.
95. Grynpas, M., Age and disease-related changes in the mineral of bone, *Calcif. Tissue Int.,* 53, S57, 1993.
96. Burr, D. B. and Martin, R. B., The effects of composition, structure and age on the torsional properties of the human radius, *J. Biomech.,* 16, 603, 1983.
97. Parfitt, A. M., Han, Z. H., Palnitkar, S., Rao, D. S., Shih, M. S., and Nelson, D., Effects of ethnicity and age or menopause on osteoblast function, bone mineralization, and osteoid accumulation in iliac bone, *J. Bone Miner. Res.,* 12, 1864, 1997.
98. Handschin, R. G. and Stern, W. B., Crystallographic and chemical analysis of human bone apatite (Crista iliaca), *Clin. Rheumatol.,* 13, s75, 1994.
99. Hanschin, R. G. and Stern, W. B., X-ray diffraction studies on the lattice perfection of human bone apatite (Crista iliaca), *Bone,* 16, 355S, 1995.
100. Dziedzic-Goclawska, A., Emerich, J., Grzesik, W., Stachowicz, W., Michalik, J., and Ostrowski, K., Differences in the kinetics of the mineralization process in endochondral and intramembranous osteogenesis in human fetal development, *J. Bone Miner. Res.,* 3, 533, 1988.
101. Aerssens, J., Van Audekercke, R., Talalaj, M., Van Vlasselaer, P., Bramm, E., Geusens, P., and Dequeker, J., Effect of 1 alpha-vitamin D3 on bone strength and composition in growing rats with and without corticosteroid treatment, *Calcif. Tissue Int.,* 55, 443, 1994.
102. Leopold, S. S., Boskey, A. L., Doty, S. B., Gertner, J. M., and Torzilli, A., Diminished material properties and altered bone structure in rat femora during pregnancy, *J. Orthop. Res.*, 13, 41, 1995.
103. Miller, S. C. and Bowman, B. M., Comparison of bone loss during normal lactation with estrogen deficiency osteopenia and immobilization osteopenia in the rat, *Anat. Rec.,* 251, 265, 1998.
104. Aoki, H., Okayama, S., Kondo, K., and Akao, M., Effect of exercise on strength and chemical composition of rat femur bone, *Biomed. Mater. Eng.,* 3, 25, 1993.
105. Tuukkanen, J., Wallmark, B., Jalovaara, P., Takala, T., Sjogren, S., and Vaananen, K., Changes induced in growing rat bone by immobilization and remobilization, *Bone,* 12, 113, 1991.
106. Einhorn, T. A., Levine, B., and Michel, P., Nutrition and bone, *Orthop. Clin. North Am.,* 21, 43, 1990.

107. Klein, G. L., Herndon, D. N., Goodman, W. G., Langman, C. B., Phillips, W. A., Dickson, I. R., Eastell, R., Naylor, K. E., Maloney, N. A., Desai, M., Benjamin, B., and Alfrey, A. C., Histomorphometric and biochemical characterization of bone following acute severe burns in children, *Bone,* 17, 455, 1995.
108. Burnell, J. M., Liu, C., Miller, A. G., and Teubner, E., Effects of dietary alteration of bicarbonate and magnesium on rat bone, *Am. J. Physiol.,* 250, F302, 1986.
109. Wohl, G. R., Loehrke, L., Watkins, B. A., and Zernicke, R. F., Effects of high-fat diet on mature bone mineral content, structure, and mechanical properties, *Calcif. Tissue Int.,* 63, 74, 1998.
110. Nicodemo, M. L., Scott, D., Buchan, W., Duncan, A., and Robins. S. P., Effects of variations in dietary calcium and phosphorus supply on plasma and bone osteocalcin concentrations and bone mineralization in growing pigs, *Exp. Physiol.,* 83, 659, 1998.
111. Kenney, M. A. and McCoy, H., Adding zinc reduces bone strength of rats fed a low-calcium diet, *Biol. Trace Elem. Res.,* 58, 35, 1997.
112. Noff, D., Simkin, A., and Edelstein, S., Effect of cholecalciferol derivatives on the mechanical properties of chick bones, *Calcif. Tissue Int.,* 34, 501, 1982.
113. Nakamura, T., Kurokawa, T., and Orimo, H., Increased mechanical strength of the vitamin D-replete rat femur by the treatment with a large dose of 24R,25$(OH)_2D_3$, *Bone,* 10, 117, 1989.
114. Navia, J. M. and Harris, S. S., Vitamin A influence on calcium metabolism and calcification, *Ann. N. Y. Acad. Sci.,* 355, 45, 1980.
115. Turan, B., Balcik, C., and Akkas, N., Effect of dietary selenium and vitamin E on the biomechanical properties of rabbit bones, *Clin. Rheumatol.,* 16, 441, 1997.
116. Verhaeghe, J., van Herck, E., Visser, W. J., Suiker, A. M., Thomasset, M., Einhorn, T. A., Faierman, E., and Bouillon, R., Bone and mineral metabolism in BB rats with long-term diabetes. Decreased bone turnover and osteoporosis, *Diabetes,* 39, 477, 1990.
117. Tein, M. S., Breen, S. A., Loveday, B. E., Devlin, H., Balment, R. J., Boyd, R. D., Sibley, C. P., and Garland, H. O., Bone mineral density and composition in rat pregnancy: effects of streptozotocin-induced diabetes mellitus and insulin replacement, *Exp. Physiol.,* 83, 165, 1998.
118. Siris, E. S., Paget's disease of bone, *J. Bone Miner. Res.,* 13, 1061, 1998.
119. Wojtowicz, A., Dziedzic-Goclawska, A., Kaminski, A., Stachowicz, W., Wojtowicz, K., Marks, S. C., Jr., and Yamauchi, M., Alterations of mineral crystallinity and collagen cross-linking of bones in osteopetrotic toothless (tl/tl) rats and their improvement after treatment with colony stimulating factor-1, *Bone,* 20, 127, 1997.
120. Boskey, A. L., Bone mineral and matrix: are they altered in osteoporosis? *Orthop. Clin. North Am.,* 21, 19, 1990.
121. Zerwekh, J. E., Antich, P. P., Mehta, S., Sakhaee, K., Gottschalk, F., and Pak, C. Y., Reflection ultrasound velocities and histomorphometric and connectivity analyses: correlations and effect of slow-release sodium fluoride, *J. Bone Miner. Res.,* 12, 2068, 1997.
122. Fleisch, H. A., Bisphosphonates: preclinical aspects and use in osteoporosis, *Ann. Med.,* 29, 55, 1997.
123. Kaastad, T. S., Reikeras, O., Madsen, J. E., Narum, S., Stromme, J. H., Obrant, K. J., and Nordsletten, L., Effects of clodronate on cortical and trabecular bone in ovariectomized rats on a low calcium diet, *Calcif. Tissue Int.,* 61, 158, 1997.
124. Civitelli, R., In vitro and in vivo effects of ipriflavone on bone formation and bone biomechanics, *Calcif. Tissue Int.,* 61, S12, 1997.
125. Weiner, S. and Traub, W., Bone structure: from ångstroms to microns, *FASEB J.,* 6, 879, 1992.
126. Landis, W. J., The strength of a calcified tissue depends in part on the molecular structure and organization of its constituent mineral crystals in their organic matrix, *Bone,* 16, 533, 1995.
127. Glimcher, M. J., Molecular biology of mineralized tissues with particular reference to bone, *Rev. Mod. Phys.,* 31, 359, 1959.
128. Anderson, H. C., Biology of disease: mechanism of mineral formation in bone, *Lab. Invest.,* 60, 320, 1989.

129. Anderson, H. C., Molecular biology of matrix vesicles, *Clin. Orthop.,* 314, 266, 1995.
130. Boskey, A. L., Boyan, B., and Schwartz, Z., Matrix vesicles promote mineralization in a gelatin gel, *Calcif. Tissue Int.,* 60, 309, 1997.
131. Boskey, A. L., Vigorita, V., and Bullough, P. G., Calcium-acidic phospholipid-phosphate complexes: promoter of mineralization common to pathologic hydroxyapatite-containing calcification, *Am. J. Pathol.,* 133, 22, 1988.
132. Hashimoto, S., Ochs, R. L., Rosen, F., Quach, J., McCabe, G., Solan, J., Seegmiller, J. E., Terkeltaub, R., and Lotz, M., Chondrocyte-derived apoptotic bodies and calcification of articular cartilage, *Proc. Natl. Acad. Sci. U.S.A.,* 95, 3094, 1998.
133. Hultenby, K., Reinholt, F. P., Oldberg, A., and Heinegard, D., Ultrastructural immunolocalization of osteopontin in metaphyseal and cortical bone, *Matrix,* 11, 206, 1991.
134. Boskey, A. L., Overview of cellular elements and macromolecules implicated in the initiation of mineralization, in *The Chemistry and Biology of Mineralized Tissues,* Butler, W. T., Ed., Ebsco Media Inc., Birmingham, AL, 335, 1985.
135. Mann, S., Hannington, J. P., and Williams, R. J. P., Phospholipid vesicles as a model system for biomineralization, *Nature,* 324, 565, 1986.
136. Caverzasio, J. and Bonjour, J. P., Characteristics and regulation of Pi transport in osteogenic cells for bone metabolism, *Kidney Int.,* 49, 975, 1996.
137. Ehrlich, M. G. and Armstrong, A. L., Aggregate degradation by growth plate proteases, *Clin. Orthop.,* 334, 298, 1997.
138. Dean, D. D., Boyan, B. D., Muniz, O. E., Howell, D. S., and Schwartz, Z., Vitamin D metabolites regulate matrix vesicle metalloproteinase content in a cell maturation-dependent manner, *Calcif. Tissue Int.,* 59, 109, 1996.
139. Ali, S. Y., Constitutive enzymes of matrix vesicles, *Bone Miner.,* 17, 168, 1992.
140. Vu, T. H., Shipley, J. M., Bergers, G., Berger, J. E., Helms, J. A., Hanahan, D., Shapiro, S. D., Senior, R. M., and Werb, Z., MMP-9/gelatinase B is a key regulator of growth plate angiogenesis and apoptosis of hypertrophic chondrocytes, *Cell,* 93, 411, 1998.
141. Narisawa, S., Frohlander, N., and Millan, J. L., Inactivation of two mouse alkaline phosphatase genes and establishment of a model of infantile hypophosphatasia, *Dev. Dyn.,* 208, 432, 1997.
142. Blair, H. C., How the osteoclast degrades bone, *Bioessays,* 20, 837, 1998.
143. Kaysinger, K. K. and Ramp, W. K., Extracellular pH modulates the activity of cultured human osteoblasts, *J. Cell Biochem.,* 68, 83, 1998.
144. Blumenthal, N. C., Mechanisms of inhibition of calcification, *Clin. Orthop.,* 247, 279, 1989.
145. Termine, J. D. and Conn, K. M., Inhibition of apatite formation by phosphorylated metabolites and macromolecules, *Calcif. Tissue Res.,* 22, 149, 1976.
146. Boskey, A. L., Hydroxyapatite formation in a dynamic gelatin gel system: effects of type I collagen, lipids, and proteoglycans, *J. Phys. Chem.,* 93, 1628, 1989.
147. Boskey, A. L., Matrix proteins and mineralization: an overview, *Connect. Tissue Res.,* 35, 357, 1996.
148. Chen, C. C., Boskey, A. L., and Rosenberg, L. C., The inhibitory effect of cartilage proteoglycans on hydroxyapatite growth, *Calcif. Tissue Int.,* 36, 285, 1984.
149. Chen, C. C. and Boskey, A. L., Mechanisms of proteoglycan inhibition of hydroxyapatite growth, *Calcif. Tissue Int.,* 37, 395, 1985.
150. Boskey, A. L., Wians, F. H., Jr., and Hauschka, P. V., The effect of osteocalcin on in vitro lipid-induced hydroxyapatite formation and seeded hydroxyapatite growth, *Calcif. Tissue Int.,* 37, 75, 1985.
151. Romberg, W. R., Werness, P. G., Riggs, B. L., and Mann, K. G., Inhibition of hydroxyapatite crystal growth by bone-specific and other calcium-binding proteins, *Biochemistry,* 25, 1176, 1986.
152. Terkeltaub, R. A., Santoro, D. A., Mandel, G., and Mandel, N., Serum and plasma inhibit neutrophil stimulation by hydroxyapatite cyrstals. Evidence that serum alpha 2-HS glycoprotein is a potent and specific crystal-bound inhibitor, *Arthritis Rheum.,* 31, 1081, 1988.

153. Garnett, J. and Dieppe, P., The effects of serum and human albumin on calcium hydroxyapatite crystal growth, *Biochem. J.,* 266, 863, 1990.
154. Boskey, A. L., Maresca, M., Ullrich, W., Doty, S. B., Butler, W. T., and Prince, C. W., Osteopontin-hydroxyapatite interactions in vitro: inhibition of hydroxyapatite formation and growth in a gelatin-gel, *Bone Miner.,* 22, 147, 1993.
155. Hunter, G. K., Kyle, C. L., and Goldberg, H. A., Modulation of crystal formation by bone phosphoproteins: structural specificity of the osteopontin-mediated inhibition of hydroxyapatite formation, *Biochem. J.,* 300, 723, 1994.
156. Gilman, H. and Hukins, D. W., Seeded growth of hydroxyapatite in the presence of dissolved albumin, *J. Inorg. Biochem.,* 55, 21, 1994.
157. Gilman, H. and Hukins, D. W., Seeded growth of hydroxyapatite in the presence of dissolved albumin at constant composition, *J. Inorg. Biochem.,* 55, 31, 1994.
158. Goldberg, H. A. and Hunter, G. K., The inhibitory activity of osteopontin on hydroxyapatite formation in vitro, *Ann. N.Y. Acad. Sci.,* 760, 305, 1995.
159. Boskey, A. L., Osteopontin and related phosphorylated sialoproteins: effects on mineralization, *Ann. N.Y. Acad. Sci.,* 760, 249, 1995.
160. Schinke, T., Amendt, C., Trindl, A., Poschke, O., Muller-Esterl, W., and Jahnen-Dechent, W., The serum protein 2-HS glycoprotein/fetuin inhibits apatite formation in vitro and in mineralizing calvaria cells. A possible role in mineralization and calcium homeostasis, *J. Biol. Chem.,* 271, 20789, 1996.
161. Hunter, G. K., Hauschka, P. V., Poole, A. R., Rosenberg, L. C., and Goldberg, H. A., Nucleation and inhibition of hydroxyapatite formation by mineralized tissue proteins, *Biochem. J.,* 317, 59, 1996.
162. Boskey, A. L., Spevak, M., Doty, S., and Rosenberg, L., Effects of bone proteoglycans, decorin and biglycan on hydroxyapatite formation in a gelatin gel, *Calcif. Tissue Int.,* 61, 298, 1997.
163. Stubbs, J. T. III, Mintz, K. P., Eanes, E. D., Torchia, D. A., and Fisher, L. W., Characterization of native and recombinant bone sialoprotein: delineation of the mineral-binding and cell adhesion domains and structural analysis of the RGD domain, *J. Bone Miner. Res.,* 12, 1210, 1997.
164. Sfeir, C. and Veis, A., Casein kinase localization in the endoplasmic reticulum of the ROS17/2.8 cell line, *J. Bone Miner. Res.,* 10, 607, 1995.
165. Worcester, E. M., Blumenthal, S. S., Beshensky, A. M., and Lewand, D. L., The calcium oxalate crystal growth inhibitor protein produced by mouse kidney cortical cells in culture is osteopontin, *J. Bone Miner. Res.,* 7, 1029, 1992.
166. Luo, G., Ducy, P., McKee, M. D., Pinero, G. J., Loyer, E., Behringer, R. R., and Karsenty, G., Spontaneous calcification of arteries and cartilage in mice lacking matrix GLA protein, *Nature,* 386, 78, 1997.
167. Cole, W. G., The Nicholas Andry Award–1996. The molecular pathology of osteogenesis imperfecta, *Clin. Orthop.,* 343, 235, 1997.
168. Fisher, L. W., Eanes, E. D., Denholm, L. J., Heywood, B. R., and Termine, J. D., Two bovine models of osteogenesis imperfecta exhibit decreased apatite crystal size, *Calcif. Tissue Int.,* 40, 282, 1987.
169. Vetter, U., Eanes, E. D., Kopp, J. B., Termine, J. D., and Gehron Robey, P., Changes in apatite crystal size in bones of patients with osteogenesis imperfecta, *Calcif. Tissue Int.,* 49, 248, 1991.
170. Traub, W., Arad, T., and Weiner, S., Origin of mineral crystal growth in collagen fibrils, *Matrix,* 12, 251, 1992.
171. Merganhagen, S. E., Martin, G. R., Rizzo, A. A., and Glimcher, M. J., Calcification *in vivo* of implanted collagens, *Biochim. Biophys. Acta,* 43, 563–565, 1960.
172. Blumenthal, N. C., Cosma, V., and Gomes, E., Regulation of hydroxyapatite formation by gelatin and type I collagen gels, *Calcif. Tissue Int.,* 48, 440, 1991.
173. Termine, J. D., Kleinman, H. K., Whitson, S. W., Conn, K. M., McGarvey, M. L., and Martin, G. R., Osteonectin, a bone-specific protein linking mineral to collagen, *Cell,* 26, 99, 1981.

174. Endo, A., Potential role of phosphoprotein in collagen mineralization—an experimental study in vitro, *J. Orthop. Assoc.,* 61, 563–569, 1987.
175. Veis, A., Mineral-matrix interactions in bone and dentin, *J. Bone Miner. Res.,* 8, S493, 1993.
176. Knott, L. and Bailey, A. J., Collagen cross-links in mineralizing tissues: a review of their chemistry, function, and clinical relevance, *Bone,* 22, 181, 1998.
177. Gerstenfeld, L. C., Riva, A., Hodgens, K., Eyre, D. R., and Landis, W. J., Post-translational control of collagen fibrillogenesis in mineralizing cultures of chick osteoblasts, *J. Bone Miner. Res.,* 8, 1031, 1993.
178. Reddi, A. H. and Sullivan, N. E., Inhibition of mineralization by experimental lathyrism during matrix-induced endochondral bone differentiation. *Proc. Soc. Exp. Biol. Med.,* 162, 445, 1979.
179. Chen, Y., Bal, B. S., and Gorski, J. P., Calcium and collagen binding properties of osteopontin, bone sialoprotein, and bone acidic glycoprotein-75 from bone, *J. Biol. Chem.,* 267, 24871, 1992.
180. Robey, P. G. and Boskey, A. L., The biochemistry of bone, in *Osteoporosis,* Marcus, R., Feldman, D., and Kelsey, J., Eds., Academic Press, San Diego, 1996, 95.
181. McKee, M. D. and Nanci, A., Postembedding colloidal-gold immunocytochemistry of noncollagenous extracellular matrix proteins in mineralized tissues, *Microsc. Res. Tech.,* 31, 44, 1995.
182. Hunter, G. K. and Goldberg, H. A., Nucleation of hydroxyapatite by bone sialoprotein, *P.N.A.S. U.S.,* 90, 8562, 1993.
183. Chen, J., Shapiro, H. S., Wrana, S. R., Heersche, J. N. M., and Sodek, J., Localization of bone sialoprotein (BSP) expression to sites of mineralized tissue formation in fetal rat tissues by in situ hybridization, *Matrix,* 11, 133–143, 1993.
184. Riminucci, M., Bradbeer, J. N., Corsi, A., Gentili, C., Descalzi, F., Cancedda, R., and Bianco, P., Vis-a-vis cells and the priming of bone formation, *J. Bone Miner. Res.,* 13, 1852, 1998.
185. Boskey, A. L., Maresca, M., Doty, S., Sabsay, B., and Veis, A., Concentration-dependent effects of dentin phosphophoryn in the regulation of in vitro hydroxyapatite formation and growth, *Bone Miner.,* 11, 55, 1990.
186. Boskey, A. L., The role of extracellular matrix components in dentin mineralization, *Crit. Rev. Oral Biol. Med.,* 2, 369, 1991.
187. Linde, A., Lussi, A., and Crenshaw, M. A., A mineral induction by immobilized polyanionic proteins, *Calcif. Tissue Int.,* 44, 286–295, 1989.
188. Doi, Y., Horiguchi, T., Kim, S. H., Moriwaki, Y., Wakamatsu, N., Adachi, M., Shigeta, H., Sasaki, S., and Shimokawa, H., Immobilized DPP and other proteins modify OCP formation, *Calcif. Tissue Int.,* 52, 139, 1993.
189. Gorski, J. P., Kremer, E. A., Chen, Y., Ryan, S., Fullenkamp, C., Delviscio, J., Jensen, K., and McKee, M. D., Bone acidic glycoprotein-75 self-associates to form macromolecular complexes in vitro and in vivo with the potential to sequester phosphate ions, *J. Cell Biochem.,* 64, 547, 1997.
190. Kaartinen, M. T., Pirhonen, A., Linnala-Kankkunen, A., and Maenpas, P. H., Transglutaminase-catalyzed cross-linking of osteopontin is inhibited by osteocalcin, *J. Biol. Chem.,* 272, 22736, 1997.
191. Zhou, H. Y., Salih, E., and Glimcher, M. J., Isolation of a novel bone glycosylated phosphoprotein with disulphide cross-links to osteonectin, *Biochem. J.,* 330, 1423, 1998.
192. Scott, P. G. and Haigh, M., Proteoglycan type I collagen fibril interactions in bone and non-calcifying connective tissues, *Biosci. Rep.,* 5, 71, 1985.
193. Glimcher, M. J., Mechanisms of calcification in bone: role of collagen fibrils and collagen-phosphoprotein complexes in vitro and in vivo, *Anat. Rec.,* 224, 139, 1989.
194. Fujisawa, R. and Kuboki, Y., Affinity of bone sialoprotein and several other bone and dentin acidic proteins to collagen fibrils, *Calcif. Tissue Int.,* 51, 438, 1992.
195. Kirsch, T., Ishikawa, Y., Mwale, F., and Wuthier, R. E., Roles of the nucleational core complex and collagens (types II and X) in calcification of growth plate cartilage matrix vesicles, *J. Biol. Chem.,* 269, 20103, 1994.

196. Wu, L. N., Genge, B. R., Dunkelberger, D. G., LeGeros, R. Z., Concannon, B., and Wuthier, R. E., Physicochemical characterization of the nucleational core of matrix vesicles, *J. Biol. Chem.,* 272, 4404, 1997.
197. Boskey, A. L. and Posner, A. S., The role of synthetic and bone extracted Ca-phospholipid-PO_4 complexes in hydroxyapatite formation, *Calcif. Tissue Res.,* 20, 23, 1978.
198. Raggio, C. L., Boyan, B. D., and Boskey, A. L., In vivo hydroxyapatite formation induced by lipids, *J. Bone Miner. Res.,* 1, 409, 1986.
199. von der Mark, K. and Mollenhauer, J., Annexin V interactions with collagen, *Cell Mol. Life Sci.,* 53, 539, 1997.
200. Gerstenfeld, L. C., Chipman, S. D., Kelly, C. M., Hodgens, K. J., Lee, D. D., and Landis, W. J., Collagen expression, ultrastructural assembly, and mineralization in cultures of chicken embryo osteoblasts, *J. Cell Biol.,* 106, 979, 1988.
201. Gerstenfeld, L. C., Uporova, T., Schmidt, J., Strauss, P. G., Shih, S. D., Huang, L. F., Gundberg, C., Mizuno, S., and Glowacki, J., Osteogenic potential of murine osteosarcoma cells: comparison of bone-specific gene expression in in vitro and in vivo conditions, *Lab. Invest.,* 74, 895, 1996.
202. Ecarot-Charrier, B., Shepard, N., Charette, G., Grynpas, M., and Glorieux, F. H., Mineralization in osteoblast cultures: a light and electron microscopic study, *Bone,* 9, 147, 1988.
203. Boskey, A. L., Stiner, D., Doty, S. B., Binderman, I., and Leboy, P., Studies of mineralization in tissue culture: optimal conditions forcartilage calcification, *Bone Miner.,* 16, 11, 1992.
204. Pockwinse, S. M., Wilming, L. G., Colon, D. M., Stein, G. S., and Lian, J. B., Expression of cell growth and bone specific genes at single cell resolution during development of bone tissue like organization in primary osteoblastic cultures, *J. Cell Biochem.,* 49, 310, 1992.
205. Ohgushi, H., Dohi, Y., Katuda, T., Tamai, S., Tabata, S., and Suwa, Y., In vitro bone formation by rat marrow cell culture, *J. Biomed. Mater. Res.,* 32, 333, 1996.
206. Collignon, H., Davicco, M. J., and Barlet, J. P., Isolation of cells from ovine fetal long bone and characterization of their osteoblastic activities during in vitro mineralization, *Arch. Physiol. Biochem.,* 105, 158, 1997.
207. Yao, K. L., Todescan, R., Jr., and Sodek, J., Temporal changes in matrix protein synthesis and mRNA expression during mineralized tissue formation by adult rat bone marrow cells in culture, *J. Bone Miner. Res.,* 9, 231, 1994.
208. Cowles, E. A., DeRome, M. E., Pastizzo, G., Brailey, L. L., and Gronowicz, G. A., Mineralization and the expression of matrix proteins during in vivo bone development, *Calcif. Tissue Int.,* 62, 74, 1998.
209. Kuboki, Y., Kudo, A., Mizuno, M., and Kawamura, M., Time-dependent changes of collagen cross-links and their precursors in the culture of osteogenic cells, *Calcif. Tissue Int.,* 50, 473, 1992.
210. Boskey, A. L., Guidon, P., Doty, S. B., Stiner, D., Leboy, P., and Binderman, I., The mechanism of β-glycerophosphate action in mineralizing chick limb-bud mesenchymal cell cultures, *J. Bone Miner. Res.,* 11, 1694, 1996.
211. Boskey, A. L., Stiner, D., Binderman, I., and Doty, S. B., The effects of proteoglycan modification on mineral formed in a differentiating chick limb-bud culture system, *J. Cell. Biochem.,* 64, 632, 1997.
212. Blumberg, P., Brenner, R., Budny, S., and Kresse, H., Increased turnover of small proteoglycans synthesized by human osteoblasts during cultivation with ascorbate and β-glycerophosphate, *Calcif. Tissue Int.,* 60, 554, 1997.
213. Chipman, S. D., Sweet, H. O., McBride, D. J., Jr., Davisson, M. T., Marks, S. C., Jr., Shuldiner, A. R., Wenstrup, R. J., Rowe. D. W., and Shapiro, J. R., Defective pro α 2(I) collagen synthesis in a recessive mutation in mice: a model of human osteogenesis imperfecta, *Proc. Natl. Acad. Sci. U.S.A.,* 90, 1701, 1993.
214. Stacey, A., Bateman, J., Choi, T., Mascara, T., Cole, W., and Jaenisch, R., Perinatal lethal osteogenesis imperfecta in transgenic mice bearing an engineered mutant pro-α1(I) collagen gene, *Nature,* 332, 131, 1988.

215. Schnieke, A., Dziadek, M., Bateman, J., Mascara, T., Harbers, K., Gelinas, R., and Jaenisch, R., Introduction of the human pro α 1(I) collagen gene into pro α 1(I)-deficient Mov-13 mouse cells leads to formation of functional mouse-human hybrid type I collagen, *Proc. Natl. Acad. Sci. U.S.A.,* 84, 764, 1987.
216. Sillence, D. O., Ritchie, H. E., Dibbayawan, T., Eteson, D., and Brown, K., Fragilitas ossium (fro/fro) in the mouse: a model for a recessive inherited type of osteogenesis imperfecta, *Am. J. Med. Genet.,* 45, 276, 1993.
217. Soriano, P., Montgomery, C., Geske, R., and Bradley, A., Targeted disruption of the c-src proto-oncogene leads to osteopetrosis in mice, *Cell,* 64, 693, 1991.
218. Jacenko, O., LuValle, P. A., and Olsen, B. R., Spondylometaphyseal dysplasia in mice carrying a dominant negative mutation in a matrix protein specific for cartilage-to-bone transition, *Nature,* 365, 56, 1993.
219. Rosati, R., Horan, G. S., Pinero, G. J., Garofalo, S., Keene, D. R., Horton, W. A., Vuorio, E., de Crombrugghe, B., and Behringer, R. R., Normal long bone growth and development in type X collagen-null mice, *Nat. Genet.,* 8, 129, 1994.
220. Ducy, P., Desbois, C., Boyce, B., Pinero, G., Story, B., Dunstan, C., Smith, E., Bonadio, J., Goldstein, S., Gundberg, C., Bradley, A., and Karsenty, G., Increased bone formation in osteocalcin-deficient mice, *Nature,* 382, 448, 1996.
221. Malone, J. D., Teitelbaun, S. L., Griffin, G. L., Senior, R. M., and Kahn, A. J., Recruitment of osteoclast precursors by purified bone matrix constituents, *J. Cell Biol.* 92, 227, 1982.
222. Glowacki, J. and Lian, J. B., Impaired recruitment and differentiation of osteoclast progenitors by osteocalcin-depleted bone implants, *Cell Differ.,* 21, 247, 1987.
223. Chenu, C., Colucci, S., Grano, M., Zigrino, P., Barattolo, R., Zambonin, G., Baldini, N., Vergnaud, P., Delmas, P. D., and Zallone, A. Z., Osteocalcin induces chemotaxis, secretion of matrix proteins, and calcium-mediated intracellular signaling in human osteoclast-like cells, *J. Cell Biol.,* 127, 1149, 1994.
224. Shaw, N. J., Rehan, V. K., Husain, S., Marshall, T., and Smith, C. S., Bone mineral density in Turner's syndrome—a longitudinal study, *Clin. Endocrinol.* (Oxford), 47, 367, 1997.
225. Heegaard, A. M., Gehron Robey, P., Vogel, W., Just, W., Widom, R. L., Scholler, J., and Fisher, L. W., Functional characterization of the human biglycan 5' flanking DNA and binding of the transcription factor c-Krox, *J. Bone Miner. Res.,* 12, 2050, 1997.
226. Rittling, S. R., Matsumoto, H. N., McKee, M. D., Nanci, A., An, X. R., Novick, K. E., Kowalski, A. J., Noda, M., and Denhardt, D. T., Mice lacking osteopontin show normal development and bone structure but display altered osteoclast formation in vitro, *J. Bone Miner. Res.,* 13, 1101, 1998.
227. Glorieux, F. H. and St-Arnaud, R., Molecular cloning of (25-OH D)-1 α-hydroxylase: an approach to the understanding of vitamin D pseudo-deficiency, *Recent Prog. Horm. Res.,* 53, 341, 1998.
228. Jena, N., Martin-Seisdedos, C., McCue, P., and Croce, C. M., BMP7 null mutation in mice: developmental defects in skeleton, kidney, and eye, *Exp. Cell Res.,* 230, 28, 1997.
229. Yamashita, T., Nifuji, A., Furuya, K., Nabeshima, Y., and Noda, M., Elongation of the epiphyseal trabecular bone in transgenic mice carrying a klotho gene locus mutation that leads to a syndrome resembling aging, *J. Endocrinol.,* 159, 1, 1998.
230. Gilmour, D. T., Lyon, G. J., Carlton, M. B., Sanes, J. R., Cunningham, J. M., Anderson, J. R., Hogan, B. L., Evans, M. J., and Colledge, W. H., Mice deficient for the secreted glycoprotein SPARC/osteonectin/BM40 develop normally but show severe age-onset cataract formation and disruption of the lens, *EMBO J.,* 17, 1860, 1998.
231. Paschalis, E. P., Betts, F., DiCarlo, E., Mendelsohn, R., and Boskey, A. L., FTIR microspectroscopic analysis of normal human cortical and trabecular bone, *Calcif. Tissue Int.,* 61, 480, 1997.
232. Glowacki, J., Rey, C., Glimcher, M. J., Cox, K. A., and Lian, J., A role for osteocalcin in osteoclast differentiation, *J. Cell Biochem.,* 45, 292, 1991.

233. Ingram, R. T., Park, Y. K., Clarke, B. L., and Fitzpatrick, L. A., Age- and gender-related changes in the distribution of osteocalcin in the extracellular matrix of normal male and female bone. Possible involvement of osteocalcin in bone remodeling, *J. Clin. Invest.,* 93, 989, 1994.
234. Lacey, D. L., Timms, E., Tan, H. L., Kelley, M. J., Dunstan, C. R., Burgess, T., Elliott, R., Colombero, A., Elliott, G., Scully, S., Hsu, H., Sullivan, J., Hawkins, N., Davy, E., Capparelli, C., Eli, A., Qian, Y. X., Kaufman, S., Sarosi, I., Shalhoub, V., Senaldi, G., Guo, J., Delaney, J., and Boyle, W. J., Osteoprotegerin ligand is a cytokine that regulates osteoclast differentiation and activation, *Cell,* 93, 165, 1998.
235. Innis, J. W. and Mortlock, D. P., Limb development: molecular dysmorphology is at hand! *Clin. Genet.,* 53, 337, 1998.
236. Augustine, K., Liu, E. T., and Sadler, T. W., Antisense attenuation of Wnt-1 and Wnt-3a expression in whole embryo culture reveals roles for these genes in craniofacial, spinal cord, and cardiac morphogenesis, *Dev. Genet.,* 14, 500, 1993.
237. Aubin, J., Lemieux, M., Tremblay, M., Behringer, R. R., and Jeannotte, L., Transcriptional interferences at the Hoxa4/Hoxa5 locus: importance of correct Hoxa5 expression for the proper specification of the axial skeleton, *Dev. Dyn.,* 212, 141, 1998.
238. ten Berge, D., Brouwer, A., Korving, J., Martin, J. F., and Meijlink, F., Prx1 and Prx2 in skeletogenesis: roles in the craniofacial region, inner ear and limbs, *Development,* 125, 3831, 1998.
239. Chow, J. W., Wilson, A. J., Chambers, T. J., and Fox, S. W., Mechanical loading stimulates bone formation by reactivation of bone lining cells in 13-week-old rats, *J. Bone Miner. Res.,* 13, 1760, 1998.
240. McLeod, K. J., Rubin, C. T., Otter, M. W., and Qin, Y. X., Skeletal cell stresses and bone adaptation, *Am. J. Med. Sci.,* 316, 176, 1998.
241. Meade, J. B., Cowin, S. C., Klawitter, J. J., Van Buskirk, W. C., and Skinner, H. B., Bone remodeling due to continuously applied loads, *Calcif. Tissue Int.,* 36, S25, 1984.

II

Techniques from Mechanics and Imaging

6

Mechanics of Materials*

Stephen C. Cowin
The City College of New York

6.1 Introduction

6.1.1 Bone and the Science of Mechanics

The discipline of mechanics is the physical science that deals with the effects of forces on objects. The concern here is with the mechanics of deformable objects, in particular, bone. Bones are physical objects that obey the laws of mechanics. The primary laws of mechanics that concern deformable objects like bone are the three laws of motion by Sir Isaac Newton in 1687 and the law of elasticity of solid materials described by Robert Hooke in 1678. The following three Newtonian laws are the basis of classical mechanics:

1. A body remains at rest or moves at a constant speed in a straight line unless acted on by a force. This is a statement of the principle of inertia.

*This chapter is a revision of Chapter 2 of *Bone Mechanics Handbook,* Cowin, Stephen C., Ed., CRC Press, Boca Raton, FL, 1989. With permission.

0-8493-9117-2/01/$0.00+$.50

2. The total force acting on a body is equal to the mass of the body times its acceleration; that is, $\mathbf{f} = m\mathbf{a}$, where $\mathbf{f}$ and $\mathbf{a}$ are vectors oriented in the same direction.
3. If a body exerts a force on a second body, the second body exerts a force on the first body that is equal in magnitude and opposite in direction to the first force. This is the law of action and reaction.

Hooke's law states that there is a linear relation between the force and deformation of a solid object. The laws of Newton and Hooke form the foundation of the mechanics of elastic objects. The mechanical behavior of bone in normal physiological situations is quite similar to the mechanical behavior of an elastic object.

6.1.2 Objective and Organization

The purpose of this chapter is to provide background information that will be used in subsequent chapters. The material covered ranges from elements of the mechanics as presented in a university-level physics course to the elements of the theory of elasticity, which is generally a graduate-level course. In the presentation of this background information, there is a great emphasis on materials with a type of anisotropy called orthotropy. A material is anisotropic when its properties differ with direction but isotropic if its properties are the same in all directions. The most common example of an orthotropic material is wood. The properties of wood are different along the grain from what they are transverse to the growth rings and different again from what they are along the near circular path following a growth ring.

The presentation is descriptive. The proofs of results are not presented. All but the last two sections have been written so that someone with some knowledge of a university-level general physics course and elementary vector and matrix algebra should not have to seek supplementary references. The last two sections contain some material from the theory of elasticity and involve the use of derivatives. The mechanics of orthotropic elastic materials are discussed in the books by Lekhnitskii,[1] Hearmon,[2] and Jones.[3]

6.2 Force and Vectors

6.2.1 Force

The primary physical entity in mechanics is force; force is used to represent the action of one object on another. There are two kinds of force, a kind that exerts its action by direct contact and a kind that exerts its action at a distance, such as gravitational or electromagnetic force. A force is characterized by its point of application, its magnitude, and its direction. A force is represented mathematically by a vector. The unit of force in the SI system is the newton (N) and the unit in U.S. customary units is the pound (lb). Since forces are represented as vectors, attention is turned to vectors.

6.2.2 Vectors

Vectors will be represented wherever possible as boldface lowercase Latin letters, for example, $\mathbf{f}$. The sum or the resultant of two vectors $\mathbf{a}$ and $\mathbf{b}$ acting at a point is denoted by $\mathbf{a} + \mathbf{b}$ and is determined by the parallelogram law of addition. A vector of magnitude or length 1 is a unit vector. Any vector may be written as the product of its magnitude and a unit vector in the same direction as the vector. For example, if $\mathbf{n}$ is a unit vector in the direction of $\mathbf{f}$, then $\mathbf{f} = f\mathbf{n}$ where f is the magnitude or length of the vector $\mathbf{f}$, $f = |\mathbf{f}|$. The scalar or dot product of two vectors $\mathbf{a}$ and $\mathbf{b}$ is denoted by $\mathbf{a} \cdot \mathbf{b}$. The value of a scalar product is a scalar equal to the magnitude of $\mathbf{a}$ times the magnitude of $\mathbf{b}$ times the cosine of the angle between $\mathbf{a}$ and $\mathbf{b}$,

$$\mathbf{a} \cdot \mathbf{b} = ab\cos\theta, \tag{6.1}$$

where a and b are the magnitudes of **a** and **b**, respectively, and where θ denotes the angle less then 180° between **a** and **b**. Note that the magnitude of a vector **a** is given by $a = |\mathbf{a}| = \sqrt{\mathbf{a} \cdot \mathbf{a}}$.

It is very useful to resolve vectors into rectangular components. This is done by introducing a Cartesian basis. In three dimensions, a Cartesian basis is determined by three mutually perpendicular unit vectors. Let these three unit vectors be denoted by $\mathbf{e}_1$, $\mathbf{e}_2$, and $\mathbf{e}_3$, where

$$\mathbf{e}_1 \cdot \mathbf{e}_1 = \mathbf{e}_2 \cdot \mathbf{e}_2 = \mathbf{e}_3 \cdot \mathbf{e}_3 = 1, \qquad \mathbf{e}_1 \cdot \mathbf{e}_2 = \mathbf{e}_2 \cdot \mathbf{e}_3 = \mathbf{e}_1 \cdot \mathbf{e}_3 = 0. \tag{6.2}$$

The projections of the vector **f** in each of the three directions $\mathbf{e}_1$, $\mathbf{e}_2$, and $\mathbf{e}_3$ are denoted by f_1, f_2, and f_3, respectively. Using the definition of the scalar product and unit vector given above it is easy to see that

$$f_1 = \mathbf{f} \cdot \mathbf{e}_1, \qquad f_2 = \mathbf{f} \cdot \mathbf{e}_2, \qquad f_3 = \mathbf{f} \cdot \mathbf{e}_3; \tag{6.3}$$

thus, for example, f_1 is the product of the magnitude f of **f** with the cosine of the angle between **f** and $\mathbf{e}_1$. It follows then that the vector **f** can be reconstructed from its projections,

$$\mathbf{f} = f_1\mathbf{e}_1 + f_2\mathbf{e}_2 + f_3\mathbf{e}_3\,. \tag{6.4}$$

The scalars f_1, f_2, and f_3 are the *components* of the vector **f** relative to the Cartesian basis $\boldsymbol{e}_1$, $\mathbf{e}_2$, and $\mathbf{e}_3$. The scalar product of two vectors **a** and **b**,

$$\mathbf{a} = a_1\mathbf{e}_1 + a_2\mathbf{e}_2 + a_3\mathbf{e}_3, \qquad \mathbf{b} = b_1\mathbf{e}_1 + b_2\mathbf{e}_2 + b_3\mathbf{e}_3, \tag{6.5}$$

is then given by

$$\mathbf{a} \cdot \mathbf{b} = a_1b_1 + a_2b_2 + a_3b_3, \tag{6.6}$$

when the results (Eq. 6.2) have been employed.

The vector product of two vectors **a** and **b** is denoted by $\mathbf{a} \times \mathbf{b}$ and is defined as

$$\mathbf{a} \times \mathbf{b} = (ab\sin\theta)\mathbf{n} \tag{6.7}$$

where θ is the angle less than 180° between **a** and **b**, and the unit vector **n** is perpendicular to the plane containing **a** and **b** in the direction given by the right-hand rule. The right-hand rule may be stated as follows: the fingers of the right hand are extended in the direction of **a**. The hand is then rotated through the angle θ to point in the direction **b**. The direction of **n** is indicated by the thumb of the right hand if the thumb is held perpendicular to the fingers of the right hand. The cross product of two vectors can be expressed in terms of a determinant,

$$\mathbf{a} \times \mathbf{b} = \begin{vmatrix} \mathbf{e}_1 & \mathbf{e}_2 & \mathbf{e}_3 \\ a_1 & a_2 & a_3 \\ b_1 & b_2 & b_3 \end{vmatrix}, \tag{6.8}$$

or by

$$\mathbf{a} \times \mathbf{b} = (a_2b_3 - a_3b_2)\mathbf{e}_1 + (a_3b_1 - a_1b_3)\mathbf{e}_2 + (a_1b_2 - a_2b_1)\mathbf{e}_3, \tag{6.9}$$

which can be obtained by expansion of the determinant.

6.2.3 Mechanical Equilibrium

Consider an object that is either not moving or moving with constant velocity. The object is subjected to a system of N forces denoted by $\mathbf{f}^{(1)}$, $\mathbf{f}^{(2)}, \ldots,$ $\mathbf{f}^{(N)}$. To satisfy the second law of Newton it is necessary that the sum of the forces acting on the object be zero,

$$\sum_{i=1}^{N} \mathbf{f}^{(i)} = \mathbf{f}^{(1)} + \mathbf{f}^{(2)} + \cdots + \mathbf{f}^{(N)} = 0. \tag{6.10}$$

This is the condition of force equilibrium for an object. To ensure complete equilibrium the object must also satisfy a condition of moment equilibrium. To obtain the condition of moment equilibrium, a point is selected and a system of vectors $\mathbf{r}^{(1)}$, $\mathbf{r}^{(2)}$, …, $\mathbf{r}^{(N)}$ from the selected point to the point of application of each force $\mathbf{f}^{(1)}$, $\mathbf{f}^{(2)}$, …, $\mathbf{f}^{(N)}$ is constructed. The vectors $\mathbf{r}^{(1)}$, $\mathbf{r}^{(2)}$, …, $\mathbf{r}^{(N)}$ are called the position vectors of the forces $\mathbf{f}^{(1)}$, $\mathbf{f}^{(2)}$, …, $\mathbf{f}^{(N)}$. The *moment* of the force $\mathbf{f}^{(1)}$ with respect to the selected point is given by the vector cross product of $\mathbf{r}^{(1)}$ with $\mathbf{f}^{(1)}$, $\mathbf{r}^{(1)}\mathbf{f}^{(1)}$. The sum of all the moments of all the forces with respect to the selected point is given by

$$\sum_{i=1}^{N} \mathbf{r}^{(i)} \times \mathbf{f}^{(i)} = \mathbf{r}^{(1)} \times \mathbf{f}^{(1)} + \mathbf{r}^{(2)} \times \mathbf{f}^{(2)} + \cdots + \mathbf{r}^{(N)} \times \mathbf{f}^{(N)}. \tag{6.11}$$

If the object in equilibrium is subjected to a set of applied couples $\mathbf{c}^{(1)}$, $\mathbf{c}^{(2)}$, …, $\mathbf{c}^{(M)}$ as well as the set of applied forces, then the condition for moment equilibrium is given by

$$\sum_{i=1}^{N} \mathbf{r}^{(i)} \times \mathbf{f}^{(i)} + \sum_{k=1}^{M} \mathbf{c}^{(k)} = 0. \tag{6.12}$$

An object whose applied forces and couples satisfy Eqs. 6.10 and 6.12 is said to be in *mechanical equilibrium*.

6.3 Stresses and Matrices

6.3.1 Normal Stresses and Shear Stresses

Stresses are mental constructs used to represent internal interactions or internal forces in an object. They are forces per unit area and are obtained by dividing forces by the areas over which they act. The unit of stress in the SI system is a pascal (Pa) which is one newton (N) per square meter (m^2) or $\mathrm{N/m}^2$. The pascal is a very small unit and is impractical for most applications. Multiples of this unit are employed in practice. These multiples include the kilopascal (kPa), the megapascal (MPa), and the gigapascal (GPa). The kilopascal is 10^3 Pa or 10^3 $\mathrm{N/m}^2$, the megapascal is 10^6 Pa or 10^6 $\mathrm{N/m}^2$, and the gigapascal is 10^9 Pa or 10^9 $\mathrm{N/m}^2$. Physiological stress levels in bone are generally at or below the MPa range because a bone breaks in the MPa range. The unit of stress in the U.S. customary unit system is pounds (lb) per square inch $(\mathrm{in.}^2)$ or psi. One psi is approximately 7 kPa, but it is exactly 6.895 kPa or 6895 Pa. Atmospheric pressure is 14.7 psi or 101.36 kPa or 0.1014 MPa.

A proper definition of stress requires that the orientation of the involved area be described by a unit vector perpendicular to the area. Since the force is also described by a vector, the definition of a stress is dependent upon two vectors, one describing the orientation of the area over which the stress acts and one characterizing the direction of the force. When two vectors are in the same direction so that the applied force is perpendicular to the area over which it acts, the stress is said to be a *normal stress*. This situation is illustrated in Fig. 6.1A. When the two vectors are perpendicular so that the applied force lies

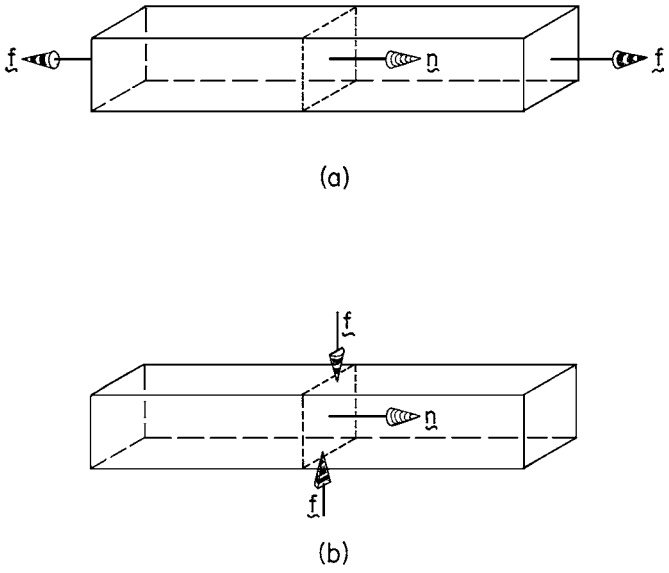

FIGURE 6.1 An illustration of the two-vector character of stress. The orientation of the area across which the force acts is characterized by a unit vector **n** and the force **f**, which is itself a vector. (A) The stress is called a normal stress if **n** and **f** are parallel. (B) The stress is called a shear stress if **n** and **f** are perpendicular. (From Cowin, S. C., *Bone Mechanics Handbook,* CRC Press, Boca Raton, FL, 1989. With permission.)

in the plane of the area over which it is acting, the stress is said to be a *shearing stress*. This situation is illustrated in Fig. 6.1B.

Consider an object acted upon by a system of forces as shown in Fig. 6.2A. An imaginary plane characterized by its normal **n** is passed through a point P in the object, dividing it into two parts. The action of the right portion of the object upon the left portion is represented by the force **f** as shown in Fig. 6.2B, where the right portion of the object has been removed. A sequence of decreasing areas $\Delta A_{(n)}$, all containing the point P as they shrink down to P, is considered. To develop the concept of stress in a Cartesian component form, a Cartesian basis $\mathbf{e}_1$, $\mathbf{e}_2$, $\mathbf{e}_3$ is introduced so that $\mathbf{e}_1$ is coincident with the normal **n** to the plane. This is illustrated in Fig. 6.2C. The force **f** is then decomposed relative to the Cartesian basis as shown in Fig. 6.2C. The sequence of decreasing areas is now denoted by ΔA_1 since the normal to the plane is in the $\mathbf{e}_1$ direction. The normal stress T_{11} and the shear stresses T_{12} and T_{13} are then defined by

$$T_{11} = \lim_{\Delta A_1 \to 0} \frac{f_1}{\Delta A_1}, \qquad T_{12} = \lim_{\Delta A_1 \to 0} \frac{f_2}{\Delta A_1}, \qquad T_{13} = \lim_{\Delta A_1 \to 0} \frac{f_3}{\Delta A_1}. \tag{6.13}$$

If two more planes are passed through the point P, one whose normal is in the $\mathbf{e}_2$ direction and one whose normal is in the $\mathbf{e}_3$ direction, then the Cartesian stress components T_{21}, T_{22}, T_{23} and T_{31}, T_{32}, T_{33}, respectively, are obtained. The notation **T** is introduced for the matrix formed by these nine stress components,

$$\boldsymbol{T} = \begin{bmatrix} T_{11} & T_{12} & T_{13} \\ T_{21} & T_{22} & T_{23} \\ T_{31} & T_{32} & T_{33} \end{bmatrix}. \tag{6.14}$$

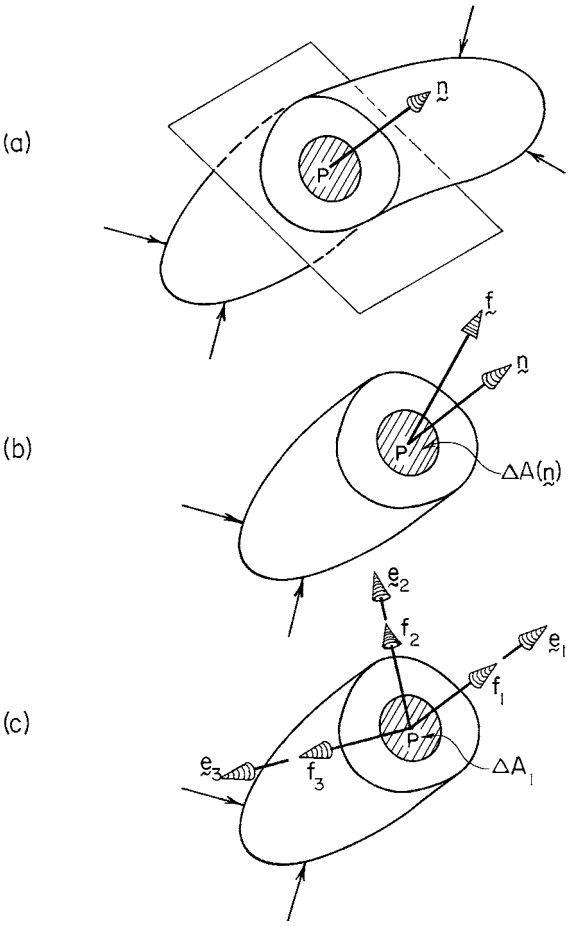

FIGURE 6.2 An illustration for the definition of stress. (A) An object bisected by a plane, whose normal is **n** and which passes through the point *P*, that divides the object into two parts. (B) The action of the removed right portion of the object on the remaining left portion of the object is represented by a force **f**. (C) The force **f** is decomposed into one component perpendicular to the plane and two lying in the plane. (From Cowin, S. C., *Bone Mechanics Handbook,* CRC Press, Boca Raton, FL, 1989. With permission.)

More precisely, **T** is the matrix of the Cartesian components of the stress tensor, but for brevity it will be called the stress matrix. A tensor is an abstract mathematical quantity of great importance in physics. Its importance in physics is due to the fact that it represents physical quantities in a manner that is independent of the observer's Cartesian basis. The matrix of components of the tensor given by Eq. 6.14 is like a shadow of the tensor. The tensor will have such a matrix component representation for every Cartesian basis, and each matrix component representation will generally be different and distinct as the Cartesian basis is distinct, but the tensor will be the same. Thus, the shadows the same tensor casts on different Cartesian bases will be different. Since the tensorial concept is abstract, it will be described again in a slightly different way. A tensor is a quantity that has a representation of the type of Eq. 6.14 for each Cartesian basis, and as the Cartesian basis is changed, the representation of the type (Eq. 6.14) changes in such a way that the tensor itself is unchanged. That is to say, the physical significance of a tensor is independent of the particular Cartesian basis used to express its components. This property was first understood for stress; hence, the name *tensor* comes from the Latin for force.

The condition of moment equilibrium, Eq. 6.12, can be shown to require that the stress matrix be symmetric, that is to say

$$\mathbf{T} = \mathbf{T}^T. \tag{6.15}$$

The transpose of a matrix is the matrix obtained by interchanging the first, second, and third row with the first, second, and third column, respectively. In terms of the components of **T**, the condition (Eq. 6.15) of symmetry requires that

$$T_{12} = T_{21}, \qquad T_{13} = T_{31}, \qquad T_{23} = T_{32}. \tag{6.16}$$

Thus, the ordering of the indices on the components of the stress matrix is no longer significant. The condition for force equilibrium will be obtained later because it requires more discussion. During the interval, stresses will be multiplied by areas to obtain forces, and equilibrium will be ensured directly by use of the condition (Eq. 6.10) of force equilibrium.

The stress matrix **T** represents the state of stress at a point *P* in an object. It is necessary to also consider the *stress vectors* **t** that act on planes with normals **n** passing through *P*. For example, the stress vector **t** acting on the plane whose normal is $\mathbf{e}_1$, the situation illustrated in Fig. 6.2C, is given by

$$\mathbf{t}(\text{on } \mathbf{e}_1) = T_{11}\mathbf{e}_1 + T_{12}\mathbf{e}_2 + T_{13}\mathbf{e}_3\,. \tag{6.17}$$

In general, the stress vector **t** at the point *P* acting on the plane whose normal is **n** is given by

$$\mathbf{t} = \mathbf{T}\mathbf{n}, \tag{6.18}$$

or, in explicit matrix notation,

$$\mathbf{t} = \begin{bmatrix} t_1 \\ t_2 \\ t_3 \end{bmatrix} = \begin{bmatrix} T_{11} & T_{12} & T_{13} \\ T_{21} & T_{22} & T_{23} \\ T_{31} & T_{32} & T_{33} \end{bmatrix} \begin{bmatrix} n_1 \\ n_2 \\ n_3 \end{bmatrix}, \tag{6.19}$$

or, in scalar notation,

$$t_1 = T_{11}n_1 + T_{12}n_2 + T_{13}n_3, \quad t_2 = T_{12}n_1 + T_{22}n_2 + T_{23}n_3, \quad t_3 = T_{13}n_1 + T_{23}n_2 + T_{33}n_3. \tag{6.20}$$

The special case (Eq. 6.17) can be recovered by setting $n_1 = 1$ and $n_2 = n_3 = 0$, which is equivalent to setting **n** equal to $\mathbf{e}_1$. The result (Eq. 6.18) shows that the stress vector **t** acting on any plane whose normal is **n** can be obtained from the stress matrix **T** by the mathematically simple operation of matrix multiplication of **n** by **T**.

6.3.2 Matrix Notation

Some matrix notation has already been introduced. The transpose of matrix **T** given by Eq. 6.14 is denoted by $\mathbf{T}^T$ and written as

$$\mathbf{T}^T = \begin{bmatrix} T_{11} & T_{21} & T_{31} \\ T_{12} & T_{22} & T_{32} \\ T_{13} & T_{23} & T_{33} \end{bmatrix}. \tag{6.21}$$

The trace of **T** is denoted by tr**T** and written

$$\text{tr}\mathbf{T} = T_{11} + T_{22} + T_{33}, \tag{6.22}$$

and the determinant of **T** is written as det**T**. The transpose of a product **C** of two matrices **A** and **B**,

$$\mathbf{C} = \mathbf{AB}, \tag{6.23}$$

is given by

$$\mathbf{C}^T = \mathbf{B}^T\mathbf{A}^T, \tag{6.24}$$

and the determinant of **C** by

$$\det\mathbf{C} = (\det\mathbf{A})(\det\mathbf{B}). \tag{6.25}$$

The trace of $\mathbf{C} = \mathbf{AB}$ is given by

$$\mathrm{tr}\mathbf{AB} = A_{11}B_{11} + A_{12}B_{21} + A_{13}B_{31} + A_{21}B_{12} + A_{22}B_{22} + A_{23}B_{32} + A_{31}B_{13} + A_{32}B_{23} + A_{33}B_{33}. \tag{6.26}$$

6.4. Strain

Strain has many similarities to stress, but it is fundamentally a different physical quantity because it is a dimensionless measure of geometric change, while stress is a measure of force per unit area. Normal and shearing strains are concepts parallel to normal and shear stresses, and strain is similar to stress in that it can be represented by a symmetric matrix of tensor components, which are here denoted by **E**:

$$\mathbf{E} = \begin{bmatrix} E_{11} & E_{12} & E_{13} \\ E_{12} & E_{22} & E_{23} \\ E_{13} & E_{23} & E_{33} \end{bmatrix}. \tag{6.27}$$

The elements E_{11}, E_{22}, and E_{33} along the diagonal of this matrix are called normal strains and the off-diagonal elements E_{12}, E_{13}, and E_{23} are called shearing strains. The normal strains are measures of change in length per unit length and shearing strains are one half the change, in radians, of an angle that was originally a right angle. Specifically, the normal strain E_{11} is the change in length per unit length in the $\mathbf{e}_1$ direction due to a deformation. Consider the situation illustrated in Fig. 6.3A. An unloaded bar on the left has length L_1. When a force **f** is applied in the $\mathbf{e}_1$ direction as indicated, the length of the bar changes to $L_1 + \delta_1$, δ_1 being the change in length. The strain E_{11} is defined as

$$E_{11} = \delta_1/L_1. \tag{6.28}$$

The normal strains E_{22} and E_{33} are defined in a similar fashion. The shearing strain E_{12} is defined as one half of the change of a right angle in the plane of $\mathbf{e}_1$ and $\mathbf{e}_2$ due to a deformation. Consider the situation illustrated in Fig. 6.3B and the right angle that is defined initially by $\mathbf{e}_1$ and $\mathbf{e}_2$. A cubic portion of an object is aligned so that its faces are perpendicular to the vectors $\mathbf{e}_1$, $\mathbf{e}_2$, and $\mathbf{e}_3$ of the basis as shown on the left of Fig. 6.3B. The system of forces then distorts the cube so that two of its faces become nonrectangular parallelograms and four of its faces, upon which the forces **f** are applied, remain squares. The angle ψ is the change in alignment of the square faces of the parallelepiped from its original shape. The shearing strain E_{12} is defined as

$$E_{12} = \psi/2. \tag{6.29}$$

The shearing strains E_{13} and E_{23} are defined similarly.

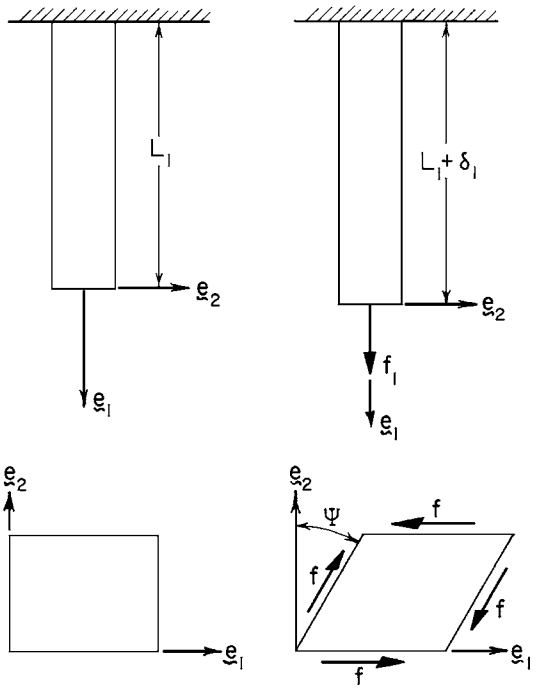

FIGURE 6.3 Illustrations for the definitions of normal and shearing strains. (A) The definition of the normal strain E_{11} is illustrated by the extension of a rectangular bar. (B) The definition of the shearing strain E_{12} is illustrated by a change in angle that was originally a right angle. (From Cowin, S. C., *Bone Mechanics Handbook,* CRC Press, Boca Raton, FL, 1989. With permission.)

From these definitions, it can be seen that it is experimentally possible to measure strains directly because they are determined in terms of lengths and angles. There is no way to measure stress directly. The definitions of strains given above are only valid for small strains. If the strains are greater than 5 or 6%, these definitions must be revised.

6.5 Axial Deformation

6.5.1 The Tensile Test

The most universal test for the purpose of determining the mechanical properties of a material is the tension test. In this test a specimen of material in the shape of a rod with a rectangular or circular transverse cross section is subjected to an axial deformation along its long axis. An idealized sketch of this situation is shown in Fig. 6.4. The long axis of the specimen is taken to lie in the $\mathbf{e}_1$ direction. The initial length of the specimen is L_1 and its cross-sectional area is A_1. Under the axial tensile force $\mathbf{f}_1$ the length of the specimen changes an amount δ_1. If the applied force $\mathbf{f}_1$ vs. the deflection δ_1 is plotted for one tension test, one of the curves in Fig. 6.5A is obtained. If the specimen length L_1 or the cross-sectional area A_1 is changed and the same test is repeated, another of the curves in Fig. 6.5a is obtained. However, if the same data are replotted with $\mathbf{f}_1$ divided by A_1 and δ_1 divided by L_1, all of the different curves of Fig. 6.5c collapse into the one curve shown in Fig. 6.5b. The initial slope of the curve in Fig. 6.5b is denoted by E_1 and called the Young's modulus in the $\mathbf{e}_1$ direction. From the discussion above,

$$E_1 \equiv f_1 L_1 / A_1 \delta_1 \tag{6.30}$$

or, since $T_{11} = f_1/A_1$, and $\mathrm{E}_{11} = \delta_1/L_1$,

$$E_{11} = T_{11}/E_{11} \tag{6.31}$$

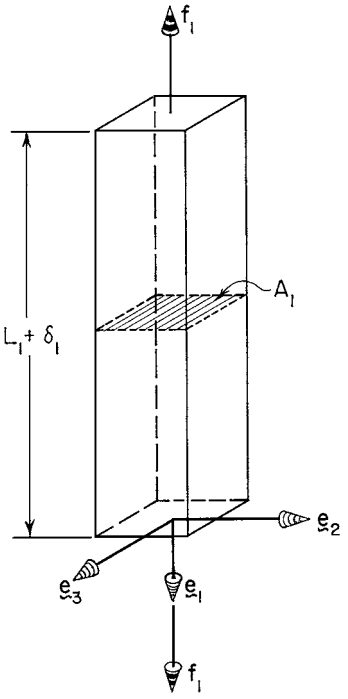

FIGURE 6.4 A schematic illustration of a tension test. (From Cowin, S. C., *Bone Mechanics Handbook,* CRC Press, Boca Raton, FL, 1989. With permission.)

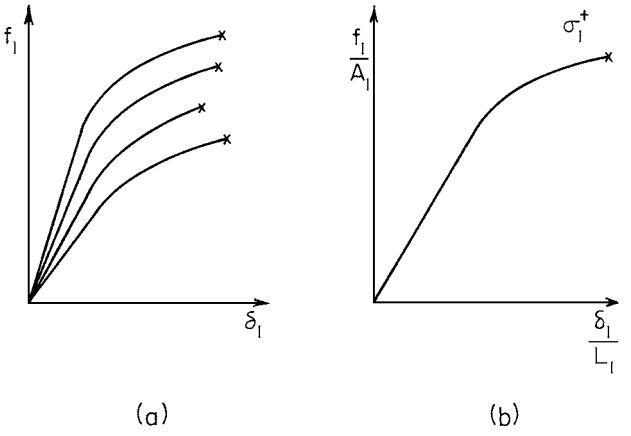

FIGURE 6.5 Illustrations of the typical curves obtained from a tension test for specimens of the same material but of different size. (A) The force vs. deformation curves for the different-sized specimens. (B) The stress vs. strain curve is the same for all the different-sized specimens. (From Cowin, S. C., *Bone Mechanics Handbook,* CRC Press, Boca Raton, FL, 1989. With permission.)

and Young's modulus is simply the ratio of the normal stress in the $\mathbf{e}_1$ direction to the normal strain in the $\mathbf{e}_1$ direction. Young's modulus is a *material property* since it is independent of the size of the specimen used to measure it. The spring constant K_1 of a particular specimen is expressed in terms of E_1 by rearranging Eq. 6.30, thus

$$K_1 \equiv f_1/\delta_1 = (A_1 E_1/L_1). \tag{6.32}$$

Clearly, the spring constant of a specimen depends upon the cross-sectional area and the length of the specimen, as well as the Young's modulus. For that reason, the spring constant is said to be a *structural property* as opposed to a material property.

The Young's modulus of a specimen along the long axis of the specimen can be measured from a tension test. A number of other mechanical properties of the material can also be measured in the tension test. The stress at which the specimen breaks in tension is called the tensile strength of the material in that direction. In the $\mathbf{e}_1$ direction, this tensile strength is denoted by σ_1^+, the plus sign indicating tensile.

6.5.2 Poisson's Ratios

There is a tendency for a solid material to try to retain its total volume as it is deformed. In the case of the tensile test situation illustrated in Fig. 6.4, the sides of the long rod will move closer together as the two ends of the rod are pulled apart. In other words, the elongation produced by the axial force $\mathbf{f}_1$ will be accompanied by a contraction in each of the transverse directions. This contraction is called the lateral strain in the associated direction. There is a lateral strain in the $\mathbf{e}_2$ direction and one in the $\mathbf{e}_3$ direction. The absolute value of the ratio of the lateral strain over the axial strain is called a Poisson's ratio; thus, two Poisson's ratios are defined for the two lateral contractions:

$$\nu_{12} = -E_{22}/E_{11}, \qquad \nu_{13} = -E_{33}/E_{11}. \tag{6.33}$$

From Eqs. 6.31 and 6.33 the lateral strains E_{22} and E_{33} are related to the applied stress T_{11} by

$$E_{22} = -\nu_{12}T_{11}/E_1, \qquad E_{33} = -\nu_{13}T_{11}/E_1. \tag{6.34}$$

In the uniaxial extension of the rod illustrated in Fig. 6.4, there is only one force applied. The one force causes only one stress, T_{11}. However, there are three strains due to T_{11}, E_{11}, E_{22}, and E_{33}.

6.6 Hooke's Law for Orthotropic Materials

6.6.1 Orthotropic Symmetry

Orthotropic symmetry may be thought of as the type of elastic material symmetry possessed by the wood tissue of a tree. Each year the new growth ring forms a laminate around a central core, and the axes of material symmetry lie in the directions tangent and normal to the growth rings or laminates and along the axis of the cylinder or tree. Most plant tissue, bone tissue, and the products of certain industrial lamination and metal-forming processes have the same type of symmetry. Formally, orthotropic symmetry is characterized by three mutually perpendicular planes of mirror symmetry. The normals to these three planes form a symmetry coordinate system for orthotropic symmetry and, relative to this coordinate system, there are only nine distinct orthotropic elastic constants for linear elasticity. One set of these nine constants consists of the *technical elastic constants,* which include three Young's moduli, E_1, E_2, and E_3, three shear moduli, G_{12}, G_{13}, and G_{23}, and six Poisson's ratios, ν_{23}, ν_{32}, ν_{13}, ν_{31}, ν_{12}, ν_{21}, only three of which are independent.

Curvilinear orthotropy is the term used to describe a material in which the orientation of the orthotropic symmetry coordinate system is different from point to point. The term *shape intrinsic orthotropy* describes the general situation when the symmetry coordinate system for orthotropic symmetry of a cylinder is coincident with the long axis of the cylinder, with the local tangent and normal to a closed family of curves, one of which forms the lateral boundary of the cylinder. The closed family of curves also delineates the laminates of the cylinder. The types of curvilinear orthotropy, known as circular (sometimes cylindrical) and elliptic orthotropy, are special cases of shape intrinsic orthotropy and are associated with circular and elliptical cylinders, respectively. Shape intrinsic orthotropy is characteristic of cylinders that are formed in growth processes like plant and animal tissue or in industrial lamination processes. In the literature of elasticity, curvilinear orthotropy is contrasted with *rectilinear orthotropy* in which the symmetry coordinate system for the material has the same orientation at all points.

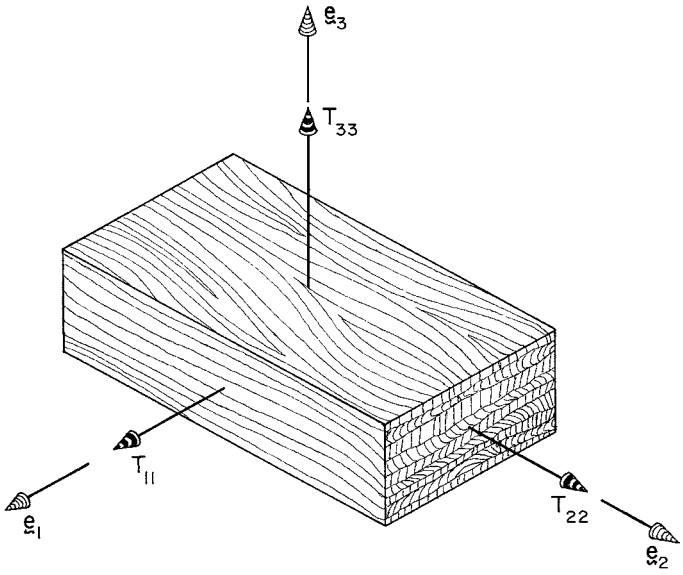

FIGURE 6.6 Illustration of a rectilinear parallelepiped specimen of an orthotropic material prepared so that its faces are each perpendicular to the mutually perpendicular symmetry axes of the material. (From Cowin, S. C., *Bone Mechanics Handbook,* CRC Press, Boca Raton, FL, 1989. With permission.)

6.6.2 Multiaxial Loading

The purpose of this section is to obtain formulas that relate the normal strain components, E_{11}, E_{22}, E_{33}, to the normal stress components, T_{11}, T_{22}, and T_{33}, for a general state of stress as an object with orthotropic elastic symmetry. A rectilinear parallelepiped specimen of the orthotropic material is prepared so that its faces are all parallel or perpendicular to the symmetry axes of the material as illustrated in Fig. 6.6. The effect of each of the stresses, T_{11}, T_{22}, and T_{33}, on the state of strain in this block will be considered separately; then the effects will be added. This addition of the results of different applied stresses is called the principle of superposition, and it is justified because, for a linear elastic material, stress is proportional to strain. Consider first the effect of T_{11}. In Section 6.5 it was noted that T_{11}, by itself, caused the following three strains:

$$E_{11} = T_{11}/E_1, \qquad E_{22} = -\nu_{12}T_{11}/E_1, \qquad E_{33} = -\nu_{13}T_{11}/E_1. \tag{6.35}$$

A repetition of the arguments leading to Eq. 6.35 will show that T_{22} by itself will give rise to the following strains:

$$E_{11} = -\nu_{21}T_{22}/E_2, \qquad E_{22} = T_{22}/E_2, \qquad E_{33} = -\nu_{23}T_{22}/E_2, \tag{6.36}$$

and T_{33}, to the set

$$E_{11} = -\nu_{31}T_{33}/E_3, \qquad E_{22} = -\nu_{32}T_{33}/E_3, \qquad E_{33} = T_{33}/E_3. \tag{6.37}$$

If all three stresses are applied, then the resulting strain is the sum of all the individual strains, thus

$$\begin{aligned} E_{11} &= (T_{11}/E_1) - \nu_{21}(T_{22}/E_2) - \nu_{31}(T_{33}/E_3), \\ E_{22} &= -\nu_{12}(T_{11}/E_1) + (T_{22}/E_2) - \nu_{32}(T_{33}/E_3), \\ E_{33} &= -\nu_{13}(T_{11}/E_1) - \nu_{23}(T_{22}/E_2) + (T_{33}/E_3). \end{aligned} \tag{6.38}$$

The six Poisson's ratios are not independent. In order that an orthotropic elastic material be consistent with the second law of thermodynamics, it is necessary that

$$-\nu_{12}/E_1 = -\nu_{21}/E_2, \qquad -\nu_{13}/E_1 = -\nu_{31}/E_3, \qquad -\nu_{23}/E_2 = -\nu_{32}/E_3. \tag{6.39}$$

If the conditions (Eq. 6.39) were not satisfied, it would be possible to extract work in a closed cycle from an orthotropic elastic material.

If the rectangular parallelepiped illustrated in Fig. 6.6 is subjected to the system of shearing forces sketched in Fig. 6.3B, then it is possible to measure the elastic shear modulus G_{12}. The shear modulus is obtained by dividing the applied shear stress T_{12} by the angle ψ,

$$G_{12} = T_{12}/\psi. \tag{6.40}$$

From Eqs. 6.29 and 6.40 it follows that E_{12} is given by

$$E_{12} = T_{12}/(2G_{12}). \tag{6.41}$$

In a similar fashion, E_{13} and E_{23} are given by

$$E_{23} = T_{23}/(2G_{23}), \qquad E_{13} = T_{13}/(2G_{13}). \tag{6.42}$$

6.6.3 Hooke's Law for Orthotropic Materials

Hooke's law for an orthotropic material expressed in the orthotropic symmetry coordinate system is given by Eqs. 6.38, 6.41, and 6.42. By combining these equations into one matrix equation, the following expression is obtained:

$$\begin{bmatrix} E_{11} \\ E_{22} \\ E_{33} \\ 2E_{23} \\ 2E_{13} \\ 2E_{12} \end{bmatrix} = \begin{bmatrix} \frac{1}{E_1} & \frac{-\nu_{21}}{E_2} & \frac{-\nu_{31}}{E_3} & 0 & 0 & 0 \\ \frac{-\nu_{12}}{E_1} & \frac{1}{E_2} & \frac{-\nu_{32}}{E_3} & 0 & 0 & 0 \\ \frac{-\nu_{13}}{E_1} & \frac{-\nu_{23}}{E_2} & \frac{1}{E_3} & 0 & 0 & 0 \\ 0 & 0 & 0 & \frac{1}{G_{23}} & 0 & 0 \\ 0 & 0 & 0 & 0 & \frac{1}{G_{31}} & 0 \\ 0 & 0 & 0 & 0 & 0 & \frac{1}{G_{12}} \end{bmatrix} \begin{bmatrix} T_{11} \\ T_{22} \\ T_{33} \\ T_{23} \\ T_{13} \\ T_{12} \end{bmatrix}. \tag{6.43}$$

Eq. 6.43 represents a rather widely used expression for Hooke's law for orthotropic materials. It must be noted that Eq. 6.43 only holds in the orthotropic symmetry coordinate system of the material and, in other systems, there will be more nonzero entries in the six-by-six matrix. Since it is quite convenient to have a shorthand notation for the result (Eq. 6.43), the following relation is employed:

$$\mathbf{E} = \mathbf{K}[\mathbf{T}]. \tag{6.44}$$

The six-by-six matrix is denoted by **K** in this notation. This matrix, which is often called the elastic compliance matrix, is usually denoted by **K**. Whenever Eq. 6.44 appears, it is to be understood that it is a shorthand notation for Eq. 6.43.

The inverse of Eq. 6.43 is denoted by

$$\begin{bmatrix} T_{11} \\ T_{22} \\ T_{33} \\ T_{23} \\ T_{13} \\ T_{12} \end{bmatrix} = \begin{bmatrix} c_{11} & c_{12} & c_{13} & 0 & 0 & 0 \\ c_{12} & c_{22} & c_{23} & 0 & 0 & 0 \\ c_{13} & c_{23} & c_{33} & 0 & 0 & 0 \\ 0 & 0 & 0 & c_{44} & 0 & 0 \\ 0 & 0 & 0 & 0 & c_{55} & 0 \\ 0 & 0 & 0 & 0 & 0 & c_{66} \end{bmatrix} \begin{bmatrix} E_{11} \\ E_{22} \\ E_{33} \\ 2E_{23} \\ 2E_{13} \\ 2E_{12} \end{bmatrix}, \tag{6.45}$$

where

$$\begin{aligned} c_{11} &= \frac{1 - \nu_{23}\nu_{32}}{\Delta E_2 E_3}, \qquad c_{12} = \frac{\nu_{21} + \nu_{31}\nu_{23}}{\Delta E_2 E_3} = \frac{\nu_{12} + \nu_{32}\nu_{13}}{\Delta E_1 E_3}, \\ c_{13} &= \frac{\nu_{31} + \nu_{21}\nu_{32}}{\Delta E_2 E_3} = \frac{\nu_{13} + \nu_{12}\nu_{23}}{\Delta E_1 E_2}, \qquad c_{22} = \frac{1 - \nu_{13}\nu_{31}}{\Delta E_1 E_3}, \\ c_{23} &= \frac{\nu_{32} + \nu_{12}\nu_{31}}{\Delta E_2 E_1} = \frac{\nu_{23} + \nu_{21}\nu_{13}}{\Delta E_1 E_2}, \qquad c_{33} = \frac{1 - \nu_{12}\nu_{21}}{\Delta E_2 E_1}, \\ c_{44} &= G_{23}, \qquad c_{55} = G_{13}, \qquad c_{66} = G_{12}, \end{aligned} \tag{6.46}$$

and where

$$\Delta = \frac{1 - \nu_{12}\nu_{21} - \nu_{23}\nu_{32} - \nu_{31}\nu_{13} - 2\nu_{21}\nu_{32}\nu_{13}}{E_1 E_2 E_3}.$$

The shorthand for Eq. 6.45 is

$$\mathbf{T} = \mathbf{C}[\mathbf{E}], \tag{6.47}$$

paralleling the shorthand Eq. 6.44 for Eq. 6.43. The relations represented by Eq. 6.45 or 6.47 are called the elastic *stress–strain relations* to distinguish them from the elastic *strain–stress relations* given by Eqs. 6.43 and 6.44.

While there appear to be 12 distinct elastic constants in Eq. 6.43, there are actually only 9 because of the relations given by Eq. 6.39. Thus, for orthotropic elastic symmetry, there are only nine distinct elastic constants. Transverse isotropy is a higher symmetry than orthotropic symmetry. Transverse isotropy has a plane of isotropy. A plane of isotropy, which is also a plane of mirror symmetry, is a plane in which every vector is a normal to a plane of mirror symmetry. For transverse isotropy, there are only five distinct elastic constants and they are obtained from the nine distinct orthotropic elastic constants by imposing the following restrictions:

$$E_1 = E_2, \qquad \nu_{12} = \nu_{21}, \qquad \nu_{31} = \nu_{32}, \qquad G_{23} = G_{31}, \qquad \mathrm{G}_{12} = \frac{E_1}{2(1 + \nu_{12})}. \tag{6.48}$$

Isotropic symmetry is the highest type of symmetry possible. For isotropic symmetry every material direction is the same, and all planes are planes of mirror symmetry and planes of isotropy. There are only two distinct elastic constants for isotropic symmetry. The isotropic elastic constants can be obtained from the orthotropic elastic constants by imposing the following restrictions:

$$\begin{aligned} E_1 = E_2 = E_3 = E, \qquad G_{23} = G_{13} = \mathrm{G}_{12} \equiv G = \frac{E}{2(1 + \nu)}, \\ \nu_{12} = \nu_{21} = \nu_{31} = \nu_{32} = \nu_{13} = \nu_{23} = \nu. \end{aligned} \tag{6.49}$$

6.6.4 Digression for a Point of Notation

In general, the notation $\mathbf{T} = \mathbf{C}[\mathbf{E}]$ introduced by Eq. 6.47 stands for

$$\begin{bmatrix} T_{11} \\ T_{22} \\ T_{33} \\ T_{23} \\ T_{13} \\ T_{12} \end{bmatrix} = \begin{bmatrix} c_{11} & c_{12} & c_{13} & c_{14} & c_{15} & c_{16} \\ c_{12} & c_{22} & c_{23} & c_{24} & c_{25} & c_{26} \\ c_{13} & c_{23} & c_{33} & c_{34} & c_{35} & c_{36} \\ c_{14} & c_{24} & c_{34} & c_{44} & c_{45} & c_{46} \\ c_{15} & c_{25} & c_{35} & c_{45} & c_{55} & c_{56} \\ c_{16} & c_{26} & c_{36} & c_{46} & c_{56} & c_{66} \end{bmatrix} \begin{bmatrix} E_{11} \\ E_{22} \\ E_{33} \\ 2E_{23} \\ 2E_{13} \\ 2E_{12} \end{bmatrix}. \tag{6.50}$$

The strain energy per unit volume of a deformed elastic object is given by

$$U = (\mathrm{tr}\mathbf{TE})/2 = (1/2)(T_{11}E_{11} + T_{22}E_{22} + T_{33}E_{33}) + T_{23}E_{23} + T_{13}E_{13} + T_{12}E_{12}. \tag{6.51}$$

To express the strain energy per unit volume in terms of strain, the representation of **T** given by Eq. 6.47 is substituted into Eq. 6.50, thus

$$U = (1/2)\mathrm{tr}(\mathbf{EC}[\mathbf{E}]). \tag{6.52}$$

The purpose of this digression is to note that $\mathrm{tr}(\mathbf{EC}[\mathbf{E}])$ is given in terms of scalars by the following expression:

$$\begin{aligned} 2U = \mathrm{tr}(\mathbf{EC}[\mathbf{E}]) = {} & c_{11}E_{11}^2 + c_{22}E_{22}^2 + c_{33}E_{33}^2 + 4c_{44}E_{23}^2 + 4c_{55}E_{13}^2 + 4c_{66}E_{12}^2 + 2c_{12}E_{11}E_{22} \\ & + 2c_{13}E_{11}E_{33} + 2c_{23}E_{22}E_{33} + 4c_{14}E_{11}E_{23} + 4c_{24}E_{22}E_{23} + 4c_{34}E_{33}E_{23} + 4c_{15}E_{11}E_{13} \\ & + 4c_{25}E_{22}E_{13} + 4c_{35}E_{33}E_{13} + 4c_{16}E_{11}E_{12} + 4c_{26}E_{22}E_{12} + 4c_{36}E_{33}E_{12} \\ & + 8c_{45}E_{23}E_{13} + 8c_{46}E_{23}E_{12} + 8c_{56}E_{13}E_{12}. \end{aligned} \tag{6.53}$$

The notation $\mathrm{tr}(\mathbf{EC}[\mathbf{E}])$ will be used elsewhere in this volume with different uppercase Latin letters. The significance in terms of scalar components is that indicated by Eq. 6.53.

6.6.5 Thermodynamic Restrictions on the Orthotropic Elastic Constants

The necessary and sufficient condition that the work done on an elastic material be strictly positive is that the strain energy U defined by Eq. 6.51 be positive for all values of the strain matrix **E** that are not identically zero. From this thermodynamic restriction it is possible to show[5,6] that

$$\begin{gathered} E_1 > 0, \quad E_2 > 0, \quad E_3 > 0, \quad G_{23} > 0, \quad G_{13} > 0, \quad G_{12} > 0, \\ 1 - \nu_{23}\nu_{32} > 0, \quad 1 - \nu_{13}\nu_{31} > 0, \quad 1 - \nu_{12}\nu_{21} > 0, \end{gathered} \tag{6.54}$$

and

$$1 - \nu_{12}\nu_{21} - \nu_{23}\nu_{32} - \nu_{31}\nu_{13} - 2\nu_{21}\nu_{32}\nu_{13} > 0.$$

Using the condition of symmetry (Eq. 6.39), it can be also shown that the following inequalities must be satisfied by the technical elastic constants:

$$|\nu_{21}| < \sqrt{\frac{E_2}{E_1}}, \qquad |\nu_{12}| < \sqrt{\frac{E_1}{E_2}}, \qquad |\nu_{32}| < \sqrt{\frac{E_3}{E_2}}, \qquad |\nu_{23}| < \sqrt{\frac{E_2}{E_3}}, \qquad |\nu_{13}| < \sqrt{\frac{E_1}{E_3}}, \qquad |\nu_{31}| < \sqrt{\frac{E_3}{E_1}},$$

$$\nu_{21}\nu_{32}\nu_{13} < \frac{1}{2} - \frac{\nu_{21}^2}{2}\frac{E_1}{E_2} - \frac{\nu_{32}^2}{2}\frac{E_2}{E_3} - \frac{\nu_{13}^2}{2}\frac{E_3}{E_1} < \frac{1}{2}. \tag{6.55}$$

If the elastic moduli are known, then these inequalities are restrictions on the Poisson's ratios, and vice versa.

6.7 Stresses in a Cylindrical Shaft

6.7.1 The Cylindrical Shaft

The purpose of this and the subsequent subsections is to describe the stresses and strains that occur in a hollow cylinder shaft with shape-intrinsic orthotropy when it is subjected to various types of loadings. The hollow cylindrical shaft with shape-intrinsic orthotropic symmetry is a model for the mid-diaphysis of a long bone. It is illustrated in Fig. 6.7. The Cartesian basis $\mathbf{e}_1$, $\mathbf{e}_2$, $\mathbf{e}_3$ is selected so that its origin is at the centroid of the transverse cross-sectional area and so that $\mathbf{e}_3$ is coincident with the long axis of the cylinder. The base vectors $\mathbf{e}_1$ and $\mathbf{e}_2$ are taken to be coincident with the principal axes of area moment of inertia of the transverse cross section of the shaft. The area moments of inertia are denoted by I_{11} and I_{22} and the cross-sectional area by A.

Shape-intrinsic orthotropy means that the material of which the cylinder is made is orthotropic in the system whose base vectors are $\mathbf{e}_n$, $\mathbf{e}_t$, and $\mathbf{e}_z$, where $\mathbf{e}_z$ is coincident with $\mathbf{e}_3$, and $\mathbf{e}_n$ and $\mathbf{e}_t$ are unit normal and tangent vectors, respectively, with respect to a closed family of curves that delineate the laminates of the cylinder, and one of which forms the lateral boundary of the cylinder. This system is illustrated in Fig. 6.7. Thus, the elastic constants that will appear in the following discussion will be E_n, E_t, E_z, G_{tn}, G_z, G_{nz}, ν_{nt}, ν_{tn}, ν_{tz}, ν_{zt}, ν_{nz}, ν_{zn} referred to the system $\mathbf{e}_t$, $\mathbf{e}_n$, $\mathbf{e}_z$. The stresses and the strains must also be referred to this system. In this system, Hooke's law (Eq. 6.43) takes a form determined by replacing the subscripts 1, 2, and 3 by n, t, and z, respectively; thus,

$$\begin{bmatrix} E_{nn} \\ E_{tt} \\ E_{zz} \\ 2E_{tz} \\ 2E_{nz} \\ 2E_{nt} \end{bmatrix} = \begin{bmatrix} \frac{1}{E_n} & \frac{-\nu_{tn}}{E_t} & \frac{-\nu_{zn}}{E_z} & 0 & 0 & 0 \\ \frac{-\nu_{nt}}{E_n} & \frac{1}{E_t} & \frac{-\nu_{zt}}{E_z} & 0 & 0 & 0 \\ \frac{-\nu_{nz}}{E_n} & \frac{-\nu_{tz}}{E_t} & \frac{1}{E_z} & 0 & 0 & 0 \\ 0 & 0 & 0 & \frac{1}{G_{tz}} & 0 & 0 \\ 0 & 0 & 0 & 0 & \frac{1}{G_{zn}} & 0 \\ 0 & 0 & 0 & 0 & 0 & \frac{1}{G_{nt}} \end{bmatrix} \begin{bmatrix} T_{nn} \\ T_{tt} \\ T_{zz} \\ T_{tz} \\ T_{nz} \\ T_{nt} \end{bmatrix}. \tag{6.56}$$

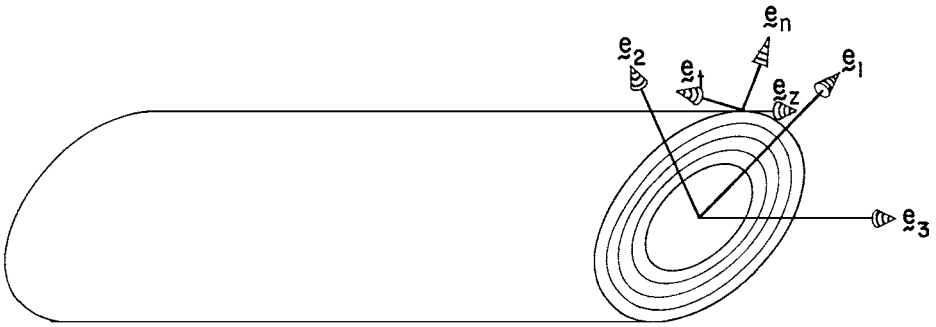

FIGURE 6.7 Illustration of a hollow cylindrical shaft with shape intrinsic orthotropic symmetry. (From Cowin, S. C., *Bone Mechanics Handbook,* CRC Press, Boca Raton, FL, 1989. With permission.)

The stress distributions presented in the following three subsections (6.7.2, 6.7.3, and 6.7.4) are exact solutions as the linear theory of anisotropic elasticity only if $\nu_{zn} = \nu_{zt}$. If $\nu_{zn} \neq \nu_{zt}$, circumferential inhomogeneities occur in the stress distribution.[1]

6.7.2 Centric Compressive Loading

Consider first the situation in which a compressive force of magnitude f_3 is applied to both ends of the shaft exactly at the origin of the $\mathbf{e}_1$, $\mathbf{e}_2$, $\mathbf{e}_3$ system. Recall that this origin was placed at the centroid of the transverse cross section. The only nonzero stress in this situation is

$$T_{zz} = -f_3/A\,, \tag{6.57}$$

where A is the cross-sectional area. The strains relative to the $\mathbf{e}_n$, $\mathbf{e}_t$, $\mathbf{e}_z$ system are obtained from Eq. 6.56; thus;

$$E_{nn} = -\nu_{zn}T_{zz}/E_z, \qquad E_{tt} = -\nu_{zt}T_{zz}/E_z, \qquad E_{zz} = T_{zz}/E_z. \tag{6.58}$$

6.7.3 Pure Bending

Consider first the situation in which the shaft illustrated in Fig. 6.7 is bent by a pure couple M_1 applied about the axis $\mathbf{e}_1$. The right-hand rule described earlier is used to determine the sense of the couple. As a result of this couple, the axis of the shaft is bent into a circular arc in the $\mathbf{e}_2$, $\mathbf{e}_3$ plane. The radius of this circular arc is denoted by ρ_1. Since strains are small, the radius ρ_1 is quite large. The radius ρ_1 is related to M_1 by

$$1/\rho_1 = M_1/(E_z I_{11}), \tag{6.59}$$

where I_{11} is the area moment of inertia of the cross-sectional area about $\mathbf{e}_1$. The only nonzero stress is T_{zz} and it is given by

$$T_{zz} = M_1 x_2/I_{11}, \tag{6.60}$$

where x_2 is the distance from the origin in the $\mathbf{e}_2$ direction. This result shows that the stress T_{zz} due to the bending couple M_1 varies linearly with x_2 across the cross section of the shaft. The strain in the $\mathbf{e}_z$ direction is given by

$$E_{zz} = x_2/\rho_1, \tag{6.61}$$

and it is also seen to vary linearly with x_2 across the cross section.

If, rather than bending about $\mathbf{e}_1$, a couple M_2 is applied about the $\mathbf{e}_2$ axis, then the central axis of the shaft forms a circular arc of radius p_2 in the $\mathbf{e}_1$, $\mathbf{e}_3$ plane where p_2 is given by

$$1/\rho_2 = M_2/(E_z I_{22}), \tag{6.62}$$

The only nonzero stress is again T_{zz} and it is given by

$$T_{zz} = -M_2 x_1/I_{22}, \tag{6.63}$$

and its associated strain by

$$E_{zz} = -x_1/\rho_2, \tag{6.64}$$

where both are seen to vary linearly with x_1 across the cross section.

If a couple is applied to the cylindrical shaft about an axis that is not $\mathbf{e}_1$ or $\mathbf{e}_2$, then the couple can be decomposed into components M_1 and M_2, and the two contributions to T_{zz} and E_{zz} can be summed; thus,

$$T_{zz} = (M_1 x_2/I_{11}) - (M_2 x_1/I_{22}), \tag{6.65}$$

and

$$E_{zz} = (x_2/\rho_1) - (x_1/\rho_2). \tag{6.66}$$

In each of these three situations the nonzero strains E_{nn}, E_{tt}, and E_{zz} can be obtained from Eq. 6.58 by substitution of the appropriate expression for T_{zz}.

6.7.4 Eccentric Axial Loading

If the applied load to the cylindrical shaft of Fig. 6.7 consists of an axial compressive force of magnitude f_3, applied at the centroid of the cross section, and two couples M_1 and M_2, applied about the $\mathbf{e}_1$ and $\mathbf{e}_2$ axes, respectively, then the total stress T_{zz} is given by the sum of Eqs. 6.57, 6.60, and 6.63,

$$T_{zz} = -f_3/A + (M_1 x_2/I_{11}) - (M_2 x_1/I_{22}). \tag{6.67}$$

If, rather than being centric, f_3 is applied eccentrically at a point x_1^*, x_2^* in the cross section, then there are couples M_1 and M_2 given by

$$M_1 = -x_2^* f_3, \qquad M_2 = x_1^* f_3, \tag{6.68}$$

set up by the eccentric application of f_3. If the eccentric application of f_3 is the only source for the couples M_1 and M_2, then it follows from Eqs. 6.67 and 6.68 that the stress T_{zz} due to the eccentric application of f_3 is given by

$$T_{zz} = -f_3\{1/A + (x_2 x_2^*/I_{11}) - (x_1 x_1^*/I_{22})\}. \tag{6.69}$$

Note that x_1^* and x_2^* are constants representing the point of application of the load f_3; hence T_{33} given by both Eqs. 6.67 and 6.69 is linear in both x_1 and x_2, and therefore the stress distribution is still linear across a cross section. The strains E_{nn}, E_{tt}, and E_{zz} in both of these situations are obtained from Eq. 6.58 using the appropriate expression for T_{zz}.

6.7.5 Torsion

The situation in which the shaft is subject to a twisting torque of magnitude T about the $\mathbf{e}_3$ axis is considered now. For simplicity, and without a great loss in generality, the cross-sectional shape of the cylinder is specialized to the case where the two bounding curves of the cross section are from the same family of ellipses. The outer boundary is given by

$$(x_1/a)^2 + (x_2/\xi a)^2 = 1, \qquad 0 < \xi < 1, \tag{6.70}$$

and the inner boundary by

$$(x_1/a_o)^2 + (x_2/\xi a_o)^2 = 1, \qquad 0 < \xi < 1, \tag{6.71}$$

where ξ is a constant for the cylindrical shaft in question. It is the ratio of the minor to the major axes of the bounding ellipses. The twist per unit length α along the cylinder is related to the torque T, ξ, and G_{tz} by

$$T = \{\alpha \xi^3 (a^4 - (a_0)^4) G_{tz}\}/(1 + \xi^2), \tag{6.72}$$

and the only nonzero stress is given by

$$T_{tz} = 2\alpha G_{tz}\left(\sqrt{\{(x_2)^2 + (x_1\xi^2)^2\}}\right)/(1 + \xi^2). \tag{6.73}$$

The strain E_{tz} is obtained by dividing T_{tz} by $2G_{tz}$.

Exact solutions for other cylinders with shape-intrinsic orthotropy are given by Cowin.[4] St. Venant observed that for most practical purposes the stresses and strains in any cylinder could be closely approximated by those in a cylinder with elliptical cross section.

6.8 The Displacement–Strain Relations

There are three basic types of movement that an object can experience. First, there is a *translational movement* in which all points of the object are moving at the same speed in the same direction. Second, there is a *rotational movement* in which the object is turning about one fixed point, and its movement at any particular point is perpendicular to a line drawn from the particular point to the fixed rotation points and its speed is proportional to the distance between the two points. Both translational and rotational movements are called rigid object movements because the distance between any two points on the object never changes during the movement. The strain matrix **E** defined in Section 6.4 is zero for any rigid body movement. The third type of movement is called *deformation* because it is a movement in which points on the same object move relative to one another. It is a basic theorem of physics that the movement of any object can be decomposed into a translational movement, a rotational movement, and a deformation. The concern here is with deformation and quantities that measure the deformation of an object independent of its translational and rotational movement.

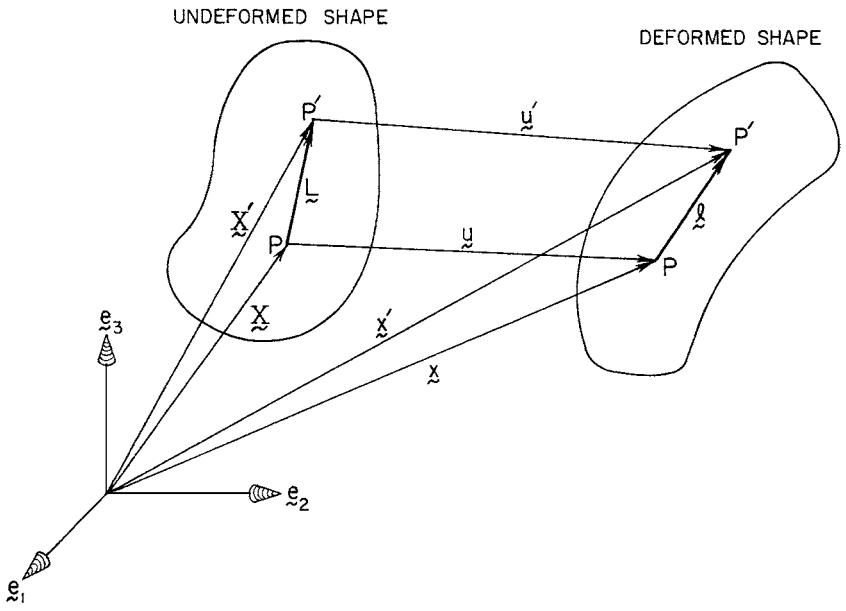

FIGURE 6.8 Illustration of an object in its undeformed shape and its deformed shape. (From Cowin, S. C., *Bone Mechanics Handbook,* CRC Press, Boca Raton, FL, 1989. With permission.)

6.8.1 Position and Displacement

Consider an undeformed object referred to a Cartesian basis $\mathbf{e}_1$, $\mathbf{e}_2$, $\mathbf{e}_3$ as shown on the left in Fig. 6.8. The location of each particle in the undeformed object is located and assigned a name by virtue of its position relative to the Cartesian basis. For example, the particle P is "named" by its position vector $\mathbf{X}$, the particle P' by its position vector $\mathbf{X}'$. The particles on the straight line between P and P' form a material filament. Let $\mathbf{L}$ be a vector representing this material filament; then

$$\mathbf{L} = \mathbf{X}' - \mathbf{X}, \tag{6.74}$$

a result that follows from the closure of the vector triangle $\mathbf{L}$, $\mathbf{X}$, and $\mathbf{X}'$.

Consider now the deformed shape of the same object as illustrated on the right-hand side of Fig. 6.8. The position of the particle P is now given by the position vector $\mathbf{x}$, that of P' by $\mathbf{x}'$. The particles now lying on the straight line between P and P' are assumed to be the same as those that lie on the straight line between P and P' in the undeformed shape. This assumption is only true if P and P' are close to each other and remain close to each other in the deformed shape. If this is the case, then

$$\boldsymbol{l} = \mathbf{x}' - \mathbf{x} \tag{6.75}$$

represents the deformed length and orientation of the material filament $\mathbf{L}$. Similarly, $\mathbf{x}$ represents the deformed position of P, and $\mathbf{x}'$ the deformed position of P'.

The displacement vector of the point P in the deformation is denoted by $\mathbf{u}$ and defined by

$$\mathbf{u} = \mathbf{x} - \mathbf{X}. \tag{6.76}$$

The displacement vector for P' is given by

$$\mathbf{u}' = \mathbf{x}' - \mathbf{X}'. \tag{6.77}$$

At this point a digression is made to introduce notation for derivatives and gradients.

6.8.2 Derivatives and Gradients

The quantities X_1, X_2, X_3 that are the Cartesian components of the position vector $\mathbf{X}$ are also Cartesian coordinates of the Cartesian basis $\mathbf{e}_1$, $\mathbf{e}_2$, $\mathbf{e}_3$. The partial derivative of a function $f(\mathbf{X})$ with respect to X_1, X_2, or X_3 is denoted by $\partial f/\partial X_1$, $\partial f/\partial X_2$, or $\partial f/\partial X_3$, respectively, and the gradient ∇ of the scalar-valued function f denoted by

$$\nabla f = \frac{\partial f}{\partial X_1}\mathbf{e}_1 + \frac{\partial f}{\partial X_2}\mathbf{e}_2 + \frac{\partial f}{\partial X_3}\mathbf{e}_3. \tag{6.78}$$

The gradient of a scalar is thus seen to be a vector. The gradient of a vector is a tensor.

The matrix of tensor components of the gradient of the displacement vector $\mathbf{u}$ is given by

$$\nabla\mathbf{u} = \begin{bmatrix} \frac{\partial u_1}{\partial X_1} & \frac{\partial u_1}{\partial X_2} & \frac{\partial u_1}{\partial X_3} \\ \frac{\partial u_2}{\partial X_1} & \frac{\partial u_2}{\partial X_2} & \frac{\partial u_2}{\partial X_3} \\ \frac{\partial u_3}{\partial X_1} & \frac{\partial u_3}{\partial X_2} & \frac{\partial u_3}{\partial X_3} \end{bmatrix}. \tag{6.79}$$

If the representation (Eq. 6.76) for $\mathbf{u}$ is substituted into Eq. 6.79, then $\nabla\mathbf{u}$ is given by

$$\nabla\mathbf{u} = \mathbf{J} - \mathbf{1}, \tag{6.80}$$

where

$$\mathbf{J} = \left[\frac{\partial\mathbf{x}}{\partial\mathbf{X}}\right] = \begin{bmatrix} \frac{\partial x_1}{\partial X_1} & \frac{\partial x_1}{\partial X_2} & \frac{\partial x_1}{\partial X_3} \\ \frac{\partial x_2}{\partial X_1} & \frac{\partial x_2}{\partial X_2} & \frac{\partial x_2}{\partial X_3} \\ \frac{\partial x_3}{\partial X_1} & \frac{\partial x_3}{\partial X_2} & \frac{\partial x_3}{\partial X_3} \end{bmatrix}, \tag{6.81}$$

and where $\mathbf{1}$ is the unit matrix. The matrix $\mathbf{J}$ is called the *Jacobian* and use will be made in later chapters of the determinant of the Jacobian,

$$\det\mathbf{J} = \begin{bmatrix} \frac{\partial x_1}{\partial X_1} & \frac{\partial x_1}{\partial X_2} & \frac{\partial x_1}{\partial X_3} \\ \frac{\partial x_2}{\partial X_1} & \frac{\partial x_2}{\partial X_2} & \frac{\partial x_2}{\partial X_3} \\ \frac{\partial x_3}{\partial X_1} & \frac{\partial x_3}{\partial X_2} & \frac{\partial x_3}{\partial X_3} \end{bmatrix}. \tag{6.82}$$

6.8.3 Strain and Rotation

Consider again the situation of the material filament $\mathbf{L}$ deformed into the orientation and length represented by $\boldsymbol{l}$. Recall that, in order to interpret $\boldsymbol{l}$ as a deformed representation of the material filament $\mathbf{L}$, it was necessary to require that $\mathbf{L}$, and thus $\boldsymbol{l}$, have small length. Let $\mathbf{L}$ be denoted by $d\mathbf{X}$ and $\boldsymbol{l}$ by $d\mathbf{x}$ and

they will be considered as differential lengths. The displacement $\mathbf{u}'$ then represents the value of the displacement at the particle $\mathbf{X} + d\mathbf{X}$ and $\mathbf{u}$ represents the value of the displacement at the particle $\mathbf{X}$,

$$\mathbf{u} = \mathbf{u}(\mathbf{X}), \qquad \mathbf{u}' = \mathbf{u}(\mathbf{X} + d\mathbf{X}). \tag{6.83}$$

When the function $\mathbf{u}(\mathbf{X} + d\mathbf{X})$ is expanded in a Taylor series of three variables about the particle $\mathbf{X}$ and only linear terms in the expansion are retained, then

$$\mathbf{u}(\mathbf{X} + d\mathbf{X}) \cong \mathbf{u}(\mathbf{X}) + (\nabla\mathbf{u})d\mathbf{X}. \tag{6.84}$$

According to Taylor's theorem, this representation can achieve any specified degree of accuracy simply by taking $\mathbf{L} = d\mathbf{X}$ to be smaller. The matrix $(\nabla\mathbf{u})$ can be written as the sum of a matrix that is symmetric and one that is antisymmetric; thus,

$$(\nabla\mathbf{u}) = \mathbf{W} + \mathbf{E}, \tag{6.85}$$

where

$$\mathbf{E} = (1/2)[(\nabla\mathbf{u}) + (\nabla\mathbf{u})^T], \tag{6.86}$$

and

$$\mathbf{W} = (1/2)[(\nabla\mathbf{u}) - (\nabla\mathbf{u})^T]. \tag{6.87}$$

It can be shown that the $\mathbf{E}$ given by Eq. 6.86 has all the properties described in Section 6.4 for the strain matrix. Thus, Eq. 6.86 is a formula relating the displacement vector to the strain matrix $\mathbf{E}$ and it is called the *strain-displacement relation*. The matrix $\mathbf{W}$ represents the infinitesimal rigid body rotation of the material filament $\mathbf{L}$ into its position *f*. Substituting Eq. 6.85 into Eq. 6.84, one obtains the formula

$$\mathbf{u}(\mathbf{X} + d\mathbf{X}) \cong \mathbf{u}(\mathbf{X}) + \mathbf{W}d\mathbf{X} + \mathbf{E}d\mathbf{X}. \tag{6.88}$$

The right-hand side of this formula can be viewed as a decomposition of the movement of the material filament into a translational movement, a rotational movement, and a deformation. The term $\mathbf{u}(\mathbf{X})$ represents the translation, the term $\mathbf{W}d\mathbf{X}$ the rotation, and the term $\mathbf{E}d\mathbf{X}$ the deformation.

6.9 The Theory of Orthotropic Elasticity

6.9.1 The Stress Equations of Equilibrium

In Section 6.2 the two conditions of mechanical equilibrium were discussed. These are the condition for force equilibrium and the condition for moment equilibrium. In Section 6.3 it was noted that the condition for moment equilibrium was expressed in terms of the stress matrix $\mathbf{T}$ by requiring that it be a symmetric matrix, Eq. 6.15. The condition for force equilibrium (Eq. 6.10) for an object can be shown to be equivalent to the requirement that the following system of equations involving the stress components be satisfied at every particle $\mathbf{X}$ of the object:

$$\begin{aligned}
\frac{\partial T_{11}}{\partial X_1} + \frac{\partial T_{12}}{\partial X_2} + \frac{\partial T_{13}}{\partial X_3} + b_1 &= 0,\\
\frac{\partial T_{12}}{\partial X_1} + \frac{\partial T_{22}}{\partial X_2} + \frac{\partial T_{23}}{\partial X_3} + b_2 &= 0,\\
\frac{\partial T_{13}}{\partial X_1} + \frac{\partial T_{23}}{\partial X_2} + \frac{\partial T_{33}}{\partial X_3} + b_3 &= 0.
\end{aligned} \tag{6.89}$$

The scalars b_1, b_2, b_3 are the components of a vector representing gravitational forces. The condition (Eq. 6.15) of symmetry of the stress matrix has been incorporated in the result (Eq. 6.89). It is customary to write Eq. 6.89 in the shorthand form:

$$\text{div}\mathbf{T} + \mathbf{b} = 0, \tag{6.90}$$

where div stands for the divergence. If the object in question is not at rest or moving with a constant velocity, then Eq. 6.90 is replaced by the stress equations of motion

$$\text{div}\mathbf{T} + \mathbf{b} = \rho\ddot{\mathbf{u}}, \tag{6.91}$$

where $\ddot{\mathbf{u}}$ represents the acceleration at the particle **X**. The acceleration is the second time derivative of the displacement vector **u**. Eq. 6.91 is a statement of Newton's second law of motion (see Section 6.1) in terms of stress.

6.9.2 The Basic System of Equations

The basic system of equations governing the stress **T**, the strain **E**, and the displacement **u** in an orthotropic elastic object in mechanical equilibrium comprises the *strain–displacement* relations,

$$\mathbf{E} = (1/2)[(\nabla\mathbf{u}) + (\nabla\mathbf{u})^T], \tag{6.86}$$

the *stress–strain* relations,

$$\mathbf{T} = \mathbf{C}[\mathbf{E}] \tag{6.47}$$

or the *strain–stress* relations,

$$\mathbf{E} = \mathbf{K}[\mathbf{T}] \tag{6.44}$$

and the *stress equations of equilibrium,*

$$\text{div}\mathbf{T} + \mathbf{b} = 0 \tag{6.90}$$

When a solution of this system of equations is sought, either the *stress–strain* relations or the *strain–stress* relations and the gravitational force **b** are known. The system of Eqs. 6.86, 6.47 or 6.44, and 6.90 is then a system of 15 equations in 15 unknowns. The 15 unknowns are the three components of the displacement vector **u**, the six components of the symmetric stress matrix **T**, and the six components of the symmetric strain matrix **E**. The equations consist of the six strain–displacement relations (Eq. 6.86), the six stress–strain relations (Eq. 6.47), or the six strain–stress relations (Eq. 6.44), and the three stress equations of equilibrium (Eq. 6.90).

6.9.3 The Formulation of Boundary-Value Problems

To solve the basic system of equations described above, particular problems must be specified. These problems are specified by the way in which the object is loaded on its boundary and are therefore called boundary-value problems. If **n** is the unit normal to a point of the boundary of an object, then the normal stress vector **t** acting on the exterior boundary at that point is related to the stress matrix **T** at the boundary point by Eq. 6.18,

$$\mathbf{t} = \mathbf{T}\mathbf{n}. \tag{6.92}$$

If the stress vector **t** on the boundary is known, then it forms a stress boundary condition. Let the portion of the boundary of the object over which **t** is known be denoted by S_t and be called the *stress boundary*.

On the other hand, it is possible that the displacement **u** is known on a portion of the object's boundary. Let S_u denote the portion of the boundary of the object over which the displacement is known. If an object has a portion of boundary over which the stress vector is specified and a portion over which the displacement vector is specified, then the boundary conditions would be written in the form:

$$\mathbf{t}^* = \mathbf{Tn}, \qquad X \in S_t, \qquad \mathbf{u}^* = \mathbf{u}, \qquad X \in S_u, \tag{6.93}$$

where $S_u + S_t$ is the total boundary of the object and where $\mathbf{t}^*$ and $\mathbf{u}^*$ are functions that are known on S_t and S_u, respectively. An elasticity problem in which a solution to the system of basic equations is sought for the boundary conditions (Eq. 6.93) is called a *mixed elastostatic boundary-value* problem. It is possible to show that for any specification of the functions $\mathbf{t}^*$ and $\mathbf{u}^*$ over appropriate domains, the solution to the mixed boundary-value problem is unique.

References

1. Lekhnitskii, S. G., *Theory of Elasticity of an Anisotropic Elastic Body,* trans. by Fern, P., Holden Day, San Francisco, 1963.
2. Hearmon, R. F. S., *An Introduction to Applied Anisotropic Elasticity,* Oxford University Press, Oxford, U.K., 1961.
3. Jones, R. M., *Mechanics of Composite Materials,* Scripta, Washington, D.C., 1975.
4. Cowin, S. C., Torsion of cylinders with shape intrinsic orthotropy, *J. Appl. Mech.,* 109, 778, 1987.
5. Lempriere, B. M., Poisson's ratio in orthotropic materials, *Am. Inst. Aeronaut. Astronaut. J.,* 6, 2226, 1968.
6. Cowin, S. C. and Van Buskirk, W. C., Thermodynamic restrictions on the elastic constants of bone, *J. Biomech.,* 19, 85, 1986.

7

Experimental Techniques for Bone Mechanics

Charles H. Turner
Indiana University

David B. Burr
Indiana University

7.1 Introduction

This chapter reviews the methods commonly used for biomechanical evaluation of bone or bone replacement materials and substantially expands upon the authors' previous review of biomechanical test methods.[1] It is assumed that the reader has a basic understanding of skeletal anatomy and mechanics of materials (these topics are covered in Chapter 1, Integrated Bone Tissue Physiology, by Jee and Chapter 6, Mechanics of Materials, by Cowin). There are a wide variety of experimental techniques available for evaluation of bone structure, microstructure, and biomechanics. Many of these are described in detail in other chapters. Techniques not covered in this chapter but covered elsewhere in the book include measurement of bone structure and mineral density using X-ray techniques (Chapter 9 by Rüegsegger and Chapter 34 by Kaufman and Siffert), quantification of trabecular structure (Chapter 14 by Odgaard), measurement of microdamage (Chapter 17 by Jepsen, Davy, and Akkus), measurement of *in vivo* bone strains (Chapter 8 by Fritton and Rubin), and measurement of viscoelastic properties of bone (Chapter 11 by Lakes).

0-8493-9117-2/01/$0.00+$.50

7.2 Specimen Handling and Considerations

Bone biomechanical properties vary with anatomical site and are affected by the age and general health of the donor. In addition, the preparation and storage of bone specimens can affect the mechanical properties of the tissue. Important factors include specimen preservation (covered in Chapter 20 by Martin and Sharkey), hydration, and temperature. Tissue autolysis begins within hours following removal of bone from the body, and with time this adversely affects the mechanical properties of bone.[2,3]

7.2.1 Bone Hydration

After it is dried, the Young's moduli and strength of bone will generally increase, but its toughness will decrease.[4,5] Evans and Lebow[6] showed a 17% increase in the Young's modulus of the whole human femur, a 31% increase in ultimate tensile strength, but a 55% decrease in toughness, after drying. For accurate testing results, therefore, it is best to test bone in its hydrated condition. This can be done by keeping specimens in physiological saline or wrapped with saline-soaked gauze during the test.

The mechanical ductility of dry cortical bone is, for the most part, recoverable by rewetting in buffered physiological saline.[7,8] It takes about 3 h in saline for bone specimens to recover their wet weight completely.[7] The mechanical properties of cortical bone, including the Young's modulus, ultimate displacement, and work to failure, were recovered after 3 h of rehydration.[7,8] However, Currey[8] found the drying/rehydration steps significantly reduced the bending strength.

7.2.2 Temperature

As in most biological materials, the mechanical properties of bone are influenced by the surrounding temperature. For accurate measurement of mechanical properties, bone specimens should be tested at 37°C. However, this is not always practical. Testing at room temperature (23°C) increases the Young's modulus of bone about 2 to 4% compared with a test at 37°C.[9–11] Thus, the error caused by testing at room temperature is not large, except for fatigue tests where bone tested at room temperature undergoes twice as many loading cycles prior to failure than bone tested at 37°C.[12] It should be noted that "room" temperature often varies considerably. The variability in biomechanical measurements can be reduced by careful control of temperature.

7.2.3 Strain Rate

The rate at which loading is applied during biomechanical testing of bone affects the measured stiffness and strength. In its natural state, bone is viscoelastic[13] (see Chapter 11 by Lakes for further discussion of bone viscoelasticity). When bone is dried, its viscous nature disappears and it behaves like a perfect spring,[14] but when bone is wet, it behaves like a spring with a small shock absorber. The resistance of the bone "shock absorber" to load varies proportionally to the rate at which the load is applied, so the mechanical properties of wet bone vary slightly with strain rate. If strain rate is increased by an order of magnitude, measured bone strength will increase by about 15%.[15] If one is trying to simulate physiological conditions, the strain rate should be between 0.01 and 0.08/s, which is within the range of strain rates that occur *in vivo*.[16]

7.3 Bone Density and Morphology Measurements

7.3.1 Direct Measurement of Bone Density

The classical method for determining density was invented by Archimedes in the third century B.C., based upon his law of buoyancy. Archimedes' principle dictates that the density of a bone sample can be determined from the dry and submerged weights

$$\rho_{\text{bone}} = \rho_{\text{fluid}} \frac{W}{W - S}, \tag{7.1}$$

where W is the dry weight, S is the submerged weight, and ρ_{fluid} is the density of the fluid in which the specimen is submerged. Bone density can be determined for hydrated bone, where W represents the hydrated weight, or for dry bone in which all of the internal water has been evaporated, e.g., by placing the specimen in a drying oven for 24 h. For cancellous bone specimens, the bone marrow must be removed before density measurement. This is typically done using a water jet to physically blow the marrow from the pores of the bone. After marrow removal by this method, there will remain a thin layer of hydrophobic residue on the trabecular surfaces. This residue causes the measurement of submerged weight in water to be highly inaccurate. One solution to this problem is to soak the bone specimen in a solvent, like acetone, for several hours to remove the hydrophobic grease from the bone surfaces. Acetone (or xylene) could cause undesirable changes in the mechanical properties of the specimen and thus may not be acceptable for some experiments. An alternative fix uses pure ethyl alcohol to determine submerged weight (thus, $\rho_{\text{fluid}} = 0.789$). This approach works because alcohol has superior wetting properties compared with water. The authors routinely use ethyl alcohol for density measurements and have found it to give better precision than the traditional technique that used distilled water. However, since alcohol has excellent wetting properties, it tends to penetrate farther into bone matrix than water. Consequently, bone volumes determined in alcohol will be slightly smaller and bone densities slightly larger than those determined in water. Alcohol tends to displace water within the bone matrix and thus tends to dry the bone. After measuring submerged weight in alcohol, bone specimens should be placed in isotonic saline for a prolonged period to rehydrate the bone tissue.

Another density measure commonly used for cancellous bone is the apparent density.[15] This is calculated as the weight of the bone specimen, after the marrow has been removed, divided by its total volume including pores. The porosity of bone can be determined from the apparent density ρ_{app} and the bone density in Eq. 7.1,

$$P = \left(1 - \frac{\rho_{\text{app}}}{\rho_{\text{bone}}}\right). \tag{7.2}$$

Using Eq. 7.2, porosity can be accurately measured for cancellous or cortical bone. Porosity also may be measured using histomorphometric techniques (see below).

7.3.2 Cross-Sectional Moment of Inertia

Cross-sectional moment of inertia (CSMI) is a measure of the distribution of material around a given axis. For the femoral midshaft, the CSMI is often estimated using the formula for a perfectly elliptical cross section.[17,18]

$$\text{CSMI} = \pi/64\ [ab^3 - (a - 2t)(b - 2t)^3], \tag{7.3}$$

where a and b are the diameters of the bone cross section and t is the average cortical thickness.

For irregular cross sections, CSMI is calculated using the parallel-axis theorem.

$$\text{CSMI} = i_c + Ad^2, \tag{7.4}$$

where i_c and A are the moment of inertia about the center axis and the area, respectively, for an element of area within the cross section, and d is the distance from the center of the element of area to a given axis on the cross section (Fig. 7.1). For a bone cross section, moments of inertia can be measured using a digitizing system or by point-counting techniques. In a digitized image, the bone cross section is made up of many rectangular elements (pixels) each with a height of h and a width of w. Eq. 7.4 then becomes

$$\text{CSMI} = \sum_{i=1}^{n} (h^3 w/12 + hwd_i^2), \tag{7.5}$$

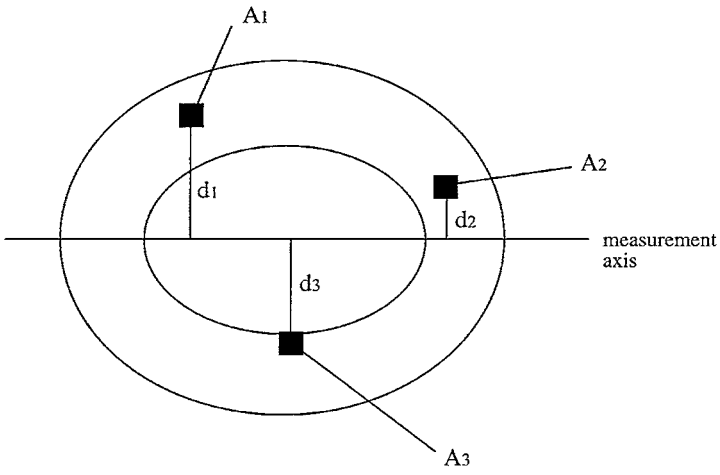

FIGURE 7.1 CSMI measurement using a digitized image of the bone cross section. The parallel-axis theorem is used for each element of area (pixel) in the image. The CSMI for the section is the sum of pixel inertia values (i_1, i_2, i_3, etc.). (From Turner, C. H. and Burr, D. B., *Bone* 14, 595–608, 1993. With permission from Elsevier Science.)

where $i_c = h^3 w/12$, $A = hw$, and d_i is the distance from the neutral axis for pixel number i. The sum of the contributions of each pixel from 1 to n gives the total CSMI for the bone section. CSMI also can be determined noninvasively using attenuation data from single photon or dual energy X-ray absorptiometry,[19–21] as well as from peripheral quantitative computed tomography (pQCT), or from microcomputed tomography (μCT).

The polar moment of inertia (J) is equal to the sum of any two cross-sectional moments of inertia around orthogonal axes or simply the sum of the maximum and minimum CSMI. J can be calculated accurately for a specimen with a circular cross-section:

$$J = \frac{\pi}{2} r^4. \tag{7.6}$$

If one is calculating J for a circular tube (like a long bone),

$$J = \frac{\pi}{2} (r_o^4 - r_i^4), \tag{7.7}$$

where r_o is the outer radius and r_i is the inner radius. Eqs. 7.6 and 7.7 are only valid for circular cross sections. For noncircular cross sections, corrections should be made to the calculation to define a more precise value of J.[22] For long bones with an irregular cross section, J is best measured computationally from a digitized image of the cross section using the polar version of the parallel-axis theorem (Eq. 7.4)

$$J = j_c + Ar^2 \tag{7.8}$$

where j_c and A are the polar moment of inertia and the area, respectively, of an element of area, and r is the radius from the center of the element of area to the center of the entire cross section.[23] For rectangular

elements of area (pixels), $j_c = (w^3h + h^3w)/12$, and $A = hw$, where h is the height and w is the width of the pixel.

7.3.3 Histomorphometry

7.3.3.1 Porosity

Porosity in human bone varies from about 70 to 80% in cancellous bone sites to 2 to 3% in cortical bone of healthy young adults. Cortical porosity may increase to 10 to 12% in disease states or in some local regions of the skeleton. In human bone, porosity increases topographically from periosteal to endosteal[24] and is greater near the endosteal surface because of the higher remodeling rates. This gradient is even more evident in bone from older people and/or from individuals with osteoporosis. Porosity is inversely and exponentially related to bone strength and modulus. Several studies suggest a cubic relationship between apparent density (which is related to porosity, see Eq. 7.2) and elastic modulus for both cortical and cancellous bone.[15] However, there is some debate about the appropriate power law relationship between apparent density and elastic modulus. Power law relationships for cancellous bone show elastic modulus proportional to apparent density raised to a power between 1 to 2,[25,26] while relationships for cortical bone show apparent density raised to powers as high as 7.[27] Nevertheless, there is general agreement that small increases in porosity can produce much larger reductions of mechanical strength and stiffness.

Porosity is most easily measured microscopically in two dimensions (areal measures) from cross sections of bone using stereological point-counting techniques. It is expressed either as a dimensionless number or as a percentage of the total (bone + nonbone) area or volume. Even for highly anisotropic structures, the porosity measurement is typically unaffected by section orientation, with the exception of cortical bone where measurement in longitudinal sections will give slightly larger values of porosity compared with measurement in cross sections. This is because of the directionality of Haversian canals. The maximum width of the canal, rather than the average width, is generally seen in a longitudinal section.[28] This optical effect causes overestimation of porosity in longitudinal sections. Consequently, it is best to measure porosity from cross sections, or using reflected light on polished longitudinal sections, which can be considered infinitely thin.

7.3.3.2 Collagen Orientation

There is a large body of work showing a close association between the predominant mode of strain and collagen fiber orientation (reviewed in Ref. 29). This was based in part on the early work of Ascenzi and Bonucci[30,31] on single osteons showing that osteons with predominantly longitudinally oriented collagen fibers were stronger and stiffer in tension than osteons with collagen fibers oriented transversely. Conversely, osteons with transversely oriented collagen fibers were stronger and stiffer in compression than those with longitudinally oriented fibers. Collagen fiber orientation is typically evaluated based on the birefringence of bone under polarized light. Under polarized light, osteons with longitudinally oriented collagen fibers appear dark, whereas those with transversely oriented collagen fibers appear light. This technique has been criticized because the birefringence pattern one observes is altered by the orientation of the tissue section with respect to the collagen fibers, and can change with alterations in the orientation of microstructural units like osteons.[32,33]

Martin and Ishida[34] developed a method of evaluating collagen orientation by using circularly polarized filters made by combining a quarter-wavelength plate with a sheet of plane polarizing material with the vibration directions oriented at 45° with respect to each other. This method is more quantitative than previous methods of evaluating collagen fiber orientation, and can be used to reduce or eliminate variations caused by differences in staining and porosity. Briefly, dark-field measurements are made using circularly polarizing filters above and below the microscope stage, and bright-field measurements are made with the lower filter removed. A light meter produces a voltage proportional to the average light intensity of a field, and a multimeter is used to measure this voltage. Illumination is adjusted in bright field to produce a standardized voltage without a histological section on the microscope stage. The analyzing

filter of a set of polarizers is rotated between bright and dark fields. Because the light intensity of a stained cross section in bright field (V_o) is dependent on staining and porosity, and intensity in dark field is dependent on these plus the birefringence of the collagen fibers when the light is polarized (V_d), a ratio can be defined (V_o/V_d) that is an approximate quantitative measure of the degree of longitudinal orientation of the collagen. The precision of this measurement was found to be about ± 5 to 6%. Using this "longitudinal structure index" (LSI), Martin and co-workers found that collagen fiber orientation is indeed a significant determinant of bone strength in tension[34] and bending.[35] While this method did not directly address the concerns about the effect of tissue orientation on the measurement, LSI has been shown to correlate with the tissue anisotropy ratio determined acoustically in cortical bone samples and in demineralized bone.[36] Interestingly, LSI was not correlated with anisotropy ratio in deproteinized bone, indicating that LSI reflects collagen fiber orientation, but not the mineral crystal orientation, in bone matrix.

7.4 Mechanical Testing Methods

7.4.1 Outcome Measures

There are a number of biomechanical parameters that can be used to characterize the integrity of bone. The key relationship is that between load applied to a structure and displacement in response to the load (Fig. 7.2). The slope of the elastic region of the load–displacement curve represents the extrinsic stiffness or rigidity of the structure. Besides stiffness, several other biomechanical properties can be derived, including ultimate load (force at failure), work to failure (area under the load–displacement curve), and ultimate displacement. Each of these measured parameters reflects a different property of the bone: ultimate load reflects the general integrity of the bone structure, stiffness is closely related to the mineralization of the bone, work to failure is the amount of energy necessary to break the bone, and ultimate displacement is inversely related to the brittleness of the bone. The biomechanical status of bone may be poorly described by just one of these properties. For example, a bone from a patient with osteopetrosis will tend be very stiff, but also very brittle, resulting in reduced work to failure and increased risk of fracture (Fig. 7.3). On the other hand, a bone from a young child will tend to be poorly mineralized and weak, but very ductile (large ultimate displacement), resulting in increased work to failure. Because of these properties, "greenstick" fractures, in which the bone undergoes large deformation but does not completely break, are sometimes observed in children.

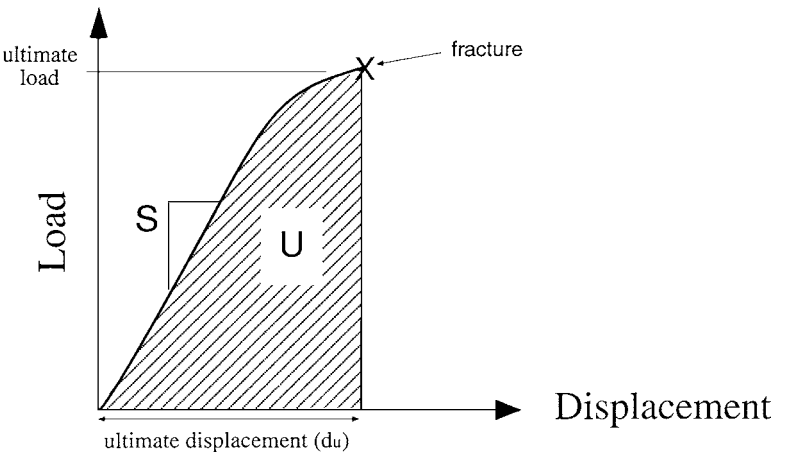

FIGURE 7.2 The load–displacement curve, illustrating the four key biomechanical parameters for the bone specimen: ultimate load, extrinsic stiffness or rigidity (S), work to failure (U), and ultimate displacement. (From Sato M. et al., *J. Med. Chem.*, 42, 1–24, 1999. With permission by the American Chemical Society.)

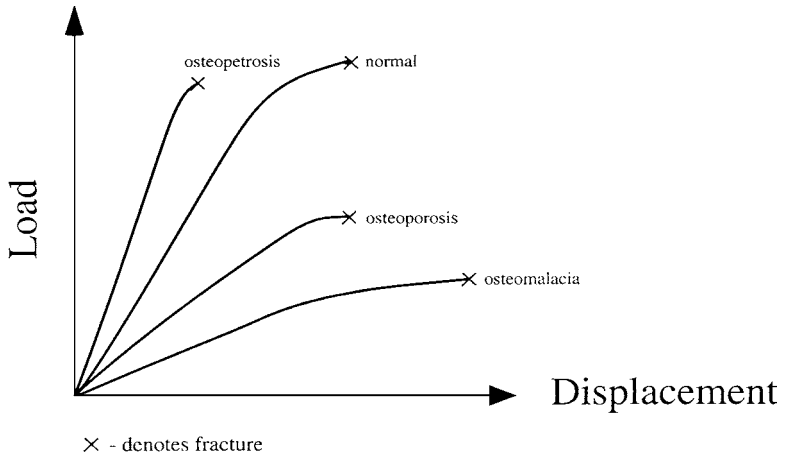

FIGURE 7.3 Bone diseases have characteristic biomechanical profiles that require measurement of several mechanical parameters to properly resolve. Osteopetrotic bone is stiff but brittle, osteomalacic bone is compliant and ductile, while osteoporotic bone is weak. Each of these diseases reduce work to failure and thus increase bone fragility. (From Sato M. et al., *J. Med. Chem.*, 42, 1–24, 1999. With permission by the American Chemical Society.)

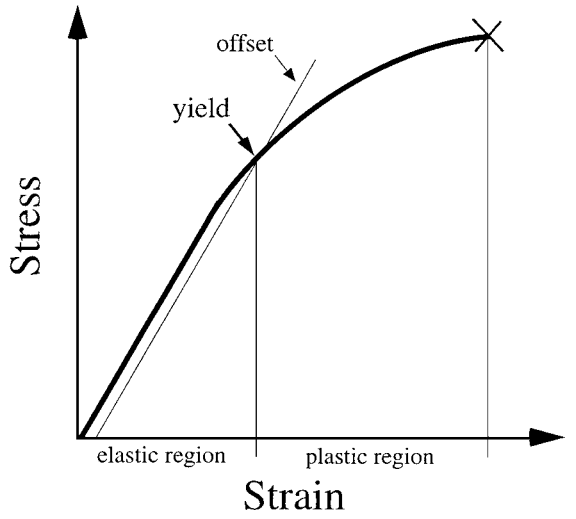

FIGURE 7.4 The stress–strain curve is divided into elastic and plastic regions by the yield point (the stress level above which permanent damage occurs in the bone matrix). The yield point is often estimated using the offset method—a line, parallel to but offset by a predetermined distance from the linear portion of the curve, is constructed and the intersection of the stress–strain curve and the offset line denotes the yield point.

When load is converted to stress and deformation converted to strain by engineering formulae, the relationship between stress and strain in bone follows a curve called the stress–strain curve (Fig. 7.4). The slope of the stress–strain curve within the elastic region is called the elastic or Young's modulus. The Young's modulus is a measure of the intrinsic stiffness of the material. The area under the stress–strain curve is a measure of the amount of energy needed to cause a fracture. This property of a material is called energy absorption or modulus of toughness.[37] The maximum stress and strain the bone can sustain are called the ultimate strength and ultimate strain, respectively. It should be noted that strength, as it is defined by the stress–strain curve, is an intrinsic property of bone. That is, these strength values are independent of the size and shape of the bone. The force required to break the bone is different from

the intrinsic strength, because ultimate load will vary with bone size. It is important to keep this distinction in mind because intrinsic strength and ultimate load can show different trends in drug or genetic studies, especially if the drug or gene affects the size of the bone. Strength measures that are not presented in units of stress do not represent the intrinsic strength of the material but are influenced by extrinsic factors like specimen size and shape.

The elastic strain region and the plastic strain region of the stress–strain curve are separated by the yield point (see Fig. 7.4). The yield point represents a gradual transition, above which stresses begin to cause permanent damage to the bone structure. In reference to the yield point, the elastic strain region is often called the pre-yield region and the plastic strain region is the post-yield region. post-yield strains (i.e., strains within the plastic strain region) represent permanent deformations of bone structure caused by slip at cement lines, trabecular microfracture, crack growth, or combinations of these. The yield point is seldom well defined when testing bone specimens. Several methods have been proposed to determine the yield point. For example, the yield point is often defined as the point where the stress–strain curve begins to become nonlinear.[38] Other techniques include offset methods where a line parallel with the linear portion of the stress–strain curve and offset by 0.03 to 0.2% strain is constructed.[39] The point where this line intersects the stress–strain curve is arbitrarily called the yield point.

7.4.2 Equipment

Basic tools for biomechanical testing of bone include a mechanical testing machine, strain measurement transducers, and a system for recording stress and strain. Testing machines can be screw driven, pneumatic, servo-hydraulic, electromagnetic, or stepper motor driven. The most versatile machines can apply loads or displacements to bone specimens at a variety of different rates and magnitudes. Many mechanical testing machines are designed for testing engineering materials and have capacities of up to tens of thousands of newtons. For biomechanical applications, maximum loads typically do not exceed 1000 or 2000 N. For testing microspecimens of bone or for testing small bones, smaller machines (often called texture analyzers) are available that allow sensitive control of loads as small as a few grams. Most mechanical testing machines contain transducers that give displacement of the loading platen, which provides data for calculating strain in the specimen. However, specimen displacement and machine displacement are never exactly equal. The test machine itself has some compliance and there will always be some displacement in the machine components during a test. The compliance of the machine can be measured by allowing the machine to apply load without a specimen in place (this should be done carefully to avoid damaging the load cell). For this test, a machine stiffness (S_M) is calculated as the applied load divided by the machine displacement. The test is then repeated with a specimen in place, resulting in an apparent stiffness (S_{app}) for the specimen. The actual stiffness of the specimen (S) is

$$S = \frac{S_{app} S_M}{(S_M - S_{app})}. \tag{7.9}$$

If S_M is much greater than S, the error caused by compliance in the machine is minimal. This is usually the case when testing bone specimens, so correction for machine compliance is not always necessary. In addition, the calculation of strain from specimen displacement may be confounded due to inhomogeneous strains within the specimen. More accurate strain measurement transducers include resistance strain gauges that can be bonded directly to the specimen with cyanoacrylate cement[40–42] and extensometers that clip onto the specimen.

Preparation of test specimens may require special fabrication. For example, one might prepare dog bone-shaped tensile specimens from the cortex of a long bone, or cubes of trabecular bone for compressive tests. A diamond wafering saw is the preferred tool for creating smooth, flat surfaces on bone specimens. It is also possible to obtain diamond-coated cylindrical cutters for boring cylindrical bone specimens from either cortical or cancellous bone sites. Preparation of complex specimen shapes requires a small mill/lathe. Several manufacturers provide small machining tools to include a mill and

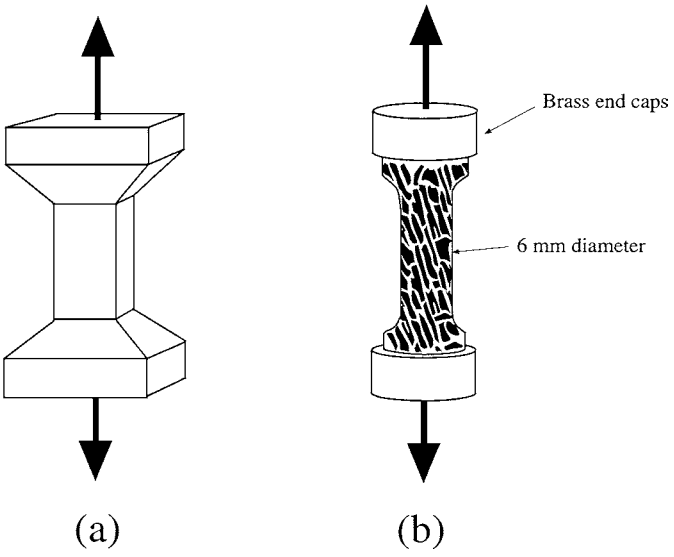

FIGURE 7.5 Tensile test specimens for cortical bone (a) and cancellous bone (b).[43,44] The design objective of a tensile test specimen is for failure consistently to occur in the central portion of the specimen. This objective is achieved by making the cross-sectional area of the central portion smaller than the ends. (Adapted from Turner, C. H. and Burr, D. B., *Bone,* 14, 595–608, 1993. With permission from Elsevier Science.)

lathe in the same unit. These instruments are ideal for fabricating small bone specimens. During fabrication it is important to keep the bone moist and to avoid heating of the specimen while cutting.

7.4.3 Tensile Testing

Tensile testing can be one of the most accurate methods for measuring bone properties, provided that force is applied without inducing a coupled bending moment. This can be accomplished by attaching universal joints to the testing fixtures. Examples of tensile test specimens for cortical bone[43] and cancellous bone[44] are shown in Fig. 7.5. These specimens are designed so that the majority of the strain will occur in the central portion of the specimen. Strain measurement can be accomplished accurately by attaching a clip-on extensometer to the midsection of the specimen.

There is a difference between intrinsic material stiffness of the specimen, and extrinsic stiffness, which is influenced by specimen size and shape. For a tensile test of bone the intrinsic stiffness is equal to the Young's modulus (E) while the extrinsic stiffness is equal to EA/L, where A is the cross-sectional area of the specimen and L is the length of the specimen.

Tensile test specimens must be relatively large and carefully machined (the specimens in Fig. 7.5 are 15 to 25 mm in length; Keaveny's specimen preparation technique begins with a 40-mm cylinder of cancellous bone[44]). This limits the usefulness of tensile testing for bone, particularly when testing cancellous bone because the specimen must be large enough to allow the trabecular structure to be treated as a continuum.[45]

7.4.4 Compressive Testing

Compressive testing of bone specimens allows the use of relatively small specimens. However, compressive tests tend to be less accurate than tensile tests due to end effects imposed on the specimen during the test. Should the faces of the bone specimen be slightly misaligned with the loading platen (Fig. 7.6a), large stress concentrations can occur causing an underestimation of both Young's modulus and strength. The placement of a pivoting platen in the load train greatly reduces misalignment error (Fig. 7.6b).

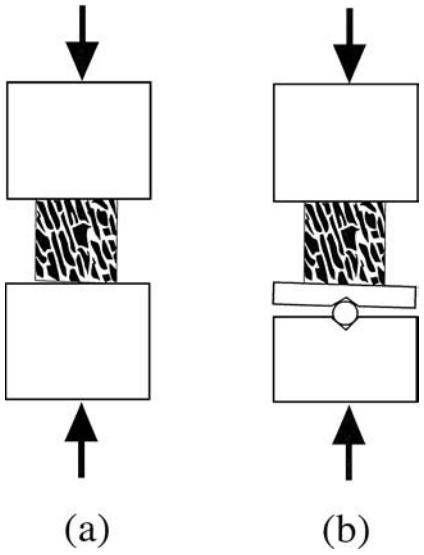

FIGURE 7.6 Compressive test of a cancellous bone cube. In (a) the loading platens are slightly misaligned with the specimen. This causes a stress concentration at the right edge of the specimen leading to inaccurate results. In (b) a pivoting platen is incorporated into the load train to correct for the misalignment. (From Turner, C. H. and Burr, D. B., *Bone,* 14, 595–608, 1993. With permission from Elsevier Science.)

Friction between the specimen and compression platen also can contribute to measurement error. When a bone specimen is compressed, it will expand in the transverse directions due to the Poisson's effect. Friction at the platen–specimen interface will interfere with this expansion and change the apparent stiffness of the specimen. Lubrication of the platens with petroleum jelly has been shown to reduce interface friction.[46]

Another problem associated with compressive testing of cancellous bone is the end effect created by machining a test specimen.[47–51] Typically cubes or cylinders of cancellous bone, about 7 to 10 mm in width, are cut using an irrigated saw or burr.[52–54] At the boundary where the specimen contacts the loading platen, the trabeculae are unsupported. For this reason, the strain tends to be much greater in the boundary region than in the middle of the specimen.[47,49,50] The elevated strains at the ends of the specimen cause overestimation of the average specimen strain, underestimation of Young's modulus, and overestimation of specimen toughness. The accuracy of the Young's modulus calculations can be improved by direct measurement of strain at the midsection of the specimen using a clip-on extensometer. The most accurate compressive testing technique was described by Keaveny et al.[44] They machined waisted specimens that were gripped with brass end caps (see Fig. 7.5). The disadvantage of Keaveny's technique is that it requires large specimens (cylinders 30 to 40 mm in length).

Although it is considerably more difficult to achieve accurate results using a compressive test compared with a tensile test, the compressive test has several advantages. First, the compressive specimens need not be as large as tensile specimens (with the exception of Keaveny's technique); this is a major advantage when testing cancellous bone. Second, fabrication of compressive specimens may not be as difficult as with tensile test specimens. Finally, in some regions of the skeleton (e.g., the vertebrae) compressive tests more closely simulate the *in vivo* loading conditions to which the bone is exposed. Even with the measurement errors discussed above, compressive tests can provide useful biomechanical data. The compressive test is preferred for measuring mechanical properties of vertebral specimens. There are several issues to consider when testing whole vertebrae in compression. Generally, the spinous processes posterior to the spinal canal should be removed, while taking care not to damage the vertebral body. In some cases, it may be desirable to test the vertebral body with the posterior processes intact. This can be done using custom loading platens that make contact only with the vertebral body (Fig. 7.7). The precision of the test can

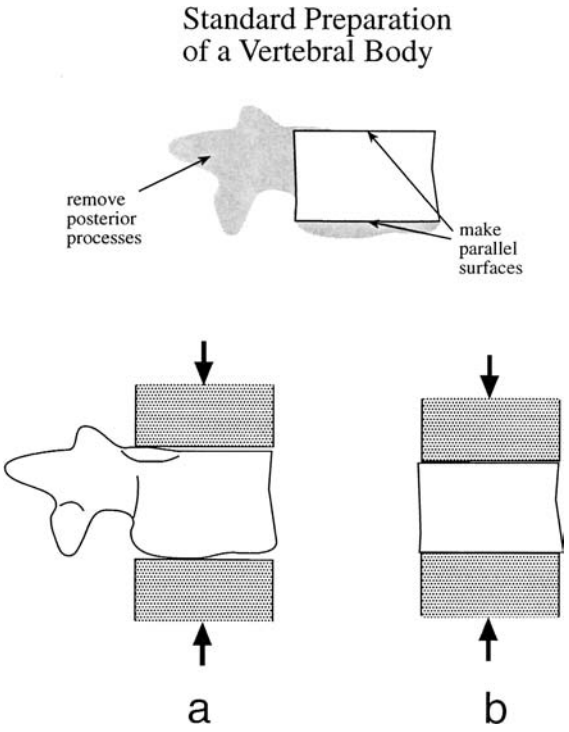

FIGURE 7.7 Compressive test of vertebral specimens. Generally the spinous processes posterior to the spinal canal should be removed. In some cases, it may be desirable to test the vertebral body with the posterior processes intact (a). The precision of the test can be improved by removing the end plates of the vertebral body with parallel cuts (b).

be improved by removing the end plates of the vertebral body with parallel cuts using a diamond wafering saw. The final specimen should have parallel faces and its height should be equal to or less than its width.

For a specimen in compression, stress is calculated as the applied force divided by the cross-sectional area of the bone specimen. However, the calculation of stress is complicated for cancellous bone specimens by the underlying trabecular microstructure. For cancellous bone, force divided by cross-sectional area gives an apparent stress, yet less than 30% of the specimen is bone tissue. Consequently, the apparent stress in the specimen and the true stress in the trabecular tissue are quite different quantities. The trabecular stress is more accurately approximated as

$$\sigma = \left(\frac{F}{A}\right)\left(\frac{1}{A_f}\right), \tag{7.10}$$

where σ is stress, F is force, A is the specimen cross-sectional area, and A_f is the area fraction of trabecular tissue. However, Eq. 7.10 must be viewed as an estimate because stress is not exactly proportional to $1/A_f$, instead it is generally accepted that σ is proportional to $1/A_f^n$.[55,56] Unfortunately, there is no consensus regarding what the value of the power n should be, except that it falls between 1 and 2.[55]

7.4.5 Bending Tests

Bending tests are useful for measuring the mechanical properties of long bones. For bones from small animals it is very difficult to machine tensile or compressive test specimens. In the bending test the whole long bone is loaded in bending until failure. Stresses due to bending can be calculated using the

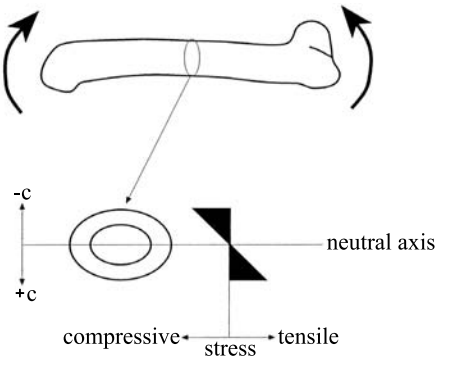

$$\sigma = Mc/I$$

σ - stress
M - bending moment
c - distance from cross-sectional center of mass
I - cross-sectional moment of inertia around the axis of bending

FIGURE 7.8 Bending causes both tensile and compressive stresses. Stress magnitude is greatest at the surface of the bone and is zero at the neutral axis. (From Turner, C. H. and Burr, D. B., *Bone,* 14, 595–608, 1993. With permission from Elsevier Science.)

beam-bending formula in Fig. 7.8. This beam-bending formula is valid for beams with symmetric cross sections. For some bones, the tibia, for example, the cross section is assymmetric and a more complicated formula is required to calculate stresses accurately.[57] Bending causes tensile stresses on one side of the bone and compressive stresses on the other. Bone is weaker in tension than compression,[58] so in a bending test failure usually occurs on the tensile side of the bone.

Bending can be applied to the bone using either three-point or four-point loading (Fig. 7.9). The advantage of three-point loading is its simplicity, but it has the disadvantage of creating high shear stresses near the midsection of the bone. Four-point loading produces pure bending between the two upper loading points, which ensures that transverse shear stresses are zero. However, four-point bending requires that the force at each loading point be equal. This requirement is simple to achieve in regularly shaped specimens but difficult to achieve in whole bone tests. Therefore, three-point bending is used more often for measuring the mechanical properties of long bones.

Stress, strain, Young's modulus, and modulus of toughness can be calculated from the force and displacement of the loaders in Fig. 7.9. For three-point loading the equations are

$$\sigma = F\left(\frac{Lc}{4I}\right), \quad \varepsilon = d\left(\frac{12c}{L^2}\right), \quad E = S\left(\frac{L^3}{48I}\right), \quad u = U\left(\frac{3c^2}{IL}\right) \tag{7.11}$$

and, for four-point loading,

$$\sigma = F\left(\frac{ac}{2I}\right), \quad \varepsilon = d\left(\frac{6c}{a(3L-4a)}\right), \quad E = S\left(\frac{a^2}{12I}\right)(3L-4a), \quad u = U\left(\frac{3c^2}{I(3L-4a)}\right), \tag{7.12}$$

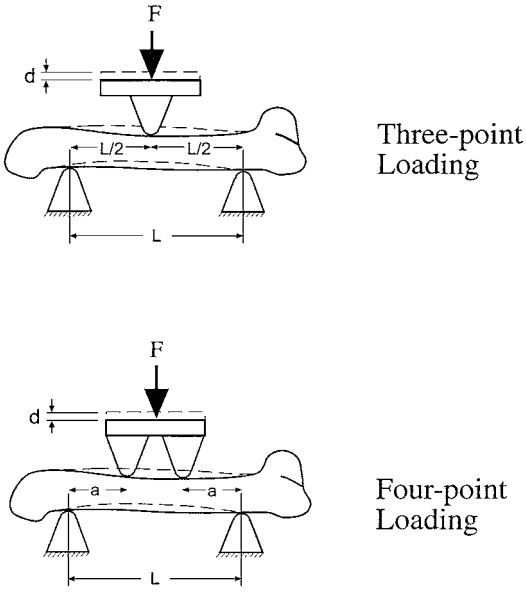

FIGURE 7.9 Bending can be applied to rodent bones and machined bone specimens using either three-point or four-point loading. *F* is the applied force and *d* is the resulting displacement. (From Turner, C. H. and Burr, D. B., *Bone,* 14, 595–608, 1993. With permission from Elsevier Science.)

where σ is stress, ε is strain, *E* is Young's modulus, *S* is stiffness, *u* is modulus of toughness, *U* is the work to failure (area under the load-displacement curve), *c* is the distance from the center of mass of the cross section (see Fig. 7.8), *I* is the cross-sectional moment of inertia about the neutral axis, *F* is applied force, *d* is displacement, and *a* and *L* are lengths given in Fig. 7.9.[37] Indirect calculation of strain is inaccurate, however, for several reasons. First, the equations given above for strain are only valid within the pre-yield region of the stress–strain curve; once the yield point is surpassed, strain is not so easy to calculate.[3] Second, substantial deformation of the specimen occurs where the loaders contact the bone. Finally, the span of the specimen that is loaded (shown as *L* in Fig. 7.9) must be sufficiently long to guarantee an accurate test. If *L* is very short, much of the displacement induced by loading will be due to shear stresses and not bending. For bone specimens, the ratio of length to width should be at least 20:1 to guarantee that shear displacements are insignificant.[59] For long bones, the length-to-width ratio is typically less than half of the recommended value, so shear stresses will cause substantial displacement (shear stresses cause 15 to 20% of the measured deformation in bending tests of whole rodent bones; Turner, unpublished data). These effects cause the measured displacement to be greater than the flexural displacement of the bone, resulting in an overestimation of strain and an underestimation of Young's modulus. Strain can be measured more accurately by using a resistance strain gauge bonded directly to the midshaft of the bending specimen. The authors found the Young's modulus of the rat tibia to be 29.4 GPa using a resistance strain gauge attached to the bone,[60] but the calculated value of Young's modulus from displacement of the loaders (using Eq. 7.12) was only 7.6 GPa.[1] Key to a successful three-point bending test for whole bones are the dimensions of the testing fixtures. Of greatest importance are the span between the lower loaders and the radius of curvature of the loading surfaces (Fig. 7.10)—the former determines the length-to-width ratio and the latter determines how much bone deformation will occur beneath the loaders.

For bending tests, it is important to distinguish between intrinsic stiffness and extrinsic stiffness of the bone. The intrinsic stiffness is equal to the Young's modulus (*E*), while the extrinsic stiffness or flexural rigidity is equal to *EI*, where *I* is the cross-sectional moment of inertia. As noted above, bending tests on whole-bone specimens give inaccurate values for Young's modulus and strain; however, accurate results can be obtained by testing a strip of bone machined from the cortical diaphysis (Fig. 7.11). For a machined specimen tested in three-point bending, the stress, strain, Young's

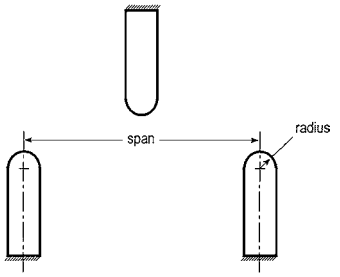

Loader Dimensions for Different Animal Species

Species (BW)	bone	Span	Radius
mouse (30 g)	femur	5 mm	0.75 mm
rat, female (350 g)	femur	15 mm	2.0 mm
rat, male (500 g)	femur	20 mm	2.0 mm
rabbit (2.3 kg)	femur	55 mm	6.0 mm
cynomolgus monkey (2.7 kg)	humerus	55 mm	6.0 mm

FIGURE 7.10 The key dimensions for a three-point bending test of a long bone are the span between the lower loaders and the radius of curvature of the loading surfaces. The table shows representative dimensions used successfully in the authors' laboratory.[68,137,139,165–168]

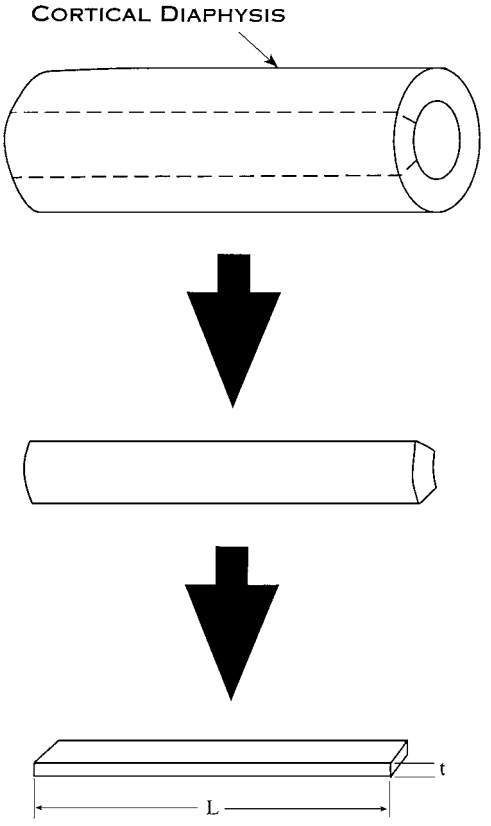

FIGURE 7.11 Accurate measurement of bone tissue properties can be obtained by testing a strip of bone machined from the cortical diaphysis, provided that the ratio of L to t is greater than 20.

modulus, and modulus of toughness are estimated by

$$\sigma = F\left(\frac{3L}{2wt^2}\right), \quad \varepsilon = d\left(\frac{6t}{L^2}\right), \quad E = S\left(\frac{L^3}{4wt^3}\right), \quad \text{and} \quad u = U\left(\frac{9}{Lwt}\right), \tag{7.13}$$

where F is applied force, d is loader displacement, S is stiffness, U is the work to failure, L is the span of the loaders, and w and t are the specimen width and thickness. Eq. 7.13 does not account for shear deformation in the specimen; yet the error associated with this simplification is minimal if the ratio of L to t is greater than 20. Spatz et al.[59] recommended designing a test for bone tissue with $L/t = 25$, whereas the American Society for Testing and Materials recommends $L/t = 16$ for plastics (D 790M-82).

7.4.6 Torsion Testing

A torsion test can be used to measure the mechanical properties of bone in shear. When a torque is applied to a circular specimen, shear stress varies from zero at the center of the specimen to a maximum at the surface (Fig. 7.12). The general equations for calculating shear stress and shear modulus of elasticity in a torsion test are

$$\tau = \frac{Tr}{J} \qquad \text{and} \qquad G = \left(\frac{TL}{\theta J}\right), \tag{7.14}$$

where τ is shear stress, G is shear modulus, T is applied torque, θ is rotational displacement, r is the radius of the specimen, L is the length of the specimen test region, and J is the polar moment of inertia of the specimen. It should be noted that the general equation for shear stress (Eq. 7.14) is inaccurate if

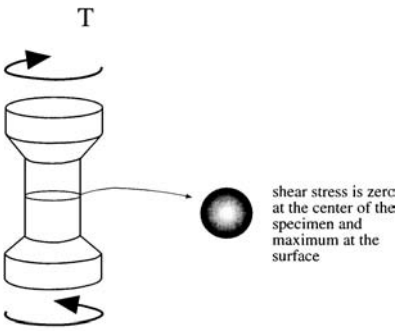

FIGURE 7.12 Torsion creates shear stresses that are greatest at the surface and are zero at the center of mass. Torsion specimens, like tensile specimens, are machined such that the central portion is more narrow so most of the displacement occurs in this region. (From Turner, C. H. and Burr, D. B., *Bone,* 14, 595–608, 1993. With permission from Elsevier Science.)

the cross section is not circular. Equations for shear stress in noncircular cross sections can be found in various references (e.g., Ref. 61).

Torsion tests are often used to measure the strength of whole bones from rodents.[62,63] A major disadvantage of torsional testing of whole bones is the difficulty of mounting the specimen ends into the testing grips. The bone ends must be embedded in blocks of plastic or a low-melting-point metal alloy to allow rigid fixation with the testing grips. Embedding adds specimen preparation time and expense for each test. There also are potential errors associated with embedding. The specimen must remain perfectly aligned while the embedding resin hardens. Any misalignment could induce a bending moment that would confound the test result. Also plastic embedding resins have significant compliance, and thus allow substantial rotation of the ends of the specimen within the grips resulting in an overestimation of rotational displacement and an underestimation of torsional rigidity. Consequently, bending, rather than torsional, testing is the preferred methodology for large-scale screening of long bones for pharmaceutical or genetic effects. However, torsion offers a distinct advantage over bending tests for measuring the biomechanical effects of fracture healing, bone defects, or bone grafts. Torsion allows the load to be applied at the ends of the bone, away from the bone defect/graft, whereas three-point bending requires loading near or directly above the defect/graft. Besides torsion, four-point bending is another useful method for testing long bones with grafts or defects.

7.4.7 Site-Specific Tests

A number of methods have been developed to measure biomechanical properties at a variety of different anatomical sites. A site of particular clinical interest is the femoral neck. With the recent acceleration in drug development for preventing hip fractures associated with osteoporosis, there has been considerable interest in the biomechanics of the femoral neck.[64,65] Biomechanical tests of the femoral neck are done routinely when assessing the effect of antiosteoporosis drugs in animal models.[66–68] To measure femoral neck strength, the proximal end of the femur is mounted in a loading fixture, either by embedding it into plastic resin or by clamping it in place, and force is applied to the femoral head until the femoral neck fractures. This test produces a load–displacement curve from which biomechanical parameters can be calculated. There are two common loading configurations for the femoral neck (Fig. 7.13): either load is applied parallel to the femoral shaft (axial configuration[69]) or in a simulated fall configuration.[70–72] The simulated fall configuration provides valuable information about the biomechanics of the human hip

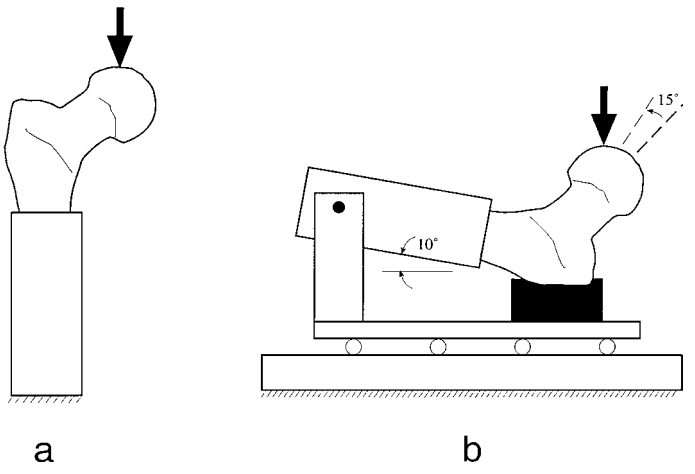

FIGURE 7.13 Biomechanical tests of the femoral neck typically use either the axial loading configuration (a) or the simulated fall configuration (b). The simulated fall configuration places the femoral neck in 15° internal rotation and 10° from horizontal.[70,72]

under realistic loading conditions. However, application of the technique in small rodent bones introduces experimental error—due to difficulty in positioning the small bones. For mouse bones, the reproducibility for the axial loading configuration is more than twice as good as the simulated fall configuration.[73]

7.4.8 Indentation Testing

Indentation tests are used to map the biomechanical properties of subchondral bone and the underlying trabecular bone near diarthrodial joints or bone adjacent to implants. The biomechanical properties of bone in these regions are clinically important in studies of osteoarthritis progression and joint replacement arthroplasty. Indentation testing also may be used for measuring Young's modulus and strength of trabecular bone specimens.[74,75] Tests are usually done with a blunt end indentor, ranging from 2.5 to 6 mm in diameter, at a displacement rate of 2 mm/min and to a depth of 0.2 to 0.5 mm.[75–78] As the indentor penetrates the specimen, a load–displacement curve is created. The strength of the bone is estimated as the maximum load divided by the cross-sectional area of the indentor. The Young's modulus is calculated as

$$E = S\left(\frac{1-\nu^2}{d}\right), \tag{7.15}$$

where S is the slope of the load–displacement curve, ν is the Poisson's ratio of the bone, and d is the diameter of the indentor.[79]

7.4.9 Pure Shear Tests

Torsion testing allows the measurement of shear properties of bone but, because of the composite nature of bone, torsion also creates tension within the structure.[14] Because of this and other difficulties with the torsion test, other methods for measuring the shear properties of materials (especially composite materials) have been developed. These include the rail shear test, the torsion tube, cross-beam specimens, and tension–compression of notched specimens (see Ref. 80). Each of these methods has limitations when applied to bone mechanics.

Methods for shear testing that can be adapted for bone specimens are those of Iosipescu and Arcan.[81–83] Both tests use a notched specimen: Iosipescu applied offset four-point loading to a knotched beam, while Arcan used a butterfly-shaped specimen rigidly attached to a special testing fixture (Fig. 7.14). For both Iosipescu and Arcan test specimens shear stress is calculated by F/ht, where F and h come from Fig. 7.14, and t is the thickness of the specimen. Shear strain is approximately equal to the total displacement between the contact points of the test fixture, assuming the test fixture is much stiffer than the bone specimen.

Pure shear tests have advantages over torsion tests because they tend to be more accurate and, for the Arcan test, smaller test specimens can be used. Nevertheless these tests require machined specimens taken from a relatively large bone, i.e., the cortex of the bone must be 5 to 10 mm thick.

7.4.10 Fracture Mechanics Testing

The goal of fracture mechanics is to describe the fracture process in a structural material. The key relationship is that between the local stress field near a crack tip and the resultant growth of the crack. A fracture mechanics test produces two key parameters: the critical stress intensity factor, K_c, and the critical strain energy release rate, G_c. K_c is also known as fracture toughness (not to be confused with the modulus of toughness described above; modulus of toughness is reported in units of N/m^2, or J/m^3, while K_c is reported in units of N/m, or J/m^2). For details about the calculation of K_c and G_c from a fracture mechanics test, see Norman et al.[84] Like pure shear tests, measurement of fracture mechanics parameters requires fairly large pieces of bone. There are several specimen geometries that are useful for determining fracture parameters. The geometry most useful in bone mechanics is the compact tension

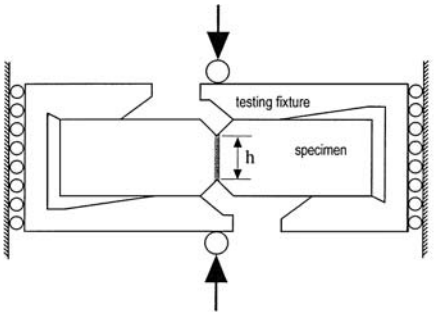

a) Iosipescu Test specimen

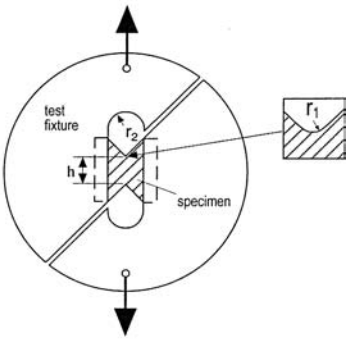

b) Arcan Test specimen

FIGURE 7.14 (a) Iosipescu and (b) Arcan test methods for producing pure shear stresses in bone. The shaded region in (a) is under pure shear when loads are applied. Iosipescu specimens are typically four times longer than they are wide with 90° notches in the center that have depths that are 20% of the specimen width, and a specimen thickness of at least 2.5 mm. For Arcan test specimens the critical dimensions are related to the width of the test region denoted h. The radius r_2 is equal to h and the fillet radius r_1 is equal to $0.14h$. It is important that the notches have fillets, because otherwise stress concentrations can be created that will cause premature failure of the test specimen. (From Turner, C. H. and Burr, D. B., *Bone,* 14, 595–608, 1993. With permission from Elsevier Science.)

specimen (Fig. 7.15).[84–90] The test standard[91] recommends the use of a thick specimen ($B = W/2$, see Fig. 7.15). This recommendation can be achieved only in bones from large animals, e.g., cattle.[84] Test specimens of human bone cannot be made with sufficient thickness because of size and geometric constraints imposed by the bone curvature and cortical thickness. Consequently, fracture mechanics parameters derived from human bone must be corrected for specimen thickness.[84,85]

7.4.11 Fatigue Testing

When a material is repetitively loaded, with loads within the pre-yield region of the stress–strain curve, its mechanical properties gradually degrade over a period of time. This degradation of strength and Young's modulus with time is called fatigue. In bone, the reduction in mechanical properties is attributed to the formation of small cracks within the bony structure. As loading continues, these cracks grow and coalesce until, ultimately, the bone will fail catastrophically. Fatigue properties can be measured using tensile, compressive, bending, or torsional loading. Fatigue testing requires a test machine capable of applying cyclic loading, e.g., a servo-hydraulic testing machine or a purpose-built fatigue machine. One of the simplest fatigue protocols is rotated beam loading.[92] According to this

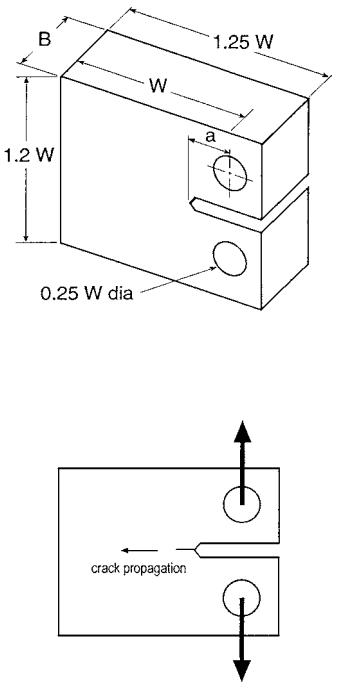

FIGURE 7.15 Compact tension specimen configuration (top). This geometry follows the recommendations of the ASTM (ASTM E 399-83), where *a* is crack length and *B* is ideally *W*/2. The specimen loading is illustrated by the bottom figure. Crack growth is typically monitored using optical methods.

protocol, waisted cylindrical specimens are rotated as a bending moment is applied, causing cyclic bending. The stress at any point on the specimen oscillates between tension and compression.

The results of fatigue tests can be summarized on an S–N diagram. The S–N diagram depicts the peak applied stress as a function of the number of fatigue cycles before failure. Generally, fatigue failure is defined as the number of cycles necessary to cause a specimen to lose 30% of its Young's modulus. The fatigue properties of bone are very sensitive to testing temperature; specimens tested at room temperature undergo twice as many loading cycles before failure compared with bone tested at 37°C.[12] Fatigue properties also will change substantially if the bone is dehydrated. Fatigue in bone can occur in two ways: creep (slippage at the cement lines[93]) or crack accumulation.[94–96] Caler and Carter[98] and Carter and Caler[99] have shown that creep is the major cause of fatigue failure if the bone is loaded in tension or at high stress (>60 MPa) while crack accumulation causes fatigue failure if the specimen is loaded in compression at low stress (<60 MPa). Consequently, creep may be a major mode of failure during extraordinary or traumatic loading while crack accumulation is the predominant damage mechanism under typical daily activities or exercise.

A major problem in designing a fatigue test is the fact that a cortical bone specimen can undergo as many as 37 million low-stress (24-MPa) loading cycles[97]; this translates to 43 days of fatigue testing at 10 cycles/s. The fatigue life is shortened considerably if the applied stress is raised to 50 MPa—5 days in tension and 45 days in compression at 2 Hz.[98] Raising the applied stress to about 60 MPa (with an applied strain of about 3000 μstrain) reduces fatigue life even farther—3 h in tension and 4 days in compression.[99] The time to do fatigue tests can be reduced by increasing the frequency at which the tests are done. Although Lafferty[100] found that loading up to 30 Hz does not change the fatigue behavior of bone, close examination of his data indicate that loading <15 Hz is recommended. While fatigue strength is an important property to quantify in bone, fatigue tests are considerably more time- and labor-consuming than most other biomechanical tests. Consequently, a fatigue test should be designed carefully with clear objectives.

7.4.12 Micro- and Nanotesting

There are a growing number of techniques to measure the biomechanical properties of bone at a microstructural or ultrastructural level. Measurements have been taken for specimens from mouse long bones, individual trabeculae, individual osteons, and individual lamellae within an osteon. Microtesting of bone began with the pioneering work of Ascenzi and Bonucci. Using specially designed equipment, they measured the mechanical properties of single osteons in tension,[30] compression,[31] and shear.[101] Ascenzi and co-workers subsequently measured single osteon properties in bending[102] and torsion,[103] and the tensile properties of single osteonal lamellae.[104] Ascenzi's studies required tremendous care in microsample preparation and a sensitive microwave extensometer to measure displacements in the microsamples.

Early mechanical tests of individual trabeculae were done by compressing the specimen along its length and extrapolating the specimen Young's modulus from its buckling behavior.[105,106] Techniques for preparation of microspecimens of bone were developed by Kuhn et al.[107] and Choi et al.[108] These specimens are about 200 μm in width by about 2000 μm in length (see Ref. 109 for a description of specimen preparation). Testing of microspecimens has been done using three-point bending,[107] four-point bending,[109,110] and tensile testing.[25] These studies open the possibility of performing tensile and bending tests with specimens machined from bones of rats and mice or for individual trabeculae. However, it should also be noted that engineering standards exist for the size and geometry of test specimens. Tests on very small specimens rarely meet these criteria, so information derived from microtensile tests must be interpreted carefully. For example, the properties derived from bending tests of microspecimens are dependent on specimen size, with lower Young's moduli being measured for smaller specimens.[108] Tensile tests of microspecimens did not show a dramatic specimen size effect, i.e., Young's moduli for microspecimens were close to those measured in standard tensile tests of bone specimens.[25] The seemingly low values for Young's modulus measured using microbending tests are probably due to stress concentrations and inhomogeneities in microspecimens caused by Haversian canals and canaliculi within the bone. These inhomogeneities have a more dramatic effect in bending testing compared with tensile testing.

Techniques for micro- and nanoindentation offer the possibility for measuring biomechanical properties in a region as small as 1 μm. Microindentation methods provide spatial resolution varying from 30 to 100 μm depending on the shape of the indentor.[111–115] Hardness measurements reflect the degree and quality of mineralization of the bone. Using the Knoop indentor, anisotropy of bone mineral hardness can be measured.[112] The newly developed nanoindentation methods offer spatial resolution from 1 to 5 μm.[116] Consequently, nanoindentation can be used to measure mechanical properties of individual lamellae in bone. Nanoindentation allows estimation of Young's modulus from the contact stiffness (S; Fig. 7.16) using the formula:

$$S = 2\pi^{-1/2}\left[\left(\frac{1-\nu_b^2}{E_b}\right)+\left(\frac{1-\nu_i^2}{E_i}\right)\right]^{-1} A^{1/2}, \tag{7.16}$$

where E and ν are the Young's modulus and Poisson's ratio, respectively, for the bone (b) and indentor (i), and A is the contact area.[117] Reasonably accurate estimates for Young's modulus have been achieved using $E_i = 1141$ GPa, $\nu_i = 0.07$, and $\nu_b = 0.3$.[118] Micro- and nanoindentation measurements require a highly polished specimen surface. Specimens are typically polished with a series of abrasive papers of decreasing grit size (600, 800, and 1200 grit). This is followed by polishing with 0.05 μm diamond powder suspended in water.

7.4.13 Acoustic Tests

The rate at which sound travels through solid matter is dependent upon its elastic properties and density or

$$v = \sqrt{\frac{E}{\rho}}, \tag{7.17}$$

where v is velocity, E is Young's modulus, and ρ is density. Eq. 7.17 can be used to determine the elastic

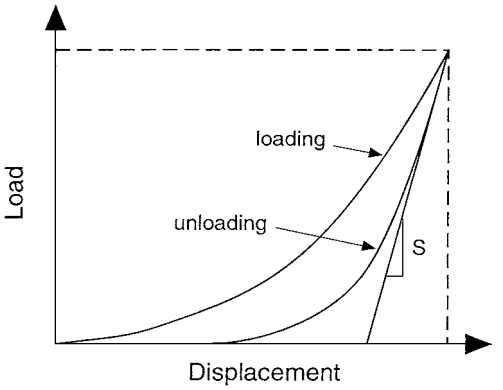

FIGURE 7.16 For the nanoindentation tests, Young's modulus was calculated from contact stiffness (S). The contact stiffness was measured from the load–displacement data as the slope of the upper portion of the unloading curve.[116] (From Turner, C. H. and Burr, D. B., *Bone,* 14, 595–608, 1993. With permission from Elsevier Science.)

properties of bone samples if the density and sound velocity are known:

$$E = \rho v^2. \tag{7.18}$$

Sound velocity can be measured by transmitting a wave through a specimen and measuring on an oscilloscope the time required for the wave to traverse the specimen; the width of the specimen divided by the time delay is the velocity.[53,119,120] Piezoelectric transducers are used to generate and detect waves for sound or ultrasound velocity measurement. Longitudinal acoustic waves can propagate through matter at two distinct velocities:[121] bulk and bar. For bar wave propagation, Eq. 7.17 is valid. However, bulk waves travel through bone about 17% faster than bar waves.[122] For bulk wave propagation

$$v = \sqrt{\frac{c}{\rho}}, \tag{7.19}$$

where c is an elasticity coefficient. For a cortical bone specimen 5 mm in diameter, bulk wave propagation will occur if the ultrasonic frequency is greater than 2 MHz; if the frequency is less than 500 kHz, bar wave propagation will occur.[122] In cancellous bone, bar wave propagation will occur if the frequency is less than 100 kHz.[120] Ultrasonic measurements are especially effective for cancellous bone because ultrasonic waves at frequencies greater than 2 MHz will travel along the individual trabeculae and allow calculation of the Young's modulus of the trabecular material.[123] In addition, shear waves can be generated in bone specimens (Fig. 7.17), and the elastic modulus in shear can be determined from the velocity of these waves:

$$G = \rho v_s^2, \tag{7.20}$$

where G is the elastic shear modulus and v_s is the propagation velocity of shear waves.

Besides the ultrasonic velocity measurements described above, there are other acoustic methods that have proved successful for measuring Young's modulus of bone. These methods include acoustic microscopy[124] and critical angle analysis.[125] Acoustic microscopy uses focused beams of acoustic energy. The acoustic velocity of a region of bone at the focal point of the acoustic beam can be measured. The advantage of acoustic microscopy is its ability to make measurements with high spatial resolution. The resolution improves as the frequency of the acoustic wave increases (resolution is 1 to 5 μm at $f = 1$ GHz).

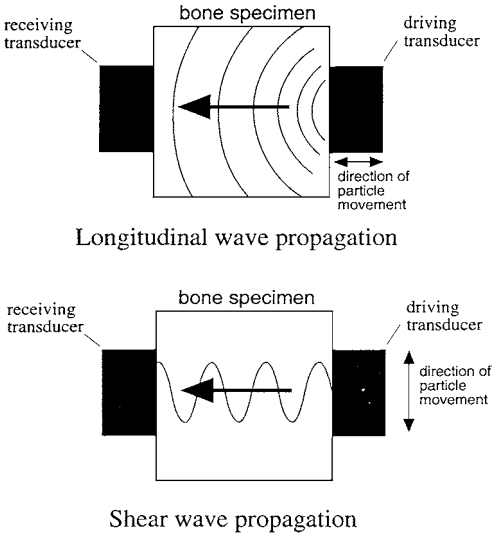

FIGURE 7.17 Ultrasound wave propagation in bone specimens. If the driving transducer vibrates in the same direction as wave propagation, longitudinal waves result. If the driving transducer vibrates in the perpendicular direction to wave propagation, shear waves result. The time delay between when the wave is sent by the driving transducer and when it is received by the receiving transducer can be used to calculate velocity. (From Turner, C. H. and Burr, D. B., *Bone,* 14, 595–608. 1993. With permission from Elsevier Science.)

Zimmerman et al.[126] developed a technique using reflected acoustic waves to provide an acoustic impedance map of bone. The acoustic impedance z is related to the elastic coefficient c of bone in the i-direction by

$$c_{ii} = z_i v_i \qquad \text{and} \qquad z_i = \rho v_i, \tag{7.21}$$

where v_i is the acoustic bulk velocity in the i-direction and ρ is density. The acoustic impedance is determined from the reflection coefficient R (this is the amplitude of the reflected wave divided by the amplitude of the incident wave):

$$z_b = \left(\frac{1+R}{1-R}\right) z_w, \tag{7.22}$$

where z_b is the impedance of the bone specimen and z_w is the impedance of the coupling medium (water). Acoustic velocity may also be measured directly using a pulse-delay technique.[127] In this method, the time delay is measured from the reflected wave on the top bone surface to the reflected wave on the bottom bone surface. The ultrasonic velocity is equal to twice the thickness of the specimen divided by the time delay (Fig. 7.18). The velocity measured using this technique represents a bulk wave velocity. Typically, specimen thickness is between 0.5 and 1 mm and the frequency of the acoustic waves is 30 to 100 MHz. It is difficult to measure velocity at frequencies higher than 100 MHz because most of the acoustic signal is attenuated within the bone specimen. Consequently, the resolution of velocity measurements is seldom better than 50 μm.

Another technique for measuring acoustic velocities in embedded biopsy specimens was developed by Antich et al.[125] This technique measures the critical angle of reflection of acoustic waves. Generally, when acoustic waves come in contact with an interface, some of the energy is reflected and the rest is refracted. When acoustic waves are propagated into the interface surface at the critical angle, all the energy is reflected and none is refracted. The value of this critical angle depends upon the acoustic velocities of the two materials making up the interface and the mode of wave propagation, i.e., longitudinal or shear (Fig. 7.19). Antich et al.[125] propagated ultrasonic waves through a water bath at various angles onto a

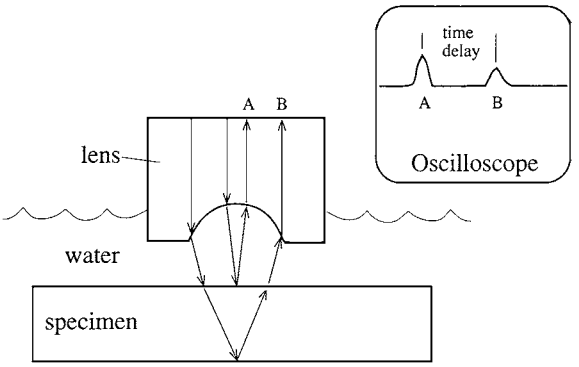

FIGURE 7.18 Acoustic velocity measurement using acoustic microscopy. The acoustic energy is reflected from the top surface of the specimen (A) and the bottom surface of the specimen (B). The two reflections can be seen on an oscilloscope and the time delay between them can be measured. The velocity is twice the thickness of the specimen divided by the time delay. (From Turner, C. H. and Burr, D. B., *Bone,* 14, 595–608, 1993. With permission from Elsevier Science.)

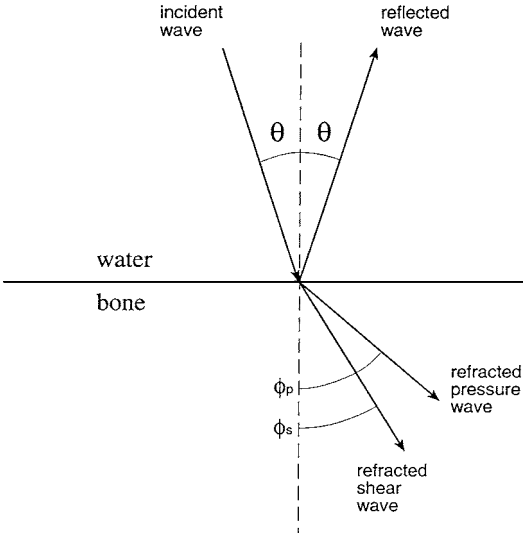

FIGURE 7.19 Acoustic propagation at a water–bone interface. The incident and reflected waves propagate at angles θ. The transmitted wave consists of a longitudinal pressure wave and a shear wave, each refracted and propagating at angles ϕ_p and ϕ_s, respectively. θ is a critical angle when either ϕ_p or ϕ_s is 90° and there is total internal reflection in water. At these angles, the reflected longitudinal or shear wave amplitudes are maximum. (Adapted from Antich, P. P. et al., *J. Bone Miner. Res.,* 6, 417–426, 1991.)

smooth bone surface to determine the critical angle. From this information they were able to calculate the ultrasonic velocity in the bone specimen. Acoustic velocities determined using critical angle analysis correlate well with those measured using transmitted acoustic waves.[128]

Acoustic test methods have advantages and disadvantages compared with the mechanical tests outlined above. The main advantage is that they are not destructive to the specimen. The measurement of velocity can be repeated several times and the results averaged to reduce experimental error. For this reason, acoustic methods can achieve much greater precision than mechanical tests—an important consideration if an experimental design requires small treatment groups.[127] Acoustic tests are versatile; they can be used to make measurements in multiple directions within a single specimen required to quantify the anisotropy

of elastic constants.[122] Acoustic tests provide accurate results in small (0.5 to 5 mm) specimens. Specimens over 10 mm in length generally cannot be used, however, because the ultrasonic waves will attenuate too much traveling through the larger specimen. The disadvantage of ultrasonic methods is that strength must be inferred,[53] because it cannot be measured directly.

There are several other acoustic methods for evaluating bone biomechanics that are not discussed in detail here. These include acoustic attenuation measurement[129–131] and $V(z)$ analysis.[132] Furthermore, also not discussed is acoustic emission, a technique used to monitor the accumulation of microdamage within bone or bone/implant interfaces. Those readers interested in this technique should refer to the comprehensive review by Kohn.[133]

7.5 Animal Models for Biomechanical Testing

7.5.1 Choice of an Animal Model

Although the animal model chosen determines, to a large extent, what biomechanical tests can be accomplished, choice of an animal model is made largely for reasons other than biomechanical necessity. For example, mice are typically used for genetic studies and the development of transgenic lines because the mouse genome is better characterized compared with other mammalian species and inbred strains of mice are well characterized physiologically and readily available.[134] Similarly, recommendations and guidelines for drug registration require that agents for prevention or treatment of osteoporosis be tested in the ovariectomized rat model and in one larger species that undergoes osteonal bone remodeling.[135,136] Studies of biomechanical stability of orthopedic implants and prosthetics requires animals with appropriate size and anatomy to allow successful surgical implantation. These studies often involve rabbits, dogs, goats, or sheep. Biomechanical testing regimens must be tailored according to the goals of the study and the special constraints associated with the animal model.

7.5.2 Biomechanical Measurements for Mice

Biomechanical testing of mouse bone is limited due to the small size of the specimens. However, long bone bending and vertebral compression tests are accomplished routinely.[137] More effort is required for long bone torsion or femoral neck biomechanical tests. Testing of tissue properties can be done using micromechanical or acoustic testing methods.[109,138] The small size of mouse bones also presents a problem for bone density measurements. X-ray densitometry techniques, with the exception of μCT, do not have sufficient resolution to represent long bone and vertebral dimensions accurately for mice, and thus provide inaccurate values for bone mineral density.

For inbred mice strains, the individual mice of each sex are genetically the same, so the biological variability in bone size and shape is minimal. Therefore, significant biomechanical changes can be measured using relatively small experimental group sizes. In their studies, the authors found that group sizes ranging from six to ten provide sufficient statistical power to detect meaningful biomechanical differences among inbred mouse strains (Turner et al., unpublished data).

7.5.3 Evaluation of Drugs for Treatment of Osteoporosis

In the past 10 years there has been an accelerated effort in research and development of drugs dedicated to the prevention and treatment of osteoporosis. Preclinical testing of new potential treatments must include tests of safety and efficacy in both the ovariectomized rat model and in one larger species that undergoes osteonal bone remodeling.[135,136] From a biomechanical standpoint, a drug is considered efficacious if it significantly improves bone strength (and work to failure) compared with the appropriate placebo-treated control, and the drug is safe if it does not induce an unacceptable decrease in tissue-level biomechanical properties of bone. Some osteoporosis therapies do not cause a safety risk; i.e., they do not impair tissue-level biomechanical properties. These include hormone therapies using estrogens or calcitonin.

Other agents improve bone strength by increasing bone size, but also impair tissue-level biomechanics. These include fluoride, which changes the bone mineral structure,[139] and parathyroid hormone, which increases porosity in cortical bone.[140] Agents in the latter category require careful scrutiny to assure that their beneficial effects outweigh any detrimental effects.

Preclinical evaluation using the ovariectomized rat model is required for registration of any potential osteoporosis drug therapy. To evaluate drug efficacy in rats, a battery of biomechanical tests is recommended. These include three-point bending of the femur, compression of a lumbar vertebra, and fracture of the femoral neck.[67,68] These tests allow the evaluation of drug effects at two clinically relevant sites—the lumbar spine and femoral neck—and a predominantly cortical bone site—the femoral diaphysis. Unfortunately, it is difficult to measure accurately the mechanical properties of cancellous bone in rats. Cancellous bone cores can be removed from lumbar vertebral bodies of rats for compressive tests.[141] However, these cancellous bone cores do not meet the requirement for a continuous structure,[45] and therefore the resulting mechanical measurements are doomed to be inaccurate. Consequently, compression tests of the whole vertebral body provide a surrogate for cancellous bone tests. It is possible to evaluate the tissue-level properties of rat cortical bone using micromechanical or acoustic testing. However, since rat cortical bone does not undergo osteonal remodeling, the rat is typically not considered an appropriate model for studying drug effects on cortical bone biomechanics. Using outbred rat strains (Sprague-Dawley is most common in bone research), the authors found that group sizes ranging from 20 to 25 provide sufficient statistical power to detect biomechanical differences among drug treatment groups.[67,68]

In addition to preclinical testing in ovariectomized rats, a potential osteoporosis drug must be tested in a larger species that undergoes osteonal bone remodeling. Several species have been evaluated as potential animal models. These include minipigs,[142] sheep,[143,144] ferrets,[145] and nonhuman primates.[146,147] Rabbits have Haversian remodeling and can be used to evaluate anabolic treatments for osteoporosis,[148] but they do not lose bone following ovariectomy and do not make a suitable model to assess treatments that only prevent bone loss. Nonhuman primates have been used most frequently for evaluation of osteoporosis drugs. A battery of biomechanical tests for measuring efficacy of the drug should be similar to those described above for rats; i.e., they should include the femoral neck, lumbar spine, and a long bone diaphysis. In addition, direct biomechanical evaluation of the bone tissue should be done to determine the drug's safety. This can be done by machining and testing tensile or bending specimens from the cortical bone shaft. These tests will demonstrate any adverse drug effect on cortical bone tissue caused by changes in the rate of osteonal remodeling, effects on the degree of mineralization or integrity of bone mineral.

7.5.4 Evaluation of Drugs for Treatment of Osteoarthritis

The main goal of a therapy for osteoarthritis (OA) is improvement of the tissue integrity of the articular cartilage. However, cartilage mechanics are affected by the stiffness of the underlying calcified cartilage, subchondral, and cancellous bone.[149,150] Consequently, the biomechanical properties of these tissues are of interest when evaluating potential treatments for OA. There are many animal models with which to study OA pathogenesis, but none is ideal.[151,152] The most commonly used models involve surgical manipulation of the joint that may include partial or full meniscectomy through a complete arthrotomy.[151,153] Of the surgical models, the Pond–Nuki model,[154,155] in which the anterior cruciate ligament is resected without arthrotomy, has become the model of choice. Significant cartilage destruction in this model requires a very long time,[156] although the speed with which cartilage lesions develop into full thickness loss can be accelerated by dorsal rhizotomy.[157] The model was developed originally using dogs, and this is still the most common model, although rabbits,[158] sheep, goat, pig, and monkeys also have been used.[159] A second class of OA models is noninvasive and does not require surgical alteration. These models involve repetitive loading or impact, usually on the knee joint, in either dogs[160] or rabbits.[161] These models lead to full thickness loss and have the added advantage that they avoid surgical intervention. However, they can be criticized on grounds that they may involve direct trauma to cartilage, which may or may not be part of the pathogenesis of the human disease. A third class of models includes those animals in which spontaneous OA occurs, e.g., guinea pigs[162] and cynomolgus monkeys.[163] These provide useful means to study the degenerative process,

but again the pathogenesis of disease in these animals may not mimic that in humans. Regardless of the choice of animal model, an effective biomechanical test of subchondral tissues should have high spatial resolution. Potential tools include micro- and nanoindentation and acoustic microscopy.

7.5.5 Evaluation of Surgical Remedies

As noted above, evaluation of the efficacy of orthopedic appliances or implants is usually done in a larger animal species. Biomechanical evaluation of the outcome may be done in a variety of different ways, depending on the goals of the study. For example, interface strength of an implant can be tested using a pullout test, in which the implant is surgically placed within the cortex of a long bone, the bone is allowed to heal, and the biomechanical force required to remove the implant is measured. Study design will vary depending on the surgical remedy that is being evaluated, but, as a minimum requirement, all study plans must (1) address ethical issues associated with animal surgery, (2) enumerate group sizes to provide sufficient statistical power, and (3) provide an appropriate control treatment (or sham surgery).

7.6 Quality Assurance

Laboratory studies that are to be used for registration of a drug or device with the U.S. Food and Drug Administration must follow the Good Laboratory Practices (GLP) guidelines.[164] The authors have implemented these practices in their laboratories over the past 7 years. The result has been an improvement in data quality, but also an increase in paperwork. What follows is a summary of the practices taken from GLP that the authors have found most worthwhile. The reader will notice that many of these practices are routinely practiced in most scientific laboratories, but others may not be as widely implemented.

7.6.1 Experimental Protocols

Each study should have a written protocol that clearly indicates the objectives and all methods for conduct of the study. The protocol should use effective experimental designs. For example, study group sizes should be sized appropriately for good statistical power and specimen numbers should be randomized after specimen collection so the individual conducting the biomechanical tests is unaware of the test group from which each specimen comes. For a large animal study, which must be accomplished in several phases, all animals should be given a unique identification number and animals within each study phase should be assigned to study groups so that each study group is equally represented. Furthermore, the protocol should anticipate and address pitfalls before beginning the study. For example, consider a long-term experiment in which specimens will be collected at several time points over the period of many months or years. Is it better to store the specimens retrieved earlier in the study and test all specimens at the end of the study, or should the specimens be tested as they are collected? If one chooses the former option, there will likely be some degradation in mechanical properties for specimens stored for many months at $-20^{\circ}C$; thus, the biomechanical properties may be changed. In the latter case, there is a risk that the testing procedures or machine calibration may change slightly with time, skewing the time-related results of the study. When faced with this choice, it is best to choose the latter option; i.e., test the specimens as they are collected because it is difficult to correct for specimen degradation during storage, yet machine calibration and testing procedures can be kept consistent with time if the appropriate practices are implemented. The key to these practices is well-documented and well-implemented protocols.

7.6.2 Standard Operating Procedures

A standard operating procedure (SOP) is a document that describes a single laboratory operation or protocol. SOPs should be drafted for all tests done routinely in the laboratory. For example, an SOP for a biomechanical test might contain the following information:

1. Protocol for specimen preparation,
2. Setup specifications for the testing machine and recording instruments,

3. Description of the test fixtures,
4. Protocol for morphology measurement and mechanical test,
5. Glossary of raw data variables,
6. Methodology for data analysis,
7. Procedure for verification of accuracy and reproducibility of the measurements, and
8. Methods to document deviations or discrepancies in the test procedures.

In addition to SOPs for laboratory tests, SOPs should be created for (1) management and storage of data, (2) receipt and logging of experimental samples, (3) operation, calibration, and maintenance of each measurement instrument, and (4) monitoring and maintenance of specimen storage freezers and refrigerators. Each laboratory employee should follow the SOP by the letter, and SOPs should be updated as test procedures change. Although creation and maintenance of SOPs require substantial time and effort, they ultimately reduce the time necessary to train new laboratory personnel and provide continuity of laboratory procedures.

7.6.3 Equipment Calibration

GLP requires that equipment "be adequately inspected, cleaned, and maintained."[164] The details of the calibration and maintenance procedures are left up to the individual laboratories. In their laboratory, the authors have calibration and maintenance protocols for the mechanical testing machine, the data acquisition systems, and the digital micrometer used to measure specimen dimensions. Each of these instruments is unlikely to fall out of calibration unless it is damaged. Nevertheless, the calibration is verified routinely before beginning a new study and the results from the calibration tests recorded. Procedures to verify instrument calibration should be created for every measurement instrument used in a given study. Furthermore, it is useful to monitor the conditions of specimen storage (e.g., freezer temperature) and the parameters of the test, (e.g., testing temperature, time required to thaw the specimens, etc.)

7.6.4 Use of Testing Standards and Data Verification

One has to establish standards for verifying instrument calibration. For example, calibrated weights are used to verify a load cell, and a set of measurement blocks is used to verify a micrometer. A mechanical test procedure could be verified by conducting several tests using a material with known mechanical properties (acrylic plastics can provide a good test surrogate for bone). As noted above, testing standards should be established for every measurement instrument. Any manipulation of the data should be verified for correctness. Analog-to-digital data acquisition systems should be verified by inputting a standard signal and comparing the acquired data to the expected outcome. Similarly, computer-generated analyses should be verified on standard data sets with known analysis outputs. It is a good policy to check individual load–displacement curves visually and compare these to the reduced biomechanical parameters to assure that the analysis did not misinterpret some artifact or glitch in the test. All data verification should be done while the investigator remains blinded to the specimens' group identification. After this code is broken, it is difficult to justify changing the values of data points, as such changes give the appearance of data manipulation.

7.6.5 Record Keeping

When conducting an experiment, record keeping is of paramount importance and it has been the authors'experience that records are seldom as detailed as they should be. For a biomechanical test, the records should include:

1. The source from which the specimens came (including all pertinent details about the source, such as age, gender, health complications, and how long diseased), the date they were collected, and how they were preserved before they were obtained;
2. Documentation of all equipment calibration and verification;
3. A description of all circumstances that may have affected the quality or integrity of the data;

4. A collection of all raw data, including the dates when they were collected, and the conditions under which they were collected; and
5. A description of the transformations, calculations, or statistical tests performed on the data.

Collection of data on handwritten records, laboratory worksheets, or instrument printouts should be dated and signed by the person recording the data. Changes in raw data should be made by striking a single line through the original datum and noting the new datum in the margin. The date and justification for the change should be noted, and the person making the change should be identified by initials or signature.

7.6.6 Archiving

GLP requires that raw data and specimens be stored in an authorized repository. This requirement is impractical for most noncommercial laboratories. However, the authors have found it useful on many occasions to reanalyze old specimens with newer measurement techniques. For this reason space for data and specimen storage was established. It is important to provide the archive materials with the appropriate identifiers so that the results from the study can be completely reconstructed from the raw data. Each study should be given a unique numbering system to avoid confusion if the specimens should become intermixed with those from other studies.

References

1. Turner, C. H., Burr, D. B., Basic biomechanical measurements of bone: a tutorial, *Bone,* 14, 595–608, 1993.
2. Sedlin, E. D., Hirsch, C., Factors affecting the determination of the physical properties of femoral cortical bone, *Acta Orthop. Scand.,* 37, 29–48, 1966.
3. Burstein, A. H., Currey, J. D., Frankel, V. H., Reilly, D. T., The ultimate properties of bone tissue: the effects of yielding, *J. Biomech.,* 5, 35–44, 1972.
4. Evans, F. G., *Mechanical Properties of Bone*, Charles C Thomas, Springfield, IL, 1973.
5. Dempster, W. T., Liddicoat, R., Compact bone as a non-isotropic material, *Am. J. Anat.,* 91, 331–362, 1952.
6. Evans, F. G., Lebow, M., Regional differences in some of the physical properties of the human femur, *J. Appl. Physiol.,* 3, 563–572, 1951.
7. Broz, J. J., Simske, S. J., Greenberg, A. R., Luttges, M. W., Effects of rehydration state on the flexural properties of whole mouse long bones, *J. Biomech. Eng.,* 115, 447–449, 1993.
8. Currey, J. D., The effects of drying and re-wetting on some mechanical properties of cortical bone, *J. Biomech.,* 21, 439–441, 1988.
9. Ashman, R. B., Ultrasonic Determination of the Elastic Properties of Cortical Bone: Techniques and Limitations, Ph.D. thesis; Tulane University, New Orleans, LA, 1982.
10. Bonfield, W., Tully, A. E., Ultrasonic analysis of the Young's modulus of cortical bone, *J. Biomed. Eng.,* 4, 23–27, 1982.
11. Bonfield, W., Li, C. H., The temperature dependence of the deformation of bone, *J. Biomech.,* 1, 323–329, 1968.
12. Carter, D. R., Hayes, W. C., Fatigue life of compact bone—I. Effects of stress amplitude, temperature and density, *J. Biomech.,* 9, 27–34, 1976.
13. Lakes, R. S., Katz, J. L., Sternstein, S. S., Viscoelastic properties of wet cortical bone—I. Torsional and biaxial studies, *J. Biomech.,* 12, 657–678, 1979.
14. Park, H. C., Lakes, R. S., Cosserat micromechanics of human bone: strain redistribution by a hydration sensitive constituent, *J. Biomech.,* 19, 385–397, 1986.
15. Carter, D. R., Hayes, W. C., The compressive behavior of bone as a two-phase porous structure, *J. Bone Joint Surg.,* 59-A, 954–962, 1977.
16. Rubin, C. T., Lanyon, L. E., Limb mechanics as a function of speed and gait: a study of functional strains in the radius and tibia of horse and dog, *J. Exp. Biol.,* 101, 187–211, 1982.

17. Turner, C. H., Akhter, M. P., Heaney, R. P., The effects of fluoridated water on bone strength, *J. Orthop. Res.,* 10, 581–587, 1992.
18. Keller, T. S., Spengler, D. M., Carter, D. R., Geometric, elastic, and structural properties of maturing rat femora, *J. Orthop. Res.,* 4, 57–67, 1986.
19. Martin, R. B., Burr, D. B., Non-invasive measurement of long bone cross-sectional moment of inertia by photon absorptiometry, *J. Biomech.,* 17, 195–201, 1984.
20. Yoshikawa, T., Turner, C. H., Markwardt, P., Burr, D. B., Cross-sectional moment of inertia of the femoral neck measured using DEXA, *J. Bone Miner. Res.,* 7 (Suppl. 1), S135, 1992.
21. Beck, T. J., Ruff C. B., Scott, Jr., W. W., Plato C. C., Tobin, J. D., Quan, C. A., Sex differences in geometry of the femoral neck with aging: a structural analysis of bone mineral data, *Calcif. Tissue Int.,* 50, 24–29, 1992.
22. Wang, C., *Applied Elasticity,* McGraw-Hill, New York, 1953.
23. Martin, R. B., Measuring the moment of inertia of irregular cross sections, *Rev. Sci. Instrum.,* 46, 838–839, 1975.
24. Smith, J. W., Walmsley, R., Factors affecting the elasticity of bone, *J. Anat.,* 93, 503–522, 1959.
25. Rho, J.-Y., Ashman, R. B., Turner, C. H., Young's modulus of trabecular and cortical bone material: ultrasonic and microtensile measurements, *J. Biomech.,* 26, 111–119, 1993.
26. Rice, J. C., Cowin, S. C., Bowman, J. A., On the dependence of the elasticity and strength of cancellous bone on apparent density, *J. Biomech.,* 21, 155–168, 1988.
27. Schaffler, M. B., Burr, D. B., Stiffness of compact bone: effects of porosity and density, *J. Biomech.,* 21, 13–16, 1988.
28. Martin, R. B., Porosity and specific surface of bone, *CRC Crit. Rev. Biomed. Eng.,* 10, 179–222, 1984.
29. Martin, R. B., Burr, D. B., *Structure, Function, and Adaptation of Compact Bone,* Raven Press, New York, 1989.
30. Ascenzi, A., Bonucci, E., The tensile properties of single osteons, *Anat. Rec.,* 158, 375–386, 1967.
31. Ascenzi, A., Bonucci, E., The compressive properties of single osteons, *Anat. Rec.,* 161, 377–391, 1968.
32. Black, J., Mattson, R., Korostoff, E., Haversian osteons: size, distribution, internal structure, *J. Biomed. Mater. Res.,* 8, 299–318, 1974.
33. Frasca, P., Harper R. A., Katz, J. L., Mineral and collagen fiber orientation in human secondary osteons, *J. Dent. Res.,* 57a, 526–533, 1978.
34. Martin, R. B., Ishida, J., The relative effects of collagen fiber orientation, porosity, density and mineralization on bone strength, *J. Biomech.,* 22, 419–426, 1989.
35. Martin, R. B., Boardman, D. L., The effects of collagen fiber orientation, porosity, density and mineralization on bovine cortical bone bending properties, *J. Biomech.,* 26, 1047–1054, 1993.
36. Takano, Y., Turner, C. H., Forwood, M. R., Owan, I., Martin, R. B., Lau, S. T., Burr, D. B., Elastic anisotropy and collagen orientation of osteonal bone are dependent upon the mechanical strain distribution, *J. Orthop. Res.,* 17, 59–66, 1999.
37. Gere, J. M., Timoshenko, S., *Mechanics of Materials,* PWS-Kent, Boston, MA, 1984.
38. Hvid, I., Jensen, J., Cancellous bone strength at the proximal human tibia, *Eng. Med.,* 13, 21–25, 1984.
39. Turner, C. H., Yield behavior of cancellous bone, *J. Biomech. Eng.,* 111, 1–5, 1989.
40. Caler, W. E., Carter, D. R., Harris, W. H., Techniques for implementing and *in vivo* bone strain gage system, *J. Biomech.,* 14, 503–507, 1981.
41. Carter, D. R., Anisotropic analysis of strain rosette information from cortical bone, *J. Biomech.,* 11, 199–202, 1978.
42. Roberts, V. L., Strain gage techniques in biomechanics, *Exp. Mech.,* 19A–22A, 1966.
43. Reilly, D. T., Burstein, A. H., Frankel, V. H., The elastic modulus for bone, *J. Biomech.,* 7, 271–275, 1974.
44. Keaveny, T. M., Guo X. E., Wachtel, E. F., McMahon, T. A., Hayes, W. C., Trabecular bone exhibits fully linear elastic behavior and yields at low strains, *J. Biomech.,* 27, 1127–1136, 1994.

45. Harrigan, T. P., Jasty, M., Mann, R. W., Harris, W. H., Limitations of the continuum assumption in cancellous bone, *J. Biomech.,* 21, 269–275, 1988.
46. Linde, F., Hvid, I., The effect of constraint on the mechanical behavior of trabecular bone specimens, *J. Biomech.,* 22, 485–490, 1989.
47. Allard, F. N., Ashman, R. B., A comparison between cancellous bone compressive moduli determined from surface strain and total specimen deflection, *Trans. Othop. Res. Soc.,* 16, 151, 1991.
48. Keaveny, T. M., Borchers, R. E., Gibson, L. J., Hayes, W. C., Trabecular bone modulus and strength can depend on specimen geometry, *J. Biomech.,* 26, 991–1000, 1993.
49. Linde, F., Hvid, I., Madsen, F., The effect of specimen geometry on the mechanical behavior of trabecular bone specimens, *J. Biomech.,* 25, 359–368, 1992.
50. Odgaard, A., Hvid, I., Linde, F., Compressive axial strain distributions in cancellous bone specimens, *J. Biomech.,* 22, 829–835, 1989.
51. Odgaard, A., Linde, F., The underestimation of Young's modulus in compressive testing of cancellous bone specimens, *J. Biomech.,* 24, 691–698, 1991.
52. Goulet, R. W., Goldstein, S. A., Ciarelli, M. J., Kuhn, J. L., Brown, M. B., Feldkamp, L. A., The relationship between the structural and orthogonal compressive properties of trabecular bone, *J. Biomech.,* 27, 375–389, 1994.
53. Turner, C. H., Eich, M., Ultrasonic velocity as a predictor of strength in bovine cancellous bone, *Calcif. Tissue Int.,* 49, 116–119, 1991.
54. Mosekilde, Li, Mosekilde, Le, Danielsen, C. C., Biomechanical competence of vertebral trabecular bone in relation to ash density and age in normal individuals, *Bone,* 8, 79–85, 1987.
55. Keaveny, T. M., Hayes, W. C., A 20-year perspective on the mechanical properties of trabecular bone, *J. Biomech. Eng.,* 115, 534–542, 1993.
56. Turner, C. H., Effects of parathyroid hormone treatment in rats [Letter to the editor], *Bone,* 19, 73–74, 1996.
57. Levenston, M. E., Periosteal bone formation stimulated by externally induced bending strains, *J. Bone Miner. Res.,* 10, 671, 1995.
58. Reilly, D. T., Burstein, A. H., The elastic and ultimate properties of compact bone tissue, *J. Biomech.,* 8, 393–405, 1975.
59. Spatz, H.-Ch., O'Leary, E. J., Vincent, J. F. V., Young's moduli and shear moduli in cortical bone, *Proc. R. Soc. Lond. B. Biol. Sci.,* 263, 287–294, 1996.
60. Akhter, M. P., Raab, D. M., Turner, C. H., Kimmel, D. B., Recker, R. R., Characterization of *in vivo* strain in the rat tibia during external application of a four-point bending load, *J. Biomech.,* 25, 1241–1246, 1992.
61. Roark, R. J., Young, W. C., *Formulas for Stress and Strain,* McGraw-Hill, New York, 1975.
62. Einhorn, T. A., Wakley, G. K., Linkhart, S., Rush, E. B., Maloney, S., Faierman, E., Baylink, D. J., Incorporation of sodium fluoride into cortical bone does not impair the mechanical properties of the appendicular skeleton of rats, *Calcif. Tissue Int.,* 51, 127–131, 1992.
63. Forwood, M. R., Parker, A. W., Effects of exercise on bone growth: mechanical and physical properties studied in the rat, *Clin. Biomech.,* 2, 185–190, 1987.
64. Greenspan, S. L., Myers, E. R., Maitland, L. A., Resnick, N. M., Hayes, W. C., Fall severity and bone mineral density as risk factors for hip fracture in ambulatory elderly, *JAMA,* 217, 128–133, 1994.
65. Hayes, W., Myers, E., Morris, J. N., Yett, H. S., Lipsitz, L. A., Impact near the hip dominates fracture risk in elderly nursing home residents who fall, *Calcif. Tissue Int.,* 52, 192–198, 1993.
66. Azuma, Y., Oue, Y., Kanatani, H., Ohta, T., Kiyoki, M., Komoriya, K., Effects of continuous alendronate treatment on bone mass and mechanical properties in ovariectomized rats: comparison with pamidronate and etidronate in growing rats, *J. Pharmacol. Exp. Ther.,* 286, 128–135, 1998.
67. Turner, C. H., Sato, M., Bryant, H. U., Raloxifene preserves bone strength and bone mass in ovariectomized rats, *Endocrinology,* 135, 2001–2005, 1994.
68. Sato, M., Zeng, G. Q., Turner, C. H., Biosynthetic human parathyroid hormone (1–34) effects on bone quality in aged ovariectomized rats, *Endocrinology,* 138, 4330–4337, 1997.

69. Dalén, N., Hellstrom, L.-G., Jacobson, B., Bone mineral content and mechanical strength of the femoral neck, *Acta. Orthop. Scand.,* 47, 503–508, 1976.
70. Bouxsein, M. L., Courtney, A. C., Hayes, W. C., Ultrasound and densitometry of the calcaneus correlate with the failure loads of cadaveric femurs, *Calcif. Tissue Int.,* 56, 99–103, 1995.
71. Cheng, X. G., Lowet, G., Boonen, S., Nicholson, P. H. F., Brys, P., Nijs, J., Dequeker, J., Assessment of the strength of proximal femur *in vitro*: relationship to femoral bone mineral density and femoral geometry, *Bone,* 20, 213–218, 1997.
72. Courtney, A. C., Wachtel, E. F., Myers, E. R., Hayes, W. C., Effects of loading rate on strength of the proximal femur, *Calcif. Tissue Int.,* 55, 53–58, 1994.
73. Jamsa, T., Tuukkanen, J., Jalovaara, P., Femoral neck strength of mouse in two loading configurations, method evaluation and fracture characteristics, *J. Biomech.,* 31, 723–739, 1998.
74. Hvid, I., Hansen, S. L., Trabecular bone strength patterns at the proximal tibial epiphysis, *J. Orthop. Res.,* 3, 464–472, 1985.
75. Sumner, D. R., Willke, T. L., Berzins, A., Turner, T. M., Distribution of Young's modulus in the cancellous bone of the proximal canine tibia, *J. Biomech.,* 27, 1095–1099, 1994.
76. Aitken, G. K., Bourne, R. B., Finlay, J. B., Rorabeck, C. H., Andreae, P. R., Indentation stiffness of the cancellous bone in the distal human tibia, *Clin. Orthop. Relat. Res.,* 201, 264–270, 1985.
77. Harada, Y., Wevers, H. W., Cooke, T. D. V., Distribution of bone strength in the proximal tibia, *J. Arthroplasty,* 3, 167–175, 1988.
78. Katoh, T., Griffin, M. P., Wevers, H. W., Rudan, J., Bone hardness testing in the trabecular bone of the patella, *J. Arthroplasty,* 11, 460–468, 1996.
79. Timoshenko, S. P., Goodier, J. N., *Theory of Elasticity,* 3rd ed., McGraw-Hill, New York, 1970, 380–409.
80. Tarnopol'skii, Iu. M., Kincis, T., *Static Test Methods for Composites,* Van Nostrand Reinhold, New York, 1985.
81. Iosipescu, N., New accurate procedure for single shear testing of metals, *J. Mater.,* 2, 537–566, 1967.
82. Walrath, D. E., Adams, D. F., The Iosipescu shear test as applied to composite materials, *Exp. Mech.,* 23, 105–110, 1983.
83. Arcan, M., Hashin, Z., Voloshin, A., A method to produce uniform plane-stress states with applications to fiber-reinforced materials, *Exp. Mech.,* 18, 141–146, 1978.
84. Norman, T. L., Vashishth, D., Burr, D. B., Fracture toughness of human bone under tension, *J. Biomech.,* 28, 309–320, 1995.
85. Behiri, J. C., Bonfield, W., Fracture mechanics of bone—the effects of density, specimen thickness and crack velocity on longitudinal fracture, *J. Biomech.,* 17, 25–34, 1984.
86. Behiri, J. C., Bonfield, W., Orientation dependence on fracture mechanics of bone, *J. Biomech.,* 22, 863–872, 1989.
87. Bonfield, W., Grynpas, M. D., Young, R. J., Crack velocity and the fracture of bone, *J. Biomech.,* 11, 473–479, 1978.
88. Melvin, J. W., Fracture mechanics of bone, *J. Biomech. Eng.,* 115, 549–554, 1993.
89. Norman, T. L., Vashishth, D., Burr, D. B., Effect of groove on bone fracture toughness, *J. Biomech.,* 25, 1489–1492, 1992.
90. Wright, T. M., Hayes, W. C., Fracture mechanics parameters for compact bone—effects of density and specimen thickness, *J. Biomech.,* 10, 419–430, 1977.
91. ASTM Standard test method for plane strain fracture toughness testing of metallic materials, *ASTM Annual Book of Standards,* Section 2, Designation E 399-83, 1985, 898–933.
92. Carter, D. R., Hayes, W. C., Compact bone fatigue damage. I. Residual strength and stiffness, *J. Biomech.,* 10, 325–337, 1977.
93. Lakes, R. S., Saha, S., Cement line motion in bone, *Science,* 204, 501–503, 1979.
94. Schaffler, M. B., Radin, E. L., Burr, D. B., Mechanical and morphological effects of strain rate on fatigue of compact bone, *Bone,* 10, 207–214, 1989.

95. Carter, D. R., Hayes, W. C., Compact bone fatigue damage. A microscopic examination, *Clin. Orthop. Relat. Res.,* 127, 265–274, 1977.
96. Forwood, M. R., Parker, A. W., Microdamage in response to repetitive torsional loading in the rat tibia, *Calcif. Tissue Int.,* 45, 47–53, 1989.
97. Schaffler, M. B., Radin, E. L., Burr, D. B., Long-term fatigue behavior of compact bone at low strain magnitude and rate, *Bone,* 11, 321–326, 1990.
98. Caler, W. E., Carter, D. R., Bone creep-fatigue damage accumulation, *J. Biomech.,* 22, 625–635, 1989.
99. Carter, D. R., Caler, W. C., A cumulative damage model for bone fracture, *J. Orthop. Res.,* 3, 84–90, 1985.
100. Lafferty, J. F., Analytical model of the fatigue characteristics of bone, *Aviat. Space Environ. Med.,* 49, 170–174, 1978.
101. Ascenzi, A., Bonucci, E., The shearing properties of single osteons, *Anat. Rec.,* 172, 499–510, 1972.
102. Ascenzi, A., Baschieri, P., Benvenuti, A., The bending properties of single osteons, *J. Biomech.,* 23, 763–771, 1990.
103. Ascenzi, A., Baschieri, P., Benvenuti, A., The torsional properties of single selected osteons, *J. Biomech.,* 27, 875–884, 1994.
104. Ascenzi, A., Benvenuti, A., Bonucci, E., The tensile properties of single osteonic lamellae: technical problems and preliminary results, *J. Biomech.,* 15, 29–37, 1982.
105. Runkle, J. C., Pugh, J., The micro-mechanics of cancellous bone. II. Determination of the elastic modulus of individual trabeculae by a buckling analysis, *Bull. Hosp. Joint Dis.,* 36, 2–10, 1975.
106. Townsend, P. R., Rose, R. M., Radin, E. L., Buckling studies of single human trabeculae, *J. Biomech.,* 8, 199–201, 1975.
107. Kuhn, J. L., Goldstein, S. A., Choi, K., London, M., Feldkamp, L. A., Matthews, L. S., Comparison of the trabecular and cortical tissue moduli from human iliac crests, *J. Orthop. Res.,* 7, 876–884, 1989.
108. Choi, K., Kuhn, J. L., Ciarelli, M. J., Goldstein, S. A., The elastic moduli of human subchondral, trabecular, and cortical bone tissue and the size-dependency of cortical bone modulus, *J. Biomech.,* 23, 1103–1113, 1990.
109. Jepsen, K. J., Schaffler, M. B., Kuhn, J. L., Goulet, R. W., Bonadio, J., Goldstein, S. A., Type I collagen mutation alters the strength and fatigue behavior of mov13 cortical tissue, *J. Biomech.,* 30, 1141–1147, 1997.
110. Choi, K., Goldstein, S. A., A comparison of the fatigue behavior of human trabecular and cortical bone tissue, *J. Biomech.,* 25, 1371–1381, 1992.
111. Amprino, R., Investigations on some physical properties of bone tissue, *Acta Anat.,* 34, 161–186, 1958.
112. Huja, S. S., Katona, T. R., Moore, B. K., Roberts, W. E., Microhardness and anisotropy of the vital osseous interface and endosseous implant supporting bone, *J. Orthop. Res.,* 16, 54–60, 1998.
113. Stea, S., Visentin, M., Savarino, L., Ciapetti, G., Donati, M. E., Moroni, A., Caja, V., Pizzoferrato, A., Microhardness of bone at the interface with ceramic-coated metal implants, *J. Biomed. Mater. Res.,* 29, 695–699, 1995.
114. Weaver, J. K., The microscopic hardness of bone, *J. Bone Joint Surg. [Am. Vol.],* 48, 273–288, 1966.
115. Ziv, V., Wagner, H. D., Weiner, S., Microstructure-microhardness relations in parallel-fibered and lamellar bone, *Bone,* 18, 417–428, 1996.
116. Rho, J.-Y., Tsui, T. Y., Pharr, G. M., Elastic properties of human cortical and trabecular lamellar bone measured by nanoindentation, *Biomaterials,* 18, 1325–1330, 1997.
117. Oliver, W. C., Pharr, G. M., An improved technique for determining hardness and elastic modulus using load and displacement sensing indentation experiments, *J. Mater. Res.,* 7, 1564–1583, 1992.
118. Turner, C. H., Rho, J., Takano, Y., Tsui, T. Y., Pharr, G. M., The elastic properties of trabecular and cortical bone tissues are similar: results from two microscopic measurement techniques, *J. Biomech.,* 32, 437–441, 1999.

119. Yoon, H. S., Katz, J. L., Ultrasonic wave propagation in human cortical bone II. Measurements of elastic properties and microhardness, *J. Biomech.,* 9, 459–464, 1976.
120. Ashman, R. B., Corin, J. D., Turner, C. H., Elastic properties of cancellous bone: measurement by an ultrasonic technique, *J. Biomech.,* 20, 979–986, 1987.
121. Kolsky, H., *Stress Waves in Solids,* Dover, New York, 1963.
122. Ashman, R. B., Cowin, S. C., Van Buskirk, W. C., Rice, J. C., A continuous wave technique for the measurement of the elastic properties of cortical bone, *J. Biomech.,* 17, 349–361, 1984.
123. Ashman, R. B., Rho, J.-Y., Elastic modulus of trabecular material, *J. Biomech.,* 21, 177–181, 1988.
124. Briggs, A., *Acoustic Microscopy,* Oxford University Press, New York, 1992.
125. Antich, P. P., Anderson, J. A., Ashman, R. B., Dowdey, J. E., Gonzales, J., Murry, R. C., Zerwekh, J. E., Pak, C. Y. C., Measurement of mechanical properties of bone material in vitro by ultrasound reflection: methodology and comparison with ultrasonic transmission, *J. Bone Miner. Res.,* 6, 417–426, 1991.
126. Zimmerman, M. C., Meunier, A., Katz, J. L., Christel, P., The evaluation of cortical bone remodeling with a new ultrasonic technique, *IEEE Trans. Biomed. Eng.,* 37, 433–441, 1990.
127. Hasegawa, K., Turner, C. H., Recker, R. R., Wu, E., Burr, D. B., Elastic properties of osteoporotic bone measured by scanning acoustic microscopy, *Bone,* 16, 85–90, 1995.
128. Ashman, R. B., Antich, P. P., Gonzales, J., Anderson, J. A., Rho, J. Y., A comparison of reflection and transmission ultrasonic techniques for measurement of cancellous bone elasticity, *J. Biomech.,* 27, 1195–1199, 1994.
129. Evans, J. A., Tavakoli, M. B., Ultrasonic attenuation and velocity in bone, *Phys. Med. Biol.,* 35, 1387–1396, 1990.
130. Langton, C. M., Palmer, S. B., Porter, R. W., The measurement of broadband ultrasonic attenuation in cancellous bone, *Eng. Med.,* 13, 89–91, 1984.
131. Serpe, L., Rho, J.-Y., The nonlinear transition period of broadband ultrasound attenuation as bone density varies, *J. Biomech.,* 29, 963–966, 1996.
132. Gardner, T. N., Elliott, J. C., Sklar, Z., Briggs, G. A. D., Acoustic microscope study of the elastic properties of fluorapatite and hydroxyapatite, tooth enamel and bone, *J. Biomech.,* 25, 1265–1277, 1992.
133. Kohn, D. H., Acoustic emission and nondestructive evaluation of biomaterials and tissues, *Crit. Rev. Biomed. Eng.,* 22, 221–306, 1995.
134. The Jackson Laboratory, http://www.jax.org, 1999.
135. Food and Drug Administration, Guidelines for preclinical and clinical evaluation of agents used in the prevention or treatment of postmenopausal osteoporosis (draft), 1995.
136. Reginster, J. Y., Compston, J. E., Jones, E. A., Kaufman, J. M., Audran, M., Bouvenot, G., Frati, L., Mazzouli, G., Gennari, C., Lemmel, E.-M., Ringe, J. D., Sebert, J.-L., Vanhaelst, L., Avouac, B., Recommendations for the registration of new chemical entities used in the prevention and treatment of osteoporosis, *Calcif. Tissue Int.,* 57, 247–250, 1995.
137. Turner, C. H., Hsieh, Y. F., Müller, R., Bouxsein, M. L., Baylink, D. J., Rosen, C. J., Donahue, L. R., Beamer, W., Differential regulation of cortical and trabecular bone strength and microstructure in inbred strains of mice, *Bone,* 23 (Suppl.), S276, 1998.
138. Geiser, A. G., Zeng, G. Q., Sato, M., Helvering, L. M., Hirano, T., Turner, C. H., Decreased bone mass and bone elasticity in mice lacking the transforming growth factor-β1 gene, *Bone,* 23, 87–93, 1998.
139. Turner, C. H., Garetto, L. P., Dunipace, A. J., Zhang, W., Wilson, M. E., Grynpas, M. D., Chachra, D., McClintock, R., Peacock, M., Stookey, G. K., Fluoride treatment increased serum IGF-1, bone turnover and bone mass, but not bone strength, in rabbits, *Calcif. Tissue Int.,* 61, 77–83, 1997.
140. Turner, C. H., Wang, Y., Hirano, T., Burr, D. B., Hock, J. M., Hotchkiss, C. E., Brommage, R., Jerome, C. P., In monkeys, treatment with PTH (1-34), LY333334, increases bone strength in lumbar vertebrae and the femoral neck without compromising cortical bone strength, in *Proceedings of the 8th World Congress of the Société Internationale de Recherche Orthopédique et de Traumatologie*, 1999.

141. Demetropoulos, C. K., Willis, C. B., Goldstein, S. A., Biomechanical characteristics of rat trabecular bone, *Trans. Orthop. Res. Soc.,* 18, 585, 1993.
142. Mosekilde, L., Weisbrode, S. E., Safron, J. A., Stills, J. F., Jankowsky, M. A., Evert, D. C., Danielsen, C. C., Søgaard, C. H., Franks, A. F., Stevens, M. L., Paddock, C. L., Boyce, R. W., Evaluation of the skeletal effects of combined mild dietary calcium restriction and ovariectomy in Sinclair S-1 minipigs: a pilot study, *J. Bone Miner. Res.,* 8, 1311–1321, 1993.
143. Turner, A. S., Alvis, M., Myers, W., Stevens, M. L., Lundy, M. W., Changes in bone mineral density and bone-specific alkaline phosphatase in ovariectomized ewes, *Bone,* 17(Suppl. 4), 395S–402S, 1995.
144. Hornby, S. B., Ford, S. L., Mase, C. A., Evans, G. P., Skeletal changes in the ovariectomized ewe and subsequent response to treatment with 17β oestradiol, *Bone,* 17(Suppl. 4), 389S–394S, 1995.
145. Mackey, M. S., Stevens, M. L., Ebert, D. C., Tressler, D. L., Combs, K. S., Lowry, C. K., Smith, P. N., McOsker, J. E., The ferret as a small animal model with BMU-based remodeling for skeletal research, *Bone,* 17 (Suppl. 4), 191S–196S, 1995.
146. Balena, R., Toolan, B. C., Shea, M., Markatos, A., Myers, E. R., Lee, S. C., Opas, E. E., Seedor, J. G., Klein, H., Frankenfield, D., Quartuccio, H., Fioravanti, C., Clair, J., Brown, E., Hayes, W. C., Rodan, G. A., The effects of 2-year treatment with the aminobisphosphonate alendronate on bone metabolism, bone histomorphometry, and bone strength in ovariectomized nonhuman primates, *J. Clin. Invest.,* 92, 2577–2586, 1993.
147. Jerome, C. P., Turner, C. H., Lees, C. J., Decreased bone mass and strength in ovariectomized cynomolgus monkeys (*Macaca fascicularis*), *Calcif. Tissue Int.,* 60, 265–270, 1997.
148. Hirano, T., Burr, D. B., Turner, C. H., Sato, M., Cain, R. L., Hock, J. M., Anabolic effects of human biosynthetic parathyroid hormone fragment (1-34), LY333334, on remodeling and mechanical properties of cortical bone in rabbits, *J. Bone Miner. Res.,* 14, 536–545, 1999.
149. Burr, D. B., Schaffler, M. B., The involvement of subchondral mineralized tissues in osteoarthrosis: quantitative microscopic evidence, *Microsc. Res. Tech.,* 37, 343–357, 1997.
150. Burr, D. B., The importance of subchondral bone in osteoarthrosis, *Curr. Opin. Rheum.,* 10, 256–262, 1998.
151. Moskowitz, R., Experimental models of degenerative joint disease, *Sem. Arthritis Rheum.,* 1, 95–116, 1972.
152. Pritzker, K. P. H., Animal models for osteoarthritis: processes, problems and prospects, *Ann. Rheum. Dis.,* 53, 406–420, 1994.
153. Hulth, A., Lindberg, L., Telhag, H., Experimental osteoarthritis in rabbits, *Acta Orthop. Scand.,* 41, 522–530, 1970.
154. Pond, M. J. and Nuki, G., Experimentally-induced osteoarthritis in the dog, *Ann. Rheumatol. Dis.,* 32, 387–388, 1973.
155. Brandt, K. D., Braunstein E. M., Visco D. M., O'Connor, B., Heck D., Albrecht, M., Anterior (cranial) cruciate ligament transection in the dog: a bona fide model of osteoarthritis, not merely of cartilage injury and repair, *J. Rheumatol.,* 18, 436–446, 1991.
156. Brandt, K. D., Myers, S. L., Burr, D. B., Albrecht, M., Changes of osteoarthritis in canine articular cartilage, subchondral bone and synovium 54 months after transection of the anterior cruciate ligament, *Arthritis Rheum.,* 232, 180–189, 1991.
157. O'Connor, B., Palmoski, M. J., Brandt, K. D., Neurogenic acceleration of degenerative joint lesions, *J. Bone Joint Surg.,* 67A, 562–572, 1985.
158. Sah, R. L., Yang, A. S., Chen, A. C., Hant, J. J., Halili, R. B., Yoshioka, M., Amiel, D., Coutts, R. D., Physical properties of rabbit articular cartilage after transection of the anterior cruciate ligament, *J. Orthop. Res.,* 15, 197–203, 1997.
159. Xerogeanes, J. W., Fox, R. J., Takeda, Y., Kim, H.-S., Ishibashi, Y., Carlin, G. J., Woo, S. L.-Y., A functional comparison of animal anterior cruciate ligament models to the human anterior cruciate ligament, *Ann. Biomed. Eng.,* 26, 345–352, 1998.

160. Thompson, R. C., Oegema, T. R, Lewis, J. L., Wallace, L., Osteoarthrotic changes after acute transarticular load, *J. Bone Joint Surg.,* 73A, 990–1001, 1991.
161. Radin, E. L., Martin, R. B., Burr, D. B., Caterson, B., Boyd, R. D., Goodwin, C., Effects of mechanical loading on the tissues of the rabbit knee, *J. Orthop. Res.,* 2, 221–234, 1984.
162. Bendele, A. M., White, S. L., Hulman, J. F., Osteoarthrosis in guinea pigs: histopathologic and scanning electron microscopic features, *Lab. Anim. Sci.,* 39, 115–121, 1989.
163. Carlson, C. S., Loeser, R. F., Jayo, M. J., Weaver, D. S., Adams, M. R., Jerome, C. P., Osteoarthritis in cynomolgus macaques: a primate model of naturally occurring disease, *J. Orthop. Res.,* 12, 331–339, 1994.
164. Code of Federal Regulations, Food and Drug Administration, Good Laboratory Practice Regulations; Final Rule, CFR 21–Part 58, 1987.
165. Sato, M., Zeng, G. Q., Rowley, E., Turner, C. H., LY353381 HCl: an improved benzothiophene analog with bone efficacy complementary to parathyroid hormone (1-34), *Endocrinology,* 139, 4642–4651, 1998.
166. Sato, M., Bryant, H. U., Iversen, P., Helterbrand, J., Smietana, F., Bemis, K., Higgs, R., Turner, C. H., Owan, I., Takano, Y., Burr, D. B., Advantages of raloxifene over alendronate or estrogen on nonreproductive and reproductive tissues in the long-term dosing of ovariectomized rats, *J. Pharmacol. Exp. Ther.,* 279, 298–305, 1996.
167. Turner, C. H., Hasegawa, K., Zhang, W., Wilson, M., Li, Y., Dunipace, A. J., Fluoride reduces bone strength in older rats, *J. Dent. Res.,* 74, 1475–1481, 1995.
168. Turner, R. T., Evans, G. L., Sluka, J. P., Adrian, M. D., Bryant, H. U., Turner, C. H., Sato, M., Differential responses to estrogen target tissues in rats including bone to clomiphene, enclomiphene, and zuclomiphene, *Endocrinology,* 139, 3712–3720, 1998.

8

In Vivo Measurement of Bone Deformations Using Strain Gauges

Susannah P. Fritton
The City College of New York

Clinton T. Rubin
State University of New York at Stony Brook

8.1 Introduction

Quantifying the mechanical input to bone is an important step in understanding the form and function of the skeleton. The forces applied to bone at the organ level must be translated to the cellular level and in some way play a role in the maintenance and adaptation of bone tissue. Determining the deformations that a bone normally experiences should help elucidate this mechanotransduction mechanism in bone. To date, the strain gauge, a device that measures the deformations of the material to which it is attached, has been the method used to quantify *in vivo* bone strains. While the strain gauge suffers from limitations, especially when used in the harsh environment of the body, this device has provided many useful measurements of bone deformations. This chapter covers the development of strain gauges for use with bone and tabulates the *in vivo* strain measurements recorded over the years to quantify the mechanical loading environment of the skeleton. While strain gauges have been used for many applications using *in vitro* bone specimens and human cadavers, this chapter will focus on the use of strain gauges to measure *in vivo* bone strains.

0-8493-9117-2/01/$0.00+$.50

8.2 The Development of Strain Gauge Procedures for Use with Bone

8.2.1 Development of the Bonded Resistance Strain Gauge

The bonded wire strain gauge was developed in the late 1930s and consisted of bonding a thin length of fine wire to a surface so that all surface strains were transmitted to the wire.[1] The change in length and diameter of the wire changes the resistance of the gauge; thus, by measuring the current through a calibrated gauge, the strain of the underlying material can be determined. This bonded wire strain gauge allowed for large-scale experimental stress analyses that were subsequently performed on airplanes and ships, in the automotive industry, railroad industry, on bridges, buildings, and highways, and on many types of machinery.[1] In the late 1950s piezoresistive strain gauges were first used experimentally.[1] These piezoresistive or semiconductor strain gauges use crystals such as silicon and have output signals approximately 50 times greater than the conventional resistance gauge. These gauges also exhibit a resistance change proportional to the strain of the material to which they are attached.

The advantages of the bonded resistance strain gauge are many: they can be made very small, they are lightweight, attachment to a test piece is relatively simple, and they are relatively inexpensive.[1] Some limitations of the strain gauge are that it only measures the deformation of the material at the point (over the area) where it is attached, and strain can only be measured along the primary axis of the gauge. To a certain extent, these limitations can be addressed by attaching more than one gauge to any given region of interest, and using gauges with several independent elements, typically two or three, to determine the strain in more than one direction.

8.2.2 Early Bone Strain Gauge Studies

The increase of automobile and air travel and the resulting accidents motivated the early strain gauge studies of bone, which were undertaken to quantify the response of the skeletal system to external forces, especially in cases of high impact. Applications included the design of windshields and safety equipment such as helmets and restraint systems.[2,3] One of the earliest uses of wire strain gauges on bone was a study of the mechanism of head injury in exposed canine crania.[4] In that early study the bone deformations were measured using a strain gauge connected to a cathode ray oscilloscope, with the recordings captured by photographing the oscilloscope screen. Another early use of strain gauges *in vivo* was the attachment of a gauge to a canine tibia as reported by Evans,[2,5] with the bone deformations as the animal walked recorded on an oscilloscope. These and other pioneering efforts to quantify *in vivo* bone deformations using strain gauges relied on a trial-and-error approach, adapting traditional mechanical engineering strain gauging methods to the harsh environment of a living animal. Specialized techniques for waterproofing, bonding to bone, and wiring had to be developed for successful *in vivo* strain gauge measurements.[3]

Some of the factors that complicate the use of strain gauges with bone include (1) presence of body fluids, including blood, bone fluid, as well as fatty tissue; (2) the body's defense mechanism to attack foreign bodies, which can play a role in long-term testing; (3) mechanical forces that act on the gauge because of muscle movement and overlying tissue; and (4) limited access to the area of interest (e.g., femoral neck).[3]

For early summaries of bone strain gauge techniques see Roberts[3] and Lanyon,[6] and for a more recent step-by-step guide to applying and using strain gauges with bone see Biewener.[7]

8.2.3 Types of Gauges Used

While some early bone experiments used semiconductor strain gauges because of their high sensitivity,[8–11] metal foil resistance strain gauges have time and time again demonstrated their usefulness in evaluating the functional strain environment. These resistance strain gauges consist of a grid made of strain-sensitive metal foil. For bone uses, these gauges are usually mounted to either a polyimide or polyester resin

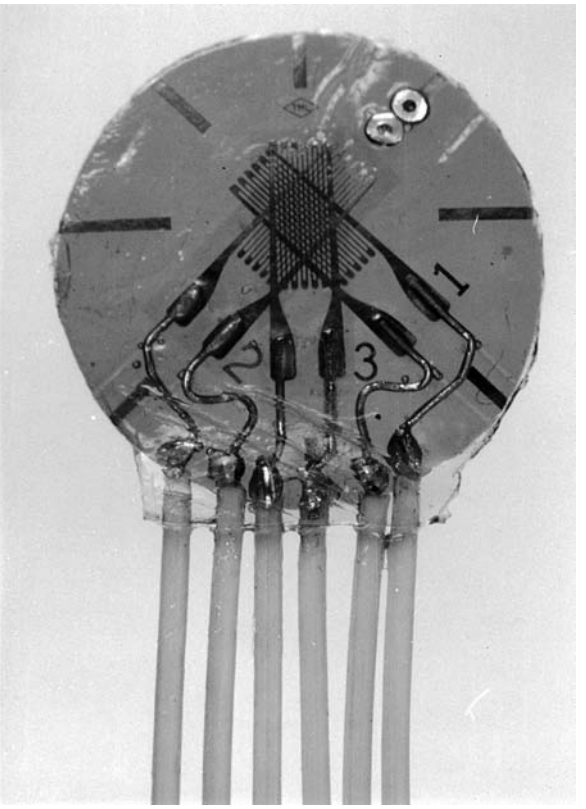

FIGURE 8.1 Triple 45° rosette strain gauge with 2-mm gauge elements. The solder dots (top right) help to determine gauge placement via radiograph. Each lead is Teflon-etched so the waterproofing adheres effectively.

backing that is flexible yet tough.[7] While investigators have used several sources for strain gauges in biological applications, they are often acquired from Tokyo Sokki Kenkyujo, Ltd., Measurements Group, Inc., or BLH Electronics.[7] Gauge resistance is usually 120 or 350 Ω with a gauge factor of around two. Because *in vivo* temperatures have a small range, temperature compensation is not a major factor to consider when choosing a gauge.[12]

The earliest strain gauge experiments used single-element gauges, but later experiments used rectangular stacked rosette gauges so that the principal strain magnitudes and their orientations could be measured at a point on a bone surface (Fig. 8.1). There are a vast array of gauge sizes and types, from single-element to multielement gauges, stacked vs. unstacked rosettes, rectangular vs. delta rosettes, etc. Given the range of gauge profiles, it is also important to record the gauge length as well as the arrangement of the gauges, as the analysis of the strain data is dependent on these factors. Barnes and Pinder[13] compared results from large (20 mm^2) and small (1 mm^2) foil resistance strain gauges and found that the small gauge size gave valid results. A commonly used gauge length is 2 mm. For very small bones such as a mouse tibia, there is often insufficient room to attach a rosette gauge and single-element gauges must be used.

8.2.4 Waterproofing Strain Gauges

Gauges and the lead wires must be protected from the body's corrosive environment for proper function. Several types of waterproofing have been tried, with varying success. Many early waterproof coatings were made of silicone rubber to protect the top surface of the gauge as well as the wiring junctions.[3,10] An advantage of using silicone rubber is that it is nontoxic and can be sterilized.[3] Because silicone rubber is not impervious to water for long periods of time, other compounds have been used with the rubber,

such as epoxy resin.[3,6] When considering short-term or even acute surgeries, it is important to note that several gauge vendors make available prewired, "waterproofed" gauges, which simplify experimental setup.

Other coatings are used to insulate the gauge. Separate polyurethane and xylene-based latex can be used to protect the gauge. Other heat-cure epoxies can be used, although slower cure times may cause extra flow of the epoxy.[7]

The effectiveness of waterproofing can be monitored by checking the resistance to ground of the gauge, which should be several megaohms. If this resistance changes, a gauge will drift and once fluid penetrates the waterproofing material, the gauge rapidly becomes ineffective.[3]

8.2.5 Bone Site Selection and Preparation

A bone site must be properly prepared to ensure successful attachment of the strain gauge. First, the site must be chosen such that a strain gauge can be attached without interference from surrounding soft tissues, especially muscle attachments. While the muscle insertions may be dissected away from the site, such a procedure will inevitably cause discomfort and potentially lameness; therefore, placement of a strain gauge should consider minimal disturbance of the surrounding soft tissues. Because investigators are often interested in determining the strains transmitted by the whole bone, the gauge site must be chosen so that it is not near local pulling (stress concentrations) caused by nearby muscles, tendons, or ligaments.[7] For long bones, gauges are usually attached at the mid-diaphysis to avoid any stress concentrations (in general, this is the region of maximum strain due to bending). The bone site must also be large enough for the strain gauge to be attached, which can be a problem with small bones such as those in mice and rats. For larger long bones, to obtain the strain distribution around a cross section, often three rosette gauges are placed on three surfaces of a bone. Such gauge placement will enable the calculation of normal and shear strains across the cross section, as well as effectively lead to a first-order approximation of the external loading conditions that caused the strain state, such as axial loads and torsional and bending moments.

It is important to emphasize that *in vivo* strain gauge experiments must be performed with proper approval and by observing the appropriate animal care guidelines. It is essential that the surgical procedure to attach the strain gauge(s) is performed under anesthesia, and that a sterile environment is secured. It should also be noted that strain gauges can be utilized without necessarily requiring euthanasia of the animal. After the data are collected and the location and orientation of the gauges are determined, the animal is again anesthetized and the gauges are simply removed.

To prepare a bone surface for gauge attachment, an incision is made and the proposed site of gauge attachment is exposed. It is strongly advised that the surgical approach first be evaluated using a cadaver specimen to identify key muscles, nerves, arteries, and veins. Using blunt dissection to reach the site of interest, a small area of the periosteum ($\sim$1 cm^2) is then scraped away from the bone using a periosteal elevator and/or a scalpel. To remove any fatty residues the site is then degreased, which is usually performed by rubbing the area "dry" using chloroform, anhydrous ether, or acetone applied to a cotton-tip applicator. Bleeding should be minimized before gauge attachment[3] until a clean, dry, and smooth surface is obtained.

8.2.6 Attachment of Gauge to Bone

The bonding material must be both a stable and nontoxic adhesive.[12] Early experiments attaching strain gauges to bone used epoxy resins and dental cement,[3] which are somewhat cumbersome and unforgiving to the ultimate goal of rapid and effective bonding of gauge to bone. Even fast-curing epoxies were undesirable because of toxic properties and exothermic cures. It was the development of the cyanoacrylate adhesives that helped to spur more physiological studies using strain gauges.[12] Cyanoacrylate (in particular, isobutyl 2-cyanoacrylate) is used most often because of the quick bonding time ($\sim$1 min), effective under even moist conditions. Methyl-cyanoacrylate adhesives (superglues) purchased at hardware stores

have also given reliable results for attaching strain gauges to bone,[7] although the container must first be sterilized. To avoid any possible toxic effects from cyanoacrylate, polymethyl methacrylate (PMMA) has recently been used to bond strain gauges to the human tibia and has been shown to produce strain magnitudes similar to those collected using cyanoacrylate (no more than 5% difference).[14–16]

Ensuring that the gauge site is still dry and accessible, the back of the strain gauge is flooded with the adhesive, minimizing any air bubbles. After applying the adhesive to the strain gauge backing, the gauge is pressed to the bone using firm pressure from a finger. Because the adhesive will also bond latex (i.e., surgical gloves), it is advised that a finger from a sterile polyvinyl glove be placed over the finger before pushing, such that the surgical glove can be withdrawn intact. For small bones, a small instrument such as a metal bar covered with a polyethylene sleeve can be used to press on the gauge.[7] While pressure should be applied for at least 1 min for cyanoacrylate, PMMA requires at least 10 min for polymerization.[14] Extreme caution is then used when lifting the finger from the site, to ensure that the gauge has not somehow stuck to the finger as well as the bone, thus potentially destroying the gauge. After carefully removing the applied pressure, the gauge attachment should be carefully examined to ensure that all edges are securely adhered to the bone. While it is unfortunate if an edge is not adhered, it is best to remove the gauge, and begin with a new gauge from the very beginning.

8.2.7 Wiring and Strain Relief

Insulated lead wires must be used to withstand the body fluids. Early experiments used cyanoacrylate to bond the lead wires to the bone to provide strain relief.[8] In these early experiments, gauges remained firmly attached to bones such as the sheep tibia for up to 4 weeks. At that time, the most common cause of failure was fatigue fracture of the leads usually near the knee joint where they underwent bending.[9] Other early experiments used flexible epoxy resin flanges that surrounded the lead wires and were bonded to bone for strain relief.[10]

It is strongly recommended that the lead wires be soldered to the strain gauge before the *in vivo* attachment of the gauge to bone; many manufacturers provide gauges with presoldered lead wires. Nevertheless, many investigators prefer to etch and solder their own Teflon-coated lead wires to the gauges, to ensure good connections with waterproofed insulation. To provide strain relief for the lead wires in smaller animals, the wires can be sutured to soft tissue near the gauge site as well as to the soft tissue below the skin and to skin outside the incision.[3] To help anchor the wires, a short polyethylene sleeve can be epoxied around the wires.[7] In larger animals, an epoxy resin flange is often used to hold the wires in place approximately 2 cm away from the gauge using a small screw (1.5 or 2 mm) tapped into the cortex[6] (Fig. 8.2).

In early experiments polytetra fluoroethylene (PTFE)-covered lead wires were connected to a sterilized epoxy-embedded multipin socket that was sutured in a small incision in the flank,[9,10] whereas more recent studies usually use a connector to which the wires are soldered and then attached externally (via tape, a small pouch, or a harness) to the animal. In either case, the leads are passed through the incision or for some animals the leads are passed subcutaneously to a convenient point that is inaccessible to the animals such as between the shoulder blades and then brought through the skin.[3] To facilitate the passing of wires to a remote location, it is advised to use a pointed stainless steel tube, which is very carefully worked subcutaneously to the remote site and then pierces the skin at an aseptic site. The wires are then passed through the tube, and the tube pulled through the stab incision, leaving the leads exposed through the new site. Obviously, it is essential to keep track of which wires go to which gauge of a double or triple rosette gauge, and thus the wires are usually color coded. To keep track of the different rosette gauges when more than one rosette is used (especially as they often come through the same exit incision), it is convenient to group the wires from each gauge together and tie small, loose knots in them for identification (e.g., 1 knot = cranial rosette, 2 knots = caudal rosette, etc.). It is strongly advised to check, and recheck, the set of leads for any given gauge.

For data collection, the external connector is hooked up to a shielded cable that leads to signal conditioning and amplifying equipment, which converts the change in resistance of each gauge to a

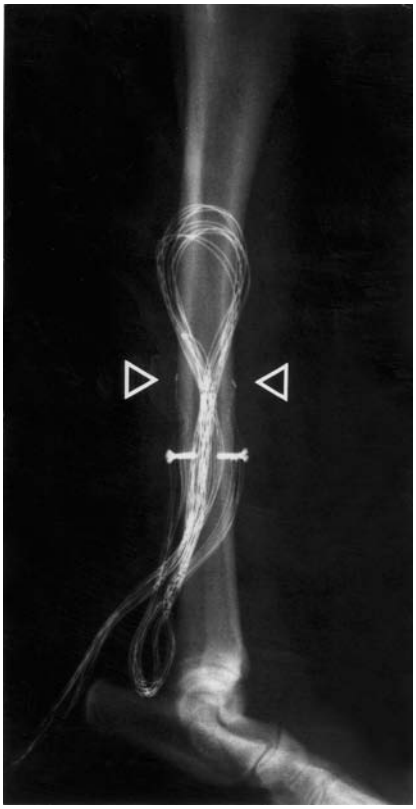

FIGURE 8.2 Radiograph showing two triple 45° rosette strain gauges attached to the cranial surface (left arrow) and caudal surface (right arrow) of a dog tibia. The epoxy resin flanges are approximately 2.5 cm away from each gauge and are screwed into the bone cortex to serve as strain relief.

change in voltage. The circuitry is usually a Wheatstone bridge, with each gauge an active arm of the bridge.

Some investigators have eliminated the difficulties of connecting the strain gauges to the data collection equipment and have developed telemetry methods of data collection.[17–20] A main advantage of telemetry is that it removes the long, trailing cable from the animal, thus allowing freer movement. Instead, the wires from the gauges are still passed through the skin of the animal, where they are connected to a transmitter that remains attached to the animal.[17,18] However, the use of telemetry often limits the resolution of the gauge readings, and may limit the number of gauges that can be simultaneously monitored. It also, invariably, adds a degree of expense to the project.

8.2.8 Verification of Gauge Attachment and Gauge Function

Before the wound is closed during surgery, the gauge function should be checked. First, the gauge resistance is checked using an ohmmeter. If this resistance has deviated from the manufacturer's specifications, the gauge may have been damaged during application and should not be used.[1] Next, the gauge should be hooked up to the measuring circuit to check for proper attachment to the bone. The strain signals should be observed on an oscilloscope to look for any evidence of problems (e.g., drift, spikes).[7] It is suggested that manual manipulation of the limb also be enacted, to determine that the gauges are in fact showing some relationship to the loads applied. A tensile and compressive calibration should also be performed to ensure an accurate conversion of the voltage output to strain magnitude. This is essential, as the gain of the amplifiers may be adjusted, intentionally or inadvertently. Most bridge

amplifier/signal conditioners (e.g., Vishay, Syminex) have built-in calibration switches. Such a calibration also can be used as a check of the integrity of the strain gauge circuits during experimental sessions.

To minimize drift because of heating of the bone, the excitation voltage should remain low, preferably at or below 2 V.[7,12] A high bridge excitation voltage can cause the gauge to heat above typical body temperatures, and may cause bone necrosis and/or discomfort for the subject.

After gauges are attached, their resistance has usually changed slightly from the original 120 or 350 Ω because of deformation of the gauge during attachment or lead wire resistance.[7] This results in a DC offset, requiring that the strain gauge circuit be balanced. While establishing a state of zero strain in a conscious animal is somewhat subjective, zero strain balancing is often performed with weightbearing removed from the instrumented limb (see Section 8.2.11 for more details on how to establish the zero-level strain).

Some early strain gauge reports included tests after animal sacrifice where harvested bones were loaded with weights and strains recorded. Then the implanted gauges were replaced with new gauges and the loading was repeated. If the strain readings were within 5% of each other, the implanted gauges were said to have been securely bonded.[12] In other studies sinusoidal loading was applied to harvested bones to confirm that the gauges were performing in the expected manner.[9] Baggott and Lanyon[21] tested the reliability of the bone–gauge bond using an extensometer after up to 3 weeks of gauge implantation. They found that the bone–gauge bond efficiently transmitted the surface bone strain and that no deterioration of the bond could be found over 3 weeks of implantation.[20] Carter et al.[22] also found that strains measured with an extensometer matched strains measured with strain gauges. In addition, Wright and Hayes[23] showed that the *in vitro* application of strain gauges to cortical bone specimens did not cause surface damage significant enough to alter the bone properties. Using these methods along with other *in vitro* experiments using strain gauges on bone specimens, early investigators confirmed that strain gauges were a useful and reliable tool to measure bone deformations.

8.2.9 Dummy Gauges

Verification of gauge function in early strain gauge experiments also involved using "dummy" gauges bonded to stainless steel placed beneath the skin to confirm that *in vivo* placement of the gauges did not affect the strain measurements.[8] Even after it was established that the *in vivo* strain gauge implantation did not cause artifacts in the strain measurements, dummy gauges were still implanted because they provided a useful check of the equipment.[10] More recent strain gauge experiments have used precision resistors external to the animal (applied at the connector) as a measurement of strain signal noise.[24]

8.2.10 Collection of Strain Gauge Data

Before data are collected, enough time must be allowed for the animal to recover fully from anesthesia. Several studies enlist a minimum of a 1-day recovery, which can extend up to a few days, with recovery determined by visually assessing the animal's movements to look for signs of limping or lameness. A force plate can also be used to measure ground reaction forces to assess lameness. Even if several days of recovery are anticipated, to ensure joint mobility and limb flexibility, it is suggested that at least some ambulatory movement be engagd. Selecting a gauge site based on minimal muscle disruption also ensures a swift and full recovery. In some short-term studies in which the gauge wiring is at risk of disruption (e.g., with primates), data collection can even begin immediately after anesthesia has worn off.[14,16,25] With careful attention to details, strain gauges can be successfully bonded to bone for weeks. Early reports showed bonding lasting up to 5 weeks.[12]

As with any signal collection, to minimize electrical noise and to avoid aliasing, the strain signals should be filtered before digitizing. This is especially important if the frequency content of the strain signals will be analyzed. The data should be sampled at a rate at least twice the highest frequency of interest. For bone, a sampling rate of 100 to 500 Hz is generally adequate. Current A/D boards provide high resolution (16-bit), which can allow strain resolutions of higher than 0.1 microstrain ($\mu\varepsilon$) along with strain ranges of approximately $\pm 2500\ \mu\varepsilon$.[24] With the large storage capacity of personal computers, data can be sampled continuously for extended periods of time and stored directly to disk.

8.2.11 Calculation of Principal Strains

Principal strains acting at a point on a surface are the largest and smallest normal strains acting at the point. These strains are perpendicular to each other and are oriented such that the shear strain at the point is zero. Using the raw strain data from a three-element stacked rosette gauge, the principal strains and their orientation at the point of gauge attachment can be determined using standard formulae.[26] To perform these calculations, the orientation of the rosette gauge on the bone surface must be quantified. Typically, this can be achieved using radiographs and measuring the angle that a specific gauge element makes with the long axis of the bone. It is advised to take a series of high-resolution radiographs with the gauge in the plane of the film and with the gauge perpendicular to the film to help define placement. As a radiograph of a gauge can be somewhat misleading in terms of whether one is viewing the front or back of the gauge, it is also advised to place a solder dot over one of the gauge elements to ensure that the radiograph orientation is correct. Gauge placement can also be confirmed by postmortem examination if possible.

To calculate the magnitude and direction of the principal strains, the point of zero strain must also be determined for each strain gauge of each rosette. The zero point is often taken to be the swing phase of walking where the limb is not touching the ground,[27] and is indicated by a broad flat region of strain during the swing phase (Fig. 8.3). Other investigators have determined the zero-level strain by putting the animals in a recumbent position so that the instrumented limb is not loaded.[22] The zero-level strain determined in this way has been found to match the level of strain measured at a point during the swing phase of gait. Measurements taken from an anesthetized animal (to further relax the muscles) are not different from measurements taken with the animal awake and lying on its side.[28] Care should be taken when measuring the zero-level strain because small errors in this measurement could lead to significant errors in the calculation of the shear strain.[22] Methods have been developed to compensate automatically for strain offsets[29] and to correct the zero-strain reference points when significant transverse loading is not present.[30] Misreadings of zero strain often become clear when principal strains are calculated, as the analyzed data do not reflect the pattern of the actual raw strain measurements.

Strains can also be reported along the structural (material) directions of the bone (the long axis, transverse axis) as outlined by Carter.[31] Such an approach is useful when comparing strains from different animals or if the material properties of the bone are known so that the stresses in the material directions of the bone can be calculated.

8.2.12 Calculation of Normal and Shear Strains Across a Bone Section

If the normal strains at three points around a planar section of a long bone are measured (either with single-element gauges aligned with the longitudinal bone axis or with rosette gauges), the distribution of normal longitudinal strains can be calculated assuming a uniform distribution across the section. The bone can be modeled as a prismatic beam of uniform cross section, and linear beam theory can be used to estimate the normal strain distribution across the bone cross section.[32–34]

When using three, three-element rosette strain gauges around a planar section of a long bone, shear strains may be similarly estimated by modeling a long bone as a prismatic cantilever subjected to end shearing forces and a torsional moment. A finite element model can be constructed of the bone cross section, using appropriate material properties. With shear strains measured at three sites around the circumference of a bone, the applied end shearing forces and torsional moment can be scaled so that the strains calculated at elements located at the three gauge sites match the strains measured *in vivo*.[34] Once the loading conditions are scaled correctly, the shear strains acting at each element across the bone cross section will be known.

While no stress data will be presented in this chapter, strain gauge measurements can be used to calculate bone stresses using the bone tissue material properties. Because bone is anisotropic, the principal stress directions may not be the same as the principal strain directions, so an anisotropic stress analysis should be performed to avoid errors.[31] In addition, the *in vivo* axial force and bending moments acting

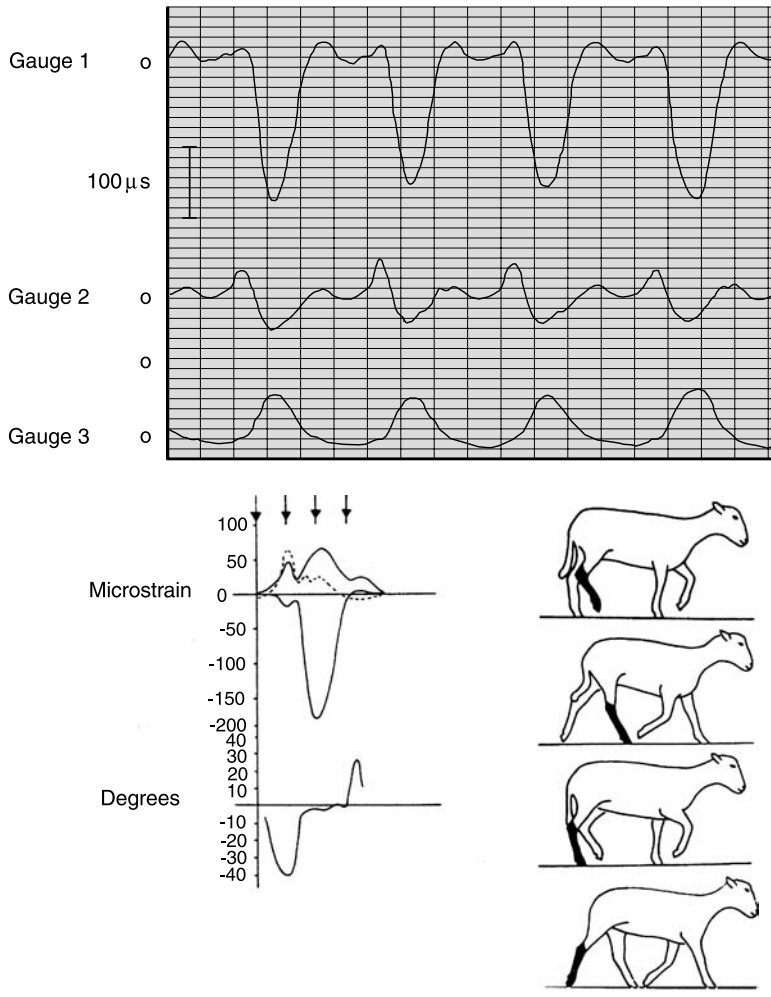

FIGURE 8.3 Strain recordings from a triple rosette gauge attached to the sheep calcaneus showing the tracing of each gauge (top) along with the principal strains and maximum shear strain (dotted) as well as the angle between the principal compressive strain and the axis of gauge 1. The animal's position at the four arrowed points (from left to right) is indicated by the leg position during walking (from top to bottom). The vertical lines in the top figure are 0.1 s apart and the label indicates 100 $\mu\varepsilon$, with tension upward and compression downward. (From Lanyon, L. E., *J. Biomech.,* 6, 41–49, 1973. With permission from Elsevier Science.)

on a long bone can be estimated using the normal longitudinal strain measurements as described above along with the bone geometry and material properties.[32] The end shearing forces and torsional moments can be estimated as described above by using shear strains measured at three points around a bone surface.[34] In essence, the use of strain gauges in this manner allows the bone to become an internal force transducer, monitoring the loads and moments that are applied to the bone. However, it is essential that the position of the gauges be carefully determined, and the cross-sectional geometry of the bone be accurately measured, as small deviations from location can have a significant influence on the calculation of loads and moments. In nonterminal experiments, computed tomography (CT) scans for this purpose have been shown to be very useful.[25] An alternative technique to calculate the external forces and moments acting on a bone involves *in vitro* calibrations performed after *in vivo* strain data collection and does not require bone elastic properties or geometry measurements.[35]

8.3 Results of *in Vivo* Strain Gauge Experiments

While the earliest bone strain gauge study focused on quantifying the maximum strains bones could withstand before fracture,[4] Lanyon and Smith[8,9] were the first to point out the need to measure the mechanical demands made on bone during normal functional activity. Since that time, strain recordings have been made for a wide variety of animals, bones, and activities to help define the functional challenges made on bone. While most of these experiments have focused on quantifying the peak strain magnitudes and strain rates during locomotory activities, several recent studies have attempted to provide a more complete strain history of bone by including measurements during less vigorous activities as well as by quantifying the frequency content of the bone strain signals.[24,36,37] These experiments are important in the sense that it is not yet clear which specific parameters in the strain milieu are actually regulating the adaptive response, and therefore it is necessary to measure all aspects to characterize fully the mechanical conditions the bone is exposed to. Results from all these *in vivo* strain gauge experiments are summarized in Table 8.1.

8.3.1 Measurement of Peak Bone Strains and Strain Rates during Various Activities

8.3.1.1 Early Sheep and Dog Measurements

The early studies of animal gait using strain gauges attached to the tibia of sheep indicated that the strain traces were reproducible and many similarities existed in the patterns between sheep, but they also showed differences in the style of gait between animals.[9] In the early gait experiments, peak tibial strain magnitudes during slow walking were found to be on the order of 300 $\mu\varepsilon$ at the site of gauge attachment for both the sheep and the dog[9,12] (see Table 8.1).

After successful bonding of strain gauges to the tibia, measurements were taken on both sides of lumbar and thoracic vertebrae.[10,11] Peak strains were measured during respiration at rest, walking, and trotting. For walking and trotting, strain magnitudes were on the order of 100 to 300 $\mu\varepsilon$ for both vertebral sites; during respiration, vertebral strains were on the order of 10 to 20 $\mu\varepsilon$ (lumbar) to 50 $\mu\varepsilon$ (thoracic)[10,11] (see Table 8.1). As expected, the strain values during respiration were greater in thoracic vertebrae than in lumbar vertebrae.[11]

All the above-mentioned experiments used single-element gauges that could only measure strain in one direction, and all except Cochran[12] used semiconductor strain gauges. To be able to calculate principal strains, Lanyon[27] began to use triple-rosette resistance strain gauges. The first use of rosette resistance gauges was compared with the single-element semiconductor gauges, and similar results were found.[27] Lanyon[38] demonstrated that during maximum deformation of the sheep calcaneus, the principal strains coincided with the direction of trabeculae, which provided some experimental support for the trajectorial theory of trabecular bone structure.

8.3.1.2 Human Measurements

Lanyon et al.[39] showed that the strains and strain rates measured in a human were similar to those in animals. The largest strains occurred when the human subject was running, producing a principal tensile strain of 850 $\mu\varepsilon$ along the long axis of the tibia (Fig. 8.4), along with a maximum strain rate of 13,000 $\mu\varepsilon$/s. The largest strains during walking occurred just before toe-off during the gait cycle, producing a compressive principal strain of -400 $\mu\varepsilon$ at 37° to the tibia's long axis and a maximum strain rate of -4000 $\mu\varepsilon$/s[39] (see Table 8.1).

In a second, more recent study that measured human tibial strains, peak principal compressive strains were -1200 $\mu\varepsilon$ and peak principal tensile strains were 740 $\mu\varepsilon$ (during uphill zigzag running)[14] (see Table 8.1). The largest strains measured were shear strains that reached nearly 2000 $\mu\varepsilon$, also during the extreme exertion of uphill zigzag running. Compressive strain rates ranged from -7000 to $-34{,}000$ $\mu\varepsilon$/s and tensile strain rates ranged from 7000 to 20,000 $\mu\varepsilon$/s for different activities[14] (see Table 8.1), similar to rates measured in other animals. In investigating the etiology of stress fractures,

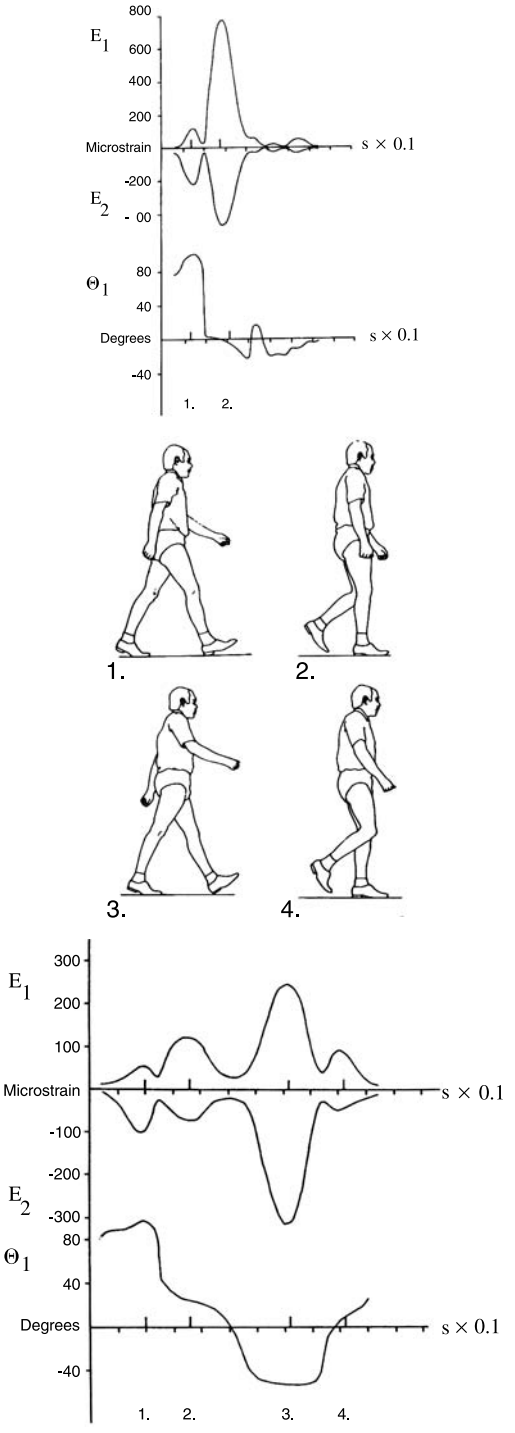

FIGURE 8.4 Strain recordings from a triple rosette gauge attached to a human tibia. (Top) Principal strains and strain angle relative to the bone's long axis during a single stride walking on the floor the day after the operation wearing shoes (note points 1 to 4). (Middle) The man's position at points 1 to 4 taken from cine film. (Bottom) Principal strains and strain angle relative to the bone's long axis during one stride running on a belt without shoes at 2.2 m/s soon after the operation. (From Lanyon, L. E. et al., *Acta Orthop. Scand.*, 46, 256, 1975. With permission.)

TABLE 8.1 Results from *in Vivo* Strain Gauge Experiments

Animal	Bone	Aspect	No. of Animals	Activity	Principal or Maximum Strains* ($\mu\varepsilon$)	Maximum Strain Rate ($\mu\varepsilon$/s)	Type of Gauge, Orientation	Ref.
Human	Tibia	Anteromedial	1	Walking	850 T	13,000	Three-element 45° foil rosette	Lanyon et al., 1975[39]
				Running	400 C	−4000		
	Tibia	Medial (midshaft)	1	Walking:			Three-element 45° unstacked foil rosette	Burr et al., 1996[14]
				Level	540 C, 440 T, 870 shear	−7,200; 11,000		
				Uphill	630 C, 440 T, 1070 shear	−8,200; 7100		
				Downhill	410 C, 530 T, 720 shear	−10,800; 9600		
				Running:				
				Jog	880 C, 630 T, 1440 shear	−27,400; 13,900		
				Sprint	970 C, 650 T, 1580 shear	−34,500; 20,200		
				Uphill	950 C, 630 T, 1560 shear	−23,800; 17,500		
				Downhill	520 C, 710 T, 980 shear	−26,300; 16,700		
				Zigzag uphill	1230 C, 740 T, 1970 shear	−20,900; 13,600		
				Zigzag downhill	1150 C, 710 T, 1870 shear	−30,000; 15,700		
Human	Femur	Lateral (proximal)	2	Two-legged stance	400 T, 115 C[a]	—	Three-element 45° foil rosette	Aamodt et al., 1997[16]
				One-legged stance	1340 T, 250 C[a]	—		
				Walking	1200 T, 390 C, 12° to long axis[b]	—		
				Stair climbing	1230 T, 570 C[a]	—		
Sheep	Tibia	Craniomedial	1[c]	Walking	−260	—	Semiconductor, aligned with long axis	Lanyon and Smith, 1970[9]
				Trotting	−310	—		

	Tibia	Cranial and caudal (distal third)	5	Walking (1 m/s)	Cranial: 710 T, 450 C, 29° to long axis	17,800	Three-element 45° foil rosette	Lanyon and Bourn, 1979[44]
					Caudal[d]: 380 T, 670 C, 22° to long axis	−16,200[d]		
	Tibia	Anterior, posterior, and medial (midshaft)	1	Normal daily activities	2 to 2000[e]	20,000	Three-element 45° foil rosette	Fritton et al., 1999[89]; 2000[24]
Sheep	Lumbar vertebrae	Bilateral: right and left sides	4	Respiration	Right side: 20	—	Semiconductor, aligned along spine axis	Lanyon, 1971[10]
					Left side: 10	—		
				Medium walk	Right side: 180	—		
					Left side: 70	—		
				Medium trot	Right side: 270	—		
					Left side: 110			
Sheep	Thoracic vertebrae	Bilateral: right and left sides	6	Respiration	Right side: 50	200[f]	Semiconductor, aligned along spine axis	Lanyon, 1972[11]
					Left side: 50			
				Walking	Right side: 130	—		
					Left side: 150			
				Trotting	Right side: 170	3,500[f]		
					Left side: 200			
Sheep	Calcaneus	Dorsal	2	Slow walk	120	1,800	Semiconductor	Lanyon, 1973[27]
				Medium walk	130	2,300		
				Fast walk–slow trot	160	2,700		
	Calcaneus	Dorsal	5	Slow walk	80 T, 170 C	2,700	Three-element 45° foil rosette	Lanyon, 1973[27]
				Medium walk	100 T, 210 C	3,600		
				Fast walk–slow trot	100 T, 220 C	4,300		
				Medium trot	120 T, 250 C	5,100		
	Calcaneus	Lateral	8	Medium walk	160 T,[g] 220 C,[g] 380 max shear	—	Three-element 45° foil rosette	Lanyon, 1974[38]
Sheep	Radius	Cranial and caudal (proximal half)	8	Walking (~1 m/s)	Cranial: 810 T, 360 C, 3° to long axis	7,900 to 14,700[h]	Three-element 45° foil rosette	Lanyon and Baggott, 1976[40]
					Caudal: 480 T, 1320 C, 2° to long axis	11,400 to 17,900[h]		

(*continued*)

TABLE 8.1 Results from *in Vivo* Strain Gauge Experiments (Continued)

Animal	Bone	Aspect	No. of Animals	Activity	Principal or Maximum Strains* ($\mu\varepsilon$)	Maximum Strain Rate ($\mu\varepsilon$/s)	Type of Gauge, Orientation	Ref.
	Radius	Cranial and caudal (midshaft)	18	Walking (~1 m/s)	Cranial: 690 T, 2° to long axis	—	Three-element 45° foil rosette	Lanyon et al., 1979[41]
					Caudal: 1160 C, 2° to long axis	—		
	Radius	Cranial and caudal (proximal)	6	Walking (1 m/s)	Cranial: 640 T, 4° to long axis	—	Three-element 45° foil rosette	Lanyon et al., 1982[42]
					Caudal: 1170 C, 4° to long axis	—		
	Radius	Cranial and caudal (midshaft)	11	Walking (1 m/s)	Cranial: 930 T, 0° to long axis	6,700 to −11,400[i]	Three-element foil rosette	O'Connor et al., 1982[43]
					Caudal: 1250 C, 0° to long axis	−10,000 to 16,400[i]		
Sheep	Femur	Medial and lateral (proximal)	4	Walking (~1 m/s)	Medial: 700 C, 180 T, 19° to long axis	—	Three-element 45° foil rosette	Lanyon et al., 1982[52]
					Lateral: 300 C, 190 T, 27° to long axis	—		
Horse	Third metacarpal	Lateral and medial	1	Walking	Lateral: 430 p-p	—	Foil, single element	Barnes and Pinder, 1974[13]
					Medial: 150 p-p			
	Metacarpus	Lateral, palmar, dorsal, and medial	1	Standing	−100 to −525[j]	—	Single-element foil	Turner et al., 1975[45]
				Walking (foot down)	−300 to −1000[j]	—		
				Trotting	100 to −1700[j]	—		
Horse (2-year-old Thoroughbred)	Third metacarpal	Dorsolateral (midshaft)	4	Maximum effort (16 – 17 m/s)	4840 C	—	Three-element 45° foil rosette	Nunamaker et al., 1990[48]
Horse (12-year-old Thoroughbred)	Third metacarpal	Dorsolateral (midshaft)	1	Maximum effort (16 – 17 m/s)	3320 C	—	Three-element 45° foil rosette	Nunamaker et al., 1990[48]
Horse (5-year-old Thoroughbred)	Third metacarpal	Medial, anterior, and lateral (midshaft)	1	Medium trot (3.6 m/s)	2400 C, 810 T, 1500 shear[k]	—	Three-element 45° foil rosette	Gross et al., 1992[34]
Horse (4- to 8-year-old Thoroughbred)	Third metacarpal	Dorsomedial	5	Walk (2 m/s)	390 C	13,200	Three-element 45° foil rosette	Davies et al., 1993[58]
				Trot (4 m/s)	1190 C	30,800		
				Trot (6 m/s)	1570 C	47,800		
				Trot/canter (8 m/s)	2030 C	60,700		
				Canter (10 m/s)	2410 C	75,300		
				Gallop (12 m/s)	3210 C[l]	—		
				Gallop (14 m/s)	4000 C[l]	—		

Horse	Radius	Lateral, caudal, cranial, and medial	1	Standing	900 to −1500[j,m]	—	Single-element foil	Turner et al., 1975[45]
				Walking (foot down)	1200 to −1900[j,m]	—		
				Pacing	1500 to −2600[j,m]	—		
Horse (adult ponies)	Radius	Caudal[n] (midshaft)	1	Slow walk (1.1 m/s)	1780 C	—	Three-element 45° foil rosette	Rubin and Lanyon, 1982[55]
				Fast walk	1970 C	—		
				Slow trot (1.5 m/s)	2630 C	—		
				Fast trot (5.2 m/s)	2670 C	—		
				Slow canter	2300 C	—		
				Gallop (7.5 m/s)	2650 C[o]	—		
Horse	Radius	Cranial, caudal, medial, and lateral (proximal, midshaft, and distal)	1	Walking	Cranial:[p] P: 900 axial, −400 shear M: 800 axial, 600 shear D: −200 axial, 900 shear	—	Three-element foil rosette	Schneider et al., 1982[46]
					Caudal:[p] P: −1400 axial, 450 shear M: –1200 axial, 600 shear D: −900 axial, 100 shear	—		
					Lateral:[p] P: –1600 axial, −400 shear M: –1100 axial, −500 shear D: –1100 axial, 650 shear	—		
					Medial:[p] P: 900 T axial, 250 shear M: 500 T axial, 400 shear D: −600 axial, 200 shear	—		

(*continued*)

TABLE 8.1 Results from *in vivo* Strain Gauge Experiments (Continued)

Animal	Bone	Aspect	No. of Animals	Activity	Principal or Maximum Strains* ($\mu\varepsilon$)	Maximum Strain Rate ($\mu\varepsilon$/s)	Type of Gauge, Orientation	Ref.
	Radius	Caudal (midshaft)	3	Fast walk (1.6 m/s)	1250 C	—	Three-element foil rosette	Biewener et al., 1983[90]; Biewener and Taylor, 1986[57]
				Slow trot (1.9 m/s)	1790 C	—		
				Fast trot (4.2 m/s)	2050 C	—		
				Canter (4.7 m/s)	2010 C			
Horse	Metatarsus	Lateral, plantar, dorsal, and medial	1	Walking (foot down)	760 to −1250[j]	—	Single-element foil	Turner et al., 1975[45]
				Walking (foot up)	250 to −290[j]	—		
				Trotting	580 to −1580[j]	—		
Horse	Tibia	Lateral, caudal, cranial, and medial	1	Standing	480 to −300[j, m]	—	Single-element foil	Turner et al., 1975[45]
				Walking (foot down)	250 to −50[j, m]	—		
				Walking (foot up)	820 to −950[j, m]	—		
				Trotting	1500 to −1600[j, m]	—		
Horse (adult ponies)	Tibia	Caudal[n] (midshaft)	2[q]	Slow walk (1.1 m/s)	940 C	—	Three-element 45° foil rosette	Rubin and Lanyon, 1982[55]
				Fast walk	1350 C	—		
				Slow trot (1.5 m/s)	2140 C	—		
				Fast trot (5.4 m/s)	2480 C	—		
				Slow canter	2660 C	—		
				Fast canter (6.8 m/s)	3170 C	—		
				Gallop (7.5 m/s)	3130 C	—		
Horse	Tibia	Cranial, caudal, medial, and lateral (proximal, midshaft, and distal)	2[r]	Walking	Cranial:[p] P: 1300 axial, 0 shear M: 1200 axial, −780 shear D: −100 axial, −1500 shear	—	Three-element foil rosette	Schneider et al., 1982[46]
					Caudal:[p] P: −1250 axial, −500 shear M: −1700 axial, −400 shear D: −800 axial, −1200 shear	—		

					Medial:[p] P: −200 axial, −1000 shear M: −300 axial, −900 shear D: −1000 axial, −1150 shear	—		
					Lateral:[p] P: 200 axial, −750 shear M: 300 axial, −900 shear D: 450 axial, −600 shear	—		
Horse (adult ponies)	Tibia	Cranial, caudal, and medial (midshaft)	6	Walking (~1.5 m/s)	Cranial:[s] 790 T, 370 C, 16° to long axis	—	Three-element 45° foil rosette	Hartman et al., 1984[47]
					Caudal:[s] 480 T, 1120 C, 13° to long axis	—		
					Medial:[s] 480 T, 690 C, 37° to long axis	—		
Horse	Tibia	Caudal (midshaft)	3	Fast walk (1.6 m/s)	1000 C	—	Three-element foil rosette	Biewener et al., 1988[91]; Biewener and Taylor, 1986[57]
				Slow trot (1.9 m/s)	1260 C	—		
				Fast trot (4.2 m/s)	1740 C	—		
				Canter (4.7 m/s)	2360 C	—		
Young pig	Radius	Craniomedial	6	Walking (~1 m/s)	Right limb: 750 C, 22° to long axis	—	Three-element 45° foil rosette	Goodship et al., 1979[49]
					Left limb: 840 C, 24° to long axis	—		

(*continued*)

TABLE 8.1 Results from *in vivo* Strain Gauge Experiments (Continued)

Animal	Bone	Aspect	No. of Animals	Activity	Principal or Maximum Strains* ($\mu\varepsilon$)	Maximum Strain Rate ($\mu\varepsilon$/s)	Type of Gauge, Orientation	Ref.
Dog	Tibia	—	2	Walking	300 (T & C)	—	Single-element foil, aligned with long axis	Cochran, 1972[12]
	Tibia	Caudal[n] (midshaft)	1	Slow walk (0.7 m/s)	700 C, 11° to long axis	4500	Three-element 45° foil rosette	Rubin and Lanyon, 1982[55]
				Fast walk (1.6 m/s)	1060 C, 16° to long axis	7700		
				Slow trot	1580 C, 4 ° to long axis	17,400		
				Fast trot (3.4 m/s)	2010 C	—		
				Slow canter	1350 C	29,600		
				Gallop (6.3 m/s)	2020 C	—		
				Max gallop (6.9 m/s)	2000 C, 1° to long axis	64,100		
	Tibia	Medial (midshaft)	2	Fast walk/slow run (1.2 m/s)	650 T, 700 C, 42° to long axis[t]	—	Three-element 45° foil rosette	Bouvier and Hylander, 1984[50]
	Tibia	Anterior, posterior, and medial (midshaft)	1	Normal daily activities	2 to 2000[e]	85,000	Three-element 45° foil rosette	Fritton et al., 1999[89]; 2000[24]
Dog	Radius	Cranial, cranial-medial, and caudal (midshaft and distal)	3[u]	Walking (~1.4 m/s)	Cranial midshaft:[v] 400 axial, −150 transverse, −650 shear	—	Three-element 45° foil rosette	Carter et al., 1980[22]
					Cranial-medial midshaft:[v] 125 axial, −75 transverse, −580 shear	—		
					Caudal distal:[v] −190 axial, 240 transverse, −410 shear	—		
	Radius	Caudal[n] (midshaft)	1[w]	Fast walk	1500 C	—	Three-element 45° foil rosette	Rubin and Lanyon, 1982[55]

				Slow trot (1.2 m/s)	1800 C	—		
				Fast trot (3.2 m/s)	2380 C	—		
				Slow canter	2090 C	—		
				Fast canter (4.0 m/s)	2250 C	—		
	Radius	Cranial and caudal (midshaft)	5	Slow running (1.1 m/s)	Cranial: 480 C Caudal: 290 C	— —	Three-element 45° foil rosette	Burr et al., 1989[51]
Dog	Ulna	Caudal-medial, cranial-lateral (midshaft)	2[u]	Walking (~1.4 m/s)	Caudal-medial:[v] −200 axial, 160 transverse, 740 shear	—	Three-element 45° foil rosette	Carter et al., 1980[22]
					Cranial-lateral:[v] 780 axial, −450 transverse, −130 shear	—		
Dog	Femur	Medial and lateral (midshaft)	5	Walking	Medial: 460 C Lateral: 240 T	— —	Three-element 45° foil rosette	Manley et al., 1982[19]
	Femur	Medial (midshaft)	6	Walking	310 C, 150 T, <30° to long axis[x]	—	Three-element 45° foil rosette	Szivek et al., 1992[54]
	Femur	Medial and lateral (midshaft, proximal, and distal)	4	Walking	Medial proximal: 410 C[y]	—	Three-element foil rosette	Page et al., 1993[53]
					Medial midshaft: 350 C[y]	—		
					Medial distal: 400 C[y]	—		
					Lateral midshaft: 300 T[y]	—		
					Lateral distal: 320 T[y]	—		
Goat	Radius	Caudal (midshaft)	3	Slow walk (0.5 m/s)	820 C	—	Three-element 45° foil rosette	Biewener and Taylor, 1986[57]
				Fast walk (1.3 m/s)	830 C	—		
				Slow trot	1300 C	—		
				Fast trot (3.3 m/s)	1750 C	—		
				Slow gallop	1580 C	—		
				Max gallop (4.3 m/s)	1850 C	—		

(*continued*)

TABLE 8.1 Results from *in vivo* Strain Gauge Experiments (Continued)

Animal	Bone	Aspect	No. of Animals	Activity	Principal or Maximum Strains* ($\mu\varepsilon$)	Maximum Strain Rate ($\mu\varepsilon$/s)	Type of Gauge, Orientation	Ref.
Goat	Tibia	Caudal (midshaft)	3	Slow walk (0.5 m/s)	730 C	—	Three-element 45° foil rosette	Biewener and Taylor, 1986[57]
				Fast walk (1.3 m/s)	850 C			
				Slow trot	1140 C	—		
				Fast trot (3.3 m/s)	1800 C	—		
				Slow gallop	1620 C	—		
				Max gallop (4.3 m/s)	1970 C	—		
Galago	Mandible	Corpus	2	Biting	−435[z]	—	Single-element foil, parallel to lower border	Hylander, 1977[59]
				Chewing	−70 to 25[aa]	—		
Macaque	Mandible	Lateral corpus	4	Mastication	10 to 360 maximum −20 to −450 minimum 90 to 760 shear	—	Three-element 45° foil rosette	Hylander, 1979[60]
	Mandible	Corpus	3–5[bb]	Mastication	110 to 470 maximum[bb] −210 to −500 minimum[bb]	Loading: 1600 to 4300[bb] Unloading: 2900 to 6700[bb]	Three-element 45° foil rosette	Hylander et al., 1987[61]
	Mandible	Symphysis	5	Mastication	40 to 820 maximum[cc]	—	Three-element 45° foil rosette	Hylander, 1984[92]
					−10 to −1040 minimum[cc]	—		
Macaque	Ulna	Medial, lateral, and posterior (slightly distal to midshaft)	3	Walking	Medial: 870 C, 450 T, 100° to long axis[dd]	—	Three-element 45° foil rosette	Demes et al., 1998[25]
					Lateral: 750 T, 360 C, 18° to long axis[dd]	—		
					Posterior: 430 C, 400 T, 33° to long axis[dd]	—		
Gibbon	Ulna	Ventral and dorsal (midshaft)	4	Brachiation	Ventral: 1420 T, 2° to long axis	—	Three-element foil rosette	Swartz et al., 1989[20]

					Dorsal: 1270 T, 6° to long axis	—		
Gibbon	Radius	Ventral and dorsal (midshaft)	4	Brachiation	Ventral: 1640 C, 1° to long axis	—	Three-element foil rosette	Swartz et al., 1989[20]
					Dorsal: 750 T, 5° to long axis	—		
Gibbon	Humerus	Ventral and dorsal (midshaft)	4	Brachiation	Ventral: 420 T, 44° to long axis	—	Three-element foil rosette	Swartz et al., 1989[20]
					Dorsal: 1490 T, 62° to long axis	—		
Owl monkey	Interorbital region, postorbital bar, postorbital septum	—	2	Mastication	Interorbital: 20 to 170 T; 50 to 180 C[ee]	—	Three-element delta foil rosette	Ross and Hylander, 1996[62]
					Lateral postorbital bar: 50 to 690 T, 70 to 640 C[ee]	—		
					Medial postorbital septum: 40 to 300 T, 60 to 230 C[ee]	—		
Rabbit	Mandible	Lateral	7	Mastication	Chewing: 320 C, 280 T	—	Three-element delta foil rosette	Weijs and de Jongh, 1977[63]
					Biting: 90 T, 60 C[ff]	—		
Fish	Operculum	Lateral	2	Strike during capture of prey	1800 C, 1600 T[gg]	615,000[hh] 15,000 to 110,000[ii]	Three-element 45° foil rosette	Lauder and Lanyon, 1980[64]
Rat	Femur	Anterior-lateral	1[jj]	Exercising wheel (0.2 m/s)	−260 axial, 120 transverse, 420 shear	—	Three-element unstacked foil rosette	Keller and Spengler, 1982[65]
Immature and mature rat	Femur	Anterior-lateral	20 immature, 20 mature	Exercising wheel (0.2 m/s)	Immature: 380 C, 230 T Mature: 410 C, 250 T	10,000 to 20,000	Three-element unstacked foil rosette	Keller and Spengler, 1989[70]

(*continued*)

TABLE 8.1 Results from *in vivo* Strain Gauge Experiments (Continued)

Animal	Bone	Aspect	No. of Animals	Activity	Principal or Maximum Strains* ($\mu\varepsilon$)	Maximum Strain Rate ($\mu\varepsilon$/s)	Type of Gauge, Orientation	Ref.
Rat	Femur	Anterior	6-week-old: 8 12-week-old: 8 52-week-old: 8	Running on treadmill (0.2 m/s)	6-week-old: 270[kk] 12-week-old: 330[kk] 52-week-old: 230[kk]	— — —	Single-element foil, aligned with long axis	Indrekvam et al., 1991[71]
Rat	Ulna	Medial (midshaft)	4	Running on solid level surface (unrestricted)	−700 to −1200	23,000 to −38,000	Single-element foil, aligned with long axis	Mosley et al., 1997[66]
				Dropping from a height of ~30 cm	−2500	−100,000		
Turkey	Ulna	Midshaft	2	Vigorous wing flapping	−3300 axial[ll]	56,000	Three-element foil rosette	Lanyon and Rubin, 1984[67]
	Ulna	Midshaft	2	Wing flapping	−1900 axial[ll]	33,000	Three-element foil rosette	Rubin and Lanyon, 1984[93]
	Ulna	Cranial, caudal, and ventral (midshaft)	3	Large wing flap	Caudal: 960; ventral: 770[mm]	—	Three-element 45° foil rosette	Adams et al., 1997[36]
				Small wing flap	Caudal: 420; ventral: 310[mm]	—		
				Shaking	Caudal: 1020; ventral: 540[mm]	—		
				Wing extension	Caudal: 290; ventral: 170[mm]	—		
				Ruffling	Caudal: 280; ventral: 80[mm]	—		
				Wing adduction	Caudal: 130; ventral: 140[mm]	—		
	Ulna	Cranial, caudal, and ventral (midshaft)	3	Normal daily activities	2 to 2000[e]	—	Three-element 45° foil rosette	Fritton et al., 2000[24]
Turkey	Tibia	Anterior, posterior, and medial (midshaft)	1	Normal daily activities	2 to 2000[e] (walking: −1500 to 1000)	35,000	Three-element 45° foil rosette	Fritton et al., 1999[89]; 2000[24]

Growing chick 4 to 17 weeks old	Tibiotarsus	Medial, caudal, and cranial (midshaft, proximal, and distal)	15	35% of maximum speed (0.5–1.2 m/s)	Medial proximal: 650 C[nn] Caudal midshaft: 1140 C[nn] Cranial midshaft: 630 T[nn] Cranial distal: 910 C[nn]	— — — —	Three-element 45° foil rosette	Biewener et al., 1986[69]
8 and 12 weeks old	Tibiotarsus	Medial, caudal, and cranial (midshaft, proximal, and distal)	6	Sedentary (small cage activity)	Medial proximal: 320 C Caudal midshaft: 290 C Cranial midshaft: 150 T Cranial distal: 360 C	Medial proximal: −2600 Caudal midshaft: −2200 Cranial midshaft: 1700 Cranial distal: −2800	Three-element 45° foil rosette	Biewener and Bertram, 1994[94]
Rooster	Tarsometatarsal	Medial, anterior, and lateral (midshaft)	3[oo]	Slow walking (0.4 m/s)	Medial: −840 axial, 770 shear[oo] Anterior: −870 axial, 630 shear[oo] Lateral: −530 axial, 800 shear[oo]	— — —	Three-element delta foil rosette	Loitz and Zernicke, 1992[72]
	Tarsometatarsal	Medial, anterior, and lateral (midshaft)	6	Running (1.7 m/s)	Maximum longitudinal: −1850 (anterior)[pp]; 1220 (posterior)[pp]; Maximum shear: 1580[qq]	—	Three-element 45° foil rosette	Judex et al., 1997[73]

(*continued*)

TABLE 8.1 Results from *in vivo* Strain Gauge Experiments (Continued)

Animal	Bone	Aspect	No. of Animals	Activity	Principal or Maximum Strains* ($\mu\varepsilon$)	Maximum Strain Rate ($\mu\varepsilon$/s)	Type of Gauge, Orientation	Ref.
12 to 16 weeks old	Tarsometatarsal	Medial, anterior, and lateral (midshaft)	6	Walking (0.5 m/s)	Maximum longitudinal: −1570 (anterior)[pp]; 860 (posterior)[pp]	38,000	Three-element 45° foil rosette	Judex and Zernicke, 2000[74]
				Running (1.5–1.8 m/s)	Maximum longitudinal: −1870 (anterior)[pp] 960 (posterior)[pp]	89,000		
Bat	Humerus	Dorsal, ventral, and medial (midshaft)	2–4	Mid-downstroke during flight	Dorsal: 1550 T, 21° to long axis	—	Three-element foil rosette	Swartz et al., 1992[75]
					Ventral: 1500 T, 22° to long axis	—		
					Medial: 2000 T, 21° to long axis	—		
				Bottom of downstroke	Dorsal: 1190 T, 31° to long axis	—		
					Ventral: 990 T, 21° to long axis	—		
					Medial: 1850 T, 22° to long axis	—		
				Top of upstroke	Dorsal: 490 T, 0° to long axis	—		
					Ventral: 570 T, 2° to long axis	—		
					Medial: 470 T, 25° to long axis	—		
Bat	Radius	Dorsal, dorsolateral, and ventral (midshaft)	2−4	Mid-downstroke during flight	Dorsal: 1810 C, 28° to long axis	—	Three-element foil rosette	Swartz et al., 1992[75]
					Dorsolateral: 2180 C, 32° to long axis	—		
					Ventral: 1280 T, 32° to long axis	—		
				Bottom of downstroke	Dorsal: 2110 C, 27° to long axis	—		

					Dorsolateral: 1910 C, 32° to long axis	—		
					Ventral: 1320 T, 29° to long axis	—		
				Top of upstroke	Dorsal: 410 C, 29° to long axis	—		
					Dorsolateral: 900 T, 21° to long axis	—		
					Ventral: 240 T, 10° to long axis	—		
Pigeon	Humerus	Dorsal and ventral (midshaft)	3[rr]	Level flight	Dorsal: 2120 C, 38° to long axis 1780 shear	—	Three-element foil rosette	Biewener and Dial, 1995[76]
					Ventral: 1380 T, 34° to long axis 1210 shear	—		
				Take-off	Dorsal: 2230 C, 36° to long axis 1650 shear	—		
					Ventral: 1540, 33° to long axis 1310 shear	—		
				Landing	Dorsal: 1660 C, 39° to long axis 1540 shear	—		
					Ventral: 1450, 34° to long axis 930 shear	—		
	Humerus	Dorsal, ventral, and anterior	3	Level flight	Dorsal: −1980 Ventral: 1260 Anterior: −1830[ss]	—	Single-element foil, aligned with long axis	Biewener and Dial, 1995[76]
				Ascent	Dorsal: −2330[ss]			
					Ventral: 1430 Anterior: −2040[ss]	—		
				Landing	Dorsal: −1500[ss]			
					Ventral: 1200 Anterior: −1240[ss]	—		

(*continued*)

TABLE 8.1 Results from *in vivo* Strain Gauge Experiments (Continued)

Animal	Bone	Aspect	No. of Animals	Activity	Principal or Maximum Strains* ($\mu\varepsilon$)	Maximum Strain Rate ($\mu\varepsilon$/s)	Type of Gauge, Orientation	Ref.
Alligator (juvenile)	Femur	Dorsal and ventral (slightly distal to midshaft)	3	Slow locomotion (0.2 m/s)	Dorsal: 350 C, 190 T, 42° to long axis 490 shear	—	Three-element 45° foil rosette	Blob and Biewener, 1999[77]
					Ventral: 340 T, 260 C, 28° to long axis 470 shear	—		
				Fast locomotion (0.4 m/s)	Dorsal: 470 C, 230 T, 47° to long axis 620 shear	—		
					Ventral: 710 T, 540 C, 29° to long axis 1030 shear	—		
Alligator (juvenile)	Tibia	Anterior (midshaft)	3	Fast locomotion (0.4 m/s)	390 T, 360 C, 35° to long axis, 680 shear	—	Three-element 45° foil rosette	Blob and Biewener, 1999[77]
				Slow locomotion (0.2 m/s)	340 T, 320 C, 36° to long axis 620 shear	—		
	Tibia	Anterior, medial, and posterior (midshaft)	2–3	Slow locomotion (0.2 m/s)	Anterior: 200[tt]	—	Single-element foil, aligned with long axis	Blob and Biewener, 1999[77]
					Medial: 510	—		
					Posterior: −470	—		
				Fast locomotion (0.4 m/s)	Anterior: 230[tt]	—		
					Medial: 420	—		
					Posterior: −890	—		
Iguana (subadult)	Tibia	Anterior, medial, and posterior (midshaft)	2–3	Walking	Anterior: 770	—	Single-element foil, aligned with long axis	Blob and Biewener, 1999[77]
					Medial: 390	—		
					Posterior: −660	—		

				Running	Anterior: 1650 Medial: 980 Posterior: −840	— — —		
Iguana (subadult)	Femur	Dorsal and anterior (slightly distal to midshaft)	1–3	Walking	Dorsal: 200[tt] Anterior: −280	— —	Single-element foil, aligned with long axis	Blob and Biewener, 1999[77]
				Running	Dorsal: −160	—		

Note: All animals were mature adults unless otherwise indicated.

[*]Principal directions and maximum shear are also given if reported. Strain values for each experiment were calculated by averaging mean values reported in each study without including the standard deviations. For strains measured using rosette gauges, C = principal compressive strain and T = principal tensile strain. For strains other than principal strains, compressive strains are indicated with a minus sign. "p-p" indicates peak-to-peak magnitude.

[a]Average of the two subjects.

[b]Data given for only one subject.

[c]Although measurements were taken for 10 animals, average peak strains were only reported for one animal.

[d]Only four animals had gauges on the caudal surface.

[e]Strains were raw strains, not principal strains. See Figs. 8.6 and 8.7 for magnitude and frequency distributions (and for the sheep tibia see Fig. 8.5).

[f]Reported for one animal.

[g]Average for the eight animals during a typical stride for each animal.

[h]Lower number is the average for all animals at "foot down"; higher number is the average for all animals at "foot up" (averaged for the 8-9 instrumented radii for a typical stride).

[i]The first number is the average for all animals at "foot down"; the second number is the average for all animals at "foot up."

[j]Range for lateral, caudal (or palmar or plantar), cranial (or dorsal), and medial gauges.

[k]These values were calculated using a combined beam theory and finite element model analysis to define the strain distribution of the bone's cross section. Maximum strains measured by the gauges were 1900 $\mu\varepsilon$ in compression (medial gauge) and 1400 $\mu\varepsilon$ in shear (anterior gauge).

[l]An average for three animals for 12 m/s and for two animals for 14 m/s.

[m]The animals showed slight lameness during data collection and were almost but not fully weight bearing on the instrumented limb.

[n]Recordings were also taken from rosette gauges on the cranial surface of all the bones, but the focus was on the results from the caudal gauges because the compressive strains were greater in magnitude.

[o]Measured from horse B (other measurements from horse A).

[p]Reported at proximal metaphysis (P), mid-diaphysis (M), and distal metaphysis (D) gauge sites for one gait cycle; axial strain is directed along the long axis of the bone; a positive shear strain indicates the bone is twisted clockwise when viewed from above.

[q]Values are the average of two animals where data for both animals were given.

[r]One animal was used for all the measurements except for the distal tibia measurements.

[s]Four animals were used for the cranial measurements, four for the caudal measurements, and three for the medial.

[t]Average for the 2 animals for day 3 (dog 1) and day 4 (dog 2).

[u]Seven animals were included in the study, but plots of the strain results were only presented for five animals (three for the radius and two for the ulna).

(*continued*)

[v]Results for each gauge location represent one animal during a single gait cycle and were estimated from plots of strain vs. time. A negative shear strain corresponds to external rotation of the proximal end of the bone under consideration.

[w]Not the same animal used to measure strains on the dog tibia in the same study.

[x]Average for the six animals.

[y]Average for all animals at each site. For the medial surface, only two animals were included in the proximal and middle measurements and only three for the distal measurements due to gauge failure.

[z]Maximum value for one animal when biting on a bite force transducer.

[aa]Maximum values for one animal.

[bb]Ranges for mean principal strains measured during mastication of an apple. Strains were measured in three animals on the working-side of the mandible during the power stroke of mastication. Strain rates were measured in five animals during the power stroke of mastication.

[cc]Ranges for mean principal strains measured during mastication of an apple.

[dd]Average for the three animals for each gauge site (except only two animals had working medial gauges).

[ee]Mean averages while chewing different foods (hard prunes and apricots, gummy bears).

[ff]Average of five animals for the biting measurements.

[gg]Peak measured in one animal.

[h]Peak measured in one animal during a very rapid strike during capture of an elusive prey.

[ii]Measured during strikes on slower prey.

[jj]38 rats were instrumented, but typical results were shown in graphical form for two gait cycles for one rat.

[kk]Not stated whether compression or tension.

[ll]Peak longitudinal (axial) strains were calculated using beam theory.

[mm]Strain values are given as absolute values—compression or tension was not indicated.

[nn]Averaged for 4-, 8-, 12-, and 17-week animals (3 to 5) per group.

[oo]Strains were measured in six other animals (younger animals and exercised animals) but are not included here. Given values were estimated from a bar plot (Fig. 6 in Loitz and Zernicke, 1992[72]).

[pp]These values were obtained using linear beam theory to numerically calculate the longitudinal (axial) normal strain distributions across the midshaft cross section.

[qq]Shear strain distribution was calculated using a finite-element mesh of the midshaft cross section of the bone.

[rr]Averages presented for one animal per gauge site only.

[ss]Average for two animals where noted for dorsal gauge; measurements for one animal for anterior gauge.

[tt]Measured using rosette gauges.

the authors had hypothesized that strains greater than 3000 $\mu\varepsilon$ would be found on the surface of the human tibia during vigorous exercise, such as that performed by military recruits; but all measured strains were below 2000 $\mu\varepsilon$, with almost all normal strains below 1000 $\mu\varepsilon$. This study reflects a critical contribution that direct strain gauge measurements will make; while it made a great deal of sense to anticipate very high strain readings at this specific site on the tibia, as this was the site of stress fracture pathology, the strain gauge readings suggest that something other than high strains are contributing to this devastating lesion.

Strains measured in the human femur of two patients undergoing surgery for "snapping hip syndrome" showed principal tensile strains of 1200 $\mu\varepsilon$ and compressive strains of -390 $\mu\varepsilon$ during walking, with the principal direction at 12° to the long axis of the femur[16] (see Table 8.1). This study demonstrates a tensile axial strain acting at the proximal lateral aspect of the femur during different activities.

8.3.1.3 Sheep Measurements

Rosette gauges attached to the cranial and caudal surfaces of sheep radii showed that during walking the cranial surface experienced tensile strain along the long axis of the bone and the caudal surface experienced a compressive strain along the same direction, with the overall loading being compression with superimposed craniocaudal bending[40–43] (see Table 8.1). Increasing the walking speed generally caused larger strain magnitudes and rates.[40,43] The principal compressive strain on the caudal surface was found to be 1.8 to 1.9 times as great as the principal tensile strain on the cranial surface.[40,41]

Strains measured on the cranial and caudal surfaces of the sheep tibia indicated that the tibia was loaded via craniocaudal bending and torque.[44] Similar to the sheep radius, the principal tensile strain (710 $\mu\varepsilon$) was larger than the principal compressive strain (-450 $\mu\varepsilon$) on the cranial cortex, while on the caudal cortex, the principal compressive strain (-670 $\mu\varepsilon$) was greater than the principal tensile strain (380 $\mu\varepsilon$)[44] (see Table 8.1). The maximum strain rates averaged 17,800 $\mu\varepsilon$/s on the cranial surface and $-16{,}200$ $\mu\varepsilon$/s on the caudal surface, with 50,000 $\mu\varepsilon$/s the highest strain rate recorded. When the slow walk was increased to a fast trot, the maximum strain values doubled and the maximum strain rates increased fivefold.[44] However, the investigators found that there was little variation in the principal strain directions during locomotion at different speeds. They also found that the secondary osteons in the tibial shaft were aligned along a direction between the long axis of the bone and the direction of the larger principal strain at peak loading of the bone (which was cranial 29°, caudal 22° to long axis), and suggested that a link between the structure and principal strain direction might exist.

8.3.1.4 Horse Measurements

Turner et al.[45] measured strains in the radius, tibia, metacarpus, and metatarsus in the horse and found strains at much higher magnitudes than those previously reported for other animals (1500 to -2600 $\mu\varepsilon$; see Table 8.1). By placing four single-element gauges around the mid-diaphysis of each bone, the authors were able to estimate the strain range across the bone cross section. Their results showed that during different activities, the strains across a long bone ranged from compressive to tensile. They also compared the strain pattern from the medial side of the sheep tibia measured by Lanyon and Smith[9] to the pattern from the medial side of the horse tibia and found that the patterns were similar, although the strain magnitudes were higher in the horse. Barnes and Pinder[13] correlated tendon tension with strains measured in the horse metacarpal during walking and showed that tendon pull makes a significant contribution to bone strain.

Other strain measurements of the horse limb during walking indicate that the proximal and mid-diaphyseal cranial cortex of the tibia is loaded in tension, while the caudal cortex is loaded in compression, with a significant amount of torsion present throughout the bone[46,47] (see Table 8.1). Again, the contribution of strain gauges is clear; while many investigators had presumed that bone would be loaded axially, and in such a manner to minimize strain due to bending, strain gauge measurements have provided key insights into the way the bone is actually challenged by physiological loading conditions. Strain distributions similar to those found in the horse femur were found in the horse radius during walking[46]

(see Table 8.1). As demonstrated in other animals, at walking speed strain measurements from the horse tibia have been found to be biphasic, consisting of an initial peak, an inflection that is approximately 55% of the peak, and then a second peak.[47]

The strains measured on the third metacarpal (cannon bone) of four 2-year-old thoroughbred racehorses at maximum effort (16 to 17 m/s) are among the highest measured in any animal: an average of $-4840\ \mu\varepsilon$ peak was found as the animals ran on a dirt racetrack[48] (see Table 8.1). A change in principal direction when the animals changed their gait from a trot to a gallop indicated a decrease in torsional loading during the gallop. Interestingly, similar measurements taken from a 12-year-old horse had an average peak principal strain of $-3320\ \mu\varepsilon$, about two thirds of the peak strains for the younger animals[48] (see Table 8.1). It must be emphasized that this work demonstrates that strains can reach very high levels under extreme conditions such as thoroughbred racing, but that other conditions, such as the age of the bone, may contribute to the ultimate strain milieu.

Gross et al.[34] measured bone strains in the third metacarpal of a 5-year-old thoroughbred running on a treadmill. The maximum strains measured when the animal was trotting at a medium speed were $1900\ \mu\varepsilon$ in compression (medial gauge) and $1400\ \mu\varepsilon$ in shear (anterior gauge). The maximum strains calculated using a combined beam theory and finite-element model analysis to define the strain distribution across the bone section were normal strains of $2400\ \mu\varepsilon$ in compression and $810\ \mu\varepsilon$ in tension, and a shear strain of $1500\ \mu\varepsilon$[34] (see Table 8.1). The analysis indicated that the third metacarpal is subjected to a complex loading consisting of bending, axial compression, end shear, and torsion during locomotion. The results from this study illustrate the widely differing strain magnitudes repeatedly experienced by different portions of a bone cross section during the stance phase of locomotion, with some portions of the bone experiencing high-magnitude normal and shear strains and some portions experiencing relatively low strains. The study also illustrates the important point that strain gauges only measure the strain of the area to which they are attached, but that, with a set of gauges, the strain state across a section of bone can be estimated.

8.3.1.5 Pig Measurements

Goodship et al.[49] measured strains on the craniomedial aspect of the radius of young pigs as part of an ulnar osteotomy-radial overload experiment and found strain values of similar magnitude to those found in other species during walking ($\sim -800\ \mu\varepsilon$; see Table 8.1).

8.3.1.6 Dog Measurements

Carter et al.[22] measured strains in mongrel dogs at five different sites along the radius and ulna and found the highest longitudinal tensile stresses were probably near the cranial or cranial-lateral aspect of the radius, caused by bending in the cranial/caudal plane. High shear strains ($\sim -600\ \mu\varepsilon$) were found in the transverse direction due to external rotation of the radius. Positive shear strains were found at the caudal-medial aspect of the mid-ulna, indicating internal rotation of the proximal ulna during stance; and large tensile longitudinal strains ($\sim 800\ \mu\varepsilon$) were found at the cranial-lateral surface of the mid-ulna, a portion of the bone that is convex[22] (see Table 8.1).

Principal strains measured on the medial surface of the dog tibia during a fast walk/slow run were found to be $650\ \mu\varepsilon$ and $-700\ \mu\varepsilon$ (see Table 8.1).[50] Burr et al.[51] measured strains on the caudal and cranial surfaces of the beagle radius and found both cortices to be in compression (see Table 8.1).

Strains measured on the dog femur during walking were found to be of similar magnitude as those in other animals, with the medial surface of the midshaft in compression ($-460\ \mu\varepsilon$) and the lateral surface in tension ($240\ \mu\varepsilon$)[19] (see Table 8.1), with higher values found toward the proximal end ($-700\ \mu\varepsilon$ on the medial surface and $-300\ \mu\varepsilon$ on the tensile surface[52]). Another study of the dog femur during walking found similar values for the medial and lateral surfaces of the proximal, midshaft, and distal aspects (-310 to $-500\ \mu\varepsilon$ on the medial surface and 250 to $450\ \mu\varepsilon$ on the lateral surface;[53] see Table 8.1). Principal strains measured from the greyhound femur medial midshaft surface were $-310\ \mu\varepsilon$ and $150\ \mu\varepsilon$ at an angle less than 30° from the long axis of the bone[54] (see Table 8.1).

8.3.1.7 Measurements in the Dog, Horse, and Goat as a Function of Speed and Gait

To observe bone strains as a function of running speed and gait, Rubin and Lanyon[55] attached rosette strain gauges to the radius and tibia of dogs and horses. They found that the peak strain magnitudes were dependent on the type of gait used, while the maximum strain rate increased linearly as the locomotory speed increased[55] (see Table 8.1). In all bones instrumented, the caudal midshaft showed a large principal compressive strain aligned with the long axis of the bone. On the cranial surface, the tensile principal strain was large in magnitude. The compressive strain on the caudal surface was larger than the tensile strain on the cranial surface, indicating axial compression with superimposed craniocaudal bending. The peak strains measured during the fastest running were approximately $-2000\ \mu\varepsilon$ in the dog tibia, $-2400\ \mu\varepsilon$ in the dog radius, $-3200\ \mu\varepsilon$ in the horse tibia, and $-2900\ \mu\varepsilon$ in the horse radius.[55] The relative magnitudes of the principal strains remained constant during the stance phase of the gait cycle, and the principal orientation did not vary much for the different gaits observed. Interestingly, while there was a large increase in strain magnitude in the transition from walk to trot, there was a large decrease in strain in the tibia and radius in the transition from trot to gallop. Presumably, this reflects a change in the manner in which the animal propels itself forward.

To compare tibial loading in different animals further, Rubin[56] calculated the relative contribution of axial to bending strain and found that the percentage of total normal strain due to bending is ~85% for the tibia of animals of widely varying sizes. In essence, rather than minimizing strains, it appears that many architectural (e.g., second moments of area) and physiological features (e.g., synergistic and antagonistic muscle activity) of the musculoskeletal system conspire to augment the strain environment of the bone, perhaps in an attempt to regulate the peak strains to which the bone is subject.

In a similar set of experiments, examining the challenge of the skeleton as a function of speed and gait, it was demonstrated that in both the goat radius and tibia, the caudal cortex was in compression and the cranial cortex was in tension.[57] Strain magnitudes increased as gait velocity increased, although again a reduction in strain at the transition from fast trot to gallop occurred due to the redistribution of forces with the change of gait.[57] Strain levels in the goat tibia at galloping speeds were similar to values reported for the dog tibia (~$2000\ \mu\varepsilon$), even though the maximum speeds were different (goat, 4.3 m/s;[57] dog, 6.9 m/s[55]).

Other measurements that investigated the variation in strain as a function of speed and gait were measurements from 4- to 8-year-old thoroughbreds running on a treadmill. These recordings showed a linear increase in strain magnitude and strain rate with an increase in locomotory velocity, with the principal directions remaining within 5° to 10° of the long axis of the bone[58] (see Table 8.1).

8.3.1.8 Galago, Macaque, Gibbon, and Owl Monkey Measurements

Hylander[59] measured mandible strains in the primate galago and found that the maximum strain while biting on a bite force transducer made from a plastic block was $435\ \mu\varepsilon$ in compression. The largest strain magnitude during biting food (a carrot) occurred when the galago initially "attacked" the carrot[59] (see Table 8.1). During chewing, strains ranged from a maximum of $70\ \mu\varepsilon$ in compression and $25\ \mu\varepsilon$ in tension. In the macaque, mandibular principal bone strains during ingestion and mastication of apples ranged from 10 to $360\ \mu\varepsilon$ for the maximum principal strain and from -20 to $-450\ \mu\varepsilon$ for the minimum principal strain, with maximum shear strains ranging from 90 to $760\ \mu\varepsilon$[60] (see Table 8.1). Strain rates in the macaque mandible during mastication ranged from 1600 to $4300\ \mu\varepsilon$/s during loading to 2900 to $6700\ \mu\varepsilon$/s during unloading[61] (see Table 8.1). During mastication in the owl monkey, higher strain magnitudes were found in the postorbital bar than in the interorbital region[62] (see Table 8.1).

Strains measured in the macaque ulna during walking showed mediolateral bending with superimposed torsion. The maximum principal compressive strain was $-870\ \mu\varepsilon$ on the medial surface, while the maximum principal tensile strain was $750\ \mu\varepsilon$ on the lateral surface[25] (see Table 8.1).

In one animal, strains during galloping were recorded and showed similar strain magnitudes as walking.

Strains measured in brachiating gibbons using radiotelemetry showed a fairly large variability in strain pattern and peak magnitude among swings (an average standard deviation for the six gauge sites in the three bones studied was approximately 24%).[20] This variability during arm swings is much higher than studies of animal locomotion using treadmills, where the movement of the animal is much more controlled and regular. The ulna was found to be loaded primarily in tension during brachiation, while the radius underwent bending and the humerus experienced a combination of tension, torsion, and bending[20] (see Table 8.1).

8.3.1.9 Rabbit Measurements

Strains measured on the lateral surface of the rabbit mandible demonstrated maximum principal strains of –320 and 280 $\mu\varepsilon$ while chewing hay or pellets[63] (see Table 8.1). Strains of lower magnitude (-150 and 150 $\mu\varepsilon$) occurred when the animals chewed a carrot. On the contralateral chewing side, strains on the order of -80 to 100 $\mu\varepsilon$ were found. Biting a carrot caused principal strains of -60 and 90 $\mu\varepsilon$.[63]

8.3.1.10 Fish Measurements

A peak principal strain of -1800 $\mu\varepsilon$ was found on the operculum (gill cover) of the sunfish during the most vigorous strikes on prey[64] (see Table 8.1). The peak strain rates measured during a very vigorous strike on an elusive prey were 615,000 $\mu\varepsilon$/s, with strain rates during less vigorous activities in the range 15,000 to 110,000 $\mu\varepsilon$/s. It is interesting to note that this is the highest strain rate that has been measured in bone, yet bone such as that in the sunfish has been reported to be acellular with limited repair or adaptive capabilities.[64]

8.3.1.11 Rat Measurements

Strains measured on the rat femur while the animal used an exercising wheel showed values similar to those found in other animals (-260 $\mu\varepsilon$ in the axial direction, 120 $\mu\varepsilon$ in the transverse direction, 420 $\mu\varepsilon$ shear;[65] see Table 8.1). Strains measured in the rat ulna using single element gauges aligned along the long axis of the bone showed medial longitudinal strains of 700 to 1200 $\mu\varepsilon$ in compression during unrestricted running on a solid level surface, with strain rates from 23,000 to $-38{,}000$ $\mu\varepsilon$/s[66] (see Table 8.1). To estimate the peak strain magnitudes during extreme activities, the rats were allowed to fall from a height of approximately 30 cm, which produced strains on the order of 2500 $\mu\varepsilon$ in compression, with a strain rate of $-100{,}000$ $\mu\varepsilon$/s.[66]

8.3.1.12 Turkey Measurements

Strains measured on the surface of the midshaft of the turkey ulna during vigorous wing flap showed peak longitudinal strains of 3300 $\mu\varepsilon$ in compression, with a maximum strain rate of 56,000 $\mu\varepsilon$/s[67] (see Table 8.1). The complex loading during wing flap consisted of bending, compression, and torsion that varied throughout the wing cycle.[68] The highest shear strains in the turkey ulna have been found to occur during large wing flaps.[36]

8.3.1.13 Growing Chicken and Rat Measurements

Bone strains measured in growing chicks indicated that the pattern of strain within the tibiotarsus did not change during the growth period from 4 to 17 weeks of age, and the magnitude and orientation of strain at four gauge sites along the bone were also very similar[69] (see Table 8.1). During this growth period, the tibiotarsus increased in mass nearly tenfold, and in length nearly threefold. Similar results were found on the anterior-lateral surface of the rat femur during a 12-week period when the rat's body weight increased over threefold and the midshaft femoral geometry increased over sixfold[70] (see Table 8.1). Strain magnitudes and orientations were not significantly different in skeletally immature (6 to 18 weeks old) as compared to skeletally mature rats ($>$18 weeks old). Another study with single-element gauges found strains on the anterior surface of the Wistar rat femur to be slightly reduced in older animals, possibly due to a lower stride frequency of the older, larger animals[71] (see Table 8.1).

8.3.1.14 Rooster Measurements

Normal longitudinal strains and shear strains in the tarsometatarsal of roosters were found to be similar to values in other animals during walking[72] (see Table 8.1). By calculating normal longitudinal strains and shear strains across the midshaft of the tarsometatarsal of the rooster while the animal was running, peak longitudinal strains in the adult rooster were 1850 $\mu\varepsilon$ in compression in the anterior cortex at the midshaft and 1220 $\mu\varepsilon$ in tension in the posterior cortex, with a maximum of 1580 in shear[73,74] (see Table 8.1). The neutral axis did not change much during the stance phase. In younger animals the peak longitudinal strains during running were 1870 $\mu\varepsilon$ in compression and 960 $\mu\varepsilon$ in tension, with lower values reported for walking[74] (see Table 8.1). Peak strain rates were 38,000 $\mu\varepsilon$/s for walking and 89,000 $\mu\varepsilon$/s for running.[74]

8.3.1.15 Bat and Pigeon Measurements

Strains measured during bat flight indicate the presence of torsion and shear.[75] Maximum principal strains were found to be 2000 $\mu\varepsilon$ in tension on the medial surface of the humerus and 2180 $\mu\varepsilon$ in compression on the dorsolateral surface of the radius during the wing downstroke[75] (see Table 8.1). Strains measured in flying pigeons also showed large torsional strains (maximum: 2700 to 4150 $\mu\varepsilon$), which were 1.5 times greater than longitudinal strains[76] (see Table 8.1). Peak longitudinal and principal strains increased approximately 50% from landing to takeoff and ascending flight. Maximum strains measured with a pigeon carrying a load equal to its body weight were only 20% greater than the maximum strains carrying no load.[76]

8.3.1.16 Immature Alligator and Iguana Measurements

Strains measured in the alligator and iguana show a large amount of torsion during locomotion.[77] The alligator femur is subjected to a combination of axial compression, bending, and torsion with principal strains of 710 $\mu\varepsilon$ (ventral) and -470 $\mu\varepsilon$ (dorsal), with shear strains more than 1000 $\mu\varepsilon$ during fast locomotion[77] (see Table 8.1). The iguana femur is loaded similarly, with the anterior cortex in tension and the dorsal cortex in compression (see Table 8.1). Like the alligator femur, the alligator tibia undergoes a combination of axial compression, bending, and torsion[77] (see Table 8.1). For both the alligator and iguana, slower locomotion yielded lower strains compared with faster locomotion[77] (see Table 8.1).

8.3.2 Quantifying the Daily Strain History of Bone

Many of the above studies focused on quantifying peak bone strains during locomotory activities, usually based on the assumption that the predominant functional stimulus is provided by locomotion and thus the structural objective of limb bones will be related to the mechanical demands that locomotion imposes.[78] While it is reasonable to assume that locomotion is the most important mechanical stimulus a bone experiences, the difficulty in isolating the mechanical parameter(s) responsible for bone adaptation by focusing on peak magnitude strains has led investigators to study the bone strains during a wider variety of functional activities and to quantify the frequency content of the strain signals.[24,36,37,79,80] It becomes a great challenge to look beyond peak strain events and investigate the overall strain environment of the bone in an attempt to determine which of the multitude of factors (e.g., amplitude, duration, frequency, number of cycles, strain rate, strain rate over time, etc.) are the critical components in defining the mass and morphology of a bone.

Two recent strain gauge investigations have quantified the loading history of bone by cataloging activities.[36,37] Adams et al.[36] observed turkeys for 24 h and cataloged several different typical activities. They found that in reality, and perhaps not overly surprising, the animals were fairly inactive and performed relatively few large-magnitude strain events. The number of relatively high magnitude strain events (greater than ~300 $\mu\varepsilon$) was found to be approximately one large wing flap, six small wing flaps, and 30 whole body shakes or wing extensions per day.[36] In this study activities with strain magnitudes

less than 50 $\mu\varepsilon$ were not considered important to the strain history of bone, so the smaller magnitude strains were not included.

Konieczynski et al.[37] quantified the daily loading history of the tibiotarsus of chickens by measuring peak strains for less than 1-h intervals of treadmill exercise, cage activity, and handling activity and then scaling these measurements to 24 h. At each gauge site, data were put into 100-$\mu\varepsilon$ bin histograms to describe a combined daily loading history, which included a 2500 cycle/day exercise program. The background loading activities (cage activity and handling activity) were found to occur 775 cycles/day at magnitudes generally less than 500 $\mu\varepsilon$. However, the magnitudes of the cyclic strains were calculated as the maximum strain after a 50% or greater strain reduction from the previous peak, which diminishes the detection of lower-magnitude strain events.

To quantify the daily strain history of bone to include the smallest- to largest-magnitude strains, Fritton et al.[24] used a data collection protocol with very fine resolution ($<$0.08 $\mu\varepsilon$, 30 times finer than the resolution of 2.44 $\mu\varepsilon$ used in the above experiments by Konieczynski et al.[37]). Strains were collected at frequencies from 102.4 to 409.6 Hz and filtered at 50 or 200 Hz to allow the analysis of the frequency content of the strain signals. Strains were measured *in vivo* for both weight-bearing and non-weight-bearing bones in the dog, sheep, and turkey and collected continuously while the animals performed their natural daily activities. The daily strain history was quantified by both counting cyclic strain events (to quantify the distribution of strain magnitudes) and by estimating the average spectral characteristics of the strain (to quantify the frequency content of the strain signals).

Strain recordings from the sheep tibia illustrate the scaling properties observed in recordings from all the animals (Fig. 8.5). The data also showed that large strains ($>$1000 $\mu\varepsilon$) occurred relatively few times a day, while very small strains ($<$10 $\mu\varepsilon$) occurred thousands of times a day (Fig. 8.6). Strain dynamics were found to be well described by a power law relationship (Fig. 8.7) and exhibited self-similar characteristics. These data demonstrated that functional strains span a wide but consistent range of frequency and amplitude. While the lower physiological strain limit has been suggested to be around 200 $\mu\varepsilon$,[81] this study indicates that the lower limit is much lower, on the order of 2 $\mu\varepsilon$.[24]

For repetitive, peak strain activities such as walking, a mid-diaphyseal bone cross section experiences a very nonuniform strain distribution with each gait cycle, ranging from high tensile strains to zero strains at the neutral axis to high compressive strains.[34] The measurements made through the daily strain history of bone demonstrate that different sites across a bone section experience a much more similar number of lower-magnitude (2 to 200 $\mu\varepsilon$) strain events compared with the higher-magnitude events.[24]

8.4 Alternative *in Vivo* Techniques to Measure Bone Strains

Because of possible problems with the long-term use of strain gauges *in vivo*, including deterioration of waterproofing and gauge attachment, some investigators have developed alternative methods to measure bone deformations. The focus of most of these studies is to establish a method for *in vivo* strain measurement for long-term applications such as a joint degeneration model[82] or space flight experiments.[83] One method uses an instrumented steel staple that is attached to bone by impacting it into predrilled holes in the bone cortex.[82] Small strain gauges are attached to the staple, which is calibrated so that staple strain is proportional to bone strain. These staples have been used *in vivo* to measure canine vertebral strains[82] and human tibial strains.[84] A second method uses calcium phosphate ceramic-coated strain gauges to avoid use of cyanoacrylate for long-term experiments.[85] These ceramic-coated gauges have been used *in vivo* to measure strains from the dog and rat femur, indicating similar results to gauges attached using cyanoacrylate after approximately 4 months of bonding time.[83,86,87] A third method has been used to measure human tibial strains using extensometers consisting of k-wires inserted into the bone cortex and joined by a custom displacement transducer.[88] While all these methods show promising results, the strain gauge is still the gold standard for measuring *in vivo* bone deformations.

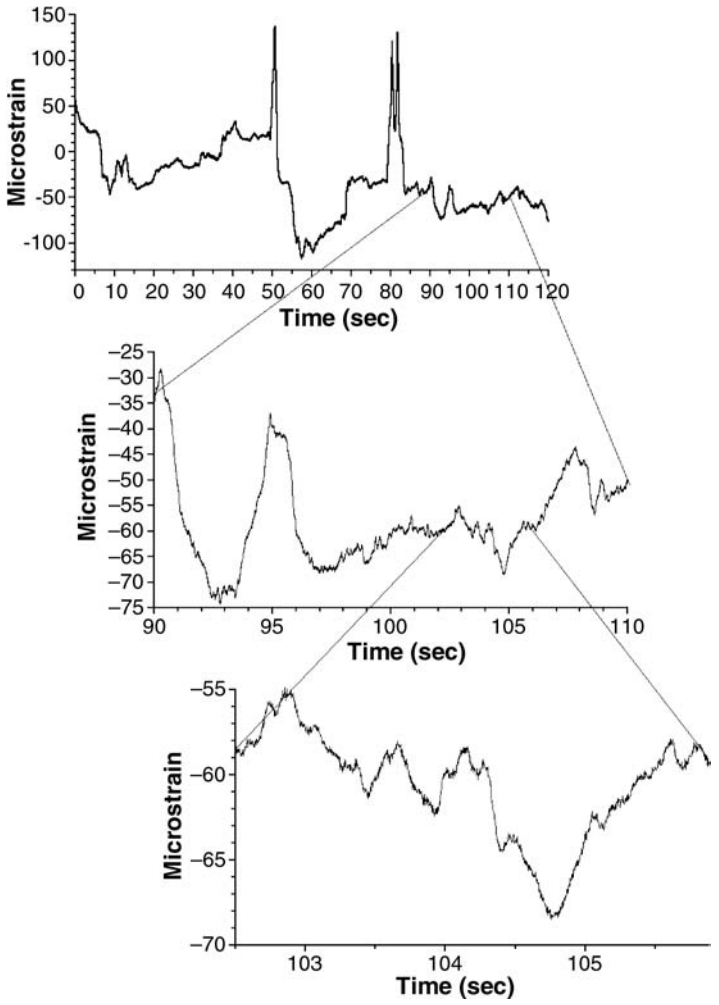

FIGURE 8.5 (Top) A 2-min strain recording from the caudal longitudinal gauge of the sheep tibia while the animal is standing and shifting its limb a few times, creating peak strains on the order of 200 $\mu\varepsilon$. (middle) A 20-s portion of that strain record shows peak strain events as large as 40 $\mu\varepsilon$. (Bottom) Further scaling down to a 3-s stretch of the strain recording illustrates events on the order of 5 $\mu\varepsilon$. (From Fritton, S. P. et al., *J. Biomech.*, 33, 317–325, 2000. With permission from Elsevier Science.)

8.5 Summary

From the 1970s to the present, strain gauges have been widely used to quantify bone strains produced by mechanical loading in many species. Bone strains and strain rates are fairly similar across species, despite variations in animal size and bone function. As previously observed by Rubin and Lanyon,[78] peak functional strains are similar for a range of animals, generally falling between -2000 and -3200 $\mu\varepsilon$ for the most vigorous activities. Strain rates generally fall under 100,000 $\mu\varepsilon$/s. At the extreme, the largest-magnitude strains were found in the horse, with a maximum of almost -5000 $\mu\varepsilon$ found in the galloping thoroughbred.[48] The increase in peak principal strains as gait speed is increased correlates with the increase in the magnitude of the ground reaction force exerted on the animal's limb.

Most animals, of course, cannot reach the speed of a galloping horse and for the most part their activities comprise far less strenuous activities. Walking produces peak strains in the leg bones or hind limbs usually less than 1000 $\mu\varepsilon$ in most animals, and considering the degree of bending in most bones,

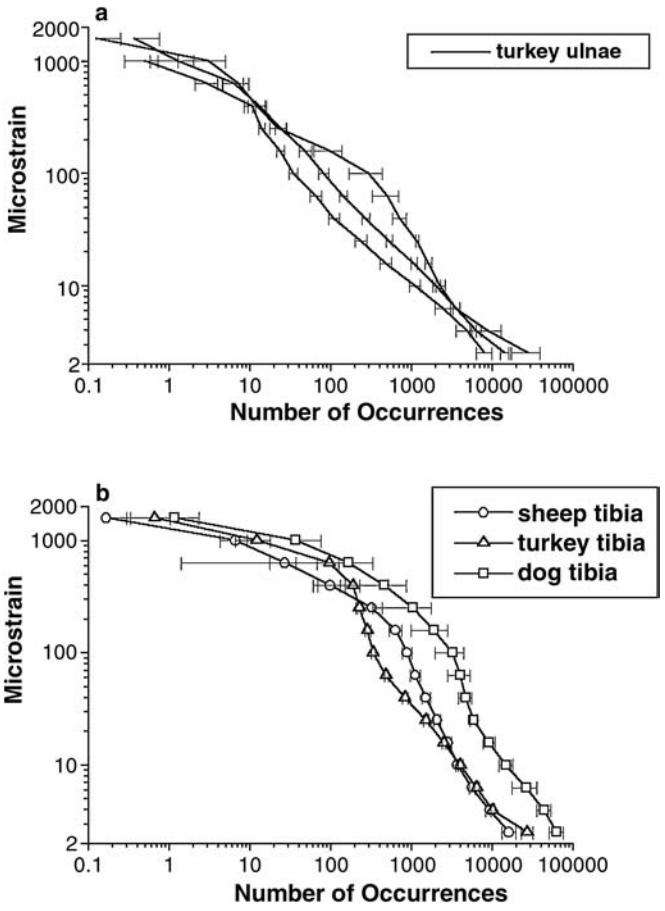

FIGURE 8.6 Log–log plots of strain magnitude (mean ± s.e. for all functional channels of strain data) vs. the number of occurrences over 12 to 24 h. (a) 24-h summation of cyclic strain events for the turkey ulnae; (b) 12-h summations for the sheep, turkey, and dog tibiae. (From Fritton, S. P., et al., *J. Biomech.*, 33, 317–325, 2000. With permission from Elsevier Science.)

much of the cortex is subjected to strains far below 1000 $\mu\varepsilon$. In humans, who arguably can be very inactive while maintaining normal bone, even the most vigorous exercises produced strains less than 2000 $\mu\varepsilon$.[14,16,39] With these data in mind, all provided by strain gauges, it seems possible that strains key to determining bone mass and morphology may not be the peak—and relatively rare—strains generated during vigorous activity, but instead that the persistent barrage of low-magnitude, higher-frequency strains may play a role in determining bone architecture.

The spectrum of strain gauge work, accumulated over several decades and by a range of investigators, has provided a rigorous indication of the mechanical demands made on the skeleton. This is work which extends beyond that which can be extrapolated through ground reaction forces or from projections made from theoretical models. In essence, the strain gauge provides a direct measure of the deformations caused by the product of all the elements of the musculoskeletal system working together. But rather than producing a simplified, uniform answer to the strains that drive bone mass and morphology, strain recordings illustrate the complexity of the *in vivo* mechanical loading of bone, complexity similar to that found in many other physiological systems.[24] Considering the full range of strain magnitudes and frequencies that a bone experiences, strain gauges will ultimately provide key insights into the organ-level, tissue-level, cellular-level, and even molecular-level signals that regulate bone architecture, and perhaps lend a unique perspective in elucidating the etiologies of metabolic bone diseases such as osteoporosis.

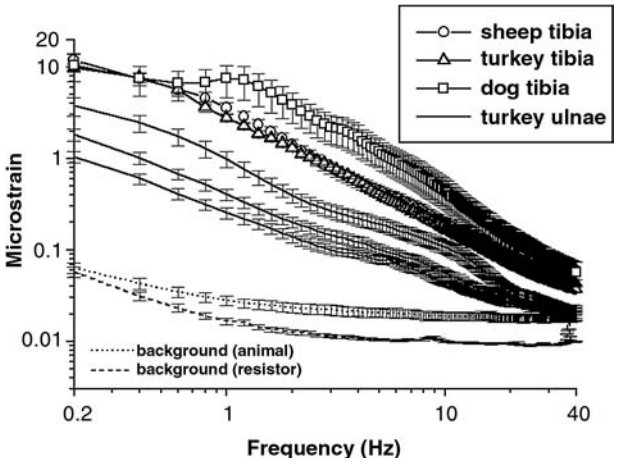

FIGURE 8.7 The 5-s spectra averaged over 12 h (mean ± s.e. for all functional channels of strain data) for each bone illustrate the power law relationship of the data. Background recordings were taken after sacrifice of the animals as well as with precision resistors replacing the strain gauges. The slopes of the curves drop off as a function of the inverse of the frequency, $1/f^{\alpha}$. (From Fritton, S. P., et al., *J. Biomech,* 33, 317–325, 2000. With permission from Elsevier Science.)

References

1. Perry, C. C. and Lissner, H. R., *The Strain Gauge Primer,* McGraw-Hill, New York, 1962.
2. Evans, F. G., *Stress and Strain in Bones: Their Relation to Fractures and Osteogenesis,* Charles C Thomas, Springfield, IL, 1957.
3. Roberts, V. L., Strain-gauge techniques in biomechanics, *Exp. Mech.,* 6, 19A, 1966.
4. Gurdjian, E. S. and Lissner, H. R., Mechanism of head injury as studied by the cathode ray oscilloscope: preliminary report, *J. Neurosurg.,* 1, 393, 1944.
5. Evans, F. G., Methods of studying the biomechanical significance of bone form, *Am. J. Phys. Anthropol.,* 11, 413, 1953.
6. Lanyon, L. E., The measurement of bone strain *in vivo, Acta Orthop. Belg.,* 42, 98, 1976.
7. Biewener, A. A., *In vivo* measurement of bone strain and tendon force, in *Biomechanics—Structures and Systems: A Practical Approach,* Biewener, A. A., Ed., Oxford University Press, New York, 1992, chap. 6.
8. Lanyon, L. E. and Smith, R. N., Measurements of bone strain in the walking animal, *Res. Vet. Sci.,* 10, 93, 1969.
9. Lanyon, L. E. and Smith, R. N., Bone strain in the tibia during normal quadrupedal locomotion, *Acta Orthop. Scand.,* 41, 238, 1970.
10. Lanyon, L. E., Strain in sheep lumbar vertebrae recorded during life, *Acta Orthop. Scand.,* 42, 102, 1971.
11. Lanyon, L. E., *In vivo* bone strain recorded from thoracic vertebrae of sheep, *J. Biomech.,* 5, 277, 1972.
12. Cochran, G. V. B., Implantation of strain gauges on bone *in vivo*, *J. Biomech.,* 5, 119–123, 1972.
13. Barnes, G. R. G. and Pinder, D. N., *In vivo* tension and bone strain measurement and correlation, *J. Biomech.,* 7, 35, 1974.
14. Burr, D. B., Milgrom, C., Fyhrie, D., Forwood, M., Nyska, M., Finestone, A., Hoshaw, S., Saiag, E., and Simkin, A., *In vivo* measurement of human tibial strains during vigorous activity, *Bone,* 18, 405, 1996.
15. Hoshaw, S. J., Fyhrie, D. P., Takano, Y., Burr, D. B., and Milgrom, C., A method suitable for *in vivo* measurement of bone strain in humans, *J. Biomech.,* 30, 521, 1997.

16. Aamodt, A., Lund-Larsen, J., Eine, J., Andersen, E., Benum, P., and Schnell Husby, O., *In vivo* measurements show tensile axial strain in the proximal lateral aspect of the human femur, *J. Orthop. Res.,* 15, 927, 1997.
17. Sumner-Smith, B., Bell, M., Manley, P., Caddell, E., and Hoare, J., Telemetric measurements of strain in the metacarpus of the horse: a pilot study, *Am. J. Vet. Res.,* 38, 1675, 1977.
18. Schatzker, J., Sumner-Smith, G., Hoare, J., and McBroom, R., A telemetric system for the strain gauge determination of strain in bone *in vivo, Arch. Orthop. Traumat. Surg.,* 96, 309, 1980.
19. Manley, P. A., Schatzker, J., and Sumner-Smith, G., Evaluation of tension and compression forces in the canine femur *in vivo*, *Arch. Orthop. Traumat. Surg.,* 99, 213, 1982.
20. Swartz, S. M., Bertram, J. E. A., and Biewener, A. A., Telemetered *in vivo* strain analysis of locomotor mechanics of brachiating gibbons, *Nature,* 342, 270, 1989.
21. Baggott, D. G. and Lanyon, L. E., An independent "post-mortem" calibration of electrical resistance strain gauges bonded to bone surfaces "*in vivo*," *J. Biomech.,* 10, 615, 1977.
22. Carter, D. R., Smith, D. J., Spengler, D. M., Daly, C. H., and Frankel, V. H., Measurement and analysis of *in vivo* bone strains on the canine radius and ulna, *J. Biomech.,* 13, 27, 1980.
23. Wright, T. M. and Hayes, W. C., Strain gauge application on compact bone, *J. Biomech.,* 12, 471, 1979.
24. Fritton, S. P., McLeod, K. J., and Rubin, C. T., Quantifying the strain history of bone: spatial uniformity and self-similarity of low magnitude strains, *J. Biomech.,* 33, 317, 2000.
25. Demes, B., Stern, J. T., Hausman, M. R., Larson, S. G., McLeod, K. J., and Rubin, C. T., Patterns of strain in the macaque ulna during functional activity, *Am. J. Phys. Anthropol.,* 106, 87, 1998.
26. Dally, J. W. and Riley, W. F., *Experimental Stress Analysis,* McGraw-Hill, New York, 1991, chap. 5.
27. Lanyon, L. E., Analysis of surface bone strain in the calcaneus of sheep during normal locomotion, *J. Biomech.,* 6, 41, 1973.
28. Caler, W. E., Carter, D. R., and Harris, W. H., Techniques for implementing an *in vivo* bone strain gauge system, *J. Biomech.,* 14, 503, 1981.
29. Schamhardt, H. C. and Hartman, W., Automatic zero strain compensation of *in vivo* bone strain recordings, *J. Biomech.,* 15, 621, 1982.
30. Bessman, E. S., Carter, D. R., McCarthy, J. C., and Harris, W. H., Accuracy enhancement of *in vivo* bone strain measurements and analysis, *J. Biomech. Eng.,* 104, 226, 1982.
31. Carter, D. R., Anisotropic analysis of strain rosette information from cortical bone, *J. Biomech.,* 11, 199, 1978.
32. Rybicki, E. F., Mills, E. J., Turner, A. S., and Simonen, F. A., *In vivo* analytical studies of forces and moments in equine long bones, *J. Biomech.,* 10, 701, 1977.
33. Carter, D. R., Harris, W. H., Vasu, R., and Caler, W. E., The mechanical and biological response of cortical bone to *in vivo* strain histories, in *Mechanical Properties of Bone,* Vol. 45, Cowin, S. C., Ed., ASME AMD, New York, 1981.
34. Gross, T. S., McLeod, K. J., and Rubin, C. T., Characterizing bone strain distributions *in vivo* using three triple rosette strain gauges, *J. Biomech.,* 25, 1081, 1992.
35. Roszek, B., Weinans, H., van Loon, P., and Huiskes, R., *In vivo* measurements of the loading conditions on the tibia of the goat, *Acta Anat.,* 146, 188, 1993.
36. Adams, D. J., Spirt, A. A., Brown, T. D., Fritton, S. P., Rubin, C. T., and Brand, R. A., Testing the daily stress stimulus theory of bone adaptation with natural and experimentally controlled strain histories, *J. Biomech.,* 30, 671, 1997.
37. Konieczynski, D. D., Truty, M. J., and Biewener, A. A., Evaluation of a bone's *in vivo* 24-hour loading history for physical exercise compared with background loading, *J. Orthop. Res.,* 16, 29, 1998.
38. Lanyon, L. E., Experimental support for the trajectorial theory of bone structure, *J. Bone Joint Surg.,* 56-B, 160, 1974.
39. Lanyon, L. E., Hampson, W. G. J., Goodship, A. E., and Shah, J. S., Bone deformation recorded *in vivo* from strain gauges attached to the human tibial shaft, *Acta Orthop. Scand.,* 46, 256, 1975.

40. Lanyon, L. E. and Baggott, D. G., Mechanical function as an influence on the structure and form of bone, *J. Bone Joint Surg.,* 58-B, 436, 1976.
41. Lanyon, L. E., Magee, P. T., and Baggott, D. G., The relationship of functional stress and strain to the processes of bone remodelling: an experimental study on the sheep radius, *J. Biomech.,* 12, 593, 1979.
42. Lanyon, L. E., Goodship, A. E., Pye, C. J., and MacFie, J. H., Mechanically adaptive bone remodelling, *J. Biomech.,* 15, 141, 1982.
43. O'Connor, J. A., Lanyon, L. E., and MacFie, H., The influence of strain rate on adaptive bone remodelling, *J. Biomech.,* 15, 767, 1982.
44. Lanyon, L. E. and Bourn, S., The influence of mechanical function on the development and remodeling of the tibia, *J. Bone Joint. Surg.,* 61-A, 263, 1979.
45. Turner, A. S., Mills, E. J., and Gabel, A. A., *In vivo* measurement of bone strain in the horse, *Am. J. Vet. Res.,* 36, 1573, 1975.
46. Schneider, R. K., Milne, D. W., Gabel, A. A., Groom, J. J., and Bramlage, L. R., Multidirectional *in vivo* strain analysis of the equine radius and tibia during dynamic loading with and without a cast, *Am. J. Vet. Res.,* 43, 1541, 1982.
47. Hartman, W., Schamhardt, H. C., Lammertink, J. L., Badoux, D. M., Bone strain in the equine tibia: an *in vivo* strain gauge analysis, *Am. J. Vet. Res.,* 45, 880, 1984.
48. Nunamaker, D. M., Butterweck, D. M., and Provost, M. T., Fatigue fractures in thoroughbred racehorses: relationships with age, peak bone strain, and training, *J. Orthop. Res.,* 8, 604, 1990.
49. Goodship, A. E., Lanyon, L. E., and McFie, H., Functional adaptation of bone to increased stress, *J. Bone Joint Surg.,* 61-A, 539, 1979.
50. Bouvier, M. and Hylander, W. L., *In vivo* bone strain on the dog tibia during locomotion, *Acta Anat.,* 118, 187, 1984.
51. Burr, D. B., Schaffler, M. B., Yang, K. H., Lukoschek, M., Sivaneri, N., Blaha, J. D., and Radin, E. L., Skeletal change in response to altered strain environments: is woven bone a response to elevated strain? *Bone*, 10, 223, 1989.
52. Lanyon, L. E., Paul, I. L., Rubin, C. T., Thrasher, E. L., DeLaura, R., Rose, R. M., and Radin, E. L., *In vivo* strain measurements from bone and prosthesis following total hip replacement, *J. Bone Joint Surg.,* 63-A. 989, 1981.
53. Page, A. E., Allan, C., Jasty, M., Harrigan, T. P., Bragdon, C. R., and Harris, W. H., Determination of loading parameters in the canine hip *in vivo, J. Biomech.,* 26, 571, 1993.
54. Szivek, J. A., Johnson, E. M., and Magee, F. P., *In vivo* strain analysis of the greyhound femoral diaphysis, *J. Invest. Surg.,* 5, 91, 1992.
55. Rubin, C. T. and Lanyon, L. E., Limb mechanics as a function of speed and gait: a study of functional strains in the radius and tibia of horse and dog, *J. Exp. Biol.,* 101, 187, 1982.
56. Rubin, C. T., Skeletal strain and the functional significance of bone architecture, *Calcif. Tissue Int.,* 36, S11, 1984.
57. Biewener, A. A. and Taylor, C. R., Bone strain: a determinant of gait and speed? *J. Exp. Biol.,* 123, 383, 1986.
58. Davies, H. M. S., McCarthy, R. N., and Jeffcott, L. B., Surface strain on the dorsal metacarpus of thoroughbreds at different speeds and gaits, *Acta Anat.,* 146, 148–153, 1993.
59. Hylander, W. L., *In vivo* bone strain in the mandible of *Galago crassicaudatus, Am. J. Phys. Anthropol.,* 46, 309, 1977.
60. Hylander, W. L., Mandibular function in *Galago crassicaudatus* and *Macaca fascicularis*: an *in vivo* approach to stress analysis of the mandible, *J. Morphol.,* 159, 253, 1979.
61. Hylander, W. L., Johnson, K. R., and Crompton, A. W., Loading patterns and jaw movements during mastication in *Macaca fascicularis:* a bone-strain, electromyographic, and cineradiographic analysis, *Am. J. Phys. Anthropol.,* 72, 287, 1987.
62. Ross, C. F. and Hylander, W. L., *In vivo* and *in vitro* bone strain in the owl monkey circumorbital region and the function of the postorbital septum, *Am. J. Phys. Anthropol.,* 101, 183, 1996.

63. Weijs, W. A. and de Jongh, H. J., Strain in the mandibular alveolar bone during mastication in the rabbit, *Arch. Oral Biol.,* 22, 667, 1977.
64. Lauder, G. V. and Lanyon, L. E., Functional anatomy of feeding in the bluegill sunfish, *Lepomis macrochirus*: *in vivo* measurement of bone strain, *J. Exp. Biol.,* 84, 33, 1980.
65. Keller, T. S. and Spengler, D. M., *In vivo* strain gauge implantation in rats, *J. Biomech.,* 15, 911, 1982.
66. Mosley, J. R., March, B. M., Lynch, J., and Lanyon, L. E., Strain magnitude related changes in whole bone architecture in growing rats, *Bone,* 20, 191, 1997.
67. Lanyon, L. E. and Rubin, C. T., Static vs. dynamic loads as an influence on bone remodelling, *J. Biomech.,* 17, 897, 1984.
68. Rubin, C. T. and Lanyon, L. E., Regulation of bone mass by mechanical strain magnitude, *Calcif. Tissue Int.,* 37, 411, 1985.
69. Biewener, A. A., Swartz, S. M., and Bertram, J. E. A., Bone modeling during growth: dynamic strain equilibrium in the chick tibiotarsus, *Calcif. Tissue Int.,* 39, 390, 1986.
70. Keller, T. S. and Spengler, D. M., Regulation of bone stress and strain in the immature and mature rat femur, *J. Biomech.,* 22, 1115, 1989.
71. Indrekvam, K., Husby, O. S., Gjerdet, N. R., Engester, L. B., and Langeland, N., Age-dependent mechanical properties of rat femur measured *in vivo* and *in vitro*, *Acta Orthop. Scand.,* 62, 248, 1991.
72. Loitz, B. J. and Zernicke, R. F., Strenuous exercise-induced remodelling of mature bone: relationships between *in vivo* strains and bone mechanics, *J. Exp. Biol.,* 170, 1, 1992.
73. Judex, S., Gross, T. S., and Zernicke, R. F., Strain gradients correlate with sites of exercise-induced bone-forming surfaces in the adult skeleton, *J. Bone Miner. Res.,* 12, 1737, 1997.
74. Judex, S. and Zernicke, R. F., Does the mechanical milieu associated with high-speed running lead to adaptive changes in diaphyseal growing bone? *Bone,* 26, 153, 2000.
75. Swartz, S. M., Bennett, M. B., and Carrier, D. R., Wing bone stresses in free flying bats and the evolution of skeletal design for flight, *Nature,* 359, 726, 1992.
76. Biewener, A. A. and Dial, K. P., *In vivo* strain in the humerus of pigeons (*Columba livia*) during flight, *J. Morphol.,* 225, 61, 1995.
77. Blob, R. W. and Biewener, A. A., *In vivo* locomotor strain in the hindlimb bones of *Alligator mississippiensis* and *Iguana iguana*: implications for the evolution of limb bone safety factor and non-sprawling limb posture, *J. Exp. Biol.,* 202, 1023, 1999.
78. Rubin, C. T. and Lanyon, L. E., Dynamic strain similarity in vertebrates: an alternative to allometric limb bone scaling, *J. Theor. Biol.,* 107, 321, 1984.
79. Rubin, C. T., McLeod, K. J., and Bain, S. D., Functional strains and cortical bone adaptation: epigenetic assurance of skeletal integrity, *J. Biomech.,* 23(Suppl. 1), 43, 1990.
80. Turner, C. H., Yoshikawa, T., Forwood, M. R., Sun, T. C., and Burr, D. B., High frequency components of bone strain in dogs measured during various activities, *J. Biomech.,* 28, 39, 1995.
81. Martin, R. B. and Burr, D. B., *The Structure, Function and Adaptation of Compact Bone*, Raven Press, New York, 1989, chap. 6.
82. Buttermann, G. R., Janevic, J. T., Lewis, J. L., Lindquist, C. M., Wood, K. B., and Schendel, M. J., Description and application of instrumented staples for measuring *in vivo* bone strain, *J. Biomech.,* 27, 1087, 1994.
83. Szivek, J. A., Anderson, P. L., Wilson, D. L., and DeYoung, D. W., Technical note: development of a model for study of *in vivo* bone strains in normal and microgravity environments, *J. Appl. Biomater.,* 6, 203, 1995.
84. Ekenman, I., Halvorsen, K., Westblad, P., Fellander-Tsai, L., and Rolf, C., Local bone deformation at two predominant sites for stress fractures of the tibia: an *in vivo* study, *Foot Ankle Int.,* 19, 479, 1998.
85. Szivek, J. A., Gealer, R. G., Magee, F. P., and Emmanual, J., Preliminary development of a hydroxyapatite-backed strain gauge, *J. Appl. Biomater.,* 1, 241, 1990.
86. Maliniak, M. M., Szivek, J. A., DeYoung, D. W., and Emmanual, J., Hydroxyapatite-coated strain gauges for long-term *in vivo* bone strain measurements, *J. Appl. Biomater.,* 4, 143, 1993.

87. Szivek, J. A., Anderson, P. L., and DeYoung, D. W., *In vivo* strain measurements collected using calcium phosphate ceramic-bonded strain gauges, *J. Invest. Surg.,* 10, 263, 1997.
88. Fyhrie, D. P., Milgrom, C., Hoshaw, S. J., Simkin, A., Dar, S., Drumb, D., and Burr, D. B., Effect of fatiguing exercise on longitudinal bone strain as related to stress fracture in humans, *Ann. Biomed. Eng.,* 26, 660, 1998.
89. Fritton, S. P., McLeod, K. J., and Rubin, C. T., The wide range of strain magnitudes and strain rates in functionally loaded bone, *Trans. 45th Orthop. Res. Soc.,* 24, 332, 1999.
90. Biewener, A. A., Thomason, J., and Lanyon, L. E., Mechanics of locomotion and jumping in the forelimb of the horse (*Equus*): *in vivo* stress developed in the radius and metacarpus, *J. Zool.,* 201, 67, 1983.
91. Biewener, A. A., Thomason, J., and Lanyon, L. E., Mechanics of locomotion and jumping in the horse (*Equus*): *in vivo* stress in the tibia and metatarsus, *J. Zool.,* 214, 547, 1988.
92. Hylander, W. L., Stress and strain in the mandibular symphysis of primates: a test of competing hypotheses, *Am. J. Phys. Anthropol.,* 64, 1, 1984.
93. Rubin, C. T. and Lanyon, L. E., Regulation of bone formation by applied dynamic loads, *J. Bone Joint Surg.,* 66-A, 397, 1984.
94. Biewener, A. A. and Bertram, J. E. A., Structural response of growing bone to exercise and disuse, *J. Appl. Physiol.,* 76, 946, 1994.

9

Imaging of Bone Structure

Peter Rüegsegger
University of Zurich and ETH

9.1 Introduction

9.1.1 About Bone Structure

Osteoporosis is a multifactorial disease, and bone removal differs widely from patient to patient with considerable consequences for the respective bone mechanics. The general features of osteoporotic abnormalities include alterations in cancellous bone such as fenestration of bone plates, and thinning and reduction of bone trabeculae. Alterations in cortical bone such as thinning of its width due to endosteal bone resorption, and increased porosity of the Haversian canals[1,2] also occur.

Dual-energy X-ray absorptiometry (DEXA) became so popular because most of the osteoporotic changes lead to a reduction of bone mass. DEXA is based on projectional images and provides the mineral content or the areal density of the examined bone. It cannot differentiate between cortical and cancellous bone loss, and it is insensitive to structural changes within cancellous bone, such as reduction of bony elements and compensatory thickening of the remaining elements, transformation of plates to rods, or alterations in connectivity and anisotropy. Projectional images are not useless per se to analyze changes in cancellous bone structure. The proximal femur, for example, has a distinctive pattern of trabecular architecture, which is disturbed in the course of osteoporosis and can be described semiquantitatively with the Singh index. The Singh index[3,4] distinguishes six grades of osteoporosis by comparing radiographs of a patient with a set of standard radiographs or with charts. The procedure proved to be useful for epidemiological studies, but was not sufficiently reliable for diagnostic purposes. Considerable efforts have been made to analyze the trabecular pattern from radiographs of the radius and the calcaneus[5–8] with the help of image analysis tools such as histogram analysis, run length methods, and fractual dimensions, just to name a few. Plain film radiography, however, does not record the real architecture of bone, but an apparent one which is created by superposition of the X-ray shadows produced by calcified tissues.

0-8493-9117-2/01/$0.00+$.50

X-ray computed tomography (CT) and magnetic resonance imaging (MRI) have the potential to study the real three-dimensional (3D) architecture of bone in a nondestructive way. Standard equipment, however, is used primarily for two-dimensional (2D) imaging. To reduce image noise it is customary to select a slice thickness that is much larger than the pixel size of the tomogram. In displaying bone structures this is a handicap, especially if cancellous bone is to be analyzed where preferential directions are not present per se. There are 3D imaging tools available for standard CT and MRI systems to depict surfaces of organs from a stack of 2D images. Similar imaging techniques can be used to display the appearance of cancellous bone, if the measurements had been made with an isotropic spatial resolution.

Although microarchitecture of cancellous bone is of primary interest in this chapter, it should be mentioned that cortical bone plays an equally important role in the assessment of bone mechanics.[9,10] At first glance it appears as if cortical bone would be much easier to assess than cancellous bone. The thickness of cortical bone in the diaphysis of a long bone seems to be measurable with simple means. Even in this "simple" case, however, there are some pitfalls: CT images are convolutions of the real object with the response function of the measuring device. Hence, the edges of cortical bone are blurred and any cortical thicknesses evaluated from the CT images are dependent on the segmentation (thresholding) procedure. The density of cortical bone is displayed correctly in the central part of the cortex only, provided cortical thickness is at least three times the width of the point spread function (PSF).[11] Furthermore, certain pathologies might cause a trabeculization of the endosteum, or cause a pronounced porosity of cortical bone (such as in hyperparathyroidism), leading to additional uncertainties. However, the diaphyses of long bones are not only of interest. The role of the cortical shell of vertebrae, femoral heads, or joint surfaces in general is underestimated at present and might be of considerable importance in future discussions about osteoporotic fractures. Radiographs of thin sections through these bones show similar thicknesses of the cortical shell and the trabecular plates and rods. It may be concluded that an advanced understanding of the biomechanics of bone requires equally high-quality imaging tools for both cancellous and cortical bone.

The traditional way to assess the mechanical competence of a bone is an empirical one: assess a certain bone feature (mass, density, fractual dimension, complexity, etc.) and relate it to a clinical outcome (fractures), or to the outcome of a mechanical test. With the availability of noninvasive, 3D imaging procedures, a second, more basic approach comes into view: assess a complete bone region, such as the hip, the ankle, or the wrist, with an adequate spatial resolution and calculate the mechanical properties of the bone under standardized loading conditions. It is not clear yet which approach will be superior. The first one appears to be much simpler but does not answer basic questions. The second one aims at a basic understanding of the processes leading to osteoporotic fractures and promises a fracture risk prediction for individual patients. A major unresolved problem of the second approach is posed by the largely unknown material properties of bony tissue.

9.1.2 About Spatial Resolution

Spatial resolution has to be selected according to the actual problem to be solved. In displaying the surface of a large bone a 1-mm resolution is usually sufficient. A 100-μm resolution appears to be adequate to analyze trabecular spacing, while other features of cancellous bone require resolutions of up to 10 μm. To study bone changes on a cellular level, a 1-μm resolution is advantageous. Even higher resolutions are required to analyze the ultrastructure of bone and the crystal structure of the bone mineral.

In real life, spatial resolution and sample size are linked together. An image matrix size of 1000 $\times$ 1000 $\times$ 1000 voxels of 1 μm side length represents a volume of 1 mm^3. A volume of interest (VOI) of 1-mm^3 within, for example, the human calcaneus, will contain either no bone at all or only one or two trabeculae. So 1-μm resolution imaging is meaningful only if the VOI can strategically be placed to study well-localized phenomena. To get representative information about a bone, larger VOIs are necessary. An optimum would be to have a complete bone, or a complete end section of a bone, within the VOI. For the human femur, radius, or calcaneus and the above-mentioned matrix size, this leads to voxel dimensions of 100 μm. What appears to be adequate for humans is not adequate for animal

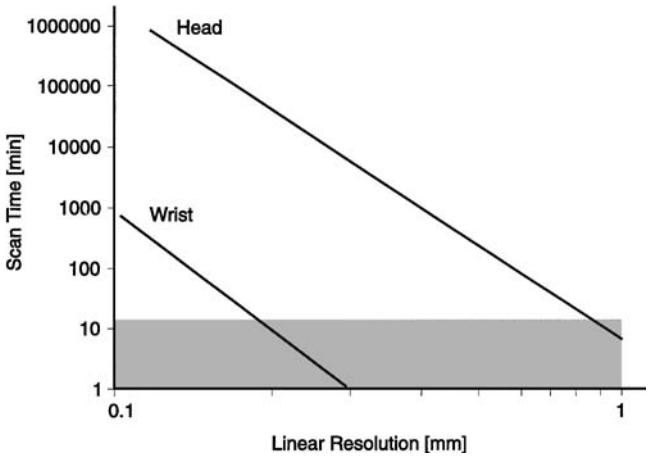

FIGURE 9.1 Scan time vs. resolution in MRI at 1.5 T to obtain a signal-to-noise ratio of approximately 10 for a head coil and a wrist coil. The crosshatched area indicates the reasonable measuring time range for *in vivo* examinations. (From Wehrli, F.W. et al., *Technol. Health Care,* 6, 307, 1998. With permission.)

models. In small laboratory animals (e.g., knockout mice), where a VOI of a few millimeter side length might contain a complete peripheral bone, voxels of a few micrometers are what is needed to assess bone biomechanics.

There are, however, also other criteria limiting the achievable spatial resolution of 3D images. In X-ray CT of patients, live laboratory animals, or living cells, radiation dose is of concern. A rough idea of the relationship between dose D, spatial resolution Δx, image noise σ, and size of the object, is given by:

$$\sigma^2 \cdot \Delta x^4 \cdot D \cong e^{\int \mu \, dx},$$

where $e^{\int \mu \, dx}$ shall be a typical attenuation of the measured object. With all other parameters held constant, dose goes up with approximately the fourth power of spatial resolution. This rule is somewhat alleviated if the object is small (then $e^{\int \mu \, dx}$ is small, and so is D), if a larger image noise is accepted, or if special procedures, such as local tomography,[12–14] are applied. Radiation dose is of no concern if MRI procedures are used. The spatial resolution of MRI, however, is limited by measuring time. Scan time vs. resolution for a given procedure was studied by Wehrli et al.[15] (Fig. 9.1). Even if a relatively small object such as the human wrist is examined with a specialized wrist coil, the measuring time is at least 10 min to obtain a spatial resolution around 150 μm. Measuring time is a critical parameter in high-resolution imaging of live objects. According to experience with patient examinations, spatial resolutions better than 200 μm can only be achieved reliably if measuring time is kept well below 5 min—even if sophisticated immobilization tools are used. As with X-ray CT, it is also possible to use special equipment with MRI to measure small laboratory animals. But even with specialized tools, it is difficult to get a spatial resolution better than 50 μm.

More detail should be given as to how spatial resolution is defined. From a scientific standpoint, it is most meaningful to provide the modulation transfer function (MTF) or the PSF. Resolution is then usually defined as $1/2\ell p$ at 10% contrast, so if 10 line pairs (lp)/mm can be resolved at 10% contrast, the resolution is said to be 50 μm. However, very often a so-called nominal resolution is given. This is simply the linear voxel size of the matrix used to display the reconstructed images. It is a subjective measure, meaningful only if the voxel size is not reduced beyond the point where detail perception is further improved. Nominal resolutions are used in Table 9.1 because MTFs are not available for all procedures.

TABLE 9.1 Typical Nominal Resolution of Some 3D Imaging Procedures

CT (*in vivo*)	$200 \times 200 \times 1000\ \mu m^3$
3D-pQCT (*in vivo*)[19]	$165 \times 165 \times 165\ \mu m^3$
Micro-CT (*in vitro*)[23]	$14 \times 14 \times 14\ \mu m^3$
3D-micro-CT (*in vivo*)[24]	$28 \times 28 \times 28\ \mu m^3$
Synchrotron-CT (*in vivo*)[66]	$8 \times 8 \times 8\ \mu m^3$
Synchrotron-CT (*in vitro*)[75]	$2 \times 2 \times 2\ \mu m^3$
MRI (*in vivo*)[39]	$150 \times 150 \times 500\ \mu m^3$
Micro-MRI (*in vivo*)[33]	$40 \times 40 \times 40\ \mu m^3$

9.2 Imaging Procedures

9.2.1 CT

CT images show 2D or 3D distributions of linear attenuation coefficients and hence are dependent on the energy of the X-rays and the atomic composition of the imaged material. With proper calibration they can be converted to density images. There are, however, limitations to be observed caused by artifacts due to the energy spectrum of the X-rays (beam hardening artifact) and artifacts due to the mismatch between spatial resolution of the measuring system and the structural dimensions (partial volume artifacts). Beam hardening artifacts can be taken care of quite efficiently by calibrating procedures and are completely missing in monochromatic synchrotron-CT images. Partial volume artifacts are omnipresent, and can be neglected only if spatial resolution is much higher than the structural dimensions. For example, with a spatial resolution of 50 μm, only the center core of a 150-μm-thick trabecula reaches the correct density. The measuring procedures for standard CT examinations are quite different from those used for bone structure analysis. Standard hospital-based CT systems used for 3D imaging either sequentially measure a stack of parallel slices or are of the spiral scanning type.[16,17] The source-detector geometry and the number of detector elements are fixed and selected such that large patients can also be scanned. This limits the in-plane resolution and, since slice thickness can hardly be reduced to no more than 1 mm, it is currently not possible to use standard equipment to depict the 3D topology of cancellous bone with these instruments. To examine peripheral bones such as the radius or the tibia, specialized equipment is available.[18] These 3D peripheral quantitative computed tomography (pQCT) systems are of the multiple fan–beam type, where line sources (line in axial direction, fan in lateral direction) and a 2D detectors are used. The individual fans are separated by a foil collimator, but all fans are measured simultaneously, so that the complete 3D structure is assessed at once (Fig. 9.2). At present, an isotropic spatial resolution of 170 μm is available for patient examinations at a local radiation dose much below 1 mSv.[19] The same technique has the potential to obtain 120 μm resolution at 5 mSv, and with local tomography, even 100 μm is achievable with the same radiation dose.[14] A resolution around 100 to obtain 120 μm appears to be critical since most of the stuctural parameters are restorable from such images with the help of normative data obtained from high-resolution micro-CT images.[20,21]

9.2.2 Micro-CT

Micro-CT was pioneered by Feldkamp et al.[22] They used a microfocus X-ray tube as a source, an image intensifier as a 2D detector, and a cone-beam reconstruction algorithm to create a 3D object with a typical resolution of 50 μm. The early work in micro-CT focused primarily on the technical and methodological aspects of the systems, and used equipment not normally available to the public at large. A more recent development emphasized the practical aspects of micro-CT and aimed to enlarge the availability of the technology in basic research as well as in clinical laboratories. That system is based on a compact fan-beam type of tomograph, also referred to as desktop micro-CT, providing a nominal resolution of 14 μm.[23] Specimens with diameters of a few millimeters to a maximum of 18 mm can be measured. By enlarging the detector array, and with a full 360° rotation, it was also possible to extend the maximal object diameter to 80 mm. These fan-beam-type instruments measure slice by slice, and since slice

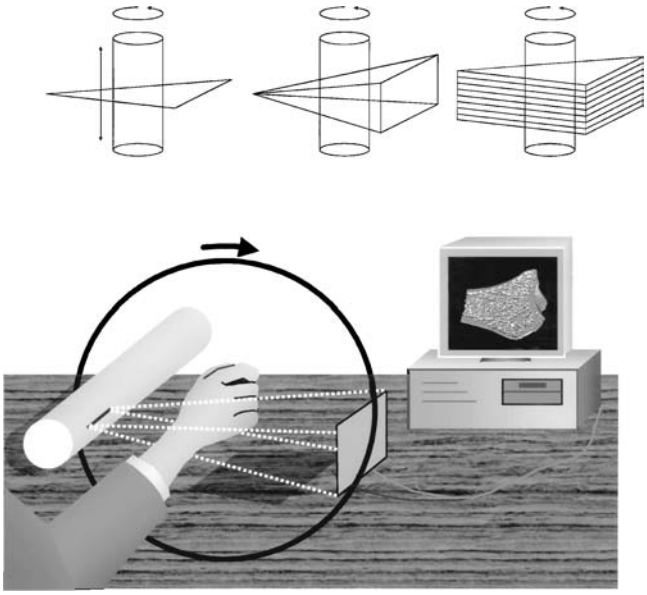

FIGURE 9.2 The basic scan geometries for 3D data acquisition. Top row from left to right: Fan-beam geometry with axial shift of the object, cone-beam geometry, stacked fan-beam geometry. A stacked fan-beam measurement of the wrist with line source and area detector is shown in the lower part of the illustration.

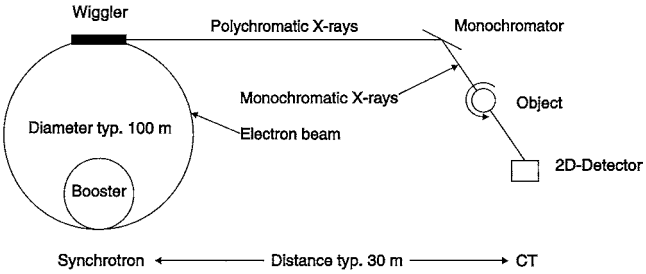

FIGURE 9.3 In synchrotron-CT electrons are accelerated to some GeV and produce a high-intensity X-ray beam. After passing a monochromator quasi-monoenergetic X-rays are available. Because of the small divergence of the X-ray beam, the photons can be considered to impinge in a parallel way onto object and area detector.

thickness has to be comparable with the lateral resolution, up to 1000 tomograms have to be measured to assess fully a bone biopsy or a rat tibia, for example. Next-generation instruments are using the same multiple fan-beam technique, as the 3D-pQCT system mentioned above.[24] Since these systems measure all necessary tomograms at once, the measuring time is reduced from several hours to a few minutes. This enables measurements of live laboratory animals and allows dynamic tests to be performed. The multiple fan-beam approach provides exact 3D reconstructions, and thus distortions known from cone-beam reconstructions are avoided.

9.2.3 Synchrotron-CT

Synchrotron radiation[25–28] is produced when relativistic electrons are accelerated by a magnetic field. Radiation is emitted into a narrow cone in the direction of the path of the electron. The combination of high electron energy, high electron current, and high magnetic fields produce intense continuous X-ray radiation over a large span of energy, typically between 5 through 60 keV. X-rays in a very narrow energy band can be extracted with monochromators (Fig. 9.3). Typical energy resolution is 10^{-4}, thus, at 25 keV

the beam incident on the specimen has an energy spread of less than 5 eV. Since the divergence of the X-ray beam is very small, parallel beam reconstruction techniques can be employed. Furthermore, the beam cross section is quite sizable so that 2D projections even of objects in the centimeter range can be obtained. The combination of quasi-monochromaticity, high intensity, and low divergency makes synchrotron radiation ideally suited for tomographic imaging. Limitations are given by the limited access to these bulky instruments and the rapid falloff of the X-ray intensity at higher energies. With synchroton-CT systems the highest-resolution nondestructive bone images have been made.

9.2.4 MRI

MR images are fundamentally different from CT images. MR images show the soft tissue components (bone marrow, fat, muscle). With the techniques used today it is not possible to analyze bone directly, at least not *in vivo*. The quality of the MR image is largely given by the available signal-to-noise ratio (SNR). SNR scales (rule of thumb) with resonance frequency ω for large objects, and with ω^2 for small objects.[29] Thus, for small objects, it is particularly advantageous to work with high resonance frequencies (high field strengths). SNR performance, however, is also dependent on the design of the radio frequency (RF) receiver coil. The coil should encompass the structure of interest as tightly as possible. This is the reason imaging small samples that fit precisely in the receiver coil is much more efficient than imaging the femoral head within the pelvis of a patient. For a given coil configuration, SNR increases linearly with the number of spins per voxel, thus with the third power of the side length of the voxel. Furthermore, SNR improves with the square root of the measuring time. Hence, measuring time increases with the reciprocal sixth power of spatial resolution. In addition, it has to be noted that spatial resolution in MRI depends also on the imaging method. In summary, small objects are measured in high-field (up to 9 T), small-bore magnets in coils that fit tightly to the object, and spatial resolution is primarily limited by the available measuring time. *In vivo* examinations of humans are usually performed with standard equipment and a field strength of 1.5 T. To achieve a sufficiently high spatial resolution at an acceptable measuring time, peripheral examination sites such as the finger,[30] radius, or calcaneus are preferred and specialized coils and imaging methods are used.

9.2.5 Micro-MRI

Micro-MRI, also known as NMR microscopy,[31–33] is used to extract morphometric parameters from trabecular bone in much the same way as micro-CT. Since any high-field NMR spectrometer equipped with microimaging tools can be used for NMR microscopy, this technique is, in principle, widely available to image bone samples and small laboratory animals. This advantage is somewhat offset by the less favorable spatial resolution. Typical resolutions with scan times on the order of 30 to 60 min are 50 to 80 μm. This is, in general, not sufficient for an accurate tissue classification, so special software tools (subvoxel classification[34]) have been developed to lessen partial volume blurring. For small samples, further improvement of spatial resolution can possibly be reached with superconducting receiver coils.[35] In some *in vitro* studies trabecular bone is imaged after removal of bone marrow and impregnating bone with MR contrast agents.[36–38]

9.3 Structural Features Analyzed from Bone Images

9.3.1 Patient Examinations

The most common fracture sites in osteoporosis are the spine, the proximal femur, and the distal radius. This is the reason these sites are most important for bone structure analysis in patients. As discussed in the previous sections, technical limitations and limitations given by the underlying physics render the central skeleton unsuitable for structural analysis. Of the three sites mentioned above, only

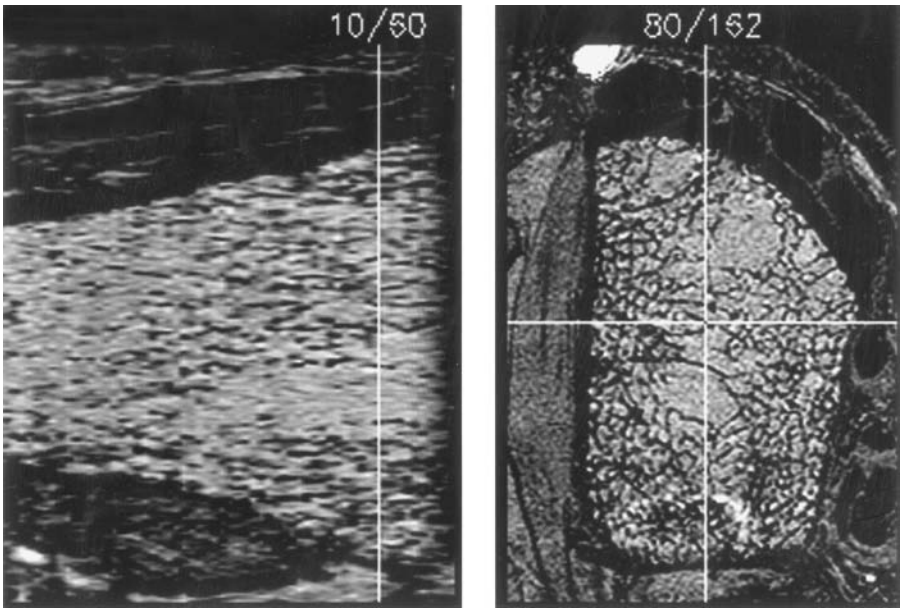

FIGURE 9.4 *In vivo* examination with a clinical 1.5 T MRI instrument: axial and transaxial cuts through the distal radius of a patient are shown. (Courtesy of Sharmila Majumdar.)

the radius is sufficiently small and accessible for high-resolution 3D imaging. CT and MRI examinations of the distal radius are at present available with a spatial resolution of approximately 150 μm, although MRI has a somewhat less favorable resolution in the axial direction. In both cases, patient examinations have to be performed with a suboptimal spatial resolution. This is leading to blurred images that prevent the direct assessment of true morphometric indices. Of course, there is always the possibility to obtain "apparent" indices using a somewhat arbitrary threshold limit and segmenting bone regions from nonbone regions. By counting the total number of "bone" voxels (bone volume, BV) and dividing them by the total number of voxels (total volume, TV) in the region of interest, an apparent relative bone volume ($(BV/TV)_{app}$) can be obtained. Similarly, an apparent trabecular thickness ($Tb.Th_{app}$) and separation ($Tb.Sp_{app}$) can be calculated. This approach was followed by Majumdar et al.[39,40] for their MR images (Fig. 9.4). An alternative approach accepts that BV/TV cannot be truly evaluated by segmentation of *in vivo* measurements, but can be derived from the mean trabecular bone density (TBD) and complement this information with a structural measure for the number of plates and rods. This approach was taken by Laib et al.[19,41] for their CT images. The structural measure of this second approach is based on ridge extraction, which allows detection of a 3D skeleton of cancellous bone irrespective of the real dimensions of the bony structures. By applying a direct distance transformation[42] to the 3D ridge image (Fig. 9.5), trabecular number (Tb.N) is calculated as the inverse of the average distances. Combining Tb.N and BV/TV leads to a mean trabecular thickness $Tb.Th = BV/TV/Tb.N$ and to a mean trabecular spacing $Tb.Sp = (1 - BV/TV)/Tb.N$, in analogy with standard histomorphometry.[43,44] The derivation of Tb.N is really 3D; the derived measures, however, implicitly assume a plate model. The complete procedure follows a specific protocol (Fig. 9.6). The distal radius is measured with a 3D-pQCT system, the outer and the inner surface of the cortical bone is detected, and the bone separated into cortical bone and cancellous bone. Average thickness and density of compact bone are determined and the cancellous bone analyzed as described above. The same procedure can be applied to the complete wrist. With the help of finite-element methods it is then possible to relate structural measures directly to mechanical properties of the same bone[45] (see also Chapter 14 in this book).

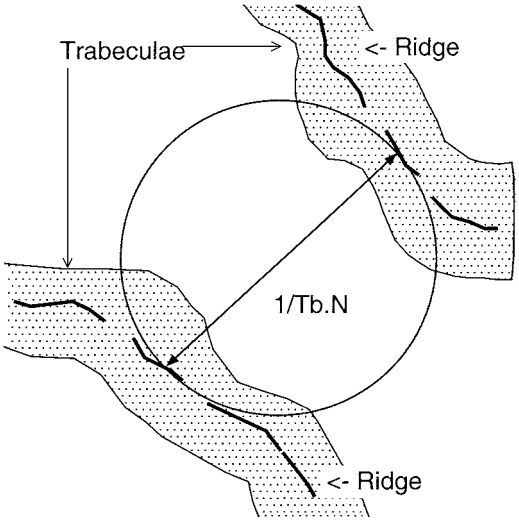

FIGURE 9.5 Determination of trabecular number from ridge images. Largest spheres (a 2D cut is shown for clarity) are fitted into the background of the 3D ridge image, then Tb.N is determined as the inverse of the average diameter of these spheres. (From Laib, A. et al., *Technol. Health Care,* 6, 329, 1998. With permission.)

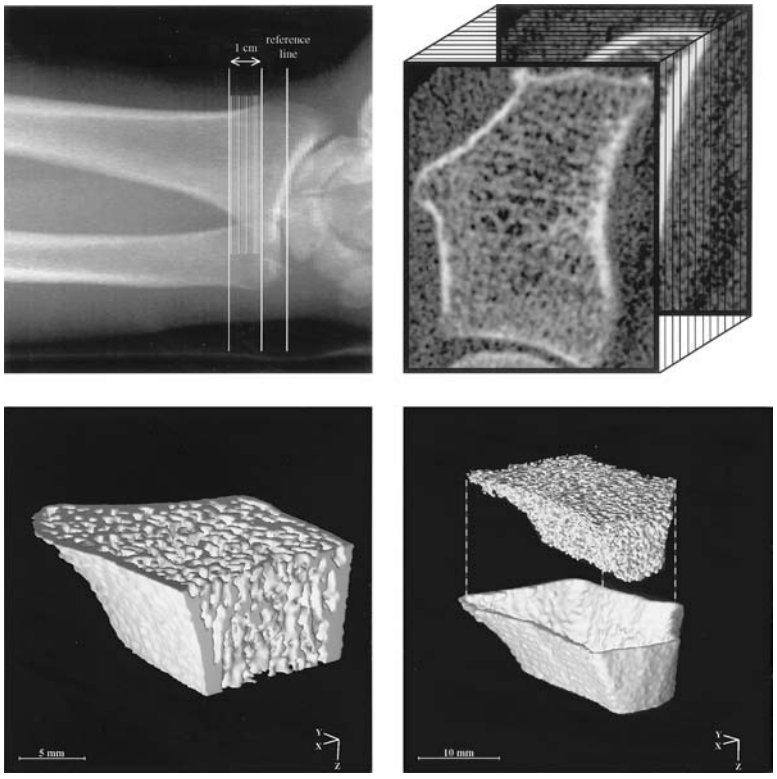

FIGURE 9.6 Procedure to extract structure and density from 3D-pQCT images. Top row: standard measuring site at the distal radius. A stack of 60 slices is measured over an axial distance of 1 cm. Bottom row: left, 3D image of the reconstructed and segmented bone (artificial cut to display the inner part of the bone); right, exploded view of cortical and cancellous bone region of the assessed VOI. (From Laib, A. et al., *Technol. Health Care,* 6, 329, 1998. With permission.)

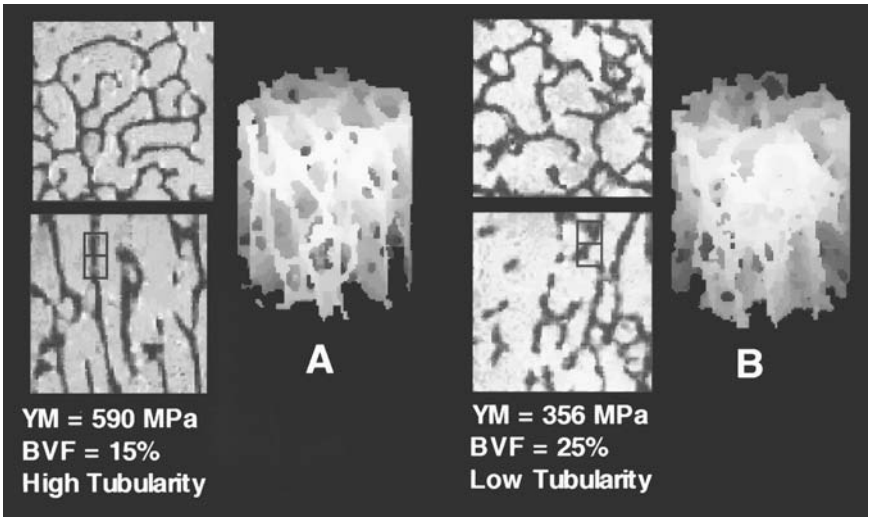

FIGURE 9.7 Stiffness and tubularity of two bone samples from the distal radius. Despite the fact that sample B has a higher bone volume fraction (BVF), its stiffness (Young's modulus,YM) is lower compared with sample A. The higher stiffness of sample A is reflected by its higher tubularity. (From Wehrli, F.W. et al., *Technol. Health Care,* 6, 307, 1998. With permission.)

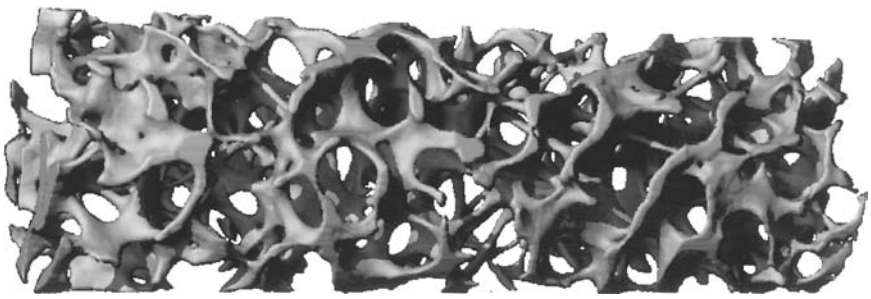

FIGURE 9.8 3D micro-CT image of a human bone biopsy from the iliac crest.

A different approach to analyze the 3D nature of the cancellous bone architecture was described by Wehrli et al. and applied to MR images of the radius. Wehrli et al.[15,38] introduced a new parameter, which they called "tubularity." Tubularity expresses the relative likelihood for two points in adjacent slices with identical in-plane coordinates to be both in bone. If the plane of section is chosen orthogonal to the principal anatomic axis, such as the direction of the forearm, then tubularity describes how cancellous architecture is oriented in axial direction. Fig. 9.7 shows two samples from the human wrist, as well as transverse and longitudinal sections. It is of special interest here to note that the sample with the higher bone density (BV/TV) is less stiff (lower Young's modulus in axial direction) than the sample with the lower bone density. This is due to the higher tubularity of the former sample.

9.3.2 Bone Samples

Bone biopsies typically taken from the iliac crest of patients for histological and histomorphometrical analyses are 4 to 8 mm in diameter and roughly 1cm in length. Such small objects can be examined with the micro-CT procedures described in Section 9.2, that is, with a spatial resolution of roughly ten times better than that of the *in vivo* radius measurements. Fig. 9.8 shows a typical example of a bone biopsy that was measured with a commercially available micro-CT system (Scanco Medical, Bassersdorf, Switzerland).

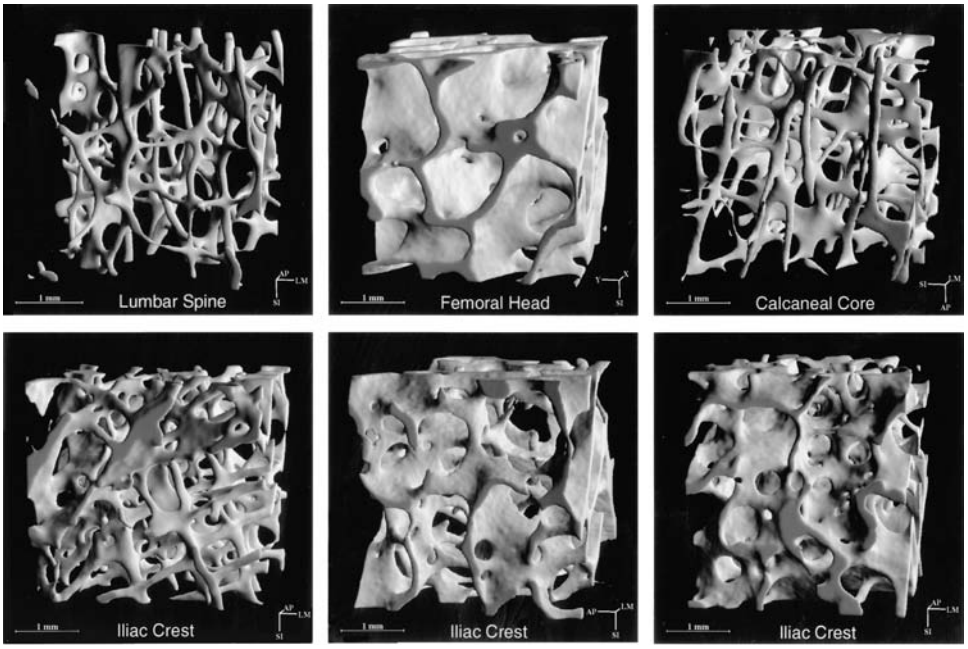

FIGURE 9.9 Typical 3D micro-CT images from various sites of the human skeleton (top), and the same site but different individuals (bottom).

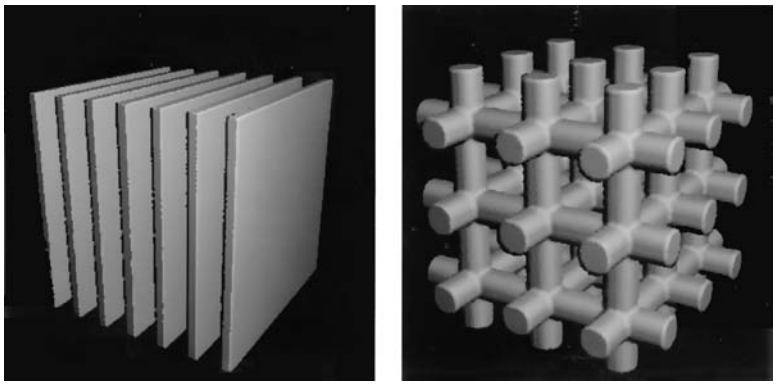

FIGURE 9.10 Plate and rod models used for the indirect calculation of structural indices.

Usually the complete volume of the biopsy is not used to analyze the structure of cancellous bone, but only the central 4 mm of a transiliac crest biopsy. Typical examples of such subvolumes are given in Fig. 9.9. It is obvious that the intersite and interindividual variability in the structure of cancellous bone is very high. From simple visual inspection, plates and rods can be distinguished; some of the plates are fenestrated and partly transformed to rods. Rods vary largely in diameter, length, and orientation. To quantitate the structural features one is tempted to follow the recommendations of the American Society for Bone and Mineral Research.[44] However, these recommendations were worked out to interpret 2D sections. The third dimension was taken into account by model assumptions. Usually plate models or rod models are used (Fig. 9.10; see also Chapter 13). The error made by assuming the wrong model can be considerable. With the availability of 3D imaging, it was necessary to develop new image analysis

tools that take full advantage of all three dimensions. Examples of such procedures are direct volume and surface determination,[46,47] model independent assessment of thickness,[30] three-dimensional connectivity estimation,[48] degree of anisotropy,[49,50] and structure type assessment.[51] Also fractal dimensions[52–55] are used for the characterization of topological properties of cancellous bone, although their usefulness is still a matter of debate. An overview on 3D methods for the quantification of cancellous bone architecture can be found in a review article written by Odgaard[56] or in his chapter in this book (Chapter 14). Here only a few definitions will be given. Bone surface area (BS)[57] can be calculated using the marching cubes algorithm[47] to triangulate the surface of the mineralized bone phase. Tetrahedrons are then used to calculate the bone volume (BV) of the triangulated surfaces. To be able to compare samples with different sizes, the normalized indices BV/TV and BS/TV are used.

3D connectivity[22,48] is defined as a measure of the degree to which a structure is multiply connected. Absolute measures of connectivity are not directly related to mechanical strength. However, changes in connectivity are connected to changes in elastic stiffness. A loss in connectivity at preserved bone mass leads to a reduction in stiffness.[58]

Directly assessed trabecular thickness is determined by filling maximal spheres into the structure with the distance transformation.[42,59] This leads to a thickness distribution (Fig. 9.11). Then the average thickness of all bone voxels is calculated. The thickness histograms might contain valuable information about cancellous bone structure; however, their potential has not yet been explored.

An estimate of the plate–rod characteristic of the structure can be achieved using the structure model index (SMI).[51] It is calculated by a differential analysis of a triangulated surface of a structure (Fig. 9.12). The surface derivative dBS/dr is calculated with the help of a simulated thickening of the structure by translating

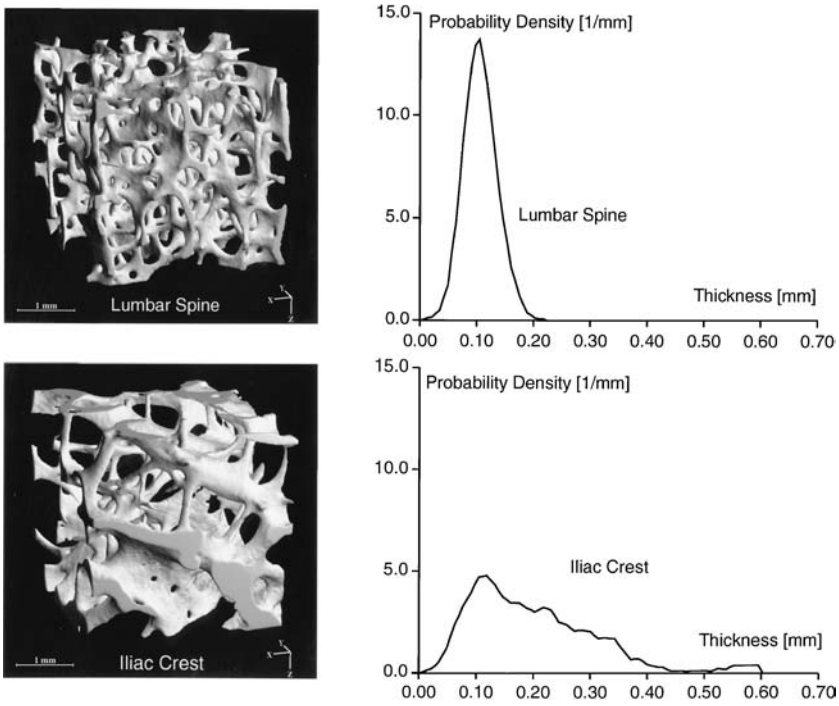

FIGURE 9.11 Two examples of directly (model independent) determined trabecular thicknesses. Top: A rodlike sample from the lumbar spine with a quite uniform trabecular thickness of 100 μm. Bottom: A platelike sample from the iliac crest with a broad thickness distribution. (From Hildebrand, T. and Rüegsegger, P., *J. Microsc.,* 185, 67, 1997. With permission.)

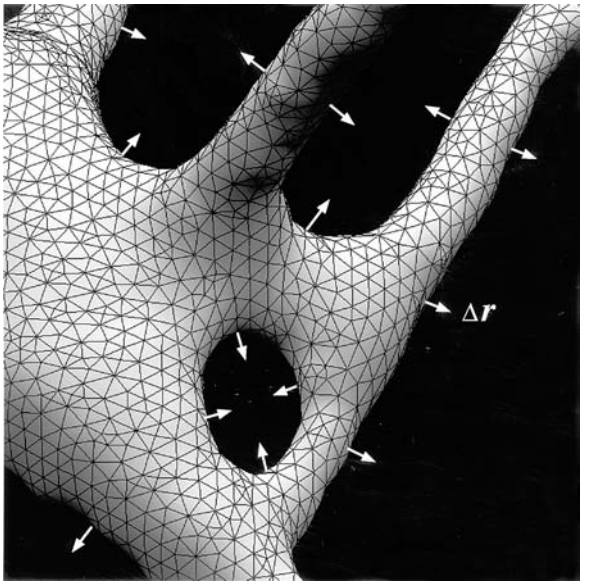

FIGURE 9.12 Surface triangulation of a voxel image used for volume, surface, and surface derivative estimation. (From Hildebrand, T. and Rüegsegger, P., *Comp. Methods Biomech. Biomed. Eng.*, 1, 15, 1997. With permission.)

the triangulated surface by a small extent in its normal direction and dividing the associated change of surface area by the length of the extent. For an ideal plate and rod structure, the SMI value is 0 and 3, respectively. For a structure with both plates and rods of equal thickness, the value is between 0 and 3, depending on the volume ratio between rods to plates. SMI can reliably be calculated only if the triangulated surface follows the surface of cancellous bone truly, that is if the spatial resolution is sufficiently high. Hence SMI can be applied safely to micro-CT images in the 15-μm resolution range, but not to patient examinations with their ten times lower resolution. An alternative to the SMI procedures that might be applicable to *in vivo* examinations was suggested by Stampa et al.[60]

The comparison between conventional histomorphometry and micro-CT-derived histomorphometry is described in Müller et al.[61] It is based on a set of 63 human transiliac bone specimens. For the conventional histomorphometric analysis,[62] two sets of four 5-μm-thick undecalcified sections were made in the mediolateral direction. The first set of four sections was made at a distance of 2 mm from the anterior edge, and the second set at a distance of 3 mm. The sections were stained to obtain high-contrast 2D images. Prior to the histological sectioning the samples were measured with a micro-CT with a 14 μm nominal resolution. The morphometric parameters were then computed for both methods using a plate model. The correlations for the morphometric parameters ranged from $r = 0.84$ to $r = 0.93$. In view of the fact that it is extremely difficult to locate the physical cut through a sample within the 3D micro-CT image stored in the computer, and since the histological sections differ in their thickness from the micro-CT sections (5 vs. 14 μm), the high correlations suggest that both procedures provide the same information with regard to 2D parameters.

The same bone samples also underwent a complete 3D analysis.[63] In fact, twofold 3D analysis was made in which model-dependent parameters were compared with model-independent parameters. An example of this comparison is given in Fig. 9.13. Trabecular thickness is systematically lower in the model-dependent (a plate model was used) case. This makes sense since cancellous bone is never completely platelike. The rod component causes an increase of the surface-to-volume ratio with the consequence of a smaller thickness if it is derived from BV/TV under the assumption of a plate model. Of interest is also the scatter of the data displayed in Fig. 9.13. The model assumption causes an

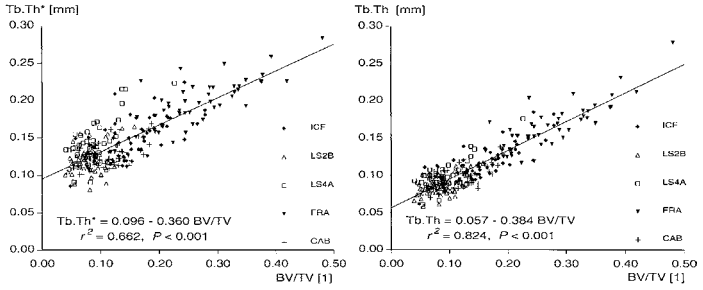

FIGURE 9.13 Relation between trabecular thickness and bone volume density for five different sites from the human skeleton (iliac crest, ICF), bodies of the second and fourth vertebrae of the lumbar spine (LS2B, LS4A), femur head (FRA), calcaneus (CAB). Left: Directly (model independently) determined. Right: Calculated by using a plate model. (From Hildebrand, T. et al., *J. Bone Miner. Res.,* 14, 1167, 1999. With permission.)

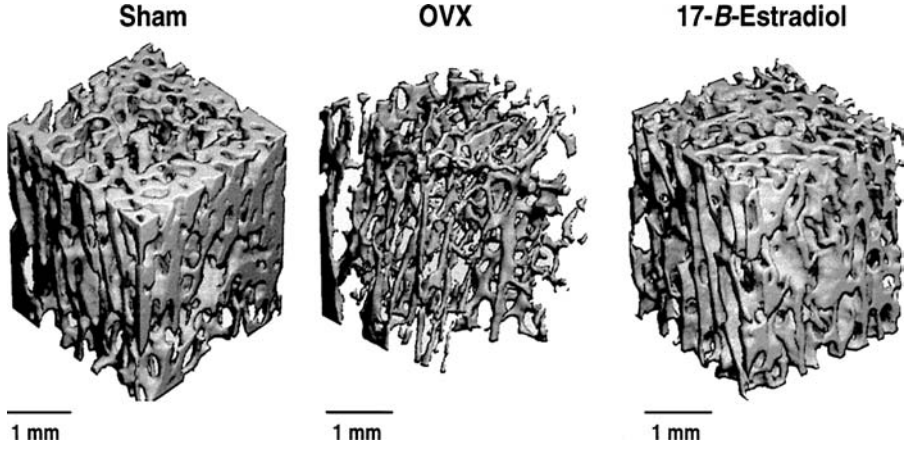

FIGURE 9.14 3D micro-CT images (12 μm voxels) of samples taken from the rat tibia showing structural changes following ovariectomy and treatment with estradiol. (From Kapadia, R.D. et al., *Technol. Health Care,* 6, 361, 1998. With permission.)

artificially reduced scatter range. The large variability of individual results is better reflected by the model-independent parameters.

9.3.3 Small Laboratory Animals

For bones of small laboratory animals such as rats and mice, the same structural analysis procedures can be used as for bone biopsies since object size and spatial resolution are comparable. Utilizing micro-CT techniques to evaluate quantitatively cancellous bone architecture of the rat proximal tibia showed a pronounced loss of trabecular bone-following ovariectomy and a marked inhibition of this loss if the rats were substituted with estrogens (Fig. 9.14).[64] A similar change in bone microarchitecture can be visualized with micro-MRI (Fig. 9.15). The availability of gene-modified models of skeletal diseases in mice[65] has led to a significant interest in developing imaging techniques to evaluate morphological differences in these models. Surface-rendered micro-CT images of the entire mouse hind limb and the proximal tibia are shown in Fig. 9.16.

The first 3D studies of bone microarchitecture in live animals were reported by Kinney et al.[66] They used synchrotron-CT to detect microscopic changes in the cancellous bone structure in the proximal

FIGURE 9.15 Micro-MR images (39 μm voxels) from rat tibiae following ovariectomy and treatment with estradiol. (From Kapadia, R.D. et al., *Technol. Health Care,* 6, 361, 1998. With permission.)

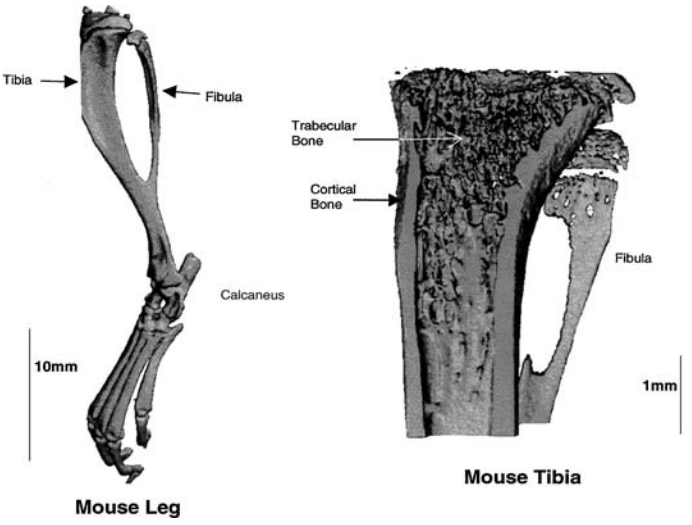

FIGURE 9.16 Micro-CT images from mouse leg (34 μm voxels) and mouse tibia (9 μm voxels). (From Kapadia, R.D. et al., *Technol. Health Care,* 6, 361, 1998. With permission.)

tibia of ovariectomized rats. The animals were anesthetized, secured to a rotating platform, and their right hind limbs elevated into the X-ray beam. The scanned region contained both cortical and cancellous bone (Fig. 9.17). The volumetric data were analyzed by standard histomorphometry and by cluster analysis[67] to obtain the connectivity (the first Betti number) . The influence of unopposed ovariectomy was dramatic, with 65% loss of BV/TV within 5 weeks (Fig. 9.18), and a drop in connectivity density. The relationship between 3D connectivity and the elastic properties of trabecular bone was studied separately[58] with the help of simulated bone atrophy and subsequent regrowth. There is no functional relationship between connectivity and elastic modulus per se because connectivity does not discriminate between rodlike connections and fenestrated plates. Although absolute measures of connectivity are not directly related to mechanical strength, there is an important relation between the respective changes. If connectivity does not recover, then elastic modulus does not reach its original value, even if bone mass is fully recovered.

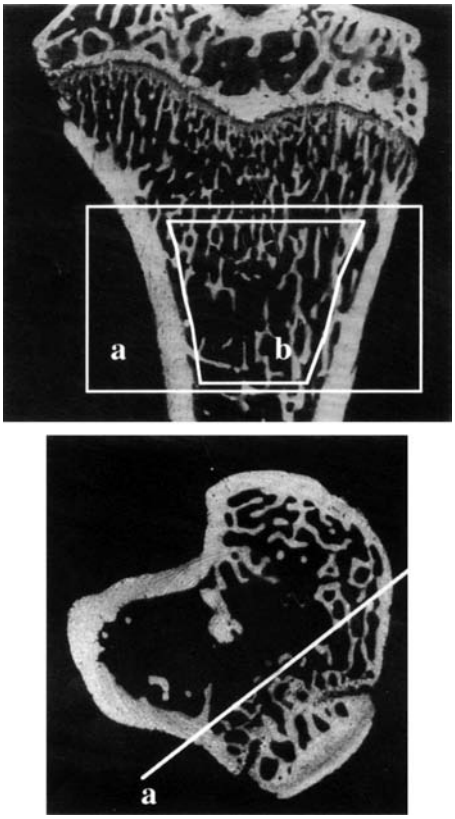

FIGURE 9.17 Axial and transaxial cuts through a 3D synchrotron-CT image (8 μm voxels) with (a) the VOI displayed in Figure 9.19, and (b) the VOI where the structural indices are determined. (From Kinney, J.H. et al., *J. Bone Miner. Res.,* 10, 264, 1995. With permission.)

9.4 Applications

9.4.1 Postmenopausal Osteoporosis

To study the feasibility of using high-resolution MRI to document osteoporotic changes in the microarchitecture of calcaneal bone, a group of 50 postmenopausal women was examined.[40] Half of the group had suffered hip fractures prior to the measurements; the other half was considered to be healthy. In this study the central ten slices of the calcaneus (the central 5 mm) were assessed (Fig. 9.19) and therein circular regions of interest (ROIs) analyzed (Fig. 9.20). The images clearly show the basic difficulty of such analyses. Cancellous bone is dramatically inhomogeneous and great care has to be taken to get representative and reproducible results. Nevertheless, significant differences in the structural parameters between the two groups were observed, with the exception of $Tb.Th_{app}$. With the voxel size of $195 \times 195 \times 500$ μm used in this study, it has to be considered that only the larger trabeculae were adequately depicted while the smaller trabeculae were subjected to partial volume effects. The apparent morphometrical measures were therefore not identical with the histomorphometrical measures. This is especially true for $Tb.Th_{app}$, where the data are primarily given by the voxel size of the MR image, and to a much lesser extent by the bone. Similar studies with similar findings were done for the human radius[39,68,69] and the phalanges.[70]

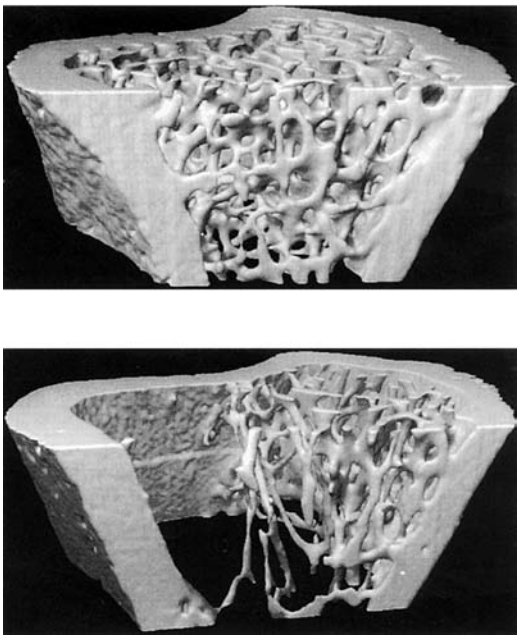

FIGURE 9.18 3D-display of the VOI shown in Fig. 9.18 of a female rat, just prior to ovariectomy (upper image) and 5 weeks after ovariectomy (lower image). (From Kinney, J.H. et al., *J. Bone Miner. Res.,* 10, 264, 1995. With permission.)

The potential of *in vivo* patient examinations with 3D-pQCT was evaluated with a group of 18 postmenopausal women.[19] These women were measured three times over a period of 1 year following the procedure described in Section 9.3.1. After carefully matching the VOIs, the individual changes relative to the baseline measurements were determined in cortical bone, as well as in cancellous bone, for bone density and structure. The results (Fig. 9.21) were surprising, and might lead to a new understanding of the processes involved in bone changes due to aging, disease, and treatment, if confirmed with larger patient groups. Bone loss after menopause has many manifestations. Either cortical bone or trabecular bone or both are lost, and in trabecular bone either the number or the thickness of trabeculae or both are reduced.

9.4.2 Simulated Bone Atrophy

It is assumed that mechanical stresses and strains influence the remodeling process and subsequently the structure and strength of bone. With the availability of precise 3D images of cancellous bone, it is therefore tempting to simulate the process of age-related bone loss and to calculate the effects on bone strength. One possible approach was presented by Müller and Hayes.[71] It is based on the remodeling sequence first described by Frost,[72] which consists of the four phases resorption–reversal–formation–quiescence. To simplify matters, the net result of a complete remodeling cycle was considered only and the length of a cycle was set to 197 days. It was assumed that the loss of bone mass observed after menopause was caused by an imbalance between the osteoblastic and osteoclastic activity. The effect of this imbalance is modeled with the help of constrained Gaussian filtration of the binarized (bone, nonbone) data set of the 3D cancellous bone images. The procedure was applied to bone specimens from various sites of the human skeleton. The specimens were measured with a micro-CT system. Fig. 9.22 shows the result of the simulation. In the left-hand upper corner the original bone structure is depicted, and the following images simulate how bone structure changes over 27 years. Quantitative structure analysis for a typical set of seven specimens was performed with the tools described in Section 9.3.2. One of the results showed the development of the degree of anisotropy over time (Fig. 9.23) with huge interindividual variability. In an early stage of the

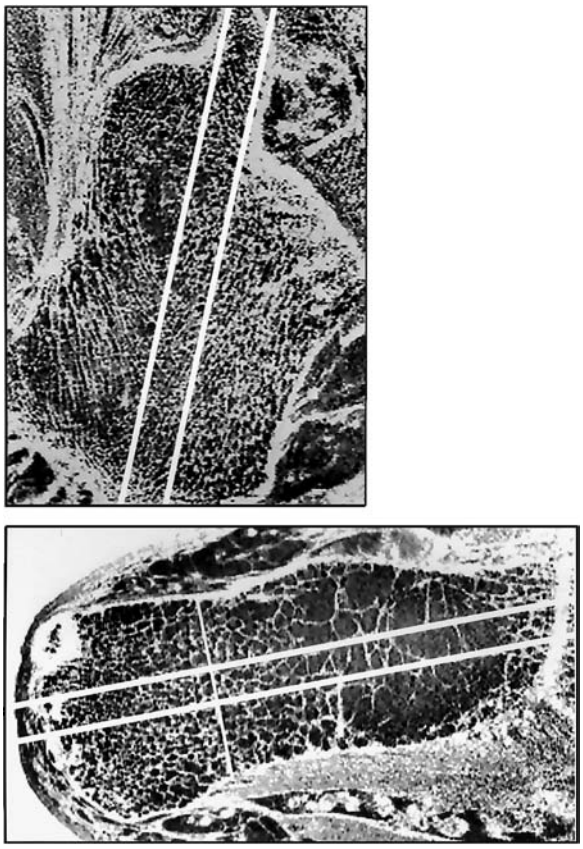

FIGURE 9.19 MRI image of the calcaneus of a patient, sagittal (top) and axial (bottom) cuts are shown. The region between the two lines was analyzed. (From Link, T.M. et al., *J. Bone Miner. Res.,* 13, 1175, 1998. With permission.)

simulation, degree of anisotropy increased for most specimens; later in the simulation it decreases again. For other specimens it remained constant over the complete simulated aging process, or increased monotonously. This means that in the majority of specimens thin but highly oriented elements were eliminated in an early stage, and later in time elements oriented in other directions were removed as well.

9.4.3 Cellular-Level Bone Changes

Standard histological examinations of the activity of bone cells is done with double labeling using fluorophores.[73] For example, in patients tetracyclines are given in fixed time intervals (2 weeks) and then a bone biopsy is taken. Cuts through the biopsy are made and the incorporated fluorophores visualized with ultraviolet light. The distance between the bone markers is determined and the bone formation rate can be calculated in micrometers per day. As all standard histomorphometric procedures, this procedure also is 2D and destructive (biopsies have to be taken, laboratory animals have to be sacrificed) and time serial examinations are not possible. It would be extremely interesting to visualize and quantitate bone formation in 3D and *in vivo*. Micro-CT or synchrotron-CT can be used for this purpose. Standard fluorophores, however, do not provide sufficient contrast for CT imaging. Heavy metal staining would be more appropriate. Ritman et al.[74] showed that $SrCl_2$ can be used as an X-ray analogue of fluorophore staining. Strontium is a calcium substitute, and localized deposits of the heavy metal behave much like the fluorophores commonly used in bone histology. Given in predefined time intervals, it appears to be possible to determine the bone formation rate *in vivo*.

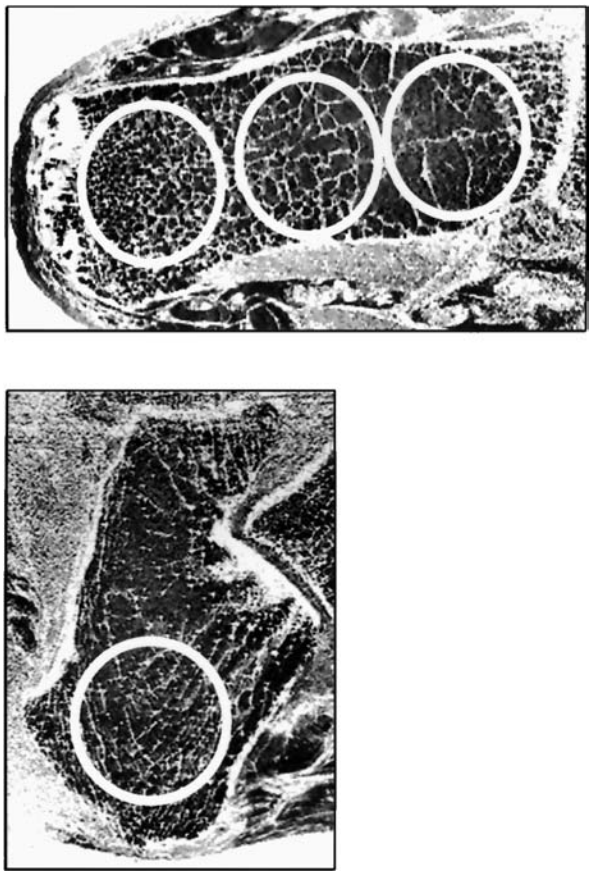

FIGURE 9.20 MRI images of the calcaneus with the circular regions of interest. (From Link, T.M. et al., *J. Bone Miner. Res.,* 13, 1175, 1998. With permission.)

Synchrotron-CT experiments in the resolution range of 1.4 μm reveal that the contours of the trabeculae are quite rough.[75] Obviously, the ultrahigh resolution allows documentation of how osteoclasts resorb trabecular bone. Inside the bone, tiny spaces are observable, interpretable as osteocytes. Hence 3D CT examinations in the spatial resolution range of 1 μm has the potential to observe cellular activity in intact bone (Fig. 9.24).

9.5 Conclusions

The analysis of bone structure from 3D images such as CT and MRI presents a formidable challenge. Neither macroscopic geometrical features nor microscopic architectural details can be neglected. The appearances of the various pathologies of skeletal diseases are extremely diverse and it is simply not known yet how to interpret them with regard to the mechanical competence of bone. An excellent help in this regard is available with large-scale finite-element analysis. It even might be that, in the future, this tool will the basis for an *in vivo* bone strength analysis. Meanwhile it enables validation of the importance of newly developed structural features. For both, the imaging task and the finite-element modeling, spatial resolution is of paramount importance. With synchrotron-CT it is now possible even to image processes on the cellular level. The procedure is nondestructive. Radiation dosage, however, is of concern and the highest resolution is available for small objects only. Nethertheless, in combination with other imaging modalities such as micro-CT and micro-MRI the link to the macroscopic scale obtainable with specialized clinical tools is feasible.

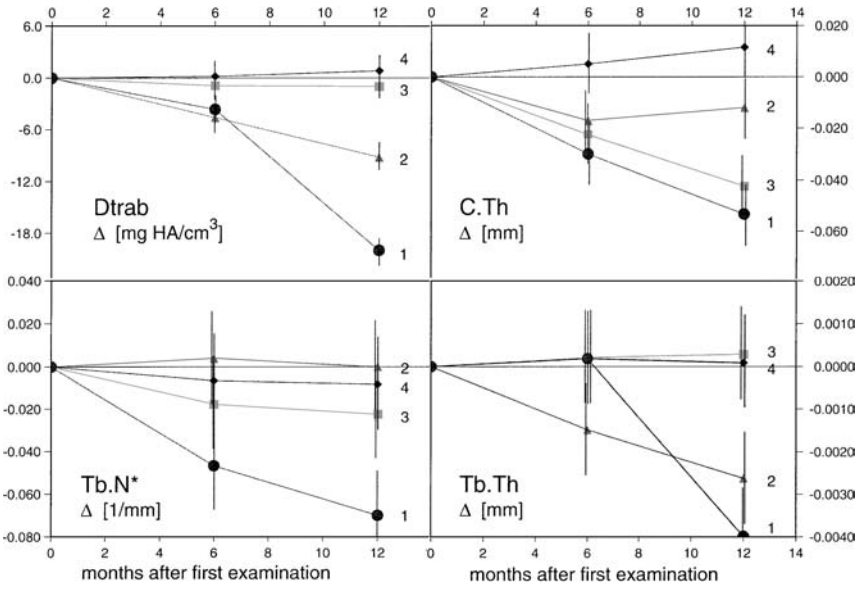

FIGURE 9.21 *In vivo* structure analysis. Changes in trabecular density, cortical thickness, trabecular number, and thickness, observed in postmenopausal women over a period of 1 year. To highlight that bone can be lost quite differently, the results are displayed in subgroups: main loss in trabecular bone (triangles), main loss in cortical bone (squares), loss in trabecular as well as in cortical bone (circles). The fourth group shows the women with no significant bone loss. (From Laib, A. et al., *Technol. Health Care,* 6, 329, 1998. With permission.)

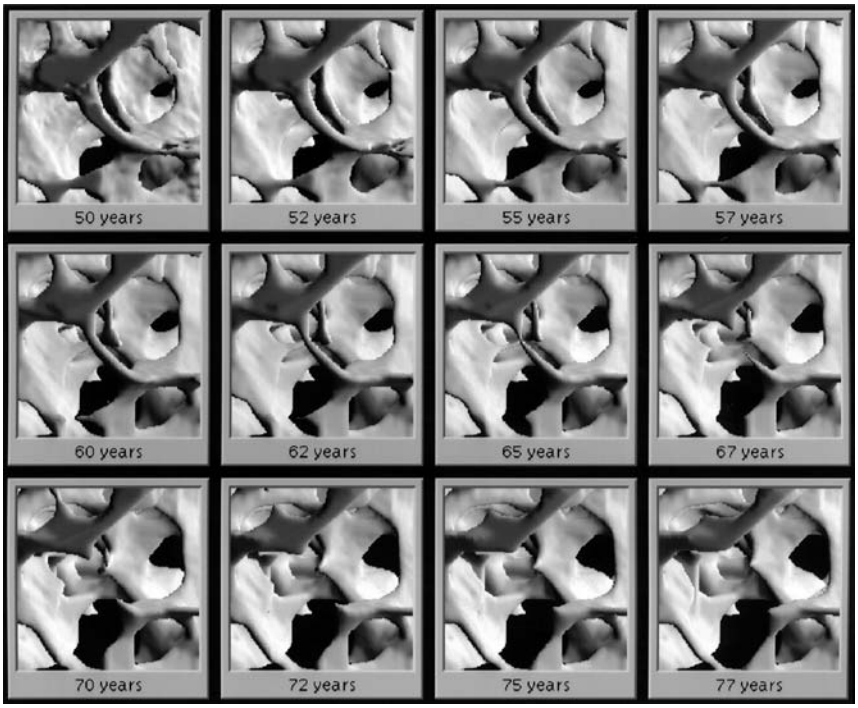

FIGURE 9.22 Simulated bone loss. The simulation starts at age 50 and covers 27 years. The rods forming the trabecular network are more and more thinned until they are perforated, and then they vanish quickly, leaving the structure less well connected. (From Müller, R. and Hayes, W.C., *Proc. SPIE,* 3149, 69, 1997. With permission.)

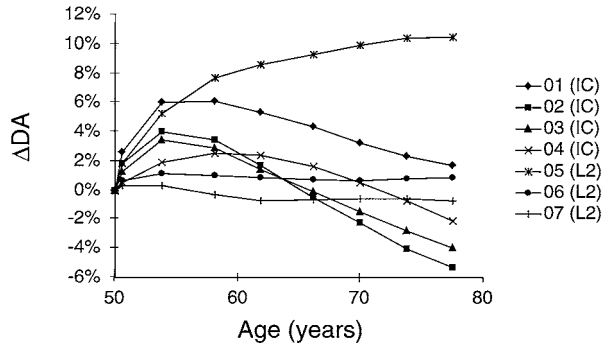

FIGURE 9.23 Relative changes in degree of anisotropy (DA) with respect to the simulated age for seven different bone samples. (From Müller, R. and Hayes, W.C., *Proc. SPIE,* 3149, 69, 1997. With permission.)

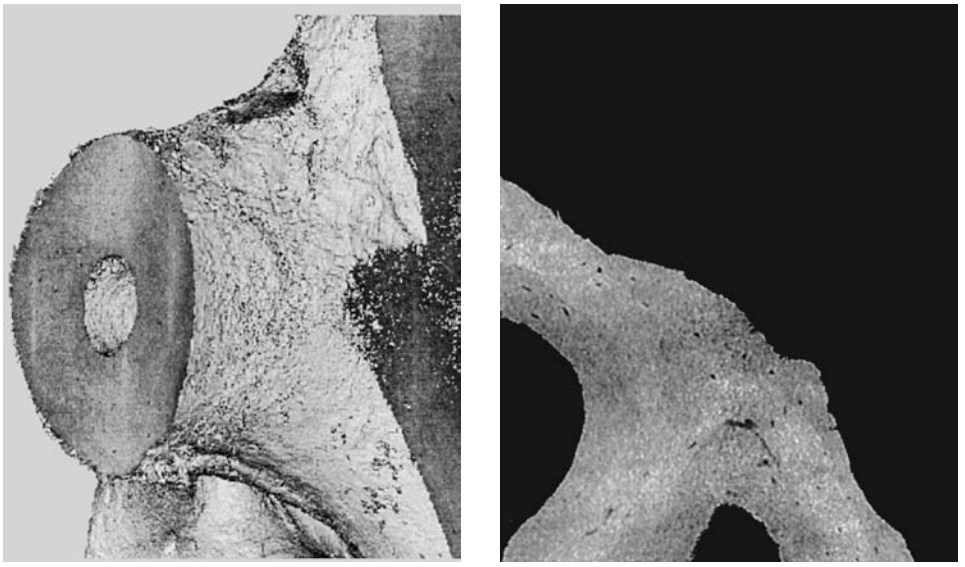

FIGURE 9.24 Synchrotron-CT images with a spatial resolution of 1.4 μm. Left: Cavity within a trabecula. Right: Section through the 3D image, showing some osteocytes. (Adapted from Peyrin, F. et al., *Technol. Health Care,* 6, 391, 1998. Courtesy of E. Ritman.)

References

1. Kanis, J.A., *Osteoporosis,* Blackwell Science Ltd., Oxford, 1994, chaps. 1 and 2.
2. Mundy, G.R., *Bone Remodeling and Its Disorders,* Martin Duniz Ltd., London, 1995, chap. 12.
3. Singh, M., Nagrath, A.R., and Malni, P.S., Changes in trabecular pattern of the upper end of the femur as an index of osteoporosis, *J. Bone Joint Surg.,* 52A, 457, 1970.
4. Wickham, C.A.C., Walsh, K., and Cooper, C., Dietary calcium, physical activity and risk of hip fracture: a prospective study, *BMJ,* 299, 889, 1989.
5. Geraets, W.G.M., Van der Stelt, P.F., Netelenbos, C.J., and Elders, P.J.M., A new method for automatic recognition of the radiographic trabecular pattern, *J. Bone Miner. Res.,* 5, 227, 1990.
6. Benhamou, C.L., Harba, R., Lespessailles, E., Jacquet, G., Toulière, D., and Jennane, R., Changes in fractal evaluation of trabecular bone in osteoporosis: a preliminary study, in *Fractals in Biology and Medicine,* Birkäuser, Basel, 1993, 292.

7. Cortet, B., Colin, D., Dubois, P., Delcambre, B., and Marchandise, X., Methods for quantitative analysis of trabecular bone structure, *Rev. Rhum.,* 62, 781, 1995.
8. Fidouh, F., Harba, R., Jacquet, G., Loussot, T., and Lespessailles, E., Long-term reproducibility optimization of an X-ray process for bone architectural evaluation during osteoporosis, *Phys. Med. Biol.,* 44, N1, 1999.
9. Mosekilde, L., Vertebral structure and strength *in vivo* and *in vitro, Calcif. Tissue Int.,* 53(Suppl. 1), 121, 1993.
10. Ritzel, H. and Amling, M., The thickness of human vertebral cortical bone and its changes in ageing and osteoporosis: a histomorphometric analysis of the complete spinal column from thirty-seven autopsy cases, *J. Bone Miner. Res.,* 12, 89, 1997.
11. Prevrhal, S., Engelke, K., and Kalender, W.A., Accuracy limits for the determination of cortical width and density: the influence of object size and CT imaging parameters, *Phys. Med. Biol.,* 44, 751, 1999.
12. Faridani, A., Ritman, E.L., and Smith, K.T., Local tomography, *SIAM J. Appl. Math.,* 51, 459, 1992.
13. Ritman, E.L., Dunsmuir, J.H., Faridani, A., Finch, D.V., Smith, K.T., and Thomas, P.J., Local reconstruction applied to x-ray microtomography, in *IMA Volumes in Mathematics and Its Applications, Inverse Problems in Wave Propagation,* vol. 90, Chavent, G., Papanicolaou, G., Sacks, P., and Symes,W., Eds., Springer Verlag, New York, 1997, 443.
14. Laib, A. and Rüegsegger, P., Local X-ray tomography for *in vivo* bone structure examinations, *Med. Phys.,* 26, 447, 1999.
15. Wehrli, F.W., Hwang, S.N., and Song, H.K., New architectural parameters derived from micro-MRI for the prediction of trabecular bone strength, *Technol. Health Care,* 6, 307, 1998.
16. Kalender, W.A., Principles and performance of spiral CT, in *Medical CT and Ultrasound: Current Technology and Applications,* Goldman, L.W. and Fowlkes, J.B., Eds., Advanced Medical Publishing, Madison, 379, 1995.
17. Kalender, W.A., Engelke, K., and Schaller, S., Spiral CT: medical use and potential industrial applications, *Proc. SPIE,* 3149, 188, 1997.
18. Kohlbrenner, A. and Rüegsegger, P., A high-speed 3D-pQCT system for structure analysis, *Osteoporosis Int.* 7, 268, 1997.
19. Laib, A., Häuselmann, H.J., and Rüegsegger, P., *In vivo* high resolution 3D-QCT of the human forearm, *Technol. Health Care,* 6, 329, 1998.
20. Müller, R., Koller, B., Hildebrand, T., Laib, A., Gianolini, S., and Rüegsegger, P., Resolution dependency of microstructural properties of cancellous bone based on three-dimensional micro-tomography, *Technol. Health Care,* 4, 113, 1996.
21. Laib, A. and Rüegsegger, P., Calibration of trabecular bone structure measurements of *in vivo* three-dimensional peripheral quantitative computed tomography with 28-μm-resolution microcomputed tomography, *Bone,* 24, 35, 1999.
22. Feldkamp, L.A., Goldstein, S.A., Parfitt, A.M., Jesion, G., and Kleerekoper, M., The direct examination of three-dimensional bone architecture *in vitro* by computed tomography, *J. Bone Miner. Res.,* 4, 3, 1989.
23. Rüegsegger, P., Koller, B., and Müller, R., A microtomographic system for the nondestructive evaluation of bone architecture, *Calcif. Tissue Int.,* 58, 24, 1996.
24. Kohlbrenner, A., Hämmerle, S., Laib, A., and Rüegsegger, P., A 3D microtomographic system with stacked fan beam geometry, *Nucl. Instrum. Meth.,* A433, 531, 2000.
25. Kinney, J.H., Ryaby, J.T., Haupt, D.L., and Lane, N.E., Three-dimensional *in vivo* morphometry of trabecular bone in the OVX rat model of osteoporosis, *Technol. Health Care,* 6, 339, 1998.
26. Kinney, J.H. and Nichols, M.C., X-ray tomographic microscopy (XTM) using synchrotron radiation, *Annu. Rev. Mater. Sci.,* 22, 121, 1992.
27. Bonse, U. and Busch, F., X-ray computed microtomography using synchrotron radiation, *Prog. Biophys. Mol. Biol.,* 65, 133, 1996.

28. Bonse, U., Busch, F., Günnewig, O., Beckmann, F., Pahl, R., Delling, G., Hahn, M., and Graeff, W., 3D computed X-ray tomography of human cancellous bone at 8 μm spatial and 10^{-4} energy resolution, *Bone Miner.,* 25, 25, 1994.
29. Hayes, C.E., Edelstein, W.A., and Schenk, J.F., Radio frequency coils, in *NMR in Medicine: The Instrumentation and Clinical Applications,* Thomas, S.R. and Dixon, R.L., Eds., American Institute of Physics, New York 1985, 142.
30. Jara, H., Wehrli, F.W., Chung, H., and Ford, J.C., High-resolution variable flip angle 3D MR imaging of trabecular microstructure *in vivo, Magn. Reson. Med.,* 29, 528, 1993.
31. Kapadia, R.D., High, W.B., Soulleveld, H.A., Bertolini, D., and Sarkar, S.K., Magnetic resonance microscopy in rat skeletal research, *Magn. Reson. Med.,* 30, 247, 1993.
32. Wehrli, F.W., Ford, J.C., Chung, H.W., Wehrli, S.L., Williams, J.L., Grimm, M.J., Kugelmass, S.D., and Jara, H., Potential role of nuclear magnetic resonance for the evaluation of trabecular bone quality, *Calcif. Tissue Int.,* 53, S162, 1993.
33. Hipp, J.A., Jansujwicz, A., Simmons, C.A., and Snyder, B.D., Trabecular bone morphology from micro-magnetic resonance imaging, *J. Bone Miner. Res.,* 11, 286, 1996.
34. Wu, Z., Chung, H.W., and Wehrli, F.W., A bayesian approach to subvoxel tissue classification in NMR microscopic images of trabecular bone, *Magn. Reson. Med.,* 31, 302, 1994.
35. Zhou, X. and Lauterbur, P.C., NMR microscopy using projection-reconstruction, in *Magnetic Resonance Microscopy,* Blümich, B. and Kuhn, W., Eds., VCH Publishers, New York, 1992, 3.
36. Chung, H., Wehrli, F.W., Williams, J.L., and Wehrli, S.L., Three-dimensional nuclear magnetic resonance microimaging of trabecular bone, *J. Bone Miner. Res.,* 10, 1452, 1995.
37. Chung, H., Wehrli, F.W., Williams, J.L., Kugelmass, S.D., and Wehrli, S.L., Quantitative analysis of trabecular microstructure by 400 MHz nuclear magnetic resonance imaging, *J. Bone Miner. Res.,* 10, 803, 1995.
38. Hwang, S.N. and Wehrli, F.W., Probability-based structural parameters from three-dimensional nuclear magnetic resonance images as predictors of trabecular bone strength, *Med. Phys.,* 24, 1255, 1997.
39. Majumdar, S., Genant, H.K., Grampp, S., Newitt, D.C., Truong, V.H., Lin, J.C., and Mathur, A., Correlation of trabecular bone structure with age, bone mineral density, and osteoporotic status: *in vivo* studies in the distal radius using high resolution magnetic resonance imaging, *J. Bone Miner. Res.,* 12, 111, 1997.
40. Link, T.M., Majumdar, S., Augat, P., Lin, J.C., Newitt, D., Lu, Y., Lane, N.E., and Genant, H.K., *In vivo* high resolution MRI of the calcaneus: differences in trabecular structure in osteoporosis patients, *J. Bone Miner. Res.,* 13, 1175, 1998.
41. Laib, A. and Rüegsegger, P., Comparison of structure extraction methods for *in vivo* trabecular bone measurements, *Comput. Med. Imag. Graphics,* 23, 69, 1999.
42. Hildebrand, T. and Rüegsegger, P., A new method for the model independent assessment of thickness in three-dimensional images, *J. Microsc.,* 185, 67, 1997.
43. Parfitt, A.M., Mathews, C.H.E., Villanueva, A.R., Kleerekoper, M., Frame, B., and Rao, D.S., Relationship between surface, volume, and thickness of iliac trabecular bone in ageing and in osteoporosis, *Calcif. Tissue Int.,* 72, 1396, 1983.
44. Parfitt, A.M., Drezner, M.K., Glorieux, F.H., Kanis, F.H., Malluche, H., Meunier, P.J., Ott, S.M., and Recker, R.R., Bone histomorphometry: standardization of nomenclature, symbols and units, report of the ASBMR histomorphometry nomenclature committee, *J. Bone Miner. Res.,* 21, 595, 1987.
45. Ulrich, D., Van Rietbergen, B., Laib, A., and Rüegsegger, P., Load transfer analysis of the distal radius from *in vivo* high-resolution CT-imaging, *J. Biomech.,* 32, 821, 1999.
46. Guilak, F., Volume and surface area of viable chondrocytes in situ using geometric modelling of serial confocal sections, *J. Microsc.,* 173, 245, 1994.
47. Lorensen, W.E. and Cline, H.E., Marching cubes: a high resolution 3D surface construction algorithm, *Comput. Graphics,* 21, 163, 1987.

48. Odgaard, A. and Gundersen, H.J.G., Quantification of connectivity in cancellous bone, with special emphasis on 3-D reconstructions, *Bone,* 14, 173, 1993.
49. Harrigan, T.P. and Mann, R.W., Characterization of microstructural anisotropy in orthotropic materials using a second rank tensor, *J. Mater. Sci.,* 19, 761, 1984.
50. Cowin, S.C., The relationship between the elasticity tensor and the fabric tensor, *Mech. Mater.,* 4, 137, 1985.
51. Hildebrand, T. and Rüegsegger, P., Quantification of bone microarchitecture with the structure model index, *Comp. Methods Biomech. Biomed. Eng.,* 1, 15, 1997.
52. Weinstein, R.S., Majumdar, S., and Genant, H.K., Fractal geometry applied to the architecture of cancellous bone biopsy specimens, *Bone,* 13, A38, 1992.
53. Cross, S.S., Rogers, S., Silcocks, P.B., and Cotton, D.W.K., Trabecular bone does not have a fractal structure on light microscopy, *J. Pathol.,* 170, 311, 1993.
54. Chung, H.W., Chu, C.C., Underweiser, M., and Wehrli, F.W., On fractal dimension of trabecular structure, *Med. Phys.,* 21, 1535, 1994.
55. Majumdar, S., Weinstein, R.S., and Prasad, R.R., Application of fractal geometry techniques to the study of trabecular bone, *Med. Phys.,* 20, 1611, 1993.
56. Odgaard, A., Three-dimensional methods for quantification of cancellous bone architecture, *Bone,* 20, 315, 1997.
57. Müller, R., Hildebrand, T., and Rüegsegger, P., Non-invasive bone biopsy: a new method to analyse and display the three-dimensional structure of trabecular bone, *Phys. Med. Biol.,* 39, 145, 1994.
58. Kinney, J.H. and Ladd, A.J.C., The relationship between three-dimensional connectivity and the elastic properties of trabecular bone, *J. Bone Miner. Res.,* 13, 839, 1998.
59. Garrahan, N.J., Mellish, R.W.E., and Compston, J.E., A new method for the two-dimensional analysis of bone structure in human iliac crest biopsies, *J. Microsc.,* 142, 341, 1986.
60. Stampa, B., Kühl, B., Heller, M., and Glüer, C.C., Rods or plates: a new algorithm to characterize bone structure using 3D magnetic resonance imaging, *Osteoporosis Int.,* 8, 503, 1998.
61. Müller, R., Van Campenhout, H., Van Damme, B., Van der Perre, G., Dequeker, J., Hildebrand, T., and Rüegsegger, P., Morphometric analysis of human bone biopsies: a quantitative structural comparison of histological sections and micro-computed tomography, *Bone,* 23, 59, 1998.
62. Schenk, R.K. and Olah, A.J., Histomorphometrie, in *Handbuch der inneren Medizin VI/1A, Knochen Gelenke Muskeln,* Kuhlencordt, F. and Bartelsheimer, H., Eds., Springer Verlag, Berlin, 1980, 437.
63. Hildebrand, T., Laib, A., Müller, R., Dequeker, J., and Rüegsegger, P., Direct 3-D morphometric analysis of human cancellous bone: microstructural data from spine, femur, iliac crest, and calcaneus, *J. Bone Miner. Res.,* 14, 1167, 1999.
64. Kapadia, R.D., Stroup, G.B., Badger, A.M., Koller, B., Levin, J.M., Coatney, R.W., Dodds, R.A., Liang, X., Lark, M.W., and Gowen, M., Applications of micro-CT and MR microscopy to study pre-clinical models of osteoporosis and osteoarthritis, *Technol. Health Care,* 6, 361, 1998.
65. Beamer, W.G., Donahue, L.R., Rosen, C.J., and Baylink, D.J., Genetic variability in adult bone density among inbred strains of mice, *Bone,* 18, 397, 1996.
66. Kinney, J.H., Lane, N.E., and Haupt, E.L., *In vivo*, three-dimensional microscopy of trabecular bone, *J. Bone Miner. Res.,* 10, 264, 1995.
67. Hoshen, J. and Kopelman, R., Percolation and cluster distribution. I. Cluster multiple labeling technique and critical concentration algorithm, *Phys. Rev. B,* 15, 3438, 1976.
68. Gordon, C.L., Webber, C.E., Christoforou, N., and Nahmias, C., *In vivo* assessment of trabecular bone structure at the distal radius from high-resolution magnetic resonance images, *Med. Phys.,* 24, 585, 1997.
69. Wehrli, F.W., Hwang, S.N., Ma, J., Song, H.K., Ford, J.C., and Haddad, J.G., Noninvasive assessment of cancellous bone volume and structure in the forearm by magnetic resonance microimaging and image processing, *Radiology,* 206, 347, 1998.

70. Kuehn, B., Stampa, B., Heller, M., and Glueer, C., *In vivo* assessment of trabecular bone structure of the human phalanges using high resolution magnetic resonance imaging, *Osteoporos Int.,* 7, 291, 1997.
71. Müller, R. and Hayes, W.C., Biomechanical competence of microstructural bone in the progress of adaptive bone remodeling, *Proc. SPIE,* 3149, 69, 1997.
72. Frost, H.M., *The Laws of Bone Structure,* Charles C Thomas, Springfield, IL, 1964.
73. Leblond, C.P., Willimson, G.W., Bilanger, L.F., and Robichon, J., Radioautographic visualization of bone formation in the rat, *Am. J. Anat.,* 86, 289, 1950.
74. Ritman, E.L., Bolander, M.E., Fitzpatrick, L.A., and Turner, R.T., Micro-CT imaging of structure-to-function relationship of bone microstructure and associated vascular involvement, *Technol. Health Care,* 6, 403, 1998.
75. Peyrin, R., Salome, M., Cloettens, P., Laval-Jeantet, A.M., Ritman, E., and Rüegsegger, P., Micro-CT examinations of trabecular bone samples at different resolutions: 14, 7, and 2 micron level, *Technol. Health Care,* 6, 391, 1998.

III

Mechanical and Architectural Properties of Bone

10

Mechanical Properties of Cortical Bone and Cancellous Bone Tissue

X. Edward Guo
Columbia University

10.1 Introduction

Age-related bone fractures impose a significant social and economic problem on our increasingly aging population. In the United States alone, hundreds of thousands of age-related hip, spine, and wrist fractures cost more than $7 billion each year.[1] Understanding the underlying mechanisms of those devastating fractures may help to generate strategies for prevention and treatment. As a result of recent data, it has been generally accepted that osteoporosis manifests not only in reduced bone mass but also in altered bone quality.[2] Therefore, quantification of bone tissue mechanical quality is important in delineating the underlying mechanisms of many metabolic bone diseases. In addition, bone tissue may constantly undergo adaptational changes in response to local alterations in mechanical conditions. These adaptational processes are very important in the pathogenesis of age-related bone fragility and success of artificial joint replacement. Quantification of bone tissue properties is prerequisite to characterizing the mechanical environment in which bone cells reside. Finally, predictive models for bone fracture require complete and accurate input of bone tissue properties.

In this chapter, the mechanical properties of both cortical and cancellous bone tissues will be reviewed. Mechanical properties of cortical bone tissue, a relatively uniform bone tissue type, have been well quantified using a variety of mechanical testing techniques such as discussed in Chapter 7. In parallel, the continuum mechanical properties of cancellous bone have been studied extensively and are reviewed in later chapters (Chapters 13 through 15). In this chapter, the focus will be on the mechanical properties of the hard bone tissue that makes up the two microscopically distinct bone types: cortical bone and cancellous bone. Special emphasis will be on the technique and results of quantification of mechanical properties of individual trabeculae (the basic microstructural units of cancellous bone). Despite numerous research efforts, controversy remains regarding whether cancellous bone tissue has the same mechanical properties as cortical bone tissue.

In this chapter, the experimental techniques to measure mechanical properties of cortical bone and cancellous bone tissue will be reviewed and their mechanical properties will be compared. The underlying microstructural features and compositional differences between these two bone tissues will be examined and compared to reconcile the differences in mechanical properties.

10.2 Microstructural and Morphological Differences

Cortical bone is a solid, compact tissue constituting the diaphyses of long bones and outer shell of the metaphyses (Fig. 10.1; Table 10.1). At a tissue level, human cortical bone consists of secondary osteons (100 to 300 μm in diameter) surrounding Haversian canals and embedded in interstitial tissue, which is the remnant of old osteons.[3] The osteons are separated from the interstitial bone tissue by a thin layer of amorphous substance deficient in collagen, called a cement line (0.5 to 1 μm).[4] Each osteon is made of concentric lamellae (1 to 5 μm thick),[5] among which the bone cells (osteocytes) reside inside ellipsoidal spaces called lacuna (10 to 50 μm). The secondary osteons are formed as the consequence of a continuous remodeling process in which old bone is replaced by new bone. The remodeling occurs at scattered locations on the bone surface. In cortical bone, remodeling is achieved through resorption (by tunneling osteoclasts) of old osteons forming cavities followed by a short period of quiescence (reversal). Next, bone-forming cells (osteoblasts) begin to refill the cavities with new bone in a concentric lamellar pattern. The boundary layer between old bone and new bone formed following the reversal is defined as a cement line. During formation, the osteoblasts first synthesize an extracellular matrix composed of collagen and other structural proteins (osteoid). Next, the osteoid is mineralized. Primary mineralization increases mineral

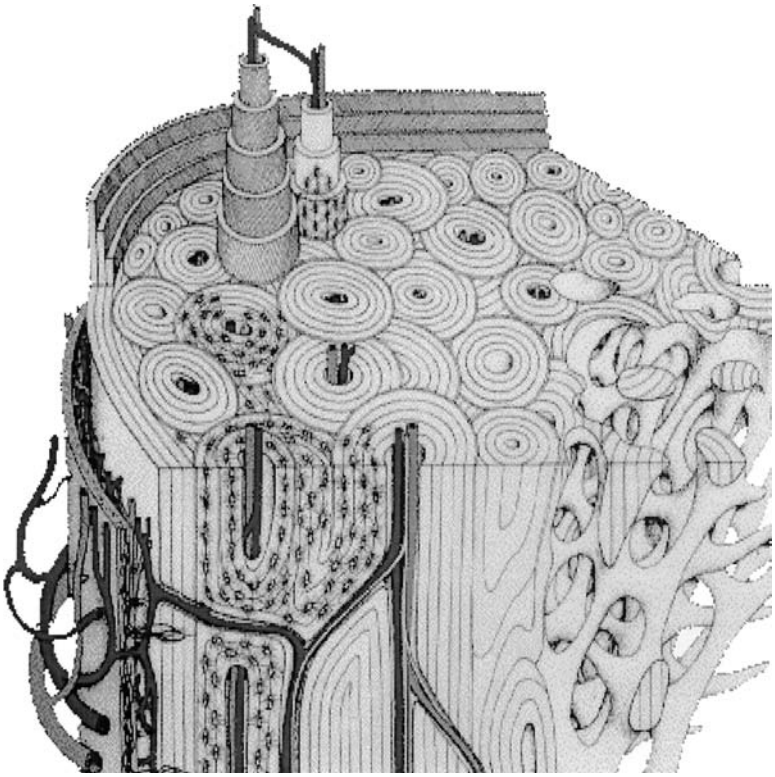

FIGURE 10.1 Schematic drawing showing microstructure of cortical and cancellous bone. (From Einhorn, T. A., Azria, M., and Goldstein, S. A., *Bone Fragility/The Biomechanics of Normal and Pathologic Bone,* Sandoz, Basel, Switzerland, 1994. With permission.)

TABLE 10.1 Microstructural and Histological Features of Cancellous and Cortical Bone Tissue

Features	Cancellous Tissue	Cortical Tissue
Microstructural	Trabecular thickness, 100–640 μm (osteon exits when thickness $>$ 350 μm)	Osteon diameter, 100–300 μm
Cement Lines	More cement lines in cancellous tissue[98]	
Lamellar thickness	1–5 μm[5]	1–5 μm[14]
	52 μm^2, 577/mm^2 [23]	30–40 μm^2, 460/mm^2 [19–23]
	38 μm^2, 245/mm^2 [24]	
	55 μm^2, 156/mm^2 (present study)	53 μm^2, 155/mm^2 (present study)
Lacunae size and distribution	294–942/mm^2 [25]	

density of the bone to about 70% of maximum in the first few days while secondary mineralization gradually increases the density to 90 to 95% of maximum after several months. As a result, recently remodeled bone tissue is usually less highly mineralized than unremodeled tissue.

While the macroscopic structure of cancellous bone is composed of an interconnected series of rods and plates (see Fig. 10.1), cancellous tissue, in general, lacks osteonal structure and consists of a mosaic of angular segments of parallel sheets of lamellae preferentially aligned with the orientation of the trabeculae. The angular groupings of lamellae, separated by cement lines, are called trabecular packets. Unlike cortical bone, which proceeds by tunneling activities of the cutting cone osteoclasts, cancellous remodeling occurs on a bone surface by directly removing old bone and then filling in the cavities with new bone (trabecular packet). Because of a high surface-to-volume ratio, cancellous bone remodeling is more active than cortical bone (26% turnover rate in cancellous bone vs. 3% in cortical bone[6]). In some transitional regions of cancellous bone, such as the calcaneus, the mastoid and the medial aspect of the proximal femur, osteons do exist in the trabeculae when the thickness of trabeculae is greater than 350 μm. These osteons have similar features to those in cortical bone, such as concentric lamellae around the Haversian canals.[7–9] These observations suggest that formation of osteons (bone lamellae formed around vascular channels) is a specific structural response to nutrient requirements. At the scale of lamellae, however, it would be reasonable to hypothesize that cancellous and cortical bone tissues should have similar properties.

There has been a significant amount of research on cortical bone tissue microstructure. The traditional concepts regarding the lamellar structure of cortical bone are that osteons are made of concentric layers of lamellae. In each lamella, all collagen fibers run in the same direction. Therefore, osteons can be classified into longitudinal, transverse, or alternating types according to the orientation of collagen fibers in the lamellae.[10–12] More recent studies, however, challenge those hypotheses, suggesting that the difference between layers of lamellae may be due to the difference between loose and dense collagen organization.[5] The thickness of lamellae ranges between 1 and 5 μm in cortical bone.[5] Most histomorphometric studies on cancellous bone have been focused on the characteristics of cancellous bone architecture, such as trabecular thickness, spacing, and orientation. Few studies have addressed the microstructural morphology of trabeculae.[13,14] The measurement of lamellar thickness in iliac cancellous bone shows similar results as in cortical bone tissue (1 to 4 μm).[14] Well-controlled and parallel studies on both cancellous and cortical bone tissue morphology are not available and therefore potential differences have not been statistically tested. Preliminary results suggest that there may be very little difference in terms of lamellar thickness. However, experimental and analytical studies of cortical bone[15–18] indicate the importance of collagen and mineral orientation (or lamellar organization and orientation) on bone tissue modulus. Clearly, it would be very valuable to compare the organization of collagen fibers in cancellous and cortical lamellae.

Another important feature in bone microstructure is the size and distribution of lacunae, which may influence stiffness and other mechanical properties (see Table 10.1). Several studies on the size and distribution of lacunae in cortical bone have reported an average area of 30 to 40 μm^2 and density of 460/mm^2.[19–23] The only available study comparing cortical bone and cancellous tissue (in dogs) indicates that cancellous tissue has more lacunae (577/mm^2) with larger sizes (52 μm^2), which would suggest that the cancellous tissue should be less stiff than cortical tissue.[23] A recent study on human vertebral cancellous

tissue suggests the mean size of lacunae is 38 μm^2 and the density is 245/mm^2.[24] In a recent detailed study osteocyte density and histomorphometric parameters were measured in cancellous bone tissue for a variety of animal species.[25] The lacuna densities were reported ranging from 294/mm^2 in cows to 942/mm^2 in rats. Recently, the author measured the size and density of lacunae in human vertebral trabeculae (55 μm^2, 156/mm^2) and vertebral cortical shell (53 μm^2, 155/mm^2) and found no statistically significant difference. It should be noted, however, that the volume fraction of lacunae is small (1 to 3%[23] and 0.2 to 2.2%, unpublished recent measurements), and how much influence these voids have on tissue modulus is unknown. Therefore, direct comparison of mechanical and morphological data for human cortical and cancellous tissue would be very helpful to identify the importance of lacunae on bone tissue properties.

Cement lines exist in both cancellous and cortical bone tissues. Schaffler and co-workers[4,26] reported that the cement lines in human cortical bone have lower calcium and phosphorus concentrations than adjacent bone, thus providing a compliant interface. Due to more active bone remodeling in cancellous bone, it is possible that there is more cement line in cancellous bone tissue than in cortical bone tissue. The existence of more extensive cement lines in cancellous tissue could influence its mechanical properties.

10.3 Compositional Differences

Each lamella in both cortical and cancellous bone tissues consists mostly of collagen and mineral in the form of hydroxyapatite crystals. The mechanical properties of bone tissues depend on the mineral and collagen compositions.[16] It has been shown that hydroxyapatite contributes significantly to the stiffness of cortical bone tissue while the collagen content governs the post-yield ductility.[27–30] Many studies have quantified cortical bone tissue composition in terms of tissue density, ash density, etc.[31–33] Recently, a quantitative mineral density method using calibrated back-scattered electron microscopy has been used to characterize local and age variations in cortical bone tissue mineralization.[34,35] It has not been applied to cancellous tissue. The few studies addressing the compositional differences in cancellous and cortical bone tissue indicate conflicting results (Table 10.2). The cancellous bone tissue has significantly lower calcium content than cortical bone tissue, although they have same phosphorus content.[36] Early work by Gong et al.[37] showed that cancellous tissue has slightly lower tissue density (1.874 g/cc) and ash fraction (33.9%) than cortical bone tissue (1.914 g/cc and 37.7%, respectively). This is consistent with a study in beagles showing cortical bone had slightly (marginally statistically significant) higher tissue density than cancellous tissue.[38] Consistent with the lower ash content, cancellous tissue has significantly higher water content (27% of volume for cancellous tissue and 23% for cortical tissue). These results are consistent with the fact that cancellous bone is more active in remodeling and freshly remodeled bone is less highly mineralized. In contrast to these studies, the relative mineral content measurements from micro-computed tomography (micro-CT) indicate that cancellous tissue has significantly higher mineral content (0.34 gray scale/area) than cortical bone tissue (0.29 gray scale/area).[39] This inconsistency could be partly explained by the remodeling characteristics along with the specimen preparation in their study, as the less-mineralized surface cancellous bone tissue was removed during the machining process. This further suggests that the nonhomogeneous distribution of material in the tissue may be important.

TABLE 10.2 Compositions of Cancellous and Cortical Bone Tissue

Properties	Cancellous Tissue	Cortical Tissue
Calcium content (mg/g)[63]	234	261 (deer)
	257	271 (bovine)
Calcium (% of ash weight)[36]	34.4	38.5 (human)
Phosphorus content (% of ash weight)[36]	18.1	17.9 (human)
Water (% volume)[37]	27.0	22.9 (human)
	28.8	22.3 (dog)
Tissue density (g/cc)[37,38]	1.874	1.914 (human)
	1.908	2.006 (dog)
Ash fraction (% volume)[37]	33.9	37.7 (human)
Mineralization (gray scale/mm^2)[39,97,98]	0.34	0.29 (human, tibia)

10.4 Mechanical Properties of Cortical and Cancellous Bone Tissue

10.4.1 Mechanical Properties of Cortical Bone

Mechanical properties of cortical bone have been well documented. Traditional mechanical testing techniques such as uniaxial tensile or compressive testing and three-point or four-point bending can be routinely used for measuring mechanical properties of cortical bone. These experimental techniques have been reviewed in Chapter 7 and will not be discussed here.

One useful method in measuring elastic properties of cortical bone is ultrasonic technique. The ultrasonic technique makes use of piezoelectric transducers applied directly to the bone specimens to transmit and receive an elastic wave.[40–59] The elastic properties can be deduced from velocity measurements of shear and longitudinal waves propagating in particular directions in the bone specimen. The elastic modulus E has a simple relation with the acoustic velocity v,

$$E = \rho v^2, \tag{10.1}$$

where ρ is the density of the material. The plane wave requirement of the application of this equation is that the wavelength of the ultrasonic wave be greater than the cross-sectional dimension of the specimen. In addition, the wavelength must also be larger than the characteristic dimension of the structure (such as the diameter of an osteon), in order for an ultrasonic wave to propagate at the velocity governed by the elasticity of gross structure. The advantage of ultrasonic method is that the fully anisotropic elastic properties of bone tissue can be determined in a same specimen by propagating ultrasonic waves along different direction of the specimen.

Microindentation tests have long been used to characterize the microhardness of bone tissue.[60–66] Microhardness H is determined by measuring the size of the impression A made by a diamond indenter, which is pressed into the tissue surface with a small known load P_{max}:

$$H = \frac{P_{max}}{A}. \tag{10.2}$$

Even though hardness is related quite closely to yield stress in plastic materials such as metals, the hardness of biological tissues such as bone is less defined. Both elastic and yield properties contribute to the hardness measurements. Therefore, it is difficult to infer only elastic properties such as elastic modulus from the hardness measurements. Direct measurements of elastic modulus in an indentation experiment have become available through the emergence of the depth-sensing indentation techniques and analytic methods for extracting the elastic modulus from the associated load-displacement data.[67,68] Within the past 10 years, a nanoindentation technique has been developed that is capable of measuring load at a resolution of 0.3 μN and displacement at 0.16 nm.[67,68] In addition, this system also provides submicron spatial resolution. The technique uses a diamond indenter to load and unload a material specimen leaving a permanent indent on the surface. Traditional hardness measurement can also be determined from the peak load and the corresponding contact area (Eq. 10.2). Doerner and Nix[67] pioneered indentation measurements of Young's modulus recognizing that the initial portion of the unloading curve is linear elastic for a variety of materials and can be modeled as an elastic punch indenting an elastic half space. The technique was then improved to address the nonlinear nature of unloading load-displacement curve for nonflat indenters.[68] This system may be a powerful tool to measure material properties such as microhardness and especially elastic modulus at the microstructural level. A typical indentation experiment results in a loading and unloading curve as shown in Fig. 10.2. The unloading data are then analyzed according to a model for the deformation of an elastic half space by rigid, axisymmetric punch derived by Sneddon.[69] The mathematical solution was adapted for the

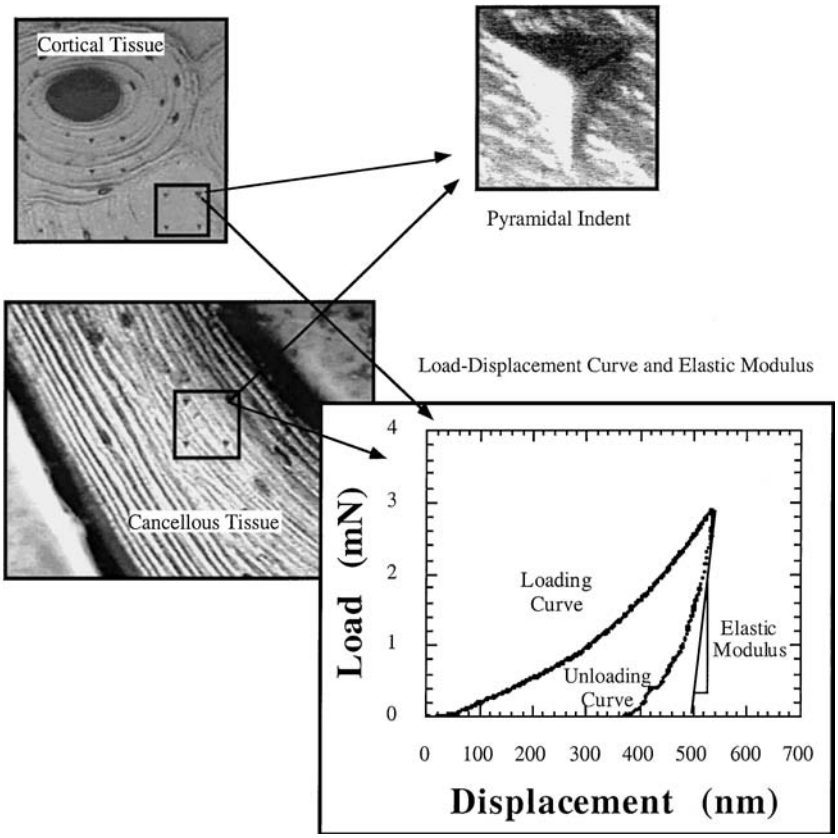

FIGURE 10.2 Nanoindentation technique for bone tissue elastic modulus measurements.

nanoindenter by Oliver and Pharr, and others.[68,70,71] The unloading stiffness S is related to the reduced modulus E_r by

$$S = \frac{dP}{dh} = \beta \frac{2}{\sqrt{\pi}} E_r \sqrt{A}, \tag{10.3}$$

where A is the projected area of contact (a function of the depth h) and β is an empirical shape factor. The reduced modulus accounts for using a nonrigid indenter and is determined by the following equation

$$\frac{1}{E_r} = \frac{(1-\nu_s^2)}{E_s} + \frac{(1-\nu_i^2)}{E_i}, \tag{10.4}$$

where E_s and ν_s are the sample modulus and Poisson's ratio, and E_i and ν_i are the indenter modulus and Poisson's ratio. In Eq. 10.4, the implicit assumption is that the sample is isotropic and the Poisson's ratio has to be assumed. The application of nanoindentation technique in measuring mechanical properties of bone tissue will be further discussed in the section of mechanical properties of cancellous bone tissue.

In general, cortical bone exhibits anisotropic elastic modulus in different anatomic directions (Table 10.3). For example, the elastic modulus in the longitudinal direction of long bone (17.4 GPa for human bone and 20.4 GPa for bovine bone) is larger than that in the transverse direction (9.6 GPa for human bone and 11.7 GPa for bovine bone). An orthotropic or transversely isotropic constitutive relation describes cortical bone elastic properties fairly well.

TABLE 10.3 Elastic Modulus of Cortical Bone Tissue

Elastic Modulus (GPa)	Human	Bovine
Longitudinal	17.4	20.4
Transverse	9.6	11.7
Bending	14.8	19.9
Shear	3.51	4.14

Source: Cowin, S.C., Ed., *Bone Mechanics,* CRC Press, Boca Raton, FL, 1988. With permission.

TABLE 10.4 Mechanical Properties of Osteons and Interstitial Bone Tissue in Cortical Bone*

Bone Tissue Type	Elastic Modulus (GPa)	Hardness (GPa)
Type L Osteon[a]		
Tension	11.7 ± 5.8	—
Compression	6.3 ± 1.8	—
Shear	3.3 ± 0.5	—
Type A Osteon[a] Tension		
Tension	5.5 ± 2.6	—
Compression	7.4 ± 1.6	—
Shear	4.1 ± 0.4	—
Type T Osteon[a]		—
Compression	9.3 ± 1.6	—
Shear	4.1 ± 0.3	
Osteon[b]	—	0.285
Interstitial	—	0.349
Osteon[c]	22.5	0.614
Interstitial	25.8	0.736
Osteon[d]	18.6	0.52
Interstitial	20.3	0.59

[a]From Refs. 10, 12, 72–83
[b]From Ref. 62.
[c]From Ref. 85.
[d]From Refs. 84, 86, 87.

Microscopic properties of osteons have been well documented from a series of remarkable research beginning in 1964 by Ascenzi, Bonucci, and their colleagues.[10,12,72–83] Ascenzi and Bonucci developed a technique for cutting cylindrical specimens from osteons contained in cross sections 500 μm thick. The specimens contained the Haversian canal and all but the outermost laminae of the osteon. Incremental dead loads were applied to the specimen and the deformation was recorded with a specially developed microwave extensometer to measure the extremely small deformation that occurred at this scale. The specimens were classified as longitudinal (type L), alternating (type A), or transverse (type T) according to the orientation of lamellae in the osteons. They reported elastic modulus in tension and compression, as well as in shear (Table 10.4). It is interesting that the moduli reported were generally lower than those at the continuum level. For example, 11.7 GPa elastic modulus was reported for longitudinal osteons in tension.

Mechanical properties of the interstitial bone tissue in cortical bone are limited. Using microhardness testing technique, Weaver[62] reported average hardness of osteons of 0.285 GPa, significantly less than that of the interstitial bone tissue 0.349 GPa. Recent data using nanoindentation confirmed his early results.[84–87] Rho et al.[85] reported average hardness of 0.614 GPa for osteons and 0.736 GPa for the interstitial bone tissue using dry specimens. In addition, elastic moduli were also measured in their study with 22.5 GPa for osteons and 25.8 GPa for the interstitial bone tissue. By using nanoindentation technique on wet cortical bone specimens,[84,86,87] elastic modulus and hardness were measured for osteons and the interstitial bone tissue (osteons: 18.6 GPa modulus and 0.52 GPa hardness; interstitial: 20.3 GPa modulus and 0.59 GPa hardness).

10.4.2 Mechanical Properties of Cancellous Bone Tissue

Measuring mechanical properties of cancellous bone tissue is far more difficult than measuring those properties of cortical bone tissue. The technical difficulties are due to the extremely small dimension of individual trabeculae in cancellous bone. More than a century ago, Wolff[88] speculated that the cancellous bone tissue modulus was similar to that of cortical bone and the apparent elastic modulus (modulus at the continuum level) differences could be contributed entirely to the difference in density. This view was shared by many others including Carter and Hayes,[32] who observed a cubic relationship between apparent elastic modulus and apparent density in cancellous bone and that the extrapolation to high-density range allowed cortical bone to be placed within the same relationship. Various direct methods have been used to determine the tissue modulus of individual trabeculae in the past 30 years. The reported cancellous bone tissue modulus has ranged from 0.76 to 20 GPa, fueling controversy concerning its measurement (Table 10.5).[89]

In this section of the chapter, the techniques and results of direct measurements of cancellous tissue modulus are examined and reviewed in detail. The most commonly used techniques for determining cancellous tissue modulus include: (1) buckling experiments of dissected, unmachined trabeculae;[90,91] (2) cantilever bending tests of unmachined trabeculae with finite-element corrections for specimen irregularity;[92] (3) uniaxial tensile test of unmachined trabeculae;[48,93] (4) ultrasonic measurements;[48,56,94–96] (5) three-point or four-point bending of machined trabeculae;[39,97,98] (6) back-calculation using two-dimensional or three-dimensional finite-element methods;[99–104] and (7) microindentation[62,63,105] and, most recently, nanoindentation.[84–87,96,105,106]

10.4.2.1 Elastic/Inelastic Buckling

Only a few studies used the buckling of single trabeculae to determine their modulus. This technique utilizes the classical Euler equation for elastic buckling of a beam:

$$\sigma_c = \frac{\pi^2}{K^2} E \left(\frac{L}{r}\right)^2, \tag{10.5}$$

where σ_c is the critical buckling stress determined from the experiments, K is a boundary condition constant, and L/r is the slenderness ratio of the specimen (Fig. 10.3). From the Euler formula, the modulus E can be determined from measuring critical buckling stress σ_c and the geometry of trabeculae. Runkle and Pugh[90] measured 8.69 GPa for dry trabeculae using this technique. When the slenderness ratio L/r is less than 100, inelastic buckling occurs and the apparent modulus determined would be less than the material modulus. By assuming a constant tissue modulus, Townsend et al.[91] established the relationship between buckling stress σ_c and the slenderness ratio L/r and extrapolated to an ideal slenderness ratio showing cancellous tissue modulus 11.38 GPa (wet) and 14.13 GPa (dry). There are several issues associated with this technique. First, it is difficult to measure accurately the dimension of unmachined trabeculae and the associated errors can be significant as the modulus is related to the square of the slenderness ratio L/r. Second, a constant modulus has to be assumed to deal with the inelastic buckling. Given the limitation of the method, it is interesting to note that the averaged modulus is about 11 GPa, 35% less than the typically reported cortical bone modulus (17 GPa), but of the same order of magnitude.

10.4.2.2 Uniaxial Tensile Testing

Several investigators designed delicate tensile testing systems to determine cancellous tissue modulus[48,93] (see Fig. 10.3). Significant technical difficulties are associated with tensile testing of small specimens. Alignment is critical to ensure a uniaxial state in determining tensile modulus but almost impossible to guarantee with irregular specimen geometry and small specimen size. In addition, irregular cancellous geometry makes it impossible to determine accurately the specimen dimensions. Ryan and Williams[93] reported very low cancellous modulus of 1.0 GPa. On the other hand, Rho et al.[48] obtained a cancellous modulus of 10 GPa and a cortical modulus of 18.6 GPa. Their cortical modulus value of 18.6 GPa from

TABLE 10.5 Mechanical Properties of Cancellous and Cortical Bone Tissue

Ref.	Bone Type	Testing Technique	Cancellous Tissue	Cortical Tissue
62	Human iliac crest	Microindentation	Hardness: Cancellous < Cortical	
99	Human distal femur	Finite-element model	Modulus: Cancellous < Cortical	
90	Human distal femur	Buckling	8.69 (3.17) GPa[a]	
91	Human proximal tibia	Inelastic buckling	11.38 GPa (wet), 14.13 GPa (dry)	
100	Human proximal tibia	Experiments and two-dimensional finite-element modeling	1.30 GPa	
101	Bovine femur Human tibia	Finite-element model	1.4–5.0 GPa	
94	Bovine femur Human femur	Ultrasonic method, bone cubes	10.9 (1.6) GPa 12.7 (2.0) GPa	
97	Human iliac crests	Three-point bending	3.81 GPa	4.89 GPa
92	Dry human femur Fresh human tibia	Cantilever bending with finite-element analysis	7.8 (5.4) GPa	
93	Bovine femur	Tensile testing	1.0 GPa	
126	Bovine tibia PMMA composites	Ultrasonic test extrapolation	8.9 GPa	
63	Bovine proximal femur	Microindentation	Hardness 43.4	Hardness 49.8
102	Human vertebra (L3)	Three-dimensional structure model	3.8 GPa	
39	Human tibia	Three-point bending	4.59 (1.60) GPa	5.44 (1.25) GPa
98	Human tibia	Four-point bending	5.72 (1.27) GPa	6.75 (1.00) GPa
48	Human tibia	Tensile test (dry) Ultrasonic test	10.4 (3.5) GPa 14.8 (1.4) GPa	18.6 (3.5) GPa 20.7 (1.9) GPa
54	Human vertebra	Scanning acoustic microscopy	Peak amplitude 68.88	Peak amplitude 71.68
105	Porcine femur	Microindentation Nanoindentation	5.9 (4.3) GPa 21.5 (2.1) GPa	11.6 (9.5) GPa 16.4 (1.3) GPa
85	Human vertebra Human tibia (osteon/interstitial)	Nanoindentation	13.4 (2.0) GPa	22.5 (1.3) GPa (osteon) 25.8 (0.7) GPa (interstitial)
96	Human femur	Nanoindentation (dry) Acoustic microscopy	18.14 (1.7) GPa 17.50 (1.12) GPa	20.02 (0.27) GPa 17.73 (0.22) GPa
86, 87	Human femur	Nanoindentation (wet)	11.4 (5.6) GPa (neck)	19.1 (5.4) GPa (diaphysis: osteon) 21.2 (5.3) GPa (diaphysis: interstitial) 15.8 (5.3) GPa (neck: osteon) 17.5 (5.3) GPa (neck: interstitial)
103	Human vertebra	Micro-CT image-based finite-element models	5.7 (1.6) GPa	
104	Human vertebra	X-ray tomographic microcopy image-based finite-element models	6.6 (1.1) GPa	
122	Bovine tibia	Serial-sectioning-based finite-element models	17.3 (2.62) GPa	
124	Human vertebra	Four-point bending	2.11 (1.89) GPa	2.50 (1.58) GPa

[a]Reported in mean (standard deviation when available).

microspecimens is very similar to the reported 17 GPa for the modulus of macroscopic cortical specimens, but their measurements may have been compromised by dehydration of the specimens and gluing the specimens to the tensile grips.

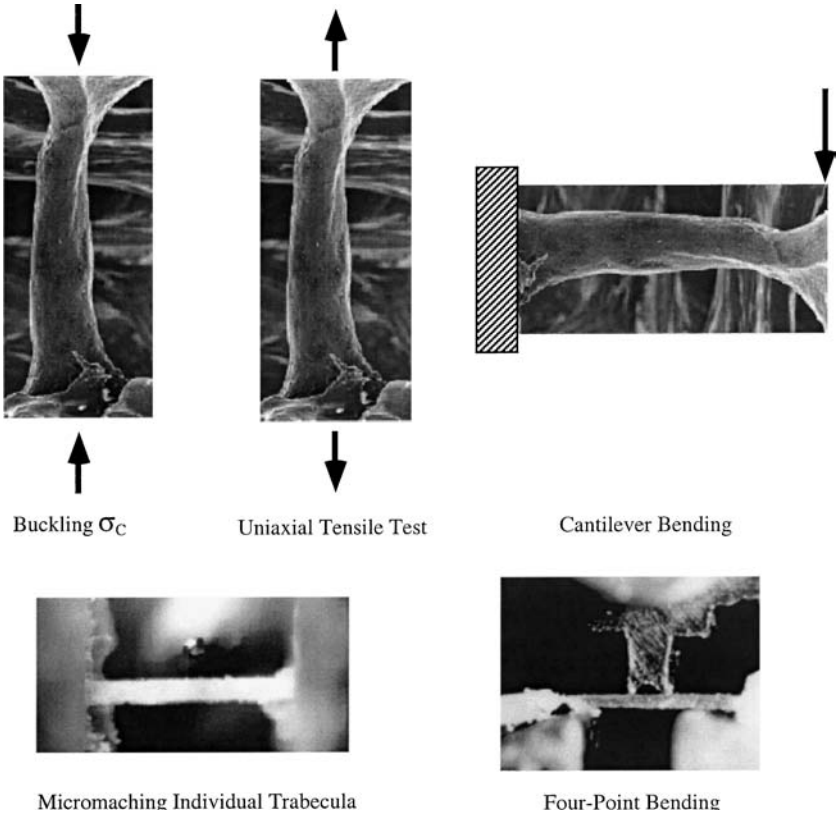

FIGURE 10.3 Microtesting techniques for measuring mechanical properties of cancellous bone tissue.

10.4.2.3 Bending Test

Bending tests have been used quite often to determine the cancellous tissue modulus (see Fig. 10.3). Advantages of a bending test include that (1) it is easy to implement and insensitive to specimen alignment; and (2) bending is an important physiological deformation mode of a trabecula. However, several concerns are raised regarding bending tests. First, anisotropy and heterogeneity of bone tissue causes complex nonlinear stress distributions and results in errors while applying a simple elastic bending formula. Second, the concentrated load at the loading head causes local stress disturbances, which may be amplified because of biological defects on the machined tissue surface (such as lacunae and cement lines). The irregular geometry of trabeculae has been taken into account by two approaches. Mente and Lewis[92] combined direct testing of a cantilever beam-type specimen, along with finite-element modeling of the specimen and the testing condition. They reported an averaged cancellous modulus of 7.8 GPa. Another approach was developed by Kuhn et al.[97] and applied extensively to quantify microscopic properties of bone tissue. This technique involves micromachining cancellous or cortical bone materials into rectangular beam specimens using a combination of diamond blade saw sectioning and micromilling (see Fig. 10.3). Then, the regular beam specimens (approximately $120 \times 120 \times 1500\ \mu m^3$) can be measured accurately for dimensions and tested under either three-point or four-point bending. The advantage of this method is the ability consistently to produce relatively uniform, regularly shaped beam specimens for microtesting. The results from their studies[39,97,98] indicate that cancellous bone tissue is about 20 to 30% less stiff than cortical bone tissue. One issue regarding these experiments is the relative low tissue modulus value for both cancellous and cortical bone tissue (5 to 7 GPa), significantly lower than the reported 17 GPa cortical bone modulus. Using varying size of specimens Choi et al.[39] showed that there is a significant size dependency of modulus measured by microbending tests and a significant correlation was also found between the modulus and the surface-to-volume ratio of the

specimen. This size dependency of modulus might be explained by the influence of biological defects such as lacunae on the machined specimen surface. Because of the local stress concentration near the loading head of the bending tests, the effects of those defects (lacunae 5 to 30 μm in size) become significant as the specimen size approaches 100 μm. Therefore, the size dependence of modulus is probably an experimental artifact related to bending tests as buckling and tensile tests do not show this apparent size-dependent phenomena. However, the conclusions that cancellous bone tissue is about 20 to 30% less stiff than cortical bone tissue are still valid as the comparison was based on similarly sized specimens and the same testing conditions.

10.4.2.4 Ultrasonic Technique

The ultrasonic technique used for measuring mechanical properties at a continuum level can also be employed for determination of cancellous bone tissue properties. The ultrasonic technique can be applied either to the continuum level cancellous volume[56,94] or to a microspecimen[48] to measure the cancellous tissue modulus. In both studies, 2.25 MHz was used to achieve a wavelength of about 1 mm. The 1-mm wavelength is larger than the cross-sectional dimension of trabeculae ($\sim$200 to 500 μm) and smaller than the continuum specimen dimension (5 mm). In the experiments using a cancellous bone cube, the tissue density for each cube was measured and used in the calculation while an averaged tissue density was assumed for the microspecimen measurements. The limitation of the ultrasonic method applied to the cancellous bone cubes stems from the fact that the actual length of the ultrasonic wave is unknown and the calculation of velocity was based on the overall length of each specimen, which probably is shorter than the actual pathway length that the ultrasonic wave traveled in the cancellous bone specimen. In addition, the modulus value is an average measure over the entire specimen neglecting the heterogeneous nature of cancellous tissue. The difficulty of applying this technique to a microspecimen lies in the fact that the tissue density of the microspecimen cannot be accurately measured. Given the limitations of the technique, applications of ultrasonic technique at both continuum and microspecimen levels provide very similar modulus values for cancellous bone tissue, which are significantly lower than the corresponding cortical bone modulus. Ashman and Rho[94] reported elastic modulus of cancellous bone tissue of 13.0 $\pm$ 1.47 GPa for human femurs and 10.9 $\pm$ 1.57 GPa for bovine femur using 2.25 MHz frequency on cancellous bone cubes. More recently, Nicholson et al.[56] used 1-MHz ultrasound pulse frequency to obtain cancellous bone tissue modulus of 9.98 $\pm$ 1.31 GPa from cancellous cubes from human vertebral bodies. Rho et al.[48] used both uniaxial tensile testing and ultrasonic techniques on individual trabeculae from human tibiae. They reported elastic modulus of 10.4 $\pm$ 3.5 GPa by mechanical testing (dry specimens) and 14.8 $\pm$ 1.4 GPa by ultrasound (wet specimens), significantly lower than those of cortical bone tissue (18.6 $\pm$ 3.5 GPa mechanical, 20.7 $\pm$ 1.9 ultrasound).

Acoustic microscopy has been used to determine the material properties of cortical and cancellous bone in human vertebrae.[95,96] By using a 90-MHz sound wave, the reflected wave from the surface of the material can be resolved at a submillimeter spatial resolution. The peak amplitude of the reflected wave is related to the acoustic impedance of the material, which in turn is related to the elastic modulus. However, there is no easy calculation or calibration between peak amplitude and elastic modulus. Nevertheless, this technique has great potential to quantify local bone tissue properties. In their preliminary results, Shieh et al.[95] found no significant difference between cancellous and cortical bone tissue in human vertebrae. More recently, Turner et al.,[96] using both acoustic microscope and nanoindentation technique (will be reviewed later in detail), reported elastic moduli for both cortical and cancellous bone tissues. By using a 50-MHz ultrasonic transducer, the acoustic velocity was calculated from 500-μm slices from both cortical and cancellous bone as twice the specimen thickness divided by the averaged delay time of the ultrasound pulse wave. Bone tissue density was measured directly and used to calculate the elastic modulus by Eq. 10.1. They reported averaged cortical bone modulus of 17.73 $\pm$ 0.22 GPa and cancellous bone tissue modulus of 17.5 $\pm$ 1.12 GPa. They concluded that the elastic properties of cancellous and cortical bone tissues are similar.

10.4.2.5 Microindentation and Nanoindentation

Microindentation has been used to characterize bone tissue properties since the early 1950s. For example, Weaver[62] used the microindentation technique and reported that the cancellous tissue was less stiff than cortical bone tissue, although no data were provided. Hodgskinson et al.[63] showed that cancellous tissue has 10 to 15% lower microhardness than cortical bone tissue.

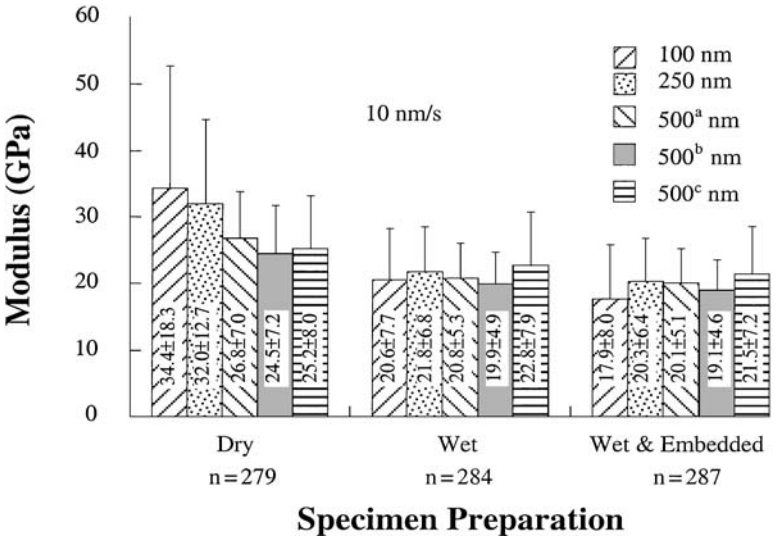

FIGURE 10.4 Modulus results for different cortical bone specimen preparation and testing conditions using nanoindentation. The superscripts a, b, and c denote the initial, immediate repeat, and delayed repeat indentation at 500 nm. The error bars show the standard deviations. The moduli of dry specimens are significantly greater than the wet, and wet and embedded specimens.

In the past 10 years, a load–displacement sensing nanoindentation instrument has been used to measure bone tissue properties. With an indenter less than 2 μm in size and a depth-sensing resolution of nanometers, the unload–displacement curve is used to calculate a material elastic modulus. The tremendous advantages of the nanoindentation technique allow bone tissue properties be probed at the microscopic level. Recently, the nanoindentation technique has been applied to biological materials, including bone tissue.[84–87,96,105–108] The experimental conditions of nanoindentation application for measuring bone tissue properties have been characterized in a recent validation study using cortical bone specimens.[84,108] Specifically, their study examined the effects of specimen preparation/testing condition (dry, wet, and wet-embedded), indentation depth (100 to 500 nm), repetitive loading, time delay (60 s), and displacement rate (5, 10, 20 nm/s). The nanoindentation experiments produced repeatable elastic moduli for human cortical bone (average value of 18.6 $\pm$ 4.2 GPa for osteons and 20.3 $\pm$ 5.1 GPa for interstitial bone tissue). In addition, the hardness measurements produced results consistent with data in the literature (average 0.52 $\pm$ 0.15 GPa for osteons and 0.59 $\pm$ 0.20 GPa for interstitial bone tissue). Consistent modulus values can be obtained from a 500-nm-deep indent. The results also indicated that the moduli and hardnesses of the dry specimens are significantly greater than those of the wet and the wet/embedded specimens, while the latter two groups were not different (Fig. 10.4). The moduli and hardnesses obtained at the 5 nm/s rate were significantly lower than the values at the 10 and 20 nm/s rates while the 10 and 20 nm/s rates were not significantly different. With this validation study in hand, the elastic properties of cancellous bone tissue have been determined using the nanoindentation technique in human femurs and compared simultaneously with cortical bone tissue from the same femoral bones[86,87] (Fig. 10.5). In diaphyseal femoral bone, the average elastic moduli were 19.1 $\pm$ 5.4 GPa in osteonal and 21.2 $\pm$ 5.3 GPa in the interstitial bone tissue. In the femoral neck, the average moduli were 15.8 $\pm$ 5.3 GPa in osteonal, 17.5 $\pm$ 5.3 GPa in interstitial, and 11.4 $\pm$ 5.6 GPa in cancellous bone tissues. In their study, the bone specimens were either kept wet from fresh or previously embedded (for cancellous bone samples).

Several other investigators have also employed the nanoindentation technique for measuring bone tissue properties. By using dry bone specimens, the average elastic modulus for vertebral trabeculae of 13.4 $\pm$ 2.0 GPa was reported and was significantly lower than those of tibial cortical bone tissues (22.5 $\pm$ 1.3 GPa for osteons and 25.8 $\pm$ 0.7 GPa for interstitial bone tissue).[85,106] However, in a more recent paper using both nanoindentation technique and ultrasonic microscopy, Turner et al.[96] reported significantly higher elastic

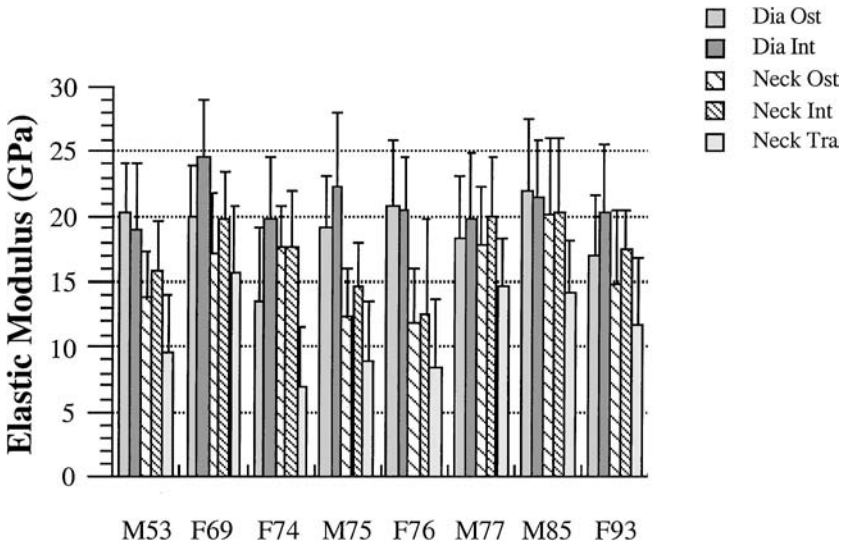

FIGURE 10.5 Elastic moduli measured by the nanoindentation technique in five microstructures in eight individual femurs (Dia Ost: Diaphyseal Osteons; Dia Int: Diaphyseal Interstitial; Neck Ost: Neck Osteons; Neck Int: Neck Interstitial; Neck Tra: Neck Trabeculae). The error bars indicate the standard deviation.

modulus for cancellous bone tissue from a distal femoral condyle (18.1 $\pm$ 1.7 GPa) and this value fell between the average (20 $\pm$ 0.27 GPa) and transverse elastic moduli (16.6 $\pm$ 0.32 GPa) of cortical bone tissue. Their results follow the same trend of the ultrasonic measurements. They concluded, therefore, that the elastic modulus of cancellous bone tissue is similar to that of cortical bone tissue. Their conclusion, however, should be interpreted with caution as dehydrated bone specimens were used in their study and they did not specify on which type of cortical bone the measurements were made (osteons vs. interstitial bone tissue).

10.4.2.6 Back-Calculation Using Finite Element Models

One of the driving forces behind the quest for mechanical properties of cancellous bone tissue comes from the need to construct mathematical or computational models for prediction of mechanical behavior of cancellous bone itself. In addition to the complexities in cancellous bone architecture, one obstacle is the input materials properties of cancellous bone tissue. From modeling of cancellous bone itself, questions have been long raised regarding the elastic modulus of cancellous bone tissue. In the early 1970s, Pugh et al.[99] found that the bone volume fraction or the modulus of cancellous bone tissue must be reduced to match the range of stiffness predictions of the structural model of cancellous with that of experiments. Later on, Williams and Lewis[100] developed two-dimensional models from proximal tibial cancellous bone. To fit the model prediction of stiffness of cancellous bone, the elastic modulus of cancellous bone tissue has to be reduced lower than that of cortical bone tissue. In three-dimensional idealized microstructural models of cancellous bone, Beaupre and Hayes[101] reached the same conclusion suggesting the elastic modulus of cancellous bone tissue (value of 13.77 GPa) was used in their models.

With the advances of new microimaging modalities such as micro-CT, synchrotron microtomography, micro-magnetic resonance imaging (micro-MRI), as well as high-resolution serial sectioning, it is possible to describe the three-dimensional microstructures of cancellous bone at the 10 to 50 μm level.[109–113] With the increasing computational power of computers, it now becomes routine that a high-resolution microscopic image of cancellous bone can be converted into a detailed, large-scale finite-element model.[104,114–119] In this type of model, the intrinsic complexities of cancellous bone microstructures such as bone volume fraction, connectivity, and anisotropy have already built into the models. It has been shown that these models can provide accurate predictions of mechanical properties of cancellous bone at a continuum level.[104,114–119]

To back-calculate the cancellous bone tissue modulus, one first will perform nondestructive mechanical tests such as uniaxial compression of cancellous bone cubes. The apparent elastic modulus of the specimens E_{Exp} can then be determined from the experimental data. Next, the cancellous bone specimens will be scanned using either a micro-CT/micro-MRI scanner or a serial grinder and the three-dimensional images will be reconstructed. The reconstructed image will then be converted into a large-scale finite-element model. Assuming an initial guess of cancellous bone tissue modulus E_0, the predicted apparent elastic modulus E_{Comp} can be calculated simulating the same boundary conditions as in the experiments. Within the linear elastic assumption, the true cancellous bone tissue elastic modulus E_s can then be determined by

$$E_s = \frac{E_{\text{Exp}}}{E_{\text{Comp}}} E_0. \tag{10.6}$$

The procedure of the back-calculation scheme is shown in Fig. 10.6.

Several researchers have employed the back-calculation scheme using high-resolution image-based, large-scale finite-element technique. Using cylindrical specimens from vertebral cancellous bone, Hou et al.[103] performed mechanical tests, micro-CT scans, and finite-element computations on 28 vertebral cancellous bone specimens (from thoracic T12 vertebrae).[103] The finite-element models predicted well the apparent elastic modulus of cancellous specimens (the coefficient of correlation between experimental measured and calculated moduli $r^2 = 0.89$), indicating the relative accuracy of this procedure. The predicted cancellous bone tissue modulus was 5.7 $\pm$ 1.6 GPa (range: 2.7 to 9.1 GPa) and this value was independent of age. Ladd et al.[104] utilized the same approach and determined the cancellous bone tissue modulus for lumbar vertebral cancellous bone. Five cancellous bone cubes were extracted from human lumbar vertebrae (lumbar L1 vertebrae). The elastic moduli in three orthogonal directions were determined using nondestructive uniaxial compression tests (inferior-superior, anterior-posterior, and lateral-medial directions). After preparation and mechanical testing, the specimens were imaged using a micro-synchrotron X-ray tomography system at 23.4 μm resolution. The images were converted into large-scale finite-element models and the apparent elastic moduli were determined for the three orthogonal directions. The cancellous bone tissue modulus was determined by comparing the average modulus taken over the three orthogonal directions from experiments to that from computation. They reported the average cancellous bone tissue modulus of 6.6 $\pm$ 1.1 GPa (range 5.5 to 7.7 GPa). In both studies, the reported elastic modulus for cancellous bone tissue is within the measurements from the microtesting of individual trabeculae but below those from nanoindentation and ultrasonic measurements. However, the apparent modulus measurements in both studies depend on the platen-to-platen measurement of displacement, which can result in 20 to 40% variation in modulus (in most cases there is an underestimation of apparent modulus).[120] This experimental artifact would bring uncertainty of the calculation of cancellous bone tissue modulus to an otherwise relatively accurate modeling procedure. For example, the estimated cancellous bone tissue modulus would be artificially low to match the experimentally underestimated apparent modulus of the specimen. To overcome this experimental uncertainty, one has to use a cancellous bone specimen embedded in the end caps with the extensometer attached to the middle of the specimen (preferably within the waisted section).[120,121] The recent data from combined accurate mechanical testing of cancellous bone using waisted specimens with end- caps and the large-scale finite-element calculation reported the calculated cancellous bone tissue modulus for bovine tibiae 17.3 $\pm$ 2.62 GPa and is about 10% less than the bovine cortical bone tissue modulus.[122] The results for human cancellous bone tissue using this accurate technique have yet to be obtained.

10.4.2.7 Fatigue Properties

In addition to static tissue modulus, characterizing the fatigue properties of cancellous and cortical bone tissue is important to better understand normal mechanical and physiological behavior as well as the response to orthopedic implants and a variety of disease states. Using the four-point bending microtesting method, Choi and Goldstein[98] demonstrated that cancellous bone tissue has significantly lower fatigue resistance than cortical bone tissue (Fig. 10.7). The significant difference in fatigue properties between cancellous and cortical specimens might have resulted from the differences in their microstructure. As

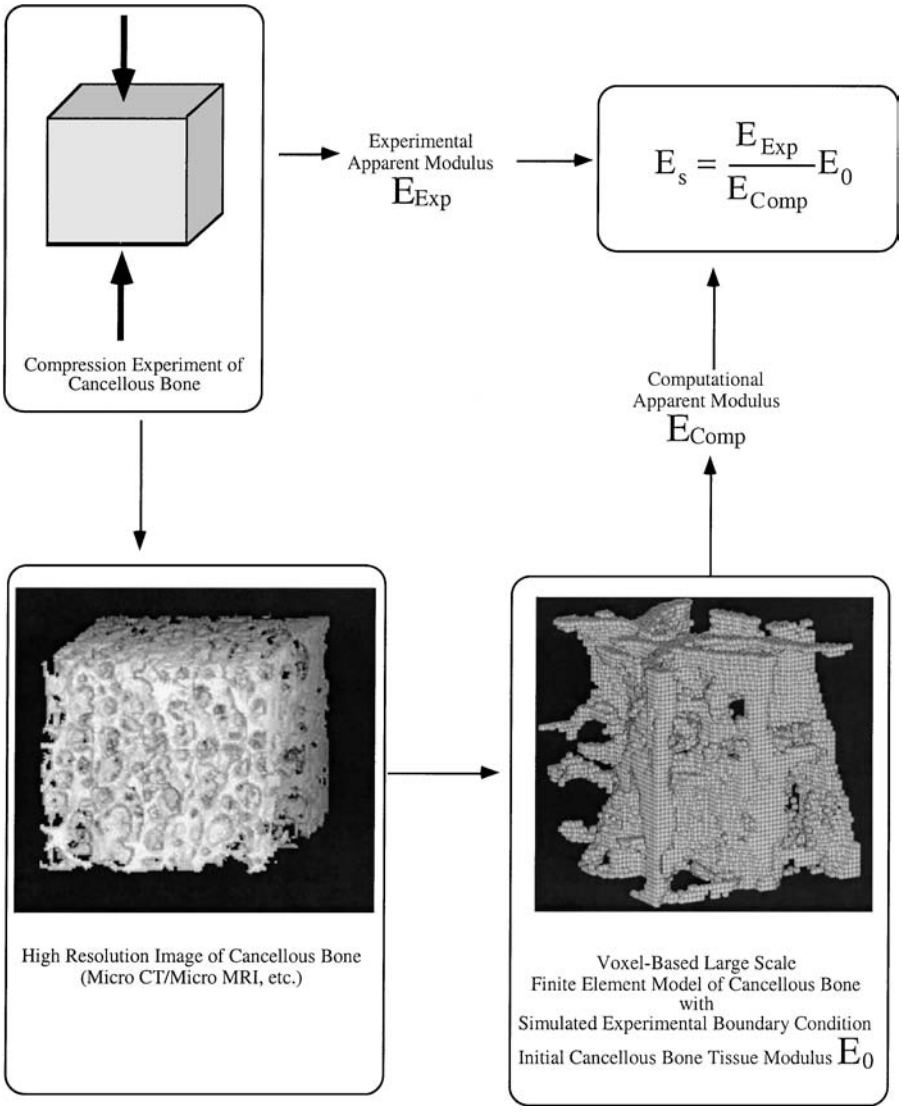

FIGURE 10.6 Estimation of elastic modulus of cancellous bone tissue using large scale micro-imaging based finite element methods.

noted earlier, microspecimens from cortical bone tissue consist of layers of lamellae parallel to the long axis of the specimen with at most only one cement line, a favorable structure to withstand bending load. On the other hand, microspecimens from cancellous bone tissue contain several cement lines and a mosaic-like microstructure with lamellae running across the long axis of the specimen.

10.5 Determinants of Cancellous Bone Tissue Modulus

Accepting that cancellous tissue modulus is 20 to 30% lower than cortical bone tissue, which factors contribute to the modulus difference? It is plausible to hypothesize that the bone tissue modulus is related to density/porosity, mineral content, and microstructural features such as lamellar orientation, lacunae, and cement lines. Choi et al.[39] showed that the modulus difference between cancellous and cortical bone tissue cannot be explained by mineralization (Fig. 10.8), despite the fact that their cancellous bone specimens

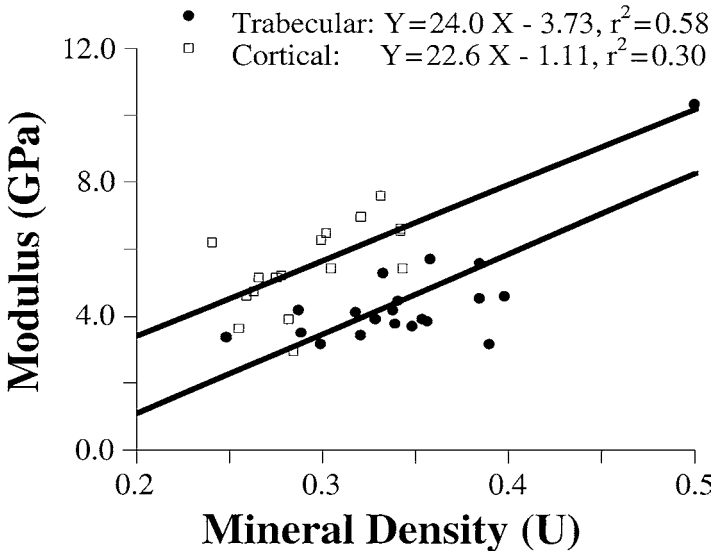

FIGURE 10.7 Correlation between the tissue modulus measured by 4-point-bending microtesting and mineral density measured by microcomputed tomography for both cancellous and cortical bone specimens. (From Choi, K. et al., *J. Biomech.,* 23, 1103–1113, 1990. With permission.)

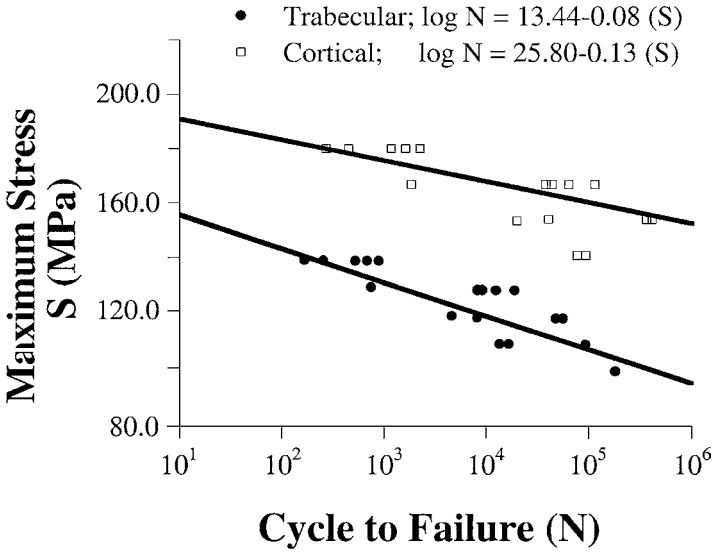

FIGURE 10.8 Median S-N curves for cancellous and cortical tissues from human tibia determined by 4-point bending testing. Cortical specimens demonstrated higher fatigue strength than cancellous specimens. (From Choi, K. and Goldstein, S. A., *J. Biomech.,* 25, 1371–1381, 1992. With permission.)

may have predominantly consisted of highly mineralized, central trabecular packets. For a specific bone type (e.g., cancellous or cortical), there is a correlation between modulus and mineralization. This result strongly suggests the importance of the microstructural differences between cancellous and cortical tissue. Since the volume fraction of lacunae is very small, the lamellar/collagen organization and orientation may be very potent determinants of tissue modulus.

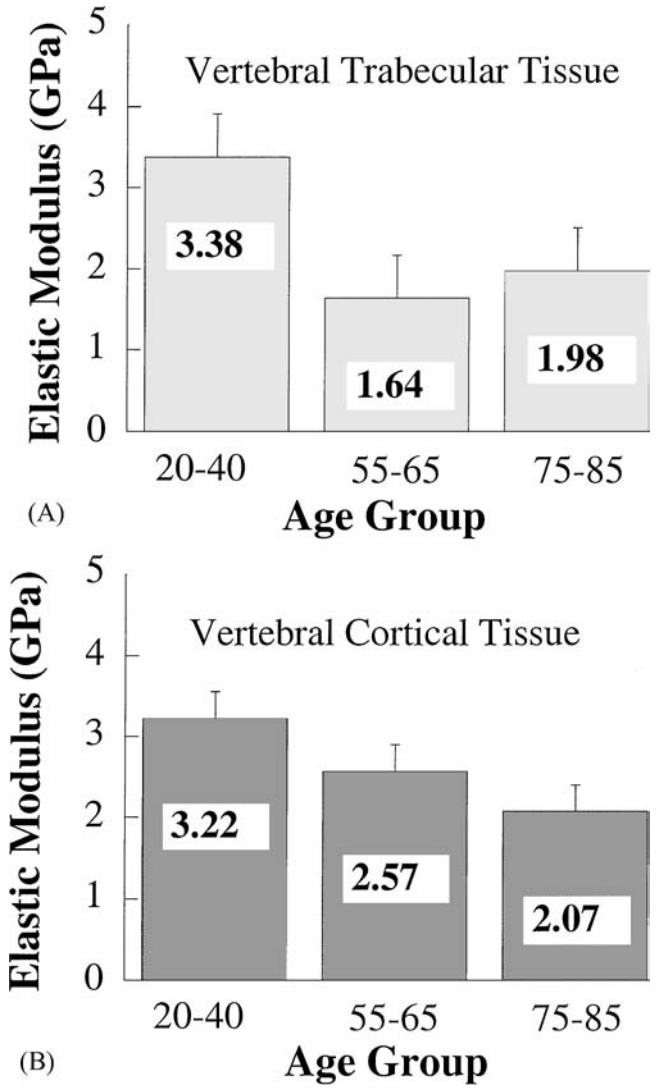

FIGURE 10.9 Tissue modulus measured from 4-point-bending microtesting for cancellous (A) and cortical (B) bone specimens from human vertebral bodies of various age groups. Cortical tissue (2.44 GPa) is 14% stiffer than cancellous tissue (2.11 GPa) ($p = 0.014$). In addition, the tissue from the younger age group (20–40) is stiffer than the older age groups (55–65 and 75–85) ($p = 0.02$).

10.6 Age-Related Changes

Using four-point bending microtesting techniques, researchers have begun to address the age-related changes in cancellous and cortical bone tissue properties, which may have profound importance in understanding bone fragility and age-related fractures.[123,124] The preliminary results in human vertebrae indicate that both cancellous and cortical bone tissue from young adults (age 20 to 40) have significantly higher moduli than the tissue from older aging adults (age 55 to 65 and 75 to 85) (Fig. 10.9). In addition, cancellous bone tissue has a lower modulus than cortical tissue. It will be of great importance to determine the underlying microstructural and compositional alterations that result in these tissue property changes.

10.7 Summary

In aggregate, there appears to be a consensus that cancellous tissue is 20 to 30% less stiff than cortical bone tissue. However, this difference cannot be explained by the difference in mineralization, suggesting that it originates from the difference in microstructures (most importantly lamellar/collagen organization and orientation). Although numerous studies demonstrate a 20 to 30% modulus difference between these tissues, the exact values of modulus for cancellous tissue is still uncertain. Continuing studies are focused on quantifying the tissue microstructure and correlating these measures to physical properties measured utilizing nanoindentation and fatigue experiments in an effort to delineate more clearly structure–function relationships in bone tissue and potential implications in fragility disorders and adaptation.

Acknowledgments

This work is supported by a grant from Whitaker Foundation (RG-97-0086) and a grant from NIH/NIAMS (RO3 AR45832-01). The author would like to acknowledge the nanoindentation data from the Orthopaedic Research Laboratories of the University of Michigan.

References

1. Melton, L. J., Epidemiology of fractures, in *Osteoporosis Etiology, Diagnosis, and Management,* Riggs, B. L. and Melton, L. J., Eds., Raven Press, New York, 1988, 133.
2. Heaney, R. P., Is there a role for bone quality in fragility fractures? [Review], *Calcif. Tissue Int.,* 53 (Suppl. 1), S3, 1993.
3. Martin, R. B. and Burr, D. B., *Structure, Function, and Adaptation of Compact Bone;* Vol. 1, Raven Press, New York, 1989, 275.
4. Schaffler, M. B., Burr, D. B., and Frederickson, R. G., Morphology of the osteonal cement line in human bone, *Anat. Rec.,* 217, 223, 1987.
5. Marotti, G., A new theory of bone lamellation, *Calcif. Tissue Int.,* 53, S47, 1993.
6. Jee, W. S. S., The skeletal tissue, in *Cell and Tissue Biology*: *A Textbook of Histology,* Weiss, L., Eds., Urban & Schwarzenberg, Baltimore, 1990, 200.
7. Lozupone, E., The structure of the trabeculae of cancellous bone. 1. The calcaneus, *Anat. Anz.,* 159, 211, 1985.
8. Sato, K., Wakamatsu, E., Sato, T., Honma, T., Kotake, H., and Byers, P. D., Histomorphometric study of trabecular channels in normal iliac bone, *Calcif. Tissue Int.,* 39, 2, 1986.
9. Lozupone, E. and Favia, A., The structure of the trabeculae of cancellous bone. 2. Long bones and mastoid, *Calcif. Tissue Int.,* 46, 367, 1990.
10. Ascenzi, A. and Bonucci, E., The tensile properties of single osteons, *Anat. Rec.,* 158, 375, 1967.
11. Ascenzi, A., Bonucci, E., Ripamonti, A., and Roveri, N., X-ray diffraction and electron microscope study of osteons during calcification, *Calcif. Tissue Res.,* 25, 133, 1978.
12. Ascenzi, A., The micromechanics versus the macromechanics of cortical bone—a comprehensive presentation, *J. Biomech. Eng.,* 8, 143, 1988.
13. Kragstrup, J., Gundersen, H. J. G., Melsen, F., and Mosekilde, L., Estimation of the three-dimensional wall thickness of complete remodeling sites in iliac trabecular bone, *Metab. Bone Dis. Relat. Res.,* 4, 113, 1982.
14. Kragstrup, J., Melsen, F., and Mosekilde, L., Thickness of lamellae in normal human iliac trabecular bone, *Metab. Bone Dis. Relat. Res.,* 4, 291, 1983.
15. Katz, J. L. and Meunier, A., The elastic anisotropy of bone, *J. Biomech.,* 20, 1063, 1987.
16. Martin, R. B. and Boardman, D. L., The effects of collagen fiber orientation, porosity, density, and mineralization on bovine cortical bone bending properties, *J. Biomech.,* 26, 1047, 1993.
17. Crolet, J. M., Aoubiza, B., and Meunier, A., Compact bone: numerical simulation of mechanical characteristics, *J. Biomech.,* 26, 677, 1993.

18. Mammone, J. F. and Hudson, S. M., Micromechanics of bone strength and fracture, *J. Biomech.,* 26, 439, 1993.
19. Hobdell, M. H., The concentration of osteocyte lacunae in human bone, *J. Anat.,* 106, 165, 1970.
20. Yeager, V. L., Chiemchanya, S., and Chaiseri, P., Changes in size of lacunae during the life of osteocytes in osteons of compact bone, *J. Gerontol.,* 30, 9, 1975.
21. Krempien, B., Manegold, C., Ritz, E., and Bommer, J., The influence of immobilization on osteocyte morphology, *Virchows Arch. A Pathol. Anat. Histol.,* 370, 55, 1976.
22. Sissons, H. A. and O'Connor, P., Quantitative histology of osteocyte lacunae in normal human cortical bone, *Calcif. Tissue Res.,* 22, 530, 1977.
23. Cane, V., Marotti, G., Volpi, G., Zaffe, D., and Palazzni, S., Size and density of osteocyte lacunae in different regions of long bones, *Calcif. Tissue Int.,* 34, 558, 1982.
24. Eadie, J. S., Riemer, B. A., and Goldstein, S. A., Quantification of vertebral trabecular bone tissue microstructure, in *41st Annual Meeting ORS,* Orlando, FL, Vol. 2, ORS, 1995, 528.
25. Mullender, M. G., Huiskes, R., Versleyen, H., and Buma, P., Osteocyte density and histomorphometric parameters in cancellous bone of the proximal femur in five mammalian species, *J. Orthop. Res.,* 14, 972, 1996.
26. Burr, D. B., Schaffler, M. B., and Frederickson, R. G., Composition of the cement line and its possible mechanical role as a local interface in human compact bone, *J. Biomech.,* 21, 939, 1988.
27. Burstein, A. H., Zika, J. M., Heiple, K. G., and Klein, L., Contribution of collagen and mineral to the elastic-plastic properties of bone, *J. Bone Joint Surg.,* 57A, 956, 1975.
28. Jepsen, K. J., Mansoura, M. K., Kuhn, J. L., Wu, H., Jaenisch, R., Bonadio, J. F., and Goldstein, S. A., An in vivo assessment of the contribution of type I collagen to the mechanical properties of cortical bone, in *38th Annual Meeting. ORS,* Washington, D.C., Vol. 1, ORS, 1992, 93.
29. Jepsen, K. J., *Characterization of the Herrarchical Composite Properties of Cortical Bone: A Transgenic Approach,* University of Michigan, Ann Arbor, 1994.
30. Jepsen, K. J., Goldstein, S. A., Kuhn, J. L., Schaffler, M. B., and Bonadio, J., Variations in the static and fatigue properties of lamellar bone associated with matrix level alterations, in *41st Annual Meeting ORS,* Orlando, FL, Vol. 1, ORS, 1995, 151.
31. Carter, D. R. and Hayes, W. C., Bone compressive strength: the influence of density and strain rate, *Science,* 194, 1174, 1976.
32. Carter, D. R. and Hayes, W. C., The compressive behavior of bone as a two-phase porous structure, *J. Bone Joint Surg.,* 59A, 954, 1977.
33. Carter, D. R. and Spengler, D. M., Mechanical properties and chemical composition of cortical bone, *Clin. Othop.,* 135, 192, 1978.
34. Skedros, J., Bloebaum, R. D., Bachus, K. N., Boyce, T. M., and Constantz, B., Influence of mineral content and composition on gray levels in backscatterd elctron images of bone, *J. Biomed. Mater. Res.,* 27, 57, 1993.
35. Crofts, R. D., Boyce, T. M., and Bloebaum, R. D., Aging changes in osteon mineralization in the human femoral neck, *Bone,* 15, 147, 1994.
36. Dyson, E. D. and Whitehouse, W. J., Composition of trabecular bone in children and its relation to radiation dosimetry, *Nature,* 217, 576, 1968.
37. Gong, J. K., Arnold, J. S., and Cohn, S. H., Composition of trabecular and cortical bone, *Anat. Rec.,* 149, 325, 1964.
38. Norrdin, R. W., Phemister, R. D., Jaenke, R. S., and Lo Presi, C. A., Density and composition of trabecular and cortical bone in perinatally irradiated beagles with chronic renal failure, *Calcif. Tissue Res.,* 24, 99, 1977.
39. Choi, K., Kuhn, J. L., Ciarelli, M. J., and Goldstein, S. A., The elastic moduli of human subchondral, trabecular, and cortical bone tissue and the size-dependency of cortical bone modulus, *J. Biomech.,* 23, 1103, 1990.
40. Williams, J. L., Ultrasonic wave propagation in cancellous and cortical bone: prediction of some experimental results by Biot's theory, *J. Acoust. Soc. Am.,* 91, 1106, 1992.

41. Antich, P. P., Anderson, J. A., Ashman, R. B., Dowdey, J. E., Gonzales, J., Murry, R. C., Zerwekh, J. E., and Pak, C. Y., Measurement of mechanical properties of bone material in vitro by ultrasound reflection: methodology and comparison with ultrasound transmission, *J. Bone Miner. Res.,* 6, 417, 1991.
42. McCarthy, R. N., Jeffcott, L. B., and McCartney, R. N., Ultrasound speed in equine cortical bone: effects of orientation, density, porosity and temperature, *J. Biomech.,* 23, 1139, 1990.
43. Lees, S., Heeley, J. D., and Cleary, P. F., A study of some properties of a sample of bovine cortical bone using ultrasound, *Calcif. Tissue Int.,* 29, 107, 1979.
44. Greenfield, M. A., Craven, J. D., Wishko, D. S., Huddleston, A. L., Friedman, R., and Stern, R., The modulus of elasticity of human cortical bone: an in vivo measurement and its clinical implications, *Radiology,* 115, 163, 1975.
45. Craven, J. D., Costantini, M. A., Greenfield, M. A., and Stern, R., Measurement of the velocity of ultrasound in human cortical bone and its potential clinical importance. An in vivo preliminary study, *Invest. Radiol.,* 8, 72, 1973.
46. Ashman, R. B. and Rho, J. Y., Use of a transmission ultrasonic technique for the in vitro evaluation of bone ingrowth, *J. Biomech.,* 23, 941, 1990.
47. Ashman, R. B., Corin, J. D., and Turner, C. H., Elastic properties of cancellous bone: measurement by an ultrasonic technique, *J. Biomech.,* 20, 979, 1987.
48. Rho, J. Y., Ashman, R. B., and Turner, C. H., Young's modulus of trabecular and cortical bone material: ultrasonic and microtensile measurements, *J. Biomech.,* 26, 111, 1993.
49. Yoon, H. S. and Katz, J. L., Ultrasonic wave propagation in human cortical bone—I. Theoretical considerations for hexagonal symmetry, *J. Biomech.,* 9, 407, 1976.
50. Yoon, H. S. and Katz, J. L., Ultrasonic wave propagation in human cortical bone—II. Measurements of elastic properties and microhardness, *J. Biomech.,* 9, 459, 1976.
51. Yoon, H. S. and Katz, J. L., Ultrasonic wave propagation in human cortical bone—III. Piezoelectric contribution, *J. Biomech.,* 9, 537, 1976.
52. Lakes, R., Yoon, H. S., and Katz, J. L., Ultrasonic wave propagation and attenuation in wet bone, *J. Biomed. Eng.,* 8, 143, 1986.
53. Zimmerman, M. C., Meunier, A., Katz, J. L., and Christel, P., The evaluation of cortical bone remodeling with a new ultrasonic technique, *IEEE Trans. Biomed. Eng.,* 37, 433, 1990.
54. Shieh, S.-J., Govind, S., Gudipaty, K., Subramanian, R., and Grimm, M. J., High resolution ultrasonic measurements of the material properties of cortical and trabecular bone in the human vertebrae, in *1995 Bioengineering Conference,* BED–Vol. 29, Hochmuth, R. M., Langrana, N. A., and Hefzy, M. S., Eds., ASME, 1995, 413.
55. Rho, J. Y., An ultrasonic method for measuring the elastic properties of human tibial cortical and cancellous bone, *Ultrasonics,* 34, 777, 1996.
56. Nicholson, P. H., Cheng, X. G., Lowet, G., Boonen, S., Davie, M. W., Dequeker, J., and Van der Perre, G., Structural and material mechanical properties of human vertebral cancellous bone, *Med. Eng. Phys.,* 19, 729, 1997.
57. Strelitzki, R., Evans, J. A., and Clarke, A. J., The influence of porosity and pore size on the ultrasonic properties of bone investigated using a phantom material, *Osteoporosis Int.,* 7, 370, 1997.
58. Strelitzki, R., Nicholson, P. H., and Evans, J. A., Low-frequency ultrasonic velocity measurements in human calcaneal trabecular bone, *Physiol. Meas.,* 18, 119, 1997.
59. Hodgskinson, R., Njeh, C. F., Currey, J. D., and Langton, C. M., The ability of ultrasound velocity to predict the stiffness of cancellous bone *in vitro, Bone,* 21, 183, 1997.
60. Carlstrom, D., Micro-hardness measurements on single Haversian system in bone, *Experientia,* 10, 171, 1954.
61. Amprino, R., Investigations on some physical properties of bone tissue, *Acta Anat.,* 34, 161, 1958.
62. Weaver, J. K., The microscopic hardness of bone, *J. Bone Joint Surg.,* 48A, 273, 1966.
63. Hodgskinson, J. D., Currey, J. D., and Evans, G. P., Hardness, an indicator of the mechanical competence of cancellous bone, *J. Orthop. Res.,* 7, 754, 1989.

64. Currey, J. D. and Brear, K., Hardness, Young's modulus and yield stress in mammalian mineralized tissues, *J. Mater. Sci. Mater. Med.,* 1, 14, 1990.
65. Evans, G. P., Behiri, J. C., Currey, J. D., and Bonfield, W., Microhardness and Young's modulus in cortical bone exhibiting a wide range of mineral volume fractions and in a bone analogue, *J. Mater. Sci. Mater. Med.,* 1, 38, 1990.
66. Blackburn, J., Hodgskinson, R., Currey, J. D., and Mason, J. E., Mechanical properties of microcallus in human cancellous bone, *J. Orthop. Res.,* 10, 237, 1992.
67. Doerner, M. F. and Nix, W. D., A method for determining the data from depth-sensing indentation instruments, *J. Mater. Res.,* 1, 601, 1986.
68. Oliver, W. C. and Pharr, G. M., An improved technique for determining hardness and elastic modulus using load and displacement sensing indentation experiments, *J. Mater. Res.,* 7, 1564, 1992.
69. Sneddon, I. N., The relation between load and penetration in the axisymmetric Boussineq problem for a punch of abitrary profile, *Int. J. Eng. Sci.,* 3, 47, 1965.
70. King, R. B., Elastic analysis of some punch problems for a layered medium, *Int. J. Solids Struct.,* 23, 1657, 1987.
71. Pharr, G. M., Oliver, W. C., and Brotzen, F. R., On the generality of the relationship among contact stiffness, contact area, and elastic modulus during indentation, *J. Mater. Res.,* 7, 613, 1992.
72. Ascenzi, A. and Bonucci, E., The compressive properties of single osteons, *Anat. Rec.,* 161, 377, 1968.
73. Ascenzi, A. and Bonucci, E., The compressive properties of single osteons as a problem of molecular biology, *Calcif. Tissue Res.,* Suppl. 44, 1968.
74. Ascenzi, A. and Bonucci, E., A micromechanic investigation on single osteons using a shearing strength test, *Isr. J. Med. Sci.,* 7, 471, 1971.
75. Ascenzi, A. and Bonucci, E., The shearing properties of single osteons, *Anat. Rec.,* 172, 499, 1972.
76. Ascenzi, A., Bonucci, E., and Simkin, A., An approach to the mechanical properties of single osteonic lamellae, *J. Biomech.,* 6, 227, 1973.
77. Ascenzi, A. and Bonucci, E., Mechanical similarities between alternate osteons and cross-ply laminates, *J. Biomech.,* 9, 65, 1976.
78. Ascenzi, A. and Bonucci, E., Relationship between ultrastructure and "pin test" in osteons, *Clin. Orthop.,* 275, 1976.
79. Ascenzi, A. and Bonucci, E., An investigation of the mechanical anisotropy of the alternately structured osteons, *Calcif. Tissue Res.,* 22 Suppl., 553, 1977.
80. Ascenzi, A., Benvenuti, A., and Bonucci, E., The tensile properties of single osteonic lamellae: technical problems and preliminary results, *J. Biomech.,* 15, 29, 1982.
81. Ascenzi, A., Benvenuti, A., Mango, F., and Simili, R., Mechanical hysteresis loops from single osteons: technical devices and preliminary results, *J. Biomech.,* 18, 391, 1985.
82. Ascenzi, A. and Benvenuti, A., Orientation of collagen fibers at the boundary between two successive osteonic lamellae and its mechanical interpretation, *J. Biomech.,* 19, 455, 1986.
83. Ascenzi, A., Boyde, A., Bianco, P., and Portigliatti Barbos, M., Relationship between mechanical properties and structure in secondary bone, *Connect. Tissue Res.,* 15, 73, 1986.
84. Guo, X. E., Zysset, P. K., Hoffler, C. E., Moore, K. E., and Goldstein, S. A., An application of nanoindentation technique to measure microscopic bone tissue properties, *J. Biomech. Eng.,* submitted, 1999.
85. Rho, J. Y., Tsui, T. Y., and Pharr, G. M., Elastic properties of human cortical and trabecular lamellar bone measured by nanoindentation, *Biomaterials,* 18, 1325, 1997.
86. Zysset, P. K., Guo, X. E., Hoffler, C. H., Moore, K. E., and Goldstein, S. A., Mechanical properties of human trabecular bone lammelae quantified by nanoindentation, *Technol. Health Care,* 6, 429, 1998.
87. Zysset, P. K., Guo, X. E., Hoffler, C. E., Moore, K. E., and Goldstein, S. A., Elastic modulus and hardness of cortical and trabecular bone lammelae measured by nanoindentation in the human femur, *J. Biomech.,* 32, 1005, 1999.
88. Wolff, J., *Das Gaesetz der Transformation der Knochen,* Hirchwild, Berlin, 1892.

89. Guo, X. E. and Goldstein, S. A., Is trabecular bone tissue different from cortical bone tissue? *Forma,* 12, 185, 1997.
90. Runkle, J. C. and Pugh, J., The micro-mechanics of cancellous bone, *Bull. Hosp. J. Dis.,* 36, 2, 1975.
91. Townsend, P. R., Rose, R. M., and Radin, E. L., Buckling studies of single human trabeculae, *J. Biomech.,* 8, 199, 1975.
92. Mente, P. L. and Lewis, J. L., Experimental method for measurement of the elastic modulus of trabecular bone tissue, *J. Orthop. Res.,* 7, 456, 1989.
93. Ryan, J. C. and Williams, J. L., Tensile testing of rodlike trabeculae excised from bovine femoral bone, *J. Biomech.,* 22, 351, 1989.
94. Ashman, R. B. and Rho, J. Y., Elastic modulus of trabecular bone material, *J. Biomech.,* 21, 177, 1988.
95. Shieh, S. J., Zimmerman, M. C., and Langrana, N. A., The application of scanning acoustic microscopy in a bone remodeling study, *J. Biomech. Eng.,* 117, 286, 1995.
96. Turner, C. H., Takano, Y., Tsui, T. Y., and Pharr, G. M., The elastic properties of trabecular and cortical bone tissues are similar: results from two microscopic measurement techniques, *J. Biomech.,* 32, 437, 1999.
97. Kuhn, J. L., Goldstein, S. A., Choi, K., London, M., Feldkamp, L. A., and Matthews, L. S., Comparison of the trabecular and cortical tissue moduli from human iliac crests, *J. Orthop. Res.,* 7, 876, 1989.
98. Choi, K. and Goldstein, S. A., A comparison of the fatigue behavior of human trabecular and cortical bone tissue, *J. Biomech.,* 25, 1371, 1992.
99. Pugh, J. W., Rose, R. M., and Radin, E. L., A structural model for the mechanical behavior of trabecular bone, *J. Biomech.,* 6, 657, 1973.
100. Williams, J. L. and Lewis, J. L., Properties and an anisotropic model of cancellous bone from the proximal tibial epiphysis, *J. Biomech. Eng.,* 104, 50, 1982.
101. Beaupre, G. S. and Hayes, W. C., Finite element analysis of a three-dimensional open-celled model for trabecular bone, *J. Biomech. Eng.,* 107, 249, 1985.
102. Jensen, K. S. and Mosekilde, L., A model of vertebral trabecular bone architecture and its mechanical properties, *Bone,* 11, 417, 1990.
103. Hou, F. J., Lang, S. M., Hoshaw, S. J., Reimann, D. A., and Hyhrie, D. P., Human vertebral body apparent and hard tissue stiffness, *J. Biomech.,* 31, 1009, 1998.
104. Ladd, A. J. C., Kinney, J. H., Haupt, D. L., and Goldstein, S. A., Finite-element modeling of trabecular bone: comparison with mechanical testing and determination of tissue modulus, *J. Orthop. Res.,* 16, 622, 1998.
105. Ko, C.-C., Douglas, W. H., and Cheng, Y.-S., Intrinsic mechanical competence of cortical and trabecular bone measured by nanoindentation and microindentation probes, in *1995 ASME Bioengineering Conference,* BED–Vol. 29, Hochmuth, R. M., Langrana, N. A., and Hefzy, M. S., Eds., ASME, 1995, 415.
106. Roy, M., Rho, J. Y., Tsui, T. Y., and Pharr, G. M., Variation of Young's modulus and hardness in human lumbar vertebrae measured by nanoindentation, *Adv. Bioeng.,* BED-33, 385, 1996.
107. Willems, G., Celis, J. P., Lembrechts, P., Braem, M., and Vanherle, G., Hardness and Young's modulus determined by nanoindentation technique of filler particles of dental restorative materials compared with human enamel, *J. Biomed. Mater. Res.,* 27, 747, 1993.
108. Hoffler, C. E., Guo, X. E., Zysset, P. K., Moore, K. E., and Goldstein, S. A., Evaluation of bone microstructural properties: effect of testing conditions, depth, repetition, time delay and displacement rate, in *Summer Conference of Bioengineering Division of ASME,* BED–Vol. 35, ASME, 1997, 567.
109. Feldkamp, L. A., Goldstein, S. A., Parfitt, A. M., Jesion, G., and Kleerekoper, M., The direct examination of three-dimensional bone architecture in vitro by computed tomography, *J. Bone Miner. Res.,* 4, 3, 1989.
110. Kinney, J. H., Lane, N. E., and Haupt, D. L., In vivo, three-dimensional microscopy of trabecular bone, *J. Bone Miner. Res.,* 10, 264, 1995.

111. Kuhn, J. L., Goldstein, S. A., Feldkamp, L. A., Goulet, R. W., and Jesion, G., Evaluation of a microcomputed tomography system to study trabecular bone structure, *J. Orthop. Res.,* 8, 833, 1990.
112. Rüegsegger, P., Koller, B., and Muller, R., A microtomographic system for the nondestructive evaluation of bone architecture, *Calcif. Tissue Int.,* 58, 24, 1996.
113. Beck, J. D., Canfield, B. L., Haddock, S. M., Chen, T. J., Kothari, M., and Keaveny, T. M., Three-dimensional imaging of trabecular bone using the computer numerically controlled milling technique, *Bone,* 21, 281, 1997.
114. van Rietbergen, B., Weinans, H., Huiskes, R., and Odgaard, A., A new method to determine trabecular bone elastic properties and loading using micromechanical finite-element models, *J. Biomech.,* 28, 69, 1995.
115. Van Rietbergen, B., Odgaard, A., Kabel, J., and Huiskes, R., Direct mechanics assessment of elastic symmetries and properties of trabecular bone architecture, *J. Biomech.,* 29, 1653, 1996.
116. van Rietbergen, B., Muller, R., Ulrich, D., Ruegsegger, P., and Huiskes, R., Quantitative assessment of tissue loading in a proximal femur using a full scale microstructural FE-Model, in *43rd Annual Meeting of Orthopaedic Research Society,* San Francisco, Vol. 1, ORS, 1997, 62.
117. Van Rietbergen, B., Odgaard, A., Kabel, J., and Huiskes, R., Relationships between bone morphology and bone elastic properties can be accurately quantified using high-resolution computer reconstructions, *J. Orthop. Res.,* 16, 23, 1998.
118. Hollister, S. H., Fyhrie, D. P., Jepsen, K. J., and Goldstein, S. A., Application of homogenization theory to the study of trabecular bone mechanics, *J. Biomech.,* 24, 825, 1991.
119. Hollister, S. J., Brennan, J. M., and Kikuchi, N., A homogenization sampling procedure for calculating trabecular bone effective stiffness and tissue level stress, *J. Biomech.,* 27, 433, 1994.
120. Keaveny, T. M., Pinilla, T. P., Crawford, R. P., Kopperdahl, D. L., and Lou, A., Systematic and random errors in compression testing of trabecular bone, *J. Orthop. Res.,* 15, 101, 1997.
121. Keaveny, T. M., Guo, X. E., Wachtel, E. F., McMahon, T. A., and Hayes, W. C., Trabecular bone exhibits fully linear elastic behavior and yields at low strains, *J. Biomech.,* 27, 1127, 1994.
122. Niebur, G. L., Hsia, A. C., Chen, T. J., and Keaveny, T. M., Simulation of trabecular bone yield using nonlinear finite element analysis, in *ASME IMECE,* BED–Vol. 43, ASME, 1999.
123. Riemer, B. A., Eadie, J. S., Weissman, D. E., Haut, K. M., Hollister, S. J., and Goldstein, S. A., Characterization of the architecture, tissue properties, and continuum behavior of aging trabecular bone, in *40th Annual Meeting of Orthopaedic Research Society,* Vol. 1, ORS, 1994, 189.
124. Riemer, B. A., Eadie, J. S., Wenzel, T. E., Weissman, D. E., Guo, X. E., and Goldstein, S. A., Microstructure and material property variations in compact and trabecular vertebral bone tissue, in *41st Annual Meeting of Orthopaedic Research Society,* Vol. 2, ORS, 1995, 529.
125. Cowin, S. C., Ed., *Bone Mechanics,* CRC Press, Boca Raton, FL, 1988.
126. Williams, J. L. and Johnson, W. J. H., Elastic constants of composites formed from PMMA bone cement and anisotropic bovine cancellous bone, *J. Biomech.,* 22, 673, 1989.

11

Viscoelastic Properties of Cortical Bone

Roderic Lakes
University of Wisconsin–Madison

Abstract—Viscoelastic damping, tan δ, in bone exhibits a broad *minimum* at frequencies 1 to 100 Hz. These frequencies are associated with normal activities. A shock-absorbing role for bone has been suggested for bone based on its viscoelastic response. However, a minimum in damping is inconsistent with such an interpretation. Moreover, the product of stiffness and damping is comparable to that of other materials. It is therefore unlikely that damping at frequencies 1 to 100 Hz has been maximized by "design." Substantial damping is observed at low frequency and substantial creep is observed at long time. The physical cause is associated with interfaces such as the cement lines.

11.1 Introduction: Viscoelastic Properties

Solid materials are often described, for small strains, by Hooke's law of linear elasticity: stress σ is proportional to strain ε. In one dimension, Hooke's law is written, $\sigma = E\varepsilon$, with E as Young's modulus. In reality, all materials deviate from Hooke's law. One form of deviation is viscoelasticity. In *viscoelastic* materials the relationship between stress and strain depends on time or upon frequency in oscillatory loading. *Anelasticity* is a special case of viscoelasticity in which full recovery ultimately occurs after removal of a transient load.

Phenomena in viscoelastic materials include the following.

1. If the stress is held constant, the strain increases with time (creep).
2. If the strain is held constant, the stress decreases with time (relaxation).
3. In a constant strain rate test, the effective stiffness depends on the strain rate.
4. If cyclic loading is applied, hysteresis (a phase lag angle δ between stress and strain) occurs, representing a dissipation of mechanical energy.
5. Acoustic and ultrasonic waves experience attenuation. The attenuation is proportional to the phase angle δ between stress and strain.

0-8493-9117-2/01/$0.00+$.50

Creep is a slow, progressive deformation of a material under constant stress σ_0. Creep tests are used in the laboratory to quantify the viscoelastic behavior of materials, and creep processes occur in the steady-state loading of materials. The creep compliance $J(t)$ is defined as the ratio of time-dependent strain $\varepsilon(t)$ to stress level σ_0.

$$J(t) = \frac{\varepsilon(t)}{\sigma_0} \tag{11.1}$$

In a creep experiment, the stress is suddenly raised to a constant level beginning at time zero, and the strain or displacement is measured as a function of time. Creep experiments can be conducted with commercial mechanical testing instruments or with custom instruments involving dead weights.

In viscoelastic materials, *linearity* refers to proportionality between stress and strain at a given time or frequency. In linearly viscoelastic materials, the creep compliance is independent of stress level. Creep curves have been classified into three regions, *primary* creep in which the curve (assuming linear scales of time and strain) is concave down, *secondary* creep in which deformation is proportional to time, and *tertiary* creep in which deformation accelerates until creep rupture occurs. Tertiary creep always, and secondary creep usually, involves damage (see Chapter 18 by Davy and Jepsen) and nonlinear viscoelasticity. Even though secondary creep is represented by a straight line in a plot of strain vs. time, that straight line has nothing whatever to do with linear viscoelasticity. Linear response involves a linear relationship between cause and effect: stress and strain at a given time in the case of creep.

Stress relaxation is the gradual decrease of stress when the material is held at constant strain. The relaxation modulus $E(t)$ is defined as the ratio of time-dependent stress $\sigma(t)$ to strain level ε_0.

$$E(t) = \frac{\sigma(t)}{\varepsilon_0} \tag{11.2}$$

In linear materials, $E(t)$ is independent of strain level, so $E(t)$ is a function of time alone. In a relaxation experiment, the strain (or displacement) is suddenly raised to a constant level beginning at time zero, and the load or torque is measured as a function of time. Relaxation experiments can be conducted with commercial mechanical testing instruments or with custom instruments involving cams to apply a prescribed displacement.

Mechanical damping refers to the phase δ between stress and strain in response to a stress $\sigma(t)$, which varies sinusoidally in time t, $\sigma(t) = \sigma_0 \sin(2\pi\nu t)$, in which frequency ν is measured in cycles per second or hertz (Hz). One usually speaks of the tangent of the phase angle, or tan δ. The dynamic stress strain relation can be expressed as

$$\sigma(t) = \left|E^*(\omega)\right| \varepsilon_0 e^{i(\omega t + \delta)}, \tag{11.3}$$

with the complex dynamic modulus represented as $E^* \equiv E' + i\,E''$ with $\tan\delta = E''/E'$ and $i = \sqrt{-1}$. The primes are conventional notation and do not represent derivatives. The complex dynamic modulus in the frequency domain is related to the creep and relaxation functions in the time domain, by Fourier transformation. Measurement of tan δ can be accomplished by direct measurement of phase at low frequency. Properties at frequencies above about 10 Hz are difficult to obtain with commercial servohydraulic or dynamic mechanical analyzer instrumentation as a result of resonances in the transducers. Damping can also be measured in custom-made instruments by study of the phase at higher frequency, of width of a dynamic compliance curve near a natural resonant frequency, by study of free-decay of resonant vibration, or by measurement of attenuation of sonic or ultrasonic waves.

Constant strain rate experiments are usually done in investigations of material strength; however, they indirectly reveal viscoelastic properties. In such an experiment, the material initially has a strain of zero; then the strain is made to increase linearly with time until fracture occurs. For a linearly viscoelastic material (Ferry, 1970; Lakes, 1998),

$$\frac{d\sigma(t)}{dt} = \frac{d\varepsilon(t)}{dt} E(t). \tag{11.4}$$

So the *slope* of the stress–strain curve of a linearly viscoelastic material is higher for a higher strain rate. $E(t)$ decreases with time; hence, the slope of a stress–strain curve decreases with strain. Consequently, the effect of viscoelasticity is for the stress–strain curve to be concave down, and its slope to increase with strain rate. The stress–strain curve is nonlinear even though the material is assumed to be linearly viscoelastic. Although the stress and strain are linearly related at a particular time t, the constant strain rate test involves strain and the time changing simultaneously. Therefore, although one can infer viscoelastic properties from such a test, it is not optimal for viscoelasticity. Commercial servohydraulic testing machines are commonly used for this kind of test.

The *constitutive equation* for linear viscoelasticity is Boltzmann's superposition integral. In linearly viscoelastic materials, the Boltzmann superposition integral has the following form in the tensorial modulus formulation. Indices i and j take on values from 1 to 3, and the repeated indices k and l are summed over via the Einstein summation convention.

$$\sigma_{ij}(t) = \int_0^t C_{ijkl}(t - \tau) \frac{d\varepsilon_{kl}}{d\tau} d\tau. \tag{11.5}$$

Given the constitutive equation and the material properties obtained from experiment, one can calculate the response to any history of stress or strain. Each component of the relaxation modulus tensor $C_{ijkl}(t)$ can have not only a different value but also a different time dependence. There are 81 components of C_{ijkl}, but taking into account the symmetry of the stress and strain tensors, only 36 of them are independent. Bone is anisotropic. Human compact Haversian bone, viewed as axisymmetric or hexagonal in symmetry, has five independent *elastic* moduli; bovine plexiform bone, viewed as orthotropic, has nine independent *elastic* moduli. Since bone is viscoelastic, each modulus term can have a different time dependence or frequency dependence. Moreover, in elastic materials one can demonstrate, since $C_{ijkl} = C_{klij}$, a reduction from 36 to 21 constants for general anisotropy via consideration of a strain energy density function. Viscoelastic materials do not have this symmetry (Rogers and Pipkin, 1963; Day, 1971): one may have an asymmetric relaxation modulus tensor $C_{ijkl}(t) \neq C_{klij}(t)$. Therefore there could be 7 independent relaxation modulus functions for human bone as a hexagonal material, and 12 for bovine bone as an orthotropic material. Thus far, experimental treatments of tensorial anisotropy of bone have dealt with the elastic aspect.

The loss tangent of a linearly viscoelastic material is related to the creep or relaxation properties by Fourier transformation. For many computational purposes as well as for visualization, $\tan \delta$ is related to the slope of the relaxation curve $E(t)$ on a doubly logarithmic scale by the following approximation, valid if the slope is not too large and the relaxation curve is slowly varying:

$$\tan \delta \approx -\frac{\pi}{2} \frac{d \ln E(t)}{d \ln t} \Big|_{t=1/\omega}. \tag{11.6}$$

Similarly, the loss tangent is related to the slope of the creep curve $J(t)$ by the following:

$$\tan \delta \approx \frac{\pi}{2} \frac{d \ln J(t)}{d \ln t} \Big|_{t=1/\omega}. \tag{11.7}$$

Viscoelastic experiment upon *tissue* such as bone is more challenging than in polymers for several reasons. For amorphous polymers, it is often possible to infer material properties over a wide range of time or frequency from test results taken at different temperatures. Viscoelasticity in such materials is studied by conducting a series of tests at different temperature, and shifting the results on a log time or log frequency scale to obtain a master curve. Materials for which the shifting process gives rise to a single curve are called thermorheologically simple. Composites, particularly those of biological origin, are not thermorheologically simple since there are multiple causal mechanisms each with a different temperature sensitivity. Direct measurement of properties over many decades is required for a full characterization of the material.

In comparisons of experimental results in this chapter, tan δ is used since it is a dimensionless measure of damping with simple physical interpretations.

11.2 Rationale: Why Is Bone Viscoelasticity of Interest?

The study of viscoelastic behavior in bone is of interest in several contexts. First, bone in its structural role in the body exhibits viscoelastic behavior, which has an influence on material performance. Second, viscoelasticity is of interest since it is causally linked to a variety of microphysical processes and can be used as an experimental probe of those processes. Third, the causal links between viscoelasticity and microstructure as well as other physical properties can be exploited in the use of viscoelastic tests as a diagnostic tool.

As an example, consider that babies have deformable heads. The head may be misshapen following the birth process, but the shape returns to normal after about 6 weeks. This is an aspect of time-dependent behavior (Lakes, 1998). If the baby sleeps in a single position, the long-term load component can cause an abnormal head shape (Largo and Duc, 1977) due to creep deformation. Abnormal head shape in infants can be corrected by a helmet-like device worn on the head (Clarren et al., 1979; Pomatto et al., 1997). The device provides a gentle pressure to gradually restore the normal shape of the head. As another example, Currey (1965) considered the loss of stiffness during creep in relation to the static component of load during standing in birds with slender legs. He considered that creep may slightly influence the "design" of limb bones so that in the presence of creep they would be somewhat bulkier than if they were purely elastic. As another example, Dimarogonas et al. (1993) found that bone damping decreased significantly following exercise training of rats, and considered damping as a possible diagnostic tool. Damping at ultrasonic frequencies is associated with attenuation of waves. Lakes et al. (1986) found attenuation to be so large in the radial direction to limit the utility of diagnostic ultrasound when passed through bone. Finally, bone is known to remodel in response to mechanical load: Wolff's law (Wolff, 1892). The process or processes by which the cells are able to sense the strain depend on transfer of mechanical energy to the cells. Such energy transfer might be probed by viscoelastic studies.

Study of bone viscoelasticity is best placed in the context of strain levels and frequency components associated with normal activities and with applications of diagnostic tools.

As for strain levels in bone *in vivo*, in a human volunteer, maximum strain along the tibia axis was about 3.5×10^{-4} during normal walking at 1.4 m/s and 8×10^{-4} during running at 2.2 m/s (Lanyon et al., 1975). Strains of similar magnitudes have been observed in animals such as sheep (Lanyon, 1973). Strain as large as 3.2×10^{-3} was observed in the tibia of a galloping horse (Rubin, 1984), and 1.2×10^{-3} to 4.2×10^{-3} in a human distal tibia during jumping (Ekenman et al., 1998).

The frequency content of normal loading histories extends to very low values as a result of the static component of force to which leg bones are subjected. Time-dependent joint forces in walking were presented by Morrison (1969) to a time resolution of 0.02 s, corresponding to a maximum frequency of about 10 Hz, were Fourier-analyzed by Lakes and Katz (1974). Frequency components beyond 100 Hz are probably not prominent in walking. Some activities, such as skiing over bumps, may generate harmonics as high as 1 kHz. Response of bone at higher frequencies in the megahertz range may be of interest in the context of diagnostic ultrasound.

11.3 Axial Properties of Bone

11.3.1 Linear Viscoelasticity

Viscoelasticity in bone has been known since Rauber (1876) studied creep as well as anisotropy and strength of bone. Results obtained for bone by various authors in tension/compression were converted to a common representation and compared by Lakes and Katz (1974). Results for axial deformation showed significant disagreement. Since more data are now available, the matter is discussed below.

As for creep, the long-term bending creep results of Currey (1965) disclose an increasing slope with log time as shown in Fig. 11.1, giving rise to an inferred tan δ increasing at progressively lower effective frequency, as shown in Fig. 11.2. Observe that a single exponential model undergoes most of its change in one decade (a factor of ten) in time, much more rapidly than the creep process in bone, and most other materials. Currey also found that after 10 days creep loading, the deformation was 33% greater than "initially." After removal of the load, most of the creep strain recovered. A further creep loading for 55 days produced a creep deformation 53% of the "initial" deformation, and most of this creep deformation was recovered after 234 days. Creep deformation under low load is therefore anelastic, or recoverable viscoelastic, rather than any form of delayed plasticity. Currey found that drying of bone slowed but did not abolish its creep response. Response of a specimen dried and rewetted was similar to the response when fresh and wet. Currey (1965) also explored the effect of temperature on bone mechanical properties. As for temperature dependence, Currey found a 0.4%/°C decrease in effective "initial" stiffness from 3 to 49 °C; the creep deformation was influenced more by temperature. In contrast to bone, echinoderm spines, which are mostly mineral, exhibited no observable creep.

As for relaxation experiments, analysis by Lakes and Katz (1974) of the axial relaxation results of Lugassy and Korostoff (1969) implies for bovine bone in the longitudinal direction, humps in tan $\delta \approx 0.045$ at 1.6×10^{-2} Hz and tan $\delta \approx 0.015$ at 1.6×10^{-3} Hz. However, as a result of limited data sets used for the transformation, the location of the humps may not be reliable; therefore, an average tan δ was computed and shown for comparison in Fig. 11.2. Lugassy and Korostoff (1969) also found relaxation to be of greater magnitude for transverse compression than for longitudinal compression. Sasaki et al. (1993) studied bending relaxation in bovine bone for times from 10 to 10^5s (about 1 day). The shortest time studied in these tests corresponds to about 0.016 Hz in the frequency domain. These results are of interest since torsion and bending can be compared for the same kind of bone. Total change of effective modulus

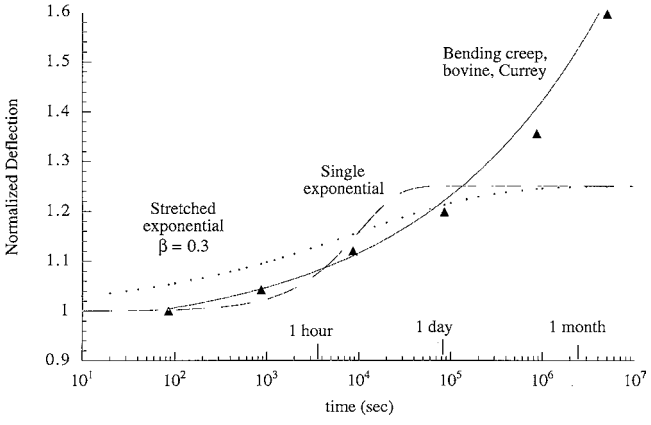

FIGURE 11.1 Creep deformation as a function of time t in bending of bovine bone (triangles), adapted from Currey (1965) and curve-fit (solid line) by $J_1(t) = at^n + bt^m + c$. Shown for comparison is a single exponential model (dashed line): $J_2(t) = 1.25 - 0.25e^{-t/\tau_c}$, with $\tau_c = 10^4$ s as a retardation time. Also shown for comparison is a stretched exponential (points): $J_3(t) = 1.25 - 0.25e^{-(t/\tau_c)^\beta}$, with $\tau_c = 10^4$ s as a retardation time and $\beta = 0.3$.

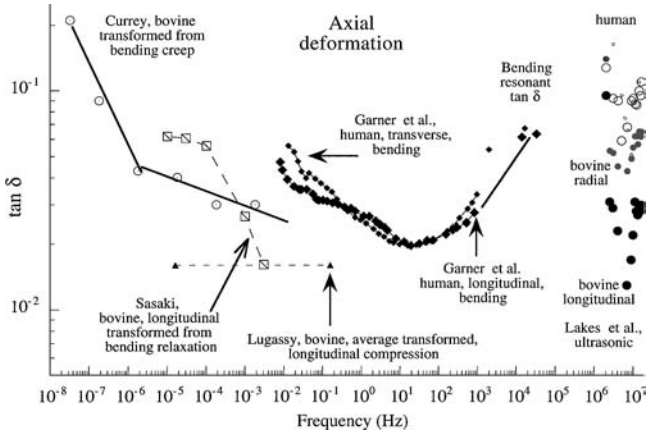

FIGURE 11.2 Tan δ for compact bone under axial deformation. Results calculated from slope of long-term creep curve for bovine bone in bending by Currey (1965), center circles, ⊙. Results calculated from integration of constitutive equation of Sasaki et al. (1993) for bending relaxation in bovine bone (slant squares, ⧅). Results calculated from average slope of bending relaxation in bovine bone by Lugassy and Korostoff (1969); triangles, ▲. Results of Garner et al. (2000) for wet human bone in bending, direct measurements of tan δ; diamonds, ♦. Results from ultrasonic attenuation by Lakes et al. (1986), human bone, open circles, ○; bovine bone solid circles ●; longitudinal direction, large symbols; radial direction, small symbols.

during relaxation was about 40% for bending and 30% for torsion. Sasaki et al. (1993) fitted their results with a superposition of a stretched exponential or KWW (after Kohlrausch, Williams, Watts) model and a Debye model; these models are discussed in Section 11.5. By numerically transforming the relaxation model of Sasaki (1993) for bending, described in detail below, one obtains tan δ shown in Fig. 11.2.

As for dynamic sinusoidal experiments, results for viable human tibia of Black and Korostoff (1973) from about 30 to 300 Hz are jagged as a function of frequency, and damping cannot be inferred. Dynamic results of Smith and Keiper (1965) are flat as a function of frequency over about one decade to 2 kHz. Since damping depends on the slope of the curve of modulus vs. frequency, these results are of insufficient resolution to reveal the damping. Direct dynamic measurements of tan δ were conducted by Garner et al. (2000) upon human compact bone in bending at ambient temperature (22°C) using an apparatus developed by Chen and Lakes (1989) and refined by Brodt et al. (1995). Damping results are shown in Fig. 11.2.

Stress–strain curves at constant strain rate from 0.001 to 1500/s were presented by McElhaney (1966). The tan δ values, e.g., 0.15 at 1.6 Hz, inferred from these results exceeded values inferred from results of other authors by about an order of magnitude. The discrepancy was attributed by Lakes and Katz (1974) to nonlinear viscoelastic behavior not accounted for in the transformation process. It is now known that nonlinearity in bone is weak up to a strain of at least 0.002; therefore, other causes are to be sought for the discrepancy, e.g., difficulties in high strain rate calibration in the results of McElhaney, or possibly differences in the bone.

At ultrasonic frequencies, Lakes and Katz (1983) found that a second, slow longitudinal wave propagated in wet bone, and attributed this wave to fluid–solid interactions in bone. The slow wave in isotropic porous materials is faster than in the pore fluid; however, in the bone the slow wave was slower than the wave speed in water. The difference may be due to bone anisotropy or due to bubbles of air in the pore fluid. Lakes et al. (1986) reported ultrasonic attenuation vs. frequency in the frequency range from less than 1 to 16 MHz. Values of damping, tan δ, inferred from the attenuation are shown in Fig. 11.2; human bone exhibited more damping than bovine. Waves propagating in the radial direction disclosed a higher tan δ than in the longitudinal direction. Wave velocity in bovine bone was highest in the longitudinal direction, 4.26 km/s; less in the circumferential direction, 3.63 km/s; and least in the radial direction, 3.38 km/s at 10 MHz. Wave velocity for human bone was 3.76 km/s longitudinal, 3.31 km/s transverse.

Ultrasonic velocity for longitudinal waves depends not on Young's modulus E but on the tensorial modulus. For the 1 direction, longitudinal wave velocity depends on C_{1111}, which is the tensorial stiffness element for tension or compression in the x (or 1) direction, when strain in the y and z directions is constrained to be zero. C_{1111} governs the propagation of longitudinal waves in an extended medium, since the waves undergo a similar constraint on transverse displacement. For isotropic elastic materials, engineering constants such as Young's modulus E and Poisson's ratio ν are related to C_{1111} as follows:

$$C_{1111} = E\frac{1-\nu}{(1+\nu)(1-2\nu)}. \tag{11.8}$$

The longitudinal wave speed in the 1 direction is $v = \sqrt{C_{1111}/\rho}$. For isotropic materials, the longitudinal wave speed may also be written

$$v = \sqrt{\left(B + \frac{4}{3}G\right)/\rho}.$$

The physical reason is the fact that compression with a restrained Poisson effect involves both volume change, governed by the bulk modulus B, and a shape change, governed by the shear modulus G (Kolsky, 1963). For anisotropic materials such as bone, C_{1111} depends in a more-complicated way on the engineering constants. For viscoelastic materials, all the material parameters may be regarded as complex–valued functions of frequency. The attenuation of longitudinal plane waves depends on tan δ for the corresponding C modulus element; this may not be the same as the tan δ corresponding to Young's modulus.

Young's modulus comparisons are as follows. Garner et al. (2000), 12.8 GPa at 1 Hz; Lugassy and Korostoff, 14 GPa at 1 Hz; Smith and Keiper, 19 GPa at 1 kHz; McElhaney, 20 GPa at 1 Hz. Ideally, comparisons should be made at the same frequency, but many of the results offer little or no overlap. The dynamic modulus depends on frequency such that the slope on a log modulus, log frequency plot is proportional to the damping, similar to Eqs. 11.6 and 11.7 for creep and relaxation. Therefore, for tan δ in the range 0.01 to 0.02, the modulus changes slowly with frequency.

Overall, the comparison of axial results leads one to conclude that the tan δ for axial deformation attains a broad minimum at frequencies that dominate in normal activities. Some of the differences in the properties may be attributed to biological variability. Indeed, Dimarogonas et al. (1993) found substantial differences in bone damping with training of rats. Trained animals had bones of lower damping (damping factor 0.02) compared with untrained animals (damping factor 0.03) as ascertained from free decay of vibration *in vitro*. Damping may be a more sensitive indicator of bone integrity than mineralization.

11.3.2 Nonlinear Viscoelasticity

Secondary creep (strain proportional to time but not proportional to stress) at relatively large stress appears to be thermally activated (Rimnac et al., 1993). Fondrk et al. (1988) observed secondary tensile creep above a threshold stress and observed that a major portion of the inelastic strain after loading in the nonlinear range was recoverable following unloading. The concept of "threshold" deserves some care in interpretation (Lakes, 1989). Secondary creep in bone requires static load levels well beyond the range that occurs during normal activities in the body. Secondary creep superficially appears to be a simpler aspect of bone viscoelastic behavior than primary creep, even though compact bone is a complex composite material; secondary creep appears simpler since history effects are usually not considered.

Creep under sufficiently large load, giving rise to an initial strain in the range 0.003 to 0.007, terminates in fracture (Mauch et al., 1992). This is well beyond the range of normal static load components in the body. These authors also found that deer antler, which has less mineral than mature bone, is more damage tolerant than bone. Moreover, antler took far longer to fracture at any given normalized stress than did bovine bone. Currey (1989) furthermore studied rate effects on antler. He found the 'final stiffness' (ultimate stress/ultimate strain) is invariant with strain rate. Reindeer antler, however, shows a considerable

post-yield increase in stress. This is difficult to accommodate in a cumulative damage model. Both creep and fatigue in bone give rise to microscopic damage (Caler and Carter, 1989)(see Davy, chapter 16). The effect of strain rate on *strength* of bone is as follows. The compressive strength σ_{ult}[in MPa] depends on the density ρ (in g/cm^3) and also varies with the strain rate $d\varepsilon/dt$ (in s^{-1}) (Carter and Hayes, 1976).

$$\sigma_{ult} = 68[d\varepsilon/dt]^{0.06}\rho^2. \tag{11.9}$$

This is a relatively weak rate dependence, since a factor 1,000 change in strain rate only changes the strength by a factor 1.5.

11.4 Shear Properties of Bone

11.4.1 Linear Viscoelasticity

Results in shear obtained by several authors are combined in Fig. 11.3. The loss tangent in shear of wet compact bone attains a broad *minimum* over the frequency range associated with most bodily activities. Also shown in Fig. 11.3 is a Debye peak (Eq. 11.13 below) in tan δ, corresponding, by Fourier transformation, to a single exponential (Eq. 11.11) in the creep or relaxation behavior, and corresponding to a three element spring–dashpot model. Observe that the loss tangent of bone occupies a much larger region of the frequency domain than a Debye peak.

As for relaxation experiments, Lakes et al. (1979) presented torsional results over a range from 1 to 10^5 s for human and bovine bone. Lakes and Katz (1979b) made use of a triangle-shaped relaxation spectrum for the long-time region (see Section 11.5). Transformed tan δ values are shown in Fig. 11.3. Sasaki et. al. (1993) studied torsional relaxation in bovine bone for times from 10 to 10^5 s, and modeled this behavior using the KWW model. Again, the dynamic behavior corresponding to the KWW relaxation (see Section 11.5) is tan δ in the form of a broad peak with tan $\delta \propto \nu^{-\beta}$ for frequencies ν well above

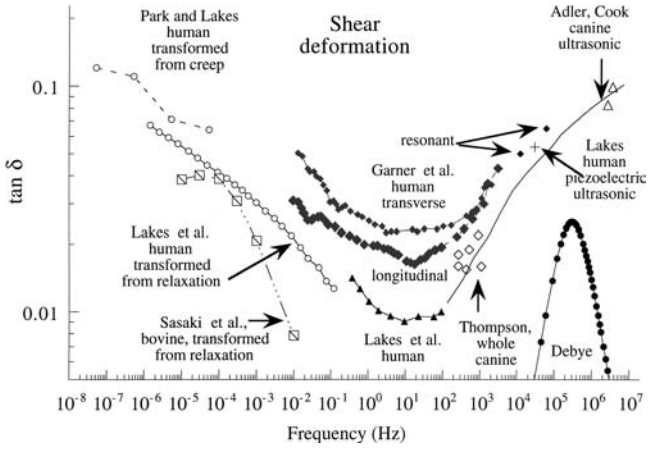

FIGURE 11.3 Tan δ for human compact bone in shear. Damping at low frequency inferred from slope of long-term creep by Park and Lakes (1986), center circles, ⊙. Results calculated from integration of constitutive equation of Sasaki et al. (1993) for torsion relaxation in bovine bone (slant squares, ▨). Results adapted from data of Lakes et al. (1979) for wet human tibial bone at 37°C (calculated from relaxation, circles, ○; directly measured, ▲). Direct measurements of tan δ by Garner et al. (2000) for wet human bone in torsion, diamonds, ♦. Damping data of Thompson (1971) for whole dog radius at acoustic frequencies (diamonds, ◊). Damping of wet human femoral bone by Lakes (1982) via a piezoelectric ultrasonic oscillator (cross, +). Damping at ultrasonic frequency for canine bone by Adler and Cook (1975) at room temperature (open triangles, △). Theoretical Debye peak corresponding to an exponential in the time domain, solid circles ●.

the peak. As shown below, the actual tan δ increases at frequencies too high to achieve in relaxation experiments; therefore, further terms would be called for in the model.

Torsional creep curves reported by Lakes and Saha (1979) and Park and Lakes (1986) were similar to the bending creep curves of Currey (1965) in that they were concave up vs. log time. As with bending creep, long-term torsional creep corresponds to high tan δ at very low effective frequency as shown in Fig. 11.3.

Direct dynamic measurements upon human compact bone of tan δ were conducted in torsion by Lakes et al. (1979) and by Garner et al. (2000). The shear modulus was 4.07 and 4.15 GPa for the former and 3.42 GPa for the latter at 1 Hz. The latter results were obtained at ambient temperature (22°C) using an apparatus capable of both torsion and bending tests upon the same specimen; they disclosed higher damping than the former, possibly because the bone was from an older donor. Lakes et al. (1979) also reported relaxation and tan δ for bovine plexiform bone. Damping was similar to that of human bone. Damping from 1 to 100 Hz exhibited little temperature dependence over the range 28 to 42°C. Also shown in Fig. 11.3 are resonant results of Lakes (1982) for human bone via a piezoelectric ultrasonic oscillator, resonant acoustic data of Thompson (1971) for whole dog radius, and ultrasonic results of Adler and Cook (1975) for canine bone at room temperature. As for ultrasonic waves in shear, for isotropic materials, the shear wave speed is $v = \sqrt{G/\rho}$, where G is the shear modulus. Attenuation is proportional to tan δ in shear. Few shear wave studies have been done.

Overall, the torsional results all lead one to conclude that the tan δ for shear attains a broad minimum at frequencies that dominate in normal activities. Damping is higher at very low frequency and at ultrasonic frequency. The bovine bone used by Sasaki et al. generally has moderately lower damping than human bone; however, the computed value at 0.01 Hz is significantly lower than values reported here and elsewhere; that frequency probably represents a short time limit of the model.

11.4.2 Nonlinear Viscoelasticity

Torsional viscoelasticity of compact bone exhibits a weak nonlinearity at strain levels associated with normal activities (Lakes et al., 1979). For human bone, neither the dynamic shear modulus nor the tan δ showed any departure from linearity for shear strains from 3.6×10^{-6} to 3.6×10^{-4}. Human bone showed an increase of stiffness by 1 to 3% with strain in relaxation, from 9×10^{-5} to 9×10^{-4}. Bovine bone showed an increase of stiffness by 6% with strain in relaxation, at strains from 4.7×10^{-5} to 6.2×10^{-4}. This nonlinearity was more pronounced in the relaxation properties than in the dynamic properties. Strain dependence of the stiffness can be accommodated by writing the relaxation modulus in Eq. 11.5 as a function of both time and strain: $G(\varepsilon,t)$. Such a formulation describes some, but not all, of the nonlinear behavior. For example, recovery following removal of applied deformation occurs somewhat more slowly than relaxation (Lakes et al., 1979). Multiple integral formulations have been used by Lakes and Katz (1979b) to describe such a situation.

11.5 Modeling

The KWW stretched exponential relaxation model is

$$E(t) = (E_0 - E_\infty)e^{-(t/\tau_r)^\beta} + E_\infty, \tag{11.10}$$

with $0 < \beta \leq 1$, E_0 and E_∞ as constants, t is time, and τ_r as a characteristic relaxation time. The dynamic behavior corresponding to the KWW relaxation is tan δ in the form of a broad peak with tan $\delta \propto \nu^{-\beta}$ for frequencies ν well above the peak.

The Debye model for relaxation in the time domain is

$$E(t) = E_2 + E_1 e^{-t/\tau_r}, \tag{11.11}$$

with τ_r as a relaxation time. For creep, the Debye model is

$$J(t) = J_2 - J_1 e^{-t/\tau_c}, \tag{11.12}$$

with τ_c as a retardation time.

The frequency domain response is related to the time domain response by Fourier transformation. The corresponding Debye peak in tan δ in the frequency domain is as follows. The peak in tan δ covers about one decade in frequency. The frequency dependence is shown in Fig. 11.3 for comparison with the behavior of bone.

$$\tan \delta(\omega) = \frac{\Delta}{\sqrt{1+\Delta}} \frac{\omega\tau_m}{1+\omega^2\tau_m^2}, \tag{11.13}$$

where $\tau_m = \tau_r\sqrt{1+\Delta}$ is a time constant, $\omega = 2\pi\nu$ is angular frequency, and ν is frequency. The *relaxation strength* Δ is defined as the change in stiffness during relaxation divided by the stiffness at long time. For small damping, the height of the peak is tan $\delta \approx \Delta/2$.

A stretched exponential and Debye model for creep are shown in Fig. 11.1 with the experimental creep results of Currey (1965). The time dependence of a Debye (single-exponential) model is more abrupt on a log timescale than that of real materials including bone. The Debye model undergoes most of its change in one decade (a factor of ten) in time. In some early studies (e.g., Bargren et al., 1974), spring–dashpot models were used in the description of viscoelastic processes. Models with three or four such elements are equivalent to the Debye model. If a linear scale of time or frequency is used to plot results, one may obtain an impression that the change in stiffness has leveled off, whereas in fact it continues to change with time or frequency. Debye models may be used as one component of a model but by themselves they are inadequate to model the viscoelasticity of bone.

In spectral modeling, one decomposes the relaxation modulus function $E(t)$ into a distribution of exponentials. The distribution function $H(\tau)$ is referred to as the relaxation spectrum, as follows. The concept of spectrum is linked to a view of the governing mechanisms considered to give rise to exponential components.

$$E(t) - E_\infty = \int_{-\infty}^{\infty} H(\tau) e^{-t/\tau} d\ln\tau = \int_0^\infty \frac{H(\tau)}{\tau} e^{-t/\tau}\, d\tau. \tag{11.14}$$

Here E_∞ is the "equilibrium" modulus, the stiffness after an infinite time of relaxation. The *box* spectrum (Tobolsky, 1960) is constant over a range of time values and zero outside that range. It was originally introduced for polymers but has been used in biomechanics. The box spectrum, if nonzero over three or more decades of time, gives a relaxation modulus that is approximately linear vs. log time and a loss modulus E'' approximately constant vs. frequency. Lakes and Katz (1979b) used a triangle spectrum $H(\tau) =$ (constant)ln(τ) to model the relaxation behavior of bone. This spectrum gives a relaxation function with a slope vs. log time increasing in magnitude with time; moreover, tan δ becomes large at progressively lower frequency.

Both the stretched exponential and the triangle spectrum have been used to model the behavior of bone for time in relaxation longer than 1 s or frequency lower than about 0.16 Hz. Since dynamic data show the damping to increase beyond 100 Hz, additional terms are called for in future models to deal with that region of behavior.

11.6 Structure and Causal Mechanisms

Viscoelasticity in bone arises from several mechanisms. Bone is a hierarchical solid that contains structure at multiple length scales (Katz, 1980; Currey, 1984; Lakes, 1993). Therefore, viscoelasticity can arise from multiple processes at the different scales, which can give rise to a distribution of relaxation times.

Such a distribution is most easily surveyed if data over many decades of time or frequency are presented on a logarithmic scale.

On the microstructural scale, osteons are large (200 μm diameter), hollow fibers composed of concentric lamellae and of pores. Porosity includes the Haversian canals that run the length of the osteons and that typically contain blood vessels. Lacunae are small ellipsoidal pores about 15 μm across, that contain the bone cells. Canaliculi are very fine channels, less than 1 μm in diameter, radiating from the lacunae. At the ultrastructural level (nanoscale) the fibers consist of a composite of the mineral hydroxyapatite and the protein collagen. The mineral phase of bone is stiff crystalline hydroxyapatite; it is considered virtually elastic. On the molecular scale, collagen as a proteinaceous phase can give rise to significant viscoelasticity (Sasaki et. al., 1993). The *shape* of the relaxation curves are similar for bone and demineralized bone following Sasaki et al. (1993). This is suggestive of a major role for collagen over the timescale studied. Collagen is a natural fibrous polymer. In polymers, viscoelasticity arises due to molecular motions. In wet bone water may facilitate molecular motions by a plasticizing action. Collagen is constrained by cross-links and close apposition with mineral crystallites; therefore, a broad distribution of tan δ is expected. Moreover, Sasaki and Yoshikawa (1993) explored the role of the mineral–collagen interface by determining the relaxation Young's modulus of bovine femoral bone as a function of mineral content. Specimens were partially demineralized chemically. The relaxation curves for specimens of different mineral contents could be superposed upon one another by shifting along the log time axis and the log stiffness axis, giving rise to a master curve. This superposition was attributed to the idea of reinforcement of the collagen matrix around the mineral inclusions. An increase in bone mineralization is associated with an increase in the average modulus and lengthens the characteristic times of the relaxation. The structure of chemically demineralized bone specimens cannot be expected to be the same as that of normal bone; therefore, inferences regarding normal bone can only be indirect. Even so, the finding of Dimarogonas et al. (1993) that bone damping decreased significantly following exercise training of rats is not inconsistent with the above view.

Bone contains other organic materials aside from collagen. A thin layer of a protein-polysaccharide substance occurs at interfaces such as the cement lines. *Interfaces* in bone include the cement lines between osteons, and the boundaries between lamellae. These interfaces are compliant (Katz, 1980). Viscous-like motion at cement lines between osteons is responsible for a portion of the viscoelasticity in bone, particularly at long times and low frequencies as ascertained experimentally in bovine bone by Lakes and Saha (1979) and in human bone by Park and Lakes (1986).

Thermoelastic coupling is a causal mechanism in which damping arises from stress-induced heat flow from the material to its environment or between heterogeneities in the material (Zener, 1938). For a single size of heterogeneity, thermoelasticity gives rise to a Debye peak in the damping. Thermoelastic damping from heat flow between osteons may account for some of the damping between 0.01 and 10 Hz (Lakes and Katz, 1979). Lamellae within osteons are smaller than osteons; therefore, thermoelastic damping from heat flow between them will occur at higher frequencies. The magnitude of the damping depends on the degree of heterogeneity, but that is not well known. Piezoelectric coupling, in which mechanical energy is converted to electrical, then dissipated via conductivity or dielectric loss, was considered by Lakes and Katz (1979). Such coupling was judged to have a negligible contribution to the damping of bone, although it can be significant in piezoelectric ceramics.

Viscoelasticity can result from fluid flow in porous media (Biot, 1941) including hard tissue such as bone (Lakes and Katz, 1979) and soft tissue such as cardiac muscle (Djerad, 1992) and spinal disks. The classical Biot (1941) theory predicts that fluid flow in porosity of a single size scale will give rise to a single exponential in relaxation $E(t)$ in the time domain, hence a Debye peak in the frequency domain. The expected time constant or characteristic frequency is not known. Johnson (1984) found by analysis that the fluid pressure in the vascular channels should have a short relaxation time, on the order of milliseconds *in vivo*. Flow in porosity associated with lacunae and canaliculi was considered more difficult to analyze; the fluid pressure in these pore systems may not relax as rapidly. As for the effects on tan δ, referring to Fig. 11.2 and Fig. 11.3, Debye peaks in damping due to fluid flow have not yet been definitively identified. A detailed presentation of theories for fluid flow in bone is given by Cowin (Chapter 23).

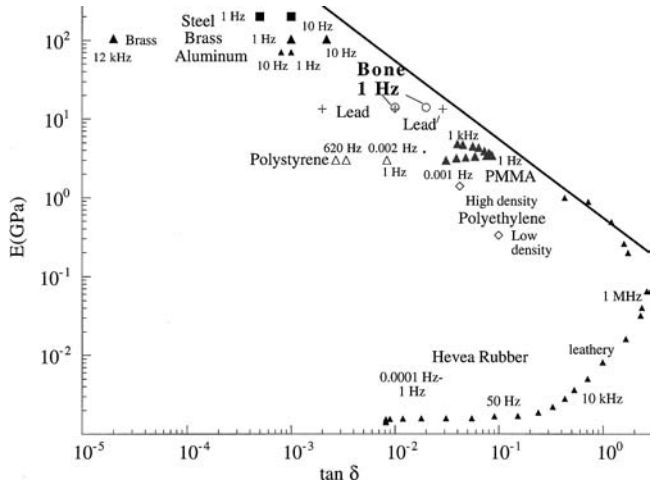

FIGURE 11.4 Comparison of stiffness and tan δ for bone compared with other materials. Common materials, including bone, lie to the lower left of the diagonal line. Damping for bone is for the frequency range 1 to 100 Hz. (Adapted from Lakes, 1998.)

The cause of the increase of viscoelasticity at the highest frequencies has not been identified. Damping increases with frequency above about 10 Hz in both wet and dry bone. That damping cannot, therefore, be primarily due to fluid flow. It may be due to segmental molecular motions in collagen.

11.7 Comparisons with Other Materials

The loss tangent, tan δ, of bone is intermediate between that of polymers and metals. Polymers exhibit values from 0.1 in the glassy state to 1 or more in the glass–rubber transition. Structural metals such as steel, brass, and aluminum exhibit small viscoelastic effects: tan δ is 10^{-3} or less, as small as tan $\delta = 3.6 \times 10^{-6}$ for some aluminum alloys. Compact bone, at physiological frequencies from 0.1 to 10 Hz, exhibits tan δ on the order 0.01 to 0.02. Both stiffness and damping of compact bone are intermediate between values seen in structural metals and polymers. The comparison is shown as a stiffness-loss map, in Fig. 11.4. The diagonal line in Fig. 11.4 presents the largest product (E tan $\delta \approx 0.6$ GPa) of stiffness E and damping, found in common materials. Stiffness is considered as the absolute value of the complex dynamic Young's modulus $|E^*|$. It is possible to achieve E tan $\delta > 0.6$ GPa in composites designed to achieve such a figure of merit (for vibration absorption), as done by Brodt and Lakes (1995). The damping of bone, by contrast, is unremarkable. It is therefore unlikely that damping at frequencies 1 to 100 Hz has been maximized by "design."

11.8 Summary

Viscoelastic damping, tan δ, in bone exhibits a broad *minimum* at frequencies 1 to 100 Hz. These frequencies are associated with normal activities. A shock-absorbing role for bone has been suggested for bone based on its viscoelastic response. However, the observed minimum in damping is inconsistent with such an interpretation. The viscoelasticity in bone may instead be a side effect of constituents in bone. For example, the cement lines give rise to toughness of bone by virtue of their compliance and viscosity and also give rise to viscoelasticity. Substantial damping is observed at low frequency and substantial creep is observed at long time. The physical cause is associated with interfaces such as the cement lines, but the biological significance is not known.

References

Adler, L. and Cook, C. V., Ultrasonic parameters of freshly frozen dog tibia, *J. Acoust. Soc. Am.,* 58, 1107–1108, 1975.

Bargren, J. H., Bassett, C. A. L., and Gjelsvik, A., Mechanical properties of hydrated cortical bone, *J. Biomech.,* 7, 239–245, 1974.

Bassett, C. A. L. and Becker, R. O., Generation of electric potentials in bone in response to mechanical stress, *Science,* 137, 1063–1064, 1962.

Biot, M. A., General theory of three-dimensional consolidation, *J. Appl. Phys.,* 12, 155–164 1941.

Black, J. and Korostoff, E., Dynamic mechanical properties of viable human cortical bone, *J. Biomech.,* 6, 435–438, 1973.

Brodt, M. and Lakes, R. S., Composite materials which exhibit high stiffness and high viscoelastic damping, *J. Composite Mater.,* 29, 1823–1833, 1995.

Brodt, M., Cook, L. S., and Lakes, R. S., Apparatus for measuring viscoelastic properties over ten decades: refinements, *Rev. Sci. Instrum.,* 66(11), 5292–5297, 1995.

Caler, W. E. and Carter, D. R., Bone creep-fatigue damage accumulation, *J. Biomech.,* 22, 625–635, 1989.

Carter, D. R. and Hayes, W. C., Bone compressive strength: the influence of density and strain rate, *Science,* 194, 1174–1176, 1976.

Chen, C. P. and Lakes, R. S., Apparatus for determining the properties of materials over ten decades of frequency and time, *J. Rheol.,* 33(8), 1231–1249, 1989.

Clarren, S., Smith, D., and Hanson, J., Helmet treatment for plagiocephaly and congenital muscular torticollis, *J. Pediatr.,* 94, 443, 1979.

Currey, J. D., Anelasticity in bone and echinoderm skeletons, *J. Exp. Biol.,* 43, 279, 1965.

Currey, J. D., *The Mechanical Adaptations of Bones,* Princeton University Press, Princetons, NJ, 1984.

Currey, J. D., Strain rate dependence of the mechanical properties of reindeer antler and the cumulative damage model of bone fracture, *J. Biomech.,* 22, 469–475, 1989.

Day, W. A., Restrictions on relaxation functions in linear viscoelasticity, *Q. J. Mech. Appl. Math.,* 24, 487–497, 1971.

Dimarogonas, A. D., Abbasi-Jahromi, S. H., and Avioli, L. V., Material damping for monitoring of strength and density of bones, *Calcif. Tissue Int.,* 52, 244–247, 1993.

Djerad, S. E., du Burck, F., Naili, S., and Oddou, C., Analyse du comportement rhéologique instationnaire d'un échantillon de muscle cardiaque, *C. R. Acad. Sci. Paris, ser. II,* 315, 1615–1621, 1992.

Ekenman, I., Halvorsen, K., Westblad, P., Fellander-Tsai, L., and Rolf, C., Local bone deformation at two predominant sites for stress fractures of the tibia: an *in vivo* study, *Foot Ankle Int.,* 19, 479–484, 1998.

Ferry, J. D., *Viscoelastic Properties of Polymers,* 2nd ed., John Wiley, New York, 1970.

Fondrk, M., Bahniuk, E., Davy, D. T., and Michaels, C., Some viscoplastic characteristics of bovine and human cortical bone, *J. Biomech.,* 21, 623–630, 1988.

Garner, E., Lakes, R. S., Lee, T., Swan, C., and Brand, R., Viscoelastic dissipation in compact bone: implications for stress-induced fluid flow in bone, *J. Biomech. Eng.,* 122, 166–172, 2000.

Gibson, L. J. and Ashby, M. F., *Cellular Solids,* Pergamon Press, Oxford, 1988.

Jendrucko, R. J., Hyman, W. A., Newell, P. H., and Chakraborty, B. K., Theoretical evidence for the generation of high pressure in bone cells, *J. Biomech.,* 9, 87–91, 1976.

Johnson, M. W., Behavior of fluid in stressed bone and cellular stimulation, *Calcif. Tissue Int.,* 36 (Suppl. 1), S72-6, 1984.

Katz, J. L., Anisotropy of Young's modulus of bone, *Nature,* 283, 106–107, 1980.

Kolsky, H., *Stress Waves in Solids,* Dover, New York, 1963.

Lakes, R. S., Dynamical study of couple stress effects in human compact bone, *J. Biomech. Eng.,* 104, 6–11, 1982.

Lakes, R. S., Comment on "Some viscoplastic characteristics of bovine and human cortical bone," *J. Biomech.,* 22, 973, 1989.

Lakes, R. S., Materials with structural hierarchy, *Nature,* 361, 511–515, 1993.

Lakes, R. S., Experimental micromechanics and viscoelasticity of biological and bio-protective materials, presented at IUTAM conference on Synthesis in Bio-Solid Mechanics, Lyngby, Denmark, 25–27 May, 1998.

Lakes, R. S., *Viscoelastic Solids,* CRC Press, Boca Raton, FL, 1998b.

Lakes, R. S. and Katz, J. L., Interrelationships among the viscoelastic functions for anisotropic solids: application to calcified tissues and related systems, *J. Biomech.,* 7, 259–270, 1974.

Lakes, R. S. and Katz, J. L., Viscoelastic properties of wet cortical bone: Part II, relaxation mechanisms, *J. Biomech.,* 12, 679–687, 1979a.

Lakes, R. S. and Katz, J. L., Viscoelastic properties of wet cortical bone: Part III, A non-linear constitutive equation, *J. Biomech.,* 12, 689–698, 1979b.

Lakes, R. S. and Quackenbush, J., Viscoelastic behaviour in indium tin alloys over a wide range of frequency and time, *Philos. Mag. Lett.,* 74, 227–232, 1996.

Lakes, R. S. and Saha, S., Cement line motion in bone, *Science,* 204, 501–503, 1979.

Lakes, R. S., Katz, J. L., and Sternstein, S. S., Viscoelastic properties of wet cortical bone. I. Torsional and biaxial studies, *J. Biomech.,* 12, 657–678, 1979.

Lakes, R. S., Yoon, H. S., and Katz, J. L., Slow compressional wave propagation in wet human and bovine cortical bone, *Science,* 220, 513–515, 1983.

Lakes, R. S., Yoon, H. S., and Katz, J. L., Ultrasonic wave propagation and attenuation in wet bone, *J. Biomed. Eng.,* 8, 143–148, 1986.

Lanyon, L. E., Analysis of surface bone strain in the calcaneus of sheep during normal locomotion, *J. Biomech.,* 6, 41–69, 1973.

Lanyon, L. E., Hampson, W. G. J., Goodship, A. E., and Shah, J. S., Bone deformation recorded *in vivo* from strain gauges attached to the human tibial shaft, *Acta Orthop. Scand.,* 46, 256–268, 1975.

Largo, R. H. and Duc, G., Head growth and changes in head configuration in healthy preterm and term infants during the first six months of life, *Helv. Paediatr.,* 32, 431–442, 1977.

Lugassy, A. A. and Korostoff, E., Viscoelastic behavior of bovine femoral cortical bone and sperm whale dentin, in *Research in Dental and Medical Materials,* Plenum Press, New York, 1969.

Mauch, M., Currey, J. D., and Sedman, A. J., Creep fracture in bones with different stiffnesses, *J. Biomech.,* 25, 11–16, 1992.

McElhaney J. H., Dynamic response of bone and muscle tissue, *J. Appl. Physiol.,* 21, 1231–1236, 1966.

Morrison, J. B., Function of the knee joint in various activities, *Bio-Med. Eng.,* 4, 573–580, 1969.

Park, H. C. and Lakes, R. S., Cosserat micromechanics of human bone: strain redistribution by a hydration-sensitive constituent, *J. Biomech.,* 19, 385–397, 1986.

Pomatto, J. K., Littlefield, T. R., Manwaring, K., and Beals, S. P., Etiology of positional plagiocephaly in triplets and treatment using a dynamic orthotic cranioplasty device, *Neurosurg. Focus,* 2, 1–4, 1997.

Rauber, A. A., *Elasticität und Festigkeit der Knochen. Anatomisch–Physiologische Studie,* Engelmann, Leipzig, 1876.

Rimnac, C. M., Petko, A. A., Santner, T. J., and Wright, T. M., The effect of temperature, stress, and microstructure on the creep of compact bovine bone, *J. Biomech.,* 26, 219–228, 1993.

Rogers, T. G. and Pipkin, A. G., Asymmetric relaxation and compliance matrices in linear viscoelasticity, *Z. Angew. Math. Phys.,* 14, 334–343, 1963.

Rubin, C. T., Skeletal strain and the functional significance of bone architecture, *Calcif. Tissue Int.,* 36, S11–S18, 1984.

Sasaki, N. and Enyo, A., Viscoelastic properties of bone as a function of water content, *J. Biomech.,* 28, 809–815, 1995.

Sasaki, N. and Yoshikawa, M., Stress relaxation in native and EDTA-treated bone as a function of mineral content, *J. Biomech.,* 26(1), 77–83, 1993.

Sasaki, N., Nakayama, Y., Yoshikawa, M., and Enyo, A., Stress relaxation function of bone and bone collagen, *J. Biomech.,* 26, 1369–1376, 1993.

Smith, R. and Keiper, D., Dynamic measurement of viscoelastic properties of bone, *Am. J. Med. Electr.,* 4, 156, 1965.

Tennyson, R. C., Ewert, R., and Niranjan, V., Dynamic viscoelastic response of bone, *Exp. Mech.,* 12, 502, 1972.

Thompson, G., Experimental Studies of Lateral and Torsional Vibration of Intact Dog Radii, Ph.D. thesis, Biomedical Engineering, Stanford University, Stanford, CA, 1971.

Tobolsky, A. B., *Properties and Structure of Polymers,* John Wiley, New York, 1960.

Wolff, J., *Das Gestz der Transformation der Knochen,* A. Hirschwald, Berlin, 1892.

Zener, C., Internal friction in solids II. General theory of thermoelastic internal friction, *Phys. Rev.,* 53, 90–99, 1938.

12

Composite Models of Bone Properties

Eliana Lucchinetti
Swiss Federal Institute of Technology

12.1 Introduction

As discussed in Chapter 1, the main constituents of bone are collagen type I and a mineral phase best defined as poorly crystalline apatite. Clearly, the mechanical properties of bone are somehow dependent upon the properties of its constituents. This means that—as shall be seen later—bone is a composite material. Moreover, not only are the molecular structure and arrangement of both the mineral and the organic phases important, but also the organization of the material "bone" at a tissue level. In other words, bone is both a composite material and a hierarchical structural composite, since several organizational levels can be identified. The necessity of looking at bone at its different structural levels was first pointed out by Katz[1] and later by many other authors, including Landis, Rho, and Weiner.[2–4] Fig. 12.1 illustrates the hierarchy in bone. The basic building blocks (level 1) are the collagen fibrils and the extremely small plate-shaped crystals of carbonate apatite, just hundreds of angstroms long and wide and some 20 to 30 Å thick.[5] These platelets are arranged in an ordered manner within the collagen framework (level 2) forming the mineralized collagen fibril. The mineralized fibrils are further arranged in parallel arrays (level 3). At the next hierarchical level, these arrays of mineral-filled collagen fibrils are organized into a three-dimensional structure (level 4). In the case of osteonal bone, the three-dimensional structure is readily seen in the bone lamellae. The lamellae can be further organized into cylindrical structures, the osteons (level 5). At any hierarchical level, the components show very different mechanical properties so that it is conceivable to consider bone an example of a hierarchical composite material.

Before an exact definition of the term *composite material* (see Section 12.2) is given, the reason a mathematical description of the material properties of bone might be useful is explained. The question to be posed is: Why is a composite model of bone of interest? A composite model of bone might help clarify the role played by bone constituents in skeletal pathologies, best described as consisting of a decrease or an increase in skeletal mass or defective mineralization. Diseases that interfere with the ability of mineral ions to be deposited within the collagen "scaffold" yield bones

0-8493-9117-2/01/$0.00+$.50

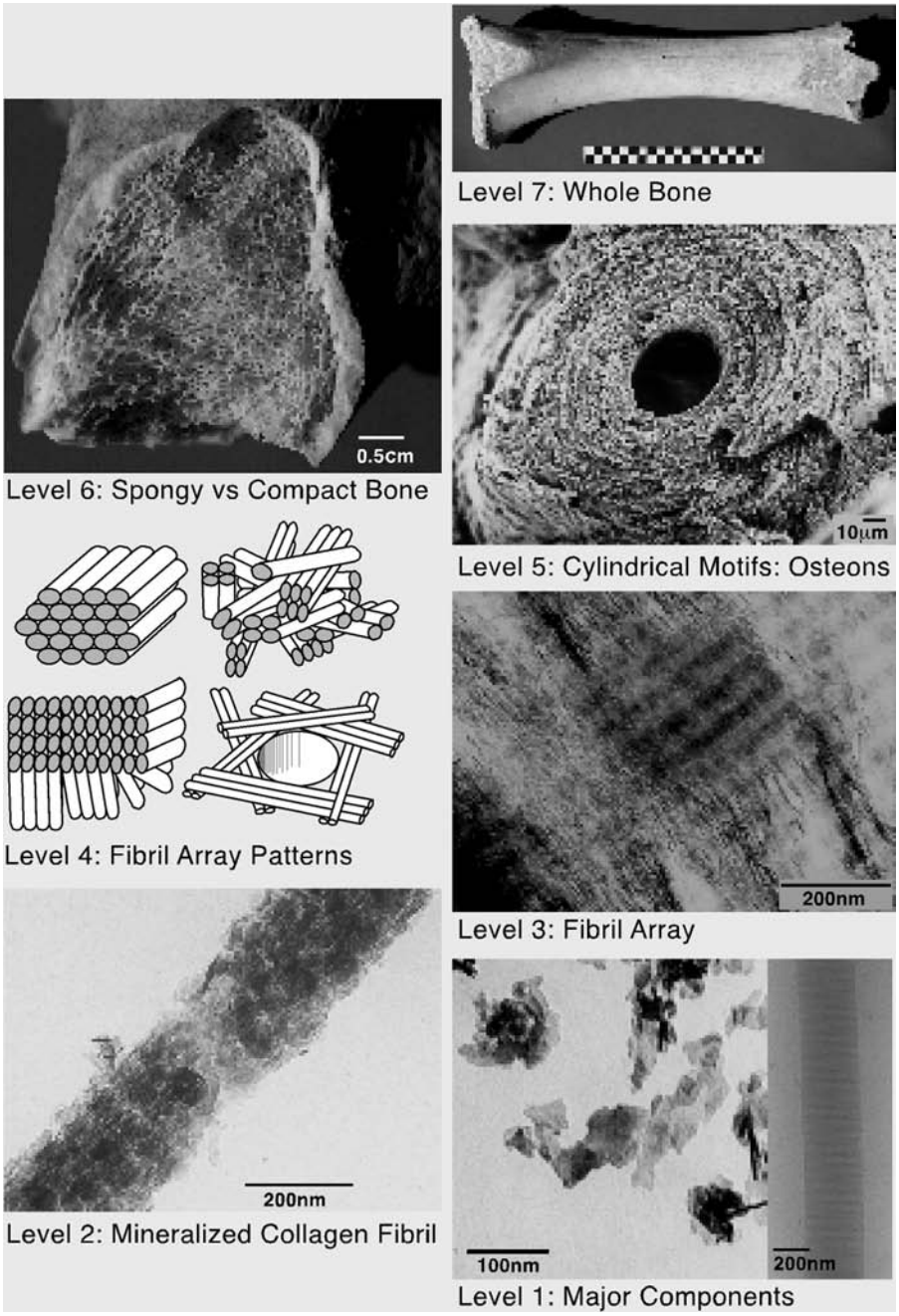

FIGURE 12.1 The seven hierarchical levels of organization of the bone family of materials. *Level 1:* Isolated crystals from human bone (left side) and unstained collagen fibrils from turkey tendon observed in vitreous ice in the TEM (right side). *Level 2:* Transmission electron microscope (TEM) micrograph of a mineralized collagen fibril from turkey tendon. *Level 3:* TEM micrograph of a thin section of mineralized turkey tendon. *Level 4:* Fibril array patterns of organization found in the bone family of materials. *Level 5:* Scanning electron microscopy (SEM) micrograph of a single osteon from human bone. *Level 6:* Light micrograph of a fractured section through a fossilized human femur. *Level 7:* Whole bovine bone (scale 10 cm). (With permission, from the Annual Review of Materials Science, Vol. 28, (c) 1998, by Annual Reviews www.annualreviews. org.)

that bend, but do not necessarily break. These diseases are usually diagnosed as "rickets" in the growing skeleton and as "osteomalacia" in the adult one. Diseases in which either the structure or the quantity of collagen fibers is "abnormal" produce brittle bones and fall under the category of "osteogenesis imperfecta." The defective collagen forms an abnormal mold into which the bone mineral is deposited, thus resulting in a material that is not as strong as normal bone. Finally, osteopenia, which means "reduced bone mass," results from, for whatever cause, an altered coupling of bone formation to its preceding resorption. The major task for clinicians is the identification of those individuals whose bones are so highly affected by osteopenia that they are to be considered at risk for fractures.

From this brief overview, it should be clear that changes in the major components of bone induce changes in its mechanical properties. This chapter is intended to illustrate the potential that a combination of the knowledge from biology, chemistry, and engineering can have on understanding of the development, maintenance, and repair of the skeleton and on the clinical management of bone diseases.

The next section is a short introduction to the mechanics of composite materials and summarizes the most common approaches to the problem of predicting the mechanical properties of a composite material starting from the properties of its constitutent phases. The application of composite models to "bone" is the subject of the subsequent section. First, the concepts discussed in greater detail by Bundy[6] are summarized to introduce the newer models. A section is dedicated to composite models, discussing further bone properties such as viscoelasticity and failure. A discussion of the assumptions employed in the proposed models for bone and of the problem of assessing the interfacial bonding between collagen molecules and apatite crystals is presented in the last section of the chapter.

12.2 Composite Materials: An Introduction to Their Mechanical Characterization

A composite material is a material that has been assembled to form one bulk without physically blending the constituents to a homogeneous material. In other words, the resulting material would still have identifiable phases. An example could be the ancient practice of combining straw with mud to make clay bricks. Commonly, composite materials consist of two separate phases, called the matrix phase and the filler phase. The combination of matrix and filler leads to improved properties over the properties of the individual components. The first industrial composite materials were developed in the 1950s to meet the needs of the aerospace industry. In fact, the combination of a strong filler and a low-density matrix allowed a significant reduction in weight. Although composites are a "technology development," they mimic to some extent the features of materials occurring in nature, such as wood and diverse bioceramics like bone or mollusk shells. To model "bone," it is therefore natural to refer to existing models describing the mechanical performance of man-made composite materials.

Composite materials can be divided into classes according to the filler's geometry. Therefore, *particulate*, *short fiber*, and *long fiber* composites can be distinguished. The filler particles in a particulate composite are roughly spherical. Short and long fiber composites are composites in which the filler has an aspect ratio (the ratio between length and diameter) greater than 1 and approaching infinity in the latter case. Long fiber composites are highly anisotropic since the fibers are usually oriented in one direction. If high stiffness and/or strength are required in multiple directions, the engineer can stack and weld together a number of sheets of a long fiber composite material, each having the fibers oriented in a different direction. The resulting material is called a cross-ply laminate; an individual sheet is called lamina or ply. The mechanical behavior of a laminate is not as straightforward as the response of a single ply loaded in the fiber direction. For example, the lateral contraction in a ply (as described by the Poisson ratio) may be resisted by other plies, generating stresses transverse to the applied load as well as shear stresses.

Since composite materials are by definition nonhomogeneous, the resulting material properties will be the combination of the properties of their constituent phases. The concept of load sharing between

the matrix and the filler is central to the understanding of the mechanical behavior of a composite material. An external load applied to a composite is partly borne by the matrix and partly by the filler. In other words, the reinforcement offered by the stiffer phase is due to a stress transfer at the interface between the former and the embedding matrix. Given that the response of the composite is elastic and the bonding between matrix and filler is ideal, the proportion of load carried by the filler will depend only on its volume fraction, shape, and orientation, as well as on the material properties of both the constituent phases. This implies that the material properties of a composite may be different in tension, in compression, and in bending, because the stress carried by the phases might be different depending upon the type of loading. The prediction of the strength and the failure properties of a composite material is more difficult, since it is not only dependent on the strength of the constituent phases, but also on the properties of the interface between the matrix and filler, as well as the presence of residual stresses.

The simplest approach to the material properties of a composite material is to consider it as a mixture of two phases, described through their volumetric fractions. Examples are the "rule of mixtures" or Voigt model of uniform strain and the Reuss model of uniform stress, both widely applied in the field of composite materials and, as shall be seen, also applied to bone (see Section 12.3). According to the Voigt equation, the elastic modulus of a mixture of Material 1 (with an elastic modulus E_1 and a volume fraction v_1) and Material 2 (with an elastic modulus E_2 and a volume fraction v_2) is given by

$$E_{\text{composite}} = v_1 * E_1 + v_2 * E_2 \tag{12.1}$$

The Voigt model can be visualized as an assembly of layers of two different materials, the layers being equally strained, i.e., with displacement continuity across the boundary (Fig. 12.2a). The Reuss or "isostress" model is described by the equation:

$$\frac{1}{E_{\text{composite}}} = \frac{v_1}{E_1} + \frac{v_2}{E_2} \tag{12.2}$$

Similarly, the Reuss model can be visualized as an assembly of layers of two different materials, the layers being equally stressed, i.e., with force continuity across the boundary (Fig. 12.2b). The calculated elastic modulus represents an upper (Voigt) and a lower (Reuss) bound to the "true" elastic modulus of the composite material, respectively. It is obvious that such a simple approach does not provide any information regarding how the different phases and their interfaces behave upon application of a nominal stress, defined as applied load divided by the cross-sectional area. However, the equations often successfully enable the engineer to understand the role that the individual phases play in the macroscopic behavior of the composite, and this may explain the popularity of the Voigt and Reuss equations. Other examples that have also found application to bone are the Hashin equations and the Halpin–Tsai equations. For a more detailed description of these models, refer to the specialized literature.[7–10]

Unit-cell-based methods consist in finding a basic, representative unit of the composite material and/or structure under consideration. The engineer will be able to investigate the overall performance of a composite material starting from the behavior of its unit cell. In fact, if the material and/or structure have a (nearly) periodic character, it is sufficient to analyze the mechanical behavior within the repeating cell. Consider a point P within an inhomogeneous material. The representative volume element (RVE) is the material volume surrounding the point P that is a statistically homogeneous representative of the material in the neighborhood of P. In this context "statistically homogeneous" means that, although the material surrounding P is not homogeneous, taking the average of the properties over the RVE yields a satisfactory description of the material overall behavior. Usually, the

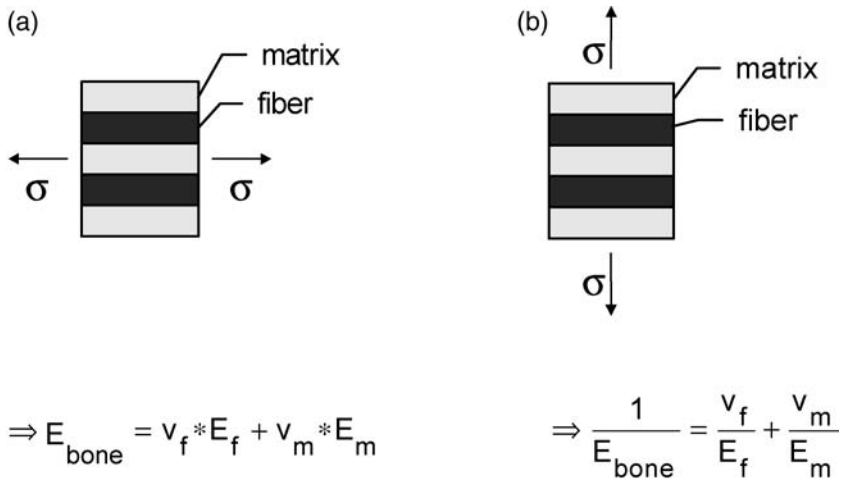

FIGURE 12.2 (a) The Voigt model of uniform stress; (b) the Reuss model of uniform strain. See Section 12.2 for details.

RVE is analyzed under the assumed boundary conditions of either uniform displacement or uniform traction because the true *in situ* boundary conditions are in general not known. The former yields an upper bound (similar to the Voigt model); the latter yields a lower bound (similar to the Reuss model) for the mechanical properties of the RVE.

A very similar mathematical framework is found in homogenization theory. In fact, the basic concept of homogenization theory is related to the concept of RVE. Given the stresses at any given point P′ within the RVE, an averaging procedure is then applied to calculate the stresses within a homogenized continuum material that describes the overall behavior of the inhomogeneous material being considered. Given a specific applied nominal stress, the homogenized equations—which entail the locally defined field equations and the geometry of the repeating unit cell—will allow a calculation of the averaged strain. In this sense, homogenization theory is very similar to the classical RVE approaches. Its distinctive feature lies in the assumption of periodic boundary conditions that will lead to a stiffness estimate whose value is between the upper (Voigt-type) and the lower (Reuss-type) bounds. Through the averaging procedure, the microstructure-related information is obviously being lost for the advantage of being able to determine aspects of the overall performance of the material under consideration. An important feature of homogenization theory is that the calculations can be carried out in the opposite direction (a process termed *localization*). Localization provides a benchmark for the constitutive equations of the material being studied by comparing the computed microstresses with experimentally collected data.

Further refinements of the homogenization procedure consist of subdividing the RVE in a given number of regions or cells (not to be confused with the previously introduced general concept of "unit cell"). The method of cells, as first introduced by Aboudi,[11,12] has an important advantage over the classical RVE methods. Since the RVE is further divided into cells, Aboudi's theory (a description of which is well beyond the purpose of this chapter) proved to be suited to analyzing not only the elastic response of a composite material, but also its viscoelastic or viscoplastic behavior. In fact, yielding or plastic flow might be different in different regions within an RVE, a region within the material that was defined to describe its elastic behavior.

It is important to note that continuum models with unit cells are not the same as finite-element (FE) models. FE analysis is a numerical method for solving the exact elasticity equations. Usually, large FE meshes are needed and a correct definition of the boundary conditions for the problem under examination might be very difficult. The use of FE analysis will not be further discussed; however, the interested reader is referred to an example given by Hogan.[13]

12.3 Assessment of the Stiffness Parameters of Compact Bone

This section specifically focuses on the modeling and prediction of the material properties of compact bone at the level 3 (i.e., arrays of mineralized collagen), level 4 (lamellae), level 5 (osteons), and level 6 (compact bone) in the hierarchy defined in Section 12.1. The importance of the interactions between the organic matrix and the mineral crystals (i.e., level 2 in the hierarchy defined in Section 12.1) is sketched in Section 12.5. This topic is discussed in greater detail in Chapter 13.

12.3.1 Review of the Older Literature[6]

The mineralized collagen fibrils constitute a platelet-reinforced fibrous material. Given that the crystals have different dimensions in the three different directions in space[5,14] and given that the three-dimensional structure of collagen is highly oriented, it is assumed that three mutually perpendicular planes of symmetry exist.[5] Therefore, mineralized collagen can be considered an orthotropic material. The first models proposed, however, were based on the notion that the mineral phase in bone is in the form of very thin, needle-shaped crystallites. Apparently, the first attempts to describe bone as a composite material were made by Currey[15] and later by Bonfield and Li.[16] These researchers applied the "law of mixtures" or Voigt model to assess the elastic modulus of bone, E_{bone}, starting from the elastic modulus of collagen E_{col}, and the elastic modulus of apatite, E_{ap}. v_{col} and v_{ap} represent the volume fractions of apatite and of collagen, respectively.

$$E_{bone} = v_{col} * E_{col} + v_{ap} * E_{ap} \tag{12.3}$$

As discussed in the previous section, the Voigt equation yields an upper bound for E_{bone}. The Reuss or "isostress" model, which gives a lower bound to the "true" elastic modulus of compact bone, is given by

$$\frac{1}{E_{bone}} = \frac{v_{col}}{E_{col}} + \frac{v_{ap}}{E_{ap}} \tag{12.4}$$

By inserting numerical values for the E_{col}, E_{ap}, v_{col}, and v_{ap} as found in the literature, it becomes obvious that this simple equation cannot account for a precise description of bone as a composite material (Table 12.1).

For this reason, Piekarski[17] proposed the Hirsch model, as it combines the Voigt and the Reuss models in a linear fashion:

$$\frac{1}{E_{bone}} = x * \left(\frac{1}{v_{col} * E_{col} + v_{ap} * E_{ap}} \right) + (1 - x) * \left(\frac{v_{col}}{E_{col}} + \frac{v_{ap}}{E_{ap}} \right) \tag{12.5}$$

The parameter x is the relative proportion of the material conforming with the upper boundary solution. In bone, x is 0.925, indicating that most of the mineral phase is arranged in such a way that deformation occurs mostly but not exclusively under uniform strain conditions.

The Voigt equation can be generalized to a universal "law of mixtures" by introducing an "efficiency of reinforcement parameter" η. This parameter accounts for diverse factors that might affect the efficiency of reinforcement, such as imperfections in the reinforcing material, defective bonding between some of the reinforcing fibers and the matrix, or fiber misalignment. The elastic modulus of bone will be

$$\Rightarrow E_{bone} = v_{col} * E_{col} + \eta * v_{ap} * E_{ap} \tag{12.6}$$

An example is the following expression, introduced first by Cox and applied to bone in 1969 by Currey.[18] In his model, Cox assumed a simple linear superposition of the properties of the constituents, proportional

TABLE 12.1 Mechanical Properties of Cortical Bone in Tension (as calculated by different authors using models and assumptions discussed in Section 12.3)

	Elastic Moduli, GPa	Comments
Voigt model ($v_{mineral}$ = 50%)	E_1 = 57.7	Cortical bone
Reuss-Model ($v_{mineral}$ = 50%)	E_1 = 2.90	Cortical bone
Sasaki[30]	E_1 = 57.7	Cortical bone
	E_2 = 14.4	
Pidaparti and Burr[29]	E_1 = 34	Cortical bone
	E_2 = 23	
Wagner and Weiner[31]	E_1 = 19.1	Lamellar properties
	E_2 = 6.26	
Crolet and Aoubiza[33]	E_1 = 26.8–40.2	Cortical bone
(homogenization theory)	E_2 = 13.6–24.2	
Lucchinetti[46]	E_1 = 13.8–21.1	Osteon properties
Mammone and Hudson[27]	E_1 = 17	Cortical bone

Note: E_1 denotes the modulus in the longitudinal direction, defined as the direction of application of the load, whereas E_2 is the modulus in a direction (in the case of a ply) or in a plane perpendicular to the longitudinal direction.

to their volumetric fraction. However, the parameter η in the fiber term accounts for the effects of the geometry of the fibers, as well as of the mechanical properties of both matrix and fibers on the mechanical properties (elastic modulus) of the composite. The Cox equation applied to bone is given by

$$E_{bone} = v_{col} * E_{col} + v_{ap} * E_{ap} * \left(1 - \frac{2}{\beta * L}\right) * \tanh\left(\frac{2}{\beta * L}\right) \tag{12.7}$$

where

$$\beta = \sqrt{\frac{2 * \pi * G_{col}}{E_{ap} * A_{ap} * \ln\left(\frac{a}{a_{ap}}\right)}}$$

L is the length, A_{ap} is the cross-sectional area, and a_{ap} is the radius of the apatite crystals. a is the mean separation distance between the crystallites and G_{col} is the shear modulus of the organic matrix.

In 1970, Padawer and Beecher[19] published a study on planar reinforced plastic resins and calculated η (the authors prefer the expression *modulus reduction factor*) in the case of a flake (or ribbon) reinforced composite:

$$\eta = \left(1 - \frac{\tanh(u)}{u}\right), \qquad \text{where} \qquad u = \alpha * \sqrt{\frac{G_{col} * v_{ap}}{E_{ap} * (1 - v_{ap})}} \tag{12.8}$$

α is the ribbon aspect ratio, α = width/thickness, and G_{col} the matrix shear modulus. This result is valid for a single reinforcing flake or for a "diluted composite." A diluted composite is a composite material where the reinforcing fibers are well separated from each other. The stress field measured in the neighborhood of one of these flakes is not influenced by the stresses measured around each of the surrounding ones. Lusis et al.[20] extended the theory to account for such flake–flake interactions and proposed the following formula for η:

$$\eta = 1 - \frac{\ln(u + 1)}{u}. \tag{12.9}$$

The Padawer and Beecher (PB) model and the Lusis (LWX) model will be referred to later in this chapter.

In 1969, Currey[18] observed that any model for the material properties of bone should be capable of predicting such properties independently of the direction of the applied load. Currey applied the tensor transformation laws for transversely isotropic materials to model the dependence of the elastic modulus of bone (treated as a unidirectional fiber composite by the Cox equation) upon the angle θ between the fibers (longitudinal direction) and the axis of the applied stress:

$$\frac{1}{E(\theta)} = \frac{\cos^4\theta}{E_{//}} + \frac{\sin^4\theta}{E_{\perp}} + \left(\frac{1}{G} - \frac{2 * \nu}{E_{//}}\right) * \sin^2\theta\cos^2\theta \tag{12.10}$$

$E_{//}$ is the elastic modulus in the longitudinal direction ($\theta = 0°$), whereas $E_{\perp}$ stands for the elastic modulus in the transverse direction ($\theta = 90°$). G is the shear modulus in the longitudinal-transverse direction. Calculations performed using these models clearly yield results, that do not fit experimental data.[16,21] Reilly and Burstein[23] also considered bone to be a transversely isotropic material and used the expression (Eq. 12.10) to fit their experimentally measured data. However, these data show a smoother dependence on the angle between the longitudinal axis and the axis of the applied stress than those collected by Bonfield and collaborators.[16,21]

It appears that treating bone as a unidirectional fiber-reinforced composite material does not lead to a correct description of its mechanical properties. Given the multiple levels of tissue organization (see Fig. 12.1), it becomes clear that cortical bone cannot *a priori* be considered transversely isotropic at the macroscopic level (i.e., levels 6 and 7 in Fig. 12.1). A possible approach to this problem has been proposed by Bundy.[22] The material properties of bone in a given direction are dependent on the orientation distribution of apatite crystals $g(\theta)$. The function $g(\theta)$ describes the relative proportion of apatite crystals oriented in a solid angle comprised between θ and $\theta + \delta\theta$.[22]

$$\bar{E}(\theta) = \int g(\theta) * E(\theta)\, d\theta, \qquad \text{where} \qquad \int g(\theta)\, d(\theta) = 1 \tag{12.11}$$

In 1981, Katz[1] pointed out that the material properties of bone can only be understood if the different levels of organization—from microstructure to macrostructure—are taken into account. The elastic properties of bone were modeled considering Haversian bone as a hierarchical composite material with two levels. The osteon is modeled as a laminated cylinder surrounding the Haversian canal (first level). On a higher scale, however, the secondary osteons are considered to be the reinforcing fibers and the surrounding interstitial bone as well as the cement line to be the matrix. The osteons are packed into a nearly hexagonal array in a transverse isotropic arrangement interfaced by the cement line. The equations of Hashin and Rosen[8] are used to calculate the elastic constants of bone.

12.3.2 Newer Theories

Newer approaches toward a modeling of the mechanical properties of plexiform and of osteonal bone have been proposed in the past few years.[24–31] These approaches can be divided in two main categories: the first category will be referred to as the "hierarchical approach" and the second one as the "global approach."

12.3.2.1 The Hierarchical Approach

The hierarchical approach consists in estimating the material properties of the mineralized collagen fibers first. Bearing in mind that the mineralized collagen fibrils constitute a plate-reinforced fibrous material, most authors use known composite theories to assess its properties. The set of material data obtained is subsequently used to calculate the material properties at the next microstructural level (lamellae), and eventually of osteons. An exception is the use of homogenization theory by Crolet and Aoubiza.[32–34]

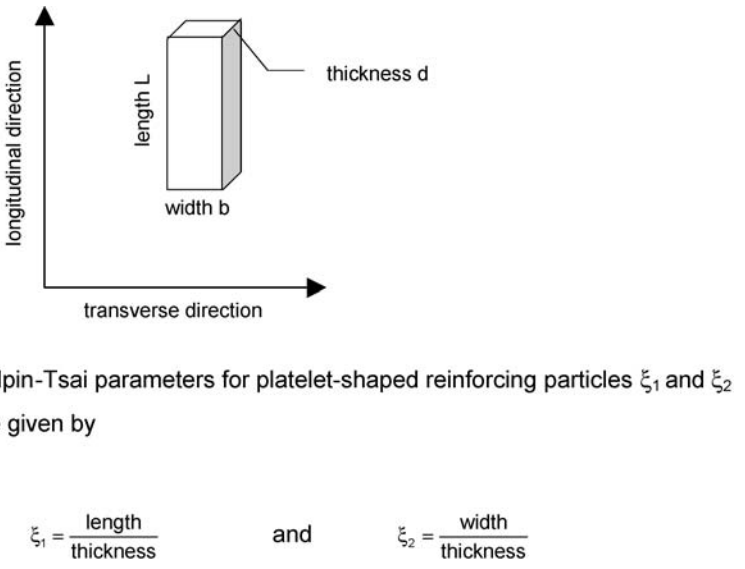

FIGURE 12.3 The HT parameters defined by the geometric characteristics of the platelets (length, width, and thickness).

The mineralized collagen fiber can be considered as an orthotropic material (Section 12.3.1). A good model should therefore take into account this anisotropy. At the lamellar level, a plywood motif has been observed in bone by several authors.[35–38] Giraud-Guille[36] analyzed the pattern of human osteonal bone and showed that the collagen fibers in adjacent and successive layers (not to be confused with bone lamellae) rotate their orientation by an angle of the order of magnitude of 10° to 15°. Weiner and collaborators[4,5,38–40] made similar observations, although they describe the existence of thin and thick lamellae and they measure a different ply-angle.

Wagner and Weiner[31] published the first model, which accounts for the platelet-like geometry of the basic reinforcing unit as well as for the different orientations of the apatite crystals in adjacent lamellae. The authors first applied three different models, namely, the PB model, the LWX model, and the Halpin–Tsai (HT) equations,[7,10] to compute the mechanical properties of mineralized collagen. While the PB and the LWX equations describe the mechanical characteristics of a flake-reinforced polymer composite, the HT equations account for a plate-shaped reinforcing phase characterized by a length L, a width w, and a thickness d ($L \geq w \geq d$; Fig. 12.3). The elastic moduli in the longitudinal and in the transverse directions are given by the following expressions:

$$\frac{E_{\text{long}}}{E_{\text{col}}} = \frac{1 + 2 * \xi_1 * \eta * \nu_{\text{ap}}}{1 - \eta * \nu_{\text{ap}}} \tag{12.12}$$

where

$$\eta = \frac{\frac{E_{\text{ap}}}{E_{\text{col}}} - 1}{\frac{E_{\text{ap}}}{E_{\text{col}}} + 2 * \xi_1}$$

$$\frac{E_{\text{transv}}}{E_{\text{col}}} = \frac{1 + 2 * \xi_2 * \eta * \nu_{\text{ap}}}{1 - \eta * \nu_{\text{ap}}} \tag{12.13}$$

where

$$\eta = \frac{\frac{E_{ap}}{E_{col}} - 1}{\frac{E_{ap}}{E_{col}} + 2 * \xi_2}$$

Again, E_{col} is the elastic modulus of the matrix (collagen), E_{ap} is the elastic modulus of apatite crystals, ν_{col} is the matrix volumetric fraction, while ν_{ap} is the mineral volumetric fraction. The HT parameter η reflects the influence of the geometry and modulus of the reinforcement on the elastic properties of the composite, whereas ξ depends on the geometry of the reinforcing fibers. For platelet-shaped reinforcing particles the shape factors ξ_1 and ξ_2 are given by

$$\xi_1 = \frac{L}{d} \quad \text{and} \quad \xi_2 = \frac{b}{d} \tag{12.14}$$

where L is the length, b is the width, and d is the thickness of the reinforcing particle. The HT equations describe a situation intermediate between a Voigt-type and a Reuss-type composite material. In fact, for $\xi \to \infty$ the HT expression reduces to the Voigt equation, whereas for $\xi \to 0$ it reduces to the Reuss model.

According to Weiner and collaborators,[4,5,14,38–41] lamellar bone appears as an assembly of thin and thick lamellae, having an alternating orientation of the collagen fibers as well as of the crystal planes in successive lamellae (rotated plywood architecture). The micromechanical model is based on a modified rule-of-mixtures to account for the two types of lamellae. In fact, an additional parameter ζ is introduced to account for the weakening effect introduced by the rotation of the crystal plane in the thick lamellae.

The authors favored the PB and the LWX models for computing the mechanical properties of mineralized collagen, because these models provide an angular dependence of the elastic modulus similar to the experimental data published by Bonfield and Li,[16] including a local maximum at an angle between 0° and 90°. The overall mechanical properties of lamellar (osteonal) bone have been subsequently calculated by simply adding the contributions from the different lamellae. Zioupos and Currey[42] have criticized this section of the paper. They pointed out that an assembly of concentric lamellae with different fiber orientations does not have an orthotropic symmetry.

Further investigations on the nature of the rotated plywood architecture[38,40] allowed the collection of more information on the structure of the transition zone between lamellae as well as a semiquantitative estimation of the plywood angle. A refined model was proposed in 1998 by Akiva et al.[24] in which the mechanical properties of an assembly of lamellae is calculated using a fully three-dimensional approach instead of using a modified rule-of-mixtures. Data are provided for parallel-fibered as well as lamellar bone and compared with microhardness values as obtained by nanoindentation.[43]

Meanwhile, a theoretical model to explain the elastic deformation of osteons was first proposed by Braidotti. et al.[44] In this model, the osteons are treated as a structure composed of several concentric tubes (the lamellae). The purpose of the calculations was, however, to study osteons as a structure per se, looking at the effects of fiber orientation and number of lamellae upon the behavior of such cylindrical structures in tension. A mismatch in the radii of two subsequent lamellae is introduced to account for the state of eigenstress of the osteons, as first reported by Ascenzi and Benvenuti in 1977.[45] As shall be seen later, the eigenstresses in osteons can be predicted by taking into account the plywood or helicoidal arrangement of the mineralized collagen fibrils.

Along similar lines, Lucchinetti[26,46] attempted to account for the actual concentric, lamellar cylindrical structure of the osteon. The author applied the HT relationships to calculate the elastic constants of a planar array of mineralized collagen fibrils as a function of mineralization, given that the mineral crystals are platelet shaped and are embedded in an ordered array within the collagen matrix (Fig. 12.4a). Since the HT formalism does not provide an expression for estimating the material properties out of the lamellar

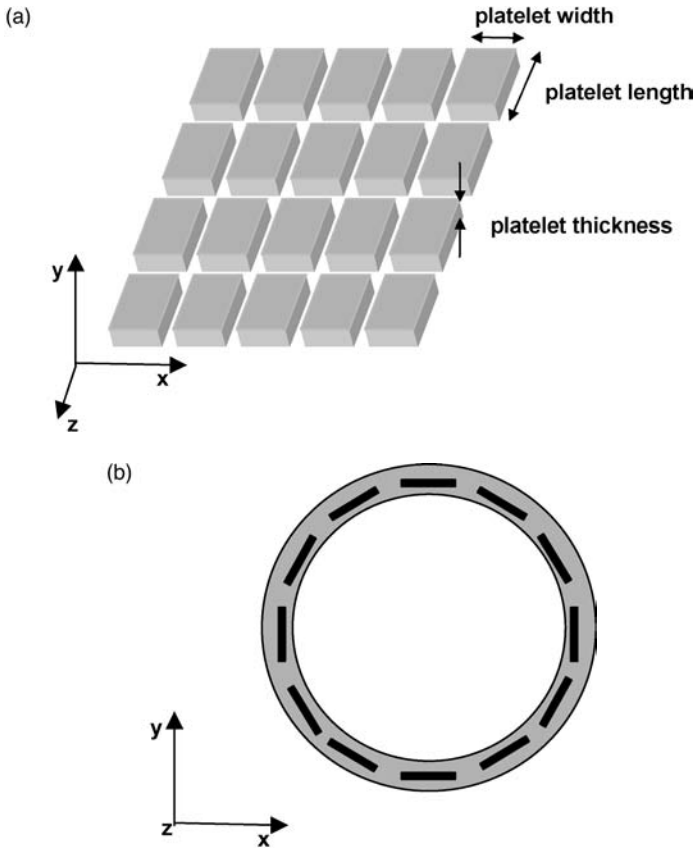

FIGURE 12.4 (a) The mineralized collagen has been treated as a platelet-reinforced composite material consisting of the plate-shaped apatite crystals embedded in a homogeneous collagen matrix. (b) The geometrical arrangement of the apatite crystals within a model osteon. The osteon axis is oriented parallel to the *z*-direction, the shortest edge of the crystals is oriented parallel to the radial direction. See Section 12.3.2 for details.

plane, thus not providing a complete description of the orthotropic composite, a generalized Reuss model was used to calculate these properties. The second step consisted of using the calculated material properties to analyze the mechanical performance of osteonic structures made of stacks of several concentric layers. Two different patterns of collagen orientation were considered. Taking 0° as the longitudinal direction, the first pattern was an alternate structure, where the orientation of the fibers changed from +45° to –45° in subsequent layers. The second pattern was a plywood structure and the rotation of the orientation of the fibers between subsequent layers was 12°.[47] The elasticity problem of loading a cylindrical composite structure in tension as well as in torsion has been solved numerically.[48] The results show very good agreement between the computed tensile properties of the osteons (see Table 12.1) and the values obtained experimentally by Ascenzi and Bonucci.[49] However, the model does not provide an adequate description of the elastic behavior of osteons in torsion.[50] The reason might lie in the fact that the shortest dimension of the platelike apatite crystals (i.e., the thickness) is oriented parallel to the radial direction, possibly weakening the composite in shear (Fig. 12.4b).

A plywood-like or helicoidal arrangement of the collagen might also explain the state of eigenstress in bone lamellae. In fact, the author[52] and Ascenzi[53] were able to predict such eigenstresses, based on Giraud-Guille's model for a twisted plywood.

Another method that allows the computation of the mechanical properties of a composite material like bone is homogenization theory. The general principle of homogenization as applied to a composite

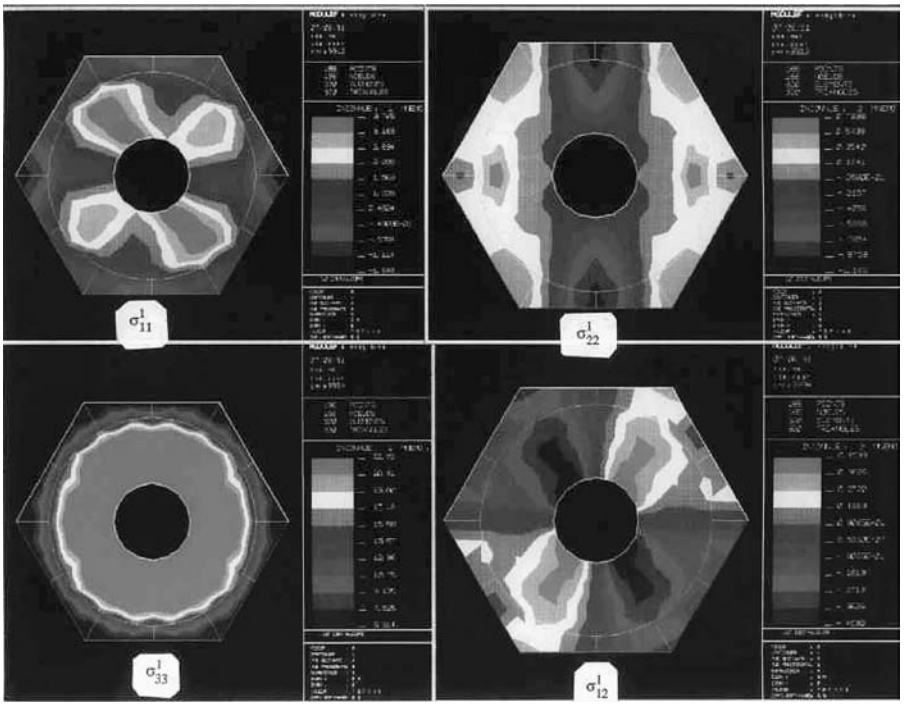

FIGURE 12.5 Stress distribution in unit cell (osteon and interstitial matrix) as calculated using the approach of Aoubiza. (From Reference 32, reproduced with permission.)

material with three hierarchical levels is the expression of the stress measured at any point x in the material as an asymptotic development as follows:

$$\sigma(x) = \sigma^0\left(x, \frac{x}{\varepsilon}, \frac{x}{\varepsilon^2}, \frac{x}{\varepsilon^3}\right) + \varepsilon * \sigma^1\left(x, \frac{x}{\varepsilon}, \frac{x}{\varepsilon^2}, \frac{x}{\varepsilon^3}\right) + \varepsilon^2 * \sigma^2\left(x, \frac{x}{\varepsilon}, \frac{x}{\varepsilon^2}, \frac{x}{\varepsilon^3}\right) + \cdots \quad (12.15)$$

where ε is a small parameter describing the order of magnitude of the structural features of the composite material ($\varepsilon < 1$). The dependence on x/ε, x/ε^2, and on x/ε^3 of these functions indicates the variation at the first, second, and third hierarchical levels, respectively. Eq. 12.15 was applied to bone by Crolet and one of his graduate students.[32–34] Bone was considered a hierarchical composite consisting of three different levels: the osteons, the lamellae, and the mineralized collagen fibrils. The authors calculated the elastic modulus of bone in the direction of the applied load to be between 27 and 40 GPa (see Table 12.1). Clearly, these values appear to be very high.

Aoubiza and Crolet also attempted the calculations in the opposite direction, a process termed *localization*. Localization permits the calculation of local stresses at any point within the composite from the knowledge of the nominal stress applied to the whole structure. The investigators applied a nominal stress of 15 MPa in the longitudinal direction (as given by the axis of the osteon). Fig. 12.5 is a plot of the stress distribution over the model's unit cell, which represents one osteon, embedded in the interstitial matrix. Application of 15 MPa nominal stress results in higher stresses toward the boundary of the osteons (outermost lamellae). A possible interpretation for this result can be found, keeping in mind that the authors did not consider the possibility that the innermost lamellae in an osteon appear to be "younger" and less mineralized than the outermost lamellae. This mineralization gradient indeed seems to exist, considering the data collected using Fourier transform infrared spectroscopy.[54] In the model, the mineralization was held constant over the cross-sectional area of the osteon. It is tempting to speculate that,

given the gradient in mineralization, the microstress distribution would be smoother. More data on compositional variations within an osteon are needed to verify such speculations.

A possible experimental verification of calculations based on localization theory is given by the assessment of the partition of stress between mineral and collagen. Borsato and Sasaki[55] were able to measure the strain within an apatite crystal using a X-ray diffraction technique. Knowing the elastic modulus of apatite, the authors calculated the stress carried by the mineral phase. Indeed, it would be very interesting to compare these data with results computed using localization theory applied to mineralized collagen.

12.3.2.2 The Global Approach

The global approach consists in documenting the anisotropy of the whole tissue first. The collected data are then related to structural features through a mathematical model. The already cited work by Reilly and Burstein[23] is an example of a global approach and other authors often utilized Reilly and Burstein's data as a benchmark for their own models. Mammone and Hudson[27] use Chow's general equations[56] to estimate the five elastic constants of a transverse isotropic composite with a finite volume concentration of filler particles having an ellipsoidal shape. The shape of the particles is characterized by an aspect ratio ρ to be the ratio of the major to the minor axes. If the filling particles are aligned in the longitudinal direction but randomly distributed, then the elastic modulus in the longitudinal and in the transverse direction, respectively, are given by the expressions[27,56]:

$$\frac{E_{\text{long}}}{E_{\text{col}}} = 1 + \frac{\left(\frac{k_{\text{ap}}}{k_{\text{col}}} - 1\right) * G_1 + 2 * \left(\frac{\mu_{\text{ap}}}{\mu_{\text{col}}} - 1\right) * K_1}{2 * K_1 * G_3 + G_1 * K_3} * \nu_{\text{ap}} \tag{12.16}$$

$$\frac{E_{90^\circ}}{E_{\text{col}}} = 1 + \frac{\left(\frac{k_{\text{ap}}}{k_{\text{col}}} - 1\right) * G_3 + \left(\frac{\mu_{\text{ap}}}{\mu_{\text{col}}} - 1\right) * (G_3 * \xi + K_3 * \zeta)}{2 * K_1 * G_3 + G_1 * K_3} * \nu_{\text{ap}} \tag{12.17}$$

Again, E_{col} is the matrix modulus, k and μ are the bulk and shear modulus of apatite, respectively, and ν_{ap} is the volume fraction of apatite. K_1, K_3, G_1, G_3 as well as the parameters ξ and ζ are functions of the bulk moduli k_{col} and k_{ap}, of the crystal aspect ratio ρ, of the volume fraction ν_{ap}, and of the Poisson ratio of collagen. The calculated longitudinal and transverse elastic moduli for cortical bone are 34.5 and 5.3 GPa, respectively. The authors conclude that bone cannot be modeled as a composite material with a perfectly oriented reinforcing phase. Based on observations by Hasegawa et al.[57] and by Sasaki et al.,[30] the authors assumed a misalignment of 30° on average. Using Eq. 12.10, they calculated a value for the elastic modulus of bone of 17 GPa.

Along similar lines, Currey et al.[25] studied the mechanical characteristics of a highly oriented natural composite, namely, dentine (narwhal tusk). The authors examined how accurately these properties can be predicted from a detailed knowledge of the properties and orientation of the constituent phases. The moduli in tension as well as the strength were measured at various fracture angles and fitted using the misalignment function (Eq. 12.10). The obtained values for $E_{//}$ and $E_{\perp}$ were used to predict the shape of the crystals using the HT equations. Most remarkably, the authors approached the problem of modeling the strength of a composite starting from the properties of its constituents and their geometric arrangement.

Pidaparti et al.[29] proposed that the elastic properties of osteonal bone can be modeled accurately as a simple fiber-reinforced composite, where most of the mineral phase resides outside the collagen fibrils and the phases are oriented in different directions (the angle is 30° on average). Stiffness measurements in canine osteonal bone specimens and in narwhal tusk were taken at increments of 10° from the longitudinal direction (which coincided with the long axis of the bone) using an acoustic microscope.

The measurements are again consistent with the experimental data of Reilly and Burstein,[23] showing a smoother angular dependence than the data collected by Bonfield and Grynpas.[21] Of the mineral, 75% is extrafibrillar, i.e., it resides outside the collagen fibers, while the remaining 25% is intrafibrillar and have the *c*-axis oriented in the same direction as the collagen fibers. The extrafibrillar mineral is oriented along the longitudinal axis of the bone and the off-axis properties are assessed using Eq. 12.10. The mechanical characteristics of the mineralized collagen fibers are modeled by a fifth-order polynomial. Furthermore two correction factors were introduced, one accounting for the loss of stiffness due to collagen imperfections, the other accounting for the anisotropy of crystal growth. Unfortunately, the introduction of a large number of different parameters is the weakness of Pidaparti's model. In fact, a good agreement between theory and experimental data can always be achieved because of the large number of parameters available. Examining each set of results obtained by varying a number of different parameters provides limited insight into the nature of bone as a composite material.

Sasaki et al.[30,58] first studied the distribution of mineral orientations from X-ray pole figure analysis and, assuming that the crystals are rod shaped, used the HT equations to calculate the properties of the mineralized collagen fibers. The contributions from the differently oriented layers were subsequently added as in a Voigt type combination of elements. The mineral fraction is assumed to be 0.5 by volume, which is rather high.

Table 12.1 summarizes the results obtained using some of the composite models of bone elasticity presented in this section. E_1 is the elastic modulus in the direction of application of the (tensile) load, whereas E_2 is the modulus calculated in the direction (or in a plane, in the case of transverse isotropy) perpendicular to the direction of load application.

It is important to point out that, in all models presented so far, a number of assumptions were made. For example, all models assume a perfect bonding between fiber and matrix, that is, in the case of bone, between collagen and mineral. This needs to be proved, and this issue will be presented in Section 12.5. A more-detailed discussion is given in Chapter 13. Moreover, it was assumed that bone is a "perfect" composite; i.e., the material does not contain any voids and the matrix is considered to be homogeneous. These assumptions are usually valid for engineering composite materials but obviously can be hardly met by bone. In fact, bone does contain voids at all levels in its hierarchical structure (see Chapter 1) and certainly the presence of these voids needs to be taken into account in order to model the failure properties of bone (see Section 12.4).

This section has reviewed the existing composite models for compact bone aimed at the prediction of its elastic properties. The different material models reflect the variety of structural models of compact bone. The collagen fiber orientation, the arrangement of the apatite crystals relative to the collagen fibers, and the mineral–matrix interfacial bonding properties have been identified as strong determinants of bone elasticity.

12.4 Approaches to the Viscoelastic and Failure Properties of Compact Bone

Most viscoelasticity models currently used to explain the mechanical response of soft tissues are usually based on continuum mechanics approaches. The ability to predict the viscoelastic properties of bone is an important aim in understanding bone biomechanics. However, bone viscoelasticity is still poorly understood and only few data are available.[59–61] Most likely, Gottesman and Hashin[62] and later Katz[1] were the only investigators who attempted a model prediction of bone viscoelasticity based on a hierarchical composite model for this tissue. Gottesman and Hashin[62] assumed that bone consisted of osteons embedded within an organic bonding material. The osteons are considered as an elastic, isotropic, and homogeneous material that reinforced the isotropic, linear viscoelastic matrix. The authors applied a correspondence principle, which directly relates the viscoelastic properties of a composite material to its effective elastic properties.

No further theoretical approaches to bone viscoelasticity are known to date. It is likely that bone viscoelasticity is closely related to the viscoelasticity of the organic matrix; see Chapter 11 for details.

In composite materials, failure depends heavily on the loading pattern. The failure mode most common in laminated composite materials is delamination, defined as the separation of one layer (ply) from the one adjacent to it. The shear strength approach consists in calculating the interlaminar stresses (shear and/or normal, depending on the loading conditions) and comparing them to the interlaminar strength (shear and/or normal, respectively). In laminates, shear failure may develop at quite low nominal stresses because of a weak interlaminar area. In bone, collagen fiber orientation shows a smooth transition at the boundary between plies.[35–38] This indeed may strengthen the interlaminar region.[51]

On the other hand, the fracture mechanics approach is based on the assessment of the stress necessary to propagate a preexisting crack. Other failure modes in the mechanics of composite materials are matrix damage per se, fiber breakage, or fiber pullout. Considering the case of bone, a prediction of its strength is even more difficult because of the sensitivity of this property to the presence of "defects" that can act as stress concentrators, such as osteocyte lacunae or Volkmann canals. Most of the failure mechanisms for anthropogenic composite materials presented so far were observed in bone specimens as well,[63] confirming the fact that bone is a composite material.

In 1970, Welch[64] assumed that in bone compressive failure occurs when Euler buckling of the apatite crystals (considered to be thin needles at that time) occurs. On the other hand, he proposed that the yield stress of bone in tension might be calculated as follows:

$$\sigma_{\text{yield, bone}} = \sigma_o * \nu_o + \sigma_i * \nu_i + \sigma_{\text{c.l.}} * \nu_{\text{c.l.}} \tag{12.18}$$

where c.l. designates the cement line and ν_o, ν_i, and $\nu_{\text{c.l.}}$ are the volume fractions of osteons, interstitial lamellae, and cement lines, respectively. The yield behavior of bone depends upon the weakest member in the above equation. Since $\nu_o + \nu_i \gg \nu_{\text{c.l.}}$, almost no load is sustained by the cement line, and failure occurs when the fracture stress of the osteons or of the interstitial lamellae is reached. Indeed, delamination and pullout at the osteonal level have been experimentally observed. However, bone strength also probably depends on the microstructural properties. The reinforcing action of apatite strongly depends on the interfacial bonding between apatite and organic matrix. This issue will be discussed in the next section and, in greater detail, in Chapter 13.

Mammone and Hudson[27] utilized an equation first derived by Chow[56] to predict the ultimate tensile strength from a calculation of the strain energy required for crack formation. If the filler particles are larger than a critical size d_c given by

$$d_c = 12 * \frac{\gamma}{E_{\text{col}} * e_{\text{col}}^2 * E_{\text{eff}}} \tag{12.19}$$

where γ is the work of adhesion and e_{col} is the ultimate strain in the matrix. The effective modulus of the composite E_{eff} is

$$E_{\text{eff}} = \frac{E - E_{\text{col}}}{E_{\text{col}} * \nu_{\text{ap}}} \tag{12.20}$$

The ultimate strength is dependent upon the inverse square root of the particle size:

$$\sigma_{\text{ult}} = \sqrt{\left(\frac{12 * \gamma * E_{\text{col}}}{d}\right) * \left(\frac{1}{E_{\text{eff}}} + \nu_{\text{ap}}\right)} \tag{12.21}$$

For calculation of the tensile strength of bone, an estimate of the work of adhesion is needed. A rough number can be provided in terms of the surface energy of apatite, which can be calculated as

$$\gamma = \frac{E * a_0}{10} \tag{12.22}$$

where E is the elastic modulus of a material and a_0 is the equilibrium separation between atomic planes. Mammone and Hudson calculated the ultimate tensile strength of bone (assuming an aspect ratio of 10 and a percentage mineralization of 65%) to be 1.7 GPa, a value that greatly overestimates the experimentally measured value of 133 MPa.[23]

As in industrial composite materials, the yield and the ultimate properties of bone appear to be strongly dependent on the properties of the interfaces found at the different hierarchical levels. The first one is the interface between matrix phase and filler phase (Section 12.2), i.e., between collagen and mineral crystals. This interface may be indeed a very important one, as illustrated in the next section and in Chapter 13. Further interfaces exist, such as between plies or lamellae, and between osteons and the interstitial bone (Chapter 1). The few models presented in this section illustrate the need for a better physicochemical characterization of the interfaces in bone.

12.5 Interfacial Bonding between Organic and Mineral Phases

In 1975, McCutchen[65] postulated that the properties of the collagen in bone are different from the properties of collagen tested on its own. In his view, the apatite and collagen are mixed at such a fine level that these materials act as though apatite struts connect the collagen molecules. These struts, upon application of a tensile load, might hinder rotation and bending of the bonds in the tropocollagen molecules ("straight-jacketing" phenomenon). Lees and Davidson[66] essentially presented the same idea as McCutchen.

In 1976, Hukins and Chapman[67] criticized McCutchen's idea mainly because the stiffening effect induced by the mineral phase is explained by introducing a novel structural feature for which no experimental evidence existed. Later, Hukins[68] proposed that bone collagen behaves like a liquid crystal of the smectic type. The collagen fibrils respond to an applied stress in the axial direction by tilting some of the molecules, thus changing their lateral arrangement within the general packing scheme. The presence of apatite crystals in bone prevents the molecules from tilting, thus having a stiffening effect. Although Hukins' idea does not represent a quantitative model, it is remarkable since no assumption on ultrastructural features (such as shape of the apatite crystals) or on the bonding strength between organic and inorganic material needs to be made. Interestingly, Landis and collaborators[69] observed that the characteristic S-shaped tensile curve of unmineralized turkey tendon disappeared upon increasing mineralization. The appearance of the tensile load–elongation curve in collagenous tissues results from a low-modulus or toe region, a linear region, and a yield and failure region. The toe region is related to the gradual disappearance of the crimp pattern, as more and more collagen fibers are straightened. The reduced toe region in mineralizing turkey tendon is attributable to an increased structural order caused by mineral deposition. The mineralization process produces a more uniform alignment of the collagen fibers along the tendon axis and eliminates the characteristic fibrillar crimp.

The interface between collagen and the reinforcing mineral phase obviously plays an important role in terms of load transfer from the weak matrix to the stiffer filler. In composite material theories, perfect bonding (as it is often assumed) is mathematically described by displacement continuity between matrix and filler. In bone, the fact that organic compounds control the growth of apatite crystals (see Chapter 5) suggests that the interfacial bonding might be quite strong. Partial debonding between these phases would result in significant modifications in the stiffness as investigated theoretically by Bundy.[70] Using the HT relationships (Eqs. 12.12 and 12.13), Bundy showed that the overall moduli of the composite decrease if a portion of the mineral phase is debonded from the collagenous matrix. Again, this means that, at least for part of the mineral crystals, the condition of displacement continuity is not ensured.

This is certainly a strongly simplified model for the interface between collagen and mineral. A better insight into the properties of the interface will be possible in the near future as a result of the constant improvements in physical and physicochemical analytical methods such as Raman spectroscopy (see Chapters 5 and 13).

12.6 Conclusions

Thus far, a number of composite models for compact bone have been proposed. These models are primarily concerned with the calculation of bone elastic properties, starting from the properties of its main components, collagen type I, and the mineral apatite. There have been few attempts to predict the yield and failure behavior of bone as a composite material. The intrinsic difficulty of this particular problem lies in the fact that the behavior at failure of a composite material not only depends on the failure properties of the constituents, but also on the properties of the interface between them. Indeed, further insight into the material properties of bone can be gained by studying the normal as well as different pathological mineralization processes. The current efforts undertaken by physical chemists, biologists, and biomedical engineers to better understand mineralization and to obtain a precise picture of the interface between organic and inorganic components in bone are presented in Chapter 13.

References

1. Katz, J. L., Composite material models for cortical bone, in *Mechanical Properties of Bone,* S. C. Cowin, Ed., American Society of Mechanical Engineers, New York, 1981.
2. Landis, W. J., The strength of a calcified tissue depends in part on the molecular structure and organization of its constituent mineral crystals in their organic matrix, *Bone,* 16, 533, 1995.
3. Rho, J. Y., Kuhnspearing, L., and Zioupos, P., Mechanical properties and the hierarchical structure of bone, *Med. Eng. Phys.,* 20, 92, 1998.
4. Weiner, S. and Wagner, H. D., The material bone: structure-mechanical function relations, *Annu. Rev. Mater. Sci.,* 28, 271, 1998.
5. Weiner, S. and Traub, W., Bone structure: from angstroms to microns, *FASEB J.,* 6, 879, 1992.
6. Bundy, K. J., Composite material models for bone, in *Bone Mechanics,* S. C. Cowin, Ed., CRC Press, Boca Raton, FL, 1989, 197.
7. Halpin, J. C., *Primer on Composite Materials Analysis,* Technomic Publ., Lancaster, PA, 1992.
8. Hashin, Z. and Rosen, B. W., The elastic moduli of fiber reinforced materials, *J. Appl. Mech.,* 31, 223, 1964.
9. Jones, R. M., *Mechanics of Composite Materials*, Hemisphere Publishing Corporation, New York, 1975.
10. Rammerstorfer, F. G. and Boehm, H. J., Micromechanics for macroscopic material description of FRPs, in *Engineering Mechanics of Fibre Reinforced Polymers and Composite Structures,* J. Hult and F. G. Rammerstorfer, Eds., Springer–Verlag, Heidelberg, 1994.
11. Paley, M. and Aboudi, J., Micromechanical analysis of composites by the generalized cells model, *Mech. Mater.,* 14, 127, 1992.
12. Aboudi, J., Micromechanical analysis of thermo-inelastic muliphase short-fiber composites, *Composites Eng.,* 5, 839, 1995.
13. Hogan, H. A., Micromechanics modeling of Haversian cortical bone properties, *J. Biomech.,* 25, 549, 1992.
14. Weiner, S. and Traub, W., Crystal size and organization in bone, *Connect Tissue Res.,* 21, 259, 1989.
15. Currey, J. D., Strength of bone, *Nature,* 195, 513, 1962.
16. Bonfield, W. and Li, C. H., Anisotropy of nonelastic flow in bone, *J. Appl. Phys.,* 38, 2450, 1967.
17. Piekarski, K., Analysis of bone as a composite material, *Int. J. Eng. Sci.,* 11, 557, 1973.
18. Currey, J. D., The relationship between the stiffness and the mineral content of bone, *J. Biomech.,* 2, 477, 1969.

19. Padawer, G. E. and Beecher, N., On the strength and stiffness of planar reinforced resins, *Polym. Eng. Sci.,* 10, 185, 1970.
20. Lusis, J., Woodhams, R. T., and Xanthos, M., The effect of flake aspect ratio on the flexural properties of mica reinforced plastics, *Polym. Eng. Sci.,* 13, 139, 1973.
21. Bonfield, W. and Grynpas, M. D., Anisotropy of Young's modulus of bone, *Nature,* 270, 453, 1977.
22. Bundy, K. J., *Experimental Studies of the Nonuniformity and Anisotropy of Human Compact Bone*, Stanford University, Palo Alto, CA, 1974.
23. Reilly, D. T. and Burstein, A. H., The elastic and ultimate properties of compact bone tissue, *J. Biomech.,* 8, 393, 1975.
24. Akiva, U., Wagner, H. D., and Weiner, S., Modelling the three-dimensional elastic constants of parallel-fibred and lamellar bone, *J. Mater. Sci.,* 33, 1497, 1998.
25. Currey, J. D., Brear, K., and Zioupos, P., Dependence of mechanical properties on fibre angle in narwhal tusk, a highly oriented biological composite, *J. Biomech.,* 27, 885, 1994.
26. Lucchinetti, E., Aufbau des Kollagen-Apatit-Verbundwerkstoffes und dessen Einfluss auf das elastische Verhalten der Osteone: Theorie und Rechenbeispiele, Diploma thesis, Department of Materials, Swiss Federal Institute of Technology, Zurich, Switzerland, 1996.
27. Mammone, J. F. and Hudson, S. M., Micromechanics of bone strength and fracture, *J. Biomech.,* 26, 439, 1993.
28. Pidaparti, R. M. and Burr, D. B., Collagen fiber orientation and geometry effects on the mechanical properties of secondary osteons, *J. Biomech.,* 25, 869, 1992.
29. Pidaparti, R. M., Chandran, A., Takano, Y., and Turner, C. H., Bone mineral lies mainly outside collagen fibrils: predictions of a composite model for osteonal bone, *J. Biomech.,* 29, 909, 1996.
30. Sasaki, N., Matsushima, N., Ikawa, T., Yamamura, H., and Fukuda, A., Orientation of bone mineral and its role in the anisotropic mechanical properties of bone—transverse anisotropy, *J. Biomech.,* 22, 157, 1989.
31. Wagner, H. D. and Weiner, S., On the relationship between the microstructure of bone and its mechanical stiffness [see comments], *J. Biomech.,* 25, 1311, 1992.
32. Aoubiza, B., Homogeneization d'un composite multi-echelle: application a une modelisation numerique de l'os haversien compact, thesis, Faculte des Sciences et Techniques, Universite de Franche-Compte, Besancon, France, 1991.
33. Crolet, J. M., Aoubiza, B., and Meunier, A., Compact bone: numerical simulation of mechanical characteristics [see comments], *J. Biomech.,* 26, 677, 1993.
34. Aoubiza, B., Crolet, J. M., and Meunier, A., On the mechanical characterization of compact bone structure using the homogenization theory, *J. Biomech.,* 29, 1539, 1996.
35. Ascenzi, A. and Bonucci, E., Mechanical similarities between alternate osteons and cross-ply laminates, *J. Biomech.,* 9, 65, 1976.
36. Giraud-Guille, M. M., Twisted plywood architecture of collagen fibrils in human compact bone osteons, *Calcil. Tissue Int.,* 42, 167, 1988.
37. Raspanti, M., Guizzardi, S., Strocchi, R., and Ruggeri, A., Collagen fibril patterns in compact bone: preliminary ultrastructural observations, *Acta Anat.,* 155, 249, 1996.
38. Ziv, V., Sabanay, I., Arad, T., Traub, W., and Weiner, S., Transitional structures in lamellar bone, *Microsc. Res. Tech.,* 33, 203, 1996.
39. Weiner, S., Arad, T., and Traub, W., Crystal organization in rat bone lamellae, *FEBS Lett.,* 285, 49, 1991.
40. Weiner, S., Arad, T., Sabanay, I., and Traub, W., Rotated plywood structure of primary lamellar bone in the rat: orientations of the collagen fibril arrays, *Bone,* 20, 509, 1997.
41. Weiner, S. and Traub, W., Organization of crystals in bone, in: Mechanisms and Phylogeny of Mineralization in Biological Systems, Symposium on Biomineralization 1990, Tokyo, Springer-Verlag, Tokyo, 1991.
42. Zioupos, P. and Currey, J. D., Comments on "On the relationship between the microstructure of bone and its mechanical stiffness" [letter; comment], *J. Biomech.,* 27, 993, 1994.
43. Ziv, V., Wagner, H. D., and Weiner, S., Microstructure-microhardness relations in parallel-fibered and lamellar bone, *Bone,* 18, 417, 1996.

44. Braidotti, P., Branca, F. P., Sciubba, E., and Stagni, L., An elastic compound tube model for a single osteon, *J. Biomech.,* 28, 439, 1995.
45. Ascenzi, A. and Benvenuti, A., Evidence of a state of initial stress in osteonic lamellae, *J. Biomech.,* 10, 447, 1977.
46. Lucchinetti, E., Modeling the elastic properties of lamellae and of osteons, in *Proceedings of the XVIth Meeting of the International Society of Biomechanics;* Tokyo, Japan, 1997.
47. Giraud-Guille, M. M., personal communication, 1996.
48. Kress, G., Minimized computational effort for the thick walled composite tube problem, *Comp. Struct.,* 54, 633, 1995.
49. Ascenzi, A., Benvenuti, A., and Bonucci, E., The tensile properties of single osteonic lamellae: technical problems and preliminary results, *J. Biomech.,* 15, 29, 1982.
50. Ascenzi, A., Baschieri, P., and Benvenuti, A., The torsional properties of single selected osteons [see comments], *J. Biomech.,* 27, 875, 1994.
51. Ascenzi, A. and Benvenuti, A., Orientation of collagen fibers at the boundary between two successive osteonic lamellae and its mechanical interpretation, *J. Biomech.,* 19, 455, 1986.
52. Lucchinetti, E., unpublished data, 1996.
53. Ascenzi, M. G., A first estimation of pre stress in so-called osteonic lamellae, *J. Biomech.,* 32, 935, 1999.
54. Paschalis, E. P., DiCarlo, E., Betts, F., Sherman, P., Mendelsohn, R., and Boskey, A. L., FTIR microspectroscopic analysis of human osteonal bone, *Calcif. Tissue Int.,* 59, 480, 1996.
55. Borsato, K. S. and Sasaki, N., Measurement of partition of stress between mineral and collagen phases in bone using X-ray diffraction techniques, *J. Biomech.,* 30, 955, 1997.
56. Chow, T. S., The effect of particle shape on the mechanical properties of filled polymers, *J. Mater. Sci.,* 15, 1873, 1980.
57. Hasegawa, K., Turner, C. H., and Burr, D. B., Contribution of collagen and mineral to the elastic anisotropy of bone, *Calcif. Tissue Int.,* 55, 381, 1994.
58. Sasaki, N. and Sudoh, Y., X-ray pole figure analysis of apatite crystals and collagen molecules in bone, *Calcif. Tissue Int.,* 60, 361, 1997.
59. Lakes, R. S., Katz, J. L., and Sternstein, S. S., Viscoelastic properties of wet cortical bone—I. Torsional and biaxial studies, *J. Biomech.,* 12, 657, 1979.
60. Lakes, R. S. and Katz, J. L., Viscoelastic properties of wet cortical bone—II. Relaxation mechanisms, *J. Biomech.,* 12, 679, 1979.
61. Lakes, R. S. and Katz, J. L., Viscoelastic properties of wet cortical bone—III. A non-linear constitutive equation, *J. Biomech.,* 12, 689, 1979.
62. Gottesman, T. and Hashin, Z., Analysis of viscoelastic behaviour of bones on the basis of microstructure, *J. Biomech.,* 13, 89, 1980.
63. Braidotti, P., Branca, F. P., and Stagni, L., Scanning electron microscopy of human cortical bone failure surfaces, *Biomech.,* 30, 155, 1997.
64. Welch, D. O., The composite structure of bone and its response to mechanical stress, in *Recent Advances in Engineering Science,* J. C. Eringer, Ed., Gordon and Breach, New York, 1970, 245.
65. McCutchen, C. W., Do mineral crystals stiffen bone by straitjacketing its collagen? *J. Theor. Biol.,* 51, 51, 1975.
66. Lees, S. and Davidson, C. L., The role of collagen in the elastic properties of calcified tissues, *J. Biomech.,* 10, 473, 1977.
67. Hukins, D. W. and Chapman, J. A., Structural hierarchy in collagenous tissues and the "straitjacket" theory of bone stiffness, *J. Theor. Biol.,* 57, 247, 1976.
68. Hukins, D. W., Bone stiffness explained by the liquid crystal model for the collagen fibril, *J. Theor. Biol.,* 71, 661, 1978.
69. Landis, W. J., Librizzi, J. J., Dunn, M. G., and Silver, F. H., A study of the relationship between mineral content and mechanical properties of turkey gastrocnemius tendon, *J. Bone Miner. Res.,* 10, 859, 1995.
70. Bundy, K. J., Determination of mineral-organic bonding effetiveness in bone—theoretical considerations, *Ann. Biomed. Eng.,* 13, 119, 1985.

13

Dense Bone Tissue as a Molecular Composite

Eliana Lucchinetti
Swiss Federal Institute of Technology

13.1 Introduction

Bone is a natural, hierarchical composite material with multiple levels of fiber–matrix organization (see Chapters 1 and 12). At the molecular level, the intricate structural interaction between the organic (mainly collagen type I) and inorganic (mineral) phases is one of the fundamental determinants of the superb mechanical properties of bone. It enables bone to absorb and distribute the mechanical stresses arising from the externally applied loads. Mechanically speaking, the function of the mineral phase is to stiffen and strengthen the compliant organic matrix. This corresponds to the idea proposed by McCutchen in 1975 that the collagen fibrils are somehow "glued" to the mineral fillings.[1] The underlying assumption is that a strong bonding between mineral and collagen allows the former to stiffen the collagen matrix through shear stress transfer. Yet, treating bone tissue as a platelet-reinforced organic matrix assuming perfect bonding between the constituents (see Chapter 12) is a rather simplistic model. As already discussed in Section 12.2, the mechanical properties of a composite material mostly depend on the following factors: the properties (geometric, mechanical, and chemical) of the phases taken separately, the relative amount of the phases, and the properties of the interface between phases. It will be seen that it is very difficult to measure these properties accurately. The hierarchical nature of bone tissue would require biomechanical testing of extremely small specimens. Also, the mechanical properties of the mineral and the mechanical properties of bone collagen (and changes thereof after maturation) are not known. Finally, it is still unclear whether the interface (if any) between organic and inorganic components in bone enables stiffening by shear stress transfer or whether the crystals prevent any rearrangements within the tertiary and quaternary structure of collagen.[2] Thus, the following questions need to be addressed: How do the

0-8493-9117-2/01/$0.00+$.50

organic and the inorganic phases interact to give bone the superb set of mechanical properties none of its constituents has? What are the properties of the main constituents? How do the cross-links within and between collagen fibrils contribute to the mechanical properties of the collagen? What is the effect of glycosylation? How is load distributed between the collagen and mineral?

Some insight can be obtained by studying models for skeletal pathologies or for defective mineralization. Improperly mineralized tissues are often the result of a defective organic template for mineral deposition. This can result from naturally occurring mutations or from transgenic and/or knockout models of the gene(s) encoding for one specific protein present in the matrix of mineralized tissues (see Chapters 4 and 5). As pointed out by Young and Yu in Chapter 4, measurements of the biomechanical properties have been performed in very few studies involving transgenic and knockout models with skeletal phenotype. The purpose of this chapter is to relate these data to the (natural or engineered) genetic defects in order to understand the role played by the different constituents in determining the material properties of bone tissue. Indeed, the discussion can only lead to partial conclusions, as the field is rapidly evolving and constantly providing new pieces of a picture far from being complete.

Section 13.2 focuses on the collagen template to learn more about the consequences of impaired fibril assembly and about the nature of post-translational modifications on the mechanical properties of collagen per se and of bone. Section 13.3 briefly discusses the consequences of ion substitution within the mineral phase. Section 13.4 is dedicated to the putative role played by noncollagenous proteins in interfacial bonding.

13.2 The Mechanical Consequences of Changes in the Collagen Template

In a paper published in 1975, Reilly and Burstein[3] provided evidence that the mineral phase is an important determinant of bone elasticity, whereas the organic phase is responsible for the bone post-yield behavior. Currey and Zioupos[4,5] reported a decrease in fracture toughness with age, which they related to increasing mineralization. In a recently published investigation, however, the authors presented data supporting the speculation that the fragility of aging bone may be also related to changes in the collagen matrix.[6] Oxlund et al.[7] measured the extractability of collagen from vertebral trabecular bone of normal subjects over a large age range and that of individuals with osteoporosis. He found a positive correlation between collagen extractability and age. The concentration of reducible cross-links (discussed below) was substantially lower in individuals with osteoporosis as compared with age-matched controls, suggesting a possible relationship between collagen quality and "bone quality," a term yet to be precisely defined. Yamauchi et al.[8] using direct chemical analysis of the bones reported a similar deficit in collagen cross-links in an animal model of disuse osteoporosis.

One factor that determines the mechanical properties of bone collagen is its hydration. Using a collagen peptide model, Bella et al.[9] demonstrated that absorbed water molecules form a highly ordered hydration network. This hydration network provides additional stability to the triple helix by the formation of additional water-mediated hydrogen bonds between all remaining backbone peptide groups that could not otherwise interact because of spatial restraints.[10] More important, however, in terms of the mechanical properties of the tissue are the post-translational modifications that occur in collagen. These modifications comprise cross-link formation and glycosylation.

13.2.1 Cross-Links and Biomechanical Properties of Bone Collagen

Type I collagen from hard tissues has essentially the same primary and secondary structure as type I collagen present in soft tissues such as tendon. In fact, the biomechanical properties of tendon are often considered a good approximation for the properties of bone collagen in composite modeling (see Chapter 12). However, this may prove to be incorrect because—as will be seen—an increasing body of literature suggests that post-translational modifications can affect the biomechanical properties of a tissue. One kind of post-translational modification in collagen is cross-link formation, described in detail by Yamauchi.[11]

TABLE 13.1 Collagen Cross-Links Anomalies Affect Bone Mechanical Properties

	Maximum Torque (Nm)			Ultimate Angular Deformation (rad)		
	Control	+ BAPN	% Changes	Control	+ BAPN	% Changes
Lathyrism (induced by BAPN)[16]	0.353 ± 0.072	0.255 ± 0.114	−28%	0.239 ± 0.068	0.174 ± 0.053	−27%
	Yield Load (N)			Fracture Load (N)		
	Control	− Vit. B_6	% Changes	Control	− Vit. B_6	% Changes
Pyridoxine (vit. B_6)-deficiency in chicks[17]	165 ± 9	124 ± 14	−25%	203 ± 35	151 ± 23	−26%
	Collagen-Linked Fluorescence (relative fluorescence/mg collagen)			Ultimate Strength (lb/mm^2)		
	Control	Diabetic	% Changes	Control	Diabetic	% Changes
Changes in bending properties in diabetic rats[21]	14.8 ± 0.7	27.3 ± 4.8	+84%	27.4 ± 3.6	13.9 ± 3.8	−49%

The inhibition of lysyl oxidase, an important enzyme involved in the formation of mature cross-links in collagen, results in increased collagen extractability. These changes can be induced either by β-aminopropionitrile (BAPN) ingestion or by feeding a pyridoxine-deficient diet. On the other hand, post-translational modifications of proteins in diabetes (and in aging) involve nonenzymatic glycation, resulting in an increased collagen autofluorescence (excitation wavelength 370 nm, emission wavelength 440 nm). Data are reported as mean ± standard deviation.

The initial cross-links between collagen molecules are nonstable, divalent, bipolar (i.e., connect two chains), and reducible forms. As the bone matures, the cross-links also mature into more stable nonreducible forms connecting more than two chains. Examples of such cross-links are hydroxylysylpyridinoline and lysylpyridinoline.[11] Correspondingly, the collagen matrix itself increases its density, stiffness, and strength.[12,13] Eyre et al.[14] showed that the content of the mature form of cross-link reaches a maximum by 10 to 15 years of age in human bone and stays in the same range throughout the adult life. The immature, reducible cross-links decrease steeply between birth and 25 years of age, but persist in significant amounts throughout life. The content of mature cross-links is lower in cancellous bone as compared to cortical bone, representing the higher turnover rate of the cancellous bone.[14]

The bone collagen cross-links are modified as mineralization proceeds. For example, lateral connection of collagen molecules is reduced by dissociation of iminium bonds as collagen is mineralized, probably induced by the deformation caused by the mineral growth.[15] A proper cross-linking of collagen is an important determinant of bone mechanical performance, as demonstrated in pathological conditions such as lathyrism, where the cross-linking pathway is blocked. Lysyl oxidase, an enzyme needed in cross-link formation, is activated in the presence of copper ions and pyridoxine (vitamin B_6). Thus, copper or pyridoxine deficiency may weaken the collagen in bone because of the reduced concentration of mature cross-links. Rats fed with a copper-deficient diet showed a significant decrease in maximal torque, ultimate angular deformation, and fracture toughness under torsion as compared to controls. No differences were found in the values of the torsional stiffness and in mineralization, measured by the ash weight, and the calcium content.[16] Similarly, Masse and co-workers[17] produced a lathyrism-like bone disorder in chicks fed with a vitamin B_6-deficient diet. The bones of these animals showed a decreased yield load and fracture load as compared with controls. The content of reducible cross-links was significantly increased compared with controls, suggesting that proper collagen cross-link maturation is important in determining the post-yield behavior of bone tissue. Table 13.1 presents the relevant changes in biomechanical data from these investigations.

13.2.2 Collagen Glycosylation

Glucose and galactose react with the hydroxy groups of hydroxylysine on collagen via the action of specific glucose and galactose collagen glycosyl transferases. Additionally there are nonenzymatic glycosylations, not specific to collagen, which occur when a variety of sugars reacts with amino groups on proteins via

the Maillard reaction[18] to form a variety of advanced glycation end (AGE) products. AGE products can modify the physicochemical properties of proteins by the formation of intermolecular cross-links, a process that is more prominent in long-lived proteins such as collagen.[12,13,19] Recently, AGE product accumulation in aging was found to affect cartilage mechanical properties,[20] and it is conceivable that similar changes may affect aging bone as well. The process of AGE formation is accelerated in diabetes because of the presence of increased amount of glucose and may contribute to diabetic osteopenia. Indeed, Tomasek et al.[21] showed that AGE products were increased in diabetic rats as compared to healthy littermates and found a significant reduction in the bending strength of long bones from diabetic animals (see Table 13.1).

13.2.3 Osteogenesis Imperfecta

Osteogenesis imperfecta (OI) is a group of diseases that primarily affect collagen type I production and assembly and that are caused predominantly by various mutations in type I collagen genes. The consequences of these mutations are either the decrease in collagen content or the production of abnormal collagen. Rowe and Shapiro[22] classified the different forms of OI into the following categories: lethal (Type II), severe (Type III), mild and deforming (Type IV), and mild and nondeforming (Type I). The common phenotype of Type I (mild and nondeforming) OI is a decreased production of type I collagen. A glycine substitution in the mid- or C-terminal region of the helix has been associated with Type IV (mild and deforming) OI. Type III (severe) OI is related to the production of α1(I) collagen trimer, whereas in Type II (lethal) OI most of the procollagen molecules formed are structurally abnormal.

Although OI is primarily caused by perturbations in the collagen template, important changes occur in the expression of noncollagenous proteins and in the mineralization,[23,24] demonstrating the importance of a proper organic template for normal mineralization.

13.2.3.1 Mouse Models for Osteogenesis Imperfecta

13.2.3.1.1 The oim/oim Mouse

The oim/oim mouse closely resembles Type III OI in humans and results from a mutation in the gene encoding for the α2(I) chain. The recessive heterozygous oim/+ mouse represents an excellent model for Type I OI in humans.

Misof et al.[25] measured the tensile properties of tendons from homozygous (oim/oim), heterozygous (oim/+) and wild-type (+/+) mice. The authors found that the ultimate stress and strain measured in oim/+ and oim/oim tendons were significantly reduced as compared with controls. Additionally, the work hardening of normal tendon in the plastic zone appeared to be lost in tendons affected by the collagen gene mutation, suggesting the collagen triple helices were mechanically compromised. Interestingly, the elastic modulus of mutated mice tendons did not differ from controls. Using high-voltage electron-microscopic tomography to study calcified tissue, Landis[26] found that the aggregation of collagen fibrils is impaired and that the hole regions from different layers of collagen fibrils do not aggregate to form "grooves" that accommodate the mineral crystals according to Weiner's model.[27] As a result, mineralization appeared to be severely impaired.

The longitudinal changes in geometric and biomechanical properties of long bones from homozygous, oim/+, and wild-type mice were measured first by McBride and collaborators.[28] Cortical thickness, cortical area, and polar moment of inertia (a measure of the distribution of bone material in respect to the longitudinal axis of the considered long bone) were significantly reduced in homozygous mice as compared with heterozygous and wild-type mice. Also, increased bone fragility (as measured by a significantly lower peak torque in a torsion test) was found in oim/oim mice at all ages. On the other hand, peak torque slightly increased with age in the wild-type mice. A decreased whole-bone torsional strength may depend on geometric and material-related factors. While the reported data do not directly support changes in the material properties per se, the oim/oim mice failed to compensate with increased age for the supposed bone fragility by changes in bone geometry. To understand exactly the determinant factors of bone fragility in this mouse model, Camacho and collaborators[29] combined biomechanical

TABLE 13.2 Mutations in the Genes Encoding for Collagen Type I Cause a Variety of Diseases Classified as OI

	Torsional Rigidity (mm^4) at 12 Months of Age			Failure Torque (N/mm) at 12 Months of Age		
	Wild-type	oim/oim	% Changes	Wild-type	oim/oim	% Changes
Age-related changes in mice with the oim/oim phenotype[28]	0.76 ± 0.19	0.4 ± 0.17	−47%	—	—	−37%[a]
	Torsional Rigidity (mm^4) at 11–13 Months of Age			Failure Torque (N/mm) at 11–13 Months of Age		
	Wild-type	oim/oim	% Changes	Wild-type	oim/oim	% Changes
Mice with the oim/oim phenotype[29]	0.48 ± 0.10	0.31 ± 0.11	−35%	—	—	−60%[a]
	Elastic Modulus E_{33} in the Longitudinal Direction (bone axis)			Poisson ratio ν_{12}		
	Wild-type	oim/oim	% Changes	Wild-type	oim/oim	% Changes
Properties of oim/oim bones measured by ultrasound critical-angle reflectometry[30]	—	—	−20%[a]	—	—	+80%[a]
	Moment of Inertia (mm^4) at 8 Weeks of Age			Failure Load (N) in Bending at 8 Weeks of Age		
	Wild-type	*Mov13*	% Changes	Wild-type	*Mov13*	% Changes
Geometric and mechanical properties of *Mov13* long bones[33]	0.128 ± 0.031	0.144 ± 0.032	+13%	21.2 ± 4.9	19.7 ± 4.0	No change
	Bending Strength (MPa) at 8 Weeks of Age (anterior quadrant)			Bending Strength (MPa) at 8 Weeks of Age (posterior quadrant)		
	Wild-type	*Mov13*	% Changes	Wild-type	*Mov13*	% Changes
Mechanical properties of small specimens taken from *Mov13* long bones[35]	196.7 ± 36.7	146.8 ± 29.6	−25%	187.1 ± 36.0	145.1 ± 30.4	−22%
	Moment of Inertia (mm^4) at 6 Weeks of Age			Failure Load (N) in Bending at 6 Weeks of Age		
	Wild-type	Transgenic	% Changes	Wild-type	Transgenic	% Changes
Geometric and mechanical properties of long bones from transgenic mice (COL1A1)[36]	0.14 ± 0.032	0.08 ± 0.033	−43%	11.6 ± 1.46	9.3 ± 3.35	−20%

The reported defective mineralization is most likely related to changes in collagen assembly and extracellular matrix expression. See text for further description of the murine models for osteogenesis imperfecta. Data are reported as mean ± standard deviation.

[a]Studies where only percent changes in mean values were reported.

measurements with physicochemical ones. The biomechanical data, some of which are presented in Table 13.2, correlated well with a lower collagen content, lower mineral content, and impaired mineral crystallinity in the oim/oim mice as compared with wild-type littermates. The measured properties of bone from the heterozygous oim/+ mice showed values consistently between the ones from the homozygous and the wild-type animals. Again, it appeared that the altered mineralization, probably due to the defective collagen template in OI, has a major effect on the mechanical properties. Using an ultrasonic technique, Mehta et al.[30] found a significant decrease in the modulus of elasticity in the longitudinal

direction in oim/oim long bones. These findings may be related to a decreased mineral content and crystallinity, although the authors did not investigate these aspects.

13.2.3.1.2 The Mov13 Mouse

In milder OI models, the bone brittleness is mainly related to a decreased production of collagen, which is the main contributor to bone ductility. In a transgenic OI animal model known as the heterozygous *Mov13* mouse strain, a retrovirus prevents initiation of transcription of one of the α1(I) collagen genes.[31,32] As a result, there is a significant reduction in (otherwise normal) type I collagen content in long bones and significant changes in the geometry and in the whole-bone brittleness.[33,34] In fact, the post-yield deflection was decreased by 61% and bending strength by 22 to 25% in specimens prepared from *Mov13* mice long bones as compared with wild-type ones. Also, a similar reduction in fatigue life and fatigue failure stress was measured.[35] These changes have been attributed to the reduced collagen content, and to the lack of crack-arresting interfaces at both the lamellar and the intermolecular levels.

13.2.3.1.3 The COLIA1 pro-alpha 1 Mutation

Another model for osteogenesis imperfecta in humans has been described by Pereira and collaborators.[36] These transgenic mice express a mutated gene for type I procollagen and show phenotypic features of OI and the occurrence of spontaneous fractures, not reported in the *Mov13* mice. Cassella et al.[37] and Pereira et al.[36,38] compared the biochemical, physicochemical, and biomechanical properties of transgenic and control mice. The defects in bone were demonstrated as a lower collagen content, a lower mineral content, and a lower Ca:P ratio. The biomechanical measurements confirmed the increased brittleness of the bones.

Some of the relevant biomechanical data from this OI model as well as from the previous ones are summarized in Table 13.2.

13.3 The Mechanical Consequences of Changes in the Mineral Phase

Bone mineral is a Ca-deficient, carboxyl-deficient apatite (either due to a substitution of Na or Mg for Ca, or a true deficiency), which contains both HPO_4 and CO_3 ions within the crystal lattice and on the surface of the crystals.[39,40] The mechanical properties of the mineral phase are assumed to be the same as the properties of the pure stochiometric hydroxyapatite,[41] although bone apatite is also hydroxyl deficient.[42] In human bone, the mineral exists in platelike shape in the molecular interstices within and between the collagen fibrils, with a characteristic size of 20 Å (thickness) $\times$ 100 Å (width) $\times$ 400 Å (length).[43] The *c*-axis of the mineral crystallization is oriented parallel to the axial direction of the collagen molecules, suggesting the role played by the collagen template in directing crystal growth. Handschin and Stern[39] did an extensive crystallographic (X-ray diffraction) and chemical (X-ray fluorescence and combustion analysis) study on bone apatite of human iliac crest ranging from 0 to 90 years old. They found that the mineral fraction and mineral crystallinity (*c*-axis size) increase significantly with age for juvenile bone (0 to 25 years) (with a decrease in crystallinity in the *a*-axis), then they stabilize over adulthood (25 to 50 years). The data at old age (50 to 90 years) show only a slight increase in *c*-axis crystallinity with age. These data seem to suggest that although aging bone may have higher percentage of mature bone apatite, the level of crystallinity does not differ much from adult bone.

13.3.1 The Hydration Shell of Bone Mineral

The phosphate groups on the surface of bone apatite can bind at least two consecutive monolayers of water molecules through electrostatic interaction and hydrogen bonding (hydration shell).[44] The water can only be removed by prolonged heating at a temperature up to 450°C or prolonged desiccation in a vacuum chamber. The heat of adsorption (a measure of adsorption strength, determined by the strength of hydrogen bonding) of water on bone mineral varies between 15 to 23 kcal/mol for the first monolayer, and it increases as the area of water coverage decreases. Additional water beyond two monolayers is bound

as strongly to the solution water as it is to the apatite-bound water, with a heat of adsorption approaching that of the heat of vaporization of water (10.5 kcal/mol). Hence, water molecules beyond two monolayers should be classified as free water.

Compared with small molecules like water, which can readily reorient themselves to attain maximal binding, the binding affinity of macromolecules (like collagen and noncollagenous proteins in bone) for bone apatite crystal depends largely on the availability of their charged groups. The noncollagenous proteins present in bone are polyanionic in nature and have a very large fixed charge density. As a result, the binding affinity of noncollagenous proteins for bone apatite is much larger than that of the aggregated collagen. This topic is discussed in Section 13.4.

13.3.2 Mineral Changes and Their Effects on Bone Biomechanical Properties

Section 13.2 reviewed a model for OI where a defective collagen template leads to changes in mineralization (crystal size and perfection as well as structural changes). As a result, the mechanical properties of OI bone were impaired. This section discusses the question whether or not it is possible to change the properties of the mineral phase selectively without affecting the organic phase. Given that the mineral phase plays a major role in determining bone stiffness,[3] it is expected that small changes in the mechanical properties of bone apatite will result in bone stiffness changes.

13.3.2.1 Effects of Ion Substitution

In vitro soaking of bone specimens in fluoride or phosphate solution for several days seems to reduce post-yield mechanical properties (Table 13.3). Walsh and Guzelsu,[45,46] who studied bovine bone, attribute this reduction to a change in the surface properties of bone apatite, which ultimately affected mineral–matrix interfacial bonding. In other words, fluoride treatment did not change the mechanical properties of bone apatite, but modified the surface chemistry of the crystal. Soaking the bone specimens

TABLE 13.3 *Ion* Substitution in the Crystal Lattice Results in Reduced Biomechanical Properties of Bone

	Ultimate Stress (MPa)			Modulus (GPa)		
	Control	NaF Treated	% Changes	Control	NaF Treated	% Changes
Compressive properties of fluoride-treated bone[45,46]	214 ± 10	127 ± 34	−41%	19.74 ± 3.09	10.43 ± 2.62	−47%
	Ultimate Torque (N/mm)			Torsional Rigidity (N/mm²/rad)		
	Control	NaF Treated	% Changes	Control	NaF Treated	% Changes
Shear properties (torsion test) of fluoride-treated bone[47]	23.2 ± 4.2	8.9 ± 1.7	−61%	693 ± 178	201 ± 69	−71%
	Ultimate Bending Moment (N/mm)			Bending Rigidity (N/mm²)		
	Control	NaF Treated	% Changes	Control	NaF Treated	% Changes
Bending properties of fluoride-treated bone[47]	22.4 ± 3.7	14.7 ± 2.6	−34%	613 ± 164	180 ± 62	−71%
	Ultimate Torque (N/mm)			Angular Deformation (rad/m)		
	Control	Male Hyp	% Changes	Control	Male Hyp	% Changes
Mechanical properties of bone in the hypophosphatemic mouse model[48]	34.4 ± 15.7	15.8 ± 6.2	−54%	9.95 ± 3.16	56.29 ± 16.18	+466%

Note: The Hyp mouse is an established animal model of X-linked hypophosphatemia, a genetic form of metabolic bone disease in humans characterized by abnormal mineralization. Data are reported as mean ± standard deviation.

in equal-strength NaCl solution did not have any effect. For the phosphate-ion solution treatment, no demineralization or removal of structural proteins was detected. Interestingly, the effect of phosphate ion solution is reversible when the phosphate ions are removed, but the fluoride ion effect is irreversible and the mechanical properties are permanently altered. This indicates a stronger binding affinity of fluoride ion for the mineral surface as compared with the phosphate ion. The fluoride ions may get incorporated into the mineral lattice and permanently alter the crystal structure of the bone mineral. Recently, Silva and Ulrich[47] reported similar results from experiments done using whole rodent bones. However, the mechanism of action of fluoride in these studies is a physicochemical one, and more studies are needed to characterize precisely the actual consequences of fluoride on the mechanical properties of bone.

13.3.2.2 The X-Linked Hypophosphatemic Mouse (*Hyp* mouse)

The *Hyp* mouse is an animal model for X-linked hypophosphatemia, a genetic disorder in humans characterized by rickets and bone deformities. The disease is associated with a renal tubular defect resulting in reduced phosphate transport. Camacho et al.[48] studied the physicochemical properties (using X-ray diffraction and Fourier transform infrared microscopy) of the mineral in the *Hyp* mouse and related them to the biomechanical behavior of long bones from these animals. Mineral content was significantly reduced in the *Hyp* mice as compared with normal mice, but crystallinity and crystal perfection were unchanged. The Ca:P ratio was significantly higher and the CO_3:PO_4 ratio was significantly reduced in the *Hyp* mice as compared with normal animals. These changes are primarily related to the reduced amount of phosphate available. The reduction in mineral content resulted in a drop of 90% in torsional stiffness of the *Hyp* whole femurs as compared with normal femurs. The post-yield behavior was also significantly affected (see Table 13.3) affected, suggesting that the molecular alterations in the *Hyp* mouse may compromise mineral–matrix interactions as well. In fact, Rifas et al.[49] have shown that that the reduced phosphate availability decreases the phosphorylation of noncollagenous matrix proteins in these bones.

13.4 The Role of Noncollagenous Proteins: Lessons from Gene-Targeted Models

The deposition of minerals within many biological tissues is a controlled process. Among the most active agents that control biological mineralization are a group of unusually acidic proteins and glycoproteins that constitute only about 10% of the total organic component in bone. Some noncollagenous proteins are responsible for organizing the collagenous matrix and mediating cell attachment; others are found to regulate the nucleation, the rate of growth, and the stability of the mineral phase crystals.[50–55] These macromolecules usually have a high negative fixed charge density and they will readily bind Ca^{2+} ions. Moreover, the β-pleated sheets and β-turns (a secondary structure represented by relatively flat aggregation of macromolecular chains) of these macromolecules often present the electronegative phosphoryl group PO_3^{2-} in a flat array that may closely match the crystal lattice of a bone apatite.[50] Because of these properties, some noncollagenous proteins have been proposed to serve as a "glue" between collagen and mineral, thus modulating mineral–matrix interfacial bonding.[56,57]

13.4.1 Interfacial Bonding in the Engineering Sense: An Introduction

To obtain an optimum bulk performance of a composite material (see Chapter 12 for a thorough discussion), the bonding properties at the interface have to be carefully designed. If the interface bonding is too strong, the fiber will fracture, together with the matrix, and the protection effect of the interface is lost. If the interface bonding is too weak, the integrity of the composite will be compromised. As shown in Fig. 13.1, the interface properties can be tuned by determining the nature of the interaction between matrix and filler (mechanical, electrostatic, or chemical). Obviously, hybrid forms can also exist. The properties of the interface can be studied by methods used in physical chemistry

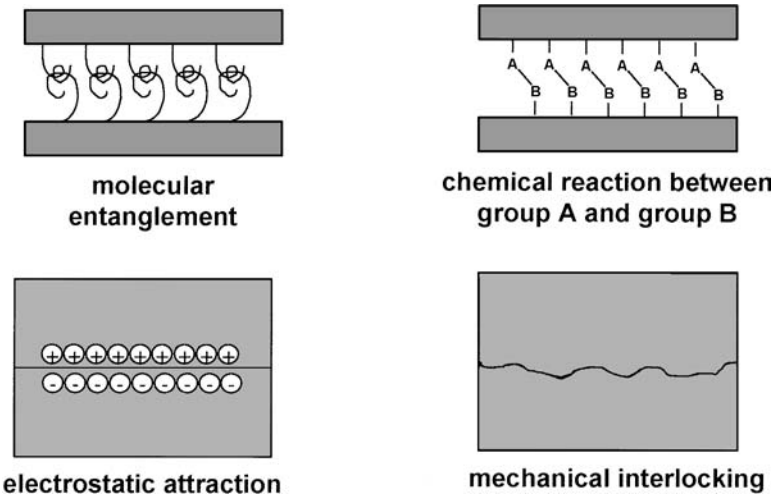

FIGURE 13.1 Interface properties in composite materials. The elasticity of a composite material mainly depends on the elasticity of the phases, their volumetric fraction, and the orientation of reinforcement phase (see Chapter 12 for a detailed discussion). On the other hand, the nature of the interfacial bonding between reinforcing phase and matrix, the homogeneity in the distribution of the reinforcing phase, and the presence of defects are very important determinants of the post-yield and failure behavior. Depending on the geometric and physicochemical characteristics of the interface between matrix and filler, interfacial bonding can be extremely strong or very weak. An example of strong bonding is given in the case covalent bonds are formed at the interface through a chemical reaction or in the case ionic bonds are formed because of the electrostatic characteristics of the surfaces in contact. A weaker bonding is given in case other intermolecular forces develop at the interface such as van der Waals forces or hydrogen bonds. Surface roughness can increase interfacial bonding by mechanical interlocking and because of an increase of the contact area.

for determining the structure and conformation of molecular compounds such as Raman spectroscopy[58,59] or solid-state nuclear magnetic resonance.[60–62] Raman spectroscopy could potentially be used to measure stresses at the molecular level.[63] In fact, a Raman band peak shifts to a lower or a higher frequency upon stretching or compressing the related molecular bond, respectively. If the stress (or strain) turns out to be a function of the frequency shift, the studied molecular bond can be considered as a "strain gauge." This approach has been recently used to study interfacial properties in anthropogenic composite materials.[64,65] It would be interesting to see whether interface properties in biological samples can be detected by Raman spectroscopy. However, two major problems need to be solved. The first is the proper calibration of the measurements. Second, the scattering volume needs to be large enough, and the bonding distinctly different at the interface than in the two substrates (L. Schadler, Rensselaer Polytechnic Institute, personal communication). In fact, compared with other artificial composite materials, which generally have dimensionally large, temporally and spatially stable interfaces, and cross-link chemistry between the phases involved, the interface between the mineral and organic phases in bone is much more minute. For these two reasons, the direct experimental approach is probably bound to fail.

13.4.2 Noncollagenous Proteins and Proteoglycans Modulate the Properties of the Material "Bone"

Some insight into the role played by noncollagenous proteins and proteoglycans in modulating the properties of the interface between the collagen and the mineral can be gained by dedicated genetic manipulation. Gene-targeted models for noncollagenous proteins have been briefly discussed in Chapter 4. Here some of them are reviewed, specifically focusing on biomechanical data.

13.4.2.1 Osteopontin

Osteopontin is a matrix protein rich in acidic amino acids and sialic acid that may be involved in the regulation of crystal growth.[53,66] In bone, osteopontin is preferentially found at tissue interfaces such as cement lines (reversal and resting lines seen in bone remodeling).[56,57] Mice lacking osteopontin were reported to appear normal based on histology,[67] but recent data indicate that the bones of the animals are increased in density and have an increased mineral content with larger mineral crystals (see Chapter 5). The osteopontin knockout mouse shows changes in wound healing,[68] suggesting that tissue repair or remodeling might be in general impaired in these animals. In a recent report, Yoshitake and collaborators,[69] showed that osteopontin knockout mice are resistant to ovariectomy-induced bone resorption, consistent with the findings that osteopontin may be important for normal osteoclast function.[67]

13.4.2.2 Osteonectin

Osteonectin (SPARC) is an acidic noncollagenous protein found in bone and dentin and shows affinity to both collagen and mineral.[70] Binding sites of this protein to hydroxyapatite were determined by a proteolytic experiment and an *in vitro* binding experiment using synthetic peptide analogues.[71] Osteonectin seems not only to be involved in development, but also in remodeling and tissue repair.[72] Also, it is interesting to note that in OI, the expression of osteonectin is reduced,[73] perhaps contributing to the reported bone fragility. Surprisingly, the osteonectin-deficient mouse[74] was reported not to have any obvious skeletal defects. However, these observations were purely qualitative since they relied only on histological investigations. Recently, Delany and collaborators[75] conducted a more-detailed investigation of bone geometry, histomorphometry, and biomechanics of bones from the osteonectin-deficient mice. The authors clearly found that bone remodeling is impaired in the osteonectin-null mouse, leading to a negative bone balance and severe osteopenia. The transgenic mice clearly showed a decreased cancellous bone volume, whereas no important changes in cortical thickness were found. Additionally, mineral-to-matrix ratio and crystal size were found to be increased in the knockout animals as compared with wild-type littermates,[76] confirming the decrease in bone formation in the osteonectin-null mouse. The bending stiffness of long bones from wild-type animals increased with age, whereas no changes were measured in bones from transgenic animals. Unfortunately, the area moment of inertia was not measured in this investigation, thus not allowing an estimate of the modulus of elasticity.

13.4.2.3 Osteocalcin

Glowacki et al.[77] proposed that osteocalcin may function as a matrix signal in the recruitment and differentiation of osteoclasts. In fact, the osteocalcin-knockout mice showed an increased bone formation.[78] Accordingly, the bending properties of long bone from osteocalcin-deficient mice were significantly higher as compared to wild-type littermates (Table 13.4). A biomechanical study done before and after ovariectomy showed that bone resorption was not impaired in the mutated animals. The mineral formed, however, was abnormal. Crystal size and crystal perfection did not increase with age, suggesting that osteocalcin is also a regulator of crystal maturation.[79] A putative role for osteocalcin in mediating mineral–matrix interfacial bonding is not proved.

13.4.2.4 Biglycan

The small proteoglycan biglycan has been shown to be expressed in bone.[80] *In vitro* studies have shown that biglycan can interact with type I collagen and consequently can have an organizing function on the assembly of the extracellular matrix.[81] Xu et al.[82] presented interesting data on the role of biglycan in mineralized tissues, creating a mouse model lacking biglycan. The biglycan knockout mice showed reduced bone formation, less mineral, but a tendency to larger crystals than their normal littermates. The biomechanical properties (yield and failure load) were significantly reduced in the biglycan deficient mouse bones (see Table 13.4).

TABLE 13.4 Changes in Biomechanical Properties of Bone after Gene-Targeted Disruption of Some of the Important Noncollagenous Proteins Present in Bone

Model	Bending Stiffness (N/mm) at 11 Weeks of Age			Bending Stiffness (N/mm) at 17 Weeks of Age		
	Wild-type	Knockout	% Changes	Wild-type	Knockout	% Changes
Bending properties in the osteonectin knockout mouse[75]	33.19 ± 2.38	32.03 ± 1.77	No difference	64.59 ± 10.93	35.77 ± 6.59	−45%
	Yield Energy (N/mm) at 6 Months of Age			Failure Load (N) at 6 Months of Age		
	Wild-type	Knockout	% Changes	Wild-type	Knockout	% Changes
Bending properties in the osteocalcin knockout mouse[78]	0.169 ± 0.020	0.257 ± 0.028	+52%	27.08 ± 3.25	33.79 ± 5.41	+25%
	Yield Energy (N/mm) at 6 Months of Age			Failure Load (N) at 6 Months of Age		
	Wild-type	Knockout	% Changes	Wild-type	Knockout	% Changes
Bending properties in the biglycan knockout mouse[82]	25.28 ± 3.99	19.95 ± 3.18	−21%	36.29 ± 9.96	28.54 ± 4.11	−21%
	Cortical Thickness (mm), Femur at 3 Months of Age			Bone Mineral Density (mg/mm^3), Femur at 3 Months of Age		
	Wild-type	Knockout	% Changes	Wild-type	Knockout	% Changes
Properties of bone from the thrombospondin 2 knockout mouse[83]	0.26 ± 0.016	0.29 ± 0.017	+12%	450.5 ± 25	498.5 ± 24	+11%

Note: In the thrombospondin 2 knockout mouse, an increased bone formation has been reported; however, biomechanical data are not available. Gene-targeted models for other non-collagenous proteins has been generated. Only the biomechanical properties of soft tissues such as skin have been measured so far. Data are reported as mean ± standard deviation.

13.4.2.5 Thrombospondin 2

The role of thrombospondin-2 in connective tissue biology is still poorly understood. In the thrombospondin-2-knockout mouse,[83] abnormal fibrillogenesis leads to changes in the biomechanical properties of skin (decreased tensile strength). The long bones in mutant mice showed increased cortical thickness and an increased bone density as measured by quantitative computer tomography (Table 13.4). Again, it would be of great interest to study the biochemistry, in particular of the organic matrix, and the biomechanical properties of bone tissue in this model.

13.5 Summary

The data presented in this chapter illustrate the increasing evidence that the mechanical properties of bone depend not only on its microstructure but also on the molecular structure of the organic and inorganic components. However, the nature of the interface between these components in bone is far from being understood. A detailed characterization of transgenic/knockout mice models with skeletal phenotype from a physicochemical standpoint (i.e., using spectroscopic methods such as Fourier transform infrared spectroscopy/imaging or Raman spectroscopy) is needed. Additionally, accurate micromechanical investigations of small bone specimens (as opposed to whole bones) using well-defined protocols should be encouraged. By using state-of-the-art technology it has become possible to measure the mechanical properties of specimens with dimensions of the order of 1 mm.[84]

A complete understanding of the interaction between organic and inorganic phase at the molecular level will provide valuable information to the materials science and bioengineering community for the manufacture of superior implant materials and bone substitutes.

References

1. McCutchen, C. W., Do mineral crystals stiffen bone by straitjacketing its collagen? *J. Theor. Biol.,* 51, 51, 1975.
2. Hukins, D. W., Bone stiffness explained by the liquid crystal model for the collagen fibril, *J. Theor. Biol.,* 71, 661, 1978.
3. Reilly, D. T. and Burstein, A. H., The elastic and ultimate properties of compact bone tissue, *J. Biomech.,* 8, 393, 1975.
4. Currey, J. D., Brear, K., and Zioupos, P., The effects of ageing and changes in mineral content in degrading the toughness of human femora, *J. Biomech.,* 29, 257, 1996.
5. Zioupos, P. and Currey, J. D., Changes in the stiffness, strength, and toughness of human cortical bone with age, *Bone,* 22, 57, 1998.
6. Zioupos, P., Currey, J. D., and Hamer, A. J., The role of collagen in the declining mechanical properties of aging human cortical Bone, *J. Biomed. Mater. Res.,* 45, 108, 1999.
7. Oxlund, H., Mosekilde, L., and Ortoft, G., Reduced concentration of collagen reducible cross links in human trabecular bone with respect to age and osteoporosis, *Bone,* 19, 479, 1996.
8. Yamauchi, M., Young, D. R., Chandler, G. S., and Mechanic, G. L., Cross-linking and new bone collagen synthesis in immobilized and recovering primate osteoporosis, *Bone,* 9, 415, 1988.
9. Bella, J., Brodsky, B., and Berman, H. M., Hydration structure of a collagen peptide, *Structure,* 3, 893, 1995.
10. Beck, K. and Brodsky, B., Supercoiled protein motifs: the collagen triple-helix and the alpha-helical coiled coil, *J. Struct. Biol.,* 122, 17, 1998.
11. Yamauchi, M., Collagen: the major matrix molecule in mineralized tissues, in *Calcium and Phosphorus in Health and Disease,* Anderson, J. J. B. and Garner, S. C., Eds., CRC Press, Boca Raton, FL, 1995, 127.
12. Bailey, A. J., Paul, R. G., and Knott, L., Mechanisms of maturation and ageing of collagen, *Mech. Ageing Dev.,* 106, 1, 1998.
13. Bailey, A. J. and Paul, R. G., The mechanisms and consequences of the maturation and ageing of collagen, *Proc. Indian Acad. Sci.-Chem. Sci.* 111, 57, 1999.
14. Eyre, D. R., Dickson, I. R., and Van Ness, K., Collagen cross-linking in human bone and articular cartilage, *Biochem. J.,* 252, 495, 1988.
15. Otsubo, K., Katz, E. P., Mechanic, G. L., and Yamauchi, M., Cross-linking connectivity in bone collagen fibrils: the COOH-terminal locus of free aldehyde, *Biochemistry,* 31, 396, 1992.
16. Jonas, J., Burns, J., Abel, E. W., Cresswell, M. J., Strain, J. J., and Paterson, C. R., Impaired mechanical strength of bone in experimental copper deficiency, *Ann. Nutr. Metab.,* 37, 245, 1993.
17. Masse, P. G., Rimnac, C. M., Yamauchi, M., Coburn, S. P., Rucker, R. B., Howell, D. S., and Boskey, A. L., Pyridoxine deficiency affects biomechanical properties of chick tibial bone, *Bone,* 18, 567, 1996.
18. Monnier, V. M., Nonenzymatic glycosylation, the Maillard reaction and the aging process, *J. Gerontol.,* 45, B105, 1990.
19. Bailey, A. J., Sims, T. J., Avery, N. C., and Halligan, E. P., Non-enzymic glycation of fibrous collagen: reaction products of glucose and ribose, *Biochem. J.,* 305, 385, 1995.
20. Bank, R. A., Bayliss, M. T., Lafeber, F. P., Maroudas, A., and Tekoppele, J. M., Ageing and zonal variation in post-translational modification of collagen in normal human articular cartilage. The age-related increase in non-enzymatic glycation affects biomechanical properties of cartilage, *Biochem. J.,* 330, 345, 1998.
21. Tomasek, J. J., Meyers, S. W., Basinger, J. B., Green, D. T., and Shew, R. L., Diabetic and age-related enhancement of collagen-linked fluorescence in cortical bones of rats, *Life Sci.,* 55, 855, 1994.
22. Rowe, D. W. and Shapiro, J. R., Osteogenesis Imperfecta, in *Metabolic Bone Disease,* 3rd ed., L. V. Avioli and S. M. Krane, Eds., Academic Press, New York, 1998, 651.
23. Vetter, U., Fisher, L. W., Mintz, K. P., Kopp, J. B., Tuross, N., Termine, J. D., and Robey, P. G., Osteogenesis imperfecta: changes in noncollagenous proteins in bone, *J. Bone Miner. Res.,* 6, 501, 1991.

24. Vetter, U., Eanes, E. D., Kopp, J. B., Termine, J. D., and Robey, P. G., Changes in apatite crystal size in bones of patients with osteogenesis imperfecta, *Calcif. Tissue Int.,* 49, 248, 1991.
25. Misof, K., Landis, W. J., Klaushofer, K., and Fratzl, P., Collagen from the osteogenesis imperfecta mouse model (oim) shows reduced resistance against tensile stress, *J. Clin. Invest.,* 100, 40, 1997.
26. Landis, W. J., The strength of a calcified tissue depends in part on the molecular structure and organization of its constituent mineral crystals in their organic matrix, *Bone,* 16, 533, 1995.
27. Weiner, S. and Traub, W., Organization of hydroxyapatite crystals within collagen fibrils, *FEBS Lett.,* 206, 262, 1986.
28. McBride, D. J., Jr., Shapiro, J. R., and Dunn, M. G., Bone geometry and strength measurements in aging mice with the oim mutation, *Calcif. Tissue Int.,* 62, 172, 1998.
29. Camacho, N. P., Hou, L., Toledano, T. R., Ilg, W. A., Brayton, C. F., Raggio, C. L., Root, L., and Boskey, A. L., The material basis for reduced mechanical properties in oim mice bones, *J. Bone Miner. Res.,* 14, 264, 1999.
30. Mehta, S. S., Antich, P. P., and Landis, W. J., Bone material elasticity in a murine model of osteogenesis imperfecta, *Connect. Tissue Res.,* 40, 189, 1999.
31. Hartung, S., Jaenisch, R., and Breindl, M., Retrovirus insertion inactivates mouse alpha 1(I) collagen gene by blocking initiation of transcription, *Nature,* 320, 365, 1986.
32. Barker, D. D., Wu, H., Hartung, S., Breindl, M., and Jaenisch, R., Retrovirus-induced insertional mutagenesis: mechanism of collagen mutation in Mov13 mice, *Mol. Cell. Biol.,* 11, 5154, 1991.
33. Bonadio, J., Jepsen, K. J., Mansoura, M. K., Jaenisch, R., Kuhn, J. L., and Goldstein, S. A., A murine skeletal adaptation that significantly increases cortical bone mechanical properties. Implications for human skeletal fragility, *J. Clin. Invest.,* 92, 1697, 1993.
34. Jepsen, K. J., Goldstein, S. A., Kuhn, J. L., Schaffler, M. B., and Bonadio, J., Type-I collagen mutation compromises the ld behavior of Mov13 long bone, *J. Orthop. Res.,* 14, 493, 1996.
35. Jepsen, K. J., Schaffler, M. B., Kuhn, J. L., Goulet, R. W., Bonadio, J., and Goldstein, S. A., Type I collagen mutation alters the strength and fatigue behavior of Mov13 cortical tissue, *J. Biomech.,* 30, 1141, 1997.
36. Pereira, R., Khillan, J. S., Helminen, H. J., Hume, E. L., and Prockop, D. J., Transgenic mice expressing a partially deleted gene for type I procollagen (COL1A1), *J. Clin. Invest.,* 91, 709, 1993.
37. Cassella, J. P., Pereira, R., Khillan, J. S., Prockop, D. J., Garrington, N., and Ali, S. Y., An ultrastructural, microanalytical, and spectroscopic study of bone from a transgenic mouse with a COL1.A1 pro-alpha-1 mutation, *Bone,* 15, 611, 1994.
38. Pereira, R., Hume, E. L., Halford, K. W., and Prockop, D. J., Bone fragility in transgenic mice expressing a mutated gene for type I procollagen (COL1A1) parallels the age-dependent phenotype of human osteogenesis imperfecta, *J. Bone Miner. Res.,* 10, 1837, 1995.
39. Handschin, R. G. and Stern, W. B., Crystallographic and chemical analysis of human bone apatite (Crista Iliaca), *Clin. Rheum.,* 13, 75, 1994.
40. Glimcher, M. J., The nature of the mineral phase in bone: biological and clinical implications, in *Metabolic Bone Disease,* 3rd ed., L. V. Avioli and S. M. Krane, Eds., Academic Press, New York, 1998, 23.
41. Gilmore, R. S. and Katz, J. L., Elastic properties of apatites, *J. Mater. Sci.,* 10, 187, 1982.
42. Rey, C., Miquel, J. L., Facchini, L., Legrand, A. P., and Glimcher, M. J., Hydroxyl groups in bone mineral, *Bone,* 16, 583, 1995.
43. Weiner, S. and Traub, W., Bone structure: from angstroms to microns, *FASEB J.,* 6, 879, 1992.
44. Posner, A. S. and Beebe, R. A., The surface chemistry of bone mineral and related calcium phosphates, *Semin. Arthritis Rheum.,* 4, 267, 1975.
45. Walsh, W. R. and Guzelsu, N., The role of ions and mineral-organic interfacial bonding on the compressive properties of cortical bone, *Biomed. Mater. Eng.,* 3, 75, 1993.
46. Walsh, W. R. and Guzelsu, N., Compressive properties of cortical bone: mineral–organic interfacial bonding, *Biomaterials,* 15, 137, 1994.

47. Silva, M. J. and Ulrich, S. R., In vitro sodium fluoride exposure decreases torsional and bending strength and increases ductility of mouse femora, *J. Biomech.,* 33, 231, 2000.
48. Camacho, N. P., Rimnac, C. M., Meyer, R. A., Jr., Doty, S., and Boskey, A. L., Effect of abnormal mineralization on the mechanical behavior of X-linked hypophosphatemic mice femora, *Bone,* 17, 271, 1995.
49. Rifas, L., Cheng, S., Halstead, L. R., Gupta, A., Hruska, K. A., and Avioli, L. V., Skeletal casein kinase activity defect in the HYP mouse, *Calcif. Tissue Int.,* 61, 256, 1997.
50. Addadi, L., Berman, A., Oldak, J. M., and Weiner, S., Structural and stereochemical relations between acidic macromolecules of organic matrices and crystals, *Connect. Tissue Res.,* 21, 127, 1989.
51. Boskey, A., Maresca, M., and Appel, J., The effects of noncollagenous matrix proteins on hydroxyapatite formation and proliferation in a collagen gel system, *Connect. Tissue Res.,* 21, 171, 1989.
52. Boskey, A. L., Maresca, M., Doty, S., Sabsay, B., and Veis, A., Concentration-dependent effects of dentin phosphophoryn in the regulation of in vitro hydroxyapatite formation and growth, *Bone Miner.,* 11, 55, 1990.
53. Boskey, A. L., Maresca, M., Ullrich, W., Doty, S. B., Butler, W. T., and Prince, C. W., Osteopontin-hydroxyapatite interactions in vitro: inhibition of hydroxyapatite formation and growth in a gelatin-gel, *Bone Miner.,* 22, 147, 1993.
54. Veis, A., Mineral-matrix interactions in bone and dentin, *J. Bone Miner. Res.,* 8, S493, 1993.
55. Weiner, S. and Addadi, L., Acidic macromolecules of mineralized tissues: the controllers of crystal formation, *Trends Biochem. Sci.,* 16, 252, 1991.
56. McKee, M. D. and Nanci, A., Osteopontin at mineralized tissue interfaces in bone, teeth, and osseointegrated implants: ultrastructural distributions and implications for mineralized tissue formation, turnover, and repair, *Microsc. Res. Tech.,* 33, 141, 1996.
57. McKee, M. D. and Nanci, A., Osteopontin: an interfacial extracellular matrix protein in mineralized tissues, *Connect. Tissue Res.,* 35, 251, 1996.
58. Frushour, B. G. and Koenig, J. L., Raman scattering of collagen, gelatin, and elastin, *Biopolymers,* 14, 379, 1975.
59. Timlin, J. A., Carden, A., and Morris, M. D., Chemical microstructure of cortical bone probed by Raman transects, *Appl. Spectrosc.,* 53, 1429, 1999.
60. Glimcher, M. J., Recent studies of the mineral phase in bone and its possible linkage to the organic matrix by protein-bound phosphate bonds, *Philos. Trans. R. Soc. Lond. B,* 304, 479, 1984.
61. Roberts, J. E., Bonar, L. C., Griffin, R. G., and Glimcher, M. J., Characterization of very young mineral phases of bone by solid state 31phosphorus magic angle sample spinning nuclear magnetic resonance and X-ray diffraction, *Calcif. Tissue Int.,* 50, 42, 1992.
62. Wu, Y., Chesler, D. A., Glimcher, M. J., Garrido, L., Wang, J., Jiang, H. J., and Ackerman, J. L., Multinuclear solid-state three-dimensional MRI of bone and synthetic calcium phosphates, *Proc. Natl. Acad. Sci. U.S.A.,* 96, 1574, 1999.
63. Leikin, S., Parsegian, V. A., Yang, W. H., and Walrafen, G. E., Raman spectral evidence for hydration forces between collagen triple helices, *Proc. Natl. Acad. Sci. U.S.A.,* 94, 11312, 1997.
64. Galiotis, C., Paipetis, A., and Marston, C., Unification of fibre/matrix interfacial measurements with Raman microscopy, *J. Raman Spectrosc.,* 30, 899, 1999.
65. Paipetis, A., Galiotis, C., Liu, Y. C., and Nairn, J. A., Stress transfer from the matrix to the fibre in a fragmentation test: Raman experiments and analytical modeling, *J. Composite Mater.,* 33, 377, 1999.
66. Boskey, A. L., Osteopontin and related sialoproteins: effects on mineralization, *Ann. N.Y. Acad. Sci.,* 760, 249, 1995.
67. Rittling, S. R., Matsumoto, H. N., McKee, M. D., Nanci, A., An, X. R., Novick, K. E., Kowalski, A. J., Noda, M., and Denhardt, D. T., Mice lacking osteopontin show normal development and bone structure but display altered osteoclast formation *in vitro*, *J. Bone Miner. Res.,* 13, 1101, 1998.
68. Liaw, L., Birk, D. E., Ballas, C. B., Whitsitt, J. S., Davidson, J. M., and Hogan, B. L. M., Altered wound healing in mice lacking a functional osteopontin gene (spp1), *J. Clin. Invest.,* 101, 1468, 1998.

69. Yoshitake, H., Rittling, S. R., Denhardt, D. T., and Noda, M., Osteopontin-deficient mice are resistant to ovariectomy-induced bone resorption, *Proc. Natl. Acad. Sci. U.S.A.,* 96, 8156, 1999.
70. Termine, J. D., Kleinman, H. K., Whitson, S. W., Conn, K. M., McGarvey, M. L., and Martin, G. R., Osteonectin, a bone-specific protein linking mineral to collagen, *Cell,* 26, 99, 1981.
71. Fujisawa, R., Wada, Y., Nodasaka, Y., and Kuboki, Y., Acidic amino acid-rich sequences as binding sites of osteonectin to hydroxyapatite crystals, *Biochem. Biophys. Acta,* 1, 53, 1996.
72. Yan, Q. and Sage, E. H., SPARC, a matricellular glycoprotein with important biological functions, *J. Histochem. Cytochem.,* 47, 1495, 1999.
73. Fisher, L. W., Drum, M. A., Robey, P. G., Conn, K. M., and Termine, J. D., Osteonectin content in human osteogenesis imperfecta bone shows a range similar to that of two bovine models of OI, *Calcif. Tissue Int.,* 40, 260, 1987.
74. Gilmour, D. T., Lyon, G. J., Carlton, M. B., Sanes, J. R., Cunningham, J. M., Anderson, J. R., Hogan, B. L., Evans, M. J., and Colledge, W. H., Mice deficient for the secreted glycoprotein SPARC/osteonectin/BM40 develop normally but show severe age-onset cataract formation and disruption of the lens, *EMBO J.,* 17, 1860, 1998.
75. Delany, A. M., Amling, M., Priemel, M., Howe, C., Baron, R., and Canalis, E., Osteopenia and decreased bone formation in osteonectin-deficient mice, *J. Clin. Invest.,* 105, 915, 2000.
76. Boskey, A., Spevak, L., Amling, M., Canalis, E., and Delany, A. M., Mineral analysis of osteonectin-deficient mouse bones confirms altered remodeling activity, *Trans. Orthop. Res. Soc. 46th Annu. Mtg.,* 25, 135, 2000.
77. Glowacki, J., Rey, C., Glimcher, M. J., Cox, K. A., and Lian, J., A role for osteocalcin in osteoclast differentiation, *J. Cell. Biochem.,* 45, 292, 1991.
78. Ducy, P., Desbois, C., Boyce, B., Pinero, G., Story, B., Dunstan, C., Smith, E., Bonadio, J., Goldstein, S., Gundberg, C., Bradley, A., and Karsenty, G., Increased bone formation in osteocalcin-deficient mice, *Nature,* 382, 448, 1996.
79. Boskey, A. L., Gadaleta, S., Gundberg, C., Doty, S. B., Ducy, P., and Karsenty, G., Fourier transform infrared microspectroscopic analysis of bones of osteocalcin-deficient mice provides insight into the function of osteocalcin, *Bone,* 23, 187, 1998.
80. Ingram, R. T., Clarke, B. L., Fisher, L. W., and Fitzpatrick, L. A., Distribution of noncollagenous proteins in the matrix of adult human bone: evidence of anatomic and functional heterogeneity, *J. Bone Miner. Res.,* 8, 1019, 1993.
81. Schonherr, E., Witsch Prehm, P., Harrach, B., Robenek, H., Rauterberg, J., and Kresse, H., Interaction of biglycan with type I collagen, *J. Biol. Chem.,* 270, 2776, 1995.
82. Xu, T., Bianco, P., Fisher, L. W., Longenecker, G., Smith, E., Goldstein, S., Bonadio, J., Boskey, A., Heegaard, A. M., Sommer, B., Satomura, K., Dominguez, P., Zhao, C., Kulkarni, A. B., Robey, P. G., and Young, M. F., Targeted disruption of the biglycan gene leads to an osteoporosis-like phenotype in mice, *Nat. Genet.,* 20, 78, 1998.
83. Kyriakides, T. R., Zhu, Y. H., Smith, L. T., Bain, S. D., Yang, Z., Lin, M. T., Danielson, K. G., Iozzo, R. V., LaMarca, M., McKinney, C. E., Ginns, E. I., and Bornstein, P., Mice that lack thrombospondin 2 display connective tissue abnormalities that are associated with disordered collagen fibrillogenesis, an increased vascular density, and a bleeding diathesis, *J. Cell Biol.,* 140, 419, 1998.
84. Lucchinetti, E., Thomann, D., and Danuser, G., Micromechanical testing of bone trabeculae—potentials and limitations, *J. Mater. Sci,* in press.

14

Quantification of Cancellous Bone Architecture

Anders Odgaard
Aarhus University Hospital

14.1 Introduction

The geometric and spatial properties of trabeculae in cancellous bone are collectively known as the *cancellous bone architecture*. The purpose of this chapter is to give an overview of methods in current use for quantification of the architecture. Only methods applied to histological sections and three-dimensional (3D) reconstructions will be discussed. Methods based on texture analysis of plain radiographs and low-resolution computed tomography (CT) scans and methods devised for studying dynamic properties of bone remodeling will not be discussed. Cancellous bone may be studied at different hierarchical levels from the ultrastructure of collagen and mineral to macroscopic density. Cancellous bone architecture is studied at the scale of individual trabeculae, i.e., at a resolution in the approximate range of 20 to 50 μm.

The trabecular arrangement in cancellous bone is obviously not random. Some regions are very dense, whereas others have only sparse trabeculae. In some regions the trabeculae are consistently coarse, whereas other regions consist of finer trabeculae. The mean orientation and degree of anisotropy are also variables that obviously change between anatomical sites and between individuals.

The variation in trabecular architecture formed the basis for the formulation of Wolff's law,[1] which links trabecular architecture to mechanical usage by adaptation, and mechanical properties to trabecular architecture by solid and—possibly—fluid mechanics. This explains the interest in cancellous bone architecture. Wolff stated that the architecture relates to the mechanical usage "in accordance with mathematical laws," but did not further specify these laws. Much has been learned over the last decade about how the architecture influences mechanical properties, but the influence of a number of architectural

0-8493-9117-2/01/$0.00+$.50

TABLE 14.1 Morphometric Parameters Encountered in Bone Mechanics

	Stereology	Direct 3D Measurement	Traditional Histomorphometry	Ad hoc 2D Measures
Density[a]	V_V	V_V	BV/TV[b]	
Surface density	S_V	S_V^b	BS/TV[b]	
Trab. dimensions[c]	star volume	thickness[e]	MTPT (Tb.Th)	direct meas.
		MTV	MTPS (Tb.Sp)	
Anisotropy	MIL	MIL		
	VO	VO		
	SVD[d]	SVD		
Topology (connectivity)	ConnEulor	Euler number	MTPD (Tb.N)	TBPf
		β_0		N.Nd, N.Tm
		β_1		Nd.Nd, Nd.Tm
		β_2		Tm.Tm, TSL
				N.Nd/N.Tm

[a]Implicitly bone density. May also be used for the marrow phase.
[b]Identical to the stereological method.
[c]Also used for quantification of marrow space dimensions.
[d]The stereological use will not be discussed. Method will be explained in detail in the section on 3-D methods.
[e]Volume weighed

features is still uncertain. One of the problems in explicit formulations relating to the cancellous bone architecture is defining and delimiting the architectural variables to be included.

A variety of methods for quantification of cancellous bone architecture has been proposed and, when first entering the field, the variety may seem confusing and without any system. In the following, the methods will be classified into (1) *basic stereological methods,* (2) *methods based on 3D reconstruction,* (3) *traditional 2D histomorphometric methods*, and (4) *ad hoc 2D methods*. This classification (Table 14.1) may assist in an understanding of the individual methods.

In much of the literature the terms *cancellous, trabecular*, and *spongy* bone are used interchangeably. Throughout this chapter, the term *cancellous bone* will be restricted to the 3D lattice-like structure composed of multiple trabeculae, and the term *trabecular bone* will be used to denote the material that constitutes individual trabeculae.[2] The term *spongy bone* will not be used. Throughout this chapter, the different morphometric methods will be illustrated on the specimen shown in Fig. 14.1.

14.2 Stereological Methods

Stereology may be defined as the study of sampling methods and estimation procedures in geometric populations. In less abstract terms it can be said to be the study of methods for obtaining estimators of geometric properties from samples of a structure. Obtaining (an estimate of) the volume fraction of a phase from point-sampling on a 2D section through a specimen is a simple example of a stereological method, and a more complex example is determining the mean volume of a cell type from measurements performed on random 2D sections.[3] Stereological methods are based on rigorous spatial statistics, and the results obtained are unbiased. These features are not true for some of the methods used in traditional histomorphometry.

Many stereological techniques have been developed, but only techniques and methods of relevance to cancellous bone architecture will be mentioned in the following. These are specifically aimed at estimating *volume fraction*, *surface density*, *star volume*, and *connectivity*.

14.2.1 Volume Fraction

The trabecular bone volume fraction, V_V(bone), is one of the fundamental architectural properties of cancellous bone, and it is defined as the trabecular volume per reference volume. For a specimen,

$$V_V(\text{bone}) = \frac{\text{trabecular bone volume}}{\text{trabecular bone volume} + \text{marrow space volume}}. \quad (14.1)$$

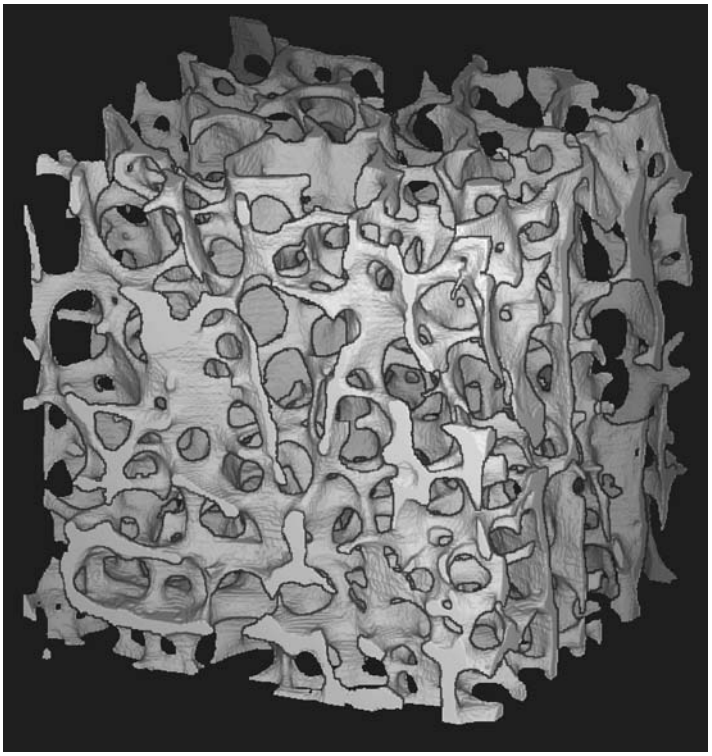

FIGURE 14.1 3D reconstruction of cubic cancellous bone specimen with side length 6.5 mm. This specimen will be used throughout this chapter for illustrating the different morphometric techniques.

The marrow space volume fraction, V_V(marrow), is defined equivalently, and V_V(bone) + V_V(marrow) = 1. For any phase, the volume fraction can be estimated unbiasedly by the area fraction A_A, the line fraction L_L and the point fraction P_P for uniformly sampled plane, line, and point probes, respectively,[4,5]

$$V_V = A_A = L_L = P_P. \tag{14.2}$$

This means that the volume fraction of cancellous bone can be estimated unbiasedly by placing a point grid on a random section and determining the fraction of points hitting bone (Fig. 14.2). There is no requirement for the orientation of the probes, and no requirement for isotropy of the structure.

14.2.2 Surface Density

The trabecular surface—or the bone-marrow interface—is highly irregular and convoluted, and its quantification may seem difficult. The surface density, or the trabecular surface area per cancellous bone volume, S_V, is related to the linear length of the border between trabeculae and marrow per examination area, B_A, as observed on a plane section through the bone.[4,5] The surface density, S_V, is also related to the number of surface intersections per line length, I_L, for a linear probe placed in the structure,[4,5]

$$S_V = \frac{4}{\pi} B_A = 2I_L. \tag{14.3}$$

The equation requires isotropy of either the trabecular surface or of the planar sections and linear probes. If the trabecular surface is isotropic, Eq. 14.3 is valid irrespective of the orientation of the planar and linear probes, and $2I_L$ and $(4/\pi)B_A$ would be unbiased estimators of S_V. If the trabecular surface is

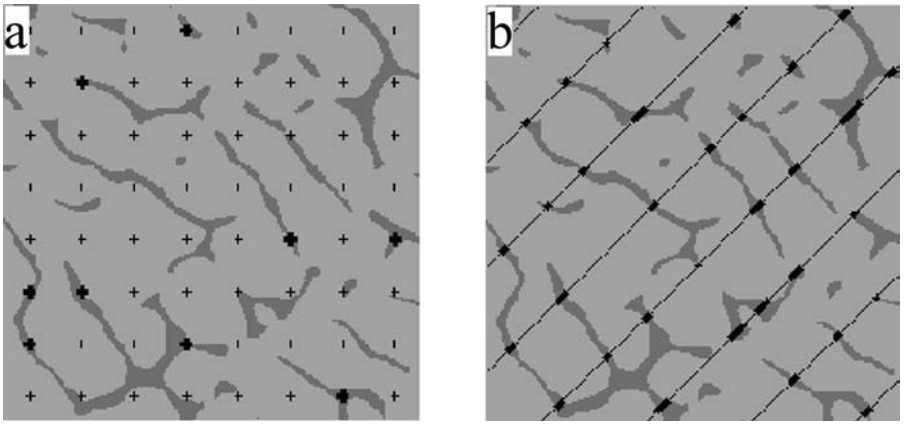

FIGURE 14.2 Random section through the specimen shown in Fig. 14.1. In (a) a point grid is shown as an overlay, and in (b) a line-grid overlay is shown. P_P from (a) is 9/64 = 0.141, and L_L from (b) is 0.118. Compare these results to the area fraction $A_A = 0.125$ of the section shown, the volume fraction $V_V = 0.131$ of the specimen in Fig. 14.1 and Eq. 14.2.

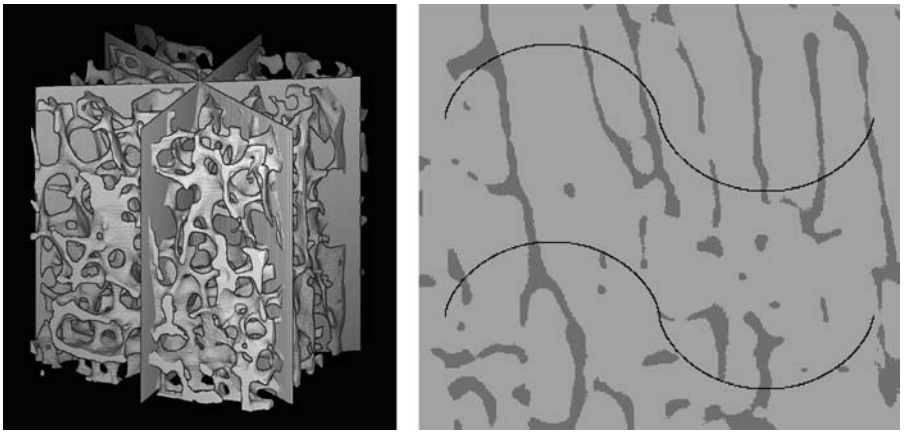

FIGURE 14.3 Three vertical sections placed through the specimen. One of these 2D sections is shown with the cycloid test system overlay. There are 28 intersections between bone–marrow interface and cycloid test system, and knowing the length of the cycloid test line system, I_L can be calculated and used in Eq. 14.3.

anisotropic, Eq. 14.3 requires isotropy of the 2D section or of the linear probes. As trabecular surfaces as a general rule are anisotropic, the isotropy requirement for the probes must be obeyed in order not to obtain biased results. Determining I_L from isotropic, random lines in 2D sections with a fixed orientation will result in unbiased values of B_A in these sections, but S_V will be biased to an unknown degree. An example of this might be determining I_L in transverse sections through iliac crest biopsies.

Vertical sections provide an elegant method for placing lines isotropically in 3D space, and hence for measuring surface density.[6,7] First an arbitrary direction is chosen, called the vertical axis, and 2D sections are made by rotating the specimen around this vertical axis. In the 2D sections obtained by this method, intersections between the trabecular surfaces and cycloid test lines are determined (Fig. 14.3). The combination of vertical sections and cycloid test lines assures isotropy of the test lines in 3D space. Knowing the length of the cycloid test lines allows direct calculation of I_L, and an unbiased estimation of S_V can be performed using Eq. 14.3.

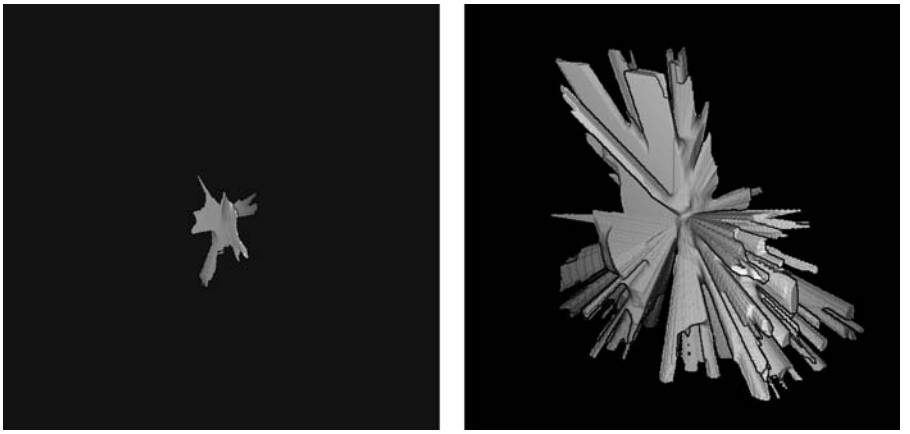

FIGURE 14.4 The star volume is the mean volume that can be seen unobscured from a random point within a phase. The left figure shows an unobscured volume around a random point in trabecular bone, and the right figure shows an unobscured volume around a random point in the marrow space. Both figures are directly comparable to Fig. 14.1.

14.2.3 Star Volume

Star volume is defined as the average volume that can been seen unobscured from a random point within a structure, and it can be applied to both the bone and the marrow phase.[8,9] The star volume is given by

$$\bar{v}_V^* = \frac{\pi}{3}\ell^3, \tag{14.4}$$

where ℓ is the average length of an intercept with random orientation through a random point. For convex particles, e.g., spheres, the star volume gives a volume weighed mean of the particle volumes. For complex trabecular structures, the star volume gives a volume weighed mean of the trabecular (or marrow) volume "visible" from a random location. See Fig. 14.4 for examples. The star volume of the marrow phase has been linked to connectivity, and it may indeed vary with connectivity.[10] It should, however, be emphasized that star volume is not a direct measure of connectivity.

14.2.4 Connectivity

Connectivity reports the number of redundant trabeculae in cancellous bone. A *redundant trabecula* is a trabecula that may be cut without increasing the number of separate parts of the bone structure. In Fig. 14.5c two redundant trabeculae exist. It should be noted that although connectivity gives the number of connections, it does not allow one to specify where a single trabecula starts or ends. A definition of trabeculae based on segments between nodes would require an abundance of *ad hoc* rules for the geometry of the structure. Even with several *ad hoc* rules, a consistent system would hardly be obtainable. One may as an example ask how long the segment D–F in Fig. 14.5c should be to be considered a proper trabecula.

The discipline of topology contains a full set of theorems for handling the connectivity of cancellous bone.[11] The central parameter is the *Euler number* χ, also known as the Euler characteristic. In 2D structures, the Euler number reports the number of particles (β_0) minus the number of holes (β_1) (see Fig. 14.5),

$$\chi = \beta_0 - \beta_1. \tag{14.5}$$

Given a 3D bone structure with β_0 separate bone particles, β_1 redundant connections, and β_2 fully enclosed marrow cavities (pores) isolated from the main marrow space,

$$\chi = \beta_0 - \beta_1 + \beta_2. \tag{14.6}$$

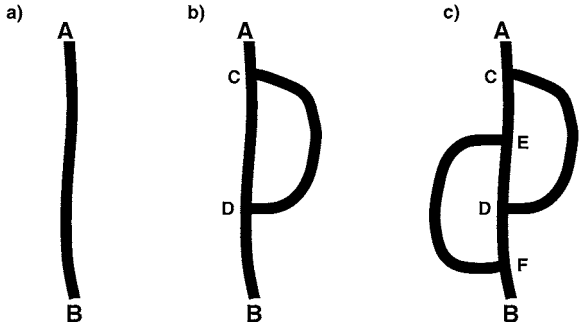

FIGURE 14.5 2D example illustrating connectivity and the number of trabeculae. A single trabecula from A to B exists in (a). To this trabecula first one and then a second trabecula are added as CD in (b) and EF in (c). The only consistent definition of a trabecula is based on counting the number of connections that may be cut without separating the structure into two parts. No matter how cuts are placed in (c), maximally two cuts can be made without creating separate particles. This means that two redundant connections exist, and this added to the initial trabecula in (a) gives a total number of three trabeculae. Using Eq. 14.5, $\chi(a) = 1 - 0 = 1$, $\chi(b) = 1 - 1 = 0$, and $\chi(c) = 1 - 2 = -1$.

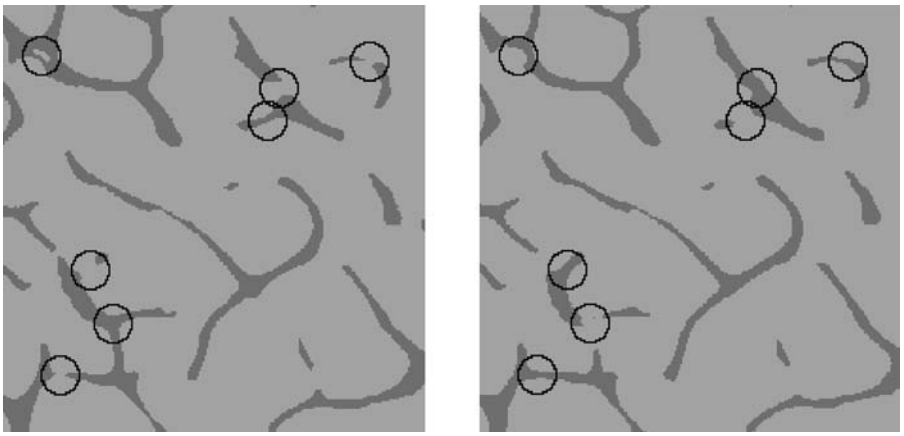

FIGURE 14.6 Two consecutive serial sections. Topological changes between the two sections are indicated by the circles. By noting and counting these occurrences, the Euler number density may be calculated.[12,48,49]

The numbers β_0, β_1, and β_2 are known as the 0th, 1st, and 2nd Betti numbers, respectively. Bone usually consists of one connected component and is without completely enclosed marrow cavities. This means that the number of redundant trabeculae in cancellous bone can be expressed by the Euler number of the structure:

$$\beta_1 = 1 - \chi. \tag{14.7}$$

The ConnEulor principle describes a method for determining the Euler number density from pairs of 2D sections.[12] The number of occurring/disappearing bone islands I, bridges B, and marrow holes H in two consecutive serial sections are determined, obeying disector counting rules,[13] and by knowing the examination area a and the distance between the sections h, the Euler number density χ_V can be determined as[12]

$$\chi_V = \frac{I - B + H}{2ha}, \tag{14.8}$$

when counting both ways in the dissector. See Fig. 14.6 for an example.

14.3 Three-Dimensional Methods

The 3D methods are based on performing morphometric measurements directly in a 3D data set. Different methods exist for 3D reconstruction of a cancellous bone region. The first published method was by Amstutz and Sissons,[14] who transferred serial sections through cancellous bone onto sheets of plastic that were stacked. Although this gave a magnified structure, it did not improve quantification of the structure. The real breakthrough in 3D reconstruction, which has been seen within the last decade, depends on developments in computer technology. 3D data sets require mass storage, and 3D analysis requires fast central processing units, efficient algorithms and compilers, and stable operating systems (mostly UNIX).

3D reconstruction can be performed using automated serial sectioning,[15] X-ray CT methods based on conventional sources or synchrotron radiation,[16–19] and magnetic resonance (MR) based methods.[20,21] No matter which method is used, the result is a 3D data set that maps the bone architecture in a voxel-data set. Usually, a purification algorithm is used to remove noise in the reconstruction.[11] In the following discussion, it is assumed that the 3D reconstruction is an accurate representation of the original specimen.

Volume fraction and surface density can easily be determined in a 3D reconstruction. Volume fraction is simply determined by the fraction of bone voxels to the total number of voxels, which may be considered an exact determination of V_V. Surface density may be determined unbiased by 3D isotropic linear probing and applying Eq. 14.3. By determining the surface directly from the voxel set, a resolution-dependent, fractal behavior of the measure will be observed.

14.3.1 Anisotropy

Different methods for quantification of anisotropy have been suggested. It may seem counterintuitive that different methods exist, but it should be noted that there is no single definition of architectural anisotropy. The specific geometric property of interest should explicitly be stated. Fig. 14.7 gives an example of a structure that yields different results depending on the specific anisotropy measure used.

Anisotropy is generally described by main directions, which are directions perpendicular to symmetry planes in the structure, and by numbers describing the concentration of directions around the main directions. *Fabric tensors* provide compact descriptions of orthotropic architectural anisotropy in the form of a 3×3 matrix, where the eigenvectors give main directions, and the eigenvalues give the degree of concentration around the main directions.[22,23]

14.3.1.1 Mean Intercept Length

The mean intercept length (MIL) measure was first introduced in cancellous bone morphometry by Whitehouse.[24] The basic principle of the MIL method consists of placing a linear grid with orientation ω onto a structure, and counting the number of intersections I between the grid and the bone–marrow

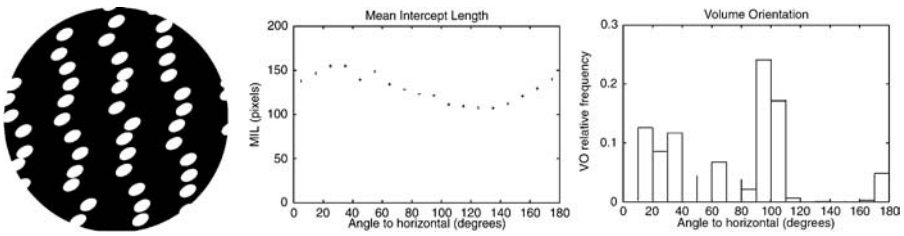

FIGURE 14.7 Example of a structure that shows different anisotropy directions dependent on the analysis method used. The result of the mean intercept length analysis shows one main direction at 30° corresponding to the orientation of the ellipses. The volume orientation analysis results in a main direction at about 100° and a second main direction around 30°. Perceived anisotropy seems better to be expressed by the VO result than by the MIL result. Structures with MIL isotropy and with strong VO anisotropy also exist.[25] The MIL and VO methods are described in detail in the text.

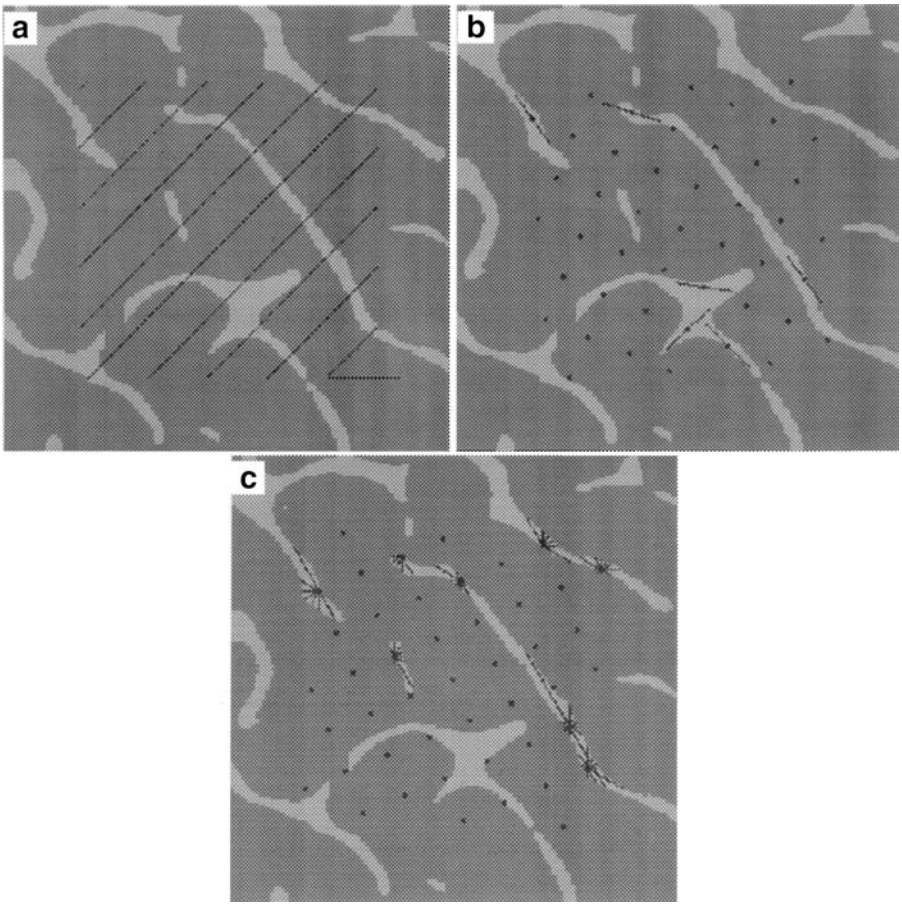

FIGURE 14.8 Principles of anisotropy methods. The linear grid of the mean intercept length (MIL) method is shown in (a). The point sampling and determination of the direction of longest intercepts used in the volume orientation (VO) method are demonstrated in (b). The point grid is also used in the star volume distribution (SVD) method, but here the lengths of intercepts in a number of directions are determined (c).

interfaces, see Fig. 14.8a. The mean length between any two intersections is then

$$\mathrm{MIL}(\omega) = \frac{L}{I(\omega)}, \tag{14.9}$$

where L is the total line length of the grid. Some authors have used a modified definition of MIL:

$$\mathrm{MIL}(\omega) = 2\frac{L}{I(\omega)}\mathrm{V}_V(\mathrm{bone}), \tag{14.10}$$

which reports the mean length of intercepts through the bone phase only. The factor $2\mathrm{V}_\mathrm{V}$ (bone), which is the only difference between Eqs. 14.9 and 14.10, however, does not provide any additional anisotropy information, and there is no advantage in using Eq. 14.10. It should be noted that the MIL method quantifies the *interface anisotropy* of a structure; see Fig. 14.7. One may easily think of structures that display interface isotropy but are yet structurally anisotropic.[25]

MIL varies with the orientation ω for structures with anisotropy of the bone–marrow interface, and Whitehouse observed that a polar plot of MIL vs. ω approximated an ellipse for planar sections through cancellous bone. A generalization of this observation into 3D space would result in an ellipsoid that

Harrigan and Mann noted could be expressed as the quadratic form of a second-rank tensor **M**, i.e., a fabric tensor.[26,27] Cowin defined a MIL fabric tensor **H** as the inverse square root of **M**.[23] The advantage of this modification is that larger values of **H** will be associated with larger values of Young's modulus, and that the eigenvalues of **H** are the MIL values in the main directions.

For an experimental data set consisting of n directions ω_i with directional cosines (x_i, y_i, z_i) and with corresponding mean intercept lengths (MIL_i), $1 \le i \le n$, a mean intercept length tensor **H** should be determined that gives the best fit of

$$\mathrm{MIL}_{\omega_i} = (x_i \;\; y_i \;\; z_i)\,\mathbf{H}\begin{Bmatrix} x_i \\ y_i \\ z_i \end{Bmatrix} = Ax_i^2 + By_i^2 + Cz_i^2 + 2Dx_iy_i + 2Ex_iz_i + 2Fy_iz_i, \tag{14.11}$$

where

$$\mathbf{H} = \begin{bmatrix} A & D & E \\ D & B & F \\ E & F & C \end{bmatrix}. \tag{14.12}$$

This may be done by solving the equation

$$\begin{bmatrix} \mathrm{MIL}_1 \\ \cdots \\ \mathrm{MIL}_i \\ \cdots \\ \mathrm{MIL}_n \end{bmatrix} = \begin{bmatrix} x_1^2 & y_1^2 & z_1^2 & 2x_1y_1 & 2x_1z_1 & 2y_1z_1 \\ & & & \cdots & & \\ x_i^2 & y_i^2 & z_i^2 & 2x_iy_i & 2x_iz_i & 2y_iz_i \\ & & & \cdots & & \\ x_n^2 & y_n^2 & z_n^2 & 2x_ny_n & 2x_nz_n & 2y_nz_n \end{bmatrix} \begin{bmatrix} A \\ B \\ C \\ D \\ E \\ F \end{bmatrix}, \tag{14.13}$$

with respect to the components of **H** using multiple regression analysis or singular value decomposition.

14.3.1.2 Volume Orientation

The realization that anisotropic structures may not show anisotropy when examined with the MIL method (see Fig. 14.7) led to the development of volume-based anisotropy measures. The first of these measures was the volume orientation (VO) method.[28]

The basic principle of the VO method is to determine the orientation of the longest intercept through randomly sampled points falling within bone; see Fig. 14.8b. This yields a sample of orientations that may be treated by a number of statistical methods.

The *orientation matrix* **V** for the sample of orientations may be thought of as a volume orientation fabric tensor.[29] Let the n orientations be given by directional cosines (x_i, y_i, z_i); then

$$\mathbf{V} = \sum_{i=1}^{n} \begin{Bmatrix} x_i \\ y_i \\ z_i \end{Bmatrix} (x_i \quad y_i \quad z_i) = \begin{bmatrix} \sum x_i^2 & \sum x_iy_i & \sum x_iz_i \\ \sum x_iy_i & \sum y_i^2 & \sum y_iz_i \\ \sum x_iz_i & \sum y_iz_i & \sum z_i^2 \end{bmatrix}. \tag{14.14}$$

A particularly interesting application of the VO principle allows the distinction between horizontal and vertical trabecular volume. By determining the local volume orientations is it possible to determine the fraction pointing for instance within 30° of the vertical direction; see Fig. 14.9.

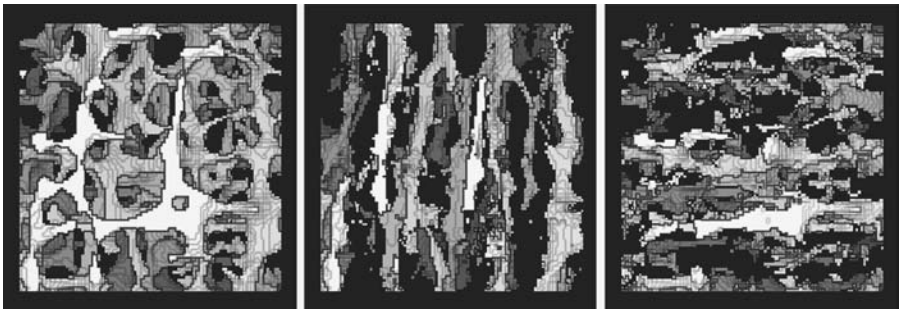

FIGURE 14.9 Volume orientation was determined for every voxel in the specimen on the left. All voxels with a volume orientation less than 30° from vertical are shown in the center, and all voxels with a volume orientation larger than 60° from vertical are shown on the right. This principle provides one method for separating the structure in vertical and horizontal elements.

14.3.1.3 Star Volume Distribution

The star volume distribution (SVD) is conceptually closely related to both VO and star volume (Section 14.2.3). In Eq. 14.4 the average length ℓ is taken over random directions, but instead of this, *a star volume component* $\bar{v}_V^*$ is defined for a single orientation ω as[30]

$$\bar{v}_V^*(\omega) = \frac{\pi}{3}\ell^3(\omega). \tag{14.15}$$

A star volume fabric tensor **S** may be defined as[29]

$$\mathbf{S} = \begin{bmatrix} \sum L_i^2 x_i^2 & \sum L_i^2 x_i y_i & \sum L_i^2 x_i z_i \\ \sum L_i^2 x_i y_i & \sum L_i^2 y_i^2 & \sum L_i^2 y_i z_i \\ \sum L_i^2 x_i z_i & \sum L_i^2 y_i z_i & \sum L_i^2 z_i^2 \end{bmatrix}, \tag{14.16}$$

where L is the star volume component in direction (x_i, y_i, z_i). The summation is done over all directions examined.

14.3.2 Connectivity

In a voxel-based 3D reconstruction, the Euler number χ (see Section 14.2.4) can be determined from the number of voxel corners α_0, voxel edges α_1, voxel faces α_2, and voxel volumes α_3 as

$$\chi = \sum (-1)^i \alpha_i = \alpha_0 - \alpha_1 + \alpha_2 - \alpha_3. \tag{14.17}$$

For a 2D surface $\alpha_3 = 0$ and $\chi = \alpha_0 - \alpha_1 + \alpha_2$. For a 1D line $\alpha_3 = \alpha_2 = 0$ and $\chi = \alpha_0 - \alpha_1$. For a 0D point, χ is 1 if the point is set; otherwise χ is 0. See Fig. 14.10 for further details. It may be tempting simply to use Eq. 14.17—or other measures for simply determining the Euler number—on a 3D reconstruction for determination of the Euler number of the data set, but this will be a biased measure.

When determining connectivity in a cancellous bone specimen that has been cut from a cancellous bone region, one must be aware that connections will be lost and that isolated bone particles may be created in the cutting process (see Fig. 14.1). If, for instance, a vertebral body is divided into halves, the sum of the connectivity of the halves will not equal the connectivity of the entire vertebral body. The consequence is that any determination of connectivity density based simply on the connectivity of a specimen will be a

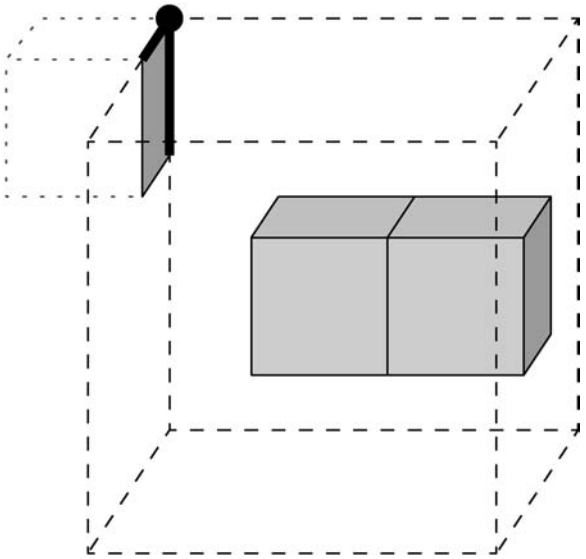

FIGURE 14.10 Volume of interest (VOI) consisting of $3 \times 3 \times 3$ voxels (the coarse dotted line). There are two bone voxels within the VOI, and one is bounded by the VOI surface. When calculating the Euler number for the volume using Eq. 14.17 it is important that voxels bounding the VOI are considered. There are two voxels, 12 faces, 24 edges, and 16 corners within the VOI. Hence, $\chi(V) = 16 - 24 + 12 - 2 = 2$. For unbiasedly calculating the contribution of the VOI to the total Euler number in the region where the VOI is placed, the edge problem must be considered. Four of the six VOI surfaces are nonvoid, and using Eq. 14.17, $\Sigma\chi(F) = (4 - 4 + 1) + (4 - 4 + 1) + (2 - 1 + 0) + (2 - 1 + 0) = 4$. Three of the 12 VOI edges are nonvoid, and $\Sigma\chi(E) = (2 - 1) + (2 - 1) + (1 - 0) = 3$. One VOI corner is set giving $\Sigma\chi(P) = 1$. Using Eq. 14.22, $\Delta\chi = 2 - \frac{4}{2} + \frac{3}{4} - \frac{1}{8} = \frac{5}{8}$.

biased estimate of the connectivity in the region from which the specimen was cut. Whenever artificial surfaces (edges) of a specimen exist, this bias must be controlled. This control is implemented in the disector counting rules used in the ConnEulor principle, but for quantification of connectivity directly from a 3D reconstruction a different approach is possible. This approach allows unbiased estimation of the Euler number density, no matter what the form of the examination volume may be.

The Euler number addition theorem provides means for controlling the effect of cutting a specimen from its surroundings. If a cancellous bone region is cut into two parts A and B, then

$$\chi(A \cup B) = \chi(A) + \chi(B) - \chi(A \cap B), \tag{14.18}$$

where $A \cap B$ is the intersection between the two sets. The equation is valid in any dimension. Fig. 14.11 shows a 2D example of using the addition theorem. To illustrate the use of the addition theorem further, the 2D case will first be described followed by a generalization to 3D reconstructions.

Given a quadratic tessellation of the plane (Fig. 14.12a), it can by use of Eq. 14.18 be shown that

$$\chi(T) = \Sigma\chi(F) - \Sigma\chi(E) + \Sigma\chi(P), \tag{14.19}$$

where the summation is done over all elements in the tessellation, and F is the 2D area of an element of the tessellation, E is a 1D edge, and P is a 0D corner. This is an expression of the so-called kinematic quermass-integral.[31] If the tessellation is changed, so that the individual elements no longer are quadratic (Fig. 14.12a and b), the equation will still be valid. The Euler number contribution of a 2D element of the tessellation to the universal Euler number can be determined by sharing the lower-dimensional (0D and 1D) contributions in Eq. 14.19 equally between the 2D elements. Each 1D element will be shared by two 2D elements, and each 0D element will be shared by four 2D elements. This means that the Euler

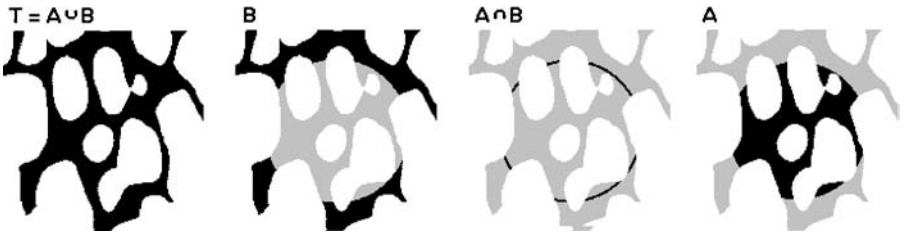

FIGURE 14.11 2D section T through cancellous bone. A circular interface $A \cap B$ separates the examination area A from the exterior B. $\chi(T) = 1 - 4 = -3$, $\chi(B) = 3 - 0 = 3$, $\chi(A) = 2 - 1 = 1$, and $\chi(A \cap B) = 7$; see Eq. 14.5. If the Euler numbers of the examination area A and the exterior B are simply added, one does not get the Euler number of the total specimen T $(1 + 3 \neq -3)$. Only by using the addition theorem, Eq. 14.18, the correct sum is obtained $(-3 = 1 + 3 - 7)$.

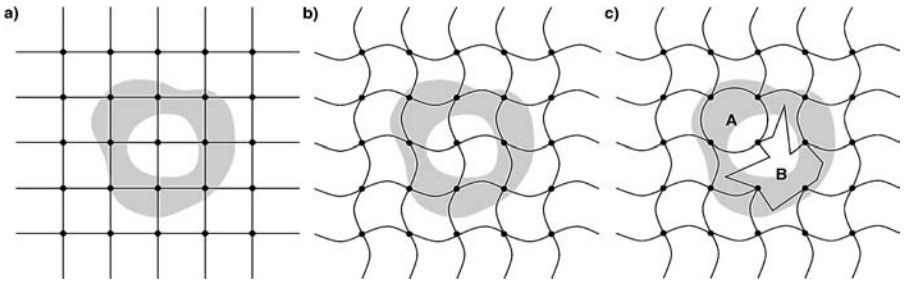

FIGURE 14.12 Tessellations of the plane. The first is a quadratic tessellation. The last is an irregular tessellation, but in spite of this, the Euler number contribution of any 2D element, e.g., A or B, may be determined using Eq. 14.20 or 14.21. In all cases, $\Sigma\Delta\chi = 0$ for the shaded ringlike figure.

number contribution of a 2D region to the universal Euler number is*

$$\Delta\chi = \chi(F) - \frac{1}{2}\sum_{i=1}^{4}\chi(E) + \frac{1}{4}\sum_{i=1}^{4}\chi(P), \tag{14.20}$$

where the sums are taken over all lower-dimensional elements bounding the 2D element (four edges and four points). If the edge of the 2D area is considered as a single continuous edge $E_c = \cup\, E$ instead of four separate edges, it can be shown that the Euler number contribution is

$$\Delta\chi = \chi(F) - \frac{1}{2}\chi(E_c) - \frac{1}{4}\sum_{i=1}^{4}\chi(P). \tag{14.21}$$

*The factors in the equation depend on the tessellation considered. If, for example, a hexagonal tessellation is studied, there are six edges and corners around each 2D element. Each edge is shared by two and each corner is shared by three. This gives the following contribution from each 2D element

$$\Delta\chi = \chi(F) - \frac{1}{2}\sum_{i=1}^{6}\chi(E) + \frac{1}{3}\sum_{i=1}^{6}\chi(P).$$

It should, however, be noted that the value $\Delta\chi$ will not be affected by the choice of the tessellation.

The consequence of the above considerations is that the Euler number contribution $\Delta\chi$ of any 2D examination area can be determined and it also means that $\Delta\chi$ of any 2D profile divided by the area of the profile will provide an unbiased estimate of the Euler number density in the examination area. The latter can be used for a sample-based estimate of connectivity density.

For 3D space, similar deductions can be made. Assuming that each 3D region is cubic and has 6 faces, 12 edges, and 8 corners, the direct equivalent of Eq. 14.20 is

$$\Delta\chi = \chi(V) - \frac{1}{2}\sum_{i=1}^{6}\chi(F) + \frac{1}{4}\sum_{i=1}^{12}\chi(E) - \frac{1}{8}\sum_{i=1}^{8}\chi(P), \tag{14.22}$$

where V is the examination volume, and the sums are taken over 6 faces, 12 edges, and 8 corner points.* See Fig. 14.10 for an example. For a 3D examination volume, the 12 edges may be placed arbitrarily, thereby defining 6 faces and 8 points.

The Euler number contribution of a rectangular parallelepiped specimen may directly be determined using Eq. 14.22, where $\chi(\star)$ ($\star$ may be replaced by V for specimen volume, F for specimen face, E for specimen edge, and P for specimen corner point) is determined by using Eq. 14.17. Often, nonparallelepiped specimen geometries may be at hand, e.g., a cylindrical specimen. By realizing that Eq. 14.22 is also valid for a single voxel, the Euler number contribution of any specimen geometry may be determined, by adding $\Delta\chi$ for all voxels in the examination volume.

By now, it has been shown how the Euler number contribution of a specimen to the Euler number in the region from which the specimen was taken can be determined. As cancellous bone 3D reconstructions will usually have been purified, so that $\chi = 1 - \beta_0$, (see Eq. 14.7), the Euler number is numerically identical to the connectivity contribution $\Delta\beta_1$ of the specimen to the total connectivity in the region from which the specimen was taken (the 1-contribution in Eq. 14.7 is neglected, as the specimen is usually much smaller than the parent bone region):

$$\Delta\beta_1 \approx -\Delta\chi. \tag{14.23}$$

The connectivity density β_{1V} is obtained by dividing by the examination volume V

$$\beta_{1V} = \frac{\Delta\beta_1}{V}. \tag{14.24}$$

If the 3D reconstruction has not been purified, β_0 and β_2 may be determined independently in the 3D data set and a modified version of Eq. 14.23 should be used.

14.3.3 Trabecular Dimensions

Trabecular dimensions have been approached by a number of qualitative and/or biased methods. The plate model-derived parameter MTPT (mean trabecular plate thickness) is an example of a thickness parameter, see Section 14.4.1. The main problem in measuring trabecular dimensions is in defining what should be measured.

Knowing the number of redundant connections from Eq. 14.23, i.e., the connectivity, the mean trabecular volume (MTV) is

$$\mathrm{MTV} = \frac{V_V(\mathrm{bone})}{\beta_{1V}} \tag{14.25}$$

where V_V (bone) is the bone volume fraction in the examination volume.

*As mentioned in the previous footnote the factors in Eq. 14.22 depend on the tessellation studied, but $\Delta\chi$ will not be affected.

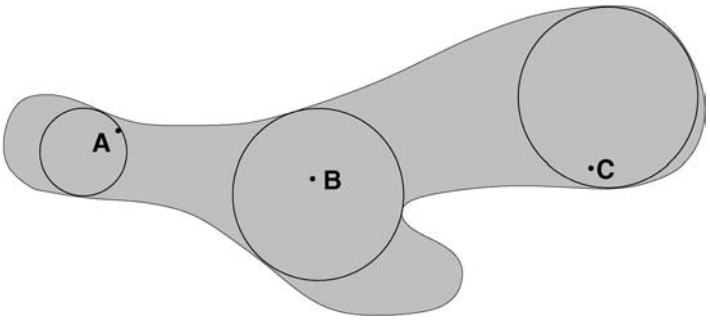

FIGURE 14.13 2D examples of local thickness. The thickness at a point is defined as the diameter of the largest enclosing circle within the structure. The thickness at the points A, B, and C is defined by the diameter of the shown circles. For 3D structures, the thickness at any point is defined as the diameter of the maximal enclosing sphere.[32]

Hildebrand and Rüegsegger[32] have suggested a rigorous and model-free definition of trabecular thickness. The thickness for a structure is defined locally for every point within the structure as the diameter of the maximal sphere fully within the structure and enclosing the point. A mean or global thickness is obtained by averaging over the volume of the structure. A general example of a local thickness is shown in Fig. 14.13. For simple geometric structures like plates, cylinders, and spheres, the definition results in correct values, i.e., plate thickness, cylinder diameter, and sphere diameter. For more complex structure, e.g., trabeculae, the definition results in a well-defined weighting of a mean value, and it is possible to study the distribution of local thickness.

14.3.4 Other Measures

A Structure Model Index has been proposed by Hildebrand and Rüegsegger for quantification of whether the structure is platelike or rodlike.[33] Fractal properties have been proposed by different groups, but consensus on the use of fractals has not yet been found.[34–36]

14.4 Traditional Histomorphometry

Traditional histomorphometry presents architectural parameters and methods for determining these. For a full description of these methods, the reader is referred to other sources.[37,38] Generally speaking, traditional histomorphometry can be divided into *dynamic* and *static* measures. The former group falls outside the scope of this chapter. The static methods can be divided into *stereologically founded measures* and *model-based measures*. The first group has already been discussed.* The model-based methods are aimed at determining properties of the trabecular architecture that are assumed to be related to mechanical properties. These measures are to some extent from a period when only 2-D examination of cancellous bone was possible, but because of their frequent use in present-day publications, they will be discussed in some detail.

14.4.1 The Plate Model

Assume that all trabecular bone is organized in infinite parallel plates with thickness MTPT and MTPS (mean trabecular plate separation) apart (see Fig. 14.14), and assume that the volume fraction V_V has been determined using Eq. 14.2 and that the surface density has been determined using Eq. 14.3; then

*Traditional histomorphometry uses the symbol BV/TV for V_V and BS/TV for S_V.[39] In this notation, BV means "bone volume," TV means "tissue volume," and BS means "bone surface." it also specifies BS/BV, which equals S_V/V_V. Measurements are performed as indicated in Section 14.2.

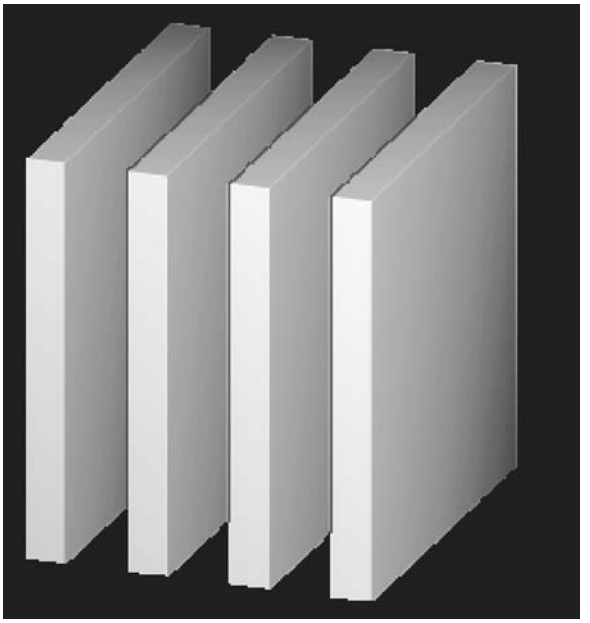

FIGURE 14.14 The plate model assumes that all trabecular material is contained in infinite parallel plates with thickness MTPT and separation MTPS.

the following relations hold:

$$V_V = \frac{MTPT}{MTPS + MTPT}, \tag{14.26}$$

$$S_V = \frac{2}{MTPS + MTPT}, \tag{14.27}$$

$$MTPD = \frac{1}{MTPS + MTPT}, \tag{14.28}$$

where MTPD (mean trabecular plate density) is the number of plates traversed by a line of unit length perpendicular to the plates.*

The Eqs. 14.26 to 14.28 may be rearranged into

$$MTPT = \frac{2 - 2V_V}{S_V}, \tag{14.29}$$

$$MTPS = \frac{2V_V}{S_V}, \tag{14.30}$$

$$MTPD = \frac{S_V}{2}. \tag{14.31}$$

*In 1988, a decision was made to change the bone histomorphometry nomenclature.[39] The parameters MTPT, MTPS, and MTPD were renamed Tb.Th (trabecular thickness), Tb.Sp (trabecular spacing), and Tb.N (trabecular number), respectively. This nomenclature is particularly unfortunate, as it does not imply any model assumptions, and this nomenclature will not be used further in this chapter.

These expressions of mean trabecular plate thickness, separation and density have been used extensively in the literature as surrogate measures of trabecular thickness, spacing, and connectivity, respectively. It should be emphasised that the above equations are valid *only* under assumption of a plate model and that S_V is correctly determined. If S_V is not based on isotropic random lines, then the measure will be biased, and the results will also be biased to an unknown degree if all trabecular bone is not organized in parallel plates. The surrogate measure of connectivity, MTPD, has units of length^{-1}, which is meaningless for a measure of connectivity. Observations by Kinney et al.[40,41] have emphasized the problem in using the plate model-derived parameter—and the problem in reviewers requiring biased methods for journal publication. Another observation by Boyce et al.[10] has demonstrated that MTPD is not related to connectivity.

The problem with the model-based approach is that if the model is not valid, any parameter extracted from the model will be biased to an unknown extent. In particular, in situations where one population is to be compared with another population, any change that would remove the structure further from the model assumptions will make observed changes impossible to interpret.

14.5 Ad Hoc Methods

14.5.1 Trabecular Thickness

Direct measurement of trabecular thickness in 2D sections has been attempted by different authors.[42,43] Generally, trabecular thickness in a 3D sense can only be determined from perimeter and area measurements in 2D sections, when a structural model is assumed, e.g., the plate model described in Section 14.4.1, and if the structure is anisotropic the 2D sections must be isotropically positioned. Attempts at determining thickness of individual trabecular populations, e.g., horizontal or vertical trabeculae, by fixing the plane orientations may seem tempting, but will provide biased measures. The only way to get unbiased, model-free thickness measures of trabeculae or of trabecular subpopulations is to perform the measurements in 3D reconstructions.

14.5.2 Connectivity

Different 2D measures have explicitly been linked to 3D connectivity, but none of these measures has any known relation to 3D connectivity, as it can be shown that determination of 3D connectivity requires 3D information.[12] These measures typically depend on the orientation of the 2D section,[44] which can be considered a demonstration of the fact that they cannot be measures of connectivity. Some of these methods have been defended by stating that the measure is a 2D measure only, but one can then question the relevance of the measure for bone mechanics. In experimental settings, the measures may show significant differences between different populations, but the significance of this remains unclear.

A trabecular bone pattern factor (TBPf) has been suggested as an indirect measure of the relative amount of convex and concave trabecular surfaces on 2D sections.[45] First the trabecular bone area (A1) and perimeter (P1) are measured in a reference region. After a dilatation of the bone phase using image processing, a second measurement of these two parameters (now A2 and P2) is done. The TBPf is defined as a quotient of the difference of the first and the second measurement: $\text{TBPf} = (P1 - P2)/(A1 - A2)$. The TBPf has been used as a direct equivalent to connectivity, but an analysis of simple structures easily shows that TBPf has no relation to connectivity.[25] The unit of length^{-1} further shows that TBPf cannot be a measure of connectivity.

By digitally skeletonizing a 2D section through cancellous bone, one obtains a node-and-strut network. Neglecting the influence of the skeletonization algorithm upon the resulting skeleton, the skeleton will represent the 2D topology of the section. As mentioned above, this has no relation to 3D connectivity, but has nevertheless been interpreted as such. A series of parameters has been determined from 2D node-and-strut networks.[46,47] These include node number (N.Nd), terminus number (N.Tm), node to node (Nd.Nd), node to terminus (Nd.Tm), terminus to terminus (Tm.Tm), cortex to terminus, and node-to-loop strut lengths, total strut length (TSL), and the node-to-terminus ratio (N.Nd/N.Tm).

14.6 Concluding Remarks

The field of bone morphometry is rapidly evolving because of the availability of 3D reconstruction. Some of the methods mentioned in this chapter may be only little used in the future, and other methods may have shown their value after this chapter was written.

The properties of trabecular bone vary depending on the composition. Osteoid and fully mineralized bone may be considered extremes of composition. There has so far not been much interest in combining information on cancellous bone architecture with its composition. One might consider studying the anisotropy of the osteoid phase compared with the mineralized phase, and studies along these lines will probably be seen in the years to come.

A final word of warning might be appropriate at this point. The huge amounts of information that can be accumulated with modern methods for 3D reconstruction can easily lead to numerous methods for quantifying the cancellous bone architecture. It is therefore important that the objectives of cancellous bone research are kept clear, and that the architectural studies are not done without an aim. Studying the fascinating architecture of cancellous bone and developing new methods for its quantification can be fun and challenging, but it should fundamentally aim at a precise understanding of the mechanics and biology of cancellous bone.

References

1. Wolff, J., Ueber die innere Architectur der Knochen und ihre Bedeutung für dir Frage vom Knochenwachstum, *Virchows Arch. Pathol. Anat. Physiol. Klin. Med.,* 50, 389, 1870.
2. Parfitt, A.M., Trabecular bone architecture in the pathogenesis and prevention of fracture, *Am. J. Med.,* 82, 68, 1987.
3. Gundersen, H.J., The nucleator, *J. Microsc.,* 151, 3, 1988.
4. Underwood, E.E., *Quantitative Stereology,* Addison-Wesley, Reading, MA, 1970.
5. Weibel, E.R., *Stereological Methods,* Vol. 2: *Theoretical Foundations,* Academic Press, New York, 1980.
6. Baddeley, A.J., Gundersen, H.J., and Cruz-Orive, L.M., Estimation of surface area from vertical sections, *J. Microsc.,* 142, 259, 1986.
7. Vesterby, A., Kragstrup, J., Gundersen, H.J., and Melsen, F., Unbiased stereologic estimation of surface density in bone using vertical sections, *Bone,* 8, 13, 1987.
8. Gundersen, H.J. and Jensen, E.B., Stereological estimation of the volume-weighted mean volume of arbitrary particles observed on random sections, *J. Microsc.,* 138, 127, 1985.
9. Vesterby, A., Gundersen, H.J., and Melsen, F., Star volume of marrow space and trabeculae of the first lumbar vertebra: sampling efficiency and biological variation, *Bone,* 10, 7, 1989.
10. Boyce, R.W., Ebert, D.C., Youngs, T.A., Paddock, C.L., Mosekilde, L., Stevens, M.L., and Gundersen, H.J., Unbiased estimation of vertebral trabecular connectivity in calcium-restricted ovariectomized minipigs, *Bone,* 16, 637, 1995.
11. Odgaard, A. and Gundersen, H.J., Quantification of connectivity in cancellous bone, with special emphasis on 3-D reconstructions, *Bone,* 14, 173, 1993.
12. Gundersen, H.J., Boyce, R.W., Nyengaard, J.R., and Odgaard, A., The Conneulor: unbiased estimation of connectivity using physical disectors under projection, *Bone,* 14, 217, 1993.
13. Sterio, D.C., The unbiased estimation of number and sizes of arbitrary particles using the disector, *J. Microsc.,* 134, 127, 1984.
14. Amstutz, H.C. and Sissons, H.A., The structure of the vertebral spongiosa, *J. Bone Joint Surg.,* 51-B, 540, 1969.
15. Odgaard, A., Andersen, K., Ullerup, R., Frich, L.H., and Melsen, F., Three-dimensional reconstruction of entire vertebral bodies, *Bone,* 15, 335, 1994.
16. Feldkamp, L.A., Goldstein, S.A., Parfitt, A.M., Jesion, G., and Kleerekoper, M., The direct examination of three-dimensional bone architecture in vitro by computed tomography, *J. Bone Miner. Res.,* 4, 3, 1989.

17. Ruegsegger, P., Koller, B., and Müller, R., A microtomographic system for the nondestructive evaluation of bone architecture, *Calcif. Tissue Int.,* 58, 24, 1996.
18. Bonse, U., Busch, F., Gunnewig, O., Beckmann, F., Pahl, R., Delling, G., Hahn, M., and Graeff, W., 3d computed X-ray tomography of human cancellous bone at 8 microns spatial and $10^{(-4)}$ energy resolution, *Bone Miner.,* 25, 25, 1994.
19. Kinney, J.H. and Nichols, M.C., X-ray tomographic microscopy (XTM) using synchrotron radiation, *Annu. Rev. Mater. Sci.,* 22, 121, 1992.
20. Chung, H.W., Wehrli, F.W., Williams, J.L., and Wehrli, S.L., Three-dimensional nuclear magnetic resonance microimaging of trabecular bone, *J. Bone Miner. Res.,* 10, 1452, 1995.
21. Majumdar, S., Newitt, D., Mathur, A., Osman, D., Gies, A., Chiu, E., Lotz, J., Kinney, J., and Genant, H., Magnetic resonance imaging of trabecular bone structure in the distal radius: relationship with X-ray tomographic microscopy and biomechanics, *Osteoporosis Int.,* 6, 376, 1996.
22. Cowin, S.C., The relationship between the elasticity tensor and the fabric tensor, *Mech. Mater.,* 4, 137, 1985.
23. Cowin, S.C., Wolff's law of trabecular architecture at remodeling equilibrium, *J. Biomech. Eng.,* 108, 83, 1986.
24. Whitehouse, W.J., The quantitative morphology of anisotropic trabecular bone, *J. Microsc.,* 101, 153, 1974.
25. Odgaard, A., Three-dimensional methods for quantification of cancellous bone architecture, *Bone,* 20, 315, 1997.
26. Whitehouse, W.J., Irregularities and asymmetries in trabecular bone in the innominate and elsewhere, in *Bone Histomorphometry, Third International Workshop,* Jee, W.S.S. and Parfitt, A.M., Eds., Societe Nouvelle de Publications Medicales et Dentaires, Paris, 1981, 271.
27. Harrigan, T.P. and Mann, R.W., Characterization of microstructural anisotropy in orthotropic materials using a second rank tensor, *J. Mater. Sci.,* 19, 761, 1984.
28. Odgaard, A., Jensen, E.B., and Gundersen, H.J., Estimation of structural anisotropy based on volume orientation. A new concept, *J. Microsc.,* 157, 149, 1990.
29. Odgaard, A., Kabel, J., van Rietbergen, B., Dalstra, M., and Huiskes, R., Fabric and elastic principal directions of cancellous bone are closely related, *J. Biomech.,* 30, 487, 1997.
30. Cruz-Orive, L.M., Karlsson, L.M., Larsen, S.E., and Wainschtein, F., Characterizing anisotropy: a new concept, *Micron Microsc. Acta,* 23, 75, 1992.
31. Santaló, L.A., *Integral Geometry and Geometric Probability,* Addison-Wesley, Reading, MA, 1976.
32. Hildebrand, T. and Rüegsegger, P., A new method for the model-independent assessment of thickness in three-dimensional images, *J. Microsc.,* 185, 67, 1997.
33. Hildebrand, T. and Rüegsegger, P., Quantification of bone architecture with the structure model index, *Comp. Methods Biomech. Biomed. Eng.,* 1, 15, 1997.
34. Chung, H.W., Chu, C.C., Underweiser, M., and Wehrli, F.W., On the fractal nature of trabecular structure, *Med. Phys.,* 21, 1535, 1994.
35. Cross, S.S., Rogers, S., Silcocks, P.B., and Cotton, D.W., Trabecular bone does not have a fractal structure on light microscopic examination, *J. Pathol.,* 170, 311, 1993.
36. Weinstein, R.S. and Majumdar, S., Fractal geometry and vertebral compression fractures, *J. Bone Miner. Res.,* 9, 1797, 1994.
37. Parfitt, A.M., Drezner, M.K., Glorieux, F.H., Kanis, J.A., Malluche, H., Meunier, P.J., Ott, S.M., and Recker, R.R., Bone histomorphometry: standardization of nomenclature, symbols, and units. Report of the ASBMR Histomorphometry Nomenclature Committee, *J. Bone Miner. Res.,* 2, 595, 1987.
38. Eriksen, E.F., *Bone Histomorphometry,* Lippincott/William & Wilkins, Baltimore, MD, 1993.
39. Parfitt, A.M., Bone histomorphometry: proposed system for standardization of nomenclature, symbols, and units, *Calcif. Tissue Int.,* 42, 284, 1988.
40. Kinney, J.H., Nichols, M.C., Lane, N.E., Majumdar, S., Marshall, G.W., and Marshall, S.J., In vivo, three-dimensional histomorphometry: new perspectives of sequential changes in bone structure, in *Trans. ORS,* 19, 1994, 56.

41. Kinney, J.H., Lane, N.E., and Haupt, D.L., In vivo, three-dimensional microscopy of trabecular bone, *J. Bone Miner. Res.,* 10, 264, 1995.
42. Bergot, C., Laval-Jeantet, A.M., Preteux, F., and Meunier, A., Measurement of anisotropic vertebral trabecular bone loss during aging by quantitative image analysis, *Calcif. Tissue Int.,* 43, 143, 1988.
43. Mosekilde, L., Age-related changes in vertebral trabecular bone architecture—assessed by a new method, *Bone,* 9, 247, 1988.
44. Amling, M., Herden, S., Posl, M., Hahn, M., Ritzel, H., and Delling, G., Heterogeneity of the skeleton: comparison of the trabecular microarchitecture of the spine, the iliac crest, the femur, and the calcaneus, *J. Bone Miner. Res.,* 11, 36, 1996.
45. Hahn, M., Vogel, M., Pompesius-Kempa, M., and Delling, G., Trabecular bone pattern factor—a new parameter for simple quantification of bone microarchitecture, *Bone,* 13, 327, 1992.
46. Garrahan, N.J., Mellish, R.W., and Compston, J.E., A new method for the two-dimensional analysis of bone structure in human iliac crest biopsies, *J. Microsc.,* 142, 341, 1986.
47. Parisien, M., Mellish, R.W., Silverberg, S.J., Shane, E., Lindsay, R., Bilezikian, J.P., and Dempster, D.W., Maintenance of cancellous bone connectivity in primary hyperparathyroidism: trabecular strut analysis, *J. Bone Miner. Res.,* 7, 913, 1992.
48. Boyce, R.W., Wronski, T.J., Ebert, D.C., Stevens, M.L., Paddock, C.L., Youngs, T.A., and Gundersen, H.J., Direct stereological estimation of three-dimensional connectivity in rat vertebrae: effect of estrogen, etidronate and risedronate following ovariectomy, *Bone,* 16, 209, 1995.
49. Thomsen, J.S., Ebbesen, E.N., and Mosekilde, L., Relationships between static histomorphometry and bone strength measurements in human iliac crest bone biopsies, *Bone,* 22, 153, 1998.

15

Elastic Constants of Cancellous Bone

Bert van Rietbergen
Eindhoven University of Technology

Rik Huiskes
Eindhoven University of Technology

15.1 Introduction

Cancellous bone is a porous type of tissue mainly found near the ends of long bones and in vertebral bodies. In long bones, it distributes the mechanical loads from the articular surfaces to the cortical shaft, whereas in vertebral bodies it is the main load-carrying constituent. Bone fractures due to conditions such as osteoporosis usually occur in cancellous bone regions. Diseases in the skeleton, such as osteoarthritis, might be related to the mechanical properties of the subchondral bone under the affected cartilage and that of the cancellous bone supporting it. Hence, the mechanical quality of cancellous bone is an important parameter for bone fracture risk and integrity.

Although cancellous bone strength is the most relevant parameter for bone fracture risk, the elastic properties determine its mechanical behavior during normal daily activities. During such activities, strains in bone usually do not exceed 3000 $\mu\varepsilon$, and experiments have shown that its constitutive behavior can be considered as linear in this range. Elastic properties determine how the loads are introduced from the joints to the subchondral bone and distributed through the bone at large. Cancellous bone elastic properties also affect bone fracture risk, since they determine the local loading conditions in fracture regions at the onset of cancellous bone failure. Finally, elastic properties are correlated with strength, so

0-8493-9117-2/01/$0.00+$.50

their values can be used to estimate fracture risk. Hence, elastic properties are important for the mechanical integrity of cancellous bone.

This chapter describes the elastic behavior of cancellous bone and how this relates to its structure. In the first sections, the elastic constants needed to characterize this behavior are discussed, as well as traditional and new methods for their determination. Based on elastic constants available for large sets of cancellous bone specimens, it is discussed in the following sections which elastic model best describes the behavior of cancellous bone and what the role of the bone structure is for its anisotropic behavior. In the last sections, it is discussed which stochastic models exist to assess cancellous bone elastic constants from measurements of its internal structure and how cancellous bone elastic constants depend on the bone tissue properties.

15.2 Cancellous Bone Structural Characterization

Cancellous bone is a highly porous material. It has a very complex internal structure, built of struts and plates, the trabeculae, which form the actual load-carrying constituent. The trabeculae are built of hydroxyapetite crystals, embedded in a collagen-fiber matrix, thus creating a stiff but also ductile material (see Chapters 5, 10, 13, and 14 for a discussion on trabecular tissue composition and material properties). The mechanical properties of the bone matrix are the first determinant for the mechanical behavior of cancellous bone. Based on measurements on bone specimens, it was concluded that the bone marrow in the pores does not significantly contribute to the stiffness of cancellous bone at normal strain rates ($\sim$1 Hz).[1,2]

The trabecular structure (or architecture) of cancellous bone is the second important factor for cancellous bone mechanical properties. The structure can resemble very different shapes such as open or closed cell structures, strutlike, platelike, or honeycomb-like architectures. In all cases, however, the average trabecular thickness or plate thickness is more or less the same (150 to 200 μm).[3] In some of these structures the trabeculae can have a very pronounced preferred orientation (e.g., strutlike and honeycomb structures); in other structures, however, such a preferred trabecular orientation is hard to recognize (e.g., open or closed spherical cells). The presence of a preferred trabecular orientation is of particular importance for the mechanical anisotropy of cancellous bone.

A large number of parameters have been suggested to characterize cancellous bone architectural morphology (see Chapter 13 for an overview). The most important of those is the bone volume fraction, which is the volume of bone tissue per unit of volume and is dimensionless. A similar scalar quality is the total mass per unit volume of bone, which is called the structural density or apparent density and which measures the degree of mineralization as well (dimensions: $kg \cdot m^{-3}$). Since the bone volume fraction does not provide any information about the actual structure of the bone (other than its density), other parameters have been developed. Among these are scalar parameters that quantify the average geometry of the trabeculae (e.g., mean trabecular thickness and spacing), the connectivity, and the fractal dimension of the trabecular network. To quantify the directionality and the anisotropy of the structure, tensor parameters have been introduced. The one most commonly used is the mean intercept length (MIL). In MIL measurements, a grid of parallel lines is projected over a cross-sectional image of the bone structure. The number of bone–marrow interfaces are then counted for a large number of grid angles. When representing the number of bone–marrow interfaces in a polar plot, an ellipse-shaped figure results (an ellipsoid in three dimensions, 3D), with its largest principal axis indicating the principal or axial direction of the material (Fig. 15.1). The ratio between the lengths of the principal axes is an indication of the anisotropy of the structure. It should be emphasized, however, that no unique definition exists for the structural anisotropy of bone; other tensor measures have been developed as well (see Chapter 13).

15.3 Cancellous Bone Mechanical Characterization

The mechanical behavior of cancellous bone is best described as viscoelastic. The elastic part of this behavior is demonstrated by the ability of trabecular bone to recover its initial geometry fully after release of an applied load that did not exceed the elastic limit. The viscous part is responsible for the dependency of stiffness on strain rate,[1,4] the ability to dissipate energy within the elastic range of deformation,[5,6] and

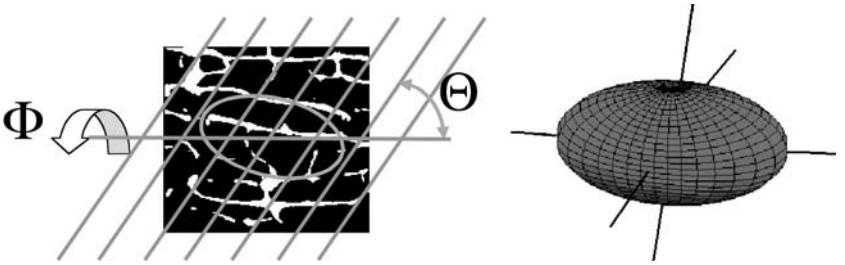

(a) (b)

FIGURE 15.1 (a) The average orientation of trabeculae in three dimensions can be obtained from, for example, MIL measurements. With these measurements, the number of bone–marrow interfaces are counted along a large number of parallel lines through the specimen for a large number of different angles Φ and **Θ**. (b) When plotting the number of bone–marrow interfaces per total line length in a 3D polar plot, the measurement points can be well fitted to the surface of an ellipsoid. The ellipsoid can be expressed as a second-rank fabric tensor. The eigendirections of this tensor indicate the principal directions of the trabecular structure. The ratios between the three eigenvalues are an indication of the structural anisotropy of the bone.

for phenomena such as stress relaxation and creep behavior of cancellous bone.[7] The viscous part can be due both to the viscous properties of the tissue material and to the marrow in the pores. The hydraulic stiffening effects on the mechanical properties due to the marrow in the pores, however, were found to be minor, except for high strain rates.[1,8] The viscoelastic properties of the trabecular tissue have been established and were found to be similar to those of cortical bone.[8] It has also been demonstrated that the creep behavior of trabecular bone is similar to that of cortical bone.[9] Although the mechanical properties such as modulus and strength are thus dependent on strain rate, the dependency is very weak. Both strength and modulus are approximately proportional to the strain rate raised to the 0.06 power.[1,4] Consequently, for strain rates as they occur during normal activities (~1 Hz), cancellous bone can be well described as an elastic material.

Cancellous bone elastic properties are defined at the continuum level, also referred to as the apparent level. At this level the bone is considered to be a continuous material with material properties that represent the average properties of a representative bone volume. Such a representative volume must hold a large number of trabeculae to provide sufficiently averaged continuum quantities. For cancellous bone a representative volume should be at least five intertrabecular lengths in size (approximately 3 to 5 mm).[10] It is not possible to define meaningful elastic properties for cancellous bone specimens smaller than this minimum size.

The apparent elastic modulus of cancellous bone can vary over a wide range (roughly speaking from 0.1 to 2000 MPa) and is dependent on the direction in which the bone is loaded. The latter demonstrates the anisotropic behavior of cancellous bone. Several models exist to describe anisotropic behavior of materials.[11–13] These models differ in the number of elastic symmetries that can be identified. For cancellous bone, it is generally assumed that at least three orthogonal planes of elastic symmetry exist (orthotropic elastic behavior). In some cases, however, cancellous bone can be described as transversely isotropic (every plane through a longitudinal axis is a plane of symmetry) or isotropic (every plane is a plane of symmetry). In this section, the elastic constants needed to characterize these elastic models for cancellous bone will be discussed.

15.3.1 Elastic Constants and Restrictions

Elastic properties of continua are fully described by the components S_{ijkl} of the fourth-rank stiffness tensor **S** or by the components C_{ijkl} of its inverse, the compliance tensor **C**, in the generalized Hooke's law

$$\sigma_{ij} = S_{ijkl}\varepsilon_{kl}, \qquad \varepsilon_{ij} = C_{ijkl}\sigma_{kl}, \mathbf{S} = \mathbf{C}^{-1}, \tag{15.1}$$

with σ_{ij} the components of the stress tensor and ε_{ij} those of the strain tensor. The stiffness and compliance tensors are usually represented by symmetric six-by-six matrices, S and C, respectively. In its most general form, these matrices hold 21 independent components that must be determined from experiments (Fig. 15.2a). If planes of elastic symmetry exist in the material, some of these coefficients are interdependent or zero when measured in a coordinate system aligned with the normals to the symmetry planes.[11–13] In the case of orthotropy, with three orthogonal planes of elastic symmetry, nine independent elastic coefficients remain to be determined. Fig. 15.2b shows the orthotropic compliance matrix in terms of the commonly used engineering constants: the Young's moduli E_i, the Poisson's ratios ν_{ij} and the shear moduli G_{ij}. Because of the thermodynamic restriction that the work done on an elastic material must be positive, the stiffness and compliance matrix must be positive definite and symmetric.[14] For the compliance matrix of an orthotropic elastic material, the necessary and sufficient conditions for this have been shown by Lempriere[15] and Cowin and van Buskirk:[16]

$$E_1, E_2, E_3, G_{23}, G_{31}, G_{12} > 0, \tag{15.2}$$

$$\begin{gathered}(1 - \nu_{23}\nu_{32}) > 0, \qquad (1 - \nu_{13}\nu_{31}) > 0, \qquad (1 - \nu_{12}\nu_{21}) > 0, \\ 1 - \nu_{12}\nu_{21} - \nu_{23}\nu_{32} - \nu_{31}\nu_{13} - 2\nu_{21}\nu_{32}\nu_{13} > 0,\end{gathered} \tag{15.3}$$

and

$$\frac{\nu_{12}}{E_1} = \frac{\nu_{21}}{E_2}, \qquad \frac{\nu_{13}}{E_1} = \frac{\nu_{31}}{E_3}, \qquad \frac{\nu_{23}}{E_2} = \frac{\nu_{32}}{E_3}. \tag{15.4}$$

As a result of these restrictions, the following inequalities must be satisfied by the engineering elastic constants:[15–17]

$$|\nu_{21}| < \sqrt{\frac{E_2}{E_1}}, \qquad |\nu_{12}| < \sqrt{\frac{E_1}{E_2}}, \qquad |\nu_{32}| < \sqrt{\frac{E_3}{E_2}}, \qquad |\nu_{23}| < \sqrt{\frac{E_2}{E_3}}, \qquad |\nu_{13}| < \sqrt{\frac{E_1}{E_3}}, \qquad |\nu_{31}| < \sqrt{\frac{E_3}{E_1}}, \tag{15.5}$$

and

$$\nu_{21}\nu_{32}\nu_{13} < \frac{1 - \nu_{21}^2\left(\frac{E_1}{E_2}\right) - \nu_{32}^2\left(\frac{E_2}{E_3}\right) - \nu_{13}^2\left(\frac{E_3}{E_1}\right)}{2} < \frac{1}{2}. \tag{15.6}$$

The number of independent engineering constants is reduced further to five for the case of transverse isotropy when each plane through a longitudinal axis is a plane of elastic symmetry. In the case when the 1–2 plane is perpendicular to the longitudinal axis, the compliance matrix takes the form of Fig. 15.2c. In this situation, the restrictions of Eq. 15.5 and 15.6 reduce to

$$-1 < \nu_{12} < 1, \qquad -\sqrt{\frac{E_3}{E_1}} < \nu_{31} < \sqrt{\frac{E_3}{E_1}}, \tag{15.7}$$

$$\nu_{12} < 1 - 2\nu_{31}^2\sqrt{\frac{E_1}{E_3}}. \tag{15.8}$$

$$C = \begin{bmatrix} c_{11} & c_{12} & c_{13} & c_{14} & c_{15} & c_{16} \\ c_{12} & c_{22} & c_{23} & c_{24} & c_{25} & c_{26} \\ c_{13} & c_{23} & c_{33} & c_{34} & c_{35} & c_{36} \\ c_{14} & c_{24} & c_{34} & c_{44} & c_{45} & c_{46} \\ c_{15} & c_{25} & c_{35} & c_{45} & c_{55} & c_{56} \\ c_{16} & c_{26} & c_{36} & c_{46} & c_{56} & c_{66} \end{bmatrix}$$

(a) Anisotropic

$$C = \begin{bmatrix} \frac{1}{E_1} & \frac{-\nu_{21}}{E_2} & \frac{-\nu_{31}}{E_3} & 0 & 0 & 0 \\ \frac{-\nu_{12}}{E_1} & \frac{1}{E_2} & \frac{-\nu_{32}}{E_3} & 0 & 0 & 0 \\ \frac{-\nu_{13}}{E_1} & \frac{-\nu_{23}}{E_2} & \frac{1}{E_3} & 0 & 0 & 0 \\ 0 & 0 & 0 & \frac{1}{G_{23}} & 0 & 0 \\ 0 & 0 & 0 & 0 & \frac{1}{G_{31}} & 0 \\ 0 & 0 & 0 & 0 & 0 & \frac{1}{G_{12}} \end{bmatrix}$$

(b) Orthotropic

$$C = \begin{bmatrix} \frac{1}{E_1} & \frac{-\nu_{21}}{E_1} & \frac{-\nu_{31}}{E_3} & 0 & 0 & 0 \\ \frac{-\nu_{21}}{E_1} & \frac{1}{E_1} & \frac{-\nu_{31}}{E_3} & 0 & 0 & 0 \\ \frac{-\nu_{23}}{E_1} & \frac{-\nu_{23}}{E_1} & \frac{1}{E_3} & 0 & 0 & 0 \\ 0 & 0 & 0 & \frac{1}{G_{23}} & 0 & 0 \\ 0 & 0 & 0 & 0 & \frac{1}{G_{23}} & 0 \\ 0 & 0 & 0 & 0 & 0 & \frac{2+2\nu_{12}}{E_1} \end{bmatrix}$$

(c) Transversely isotropic

$$C = \begin{bmatrix} \frac{1}{E} & \frac{-\nu}{E} & \frac{-\nu}{E} & 0 & 0 & 0 \\ \frac{-\nu}{E} & \frac{1}{E} & \frac{-\nu}{E} & 0 & 0 & 0 \\ \frac{-\nu}{E} & \frac{-\nu}{E} & \frac{1}{E} & 0 & 0 & 0 \\ 0 & 0 & 0 & \frac{2+2\nu}{E} & 0 & 0 \\ 0 & 0 & 0 & 0 & \frac{2+2\nu}{E} & 0 \\ 0 & 0 & 0 & 0 & 0 & \frac{2+2\nu}{E} \end{bmatrix}$$

(d) Isotropic

FIGURE 15.2 (a) In its most general form the compliance matrix holds 21 different elastic coefficients. In the case of orthotropy, with three orthogonal planes of elastic symmetry, nine independent elastic coefficients remain as a result of thermodynamic restrictions (Eqs. 15.2 to 15.6). This becomes apparent when the matrix is expressed in a coordinate system that is aligned with the symmetry planes, in which case the matrix takes the form (b). For the case of transverse isotropy, when each plane through a longitudinal axis is a plane of elastic symmetry, the number of independent engineering constants is reduced further to five because of more stringent thermodynamic restrictions (Eqs. 15.7 and 15.8). In this case, the matrix takes the form of (c) for a coordinate system in which the third axis is aligned with the longitudinal axis. For isotropic materials two elastic coefficients remain and the matrix is of the form (d) for any coordinate system.

In the case of isotropy only two independent engineering constants remain (Fig. 15.2d) and the restriction 15.5 and 15.6 reduce to

$$-1 < \nu < 0.5. \tag{15.9}$$

It should be emphasized that even for perfectly orthotropic materials, the typical forms of the compliance matrices shown in Fig. 15.2 are only obtained if the measurement coordinate system coincides with the symmetry coordinate system. If this is not the case, the matrix will take the general form of Fig. 15.2a and the mechanical symmetries are not immediately apparent. For perfectly orthotropic materials, however, a coordinate transformation exists that transforms the stiffness matrix in its orthotropic representation. Cowin and Mehrabadi[18] developed a mathematical method to find this coordinate transformation. With this method, the stiffness tensor **S** is decomposed in two second rank tensors **A** and **B**. If **A** and **B** have common eigenvectors, these eigenvectors form the symmetry coordinate system. After transformation of the stiffness tensor into this symmetry coordinate system, the corresponding stiffness matrix takes the form of Fig. 15.2b. A practical problem with this method is, however, that the eigenvectors are never exactly the same, due to the fact that materials are never perfectly orthotropic and due to measurement errors. To overcome these problems, numerical algorithms have been developed to determine the best orthotropic representation of a stiffness matrix based on an error minimization algorithm.[19] With these methods, the coordinate transformation is found that results in the smallest possible value for those matrix entries that are zero for perfect orthotropic materials. These entries are then set to zero such that an orthotropic stiffness (or compliance) matrix results that is the best orthotropic estimate of the material. Recently, Cowin and Yang[20] developed a new method based on a spectral decomposition of the stiffness matrix. With this method the fourth-rank stiffness tensor is represented as a second-rank tensor in a six-dimensional space.[21] Unlike the traditional representation of the stiffness matrix in a 6×6 matrix, which does not form a tensor, the eigenvectors and eigenvalues of this second-rank six-dimensional stiffness tensor form a meaningful eigenbasis. By averaging the eigenbases of these second-rank tensors for different measurements of the elasticity tensor components, it is possible to determine an average eigenbasis and average eigenvalues, from which the orthotropy assumption can be evaluated.

15.3.2 Compressive and Tensile Mechanical Properties

Traditionally, cancellous bone elastic constants have been determined using compression tests on excised bone specimens. The elastic constants measured represent the compressive elastic constants of the bone. Cancellous bone elastic properties for tensile loading have been determined as well in a number of studies.[22–25] The conclusion of these studies was that there are no differences between the tensile and compressive elastic constants of cancellous bone.

A large number of investigators have reported a strong linear relationship between the axial elastic modulus of cancellous bone and axial compressive strength.[26–30] Correlation coefficients between strength and modulus are usually higher than those between strength and structural density, indicating that modulus is a better predictor for strength than structural density. The tensile strength of cancellous bone, however, is less than the compressive strength.[31–33] It has been found that a strong correlation between tensile strength and modulus exists as well, but, since compressive and tensile strength are different, this relationship is not the same as that between compressive strength and modulus.[33]

15.4 Assessment of Cancellous Bone Elastic Constants

15.4.1 Experimental Assessment

With the traditional compression test, the specimen is compressed between polished steel platens while measuring the forces and axial deformation. Since cancellous bone displays viscoelastic properties, the reproducibility of a single mechanical test at a given strain rate is not very good.[5] To increase the reproducibility of the results, the test protocol usually involves a number of precycles to reach a steady state before the

measurement is started.[5,34] A line is fit through the linear part of the resulting stress–strain curve that is calculated from the measured data, and the longitudinal Young's modulus is calculated from the slope of this line. For cubic specimens, this procedure can be repeated in the three spatial directions to provide all three Young's moduli. The determination of Poisson's ratios and shear moduli from compression tests, however, is difficult, requiring sophisticated experiments (see Chapter 7).[35,36] As an alternative to compression tests, ultrasound measurements have been used to determine cancellous bone elastic constants. With this method, it is possible to determine nine orthotropic elastic constants for a bone specimen.[24,37] More recently, test protocols have been developed that use waisted cylindrical specimens, with the ends of the specimen glued in end caps.[38] These protocols allow torsion tests to determine shear moduli and compression and tension tests to determine the elastic moduli. A disadvantage of these tests is, however, the large volume of bone that is needed to cut a specimen with the correct geometry. For this reason, most of these tests have been done with bovine bone.

All of the test methods mentioned have a number of limitations and problems. First, these tests provide, at best, nine elastic constants. For this reason, the assumption that bone can be considered an orthotropic elastic material must be made *a priori*, and it is not possible to check this assumption based on the results of the experiments. Second, the elastic constants measured only represent the orthotropic elastic constants if the measurement coordinate system is aligned with the orthotropic symmetry coordinate system. If this is not the case, errors will result, dependent on the misalignment of the coordinate system. For a misalignment angle of 10°, the average error for the calculated moduli is 9.5% and considerably higher for the Poisson's ratios.[39,40] Third, the results of experimental tests are affected by systematic and random errors.[41–44] The most important source of errors are the end artifacts that emerge when a specimen is extracted from the surrounding tissue. Trabeculae near the boundaries of the specimen, which were connected to the neighboring bone, are cut off after extraction. When the specimen is loaded at its surface, these cut trabeculae exhibit deformation modes (bending, sliding) that were compressed when the specimen was *in situ*. As a result, the specimen is less stiff than it was *in situ*. This effect is inherent to the extraction of the specimen, and would occur even if the extraction process causes no damage. The underestimation of the stiffness due to end artifacts is in the range of 20 to 40%.[42] This error is less severe in a test protocol that uses waisted specimens glued in end caps, since in these tests all measurements are done on a subvolume of the specimen which, thus, is still connected to its environment. In addition, the results of mechanical tests also depend on specimen size, aspect ratio, geometry,[45,46] as well as the storage method, strain rate, and dry/wet conditions during testing (see Chapters 7 and 20).[47]

15.4.2 Numerical Assessment from Structure Measurements

15.4.2.1 Micro-Finite-Element Analyses

As an alternative to mechanical tests, micro-finite-element (μFE) analyses have been developed to calculate the elastic constants of bone specimens directly from computer models representing the actual trabecular structure of cancellous bone in full detail. This method uses two recent developments. The first is a method for the 3D graphics reconstruction of trabecular structure. With this method, high-resolution images of sequential cross sections of a cancellous bone region are created. These images are digitized and stored. By stacking the cross-sectional images, the original structure can be rebuilt in the computer as a 3D voxel (i.e., 3D pixel) grid (see Chapter 9). Methods to create the high-resolution images can be destructive (e.g., serial sectioning and serial milling techniques[48,49]) or nondestructive (e.g., micro-computed tomography (μCT) and micro-magnetic resonance (μMR) imaging[50–53]). In both cases a resolution of 50 μm or better can usually be obtained for cancellous bone regions of approximately 1 cm in size.

The second recent development is a method to create finite element models based on these reconstructions in a fully automated way. Two methods are now available for this. With the first of these, the voxel conversion technique, voxels in the computer reconstruction representing bone tissue are converted to equally shaped brick elements in an FE model, with elastic properties representing bone tissue.[54–57] The voxels representing marrow are either deleted or converted to brick elements with elastic properties

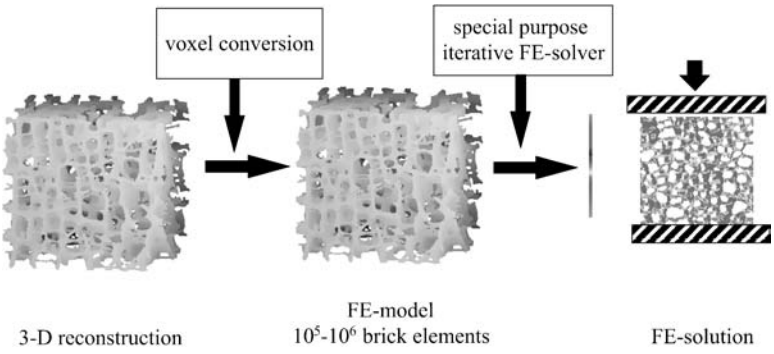

FIGURE 15.3 Summary of the micro-FE approach for the calculation of mechanical properties of trabecular bone. A 3D reconstruction of a trabecular bone specimen (left) is converted to an FE model by converting all bone voxels in the reconstruction to equally sized brick elements in the FE model. The resulting FE model (middle) has exactly the same geometry as the reconstruction it is based on. For a 10-mm specimen, the FE model consists of on the order of 10^5 to 10^6 elements. To solve these large FE problems, special-purpose iterative solvers are used. By applying the appropriate boundary conditions, the FE models can be used to simulate compression test experiments and, after solving the corresponding FE problem, to calculate the elastic properties of the specimen.

representing bone marrow. The resulting FE model generally consists of a very large number of brick elements, on the order of 10^5 to 10^6 elements for 1 cm^3 of cancellous bone. Special-purpose solvers have been developed to enable the solving of such large problems within reasonable CPU-time limits.[58] With this voxel conversion meshing technique, the geometry of the FE model is exactly the same as that of the graphics reconstruction it is derived from. Since the element size is the same as the voxel size in μCT images, these FE models are referred to as μFE models. An overview of the voxel conversion method is given in Fig. 15.3.

The second automated meshing technique that has been used to generate μFE models of cancellous bone is based on a marching cubes algorithm.[57,59,60] With this method, the bone voxels are subdivided into tetrahedron elements of varying sizes. An advantage of this algorithm is that the μFE models created have smooth trabecular surfaces. Disadvantages are the lesser accuracy of tetrahedron elements and the increased computational effort to solve these models.

μFE models can be used to calculate elastic constants of cancellous bone by simulating experimental tests on bone specimens. In these simulations, many uncertainties that play a role in real tests (e.g., bone–platen interface conditions, protocol errors) can be eliminated or well controlled. The μFE models also enable simulation of tests that are difficult or impossible in reality. For example, it is possible to apply boundary conditions that represent a pure state of uniaxial stress or strain, or simulate experiments in which a shear loading is applied to the specimen.

Limitations of this technique should be mentioned as well. At this moment, no methods exist to determine the spatial distribution of the (visco-) elastic properties and inhomogeneity of the bone tissue itself. Consequently, in most of the μFE studies performed to date, homogenous and isotropic elastic properties are specified for the elements representing the bone tissue. Although this may seem a crude simplification of reality, it has long been hypothesized that only its macroarchitecture is important for its mechanical behavior at the apparent level (i.e., for the specimen as a whole).[18] This point is further discussed in Sections 15.2 and 15.7. Whereas the simplified modeling of bone tissue is a limitation for studies where the aim is to predict accurate absolute values for elastic constants of bone specimens, it is an advantage for studies where it is aimed to correlate mechanical and morphological parameters. By specifying homogeneous isotropic tissue properties for bone tissue, the effect of bone tissue inhomogeneity and anisotropy on the elastic properties of a bone specimen can be excluded. In this way it is possible to determine the bone elastic properties that are purely due to its structure. This point is further discussed in Section 15.6.

15.4.2.2 Calculation of Stiffness Tensor and Mechanical Symmetries

As discussed earlier, compression tests that are commonly used to determine bone elastic constants suffer from a number of limitations (e.g., only a limited number of constants can be determined) and problems (e.g., limited accuracy). An important aspect of compression tests is that all measurements are done at the surface of the specimen. For example, the moduli are calculated from the measured displacement and reaction forces at the bone surfaces adjacent to the platens of the machine. With the introduction of μFE analyses, however, it has become possible to obtain information about the deformation and loading throughout a specimen. This enables the use of averaging techniques to calculate apparent elastic properties from measurements of the average tissue loading rather than from surface measurements. Advantages of these techniques are that they account for the deformation throughout the specimen and that they enable the determination of the full stiffness or compliance matrix.

In the field of micromechanics of composite materials, such averaging techniques have been developed to determine the overall elastic stiffness tensor **S** or compliance tensor **C** for inhomogenous material.[61,62] These techniques require knowledge about the stress and strain state within each component of the material for different external loading conditions. In the case of cancellous bone, there is only one load-carrying component (the bone matrix), and the stresses and strains in this matrix due to external loading can be calculated from μFE analyses. Using these averaging techniques, a total of six μFE analyses are needed to determine the stiffness or compliance tensor of a bone specimen. For the calculation of the stiffness matrix, each of these analyses should represent a state of uniaxial strain at the apparent level (i.e., for the specimen as a whole). From the results of these analyses, a local structure tensor **M**[63] (also called strain localization tensor[64]) is calculated that relates the strains at the apparent level to those at the tissue level, according to

$$\boldsymbol{\varepsilon} = \mathbf{M}\bar{\boldsymbol{\varepsilon}} \tag{15.10}$$

with $\boldsymbol{\varepsilon}$ the tissue strain tensor and $\bar{\boldsymbol{\varepsilon}}$ the apparent strain tensor. The stiffness tensor **S** is calculated from the relationship:[61,63]

$$\mathbf{S} = \frac{1}{V}\int \mathbf{S}_{\text{tissue}}\mathbf{M}\, dV \tag{15.11}$$

where $\mathbf{S}_{\text{tissue}}$ is the stiffness tensor of the bone tissue and V is the volume of the cancellous bone region analyzed. Using a similar procedure, but applying boundary conditions that represent six states of uniaxial *stress* rather than strain, the compliance tensor can be derived.[61,62] It should be noted, however, that for inhomogeneous materials the stiffness tensor calculated from six uniaxial strain analyses will not equal the inverse of the compliance tensor calculated from six uniaxial stress analyses. This is because boundary conditions also determine the stiffness of a specimen. In general, strain boundary conditions provide an upper bound on the stiffness, whereas stress boundary conditions provide a lower bound.[61,62] Consequently, it should be kept in mind that the constitutive properties measured for cancellous bone with these techniques are also dependent on the boundary conditions chosen for the analyses. Recently, homogenization theory developed for periodic materials has been used to analyze the bone microstructure.[54,63] With this theory, periodic boundary conditions are applied to the region of cancellous bone analyzed. It has been shown that periodic boundary displacements provide estimates of effective stiffness between the upper- and lower-bound estimates given by strain and stress boundary conditions. However, in general, bone cannot be considered a periodic material, and it thus is not clear if homogenization theory will provide better results than other averaging techniques in all situations.

15.5 The Anisotropic Elastic Properties of Cancellous Bone

Materials can display different types of elastic behavior (see Section 15.3.1), ranging from isotropic (every plane is a plane of elastic symmetry) to fully anisotropic (no planes of elastic symmetry). It is generally assumed that cancellous bone has at least orthotropic symmetries. This assumption is based on the fact that mean intercept measurements (MIL) of its structure can be well fitted to an ellipsoid-shaped

TABLE 15.1 Overview of the Aarhus Data

Site	No. of Specimens
Vertebral body	26
Calcaneus	28
Proximal tibia	20
Distal femur	24
Proximal femur	24
Proximal humerus	19
Total	141

second-rank fabric tensor (see Chapter 13), suggesting that three orthogonal symmetry planes exist. It is also implicitly assumed that these fabric symmetry planes coincide with the planes of orthotropic symmetry. A validation for these assumptions, however, was not possible from results of experimental methods, since these can provide, at best, 9 elastic constants (see Section 15.4.1.) rather than all 21 elastic constants that are required to verify the assumptions.

With recently developed μFE methods, however, all 21 elastic constants can be obtained. Using the methods described in Section 15.3.1 it is possible to determine the best orthotropic representation of bone specimens and their principal orthotropic directions, without the need of fabric measurements and without the need to test specimens aligned with anatomical or fabric axes. In this section, results of μFE analyses for a large number of specimens will be presented. A summary will be given of literature studies that have used this, or similar data, to determine bone orthotropic elastic constants, to identify the role of the bone structure for its anisotropic behavior and to evaluate the orthotropy assumption.

15.5.1 Elastic Constants for Two Large Sets of Specimens

At present, all 21 elastic constants calculated from μFE analyses are available for two large sets of cancellous bone samples. The first of these was analyzed in Aarhus (Denmark) and will be referred to as the "Aarhus data." This data set consists of 141 specimens obtained from a total of 56 donors and six sites (Table 15.1).[81] All specimens were cubic with sides of approximately 8 mm. A serial sectioning procedure was used to create sequential images from which computer reconstructions and μFE models were derived. The element size in the μFE models was in the range of 60 to 75 μm. An important feature of this data set is that the donors were relatively young (mean age 58 years) and none of them experienced any known chronic disease. The data set is thus considered a sample of healthy cancellous bone. The methods discussed in Section 15.4.2.2 were used to determine the full compliance matrices of reconstructed bone specimens from six μFE analyses per specimen. Numerical methods[19] were used to determine the best orthotropic representation of each compliance matrix and the commonly used nine engineering constants (three Young's and shear moduli and three Poisson's ratios). The plot of Fig. 15.4 shows the calculated engineering constants (Young's and shear moduli and Poisson's ratios) for these 141 specimens as a function of their volume fraction. The moduli are normalized to a unit bone tissue Young's modulus and therefore have no dimensions. The figures suggest that there is a strong correlation between bone volume fraction and the three Young's and shear moduli, but not for the Poisson's ratios.

The second set of cancellous bone specimens for which detailed μFE results are available is the "Biomed data" set. This set consists of 242 cubic specimens from 70 donors and four sites (Table 15.2). The specimens originate from the EU-BIOMED I study "Assessment of bone quality in osteoporosis."[65,66] Many of the donors (average age 69 years, standard deviation 15 years) experienced trabecular fractures. All specimens, which were cubic with 4 mm sides, were scanned with a μCT scanner and reconstructed in a computer. The element size in the μFE model was 28 μm. Since the average age of the donors was relatively high and many donors experienced fractures or chronic diseases, this data set represents a sample of cancellous bone at risk. The plot of Fig. 15.5 shows the calculated engineering constants for these samples as a function of their volume fraction. For this data set also, a strong correlation between

TABLE 15.2 Overview of the Biomed Data

Site	No. of Specimens
Vertebral body	63
Calcaneus	60
Femoral head	58
Iliac crest	61
Total	242

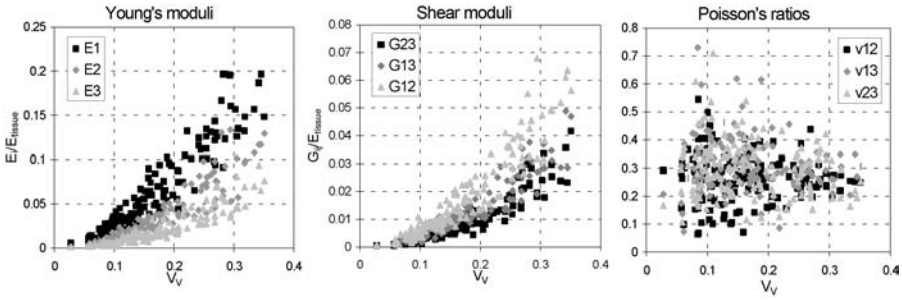

FIGURE 15.4 Orthotropic elastic constants calculated from μFE analyses of the Aarhus data[81] (Table 1). The average age of the donors from which these specimens were obtained was relatively low (58 years) and none of the donors had a record of diseases that are known to affect the bone. The data are thus considered a sample of healthy cancellous bone. The moduli are normalized to a unit tissue Young's modulus and thus are dimensionless.

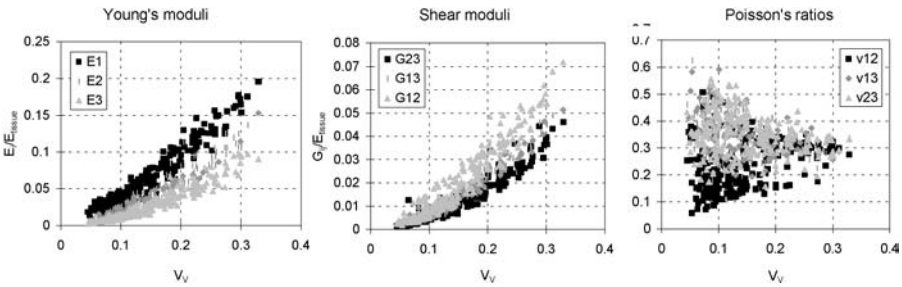

FIGURE 15.5 Orthotropic elastic constants calculated from μFE analyses of the Biomed data[65,66] (Table 2). The average age of the donors from which these specimens were obtained was high (69 years) and many of the donors experienced bone fractures. The data are thus considered a sample of cancellous bone that is suspect to osteoporosis. The moduli are normalized to a unit tissue Young's modulus and thus are dimensionless.

Young's and shear moduli and volume fraction is apparent, but not for the Poisson's ratios. A drawback of this data set is the relatively small size of the specimens, which is close to the minimum required for meaningful continuum properties.[10]

15.5.2 The Role of the Structure for Cancellous Bone Anisotropy

The anisotropy of cancellous bone as measured in mechanical tests is the result of both its trabecular structure and the anisotropy of its trabecular bone matrix. Information about the role of the trabecular structure on the apparent anisotropy is of particular importance to establish an upper limit on the accuracy for relationships that correlate mechanical and morphological parameters. If anisotropy of the bone tissue plays an important role for the anisotropy of cancellous bone at the apparent level,

the anisotropic behavior of cancellous bone cannot be accurately predicted from measurements of its architecture (e.g., fabric measurements) alone.

With the μFE method, homogeneous linear elastic and isotropic tissue properties can be specified, such that the calculated anisotropy of the FE model is due only to the trabecular structure. By comparing the anisotropy thus calculated with that measured in experiments, it becomes possible to evaluate the role of the structure for the anisotropy of cancellous bone. With this approach, it was found in many studies that, indeed, most of the anisotropy of cancellous bone at the apparent level is due to its trabecular structure only, and thus, that the anisotropy of the tissue material plays no important role.[36,67–70] A perfect match between the results of standard compression tests and μFE simulation of these tests, however, cannot be expected since the tissue material is not perfectly homogeneous, isotropic, and linear elastic, and since the experimental results also reflect a number of artifacts mentioned before (see Section 15.4.1).

To reduce these artifacts as much as possible, Kabel et al.[36] used bone specimens from a whale vertebral body. Due to the large size of this bone, it was possible to obtain 29 specimens that could be considered homogeneous, whereas there was still considerable structural variation between specimens. They found a coefficient of determination of 0.92 for the correlation between the three elastic moduli determined from compression test experiments and those calculated from μFE simulations with unique tissue elastic properties. This coefficient could be increased to 0.95 if the isotropic tissue modulus of each model were chosen such that the best agreement between the average experimental and simulation modulus was obtained for each individual specimen. In another study,[68] the experimental artifacts were reduced by gluing the specimens to the platens of the test machine. In this way, it was possible to get a very close match between experimental and μFE results.

15.5.3 The Orthotropy Assumption

As discussed in the introduction of this section, it is generally assumed that cancellous bone has at least orthotropic symmetries and that planes of orthotropic symmetry coincide with those of a fabric tensor. Since μFE results are now available for large numbers of diverse bone specimens, it is possible to verify these assumptions.

Techniques for determining the full stiffness matrices and their best orthotropic representation were demonstrated by van Rietbergen et al.[19] for two cancellous bone specimens taken from a whale vertebral body. It was found that errors in the stress–strain calculation when using the orthotropic stiffness matrices rather than the full stiffness matrices were less than a few percent, indicating that the two bone specimens investigated could well be considered orthotropic.

A more rigorous validation of the orthotropy assumption for a large set of diverse human specimens was performed by Yang et al.[71] In that study, the spectral decomposition method[20] was applied to the 141 specimens of the Aarhus data set to find the average eigenbasis of the stiffness matrices. Observing that the elements in the average eigenvector basis associated with other than orthotropic symmetry were near zero, the eigenvector basis was statistically tested for its closeness to orthotropic symmetry. It was found that this set of human cancellous bone specimens had orthotropic symmetry at the 95% confidence level.

Using a combination of μFE and morphometry analyses, Odgaard et al.[72] investigated the assumption that fabric and orthotropic coordinate systems are aligned for 29 specimens obtained from a whale vertebral body. It was found that, indeed, fabric and mechanical principal directions were closely aligned. Differences in the primary principal directions were less than 1.4° when using MIL as a fabric tensor and even slightly less when using volume-based fabric tensors (See Chapter 13).

15.6 Cancellous Bone Elastic vs. Structural Parameters

At present, no experimental techniques exist to measure cancellous bone elastic constants *in vivo*. It is possible, however, to quantify cancellous bone density and structure from imaging techniques such as dual-energy X-ray absorptiometry (DEXA), CT, and MR scanning (see Chapters 9 and 34). Hence, if it is possible to find accurate and generally valid relationships between bone elastic constants and such structural parameters measured from images, this would enable the determination of bone elastic constants

in vivo in an indirect way from morphology measurements. Such relationships could also provide a better understanding of the effect of architectural features of cancellous bone structure on its mechanical properties. This section discusses some of the structure–property relationships that have been described in the literature and their predictive value. Special attention will be given to recently developed relationships that used μFE techniques for the determination of cancellous bone elastic constants.

15.6.1 Determination of Structure–Property Relationships

Theoretical relationships between structural aspects of constructions and their elastic properties can be derived only for the most simple constructions. In some cases, however, it is possible to idealize the trabecular architecture in a region of cancellous bone as a repetitive structure built of relatively simple unit cells (e.g., open or closed cell or strut models). Such idealized models have been used to derive a theoretical basis for relationships between bone volume fraction and mechanical parameters. Explicit expressions for the bulk elastic modulus and compressive strength of 2D and 3D isotropic high-porosity open and closed cell material have been developed.[73–75] Although these models can provide insight into the relationships between structural parameters and mechanical properties, they do not represent trabecular architectures very well. For this reason, idealized models will not be discussed in this chapter and the interested reader is directed to the literature.[73–76]

Most studies aimed at finding relationships between elastic constants and structural parameters are of a more empirical nature. The protocol used in these studies is largely the same: mechanical and structural parameters are measured for a large number of cancellous bone specimens, and a statistical model is used to correlate the results. Although many investigators have found statistically significant and strong correlations between cancellous bone elastic constants and structural parameters, the precise form of such relationships remains controversial, because of insufficient knowledge of the underlying causes responsible for observed differences. In most of the studies performed to date, mechanical tests (compression tests, ultrasound measurements) were used to determine the bone elastic properties, whereas structural parameters were measured from 2D cross sections or the surface of the specimens. The results of these studies are inevitably affected by inaccuracies in the experimental tests, inaccuracies in the measurements of structural parameters, and by differences in the tissue properties between specimens, which cause variations in the specimens elastic properties that are not reflected by structural parameters. These effects could explain why relationships found in one study do not produce accurate results in another study.

With the recent introduction of high-resolution computer reconstructions and μFE-based analyses, many of the uncertainties mentioned before can be excluded. As explained in the previous section, these models enable the determination of cancellous bone elastic properties that are purely related to its structure. For this reason, recent studies have used μFE results rather than experimental tests for the determination of bone elastic properties. In addition, the computer reconstructions also enable an accurate and real 3D evaluation of structural parameters. For these reasons, it is expected that relationships based on computer reconstructions can be more accurate than those based on experimental tests and surface structure measurements.

15.6.2 Structural Density Relationships

The best-established relationship is that between cancellous bone elastic constants and its structural density. In an often-cited study by Carter and Hayes,[1] a cubic relationship was found between the axial modulus and structural density for a set of human and bovine cancellous and cortical bone specimens. Later studies have indicated that a square relationship will yield more accurate results for human cancellous bone alone. In an extensive overview, Rice et al.[77] combined the results of different earlier studies and found that a cubic relationship explained 74% of the variance in the axial modulus, whereas a square model explained 78%. They thus concluded that a square model fits the data better. More recent studies have not limited the relationships between modulus E and structural density ρ to square or cubic representation but used a more general form: $E = a\rho^p$. The results of these studies have indicated that the power p between the longitudinal modulus and structural density is close to two,[78,79] although somewhat higher values were

found ($p = 2.6$) in studies that included specimens with a large range of densities and sites.[80] Very high correlation coefficients have been found between cancellous bone structural density and the mean elastic modulus. Hodgkinson and Currey[78] determined such a relationship for 24 human cancellous bone specimens with a large range of apparent densities, and found a relationship that could explain 94% of the variation in the mean Young's modulus:

$$E_{\text{mean}} = 0.003715\rho^{1.96} \tag{15.12}$$

with ρ in kg·m^{-3}.

In all studies mentioned before, experimental tests have been used for the measurement of bone elastic moduli. In a recent study, Kabel et al.[81] correlated the mean Young's modulus determined from μFE analyses for the Aarhus specimens with their volume fraction. They found that bone volume fraction alone could explain 94% of the variation in the mean Young's moduli, the same value as found in the study by Hodgskinson and Currey.[78] It is interesting to note that the relationship between the mean Young's modulus and density found by Hodgskinson and Currey is very similar to the relationship derived by Kabel et al. After conversion of the volume fraction V_V to structural density ρ, using $\rho = 1800\,V_V$ (kg·m^{-3}), the relationship derived by Kabel et al. can be written as:

$$E = E_{\text{tissue}}813\,V_V^{1.93} = E_{\text{tissue}}813(\rho/1800)^{1.93} = E_{\text{tissue}}(0.000424\rho^{1.93}) \tag{15.13}$$

with E_{tissue} the isotropic tissue Young's modulus in GPa, which is left as a parameter in the μFE results. For a realistic tissue modulus of 10 GPa, both relationships would predict very similar values for the mean modulus.

Recently, Yang et al.[71] analyzed the same data with the spectral decomposition method. With this method, the average of the stiffness tensor eigenbases of all 141 specimens was determined and the stiffness tensor of each specimen was referred to this average eigenbasis. The orthotropic elastic constants of this common eigenbasis were regressed against the volume fraction V_V, providing relationships and coefficients of determination (R^2) for all nine engineering elastic constants:

$$\begin{aligned}
&E_{11} = E_{\text{tissue}}(1240V_V^{1.8}), \quad E_{22} = E_{\text{tissue}}(885V_V^{1.89}), \quad E_{33} = E_{\text{tissue}}(529V_V^{1.92}), \quad (R^2 = 0.924)\\
&G_{23} = E_{\text{tissue}}(533.3V_V^{2.04}), \; G_{13} = E_{\text{tissue}}(633.3V_V^{1.97}), \quad G_{12} = E_{\text{tissue}}(972.6V_V^{1.98}), \quad (R^2 = 0.884)\\
&\nu_{23} = E_{\text{tissue}}(0.256V_V^{-0.086}), \; \nu_{13} = E_{\text{tissue}}(0.316V_V^{-0.191}), \; \nu_{12} = E_{\text{tissue}}(0.176V_V^{-0.248}), (R^2 = 0.755)
\end{aligned} \tag{15.14}$$

In these relationships, bone volume fraction alone can explain more than 92% of the variation in the Young's moduli, more than 88% of that in the shear moduli and most of the variation (76%) in the Poisson's ratios. Clearly, however, no information about the directionality of the structure can be derived from bone volume fraction, which is a scalar. To overcome this problem, Cowin et al. introduced the term *trabecular grain*, which was defined in analogy with the idea of the grain of wood. Trabecular grain represents a set of three ordered orthogonal directions, the first of which lies along the predominant trabecular direction. It is suggested that the trabecular grain be directly related to the anatomical site, such that knowledge of the site and the volume fraction would provide all information needed for the determination of the orthotropic elastic constants and the orthotropic principal directions.

The plot of Fig. 15.6 compares different relationships published in the literature for the dependency of the axial, the mean, and the lower and higher Young's modulus on structural density.

15.6.3 Other Structural Scalar Parameters

The high coefficients of determination (R^2) mentioned in the previous section are found in studies where the cancellous bone density varies over a wide range. In spite of these high coefficients, the prediction for individual specimens can be rather poor. Using a subset of the Biomed specimens, Ulrich et al.[82] demonstrated that while more than 86% of the variation in the elastic properties of this subset could be explained

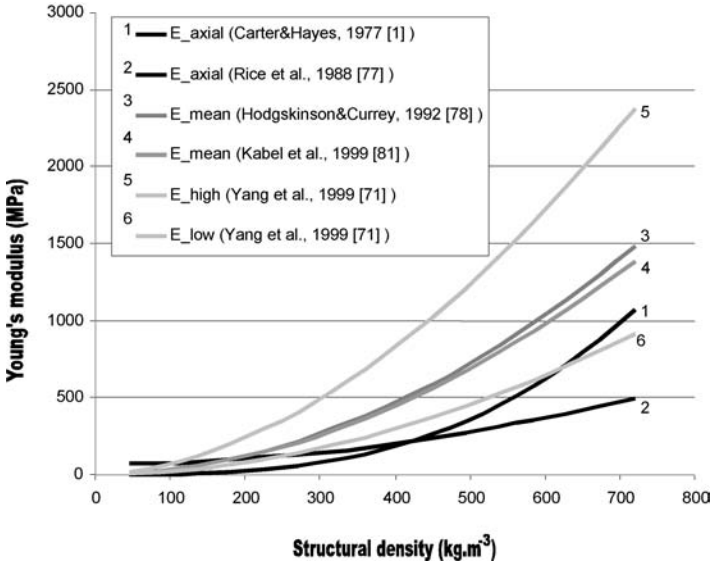

FIGURE 15.6 Different models published in the literature for the dependency of the axial, mean, high, and low Young's modulus of cancellous bone on its structural density. Results for Kabel et al.[81] and Yang et al.[71] are scaled for a tissue Young's modulus of 10 GPa.

by bone volume fraction, differences in moduli between samples with the same bone volume fraction could be as large as 53%. It has been investigated if the inclusion of other structural parameters in predictive relationships could possibly reduce the remaining variance in predicted elastic constants. In the osteoporosis literature, connectivity density is generally believed to be an important parameter. However, the results of studies investigating the role of connectivity density on cancellous bone elastic properties are not consistent. Some authors found that connectivity density was highly correlated with structural density (or volume fraction), implying that it cannot explain any variation in the elastic moduli that is not already explained by structural density.[79,83,84] Results of other studies, however, indicated that connectivity density was not or only partly related to volume fraction.[50,85,86] In the study by Kabel et al.[81] mentioned in the previous section, the role of connectivity density on the mean elastic modulus of the Aarhus specimens was investigated as well. In this study, it was found that adding connectivity density to the relationship only marginally improved the prediction of the mean elastic modulus (by 0.2%). Kinney and Ladd[87] investigated the role of connectivity density on changes in trabecular structure. In this study a computer algorithm was used to degrade and recover a trabecular structure and μFE techniques were used to determine the elastic properties of the resulting structures. Although no functional relationship was found between connectivity and elastic modulus, there was a linear relationship, after a full cycle of atrophy and recovery, between the loss of elastic modulus and the overall loss of connectivity. These results indicate that recovery of mechanical function depends on preserving or restoring trabecular connectivity.

In a study by Ulrich et al.[82] the predictive value of several structural parameters for the elastic properties for subsets of the Biomed specimens was investigated. These subsets were chosen to represent specimens of one of four investigated sites that could not be identified as osteoporotic or normal from their volume fraction alone. When only volume fraction was included in the predictive relationship, coefficients of determination for the subgroups were rather low and considerably less than the one for the whole group (e.g., 52% rather than 72% for the whole group). They demonstrated that the coefficients of determination could be increased by as much as 39% if other structural indices (Tb.Sp, MIL ratio, and Tb.N) were included in the predictive relationship. However, the most effective indices were not the same for different skeletal sites. It is interesting to note that the latter result was predicted by Keaveny [75] based on structural analyses of simplified models.

15.6.4 Relationships Based on Fabric Tensors

Since the anisotropy of cancellous bone is determined by its structure, it seems an obvious idea to find relationships between bone elastic constants and the constants of a fabric tensor that represents the anisotropy of the trabecular structure. However, bone elastic constants are described by a fourth-rank tensor and fabric by a second-rank tensor, and a correlation between both thus requires a mathematical framework. Such a framework was first developed by Cowin.[88] He developed a general representation between the elastic constants and structural density ρ and a fabric tensor **H**, based on the notion that the matrix material is isotropic and that all of the anisotropy is characterized by the fabric tensor. The mathematical statement of this notion is that the stress tensor **T** is an isotropic function of the strain tensor **E** and the fabric tensor **H** as well as the structural density ρ. The general relationship developed by Cowin[88] depended upon terms of the fourth order in $\boldsymbol{H}$ and contained nine functions of the isotropic invariants in **H** and structural density that must be determined from experiments. To simplify the relationship an approximation that retains terms of order two in **H** was developed and the fabric tensor eigenvalues H_i were normalized with the requirement $H_1 + H_2 + H_3 = 1$. The latter normalization is based on the assumption that, given constant volume fraction, the elastic properties of bone are not dependent on pore size. The resulting relationships between the elastic constants and normalized fabric tensor eigenvalues are[37,88]

$$\begin{aligned}
&\begin{cases} S_{iiii} &= k_1 + 2k_6 + (k_2 + 2k_7)\mathrm{II} + 2(k_3 + 2k_8)H_i + (2k_4 + k_5 + 4k_9)H_i^2 \\ S_{iijj} &= k_1 + k_2\mathrm{II} + k_3(H_i + H_j) + k_4(H_i^2 + H_j^2) + k_5 H_i H_j \\ S_{ijij} &= k_6 + k_7\mathrm{II} + k_8(H_i + H_j) + k_9(H_i^2 + H_j^2) \end{cases} \\
&i,j = 1,2,3; \qquad i \neq j
\end{aligned} \tag{15.15}$$

with S_{ijkl} the components of the stiffness tensor **S**, $\mathrm{II} = H_1H_2 + H_2H_3 + H_1H_3$ the second invariant of **H**, and k_1 to k_9 nine functions of structural density or volume fraction. The same relationship can be used to correlate the components of the compliance tensor **C** with fabric, in which case the stiffness tensor entries on the left-hand side are replaced by the compliance tensor entries C_{ijkl}. The functions k_i are usually chosen as $k_i = a_i + b_i\rho^p$, with a_i and b_i two constants and p the power for relationships with the stiffness tensor, and as $k_i = a_i + b_i\rho^{-p}$ for relationships with the compliance tensor. Consequently, a total of 18 constants must be determined from experiments in order to quantify these relationships.

An alternative model was developed by Zysset and Curnier.[89] They simplified the general relationship developed by Cowin by requiring that the stress be homogeneous in the fabric for all strain states and the application of the *a priori* condition that the stiffness matrix be positive definite and invertable. In its final form, their relationship

$$\begin{aligned}
&\begin{cases} S_{iiii} &= (\lambda_c + 2\mu)H_i^{2k} \\ S_{iijj} &= \lambda_c H_i^k H_j^k \\ S_{ijij} &= 2\mu_c H_i^k H_j^k \end{cases} \\
&i,j = 1,2,3; \qquad i \neq j
\end{aligned} \tag{15.16}$$

with μ_c and λ_c Lamé like constants, requires only five independent parameters (μ_c, λ_c, k, H_1, and H_2; note that $H_3 = 1 - H_1 - H_2$ and thus is not an independent parameter) to identify the nine orthotropic elastic constants. An advantage of this model is the fact that all these constants have a physical meaning. A disadvantage, however, is the fact that it cannot represent all forms of orthotropy, which would require nine independent constants. Hence, the model is more restrictive than the one developed by Cowin.[88] Whether this restricted form of orthotropy is a serious limitation for cancellous bone remains to be investigated.

Using the model developed by Cowin,[88] Turner et al.[37] were the first to quantify a relationship between the elastic constants and fabric. They fitted the MIL fabric tensor for human and bovine specimens against the compliance tensor, but used an uncoupled form of Eq. 15.15. such that relationships for the Young's moduli and shear moduli could be determined independently. In their study, ultrasound measurements were used to determine the engineering elastic constants (E_i and G_{ij}) for bovine and human cancellous bone specimens. Eigenvalues of the fabric tensor (H_i) were determined from mean intercept measurements on the six surfaces of the cubic specimens. The power p in the functions of structural density $k_i = a_i + b_i\rho^{-p}$ was chosen to be 1, 2, and 3. The relationship found for human bone and using square power functions was

$$\begin{aligned}
\frac{1}{E_i} &= 0.01575 + \frac{-0.0006}{\rho^2} + \left(-0.01622 + \frac{0.00071}{\rho^2}\right)\mathrm{II} + \left(-0.05088 + \frac{0.00289}{\rho^2}\right)H_i \\
&\quad + \left(0.06586 + \frac{-0.00442}{\rho^2}\right)H_i^2 \\
\frac{1}{G_{ij}} &= -0.03341 + \frac{0.0042}{\rho^2} + \left(0.27419 + \frac{-0.01938}{\rho^2}\right)\mathrm{II} + \left(-0.14621 + \frac{0.00761}{\rho^2}\right)(H_i + H_j) \\
&\quad + \left(0.19319 + \frac{-0.01147}{\rho^2}\right)(H_i^2 + H_j^2) \\
i, j &= 1, 2, 3; \qquad i \neq j
\end{aligned} \tag{15.17}$$

The coefficients of determination (R^2) were 0.70 and 0.80 for the Young's and shear moduli, respectively. Similar coefficients of determination were found when using linear or cubic functions of structural density.

The use of high-resolution microstructural computer models for the μFE calculation of all orthotropic elastic constants of bone cubes and real 3D fabric measurements was introduced in a study by van Rietbergen et al.[90] They also demonstrated that this approach enables the determination of all 18 constants in Eq. 15.15 and that very high coefficients of determination can be obtained. Kabel et al.[91] applied these techniques to analyze the Aarhus data. In their study, the authors regressed both the components of the compliance and those of the stiffness tensor using separate relationships, with several fabric measures (MIL and volume-based fabric measures). Best correlations were found for the regression of MIL eigenvalues with the components of the stiffness tensor (Fig. 15.7), using functions of volume

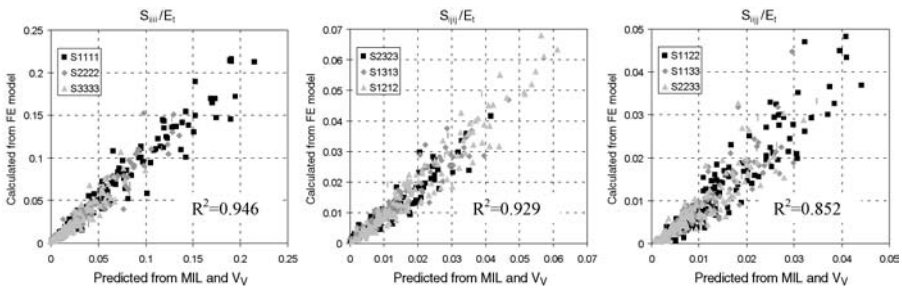

FIGURE 15.7 Components of the stiffness tensor S predicted from MIL and volume fraction (V_V) using Eq. 15.19 (horizontal axes) vs. those calculated from μFE analyses (vertical axes). (From Kabel, J. et al., *Bone,* 25, 481, 1999. With permission.)

fraction V_V of the form $k_i = a_i + b_i V_V^{1.6}$. After substituting the 18 constants, the relationship takes the form

$$\begin{cases} S_{iiii} = E_{\text{tissue}}\{0.0291 + 0.8650V_V^{1.6} + (0.1332 - 5.506V_V^{1.6})\text{II} + (-0.5109 + 5.1440V_V^{1.6})H_i \\ \qquad + (0.8208 - 0.0700V_V^{1.6})H_i^2\} \quad (R^2 = 0.946) \\ S_{iijj} = E_{\text{tissue}}\{-0.0065 + 0.6238V_V^{1.6} + (0.2758 + 11.570V_V^{1.6})\text{II} + (-0.2631 - 13.430V_V^{1.6}) \\ \qquad (H_i + H_j) + (0.2629 + 11.590V_V^{1.6})(H_i^2 + H_j^2) + (0.2739 + 18.790V_V^{1.6})H_iH_j\} \\ \qquad (R^2 = 0.852) \\ S_{ijij} = E_{\text{tissue}}\{0.0178 + 0.1206V_V^{1.6} + (-0.0713 - 8.5380V_V^{1.6})\text{II} + (0.0038 + 8.0010V_V^{1.6}) \\ \qquad (H_i + H_j) + (0.0053 - 10.510V_V^{1.6})(H_i^2 + H_j^2)\} \quad (R^2 = 0.929) \\ i, j = 1, 2, 3; \qquad i \neq j \end{cases} \tag{15.18}$$

with S_{ijkl} the components of the stiffness tensor, E_{tissue} the isotropic tissue Young's modulus, and H_i the eigenvalues of the MIL fabric tensor. The coefficient of determination for the pooled data was 0.97. After calculating the Young's and shear moduli from the predicted stiffness matrix, it was found that these engineering constants were accurately predicted as well ($R^2 > 0.93$). The Poisson's ratios calculated from the predicted stiffness matrix, however, did not correlate with those calculated from the μFE analyses ($R^2 = 0.07$). Coefficients of determination for the regression with the components of the compliance tensor were somewhat less (for the pooled data $R^2 = 0.89$) and there was no significant correlation between the moduli and Poisson's ratios calculated from the predicted compliance matrices and those calculated from the μFE analyses. The fact that elastic moduli can be predicted from relationships based on the stiffness tensor, but not from relationships based on compliance tensor, is likely due to the fact that entries in the stiffness tensor are linearly related to the moduli, whereas those in the compliance tensor are inversely related to the moduli. A good prediction of the stiffness tensor thus also ensures a good prediction of the moduli, which is not necessarily so in the case when a good prediction of the compliance tensor is obtained.

In a later study, van Rietbergen et al.[92] used the same methods to investigate if an accurate relationship exists for the bone of the Biomed data set as well, and if the earlier-found relationship for healthy bone of the Aarhus sample also yields accurate predictions for elastic properties of this data set. In this study, square functions of apparent density were used and only MIL measurements were used to determine the bone fabric. It was found that, for this data set as well, an excellent fit between the components of the stiffness tensor and MIL and volume fraction could be obtained, with coefficients of determination of 0.963, 0.933, 0.944, and 0.97 for the stiffness tensor components S_{iiii}, S_{iijj}, S_{ijij}, and the pooled data, respectively. Although the 18 constants found in this relationship were very different from those found for the healthy bone (Eq. 15.18), it was found that the relationship for healthy bone could also predict the elastic constants of the Biomed specimens with the same coefficients of determination ($R^2 = 0.97$ for the pooled data). The slope of the regression line, however, was less than one, such that the elastic constants of the Biomed specimens were underestimated when using relationship 15.18. This underestimation could be explained by the differences in specimen size between both studies, which was only 4 mm for the Biomed specimens and 8 mm for the Aarhus specimens. The displacement boundary conditions applied during the μFE analyses have a more-pronounced effect for small specimens because a relatively larger number of the degrees of freedom in the model are prescribed. It was thus concluded that the relationship for healthy bone (Eq. 15.18) better represents the *in vivo* elastic constants of cancellous bone, and can accurately predict the elastic constants for both the young Aarhus and the older Biomed specimens.

15.7 Dependency of Elastic Constants on Bone Tissue Properties

In the previous paragraphs it was shown that the anisotropic elastic properties of cancellous bone are well represented by μFE models with isotropic tissue properties. Looking at the microarchitecture of the cancellous bone tissue, it seems unlikely that the bone tissue indeed is an isotropic material; the collagen fibers are largely oriented along the trabecular longitudinal direction. It thus seems more likely that the bone tissue will behave as a transversely isotropic material. Most of the trabeculae, however, are loaded in compression or bending. For these loading modes, only the longitudinal Young's modulus is of importance. Consequently, the anisotropic tissue material can be well represented as an isotropic material with an "effective" isotropic tissue modulus that represents the longitudinal stiffness of the bone tissue.

The actual value for this "effective" isotropic tissue Young's modulus can be determined by comparing the results of μFE analyses with those of experimental tests for the same specimen.[36,55,68,69] The isotropic tissue modulus chosen in the μFE analyses determines the absolute values of the elastic constants of cancellous bone just like a linear scaling factor; if the tissue Young's modulus is chosen twice as high, the calculated cancellous bone elastic constants will be twice as high as well. By specifying an arbitrary initial Young's modulus E_{init} for the μFE analyses, the scaling factor k can be determined that gives the best agreement between experimental and μFE-calculated moduli. The tissue Young's modulus is then calculated as $E_{\text{tissue}} = kE_{\text{init}}$. The values found for the tissue Young's modulus when using this approach are generally in the range 4 to 8 GPa,[36,55,69] although higher values (14.6 GPa) have been reported as well.[68]

In earlier studies the tissue elastic properties and strength have been measured using standard engineering test methods such as tensile tests, three- or four-point bending tests, and buckling tests. Values found for the tissue modulus range from 0.76 to 10 GPa when using tensile tests, from 3.2 to 5.4 GPa for three- or four-point bending tests and from 8.7 to 14 GPa for buckling tests (for an overview see Rho et al. [93]). A major problem when using standard engineering test methods for the determination of bone tissue properties is the small size of trabeculae (thickness; 100 to 200 μm; length, 1 to 2 mm), resulting in inaccuracies in the displacement measurements and thus in the calculation of moduli. Another problem is the irregular shape of trabeculae, where standard engineering tests require standardized specimen geometry. To overcome the latter problem, some studies have used machined specimens,[94,95] but it is unclear to what extent machining artifacts can affect the stiffness of the specimens. Other engineering test methods for the measurement of tissue elastic properties include ultrasound measurements. Values found with this method are generally higher than those obtained from the standard tests: 11 to 15 GPa.[93,96] Recently, nanoindentation test have been developed for the measurement of tissue elastic properties,[97] providing a tissue modulus at the microlevel ranging from 15 to 20 GPa.

Based on the large variation in the results obtained from these studies, it has been questioned if the tissue properties of trabecular bone can be defined at all. Bone tissue is a structure at all levels of organization[98] and, consequently, different properties will be found if different test methods are performed at different levels. It has been proposed that each test will measure "a stiffness" for some level of organization rather than an intrinsic property of bone material.[94] The tissue modulus determined by comparing results of mechanical tests and μFE analyses measures the effective tissue modulus at the level of intact trabeculae *in situ*. These results thus could differ from those of measurements that use extracted or machined trabeculae or that measure at a very local level (e.g., nanoindentation).

The tissue Poisson's ratio cannot be determined by simply scaling μFE to experimental results. Since the isotropic tissue properties are not a linear function of the Poisson's ratio (see Fig. 15.1d), no scaling factor for the Poisson's ratio exists to fit μFE and experimental results. However, results of μFE analyses have demonstrated that the Poisson's ratio of the bone tissue has a negligible effect on cancellous bone elastic constants at the apparent level.[56] Consequently, most of the studies performed to date have chosen a reasonable value (usually 0.3) for the tissue material properties.

References

1. Carter, D.R. and Hayes, W.C., The compressive behavior of bone as a two-phase structure, *J. Bone Joint Surg. (Am.),* 59, 954, 1977.
2. Linde, F., Elastic and viscoelastic properties of trabecular bone by a compression testing approach, *Dan. Med. Bull.,* 41, 119, 1994.
3. Mullender, M.G., Huiskes, R., Versleyen, H., and Buma, P., Osteocyte density and histomorphometric parameters in cancellous bone of the proximal femur in five mammalian species, *J. Orthop. Res*., 14, 972, 1996.
4. Linde, F., Nørgaard, P., Hvid, I., Odgaard, A., and Søballe, K., Mechanical properties of trabecular bone: dependency on strain rate, *J. Biomech*., 24, 803, 1991.
5. Linde, F., Hvid, I., and Jensen, N.C., Material properties of cancellous bone in repetative axial loading, *Eng. Med.,* 14, 173, 1985.
6. Linde, F., Hvid, I., and Pongsoipetch, B., Energy absorptive properties of human trabecular bone specimens during axial compression, *J. Orthop. Res.,* 7, 432, 1989.
7. Zilch, H., Rohlmann, A., Bergman, G., and Kölbel, R., Material properties of femoral cancellous bone in axial loading. Part II: Time dependent properties, *Arch. Orthop. Traumat. Surg*., 97, 257, 1980.
8. Pugh, J.W., Rose, R.M., and Radin, E.L., Elastic and viscoelastic properties of trabecular bone: dependency on structure, *J. Biomech.,* 6, 475, 1973.
9. Bowman, S.M., Keaveny, T.M., Gibson, L.J., Hayes, W.C., and McMahon, T.A., Compressive creep behavior of bovine trabecular bone, *J. Biomech.,* 27, 301, 1994.
10. Harrigan, T. P., Jasty, M., Mann, R. W., and Harris, W. H., Limitations of the continuum assumption in cancellous bone, *J. Biomech.,* 21, 269, 1988.
11. Nye, J.F., *Physical Properties of Crystals: Their Representation by Tensors and Matrices,* Clarendon Press, Oxford, 1957.
12. Bunge, H.J., *Texture Analysis in Material Science,* Butterworths, London, U.K., 1982.
13. Cowin, S.C. and Mehrabadi, M., On the identification of material symmetry for anisotropic elastic materials, *Q. J. Mech. Appl. Math.,* 40, 451, 1987.
14. Gurtin, M.E., *The Linear Theory of Elasticity,* Handbuch der Physik, VIa/2, 1972.
15. Lempriere, B.M., Poisson's ratios in orthotropic materials, *Am. Inst. Aeronaut. Astronaut., J.,* 6, 2226, 1968.
16. Cowin, S.C. and van Buskirk, W.C., Thermodynamic restrictions on the elastic constants of bone, *J. Biomech.,* 19, 85, 1986.
17. Jones, R.M., *Mechanics of Composite Materials*, 2nd. ed., Taylor & Francis, Philadelphia, 1999.
18. Cowin, S.C. and Mehrabadi, M., Identification of the elastic symmetry of bone and other materials, *J. Biomech.,* 22, 503, 1989.
19. van Rietbergen, B., Odgaard, A., Kabel, J., and Huiskes, R., Direct mechanics assessment of elastic symmetries and properties of trabecular bone architecture, *J. Biomech.,* 29, 1653, 1996.
20. Cowin, S.C. and Yang, G., Averaging anisotropic elastic constant data, *J. Elast*., 46, 151, 1997.
21. Mehrabadi, M.M. and Cowin, S.C., Eigentensors of linear anisotropic elastic materials, *Q. J. Mech. Appl. Math.,* 43, 15, 1990.
22. Carter, D.R., Schab, G.H., and Spengler, D.M., Tensile fracture of cancellous bone, *Acta Orthop. Scand.,* 51, 733, 1980.
23. Benusan, J.S., Davy, D.T., Heiple, K.G., and Verdin, P.J., Tensile, compressive and torsional testing of cancellous bone, *Trans. Orthop. Res. Soc.,* 8, 132, 1983.
24. Ashman, R.B., Rho, J.Y., and Turner, C.H., Anatomical variation of orthopedic elastic modula of proximal human tibia, *J. Biomech.,* 22, 895, 1989.
25. Røhl, L., Larsen, E., Linde, F., Odgaard, A., and Jørgensen, J., Tensile and compressive properties of cancellous bone, *J. Biomech.,* 24, 1143, 1991.

26. Williams, J.L. and Lewis, J.L., Properties and an anisotropic model of cancellous bone from the proximal tibial epiphysis, *J. Biomech. Eng.,* 104, 50, 1982.
27. Goldstein, S.A., Wilson, D.L., Sonstegard, D.A., and Matthews, L.S., The mechanical properties of human tibial trabecular bone as a function of methaphysial location, *J. Biomech.,* 16, 965, 1983.
28. Turner, C.H., Yield behavior of bovine cancellous bone, *J. Biomech. Eng.,* 111, 256, 1989.
29. Ciarelli, M.J., Goldstein, S.A., Kuhn, J.L., Cody, D.D., and Brown, M.B., Evaluation of orthogonal mechanical properties and density of human trabecular bone from the major metaphysial regions with materials testing and computed tomography, *J. Orthop. Res.,* 9, 674, 1991.
30. Hodgskinson, R. and Currey, J.D., Seperate effects of osteoporosis and density on the strength and stiffness of human cancellous bone, *Clin. Biomech.,* 8, 262, 1993.
31. Stone, J.L., Beaupré, G.S., and Hayes, W.C., Multiaxial strength characteristics of trabecular bone, *J. Biomech.,* 18, 743, 1983.
32. Kaplan, S.J., Hayes, W.C., and Stone, J.L., Tensile strength of bovine trabecular bone, *J. Biomech.,* 18, 723, 1985.
33. Keaveny, T.M., Wachtel, E.F., Ford, C.M., and Hayes, W.C., Differences between the tensile and compressive strengths of bovine tibial trabecular bone depend on modulus, *J. Biomech.,* 27, 1137, 1994.
34. Linde, F. and Hvid, I., Stiffness behavior of trabecular bone specimens, *J. Biomech.,* 20, 83, 1987.
35. Snyder, B.D. and Hayes, W.C., Multiaxial structure-property relations in trabecular bone, in *Biomechanics of Diarthrodial Joints,* Mow, V.C., Ratcliffe, A., and Woo, S.L-Y., Eds., Springer-Verlag, New York, 1990, 31.
36. Kabel, J., van Rietbergen, B., Dalstra, M., Odgaard, A., and Huiskes, R., The role of an effective isotropic tissue modulus in the elastic properties of cancellous bone, *J. Biomech.,* 32, 673, 1999.
37. Turner, C.H., Cowin, S.C., Rho, J.Y., Ashman, R.B., and Rice, J.C., The fabric dependence of the orthotropic elastic constants of cancellous bone, *J. Biomech.,* 23, 549, 1990.
38. Keaveny, T.M., Guo, X.E., Wachtel, E.F., McMahon, T.A., and Hayes, W.C., Trabecular bone exhibits fully linear elastic behavior and yields at low strains, *J. Biomech.,* 27, 1127, 1994.
39. Turner, C.H. and Cowin, S.C., Errors induced by off-axis measurement of the elastic properties of bone, *J. Biomech. Eng.,* 110, 213, 1988.
40. Cowin, S.C., Sadegh, A.M., and Luo, G.M., Correction formulae for the misalignment of axes in the measurement of the orthotropic elastic constants, *J. Biomech.,* 24, 637, 1991.
41. Odgaard, A. and Linde, F., The underestimation of Young's modulus in compressive testing of cancellous bone specimens, *J. Biomech.,* 24, 691, 1991.
42. Keaveny, T.M., Pinilla, T.P., Crawford, R.P., Kopperdahl, D.L., and Lou, A., Systematic and random errors in compression testing of trabecular bone, *J. Orthop. Res.,* 15, 101, 1997.
43. Keaveny, T.M., Borchers, R.E., Gibson, L.J., and Hayes, W.C., Theoretical analysis of the experimental artifact in trabecular bone compressive modulus, *J. Biomech.,* 26, 599, 1993.
44. Zhu, M., Keller, T.S., and Spengler, D.M., Effects of specimen load-bearing and free surface layers on the compressive mechanical properties of cellular materials, *J. Biomech.,* 27, 57, 1994.
45. Keaveny, T.M., Borchers, R.E., Gibson, L.J., and Hayes, W.C., Trabecular bone modulus and strength can depend on specimen geometry, *J. Biomech.,* 26, 991, 1993.
46. Linde, F., Hvid, I., and Madsen, F., The effect of specimen geometry on the mechanical behaviour of trabecular bone specimens, *J. Biomech.,* 25, 359, 1992.
47. Linde, F. and Sorensen, H.C., The effect of different storage methods on the mechanical properties of trabecular bone, *J. Biomech.,* 26, 1249, 1993.
48. Odgaard, A., Andersen, K., Melsen, F., and Gundersen, H.J.G., A direct method for fast three-dimensional serial reconstruction, *J. Microsc.,* 159, 335, 1990.
49. Beck, J.D., Canfield, B.L., Haddock, S.M., Chen, T.J., Kothari, M., and Keaveny, T.M., Three-dimensional imaging of trabecular bone using the computer numerically controlled milling technique, *Bone,* 21, 281, 1997.

50. Feldkamp, L.A., Goldstein, S.A., Parfitt, A.M., Jesion, G., and Kleerekoper, M., The direct examination of three-dimensional bone architecture *in vitro* by computed tomography, *J. Bone Miner. Res.,* 4, 3, 1989.
51. Rüegsegger, P., Koller, B., and Muller, R., A microtomographic system for the nondestructive evaluation of bone architecture, *Calcif. Tissue Int.,* 58, 24, 1996.
52. Bonse, U., Busch, F., Gunnewig, O., Beckmann, F., Pahl, R., Delling, G., Hahn, M., and Graeff, W., 3D computed X-ray tomography of human cancellous bone at 8 microns spatial and 10(-4) energy resolution, *Bone Miner.,* 25, 25, 1994.
53. Hipp, J.A., Jansujwicz, A., Simmons, C.A., and Snyder, B.D., Trabecular bone morphology from micro-magnetic resonance imaging, *J. Bone Miner. Res.,* 11, 286, 1996.
54. Hollister, S.J., Brennan, J.M., and Kikuchi, N., A homogenization sampling procedure for calculating trabecular bone effective stiffness and tissue level stress, *J. Biomech.,* 27, 433, 1994.
55. van Rietbergen, B., Weinans, H., Huiskes, R., and Odgaard, A., A new method to determine trabecular bone elastic properties and loading using micromechanical finite-element models, *J. Biomech.,* 28, 69, 1995.
56. Ladd, A.J. and Kinney, J.H., Numerical errors and uncertainties in finite-element modeling of trabecular bone, *J. Biomech.,* 31, 941, 1998.
57. Ulrich, D., van Rietbergen, B., Weinans, H., and Ruegsegger, P., Finite element analysis of trabecular bone structure: a comparison of image-based meshing techniques, *J. Biomech.,* 31, 1187, 1998.
58. van Rietbergen, B., Weinans, H., Polman, B.J.W., and Huiskes, R., Computational strategies for iterative solutions of large FEM applications employing voxel data, *Int. J. Numer Methods Eng.,* 39, 2743, 1996.
59. Frey, P., Sarter, B., and Gautherie, M., Fully automated mesh generation for 3-D domains based upon voxel sets, *Int. J. Numer Methods Eng.,* 37, 2735, 1994.
60. Müller, R. and Rüegsegger, P., Three-dimensional finite element modelling of non-invasively assessed trabecular bone structures, *Med. Eng. Phys.,* 17, 126, 1995.
61. Hill, R., Elastic properties of reinforced solids: some theoretical principles, *J. Mech. Phys. Solids,* 11, 357, 1963.
62. Nemat-Nasser S. and Hori, M., *Micromechanics: Overall Properties of Heterogeneous Materials,* Vol. 37, North-Holland, Amsterdam, 1993.
63. Hollister, S.J., Fyhrie, D.P., Jepsen, K.J., and Goldstein, S.A., Application of homogenization theory to the study of trabecular bone mechanics, *J. Biomech.,* 24, 825, 1991.
64. Suquet, P.M., Elements of homogenization theory for inelastic solid mechanics, in *Homogenization Techniques for Composite Media,* Sanchez-Palencia, E. and Zaoui, A., Eds., Springer, Berlin, 1985.
65. Dequeker, J., Assessment of quality of bone in osteoporosis—BIOMED I: Fundamental study of relevant bone, *Clin. Rheum.,* 13 (Suppl. 1), 7, 1994.
66. Hildebrand, T., Laib, A., Müller, R., Dequeker, J., and Rüegsegger, P., Direct three-dimensional morphometric analysis of human cancellous bone: microstructural data from spine, femur, iliac crest, and calcaneus, *J. Bone. Miner. Res.,* 14, 1167, 1999.
67. van Rietbergen, B., Huiskes, R., Weinans, H., Odgaard, A., and Kabel, J., The role of trabecular architecture in the anisotropic mechanical properties of bone, in *Bone Structure and Remodeling,* Odgaard, A. and Weinans, H., Eds., World Scientific, Singapore, 1995.
68. van Rietbergen, B., Kabel, J., Odgaard, A., and Huiskes, R., Determination of trabecular bone tissue elastic properties by comparison of experimental and finite element results, in *Material Identification Using Mixed Numerical Experimental Methods,* Sol, H. and Oomens, C.W.J., Eds., Kluwer Academic Publishers, Dordrecht, The Netherlands, 1997.
69. Ladd, A.J., Kinney, J.H., Haupt, D.L., and Goldstein, S.A., Finite-element modeling of trabecular bone: comparison with mechanical testing and determination of tissue modulus, *J. Orthop. Res.,* 16, 622, 1998.

70. Hou, F.J., Lang, S.M., Hoshaw, S.J., Reimann, D.A., and Fyhrie, D.P., Human vertebral body apparent and hard tissue stiffness, *J. Biomech.,* 31, 1009, 1998.
71. Yang, G., Kabel, J., van Rietbergen, B., Odgaard, A., Huiskes, R., and Cowin, S.C., The anisotropic Hooke's law for cancellous bone and wood, *J. Elasticity,* 53, 125, 1999.
72. Odgaard, A., Kabel, J., van Rietbergen, B., Dalstra, M., and Huiskes, R., Fabric and elastic principal directions of cancellous bone are closely related, *J. Biomech.,* 30, 487, 1997.
73. Silva, M.J. and Gibson, L.J., Modeling the mechanical behavior of vertebral trabecular bone: effects of age-related changes in microstructure, *Bone,* 21, 191, 1997.
74. Gibson, L.J., The mechanical behaviour of cancellous bone, *J. Biomech.,* 18, 317, 1985.
75. Keaveny, T.M., Mechanistic approaches to analysis of trabecular bone, *Forma,* 12, 267, 1997.
76. Gibson, L.J. and Ashby, M.F., *Cellular Solids: Structures & Properties,* Pergamon Press, Oxford, 1988.
77. Rice, J.C., Cowin, S.C., and Bowman, J.A., On the dependence of the elasticity and strength of cancellous bone on apparent density, *J. Biomech.,* 21, 155, 1988.
78. Hodgskinson, R. and Currey, J.D., Young's modulus, density and material properties in cancellous bone over a large density range, *J. Mater. Sci. Mater. Med.,* 3, 377, 1992.
79. Goulet, R.W., Goldstein, S.A., Ciarelli, M.J., Kuhn, J.L., Brown, M.B., and Feldkamp, L.A., The relationship between the structural and orthogonal compressive properties of trabecular bone, *J. Biomech.,* 27, 375, 1994.
80. Keller, T.S., Predicting the compressive mechanical behavior of bone, *J. Biomech.,* 27, 1159, 1994.
81. Kabel, J., Odgaard, A., van Rietbergen, B., and Huiskes, R., Connectivity and the elastic properties of cancellous bone, *Bone,* 24, 115, 1999.
82. Ulrich, D., van Rietbergen, B., Laib, A., and Rüegsegger, P., The ability of 3-D structural indices to reflect mechanical aspects of trabecular bone, *Bone,* 25, 55, 1999.
83. Hodgskinson, R. and Currey, J.D., Effects of structural variation on Young's modulus of non-human cancellous bone, *Proc. Inst. Mech. Eng.,* 204, 43, 1990.
84. Goldstein, S.A., Goulet, R., and McCubbrey, D., Measurement and significance of three-dimensional architecture to the mechanical integrity of trabecular bone, *Calcif. Tissue Int.,* 53 (Suppl. 1), 127, 1993.
85. Wessels, M., Mason, R.P., Antich, P.P., Zerwekh, J.E., and Pak, C.Y., Connectivity in human cancellous bone by three-dimensional magnetic resonance imaging, *Med. Phys.,* 24, 1409, 1997.
86. Odgaard, A. and Gundersen, H.J., Quantification of connectivity in cancellous bone, with special emphasis on 3-D reconstructions, *Bone,* 14, 173, 1993.
87. Kinney, J.H. and Ladd, A.J., The relationship between three-dimensional connectivity and the elastic properties of trabecular bone, *J. Bone Miner. Res.,* 13, 839, 1989.
88. Cowin, S.C., The relationship between the elasticity tensor and the fabric tensor, *Mech. Mater.,* 4:137, 1985.
89. Zysset, P.K. and Curnier, A., An alternative model for anisotropic elasticity based on fabric tensors, *Mech. Mater.,* 21, 243, 1995.
90. Van Rietbergen, B., Odgaard, A., Kabel, J., and Huiskes R., Relationships between bone morphology and bone elastic properties can be accurately quantified using high-resolution computer reconstructions, *J. Orthop. Res.,* 16, 23, 1998.
91. Kabel, J., van Rietbergen, B., Odgaard, A., and Huiskes, R., The constitutive relationships of fabric, density and elastic properties in cancellous bone architecture, *Bone,* 25, 481, 1999.
92. van Rietbergen, B., Ulrich, D., Kabel, J., and Rüegsegger, P., Estimates in normal versus osteoporotic bone, *Proc. of the 14th European Society for Biomaterials,* 14, OST13, 1998.
93. Rho, J.Y., Ashman, R.B., and Turner, C.H., Young's modulus of trabecular and cortical bone material: ultrasound and microtensile measurements, *J. Biomech.,* 26, 111, 1993.
94. Choi, K., Kuhn, J.L., Ciarelli, M.J., and Goldstein, S.A., The elastic moduli of human subchondral, trabecular and cortical bone tissue and the size-dependency of cortical bone modulus, *J. Biomech.,* 23, 1103, 1990.

95. Choi, K. and Goldstein, S.A., A comparison of the fatigue behavior of human trabecular and cortical bone tissue, *J. Biomech.,* 25, 1371, 1992.
96. Ashman R.B. and Rho, J.Y., Elastic modulus of trabecular bone material, *J. Biomech.,* 21, 177, 1988.
97. Rho, J.Y., Roy, M.E., Tsui, T.Y., and Pharr, G.M., Young's modulus and hardness of trabecular and cortical bone in the various directions determined by nanoindentation, *Proc. 43rd Annu. M. ORS,* 43, 811, 1997.
98. Reilly D.T. and Burstein, A.H., The mechanical properties of cortical bone, *J. Bone Joint Surg.,* 56A, 1001, 1974.

16

Strength of Trabecular Bone

Tony M. Keaveny
University of California

16.1 Introduction

The strength behavior of trabecular bone is integral to musculoskeletal applications such as bone fracture and loosening of bone-implant systems. Since bone remodeling is thought to be stimulated in part by damage, trabecular strength may also have direct biological relevance. The overall goal of this chapter is to describe what is known about the strength properties of trabecular bone and to identify areas where gaps exist in this knowledge. Emphasis is placed on recent theoretical developments in the field, although the earlier foundational work is also summarized. The uniaxial strength properties of trabecular bone are described first, with emphasis on issues such as heterogeneity, anisotropy, and aging. The description of failure properties in terms of strains is also addressed since use of nondimensional measures of loading can greatly simplify mathematical description of the failure properties. Micromechanical modeling is then addressed since this provides an intuitive basis for understanding the empirical data. This is followed by a fairly detailed treatment of the multiaxial failure behavior and its theory. Then, the reloading and damage behaviors are discussed, including descriptions of loading–unloading–reloading behavior and the accompanying mechanical property changes, as well as direct measurements of the underlying physical damage patterns. Finally, there is a section on time-dependent properties, including creep and fatigue. Taken together, this chapter attempts to cover most of what is known about trabecular strength from a mechanics perspective.

16.1.1 Terms and Definitions

Before describing the strength characteristics of trabecular bone, some preliminary comments are appropriate. First, it is important to clarify the terminology used to distinguish between mechanical behavior at the continuum level of the whole specimen—the *apparent properties*—as opposed to those at the level of individual trabeculae—the *tissue properties*. Thus, for example, one talks of apparent vs. tissue modulus for trabecular bone for the whole specimen and trabecular hard tissue, respectively, and the apparent vs. tissue yield strains. Unless noted otherwise, the discussion here will assume the properties are at the apparent level. It has been argued that at least five trabecular characteristic dimensions should exist in the specimen for continuum behavior to be manifested.[1] Thus, test specimens should not be less than about 5 mm in any dimensions, but should be larger if possible. Limitations on producing homogeneity of volume fraction and architecture within the test specimen limit its size, however, as does the relatively small geometry of many metaphyses.

First, even the term *strength* requires some qualification! Typically, this term refers to the stress at which the specimen fails. Failure may be defined by an offset yield point, or, at the maximum load carrying capacity, i.e., the ultimate point. However, strength in some situations may refer to more generic failure of the specimen, which could be characterized by the strain at which the specimen fails. In this discussion, the term *strength* is used generically as the stress at which a specimen fails. Terms such as *failure stress, ultimate stress, failure strain, yield strain* are used, when necessary, to be more specific.

Second, it is essential to appreciate the *heterogeneity* in volume fraction and architecture of trabecular bone (Fig. 16.1). Such heterogeneity, which can be both intra- and interspecimen, makes it difficult to generalize about the elastic and strength properties. As will be seen, however, use of strains and nondimensional measures of stress can overcome many apparent-level, interspecimen heterogeneity issues. The effects of intraspecimen heterogeneity are not well understood, but will be discussed briefly.

Third, the term *architecture* is used to refer to the spatial arrangement of the individual trabeculae, their topology, and geometry. Due to the complexity and heterogeneity of trabecular architecture, and the fact that many indices of architecture are highly correlated with volume fraction,[2–4] it has been difficult so far to characterize architecture in a fashion that successfully explains variations in strength not accounted for by variations in volume fraction. This issue is discussed in more detail below but remains an area that requires further research.

And fourth, since trabecular bone is anisotropic at the apparent level, it is important to distinguish between its behavior in its principal material coordinate system compared with an arbitrary coordinate system. The former is characterized mathematically as when the elastic stiffness matrix is sparse, i.e., that coordinate system for which there is no coupling between the shear and normal elastic behaviors. It has been shown analytically[5] and using high-resolution finite-element models[6] that if the anisotropy of the trabecular hard tissue is ignored—a reasonable assumption since the individual trabeculae are loaded mostly uniaxially—the principal material coordinate system of elastic anisotropy at the apparent level coincides with the principal microstructural coordinate system of the trabecular network as derived from the fabric tensor. For simplicity of nomenclature, the term *on-axis* is used here to describe the situation when loading is along the main trabecular orientation, and *off-axis* refers to when loading is oblique to this. On-axis elastic and strength properties for orthotropic or higher symmetry materials are considered as the inherent material properties since the off-axis properties (except for those at 90° off-axis) depend on both the on-axis properties and the angles of misalignment between the on- and off-axis coordinate systems. Thus, the strength properties of primary interest from a constitutive modeling perspective are those measured in the on-axis coordinate system.

16.2 Uniaxial Properties

16.2.1 Heterogeneity, Anisotropy, and Asymmetry

The strength of trabecular bone depends on volume fraction, architecture, and the tissue material properties, in that order of importance. Since volume fraction and architecture depend so much on anatomic site, species, age, and pathologies such as osteoporosis, there is tremendous variation in trabecular bone

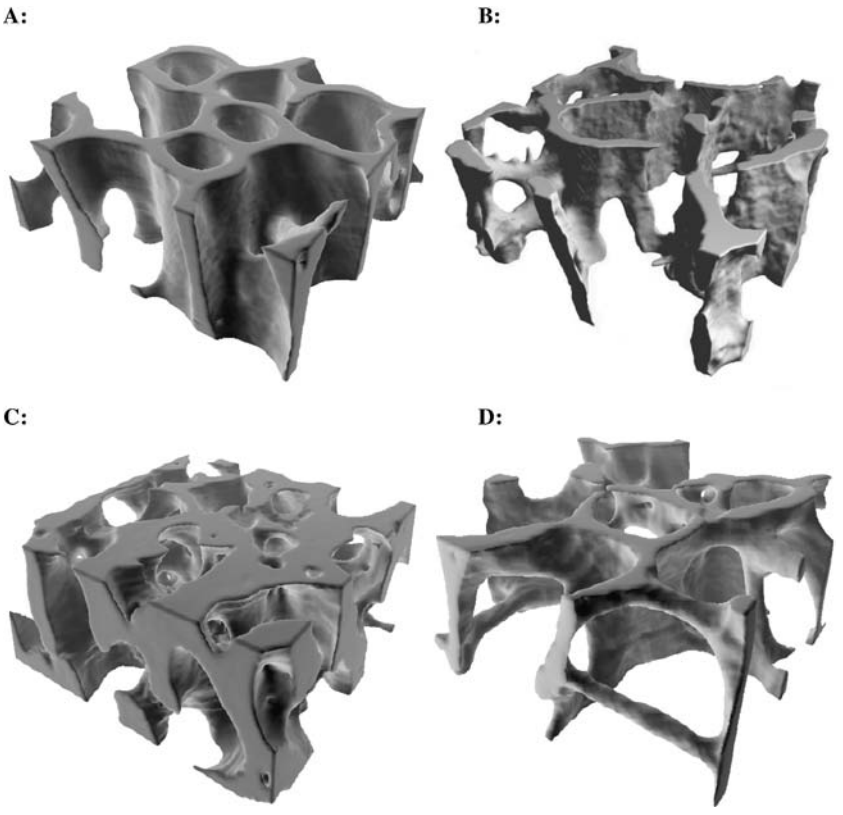

FIGURE 16.1 Volume rendering (20 micron resolution) of bovine proximal tibial (A), human proximal tibial (B), human femoral neck (C), and human vertebral (D) tradecular bone. All specimens have the same bulk dimensions ($3 \times 3 \times 1$ mm^3) and have the main trabecular orientation aligned with the vertical axis. Note the different volume fractions and architectures. The vertebral bone has a strong rod-type architecture whereas the bovine tibial bone is more plate type; the other two types of bone are not so easily classified.

failure stresses. Mean values per site for human bone can vary threefold from as low as about 2 MPa in the vertebral body[11–12] to over 7 MPa in the distal femur (Table 16.1).[7–9] Other sites such as the bovine proximal tibia when loaded on-axis can have average strengths of over 23 MPa.[10] Regarding the effects of aging (Fig. 16.2), ultimate stress is reduced by an average of almost 7% per decade for the human proximal femur from ages 20 to 100, due mostly to decreases in volume fraction,[3] and by almost 11% per decade for vertebral bone over a similar age range.[11,12] Age effects, particularly changes in strength in the transverse loading direction, can be accentuated for females at about age 50,[13] due presumably to hormonal changes associated with menopause. For the human proximal tibia, highest strength has been reported to occur between ages 40 and 50 years.[14] Indeed, similar trends are observable also for the spine, where, despite an average linear decrease of strength from age 20, maximum values of strength occurred in those specimens in the age range 30 to 40.[11,12] Thus, realizing that age is not the sole explanatory variable for observed strength variations ($r^2 = 0.50$ to 0.65), it appears that strength does not decrease in any significant manner until after about age 30, perhaps even later depending on site.

Because trabecular bone is anisotropic, strength also depends on the orientation of the specimen with respect to the loads. Interestingly, this dependence can also change with aging, reflecting changes in density and architecture. For example, the compressive strength anisotropy ratio (defined as the ratio of longitudinal to transverse compressive strengths) for human vertebral trabecular bone increases from about 2.1 at age 20 (high density) to 3.4 at age 70 (low density).[11] A series of studies on bovine tibial bone,[10,15,16] which has a much more plate-type architecture than the human vertebral bone (see Fig. 16.1),

TABLE 16.1 Mean Values (S.D.) of Wet Apparent Density, Elastic Modulus, and Compressive Ultimate Properties for Human Trabecular Bone Specimens Taken from a Range of Anatomic Sites

Study	Cadavers No.	Cadavers Ages	Specimens, No.	Density (g/cm^3)	Modulus (MPa)	Ultimate Stress (MPa)	Ultimate Strain (%)
Proximal tibia							
Linde et al.[7a]	9	59–82	121	0.29 (0.10)	445 (257)	5.33 (2.93)	2.02 (0.43)
Femur							
Lotz et al.[8b]	4	25–82	49	—	441 (271)	6.76 (4.84)	—
Rohlmann et al.[9a,e]	10	58–83	299	0.50 (0.16)	389 (270)	7.36 (4.00)	—
Lumbar spine							
Mosekilde et al.[12a]	42	15–87	40	0.24 (0.07)	67 (44)	2.45 (1.52)	7.40[e]
Kopperdahl and Keaveny[20d]	11	32–65	22	0.17 (0.04)	291 (113)	2.23 (0.95)	1.45 (0.33)

Note: Typical ranges can be estimated as about ±2 S.D. about the mean. Note the wide variation in some properties across sites, but more surprisingly within sites (across different studies). The latter is probably due to differences in measurement techniques including the presence of end artifacts, different definitions of modulus, and differences in populations. These parameters should be carefully considered when interpreting the literature. All mechanical data from tests with specimens oriented in the inferior-superior direction, unless noted.

—Data were noted reported.

[a]The dry or ash densities that were originally reported have been converted to wet densities.

[b] Proximal femur only, specimens were oriented along the femoral neck axis.

[c] Proximal and distal femur pooled; proximal specimens oriented approximately along the femoral neck axis.

[d] End artifacts were minimized, accounting for the relatively high values of modulus and low values of ultimate strain.

[e] A standard error of 0.002% was reported.

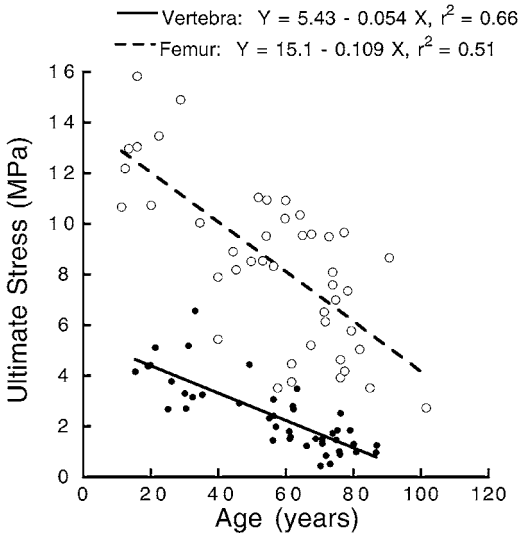

FIGURE 16.2 Dependence of compressive strength on age for human vertebral[11] and distal femoral[3] trabecular bone cores. From the regression models, it is seen that average strength is reduced 47% from 12.92 to 6.83 MPa from ages 20 to 80, respectively, for the femur, with corresponding values of 4.35 and 1.11 MPa for the vertebra, a 74% decrease. Over these 7 decades, this represents average strength loss of 6.7 and 10.6% per decade for the femur and vertebra, respectively. Redrawn, with permission, based on data from Mosekilde and Mosekilde, *Bone,* 7, 207–212 (1986) and McCalden et al., *J. Bone Joint Surgery,* 79-A, 421–427 (1997).

TABLE 16.2 Apparent Yield Stress (σ_y in MPa) vs. Apparent Density (ρ in g/cm^3) Empirical Power Law Functions for Tensile, Compressive, and Shear Loading, Each for Longitudinal and Transverse Loading

Direction	Loading Mode	Sample Size	Strength Variable[a]	$\sigma_{yi} = a_i \rho^{b_i}$		
				a_i	b_i	r^2
Longitudinal	Compression	20	σ_{y1}^C	−86.4	1.99	0.83
	Tension	20	σ_{y1}^T	46.9	1.68	0.95
	Torsion	25	σ_{y4}	10.1	1.30	0.62
Transverse	Compression	27	σ_{y2}^C	−22.4	2.58	0.80
	Tension	24	σ_{y2}^T	10.8	1.59	0.74
	Torsion	23	σ_{y5}	7.4	1.58	0.68

Note: These equation are from experiments on 139 specimens of bovine proximal tibial trabecular bone tested without end artifacts in the principal material coordinate system. Longitudinal direction specimens were tested with the long axis of the cylindrical specimen orientated parallel to the principal trabeuclar orientation; transverse direction specimens were perpendicular to this orientation.

[a] This nomenclaure is used in Eq. 16.16.

Source: Keaveny, T. M. et al., *J. Biomech. Eng.*, 121, 99–107, 1999. With permission.

provide data (Table 16.2) that can be used to show how the strength anisotropy–density relation depends on both density and loading mode (tension vs. compression vs. shear, Fig. 16.3). Specifically, the strength anisotropy ratio varies from about 2 to 10 across a typical range of densities, being higher for lower-density bone, greatest for compression, and least for shear. Such data are not currently available for human bone for any site. It is cautioned that extrapolation of the bovine-based data to various human sites may not be valid because of substantial differences in architecture between the sites.

The shear strength of trabecular bone is relatively low compared with its compressive and tensile strengths.[16] The ratio of axial to shear strength increases with increasing density. For example, the empirical strength–density relations in Table 16.2 indicate that the ratio of longitudinal tensile to shear strengths for bovine tibial bone increases from 2.5 at an apparent density of 0.20 g/cm^3 to about 3.8 at a density of 0.60 g/cm^3. For comparison purposes, the ratio of tensile to shear strengths for a von Mises yielding material is 1.73. Thus, trabecular bone, compared with a von Mises material, is particularly weak in shear.

When all these findings are considered together, it is clear that the failure (yield and ultimate) stresses of trabecular bone vary substantially with anatomic site and age—reflecting underlying variations in volume fraction and architecture—and loading direction. Trabecular strength is therefore heterogeneous, anisotropic, and asymmetric (different between tension and compression). It follows then that a simple question such as "what is the strength of trabecular bone?" is overly vague since one cannot provide a precise answer without first specifying factors such as the anatomic site, age, species, loading direction, and loading mode.

16.2.2 Strength–Density Relations

The precise relationship between the yield or ultimate stress of trabecular bone vs. apparent density or volume fraction remains an open question. The most common relation used is from the early work of Carter and Hayes:[17]

$$\sigma_{\text{ult}} = 68 \dot{\varepsilon}^{0.06} \rho^2 \tag{16.1}$$

where σ_{ult} is ultimate stress (in MPa), ρ is apparent density (in g/cm^3), and $\dot{\varepsilon}$ is strain rate (in s^{-1}). This equation was developed to describe the strength of pooled cortical and trabecular bone specimens. Statistical analysis of pooled literature data for only trabecular bone but from many sites subsequently found that a squared relationship worked best,[18] supporting the power law model. However, it is currently not known if this relationship depends on anatomic site. For human bone, the reported strength–density relationships do not vary tremendously across sites (Table 16.3).[7,8,11,19,20] However, differences in architecture that can occur for the different density ranges do have an effect on the

TABLE 16.3 Power Law Regression between Ultimate Stress (σ in MPa) and Wet Apparent Density (ρ in g/cm^3) for Compressive Loading of Human Trabecular Bone Specimens Loaded at "Low" Strain Rates ($\leq$ 1.0/s) and Taken from a Range of Anatomic Sites

	Cadavers			$\sigma = a\rho^b$		
Study	No.	Age	Specimens, No.	a	b	r^2
Proximal tibia						
Linde et al.[7]	9	59–82	121	23.7	1.56	0.79
Proximal femur						
Lotz et al.[8]	4	25–82	49	25.0	1.80	0.93
Lumbar spine						
Hansson et al.[19]	3	71–84	231	50.3	2.24	0.76
Mosekilde et al.[12]	42	15–87	40	24.9	1.80	0.83
Kopperdahl and Keaveny[20a]	11	32–65	22	33.2	1.53	0.68

Note: See Table 16.1 for legends.
[a] 0.2% offset yield stress is reported instead of ultimate stress since the latter was not measured.

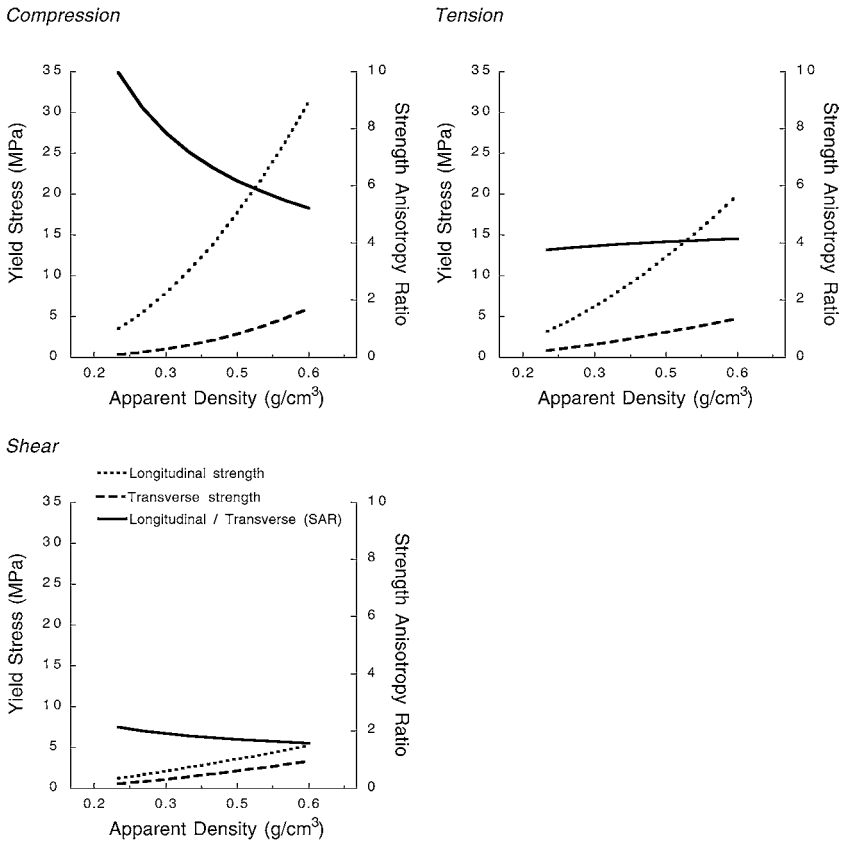

FIGURE 16.3 Yield stress for longitudinal vs. transverse loading, and their ratio (SAR), plotted as a function of apparent density for three different loading modes (compression, tension, and shear). The curves, derived from the data shown in Table 16.2 for bovine tibial trabecular bone, demonstrate the complexity of the strength properties of trabecular bone. Strength (dashed lines) always increases with increasing density and depends critically on loading direction and mode. The strength anisotropy ratio (solid lines) varies from approximately 2–10. It, too, depends on density and loading mode, being greatest for compression and least for shear.

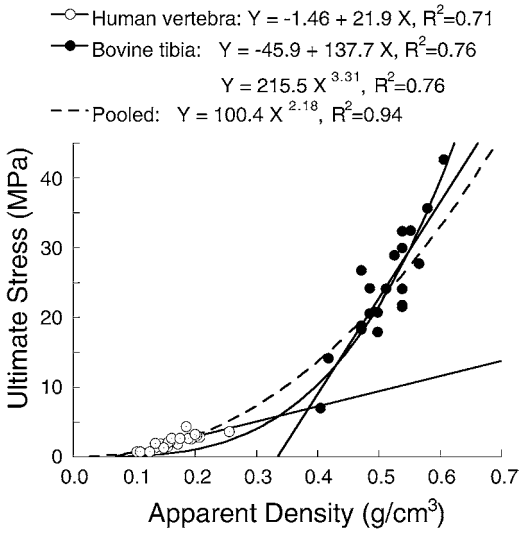

FIGURE 16.4 Compressive on-axis ultimate stress for human vertebral and bovine tibial trabecular bone, plotted as a function of apparent density. For each site, a linear regression model fits the data well. A power model for the bovine tibia is also shown (exponent = 3.31, solid line) and works about the same as the linear model over the range of data. Since the slope for the linear regression model for the bovine tibial bone is over six times that for the vertebral bone, extrapolation of such models across sites is not valid. Interestingly, a power law model (exponent = 2.18, dashed line) fits the pooled data well in terms of R^2 value, but is different than for any one of the sites. These data were obtained from experiments described in the literature.[10,20]

strength–density relationship. For example, if the on-axis strength–density relation for human vertebral bone, which has a mostly rod-type architecture, is extrapolated to sites of higher density such as the bovine tibia, which is very platelike, substantial errors can result (Fig. 16.4).

So, the question arises regarding what type of relationship between strength and density should be used. The definitive study on the effects of site on the strength–density relationship has not been reported. Such a study would need to eliminate orientation effects by ensuring all specimens are loaded to failure on-axis; otherwise, intersite differences, or similarities, will be confounded by misorientation effects, which may not reflect true architecture effects. In the meanwhile, it is this author's opinion that for a specific site, a linear or power law model can be used, since typically the predictive power of these models is similar in this circumstance (see Fig. 16.4). For multiple sites, care must be taken to avoid extrapolation errors. In such circumstances, it appears that a power law model, fit to the pooled data, is most appropriate. Even so, it is recommended to use a site-specific model, if available, for those situations where analysis is confined to a single site.

One issue related to the strength–density relation is the inference of microstructural failure mechanisms from the apparent level test results. Based on arguments from cellular solid theory[21–23] (see Section 16.2.5.1 below for more details), it is expected that the microstructural mechanisms of deformation and failure of the individual trabeculae can be different between off-axis and on-axis loading depending on the architecture of the specimen. These mechanisms determine both constants in the power law relation. Also, if tested off-axis, the resulting properties do not reflect the inherent (on-axis) properties. Thus, since trabecular orientation has not been controlled in many previous experiments, most power law relations reported thus far provide only limited insight into possible failure and deformation mechanisms for on-axis loading. Besides its importance for providing a basis for anisotropic constitutive relations, on-axis behavior may be most relevant to the study of bone adaptation and "normal" behavior since, by way of Wolff's Law, it is generally accepted that, for habitual loading, stresses are oriented primarily along the principal material coordinate directions.[24–26]

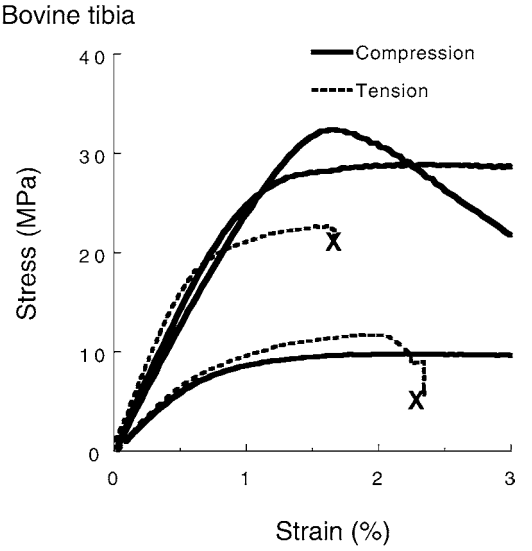

FIGURE 16.5 Stress-strain curves for compressive and tensile loading to failure of five bovine trabecular bone specimens. Loading was stopped at 3% strain, but fractures occurred earlier for the tensile specimens as denoted by the X. This behavior illustrates that for high stiffness specimens, the bone is markedly stronger in compression, whereas for lower stiffness specimens, the bone has about the same strength in tension and compression. Similar behavior occurs for human bone. (From Keaveny et al., *J. Biomech.,* 27, 1137–1146, 1994. With permission.)

16.2.3 Tensile vs. Compressive Strengths

One fundamental issue that has been somewhat controversial in the literature but which now appears to be resolved is the difference between the tensile and compressive strengths for trabecular bone. By contrast to the large post-yield region that exists in the stress–strain curve for compressive loading, the post-yield region for tensile loading is small (Fig. 16.5). Thus, the load-carrying capacity of trabecular bone is negligible after tensile fracture, whereas it is substantial after compressive fracture. The issue of whether the bone is stronger in tension vs. compression, however, has been less clear.

Up through 1991, one peer-reviewed study had concluded that the tensile and compressive strengths were equal,[27] two that the compressive strength was higher,[28,29] and one that the tensile strength was higher.[30] Then, a study on bovine bone,[10] performed with all specimens in the on-axis configuration and using the same testing techniques for both loading modes that eliminated end artifacts, demonstrated that the difference between the tensile and compressive strengths increased in a linear fashion with increasing modulus (Fig. 16.6), such that at low modulus there was a negligible difference between the tensile and compressive strengths, and at high modulus the difference was large. A similar trend has since been reported for low-density human vertebral bone,[20] suggesting that this modulus-dependent strength asymmetry is a general characteristic of trabecular strength behavior.

As will be discussed next, however, such complexity in description of the strength asymmetry can be eliminated if strains are used to describe the failure characteristics. This is because the modulus-dependent asymmetry is simply a reflection that the yield strains are higher in compression than tension, and that they are generally independent of modulus within an anatomic site. In that case, the approximate difference between the tensile and compressive yield stresses $\Delta\sigma_y$ can be expressed as a linear function of modulus E as follows:[10]

$$\Delta\sigma_y = \sigma_y^C - \sigma_y^T = E(\varepsilon_y^C - \varepsilon_y^T) = E\Delta\varepsilon_y \tag{16.2}$$

where the subscripts refer to compression (C) and tension (T), E is the elastic modulus (which is

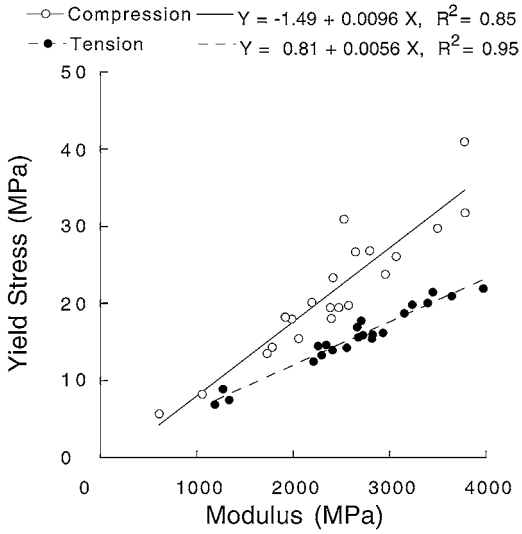

FIGURE 16.6 Yield stress vs. modulus for bovine tibial trabecular bone, loaded in an on-axis configuration without end-artifacts in either tension or compression. These data demonstrate that tension-compression strength asymmetry for trabecular bone increases with increasing stiffness. (From Keaveny et al., *J. Biomech.,* 27, 1137–1146, 1994. With permission.)

the same for tensile and compressive loading), and ε_y is the yield strain, which is independent of modulus.

16.2.4 Failure Strains

Perhaps one of the most important characteristics to emerge in trabecular bone strength biomechanics is the relative homogeneity of yield strains despite substantial variations in volume fraction and architecture. As a consequence of the similarity between the modulus–density and strength–density relationships, there have been many reports of strong linear relationships between compressive strength and modulus.[10,31–38] These findings indicate that stiffer trabecular bone is also proportionally stronger, implying that a major parameter controlling failure in trabecular bone (at the apparent level) is the maximum level of apparent strain. This concept now has broad support from experiments showing that the yield (or ultimate) strain of trabecular bone has only a weak dependence, if any, on apparent density.[10,20,30,35,38–42]

Since accurate measurement of strains for trabecular bone is difficult due to the presence of end artifacts,* rigorous testing of the hypothesis of homogeneity of yield strains has only been done recently. By comparing bovine tibial vs. human vertebral bone loaded in the on-axis configuration, it was found that tensile yield strains were statistically similar across both sites, but that compressive yield strains were higher for the bovine bone (Fig. 16.7).[10,20,30,35,38–42] Preliminary reports on analysis of yield strains for a variety of human sites indicate that both on-axis tensile and compressive failure strains can depend on site.[49] However, the scatter within sites was small, as evidenced by standard deviations on the order of only one tenth of the mean. Thus, while failure strains are heterogeneous across sites, within a single site they tend to be homogeneous. Demonstrating the significance of these findings, use of such an intrasite homogeneous yield strain failure criterion worked well for finite-element prediction of compressive failure of 10-mm-thick, full sagittal slices ($n = 18$) of the human vertebral body.[50]

*Correct measurement of strain requires the elimination of end artifacts.[34,43–48] Thus, appropriate testing techniques should be used for studies on yield and ultimate strains for trabecular bone or else substantial random and systematic errors[46,48] can be introduced that can obscure real behavior. See Chapter 7 for more details on experimental testing techniques.

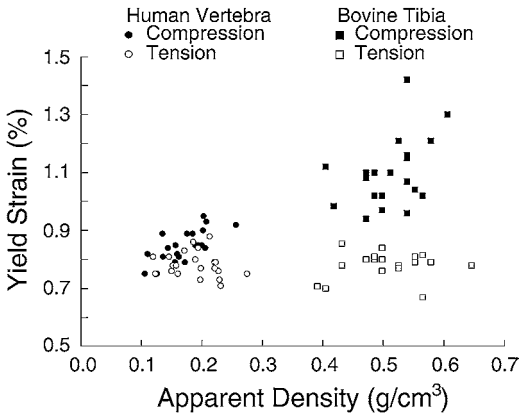

FIGURE 16.7 Dependence of yield strain on apparent density for human vertebral and bovine tibial trabecular bone, for tensile (open symbols) and compressive (solid symbols) on-axis loading. Note the small range on the scale of the vertical axis. In tension, the yield strain did not depend on anatomic site or density, whereas in compression it did. Further, in compression there were trends of increasing yield strain with increasing density and mean values were different between the two sites. (Adapted from Kopperdahl and Keaveny, *J. Biomech.,* 31, 601–608, 1998. With permission.)

The issue of isotropy of yield strains is also of interest. Turner[35] found no significant relation between compressive yield strain and a fabric tensor-based measure of trabecular orientation for bovine distal femoral bone. These findings suggested that yield strains for trabecular bone are isotropic. However, all specimens in that study were in the off-axis configuration such that the potentially high sensitivity of failure strain to orientation near the on-axis configuration was not explored. By contrast, Mosekilde et. al.[11] concluded that on-axis compressive ultimate strains were anisotropic for human vertebral bone. However, end artifacts in that study may have compromised the accuracy of the failure strain comparisons. Using testing techniques designed to eliminate such artifacts, Ford and Keaveny[16] found only slight anisotropy of shear yield strains for bovine tibial trabecular bone. A more recent study on bovine tibial bone was then designed to test the isotropy hypothesis explicitly.[51] Different groups of specimens were tested to failure in on-axis or off-axis configurations, in uniaxial tension or compression. The results established that the yield strains for this type of bone were indeed isotropic (Fig. 16.8). However, since bovine tibial trabecular bone is of high density and has a strong plate-type, anisotropic architecture, additional experiments are required to extend these findings to human bone, which is typically lower density and more rod-type. Understanding the phenomenon of homogeneity and isotropy of failure strains from a structure–function perspective is important since it may hold a key to understanding the development and adaptation of trabecular microstructure.

16.2.5 Micromechanical Modeling

Although there are now many data available describing empirical relations between the strength properties of trabecular bone and various explanatory variables, to understand the *mechanisms* of these relationships some type of model is required. The need for improved mechanistic understanding of the latter is particularly timely since the role of architecture on the failure strains and strength–density relations is not understood and yet this issue is at the core of important clinical problems such as osteoporosis, as well as basic biological issues such as bone formation and adaptation. For example, if architecture–mechanical property relations that are independent of density can be identified under controlled *in vitro* conditions, then the specific architecture parameters thus identified might be effective clinically in screening weak bone. The corollary may also be helpful since it would signal the futility of attempting to find clinically relevant architectural parameters that are independent of bone density.

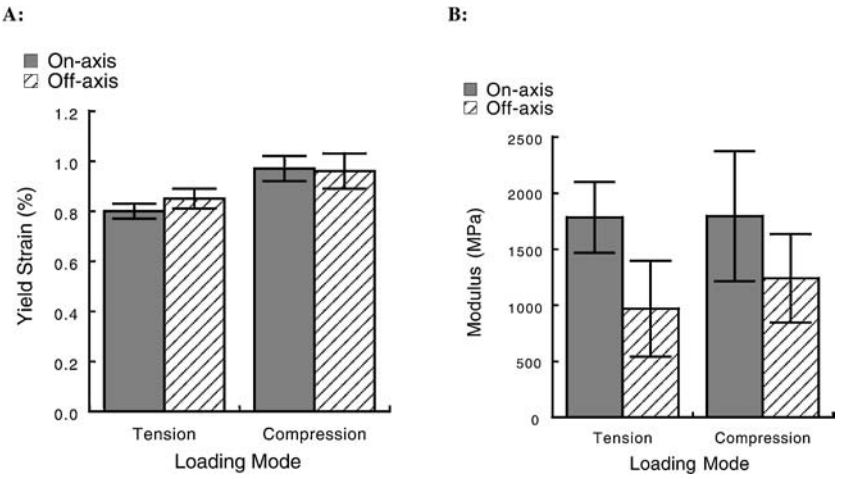

FIGURE 16.8 Isotropy of uniaxial yield strains for bovine tibial trabecular bone (error bars show ±1 S.D.). Specimens were tested in uniaxial tension or compression, and were prepared with the main trabecular orientation either parallel with the cylindrical specimen axis (on-axis) or 30–40° oblique to this (off-axis). (**A**) yield strains; and (**B**) corresponding moduli. Statistically, the yield strains did not depend on orientation but did depend on loading mode. The modulus data confirm the substantial elastic anisotropy of the bone tested. (From Chang et al., *J. Orthop. Res.,* 17, 582–585, 1999. With permission.)

Three mechanistic approaches are reviewed here: one based on relatively simple analytical and highly idealized geometric "cellular solid" models; another on a class of lattice-type finite-element models that are based on the cellular solid paradigm; and a third on much more complex computational "high-resolution" finite-element models that include detailed descriptions of the trabecular microstructure.

16.2.5.1 Cellular Solid Theory

Closed-form cellular solid analysis is an established engineering theory (see Gibson and Ashby's book[52] for a comprehensive treatment) that has provided substantial insight into the uniaxial failure properties of trabecular bone.[20–23,35] These simple analytical models, first proposed by both Gibson[21] and Rajan[22] for trabecular bone, can be used to explain why strength (and modulus) of the whole specimen should vary with apparent density (or volume fraction) by either a power law or linear relationship. Depending on the structure and loading direction, individual trabeculae are assumed to deform primarily axially or in bending, and to fail by either elastic buckling or formation of plastic hinges, or in a brittle manner. Strength can vary with volume fraction from a power of 1 to 3, depending on the cell geometry, failure mechanism, and loading direction. As will be shown below, the theory also establishes the effects of architecture and tissue material properties, and identifies interactions between architecture and volume fraction.

At the basis of cellular solid theory is the assumption that the continuum-level behavior reflects that of a sufficiently large number of identical repeating unit cells at the microstructural level. The apparent level behavior can therefore be derived by analysis of just a single unit cell. Relations can be derived between either apparent modulus and strength (or failure strain) vs. volume fraction, quantitative measures of architecture, and the tissue material properties (of the unit cell material). For the derivation presented here, each cell is assumed to have a hexagonal shape, but other shapes can just as easily be assumed (Fig. 16.9). The analysis will be restricted to two-dimensional "honeycombs," as opposed to three-dimensional "foams," although the two are conceptually equal.

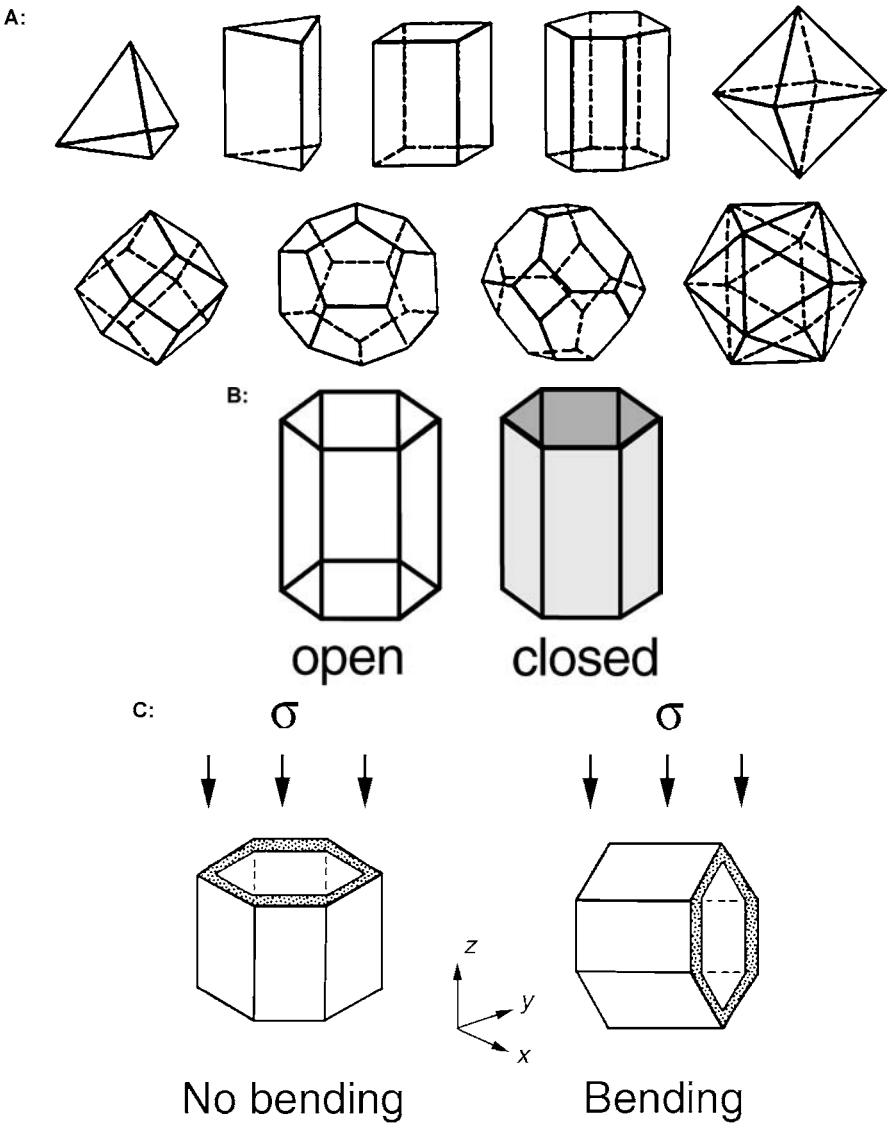

FIGURE 16.9 (A) Various three-dimensional geometries for the unit cell in cellular solid analysis. (B) Cells can be open or closed, depending on whether the walls are solid or hollow. The former results in a plate type structure, while the latter is more rod type. (C) A structure can be loaded so as to produce only axial loading without any bending, or, to cause bending of obliquely oriented struts. A derivation for the latter is included in the text. ((A) Adapted from Gibson, L. J. and Ashby, M. F., *Cellular Solids: Structures* & *Properties,* 2nd ed., Oxford, Pergamon, 1997. With permission.)

The overall derivation has three parts. First, the apparent-level external loads are related to the internal loads acting on each strut of the unit cell. The case is considered here where the apparent loads are aligned parallel to the vertical direction of the hexagon as shown in Fig. 16.9c. Taking a free body analysis of a sectioned cell (Fig. 16.10), it is seen that the vertical force equivalent of the external apparent stress σ must be equilibrated internally by the total axial force $2P$ in each vertical strut, such that $P = \sigma bL\cos\theta$, where L is the length of the oblique strut, b its thickness (into the page), and θ is its angle with respect to the horizontal. Moment equilibrium for an entire oblique strut and symmetry dictates that the internal

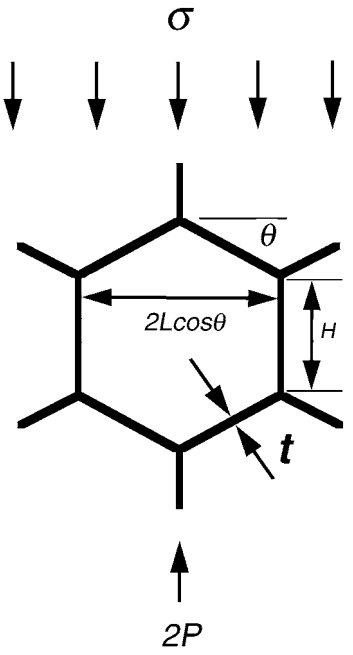

FIGURE 16.10 Hexagonal unit cell exposed to an external apparent level stress σ in the axial direction. L is the length of the oblique strut, θ its angle with respect to the horizontal, and t its thickness in the plane of the hexagonal. H is the length of the vertical strut. The force $2P$ is the total internal axial force on the vertical strut, i.e., along the direction of the applied external stress. This force must equilibrate the apparent stress σ over the equivalent area of the unit cell, given by the product of $2L\cos\theta$ and the thickness b of the unit cell into the page (not shown).

bending moment M at the end of each strut is the same, and has a value given by $M = (PL\cos\theta)/2$. This value also represents the maximum bending moment in the strut.

Second, the deformations due to these internal loads are found for each strut. Since it is commonly assumed for these analyses that the deformation of the vertical struts is negligible compared to that from bending of the oblique strut, only the latter is included in the derivation (the geometric conditions for which these assumptions are most reasonable are discussed elsewhere[52]). Simple beam theory is then used to calculate these deformations. The axial force P acting on each oblique strut is resolved into components along and transverse to the strut. Again, deformations due to the former are neglected. The deflection δ_P from the transverse component of the axial force acting on each oblique strut is obtained from elementary strength of materials as

$$\delta_P = \frac{PL^3\cos\theta}{3E_tI}, \tag{16.3}$$

where E_t is the tissue modulus, and I the areal moment of inertia of the strut. This deflection is transverse to the strut axis. Similarly, the internal bending moment causes a deflection of the oblique strut in the opposite direction, given by

$$\delta_M = \frac{PL^3\cos\theta}{4E_tI}. \tag{16.4}$$

The net deflection transverse to the strut is therefore given by

$$\delta = \frac{PL^3\cos\theta}{12E_tI} = \frac{\sigma bL^4\cos^2\theta}{12E_tI}. \tag{16.5}$$

The third part of the derivation is to calculate the apparent-level strains from these deformations, and from that, the apparent modulus. The gauge length for strain calculation per hexagonal cell is $L\sin\theta + H$, where H is the length of a complete vertical strut. The component of strut deformation in the direction of the apparent load is $\delta\cos\theta$. Thus, for the closed-cell hexagonal structure shown in Fig. 16.9c (where $I = bt^3/12$, t = strut thickness), the axial strain is

$$\varepsilon = \frac{\sigma L^4\cos^3\theta}{E_tt^3(H + L\sin\theta)}. \tag{16.6}$$

Dividing the apparent level stress σ by this quantity gives the following expression for the apparent modulus:

$$E = E_t\left\{\frac{t}{L}\right\}^3\left\{\frac{H/L + \sin\theta}{\cos^3\theta}\right\}. \tag{16.7}$$

Most interestingly for a clinical biomechanics perspective, this expression can be expressed in terms of volume fraction, architecture, and tissue material properties. It can be shown by simple geometric analysis (accounting for all shared struts between neighboring unit cells) that the volume fraction of bone tissue for the closed-cell hexagonal is given by

$$V_f = \left\{\frac{t}{L}\right\}\left\{\frac{H/L + 2}{(H/L + \sin\theta)2\cos\theta}\right\}. \tag{16.8}$$

It follows then that the apparent modulus is given as

$$E = V_f^3a_1E_t, \tag{16.9}$$

where

$$a_1 = \frac{8(H/L + \sin\theta)^4}{(H/L + 2)^3}$$

This equation explicitly describes the relationship between an apparent mechanical property (modulus, E) and each of volume fraction (V_f), architecture (denoted by the parameter a_1), and tissue material properties (tissue modulus, E_t). In this particular example, volume fraction is raised to the third power, and the architectural parameter a_1 is a nonlinear function of the length ratio of the vertical to oblique struts as well as their relative angle. For other cell geometries, these characteristics would change, with powers ranging from 1 to 3 for the dependence on volume fraction and a variety of different architectural relations.

A number of different failure mechanisms can be assumed for any given cell geometry, such as Euler buckling, plastic yielding, or brittle fracture. The case of plastic yielding is considered here for the closed-cell hexagonal structure, where the tensile and compressive strengths of the tissue are assumed to be different, just as with cortical tissue.[53] Even for this assumed failure mode, there are two possible dominant failure mechanisms: yielding of either the vertical or the oblique struts. For the former, tissue-level yielding will occur when the axial force $2P$ in the vertical strut equals its load-carrying capacity, i.e., when $P = \sigma_{y-t}^Tbt/2$, where $\sigma_{y-t}^T(\sigma_{y-t}^C)$ is the tensile (or compressive) yield stress of the trabecular tissue. Relating P to the apparent-level stress, and expressing the result in terms of volume fraction V_f and an architectural

parameter a_2 leads to the following expression for the tensile and compressive apparent-level strengths (subscripts *pl* and *vert* denote assumed plastic yielding and failure within the vertical struts, respectively):

$$\sigma^T_{\text{pl}-\text{vert}} = V_f a_2 \sigma^T_{y-t}; \qquad \sigma^C_{\text{pl}-\text{vert}} = V_f a_2 \sigma^C_{y-t}, \qquad \text{where} \quad a_2 = \left(\frac{H/L + \sin\theta}{H/L + 2}\right). \tag{16.10}$$

In this case, it is seen that the strength is directly proportional to volume fraction, and the architectural parameter a_2 is different from that for elastic modulus.

Consider now the situation where failure is assumed instead to be dominated by yielding of the oblique struts. It is commonly assumed that the compressive or tensile component of axial loading along each oblique strut produces small stresses compared with those from bending. Thus, failure is analyzed for the case of combined transverse end loading and pure bending of the oblique struts. It is further assumed that apparent failure occurs only when all material in the strut cross section has failed. Since the tensile and compressive strengths of the tissue are assumed to be different (stronger in compression), the position of the neutral axis is no longer along the centroidal axis for full yielding. By using the condition that the resultant of all axial stresses in the strut is zero for pure bending, the location of the neutral axis from the centroid is given by

$$\hat{y} = \frac{t}{2}\left(\frac{1-c}{1+c}\right), \tag{16.11}$$

where c is the ratio of the magnitudes of the compressive to tensile strengths of the tissue ($c > 1$ represents tissue that is stronger in compression, and results in a displacement of the neutral axis up to the compressive stress side of the strut, denoted here by a positive value of $\hat{y}$). Let M_{pl} be the moment on the strut when it reaches a state of full yielding through the cross section. By equilibrium, this moment must equal the integral of the first moment of the stresses across the beam cross section. Relating this moment to the apparent level stress at failure, and substituting for volume fraction as described above, the following expression results (subscript *oblq* denotes failure within the oblique struts):

$$\sigma_{\text{pl}-\text{oblq}} = V_f^2 a_3 \left\{\frac{2}{1+c}\,\sigma^T_{y-t}\right\}, \qquad \text{where} \qquad a_3 = 2\left(\frac{H/L + \sin\theta}{H/L + 2}\right)^2 \tag{16.12}$$

In this instance, apparent strength is proportional to the square of the volume fraction, the architectural parameter is again different than those for the other cases, and the tissue material property term contains the parameter c that describes the tissue strength asymmetry. Note, however, that the strength for this case is the same for apparent tensile and compressive loading since failure is assumed to be due to bending at the microstructural level and it does not matter if the struts bend up or down (this may not be true for large deformations, but that case is not considered here). Recall also that this analysis did not account for the axial stresses that develop due to the action of the component of P that acts along the length of the strut. If that component is large, the resulting axial stress could be large, thus influencing the apparent strength asymmetry.

Finally, one can derive an expression for the strain at failure simply as the ratio of the failure stress to the modulus. Thus, if failure is assumed to occur by plastic yielding of the oblique struts, the corresponding apparent level failure strain is given by

$$\varepsilon_{\text{pl}-\text{oblq}} = V_f^{-1/3}\left\{\frac{a_3}{a_1}\right\}\left\{\frac{2}{1+c}\,\varepsilon^T_{y-t}\right\}, \tag{16.13}$$

where $\varepsilon^T_{y-t} = \sigma^T_{y-t}/E_t$ is the tissue tensile yield strain. Here, it is seen that the dependence on volume fraction is weak, there remains a dependence on architecture, and the tissue material properties still contain a term related to the tissue strength asymmetry.

By using this approach, relations between either failure stresses or strains vs. volume fraction, architecture, and tissue properties can be derived for different types of assumed unit cell geometries for a variety of assumed failure modes. While these simple models do not account for the complex architecture of trabecular bone, they nevertheless provide a basic, intuitive understanding of possible deformation and failure mechanisms for individual trabeculae. For example, experiments on bovine tibial trabecular bone when loaded on-axis to failure demonstrated that the apparent modulus was related to apparent density by an approximately linear relationship, and that the apparent yield strains were independent of modulus but were higher in compression than tension.[10] These trends are predicted by a cellular solid model that has minimal bending when loaded (Fig. 16.9c), and for which the failure occurs by some form of plastic yielding with the strut material being stronger in compression than tension. The implication is that bending of trabeculae may not dominate failure of this type of trabecular bone when loaded on-axis. As usual, one must be careful not to extrapolate these mechanisms to other architecture types and to other loading conditions since it is well conceivable that bending of trabeculae would not be negligible in all situations.

Two additional points are worth emphasizing based on these closed-form solutions. First, the combined experimental data and cellular solid analysis for the bovine tibial bone imply that in order for there to be asymmetry of apparent yield strains, tensile-compressive strength asymmetry must exist at the tissue level.[10,23] Second, the relations for both volume fraction V_f and architecture a_i ($i = 1$ to 3), expressed as functions of the direct physical characteristics of the specimen, e.g., length, thickness, and orientation of the struts, demonstrate that architecture and volume fraction are inherently related to each other by way of their dependence on these underlying parameters. Thus, it may be difficult to find architectural parameters empirically for trabecular bone that are truly independent of volume fraction. The cellular solid theory is instructive in providing equations that identify these interactions.

16.2.5.2 Lattice-Type Finite-Element Modeling

Clearly, the cellular solid analytical models are overly simplistic since they do not account for the irregular geometry of real trabeculae. To account for some of this geometric complexity and yet maintain the simplicity that allows development of an intuitive understanding of the system, generic finite-element models (Fig. 16.11) have been developed using the paradigm of the cellular solid as the structural framework.[54–62] Results from these analyses are briefly reviewed here, with emphasis on those that have addressed strength.

To describe the trabecular geometry in a generic sense, one strategy has been to incorporate the salient features of the trabecular architecture based on published histomorphometric studies. In one such approach, Jensen et al.[58] assembled an irregularly spaced lattice of beam elements to represent vertebral bone. The mean thickness and spacing of each trabecular element was determined from age-related regressions,[63] and separate values were determined for vertically and horizontally oriented trabeculae. Nodes of the lattice were then randomly perturbed to better represent varying angular orientations and spacing. Yeh and Keaveny[62] extended this approach by including intraspecimen variations in trabecular thickness (Fig. 16.11c), employing β distributions of thickness from the literature.[64–66]

The incorporation of statistical distributions of spacing, angular orientation, and thickness into these finite-element models resulted in a combination of deformation modes, namely, axial deformation and bending. The amount of bending vs. axial deformation in the model is a function of the amount of "disorder" in the model. For example, trabeculae oriented along the loading direction axially deform whereas oblique trabeculae bend. By comparing the elastic behavior of the models against histomorphometric and mechanical data, the amount of disorder can be calibrated. Jensen et al.[58] introduced a parameter α, which is a relative measure of the distance that each node of the lattice can be perturbed compared to its length. Through comparison with photographs of bone specimens as well as apparent modulus data, α values of 0.4 to 0.8 were considered most appropriate for vertebral bone. In a much earlier study, Pugh et al.[57] used a model composed of a network of cortical bone plates to simulate trabecular

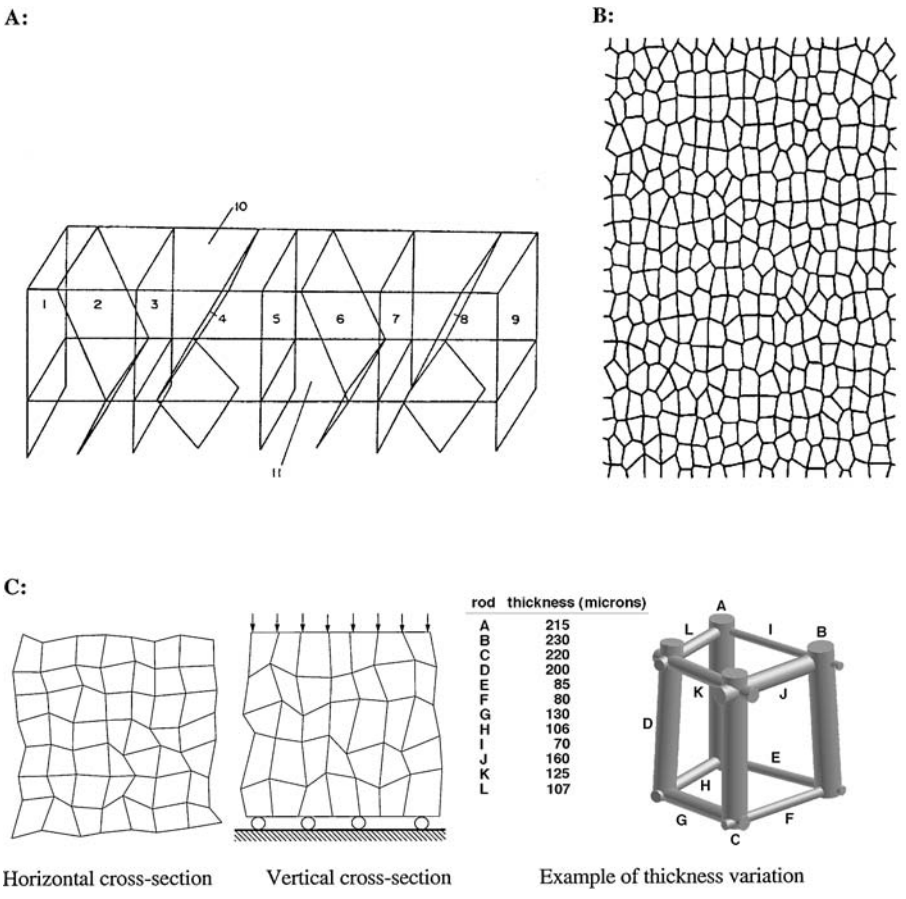

FIGURE 16.11 Various geometrics of the generic lattice-type finite element models that have been used for analysis of trabecular bone micromechanics. (**A**) Early three-dimensional model of distal femoral bone composed of 11 plate elements. (**B**) Two-dimensional model generated from the Voronoi technique. (**C**) Three-dimensional lattice disorder type model, where each trabecula has a different thickness. (From, respectively, Pugh et al., *J. Biomechanics,* 6, 657–670, 1973; Silva and Gibson, *Intern. J. Mech. Sci.,* 39, 549–563, 1997; and Yeh and Keaveny, *Bone,* 25, 223–228, 1999. With permission.)

bone at the distal femur (Fig. 16.11a). The plate elements were oriented by as much as 37° from the loading direction based on qualitative comparisons with thin sections of subchondral bone. With this arrangement, they concluded that bending was a primary mode of trabecular deformation. Furthermore, because of the aspect ratio of these plates, it was suggested that buckling and fatigue fracture were the likely failure modes. Clearly, the key to the success of this overall approach is the degree of representation of the real structure. If the model contains oblique trabeculae, for example, cellular solid theory dictates that bending will be a dominant deformation mode.

In a different approach (Fig. 16.11b), nonperiodic Voronoi distributions of the trabecular struts have been incorporated into a honeycomb-type two-dimensional model.[61] These models predicted how strength can be reduced by an irregular arrangement of the trabeculae as well as defects in the trabecular network. In one study,[61] the strength of a random two-dimensional Voronoi honeycomb of beam elements was shown to be 30% less than that of a periodic, hexagonal arrangement. This demonstrates the need to introduce geometric irregularities into these models if good agreement with real behavior is to be expected. Yeh and Keaveny[62] showed similar effects as the variance in trabecular thickness within a model

was increased. With volume fraction held constant, apparent modulus decreased by about 22% when the coefficient of variation in trabecular thickness within the model was increased from 25 to 40%. By using the nonperiodic Voronoi honeycomb of beam elements, the effects of defects (removing trabecular elements) vs. uniform thinning of trabecular elements have also been compared.[60] These analyses indicated that for a 10% reduction in volume fraction simulated by either removal or thinning of longitudinal trabeculae, loss of trabeculae reduced strength by approximately 70% whereas uniform thinning reduced strength by only 20%. Although these effects may be accentuated for a two-dimensional model, they nevertheless demonstrate the potentially important role of stark interruptions in the trabecular network vs. more uniform thinning.

Whereas the above-mentioned studies considered only randomly placed defects in the trabecular network, one study[56] reported on a more mechanistic basis for removal of trabeculae. By using a two-dimensional regular hexagonal model of beam elements, a Paris law crack propagation rule and a creep rule, both developed from cortical tissue properties, were incorporated into the model to allow crack propagation in regions where randomly introduced cracks exceeded the stress intensity factor. The study demonstrated that after reductions of apparent modulus of about 15%, further removal of trabeculae from fatigue crack propagation produced apparent modulus reductions that were greater than for random removal (fracture) of trabeculae (Fig. 16.12). The relative effects of trabeculae fracture vs. microdamage accumulation within trabeculae are still not understood. Preliminary reports[67] using a three-dimensional distorted array model with intraspecimen variations in trabecular thickness suggest that diffuse microdamage within many trabeculae, with associated reductions in tissue modulus consistent with cortical bone behavior, can successfully explain reported reductions (see Fig. 16.19a) in apparent modulus vs. applied strain. Additional work is required to provide more understanding of these issues.

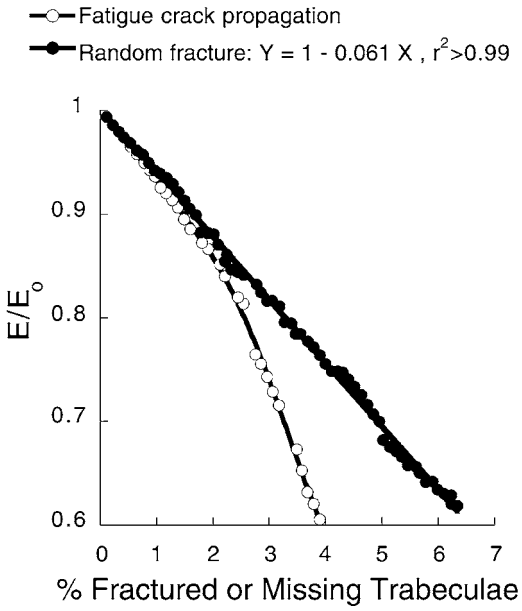

FIGURE 16.12 Results from various lattice-type finite element analyses. Loss of stiffness for incremental removal in response to propagation of fatigue fracture of trabeculae vs. random removal of trabeculae. Stiffness loss is greatest when fractures coalesce, but only after a certain number of fractures have developed. (Adapted from Guo et al., *J. Biomech.,* 27, 145–155, 1994. With permission.)

16.2.5.3 High-Resolution Finite-Element Modeling

The generic lattice-type finite-element models, although continuing to evolve in geometric complexity, still do not capture the detail of the real trabecular geometry. Recent advances in high-resolution imaging techniques have provided a variety of means to capture such detail at resolutions as high as 10 μm.[68–74] As described in Chapter 15, the strategy is to convert each voxel from the imaging process into a single finite element, resulting in three-dimensional models of particular specimens that contain upward of hundreds of thousands of elements.[75,76] Specialized algorithms that exploit the similarity of all elements in the voxel model now allow models with millions of elements to be solved.[77–79] It is expected therefore that continued developments in computer hardware will soon make such analyses routine.

To date, the high-resolution finite-element models have been applied to a wide range of applications in trabecular bone biomechanics. For example, Hollister and co-workers[76,80,81] used homogenization sampling with these models to show that strains within the trabecular tissue can be much higher than the continuum-level applied strains, and van Rietbergen et al.[75] found similar results. Other work[38,80] predicted that most highly stressed regions in the trabeculae were due to bending of struts and stress concentrations around perforations in plates. The high-resolution modeling technique has also been used to predict the biomechanical consequences of bone atrophy,[82,83] investigate the elastic symmetries of trabecular bone and their relationship to the fabric tensor and architecture,[6,79,84,85] and determine tissue elastic properties from apparent properties.[38,75,84,86] This modeling technique undoubtedly has enormous potential for study of trabecular bone failure.

Due in large part to the technical difficulty of running iterative nonlinear analyses for failure analysis of these huge models, only preliminary reports on such analyses have appeared.[87–89] Fyhrie and Hou[87] modeled the failure behavior of a single human vertebral specimen and found that their predictions were sensitive to the assumed hard tissue properties. Then, by using specimen-specific hard tissue elastic properties, van Rietbergen et al.[88] successfully predicted ultimate stresses to within 15% of the corresponding experimental data for five specimens taken from two human femurs. However, their predictions of apparent ultimate strain were low by as much as 35%, suggesting that the assumed hard tissue yield criterion may have been incorrect. Both of these studies used the von Mises yield criterion to model the hard tissue failure. Cortical bone tissue, however, is stronger in compression than tension[53] and evidence now suggests similar elastic and even failure behaviors between cortical and trabecular tissue.[10,23,90,91] Because the von Mises yield criterion does not allow this type of behavior, it has long been suggested that such a criterion may not be appropriate for trabecular hard tissue.[57] A recent study by Niebur et al.,[89] who used asymmetric tissue yield strains typical of cortical bone and specimen-specific values of tissue elastic modulus, showed excellent agreement for predicted apparent compressive and tensile strengths, as well as failure strains, of seven bovine tibial specimens vs. literature data for the same type of bone (Fig. 16.13). Thus, it appears that the high-resolution finite-element technology has the potential to qualify as a surrogate for actual test experiments—"virtually real" experiments. The challenges remain to extend the technique to bone of low density where large deformations may be important, and to verify that the strength predictions work for arbitrary loading conditions.

One great advantage of the high-resolution technique is that a single specimen can be tested—in cyberspace—to failure multiple times using any type of loading condition, and in that sense can serve as its own repeated measure. This strategy, used to investigate elastic behavior as described in Chapter 15, could also be used to develop a multiaxial failure criterion, which can then be validated or tested using a small set of real experiments. Underlying failure mechanisms can also be studied in great detail. An example is presented from ongoing work in the author's laboratory (Fig. 16.14). Here, regions of bovine trabecular hard tissue that were predicted to fail microstructurally are shown when the whole specimen was loaded to its apparent yield point. The model indicates that about one third of the tissue failed by tension for apparent compressive loading, but almost no tissue failed by compression for apparent tensile loading. This effect, due to the assumed asymmetry in the tissue-level failure strains, illustrates the subtle role of tensile tissue failure for apparent compressive loading, and begs the question as to whether or not there is a biological response specific to tissue-level tensile vs. compressive failure.

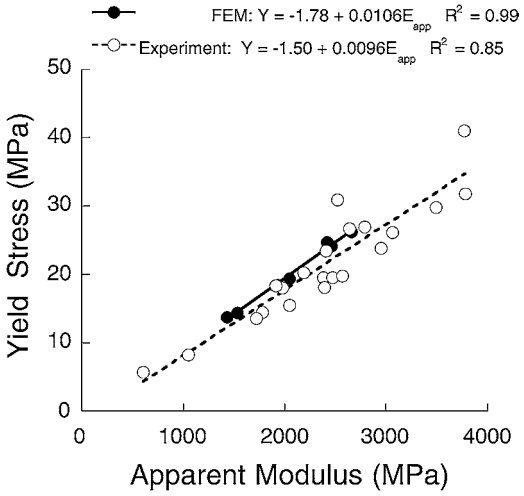

FIGURE 16.13 Predictions of strength-modulus relation for compressive loading from non-linear high-resolution finite element analysis of seven bovine tibial specimens (solid points). The predictions are compared with literature experimental data (open points) for the same type of bone, but tested earlier[10] (shown also in Figure 16.6). Asymmetric failure strains (0.71% tension, 1.10% compression) similar to those for cortical bone were assumed for the trabecular tissue in all these analyses, and the trabecular tissue modulus was calibrated on a specimen-specific basis by matching predicted and experimentally measured apparent modulus values for each specimen (mean ±S.D. of the resulting tissue modulus for the seven specimens was 18.7 ± 3.4 GPa). The good agreement between the predictions of the strength-modulus relation vs. the literature data demonstrates the capability of the non-linear analysis technique to predict the failure behavior of trabecular bone. Finite element data courtesy of Glen L. Niebur, Orthopaedic Biomechanics Laboratory, University of California, Berkeley, California.

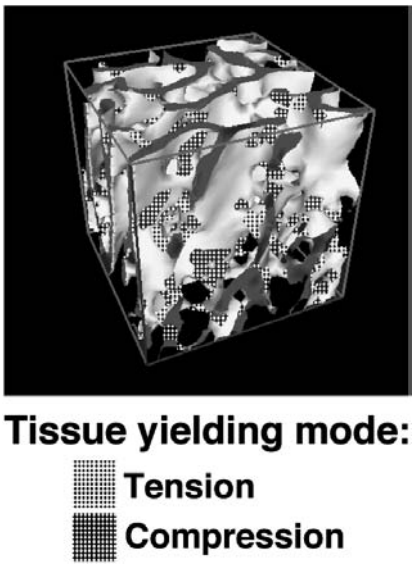

FIGURE 16.14 Distribution of failed tissue at the apparent level compressive 0.2% offset yield point, as predicted by nonlinear finite element analysis (corresponding to the analyses shown in Figure 16.13). Loading of this bovine tibial specimen was applied along the vertical axis. A 3-mm cubic region, taken from the center of the larger specimen that was analyzed, is shown. The different highlighted regions indicate tissue which exceeded the tissue tensile or copressive yield strain. Note that for this compressive apparent loading, there was failure in both compression and tension. Courtesy of Glen L. Niebur, Orthopaedic Biomechanics Laboratory, University of California, Berkeley, California.

Looking to the future, it is expected that by combining such high-resolution finite-element analyses and experiments, substantial insight will soon be gained into a variety of issues related to trabecular bone mechanics. These include describing the micromechanical changes that occur with aging and their biomechanical effects, understanding apparent-level mechanical behavior such as the reported failure strain isotropy, developing a complete multiaxial failure criterion for bone from multiple anatomic sites, predicting and assessing the effects of various drug treatments, and eventually understanding the biological response to different types and magnitudes of strain and damage at the tissue level. This modeling technology may also provide a framework for design of tissue-engineered trabecular bone, where both mechanical and biological effects can be considered in a quantitative and interdependent manner.

16.3 Multiaxial Behavior

Multiaxial behavior is important clinically since multiaxial stresses can occur during falls, trauma, and at the bone–implant interface.[25,92–101] Besides an exploratory study on axial-shear behavior of bovine humeral trabecular bone,[29] it is only recently that significant attention has turned to determination of a multiaxial failure criterion for trabecular bone. Formulation of a multiaxial failure criterion for trabecular bone is particularly challenging since it is necessary to account for interspecimen variations in volume fraction and architecture. This issue does not arise with most engineering materials nor with cortical bone because of their relatively homogeneous natures.

Attention so far[15,102–104] has focused mostly on application of the Tsai–Wu quadratic criterion[105,106] since it can account for strength asymmetry and anisotropy, as well as interactions between strengths in the different loading directions. Other work[104] has also used ideas from cellular solid theory.[52,107–110] In addition, criteria based on nondimensional measures of stress have received attention. The latter approach was motivated by observations that uniaxial failure strains, at least for a single anatomic site, do not depend much on volume fraction. The Tsai–Wu and cellular solid theories are reviewed here, and are then viewed in the light of available experimental data.

16.3.1 Tsai–Wu Criterion

The Tsai–Wu quadratic criterion,[105,106] developed originally for fiber-reinforced composite materials, has been applied with various degrees of success to cortical bone[111–113] and has been formulated in terms of the fabric tensor.[102,103] However, applications to experimental data for trabecular bone have only been reported for bovine bone, and only recently at that. This is due largely to the lack of multiaxial normal stress data required for its complete formulation.

The most common formulation of the Tsai–Wu criterion (using contracted tensor notation) is in terms of six-dimensional stress (σ_i) space resolved to the principal material coordinate system 1–2–3:

$$F_i\sigma_i + F_{ij}\sigma_i\sigma_j = 1, \qquad i, j = 1 \text{ to } 6, \tag{16.14}$$

where indices $i = 1$ to 3 correspond to normal stresses σ_{11}, σ_{22}, σ_{33}, indices $i = 4$ to 6 correspond to shear stresses σ_{12}, σ_{23}, σ_{31}, respectively, and F_i and F_{ij} are the experimentally derived Tsai–Wu coefficients, the latter of which is a second-order tensor. Eq. 16.14 represents a general quadratic equation. For failure to occur for all stress states, the tensor F_{ij} must be positive definite. In principal stress space, this would correspond to the requirement that Eq. 16.14 represents a closed ellipsoid. For biaxial stress states, this requirement reduces to the following constraint on the so-called "strength interaction" coefficients F_{ij} $(i \neq j)$:

$$\|F_{ij}\| \leq \sqrt{F_{ii}F_{jj}} \qquad \text{(no sum on } i \text{ or } j\text{)}; \qquad F_{ij} = F_{ji} \text{ assumed.} \tag{16.15}$$

16.3.1.1 Derivation Using Strength–Density Relations—Triaxial Loading

The Tsai–Wu criterion has been developed experimentally for bovine bone for the special case of transverse isotropy,* where seven independent coefficients must be calibrated experimentally.** Six coefficients are found from uniaxial tension, compression, and torsion tests performed on longitudinally and transversely

oriented specimens, and the seventh coefficient, the strength interaction term F_{12}, is found from a biaxial, triaxial, or off-axis uniaxial test. The coefficients can be expressed in terms of the normal (σ_{yi}, i = 1 and 2 or 3) and shear (σ_{yi}, i = 5 and 4 or 6) yield stresses as follows:

$$
\begin{aligned}
&F_1 = \frac{1}{\sigma_{y1}^T} + \frac{1}{\sigma_{y1}^C} \quad F_2 = \frac{1}{\sigma_{y2}^T} + \frac{1}{\sigma_{y2}^C} \quad F_3 = F_2 \quad F_4 = F_5 = F_6 = 0\\
&F_{11} = -\frac{1}{\sigma_{y1}^T \sigma_{y1}^C} \quad F_{22} = -\frac{1}{\sigma_{y2}^T \sigma_{y2}^C} \quad F_{33} = F_{22}\\
&F_{44} = \frac{1}{\sigma_{y4}^2} \quad F_{55} = \frac{1}{\sigma_{y5}^2} \quad F_{66} = F_{44}\\
&F_{12} = F_{13} \neq 0 \quad F_{23} \neq 0 \text{ (dependent)} \quad F_{i4} = F_{i5} = F_{i6} = 0 \quad (i = 1 \text{ to } 6, \text{i} \neq j),
\end{aligned}
\tag{16.16}
$$

where the superscripts T and C refer to the tensile and compressive strengths, respectively; compressive strengths should be given negative signs ($F_i = 0$ if the tensile and compressive strengths are equal, for example); and σ_{y4} and σ_{y5} are determined from torsion tests about longitudinal and transverse axes using cylindrical specimens, respectively. The terms F_i (i = 4 to 6) and $F_{ij} = F_{i4}, F_{i5}, F_{i6}$ (i = 1 to 6, $i \neq j$) are all zero so as to enforce the condition that the failure criterion is independent of the sign of the applied shear stress.

The F_{23} coefficient for a transversely isotropic material can be expressed in terms of the other coefficients based on symmetries in the microstructure.[102] The F_{12} coefficient can then be found from a multiaxial test as a function of the failure stress in that test and the other Tsai–Wu coefficients. For example, for a triaxial axial-radial compression test with a measured axial yield stress $-\sigma_y$ and radial yield pressure $-p_y$, F_{12} is given as follows:[15]

$$
F_{12} = \frac{1}{4\sigma_y p_y}\{1 + F_1\sigma_y + 2F_2 p_y - F_{11}\sigma_y^2 - 2F_{22}p_y^2 - 2F_{23}p_y^2\} \tag{16.17}
$$

For a material such as trabecular bone with large interspecimen variations in architecture and density, the interspecimen heterogeneity must also be accounted for. One approach is to control architecture by confining attention to a single anatomic site, and to then use a series of strength–density regressions for that site for different loading modes and directions (see Table 16.2) to calculate the Tsai–Wu coefficients as functions of apparent density ρ. F_{12} can be found empirically as a function of ρ using these coefficients and calibration multiaxial tests with associated equations such as Eq. 16.17. In this way, all Tsai–Wu coefficients can be determined from density and the heterogeneous formulation is complete for that particular anatomic site.

An experimental program has been completed using this strategy[15] using uniaxial strength–density data[10,16] from 139 bovine tibial specimens, and multiaxial data from 9 similar specimens tested at a specific ratio of axial stress to radial pressure. The failure criterion was then used to make predictions of failure for more general triaxial normal loading (Fig. 16.15). These predictions indicated that the orientation of the failure ellipsoid depended on apparent density, but was relatively well aligned with the principal material directions. This suggests that the strength interactions may not be important. Although the bone was assumed to be transversely isotropic, the ellipsoids had three different major diameters. This was a consequence of an interaction between the transverse isotropy and the tension–compression strength asymmetry.

When the theory was used to predict the behavior of additional specimens under different triaxial compression conditions, the average ($\pm$S.D.) error was $-32.6 \pm 10.6\%$.[15] The reason for this discrepancy

*For transverse isotropy, there are two distinct principal material directions—longitudinal (direction 1) and transverse (directions 2 and 3 in the plane of isotropy). The indices 2 and 3 of the Tsai–Wu coefficients in Eq. 16.14 are interchangeable, as are the indices 4 and 6.

**Cowin[102] provided a complete analysis of the quadratic Tsai–Wu criterion for higher and lower degrees of symmetry than transverse isotropy.

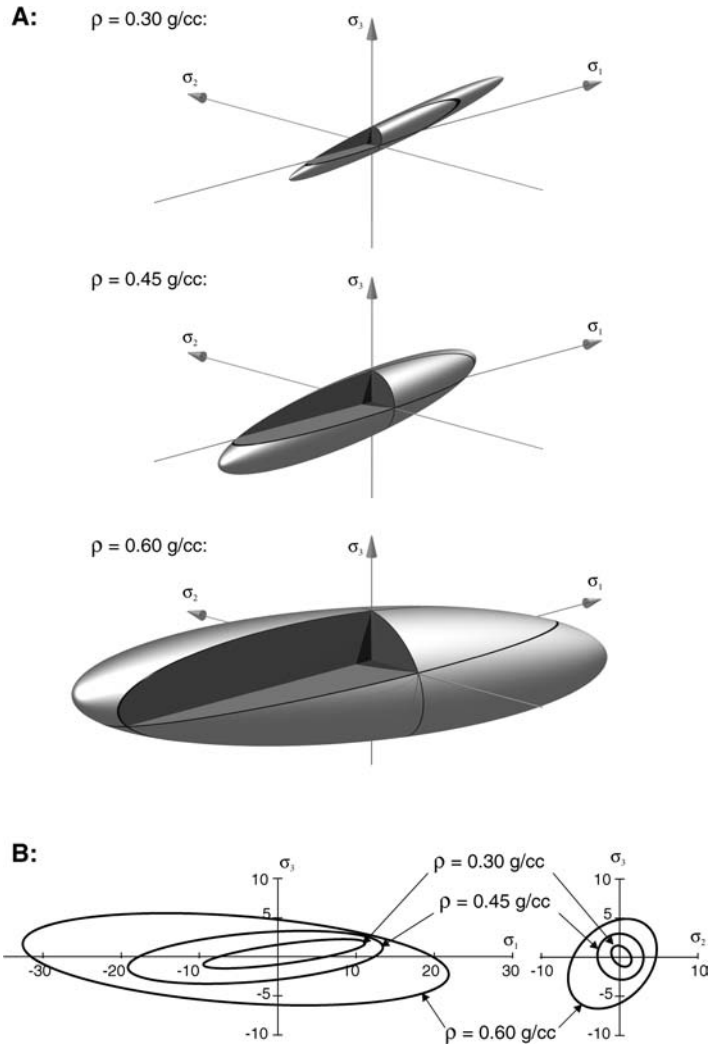

FIGURE 16.15 Tsai-Wu predictions of the three-dimensional failure ellipsoids for general triaxial normal loading (A) for three values of apparent density ρ, and corresponding failure ellipses for biaxial normal loading (B). Due to the underlying transverse isotropy, the σ_2 and σ_3 axes can be interchanged. This criterion was formed for bovine tibial bone using the strength-density relations in Table 16.2, Equation 16.16, and the following expressions for the strength interaction coefficients.[15,102]

$$F_{23} = F_{22} - \frac{F_{55}}{2}, \qquad F_{12}(\rho) = \left\{12.9 - \frac{3.16}{\rho^{2.02} - 54.2 \times 10^{-3}}\right\} \times 10^{-3}.$$

While the orientation of the ellipsoids depends on apparent density, they are well aligned with the principal material directions (the $\sigma_1 - \sigma_2 - \sigma_3$ coordinate axes), suggesting that strength interactions may not be important. (From Keaveny et al., Application of the Tsai-Wu quadratic multiaxial failure criterion to bovine trabecular bone, *J. Biomech. Eng.,* 121, 99–107, 1999. With permission.)

is not clear. Since the triaxial experiments are so technically challenging, one possibility is that the experimental data themselves do not properly match the stress states assumed in the theory. However, it was noted that most specimens in these triaxial compression experiments failed close to their uniaxial values, consistent with behavior of some cellular solid materials.[107,108,110,114] Thus, there appears to be a

precedence for the observed behavior, suggesting that the Tsai–Wu quadratic envelope may be too restrictive for this type of trabecular bone. Further research is required to resolve these issues and extend analysis to human bone. In the meanwhile, the criterion presented here represents the most-detailed multiaxial failure criterion available for trabecular bone and should improve performance in finite-element models compared with much simpler alternatives such as the von Mises criterion.

16.3.1.2 Derivation Using Normalized Stresses—Axial-Shear Loading

In an attempt to reduce the effects of interspecimen heterogeneity of density, the stress-based Tsai–Wu criterion can be normalized by modulus to produce a nondimensional measure of stress. For a combined axial stress σ and shear stress τ, the Tsai–Wu criterion describes a two-dimensional ellipse and can be expressed in nondimensional stress space ($\sigma^* = \sigma/E, \tau^* = \tau/G$) as[104]

$$K_1\sigma^* + K_{11}(\sigma^*)^2 + K_{44}(\tau^*)^2 = 1, \tag{16.18}$$

where

$$K_1 = F_1E = \frac{1}{(\varepsilon_y^T - 0.002)} + \frac{1}{(\varepsilon_y^C + 0.002)}$$

$$K_{11} = F_{11}E^2 = -\frac{1}{(\varepsilon_y^T - 0.002)(\varepsilon_y^C + 0.002)}$$

$$K_{44} = F_{44}G^2 = \frac{1}{(\gamma_y - 0.002)^2}$$

and E and G are the appropriate anisotropic Young's and shear moduli, respectively, and the K terms are nondimensional coefficients that are functions of the yield strains. This elliptical envelope in $\sigma^* - \tau^*$ space is independent of apparent density since the yield strains are assumed to be constant. The ellipse has a maximum value of τ^* at $\sigma^* = (\varepsilon_y^T + \varepsilon_y^C)/2$, which indicates that the maximum shear capacity will occur at a negative axial stress, i.e., in compression, if the uniaxial yield strain is greater in compression than tension.

One set of experiments on bovine tibial bone has been performed to test this formulation using data from separate uniaxial tests to calibrate the criterion.[104] Results indicate that the theory worked reasonably well, particularly for tension-shear (Fig. 16.16). For example, shear capacity peaked with superposition of small compressive stresses, in agreement with theory. One consequence of these findings is that the von Mises criterion should not be used when there are large shear stresses.[104] It should also be appreciated that normalization of failure stress by modulus had a dramatic effect since it allowed a single envelope to represent behavior of *all* specimens, despite modulus values that varied by a factor of over three.

16.3.1.3 Fabric-Based Formulation

In terms of extending the above site-specific empirical approaches to incorporate other architectures in a single theory, Cowin[102,103] presented explicit terms in an analytical treatment of the Tsai–Wu quadratic criterion to characterize the dependence of the Tsai–Wu coefficients on the structural anisotropy of the bone by way of the fabric tensor. Terms were also included to account for interspecimen variations in apparent density. This approach is summarized briefly here, but is described in more detail elsewhere, including the previous edition of this book.[102,103]

In general, the theory predicts a failure envelope for a given specimen when the following condition is met:

$$f(\rho, \mathbf{H}, \mathbf{T}) = 1, \tag{16.19}$$

where f is a function that describes the overall Tsai–Wu criterion, ρ is the apparent density of that specimen, $\mathbf{H}$ is the fabric tensor that describes the structural anisotropy of that specimen,[5,115–119] and $\mathbf{T}$ is the stress tensor. It is then assumed that the anisotropy in the criterion is dominated by the anisotropy contained within the fabric tensor, i.e., any anisotropy within the trabecular tissue is

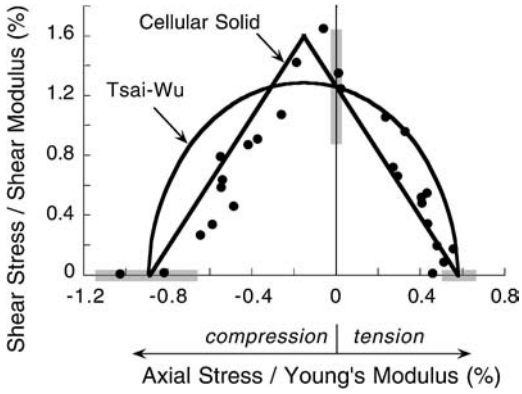

FIGURE 16.16 Biaxial axial-shear behavior of bovine proximal tibial trabecular bone. The stress axes are normalized by modulus, since use of non-dimensional units allows data from many specimens to adhere to a single failure envelope. Both the Tsai-Wu and Cellular Solid criteria were calibrated to fit through the uniaxial tension, compression, and shear failure points (gray bars show ±1 SD of those data). Note that the maximum shear capacity occurs with superposition of small compressive stresses, in agreement with both theories. The Tsai-Wu criterion worked quite well for this bone, but the Cellular Solid criterion worked better. (From Fenech and Keaveny, *J. Biomechan. Eng.,* 121, 414–422, 1999. With permission.)

unimportant compared with that contained in the larger-scale trabecular structure. This implies that the function f is an isotropic function of the tensors **H** and **T**, allowing the function f to be specified as a function of specific combinations of the trace of **H** and **T** (such as tr**H**, tr**T**, tr**HT**, tr(**HT**)^2, etc.). Restricting the analysis to material symmetries of at least orthotropy, normalizing **H** to have a trace of unity, and neglecting all terms of order three and greater in **H**, it is possible to express the orthotropic Tsai–Wu coefficients in terms of some functions s_i (i = 1 to 4) and t_j (j = 1 to 9), each of which depends only on apparent density, and the three nonzero elements (H_1, H_2, and H_3) of the diagonalized fabric tensor:

$$
\begin{aligned}
F_1 &= s_1 + s_2 II + s_3 H_1 + s_4 H_1^2 \\
F_2 &= s_1 + s_2 II + s_3 H_2 + s_4 H_2^2 \\
F_3 &= s_1 + s_2 II + s_3 H_3 + s_4 H_3^2 \\
F_{11} &= t_1 + 2t_6 + (t_2 + 2t_7) II + 2(t_3 + 2t_8) H_1 + (2t_4 + t_5 + 4t_9) H_1^2 \\
F_{22} &= t_1 + 2t_6 + (t_2 + 2t_7) II + 2(t_3 + 2t_8) H_2 + (2t_4 + t_5 + 4t_9) H_2^2 \\
F_{33} &= t_1 + 2t_6 + (t_2 + 2t_7) II + 2(t_3 + 2t_8) H_3 + (2t_4 + t_5 + 4t_9) H_3^2 \\
F_{44} &= 4(t_6 + t_7 II) + 4t_8(H_1 + H_2) + 4t_9(H_1^2 + H_2^2) \\
F_{55} &= 4(t_6 + t_7 II) + 4t_8(H_2 + H_3) + 4t_9(H_2^2 + H_3^2) \\
F_{66} &= 4(t_6 + t_7 II) + 4t_8(H_3 + H_1) + 4t_9(H_3^2 + H_1^2) \\
F_{12} &= t_1 + t_2 II + t_3(H_1 + H_2) + t_4(H_1^2 + H_2^2) + t_5 H_1 H_2 \\
F_{23} &= t_1 + t_2 II + t_3(H_2 + H_3) + t_4(H_2^2 + H_3^2) + t_5 H_2 H_3 \\
F_{31} &= t_1 + t_2 II + t_3(H_3 + H_1) + t_4(H_3^2 + H_1^2) + t_5 H_3 H_1,
\end{aligned}
\tag{16.20}
$$

where $II = \frac{1}{2}[(\mathrm{tr}\mathbf{H})^2 - \mathrm{tr}\mathbf{H}^2]$.

The experimental strategy to calibrate this criterion is to test a number of specimens uniaxially for each loading mode (tension, compression, shear, and in each of the three orthogonal 1–2–3 directions),

and measure both the apparent density and three-dimensional fabric tensor for each specimen. Then, one would assume specific forms of the $s_i(\rho)$ and $t_j(\rho)$ functions. For example, one could assume linear ($s_i = a_i + b_i\rho$) or quadratic ($s_i = a_i + b_i\rho + c_i\rho^2$) functions, which would introduce two or three constant coefficients, respectively, for each *i*th function. These coefficients would then be quantified by statistical curve-fitting against the experimental measurements. Once known, the $t_j(\rho)$ functions would be used to characterize the strength interaction coefficients $F_{ij}(i \neq j)$. This calibrated criterion would then have to be tested against a new set of specimens, preferably from a different anatomic site than those used for calibration, for a variety of multiaxial stress states. Clearly, this approach is difficult since it would require mechanical testing and fabric analysis of probably 200 or more specimens for the complex statistical calibration given the large number of unknown coefficients ($13 \times 2 = 26$ for the linear form of the $s_i(\rho)$ and $t_j(\rho)$ functions). More serious is the limitation that the theory requires simultaneous measures of the tensile and compressive strengths for the same specimen, which of course is not possible. Thus, this theory has not yet been implemented experimentally, although use of the high-resolution finite-element modeling technique combined with more selective experiments offers a promising strategy.

16.3.2 Mechanistic Analysis

The Tsai–Wu, von Mises, and most engineering multiaxial failure criteria[120] are all phenomenological in that they rarely assume or even address potential mechanisms of failure. For trabecular bone, the problem with the phenomenological approach, as discussed above in Section 16.3.1.1, is that the assumed form of the failure envelope may not apply to trabecular bone for all stress states due to the complexity of its failure mechanisms, which depend on loading mode (tension vs. compression vs. shear), architecture, and orientation.[4,20,21,23,121] Thus, there is interest in development of a criterion based on a mechanistic approach, where assumptions are made about the dominant failure mechanisms of the microstructure to predict the apparent behavior. If the assumptions about the tissue failure mechanisms are correct, it should be possible to predict apparent failure for any state of stress.

Cellular solid theory[52] is an example of such a mechanistic approach, and multiaxial failure criteria have been developed for various types of cellular materials.[52,107–110,114] This general approach has been applied to analysis of bovine tibial trabecular bone loaded to failure in combined axial shear in the principal trabecular orientation.[104] A two-dimensional approach was used where it was assumed that the individual trabeculae can be modeled as an array of longitudinally and transversely oriented uniform unit cells that behave like cantilever beams. The unit cell was taken as a vertical beam of arbitrary cross section with cantilever-type fixed boundary conditions on each end representing the reaction of the surrounding bone. The key assumption was that apparent axial loading causes mostly axial loading at the tissue level, and that any important bending at the tissue level is due to apparent-level shear loading. The tissue was also assumed to be stronger in compression than tension, similar to cortical bone. As the specimen is loaded by combined apparent axial and shear stresses, there is combined axial and bending, respectively, which superimpose linearly. Failure then occurs at the tissue level either by excessive tensile or compressive tissue stress.

If failure occurs at the tissue level by excessive tensile stresses, then the following apparent level criterion results:[104]

$$\sigma^* + \left(\frac{\varepsilon_y^T - 0.002}{\gamma_y - 0.002}\right)\tau^* = \varepsilon_y^T - 0.002, \tag{16.21a}$$

where $\sigma^* = \sigma/E$ and $\tau^* = \tau/G$ are the nondimensional axial and shear apparent stresses, respectively; and ε_y^T and γ_y are the apparent uniaxial tensile and shear yield strains, respectively (the 0.002 terms come from the definition of the yield point by the 0.2% offset criterion). A similar expression can be derived for the case where *compressive* failure occurs in the tissue,

$$\sigma^* - \left(\frac{\varepsilon_y^T - 0.002}{\gamma_y - 0.002}\right)\tau^* = \varepsilon_y^C - 0.002, \tag{16.21b}$$

where ε_y^C is the apparent uniaxial compressive yield strain.

The failure envelope described by Eq. 16.21 is an isosceles triangle and describes the failure behavior for specimens of any density. The apex is offset from zero in the normalized axial stress direction by the same amount as it is for the normalized Tsai–Wu criterion. The criterion predicts a bilinear (triangular) envelope because axial and shear apparent stresses combine linearly at the microstructural level. The isosceles nature of the envelope arises because apparent level shear loading is the dominant source of bending at the unit cell level and the incremental increase in tissue stress due to this bending does not depend on the sign of the superimposed apparent axial stress.

The criterion has been applied so far to bovine tibial[104] bone (see Fig. 16.16). The mean ($\pm$S.D.) percentage error between prediction and observation was only $7.7 \pm 12.6\%$ for compression-shear and $-5.2 \pm 11.8\%$ for tension-shear. This is excellent performance considering the complexity of the loading and heterogeneity of the bone. The main significance of these results is that they establish the ability of relatively simple mechanistic models to provide insight into the empirical results, thereby improving overall understanding of the apparent behavior. However, the assumptions made in this analysis may not be appropriate for human bone because of architectural and density differences, and further work in this area would be beneficial.

16.4 Post-Yield Behavior and Damage Mechanisms

Damage and repair of individual trabeculae are now recognized as almost normal physiological processes[122,123] that tend to increase with age[124–126] (Fig. 16.17) and which may have clinical and basic biological relevance. Fractures of individual trabeculae have been observed in the vertebral body,[127,128] acetabulum,[129] proximal femur,[130–133] and proximal tibia[134] of postmortem human specimens and in the proximal tibia of rabbits.[135] Tiny cracks of or within individual trabeculae (microfractures, or microcracks—not to be confused with "microdamage," which refers to a more subtle damage pattern not involving overt cracks) apparently can be repaired by callus formations, similar to callus formation in fractures of long bones, resulting in the appearance of a "node" of new woven or lamellar bone about the original crack.[136,137] It has long been suggested that these *in vivo* microcracks are due to fatigue loading,[133] and this has been demonstrated in a canine model,[138] although microcracks can also occur from isolated overloads, at least in a laboratory setting.[37,139] Such damage has been proposed to increase osteoporotic fracture risk,[37,122,139,140] act as a stimulus for remodeling,[134] occur during implantation of prostheses, particularly in the elderly spine where the bone is very fragile,[140] or be involved in aseptic necrosis of the femoral head, degenerative joint disease,[132,135] and other bone disorders.[129]

16.4.1 Post-Yield Mechanical Behavior

Fundamental to any discussion of constitutive failure behavior related to damage is the material's behavior for reloading after failure, the so-called post-yield behavior. It is important to be precise about terminology here. "Yielding" is usually associated with mechanisms of failure in metals consisting of slipping of planes of atoms along directions of maximum shear. By contrast, in trabecular bone biomechanics, the term *yield* is more often used to denote a point on the apparent-level stress–strain curve where the behavior has clearly exceeded the linear elastic range,[10,35] typically using a standard definition such as the 0.2% offset yield point. The term *yield* in this discussion therefore does not imply any specific type of microstructural failure mechanism.

It has now been established from experiments on machined specimens of bovine tibial[141,142] and human vertebral[140] trabecular bone that when trabecular bone is loaded past its yield point, it unloads to a residual strain at zero stress (Fig. 16.18). Regardless of volume fraction, there is a similar time-dependent recovery

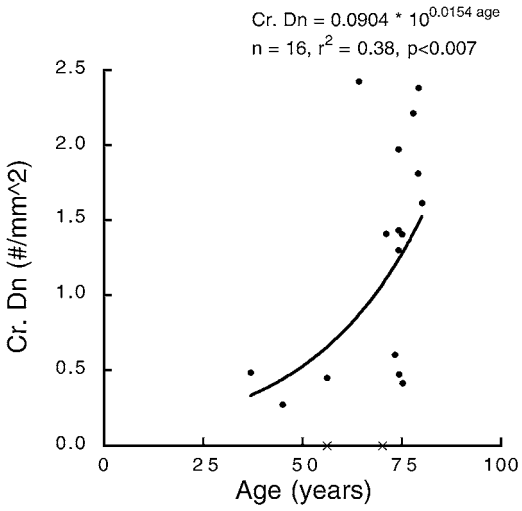

FIGURE 16.17 Crack density (Cr.Dn) vs. age for trabecular bone specimens taken from the intertrochanteric region of the proximal femur of 18 patients undergoing total hip replacement (male and female, average age about 63 years). Specimens were excised and analyzed for damage using basic fuchsin stain without any mechanical testing. Crack density was defined as the number of cracks observed per unit cross-sectional apparent area of the test section (two data points, shown as X, did not display damage and were not included in the reported regression). An exponential model was fit to the data in the original analysis and is shown here over the range of the data. It was concluded from these data that damage increases with age. (Adapted from Fazzalari et al., *Bone,* 22, 381–388, 1988. With permission.)

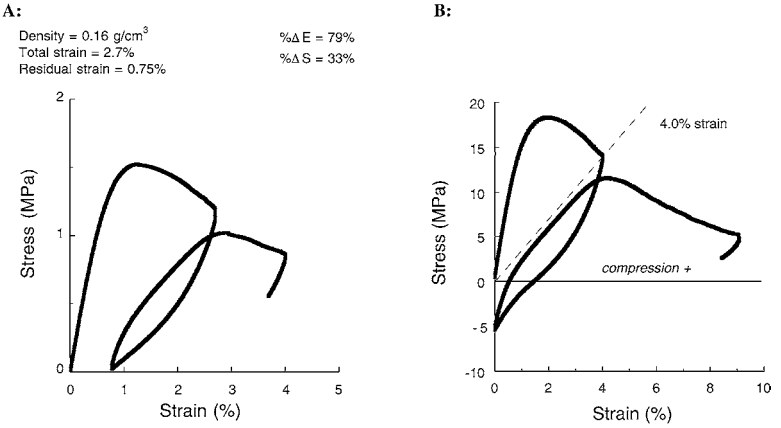

FIGURE 16.18 Load-unload-reload "post-yield" behavior of human vertebral (A) and bovine tibial (B) trabecular bone. The human bone was loaded to 2.7% strain and unloaded to zero stress before reloading, whereas the bovine bone was loaded to 4.0% strain and unloaded to zero strain (and therefore went into tension at full unloading, denoted here by a negative stress). The vertebral specimen had reductions in modulus and strength of 79 and 33%, respectively, and developed a residual strain of 0.75% after the initial overload. For multiple specimens, the secant modulus (dashed line in B) is statistically similar to the slope of the main linear region in the reloading curve, and the initial slope of the reloading curve is statistically similar to the modulus of the initial loading cycle. (From (A) Keaveny et al., *J. Orthop. Res.,* 17, 346–353, 1999; (B) Keaveny et al., *J. Biomech.,* 27, 1309–1318, 1994. With permission.)

of residual strain $\varepsilon_{\text{RESIDUAL}}$ after unloading to zero stress over a 100-s interval. This has been described well for bovine bone by a classical exponential decay model:[140]

$$\varepsilon_{\text{RESIDUAL}} = 0.084e^{-t/16.3} + 0.79. \tag{16.22}$$

This equation indicates that the residual strain immediately after unloading is a good approximation of the permanent residual strain. For human vertebral bone, it has been shown that residual strains of up to 1.05% strain occur with compressive loading of up to 3.0% strain, and increase in a slightly nonlinear fashion with increasing total applied strain:[140]

$$\varepsilon_{\text{RESIDUAL}} = -0.046 + 0.104\varepsilon_{\text{TOTAL}} + 0.073\varepsilon^2_{\text{TOTAL}}, \qquad r^2 = 0.96. \tag{16.23}$$

These residual strains do not depend on volume fraction.

After unloading, trabecular bone then reloads with an initial modulus similar to its intact Young's modulus but then quickly loses stiffness toward a value (the "residual" modulus) that would occur if the material were cracking in a perfectly brittle manner (see Fig. 16.18). This residual modulus is statistically similar to a secant modulus from the origin to the point of unloading.[140,141] In general, the reloading stress–strain curve tends to reload back toward the extrapolated envelope of the original curve. Trabecular bone therefore exhibits elements of both classical plasticity, i.e., development of permanent deformations after unloading, and brittle damage behavior, i.e., reduction in stiffness upon reloading.

The reductions in modulus and strength that occur for reloading after monotonic overloading are substantial, depend strongly on the magnitude of the applied strain, but are mostly independent of volume fraction. In an experiment performed on machined specimens of human vertebral trabecular bone,[140] percent modulus reductions (between the intact Young's and the residual moduli) were over 90% for applied apparent strains of only up to 3.0%. Percent modulus reduction $\%\Delta E$ increased with increasing plastic* strain in a nonlinear fashion (Fig. 16.19a), and at larger strains tended to level off at about 85%:

$$\%\Delta E = \frac{111\,\varepsilon_{\text{PLASTIC}}}{\varepsilon_{\text{PLASTIC}} + 0.751}. \tag{16.24}$$

By using concepts of continuum damage mechanics for brittle materials,[143] these percentage reductions in modulus can be interpreted as quantitative measures of *effective mechanical damage* in the specimen. Thus, a modulus reduction of 85% corresponds to 85% damage from a mechanical perspective.

Consistent with these findings, Zysset and Curnier[142] developed a successful rate-independent continuum damage model for trabecular bone. The theory contains a scalar damage state variable α that is a measure of accumulated plastic strain, and a function f that describes the fractional reduction in elastic properties. It was assumed that f is a monotonically decreasing function of the damage state variable α. By using nonlinear regression analysis of experimental data from compression, tension, and torsion load–reload tests of bovine tibial trabecular bone specimens, and using the fabric tensor to account for the trabecular microstructure, the form of f was found as follows:

$$f(\alpha) = 1 - f_c(1 - e^{-\alpha/\alpha_f}), \tag{16.25}$$

and the constants f_c (maximum reduction in modulus before failure, where $\alpha = \alpha_f$) and α_f were calibrated by curve fitting. The reported value for f_c for compression was 0.37, and $\alpha_f = 0.37$ MPa$^{1/2}$. Interestingly,

*"Plastic strain" is defined as the permanent strain that would occur if the material behaved as an elastic, perfectly plastic material. It is easily calculated from the shape of the monotonic stress–strain curve.[140]

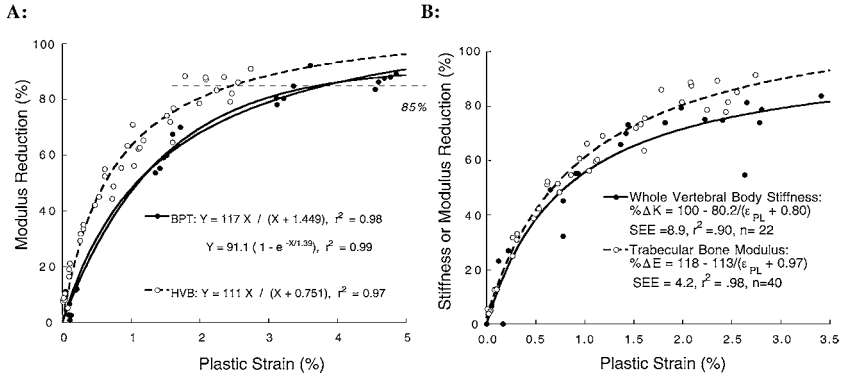

FIGURE 16.19 Dependence of percentage modulus (or stiffness) reduction, for reloading after overloading to various strains, on the applied strain level for cores specimens of vertebral trabecular bone (A) and the whole vertebral body (B). Data for bone from the bovine proximal tibial (BPT) cores are also shown in (A). This post-yield behavior is similar for bovine tibial and human vertebral bone, despite the large differences in denisty and architecture. Further, the behavior of the cores is similar to that of the whole vertebral body (B). Perhaps most surprisingly are the very high correlations between these percent reductions vs. just plastic strain. The same experimental data were used for the vertebral trabecular bone in each graph. The minor differences when plotted are due to the different horizontal scales on each chart, and subtle differences in the definition of the reloading modulus used in the two studies. Different regression models were also used to describe the trends. (Adapted from (A) Keaveny et al., *J. Orthop. Res.,* 17, 346–353, 1999; and (B) Kopperdahl et al., *J. Orthop Res.,* 18, 685–690, 2000. With permission.)

if data for bovine tibial bone equivalent to those described earlier for the human vertebral bone are fit to the same type of exponential model, an excellent fit occurs ($r^2 = 0.99$, Fig. 16.19a). Thus, there is good agreement between these different studies in the general form of the damage function *f*. The discrepancy in specific values of the constants in the regressions is likely because the parameter α does not equal the definition of plastic strain used here, fully reversed tension–compression loading was used in one experiment vs. purely compression in the other, and the same specimen was progressively loaded to higher strains in one test, whereas in the other test only one load level was applied to any one specimen. Further research is required therefore to determine the generality of this rate-independent continuum damage model.

Regarding the sensitivity of damage behavior to anatomic site, a comparison of percent modulus reduction data for human vertebral vs. bovine tibial bone shows substantial similarities (Fig. 16.19a). This suggests that the post-yield behavior is not overly sensitive to volume fraction or architecture once interanatomic differences in the uniaxial yield strain are accounted for by use of the plastic strain as the independent variable. Interestingly, comparison of the damage behaviors for trabecular bone vs. the whole vertebral body also shows substantial similarities (Fig. 16.19b).[144] This indicates that either the trabecular bone dominates the damage behavior or the cortical shell displays similar damage behavior as the trabecular bone. The former is not unreasonable given the small thickness (<0.5 mm) of the cortical shell in the vertebral body,[145] whereas the latter is not unreasonable given the reported damage behavior of cortical bone.[146]

16.4.2 Observations of Damage Mechanisms

The physical damage that occurs with such overloading has also been investigated. Compression tests performed on bovine trabecular bone to various strain levels followed by microscopic damage analysis at up to 200 × magnification demonstrated four types of damage:[139] transverse cracks, shear bands, parallel cracks, and complete fractures (Fig. 16.20), of which the first two were dominant. Statistical analysis of the amount of damage vs. applied strain indicated that the damage at initial yielding was not easily

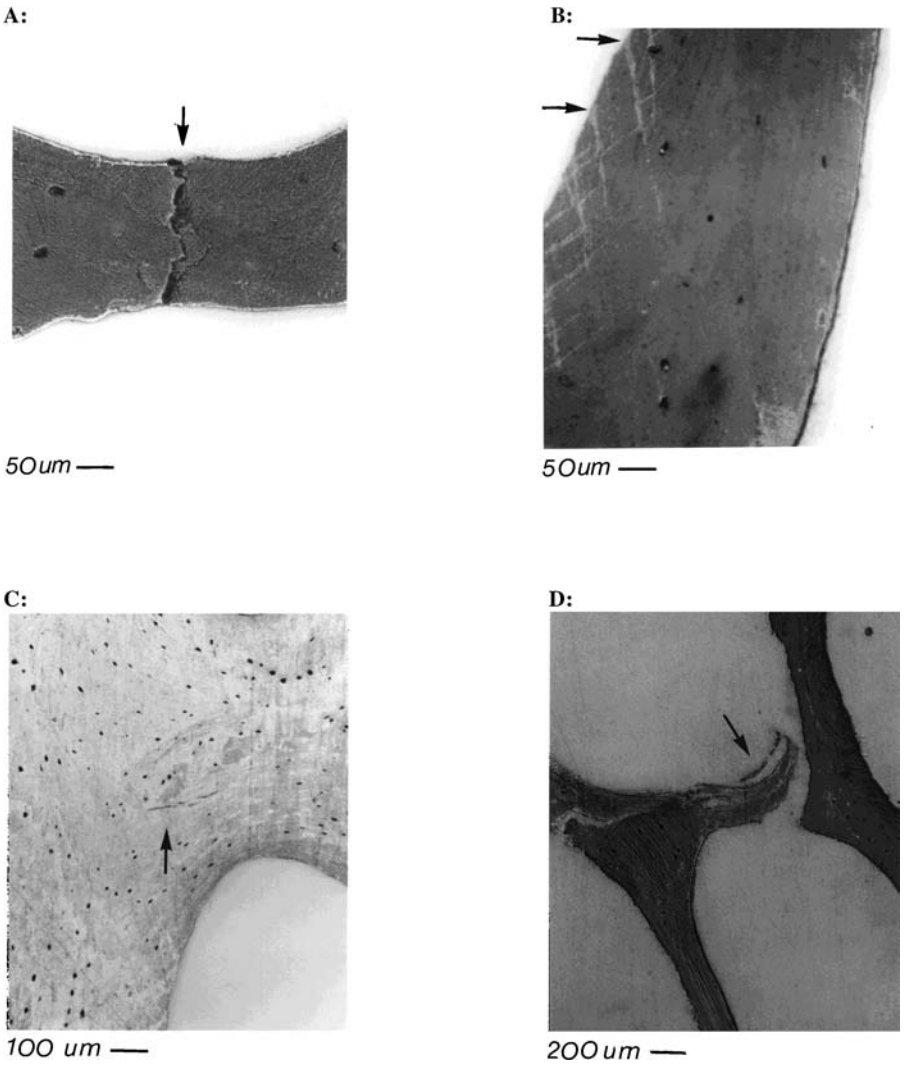

FIGURE 16.20 Various types of physical damage patterns observed in bovine trabecular bone after overloading. (**A**) transverse cracks; (B) shear bands; (**C**) parallel cracks; and (**D**) complete fracture. (From Wachtel and Keaveny, *J. Orthop. Res.,* 15, 781–787, 1997. With permission.)

detectable at 200 × magnification* and that fractures of whole trabeculae were present only past the ultimate strain.

Since percent modulus reductions associated with overloading to the yield point are on the order of 30 to 40% (strength is not reduced until after the yield point),[141] it is clear that what appears to be subtle damage within trabeculae can cause relatively large reductions in modulus upon reloading. Consistent with this, Fyhrie and Schaffler[37] reported on failure mechanisms for human vertebral trabecular bone, based on postloading histological observations of damage in specimens loaded in compression to 15% strain. They found that the primary mechanism of failure was microscopic cracking rather than overt failure of individual trabeculae. Complete fracture of trabeculae was confined to elements oriented transversely to the loading direction. Laser scanning confocal microscopy[149] has shown that crosshatch shear-band-type staining and

*It is possible that use of more sensitive detectors of microdamage such as the basic fuchsin technique[147,148] may have shown up more subtle damage at yielding.

more diffuse staining observed with basic fuchsin included "ultramicro-cracks" about 10 μm in length. The implication is that cracking can occur at very small scales. Zysset and Curnier[142] came to a similar conclusion after observing similarities in post-yield and damage behaviors between bovine trabecular bone they tested and cortical bone from the literature. Further, as noted above, preliminary results from use of the lattice-type finite-element models have predicted that microdamage within trabeculae can indeed account for the large reductions with apparent modulus at these strain levels.[67] Thus, subtle but widespread damage may account for the large changes in mechanical properties of overloaded trabecular bone. One clinical implication is that an isolated overload may result in damage that produces substantial temporary reductions in mechanical properties. Presumably, an individual with such damage would be at increased risk of fracture until biological healing of the damage is completed and mechanical properties restored. The problem is, because of its subtle nature, it will be difficult to detect this damage clinically.

Finally, despite current limitations on direct measurement of trabecular damage, some consistent trends are now emerging on the biomechanical consequences of damage in trabecular bone. Keyak et al.[150] and Fyhrie and Schaffler[37] reported on how the load-carrying capacity of human tibial and vertebral trabecular bone, respectively, is reduced after loading beyond the ultimate point. The load–reload experiments[140–142] have established that when trabecular bone is reloaded after damage, the stress-strain curve moves toward the original envelope, initially with a stiffness equal to its intact value but primarily bounded by the straight line defining the secant modulus. As a result, factors that decrease the monotonic load-carrying capacity of trabecular bone immediately after the ultimate stress is reached will also cause reductions in residual strength upon reloading, and perhaps residual modulus, too. One such factor is the strain rate—loading at higher strain rates reduces the reduction in stress after the ultimate point is reached.[140] Consistent with this, Fyhrie and Schaffler[37] noted for vertebral trabecular bone that physical damage was less at higher strain rates. It is also known that elderly cortical bone, which is less ductile than younger bone,[151,152] damages more easily than younger tissue when subjected to the same strain.[153] Preexisting trabecular damage at the hip is higher in subjects with lower bone density,[125,126] and percent strength reduction after reloading increases slightly with decreasing apparent density.[140] Taken together, these findings suggest the hypothesis that the biomechanical effects of damage from a nonfracturing fall or overload may be most severe in elderly individuals having brittle bone tissue and low bone density but who are subjected to loads at relatively low strain rates.

16.5 Time-Dependent Behavior

Time effects are also important for trabecular bone strength properties. While there are almost no data available for time-dependent behavior of human trabecular bone, it is clear from bovine studies that trabecular bone exhibits strain rate sensitivity, creep, and fatigue. Clinically, this behavior is important since it is possible that accumulation of trabecular damage from cyclic or creep loading may compromise the strength of a whole bone, thereby increasing the risk factor for fracture. Indeed, accumulated deformations over time may actually represent noncomminuted fractures such as vertebral wedge or crush fractures. Loosening of implants may also be related to time-dependent failure of the supporting trabecular bone.

16.5.1 Strain Rate Effects

It has been long shown that the viscoelastic response of individual trabeculae is similar to that of cortical bone,[154] the marrow plays a negligible role for machined specimens of trabecular bone except perhaps at hyper-physiological strain rates,[154,155] and the strength of trabecular bone is only weakly dependent on strain rate $\dot{\varepsilon}$.[31,32,155,156] With a strain rate exponent of 0.06 (see Eq. 16.1), a 100-fold increase in strain rate would increase strength by about 30%. It is certainly possible that such rate effects may be manifested in differential responses to normal slow habitual loading vs. some type of traumatic event, such as a fall, sports impact, or certainly a vehicular impact. Consistent with this, the proximal femur is about 20% stronger when loaded slowly (2 mm/s) vs. more rapidly (100 mm/s).[157] Results from a series of studies on loading of canine femoral heads with and without marrow suggest that there may also be a hydraulic stiffening effect of marrow *in vivo* due to the constraining effect of the cortex on marrow flow.[158] This is discussed further in Chapter 25.

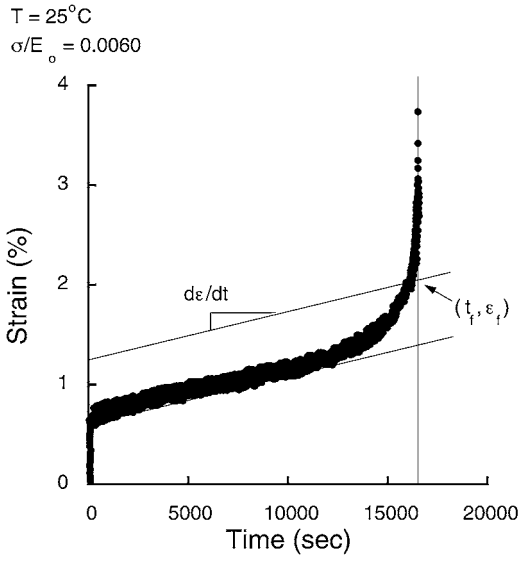

FIGURE 16.21 Creep behavior of bovine trabecular bone, showing the three classical phases. This specimen was tested at 25°C at a non-dimensional stress level of 0.60%. For reference, the reported mean compressive yield strain for this type of bone is about 1%.[10,51] The steady state creep rate ($d\varepsilon/dt$), strain-to-failure (ε_f), and time-to-failure (t_f) are defined from this curve. (From Bowman et al., *J. Biomech. Eng.,* 120, 647–654, 1998. With permission.)

16.5.2 Creep and Fatigue

Following up on some preliminary reports on time-dependent failure modes of trabecular bone,[159,160] it has now been established that trabecular bone—at least bovine—has similar (compressive) fatigue and creep characteristics to cortical bone[161–163] (no tensile creep or fatigue behavior has been reported for trabecular bone). The creep characteristics exhibit the three classical phases of an initial rapid response, a steady-state creep at a constant creep rate, and a rapid increase in strain just before fracture (Fig. 16.21). Regarding fatigue, cyclic loading results in cumulative creep deformations in addition to loss of stiffness (Fig. 16.22). Standard S–N and creep stress–time curves, using nondimensional measures of stress, have now been reported (Fig. 16.23) which can serve as input into whole bone and bone-implant structural analyses. These findings indicate that the compressive strength of (devitalized) trabecular bone can be reduced by up to 70% after 10^6 cycles of loading. Of course, *in vitro* creep or fatigue experiments preclude biological healing, and thus the resulting fatigue S–N or creep stress–time curves might best be considered as lower bounds on the specimen life, i.e., one can expect a longer life if biological healing of the fatigue- or creep-related damage occurs. However, it has been suggested that osteoclastic resorption during the remodeling process can in some situations reduce strength if the resulting Howslip's lacunae serve as significant stress concentrations.[164] If that is the case, then the *in vitro* fatigue characteristics described above may represent upper bounds on the *in vivo* fatigue life, at least perhaps in sites of low-thickness trabeculae. These issues are currently not well understood.

As with the monotonic behavior, once the applied stress is normalized by its modulus, the resulting fatigue and creep behaviors become insensitive to volume fraction. Further analysis of the fatigue behavior has indicated that creep-related mechanisms appear to dominate the cyclic loading response; i.e., the deformations that develop by translation of the stress–strain curve during cyclic loading are larger than those due to loss of stiffness[163] (see Fig. 16.22). Another interesting finding that has emerged from these bovine compressive creep and fatigue studies[162,163] is that the level of strain at failure after such loading is about the same for a given loading type, that this strain level is independent of volume fraction, and that it is greater for creep than for cyclic loading. For example, for compressive creep loading, the average strain to failure is about 2.2% compared to about 0.42% for zero-compression cyclic loading.[163]

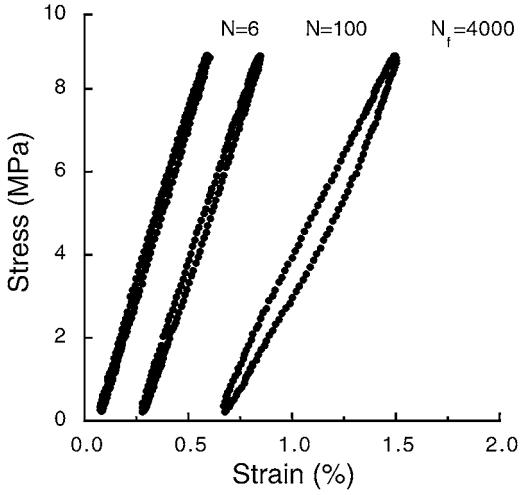

FIGURE 16.22 Stress-strain response during cyclic zero-compression loading of (bovine) trabecular bone to a specified stress level (8.8 MPa in this case, about half its static strength), after 6, 100, and 4,000 cycles. As cyclic loading progresses, the curve translates to the right, representing accumulation of creep strain. The curve also tilts over, displaying a progressively reduced secant modulus. This represents fatigue damage accumulation (loss of stiffness). This specimen failed at 4,000 cycles, as defined by a 10% reduction in secant stiffness. (From Bowman et al., *J. Biomech. Eng.,* 120, 647–654, 1998. With permission.)

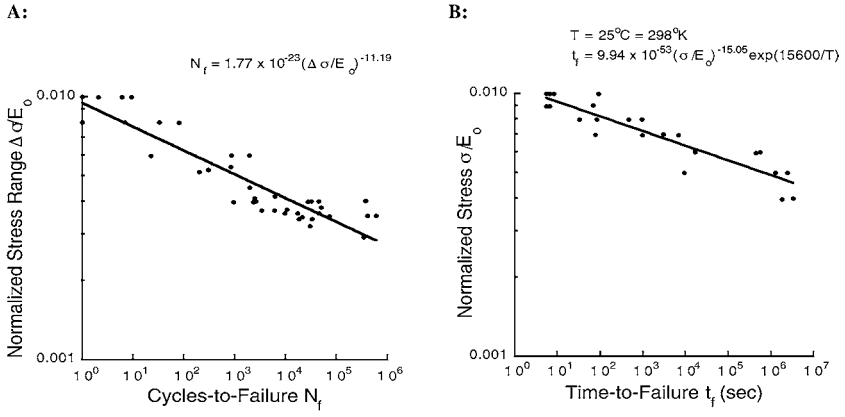

FIGURE 16.23 Traditional S-N fatigue curve (A) for bovine trabecular bone for zero-compression cyclic loading, compared with an equivalent S-t creep curve (B) for compressive creep loading. The fatigue tests were performed at room temperature, whereas the reported regression model for creep was developed from tests done at a variety of temperatures. The data indicate that cyclic or creep loading can reduce strength by up to 70%. (From Bowman et al., *J. Biomech. Eng.,* 120, 647–654, 1998. With permission.)

The creep and fatigue characteristics for human trabecular bone are not known, neither are any tensile creep or fatigue characteristics, nor how any of these behaviors may depend on aging or disease, nor how biological remodeling may potentially accentuate fatigue damage. More importantly, all studies reported to date on trabecular bone have used relatively high loading levels that are probably outside the range of habitual load levels. Thus, despite novel work over the past 10 years on characterization of the time-dependent behavior of trabecular bone, there remains much to be done.

16.6 Summary

Since the last edition of this book, there have been substantial advances in the characterization and understanding of the strength behavior of trabecular bone. Description of the properties in terms of strain greatly simplifies characterization since failure strains do not depend much on apparent density and they are also isotropic (at least for bovine bone). Thus, despite multiple-fold intersite differences in average strength values, failure strains vary little. The precise mechanisms by which bone has adapted to achieve this state remain to be elucidated, but based on the success so far of the lattice-type and high-resolution finite-element models, such insight should soon be forthcoming. These models also show promise for complementing available experimental data to elucidate the multiaxial failure behavior, where, again, the importance of using nondimensional parameters to describe the failure properties is evident. It is also becoming evident that trabecular bone also displays damage, creep, and fatigue characteristics strikingly similar to those for cortical bone. Together, this suggests that the dominant failure mechanisms occur at the lamellar or even sublamellar regions for trabecular bone where micron-level cracks can develop. Even so, most work on multiaxial, damage, and time-dependent properties has been reported for bovine bone. Additional experimental data are required to describe further these complex properties for human bone, and how they may depend on volume fraction, architecture, and tissue properties and, in turn, on age, disease, and drug treatment. With the advent of sophisticated specimen-specific nonlinear computational analysis of trabecular bone, the stage also appears to be set to probe the relationship between increasing understanding of trabecular micromechanics and the associated biological responses.

Acknowledgments

The author acknowledges financial support from the National Institutes of Health (AR41481, AR43784) and the National Science Foundation (BES-9625030). Thanks to the anonymous reviewer, and to the following students for helpful discussion and manuscript preparation: Glen Niebur, Elise Morgan, Oscar Yeh, Eric Nauman, Bill Palm, Julia Fox, Mike Feldstein, Andy Burghardt, and Erika Iverson. Computer resources for Figs. 16.13 and 16.14 were provided in part by the National Partnership for Advanced Computing Infrastructure (UCB 254) and Lawrence Livermore National Laboratory (ISCR B291837, 97-06 and 98-04).

References

1. Harrigan, T. P., Jasty, M., Mann, R. W., and Harris, W. H., Limitations of the continuum assumption in cancellous bone, *J. Biomech.,* 21, 269–275, 1988.
2. Goldstein, S. A., Goulet, R., and McCubbrey, D., Measurement and significance of three-dimensional architecture to the mechanical integrity of trabecular bone, *Calcif. Tissue Int.,* 53S, S127–S133, 1993.
3. McCalden, R. W., McGeough, J. A., and Court-Brown, C. M., Age-related changes in the compressive strength of cancellous bone. The relative importance of changes in density and trabecular architecture, *J. Bone Joint Surg. (Am.),* 79, 421–427, 1997.
4. Snyder, B. and Hayes, W., Multiaxial structure–property relations in trabecular bone, in *Biomechanics of Diarthrodial Joints*, V. C. Mow, A. Ratcliffe, and S.-Y. Woo, Eds., Springer-Verlag, New York, 1990, 31–59.
5. Cowin, S. C., The relationship between the elasticity tensor and the fabric tensor, *Mech. Mater.,* 4, 137–147, 1985.
6. van Rietbergen, B., Odgaard, A., Kabel, J., and Huiskes, R., Direct mechanics assessment of elastic symmetries and properties of trabecular bone architecture, *J. Biomech.,* 29, 1653–1657, 1996.
7. Linde, F., Hvid, I., and Pongsoipetch, B., Energy absorptive properties of human trabecular bone specimens during axial compression, *J. Orthop. Res.,* 7, 432–439, 1989.

8. Lotz, J. C., Gerhart, T. N., and Hayes, W. C., Mechanical properties of trabecular bone from the proximal femur: a quantitative CT study, *J. Comput. Assist. Tomogr.,* 14, 107–114, 1990.
9. Rohlmann, A., Zilch, H., Bergmann, G., and Kolbel, R., Material properties of femoral cancellous bone in axial loading. Part I: Time independent properties, *Arch. Orthop. Trauma Surg.,* 97, 95–102, 1980.
10. Keaveny, T. M., Wachtel, E. F., Ford, C. M., and Hayes, W. C., Differences between the tensile and compressive strengths of bovine tibial trabecular bone depend on modulus, *J. Biomech.,* 27, 1137–1146, 1994.
11. Mosekilde, L., Mosekilde, L., and Danielsen, C. C., Biomechanical competence of vertebral trabecular bone in relation to ash density and age in normal individuals, *Bone,* 8, 79–85, 1987.
12. Mosekilde, L. and Mosekilde, L., Normal vertebral body size and compressive strength: relations to age and to vertebral and iliac trabecular bone compressive strength, *Bone,* 7, 207–212, 1986.
13. Mosekilde, L., Sex differences in age-related loss of vertebral trabecular bone mass and structure—biomechanical consequences, *Bone,* 10, 425–432, 1989.
14. Ding, M., Dalstra, M., Danielsen, C. C., Kabel, J., Hvid, I., and Linde, F., Age variations in the properties of human tibial trabecular bone, *J. Bone Joint Surg. (Br.),* 79, 995–1002, 1997.
15. Keaveny, T. M., Wachtel, E. F., Zadesky, S. P., and Arramon, Y. P., Application of the Tsai-Wu quadratic multiaxial failure criterion to bovine trabecular bone, *J. Biomech. Eng.,* 121, 99–107, 1999.
16. Ford, C. M. and Keaveny, T. M., The dependence of shear failure properties of bovine tibial trabecular bone on apparent density and trabecular orientation, *J. Biomech.,* 29, 1309–1317, 1996.
17. Carter, D. R. and Hayes, W. C., The compressive behavior of bone as a two-phase porous structure, *J. Bone Joint Surg.,* 59-A, 954–962, 1977.
18. Rice, J. C., Cowin, S. C., and Bowman, J. A., On the dependence of the elasticity and strength of cancellous bone on apparent density, *J. Biomech.,* 21, 155–168, 1988.
19. Hansson, T. H., Keller, T. S., and Panjabi, M. M., A study of the compressive properties of lumbar vertebral trabeculae: effects of tissue characteristics, *Spine,* 11, 56–62, 1986.
20. Kopperdahl, D. L. and Keaveny, T. M., Yield strain behavior of trabecular bone, *J. Biomech.,* 31, 601–608, 1998.
21. Gibson, L. J., The mechanical behavior of cancellous bone, *J. Biomech.,* 18, 317–328, 1985.
22. Rajan, K., Linear elastic properties of trabecular bone: a cellular solid approach, *J. Mater. Sci. Lett.,* 4, 609–611, 1985.
23. Keaveny, T. M., Mechanistic approaches to analysis of trabecular bone, *Forma,* 12, 267–275, 1997.
24. Turner, C. H., On Wolff's law of trabecular architecture, *J. Biomech.,* 25, 1–9, 1992.
25. Cowin, S. C., Wolff's law of trabecular architecture at remodeling equilibrium, *J. Biomech. Eng.,* 108, 83–88, 1986.
26. Cowin, S. C., Sadegh, A. M., and Luo, G. M., An evolutionary Wolff's law for trabecular architecture, *J. Biomech. Eng.,* 114, 129–136, 1992.
27. Carter, D. R., Schwab, G. H., and Spengler, D. M., Tensile fracture of cancellous bone, *Acta Orthop. Scand.,* 51, 733–741, 1980.
28. Kaplan, S. J., Hayes, W. C., Stone, J. L., and Beaupre, G. S., Tensile strength of bovine trabecular bone, *J. Biomech.,* 18, 723–727, 1985.
29. Stone, J. L., Beaupre, G. S., and Hayes, W. C., Multiaxial strength characteristics of trabecular bone, *J. Biomech.,* 16, 743–752, 1983.
30. Rohl, L., Larsen, E., Linde, F., Odgaard, A., and Jorgensen, J., Tensile and compressive properties of cancellous bone, *J. Biomech.,* 24, 1143–1149, 1991.
31. Brown, T. D. and Ferguson, A. B., Mechanical property distributions in the cancellous bone of the human proximal femur, *Acta Orthop. Scand.,* 51, 429–437, 1980.
32. Ducheyne, P., Heymans, L., Martens, M., Aernoudt, E., Meester, P., and Mulier, J., The mechanical behavior of intracondylar cancellous bone of the femur at different loading rates, *J. Biomech.,* 10, 747–762, 1977.

33. Goldstein, S. A., Wilson, D. L., Sonstegard, D. A., and Matthews, L. S., The mechanical properties of human tibial trabecular bone as a function of metaphyseal location, *J. Biomech.,* 16, 965–969, 1983.
34. Odgaard, A., Hvid, I., and Linde, F., Compressive axial strain distributions in cancellous bone specimens, *J. Biomech.,* 22, 829–835, 1989.
35. Turner, C. H., Yield behavior of bovine cancellous bone, *J. Biomech. Eng.,* 111, 256–260, 1989.
36. Williams, J. L. and Lewis, J. L., Properties and an anisotropic model of cancellous bone from the proximal tibial epiphysis, *J. Biomed. Eng.,* 104, 50–56, 1982.
37. Fyhrie, D. P. and Schaffler, M. B., Failure mechanisms in human vertebral cancellous bone, *Bone,* 15, 105–109, 1994.
38. Hou, F. J., Lang, S. M., Hoshaw, S. J., Reimann, D. A., and Fyhrie, D. P., Human vertebral body apparent and hard tissue stiffness, *J. Biomech.,* 31, 1009–1015, 1998.
39. Hansson, T. H., Keller, T. S., and Panjabi, M. M., A study of the compressive properties of lumbar vertebral trabeculae: effects of tissue characteristics, *Spine,* 12, 56–62, 1987.
40. Hvid, I., Bentzen, S. M., Linde, F., Mosekilde, L., and Pongsoipetch, B., X-ray quantitative computed tomography: the relations to physical properties of proximal tibial trabecular bone specimens, *J. Biomech.,* 22, 837–844, 1989.
41. Hvid, I., Jensen, N. C., Bunger, C., Solund, K., and Djurhuus, J. C., Bone mineral assay: its relation to the mechanical strength of cancellous bone, *Eng. Med.,* 14, 79–83, 1985.
42. Mosekilde, L., Bentzen, S. M., Ortoft, G., and Jorgensen, J., The predictive value of quantitative computed tomography for vertebral body compressive strength and ash density, *Bone,* 10, 465–470, 1989.
43. Linde, F. and Hvid, I., Stiffness behaviour of trabecular bone specimens, *J. Biomech.,* 20, 83–89, 1987.
44. Linde, F. and Hvid, I., The effect of constraint on the mechanical behaviour of trabecular bone specimens, *J. Biomech.,* 22, 485–490, 1989.
45. Linde, F., Hvid, I., and Madsen, F., The effect of specimen geometry on the mechanical behaviour of trabecular bone specimens, *J. Biomech.,* 25, 359–368, 1992.
46. Odgaard, A. and Linde, F., The underestimation of Young's modulus in compressive testing of cancellous bone specimens, *J. Biomech.,* 24, 691–698, 1991.
47. Keaveny, T. M., Borchers, R. E., Gibson, L. J., and Hayes, W. C., Trabecular bone modulus and strength can depend on specimen geometry, *J. Biomech.,* 26, 991–1000, 1993.
48. Keaveny, T. M., Pinilla, T. P., Crawford, R. P., Kopperdahl, D. L., and Lou, A., Systematic and random errors in compression testing of trabecular bone, *J. Orthop. Res.,* 15, 101–110, 1997.
49. Morgan, E. F., Arramon, Y. P., Kopperdahl, D. L., and Keaveny, T. M., Dependence of yield strain on anatomic site for human trabecular bone, *Adv. Bioeng.,* Nashville TN, ASME BED–Vol. 43, 23–24, 1999.
50. Silva, M. J., Keaveny, T. M., and Hayes, W. C., Computed tomography-based finite element analysis predicts failure loads and fracture patterns for vertebral sections, *J. Orthop. Res.,* 16, 300–308, 1998.
51. Chang, W. C. W., Christensen, T. M., Pinilla, T. P., and Keaveny, T. M., Isotropy of uniaxial yield strains for bovine trabecular bone, *J. Orthop. Res.,* 17, 582–585, 1999.
52. Gibson, L. J. and Ashby, M. F., *Cellular Solids: Structures & Properties,* 2nd ed., Pergamon Press, Oxford, 1997.
53. Reilly, D. T. and Burstein, A. H., The elastic and ultimate properties of compact bone tissue, *J. Biomech.,* 8, 393–405, 1975.
54. McElhaney, J., Alem, N., and Roberts, V., A porous block model for cancellous bone, *Trans. ASME,* 1, 9, 1970.
55. Beaupre, G. S. and Hayes, W. C., Finite element analysis of a three-dimensional open-celled model for trabecular bone, *J. Biomech. Eng.,* 107, 249–256, 1985.
56. Guo, X. E., McMahon, T. A., Keaveny, T. M., Hayes, W. C., and Gibson, L. J., Finite element modeling of damage accumulation in trabecular bone under cyclic loading, *J. Biomech.,* 27, 145–155, 1994.

57. Pugh, J. W., Rose, R. M., and Radin, E. L., A structural model for the mechanical behavior of trabecular bone, *J. Biomech.,* 6, 657–670, 1973.
58. Jensen, K. S., Mosekilde, L., and Mosekilde, L., A model of vertebral trabecular bone architecture and its mechanical properties, *Bone,* 11, 417–423, 1990.
59. Silva, M. J. and Gibson, L. J., The effects of non-periodic microstructure on the elastic properties of two-dimensional cellular solids, *Int. J. Mech. Sci.,* 37, 1161–1177, 1995.
60. Silva, M. J. and Gibson, L. J., Modeling the mechanical behavior of vertebral trabecular bone: effects of age-related changes in microstructure, *Bone,* 21, 191–199, 1997.
61. Silva, M. J. and Gibson, L. J., The effects of non-periodic microstructure and defects on the compressive strength of two-dimensional cellular solids, *Int. J. Mech. Sci.,* 39, 549–563, 1997.
62. Yeh, O. C. and Keaveny, T. M., Biomechanical effects of intra-specimen variations in trabecular architecture: a three-dimensional finite element study, *Bone,* 25, 223–228, 1999.
63. Mosekilde, L., Age-related changes in vertebral trabecular bone architecture—assessed by a new method, *Bone,* 9, 247–250, 1988.
64. Wakamatsu, E. and Sissons, H. A., The cancellous bone of the iliac crest, *Calcif. Tissue Res.,* 4, 147–161, 1969.
65. Aaron, J. E., Makins, N. B., and Sagreiya, K., The microanatomy of trabecular bone loss in normal aging men and women, *Clin. Orthop.,* 215, 260–271, 1987.
66. Kothari, M., Keaveny, T. M., Lin, J. C., Newitt, D. C., Genant, H., and Majumdar, S., Measurement of intra-specimen variations in cancellous bone architecture, *Bone,* 25, 245–250, 1999.
67. Yeh, O. C. and Keaveny, T. M., Roles of microdamage and microfracture in the mechanical behavior of trabecular bone, *Trans. Orthop. Res. Soc.* (Orlando), 25, 34, 2000.
68. Feldkamp, L. A., Goldstein, S. A., Parfitt, A. M., Jesion, G., and Kleerekoper, M., The direct examination of three-dimensional bone architecture in vitro by computed tomography, *J. Bone Miner. Res.,* 4, 3–11, 1989.
69. Müller, R., Hahn, M., Vogel, M., Delling, G., and Rüegsegger, P., Morphometric analysis of non-invasively assessed bone biopsies, comparison of high-resolution computed tomography and histologic sections, *Bone,* 18, 215–220, 1996.
70. Odgaard, A., Andersen, K., Melsen, F., and Gundersen, H. J., A direct method for fast three-dimensional serial reconstruction, *J. Microsc.,* 159, 335–342, 1990.
71. Beck, J. D., Canfield, B. L., Haddock, S. M., Chen, T. J. H., Kothari, M., and Keaveny, T. M., Three-dimensional imaging of trabecular bone using the Computer Numerically Controlled Milling technique, *Bone,* 21, 281–287, 1997.
72. Kinney, J. H., Lane, N. E., and Haupt, D. L., In vivo, three-dimensional microscopy of trabecular bone, *J. Bone Miner. Res.,* 10, 264–270, 1995.
73. Chung, H. W., Wehrli, F. W., Williams, J. L., and Wehrli, S. L., Three-dimensional nuclear magnetic resonance microimaging of trabecular bone, *J. Bone Miner. Res.,* 10, 1452–1461, 1995.
74. Hipp, J. A., Jansujwicz, A., Simmons, C. A., and Snyder, B. D., Trabecular bone morphology from micro-magnetic resonance imaging, *J. Bone Miner. Res.,* 11, 286–297, 1996.
75. van Rietbergen, B., Weinans, H., Huiskes, R., and Odgaard, A., A new method to determine trabecular bone elastic properties and loading using micromechanical finite element models, *J. Biomech.,* 28, 69–81, 1995.
76. Hollister, S. J., Brennan, J. M., and Kikuchi, N., A homogenization sampling procedure for calculating trabecular bone effective stiffness and tissue level stress, *J. Biomech.,* 27, 433–444, 1994.
77. van Rietbergen, B., Müller, R., Ulrich, D., Rüegsegger, P., and Huiskes, R., Tissue stresses and strain in trabeculae of a canine proximal femur can be quantified from computer reconstructions, *J. Biomech.,* 32, 165–173, 1999.
78. Ulrich, D., van Rietbergen, B., Laib, A., and Rüegsegger, P., Load transfer analysis of the distal radius from in-vivo high-resolution CT-imaging, *J. Biomech.,* 32, 821–828, 1999.

79. van Rietbergen, B., Weinans, H., Huiskes, R., and Polman, B. J. W., Computational strategies for iterative solutions of large FEM applications employing voxel data, *Int. J. Numer. Methods. Eng.,* 39, 2743–2767, 1996.
80. Hollister, S. J., Fyhrie, D. P., Jepsen, K. J., and Goldstein, S. A., Application of homogenization theory to the study of trabecular bone mechanics, *J. Biomech.,* 24, 825–839, 1991.
81. Hollister, S. J., Kikuchi, N., and Goldstein, S. A., Do bone ingrowth processes produce a globally optimized structure? *J. Biomech.,* 26, 391–407, 1993.
82. Muller, R. and Ruegsegger, P., Analysis of mechanical properties of cancellous bone under conditions of simulated bone atrophy, *J. Biomech.,* 29, 1053–1060, 1996.
83. van Rietbergen, B., Weinans, H., and Huiskes, R., Prospects of computer models for the prediction of osteoporotic bone fracture risk, *Stud. Health Technol. Inform.,* 40, 25–32, 1997.
84. van Rietbergen, B., Odgaard, A., Kabel, J., and Huiskes, R., Relationships between bone morphology and bone elastic properties can be accurately quantified using high-resolution computer reconstructions, *J. Orthop. Res.,* 16, 23–28, 1998.
85. Kinney, J. H. and Ladd, A. J., The relationship between three-dimensional connectivity and the elastic properties of trabecular bone, *J. Bone Miner. Res.,* 13, 839–845, 1998.
86. Ladd, A. J., Kinney, J. H., Haupt, D. L., and Goldstein, S. A., Finite-element modeling of trabecular bone: comparison with mechanical testing and determination of tissue modulus, *J. Orthop. Res.,* 16, 622–628, 1998.
87. Fyhrie, D. P., and Hou, F. J., Prediction of human vertebral cancellous bone strength using nonlinear, anatomically accurate, large-scale, finite element analysis, *Proc. Bioeng. Conf.,* Beaver Creek, CO. ASME, ASME BED–Vol. 29, 301–302, 1995.
88. van Rietbergen, B., Ulrich, D., Pistoia, W., Huiskes, R., and Rüegsegger, P., Prediction of trabecular bone failure parameters using a tissue failure criterion, *Trans. Orthop. Res. Soc.,* New Orleans, 23, 550, 1998.
89. Niebur, G. L., Hsia, A. C., Chen, T. J., and Keaveny, T. M., Simulation of trabecular bone yield using nonlinear finite element analysis, *Adv. Bioeng.,* Nashville TN, ASME BED–Vol. 43, 175–176, 1999.
90. Turner, C. H., Rho, J., Takano, Y., Tsui, T. Y., and Pharr, G. M., The elastic properties of trabecular and cortical bone tissues are similar: results from two microscopic measurement techniques, *J. Biomech.,* 32, 437–441, 1999.
91. Rho, J. Y., Tsui, T. Y., and Pharr, G. M., Elastic properties of human cortical and trabecular lamellar bone measured by nanoindentation, *Biomaterials,* 18, 1325–1330, 1997.
92. Brown, T. D., Mutschler, T. A., and Ferguson, A. B., A non-linear finite element analysis of some early collapse processes in femoral head osteonecrosis, *J. Biomech.,* 15, 705–715, 1982.
93. Carter, D. R., Orr, T. E., and Fyhrie, D. P., Relationships between loading history and femoral cancellous bone architecture, *J. Biomech.,* 22, 231–244, 1989.
94. Carter, D. R. and Vasu, R., Stress changes in the femoral head due to porous ingrowth surface replacement arthroplasty, *J. Biomech.,* 17, 737–747, 1984.
95. Cheal, E. J., Hayes, W. C., Lee, C. H., Snyder, B. D., and Miller, J., Stress analysis of a condylar knee tibial component: influence of metaphyseal shell properties and cement injection depth, *J. Orthop. Res.,* 3, 424–434, 1985.
96. Cheal, E. J., Snyder, B. D., Nunamaker, D. M., and Hayes, W. C., Trabecular bone remodeling around smooth and porous implants in an equine patellar model, *J. Biomech.,* 20, 1121–1134, 1987.
97. Fyhrie, D. P. and Carter, D. R., Femoral head apparent density distribution predicted from bone stresses, *J. Biomech.,* 23, 1–10, 1990.
98. Hayes, W. C., Swenson, L. W., Jr., and Schurman, D. J., Axisymmetric finite element analysis of the lateral tibial plateau, *J. Biomech.,* 11, 21–33, 1978.
99. Vasu, R., Carter, D. R., and Harris, W. H., Stress distributions in the acetabular region. I. Before and after total joint replacement, *J. Biomech.,* 15, 155–164, 1981.

100. Lotz, J. C., Cheal, E. J., and Hayes, W. C., Fracture prediction for the proximal femur using finite element models: Part II—Nonlinear analysis, *J. Biomech. Eng.,* 113, 361–365, 1991.
101. Lotz, J. C., Cheal, E. J., and Hayes, W. C., Fracture prediction for the proximal femur using finite element models: Part I—Linear analysis, *J. Biomech. Eng.,* 113, 353–360, 1991.
102. Cowin, S. C., Fabric dependence of an anisotropic strength criterion, *Mech. Mater.,* 5, 251–260, 1986.
103. Cowin, S. C., *Bone Mechanics,* CRC Press, Boca Raton, FL, 1989.
104. Fenech, C. and Keaveny, T. M., A cellular solid criterion for predicting the axial-shear failure properties of trabecular bone, *J. Biomech. Eng.,* 121, 414–422, 1999.
105. Tsai, S. and Wu, E., A general theory for strength of anisotropic materials, *J. Comp. Mater.,* 5, 58–80, 1971.
106. Wu, E., Phenomenological anisotropic failure criterion, in *Mechanics of Composite Materials,* G. Sendecky, Ed., Academic Press, New York, 1974, 353–431.
107. Triantafillou, T. C., Zhang, J., Shercliff, T. L., Gibson, L. J., and Ashby, M. F., Failure surfaces for cellular materials under multiaxial loads—II. Comparison of models with experiment, *Int. J. Mech. Sci.,* 31, 665–678, 1989.
108. Gibson, L. J., Ashby, M. F., Zhang, J., and Triantafillou, T. C., Failure surfaces for cellular materials under multiaxial loads—I. Modelling, *Int. J. Mech. Sci.,* 31, 635–663, 1989.
109. Triantafillou, T. C. and Gibson, L. J., Multiaxial failure criteria for brittle foams, *Int. J. Mech. Sci.,* 32, 479–496, 1990.
110. Patel, M. R., The Deformation and Fracture of Rigid Cellular Plastics under Multiaxial Stress, Ph.D. dissertation, University of California, Berkeley, CA, 1969.
111. Cezayirlioglu, H., Bahniuk, E., Davy, D. T., and Heiple, K. G., Anisotropic yield behavior of bone under combined axial force and torque, *J. Biomech.,* 18, 61–69, 1985.
112. Hayes, W. C. and Wright, T. M., An empirical strength theory for compact bone, *Fracture,* 3, 1173–1179, 1977.
113. Cowin, S. C., On the strength anisotropy of bone and wood, *J. Mech.,* 46, 832–838, 1979.
114. Zaslawsky, M., Multiaxial-stress studies on rigid polyurethane foam, *Exp., Mech.,* 2, 70–76, 1973.
115. Cowin, S. C. and Turner, C. H., On the relationship between the orthotropic Young's moduli and fabric, *J. App. Biomech.,* 25, 1493–1494, 1992.
116. Turner, C. H., Cowin, S. C., Rho, J. Y., Ashman, R. B., and Rice, J. C., The fabric dependence of the orthotropic elastic constants of cancellous bone, *J. Biomech.,* 23, 549–561, 1990.
117. Harrigan, T. and Mann, R., Characterization of microstructural anisotropy in orthotropic materials using a second rank tensor, *J. Mater. Sci.,* 19, 761–767, 1984.
118. Whitehouse, W. J., The quantitative morphology of anisotropic trabecular bone, *J. Microsc.,* 2, 153–168, 1974.
119. Whitehouse, W. J., A stereological method for calculating internal surface areas in structures which have become anisotropic as the result of linear expansions or contractions, *J. Microsc.,* 101, (2), 169–176, 1974.
120. Rowlands, R. E., Strength (failure) theories and their experimental correlations, in *Handbook of Composites,* Vol. 3, G. C. Sih and A. M. Skudra, Eds., Elsevier Science, Amsterdam, 1985, 71–125.
121. Galante, J., Rostoker, W., and Ray, R. D., Physical properties of trabecular bone, *Calcif. Tissue Res.,* 5, 236–246, 1970.
122. Burr, D. B., Forwood, M. R., Fyhrie, D. P., Martin, R. B., Schaffler, M. B., and Turner, C. H., Bone microdamage and skeletal fragility in osteoporotic and stress fractures, *J. Bone Miner. Res.,* 12, 6–15, 1997.
123. Hansson, T. and Roos, B., Microcalluses of the trabeculae in lumbar vertebrae and their relation to the bone mineral content, *Spine,* 6, 375–380, 1981.
124. Hahn, M., Vogel, M., Amling, M., Ritzel, H., and Delling, G., Microcallus formations of the cancellous bone: a quantitative analysis of the human spine, *J. Bone Miner. Res.,* 10, 1410–1416, 1995.

125. Mori, S., Harruff, R., Ambrosius, W., and Burr, D. B., Trabecular bone volume and microdamage accumulation in the femoral heads of women with and without femoral neck fractures, *Bone,* 21, 521–526, 1997.
126. Fazzalari, N. L., Forwood, M. R., Smith, K., Manthey, B. A., and Herreen, P., Assessment of cancellous bone quality in severe osteoarthrosis: bone mineral density, mechanics, and microdamage, *Bone,* 22, 381–388, 1998.
127. Vernon, R. B. and Pirie, C. J., Healing trabecular microfractures in the bodies of lumbar vertebrae, *Ann. Rheum. Dis.,* 32, 406–412, 1973.
128. Wenzel, T. E., Schaffler, M. B., and Fyhrie, D. P., In vivo trabecular microcracks in human vertebral bone, *Bone,* 19, 89–95, 1996.
129. Ohtani, T. and Azuma, H., Trabecular microfractures in the acetabulum. Histologic studies in cadavers, *Acta Orthop. Scand.,* 55, 419–422, 1984.
130. Urovitz, E. P., Fornasier, V. L., Risen, M. I., and MacNab, I., Etiological factors in the pathogenesis of femoral trabecular fatigue fractures, *Clin. Orthop.,* 1977, 275–280, 1977.
131. Koszyca, B., Fazzalari, N. L., and Vernon, R. B., Trabecular microfractures. Nature and distribution in the proximal femur, *Clin. Orthop.,* 244, 208–216, 1989.
132. Benaissa, R., Uhthoff, H. K., and Mercier, P., Repair of trabecular fatigue fractures. Cadaver studies of the upper femur, *Acta Orthop. Scand.,* 60, 585–589, 1989.
133. Todd, R. C., Freeman, M. A., and Pirie, C. J., Isolated trabecular fatigue fractures in the femoral head, *J. Bone Joint Surg. (Br.),* 54, 723–728, 1972.
134. Pugh, J. W., Rose, R. M., and Radin, E. L., A possible mechanism of Wolff's law: trabecular microfractures, *Arch. Int. Physiol. Biochim.,* 81, 27–40, 1973.
135. Radin, E. L., Parker, H. G., Pugh, J. W., Steinberg, R. S., Paul, I. L., and Rose, R. M., Response of joints to impact loading. 3. Relationship between trabecular microfractures and cartilage degeneration, *J. Biomech.,* 6, 51–57, 1973.
136. Fazzalari, N. L., Trabecular microfracture, *Calcif. Tissue Int.,* 53, S143–S147, 1993.
137. Mosekilde, L., Consequences of the remodelling process for vertebral trabecular bone structure: a scanning electron microscopy study (uncoupling of unloaded structures), *Bone Miner.,* 10, 13–35, 1990.
138. Hasegawa, K., Turner, C. H., Chen, J., and Burr, D. B., Effect of disc lesion on microdamage accumulation in lumbar vertebrae under cyclic compression loading, *Clin. Orthop.,* 311, 190–198, 1995.
139. Wachtel, E. F. and Keaveny, T. M., Dependence of trabecular damage on mechanical strain, *J. Orthop. Res.,* 15, 781–787, 1997.
140. Keaveny, T. M., Wachtel, E. F., and Kopperdahl, D. L., Mechanical behavior of human trabecular bone after overloading, *J. Orthop. Res.,* 17, 346–353, 1999.
141. Keaveny, T. M., Wachtel, E. F., Guo, X. E., and Hayes, W. C., Mechanical behavior of damaged trabecular bone, *J. Biomech.,* 27, 1309–1318, 1994.
142. Zysset, P. K. and Curnier, A., A 3D damage model for trabecular bone based on fabric tensors, *J. Biomech.,* 29, 1549–1558, 1996.
143. Krajcinovic, D. and Lemaitre, J., *Continuum Damage Mechanics, Theory and Applications,* Springer-Verlag, New York, 1987.
144. Kopperdahl, D. L., Pearlman, J. L., and Keaveny, T. M., Biomechanical consequences of an isolated overload on the human vertebral body, *J. Orthop. Res.,* 18, 685–690, 2000.
145. Silva, M. J., Keaveny, T. M., and Hayes, W. C., Direct and computed tomography thickness measurements of the human lumbar vertebral shell and endplate, *Bone,* 15, 409–414, 1994.
146. Fondrk, M., Bahniuk, E., Davy, D. T., and Michaels, C., Some viscoplastic characteristics of bovine and human cortical bone, *J. Biomech.,* 21, 623–630, 1988.
147. Burr, D. B. and Stafford, T., Validity of the bulk-staining technique to separate artifactual from in vivo bone microdamage, *Clin. Orthop.,* 260, 305–308, 1990.
148. Burr, D. B. and Hooser, M., Alterations to the en bloc basic fuchsin staining protocol for the demonstration of microdamage produced in vivo, *Bone,* 17, 431–433, 1995.

149. Fazzalari, N. L., Forwood, M. R., Manthey, B. A., Smith, K., and Kolesik, P., Three-dimensional confocal images of microdamage in cancellous bone, *Bone,* 23, 373–378, 1998.
150. Keyak, J. H., Lee, I. Y., Nath, D. S., and Skinner, H. B., Postfailure compressive behavior of tibial trabecular bone in three anatomic directions, *J. Biomed. Mater. Res.,* 31, 373–378, 1996.
151. McCalden, R. W., McGeough, J. A., Barker, M. B., and Court-Brown, C. M., Age-related changes in the tensile properties of cortical bone. The relative importance of changes in porosity, mineralization, and microstructure, *J. Bone Joint Surg. (Am.),* 75, 1193–1205, 1993.
152. Burstein, A. H., Reilly, D. T., and Martens, M., Aging of bone tissue: mechanical properties, *J. Bone Joint Surg. (Am.),* 58, 82–86, 1976.
153. Courtney, A. C., Hayes, W. C., and Gibson, L. J., Age-related differences in post-yield damage in human cortical bone. Experiment and model, *J. Biomech.,* 29, 1463–1471, 1996.
154. Pugh, J. W., Rose, R. M., and Radin, E. L., Elastic and viscoelastic properties of trabecular bone: dependence on structure, *J. Biomech.,* 6, 475–485, 1973.
155. Carter, D. R. and Hayes, W. C., Bone compressive strength: the influence of density and strain rate, *Science,* 194, 1174–1176, 1976.
156. Linde, F., Norgaard, P., Hvid, I., Odgaard, A., and Soballe, K., Mechanical properties of trabecular bone. Dependency on strain rate, *J. Biomech.,* 24, 803–809, 1991.
157. Courtney, A. C., Wachtel, E. F., Myers, E. R., and Hayes, W. C., Effects of loading rate on the strength of the proximal femur, *Calcif. Tissue Int.,* 55, 53–58, 1994.
158. Ochoa, J. A., Sanders, A. P., Kiesler, T. W., Heck, D. A., Toombs, J. P., Brandt, K. D., and Hillberry, B. M., In vivo observations of hydraulic stiffening in the canine femoral head, *J. Biomech. Eng.,* 119, 103–108, 1997.
159. Schoenfeld, C. M., Lautenschlager, E. P., and Meyer, P. R. J., Mechanical properties of human cancellous bone in the femoral head, *Med. Biol. Eng.,* 12, 313–317, 1974.
160. Zilch, H., Rohlmann, A., Bergmann, G., and Kolbel, R., Material properties of femoral cancellous bone in axial loading. Part II: Time dependent properties, *Arch. Orthop. Trauma Surg.,* 97, 257–262, 1980.
161. Michel, M. C., Guo, X. D., Gibson, L. J., McMahon, T. A., and Hayes, W. C., Compressive fatigue behavior of bovine trabecular bone, *J. Biomech.,* 26, 453–463, 1993.
162. Bowman, S. M., Keaveny, T. M., Gibson, L. J., Hayes, W. C., and McMahon, T. A., Compressive creep behavior of bovine trabecular bone, *J. Biomech.,* 27, 301–310, 1994.
163. Bowman, S. M., Guo, X. E., Cheng, D. W., Keaveny, T. M., Gibson, L. J., Hayes, W. C., and McMahon, T. A., Creep contributes to the fatigue behavior of bovine trabecular bone, *J. Biomech. Eng.,* 120, 647–654, 1998.
164. Martin, R. B., Gibson, V. A., Stover, S. M., Gibeling, J. C., and Griffin, L. V., Residual strength of equine bone is not reduced by intense fatigue loading: implications for stress fracture, *J. Biomech.,* 30, 109–114, 1997.

17

Observations of Damage in Bone

Karl J. Jepsen
Mount Sinai School of Medicine

Dwight T. Davy
Case Western Reserve University

Ozan Akkus
Case Western Reserve University

17.1 Introduction

This chapter focuses on experimental issues in bone damage mechanics. Reifsnider[1] expresses the historical definition for the term *damage* as "harm or injury that diminishes the value or usefulness of the object which is 'damaged.'" This is a convenient starting place for the considerations here, which involve the physical evidence for damage (i.e., the "harm or injury") and the mechanical effects of damage (i.e., the "diminished usefulness") in bone. Although the sources of damage can be numerous, here the definition will be sharpened to identify damage as the loss of material continuity. In the context of mechanics, this allows one to distinguish damage from other behaviors such as anelasticity and plasticity.

The above definition permits drawing two inferences. One regards the mechanical effects of damage. The loss of continuity will cause most, if not all, mechanical properties to be degraded. This degradation is the basis for mechanical investigations of damage effects and helps define appropriate measurements. The second inference regards the physical appearance of damage. At least at some scale, the loss of continuity should be manifested as cracks and voids. This is the motivation behind a number of investigations seeking to characterize damage using histological and histomorphometric techniques. It is also reasonable to expect that there is a correlation between physical observations of damage and mechanical effects of damage, motivating studies combining mechanical and histological measurements.

As shown elsewhere in this volume, bone tissue has a significant volume of voids that are naturally occurring and distinct from damage. The existence of microcracks in bone tissue that are not part of these voids is also a well-established fact.[2] Damage accumulation is a normal response of composite materials to mechanical loading and it is this damageability that contributes to the superior fatigue resistance and toughness of composite materials compared with monolithic materials.[1] In bone, the presence of damage

0-8493-9117-2/01/$0.00+$.50

also has a biological consequence. Since microcracks exist at some volume in normal, healthy bone, they may play a role in the "normal" turnover process as well as adaptive behavior of bone.[3,4]

There is some debate concerning the point at which the physical evidence of damage (microcracks) should be regarded as consequential in terms of mechanical behavior.[5] A strict interpretation of damage as loss of continuity implies that mechanical properties will necessarily be degraded, whether or not they are discernible by common testing techniques. For experimental studies of bone damage, a more practical interpretation is in terms of significant increases in histological measures of damage or significant decreases in mechanical properties compared with "normal" values.

This chapter examines three independent but complementary methods of characterizing damage in bone: the mechanical characterization of damage based on property degradation, the physical characterization of damage via histological and histomorphometric means, and real-time characterization of damage based on acoustic emission. Reifsnider[6] put forth two important questions regarding how an engineer should assess the overall performance of structural materials in terms of strength: "What physical 'damage' processes are observed, and what changes in material properties are caused by these processes?" The purpose of this chapter is to address these questions in the context of these three methods of characterizing damage.

17.2 Mechanical Property Degradation as a Measure of Damage

17.2.1 Bone Inelasticity

Damage accumulation is manifested mechanically as inelastic stress–strain behavior. However, bone also exhibits behaviors consistent with plastic flow and viscous creep. It is important to distinguish between damage behavior and these other inelastic behaviors, particularly when using mechanical property degradation as a measure of the damage state. Mechanical property degradation is used as an end point to assess the physical nature of damage,[7,8] the effects of damage on bone strength,[9] or the biological response to damage.[10] To understand how mechanical property degradation relates to the physical evidence of damage, it is necessary to assess and interpret mechanical property degradation properly.

For purposes of this chapter (see also Chapter 18), the following definitions will be adopted. Inelastic behavior will be defined as the deviation from elastic behavior. Sources of inelastic behavior will be defined as (1) damage as loss of material continuity via formation of cracks or voids, which degrades stiffness as well as other mechanical properties; (2) plasticity as evidence of flow processes that do not change the stiffness of the material but create irrecoverable strains upon unloading as well as strain hardening; (3) anelasticity or delayed elasticity as dissipative (viscous) processes that increase stiffness with increased loading rate but do not involve irrecoverable strains. Accordingly, the total strain (ε_T) is the sum of elastic strain (ε_E) and inelastic strain due to damage accumulation (ε_d) and plastic flow (ε_p) and recoverable (anelastic) strains due to viscous creep (ε_v), such that $\varepsilon_T = \varepsilon_E + \varepsilon_d + \varepsilon_p + \varepsilon_v$.

If a machined cortical bone sample is subjected to a monotonic tensile load, the stress–strain curve can be divided into three phases[11,12] as shown in Fig. 17.1. Bone samples loaded below some strain level (Phase I, Fig. 17.1) would recover to zero strain if unloaded.[13,14] For cyclic loading, Pattin et al.[15] proposed 2500 $\mu\varepsilon$ in tension and 4000 $\mu\varepsilon$ in compression as limits for this regime. Phase II is commonly identified as the yield and post-yield region and is associated with the onset of inelastic processes. Phase III is the prefailure phase in which crack growth leads rapidly to rupture in a tensile test.

It is not possible to distinguish the roles of viscosity, plasticity, and damage in the accumulation of inelastic strains in a monotonic test to failure. To do so, it is necessary to examine unloading and reloading characteristics. Fig. 17.2 shows some possible stress–strain histories for a subfailure load cycle under strain control into the inelastic range. If damage alone accounted for the inelasticity, the load–unload cycle would appear as Fig. 17.2a, returning to zero strain at zero stress. If plastic behavior alone accounted for the inelasticity, the load–unload cycle would appear as Fig. 17.2b. If purely viscoelastic behavior accounted for the inelastic behavior, it would appear as Fig. 17.2c. Shown in Fig. 17.2d is an actual tensile

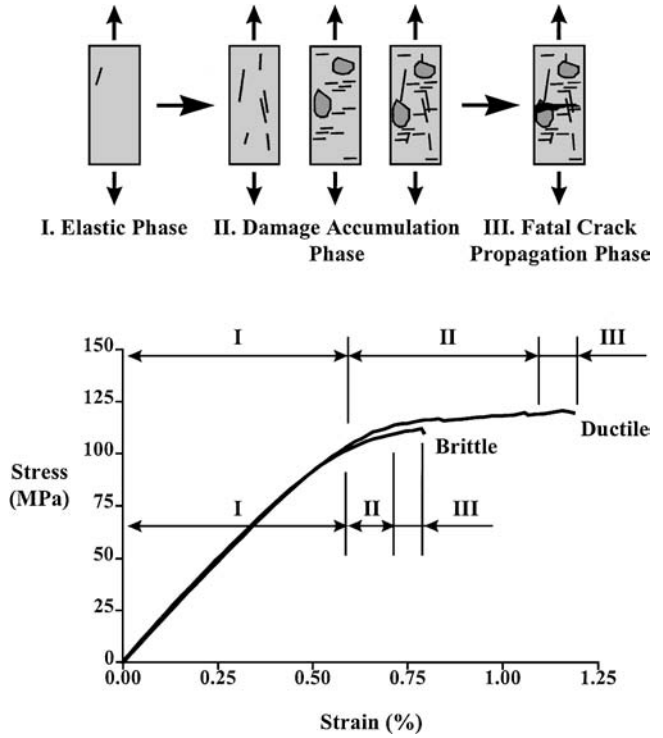

FIGURE 17.1 Segregation of stress–strain curves into elastic, damaging, and fracture regimes for cortical bone tensile tests demonstrating more ductile and more brittle behavior. (Based on Currey and Brear.[12])

stress–strain curve for human bone, which exhibits some features of each of these behaviors. The reduced stiffness on unloading is evidence that damage has occurred. However, there is clear evidence of behaviors consistent with both viscous and plastic flow. This observation is of particular importance when considering ways to assess damage.

17.2.2 The Mechanical Consequences of Damage

The stress–strain behavior of cortical and trabecular bone that has been previously damaged is qualitatively consistent across various loading modes and is similar to that for synthetic composites.[16] Upon unloading from a damaging event, both cortical and trabecular tissues show a recovery of 70 to 80% of the total inelastic strains. This behavior is illustrated for tensile loading of cortical bone in Fig 17.3. During reloading, damaged bone shows relatively small changes in the initial tangent modulus, so the effects of damage may not be apparent at lower (i.e., physiological) strain levels. The effects of damage are more apparent with increased load levels. One of the more obvious changes is that the stress–strain behavior becomes noticeably more curvilinear, giving the appearance of a reduced yield stress (Fig. 17.3). This increased curvilinear behavior may be a manifestation of crack opening or altered viscous properties. Fondrk et al.[17] proposed this reloading behavior was consistent with the presence of residual stresses resulting from the combination of damage and flow (slip) processes, stresses that must be relieved on reloading before the effects of damage on stiffness are fully appreciated.

Cyclically (fatigue) loaded human and bovine cortical bone samples show progressive reductions in stiffness and strength and progressive increases in hysteresis with increased cycle number.[9,15,18–20] During cyclic tensile loading, machined human cortical bone samples exhibit primary, secondary, and tertiary phases of degradation similar to that observed for synthetic composite materials.[1] The primary phase, consisting of an initial 5 to 10% degradation of secant modulus (see definition below) within the first 10% of life fraction, is followed by the secondary phase where the degradation rate levels off. The tertiary

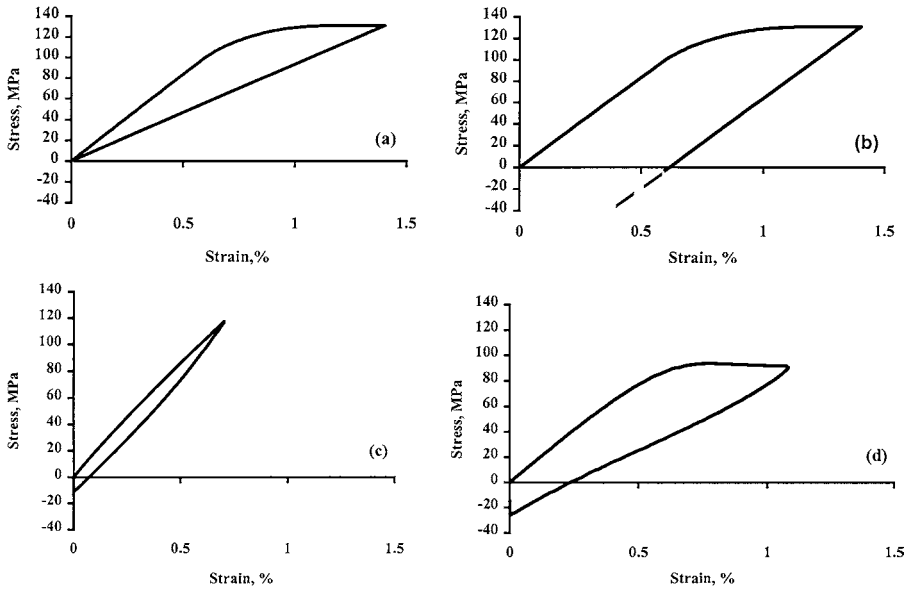

FIGURE 17.2 Stress–strain curves representing various inelastic behaviors under strain-controlled tensile loading. (a) "Perfect damage" behavior: Unloading curve returns to zero stress at zero strain. (b) Classical elastic–plastic behavior: unloading curve is parallel to initial elastic curve, and continues until compressive yielding occurs (not shown). (c) Viscoelastic behavior: closed hysteresis loop results from relaxation to zero stress at zero strain. (d) Actual stress–strain curve for human cortical bone sample strained to about 1.1% at 1%/s and unloaded at the same rate. The unloading curve crosses zero stress at about 0.25% strain at a slope approximately 2/3 the initial modulus. The residual compressive stress of about 26 MPa at zero strain relaxes to 15.7 MPa at about 15 s postloading. At this point the recovery rate is probably not zero, but is nearly undetectable over the last 5 s. (Based on authors' unpublished data.)

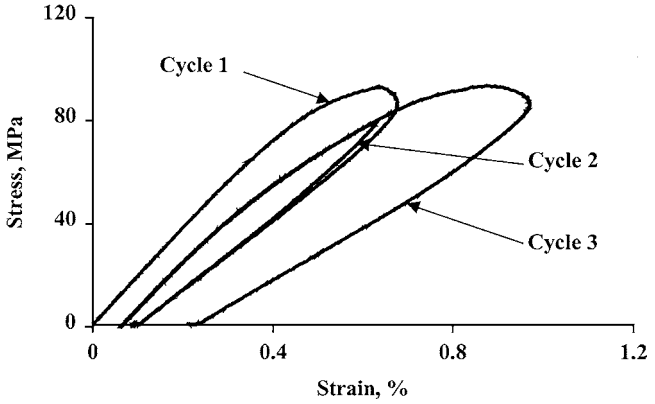

FIGURE 17.3 Example of load–unload–reload behavior. Data are from a tensile test of human femoral bone subjected to three load cycles under stress control. Loading and unloading rates were 10 MPa/s. The second load cycle was reversed at the strain corresponding to the peak stress on the first cycle, and the third cycle was reversed at 50% greater strain. The recovery period between successive loading cycles was 3 min. The third loading cycle is nearly coincident with the second until load reversal of the second cycle. The initial tangent slope of the second and third cycles is very nearly the same as the initial elastic modulus, but the loading curve is much more curvilinear. For the first and second load cycles, the residual strain was approximately 35% of the maximum inelastic strain achieved, and for the fourth cycle it was approximately 39%. (Based on Wilson,[68] unpublished data.)

phase involves the final 5% of fatigue life and is associated with a precipitous drop in secant modulus prior to fracture. This progression is mode dependent as well as load-amplitude dependent.[15,19] The fatigue life of human cortical bone is significantly greater under cyclic compression than under cyclic tension.[21] Stiffness degradation under compressive loads lacks the initial primary phase that is observed under tensile loading.[15] The mechanical effects of damage accumulation processes in nonhomogeneous strain states, such as bending, is complicated by these mode-dependent differences.[8]

17.2.3 Methods of Experimental Study of Damage Mechanics

In bone, the *damage state* (i.e., the amount of accumulated damage) can be inferred by measuring permanent changes in mechanical behavior following a *damaging event* (i.e., a subfailure loading event). A damaging event could be a single load–unload cycle, creep loading, relaxation loading, or fatigue loading. The mechanical properties most commonly used as measures of the damage state are stiffness and strength.[9] Other mechanical properties include hysteresis,[11] creep rate,[17] relaxation,[23] yield stress or yield strain,[23] microhardness,[24] residual strain,[17] and residual strength behavior.[25]

There are at least three important factors to consider when experimentally characterizing the damage state of a material. First, the choice of mechanical property that will be used as a quantitative measure of the damage state is important since not all properties degrade in the same manner or at the same rate.[23,25] Second, the definition of the "undamaged" state is critical for calculating degradation of the chosen property.[16] Third, the measurement should characterize only permanent changes in mechanical behavior.[13,14,26]

17.2.3.1 Measurement of Stiffness Degradation

In continuum damage mechanics,[16,27] the damage state of a material is assumed to be represented by an internal state variable (in general, a tensor, see Chapter 18), which characterizes the loss of continuity. Consider a damaging elastic (or quasi-brittle[28]) material, i.e., one to which the entire inelastic behavior can be attributed to damage. If this material is subjected to a simple tensile load, the loss of continuity leads to a decrease in stiffness. For the damaged state, an effective stress–strain relationship could be writen as

$$\sigma = E(1 - D)\varepsilon, \tag{17.1}$$

where σ = stress, ε = strain, E = initial (undamaged) modulus. The damage parameter D is often interpreted as the ratio of the damaged area (which no longer carries the load) to the total area (see Chapter 18). This corresponds to a material with an effective modulus $E_{\text{effective}} = E(1 - D)$. Correspondingly, the damage parameter is

$$D = 1 - E_{\text{effective}}/E \tag{17.2}$$

The measurement of an $E_{\text{effective}}$ is one of the most common characterizations of property degradation. One choice is the so-called perfect damage modulus, which is defined as the ratio (stress at maximum strain)/(maximum strain). As will be seen, this measure tends to overestimate the damage state in bone, because bone is not a quasi-brittle material. Other measurements that have been proposed are discussed below.

There is not yet any consensus regarding the best definition of $E_{\text{effective}}$ for bone. For engineering materials, particularly synthetic fiber–reinforced composites, the unloading modulus is the recommended measure for $E_{\text{effective}}$.[16] To eliminate small nonlinearities owing to viscous or hardening effects and experimental devices, it has been recommended that $E_{\text{effective}}$ be defined between 0.15 and 0.85 of the unloading curve. For bone, it has not been established that this approach is fully reliable because the other sources of inelastic behavior, particularly anelastic effects, are not insignificant.[13,14,26]

In fatigue studies, secant modulus is most often used. The stress range divided by the strain range for a single load cycle (Fig. 17.4) defines secant modulus. Typically, it is calculated at discrete intervals and plotted against the cycle number.[9,15,29–31] This measure is attractive because (1) it is simple to calculate; (2) it provides "on-the-fly" quantitative feedback regarding the damage state of the material; and (3) it is

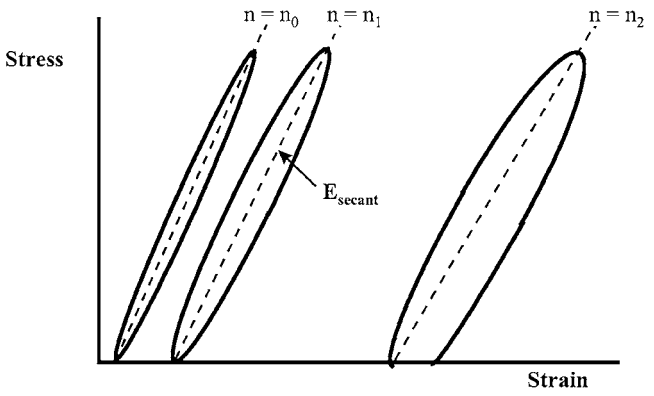

FIGURE 17.4 Secant modulus measurement for fatigue loading under stress control. For increasing loading cycle number, i, the value of $(E_{secant})_i$ decreases. Typically the curves show increased hysteresis along with increased average slope and progressive strain offset, all of which can contribute to changes in the secant modulus.

readily normalized by an initial (first-cycle) value to accommodate sample-to-sample variability. However, stress–strain behavior becomes progressively more curvilinear.[17,32,33] Consequently, secant modulus decreases may reflect stiffness degradation plus the progressive changes in other inelastic behaviors.

For load–unload–reload investigations, several methods are used to define $E_{effective}$. Zioupos et al.[32] defined the nondamaged modulus, E, as the initial tangent modulus of the first load cycle. $E_{effective}$ was calculated from the secant straight line defined from the origin of the ith cycle to the intersection of the unloading curve of the previous cycle and the loading curve of the ith cycle. Given this definition, this damage state depended on the curvilinear behavior observed during unloading and immediate reloading.

Courtney et al.[34] defined E in a similar way for machined human cortical bone samples which were loaded to 1% tensile strain, unloaded to 0.4% strain, reloaded to 1% strain, unloaded to 0.4% strain, and then unloaded to zero load. To determine $E_{effective}$, they calculated a reloading or "hysteresis" modulus by fitting a line to the entire unloading–reloading curve. They also compared the reloading modulus to a "perfect damage" modulus corresponding precisely to Eq. 17.2. The perfect damage modulus overestimated the stiffness loss by about 35% compared with the hysteresis modulus.

A third approach is represented by the work of Keaveny et al.[35] who subjected human vertebral trabecular bone to a load–unload–reload experimental protocol. Samples were loaded to 1 of 10 strain levels (0.3 to 4.0% strain) at 0.5%/s, unloaded under load control at 200 N/s to zero stress, and then immediately reloaded to 4% strain at 0.5%/s. They defined a perfect damage modulus (E_{PD}) similar to Courtney et al.[34] for the first load cycle. They also defined a residual modulus ($E_{RESIDUAL}$) as the slope of the linear portion of the second load cycle and measured at the point where the slope of the tangent modulus vs. strain curve approached zero. They also defined E as the initial tangent modulus of the first load cycle. The initial reloading modulus showed only a small decrease compared with the first loading cycle. However, the degradation of $E_{RESIDUAL}$ was in the range of 5.2 to 91.0%, depending on the applied strain level.

Jepsen and Davy[23] developed a loading protocol that takes anelastic effects into consideration and also provides additional measures of damage accumulation such as viscous property changes. This loading protocol requires that any damaging event (monotonic, fatigue, creep) be preceded and followed by diagnostic load cycles and that there is a recovery period between the damaging event and the second diagnostic cycle. Degradation was quantified by comparing changes in elastic and viscous properties of the pre- and postdamage diagnostic cycles. The recovery period allowed anelastic effects to dissipate so changes in mechanical properties between the two diagnostic cycles could be considered permanent and indicative of the presence of damage alone.

Jepsen et al.[26] compared three measures of damage accumulation for human cortical bone loaded in tension at various strain magnitudes (Fig. 17.5):

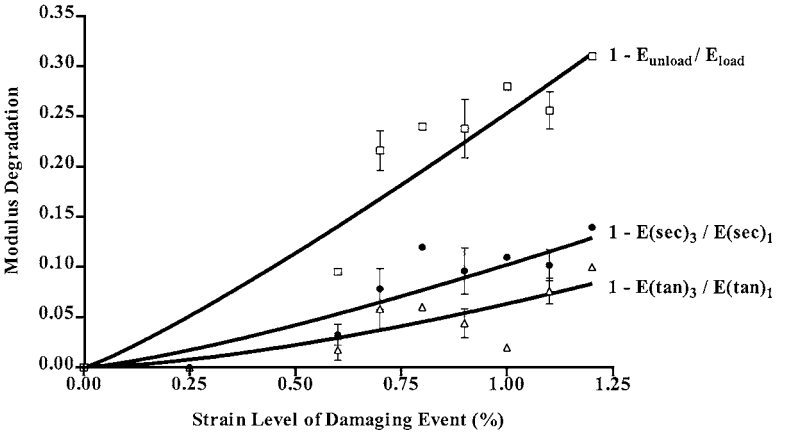

FIGURE 17.5 Comparison of three secant modulus degradation equations for human cortical bone samples subjected to a tensile load–unload protocol. The subscripts "load" and "unload" refer to moduli calculated during the loading and unloading portion of the damaging event. The subscripts 3 and 1 refer to moduli calculated from the pre- and postdamage diagnostic cycles. Standard error bars are shown where multiple data points were averaged.

1. D = 1 − initial tangent modulus ratio = 1 − $(E_{tan})_3/(E_{tan})_1$,
2. D = 1 − secant modulus ratio = 1 − $(E_{sec})_3/(E_{sec})_1$,
3. D = 1 − E_{unload}/E_{load}.

The secant moduli [$(E_{sec})_1$, $(E_{sec})_3$] and the initial tangent moduli [$(E_{tan})_1$, $(E_{tan})_3$] were calculated from the two diagnostic cycles [1 = predamage cycle; 3 = postdamage cycle]. E_{unload} and E_{load} were calculated from the damaging cycle and E_{unload} was calculated from the steepest part of the unload curve to achieve the smallest magnitude of degradation possible. They found that the initial tangent modulus exhibited only a small amount of degradation, consistent with previous investigations.[17,32,33] However, because of the increased curvilinear response during unloading and reloading following damage accumulation, they observed greater degradation of $(E_{sec})_3/(E_{sec})_1$ and E_{unload}/E_{load} compared to the initial tangent modulus degradation. The most important outcome of this study is that the magnitude of the damage state, as determined by stiffness degradation, is highly dependent on the method of calculation. These results demonstrate that using secant modulus as a measure of damage reflects both the change in the initial tangent modulus plus additional effects of damage associated with the increased nonlinear behavior characteristic of damaged bone. Further, the large differences between E_{unload} and $(E_{tan})_3$ indicate that the initial unloading behavior of bone may include anelastic deformations that lead to an overestimation of the damage state.

17.2.3.2 Measurement of Strength Degradation

Strength degradation due to damage accumulation and its associated property, damage tolerance, are of major clinical importance. In fact, strength degradation provides more desirable information in many circumstances than stiffness degradation. However, characterizing strength degradation is more difficult because there is no simple way to establish a nondamaged strength value. If strength is defined in terms of a failure event (rupture, collapse), then the only means of evaluation is to compare across sample populations. If some nominal subfailure measure is used, such as maximum load without frank fracture or collapse, it may be possible to make before-and-after comparisons in the same sample.

Several methods have been used to characterize the residual strength in bone. Carter and Hayes[9] examined the residual strength of machined bovine cortical bone samples subjected to cyclic bending. Degradation was determined by comparing the residual strength of each sample to the predicted monotonic tensile strength of that sample. The predicted monotonic tensile strength of each sample was obtained using an empirical relationship between strength and density. Martin et al.[25] examined the fatigue behavior of equine cortical bone, and they normalized their residual strength data to the mean

value of a group of nonfatigued control samples. Hoshaw et al.[36] subjected the canine proximal femur to cyclic compressive loading and used the monotonic failure strength of the contralateral femur as the nondamaged strength value. Keaveny et al.[35] subjected human trabecular bone to a load–unload–reload protocol and defined "residual strength degradation" by comparing the maximum stress attained during the reload cycle to the maximum stress attained during the first load cycle. Each of the above methods has its strengths and its limitations. Comparing population means may require large numbers of tests. Population strength values can exhibit standard deviations as high as 15 to 20% of the mean value. Residual strength degradation of only 5 to 10% may be lost in this variability. The estimation of initial strength from empirical rules is dependent on the reliability of the model and its parameters. The right–left comparisons rely on anatomical symmetry. The load–unload–reload protocol is valid only if maximum stresses are achieved on the first cycle. As for stiffness, there is not yet any consensus on the best method to characterize residual strength.

17.2.3.3 Other Mechanical Measures of Damage Accumulation

There have been numerous other mechanical measures of the damage state in addition to stiffness and strength. However, the utility of some of these measures is not as obvious. Residual strains represent clear evidence that permanent changes have occurred within bone tissue following a damaging event. The amount of residual strain is surprisingly consistent over a variety of loading conditions. These studies have revealed that roughly 25 to 35% of the total inelastic strains incurred during loading are not recovered on unloading.[13,14,17,35,37] These permanent strains are consistent for both cortical and trabecular tissue and could be attributed to plastic flow or incomplete crack closure after unloading.[17] As such, they are a manifestation of damage but not a clear measure.

Fondrk et al.[38] determined volumetric strains for human and bovine cortical bone subjected to tensile damage events and found significant volume increases and corresponding residual volumetric strains. These results were interpreted as evidence of damage accumulation. Volumetric strain measurement provides a fairly direct measure of damage, since it quantifies void volume increases. However, it has not yet been used to any extent as a degradation measure.

Yield stress, yield strain, and viscous properties have been shown to be five to ten times more sensitive to the presence of damage than traditional measures such as strength and modulus.[23,24] Torsional stiffness and strength exhibited similar degradation magnitudes between 0 and 6% for human cortical bone samples loaded to 80% of the twist at peak torque.[23] The yield strain and yield stress degraded to 27 and 41% of their initial values, respectively. Changes in relaxation were on the order of 60% of initial values and were observed at lower strain levels compared with other properties. The effects of prior damage on microhardness have been examined as a potential mechanical measure of ultrastructural level damage. The changes in microhardness following damage were similar in magnitude to modulus degradation (6%).[24]

Along with differential effects on various properties and different effects among loading modes, the effects of damage on mechanical properties may be anisotropic. The presence of longitudinal cracks would be anticipated to reduce the transverse stiffness and strength more than longitudinal stiffness and strength. Conversely, the evidence of decreased stiffness and strength properties in the longitudinal direction would be more consistent with transverse cracks than with longitudinal cracks. The presence of transverse cracks would also be expected to have much less influence on longitudinal compressive properties than on tensile properties due to crack closure effects. These observations suggest that it would be useful to study effects of damage on properties in loading modes other than the mode used to induce damage.

17.3 Histological Measures of Damage Accumulation

17.3.1 Histological Methods of Damage Characterization

Histological evidence of damage is critically important for understanding the quality and character of the damage responsible for mechanical property degradation. The use of basic fuchsin and other stains to differentiate microcracks in bone has brought about significant advances in understanding of the

physical nature of *in vivo* damage as well as the damage induced during laboratory mechanical tests. The rationale behind *en bloc* staining of bone is to differentiate cracks generated during dehydration, sectioning, and polishing from those that existed in the tissue prior to processing. Differential staining is particularly important for bone since microcracks can form if the tissue is not properly dehydrated. The number of artifactual cracks can be on the same order of magnitude as the number of *in vivo* cracks.[39] The stains are chosen to be insoluble in water so the dye does not leach out and stain the artifactual cracks induced during sectioning.[40]

Basic fuchsin staining was introduced by Frost,[2] later validated by Burr and Stafford,[39] and revised by Burr and Hooser.[41] Lee et al.[40] demonstrated that microcracks can be quantified by examining sections under transmitted light microscopy, green epifluorescence (wavelength = 546 nm), and ultraviolet (UV) epifluorescence (wavelength = 365 nm). Other methods used to visualize damage in nondecalcified bone include staining with a fluorescein solution and examining the sample under laser scanning confocal microscopy,[32] staining with a heavy metal solution of lead-uranyl acetate and examining the sample under backscattered scanning electron microscopy,[42] and staining with Villanueva mineralized bone stain and examining the sample under transmitted light.[43] Sokoloff[44] presented a paraffin embedding method to stain microcracks in decalcified subchondral bone of the patella, femoral head, and tibial condyle.

Histologically evident damage can be separated into two general categories: linear microcracks and diffuse damage. Linear microcracks are 10 to 200 μm long,[2] have well defined edges, and can be classified as interfacial cracks and cross-lamellar cracks. Linear microcracks that exist within lamellar and cement line interfaces are smooth and typically have pointed ends. Cross-lamellar microcracks are jagged, apparently as a result of microdeviations at lamellar interfaces during growth. An intermediate form of microcracks has been described as "wispy" microcracks,[8] which have poorly defined boundaries.

Diffuse damage appears as a region of increased uptake of basic fuchsin or heavy metal stains.[8,42,45] When viewed at high magnification under laser scanning confocal microscopy, these diffusely stained regions exhibit a sublamellar level disorganization associated with hundreds of matrix level cracks or discontinuities. These cracks can be distinguished from generalized staining of the canaliculi. Diffuse damage has been observed at the boundaries of linear microcracks and in regions without any microcracks present. It is unclear whether diffuse damage is an independent form of damage or is a precursor in the evolution of microcrack initiation. Frost's[2] original criteria for counting cracks excluded microcracks with increased stain uptake along the crack border. Currently, these microcracks are included in most crack-counting analyses.

17.3.2 *In Vivo* Damage Accumulation

The formation of microcracks in bone is a real, physiological event. Linear microcracks have been observed in human cortical and trabecular bone and these cracks have been attributed to *in vivo* fatigue loading.[2] *In vivo* damage has been assessed in cortical bone from the human rib,[2,39,40,42] femur,[46,47] and tibia.[47] *In vivo* damage has been observed in trabecular bone from the human vertebrae[45] and proximal femur[43,48,49] and in subchondral bone from the proximal femur[43] and from the patella, femoral head, and tibial condyle.[44] Numerous studies have quantified *in vivo* microcracks. No studies have quantified *in vivo* diffuse damage accumulation as an independent damage source, although *in vivo* diffuse damage has been observed qualitatively in association with microcracks.[42,45]

In vivo microcracks are distributed through the local microstructure,[2] preferentially found within the interstitial tissue, and tend to exhibit similar crack lengths regardless of the tissue under examination (Table 17.1). Although the magnitudes of crack density vary greatly between investigators, approximately half to two thirds of the total *in vivo* cracks have been observed in the interstitial tissue.[2,46,47] Only a small fraction of the cracks were observed entirely within osteons.[2,46] The prevalence of cracks in the interstitial tissue is consistent with increased mineral content of the interstitial tissue,[46] which would be expected to be more brittle and a site of increased damage accumulation.[50] Interestingly, the lamellar and cement line interfaces also appear to keep damage in a subcritical mode by interrupting crack propagation and preventing cracks from coalescing to form a fatal crack.[47] A biological advantage of this tissue-level

TABLE 17.1 Summary of *in vivo* Microcrack Density Measurements from Normal (Healthy) Individuals

Ref.	Source	Section	Density (No/cm^2)	Length (μm)
2	Rib	Transverse	7.5/section	—
39	Rib	Transverse	14.25	88
69	Subchondral; calcified cartilage	Midfrontal	—	56.3 (5.7)
42	Rib	Transverse	14–23	—
46	Female femur	Transverse	0–500	—
	Male femur	Transverse	0–300	—
45	Vertebra	Longitudinal	220–760	53–79
47	Female tibia/femur	Transverse	22.7	2–50
	Male tibia/femur	Transverse	15.2	2–50
48	Femoral trabecular	—	16–36	—
40	Rib	Transverse	7.18	82
49	Femoral trabecular	Longitudinal	50–250	—

damage tolerance is that microcracks remain in a subcritical state to allow time for biological repair processes to replace the damaged tissue with new tissue.

In trabecular bone two types of *in vivo* microcracks have been observed, linear and crosshatched. Linear microcracks of comparable length to those in cortical bone have been found within the cement lines, interstitial tissue, and along the surface of individual trabeculae.[45,49] The crosshatched microcracks have been found primarily in axially oriented trabeculae and are often surrounded by an area of diffuse staining.[45] Trabecular bone density appears to be an important determinant of crack density, since crack density increases with a decrease in trabecular area.[45,48]

The magnitude of *in vivo* microcrack density depends on the age, gender, and race of the donor. Microcrack density in human femoral cortical bone increases significantly with age, and is greater for females than males at a comparable age.[46,47,49] Schaffler et al.[46] found that crack density for males increased from nearly 0 at 40 years of age to 2 to 3 cracks/mm^2 at 60 to 70 years of age. Crack density for females increased from nearly 0 at 40 years to more than 5 cracks/mm^2 at 50 to 60 years of age. Similar age-related increases in crack density were observed in cortical bone from the tibia[47] and in trabecular bone from both the proximal femur[48] and intertrochanteric region.[49] Although crack density increases with age, crack length appears to be independent of age.[49] Although Wenzel et al.[45] did not find an age-related increase in microcrack density in human vertebral bone, they did find that *in vivo* microcrack density depended on the race of the donor.

The magnitude of *in vivo* microcrack density also depends on the pathological condition of the donor. The number of microcracks in subchondral bone from individuals with osteoarthritis is significantly higher than from normal, age-matched individuals.[43,44] Mori et al.[48] found that *in vivo* microcrack density was significantly higher in the femoral head (trabecular tissue) of older women ($\approx$36/cm^2) compared with younger women ($\approx$16/cm^2). However, there were no differences in damage density for women who sustained a femoral neck fracture compared with age-matched women that did not sustain a fracture.

17.3.3 Damage Induced during Laboratory Mechanical Tests

17.3.3.1 Damage Induced by Compressive Loading

Damage formed under compressive loads has consistently been associated with the appearance of oblique shear cracks (Fig. 17.6a).[51] This damage mode is consistent for machined bone samples,[51] intact bones,[3] and single osteons.[52] The angle of orientation and degree to which the crack interacts with the microstructure depends on the orientation of the osteons relative to the loading axis.[51,53] Compressive loads applied along the longitudinal bone axis are associated with cracks forming angles of $\pm 30^\circ$ to the loading axis.[51,53] Although these oblique cracks have jagged edges[51] indicative of some lamellar level involvement, these oblique cracks appear to initiate and propagate independently of the microstructure.[3,51–53] In contrast,

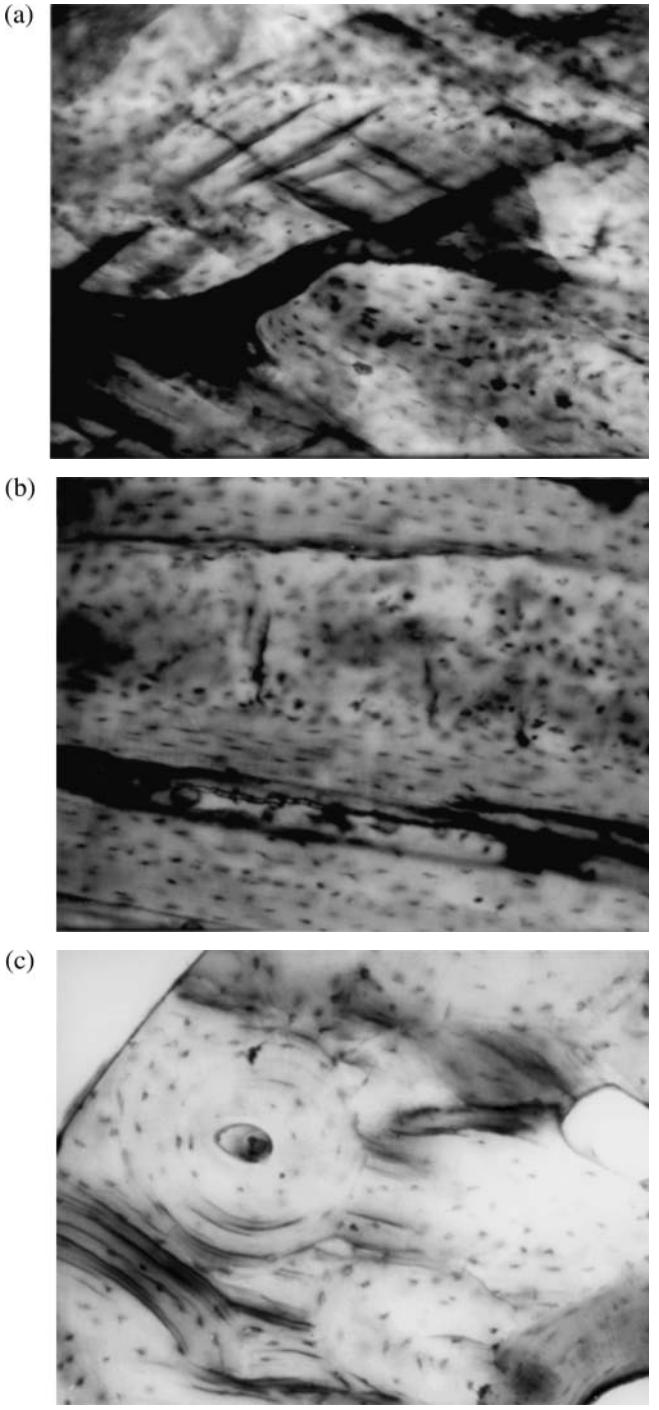

FIGURE 17.6 Black-and-white photos of stained sections showing damage in bone. (a) Stained longitudinal section of compression sample showing oblique microcracks. Test and bone axis are left to right. (b) Stained longitudinal section of tension sample showing both longitudinal (horizontal) and transverse (vertical) microcracks. Test and bone axis is left to right. (c) Stained transverse section of torsion sample showing interlamellar debonding. Curved edge is outer surface of circular section (note the radial orientation of the microcracks). All samples are strained with basic fuchsin at comparable magnifications.

compressive loads applied along the radial or tangential material axes generated cracks with relatively smooth shear planes. These cracks formed an angle of $\pm 45°$ with respect to the longitudinal axis.[51] The angle of inclination of cracks (fissures) within single human osteons was fairly constant at $\pm 30°$ to $\pm 35°$ with respect to the longitudinal axis, independent of collagen organization.[52]

17.3.3.2 Damage Induced by Tensile Loading

Tensile damage is qualitatively different from compressive damage and appears at lower stress levels (Fig. 17.6b).[54,55] Currey and Brear[54] and later Choi et al.[55] observed that cortical bone samples loaded in bending became opaque in the tensile region when yielded. The samples that had yielded exhibited "tension lines" that were transverse to the load direction and exhibited indefinite edges. These tension lines were distinctly different from the oblique slip lines found in compression that exhibited definite edges. Boyce et al.[8] confirmed the presence of transverse cracks in the tensile region for human bone samples loaded in cyclic bending.

In addition to the transverse damage, which is either bands of diffuse damage or linear microcracks,[32,54,56] tensile loading induces longitudinally oriented linear microcracks.[29,34] In investigating the evolution of tensile damage accumulation within human cortical bone samples, Jepsen et al.[24] found that linear microcracks oriented parallel to the loading direction were the first histologically evident damage. These cracks were first observed at pre-yield strain magnitudes and were found at lamellar and cement line interfaces. Formation of these cracks at low strain levels suggests early shear failure at these interfaces. Transverse damage appeared later at yield and post-yield strain levels, initially in a very diffuse form and then as linear cross-lamellar cracks at higher post-yield strain levels. These results provide a working model of the damage evolution process under monotonic tensile loading.

17.3.3.3 Damage Induced by Torsional Loading

Damage induced by torsional loading is clearly evident under histological examination. Forwood and Parker[31] subjected intact rat tibia to torsional fatigue loading and categorized histologically evident damage (microcracks) into four types based on their relationship to the microstructure (parallel or perpendicular to lamellae) and their relationship to vascular canals. The histological results revealed differences in the magnitude of the four damage types and a strong dependence between the level of loading and the probability of a section having a crack. For human cortical bone samples loaded in torsion to post-yield strains, Jepsen et al.[57] found damage was in the form of interlamellar and cement line cracks oriented primarily along the radial direction. Damage was observed within interstitial tissue, cement lines, and within osteons. Damage was nonuniformly distributed within the cross section of the bone section, consistent with the internal shear stress distribution (i.e., greater damage density at the periphery of the sample compared to the interior). They observed large numbers of shear cracks in torsion (1.1 to 43.3 cracks/mm^2), and they concluded that the microstructure of human cortical bone is well adept at keeping these cracks in a subcritical state. This damage tolerance may explain why human cortical bone exhibits dramatic post-yield deformation in torsion.

17.3.3.4 Damage Induced in Trabecular Bone

Damage accumulation in trabecular bone has been assessed for samples machined from human vertebrae,[37] the intertrochanteric region of the proximal human femur,[49] the proximal bovine tibia,[33] and for the intact proximal human femur.[36] For trabecular bone subjected to compressive overloads, the primary mechanism of failure was microscopic cracking rather than complete fracture of individual trabecular struts.[37,49] The only trabeculae to fail completely were those oriented transverse to the loading direction (i.e., horizontal trabeculae).

There are four types of damage that have been consistently found following compressive loading of trabecular specimens: complete fracture, microcracks along lamellar interfaces, microcracks in a cross-hatched pattern crossing lamellae, and diffuse damage. These damage types were consistent with those observed *in vivo*[45] and have been attributed to shear stresses associated with compression and bending of trabeculae during loading.[37] Similar damage patterns were observed for samples subjected to a single

load cycle to post-yield strain magnitude[33] and for cyclic loading of intact proximal femurs to 40% stiffness degradation.[36] Wachtel and Keaveny[33] found that damage for specimens compressed to nominal yield (1%) was not greater than for pre-yield loading (0.4%), but that post-yield strain (2.5%) produced a threefold increase in damage. Fyhrie and Schaffler[37] found that trabecular bone strained to 15% recovered 94% of the original sample height after being unloaded. This ability of trabecular tissue to damage rather than fracture has important mechanical benefits and may also have important implications for biological repair and maintenance of trabecular architecture.

17.3.4 The Relationship between Damage and Degradation

The effect of damage on mechanical properties is complex since a crack can affect the mechanical properties of the surrounding matrix, a crack can act as a local stress riser, and a crack can further exacerbate the heterogeneous and anisotropic character of bone.[58] The full effect of matrix cracks on bone properties is not well understood even for simple properties such as strength and stiffness.

One approach to understanding these effects is to develop correlations between the physical nature of the damage and the associated degradation state. At least three challenges exist in making these correlations. As previously noted, the degradation measure must be representative of permanent changes in mechanical properties. Second, it is essential to establish appropriate histological methods to stain and image all forms of damage. Basic fuchsin staining is appropriate for quantifying microcracks but its use as a stain to quantify diffuse or ultrastructural damage has yet to be determined. Third, it is important to establish appropriate methods to count microcracks and areas of diffuse damage. The question arises whether all cracks should be weighted equally when counted. Would a 10-μm-long interfacial crack located in the cement line contribute in the same manner to global property degradation as a 250-μm-long cross-lamellar crack located in the interstitial tissue? A more mechanistic approach is needed to determine whether cracks should be weighted on the basis of size, orientation, local density, or the relationship to local microstructure. These factors need to be addressed to understand fully the relationship between damage and degradation.

The relationship between damage accumulation and mechanical property degradation has typically been examined by subjecting intact or machined bone samples to a specific loading event, quantifying mechanical degradation, and then quantifying crack number, crack density, crack length, or crack area fraction using standard stereological techniques. Initial studies of damage–degradation relationships include tensile fatigue of bovine cortical bone,[29] torsional fatigue of intact rat tibia,[31] bending fatigue of intact canine femurs,[7] cyclic bending of human tibial cortical bone,[8] monotonic tension and torsion of human cortical bone,[23,24,34,57] and monotonic compression of bovine trabecular bone.[33] Several studies have examined the damage accumulation responsible for a single degradation state, but only a few studies have examined damage associated with a large number of degradation states that would enable damage–degradation regressions to be generated.

The relationship between damage and degradation depends on the damage measure[7] as well as the degradation measure.[57] For intact canine femurs subjected to cyclic four-point bending, the relationship between stiffness loss and crack density was approximately quadratic whereas the relationship between stiffness loss and crack area was linear.[7] For machined human cortical bone samples subjected to a single torsional load cycle at a post-yield twist level, secant stiffness degradation increased in a linear manner with increased microcrack density; however, changes in viscous properties showed no correlation with microcrack density.[57]

Secant stiffness degradation has been the property of choice for most damage–degradation correlations. These correlations depend on many factors such as tissue type, loading mode, histological sectioning method, and the method of calculating stiffness degradation. A 2 to 5% reduction in secant stiffness for bovine cortical bone loaded in cyclic tension is associated with a 33 to 50% increase in longitudinal microcrack density, depending on the loading rate.[29] In contrast, a 33 to 34% reduction in hysteresis modulus is associated with a 50% increase in microcrack density in cortical bone samples from an elderly donor loaded monotonically to 1% tensile strain, but with no discernible increase in microcrack density in young adult cortical tissue.[34]

The interpretation of stiffness degradation for more-complex loading situations such as bending is difficult. Boyce et al.[8] demonstrated that cortical bone samples loaded in bending exhibit several different

forms of damage associated with the tensile, compressive, and shear strain fields, and that there are differences in the amount of damage within each strain field. When this complex damage process is correlated with a single, global mechanical measure, i.e., bending stiffness, it is unclear how each of these damage factors (amount, type, distribution) contributes to the degradation. Burr et al.[7] found that for intact canine femurs loaded in bending fatigue, measurable microcrack area was absent prior to 15% bending stiffness degradation. This was taken as evidence that ultrastructural-level damage precedes the formation of microcracks.

The damage state induced during torsional loading is not as complex as in bending since one damage mode, interfacial cracks, is dominant. Total damage density increases, and the distribution of damage within the sample changes with increased stiffness degradation.[57] With increased modulus degradation, damage density saturates in the peripheral region and then increases in the middle region. This internal redistribution of microcrack density may be largely responsible for the ability of human cortical bone to undergo extensive post-yield deformation under torsional loads without rupture.

Most studies have shown that an increase in cycle number during fatigue tests and an increase in strain level during load–unload–reload tests are associated with an increase in the total amount of histologically evident damage. Furthermore, an increased amount of damage is associated with increases in mechanical property degradation. However, we are still far short of any quantitative description of relationships between histological measures of damage and property degradation.

17.4 Acoustic Emission as a Measure of Damage Accumulation

Acoustic emission (AE) has been used by several investigators to study the onset of yield and post-yield behavior of bone. Part of the stored elastic energy released during initiation and propagation of a crack goes into elastic wave energy, which is detected as an acoustic event.[59] AE measurements during mechanical loading can be used to quantify the number of events and characterize the energy content of the events. AE measurements using transducers at multiple locations can be used to locate the sources of the events.[60]

Although AE is associated with damage, it may involve numerous types of events beyond crack initiation, including motion between existing crack surfaces, crack growth, cleavage, and tearing. Other sources may be more associated with plastic type of behavior such as dislocation motion, slip, or twinning.[59] However, the primary sources of AE are associated with damage events, making it a particularly useful tool in studies of bone damage accumulation.

The results of AE studies support the conclusion that yielding is largely a damage accumulation phenomenon. A number of investigations of inelastic tensile behavior have observed that the first AE event is coincident with the onset of yielding.[32,61–64] The amount of activity within the post-yield region appears to vary with bone type,[32] composition,[62,65] loading rate,[64] and loading direction.[66] These studies also demonstrated that AE activity follows a power law relationship, consistent with the conclusion from other studies that damage accumulation rate is a highly nonlinear function of load level. Jonsson and Eriksson[63] detected AE events during loading into the nonlinear range and during the initial part of unloading for intact canine femurs subjected to a sequence of torsional loads with increasing amplitudes.

AE results provide further evidence that the scale and type of damage vary with the nature of the loading event. Inoue et al.[66] found that low-amplitude AE occurred at yield and high-amplitude AE occurred at the failure regions for bovine bone loaded in the longitudinal direction. However, transverse specimens exhibited AE only at failure. The AE amplitudes of the 90° group at failure were of the same amplitude with the AE amplitudes at the yield of 0° group. It was suggested that the low-amplitude AE patterns were pertinent to debonding and fracture at the cement line while the high-amplitude bursts belonged to rupture and destruction of the osteons. Inoue et al.[67] also found that low-amplitude bursts were distributed through the gauge length while the high-amplitude bursts that occurred prior to fracture tended to accumulate in close vicinity to the failure surface for the longitudinal specimens. Low-amplitude bursts tended to accumulate at fracture surface in the case of the 90° specimens.

Considerable work remains to develop fully the potential of AE to characterize damage accumulation. The results to date suggest that potential is considerable, particularly when combined with the histological and mechanical property measures currently being used.

17.5 Summary/Conclusions

The current state of knowledge in damage processes in bone is summarized briefly as follows.

1. There is ample experimental support for the major role of damage accumulation processes in the inelastic behavior in all loading modes that have been examined.
2. The histological evidence indicates that damage occurs at the microstructural level (microcracks) and at ultrastructural levels (diffuse damage).
3. There are correlations between histologically observed damage, mechanical property degradation, and AE measurements. However, understanding of these relationships is very much incomplete, and there is no consensus on methods for characterizing mechanical property degradation.

It is clear that the degradation of any particular property depends on how the damage state interrupts a particular structure–function relationship.[23] Since bone stiffness, strength, and creep exhibit different (albeit overlapping) structure–function relationships, it is not surprising that a particular damage state will affect these properties differently.[23] In this context, expanding the repertoire of damage and degradation measures is crucial to achieving a more thorough understanding of bone as a damaging composite material.

References

1. Reifsnider, K. L., Damage and damage mechanics, in *Fatigue of Composite Materials,* Reifsnider, K. L., Ed., Elsevier, New York, 1991, 11–77.
2. Frost, H. L., Presence of microscopic cracks *in vivo* in bone, *Henry Ford Hosp. Med. Bull.,* 8, 25, 1960.
3. Tschantz, P. and Rutishauser, E., La surcharge mechanique de l'os vivant, *Ann. Anat. Pathol.,* 12, 223, 1967.
4. Martin, R. B. and Burr, D. B., A hypothetical mechanism for the stimulation of osteonal remodeling by fatigue damage, *J. Biomech.,* 15, 137, 1982.
5. Burr, D. B., Forwood, M. R., Fyhrie, D. P., Martin, R. B., Schaffler, M. B., and Turner, C. H., Bone microdamage and skeletal fragility in osteoporotic and stress fractures, *J. Bone Miner. Res.,* 12, 6, 1997.
6. Reifsnider, K. L., Introduction, in *Fatigue of Composite Materials,* Reifsnider, K. L. Ed., Elsevier, New York, 1991, 1–10.
7. Burr, D. B., Turner, C. H., Naick, P., Forwood, M. R., Ambrosius, W., Hasan, M. S., and Pidaparti, R., Does microdamage accumulation affect the mechanical properties of bone? *J. Biomech.,* 31, 337, 1998.
8. Boyce, T. M., Fyhrie, D. P., Glotkowski, M. C., Radin, E. L., and Schaffler, M. B., Damage type and strain mode associations in human compact bone bending fatigue, *J. Orthop. Res.,* 16, 322, 1998.
9. Carter, D. R. and Hayes, W. C., Compact bone fatigue damage—I. Residual strength and stiffness, *J. Biomech.,* 10, 325, 1977.
10. Mori, S. and Burr, D. B., Increased intracortical remodeling following fatigue damage, *Bone,* 14, 103, 1993.
11. Chamay, A., Mechanical and morphological aspects of experimental overload and fatigue in bone, *J. Biomech.,* 3, 263, 1970.
12. Currey, J. D. and Brear, K., Fractal analysis of compact bone and antler fracture surfaces, *Biomimetics,* 1, 103, 1992.
13. Bonfield, W. and Li, C. H., Deformation and fracture of bone, *J. Appl. Phys.,* 37, 869, 1966.
14. Bonfield, W. and Li, C. H., Anisotropy of nonelastic flow in bone, *J. Appl. Phys.,* 38, 2450, 1967.

15. Pattin, C. A., Caler, W. E., and Carter, D. R., Cyclic mechanical property degradation during fatigue loading of cortical bone, *J. Biomech.,* 29, 69, 1996.
16. LeMaitre, J., *A Course on Damage Mechanics,* Springer-Verlag, New York, 1992, 1–10.
17. Fondrk, M., Bahniuk, E., Davy, D. T., and Michaels, C., Some viscoplastic characteristics of bovine and human cortical bone, *J. Biomech.,* 21, 623, 1988.
18. Carter, D. R., Caler, W. E., Spengler, D. M., and Frankel, V. H., Fatigue behavior of adult cortical bone: the influence of mean strain and strain range, *Acta Orthop. Scand.,* 52, 481, 1981.
19. Zioupos, P., Wang, X. T., and Currey, J. D., Experimental and theoretical quantification of the development of damage in fatigue tests of bone and antler, *J. Biomech.,* 29, 989, 1996.
20. Zioupos, P. and Casinos, A., Cumulative damage and the response of human bone in two-step loading fatigue, *J. Biomech.,* 31, 825, 1998.
21. Caler, W. E. and Carter, D. R., Bone creep-fatigue damage accumulation, *J. Biomech.,* 22, 625, 1989.
22. Griffin, L. V., Gibeling, J. C., Martin, R. B., Gibson, V. A., and Stover, S. M., Model of flexural fatigue damage accumulation for cortical bone, *J. Orthop. Res.,* 15, 607, 1997.
23. Jepsen, K. J. and Davy, D. T., Comparison of damage accumulation measures in human cortical bone, *J. Biomech.,* 30, 891, 1997.
24. Jepsen, K. J., Krzypow, D. J., Dutta Roy, T., and Pizzuto, T., Damage accumulation during tensile yielding of human cortical bone. *Trans. Orthop. Res. Soc.,* 24, 236, 1999.
25. Martin, R. B., Gibson, V. A., Stover, S. M., Gibeling, J. C., and Griffin, L. V., Residual strength of equine bone is not reduced by intense fatigue loading: implications for stress fracture, *J. Biomech.,* 30, 109, 1997.
26. Jepsen, K. J., Krzypow, D. J., and Dutta Roy, T., unpublished data.
27. Kachanov, L. M., *Introduction to Continuum Damage Mechanics,* Martinus Nijhoff Publishers, Boston, 1986.
28. Krajcinovic, D. and Mastilovic, S., Some fundamental issues of damage mechanics, *Mech. Mater.,* 21, 217, 1995.
29. Schaffler, M. B., Radin, E. L., and Burr, D. B., Mechanical and morphological effects of strain rate on fatigue of compact bone, *Bone,* 10, 207, 1989.
30. Schaffler, M. B., Radin, E. L., and Burr, D. B., Long-term fatigue behavior of compact bone at low strain magnitude and rate, *Bone,* 11, 321, 1990.
31. Forwood, M. R. and Parker, A. W., Microdamage in response to repetitive torsional loading in the rat tibia, *Calcif. Tissue Int.,* 45, 47, 1989.
32. Zioupos, P., Currey, J. D., and Sedman, A. J., An examination of the micromechanics of failure of bone and antler by acoustic emission tests and Laser Scanning Confocal Microscopy, *Med. Eng. Phys.,* 16, 203, 1994.
33. Wachtel, E. F. and Keaveny, T. M., Dependence of trabecular damage on mechanical strain, *J. Orthop. Res.,* 15, 781, 1997.
34. Courtney, A. C., Hayes, W. C., and Gibson, L. J., Age-related differences in post-yield damage in human cortical bone, experiment and model, *J. Biomech.,* 29, 1463, 1996.
35. Keaveny, T. M., Wachtel, E. F., and Kopperdahl, D. L., Mechanical behavior of human trabecular bone after overloading, *J. Orthop. Res.,* 17, 346, 1999.
36. Hoshaw, S. J., Cody, D. D., Saad, A. M., and Fyhrie, D. P., Decrease in canine proximal femoral ultimate strength and stiffness due to fatigue damage, *J. Biomech.,* 30, 323, 1997.
37. Fyhrie, D. P. and Schaffler, M. B., Failure mechanisms in human vertebral cancellous bone, *Bone,* 15, 105, 1994.
38. Fondrk, M. T., Bahniuk, E., and Davy, D. T., Inelastic strain accumulation during rapid transient tensile loading of cortical bone, *J. Biomech. Eng.,* 121, 616, 1999.
39. Burr, D. B. and Stafford, T., Validity of the bulk-staining technique to separate artifactual from *in vivo* bone microdamage, *Clin. Orthop. Relat. Res.,* 260, 305, 1990.
40. Lee, T. C., Myers, E. R., and Hayes, W. C., Fluorescence-aided detection of microdamage in compact bone, *J. Anat.,* 193, 179, 1998.

41. Burr, D. B. and Hooser, M., Alterations in en bloc basic fuchsin staining protocol for the demonstration of microdamage produced *in vivo, Bone,* 17, 431, 1995.
42. Schaffler, M. B., Pitchford, W. C., Choi, K., and Riddle, J. M., Examination of compact bone microdamage using back-scattered electron microscopy, *Bone,* 15, 483, 1994.
43. Villanueva, A. R., Longo III, J. A., and Wiener, G., Staining and histomorphometry of microcracks in the human femoral head, *Biotech. Histochem.,* 69, 81, 1994.
44. Sokoloff, L., Microcracks in the calcified layer of articular cartilage, *Arch. Pathol. Lab. Med.,* 117, 191, 1993.
45. Wenzel, T. E., Schaffler, M. B., and Fyhrie, D. P., *In vivo* trabecular microcracks in human vertebral bone, *Bone,* 19, 89, 1996.
46. Schaffler, M. B., Choi, K., and Milgrom, C., Aging and matrix microdamage accumulation in human compact bone, *Bone,* 17, 521, 1995.
47. Norman, T. L. and Wang, Z., Microdamage of human cortical bone: incidence and morphology in long bones, *Bone,* 20, 375-379, 1997.
48. Mori, S., Harruff, R., Ambrosius, W., and Burr, D. B., Trabecular bone volume and microdamage accumulation in the femoral heads of women with and without femoral neck fractures, *Bone,* 21, 521, 1997.
49. Fazzalari, N. L., Forwood, M. R., Smith, K., Manthey, B. A., and Herreen, P., Assessment of cancellous bone quality in severe osteoarthrosis: bone mineral density, mechanics, and microdamage, *Bone,* 22, 381, 1998.
50. Currey, J. D., The mechanical consequences of variation in the mineral content of bone, *J. Biomech.,* 2, 1, 1969.
51. Dempster, W. T. and Liddicoat, R. T., Compact bone as a non-isotropic material, *Am. J. Anat.,* 91, 331, 1952.
52. Ascenzi, A. and Bonucci, E., The compressive properties of single osteons, *Anat. Rec.,* 161, 377, 1968.
53. Frost, H. M., Roth, H., and Villanueva, A. R., Physical characteristics of bone Part IV, *Henry Ford Hosp. Med. Bull.,* 9, 163, 1961.
54. Currey, J. D. and Brear, K., Tensile yield in bone, *Calcif. Tiss. Res.,* 15, 173, 1974.
55. Choi, K., Fyhrie, D. P., and Schaffler, M. B., Failure mechanisms of compact bone in bending: a microstructural analysis, *Trans. Orthop. Res. Soc.,* 19, 425, 1994.
56. Zioupos P. and Currey J. D., The extent of microcracking and the morphology of microcracks in damaged bone, *J. Mater. Sci.,* 29, 978, 1994.
57. Jepsen, K. J., Davy, D. T., and Kryzpow, D.J., The role of the lemallar interface during torsional yielding of human cortical bone, *J. Biomech.,* 32, 303, 1999.
58. Nicolella, D. P., Nicholls, A. E., and Lankford, J., Micromechanics of creep in cortical bone, *Trans. Orthop. Res. Soc.,* 23, 137, 1998.
59. Kohn, D. H., Acoustic emission and nondestructive evaluation of biomaterials and tissues, *Crit. Rev. Biomed. Eng.,* 22, 221, 1995.
60. Enoki, M. and Kishi, T., Development and future aspects in AE source characterization, in *Acoustic Emission: Current Practice and Future Directions,* ASTM STP 1077, Sachse, W., Roget, J., and Yamaguchi, K., Eds., American Society for Testing and Materials, Philadelphia, 1991.
61. Netz, P., Eriksson, K., and Stromberg, L., Material reaction of diaphyseal bone under torsion. An experimental study on dogs, *Acta Orthop. Scand.,* 51, 223, 1980.
62. Wright, T. M., Vosburgh, F., and Burstein, A. H., Permanent deformation of compact bone monitored by acoustic emission, *J. Biomech.,* 14, 405, 1981.
63. Jonsson, U. and Eriksson, K., Microcracking in dog bone under load. A biomechanical study of bone viscoelasticity, *Acta Orthop. Scand.,* 55, 441, 1984.
64. Fischer, R. A., Arms, S. W., Pope, M. H., and Seligson, D., Analysis of the effect of using two different strain rates on the acoustic emission in bone, *J. Biomech.,* 19, 119, 1986.
65. Hirai, T., Katayama, T., Yamamoto, H., Inada, M., Inoue, N., Watanabe, Y., and Arai, Y., Nonlinear behavior with AE of cortical bone treated with acid under tensile loading, in *Progress in Acoustic Emission VI,* Japanese Society of NDI, 1992, 317.

66. Inoue, S., Sakakida, K., Yamasita, F., Kusakabe, T., and Inoue, N., Acoustic emission characteristics of the cortical bone under tensile loading, in *Progress in Acoustic Emission III,* Japanese Society of NDI, 1986, 244 .
67. Inoue, N., Sakakida, K., Yamasita, F., Inoue, S., Hirai, T., Katayama, T., and Hayashibara, M., Acoustic emission source location during tensile test of cortical bone, in The *Progress in Acoustic Emission IV,* Japanese Society of NDI, 1988, 177.
68. Wilson, J., Simple Predictors for Tensile Failure for Human Cortical Bone, M.S. thesis, Department of Mechanical and Aerospace Engineering, Case Western Reserve University, Cleveland, 1998.
69. Mori, S., Harruff, R., and Burr, D. B., Microcracks in articular calcified cartilage of human femoral heads, *Arch. Pathol. Lab. Med.,* 117, 196, 1993.

18

Bone Damage Mechanics

Dwight T. Davy
Case Western Reserve University

Karl J. Jepsen
Mount Sinai School of Medicine

18.1 Introduction

This chapter focuses on the modeling of damage behavior of bone. As described in the previous section, damage accumulation is an established feature of the nonlinear behavior of bone. However, it is seldom incorporated into stress analysis models of bones. The most obvious reason is that for most circumstances, it is simply unnecessary. Creep damage or low-cycle fatigue damage, i.e., damage resulting from high imposed strains, is an unlikely occurrence under normal loading for bone. High-cycle fatigue damage, i.e., damage accumulating at low strain amplitudes, is probably occurring routinely, but is usually repaired by normal bone turnover. Hence, stress analyses of skeletal structures usually do not require the incorporation of any damage process. This is also true for other complications in modeling bone mechanics, e.g., viscous or plastic behavior. Nonetheless, there are several good reasons for attempting to develop mathematical models for the damaging behavior of bone.

One reason stems from evidence that the nonlinear behavior of bone is to a significant degree the result of damage processes. It can be argued that the maximum permissible working stresses for bone are more appropriately defined in terms of critical rates of damage accumulation than in terms of a yield or failure stress.[1,2] Hence models that predict damage accumulation would potentially provide better predictions of failure risk under a given load.

A second reason follows from the fact that fatigue failure can indeed occur in real life. This makes the prediction of fatigue failure a highly desirable capability in practical application. Both the issues of creep damage and fatigue damage are relevant to the class of clinical problems that generally are called skeletal fragility[3] (see also previous chapter). The ability to predict the effects of damage on functional load-bearing behavior and the ability to predict the effects of changes in bone composition and organization on the accumulation of damage are relevant to both clinical medicine and biomedical research.

0-8493-9117-2/01/$0.00+$.50

A third reason that models for predicting damage accumulation are desirable is that they provide the ability to incorporate damage into models describing the relationship between mechanical environment and bone biology. The extent to which damage accumulation plays a role in normal bone biology is still controversial. However, it is clear that damage under some circumstances does indeed influence bone biology. Also, it is evident that damage could be included as a component of feedback models of bone adaptation. The ability to model the damage accumulation process adequately is a prerequisite for developing damage-repair models to assess the role damage might play vis-à-vis other stimuli to bone biology.

The following examines the mathematical modeling problem for damage accumulation in bone. The focus of this chapter is on models that can be regarded as continuum damage mechanics models. Several kinds of models that are candidates for describing the behavior that has been observed experimentally and described in the previous literature are considered.

18.2 Basic Concepts of Continuum Damage Mechanics

Over the past few decades a considerable literature has developed in continuum damage mechanics, which provides a fairly mature theoretical basis for such work.[4–6] The conceptual basis for the mechanics is relatively simple, namely, that damage results in a loss of continuity in the material that degrades its mechanical properties. The most notable properties would be stiffness and maximum load-carrying capability. For the simple case of one-dimensional stress, the damage can be regarded as a loss of load-carrying area due to the presence of cracks or voids. Consider for example a tensile test of such a damaged material. If the total cross-sectional area of the sample is A and the total area of damage across the section is defined as A_D, then the damage can be simply defined as[6]

$$D = \frac{A_D}{A}. \tag{18.1}$$

When there is no damage, $D = 0$ and when the material is ruptured, $D = 1$. If the material behaves elastically up to some limit, and the modulus of the undamaged material is E, then the load-extension behavior of the damaged material in a tensile test would be given by

$$\Delta = \frac{P \cdot L}{(A - A_D) \cdot E}. \tag{18.2}$$

Accordingly, the apparent stiffness would be

$$P/\Delta = E(A - A_D)/L = (1 - D)E \cdot A/L. \tag{18.3}$$

Hence, the damaged material could be regarded as a material with the modulus reduced by the factor $(1 - D)$. If the undamaged material demonstrated a yield strength of σ_Y, the yield load of the damaged material would be

$$P_Y = \sigma_Y \cdot (A - A_D) = \sigma_Y \cdot (1 - D) \cdot A. \tag{18.4}$$

Hence the damage could also be regarded as reducing the yield strength of the material by the factor $(1 - D)$. Similar arguments can be made for the effect of damage on other basic material properties, including plastic, viscoelastic, hardness, and other properties.[5]

In a more general circumstance, the loss of load-carrying area may vary with the orientation of the plane of loading (Fig. 18.1). In that case, the relationship between tensile load and cross-sectional area of

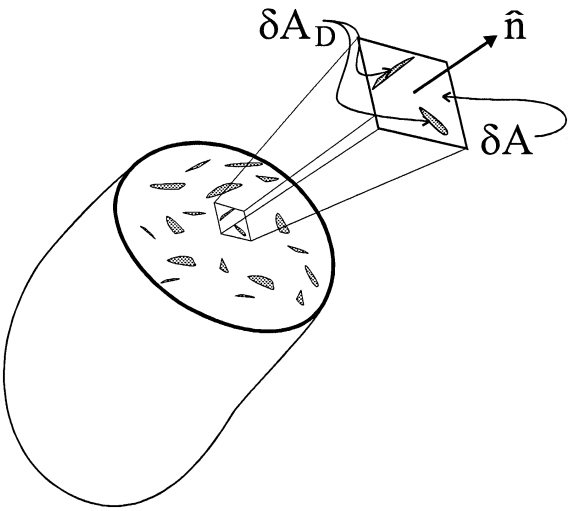

FIGURE 18.1 Schematic of a volume of material with damage distributed in the form of cracks and voids. A cut through an arbitrary plane results in a fractional loss of the area that varies as a function of the orientation of the cut if the damage is anisotropic.

a representative volume element must be altered to account for directional variation of the properties:[2]

$$D(\bar{x}, \hat{n}) = \frac{\delta A_D^{(\hat{n})}}{\delta A^{(\hat{n})}}, \tag{18.5}$$

where $\bar{x}$ defines the location within the material, $\hat{n}$ is a direction vector defining the orientation of the cross section, and $\delta A_D^{(\hat{n})}$ and $\delta A^{(\hat{n})}$ are the area of damage and the total area associated with that orientation. Clearly, this anisotropy could greatly complicate the situation depending on the nature of damage. In fact, a second-, fourth-, or even higher-order tensor may be required to describe it.[5] The recognizable composite nature of bone[7] (see also Chapter 12) suggests that bone damage would require anisotropic models. However, the ideas represented by the isotropic damage model are still of considerable use in a number of circumstances corresponding to the common practice of mechanical testing along principal material axes (see Chapter 17). In these cases, a scalar damage variable is sufficient to characterize the observed behavior even if the damage is oriented.

Another complication is the variation in the effect of damage as the mode of loading changes. It is obvious that the same damaged material loaded in compression could behave differently than in tension, since closed cracks could transmit the compressive load. Hence, the same physical damage might result in a different value of the damage parameter D in Eq. 18.1 for compressive loads. The same might also be true for shear loading. This suggests that the continuum damage models should be grounded in the micromechanics of the damage. Such modeling is the subject of fairly intense efforts in mechanics of materials research, but beyond the scope of the present work.

18.3 Constitutive Models for Damaging Materials

18.3.1 State Variable Models

The basic elements of continuum damage models are those of the nonlinear behavior of materials in general, which are most conveniently represented using state variable models.[8] In this case, the model equations consist of the differential equations of motion (or most often for purposes here, equations of

static equilibrium), the definitions of stress and strain, the compatibility equations, and the constitutive equations, which must obey the first and second laws of thermodynamics. By using the state variable approach, the constitutive equations are represented as

$$\tilde{\varepsilon} = \tilde{\varepsilon}(\tilde{\sigma}, T, \bar{\alpha}, \tilde{D}), \tag{18.6a}$$

$$\dot{\bar{\alpha}} = \bar{g}_{\alpha}(\tilde{\sigma}, T, \bar{\alpha}, \tilde{D}), \tag{18.6b}$$

$$\dot{\tilde{D}} = \bar{g}_{D}(\tilde{\sigma}, T, \bar{\alpha}, \tilde{D}), \tag{18.6c}$$

where $\tilde{\varepsilon}$, $\tilde{\sigma}$, T are the strain tensor, stress tensor, and temperature (external or observable state variables); $\tilde{D}$ is the (internal) state variable representing damage, and $\bar{\alpha}$ is a vector of other internal variables. As discussed below, $\tilde{D}$ in the most general case is a tensor quantity. Most often the other internal variables represent inelastic strains. For present purposes, temperature can be regarded as constant. Note also that in many circumstances it will be possible to invert Eq. 18.6a to express stress as a function of strain and the internal variables.

The development of a damage model for bone is the matter of defining the relationship between damage and the material behavior (Eq. 18.6a) and the evolution of the internal state variables with loading or deformation history (Eqs. 18.6b and c). One very helpful concept to guide the development is the concept of effective stress.[6] For the simple axial stress state considered in Eqs. 18.1 through 18.4, the effective stress is the load per unit undamaged area, i.e., $\sigma_a = P/(A - A_D)$. Hence, the effective stress is related to the apparent stress by $\sigma_a = \sigma/(1 - D)$. For a general state of stress, the effective stress at a point is assumed to be related to the apparent stress by a linear transformation (in general, a fourth-order tensor[4]), which is a function of the damage state, i.e.,

$$\tilde{\sigma}_a = \tilde{M}(\tilde{D}) \cdot \tilde{\sigma}, \tag{18.7}$$

where $\tilde{\sigma}_a$ is the effective stress tensor, $\tilde{\sigma}$ is the apparent (usual) stress tensor; $\tilde{D}$ is the damage tensor; and $\tilde{M}$ is the damage effect tensor.

A second useful concept is the principle of strain equivalence.[5] The principle of strain equivalence states that the strain associated with a damaged state under the applied stress $\tilde{\sigma}$ is equivalent to the strain associated with the undamaged state under the effective stress $\tilde{\sigma}_a$. According to the strain equivalence principle, if the constitutive law for the undamaged material is

$$\tilde{\varepsilon} = \tilde{F}(\tilde{\sigma}, \ldots), \tag{18.8}$$

then the corresponding stress–strain law for the damaged material is of exactly the same form with the stress replaced by the effective stress, i.e.,

$$\tilde{\varepsilon} = \tilde{F}(\tilde{\sigma}_a, \ldots). \tag{18.9}$$

The strain equivalence principle leads to some restrictive conclusions regarding the damaged constitutive equations.[4,9] Several alternative hypotheses to achieve greater generality have been proposed, such as elastic energy equivalence or total energy equivalence.[10,11] While such principles are not fully general, the development of specific constitutive laws is greatly facilitated by their use. For example, using the strain equivalence principle, a damaging elastic material, i.e., a material that is linear elastic but accumulates damage, is represented by

$$\tilde{\sigma} = \tilde{M}^{-1}(\tilde{D}) \cdot \tilde{\sigma}_a = \tilde{M}^{-1}(\tilde{D}) \cdot \tilde{C}^0 \cdot \tilde{\varepsilon}, \tag{18.10}$$

where $\tilde{C}^0$ is the stiffness tensor for the undamaged material. Hence, the material is an elastic material with an effective modulus defined by the product of the inverse of the damage effect tensor and the undamaged stiffness tensor, i.e., $\tilde{C} = \tilde{M}^{-1}(\tilde{D}) \cdot \tilde{C}^0$.

One can take advantage of symmetry of the stress and strain tensors and represent them as six-element vectors: $[\sigma_{11}, \sigma_{22}, \sigma_{33}, \sigma_{23}, \sigma_{31}, \sigma_{12}]^T$, $[\varepsilon_{11}, \varepsilon_{22}, \varepsilon_{33}, \varepsilon_{23}, \varepsilon_{31}, \varepsilon_{12}]^T$ (see Chapter 6). Then for isotropic damage, the damage effect tensor is

$$\tilde{M}(\tilde{D}) = \frac{1}{1 - D}\,\tilde{I}, \tag{18.11}$$

where $\tilde{M}$ is a 6×6 diagonal matrix defined by a constant multiplying the identity matrix. For anisotropic damage, various formulations have been proposed. For orthotropic damage, Chow and Wang[12] proposed the following formulation referenced to the principal axes of damage:

$$\begin{aligned} \tilde{M} = \operatorname{diag}\Bigg[& \frac{1}{1 - D_1}, \frac{1}{1 - D_2}, \frac{1}{1 - D_3}, \frac{1}{\sqrt{(1 - D_2)(1 - D_3)}}, \\ & \frac{1}{\sqrt{(1 - D_3)(1 - D_1)}}, \frac{1}{\sqrt{(1 - D_1)(1 - D_2)}} \Bigg], \end{aligned} \tag{18.12}$$

where D_1, D_2, D_3 = damage variables in their principal axes. In this case, the damage tensor $\tilde{D}$ is a second-order tensor while the damage effect tensor $\tilde{M}$ is fourth order. In the case of an anisotropic material with anisotropic damage, a higher-order definition of $\tilde{D}$ may be necessary.[12,13] Other formulations have been proposed for the orthotropic case, including those developed on the basis of micromechanical considerations.[14] Given the architecture of cortical bone, it seems reasonable to expect that an orthotropic model adequately describes cortical bone damage. A similar statement could be made for cancellous bone when regarded at the continuum level, consistent with assuming orthotropy for the undamaged properties. If the principal axes of damage and the principal material axes of the orthotropic material coincide, which also seems a reasonable assumption for bone, the development of damage rules is greatly simplified. The degree of anisotropy required for the damage effect tensor in cortical bone and cancellous bone is an issue yet to be explored experimentally.

18.3.2 One-Dimensional Models

18.3.2.1 Damaging Elastic Model

Much of the experimental work to date regarding the damage behavior of bone has been limited to simple loading circumstances where one-dimensional models of damage are sufficient. In problems where the stress state can be described by a scalar (simple tension or compression, bending of prismatic beams about principal material axes, torsion of circular cylinders about an axis of material symmetry), damage can be described by a scalar variable. (*Note*: This may be inadequate to describe the response of the damaged material to any other loading mode, because the induced damage may be anisotropic.) As illustrated in the following, the field equations for the scalar problem can usually be formulated in a straightforward fashion. Writing appropriate forms of Eqs. 18.6a and b, and writing an appropriate form of Eq. 18.6c describing the evolution of the scalar parameter D complete the problem formulation.

Consider the case of a damaging elastic material loaded in uniaxial tension. The stress is expressed in terms of the strain by writing the scalar version of Eqs. 18.10 and 18.11, i.e.,

$$\sigma = E^0 \cdot (1 - D) \cdot \varepsilon, \tag{18.13}$$

where E^0 represents the undamaged modulus. The entire nonlinear behavior is due to the evolution of the damage variable D. One of the classic models for the evolution of D (Eq. 18.6c) was proposed by

Kachanov[6] based on the idea that damage evolves as a power law function of the effective stress:

$$\dot{D} = B \cdot (\sigma_a)^N = B \cdot \left(\frac{\sigma}{1-D}\right)^N = \left(\frac{\sigma}{\sigma_{\text{ref}}(1-D)}\right)^N, \tag{18.14}$$

where B (or σ_{ref}) and N are experimentally determined material parameters. This model was developed in the context of damage in metals, and predicts damage accumulation at an accelerating rate for a constant hold stress. Specifically, assuming $\sigma = \sigma_0$, a constant, assuming $D(t = 0) = 0$, and assuming failure is defined by $D = 1$, the time to failure is

$$t_r = \frac{1}{(N+1)(\sigma_0/\sigma_{\text{ref}})^N}. \tag{18.15}$$

The model can be integrated under an arbitrary load history to determine the nature of softening due to the accumulation of tensile damage. For a simple tensile test to failure under stress control, i.e., $\sigma = \dot{\sigma}_0 t$, integrating Eq. 18.14 yields the following strain history:

$$\varepsilon = \frac{\dot{\sigma}_0 \cdot t}{E^0(1 - B \cdot \dot{\sigma}_0^N t^{N+1})^{1/(N+1)}}, \tag{18.16}$$

where E^0 is the undamaged value of the tensile modulus. A corresponding result for loading at a constant strain rate is readily obtained.

It was found that Kachanov's model for the evolution of D (Eq. 18.14) tended to overpredict the softening (i.e., the damage accumulation) in simulations of tensile loading experiments for human or bovine bone. Based on observed creep behavior of bone at high tensile loads, Fondrk[18] proposed the following tensile damage evolution model:

$$\dot{D} = B \cdot \left[\frac{(1-D)}{\varepsilon}\right] \cdot \sigma^N = \left[\frac{(1-D)}{\varepsilon}\right] \cdot \left(\frac{\sigma}{\sigma_{\text{ref}}}\right)^N. \tag{18.17}$$

With the use of Eq. 18.13, this expression is readily written in the standard form of the state variable model, Eq. 18.6c.

Shown in Fig. 18.2 are the results of using Kachanov's model and Fondrk's model to simulate loading a human bone sample at a constant stress rate. It is evident that either Kachanov's model or Fondrk's

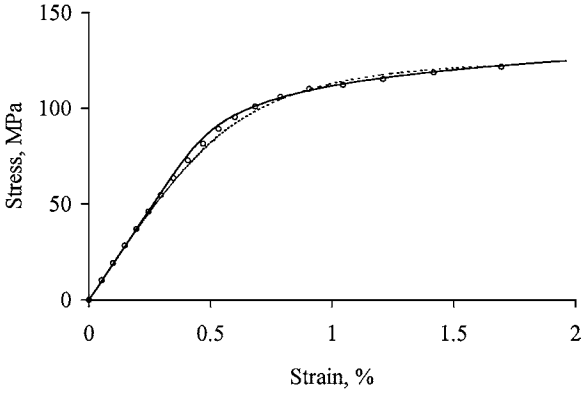

FIGURE 18.2 Plots of experimental stress–strain history[48] for monotonic tensile test of human cortical bone under stress control at 100 MPa/s (open circles) and simulations for a damaging elastic material according to Kachanov's rule (Eq. 18.14, dashed line) and Fondrk's rule (Eq. 18.17, solid line). The constants for Kachanov's rule are $\sigma_{\text{ref}} = 146$ and $N = 1.63$, and for Fondrk's rule they are $\sigma_{\text{ref}} = 162$ and $N = 9.25$. The undamaged modulus was $E^0 = 19$ GPa.

model can be made to fit the monotonic test data closely for a given test. However, Fondrk's model can describe the secondary tensile creep behavior of bone, which is strongly dependent on stress amplitude.[2] Kachanov's model (Eq. 18.14) has the potential to describe better the tertiary phase of creep, which signals the onset of creep rupture, and which is a behavior appropriate for metals. However, much of the damage in bone appears to accumulate prior to the tertiary phase of strain accumulation near rupture (see Chapter 16). Fondrk's model is more effective at representing this region of nonlinear behavior prior to the tertiary phase.

A damaging elastic model for cortical bone was proposed by Krajcinovic et al.[15] on the basis of a simple statistical model for fiber pullout. The model describes the damage as a linear function of the strain, i.e., $D = K\varepsilon$. This produces a stress–strain curve that is a simple parabola under strain-controlled loading. This model does not fit into the class of state variable models represented by Eqs 18.6a and b, since damage rate would be determined by stress rate, not stress alone. However, it is an example of a powerful approach using statistical models to describe underlying damage mechanisms, and it can be generalized to accommodate damaging elastic–plastic behavior.[4]

A fourth version of a simple damage evolution rule, which is sometimes used in fatigue damage models, is a simple power law relationship between damage rate and stress (not effective stress) amplitude, i.e.,

$$\dot{D} = B\sigma^n. \tag{18.18}$$

As discussed in Section 18.3.3, this rule has been used successfully in application to fatigue data. Like Eqs. 18.14 and 18.17, it can be made to fit a given stress–strain curve reasonably well. It suffers less from the problems found for Kachanov's rule in application to creep behavior, but was not as robust as Fondrk's rule for varying loading conditions.

Damaging elastic models can do a reasonable job of capturing stress–strain behavior observed in axial tests of cortical bone for a fixed loading rate. In fact, from the results in Fig. 18.2 one might conclude that they can represent nonlinear behavior quite well. However, they are not capable of describing the general nonlinear behavior of bone. One reason is the known rate dependence of the inelastic strain behavior of bone[16,17] (see Chapter 16). Second, bone can exhibit significant residual strains upon unloading from sufficiently high tensile stress amplitudes.[2,16] These behaviors are consistent with viscoelasticity, and plasticity or viscoplasticity models. Damaging elastic models cannot capture these behaviors.

18.3.2.2 Damaging Viscoelastic Model

Fondrk et al.[18,19] developed the idea of a damaging viscoelastic model for tensile behavior of bone. The stress–strain equation (Eq. 18.6a inverted for stress in terms of strain and internal variables) and the evolution equation for the internal strain (Eq. 18.6b) are defined as

$$\sigma = E_1 \cdot (\varepsilon - \alpha), \tag{18.19}$$

$$\dot{\alpha} = c^{-1} \cdot [E_1 \cdot (\varepsilon - \alpha) - E_2 \cdot \alpha]. \tag{18.20}$$

This model can be interpreted as a damaging standard viscoelastic solid, in which the internal variable α represents the internal viscous strain across the Kelvin–Voigt element. Parameters E_1, E_2, c correspond to the series elastic, parallel elastic, and viscous coefficients, respectively. Based on experimental evidence,[18,19] Fondrk et al. assumed that for tensile loading all material parameters are modified by the damage, i.e.,

$$E_1 = (1 - D) \cdot E_1^0; \qquad E_2 = (1 - D) \cdot E_2^0; \qquad c = (1 - D) \cdot c^0, \tag{18.21}$$

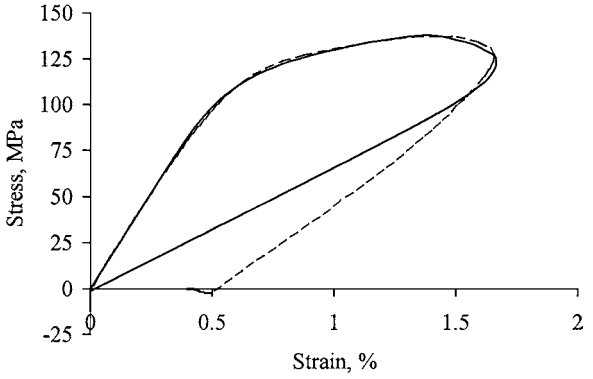

FIGURE 18.3 Plots of experimental stress–strain data for a tensile loading cycle with a triangular waveform (dashed line), and for a simulation using Fondrk's model for a damaging viscoelastic material (Eqs. 18.17 and 18.19 through 18.21, solid line). The loading and unloading rates were approximately 420 MPa/s. The values for the parameters in the model are $E_1^0 = 21$ GPa, $E_2^0 = 18$ GPa, $c^0 = 110$ GPa-s, $\sigma_{ref} = 43.5$ MPa, and $N = 8.3$. (From Fondrk, M T. et al., *J. Biomech. Eng.*, October, 1999. With permission.)

where the superscript 0 denotes the undamaged material properties. Note that this assumption is consistent with the strain equivalence principle. This model will allow prediction of time-dependent behaviors such as rate dependence, creep, and relaxation, which cannot be done with the damaging elastic models. Shown in Fig. 18.3 is the result of simulating a loading of a cortical bone sample at a constant stress rate to a high stress level and unloading at a constant stress rate. Until the strain reverses, the model can simulate the tensile loading quite closely.

18.3.2.3 Fondrk's Viscoplastic Model

Under the conditions of strain reversal, neither a damaging elastic nor damaging viscoelastic model can adequately describe the observed behavior because neither predicts residual strain or stress accumulation. If, for example, cortical bone is loaded in tension into the nonlinear strain range and unloaded to zero stress, a residual strain persists and is for all intents and purposes a permanent strain.[16,20,21] Fondrk[18,19] developed a model that accommodates this kind of behavior by including rate-dependent plastic behavior. The model can be regarded as a damaging version of a rheological model represented by an elastic element E_1, in parallel with two elements that are in series, a viscoplastic element and a second elastic element E_2.[19] The viscoplastic element, which allows the slip to occur, consists of a viscous element c in parallel with a Saint Venant (dry friction) element s. All elements in the model are assumed to change with damage. The corresponding constitutive equations for the one-dimensional case are as follows. The stress is defined in terms of the strains as

$$\sigma = E_1\varepsilon + E_2(\varepsilon - \alpha), \tag{18.22}$$

where ε is the total strain and α is the internal strain across the viscoplastic element. The current moduli E_1 and E_2 are defined as $E_1 = E^0(1 - D)$ and $E_2 = E^0 \cdot D$. This produces an initial tangent modulus unchanged by damage, which is consistent with experimental observations.[18] The evolution equation for the internal strain is given by

$$\dot{\alpha} = 0, \qquad \text{if} \quad s_C(\varepsilon, \alpha, D) < s(\varepsilon, \alpha, D) < s_T(\varepsilon, \alpha, D), \tag{18.23a}$$

$$\dot{\alpha} = c^{-1}(\varepsilon,\alpha,D) \cdot [E_1 \cdot (\varepsilon - \alpha) - E_2 \cdot \alpha - s(\varepsilon,\alpha,D)], \qquad \text{otherwise}, \tag{18.23b}$$

where $s(\varepsilon, \alpha, D)$ is the stress in the friction element and $c(\varepsilon, \alpha, D)$ is the viscosity parameter. During positive slip, the friction stress $s(\varepsilon, \alpha, D) = s_T(\varepsilon, \alpha, D)$, and during negative slip, $s(\varepsilon, \alpha, D) = s_C(\varepsilon, \alpha, D)$. The functions s_T and s_C were defined on the basis of the observed experimental behavior in stepwise

varied creep and under reversed loading. Under increasing tensile loads, the onset of significant nonlinear creep is taken to be proportional to a power of stress, and the residual strain is very nearly linearly proportional to the maximum inelastic strain. On this basis, a final form for s_T is[19]

$$s_T(\varepsilon, \alpha, D) = k_3 \cdot E^0 \cdot (1 - D) \cdot \varepsilon_r, \tag{18.24}$$

where ε_r is an approximate value of the residual strain given by

$$\varepsilon_r = k_1 \frac{\sigma_{\text{th}}}{E^0}(1/(1 - D) - 1), \tag{18.25}$$

where σ_{th} is a reference stress.[19]

The expression for s_c is

$$s_C(\varepsilon, \alpha, D) = -E^0 \cdot (1 - D) \cdot \varepsilon_r \cdot \hat{s}(\varepsilon, D), \tag{18.26}$$

where $\hat{s}(\varepsilon, D)$ is the following function that ranges from zero at strain reversal to one at zero stress:

$$\hat{s}(\varepsilon, D) = \frac{(1 - D) \cdot E^0 \cdot \varepsilon - k_2 \cdot \sigma_{\text{th}}}{(1 - D) \cdot E^0 \cdot \varepsilon_r - k_2 \cdot \sigma_{\text{th}}} \tag{18.27}$$

This model was found to represent the nonlinear strain history under reversed tensile loading quite adequately. It does omit the linear viscoelastic component of behavior, an omission that does not appreciably affect the accuracy when any significant nonlinear strains occur. Shown in Fig. 18.4 is a plot of the same test data as in Fig. 18.3, along with a simulation using Fondrk's viscoplastic model.

18.3.2.4 Elastic–Plastic and Elastic–Viscoplastic Models Incorporating Damage

By using the concepts of effective stress and strain equivalence, the models of classical plasticity or viscoplasticity are readily adapted to damaging materials. Because of the rate effects evident for cortical bone, particularly nonlinear creep behavior, the viscoplastic models would seem more likely to be applicable. The general nature of such models, incorporating either viscoplasticity or rate-independent plasticity,

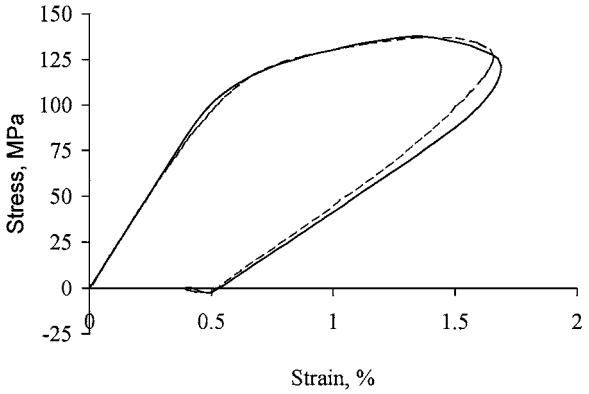

FIGURE 18.4 Plots of experimental stress–strain data for a triangular loading history under stress control (dashed line), and simulation using Fondrk's model for a damaging viscoplastic material (solid line). The experimental data are the same as in Fig. 18.3. The values for the parameters in the model are $E^0 = 21$ GPa, $\sigma_{\text{ref}} = 43.5$ MPa, $N = 8.3$, $k_1 = 0.875$, $k_2 = 1.6$, $k_3 = 0.0$, $c = \text{const.} = 34.5$ if $\dot{\alpha} > 0$, and $c = \text{const.} = 345$ if $\dot{\alpha} < 0$. (From Fondrk M.T. et al., *J. Biomech. Eng.,* October, 1999. With permission.)

is illustrated by the following example described by Lemaitre[5] for the one-dimensional case. The stress is taken to be

$$\sigma = E \cdot (\varepsilon - \alpha) = E^0 \cdot (1 - D) \cdot (\varepsilon - \alpha), \tag{18.28}$$

where α is the internal (plastic or viscoplastic) strain. The evolution of the plastic/viscoplastic strain is given by

$$\dot{\alpha} = 0, \qquad \text{if } \left| \frac{\sigma}{1 - D} - X \right| - R - \sigma_Y \leq 0; \qquad \dot{\alpha} \neq 0 \text{ otherwise.} \tag{18.29}$$

The inequality is a statement of the usual yield criterion modified by damage. The parameters X and R are the so-called back stress associated with kinematic hardening and the isotropic hardening stress, respectively, and σ_Y is the yield stress at $X = 0$, $R = 0$, $D = 0$.[5]

With appropriate definitions of X and R, this model could be made quite similar to Fondrk's viscoplastic model. Instead, an assumption commonly adopted in plasticity theory,[8,5] that X and R are saturating variables, will be followed. This accounts for strain stabilization under fully reversed loads, which has been demonstrated for engineering materials, especially metals. This idea is used with the disclaimer that such behavior has not been examined for bone. Following Lemaitre,[5] the evolutionary equations for X and R are written as

$$\dot{R} = b \cdot (R_\infty - R) \cdot |\dot{\alpha}|, \tag{18.30}$$

$$\dot{X} = a \cdot (X_\infty \cdot \dot{\alpha} - X \cdot |\dot{\alpha}|), \tag{18.31}$$

where a, b, R_∞, X_∞ are experimentally determined parameters. The additional required equations are the evolutionary equations for α and D. When the yield condition is violated, i.e., $\dot{\alpha} \neq 0$, one evolution equation for α proposed for viscoplastic materials is[5]

$$\dot{\alpha} = \left(\frac{\sigma_v}{B_v} \right)^m, \tag{18.32}$$

where B_v and m are experimentally determined parameters, and σ_v is the viscoplastic stress given by

$$\sigma_v = \left| \frac{\sigma}{1 - D} - X \right| - R - \sigma_Y > 0. \tag{18.33}$$

The evolution equation for D is based on physical and thermodynamic arguments for coupling the damage rate to the strain energy release rate and the accumulated plastic strain rate beyond a plastic strain threshold. One model that seeks to accommodate possible brittle (fatigue) damage mechanisms and ductile (microcavity nucleation and microcavity growth) mechanisms is the following:[5]

$$\dot{D} = \frac{\sigma^2}{2 \cdot S \cdot E^0 \cdot (1 - D)^2} \cdot |\dot{\alpha}| \qquad \text{if } \alpha \geq \alpha_0, \tag{18.34a}$$

$$\dot{D} = 0 \qquad \text{if } \alpha < \alpha_0. \tag{18.34b}$$

where S is an experimentally determined parameter called the energy strength of damage, α_0 is a strain corresponding to a damage threshold. Note that the model assumes that the damage accumulation rate and the inelastic strain rate are proportional. The model represented by Eqs. 18.28 through 18.34 contains a total of nine parameters (in addition to the undamaged elastic stiffness E^0) to be determined experimentally. This gives considerable flexibility in fitting the model to the data.

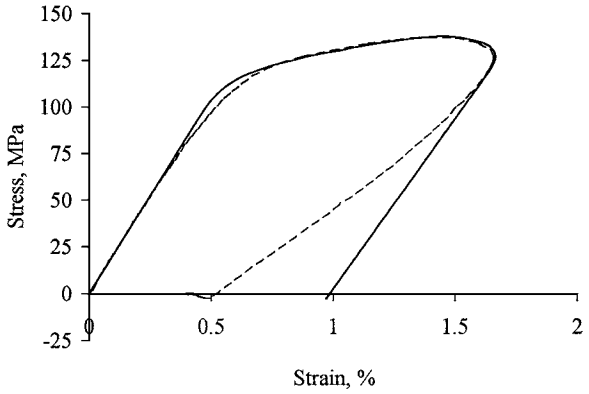

FIGURE 18.5 Plots of experimental stress–strain data for a triangular loading history under stress control (dashed line) and simulation using the general model described by Lemaitre for a damaging elastic–plastic material (Eqs. 18.28 through 18.34). The experimental data are the same as in Figs. 18.3 and 18.4. The values for the parameters in the model are $E^0 = 21$ GPa, $\sigma_Y = 70$ MPa, $a = 10, b = 10$, $R_\infty = 200$ MPa, $X_\infty = 200$ MPa, $B_\nu = 70$ MPa, $m = 7, S = 0.035, \alpha_0 = 0$.

Shown in Fig. 18.5 is a curve-fit generated with the above model for the same data as in Figs. 18.3 and 18.4. The large number of constants associated with the strain hardening and with the inelastic strain rate allows the loading portion of the curve to be fit reasonably well even without including damage. However, the unloading phase is poorly represented without damage. Even over a wide range of parameter combinations, the authors were unable to do a good job of simulating these experimental data for a load–unload cycle. Similar to Eq. 18.14, Eq. 18.34 tends to predict a rapidly accelerating damage process due to the presence of the damage term in the denominator. Although the authors would not rule out the possibility that a satisfactory fit can be achieved, the model was extremely sensitive to the parameter values in Eq. 18.34. For bone, which shows a recovery of 60 to 70% of inelastic tensile strains,[16] the model is not robust in simultaneously simulating realistic nonlinear strain accumulation and the corresponding stiffness loss on unloading.

18.3.2.5 Model of Zysset and Curnier

Zysset[22] and Zysset and Curnier[23] proposed the most general damage model to date in application to bone. Although they applied the model to cancellous bone, it is quite general enough to apply to either cancellous or cortical bone. As for the previous model, their model is derived using the formalism of generalized standard materials,[8] but does not require the potentially restrictive assumptions of an equivalence principle for strain, stress, or energy. The model is also completely general in the sense that it is three-dimensional and does not assume small strains. Here a version reduced to one dimension is presented in order that it can be readily compared with the previous models. As for the above model, the central assumption of Zysset and Curnier's model is that plastic flow and damage accumulation are intrinsically related. For the one-dimensional case, a measure of damage d is related to the plastic strain α by

$$\dot{d} = |\dot{\alpha}|. \tag{18.35}$$

(*Note*: The term d is used deliberately to distinguish it from the term D, which was defined in a more heuristic fashion.) The stress is given by

$$\sigma = \phi(d) \cdot E^0 \cdot (\varepsilon - \alpha), \tag{18.36}$$

where $\phi(d)$ is a damage function whose form is to be determined experimentally. The material is assumed to undergo isotropic hardening or softening as defined by a function $g(d)$, where $g(0)$ defines the undamaged hardening behavior. The yield is then given by

$$y = \left|S^\alpha\right| + S^d - h(d) - y_0 \leq 0, \tag{18.37}$$

where y_0 is the initial undamaged yield stress. The parameter S^α is the hardening stress, and is given by

$$S^\alpha = \begin{cases} -[y_0 + g(d)] & \text{if } \dot{\alpha} < 0 \\ [-(y_0 + g);\ +(y_0 + g)] & \text{if } \dot{\alpha} = 0 \\ +[y_0 + g(d)] & \text{if } \dot{\alpha} > 0 \end{cases} \tag{18.38}$$

The parameter S^d is associated with the damage flow and is defined by

$$S^d = \begin{cases} 0 & \text{if } \dot{d} < 0 \\ [-\infty;\ h(d) - g(d)] & \text{if } \dot{d} = 0 \\ h(d) - g(d) & \text{if } \dot{d} > 0 \end{cases} \tag{18.39}$$

The function $h(d)$ reflects the energy dissipation associated with the evolution of the damaged elastic modulus, and is given by[22]

$$h(d) = -y_0^2 \frac{\phi'(d)}{2E^0 \phi^2(d)}. \tag{18.40}$$

Based on experimental studies of trabecular bone, Zysset and Curnier[22, 23] proposed the following form for the function $\phi(d)$:

$$\phi(d) = 1 - \phi_c(1 - e^{-d/d_\phi}), \tag{18.41}$$

where ϕ_c and d_ϕ are experimentally determined parameters. Zysset and Curnier[23] also provide an empirical result for the function $g(d)$ for trabecular bone, although in a different form based on a modified definition of the damage parameter d that is amenable to three-dimensional problems. The combination of the damage function (Eq. 18.41), the yield and hardening functions (Eqs. 18.37 through 18.39), and the initial parameters are sufficient to investigate the nature of the damage evolution process. An evolution equation for the parameter d is not explicitly formulated for the rate-independent case.

Zysset[22] also developed a model that incorporates rate (viscous) effects as well as kinematic hardening, although Zysset and Curnier did not utilize it in their application to cancellous bone. Their elegant model also allows for the incorporation of anisotropic material properties using Fourier series expansions of the elasticity tensor, and it has been incorporated into a three-dimensional finite-element algorithm as described in Section 18.4.3 below.

18.3.3 Fatigue Damage Models

The discussion to this point has focused on the behavior of bone at relatively large strains. However, it has long been known that damage accumulation due to fatigue loading can accumulate at low strains (see Chapter 10). In fact, it was this behavior that first stimulated the investigation of damage models for bone. Carter and Caler[24] proposed one of the first models for damage accumulation in the context of fatigue life models based on a rupture time at constant stress defined by a power law:

$$t_r = B^* \cdot \sigma_0^{-N}. \tag{18.42}$$

As discussed below, this rule corresponds to the simple damage rule (Eq. 18.18) as well as Kachanov's rule (Eq. 18.14) for tensile fatigue loading. In more general terms, for any damage rule that has a separable form, i.e.,

$$\dot{D} = f_1(D) \cdot f_2(\sigma), \tag{18.43}$$

the time to rupture ($D = 1$) for any given constant stress σ_0 is given by

$$t_r = \frac{1}{f_2(\sigma_0)} \cdot \int_0^1 \frac{dD}{f_1(D)} = F(\sigma_0) \tag{18.44}$$

Assuming that damage is a continuous function of time, this leads to the following rule for a general stress history $\sigma(t)$.

$$\int_0^{t_r} \frac{d\tau}{t_r(\tau)} = 1, \tag{18.45}$$

where $t_r(\tau) = F(\sigma(\tau))$.

Using Eq. 18.42, Carter and Caler[24] derived an expression for time to failure under Haversine loading (their Equation 9). Converting to cycles to failure leads to the following expression:

$$n_r = \frac{B^* \cdot \Delta\sigma^{-N}\omega}{\frac{1}{2^N}\int_0^1 [1 + \sin(2\pi t)]^N dt}, \tag{18.46}$$

where $\Delta\sigma$ is the stress range, ω is the frequency, and $n_r = \omega t_r$. Carter and Caler note that this model predicts that the number of cycles to failure is proportional to frequency, but time to failure is not.

In later work, Carter and Caler[25] proposed a more general model by assuming that creep and fatigue damage obeyed two different rules; i.e., damage was the sum of three components

$$D = D_c + D_F + D_I \tag{18.47}$$

where the first and second terms are due to creep and fatigue damage and the third is an interaction term. They used Eq. 18.42 for creep damage and a second power law relating fatigue life to stress range resulting in the following equation for time to rupture:

$$\int_0^{t_r} \left(\frac{d\tau}{B^* \cdot \sigma(\tau)^{-N}} \right) + \frac{\omega t_r}{\Lambda \cdot \Delta\sigma^{-\beta}} = 1, \tag{18.48}$$

where Λ, β are constants in the fatigue life power law (and D_I is assumed to be zero). Carter and Caler[25,26] applied this model to their cyclic loading in zero tension and compression tension. The results suggest that such a distinction may be necessary for general axial behavior of bone, a notion that has been found to be useful for other materials.[27]

Other authors have applied this model to fatigue loading as well as monotonic loading to failure.[28,29] This specific characterization of damage is limited to addressing the question of rupture of a material. However, if the damage accumulation process is interpreted in the way expressed by Eq. 18.1, the history of the stress–strain cycles can be used to test a given formulation for the damage evolution rule as well as define the parameters in the rule. If the equation for the damage evolution rate is in the separable form of Eq. 18.43, as are Eqs. 18.14, 18.17, and 18.18, then $D(t)$ can be obtained by direct integration. For example, the evolution of D for a haversine loading would be given by

$$\int_0^D \frac{dD}{f_1(D)} = \frac{1}{\omega}\int_0^n f_2\left[\frac{\Delta\sigma}{2}(1 - \cos(2\pi n))\right] dn \tag{18.49}$$

TABLE 18.1

	$f_1(D)$	$f_2(\sigma)$	D	n_r
Simple damage rule (Eq. 18.18)	1	$B\sigma^N$	$K_1 B\sigma_0^N \frac{n}{\omega}$	$\frac{\omega}{K_1 B\sigma_0^N}$
Kachanov's damage rule (Eq. 18.14)	$(1-D)^{-N}$	$B\sigma^N$	$1-\left[1-(N+1)\left(K_1 B\sigma_0^N \frac{n}{\omega}\right)\right]^{\frac{1}{N+1}}$	$\frac{\omega}{(N+1)K_1 B\sigma_0^N}$
Fondrk's damage rule (Eq. 18.17)	$(1-D)^2$	$BE^0\sigma_0^{N-1}$	$\frac{K_2 BE^0 {\sigma_0}^{N-1}\frac{n}{\omega}}{1+K_2 BE^0 {\sigma_0}^{N-1}\frac{n}{\omega}}$	∞
$K_1 = 2^{-N}\int_0^1 (1-\cos 2\pi\eta)^N d\eta$			$K_2 = 2^{-(N-1)}\int_0^1 (1-\cos 2\pi\eta)^{(N-1)} d\eta$	

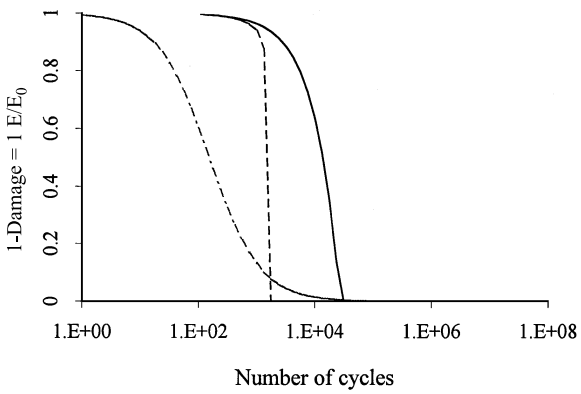

FIGURE 18.6 Predicted stiffness reduction for haversine loading using the simple damage rule (Eq. 18.18, solid line), Kachanov's damage rule (Eq. 18.14, dashed line), and Fondrk's damage evolution rule (Eq. 18.17, broken line). Parameter values for the simple damage rule and Kachanov's rule are $B = 3.314 \times 10^{-36}$ and $N = 17.95$ (Carter and Caler[25]), and the values for Fondrk's model are $\sigma_{\text{ref}} = 162$ and $N = 9.25$, which are the same values used in the monotonic loading simulation, Fig. 18.2. For all cases, $\sigma_0 = 60$ MPa, $\omega = 1$.

The changing compliance is then estimated by $(E/E^0) = (1 - D)$. The simple damage rule (Eq. 18.18), Kachanov's rule (Eq. 18.14), and Fondrk's rule for the elastic case (Eqs. 18.17 and 18.13) can be substituted into Eq. 18.48 and integrated. The results are summarized in Table 18.1. The predicted cycles to failure in Table 18.1 show that Eq. 18.46 corresponds to the life prediction ($t_r = n_r/\omega$) using either the simple damage rule or Kachanov's rule and the appropriate definitions of constants. However, the stiffness degradation rate is different for the two models (Table 18.1). Fondrk's model predicts an infinite time to rupture (Table 18.1) corresponding to an asymptotically decaying damage rate. This is unrealistic for the tertiary phase of damage growth where the stiffness loss accelerates.[1,30]

Shown in Fig. 18.6 are some numerical solutions for E/E^0 predicted by the three damage evolution rules in Table 18.1. The constants used for Fondrk's rule are those used for the monotonic curve fit (see Fig. 18.2). The values used for Kachanov's rule and for the simple rule correspond to those obtained by Carter and Caler.[25] Kachanov's rule leads to a more precipitous drop in the stiffness because of the effect of damage during the final phase of fatigue life. Fondrk's rule leads to a sigmoid-shaped decay curve, which means that the later phase of behavior is not consistent with experimental data. However, Fondrk's rule was reasonably robust with respect to using a single set of parameters in both the monotonic loading situation (Fig. 18.2) and fatigue (Fig. 18.6). When the authors attempted to use the parameters from Fig. 18.6 for

Kachanov's rule and the simple damage rule in the monotonic loading situation (Fig. 18.2), unbounded strains were predicted at stresses well below the actual peak values.

Relatively few attempts have been made to characterize the evolution of damage in experimental fatigue studies. Pattin et al.[30] characterized the fatigue damage accumulation process in tension and compression in terms of compliance change and energy dissipation. Specifically, they found the following two rules described the change in compliance in tensile fatigue and compressive fatigue, respectively.

$$1 - \frac{E(n)}{E_0} = a_0 + a_1 \log\left(\frac{n}{n_f}\right), \tag{18.50}$$

$$1 - \frac{E(n)}{E_0} = b_1 \log\left(\frac{1}{1 - n/n_f}\right), \tag{18.51}$$

where the constants a_0, a_1, b_1 are each of the form

$$(\,) = c^*\left(\frac{\Delta\sigma}{E^*} - c^{**}\right). \tag{18.52}$$

In these equations, $E(n)$ = secant modulus at cycle n = (stress range)/(strain range), E_0 = maximum secant modulus, n_f = fatigue life, $\Delta\sigma$ = stress range, E^* = initial elastic modulus, and c^* and c^{**} = parameters derived from curve fits of the data. The left-hand term in Eqs. 18.50 and 18.51 corresponds to damage D for a damaging elastic material (see Eq. 18.13), and has been used in other experimental studies.[31,32] Although the form of the evolution equations is implicit in empirical curve-fits such as Eqs. 18.50 and 18.51, they cannot in general be used to define the analytical forms of the evolution functions represented by Eqs. 18.14 and 18.17.

18.4 Applications to Nonhomogeneous Loading

Thus far, the focus has been on the simplest of stress states, allowing for relatively straightforward formulations of damage models. For general multiaxial stress states, the problem formulation is potentially quite complex. However, for some simple nonhomogeneous stress states, specifically bending of a prismatic beam and torsion of a circular cylinder, the incorporation of damage accumulation into stress analysis is still fairly straightforward. These two situations are of particular interest because they reflect some common experimental configurations. Formal expressions for the solutions for these cases are also fairly easily developed, although analytical solutions are usually not available. More complex loadings are better addressed using finite-element analysis (FEA) models that incorporate damage algorithms.

18.4.1 Symmetric Bending of a Prismatic Beam

The equations for symmetric bending of a prismatic beam are readily developed based on the assumption that plane sections remain plane and the equilibrium equations across the section are satisfied. The corresponding field equations to be satisfied at any cross section are

$$\int_{\text{Area}} \sigma dA = F(t), \tag{18.53}$$

$$\int_{\text{Area}} \sigma y dA = M(t), \tag{18.54}$$

$$\varepsilon = a(t) \cdot y + b(t), \tag{18.55}$$

where $F(t)$ and $M(t)$ are the time-dependent resultant axial force and resultant moment acting on the cross section, respectively, y is the coordinate defining position across the section, ε = strain at position

y across the section, and parameters $a(t)$ and $b(t)$ define the time-dependent strain distribution across the section. It is convenient to write Eq. 18.55 as

$$\varepsilon = \frac{y - \bar{y}(t)}{\rho(t)}, \tag{18.56}$$

where $\bar{y}(t)$ are $\rho(t)$ the neutral axis location and radius of curvature of the neutral axis, respectively. Combining the above equations with the constitutive rules for the material, the parameters $a(t)$ and $b(t)$, or $\bar{y}(t)$ and $\rho(t)$, can be determined as a function of $F(t)$ and $M(t)$, or vice versa. For example, if the instantaneous elastic behavior is described by an equation such as Eq. 18.19 (or Eq. 18.28), Eqs. 18.53 through 18.55 can be combined to yield

$$\left\{\int_A E_1 y dA\right\}a + \left\{\int_A E_1 dA\right\}b - \left\{\int_A E_1 \alpha dA\right\} = F(t) \tag{18.57}$$

$$\left\{\int_A E_1 y^2 dA\right\}a + \left\{\int_A E_1 y dA\right\}b - \left\{\int_A E_1 \alpha y dA\right\} = M(t), \tag{18.58}$$

where modulus E_1 varies with time due to damage accumulation. The problem is completed by adding the equation for the relationship between E_1 and the damage, plus the evolution equation for the damage. Typically, the damage evolution models will result in nonlinear integral-differential equations that must be solved numerically. Because the derivatives are with respect to time and the integrals are with respect to spatial coordinates, the numerical solution is relatively easy to implement.

Using the damaging viscoplastic model (Eqs. 18.22 through 18.27) for the tensile damage only, Fondrk[19] simulated experimental cantilever loading tests of machined bovine samples. In the simulations, the input was the measured $M(t)$; ($F(t)$ was zero). The model outputs were $a(t)$ and $b(t)$, which were used to calculate outer fiber strains. Shown in Fig. 18.7 are model results along with the experimentally measured outer fiber strains from one test.

Griffin et al.[33] used a somewhat different approach to characterize bending fatigue behavior of machined samples of human bone. Their work is one of few efforts to incorporate composite models into the damage accumulation process as well as recognize different damage accumulation processes in tension

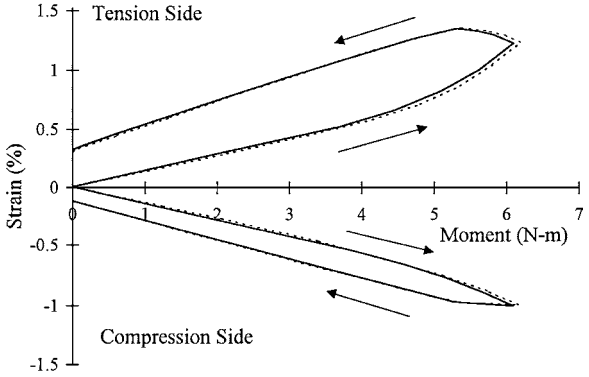

FIGURE 18.7 Experimental measurements (dashed lines) and simulation results by Fondrk et al.[19] of strain–moment curves for a cantilever beam of bovine bone subjected to a trapezoidal end-deflection history. The beam was deflected at a rate that produced approximately 1.5% outer fiber strains at the root in 1 s, held for 4 s, and unloaded at the same rate. Outer fiber strains were measured near the clamped end. The dashed line shows the experimental data, and the two solid lines show the predictions using Fondrk's viscoplastic model using model data obtained from bovine tensile tests. Only tensile damage was modeled. (From Fondrk, M.T. et al., *J. Biomech. Eng.,* October, 1999. With permission.)

and compression. They assumed the behavior to be represented by a fiber-reinforced composite, in which the fibers are the osteons and the matrix is the interstitial bone. They used the following rule of mixtures to define the evolution of the effective modulus. The local modulus is given by

$$E = (1 - D_f)E_f V_f + (1 - D_m)E_m V_m \tag{18.59}$$

where $D_{[]}$, $E_{[]}$, $V_{[]}$, are the damage parameter, undamaged modulus, and volume fraction for matrix and fiber. The evolution of tensile damage in the matrix is assumed to involve a self-limiting process and is described by

$$\frac{dD_m}{dn} = K_1(D_s - D_m). \tag{18.60}$$

D_s is a saturation density of damage assumed to be proportional to cyclic stress amplitude, i.e., $D_s = K_2\sigma_a^q$ where K_2, q are experimentally determined constants. The evolution of damage in the fibers (osteons) is not self-limiting and is assumed to be proportional to both fiber and matrix damage:

$$\frac{dD_f}{dn} = (K_3 D_f + K_4 D_m), \tag{18.61}$$

where K_3, K_4 are constants. The damage in compression is assumed to be a single process for fiber and matrix given by

$$\frac{dD_c}{dn} = K_5(D_c + D_{sr}). \tag{18.62}$$

D_{sr} represents damage initiator effects and is taken as $D_{sr} = K_6\sigma_a^p$, where K_5, K_6, and p are constants. Values for model constants were estimated using data from Pattin et al.[30] Using a laminated beam model in which each laminate is damaged according to Eqs. 18.60 through 18.62, Griffin et al. obtained good results for simulations of the fatigue histories of human cortical bone in four-point bending (Fig. 18.8).

18.4.2 Torsion of a Circular Cross Section

Assuming damage can be represented by a scalar variable in torsion, the torque–twist relationship for a given loading history can be determined from the following field equations. It is assumed that the circumferential shear strain γ varies linearly across the section, i.e.,

$$\gamma = \Theta r, \tag{18.63}$$

where r = the radius and Θ = twist per unit length. Global equilibrium requires that

$$2\pi\int_0^a \tau r^2 dr = T(t), \tag{18.64}$$

where τ = the circumferential shear stress, a = the maximum radius of the cross section, and $T = T(t)$ the external applied torque. Assuming the material behaves in shear according to a rule similar to Eq. 18.19 or 18.28, one can write

$$\tau = G \cdot (\gamma - \alpha) = G^0 \cdot (1 - D) \cdot (\gamma - \alpha), \tag{18.65}$$

where γ = circumferential shear strain, α = internal inelastic strain, G^0 = undamaged instantaneous shear modulus, and D = damage. Substituting Eqs. 18.63 and 18.65 into Eq. 18.64 yields the following equation relating torque history and twist history.

$$\Theta(t)\int_0^a (1 - D)r^3 dr - \int_0^a (1 - D)\alpha r^2 dr = T(t)/(2\pi G^0). \tag{18.66}$$

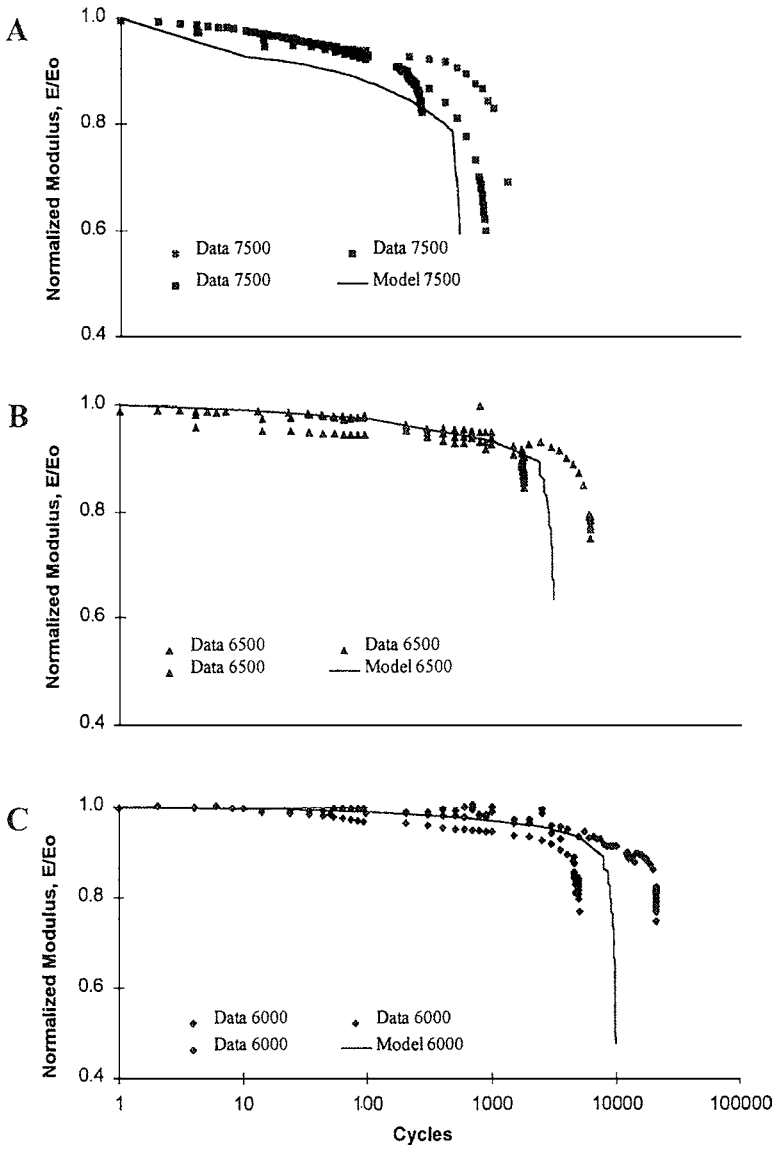

FIGURE 18.8 Results by Griffin et al.[33] for the fatigue history of equine bone under fatigue loading in four point bending. Experimental data are shown with symbols and the model (Eqs. 18.59 through 18.62) results are the solid lines. (From Griffin, L.V. et al., *J. Orthop. Res.,* 15, 607, 1997. With permission.)

As for the bending problem, this integral equation must be solved in combination with the differential equations describing the evolution of the two internal state variables α and D, which will necessitate a numerical solution procedure.

Shown in Fig. 18.9 are simulations of experimental data using the damaging viscoelastic model of Fondrk for two circumstances, monotonic loading under twist control and monotonic loading under torque control. The viscoelastic damage models that were used successfully for tensile behavior did not fare as well for the torsion problem. In particular, when the parameters derived from fitting monotonic tests were used in simulations of relaxation response, they substantially overpredicted the relaxation. Conversely, models fit to the relaxation data underpredicted strains for monotonic load simulations. It appears likely that more complex models will be required for characterizing inelastic strains and damage evolution for general torque–twist histories.

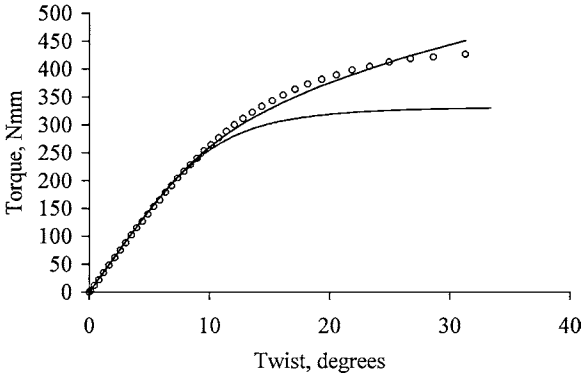

FIGURE 18.9 Torque–twist curves for a damaging viscoelastic material. The values for the model parameters are G^0 = instantaneous modulus = 3.5 GPa; G^e = equilibrium modulus = 3.08 GPa; c^0 = viscous parameter = 6.16 GPa-s, τ_{ref} = constant in damage evolution equation (Eq. 18.17) = 40 MPa; N = constant in damage evolution equation (Eq. 18.17) = 3.9. The upper line is a simulation at a constant torque rate, dT/dt = 330 Nmm/s and the lower line assumes a constant twist rate, $d\Theta/dt$ = 11°/s. Also shown are experimental data[49] (open circles) for a torque-controlled test of human bone at a twist rate of 330 Nmm/s.

18.4.3 More General Problems, FEA Models

The prediction of damage effects and damage evolution in more complex situations, particularly multiaxial stress analysis problems, is most readily addressed using FEA models. There are several potential levels of analysis. One is to investigate the effects of existing damage without concern for the damage evolution process. Another is to examine the micromechanics of damage. A third is to solve the full-blown problem of damage evolution. Relatively little work has been done in any of these areas to date, especially the third. Each of these types of applications is illustrated by an example in the following.

Pidaparti and Liu[34] used an FEA model to investigate the effect of longitudinally and transversely oriented damage on axial, bending, and torsional behavior. The bone was modeled as a circular tube, and the material and damage were assumed to be orthotropic and homogeneous. They used a damage effect transformation based on the notion of complementary strain energy equivalence, which resulted in a damaged compliance matrix of the following form:[35]

$$[C]^{-1} = \begin{bmatrix} \frac{1}{E_1} & -\frac{\nu_{21}}{E_2} & -\frac{\nu_{31}}{E_3} & 0 & 0 & 0 \\ -\frac{\nu_{12}}{E_1} & \frac{1}{E_2} & -\frac{\nu_{32}}{E_3} & 0 & 0 & 0 \\ -\frac{\nu_{13}}{E_1} & -\frac{\nu_{23}}{E_2} & \frac{1}{E_3} & 0 & 0 & 0 \\ 0 & 0 & 0 & \frac{1}{G_{23}} & 0 & 0 \\ 0 & 0 & 0 & 0 & \frac{1}{G_{31}} & 0 \\ 0 & 0 & 0 & 0 & 0 & \frac{1}{G_{12}} \end{bmatrix}, \tag{18.67}$$

where

$$E_i = (1 - D_i)^2 E_i^0, \tag{18.68a}$$

$$\nu_{ij} = \frac{1 - D_i}{1 - D_j} \nu_{ij}^0, \tag{18.68b}$$

$$G_{ij} = \frac{2(1 - D_i)^2 (1 - D_j)^2}{(1 - D_i)^2 + (1 - D_j)^2} G_{ij}^0. \tag{18.68c}$$

In Eqs. 18.68a to c, the subscripts $i, j = 1$, 2, or 3 (no summation implied), and the superscript 0 indicates undamaged values for the engineering constants. It is noteworthy that complementary energy equivalence results in a damage effect tensor with terms that involve $(1 - D_i)^2$ rather than the first-order terms of the strain equivalence principle (see Eqs. 18.13 and 18.21). Using this model, Pidaparti and Liu[34] demonstrated the variable effect of oriented damage (in this case transverse or longitudinal) on the structural stiffness as a function of loading mode.

The use of FEA models to explore damage accumulation at the microstructural level is illustrated by the work of Guo et al.[36] They modeled the two-dimensional structure of cancellous bone as hexagonal cells, in which each cell wall represented a trabecula. The trabeculae were modeled as linear elastic beams, and two cracks of random length were incorporated into each oblique trabecula. Crack growth under cyclic loading was calculated using a Paris law, and trabeculae with critical crack lengths were removed from the mesh after each load cycle. In this way they predicted stiffness loss as a function of load cycles for an idealized geometry.

The work of Zysset and Curnier[37] appears to be the only example to date of the implementation of a continuum damage mechanics model to investigate damage evolution in a skeletal structure. They incorporated the previously described damaging elastic–plastic model in an FEA algorithm to examine the accumulation of damage in a femur around a total hip arthroplasty component. The highly nonlinear behavior is evident from the results of their model for hip joint loads of nominally three, four, and seven times body weight. This model is the most realistic representation to date of the accumulation of inelastic strains under complex loading, and is capable of predicting the loss of compliance as well as the residual strains that are observed experimentally (see Chapter 17).

18.5 Micromechanical Models

In continuum damage mechanics models, the model parameters are often treated phenomenologically in the sense that they are evaluated by macroscopic measurements of damaged stress–strain behavior. The alternative is to use micromechanical models that attempt to capture explicit mechanisms of damage. Although there is a considerable volume of work in the development of micromechanical models for damage accumulation, relatively little work has been done in application to bone.

One illustration of such models is the work of Fondrk et al.,[38] who used a so-called self-consistent model to estimate the relationship between crack size and density, and compliance changes for cortical bone. This particular approach involves the use of a crack model of an assumed shape and distribution of orientations, and a means of approximating the homogenized properties of the material containing the cracks at a particular size and density. The fundamental equations for the analysis of Fondrk et al. include a relationship between the crack characteristics (size, density, shape, and orientation) and a continuum (averaged) damage parameter. For Fondrk et al.'s oriented crack model, the scalar equation for the nondimensional crack density has the following form:

$$\omega = f_s N\{a^3\} \tag{18.69}$$

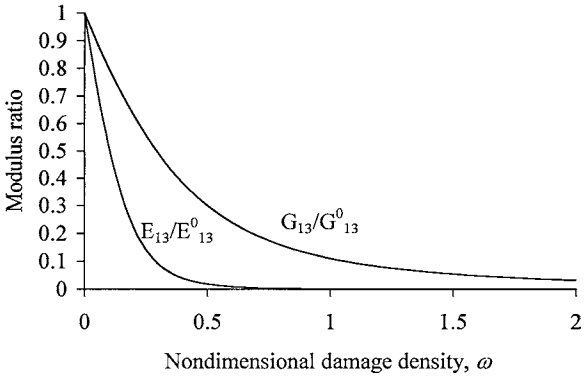

FIGURE 18.10 Results for predicted stiffness reductions from Fondrk's penny-shaped crack model (Eqs. 18.69 and 18.70). The abscissa corresponds to the parameter ω in Eq. 18.69. The normalized stiffness values correspond to the compliance terms C_{11}/C^0_{11} and C_{44}/C^0_{44} in Eq. 18.70. The solution is based on estimates of human bone anisotropic constants from the literature.[38] (From Fondrk M. T. et al., *J. Biomech. Eng.*, October, 1999. With permission.)

where N is the density of cracks per unit volume, and $\{a^3\}$ is the average of a characteristic dimension and f_s is a shape factor.[39] The relationship between the damaged and undamaged compliance tensor is

$$\tilde{C} = \tilde{C}^0 + \omega\tilde{H}(\tilde{C}), \tag{18.70}$$

i.e., the current compliance is determined by adding a correction $\tilde{H}$ to the undamaged compliance. In the self-consistent model, tensor $\tilde{H}$ is an implicit function of the current compliance; its specific form is obtained from a model of the effect of an individual crack on the compliance of a representative volume element. The form of $\tilde{H}$ in the model of Fondrk et al.[38] is defined based on the assumption that the penny-shaped cracks are oriented along the x_3 axis, which is also perpendicular to the plane of transverse isotropy. Adopting the vector notation for the stress tensor, there are only three nonzero terms in the 6×6 matrix $[H]$. These are H_{33}, corresponding to the axial compliance, and $H_{44} = H_{55}$, the compliances corresponding to the axial-transverse shear planes. Shown in Fig. 18.10 are the results predicted by the model for the decrease in longitudinal modulus and axial-transverse shear modulus as a function of damage density for human cortical bone.

The composite model of Courtney and co-workers[40] arguably falls into the class of micromechanical models. It is based on a model for local slip at the osteonal (fiber) level. They assume that debonding of the osteons results in slip along the interface with the surrounding matrix and a load transfer defined by a constant shear stress at the slipping interface. The resulting expression for the average stress–strain curve is

$$\bar{\sigma} = E\bar{\varepsilon} - \rho f(\bar{\varepsilon})\tau\frac{L}{R}\left(\frac{\bar{\varepsilon}}{\bar{\varepsilon}_0}\right)^2, \tag{18.71}$$

where $\bar{\sigma}$, $\bar{\varepsilon}$ are averaged stress and strain, $\bar{\varepsilon}_0$ is average strain at full osteonal debonding, τ is the interface shear stress, R, L, and ρ are the osteonal radius, length, and density, and $f(\bar{\varepsilon})$ is the volume fraction of damaged osteonal bone. This model was used by Courtney et al.[40] to investigate the increase in $f(\bar{\varepsilon})$ on the basis of observed decreases in stiffness. Note that Eq. 18.71 corresponds to the form of Eq. 18.70, where the initial undamaged stiffness is modified by a nonlinear term reflecting the accumulation of damage. This simple mechanistic model also incorporates two qualitative behaviors of the damaging elastic–plastic models that appear necessary for bone, namely, the loss of compliance and the frictional forces associated with nonlinear straining.

The previously cited composite beam bending model of Griffin et al.[33] and the FEA model of Guo et al.[36] also represent micromechanical models of damage in the sense that the mechanics of a micromechanical

element is used to predict the macroscopic behavior of a damaged material. There are a number of other examples of modeling micromechanics of crack formation and propagation in bone in the context of fracture mechanics. Discussion of them will be omitted here, as they are better addressed in that context.

18.6 Damage and Repair Models

As noted in the introduction to this chapter, *in vivo* damage accumulation would be coupled with a repair process. It is a natural and appealing idea to extend damage accumulation models to include repair. Elsewhere in this book, feedback models for bone adaptation are discussed in detail. Here, the issues and published work specific to feedback models for repair of damage accumulation will only be reviewed in brief fashion. In an operational sense, the models for adaptation and repair are quite similar. Both involve a coupling between some current mechanical state and biological processes, which changes the structure. In the case of adaptation, the usual assumption is that the bone seeks a new homeostatic state, usually associated with a target strain or strain energy state (see Chapters 29 and 30). In the case of damage and repair, a similar assumption is explicit or implicit in the model. Martin[41,42] proposed a damage repair model based on fatigue damage accumulation and repair. His model assumes the net rate of damage accumulation $\dot{D}$ is the difference between a damage formation rate (described by a model of the form of Eq. 18.49) and a rate of repair that reflects the local biology, i.e.,

$$\dot{D} = \dot{D}_F - \dot{D}_R. \tag{18.72}$$

The damage formation rate $\dot{D}_F$ is given by

$$\dot{D}_F = k_D s^N R_L, \tag{18.73}$$

where k_D is a rate constant, s^N is a stress[41] or effective strain range,[42] and R_L is a daily loading rate. The repair rate is given by

$$\dot{D}_R = D f_a \pi r_c^2 F_s, \tag{18.74}$$

where f_a is an activation rate for a basic multicellular unit, r_c is the radius of an osteon, and $F_s > 1$ is a damage repair specificity factor. Martin[42] combined the rules for damage formation and repair with a rule for periosteal apposition and showed that this model would predict "healing" (convergent solutions) or fatigue fracture (unstable solutions) above a critical daily loading rate.

Prendergast and Taylor[43] also developed a damage-repair model based on fatigue damage. In their model, they assume excess damage is a stimulus to remodeling and takes the form:

$$\Delta D = D - D_{\text{ref}}, \tag{18.75}$$

where D is the damage measure and D_{ref} is the reference value of damage corresponding to an equilibrium between damage accumulation and repair. Both D and D_{ref} are functions of time as well as position. They assume that a remodeling measure X is linearly related to ΔD, i.e.,

$$\dot{X} = C \cdot \Delta D = C \int_{t_0}^{t_1} (\dot{D} - \dot{D}_{\text{ref}}) dt \tag{18.76}$$

Note that this is similar to but not equivalent to Martin's model, since a second-order rather than a first-order dynamic form is implied by Eq. 18.76. Prendergast and Taylor used an equation equivalent to Eq. 18.49 to define damage accumulation rate, i.e.,

$$\dot{D} = B\sigma^N, \tag{18.77}$$

where B and N are constants. The position-dependent values for $\dot{D}_{\text{ref}}$ were determined using Eq.18.77 and stress values calculated for normal physiological loads. Using this model to investigate the change in geometry of a bone experiencing a reduction in torsional load, they predicted a nonmonotonic adaptation of geometry to achieve an adapted state. In subsequent work, McNamara et al.[44] applied this model to adaptation of bone around a noncemented femoral prosthesis. In this work, they introduced a nonlinear (power law) relationship between damage accumulation rate and fatigue life fraction, and developed the rule so that D_{ref} was a global value. They also show the circumstances under which the damage-based adaptation algorithm coincides with strain-based algorithms used elsewhere.

Levenston and Carter[45] proposed a model that also strongly parallels the ideas of strain-based adaptation models. Specifically, a stimulus due to damage is added to the strain stimulus of their previous models.

$$S = S_{ND} + S_D, \tag{18.78}$$

where S is the total daily adaptation stimulus, and S_{ND} and S_D are the nondamage stimulus and the damage stimulus. The damage stimulus is proportional to the rate of energy dissipation due to damage accumulation. It is represented by the hysteresis in loading cycles beyond that which is attributed to viscous effects, i.e.,

$$S_D \propto H_{\text{TOT}} - H_V, \tag{18.79}$$

where H_{TOT} and H_V are the total hysteresis and the hysteresis due to viscous effects, respectively. Based on the data of Pattin et al.,[30] Levenston and Carter[45] demonstrated that this model predicts a differential response to compressive loading and tensile loading, a result that distinguishes it from the strain-energy-based adaptation models.

There are obvious similarities among the above models, although each approaches the coupled damage and repair process from a different perspective. Typically, they represent the damage mechanics in the simplest possible terms. Determining which model will prove to be more realistic will require considerably more experimental work.

The use of micromechanical models offer potential for investigating damage-repair relationships at the mechanistic level. One example is the work of Prendergast and Huiskes,[46] who used a microstructural FEA model to examine the influence of interlamellar debonding and cement line cracks on local strains at the osteocyte level. These changes were interpreted as potential signals stimulating remodeling response. This work is an interesting combination of micromechanical modeling of damage and micromechanical modeling of adaptive behavior (strain stimulus at the cellular level).

A different example of a model which incorporates micromechanics is the recent work of Taylor.[47] His model assumes a nonmonotonic crack growth rate vs. crack length relationship and an assumed constant crack repair rate for bone. The model suggests there exists a range of applied stress amplitudes for which cracks below a critical length will tend toward an equilibrium length. Taylor observes that this behavior offers a damage-based explanation for the so-called lazy zone of bone adaptation (see Chapter 30).

18.7 Summary

The focus of this chapter has been on continuum-level models of damage, which are most readily incorporated into global stress analyses. A primary goal has been to provide some simple examples of applications, particularly those that correspond to common modes of testing. Using continuum damage models, the damage accumulation process in bone is a tractable problem at several levels. The models can be used to predict the inelastic behavior and the damage accumulation processes under conditions of overload and fatigue. More importantly, they can be used in conjunction with experimental studies to refine descriptions of these behaviors. Implicit or explicit mechanisms in the models can be tested in the process, thereby increasing understanding of the relationships among the structure and composition of the bone and the mechanical behavior of the bone. The continuum models can be placed in the context

of well-developed mechanics principles. However, there are numerous specifics about the effects of loading direction, loading mode, loading rate, etc. that remain to be explored. Given the complex structure and complex mechanical behavior of bone, damage model development will require substantial accompanying experimental research in damage behavior.

References

1. Carter, D. R. and Hayes, W. C., Compact bone fatigue damage—I. Residual strength and stiffness, *J. Biomech.,* 10, 325, 1977.
2. Fondrk, M., Bahniuk, E., Davy, D. T., and Michaels, C., Some viscoplastic characteristics of bovine and human cortical bone, *J. Biomech.,* 21, 623, 1988.
3. Burr, D. B., Forwood, M. R., Fyhrie, D. P., Martin, R. B., Schaffler, M. B., and Turner, C. H., Bone microdamage and skeletal fragility in osteoporotic and stress fractures, *J. Bone Miner. Res.,* 12, 6, 1997.
4. Krajcinovic, D., *Damage Mechanics,* North-Holland Elsevier, New York, 1996.
5. Lemaitre, J., *A Course in Damage Mechanics,* 2nd ed., Springer-Verlag, Berlin, 1996.
6. Kachanov, L. M., *Introduction to Continuum Damage Mechanics,* Martinus Nijhoff, Dordrecht, The Netherlands, 1986.
7. Katz, J. L., Hard tissue as a composite material. I. Bounds on the elastic behavior, *J. Biomech.,* 4, 455, 1971.
8. Lubliner, J., *Plasticity Theory,* Macmillan, New York, 1990.
9. Chaboche, J. L., Lesne, O., and Pottier, T., Continuum damage mechanics of composites: towards a unified approach, in *Damage Mechanics in Engineering Materials,* Voyiadjis, G. Z., Ju, J.-W., and Chaboche, J.-L., Eds., Elsiever, Amsterdam, 1998, 3–26.
10. Cordebois, J. P. and Sidoroff, F., Damage induced elastic anisotropy, in *Mechanical Behavior of Anisotropic Solids,* Boehler, J.P., Ed., Martinus Nijhoff, Boston, 1983, 761–774.
11. Chow, C. L. and Lu, T. J., An analytical and experimetnal study of mixed-mode ductile fracture under nonproportional loading, *Int. J. Damage Mech.,* 1, 191, 1992.
12. Chow, C. L. and Wang, J., An anisotropic theory of elasticity for continuum damage mechanics, *Int J. Fracture,* 33, 2, 1987.
13. Ju, J. W., Isotropic and anisotropic damage variables in continuum damage mechanics, *J. Eng. Mech.* 116, 2764, 1990.
14. Krajcinovic, D., Damage mechanics, *Mech. Mater.,* 8, 117, 1989.
15. Krajcinovic, D., Trafimow, J., and Sumarac, D., Simple constitutive model for a cortical bone, *J. Biomech.,* 20, 779, 1987.
16. Fondrk, M. T., Bahniuk, E. H., and Davy, D. T., Inelastic strain accumulation in cortical bone during rapid transient tensile loading, *J. Biomech. Eng.,* 121, 616, 1999.
17. Jepsen, K. J. and Davy, D. T., Comparison of damage accumulation measures in human cortical bone, *J. Biomech.,* 30, 891, 1997.
18. Fondrk, M.T., An Experimental and Analytical Investigation into the Nonlinear Constitutive Equation of Cortical Bone, Ph.D. dissertation, Department of Mechanical and Aerospace Engineering, Case Western Reserve University, Cleveland, OH, 1989.
19. Fondrk, M. T., Bahniuk, E. H., and Davy, D. T., A damage model for nonlinear tensile behavior of cortical bone, *J. Biomech. Eng.,* 121, 533, 1999.
20. Bonfield, W. and O'Connor, P. O., Anelastic deformation and the friction stress of bone, *J. Mater. Sci.,* 13, 202, 1978.
21. Burstein, A. H., Reilly, D. T., and Frankel, V. H., Failure characteristics of bone and bone tissue, in *Perspectives in Biomedical Engineering,* Kenedi, R. M., Ed., Macmillan, London, 1973.
22. Zysset, P. K., A Constitutive Law for Trabecular Bone, Ph.D. thesis, Ecole Polytechnique Federale de Lausanne, 1994.
23. Zyssett, P. K. and Curnier, A., A 3D damage model for trabecular bone based on fabric tensors, *J. Biomech.,* 29, 1549, 1996.

24. Carter, D. R. and Caler, W. E., Cycle-dependent and time-dependent bone fracture with repeated loading, *J. Biomech. Eng.,* 105, 166, 1983.
25. Carter, D. R. and Caler, W. E., A cumulative damage model for bone fracture, *J. Orthop. Res.,* 3, 84, 1985.
26. Caler, W. E. and Carter, D. R., Bone creep-fatigue damage accumulation, *J. Biomech.,* 22, 625, 1989.
27. Ellyn, F., *Fatigue Damage, Crack Growth and Life Prediction,* Chapman and Hall, London, 1997.
28. Currey, J. D., Strain rate and mineral content in fracture models of bone, *J. Orthop Res.,* 6, 32, 1988.
29. Mauch, M., Currey, J. D., and Sedman, A. J., Creep fracture in bones with different stiffnesses, *J. Biomech.,* 25, 11, 1992.
30. Pattin, C. A., Caler, W. E., and Carter, D. R., Cyclic mechanical property degradation during fatigue loading of cortical bone, *J. Biomech.,* 29, 69, 1996.
31. Zioupos, P., Wang, X.T., and Currey, J. D., Experimental and theoretical quantification of the development of damage in fatigue tests of bone and antler, *J. Biomech.,* 29, 989, 1996.
32. Zioupos, P. and Casinos, A., Cumulative damage and the response of human bone in two-step loading fatigue, *J. Biomech.,* 31, 825, 1998.
33. Griffin, L. V., Gibeling, J. C., Martin, R. B., Gibson, V. A., and Stover, S. M., Model of flexural fatigue damage accumulation for cortical bone, *J. Orthop. Res.,* 15, 607, 1997.
34. Pidaparti, R. M. and Liu, Y., Bone stiffness changes due to microdamage under different loadings, *Bio-Med. Mater. Eng.,* 7, 193, 1997.
35. Valliappan, S., Murti, V., and Wohua, Z., Finite element analysis of anisotropic damage mechanics problems, *Eng. Fract. Mech.,* 35, 1061, 1990.
36. Guo, X. E., McMahon, T. A., Keaveny, T. M., Hayes, W. C., and Gibson, L. J., Finite element modeling of damage accumulation in trabecular bone under cyclic loading, *J. Biomech.,* 27, 145, 1994.
37. Zysset, P. and Curnier, A., An implicit projection algorithm for simultaneous flow of plasticity and damage in standard generalized materials, *Int. J. Numer. Methods Eng.,* 39, 3065, 1996.
38. Fondrk, M., Bahniuk, E. B., and Davy, D. T., Crack density versus crack size predictions for cortical bone using a penny-shaped crack model, *Proc. 1997 ASME Bioengr. Conf.,* June 11–15, Sun River, OR, 1997.
39. Laws, N. and Brockenbrough, J. R., The effect of micro-crack systems on the loss of stiffness of brittle solids, *Int. J. Solids Struct.* 23, 1247, 1987.
40. Courtney, A. C., Hayes, W. C., and Gibson, L. J., Age-related differences in post-yield damage in human cortical bone. Experiment and model, *J. Biomech.,* 29, 1463, 1996.
41. Martin, B., A theory of fatigue damage accumulation and repair in cortical bone, *J. Orthop. Res.,* 10, 818, 1992.
42. Martin, B., Mathematical model for repair of fatigue damage and stress fracture in osteonal bone, *J. Orthop. Res.,* 13, 309, 1995.
43. Prendergast, P. J. and Taylor, D., Prediction of bone adaptation using damage accumulation, *J. Biomech.,* 27, 1067, 1994.
44. McNamara, B. P., Taylor, D., and Prendergast, P. J., Computer prediction of adaptive bone remodelling around noncemented femoral prostheses: the relationship between damage-based and strain-based algorithms, *Med. Eng. Phys.,* 19, 454, 1997.
45. Levenston, M. E. and Carter, D. R., An energy dissipation-based model for damage-stimulated bone adaptation, *J. Biomech.,* 31, 579, 1998.
46. Prendergast, P. J. and Huiskes, R., Microdamage and osteocyte-lacuna strain in bone: a microstructural finite element analysis, *J. Biomech. Eng.,* 118, 240, 1996.
47. Taylor, D., Bone maintenance and remodeling: a control system based on fatigue damage, *J. Orthop. Res.,* 15, 601, 1997.
48. Wilson, J., Simple Predictors for Tensile Failure for Human Cortical Bone, M.S. thesis, Department of Mechanical and Aerospace Engineering, Case Western Reserve University, Cleveland, OH, 1998.
49. Bensusan, J., Jepsen, K., and Davy, D., Unpublished data, Department of Mechanical and Aerospace Engineering, Case Western Reserve University, Cleveland, OH, 1999.

19

Ontogenetic Changes in Compact Bone Material Properties

John D. Currey
University of York

19.1 Introduction

The aim of this chapter is to show how the properties of bone material in a single individual are not fixed, but change during life. The first section deals with the development of bone, and the second with mechanical changes occurring at different stages in life. The third considers whether the changes occurring up to maturity are adaptive, the fourth considers possible causes for the decline in mechanical properties associated with aging, and the last section discusses the covariation of material properties and whole bone architecture that results in a mechanically effective bone.

Bones change in many ways during life. They grow, of course, in size. They also, however, change in their material properties, and these changes may interact in complex ways.[1,2] The bone material of a young child is very different in its mechanical properties from those of a young adult, yet at all intermediate times the bone must remain functional. As people grow old, their bone continues to change, usually for the worse, and these changes are of concern to the clinician and of interest to people trying to understand the mechanical properties of bone.

19.1.1 The Development of Primary Bone

An understanding of the development of bone is needed to make sense of the changes in mechanical properties it undergoes. The development of a bone is complex. This is particularly so at the epiphyses, where it is growing in length, and the bone is preformed in cartilage. Away from the epiphyses, most compact bone grows by accretion on preexisting bony surfaces, and development is relatively simpler. If the bone is growing very slowly, the bone lining cells simply lay down osteoid beneath themselves, and this is then mineralized. Blood vessels are periodically left in the bone, to supply the needs of the

0-8493-9117-2/01/$0.00+$.50

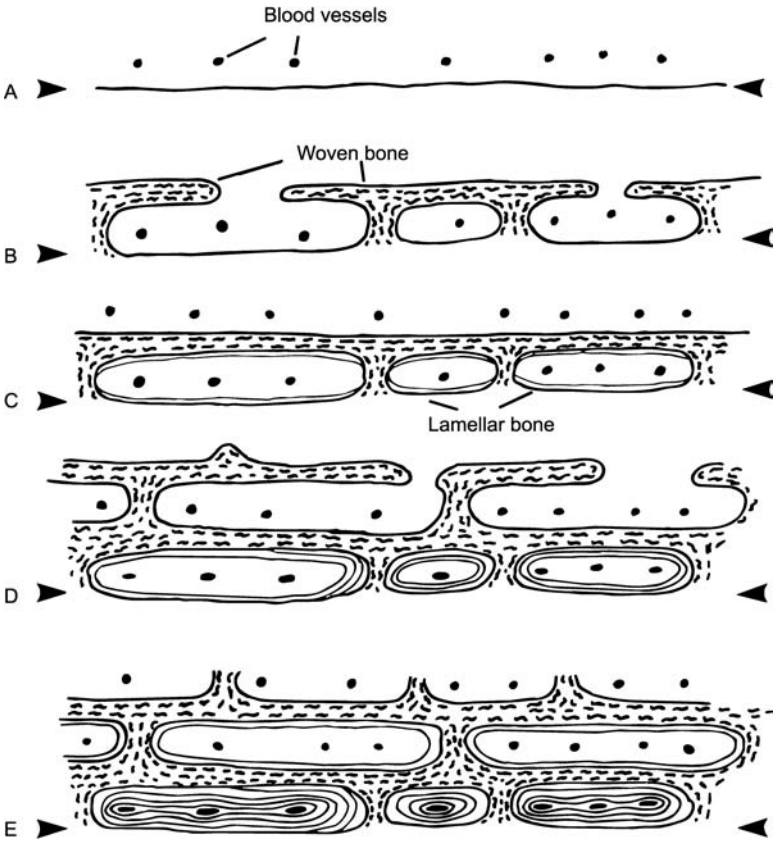

FIGURE 19.1 The formation of fibrolamellar bone. These are cross sections of the outer surface of a rapidly growing bone. The arrowheads show the position of the original surface. Blood vessels are shown by black blobs. (A) The initial situation. (B) Woven bone, shown by squiggly lines, grows very quickly to form a scaffolding clear of the original surface. (C) Lamellar bone, shown by fine lines, starts to fill in the cavities. (D) As more lamellar bone is laid down, so is another scaffolding of woven bone. (E) By the time the first row of cavities is filled, the outer surface of the bone is far away.

osteocytes, which also remain entombed. The resulting bone is lamellar bone and has good mechanical properties. However, there is a difficulty with this process, and that is that there is an absolute rate at which bone can be laid down in this way. It seems to be about 1 μm/day at most. Many bones need to grow faster than this. Woven bone can be laid down considerably faster. However, although there is little direct evidence for this, woven bone is almost certainly inferior to lamellar bone in its mechanical properties.

The difficulty is overcome by the development of an extremely characteristic type of bone called plexiform, laminar, or fibrolamellar bone.[3–6] If a bone has to grow radially faster than lamellar bone can be laid down, woven bone must be laid down instead. The undesirable mechanical results of having a bone made from woven bone are partially obviated by the production of fibrolamellar bone. Essentially a series of laminae are produced. In each one an insubstantial scaffolding of woven bone is laid down quickly to be filled in more leisurely with lamellar bone (Fig. 19.1). In bovine bone, each lamina is about 200 μm thick. In the middle there is a two-dimensional network of anastomosing blood vessels sandwiched between layers of lamellar bone. On each side of this layer is a layer of woven bone, which is more heavily mineralized than the lamellar bone (Fig. 19.2). This description is of particularly neatly arranged fibrolamellar bone. Frequently the blood channels are more irregularly disposed or do not form a network, and the laminar arrangement gives way to one in which the blood vessels anastomose in three dimensions, rather than two, and each is surrounded by more or less concentric layers of lamellar bone. This produces an appearance like that of secondary osteons, and the structures around the blood

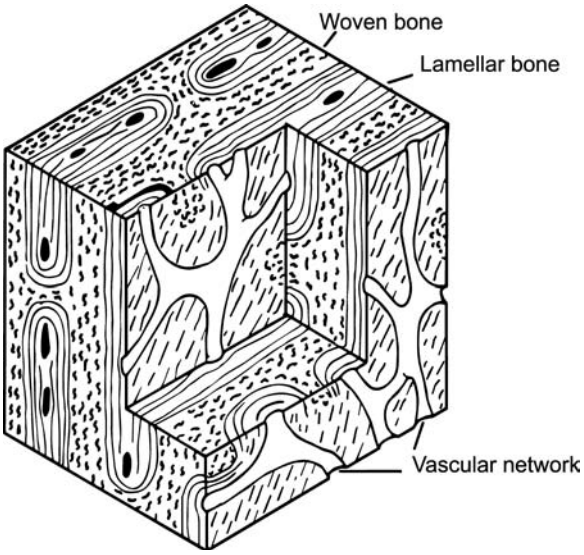

FIGURE 19.2 Block diagram of fibrolamellar bone. Conventions concerning histological type as in Fig. 19.1. Two-dimensional networks of blood channels, sheathed by lamellar bone, alternate with layers of woven bone. The longitudinal axis of the bone is up and down the page; endosteal to periosteal is southeast to northwest.

vessels are called "primary" osteons. However, there is a most important difference between primary osteons and secondary osteons (often called Haversian systems): secondary osteons are *secondary*, that is, they replace bone that has existed previously. The distinction between the two types of osteon is not mere semantic hair-splitting, because differences between primary osteonal bone and Haversian bone correlate with differences in mechanical behavior; usually Haversian bone is weaker than primary osteonal bone and fibrolamellar bone.[7–10]

The kind of primary bone laid down depends on the rate of accretion. In humans and many other mammals, the bone that is laid down in the fetus is mainly woven, and in the young child fibrolamellar bone predominates; then as the rate of growth slows circumferential lamellae appear, and then Haversian remodeling takes over.[11] Such changes could, perhaps, merely be indicating a maturation of the skeleton, and not be related to rate of growth. However Castanet et al.[12] related the changes in the histology of bones of the mallard duck *Anas platyrhyncos* to the rate of accretion, which the authors determined by periodic labeling with a fluorescent dye. Different bones grew at different rates, and they were able to see the different kinds of histology being laid down at the same time, so the differences they found were not aging or maturation effects.[12] The humerus was the fastest-growing bone, and initially, at 7 weeks of age, had a rate of accretion of about 25 μm/day and the bone was completely fibrolamellar. As the rate of accretion diminished, the fibrolamellar bone gave way to anatomizing primary osteons, and finally, when the accretion rate was only about 1 μm/day, the blood vessels were sparse, all parallel to the long axis of the bone, and the bone was completely lamellar. The phalanges, on the other hand, which had a much lower accretion rate right from the start, never showed any sign of fibrolamellar histology.

Stover et al.[6] showed that in bone that grows very fast radially, such as in the young foal, the outer sheet of woven bone may initially be connected to the rest of the bone by bony struts so sparsely, if at all, that they are effectively lying lie free in the periosteum.[6] The outer sheet becomes connected to the rest of the bone only when mineralization is well under way. This process, which they call "saltatory primary osteonal bone formation," allows growth to be even more rapid than the process described above. Indeed, Stover (personal communication) states that, very occasionally, two layers of free-floating bone can be seen. However, this is obviously a somewhat risky process, because a blow to the periosteum would cause the relative positions of the outer sheet and the main bone to become deranged.

19.1.2 Mineralization

Younger human bone is less well mineralized than mature bone. This has been confirmed by a number of studies in humans, e.g., References 13 to 15, although surprisingly Bigot et al.[16] did not find such a relationship in horses aged from 1 day to 4 years. There is no clear trend in bone in people aged over about 40.[14,15,17–19] Some of the increase that seems to occur in some studies of older people may be accounted for by the fact that older bones tends to develop regions of hypermineralization, in which patches of very densely mineralized bone form in the midst of more normal bone.[20,21] When averaged over a large volume, such regions may produce the appearance of a *general* increase in mineralization. As well as showing an increase in mineralization during maturation, the crystallinity of the bone changes; the mineral crystals become more perfect with time (Chapter 5 by Boskey).

19.1.3 Remodeling

Once bone has been laid down, the changes that can take place in it are further mineralization, and degradation, such as may be caused by the development of microcracks, and the degradation of the collagen itself.[22,23] Schaffler et al.[24] showed that the number of *in vivo* microcracks present in the cortex of long bones increases exponentially with age. Such microcracking is clearly likely to reduce the strength and stiffness of the bone. If bone is remodeled, things can be altered. Remodeling, resulting in the production of secondary osteons (Haversian systems), can alter the grain of the bone, by altering the predominant direction of the collagen; it can remove microcracks; it can replace dead osteocytes and old collagen and mineral, which may be degraded or otherwise modified, with new cells, collagen, and mineral. Which of these features is particularly important varies from site to site. One of the effects of remodeling is that the age of the bone is not the same as the age of the individual. Furthermore, unlike, for example, the liver, which undergoes a continual renewal of all its cells, so that the liver as a whole is of roughly the same age and considerably younger than the calendar age of the individual, bone will be present in a whole set of roughly equal-aged packets, and some of these packets may be old and be contiguous to packets that have formed in the last few weeks. Once osteoid is laid down and mineralized, bone tissue can be considered to have formed. However, although mineralization initially proceeds very rapidly, it inevitably slows down as the presence of mineral itself impedes the flow of ions though the bone.[25] The resulting small differences in neighboring parts of the tissue might seem unimportant, but are not, because the mechanical properties of bone vary considerably as a function of mineralization over just the range of mineralizations in which the process becomes slow.[13]

Not only may contiguous parts of the bone be of different ages and therefore have different amounts of mineralization, but the same may be true of parts that are contiguous and of almost the same age. The age of the bone at a particular level in a secondary osteon is almost the same to within a few weeks. However, mineralization proceeds from the nearest blood vessel, and as the bone becomes more mineralized, the process becomes slower and slower. This results in a density gradient of mineralization in secondary osteons, with the bone nearer the central canal being more highly mineralized than the bone near the outer limit of the osteon.[26] As a result, there are differences in the mechanical properties within the secondary osteon.[27]

19.2 Changes in Mechanical Properties

It is important to keep clear the distinction between the changes that take place during maturation (in humans from conception to about 30 years of age) and senescence (in humans from about 30 years onward). Both these periods involve important mechanical changes, but only the former can be considered adaptive, in that they probably fit the bone for its particular requirements at different stages of life. Senescent changes show bone at best making the best out of a bad job. Senescent changes are, of course, of great interest to clinicians.

TABLE 19.1 Young's Modulus of the Fetal Femora, Determined from Nanoindentation Hardness

Fetal Age (weeks)	Elastic Modulus (GPa)	
	Inner	Outer
19	13.8	4.2
19	15.9	10.8
26	13.6	10.3
26	15.9	9.2

Note: It is likely that the nanoindentation method produces considerably greater values than more conventional tests.

19.2.1 Fetal Bone

Little is known about fetal bone. McPherson and Kriewall[28,29] show that the bone in the calvaria of the human fetal skull has a Young's modulus of about 4 GPa at birth.[28,29] This value is about one third of the value for femoral cortical bone of a 12-year-old. Fetal calvarial bone is unlike adult calvarial bone in that it does not consist of two layers of compact bone separated by cancellous bone; rather, it is uniform, although somewhat porous. Its very low modulus and very high ultimate strain allow the skull to be molded without cracking as it passes down the birth canal. The father of Tristram Shandy (the hero of one of the most remarkable experimental novels ever written in English) remarks "that the lax and pliable state of the child's head in parturition, the bones of the cranium having no sutures at that time, was such … it so happened in 49 instances out of 50, the said head was compressed and moulded into the shape of an oblong piece of dough, such as a pastry-cook generally rolls up in order to make a pie of."[30] The fetal skull grows very quickly, and so most of the bone in it must be recently formed. One would expect it, therefore, to be rather lightly mineralized and inevitably to have a low Young's modulus. However, Kriewall et al.[31] claim that the mineral content at term is not significantly different from that of an adult. This seems most improbable. Certainly Boskey (Chapter 5) shows clear differences among the fetal skull bones, fetal long bone shafts, and the shafts of calves.

Su et al.[32] examined the femoral bone of human fetuses aged 19 and 26 weeks. This bone is mainly woven bone, with a rather random orientation of the fibrils, with considerable spaces between successive layers. They measured the nanoindentation hardness of the material. Nanoindentation measures the hardness of very small parts of bone, and from this the elastic modulus may be determined. They found considerable variations in the elastic modulus as a function of position in the bone, with the inner, more aged part being the stiffest. The range of values they found for the elastic modulus for four femora is shown in Table 19.1. The higher values for elastic modulus are about those one would expect for adult human bone tested by conventional methods, and are surprisingly high. However, Dr. Wang (personal communication) writes that mature human ulnar cortical bone, tested in the same way, had values of Young's modulus varying between 26 and 30 GPa. This is very high compared with most values for mature bone in the literature, and suggests that the nanoindentation methods produces values systematically higher than other methods. If so, these results taken together indicate that the elastic modulus of fetal bone is low, about one half to one eighth that of mature cortical bone.

19.2.2 Maturation and Aging

Currey and Butler[33] investigated various bending properties of femoral specimens of humans aged from 2 to 48 years. They tested the modulus of elasticity, the bending strength, the work under the load–deformation curve, and the deflection of the specimen before fracture (all specimens had virtually the same dimensions). The results are shown in Fig. 19.3a to d. The modulus of elasticity increases markedly with age, particularly in the earliest years The bending strength increases slowly. On the other hand, the deflection at break and the work under the curve decrease with age. The changes are caused mainly by

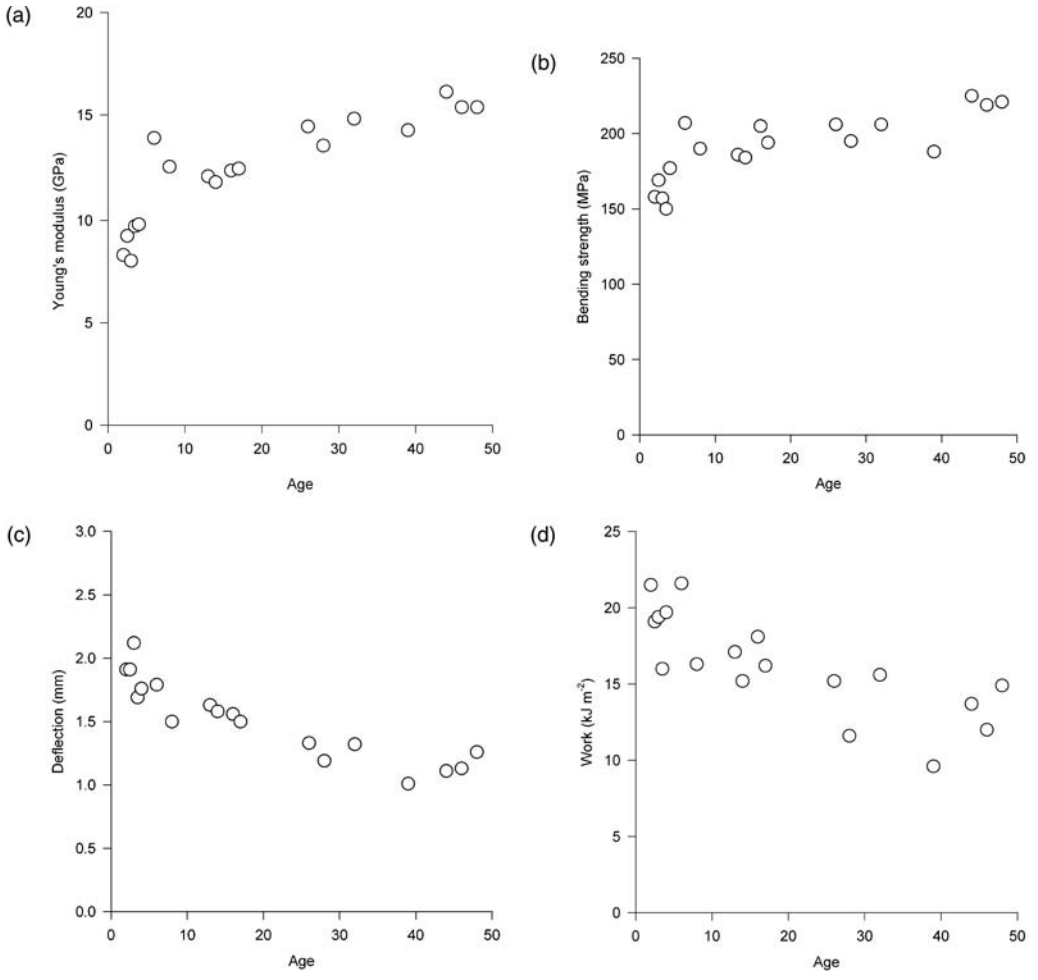

FIGURE 19.3 Bending properties of specimens taken from the femora of 18 people aged from 2 to 48. Each circle represents the femur from one person, and is the mean of from 4 to 10 specimens. (From Currey, J. D. and Butler, G., *J. Bone Joint Surg.,* 57-A, 810, 1975. With permission.)

changes in the mineralization of the bone: greater mineralization leads to reduced energy absorption but to an increase in other values. Similar mechanical findings have been made for the cannon bones of horses.[16]

A large study by McCalden et al.[18] on human femoral tensile specimens gave information over an age range from 20 to 95 (Table 19.2).

1. Tensile strength declined from about 120 MPa at age 20 to 65 MPa at age 95.
2. Ultimate tensile strain declined from about 3.5% at age 20 to about 1% at age 95.
3. Young's modulus in the longitudinal direction ranged overall from about 11 to 20 GPa, but did not vary significantly with age.

A similar study by Burstein et al.[34] on the femur and tibia showed similar but less marked changes (Table 19.2).

Currey[19] tested the impact energy absorption of human femoral specimens from subjects aged from 2 to 96 (Fig. 19.4). There was a steady decline in the energy absorbed. The porosity of the bone, which is highest at the two ends of the life span, is not dangerous in the young bone, but seems to exacerbate the decline in material properties that occurs with age.

TABLE 19.2 Mechanical Properties as a Function of Age[18,34]

Bone	Age Range	Strength (MPa)		Ultimate Strain	Young's Modulus (GPa)	
		Tensile	Compressive	Tensile	Tensile	Compressive
Femur[34]	20–29	140	209	0.034	17.0	18.1
Femur[34]	70–79	129	190	0.025	16.3	18.0
Tibia[34]	20–29	161	213[a]	0.040	18.9	35.3[a]
Tibia[34]	70–79	145	183	0.027	19.9	26.7
Femur[18]	20	120	—	0.035	11–20: not age related	
Femur[18]	95	65	—	0.010		

[a]Age range 30 to 39. (Note the tibia has many values considerably higher than in the femur. In particular, one Young's modulus value is very high.)

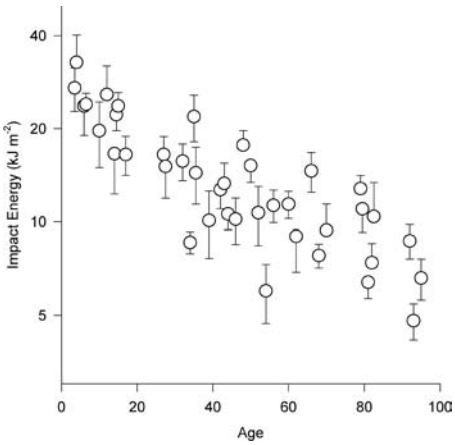

FIGURE 19.4 Impact energy absorption of human bone as a function of age. The error bars are standard errors. (From Currey et al., *J. Biomech.,* 29, 257, 1996. With permission.)

Currey et al.[14] also found that the work of fracture (which is a static test) and impact energy absorption declined with age, and altered *pari passu*, showing that both static and dynamic loading produced the same kind of results (Fig. 19.5).

Zioupos and Currey[35] examined a number of mechanical properties, including fracture mechanics properties, of three specimens from each of ten femora from subjects aged 35 to 92. They demineralized the mechanical specimens and determined two properties of the collagen (shrinkage temperature and force exerted during shrinkage), which are indications of the stability of the collagen. There was a significant decline in all the properties, with the greatest decline being in the work of fracture, which declined by about 9% per decade (Table 19.3).

Wang et al.[36] investigating baboons, found no change in strength or stiffness with age but, like Zioupos and Currey, found a decrease in fracture toughness. Torzilli et al.,[37] on the other hand, compared immature (16 weeks) with adult (~120 weeks) dog specimens in tension and compression. They found no decrease in ultimate strain, but roughly a doubling in elastic modulus and ultimate stress.

Taking all these results together, the consensus seems to be that, compared with juvenile bone, mature human bone is stiffer, stronger in bending, but less tough. Compared with mature individuals' bone, older human bone material has roughly the same stiffness, a somewhat reduced tensile strength, a considerably reduced final strain before it breaks, and a considerably reduced impact strength. Other fracture mechanics properties (which are measures of toughness) are also reduced with age. In short, older bone material is more *brittle* than younger bone material. (The same is sometimes true of other animals' bone, but there is less information about senile changes.) In general, the mechanical properties

TABLE 19.3 Least Squares Linear Regression for Various Variables as a Function of Age in the Equation: Variable $= a + b \times$ Age (with the variance ratios $F_{1,8}$ and the P value for the slope)

Variable	a	b	F	P	At 35 Years of Age	Decline per Decade, %
E(GPa)	16.4	−0.035	7.27	0.027	15.2	2.3
s_f (MPa)	191	−0.625	11.2	0.010	170	3.7
K_c (MPa m$^{1/2}$)	7.33	−0.026	19.09	0.002	6.42	4.1
J (kJ m^{-2})	1.34	−0.004	5.35	0.049	1.20	3.0
W_f (kJ m^{-2})	4.42	−0.030	10.31	0.012	3.37	8.7
$T_{s\text{-}up}$ (°C)	57.5	−0.053	5.27	0.050	55.6	1
${}_nRF_{max}$ (N s^{-1} mm^{-3})	2.26	−0.016	12.4	0.008	1.7	9.4

The value of each property at 35 years of age and its decline (%) per decade of later life is also shown. E: Young's modulus of elasticity; s_f: tensile strength; K_c: stress intensity factor; J: J integral; W_f: work of fracture; $T_{s\text{-}up}$: temperature at which the bone collagen starts to shrink; ${}_nRF_{max}$: force of contraction.[22,35]

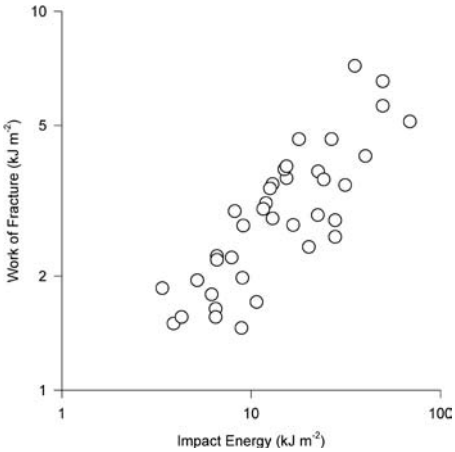

FIGURE 19.5 Relationship between impact energy and work of fracture in paired specimens from human femora. Note the log scales.

of bone seem to a large extent to be determined by its mineralization. Some properties, like Young's modulus, are also very sensitive to the porosity of the bone. Fig. 19.6, drawn from specimens of many species, rather than of different age, shows this in a three-dimensional diagram.

That young human bone is less brittle is shown clearly by the tendency of children to undergo greenstick fractures, and not to suffer fractures that break the bone cleanly across. Youths and young adults may occasionally suffer a traumatic bowing of limbs, leaving the bone permanently bowed (until remodeling straightens it.)[38,39] The material of these bones has in places been loaded well into the post-"yield" region, but the bone does not fracture. It would be extremely difficult to produce such a permanent bowing in the well-mineralized long bone of a 30-year-old.

19.2.3 Pregnancy and Lactation

Many things can affect the mechanical properties of bone during life, for example, physical exercise and endocrine disorders. For space reasons these will not be discussed here, but a life-history event that potentially can affect half the readers of this chapter must be dealt with. Little is known about the effects of pregnancy and lactation on the mechanical properties of bone, and what little knowledge there is comes almost entirely from animal, as opposed to human, experiments. Currey[40] showed that in rats the femora were stronger at the end of pregnancy than those of virgins of the same age. During lactation, the femora became weaker, and at the end of lactation the femora had about the same strength as those of virgins of

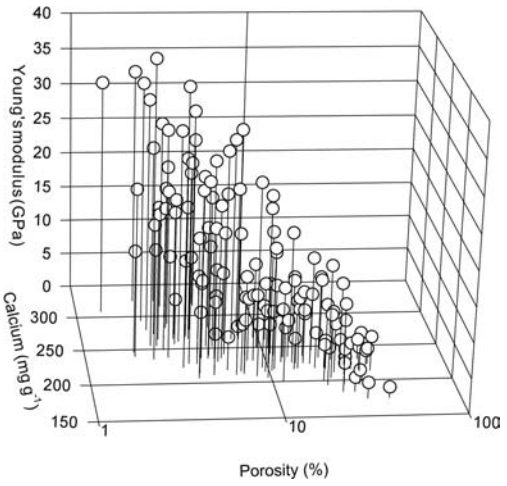

FIGURE 19.6 Three-dimensional diagram showing how the Young's modulus of bone is a function of both mineral content and porosity. Because porosity and mineral content are themselves related, it is difficult to separate the effects by eye, although the separate effects are clear statistically. (Values derived from data used by Currey.[13])

the same age. It is as if the bones became stronger in anticipation of the metabolic stresses that would be put upon them by lactation. However, a simpler explanation is that the bones of the pregnant rat were simply responding adaptively to the increased mass of the expectant mother, and when she became lighter after parturition, the bones lost mass and, therefore, became weaker. Similar findings were made by Ott et al.[41] in a huge study in macaques. Unfortunately, these two studies refer to whole bones, and not to bone material properties. However, Leopold et al.[42] found that in the growing rat (it is difficult to interest skeletally mature rats in sex!) the torsional mechanical properties of whole femora were little changed throughout pregnancy, but that in the later stages the material properties declined; however, this was made up for by growth in cross-sectional area, in particular the cortical thickness increased. Hawkins and Stover[43] found little effect of pregnancy and parturition on the mechanical properties of the bone material of cannon bones of horses.

19.3 Are Youthful Changes Adaptive?

The fact that the bones vary, apparently often adaptively, in their mechanical properties might simply be due to luck. It is useful to consider whether this is the case. For example, a possible explanation of the reduction of impact strength with age is that the higher impact strength of the young bones is merely a correlate of their necessarily lower mineralization. Bone takes time to become fully mineralized. Natural selection produces a bone with a particular stiffness, and this requires some particular amount of mineralization. The immature bone is on its way to the fully mineralized state and meanwhile happens, fortuitously, to be stronger in impact than adult bone material.

On the other hand, it may be that bone at each age is well adapted. In prehistory, efficiency in locomotion would have been of great importance. For this, high stiffness would be the feature most highly selected. It is the *prime* necessity of bone to be stiff; the stiffer the bone material, the lighter the bones can be and still allow efficient locomotion. It is possible to estimate the optimum stiffness for bones, so that the mass of bone and muscle is minimized.[44] The stiffness of whole bones turns out to be about right to minimize the total mass. Bone is capable of having a wide range of values of mineralization. The whale's tympanic bulla achieves in a year a mineralization that the femur of humans never achieves. It would be *possible*, therefore, for the femur to be stiffer than it actually is by increasing its mineralization. The fact that the stiffness is not greater must mean that the tendency to increased mineralization is balanced by some disadvantage. Since the resistance to impact decreases with increasing mineralization, it is probable that this is the counterbalancing disadvantage.

Children are acted on by different pressures from those of their parents. They do not trot for miles and miles after wounded prey nor, when really young, walk for miles and miles collecting berries or fetching water. For children, locomotory efficiency is not very important. On the other hand, they are extremely exploratory and tend to fall a lot. For children, bones that do not break easily are of great selective importance. The mechanical properties of their bones fit very well with their requirements. Although they are not very stiff, they are remarkably resistant to impact. When children's bones break, they do not break cleanly; often the crack runs out of energy, and a greenstick fracture results which, even in societies devoid of orthopedic surgeons, may heal pretty well.

This explanation of the ontogeny of the mechanical properties of bone seems reasonable, but it is hardly conclusive. However, it is possible to perform a natural experiment, by looking at bones that have a different set of selective pressures during life. Unlike humans, ungulates such as sheep and deer must be able to stand very shortly after birth, and run within a few hours or so. Therefore, one would expect the time during which the bones are compliant to be very short. An example is given here. The mechanical properties of a full-term fetus of an *Axis* deer, and its mother were investigated (Fig. 19.7a to d).[45] The

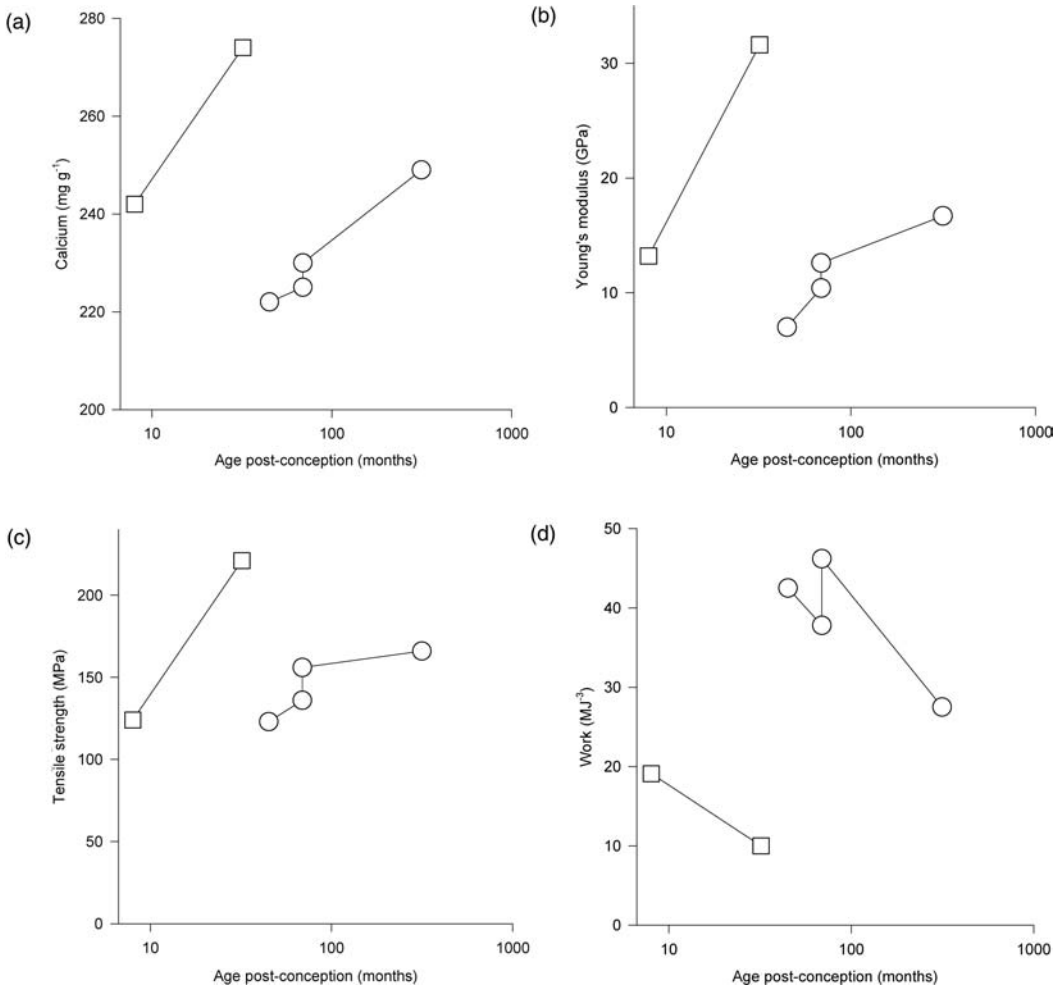

FIGURE 19.7 The relationship between three mechanical properties, measured in tension, and mineral content, with age in *Axis* deer and humans. The age scale is logged for convenience, and not to conform to any hypothetical model. The points for each species are joined, again for convenience. Squares: *Axis* deer; circles: human. Work: work under the tensile stress–strain curve.

mother had an extremely high Young's modulus (32 GPa) and, correspondingly, the fetus had a Young's modulus that might be found in a 5-year-old human child The mother's bone had a high tensile strength; this and the high Young's modulus were probably caused by the extremely precise orientation of the bone material along the length of the bone, as well as its high mineralization. The energy absorption of the deer's bones was very low, however. The deer, both mother and newborn, have much stiffer bones than humans at comparable ages, but pay for it by having bones that are much less resistant to impact.

19.4 Adaptive Changes in Histology

One of the interesting possibilities associated with maturation is that the histology of the bone tissue may become adapted to the loading situation. This is seen very clearly in the radius of the horse. This has a gentle anterior curvature and, as a result, because it is loaded primarily longitudinally, the curvature interacts with the longitudinal forces to produce bending, so that the anterior cortex is loaded in tension, and the posterior cortex is loaded in compression.[46,47] Riggs et al.[48,49] showed that this difference in loading pattern is associated with differences in histology.

The anterior and posterior cortices initially have a rather longitudinal orientation of the collagen and mineral. The anterior cortex remodels rather little, and such secondary osteons as are formed have a predominantly longitudinal orientation of their constituents. The posterior cortex remodels considerably, and the secondary osteons so formed have a much more transverse orientation of their mineral and collagen.[48] This difference in the arrangement of the tissue was confirmed by Fratzl et al.[50] using small-angle X-ray scattering.

These histological differences in the two cortices are in turn associated with differences in mechanical-properties.[49,51–53] Indeed, the only property in which the highly remodeled posterior cortex is superior is compressive strength (Table 19.4). Only in a case like this, probably quite unusual, in which bone is loaded strongly in only one mode (tension or compression) is it possible to fine-tune the histological structure so as to maximize the appropriate mechanical property.

Nevertheless, it seems unlikely that secondary remodeling usually has this beneficial effect since, as already mentioned, remodeled bone is in general weaker than primary bone. It is more likely that remodeling usually functions to take out microcracks or to replace dead bone.[54,55]

19.5 Causes of Mechanical Decline

In the transition from childhood to maturity a general increase in mineralization is probably important, increasing as it does the stiffness and bending strength, but reducing the toughness.[14] However, senile changes are less associated with an increase in mineral, and other factors are important. There are a number of likely candidates.

TABLE 19.4 Mechanical Properties of the Bone Material from the Anterior and Posterior Cortices of the Equine Radius

	E(GPa)		Strength (MPa)		Impact (kJ m^{-2})	
Cortex Loading in Life	Anterior Tension	Posterior Compression	Anterior Tension	Posterior Compression	Anterior Tension	Posterior Compression
Tension[49]	22.1	15.0	161	105	—	—
Compression[49]	18.6	15.3	185	217	—	—
Bending[53]	20.1	16.2	249	217	—	—
Bending[52]	21.1	15.5	232	203	—	—
Bending[51]	17.9	13.5	201	154	32.6	17.5

E : Young's modulus of elasticity.

TABLE 19.5 Correlation Coefficients between the Different Variables (eight degrees of freedom) for the Same Specimens as Described in Table 19.3.

	Age	E	S_f	K_C	J	W_f	${}_nRF_{\max}$
E	-0.69^{*}						
s_f	-0.76^{**}	0.84^{**}					
		0.67^{*}					
K_C	-0.84^{**}	0.68^{*}	0.78^{**}				
		0.26	*0.38*				
J	-0.63^{*}	0.38	0.22	0.61•			
		−0.10	*−0.53*	*0.18*			
W_f	-0.75^{*}	0.57•	0.76^{**}	0.71^{*}	0.57•		
		0.11	*0.44*	*0.22*	*0.19*		
${}_nRF_{\max}$	-0.78^{**}	0.52	0.51	0.65^{*}	0.86^{**}	0.83^{*}	
		−0.04	*−0.22*	*−0.02*	*0.76**	*0.59*	
$T_{s\text{-}up}$	-0.63^{*}	0.12	0.33	0.56•	0.64^{*}	0.77^{**}	0.72^{*}
		−0.56	*−0.29*	*−0.06*	*0.40*	*0.57*	*0.47*

The levels required for significance are $P = 0.10$, $R = 0.55$; $P = 0.05$, $R = 0.63$; $P = 0.01$, $R = 0.76$. Levels of significance shown thus: • $P < 0.10$; $^{*}P < 0.05$; $^{**}P < 0.01$. The numbers in italics are the partial correlation coefficients for the pairs of variables, once their respective correlations with age have been partialed out. One loses one degree of freedom in doing this, so the significance of the correlations is slightly reduced for any given value of the coefficient ($P = 0.1$, $R = 0.58$; $P = 0.05$, $R = 0.67$; $P = 0.01$, $R = 0.80$). E: Young's modulus of elasticity; S_f: tensile strength; K_c : stress intensity factor; J:J integral; W_f: work of fracture; $T_{s\text{-}up}$: temperature at which the bone collagen starts to shrink; ${}_nRF_{\max}$: force of contraction of the collagen.

Source: Zioupos, P. et al., *Bone,* 17, 521, 1995. With permission.

Change in Collagen: Older bone's collagen shows a change in its shrinkage behavior that indicates that it is less stable, and these changes are associated, in the same specimens, with a decline in toughness properties (Table 19.5).[23]

Microcracking: Older bone develops ever-increasing numbers of microcracks, which do not heal, and is more prone to develop microcracking when loaded into the post-yield region; such changes are likely to have a bad effect on the mechanical properties.[24,56]

Remodeling Defects: As bone gets older, the process of internal remodeling seems to get less efficient, and the bone removed in the early stages of the formation of secondary osteons is not replaced promptly or, sometimes, at all. This leads to an increased porosity of the bone, which is mechanically deleterious.[1] The secondary osteons that do form in old age often have defective structures, such as hypermineralized lamellae and irregular central canals, or are in general poorly mineralized.[58]

Hypermineralization: The isolated regions of hypermineralization that occur in older bone may act as sites for the development of long, dangerous cracks.[20] (Bones such as the periotic, which are naturally very highly mineralized, seem to undergo fatigue fractures with no special trauma at all.[58])

19.6 Ontogenetic Changes and Whole-Bone Behavior

Bones change in two ways during maturation: the mechanical properties of their material changes, and the architectural properties of the whole bone change. One would expect these changes to be linked adaptively in some way. Two examples of such linkage are given here.

19.6.1 Polar Bears

Brear et al.[59] examined the femora of five wild polar bears (*Ursus maritimus*) of known age and weight. The ages ranged from 3 months to 7 years (maturity occurs at about $2^1/_2$ years) and the weight from 9.5 to 400 kg. In the younger animals' bones, the bone material was both weaker and less stiff. These differences correlated well with the lower degree of mineralization of the younger bones. Does this mean that the

TABLE 19.6 Properties of the Femora of Polar Bears[59]

Bear Mass (kg)	Bone Length (mm)	Yield Stress (MPa)	Young's Modulus (GPa)	Bone "strength"	"Shape Change"
9.5	160	63	6.7	3.07	4.9
58	240	88	11.2	1.56	8.9
197	396	107	16.5	1.20	13.4
251	435	123	18.6	1.23	14.3
407	490	129	22.2	1.25	15.4

Mass: mass of the bear. Bone "strength": relative strength of the bone, taking into account the mass of the animal, the length of the bone, the geometry of the bone, and the strength of the bone material. "Shape change": relative change in shape on loading taking into account the mass of the animal, the length of the bone, the geometry of the bone, and the Young's modulus of the bone material.

bones themselves were less strong and stiff? The authors assumed that the characteristic loading on the bone was proportional to the weight of the bear times the length of the bone. The strength ("resistance to yielding") of the bone was assumed to be proportional to the strength of the bone material times the second moment of area divided by the depth of the section, and that the stiffness of the bone would be measured by the relative shape change, that is, the deflection of the end of the bone divided by the length of the bone. Beam theory was used to calculate the deflection. Bones with the same proportional deflection will be bent to the same shape, although, of course, the absolute deflection of the longer bone will be greater.

Table 19.6 shows how the strength and stiffness of the bone material, and also the relative whole-bone strength and shape change, when the size of the bear has been taken into account. Considering that the weights of the bears vary by a factor of 40, and the lengths of the bones by a factor of about 3, producing bending moments that vary by a factor of 130, the range of resistances to yielding (a factor of 2.5) and in the relative shape change (a factor of 3.1) is small. The subadults and adults (the last three) are remarkably similar, with the values for strength virtually identical and the values for shape change varying over a range of only 15%, despite the mass of the heaviest bear being 2.1 times greater than the mass of the lightest, and its femur 23% longer, producing together a bending moment 2.5 times greater.

The implication of these calculations, which, it must be remembered, are based on somewhat simplistic assumptions about loading, is that the architecture of the bones is rather precisely adapted to the loads placed on them *and* to the mechanical properties of the bone material. If the bone material in all the bones had identical mechanical properties, but the shapes were as one had measured them, then the resistance to yielding would have had a range of 5, rather than 2.5, and the shape change would have a range of 10.3, rather than 3.1.

19.6.2 Gulls

A study in Californian gulls by Carrier and Leon[60] shows similar features to the polar bears, but here it was possible to study the different behavior of the leg bones (used almost from hatching) and the wing bones (which only grew much in diameter just before the juvenile started to fly). The bone *tissue* was initially weak in both arms and legs. In the legs this tissue weakness and compliance was compensated for by a relatively large cross-sectional shape. The wing bones grew in length quite steadily, although there was a spurt just before flight. However, they remained quite slender, and therefore very feeble and compliant, until just before flying started, when there was a very large growth spurt in diameter. Bones of both limbs were functional, therefore, when they were needed, but the extra diameter needed to compensate for the feeble tissue was needed only in the legs, but not the wings.

Two general questions arise from this last section: (1) Are these ontogenetic changes genetically determined? (2) Can changes in activity affect mineralization? (Changes in activity can, of course, affect bone architecture; see Chapter 26 of this book.) In the bears and gulls, there is no direct evidence. However, the differences between humans and deer, discussed in Section 19.3, in which apparently adaptive differences in mineralization appear *in utero* strongly argues for there being a strong genetic determinant. There was an old experiment by Woo et al.[61] in which pigs were made to exercise very hard, producing large

changes in architecture in the bones, but no changes in *material* properties, either in mechanical properties or mineralization. Again, this suggests that differences in the amount of mineralization are not affected by loading.

19.7 Conclusions

The aim of this chapter was to show how the properties of bone material in a single individual are not fixed, but change during life. In the fetal stage, the bone is growing extremely fast, and its mechanical properties are probably not very important, although in mammals it is vital that the skull should not be so stiff as to impede the passage of the fetus down the birth canal. During maturation, the properties change markedly, mainly as a result of an increase in mineralization. The stiffness of the bone increases, but, at the same time, the toughness decreases. There are reasons for thinking that these changes are not merely an inevitable result of the time taken for bone to mature, but are adaptive at every stage. Changes from maturity onward are senescent, and should not be considered adaptive, although they are of great interest to clinicians. The causes of the mechanical changes seen are a whole suite of deleterious alterations in the bone material, whose effects at the moment are far from being quantified.

Finally, it must be remembered that it is the whole bone that breaks, or deflects too much, and that therefore it is important to marry the mechanical properties of the bone *material* to the structure of the *whole bone*. There are instructive examples showing how these two features of bones are related to each other in an adaptive way.

References

1. Martin, B., Heaney, R. P., Marotti, G., and Burr, D. B., Aging and strength of bone as a structural material, *Calcif. Tissue Int.,* 53 (Suppl. 1), S34, 1993.
2. Seeman, E., From density to structure: growing up and growing old on the surfaces of bone, *J. Bone Miner. Res.,* 12, 509, 1997.
3. Currey, J. D., Differences in the blood-supply of bone of different histological types, *Q. J. Microsc. Sci.,* 101, 351, 1960.
4. De Ricqlès, A., Recherches paléohistologiques sur les os longs des tétrapodes VII (deuxième partie, fin), *Ann. Paléontol.,* 63, 133, 1977.
5. Francillon-Vieillot, H., De Buffrénil, V., Castanet, J., Géraudie, J., Meunier, F. J., Sire, J. Y., Zylberberg, L., and de Ricqlès, A., Microstructure and mineralization of vertebrate skeletal tissues, in *Skeletal Biomineralization: Patterns, Processes and Evolutionary Trends,* Vol. 1, Carter, J. G., Eds., Van Nostrand Reinhold, New York; 1990, 471.
6. Stover, S. M., Pool, R. R., Martin, R. B., and Morgan, J. P., Histological features of the dorsal cortex of the third metacarpal bone mid-diaphysis during postnatal growth in thoroughbred horses, *J. Anat.,* 181, 455, 1992.
7. Currey, J. D., Differences in the tensile strength of bone of different histological types, *J. Anat.,* 93, 87, 1959.
8. Heřt, J., Kućera, P., Vávra, M., and Voleník, K., Comparison of the mechanical properties of both the primary and Haversian bone tissue, *Acta Anat.,* 61, 412, 1965.
9. Reilly, D. T. and Burstein, A. H., The elastic and ultimate properties of compact bone tissue, *J. Biomech.,* 8, 393, 1975.
10. Vincentelli, R. and Grigorov, M., The effect of Haversian remodeling on the tensile properties of human cortical bone, *J. Biomech.,* 18, 201, 1985.
11. Amprino, R., A contribution to the functional meaning of the substitution of primary by secondary bone tissue, *Acta Anat.,* 5, 291, 1948.
12. Castanet, J., Grandin, A., Abourachid, A., and De Riqlès, A., 1996 Expression de la dynamique de croissance dans la structure de l'os périostique chez *Anas platyrhyncos, C. R. Acad. Sci. Paris Sci. Vie.,* 319, 301, 1996.

13. Currey, J. D., The evolution of the mechanical properties of amniote bone, *J. Biomech.,* 20, 1035, 1987.
14. Currey, J. D., Brear, K., and Zioupos, P., The effects of ageing and changes in mineral content in degrading the toughness of human femora, *J. Biomech.,* 29, 257, 1996.
15. Reid, S. A. and Boyde, A., Changes in the mineral density distribution in human bone with age: image analysis using backscattered electrons in the SEM, *J. Bone Miner. Res.,* 2, 3, 1987.
16. Bigot, G., Bouzidi, A., Rumelhart, C., and Martinrosset, W., Evolution during growth of the mechanical properties of the cortical bone in equine cannon bones, *Med. Eng. Phys.,* 18, 79, 1996.
17. Boyde, A., Jones, S. J., Aerssens, J., and Dequeker, J., Mineral density quantitation of the human cortical iliac crest by backscattered electron image analysis: variations with age, sex and degree of osteoarthritis, *Bone,* 16, 619, 1995.
18. McCalden, R. W., McGeough, J. A., Barker, M. B., and Court-Brown, C. M., Age-related changes in the tensile properties of cortical bone: the relative importance of changes in porosity, mineralization and microstructure, *J. Bone Joint Surg.,* 75-A, 1193, 1993.
19. Currey, J. D., Changes in the impact energy absorption of bone with age, *J. Biomech.,* 12, 459, 1979.
20. Boyce, T. M. and Bloebaum, R. D., Cortical aging differences and fracture implications for the human femoral neck, *Bone,* 14, 769, 1993.
21. Simmons, E. D., Pritzker, K. P. H., and Grynpas, M. D., Age-related changes in the human femoral cortex, *J. Orthop. Res.,* 9, 55, 1991.
22. Danielsen, C. C., Mosekilde. Li., Bollerslev. J., and Mosekilde, Le., Thermal stability of cortical bone collagen in relation to age in normal individuals and in individuals with osteoporosis, *Bone,* 15, 91, 1994.
23. Zioupos, P., Currey, J. D., and Hamer, A. J., The role of collagen in the declining mechanical properties of ageing human cortical bone, *J. Biomed. Mater. Res.,* 45, 108, 1999.
24. Schaffler, M. B., Choi, K., and Milgrom, C., Aging and bone matrix microdamage accumulation in human compact bone, *Bone,* 17, 521, 1995.
25. Wong, F. S. L., Elliott, J. C., Anderson, P., and Davis, G. R., Mineral concentration gradients in rat femoral diaphyses measured by X-ray microtomography, *Calcif. Tissue Int.,* 56, 62, 1995.
26. Courtney, A. C., Crofts, R. D., Boyce, T. M., and Bloebaum, R. D., Aging changes in osteon mineralization in the human femoral neck, *Bone,* 15, 147, 1994.
27. Rho, J. Y., Zioupos, P., Currey, J. D., and Pharr, G. M., Variations in the individual thick lamellar properties within osteons by nanoindentation, *Bone,* 25, 295, 1999.
28. McPherson, G. K. and Kriewall, T. J., The elastic modulus of fetal cranial bone: a first step towards an understanding of the biomechanics of fetal head molding, *J. Biomech.,* 13, 9, 1980.
29. McPherson, G. K. and Kriewall, T. J., Fetal head molding: an investigation utilizing a finite element model of the fetal parietal bone, *J. Biomech.,* 13, 17, 1980.
30. Sterne, L., *The Life and Opinions of Tristram Shandy,* 1767.
31. Kriewall, T. J., McPherson, G. K., and Tsai, A. C., Bending properties and ash content of fetal cranial bone, *J. Biomech.,* 14, 73, 1981.
32. Su, X. W., Feng, Q. L., Cui, F. Z., and Zhu, X. D., Microstructure and micromechanical properties of the mid-diaphyses of human fetal femurs, *Connect. Tissue Res.,* 36, 271, 1997.
33. Currey, J. D. and Butler, G., The mechanical properties of bone tissue in children, *J. Bone Joint Surg.,* 57-A, 810, 1975.
34. Burstein, A. H., Reilly, D. T., and Martens, M., 1976 Aging of bone tissue: mechanical properties, *J. Bone Joint Surg.,* 58-A, 82, 1976.
35. Zioupos, P. and Currey, J. D., Changes in the stiffness, strength and toughness of human cortical bone with age, *Bone,* 22, 57, 1998.
36. Wang, X. D., Masilamani, N. S., Mabrey, J. D., Alder, M. E., and Agrawal, C. M., Changes in the fracture toughness of bone may not be reflected in its mineral density, porosity, and tensile properties, *Bone,* 23, 67, 1998.
37. Torzilli, P. A., Takebe, K., Burstein, A. H., Zika, J. M., and Heiple, K. G., The material properties of immature bone, *J. Biomech. Eng. (Trans. ASME),* 104, 12, 1982.

38. Borden IV, S., Traumatic bowing of the forearm in children, *J. Bone Joint Surg,* 56–A, 611, 1974.
39. Reisch, R. B., Traumatic bowing deformity of the radius and ulna in a skeletally mature adult, *J. Orthop. Res.,* 8, 258, 1994.
40. Currey, J. D., Interactions between age, pregnancy and lactation, and some mechanical properties of the femora of rats, *Calcif. Tissue Res.,* 13, 99, 1973.
41. Ott, S. M., Lipkin, E. W., and Newell Morris, L., Bone physiology during pregnancy and lactation in young macaques, *J. Bone Miner. Res.,* 14, 1779, 1999.
42. Leopold, S. S., Boskey, A. L., Doty, S. B., Gertner, J. M., Peterson, M. G. E., and Torzilli, P. A., Diminished material properties and altered bones structure in rats' femora during pregnancy, *J. Orthop. Res.,* 13, 41, 1995.
43. Hawkins, D. L. and Stover, S. M., Pregnancy-associated changes in the material properties of the third metacarpal cortical bone in mares, *Am. J. Vet. Res.,* 58, 182, 1997.
44. Alexander, R. McN., Ker, R. F., and Bennett, M. B., Optimum stiffness for leg bones, *J. Zool.* (London), 222, 471, 1990.
45. Currey, J. D. and Pond, C. M., Mechanical properties of very young bone in the axis deer (*Axis axis*) and humans, *J. Zool.* (London), 218, 59, 1989.
46. Rubin, C. T. and Lanyon, L. E., Limb mechanics as a function of speed and gait: a study of functional strains in the radius and tibia of horse and dog, *J. Exp. Biol.,* 101, 187, 1982.
47. Biewener, A. A., Thomason, J., Goodship, A. E., and Lanyon, L. E., Bone stress in the horse forelimb during locomotion at different gaits: a comparison of two experimental methods, *J. Biomech.,* 16, 565, 1983.
48. Riggs, C. M., Lanyon, L. E., and Boyde, A., Functional associations between collagen fibre orientation and locomotor strain direction in cortical bone of the equine radius, *Anat. Embryol.,* 187, 231, 1993.
49. Riggs, C. M., Vaughan, L. C., Evans, G. P., Lanyon, L. E., and Boyde, A., Mechanical implications of collagen fibre orientation in cortical bone of the equine radius, *Anat. Embryol.,* 187, 239, 1993.
50. Fratzl, P., Schreiber, S., and Boyde, A., Characterization of bone mineral crystals in horse radius by small angle X-ray scattering, *Calcif. Tissue Int.,* 58, 341, 1996.
51. Batson, E. L., Reilly, G. C., Currey, J. D., and Balderson, D. S., Post-exercise and positional variation in mechanical properties of the radius in young horses, *Equine Vet. J.,* (in press).
52. Reilly, G. C. and Currey, J. D., The development of microcracking and failure in bone depends on the loading mode to which it is adapted, *J. Exp. Biol.,* 202, 543, 1999.
53. Schryver, H. F., Bending properties of cortical bone of the horse, *Am. J. Vet. Res.,* 39, 25, 1978.
54. Mori, S. and Burr, D. B., Increased intracortical remodeling following fatigue damage, *Bone,* 14, 103, 1993.
55. Qiu, S.-J., Boyce, T. M., and Schaffler, M. B., Osteocyte loss and microdamage in aging human compact bone, *43rd Meeting, Orthopaedic Research Society,* San Francisco. 1997, 88.
56. Courtney, A. C., Hayes, W. C., and Gibson, L. J., Age-related differences in post-yield damage in human cortical bone, experiment and model, *J. Biomech.,* 29, 1463, 1996.
57. Nyssen-Behets, C., Duchesne, P.-Y., and Dhem, A., Structural changes with aging in cortical bone of the human tibia, *Gerontology,* 43, 316, 1997.
58. Sørensen, M. S., Bretlau, P., and Jørgensen, M. B., Fatigue microdamage in perilabyrinthine bone, *Acta Otolaryngol.* (Stockholm), Suppl., 496, 20, 1992.
59. Brear, K., Currey, J. D., and Pond, C. M., Ontogenetic changes in the mechanical properties of the femur of the polar bear *Ursus maritimus, J. Zool.* (London), 222, 49, 1990.
60. Carrier, D. and Leon, L. R., Skeletal growth and function in the California gull (*Larus californicus*), *J. Zool.* (London), 222, 375, 1990.
61. Woo, S. L.-Y., Kuei, S. C., Amiel, D., Gomez, M. A., Hayes, W. C., White, F. C., and Akeson, W. H., The effect of prolonged physical training on the properties of long bone: a study of Wolff's law, *J. Bone Joint Surg.,* 63-A, 780, 1981.

20

Mechanical Effects of Postmortem Changes, Preservation, and Allograft Bone Treatments

R. Bruce Martin
University of California at Davis Medical Center

Neil A. Sharkey
The Pennsylvania State University

20.1 Introduction

A topic of fundamental importance in bone mechanics is how accurately the mechanical properties of bone, measured in some postmortem, *ex vivo* state, represent bone tissue as it exists in the living body. The central questions here are (1) How do the mechanical properties of bone tissue change when its cells die and/or it is removed from the body? (2) How do various means of preserving bone tissue against postmortem changes alter its *in vivo* mechanical properties? These questions are manifest in two broad areas of orthopedic research. First, they are of obvious concern to those experimentalists who wish to understand structure–function relationships in bone, and others who wish to define changes in mechanical properties caused by genetic variability, aging, disease, medical treatments, and so forth. Second, they are of interest to the surgeon in the context of bone allografts. The storing of bone for these purposes raises questions analogous to those encountered by the experimentalist. In addition, treatment of allografts to prevent immune responses or the transmission of infectious organisms may also affect mechanical properties. This chapter reviews a diverse literature concerning these interrelated and important questions.

For the sake of historical perspective the work in each subsection will be reviewed in more or less chronological order. Then a summary of the subsection will be presented with a table that attempts to organize the results according to modifications in treatment variables.

0-8493-9117-2/01/$0.00+$.50

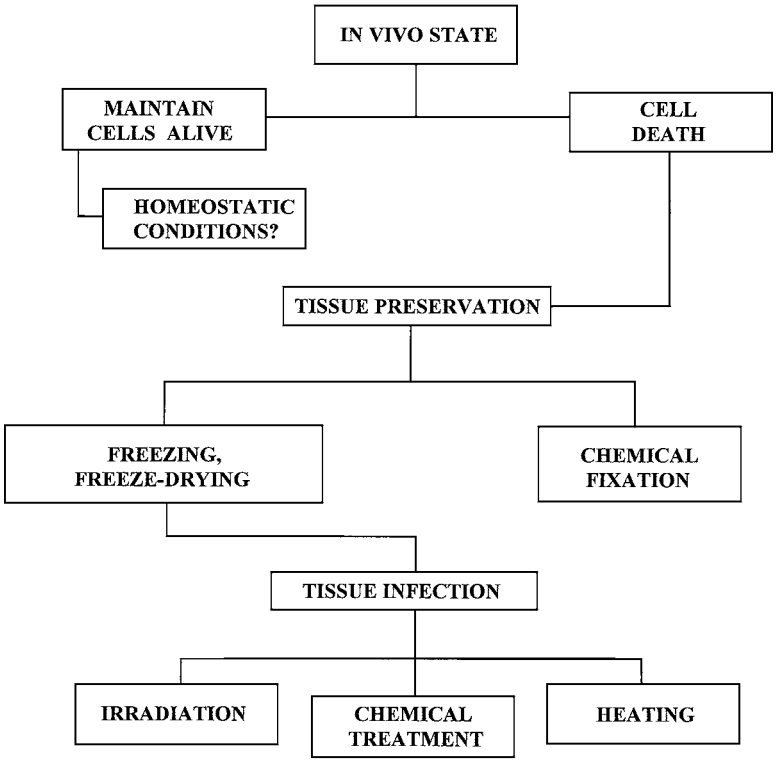

FIGURE 20.1 Flowchart for examining the kinds of postmortem mechanical changes that may occur in bone, and how various means of preserving and treating bone against such changes may introduce their own mechanical effects.

20.2 Postmortem Changes in Mechanical Properties

Suppose that a specimen of bone is removed from a living skeleton for determination of its mechanical properties. What postmortem changes would one expect to occur in these properties, and how would various preservation methods affect these changes? Fig. 20.1 attempts to identify the principal variables in this problem. One possible approach to preventing postmortem changes would be to keep the cells of the specimen alive following its removal from the body so that the tissue does not actually die. Assuming that this could be done, one might still find the mechanical properties of the tissue changing over time because an environment sufficient to keep the cells alive may nevertheless allow the tissue to change. For example, the composition of the culture medium could allow mineral to move out of the bone matrix, or the dissection process might activate remodeling within the specimen that would eventually change its porosity and mechanical properties. Thus, it would not be enough simply to keep the cells of the tissue alive; both the cells and the extracellular matrix must be maintained in a homeostatic condition relative to the *in vivo*, *in situ* state.

Alternatively, if the cells of the specimen are allowed to die, its mechanical properties are almost sure to change over time. Temperature changes and (especially) drying alter the mechanical properties of bone. If the specimen is maintained in a wet state at body temperature, lytic enzymes are likely to be produced, either by introduced bacteria or through autolysis of the cells of the specimen. These enzymes would affect the organic matrix of the bone, and if the aqueous environment were not properly buffered with respect to bone mineral, the mineral matrix would deteriorate as well. There are two basic means of preserving the tissue to prevent these problems: chemical fixation and freezing.

Chemical fixation of tissues usually involves substances that denature the proteins within cells so that lysis is prevented and the structure of the cell is "chemically frozen" in its *in vivo* spatial arrangement. These techniques were developed primarily by histologists to examine cell structures; the problem with their use by biomechanicians is that they may denature the proteins in the extracellular matrix as well, producing changes in mechanical properties. Freezing, on the other hand, prevents lysis by slowing chemical reactions, but questions arise regarding the long-term prevention of lytic changes by temperatures only slightly below freezing, and the physical effects that freezing and thawing may have on the bone tissues.

One may also be concerned about the presence of infectious bacteria or viruses in bone. This is particularly true if the bone is to be used as a graft, but it is also a concern when bones are to be used in laboratory experiments, especially if they are human bones. Chemical fixation methods kill such organisms, but freezing may not. Therefore, methods for sterilizing fresh or frozen bone are needed, and there is an interest in how these methods affect the mechanical properties of the tissue. Radiation of sufficient intensity kills bacteria and viruses, thereby preventing transmission of infectious agents when bones are used as allografts, but radiation may also damage the physical structure of the calcified matrix. Another means of sterilization is heating, and this, too, may alter the mechanical properties of bone.

This section reviews what is known about the postmortem changes in the mechanical properties of bone under varying conditions, including the *in vivo* environment, chemical treatments, freezing, heating, and irradiation.

20.2.1 Postmortem Changes without Preservation

When a specimen is isolated from its blood supply, and no alternative measures are taken to provide for the viability of its cells, the cells will die in a matter of hours. Indeed, cell organelles start to show degenerative changes about 5 min after the blood supply to the tissue is lost.[1] To investigate the immediate effects of cell death on the mechanical properties of bone, Greenberg and co-workers[2] nondestructively loaded intact skulls and tibias within living, anesthetized dogs and again immediately after killing the animal. Structural stiffness changes (1 to 2%) were not significantly affected by death per se in either the skull or the tibia. Although the proportion of the bone cells in these specimens that had died at the time of the postmortem tests may have been small, this experiment supports the common assumption that, in bone, the direct effects of cell death on mechanical properties should be minor because these properties depend primarily on the calcified extracellular matrix.

However, when bone cells are sufficiently deprived of nutrition, they can be expected to die by necrosis (as opposed to apoptosis), which will produce enzymes capable of compromising the physical structure and mechanical properties of the extracellular matrix. Indeed, Black[3,4] argued against the practice of assuming that the initial, irreproducible responses of a tissue to mechanical testing are preconditioning artifacts and should be ignored in favor of subsequent, reproducible responses. The earliest responses may be equally representative of the *in vivo* behavior because the mechanical properties are load-history dependent, or they may be more representative than later results because of postmortem degradation of the tissue by lytic enzymes following cell necrosis.

Another way that cell death could alter the mechanical properties of bone tissue is through changes in mineral content. It is well documented that the mechanical properties of bone are very sensitive to this variable.[5] Gustafson et al.[6] found that storing $4 \times 10 \times 100$ mm equine bone specimens in normal saline at room temperature for 10 days diminished their bending stiffness by 2.4%, and that storing such specimens in saline buffered with $CaCl_2$ prevented such changes. The opposite effect, gain of mineral and stiffness in specimens stored in supersaturated solutions, has apparently not been studied, but artifactual mineral deposits occur in specimens fixed with formaldehyde- or glutaraldehyde-containing phosphate buffers.[7] Frost[8] suggested that bone cells not only participate in the mineralization of new bone matrix, but also maintain the degree of mineralization at an appropriate level thereafter. He hypothesized that, because body fluids are supersaturated relative to the hydroxyapatite mineral of bone,

osteocytes must continuously transport mineral ions out of the bone matrix. This concept arose from the observation that, when the osteocytes in a region of bone die, the surrounding matrix becomes hypercalcified. If this theory is valid and a bone specimen is stored in a similarly supersaturated solution, it is possible that the mineral content of the specimen could increase during storage. It is prudent to keep the possibility of mineral leaching or addition in mind when considering results from experiments where specimens are stored or treated while immersed in fluid.

20.2.2 Changes in a Necrotic Bone that Remains in the Living Organism

In 1962, Stevens and Ray[9] used "living and dead bone" from Long-Evans rats to explore the time course of *in vivo* changes occurring within devitalized bone. In each rat, one tibia was removed, subjected to repeated freezing and thawing to devitalize its tissues, and implanted into the animal's abdomen. In the study, 16 groups of rats were killed at intervals ranging from 1 h to 120 days after this procedure, and the dead and contralateral (control) tibias were immediately removed, cleaned, and mechanically tested in three-point bending. The dead bones tended to lose weight over the course of the experiment (about 10% at 120 days). When strength was defined as breaking load normalized to bone weight, the strengths of the dead and control tibias were comparable in the first month after devitalization. Subsequently, dead bone strength was 79 and 75% of the control value, respectively, at 60 and 120 days. Compared with the bones of the animals killed within 24 h, the control tibias gained strength (16% at 120 days) and the dead tibias lost strength (12% at 120 days). However, none of these changes was statistically significant, and the methods used in this work were crude by today's standards.

20.2.3 Postmortem Changes in Unpreserved, Explanted Bones

Weaver[10] tested the effects of storage in cold saline on the hardness of human cortical bone from the fibula and tibia. The hardness of specimens stored in saline at 4°C for 24 h was 20% less than fresh specimens. Tennyson et al.[11] studied the dynamic response of bovine cortical bone in longitudinal impactive compression at postmortem times up to 38 days. They found that the specimens could be modeled as a Voigt viscoelastic material,

$$\sigma = E\varepsilon + \eta d\varepsilon/dt \tag{20.1}$$

where σ is stress, ε is strain, E is elastic modulus, and η is viscosity. They used strain rates from near zero to 450/s, and stored their specimens in water (not saline) at 1.7 °C. By repeated measurements of the same specimens they found that E was constant at about 21 GPa during the first week, diminished about 33% during the second week, and remained constant thereafter. The viscosity coefficient, on the other hand, seemed to decrease rapidly from about 55 to 20 kPa/s during the first 3 postmortem days and then remain constant, out to the 11-day limit of observation. Thus, substantial postmortem changes were recorded for bone stored in cold water, but the methods did not include a rigorous statistical analysis.

Fitzgerald[12] reported room temperature postmortem changes in the bone dynamic shear compliance over a longer period of time. In studies of two samples of human cancellous bone, tests were initiated within a few hours of procurement and continued at varying intervals for at least 40 h. The specimens were kept in water at 24°C. Both samples displayed a steady decline in the elastic and viscous components of the dynamic shear compliance with time. In both cases, the rate of decline abruptly became much more gradual at 5 h postmortem. This unexplained transition in behavior at 5 h was also present in skeletal muscle and intervertebral disks.

In an experiment designed to keep the cells of the specimen alive, Brown et al.[13] repeatedly measured the postmortem compressive elastic modulus in four human cortical bone specimens (cubes 4 mm on edge) maintained in tissue culture medium at 37°C. The modulus decayed exponentially, asymptotically approaching ~40% of the initial value 96 h postmortem. Extrapolation backward from the initial

measurement, made 2 to 3.5 hours postmortem, suggested that this value was itself 25% less than the original, *in vivo* modulus. Subsequently, Ashman et al.[14] made repeated ultrasonic measurements of the longitudinal elastic modulus in canine cortical bone specimens at multiple postmortem times. In eight specimens maintained in saline at room temperature for 100 postmortem hours, they found that the elastic modulus consistently diminished, but only about 2%. Neither of these studies reported a statistical test of the postmortem effect, but the recorded changes appear significant in both cases. The higher storage temperature of the Brown group could have accelerated enzymatic tissue degradation, but mechanical factors may also have contributed to the discrepancy in results. The Ashman group suggested that repeated testing at relatively large strains in Brown's study produced mechanical damage: test strains were apparently 4000 to 8000 microstrain ($\mu\varepsilon$), substantially exceeding the physiological range of bone (2000 to 3000 $\mu\varepsilon$). In addition, the strain rate was quite low (0.006/s) so that creep may have introduced damage as well. Both creep and fatigue failure times are very sensitive to strain range.[15] This, and the elevated test temperature, could have combined to produce microdamage that added to the effects of tissue degradation in the Brown study. Conversely, postmortem changes during lengthy fatigue experiments at physiological strains presumably degrade mechanical properties concurrently with mechanical damage.

Linde and Sorensen[16] studied short-term postmortem effects at room temperature on the compressive elastic modulus of 74 trabecular samples from the proximal tibial epiphysis of two males with amputated limbs (35 and 61 years of age). Cylinders 6.5 mm in diameter and 6.5 mm long were tested in axial compression to a nondestructive strain (0.45%) within 2.5 h of removal of the limb, and then again after 24 h of storage in saline at room temperature. In each case, specimens were cyclically compressed at a strain rate of 0.01/s until steady state behavior was observed, then elastic modulus, unloading energy, and hysteresis energy were obtained from five consecutive cycles. The samples exhibited a significant 10% decrease in modulus after 24 h of room-temperature storage. In addition, there was a significant decrease in the area under the unloading portion of the stress–strain curve.

The results from these experiments are summarized in Table 20.1. They provide convincing evidence that the elastic modulus and hardness of bone diminish postmortem, even if the specimen is refrigerated in saline. While no studies have established that lytic enzymes are responsible for these changes, they are suspected, even though similar effects could be produced by mineral leaching when bone is kept in water or saline.

TABLE 20.1 Summary of the Effects of Postmortem Changes in the Mechanical Properties of Bone without Freezing or Chemical Preservation

Authors, Year	Storage Environment	Type of Bone	Type Test	Result
Greenberg et al., 1968[2]	Animal death	Dog skull, tibia	Bending, S Bending, S	No change No change
Stevens and Ray, 1962[9]	Necrotic change *in vivo*	Rat tibia	Bending, S	σ − (n.s.)
Brown et al., 1981[13]	**Tissue cult. med., 37°C**	Human cortical	Compression, M	E−
Fitzgerald, 1977[12]	**Water, 24°C**	Human trabecular	Dynamic shear, M	E−
Tennyson et al., 1972[11]	**Water, 1.7°C**	Cow cortical	Dynamic compression, M	E−
Linde and Sorensen, 1993[16]	**Saline, room temp.**	Human trabecular	Compression, M	E−, U+
Gustafson et al., 1995[6]	**Saline, room temp.**	Equine cortical	Bending, M	E−
Ashman et al., 1982[14]	**Saline, room temp.**	Dog femur	Ultrasonic, M	E−
Weaver, 1966[10]	**Saline, 4°C**	Human cortical	Hardness, M	H−

Note: Bold typeface in the storage environment column indicates that a change was seen. S = structural test; σ = failure stress or load; + = increased; − = decreased; n.s. = not significant; M = material test; H = hardness; E = elastic modulus or structural stiffness; U = energy-to-failure.

20.3 The Mechanical Effects of Preserving Bone

If, based on the above few experiments, it is decided that the mechanical properties of bone do suffer postmortem changes unless preserved in some way, the next question is, how can such changes be prevented? Generally speaking, there are only two candidate methods for preserving bone (or other biological tissues) against portmortem degradation: freezing and chemical fixation (including embalming).

20.3.1 Freezing

Freezing would appear to be an attractive means of preventing postmortem changes in the mechanical properties of bone. However, a little thought about this method soon raises concerns. If freezing and thawing introduce mechanical damage in roads, sidewalks, and rocks, could not the same thing happen in bone? As ice crystals form and expand within the bone, could they produce microscopic damage and alter mechanical behavior? Such effects would seem to be dependent on the method and temperature of freezing, and also on sample size. Longitudinal crack formation has been reported in bones frozen quickly.[17] Freezing a mechanical test specimen may also affect the degradation of its cells on thawing. There are complex relationships between rate of cooling, cryoprotective substances (e.g., glycerol), and cell damage. When ice crystals form in the extracellular water first, and then within cells, an osmotic gradient is produced across cell membranes, and the cells become hypertonic and dehydrated. On thawing, damaged cells may lyse more quickly, and this may accelerate enzymatic release and its associated effects on tissue mechanical properties. At certain cooling rates, and with certain cryopreservatives, such effects may in principle be reduced, but specific methods for minimizing lysis of bone cells were not found in the large literature on cryopreservation. In fact, cell death is considered advantageous in bone allografts because it decreases the antigenic load to host tissue by destroying histocompatibility complexes concentrated in cell membranes.

Several studies have examined the effects of freezing on the mechanical properties of bone, partly because freezing is a preferred mode of storage for bone intended for transplantation. Some investigations have measured actual material behavior but many measure structural behavior, which makes interpretation more difficult. Frankel[18] stated that storing specimens at −25°C did not affect structural strength of the proximal femur, but no data were provided. Sedlin[19] tested small beams of human femoral cortical bone in bending within 3 h of removal from the body ($N = 43$) or after freezing at −20°C for 3 to 4 weeks and then warming to 37°C ($N = 31$). Ultimate fiber stress, modulus of elasticity, and energy absorbed to failure were statistically the same in the two groups. Weaver[19] found that the hardness of cortical bone from the human fibula and tibia was unaffected by freezing at −20°C for 48 h.

Sonstegard and Matthews[20] nondestructively tested 10-mm-diameter trabecular bone cylinders from the distal human femur and proximal tibia, compressing them at a strain rate of 32/s. In the study, 16 specimens were tested fresh and retested after being frozen for 2 weeks at −10°C. Freezing caused a significant 12% decrease in the elastic modulus. The authors postulated that freezing causes expansion of interstitial fluids, damaging the delicate trabecular network.

Pelker and colleagues[21,22] tested 90 rat femurs and 324 rat vertebral bodies, comparing fresh specimens to other specimens frozen for 2 weeks at −20, −70, or −196°C. Whole femurs were tested to failure in torsion at 13.2 rad/s and whole vertebrae were compressed to failure at 0.5 mm/s. Freezing at −20 and −70°C did not alter the torsional strength or stiffness properties of the femurs. Femurs frozen at liquid nitrogen temperature (−196°C) displayed a significant 65% increase in angular deformation to failure and a corresponding decline in torsional stiffness, but torsional strength and energy-to-failure were unaffected. The failure stress and elastic modulus of the vertebral specimens were significantly elevated about 25% by freezing at −20 and −70°C. Freezing at −196°C significantly elevated the failure stress, strain, and energy-to-failure about 15 to 20%, but did not alter the elastic modulus. These vertebral results should more properly be considered structural properties because they were calculated assuming a uniform cross-sectional area and homogeneous structure for all the specimens. This is in contrast to the method of Sonstegard and Matthews,[20] who used machined, purely trabecular samples. While the

latter investigators found no change in modulus after freezing at −10°C, the Pelker results suggest that freezing produces mild temperature-dependent changes in the mechanical properties of bone that could affect the outcome of studies aimed at defining the mechanical properties of either cortical or trabecular bone. Kang and Kim,[23] using an experimental approach similar to Pelker's, reported somewhat different results, however. They found that freezing at −80°C significantly decreased both the bending strength of rat femurs (by 7.2%) and the compressive strength of rat vertebrae (by 11.0%). The length of time that the bones were frozen (2, 6, and 12 weeks) had no effect.

Roe et al.[24] measured the compressive strength, screw pullout force, and screw-stripping torque in the diaphyses of canine femurs, comparing the results in specimens stored at 4°C for 4 h with contralateral samples stored at −20°C for 1, 16, and 32 weeks. Each of these three treatment groups had three subgroups (ignoring a partially decalcified subgroup): (1) aseptically harvested but not sterilized, (2) ethylene oxide gas sterilized, (3) methanol-chloroform (1:1) sterilized; $N = 15$ in each subgroup. Compressive strength was about 20% greater after freezing for 1 week, and this was significant in subgroups 1 and 2, but not in subgroup 3. However, after 16 or 32 weeks, compressive strength had returned to normal in subgroup 1 and fallen below control values in the chemically sterilized subgroups. Similar results tended to occur for screw pullout force, but screw-stripping torque was not affected by any of the protocols. Consequently, this study suggests that the mechanical effects of freezing are time dependent, with an initial increase in strength that is canceled by subsequent deterioration.

Goh and co-workers[25] studied the effects of freezing at −20°C for 3 or 21 days using 24 pairs of feline humeri and femora. The contralateral control specimens were tested immediately after harvesting. The humeral diaphyses were tested to failure in torsion and the femoral diaphyses were tested in four-point bending. None of these quasi-static test results was significantly affected by freezing.

Linde and Sorensen[16] studied the effects of freezing and freeze–thaw cycles on the compressive behavior of machined human trabecular bone specimens (see descriptions of other aspects of the same study above). All cylinders were initially tested nondestructively within 2.5 h after removal of the limb and then again after 24 h of storage in saline at room temperature. Subsequently, specimens were frozen at −20°C for 1 day ($N = 19$), 10 days ($N = 18$), or 100 days ($N = 18$) of freezing. All specimens were thawed and conditioned in saline for 3 h before testing. After testing the 1- and 10-day samples, they were refrozen for 1 day, thawed, conditioned, and tested again. This procedure was repeated four times to determine the effects of multiple freeze–thaw cycles. The mechanical behavior of the samples initially frozen for 1, 10, and 100 days was not significantly different from the behavior measured at 24-h postmortem. The mechanical properties were also unaffected by multiple freeze–thaw cycles. The initial storage of the specimens at room temperature for 24 h and the multiple testing cast a shadow on these results, in that they may have introduced some deterioration. Otherwise, they are quite compelling.

Equally convincing are the results of Borchers et al.,[26] who examined the mechanical effects of freezing bovine cancellous bone to either −20 or −70°C for 8 days, or the effects of 8 daily freeze–thaw cycles to −20°C. Each experimental group contained 24 samples cored from the head and metaphyseal region of three fresh bovine humeri. The 5.1-mm-diameter, 10-mm-long cylinders were quasi-statically compressed to failure. When the experimental groups were compared with fresh controls (with or without normalizing for apparent density), neither elastic modulus nor strength was found to be significantly affected by any of the freezing treatments.

When freezing bone for storage, it may be important to package the specimens so that their moisture content is maintained. Freezing freshly harvested whole canine bones at −20°C for 1 year in a sealed polyethylene container, Griffon et al.[27] found that adding saline to the container prior to freezing significantly increased their bending toughness. (Torsional properties were not affected, however.)

Using freshly harvested specimens as controls, Huss et al.[28] found that storage at −20 or −70°C for 14 or 28 days did not significantly increase the force required to pull unthreaded Steinman pins from the diaphyses of dog femurs. Hamer et al.[29] found that freezing human femoral cortex specimens to −70°C for an unspecified period of time did not alter mechanical properties measured in an unconventional bending test. Kang et al.[30] also found no effects of five daily freeze–thaw cycles

TABLE 20.2 Summary of the Effects of Freezing on the Mechanical Properties of Bone

Authors, Year	Storage Environment	Type of Bone	Type Test	Result
Sonstegard and Matthews, 1977[20]	**Freezing, −10°C**	Human trabecular	Compression, M	E−
Sedlin, 1965[19]	Freezing −20°C	Human cortical	Bending, M	No change
Weaver, 1966[10]	Freezing, −20°C	Human cortical	Hardness, M	No change
Linde and Sorensen, 1993[16]	Freezing, −20°C	Human trabecular	Compression, M	No change
Roe et al., 1988[24]	**Freezing, −20°C**	Dog femur	Compression, S	σ+ then σ−
			Screw pullout	No change
			Screw strip	No change
Huss et al., 1995[28]	Freezing, −20°C	Dog femur	Pin pullout	No change
Goh et al., 1989[25]	Freezing, −20°C	Cat femur	Bending, S	No change
		Cat humerus	Torsion, S	No change
Borchers et al., 1995[26]	Freezing, −20°C	Cow trabecular	Compression, M	No change
Kang et al., 1997[30]	Freezing, −20°C	Cow Trabecular	Indentation, M	No change
Pelker et al., 1984[22]	Freezing, −20°C	Rat femur	Torsion, S	No change
	Freezing, −20°C	Rat Vertebra	Compression, S	σ+, E+
Frankel, 1960[18]	Freezing, −25°C	Human femur	Compression, S	No change
Hamer et al., 1996[29]	Freezing, −70°C	Human femur	Bending, S	No change
Huss et al., 1995[28]	Freezing, −70°C	Dog femur	Pin pullout	No change
Pelker et al., 1984[22]	Freezing, −70°C	Rat femur	Torsion, S	No change
	Freezing, −70°C	Rat vertebra	Compression, S	σ+, E+
Borchers et al., 1995[26]	Freezing, −70°C	Cow trabecular	Compression, M	No change
Kang and Kim, 1995[23]	**Freezing, −80°C**	Rat femur	Bending, S	σ−
	Freezing, −80°C	Rat vertebra	Compression, S	σ−
Pelker et al., 1984[22]	**Freezing, −196°C**	Rat femur	Torsion, S	ε+, E−
	Freezing, −196°C	Rat vertebra	Compression, S	σ+, ε+, U+

Note: Bold typeface in the storage environment column indicates that a change was seen. S = structural test; M = material test; + = increased; − = decreased; ε = failure strain or displacement; σ = failure stress or load; E = elastic modulus or structural stiffness; U = energy-to-failure.

(to −20°C) on indentation tests of bovine tibial cancellous bone, regardless of whether the specimens were frozen in saline wraps and thawed in saline solution or frozen without saline wraps and thawed in air.

Finally, in the context of freezing bones to be used as allografts, Wohl et al.[31] found that different methods used to freeze osteochondral grafts did not affect the mechanical properties of the graft so much as the adaptive responses of the surrounding bone. In other words, by disrupting cells, freezing may affect the biological characteristics of the bone more than mechanical properties.

Table 20.2 summarizes the results of 17 studies containing 24 tests of the effects of freezing and thawing on bone mechanical properties. Eight tests found that freezing did change bone mechanical properties, and 16 did not. In most of the cases where changes were found, the temperatures were −70°C or lower and the bones were from rats rather than larger animals. There also was a tendency for structural variables to be changed more than material properties. The nature of the changes was also mixed: usually strength was increased and stiffness decreased, but not always. The greatest change reported was a 65% decrease in torsional stiffness in rat femurs frozen to −196°C.[22] Most changes were on the order of 10 to 25%. While the variability of methods prevents direct comparisons, it is interesting that they usually involved increased strength and/or decreased stiffness, which is contrary to a simple hypothesis that freezing and thawing would tend to crack or otherwise damage bone structure. Time dependence may also play a role in the variability of the results, as suggested by the results of Roe et al.[24] In summary, the preponderance of the data indicates that freezing to a temperature of −20°C, under conditions that assure maintenance of the moisture content of the specimen, is unlikely to significantly change the mechanical properties of cortical or trabecular bone relative to the normal variability within a typical experimental sample.

20.3.2 Chemical Preservation

Chemical preservation (fixation) methods were developed by histopathologists not only to prevent tissue decay, but also to preserve cell structure for microscopic examination. The fixatives commonly used in bone work today have been selected for their capacity to penetrate the specimen quickly and completely while extracting marrow fat and avoiding changes to the mineral content of the specimen. These solutions usually contain formaldehyde, alcohol, or glutaraldehyde. Formaldehyde, HCHO, is a powerful disinfectant gas. Formalin is a saturated (37% by weight) solution of formaldehyde gas in water. A 10% solution of formalin in saline is commonly used for preserving all sorts of biological tissues because it prevents bacteriological decay and maintains cell membranes in an intact state. The principal disadvantage of using formalin to preserve bone is that it is easily oxidized to form formic acid, which can cause dissolution of mineral. For this reason, formalin should be buffered and its pH neutralized to produce neutral buffered formalin: 100 ml formalin, 900 ml distilled water, 4 g monobasic sodium phosphate (monohydrate), and 6 g dibasic sodium phosphate (anhydrous).[1] Ethyl alcohol (ethanol, C_2H_5OH) is often recommended for fixation of bone tissue. The usual concentration is 70% by volume in water. It is pH neutral and avoids mineral dissolution, but it does not preserve cell membranes as well as formaldehyde and penetrates bone relatively slowly. For these reasons, using a precooled solution and refrigerating specimens at 4 to 7°C has been suggested.[32] The third commonly used chemical fixative is derived from the chemical glutaraldehyde, $C_5H_8O_2$. Glutaraldehyde concentrate, also known as glutaral, is a 50% solution of glutaraldehyde in water. A 2 to 6% solution of buffered glutaraldehyde is superior to formalin for cell fixation but penetrates tissues slowly.

Chemical fixatives may cross-link proteins in the tissue (an effect similar to that seen in a hard-boiled egg), or denature and precipitate them, or both. Alcohol probably precipitates proteins by eliminating their solvent in the tissues: water. Gluteraldehyde is known for its ability to form protein cross-links. Formalin, on the other hand, may function by forming a network of paraformaldehyde polymer throughout the tissue. Generally speaking, such effects tend to make the tissue stiffer. However, the chemistry of interactions between fixatives and various tissues is poorly understood, and there is no theory to predict the effects of fixatives on tissue mechanical properties.

20.3.2.1 Ethyl Alcohol

Only three studies were found concerning the effects of ethanol fixation on bone mechanical properties. In the first, Sedlin[19] tested cortical bone beams machined from human femurs. He found that 5 and 10 days' fixation in 40% alcohol resulted in significant 2.5 and 4% increases, respectively, in flexural modulus. Ashman[33] reported that storing bone specimens in 50% ethyl alcohol does not affect elastic modulus calculated from measurements of sound velocity. The third study was part of the previously mentioned experiment by Linde and Sorensen.[16] They examined the effects of storage in 70% ethanol at +10°C on the compressive mechanical properties of human trabecular bone. Testing each specimen nondestructively after 1, 10, and 100 days in alcohol, they found that the compressive elastic modulus tended to decrease, but the change was not significant. There was a significant 34% increase in hysteresis energy, however. (It should be noted that these specimens had previously been stored at room temperature for 24 h and were tested multiple times.) It is interesting that these modest mechanical effects have been associated with alcohol, which seems to function by precipitating proteins, while greater effects have been associated with formalin, which may create a paraformaldehyde network in the tissue.

20.3.2.2 Formalin

Weaver[10] tested the effect of formalin fixation on the hardness of human cortical bone from the fibula or tibia of four individuals aged 12 to 35 years. Specimens were tested fresh and after storage in 10% neutral buffered formalin for 24 h. Storage in formalin produced a 20% increase in bone hardness. Greenberg and co-workers[2] tested whole tibia–fibula complexes in dogs using a three-point bending arrangement that allowed testing *in situ* before and after death, and then after extraction and fixation in

10% formalin for 1 week. Structural stiffness (load/deflection) of the complexes was elevated after formalin immersion in 9 of 12 specimens, with an overall mean increase of 9%. Although the authors concluded that formalin fixation produces slightly stiffer bones, the differences they measured are not statistically significant. This result was in concert with that of Sedlin and Hirsch,[19,34] who reported that the tensile elastic modulus of human femoral cortical bone was the same following 3 weeks of fixation in 10% formalin as it had been when the same specimens were nondestructively tested in a fresh state.

Goh and co-workers[25] tested 24 pairs of feline humeri and femora. The control specimens were tested immediately, and the contralateral bones were fixed in 10% formalin for 3 or 21 days. The humeral diaphysis was tested in torsion, and the femoral diaphysis was tested in four-point bending, both quasi-statically. Formalin fixation significantly reduced the energy absorption to failure during torsion by 40% and during bending by 50%.

Edmondston et al.[35] examined the effects of fixation in 10% buffered formalin for 4 weeks on the mechanical properties of sheep spine segments loaded in compression. There were two groups of ten lumbar spines, each cut into two to three test segments consisting of a vertebral body, half of each adjacent body, and the intervening disks. To control for the effects of variability in bone density, they plotted failure load as a function of dual energy X-ray absortiometry measured bone mineral density (BMD). The failure load vs. BMD regression lines were significantly different for the fresh and fixed groups. The slopes were similar, indicating that the BMD dependence of strength was similar in each group, but the intercept of the fixed group was significantly higher ($p < 0.0005$), showing that formalin fixation had increased the strength about 13%. There was no change in stiffness.

These few studies suggest that 10% formalin does not alter bone stiffness but does increase compressive strength of trabecular bone. It may also increase hardness and reduce toughness, and perhaps affect other post-yield behavior.

20.3.2.3 Embalming

The use of embalmed bone is perhaps best justified in studies of the mechanical behavior and efficacy of fracture fixation devices, joint prostheses, and other reconstructive orthopedic devices. Given the difficulty and expense involved in obtaining sufficient quantities of fresh bones appropriate for such work, and the risks to investigators of undetected viral infection in fresh human bones, embalmed bones present an attractive alternative and are often relatively plentiful in teaching centers. Nevertheless, studies such as these require bones that reflect *in vivo* behavior reasonably well.

Embalming may be defined as fixation of an entire cadaver, but beyond the prevention of decay the goals and methods are obviously quite different. Embalming fluids vary widely in their chemical compositions, although most contain alcohol (ethyl or isopropyl), formalin, phenol, and glycerin. The manufacturers of commercial embalming fluids offer a cornucopia of formulae, almost all of which have cosmetic goals and proprietary compositions. Furthermore, the composition of the fluid used is often varied to suit the circumstances of a particular body, even in university anatomy laboratories. Thus, the term *embalmed* has no precise meaning, and it is futile to try to determine accurately the effects of this inconstant process on bone mechanical properties, regardless of how well the original tissue and the mechanical test are defined. The best one can do is to investigate the effects of some examples of embalming fluids, and by reference to many such experiments obtain an estimate of the overall effects of embalming on mechanical properties.

Calabrisi and Smith[36] were apparently the first to examine systematically the effects of embalming on the mechanical behavior of cortical bone. These investigators tested pairs of diaphyseal cylinders milled from three amputated human femurs and four amputated tibias. Each cylinder was compressed to failure to determine strength; one cylinder from each bone was tested fresh (time from amputation to testing or fixation was not provided) and the other was tested after being immersed in embalming fluid for 7 weeks. Mean compressive strength of the embalmed bone was 13% less than that of the fresh bone. No statistical analysis was performed by the authors, but using a paired *t*-test, we found this difference to be marginally significant ($p < 0.06$). However, the statistical power was low (0.41).

TABLE 20.3 Structural Characteristics of Fresh vs. Embalmed Femurs

Treatment	Structural Stiffness (N/mm)	Energy Loss (per cycle, %)
Fresh ($n = 4$)	1455 ± 99	8.8 ± 1.9
Embalmed ($n = 10$)	1411 ± 233	9.9 ± 6.0

Note: Mean values ± SD.
Source: Data from Ziran et al.[39]

McElhaney and colleagues[37] used standardized tension and compression specimens of bovine cortical bone to assess the effect of embalming under quasi-static conditions. Hardness was also tested using a Rockwell tester. Matched samples were tested within 48 h of death or after 15 h immersion in one of four varieties of embalming fluid. (The results from these different solutions were apparently pooled.) Embalming caused a significant 12% reduction in compressive strength, but no change in compressive modulus, tensile strength, tensile modulus, or hardness was found. Except for ultimate compressive strength, the differences between embalmed and unembalmed properties were much less than the intrinsic variability in the sample.

On the other hand, when Evans[38] compared the tensile properties of 150 embalmed and 250 unembalmed samples of human tibial cortical bone, he found that embalming significantly increased tensile strength by 10% and tensile modulus by 16%. Similarly, Sonstegard and Matthews[20] found that soaking human trabecular bone cylinders in embalming fluid increased their compressive elastic modulus by 10%, but this result was confounded by the fact that the modulus of the specimens had previously been decreased 12% by storage while frozen.

Ziran et al.[39] compared the structural behavior of four fresh human femurs and ten embalmed femurs. The femurs were loaded anatomically through the femoral head, with the head aligned over the medial epicondyle in the sagittal plane and the condyles parallel to the floor in the coronal plane. All bones were compressed at 0.17 mm/s to peak loads well within their elastic limit. After five conditioning cycles, data were collected for five additional cycles and averaged to obtain structural stiffness and energy loss per cycle. Embalming did not have a significant effect on the mean stiffness or energy loss, but the fresh specimens demonstrated less variation (Table 20.3).

Finally, Porta et al.[40] studied the qualitative effects of embalming on the trauma produced when cadaveric human lower extremities were impacted by a weight; they found that embalming increased soft tissue damage but decreased bone fragmentation.

20.3.2.4 Summary

Table 20.4 summarizes the effects of chemical preservatives on bone mechanical properties. Relatively few experiments have studied these effects, and the available data are equivocal. There is a slight preponderance of data showing that ethanol and formalin fixation alter mechanical properties, and five out of six studies found that embalming changed mechanical behavior. However, clear trends regarding the direction of such changes are lacking, and many studies suffer either from a lack of adequate experimental control or low experimental numbers. Without question, the most extensive investigations are those by Evans and colleagues, who reported that embalming significantly increased tensile strength and modulus. It should be emphasized that the choice of embalming medium is variable across studies and in some cases it is never defined. Indeed, as stated above, the term *embalmed* has no scientific definition because a great variety of embalming fluids are in common use. This in itself makes the question "How does embalming affect the mechanical properties of bone?" unanswerable. Even if one narrows the question to one particular embalming formula, or one fixative such as a 10% formalin solution, there are still many other aspects of the problem that need to be controlled, and scientifically sound answers may not be worth the cost.

TABLE 20.4 Summary of the Effects of Chemical Fixation Methods on Postmortem Changes in the Mechanical Properties of Bone

Authors, Year	Storage Environment	Type of Bone	Type Test	Result
Sedlin, 1965[19]	**40% ethanol**	Human cortical	Bending, M	E+
Ashman, 1982[14]	50% ethanol	Dog cortical	Ultrasonic, M	No change
Linde and Sorensen, 1993[16]	**70% ethanol**	Human trabecular	Compression, M	U+
Weaver, 1966[10]	**10% formalin**	Human cortical	Hardness, M	H+
Sedlin and Hirsch, 1966[34]	10% formalin	Human cortical	Tension, M	No change
Greenberg et al., 1968[2]	10% formalin	Dog tibia-fibula	Bending, S	No change
Goh et al., 1989[25]	**10% formalin**	Cat femur	Bending, S	U−
	10% formalin	Cat humerus	Torsion, S	U−
Edmondston et al., 1994[35]	**10% formalin**	Sheep spine	Compression	σ+
Ziran et al., 1997[39]	Embalming	Human femur	Compression	No change
Evans, 1973[38]	**Embalming**	Human tibia	Tension	σ+, E+
Calabrisi and Smith, 1951[36]	**Embalming**	Human cortical	Compression, M	σ− (m.s.)
Sonstegard and Matthews, 1977[20]	**Embalming**	Human trabecular	Compression, M	E+
McElhaney et al., 1964[37]	**Embalming**	Cow cortical	Tension, M	No change
			Compression, M	σ−
			Hardness	No change

Note: Bold typeface in the storage environment column indicates that a change was seen. S = structural test; σ = failure stress or load; + = increased; − = decreased; m.s. = marginally significant; M = material test; H = hardness; E = elastic modulus or structural stiffness; U = energy-to-failure.

20.4 The Mechanical Effects of Storing and Treating Allograft Bone

When bone is transplanted from one person to another, there are two unique features of the operation compared with transplantation of other tissues. First, unlike most other tissues, bone can be frozen and stored for years prior to use as an allograft. This is because the functionality of the transplanted bone does not depend on the viability of its cells. Short-term functionality of a bone allograft depends instead on the mechanical integrity of the extracellular matrix. This importance of the extracellular matrix and its mechanical properties is the second unique feature of bone allografting. The graft will function indefinitely if the host's cells can "incorporate" the graft bone into the remainder of the skeleton and maintain it during its subsequent mechanical usage. However, the advantage of not having to keep the cells of the bone graft alive is only realized if the storage methods do not compromise its initial mechanical properties or its receptivity to incorporation by the host's cells. Here, obviously, the former concern should be addressed.

Also of concern is another aspect of these operations that could affect the mechanical properties of the graft. When any tissue is transplanted from one person to another, the surgeon must try to avoid both the incitement of an antigenic response in the patient and the transmission of an infectious organism in the graft tissue. If the graft is treated in some way to reduce these risks, there must be concern that these treatments do not degrade its mechanical properties. This section therefore also reviews data addressing the mechanical effects of these kinds of treatments.

There are two methods of storing bone harvested for use as allografts—freezing and freeze-drying. For the purposes of storing bone grafts, freezing below −20°C is recommended and freezing at −70 to −80°C is common practice.[41] The mechanical effects of freezing bone have already been reviewed. Table 20.2 shows that freezing to these temperatures has been found to alter the mechanical properties of rat bone, but usually has not affected bones from larger animals, including humans. Now the mechanical effects of freeze-drying will be considered.

20.4.1 Freeze-Drying

Freeze-drying, also known as lyophilization, is accomplished by deep-freezing the bone (e.g., −80°C), introducing a strong vacuum, and gradually raising the temperature as the frozen water sublimates, but still keeping the temperature well below freezing. The end point of the process is usually defined as occurring when the residual water content of the specimen is less than 5%. The freeze-dried bone may be stored for 4 to 5 years at room temperature so long as it is sealed against the return of moisture. In addition, there is evidence that freeze-drying reduces the antigenicity of bone grafts without affecting their osteoinductive potential.[42] However, several studies have shown that freeze-drying has a more detrimental effect on the mechanical behavior of *cortical* bone than does freezing; the effects of freeze-drying on *trabecular* bone appear to be less severe.

Triantafyllou and colleagues[43] tested bovine cortical bone in three-point bending, comparing freeze-dried specimens to controls that had been frozen at −35°C. The freeze-dried specimens were rehydrated in normal saline for 2 h at 20°C. The bending strength of the freeze-dried specimens was 55 to 90% of the controls. The authors did not directly measure elastic modulus, nor did they report a statistical analysis, but their graphical presentation of ultimate load and deflection data strongly suggests that freeze-drying reduced modulus, failure strain, and energy-to-failure as well.

Bright and Burstein[44] studied the importance of rehydration time on freeze-dried parallelepiped specimens of human femoral cortical bone in longitudinal tension and compression at high strain rates. Rehydration times in normal saline (temperature unreported) were varied from 0.5 to 24 h. They found that freeze-drying without rehydration did not significantly alter elastic modulus, ultimate stress, or ultimate strain, but did lower yield stress and raise the plastic modulus (i.e., the slope of the stress–strain curve beyond the yield point). Rehydration gradually restored the post-yield behavior of the bone, but after 24 h in saline the plastic modulus was still significantly greater than the frozen controls. A repeated cycle of freeze-drying and rehydration did not further alter mechanical properties. The authors also noticed that the embrittlement produced by freeze-drying caused the specimens to crack longitudinally, especially when cut in the transverse direction. They stated that freeze-dried femurs had virtually no hoop strength, and that this had obvious implications for their use with intramedullary devices. They also pointed out that the changes in post-yield behavior suggested that freeze-drying affected the collagen component of the bone matrix more than the mineral component.

Pelkar and co-workers[21,22] found that freeze-dried rat femurs rehydrated in saline for 24 h were mechanically inferior to fresh or fresh-frozen femurs. Freeze-drying reduced the failure torque and torsional stiffness by over 50%. They also noticed that the freeze-dried bones sometimes developed longitudinal surface cracks when rehydrated. On the other hand, freeze-dried, rehydrated rat vertebrae tested in axial compression were 10% stronger than fresh controls, and their stiffness was unaffected. Similar results were obtained by Kang and Kim,[23] who found that freeze-drying significantly reduced the bending strength of rat femurs by 9.7% but did not alter the compressive strength of rat vertebral bodies. Malinin et al.[45] tested freeze-dried segments of paired human femoral diaphyses in diametrical compression. (This is of particular interest because the mode of failure involved circumferential bending with periosteal tension similar to a hoop stress; recall the above comment of Bright and Burstein.) Contralateral specimens were compared, one fresh and the other freeze-dried and rehydrated in saline for 24 h. The mean strength of the freeze-dried, rehydrated specimens was 19% less than controls, a marginally significant result. When holes were drilled through the cortex at the expected failure site prior to testing, freeze-drying did not exacerbate the effect of this stress concentration. Simonian and associates[46] found that freeze-dried cortical bone specimens from human tibias, when rehydrated for 2 h in saline, required only two thirds as much force to pull screws out as did control specimens.

Conrad and co-workers[47] examined the effects of freeze-drying on cancellous bone cored from pairs of human femurs and tibias within 24 h of death. Specimens 14 mm in diameter and 15 mm long were taken from identical sites in each pair of bones, stored at −80°C, and freeze-dried. Freeze-dried specimens were axially compressed to failure after being rehydrated in saline at 37°C for 24 h, and the results were compared to contralateral fresh-frozen specimens thawed at 37°C for 10 min. Strength and stiffness were normalized by the square of the apparent density of the specimen and expressed as a ratio of the freeze-dried value to

TABLE 20.5 Summary of the Effects of Various Treatments Relevant to Allograft Bone on Mechanical Properties

Authors, Year	Treatment	Type of Bone	Type Test	Result
Bright and Burstein, 1978[44]	**Freeze-dried, rehydrated**	Human cortical	Tens/compression, M	$\sigma_{yld}-$, $E_{Plas}+$
Malinin et al., 1989[45]	**Freeze-dried, rehydrated**	Human cortical	Bending, S	$\sigma-$
Simonian et al., 1994[46]	**Freeze-dried, rehydrated**	Human cortical	Screw pullout	$\sigma-$
Conrad et al., 1993[47]	Freeze-dried, rehydrated	Human trabecular	Compression, M	No change
Triantafyllou et al., 1975[43]	**Freeze-dried, rehydrated**	Cow cortical	Bending, M	$\sigma-$
Borchers et al., 1995[26]	Freeze-dried, rehydrated	Cow trabecular	Compression, M	No change
Pelker et al., 1984[22]	**Freeze-dried, rehydrated**	Rat femur	Torsion, S	$\sigma-$, E−
	Freeze-dried, rehydrated	Rat vertebra	Compression, S	$\sigma+$
Kang and Kim, 1995[23]	**Freeze-dried, rehydrated**	Rat femur	Bending, S	$\sigma-$
	Freeze-dried, rehydrated	Rat vertebra	Compression, S	No change
Komender, 1976[56]	γ radiation, 10 kGy	Human cortical	Compression, M	No change
	γ radiation, 10 kGy	Human cortical	Torsion, M	No change
	γ radiation, 10 kGy	Human cortical	Bending, M	No change
Anderson et al., 1992[57]	γ radiation, 10 kGy	Human trabecular	Compression, M	No change
Simonian et al., 1994[46]	γ radiation, 16–19 kGy	Human tibia	Screw pullout	No change
Currey et al., 1997[58]	**γ radiation, 17 kGy**	Human cortical	Bending, M	$\sigma-$
Komender, 1976[56]	γ radiation, 30 kGy	Human cortical	Compression, M	No change
	γ radiation, 30 kGy	Human cortical	Torsion, M	No change
	γ radiation, 30 kGy	Human cortical	Bending, M	No change
Currey et al., 1997[58]	**γ radiation, 30 kGy**	Human cortical	Bending, M	$\sigma-$
Hamer, et al., 1996[29]	**γ radiation, 30 kGy**	Human femur	Bending, S	$\sigma-$, U−
Triantafyllou et al., 1975[43]	**γ radiation, 30 kGy**	Cow cortical	Bending, M	$\sigma-$
Anderson et al., 1992[57]	γ radiation, 31 kGy	Human trabecular	Compression, M	No change
	γ radiation, 51 kGy	Human trabecular	Compression, M	No change
Bright and Burstein, 1978[44]	**γ radiation, unspecified**	Human cortical	Tens./compression, M	$E_{Plas}+$
Komender, 1976[56]	**γ radiation, 60 kGy**	Human cortical	Compression, M	$\sigma-$
	γ radiation, 60 kGy	Human cortical	Torsion, M	$\sigma-$
	γ radiation, 60 kGy	Human cortical	Bending, M	$\sigma-$
Anderson et al., 1992[57]	**γ radiation, 60 kGy**	Human trabecular	Compression, M	$E-$, $\sigma-$
Currey et al., 1997[58]	**γ radiation, 95 kGy**	Human cortical	Bending, M	$\sigma-$

Note: Bold typeface in the treatment column indicates that a change was seen. S = structural test; σ = failure stress or load; + = increased; − = decreased; M = material test; E = elastic modulus or structural stiffness; E_{Plas} = plastic (post-yield) modulus; U = energy-to-failure.

the control value. The ultimate strength and stiffness of the freeze-dried, rehydrated samples were not significantly different from those of controls. In another experiment, they found that unrehydrated freeze-dried specimens were 89% stronger than rehydrated contralateral specimens; stiffness was also greater but not significantly so. Evidence was also obtained that rehydration *in vacuo* is more effective than at atmospheric pressure. Freeze-dried cancellous bone was also examined in the previously cited work by Borchers et al.[26] Cylinders of freeze-dried bovine trabecular bone were compressed to failure after rehydration for 24 h in saline and compared with fresh controls. The elastic modulus and strength of the fresh and freeze-dried, rehydrated bone were comparable.

Table 20.5 summarizes the results from these experiments on the mechanical effects of freeze-drying. These data indicate that freeze-drying degrades the mechanical properties of cortical bone but not cancellous bone. However, most of these studies have been limited in their mechanical sophistication. As in the studies of freezing effects, the results of Bright and Burstein again suggest that more complete testing methods, examining post-yield behavior and structural vs. material properties, would be likely to produce a clearer picture. It should also be noted that Burchardt et al.[48] showed that freeze-dried grafts were as strong mechanically as fresh grafts 6 months after they were actually used to repair a fibular defect in a canine model.

20.4.2 Irradiation

There are several circumstances related to allografting that provoke an orthopedic surgeon's interest in the mechanical effects of gamma irradiation on bone. Two such situations involve the treatment of a malignant bone tumor. One approach to this problem is to resect the affected bone tissue and replace it with an allograft, or an autograft from another part of the patient's body. However, each of these strategies has disadvantages that might be avoided by resecting the affected region of bone, irradiating it to kill the tumor cells, and reimplanting it.[49,50] Alternatively, one may attempt to use radiation to treat the bone tumor *in situ*. Each of these approaches would be less attractive if irradiation had a negative effect on the mechanical properties of bone.

Another reason for irradiating transplanted bone is to eliminate infectious organisms. Concern about this grew with the proliferation of the human immunodeficiency virus and the AIDS epidemic in the 1980s. Because of the life-threatening consequences of human immunodeficiency virus (HIV) transmission in allograft bone, methods for effectively killing the virus and other infectious agents in bone were sought. Marrow removal and freeze–thaw cycles proved ineffective as methods for preventing retroviral transmission.[51] The remaining principal candidates for sterilizing bone allografts were ethylene oxide gas and gamma irradiation. It has since been learned that ethylene oxide gas sterilization of bone allografts results in an unacceptable rate of failure due to host reactions.[52,53] Consequently, surgeons have been left with irradiation as the primary method for sterilizing bone allografts.

The International Atomic Energy Agency long ago adopted a dose of 25 kGy of gamma radiation as the standard dose for sterilization of medical products,[54] and tissue banks have used doses of 15 to 25 kGy. (The SI unit of absorbed radiation dosage is the gray; 1 gray = 1 Gy = 100 rad; 1000 gray = 1 kGy.) However, Fideler et al.[55] found that the dose required to inactivate HIV genes effectively is no less than 30 kGy. Thus, dosages in the 30 to 60 kGy range are currently of interest for treating frozen bone allografts, and this dose raises serious concern about physical damage to the bone extracellular matrix.

In considering the effects of irradiation on bone mechanical properties, it is important to understand some of the physics involved. The photons produced by a gamma ray source transfer energy to atoms in the tissue, producing high-speed electrons in a Compton interaction. The resulting high-energy Compton electrons, rather than the gamma rays themselves, are the damaging agent, and each may ionize thousands of other atoms. Ultimately, these disruptions may weaken the molecular structure of a material. However, if the radiation travels less than 2 mm to pass through the specimen, the full potential for damage is not realized because the Compton electrons leave the tissue before achieving their full ionizing potential. Thus, the radiation dose "builds up" through the first few millimeters of bone, and larger specimens will be expected to suffer more damage than very thin ones experiencing the same level of incident radiation.

The earliest studies of the effects of irradiation on bone mechanical properties were done in the 1970s. Komender[56] tested samples of human cortical bone in compression, torsion, and bending after subjecting them to 10, 30, or 60 kGy of gamma irradiation. Irradiation at 10 or 30 kGy did not alter bone strength relative to fresh controls, but 60 kGy significantly reduced compressive strength by 20%, torsional strength by 35%, and bending strength by 30%.

Triantafyllou and colleagues,[43] in the lyophilization study described above, also tested the effects of irradiation on the flexural properties of bovine cortical bone. A radiation dose of 30 kGy reduced bending strength to 50 to 75% of the mean value for controls that had only been frozen. As with their freeze-drying data, it appears that irradiation also reduced elastic modulus, failure strain, and energy-to-failure. Indeed, there was considerable overlap in the results for the freeze-dried and irradiated specimens. In a third experimental group they tested the combined effects of freeze-drying and irradiation, and found that the strength of these beams was reduced to only 10 to 30% of control values. Bright and Burstein[44] studied the effects of irradiation on the tensile and compressive properties of human femoral cortical bone. Without specifying the dose, they reported that radiation increased the post-yield plastic modulus (as freeze-drying had), without affecting other test results. They found that the combination of irradiation and freeze-drying/rehydration increased the plastic modulus and decreased the yield stress and ultimate strain as well.

In considering the combined effects of freeze-drying and irradiation, it is noteworthy that Pelker and Friedlaender[41]cite unpublished data showing that mechanical degradation is greater when freeze-drying precedes irradiation rather than the other way around. Triantafyllou et al. did not specify the order of their treatments, but their wording suggests that lyophilization preceded irradiation, and the result was a more severe reduction in strength than either irradiation or freeze-drying produced. Bright and Burstein's paper, on the other hand, implies that irradiation preceded freeze-drying, and while they do not give quantitative results, their wording suggests that the combined effect in this order was not severe. Thus, these reports, abridged as they may be, are in concert with Pelker and Friedlaender's assertion.

Anderson and colleagues[57] examined the effects of gamma radiation on the mechanical properties of human cancellous bone taken from the proximal tibial epiphysis. Parallelepiped specimens measuring $10 \times 10 \times 20$ mm were cut from two pairs of elderly male tibias. Experimental groups ($N \geq 6$) were subjected to 10, 31, 51, or 60 kGy, then quasi-statically compressed to failure. Relative to site-matched contralateral controls, elastic modulus and failure stress and strain were unchanged except in the 60 kGy group, which experienced significant reductions in failure stress (64%) and elastic modulus (58%).

Simonian and associates[46] found that 16 to 19 kGy of irradiation applied to human tibial cortices did not decrease screw pullout force compared with controls. Hamer and co-workers[29] irradiated cross-sectional slabs of human femur cortices using a ^{60}Co source. With an unconventional bending test, they found that radiation did not alter bone stiffness, but did reduce yield and failure loads and work-to-failure. They also found that embrittlement of the tissue increased steadily with doses above about 9 kGy, to the extent that 60 kGy destroyed almost all the plastic behavior of bone.

Most recently, Currey et al.[58] examined the effects of ionizing radiation on the flexural behavior of human cortical bone from four pairs of fresh-frozen human femurs. Diaphyseal segments from one femur of each pair were exposed to 17, 30, or 95 kGy. Subsequently, $40 \times 3.4 \times 2.0$ mm beams were machined from these segments and from matching segments in the contralateral bone, and all were tested in quasi-static three-point bending. The modulus of elasticity was unaffected by irradiation regardless of dosage, but bending strength decreased with radiation dose: strength was reduced by 12% at 17 kGy, 20% at 30 kGy, and by more than 60% at 95 kGy. Energy-to-failure was dramatically reduced by irradiation: 45, 70, and 95% reductions were seen following the low, medium, and high dosages, respectively. Other specimens were subjected to impact testing with similar dose-dependent decreases in energy-to-failure.

These *in vitro* experimental results are reinforced by a very telling *in vivo* experiment by Voggenreiter et al.[59] Tibial diaphyses were removed from rats, irradiated, and reimplanted as autografts. After 3 weeks, two thirds of the grafts irradiated at 50 kGy were fractured. Furthermore, at 12 weeks there were dose-dependent 16, 24, and 50% reductions in incorporation of grafts treated at 1, 5, and 25 kGy, respectively. It is hypothesized that this diminishment of incorporation was caused by radiation-induced necrosis of bone cells. Thus, there are strong biological as well as mechanical reasons why gamma radiation is problematic as a means of killing tumor cells or viruses in bone grafts.

As summarized in Table 20.5, these studies provide compelling evidence that exposing bone to ionizing radiation adversely affects mechanical properties in a dose-dependent way. Figure 20.2 shows this graphically by merging data from several of the above studies into plots of percent diminishment in strength and work-to-failure as a function of radiation dose. These graphs suggest that strength decreases linearly with dose, but toughness (work-to-failure) drops off nonlinearly and at relatively low levels of irradiation. Because work-to-failure usually depends more on the ability of a material to resist loading after the yield point is reached, and in bone this capacity derives largely from collagen, it is useful to examine the effects of ionizing radiation on tendinous tissues.

Salehpour et al.[60] tested the effects of irradiation on the mechanical properties of bone–patellar tendon–bone specimens; their strength and toughness data are shown in Fig. 20.2. In addition, they noted that a dose of 60 kGy reduced stiffness about 35%, while reducing the density of hydroxypyridinium cross-links by only 12%. It is thought that lower levels of gamma radiation (10 to 50 kGy) can produce minor cleavage of collagen α chains as well as break inter- and intramolecular hydrogen bonds.[61]

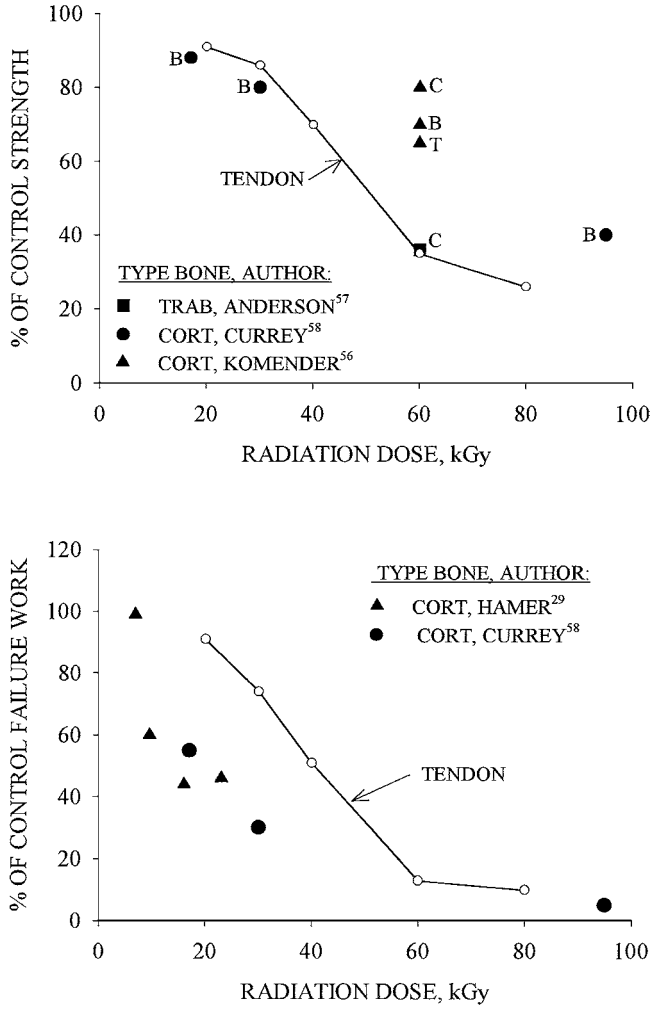

FIGURE 20.2 Graphs showing effects of irradiation on strength (above) and work-to-failure (below) of bone (solid symbols) and patellar tendon (open symbols, lines). The tendon data are from Salehpour et al.;[60] the bone data are from various sources, as shown. In the upper graph, the letters B, C, and T indicate bending, compression, and torsion tests, respectively. In the lower graph, all the bone data are from bending tests. As the radiation dose increases, work-to-failure diminishes more rapidly in bone than in tendon. Strength, on the other hand, diminishes less rapidly in bone than in tendon.

Conversely, higher levels (50 to 1000 kGy) are capable of cross-linking collagen.[61] However, it seems that, within the dose range of interest here, degradation of collagen structure in tendon far exceeds any possible compensation by radiation-induced additional cross-linking. A useful hypothesis would be that the same is true in bone, and the radiation-dependent decline of bone mechanical properties is due primarily to collagen damage. Note, however, that the susceptibility of bone and tendon to radiation damage is different. Bone toughness drops off quickly at relatively low levels of radiation, much earlier than for tendon. Conversely, bone strength does not appear to diminish nearly so much at these lower radiation levels and, at dosages above 30 kGy, bone seems to maintain its strength better than tendon.

The sensitivity of bone toughness to irradiation suggests that some parallels may exist between the effects of radiation on bone and the effects seen in osteogenesis imperfecta or other diseases arising from a defect in the genes for type I collagen. While osteogenesis imperfecta reduces bone strength, it appears

to reduce the capacity for post-yield deformation even more.[62] The resulting bone fragility may stem not only from reduced monotonic strength, but a diminished ability of the bone microstructure to sustain plastic deformation and limit damage formation. Normally, these kinds of microscopic structural changes would be repaired by remodeling, but remodeling may be delayed in an allograft, and even if it were not, a stress fracture-like phenomenon may lead to fracture.[63] This scenario would be compatible with the experimental results of Voggenreiter et al.[59] mentioned above.

20.4.3 Methanol and Chloroform Treatment

The use of ethyl alcohol as a fixative was described above. Methyl alcohol (methanol, CH_3OH), on the other hand, is a poisonous solvent that may be used to kill bacteria and extract fats. There would be obvious benefits to killing bacteria in allograft bone, and removal of lipids from such allografts has been postulated to reduce their antigenicity.[64] One approach to accomplishing these goals is soaking the graft bone in a 1:1 volumetric mixture of methanol and chloroform. Chloroform is an even stronger fat solvent, but one that is not miscible in water, as methanol is. In addition to sterilizing and removing lipids, could this solution alter the bone mechanical properties? The previously cited study by Roe and co-workers[24] studied the mechanical effects of this treatment. Canine femur diaphyseal segments were soaked in a 1:1 methanol–chloroform solution at 21°C for 24 h and then frozen at −20°C. When these specimens were compared with controls that had only been frozen, it was found that compressive strength and screw pullout force were increased. On the other hand, Thoren et al.[65] found that when previously frozen bovine trabecular bone cylinders were immersed overnight in methanol–chloroform solution, the compressive mechanical properties were unaffected. The divergent results of these two experiments are summarized in Table 20.6. It is impossible to know whether the different results were due to the kind of bone tested or the different treatment and testing methods.

TABLE 20.6 Summary of the Effects of Chemical and Thermal Sterilization on the Mechanical Properties of Allograft Bone

Authors, Year	Treatment	Type of Bone	Type of Test	Result
Thoren et al., 1995[65]	Methanol–chloroform	Cow trabecular	Compression, M	No change
Roe et al., 1988[24]	**Methanol–chloroform**	Dog femur	Compression, S	$\sigma+$
			Screw pullout	$\sigma+$
			Screw strip	No change
Sharkey et al., 1991[68]	Heating, 56°C	Cow cortical	Bending, M	No change
	Heating, 56°C	Cow trabecular	Compression, M	No change
Zimmerman et al., 1992[69]	Heating, 60°C	Human trabecular	Compression, M	No change
Sharkey et al., 1991[68]	Heating, 60°C	Cow cortical	Bending, M	No change
	Heating, 60°C	Cow trabecular	Compression, M	E−, $\varepsilon_{yld}+$
VonGarrel and Knaepler, 1993[70]	Heating, 60°C	Pig trabecular	Compression, M	No change
Sharkey et al., 1991[68]	Heating, 60°C	Dog femur	Torsion, S	No change
	Heating, 60°C	Dog trabecular	Compression, M	No change
	Heating, 65°C	Cow cortical	Bending, M	E−, $\sigma-$
VonGarrel and Knaepler, 1993[70]	Heating, 80°C	Pig trabecular	Compression, M	No change
	Heating, 100°C	Pig trabecular	Compression, M	$\sigma-$
	Heating, 134°C	Pig trabecular	Compression, M	$\sigma-$
Borchers et al., 1995[26]	**Boiling**	Cow trabecular	Compression, M	$\sigma-$
	Autoclaving	Cow trabecular	Compression, M	E−, $\sigma-$

Note: Bold typeface in the treatment column indicates that a change was seen. S = structural test; M = material test; + = increased; − = decreased; U = energy-to-failure; σ = failure stress or load; E = elastic modulus or structural stiffness; ε_{yld} = yield strain or deformation.

20.4.4 Thermal Sterilization

Heating of bone tissue has been proposed as a safe and effective means of protecting laboratory workers from HIV and preventing its transmission via bone allografts. Separate studies by McDougal et al.[66] and Spire et al.[67] independently conclude that 30 min of incubation at 56°C is sufficient for viral inactivation. McDougal and colleagues definitively state that heating lyophilized blood components at 60°C for 20 h provides a "large if not absolute margin of safety against HIV transmission."[66] For this reason, more recent studies examining the effect of supraphysiological temperatures on the material behavior of bone have used temperature ranges at or slightly above the minimum threshold values of 56 to 60°C. The mechanical consequences of more extreme treatments, including boiling and steam autoclaving, have also been investigated.

To help determine an appropriate protocol for thermal HIV inactivation in bone, the authors studied the effects of temperature and incubation time on the mechanical or structural properties of bone.[68] These experiments employed bovine and canine bone frozen whole at −5°C before being prepared and pasteurized. To assess material changes in cortical bone, 150 beams measuring 30 × 10 × 1 mm were cut from the mid-diaphysis of bovine femurs. The long axis of the beams was parallel to the long axis of the bone. Samples were immersed in saline and randomly assigned to an incubation temperature of 56, 60, or 65°C. The 50 specimens assigned to each temperature group were then randomly assigned to subgroups ($N = 10$) with incubation times of 0 (control) 3, 6, 10, and 20 h. Immediately following incubation the samples were tested in three-point bending. Heating the compact bovine bone for 20 h at 65°C caused significant 13% reductions in both ultimate stress and elastic modulus. Failure strengths for all other temperatures and times were not significantly changed and always within 10% of control values. Failure strains were not significantly affected by heating, but the strains measured after any incubation period at 60 and 65°C always exceeded control values.

To investigate heat-induced changes in cancellous bone, cylindric samples, 8 mm in diameter and one half the vertebral body height were cored from 20 bovine tail vertebrae, freed with a crosscut, and placed in saline as control specimens. The remaining vertebral bodies were incubated in saline for 20 h at either 56 or 60°C ($n = 10$ in each group). After incubation cylinders were cut from the remaining height of the vertebral body. Parallel end cuts were made on each specimen to yield test samples approximately 7 mm high. Samples were compressed to failure and stress and strain at yield and elastic moduli were calculated. Incubating cancellous bovine bone at 60°C for 20 h significantly increased yield strain by 47% and significantly decreased elastic modulus by 25%. No alterations in mechanical behavior were detected after incubation for 20 h at 56°C.

In a separate set of experiments, ten freshly harvested adult canine femora were incubated in saline at 60°C for 20 h while holding the ten contralateral control femurs at room temperature. Following treatment, cylinders of cancellous bone were cored from the femoral heads and both condyles of each femur and compressed to failure using a protocol similar to that described for the bovine vertebral bone. The remaining diaphyses were torsionally tested in external rotation. Torque, angular deformation, and absorbed energy at failure were determined. The yield stress, yield strain, and modulus measured in these trabecular bone samples were not appreciably different from values for matched controls. The torsional properties of the femoral diaphysis were also very similar in the matched pairs and unaffected by heating.

The authors concluded that both cortical and cancellous bone can withstand temperatures as high as 56°C for 20 h without significant effects on their material properties. Mild changes do occur within trabecular bone after incubation for 20 h at 60°C and within cortical bone after incubation for 20 h at 65°C. The increased susceptibility of trabecular bone may reflect its greater surface area. Although not directly investigated in these studies, it seems likely that the collagen component of bone is responsible for the changes noted. Proteins denature at these temperatures and collagen has been shown to be heat sensitive.

Zimmerman and co-workers[69] pasteurized eight cancellous dowels machined from the proximal and distal femur of human femurs and compared their post-treatment properties with the properties

of eight matched controls from contralateral bones. Experimental specimens were heated in water at 60°C for 10 h. Control specimens were held frozen during the treatment period. The 12 × 15 mm cylinders were subsequently loaded to failure in compression. Ultimate stress and the associated strain, elastic modulus, and energy absorption at failure were examined. Heated specimens demonstrated a 17% reduction in strength and failure strain, but these parameters were not statistically different than the matched controls. In the authors' experiments, the incubation period was twice as long as in the Zimmerman experiments, which may have produced greater changes in the organic constituents of bone.

Von Garrel and Knaepler[70] examined the effects of heating at 60, 80, 100, and 134°C (autoclaving) on cylinders of cancellous bone machined from porcine femoral heads. They reported that temperatures above 80°C caused significant reductions in mechanical strength. Incubation times and other details of their experiment were not provided. In the freezing experiment noted above, Borchers et al.[26] also tested the effects of heating on the compressive properties of bovine cancellous bone. Cylindrical test specimens were boiled (at 100°C) for 1 h in normal saline or autoclaved at 127°C for 10 min. The elastic moduli of the boiled and autoclaved specimens were reduced by 25 and 47%, respectively, with the latter statistically significant. The compressive strengths of the boiled and autoclaved specimens were reduced by 32 and 48%, respectively, both being significant reductions.

In summary, bones subjected to temperatures of 56°C or less, even for prolonged periods of up to 20 h, appear to maintain their normal biomechanical characteristics. However, this statement is based on only a few studies and more work should be conducted before drawing definitive conclusions. Heating bone to 60°C or more can significantly alter its material behavior. Unsurprisingly, the more intense the heat, the greater the material alterations, so that bone subjected to boiling or autoclaving behaves radically different than bone subjected to milder temperatures. Clinical experience with transplanted bones that have been autoclaved or boiled has also been somewhat disappointing in terms of osteoinduction, host bone in-growth, and graft incorporation.[71] In this regard, allografts treated at milder pasteurization temperatures behave similarly to nonheated grafts.[72,73] It is known that collagen solubilizes at high temperature. Cleavage of noncovalent bonds may occur at temperatures between 50 and 70°C and cleavage of covalent cross-links at temperatures between 70 and 100°C.[74] Heating collagen to 100°C or more induces random hydrolysis of the entire molecule. This behavior fits nicely with the experimental data reviewed.

20.4.5 Summary

The functional mechanical properties of bone to be used as an allograft will depend on its incorporation by the host as well as changes induced by storage methods and treatments to guard against immune responses and transmission of infections. In this context, freezing the bone for storage is unlikely to reduce load-bearing capacity seriously. Freeze-drying followed by rehydration may be somewhat more compromising than freezing for cortical bone, but appears to have little or no effect on the mechanical properties of cancellous bone.

Irradiation of bone may severely weaken it, particularly with respect to toughness, when dosages reach 60 kGy. Dosages below 20 kGy appear to have little effect on strength, but are also ineffective against HIV. Unfortunately, the intermediate dosages present uncertainty with respect to both mechanical effects and antiviral efficacy. A similar situation exists with regard to thermal inactivation of HIV in allograft bone. There appears to be a narrow window of temperature near 60°C within which viruses can be destroyed without damaging the mechanical integrity of the bone. The effect of treating bone with methanol–chloroform mixtures has not been studied sufficiently to reach any useful conclusions.

Acknowledgments

The authors thank Drs. Steven Olson and Larry Rose for their helpful advice.

References

1. Anderson, C., *Manual for the Examination of Bone,* CRC Press, Boca Raton, FL, 1982.
2. Greenberg, S. W., Gonzalez, D., Gordjian, E. S., and Thomas, L. M., Changes in physical properties of bone between the *in vivo,* freshly dead, and embalmed conditions, *The Twelfth Stapp Car Crash Conference Proceedings,* Society of Automotive Engineers, New York, 1968, 271.
3. Black, J., Dead or alive: the problem of *in vitro* tissue mechanics, *J. Biomed. Mater. Res.,* 10, 377, 1976.
4. Black, J., Tissue properties: relationship of *in vitro* studies to *in vivo* behavior, in *Natural and Living Biomaterials,* Hastings, G. W. and Ducheyne, P., Eds., CRC Press, Boca Raton, FL, 1984, 5.
5. Currey, J. D., The mechanical consequences of variation in the mineral content of bone, *J. Biomech.,* 2, 1, 1969.
6. Gustafson, M. B., Martin, R. B., Gibson, V., Storms, D. H., Stover, S. M., Gibeling, J., and Griffin, L., Calcium buffering is required to maintain bone stiffness in saline solution (technical note), *J. Biomech.,* 29, 1191, 1996.
7. Dickson, G. R., Chemical fixation and the preparation of calcified tissues for transmission electron microscopy, in *Methods of Calcified Tissue Preparation,* Dickson, G. R., Ed., Elsevier, New York, 1984, 79.
8. Frost, H. M., Some aspects of the mechanics and dynamics of blood-bone interchange, *Henry Ford Hosp. Med. Bull.,* 8, 36, 1960.
9. Stevens, J. and Ray, R. D., An experimental comparison of living and dead bone in rats. I. Physical properties, *J. Bone Joint Surg.,* 44B, 412, 1962.
10. Weaver, J. K., The microscopic hardness of bone, *J. Bone Joint Surg.,* 48-A, 273, 1966.
11. Tennyson, R. C., Ewert, R., and Niranjan, V., Dynamic viscoelastic response of bone, *Exp. Mech.,* 12, 502, 1972.
12. Fitzgerald, E. R., Postmortem transition in the dynamic mechanical properties of bone, *Med. Phys.,* 4, 49, 1977.
13. Brown, N., Saputa, C., and Black, J., Young's modulus of living human bone, *Trans. Orthop. Res. Soc.,* 6, 41, 1981.
14. Ashman, R. B., Donofrio, M., Cowin, S. C., and VanBuskirk, W. C., Portmortem changes in the elastic properties of bone, *Trans. Orthop. Res. Soc.,* 7, 63, 1982.
15. Caler, W. E. and Carter, D. R., Bone creep-fatigue damage accumulation, *J. Biomech.,* 22, 625, 1989.
16. Linde, F. and Sorensen, H. C. F., The effect of different storage methods on the mechanical properties of trabecular bone, *J. Biomech.,* 26, 1249, 1993.
17. Bright, R. W. and Burchardt, H., The biomechanical properties of preserved bone grafts, in *Osteochondral Allografts: Biology, Banking, and Clinical Applications,* Friedlaender, G. E., Mankin, H. J., and Sell, K. W., Eds., Little, Brown, Boston, 1983, 241.
18. Frankel, V. H., *The Femoral Neck. Function. Fracture Mechanism. Internal Fixation. An Experimental Study,* Almqvist and Wiksell, Goteborg, Sweden, 1960.
19. Sedlin, E. D., A rheological model for cortical bone, *Acta Orthop. Scand.,* 83, 1, 1965.
20. Sonstegard, D. A. and Matthews, L. S., Mechanical property dependence on storage technique and locale of knee joint trabecular bone, *Trans. Orthop. Res. Soc.,* 2, 283, 1977.
21. Pelker, R. R., Friedlaender, G. E., and Markham, T. C., Biomechanical properties of bone allografts, *Clin. Orthop. Relat. Res.,* 174, 54, 1983.
22. Pelker, R. R., Friedlaender, G. E., Markham, T. C., Panjabi, M. M., and Moen, C. M., Effects of freezing and freeze-drying on the biomechanical properties of rat bone, *J. Orthop. Res.,* 1, 405, 1984.
23. Kang, J. S. and Kim, N. H., The biomechanical properties of deep freezing and freeze drying bones and their biomechanical changes after *in vivo* allograft, *Yonsei Med. J.,* 36, 332, 1995.
24. Roe, S. C., Pijanowski, G. J., and Johnson, A. L., Biomechanical properties of canine cortical bone allografts: effects of preparation and storage, *Am. J. Vet. Res.,* 49, 873, 1988.
25. Goh, J. C., Ang, E. J., and Bose, K., Effect of preservation medium on the mechanical properties of cat bones, *Acta Orthop. Scand.,* 60, 465, 1989.

26. Borchers, R. E., Gibson, L. J., Burchardt, H., and Hayes, W. C., Effects of selected thermal variables on the mechanical properties of trabecular bone, *Biomaterials,* 16, 545, 1995.
27. Griffon, D. J., Wallace, L. J., and Bechtold, J., Biomechanical properties of canine corticocancellous bone frozen in normal saline solution, *Am. J. Vet. Res.,* 56, 822, 1995.
28. Huss, B. T., Anderson, M. A., Wagner-Mann, C. C., and Payne, J. T., Effects of temperature and storage time on pin pull-out testing in harvested canine femurs, *Am. J. Vet. Res.,* 56, 715, 1995.
29. Hamer, A. J., Strachen, J. R., Black, M. M., Ibbotson, C. J., Stockley, I., and Elson, R. A., Biomechanical properties of cortical allograft bone using a new method of bone strength measurement. A comparison of fresh, fresh-frozen and irradiated bone, *J. Bone Joint Surg.,* 78B, 363, 1996.
30. Kang, Q., Yuehuei, H., and Friedman, R. J., Effects of multiple freeze-thawing cycles on ultimate indentation load and stiffness of bovine cancellous bone, *Am. J. Vet. Res.,* 58, 1171, 1997.
31. Wohl, G., Goplen, G., Ford, J., Novak, K., Hurtig, M., McPherson, R., McGann, L., Schachar, N., and Zerniche, R. F., Mechanical integrity of subchondral bone in osteochondral autografts and allografts, *Can. J. Surg.,* 41, 228, 1998.
32. Schenk, R. K., Olah, A. J., and Herrmann, W., Preparation of calcified tissues for light microscopy, *Methods of Calcif. Tissue Preparation,* Dickson, G. R., Ed., Elsevier, New York, 1984, 1.
33. Ashman, R. B., Ultrasonic Determination of the Elastic Properties of Cortical Bone: Techniques and Limitations, doctoral thesis, Tulane University, New Orlean, LA, 1982.
34. Sedlin, E. D. and Hirsch, C., Factors affecting the determination of the physical properties of femoral cortical bone, *Acta Orthop. Scand.,* 37, 29, 1966.
35. Edmondson, S. J., Singer, K. P., Day, R. E., Breidahl, P. D., and Price, R. I., Formalin fixation effects on vertebral bone density and failure mechanics: an *in-vitro* study of human and sheep vertebrae, *Clin. Biomech.,* 9, 175, 1994.
36. Calabrisi, P. and Smith, F. C., The effects of embalming on the compressive strength of a few specimens of compact bone, *Naval Med. Res. Inst. Memo. Rep.,* 51-2, 1, 1951.
37. McElhaney, J. H., Fogle, J., Byars, E., and Weaver, G., Effect of embalming on the mechanical properties of beef bone, *J. Appl. Physiol.,* 19, 1234, 1964.
38. Evans, F. G., *Mechanical Properties of Bone,* Charles C Thomas, Springfield, IL, 1973.
39. Ziran, B. H., Sharkey, N. A., Smith, T. S., Wang, G., and Chapman, M. W., Modified transverse locking nail fixation of proximal femoral fractures, *Clin. Orthop. Relat. Res.,* 339, 82, 1997.
40. Porta, D. J., Kress, T. A., Fuller, P. M., and Snyder, J. N., Fractures of experimentally traumatized embalmed versus unembalmed cadaver legs, *Biomed. Sci. Instrum.,* 33, 423, 1997.
41. Pelker, R. R. and Friedlaender, G. E., Biomechanical considerations in osteochondral grafts, in *Bone and Cartilage Allografts: Biology and Clinical Applications,* Friedlaender, G. E. and Goldberg, V. M., Eds., American Academy of Orthopaedic Surgeons, Park Ridge, IL, 1990, 155.
42. Friedlaender, G. E., Guidelines for banking osteochondral allografts, in *Osteochondral Allografts: Biology, Banking, and Clinical Applications,* Friedlaender, G. E., Mankin, H. L., and Sell, K. W., Eds., Little, Brown, Boston, 1983, 177.
43. Triantafyllou, N., Sotiropoulos, E., and Triantafyllou, J. N., The mechanical properties of the lyophylized and irradiated bone grafts, *Acta Orthop. Belg.,* 41, 35, 1975.
44. Bright, R. W. and Burstein, A. H., Material properties of preserved cortical bone, *Trans. Orthop. Res. Soc.,* 7, 210, 1978.
45. Malinin, T., Latta, L., Milne, E., Saitoh, S., Winter, R., Flores, A., and Buck, B., Effects of freeze-drying on the flexural strength and notch sensitivity of human femoral diaphysis, *Trans. Orthop. Res. Soc.,* 14, 112, 1989.
46. Simonian, P. T., Conrad, E. U., Chapman, J. R., Harrington, R. H., and Chansky, H. A., Effect of sterilization and storage treatments on screw pullout strength in human allograft bone, *Clin. Orthop. Relat. Res.,* 302, 290, 1994.
47. Conrad, E. U., Ericksen, D. P., Tencer, A. F., Strong, D. M., and MacKenzie, A. P., The effects of freeze-drying and rehydration on cancellous bone, *Clini. Orthop. Relat. Res.,* 290, 279, 1993.

48. Burchardt, H., Jones, H., Glowczewskie, F., Rudner, C., and Enniking, W. F., Freeze-dried allogeneic segmental cortical-bone grafts in dogs, *J. Bone Joint Surg.,* 60-A, 1082, 1978.
49. Spira, E., Brenner, H. T., and Lubin, E., Extracorporeal irradiation of malignant bone tumors, in *Operative Treatment of Bone Tumors,* Chapchal, G., Ed., Thieme Verlag, Stuttgart, 1970, 136.
50. Uyttendaele, D., DeSchryver, A., Claessens, H., Roels, H., Berkvens, P., and Mondelaers W., Limb conservation in promary bone tumors by resections, extracorporeal irradiation and re-implantation, *J. Bone Joint Surg.,* 70-B, 348, 1988.
51. Nemzek, J. A., Arnoczky, S. P., and Swenson, C. L., Retroviral transmission in bone allotransplantation. The effects of tissue processing, *Clin. Orthop. Relat. Res.,* 324, 275, 1996.
52. Jackson, D. W., Windler, G. E., and Simon, T. M., Intraarticular reaction associated with the use of freeze-dried, ethylene oxide sterilized bone-patellar tendon-bone allografts in the reconstruction of the anterior cruciate ligament, *Am. J. Sports Med.,* 18, 1, 1990.
53. Jorgenson, S. S., Lowe, T. G., France, J., and Sabin, J., A prospective analysis of autograft versus allograft in posterolateral lumbar fusion in the same patient: a minimum of 1-year followup in 144 patients, *Spine,* 19, 2048, 1994.
54. VanWinkle, W., Borick, P. M., and Fogarty, M., Destruction of radiation-resistant micro-organisms on surgical sutures by 60 Co-irradiation under manufacturing conditions, in *Radiosterilization of Medical Products. Proceedings of a Symposium,* Budapest, June 5–9, 1967, and Recommended Code of Practice, International Atomic Energy Agency, Vienna, 1967, 169.
55. Fideler, B. M., Vangsness, C. T., Moore, T., Li, Z., and Rasheed, S., Effects of gamma irradiation on the human immunodeficiency virus, *J. Bone Joint Surg.,* 76-A, 1032, 1994.
56. Komender, A., Influence of preservation on some mechanical properties of human Haversian bone, *Mater. Med. Pol.,* 8, 13, 1976.
57. Anderson, M. J., Keyak, J. H., and Skinner, H. B., Compressive mechanical properties of human cancellous bone after gamma irradiation, *J. Bone Joint Surg.,* 74-A, 747, 1992.
58. Currey, J. D., Foreman, J., Laketic, I., Mitchell, J., Pegg, D. E., and Reilly, G. C., Effects of ionizing radiation on the mechanical properties of human bone, *J. Res.,* 15, 111, 1997.
59. Voggenreiter, G., Ascherl, R., Blumel, G., and Schmit-Neuerburg, K. P., Extracorporeal irradiation and incorporation of bone grafts, *Acta Orthop. Scand.,* 67, 583, 1996.
60. Salehpour, A., Butler, D. L., Proch, F. S., Schwartz, H. E., Feder, S. M., Doxey, C. M., and Ratcliffe, A., Dose-dependent response of gamma radiation on mechanical properties and related biochemical composition of goat bone-patellar tendon-bone allografts, *J. Orthop. Res.,* 13, 898, 1995.
61. Grant, R. A., Cox, R. W., and Kent, C. M., The effects of gamma irradiation on the structure and reactivity of native and cross-linked collagen fibres, *J. Anat.,* 115, 29, 1973.
62. Jepsen, K. J., Goldstein, S. A., Kuhn, J. L., Schaffler, M. B., and Bonadio, J., Type I collagen mutation compromises the post-yield behavior of Mov13 long bone, *J. Orthop. Res.,* 14, 493, 1996.
63. Martin, R. B., A mathematical model for fatigue damage repair and stress fracture in osteonal bone, *J. Orthop. Res.,* 13, 309, 1995.
64. Thoren, K., Aspenberg, P., and Thorngren, K.-G., Lipid-extraction decreases the specific immunologic response to bone allograft in rabbits, *Acta Orthop. Scand.,* 64, 44, 1993.
65. Thoren, K., Aspenberg, P., and Thorngren, K.-G., Lipid-extracted bank bone. Bone conductive and mechanical properties, *Clin. Orthop. Relat. Res.,* 311, 232, 1995.
66. McDougal, J. S., Martin, L. S., Cort, S. P., Mozen, M., Heldebrant, C. M., and Evatt, B. L., Thermal inactivation of the acquired immunodeficiency syndrome virus, human T lymphotropic virus-III lymphadenopathy-associated virus, with special reference to antihemophilic factor, *J. Clin. Invest.,* 76, 875, 1985.
67. Spire, B., Dormont, D., Barre-Sinoussi, F., Montagnier, L., and Chermann, J. C., Inactivation of lymphadenopathy-associated virus by heat, gamma rays, and ultraviolet light, *Lancet,* 1(8422), 188, 1985.

68. Sharkey, N. A., Hollstein, S. B., and Martin, R. B., Thermal inactivation of HIV in cadaveric specimens: biomechanical effects on bone, in *Transactions of the Combined Meeting of the Orthopaedic Research Societies of the USA, Japan, and Canada,* Oct. 21–23, 279, 1991.
69. Zimmerman, R., Bechtold, J. E., Eastlund, D. T., and Bianco, P. T., Effect of pasteurization on the mechanical properties of human cancellous bone, *Proceedings of the Second North American Congress on Biomechanics,* Aug. 24–28, Chicago, 17, 1992.
70. VonGarrel, T. and Knaepler, H., Thermal incubation of allogenic bone transplants, *J. Bone Joint Surg.,* 75-B Suppl. II, 107, 1993.
71. Knaepler, H., VonGarrel, T., Seipp, H. M., Ascherl, R., and Gotzen, L., Autoklavierung von allogenen Knochentransplantaten als Alternative zur konventionellen Knochenbank? *Orthop. Prax.,* 1, 18, 1992.
72. Kuhne, J. H., Bartl, R., Hammer, C., Refior, H. J., Janssen, V., and Zimmer, M., Moderate heat treatment of bone allografts. Experimental results of osteointegration, *Arch. orthop. Trauma Surg.,* 112, 18, 1992.
73. Hofmann, C., VonGarrel, T., and Gotzen, I., The use of a thermic disinfection system for allogenic bone banking, *J. Bone Joint Surg.,* 77-B, 225, 1995.
74. Jackson, D. S., Ayad, S., and Mechanic, G., Effect of heat on some collagen cross-links, *Biochim. Biophys. Acta,* 336, 100, 1974.

IV

Flow of Fluids in Bone

21

Blood Flow in Bone

Howard Winet
Orthopaedic Hospital and University of California at Los Angeles

21.1 Organization of Bone Vasculature

Bone blood flow studies have long been driven by the need to know which vessels could be sacrificed during surgery without compromising the bone of interest. The routine use of internal fixation devices, which began in the 1950s with development of the Charnley hip,[1] required reaming and plating of the bone, and concern arose over the effects of loss of blood vessels from these procedures. Angiography was the principal investigative tool used to study this problem because the technique had a 200-year history of application to normal bone blood supply. Extending the pioneering angiography study of Albinus,[2] who in 1754 was the first to inject a form of ink into cortical vessels, Brookes and Harrison,[3] Crock,[4,5] Kelly,[6] Rhinelander,[7] and Trueta[8] injected India ink, barium sulfate, or radiopaque latex into nutrient vessels feeding various bones, primarily tibias and femurs. The goal of these studies was to determine where blood goes and what kinds of vessels carry it. Brookes incorporated some of these studies and more physiological results into his definitive tome on blood supply of bone which was first published in 1971[9] and revised in 1998.[2]

21.1.1 Circulatory Morphology

That the dead bone of fossils is a far cry from its vascularized living counterpart has been known at least since 1674 when van Leeuwenhoek described periosteal veins (not visible in dried dead bone) and Volkmann canals (without using these terms, of course) in cow tibias.[10] It was not until 1875 that a definite map of bone circulatory morphology was established by Langer, who perfused human cadaver bones with Prussian blue + vermilion and reconstructed a primitive three-dimensional picture from tissue sections.[10]

As it progresses through a typical organ, blood traverses the following vascular levels: arteries → arterioles → arteriolar capillaries → capillaries → venular capillaries → venules → veins. Precapillary vessels are "afferent," characterized by increase in branch number. Postcapillary vessels are "efferent," characterized by merging of branches. There are no hard rules about vessel size, so the caliber ranges presented should not be used for modeling. The largest are arteries ($>50\ \mu$m) and veins ($>60\ \mu$m). But some arterioles (10 to 50 μm) and venules (10 to 60 μm) may have larger calibers than smaller arteries and veins, respectively. Similarly, some capillaries ($<10\ \mu$m) may exceed the calibers of small arterioles and venules. The critical determinant of vessel identity (second to flow direction relative to the heart) is wall structure.

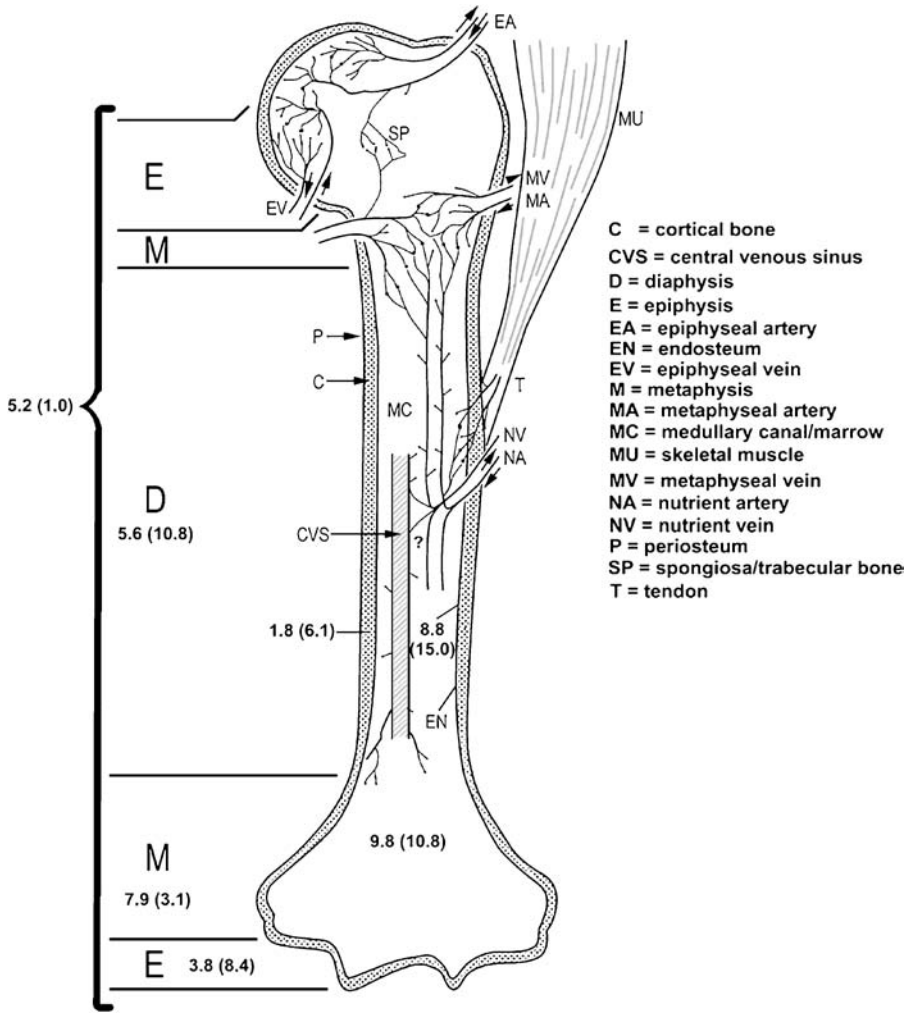

FIGURE 21.1 Idealized afferent and efferent vascular subsystems feeding a typical mature long bone. Note that veins and arteries penetrating the bone surface are concomitant (paired in proximity). This drawing is diagrammatic, with no attempt made to include the entire structure or preserve its scale. Periosteal arteries and veins are continuous not only with tendon vessels, but also with those of fascia (not shown) and branches of the metaphyseal subsystem. Cartilage that covers bone within the joint has no vasculature. It must obtain nutrients from subchondral bone vessels, synovium, and meniscus (at side of joint space and not shown, but vessels that feed them are suggested). Numbers in parentheses are Q (volumetric flow rate) in $cm^3/min/100$ g tissue, the standard representation of bone blood supply. Other numbers are vascular volume in $cm^3/100$ g. Values are from growing dogs. Adult pigs yield 8, 7, 14, and 4 $cm^3/min/100$ g for Q of total femur, cortex, cancellous bone, and marrow, respectively.[120]

21.1.1.1 Afferent Vessels: Arteries and Arterioles

Larger arteries have walls with smooth muscle thick enough to require its own blood supply, the intima circulation, fed by branches usually coming from adjacent soft tissue. Arterioles have thinner walls and relatively thin layer(s) of smooth muscle with no intima. The classical model for bone circulation is based on the angiography studies cited above and summarized in Fig. 21.1. A typical mature long bone is supplied by four afferent vessel subsystems: (1) nutrient, (2) epiphyseal, (3) metaphyseal, and (4) periosteal arteries. Calvaria (skull), ribs, and other flat bones, which carry little load; vertebrae and pelvic bones, which have more complex geometry; and foot and hand nondigit bones, which are nonelongated, show differences

in vascular pattern easily traced to their mechanical environment. That is, they tend to orient parallel with the major tension vector. But accumulating evidence supports the notion that this effect has more of a fluid than a solid mechanical basis.[11] Accordingly, capillaries in cortical bone are in Haversian canals which are predominantly parallel with the bone long axis in tibias and ribs. Orientation of this long axis is largely determined embryologically by the *in utero* mechanical environment,[12] and Haversian canal formation is determined throughout life by remodeling cells responding to mechanical stimuli.[13] Such ancillary issues as the direct influence on angiogenesis of vessel stretching by soft tissue adjacent to bone, which shares the same vessels, have apparently not been studied.

Brookes has extensively reviewed developmental and mature vascular patterns in these bones,[2] concluding that afferent patterns vary between mature and immature individuals. After the embryological transformations, that culminate at birth, the growth plate, which acts as a barrier between epiphysis and metaphysis, does not disappear until late adolescence. While the plate is present, the epiphysis and metaphysis must depend upon themselves for blood. With disappearance of the growth plate at skeletal maturity, vasculature between the two physes becomes well anastomosed (linked) and the epiphysis can "borrow" blood from its neighbor, as indicated in Fig. 21.1. Bones in elderly subjects tend to be less mineralized and more osteoporotic, with reduced vasculature, primarily in the medullary canal; although periosteal blood supply increases.[2]

Epiphyseal blood vessels are subchondral (just below joint cartilage) and can be expected to be strongly influenced by joint pressures. They penetrate bone well below the joint, avoiding impingement by articulating surfaces. They give off circling branches and are one source of nutrition for joint cartilage—by transport through the extravascular matrix, since cartilage has no vessels—and subchondral bone. Porous flow models for this transport have been developed by Knight and Levick.[14–19]

Metaphyseal arteries enter near the base of the condyles (knobby part of long bone ends). After penetrating a relatively thin cortical layer, their branches (1) feed trabecular bone and (2) anastomose with epiphyseal microvasculature, or anastomose with nutrient artery microvasculature as indicated in Fig. 21.1. Since blood must flow down, a pressure gradient at the anastomoses and local conditions may change gradient directions, the flow arrows in the figure merely show an *initial* tendency for the vessel indicated. Microvascular branches to trabeculae remain on the trabecular endosteal (facing the medullary canal) surface unless spicule width is greater than about 200 μm.[20] Thicker trabeculae get additional vessels down their centers from adjacent cortical bone. It is not clear how much diaphyseal medullary blood supply comes from metaphyseal afferents in healthy mature bone. Shaw[21] found evidence in the cat that it is a significant fraction.

The nutrient arteries (generally no more than two), which were first described by Havers in 1691,[10] penetrate through a foramen near the midpoint in the diaphysis (shaft), as shown in Fig. 21.1. In the thigh the nutrients arise from the profunda femora[20] and in the leg from the posterior tibial arteries.[22] A typical human nutrient artery supplies about 20% of the total tibial blood supply.[23] It gives off no branches until well within the medullary canal. There it bifurcates into superior (upward) and inferior (downward) branches, which divide to produce the nutrient network as is shown in Fig. 21.2.

It is generally accepted from angiographic and injected latex cadaver studies that in humans each of the nutrient bifurcations branch into two subnetworks: (1) medullary afferent (branches remaining in the medullary canal) and (2) cortical afferent (branches penetrating the cortex). All along the length of a nutrient bifurcation cortical afferent branches penetrate the endosteal surface and subdivide into capillaries, which follow Haversian canals, primarily parallel with the bone long axis. There is an apparent radial gradient of vascular size, with larger calibers more prevalent near the endosteal surface.[22] However, Brookes has challenged the techniques that led to observations underlying these conclusions. His criticisms are worth noting because they reveal the primitive state of research into bone vascularity. They range from failure to monitor animal age to assuming perfusion of all microvasculature by injected media. Indeed, a study by Albrektsson[24] of injected India ink and micropaque (barium sulfate) suspensions (particle sizes 1.0 μm or less), which have much lower interfacial tensions than microfil (latex), showed a filling incidence of about 47% with India ink and 33% with micropaque, for vessels with calibers less than 30 μm.

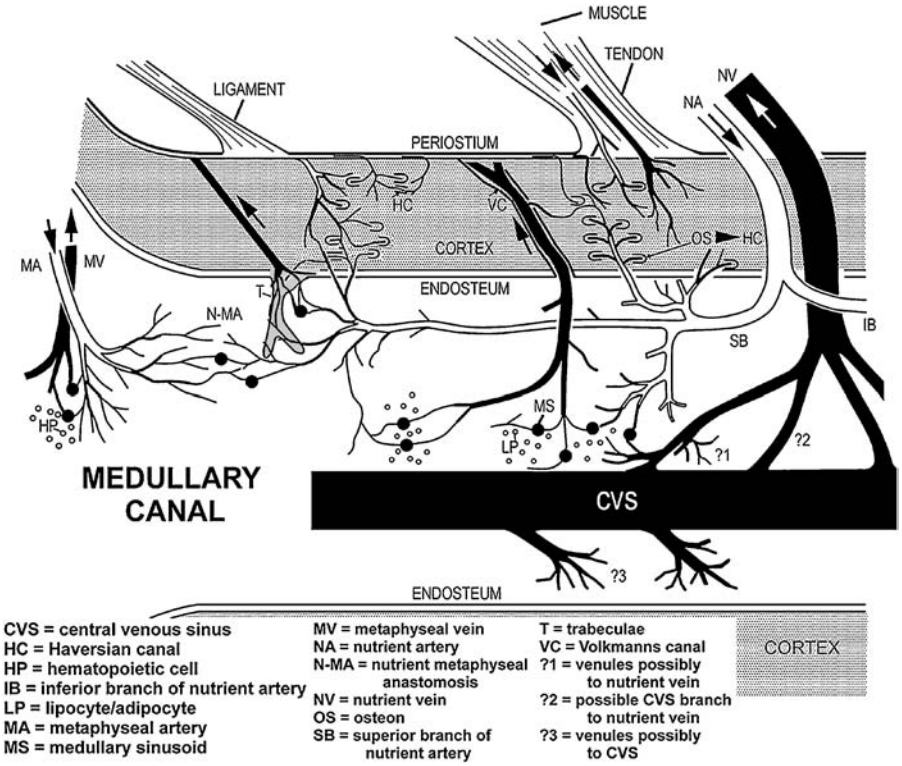

FIGURE 21.2 Simplified anatomical relationships of vasculature within a typical long bone. Focus is on diaphysis near its junction with the metaphysis. Fascia (not shown) and tendons provide most of periosteal circulation. Nutrient artery is major afferent for epiphyseal cortical bone and circulates in retrograde (making a U-turn; a direction opposite to its direction when it entered the bone) fashion. The "?" (adjacent to numbers near CVS) denotes unclear relationships among medullalry canal microcirculation, central venous sinus, and branches to the nutrient vein as summarized by Oni et al.[121] Within the cortex, some osteons (OS, which have a $\subset$ or $\supset$ shape) and a Haversian canal (HC) are diagrammed. Osteons are the multicellular modules that form a Haversian canal and remain at its center as a basic multicellular unit (BMU) as long as it remodels. Osteons near the endosteum may be larger than those near the periosteum. Only one branched trabeculum (T) is shown. Note that its trunk has a Haversian canal (identifiable from vessels down its center) indicating a trabecular thickness is greater than 200 μm. The thinner trabeculae have vessels only on their endosteal (facing the medullary canal) surface. In the medullary canal adipocytes (LP = fat cells) are abundant, as are sinusoids (MS). In contrast to the yellow marrow-endowed (high in lipocytes) diaphysis, red marrow (high in hematopoietic cells, HP) is more prevalent in the metaphysis, indicating a greater concentration of hematopoietic tissue, which produces nearly all the blood cells (RBCs, leukocytes, etc.), osteoclast precursors, and mesenchymal stem cells, which become fibroblasts, endothelial cells, pericytes, and osteoblasts.

The medullary blood supply has traditionally been left to hematologists as the two fields avoided overlapping. However, orthopedic disease states, particularly ischemic osteonecrosis (ION, formerly known as "avascular necrosis") have been shown to involve bone marrow circulation to such an extent that its conceptual segregation is not logical. Vessels branching from the medullary nutrient afferents are surrounded by lipocytes (fat cells, adipocytes) and mesenchymal stem and stromal cells, which give rise to red blood cells, platelets, bone cell progenitors, and most leukocytes. As would be expected, vascularity is greater in red marrow, which tends to be increasingly limited to the metaphysis with age, than yellow marrow, which surrounds vessels with fat cells and tends to occupy the diaphysis increasingly with age.[25] Arterioles are evident[2] and innervated[26] in the medullary canal. They branch to form capillaries that become sinusoids on their venular side as is indicated in Figure 21.2.

21.1.1.2 Efferent Vessels: Venules and Veins

Efferent vasculature usually begins with venular capillaries. These have unevenly spaced smooth muscle cells and no valves. There is some disagreement about the definition of efferent vessels in Haversian canals. Heppenstall[27] contends there are venules. However, most investigators consider all such vessels capillaries because they have no smooth muscle cells over their endothelium.[28] Otherwise, venules and veins (which have valves and continuous, but thin layers of smooth muscle) are evident throughout cortical bone and the medullary canal.

Although the existence of marrow veins has been known since Bizzozero's demonstration of them in 1868,[10] efferent circulation pathways are still a subject of controversy.[2] Angiography has revealed little of the detail of bone efferent vessel circulation. A combination of India ink and micropaque studies[22] has indicated that efferent vascular volume in bone is six to eight times that of afferent volume.[20,29] This is not an unexpected ratio, given the high distensibility of veins and their consequent role as the body's blood reservoir. Accordingly, one may expect a significant amount of blood pooling unless the incidence of natural blockages in venules is high. There are apparently two blood drainage systems in a long bone,[30] as is indicated in Fig. 21.2. One accepts fluid from nearby interstitium and transports it through cortical Volkmann canals in emissary veins or in "large transcortical venous channels." The emissary veins connect with fascicular or tendon veins at points of attachment and the venous channels apparently supply periosteal venular capillaries that feed into periosteal veins (not shown in the figure). The other drainage system is less clear in its function. It must involve the central venous sinus (CVS), a large longitudinal medullary vessel, and the nutrient vein(s) that is concomitant with the nutrient arter(ies). The CVS is well innervated, but the function of these nerve fibers is unknown.[2] Connection between the CVS and the nutrient vein has not been demonstrated, nor has the drainage from medullary capillaries to the nutrient vein. Location of this vein as a nutrient artery concomitant suggests to Oni and Gregg[30] potential for countercurrent nutrient exchange. The existence of unanswered questions about efferent relationships is indicated by question marks in Fig. 21.1 and 21.2.

21.1.1.3 Microvasculature

Capillaries are the vessels between venules and arterioles that have no smooth muscle cells. Capillaries have one layer of endothelial cells (ECs), 0.1 to 0.5 μm thick[31] and intermittently encircled by single pericytes as shown in Fig. 21.3. They display one of three levels of continuity, which may correlate with permeability depending on opening/pore sizes:

1. Continuous: with continuous basement membranes and ECs overlapping at junctions,
2. Fenestrated: with continuous basement membranes and tenuous EC junctions, and
3. Discontinuous: with holes in basement membranes and clear fissures in EC junctions.[32]

Fenestrated capillaries are characteristic of red marrow and continuous capillaries dominate yellow marrow and cortical bone.[33]

There are essentially two capillary morphologies in bone, linear/continuous and sinusoidal/discontinuous. Haversian canals, which connect vascular channels or Volkmann canals in the cortex, run predominately parallel with the long bone axis. Each contains one or two (sometimes up to four) vessels, which are capillaries or venules,[27] rarely arterioles.[22] Linear capillaries are classically cylindrical with calibers ranging from smaller than 4 μm at the periosteal surface[34] (in the guinea pig) to more than 30 μm[24] elsewhere—presumably the endosteal surface.[22] Transcapillary clefts (4 to 20 nm wide) between ECs[31] and intracellular vesicles have been observed[35] in these vessels. In other tissues linear capillaries have been shown to have functional pores:[36] (1) nonfenestrated continuous capillaries have effective pore sizes at tight junctions of 10 and 50 nm, (2) fenestrated continuous capillaries have additional tight junction pores of 70 nm, and (3) discontinuous capillaries have pores easily permeable to molecules larger than 100 kDa. These "resting" pore sizes may be increased by contraction of EC myosin light-chain kinases sliding on F-actin filaments and pulling adjacent cells apart.[36] Various leukocytes may also create temporary

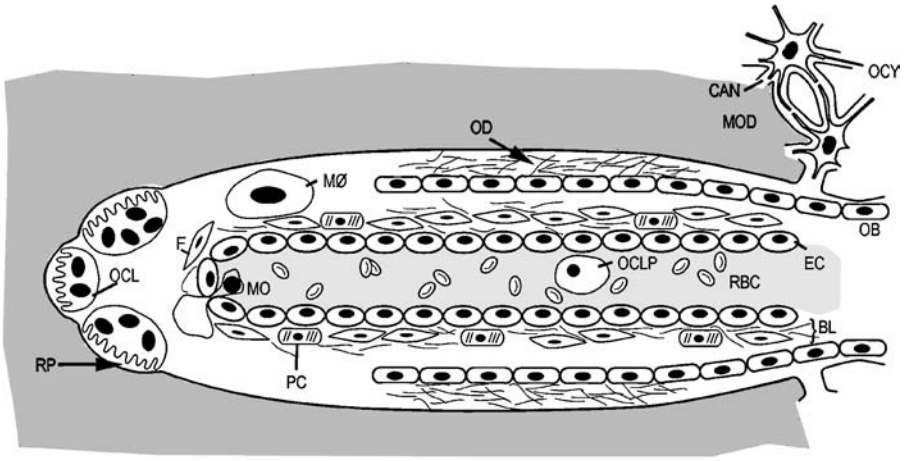

BL = basement membrane
CAN = canaliculus
EC = endothelial cell
F = fibroblast
MO = monocyte (pre-macrophage)
Mϕ = macrophage
MOD = mineralized osteoid
OB = osteoblast
OCL = osteoclast forming Howships lacuna
OCLP = osteoclast precursor (from marrow)
OCY = osteocyte
OD = osteoid
PC = pericyte
RBC = red blood cell
RP = resorption pit

FIGURE 21.3 Diagrammatic osteon. Advancing tip of a single osteon ("cutting cone") when it is the first excavation establishing a Haversian canal. A cutting cone in newly forming bone is a primary osteon, while one in remodeling bone is a secondary osteon. Primary osteons do not align with the long bone axis, nor do they lay down multiple bone layers (lamellae). Thus, they are not harbingers of Haversian canals, as are initial secondary osteons. When a secondary osteon excavates through to a radially oriented vascular channel, a Haversian canal has been completed.

Vessels in an osteon have not been shown to contain smooth muscle, so changes in blood flow controlled by smooth muscle must be initiated by upstream arterioles. In most cases an osteon contains one vessel,[25] which must be sufficiently permeable (at least at its tip) to allow perfusion.

On the basis of required permeability and tendency toward calibers of the order of 20 μm (see Fig. 21.4), it has been proposed that canal vessels be considered sinusoidal.[116] Diameter of an osteon is not the same throughout its length because osteoclasts (OCL) make a large channel which trailing osteoblasts (OB) narrow by laying down concentric cylinders (like stream tubes) of collagen I (osteoid), which become mineralized matrix.[122]

leak points when they exit vessels by crawling between cells, a process termed *diapedesis*. EC intracellular vesicles have been shown to enhance extravasation by carrying macromolecules from their luminal to their abluminal surfaces.[37]

Sinusoids are discontinuous capillaries that occur in the medullary canal. They are bulbous segments 12 to 30 μm in caliber, which allow transport of extravascular cells, platelets, and fat globules into the blood. Their surrounding basal lamina is also discontinuous according to Marshall et al.[38] Brookes, however, suggests that histological studies of sinusoids are suspect because it is extremely difficult to maintain the integrity of sinusoidal walls under the stresses of fixation or the abnormal perfusion pressures used for processing. He allows that the walls are certainly sufficiently tenuous to allow easy intravasation of marrow elements but not porous enough to allow escape of red bloow cells (RBCs).[2] So-called cortical sinusoids have the same morphology as nonfenestrated continuous capillaries. Their name derives from having calibers exceeding 30 μm and no smooth muscle cells.

ECs are capable of constriction because they contain F-actin filaments. These filaments form the backbone of each EC cytoskeleton and are referred to as "stress" fibers.[39] They attach to integrins (transmembrane heterodimer proteins), which function as extracellular matrix receptors and transduce

mechanical into chemical signals. Integrins bind to exposed RGD (R = arginine, G = glycine, D = aspartic acid) amino acid sequences of extracellular glycoproteins such as fibronectin. Members of the integrin family are usually designated by $\alpha_i\beta_j$ where *i* and *j* are code characters, in accordance with their adhesion targets. For example, ECs forming branches during angiogenesis may control their migration rate on a fibronectin-coated matrix by the number of available $\alpha_4\beta_1$ and $\alpha_5\beta_1$ integrin receptors on their contact surface.[40] On their luminal side ECs are covered with a glycocalyx, which contains carbohydrates, proteins, and glycoproteins[32] such as fibronectin (300 μg/ml in plasma[41]). In circumstances where this glycocalyx is covered by a layer of static plasma (a no-slip boundary) the two layers may be thought of as one unstirred layer. On its abluminal or basal laminar (basement membrane) side (see Fig. 21.3) the EC faces an extracellular matrix which features the RGD glycoprotein laminin and the protein collagen IV.[41] Integrins also bind to these matrix molecules.

Until recently it was assumed that ECs are the same in all organs and differences in their behavior may be attributed to their environment. As a consequence, one could extrapolate data from other organs to bone by merely factoring in mechanical or other influences of osseous tissue. There is increasing evidence, however, that endothelium of diverse tissues is inherently different morphologically and developmentally.[42] Efforts to use this difference as a basis for confirming the prediction of Trueta,[43,44] that bone ECs are capable of transformation to pre-osteoprogenitor cells (relatively primitive cells that can become osteoprogenitor cells, the last stage before developmental branching toward chondroblast or osteoblast), have failed.[45]

In contrast, there is evidence that pericytes have the potential to transdifferentiate into pre-osteoprogenitors,[46] a notion also championed by Trueta.[8] They also have contractile ability, which may play a part in local regulation of capillary diameters.[47] The basal lamina is a relatively porous sheath which surrounds and provides some mechanical support for capillaries, as indicated in Fig. 21.3. This abluminal glycocalyx is essentially a "fiber matrix," which moderates capillary permeability.[48] The sheath contains collagen IV and an abundance of the glycoprotein laminin. Nutrient exchange and angiogenesis appear to occur predominantly in microvascular branches where there is a transition from capillary to venule. Such segments are called venular capillaries.

21.1.1.4 Lymphatics

Evidence for lymphatic capillaries below the periosteum is controversial.[20] No lymph vessels have been detected in the medullary canal, trabecular, or cortical bone. Lymphatic uptake of excess fluid is replaced by increased interstitial porosity that is often great enough to constitute "prelymphatic channels," which end in periosteal lymphatic capillaries[33] and which extend into surrounding soft tissue.[28]

21.1.2 Macrocirculation (Veins and Arteries) in a Typical Long Bone

21.1.2.1 Distribution of Blood Flow

Under normal conditions, the skeleton receives about 7 to 10% of cardiac output[23] and the average volumetric flow rate in humans is 5 cm^3/s.[49] For the blood supplied to hind limbs in the two common iliac arteries formed by bifurcation of the abdominal aorta, the volumetric flow rates are undoubtedly higher. It might seem a simple matter to measure distribution of blood from this bifurcation. However, the left and right common iliacs do not completely separate limb blood supplies. Crossover vessels that are undoubtedly acting as collaterals to contralateral (opposite) limbs have been found.[50]

Collateral circulation is an example of evolutionary redundancy. As indicated in Fig. 21.1, three of the four alternative afferent vessel subsystems can act as collaterals to the same long bone cortex (the reference cortex is the diaphysis, which cannot normally be served by the epiphyseal subsystem), an extravagance that may appear to violate the common engineering assumption of optimization. It does not because this redundancy allows bone to survive the test of natural selection: when one afferent pathway is compromised by trauma, its collateral substitutes.

It is generally agreed that under normal conditions, two thirds of diaphyseal cortical volume is serviced by the nutrient network in a normal adult. The other third is serviced by periosteal vessels that originate (1) in fascia and tendons at their bone attachment points or (2) from a nearby artery such as the anterior

tibial artery.[22] Since vessel diameter may be larger in endosteal than in periosteal cortex,[22] the actual blood supply ratio may be greater than 2:1, between the nutrient and periosteal vessels.

When nutrient arteries are traumatized, periosteal vessels act as the first and metaphyseal the second backups. A change in circulation pattern results. Whereas normal flow in the cortex is centrifugal (a term commonly used in orthopedics to mean away from the bone long axis, toward the periosteum), periosteal substitution makes it centripetal (toward the long bone axis).[51] Similarly, diaphyseal afferents in the medullary canal, which normally flow toward the metaphysis, reverse to flow toward the midshaft. Similar shifts occur in the epiphysis. The femur epiphysis normally receives 90% of its blood supply from circumflex arteries that penetrate the femoral head high up on its neck; 10% of blood supply to the same region comes across the middle of the joint from the pelvis, through a ligament (ligamentum teres). Unfortunately, 10% is not good enough and trauma to the circumflex arteries often leads to femoral head death. The relative ease with which bone cortical vessels can reverse their flow is consistent with the dearth of arterioles and consequent absence of nerve endings.

21.1.2.2 Levels of Control of Macrocirculation

Direct control of intravascular convective flow occurs at three levels: (1) nervous, (2) humoral, and (3) local. Like the circulation itself, the nervous system and hormones (conveyed by blood vessels) provide systemic communication between bone organs and the rest of the body. Some humoral agents affect bone microcirculation only, while others act on vessels external to bone. Accordingly, humoral controls as a group define a transition from systemic to local regulation. Local controls are essentially microcirculatory, acting mainly on ECs, pericytes, and arteriolar smooth muscle cells.

21.1.2.2.1 Direct Neuronal (Nervous) Control

Nerves in bone were first described by Gros in 1846,[10] and little was added to the understanding of their role in osseous circulation until Zinn and Griffith described the effect of sympathectomy on blood supply in 1941.[10] Nerve fibers in bone vasculature have been observed only at smooth muscle cells, which are absent in capillaries. Since arterioles are scarce in cortical bone,[2] the nearest upstream neuronal control for cortical microcirculation is in arterioles and arteries of periosteum and the medullary canal. Shaw[21] maintained, "there is no convincing evidence for direct nervous control of blood vessels in bone." More recent observations suggest nervous influence of vasoconstriction and even metabolism. Both adrenergic (release adrenaline/epinephrine, which tends to constrict smooth muscle) and cholinergic (release acetylcholine, which tends to dilate smooth muscle) nerve fibers are found in bone.[52]

Sympathetic control has been studied by stimulation or nerve transection. Evidence was presented by Gross et al.[53] that bone vascular smooth muscle dilated (local blood flow increased without change in cardiac output) when carotid sinus baroreceptors were stimulated, and constricted (local blood flow decreased) when they were denervated. Sciatic nerve transection caused dilation[52] and stimulation constriction[54] of bone vascular smooth muscle in the lower limbs. In none of these studies were vessels observed directly so that one could determine precise location of the affected smooth muscle. However, constriction of vessel diameter by arteriolar smooth muscle has been shown in other organs to be a major contributor to microvascular resistance. Sympathetic nerve fibers containing VIP (vasoactive intestinal peptide) have been found in bone vasculature.[55] It is unlikely, however, that vasodilation is the primary function of these fibers. Osteoblasts are highly responsive to VIP, which, if secreted by the fibers, may provide a mechanism for neural control of bone metabolism.[55] A similar case can be made for recently discovered glutamate (for which bone cells have receptors)-secreting nerve fibers, which occur in the proximity of trabecular bone cells.[56] Studies on isolated arteries from human bone indicate that their adrenergic responses are mediated through α_1 receptors.[57] The high incidence of arterioles in medullary vasculature and low incidence in cortical vasculature suggest that direct nervous control in bone is not a cortical event.[58] It is therefore surprising that adrenergic fibers have been detected in Haversian canals.[55]

21.1.2.2.2 Humoral Control

In order for blood (humorally)-borne agents to control smooth muscle or pericytes directly, they must pass through the endothelium and bind with receptors on their target cells. There is mounting evidence, however, that such a direct pathway is not used.[59] Instead, ECs are the primary target for humoral agents

and are induced to secrete other agents, which diffuse to extravascular cells. Nonlocal (secreted at a distant site) humoral substances affecting vasculature include serotonin, vasopressin, norepinephrine/noradrenaline, epinephrine/adrenaline, adenosine, endothelin, acetylcholine, parathyroid hormone (PTH), calcitonin, estradiol, and testosterone.[2,60] The direct effect of a systemic agent on bone circulation is difficult to study because the source and/or the targets are difficult to compartmentalize. Nevertheless, observations by Brindley et al.[61] have supported Shaw's[21] conclusion that humoral effects on bone vasculature dominate any neuronal influence. Where a single gland is the source (e.g., the parathyroid gland) its removal allows one to establish a baseline for dose-dependent responses. When such removal is life-threatening, the baseline must be maintained at some nonzero value by constant perfusion.

Hormones (agents secreted by endocrine glands) can be studied this way. For bone the important hormones are PTH, a vasodilator[61–63] that tends to increase bone resorption, calcitonin, a vasoconstrictor[64,65] that tends to decrease bone resorption and estrogen, a vasoconstrictor[2] that tends to increase osteoblast activity. Circulating nonhormones adrenaline[66] and noradrenaline induce vasoconstriction, and bradykinin induces dilation of bone vessels.[23] Moreover, Pooley et al.[66] concluded that circulating adrenaline opens shunts between the nutrient artery and central venous sinus.

A primary target for hormonal control of circulation is the smooth muscle cell. Observations by Brindley et al.[61] suggested that the smooth muscle cells affected by PTH were extraosseous. But Verhas et al.[67] found no similar PTH vascular effect in rats. Brånemark (cited in Shaw[21]), using intravital microscopy, directly observed slowing of blood flow in marrow capillaries following intravenous injection of histamine (a mast cell secretion). The effect took 1 to 2 min to be established and started to abate 3 to 4 min later. Osteoblast responses to calcitonin and PTH and their interactions with ECs have been implicated in calcium transport in bone. According to the emerging model, osteoblasts lining an osteon, as shown in Fig. 21.3, can act as an active-transport semipermeable membrane, in effect, a blood–bone barrier.[68] Interstitial calcium pools exist on both the vascular and mineralized matrix sides of the osteoblast layer. Calcium concentration within them would be determined by the osteoblasts, which, by secretion of a local factor, prostacyclin (PGI_2), can cause vasodilation,[69] thereby controlling blood flow and calcium delivery.[65] The relevant target smooth muscle cells in this scenario would be venous.

McCarthy and Hughes,[68] using metabolic inhibitors (KCN), obtained evidence that calcium transport between endothelium and the interstitium was an active (not merely diffusive) process in the presence of PTH. Bone EC receptors to systemic agents may yet be shown to differ inherently from those in other organs in accordance with the observation that endothelium differs from organ to organ.[42] This suggestion does not appear to have been considered in current reviews of bone ECs, which assume that differences between their behavior and that of ECs in other organs are due to their environment of osteoblasts, osteoclasts, etc.[70]

21.1.2.3 Local Control of Microcirculation

Local control/regulation refers to the effects on microcirculation of chemical agents from nearby cells or of physical effects generated locally. The responding cells are smooth muscle cells, pericytes, and ECs. Since all three contain contractile fibers,[71,72] it might seem that determination of which cells cause vessel constriction would be difficult. However, data from other organs indicate that the EC acts as the sensory and the smooth muscle cell the motor device of this stimulus–response mechanism.[72] Three categories of stimulus may be distinguished: (1) local chemical regulation, (2) interactions with blood elements, and (3) fluid mechanical effects of blood. "Local," for purposes here will include adjacent musculoskeletal tissue. Examples of local regulation are presented in Table 21.1

21.1.2.3.1 Local Chemical Regulation

The concept of local chemical regulation of microcirculation differs from humoral control in that the initiating agents are produced locally. The most-studied chemical regulator in the general field of microcirculation is oxygen and its metabolic byproducts, such as CO_2. These metabolites exert their influence

TABLE 21.1 Local Regulation of Blood Flow

Tissue	Agent: Physical	Agent: Metabolic	Agent: Blood	Agent: Eccrine/ Exocrine	Endothelial Cell Response	Effect	Ref.
O				Acetylcholine	NO + PGI_2	Dilation, inhibit	23
O				Angiotensin I	→ Angiotensin II	Constriction	59
O				Bradykinin	Degradation	Dilation	59
O	Pulsatile pressure				PGI_2	Dilation, inhibit	59
O	Trauma		Thrombin		Plasminogen activators	Dissolve thrombi	59
O	Trauma		Thrombo-		Surface change	Coagulation	59
O	Trauma				Endothelins	Constriction	59
O		Acidosis				Dilation	75
O			Thrombin		Endothelins	Constriction	76
O				Angiotensin II	Endothelins	Constriction	76
O				TGF-b	Endothelins	Constriction	76
O	Shear stress				Release of cytosolic Ca^{2+} →	Dilation, increased	36
O		Hypoxia			Endothelins	Constriction	76
B		Alkalosis			Endothelins	Constriction	76
B				Bradykinin	Degradation	Dilation	23
B				Noradrenalin	Endothelins	Constriction	23

Sampling of local blood flow regulation agents. O = other; B = bone. While endocrine/hormonal agents such as PTH may be secreted locally, they are considered humoral and are discussed in the text.

by inducing ECs to secrete NO, PGI_2 endothelin, and other agents from their abluminal surfaces onto adjacent smooth muscle cells or into the extravascular matrix, where they can diffuse to smooth muscle cells. Research on bone endothelium control of microcirculation has emerged only in the last 10 years. Even as late as 1994, a typical review of this tissue was preoccupied with resorption, angiogenesis, and pericytes as potential osteoprogenitors.[70] Studies of bone endothelium regulation of vascular resistance have apparently been performed primarily in the laboratories of M.B. Wood[73–79] and E. Hansen.[23,80] In Wood's *ex vivo* model tibias were isolated and perfused artificially through their nutrient arteries. Norepinephrine and other humoral agents were used to control baseline values and it was assumed that their effects were on smooth muscle cells. However, as has been the case with metabolite studies, no method was employed to separate contractile activities of smooth muscle cells from EC and pericyte contraction, which are affected by the same agents,[36] and resistance, not flow, was observed in this model. Accordingly, their conclusions will be taken to apply to local control as a "gray box" (as opposed to a "black box" since ECs are clearly the target cells). Their results, interpreted as effects on arteriolar smooth muscle, indicated that (1) alkalosis increased constriction and acidosis decreased constriction[79] and (2) ischemia increased constriction.[77]

21.1.2.3.2 Blood Element Regulation

Except where noted, all information in this section comes from nonbone tissue. In smaller vessels, formed blood components will alter bulk viscosity or interact with the vessel wall directly to influence the shear stress sensed by ECs. The ECs may respond by releasing chemical agents that alter flow by acting on smooth muscle cells downstream (or even upstream in a countercurrent system[81]).

Blockage of vessels may result from RBCs, platelets, and/or leukocytes. RBCs have a diameter of about 7.5 μm and are the most numerous blood cells, achieving normal volume fractions (hematocrits) as high as 0.48. They do not by themselves initiate clotting but are trapped in the forming clot matrix. In regions of slow flow, they may form longitudinal stacks called "rouleaux," which alter plasma flow. In capillaries of caliber less than 13 μm they are bent into parachute shapes enhancing their release of O_2. Bone was the

first tissue in which this deformation was observed.[82] In capillaries, where diameters of formed elements are the size order of vessel caliber, blood must be considered a suspension of large interacting bodies rather than a uniform Newtonian fluid. These conditions will considerably increase nonlinearity of constitutive equations in any accurate fluid mechanical model.

Platelets are subcellular and the main elements in blood clots (thrombi). They can secrete active agents called cytokines (chemokines), which influence tissue response to trauma. Their stimulation by platelet activating factor helps start the clotting cascade, which converts the soluble protein prothrombin into a rigid thrombin matrix within which they become entrapped. Their surface contains the complex integrin receptor CD11/CD18, which binds to the glycoprotein E-selectin found on the surface of ECs, to establish the clot focus.

Leukocytes come in may forms, the rheologically most important of which are neutrophils (polymorphonuclear leukocytes, PMNLs or PMNs, the most numerous white cells in blood), lymphocytes, and monocytes. They are roughly twice the size of RBCs (when spread out on a solid surface) and do not form blood clots. Neutrophils may interfere with blood flow in vessels the size of arterioles because they are large and sufficiently numerous to clump. There is evidence that they are a prime cause of stroke.[83] Neutrophils carry integrin receptors for the glycoproteins E-selection and P-selectin, which are on the surface of ECs. Their E-selectin sites are activated by interleukin-1 (IL-1) and tumor necrosis factor (TNF) and their P-selectin sites by histamine and bradykinin, all inflammatory agents. They also contain receptors for immunoglobulin cell adhesion molecules (CAMs), in particular ICAM-1, ICAM-2, and VCAM. In response to blood slowing, as occurs during ischemia, neutrophils become receptive to the selectins and migrate to the endothelium, where they roll. Eventually, the CAM receptors bind to the CAMs and they adhere. A series of events may follow that activates platelets and results in a thrombus. Alternatively, they may be stimulated by chemotactic gradients originating outside the vessel to diapedese past the basal lamina to the extravascular matrix. In an osteon this excursion would place neutrophils in the proximity of osteoclasts or osteoblasts, as indicated in Fig. 21.3. Such a meeting is most likely early in wound healing when neutrophils are plentiful in the extravascular matrix. However, little is known of the resulting interactions. Monocytes are the intravascular form of macrophages that control wound healing, particularly angiogenesis. Some are osteoclast precursors. Lymphocytes have VCAM receptors. Their contributions to control of the microcirculation are less important than macrophages and almost nonexistent when compared with neutrophils. However, they are major players in responses to foreign bodies ranging in size from bacteria to implants. Under these circumstances their influence on blood flow regulation through inflammation and immune reactions (cell-mediated and humoral) may be profound.

21.1.2.3.3 Fluid Mechanical Regulation

Microcirculation is also controlled by mechanical factors. The hydrostatic pressure derived from heart muscle pumping and gravity not only creates a flow-maintaining pressure gradient, but also may subject ECs of the vessel wall to circumferential tension, which will evoke a stretch response. If intravascular hydrostatic pressure increases enough to stretch the endothelium significantly, tight junctions will open up, allowing macromolecules larger than 50 nm to extravasate. Transluminal hydraulic conductivity will increase, flooding extravascular spaces, and, unless prelymphatic channels and lymph capillaries can siphon off this excess, the tissue will swell, producing edema. Bone, because of its rigidity, allows virtually no swelling and the absence of lymphatic capillaries below the periosteum level assures that under the conditions described extravascular bone pressure will rise. Given the large pooling capacity of bone venous volume (six to eight times that of arterial volume[20,29]), this scenario might seem baseless. Patients suffering from bone marrow edema syndrome (BMES), however, provide evidence that vascular efflux can indeed be blocked in bone. There is evidence that under certain conditions (e.g., hyperlipidemia) the venular capillaries, particularly where sinusoids are plentiful, become engorged with fat globules (from adipocytes)—in effect fat emboli—which can block vessels downstream,[84] in spite of the fact that efflux vessels tend to increase in caliber as one progresses to veins. One explanation for this apparent paradox is that the decrease in flow caused by initial formation of the emboli stimulates downstream neutrophils to adhere to endothelial walls thereby *decreasing* the effective vessel caliber.

How do neutrophils "know" they are in slow-moving plasma? Amoeba-like, deformable cells, neutrophils sense the shear rate du/dr (with u the fluid particle velocity and r the distance from the tube center) as they cross stream tubes in vessels less than ten times their diameter. The same velocity profile includes a vessel wall lined with ECs, which feel the resultant change in shear stress τ in proportion to fluid viscosity η, or

$$\tau = \eta(du/dr) \tag{21.1}$$

As noted above, η is not constant in vessels with the calibers of interest. The presence of deformable cells and remnants of pulsatile waves (from heartbeat and/or upstream vascular smooth muscle responses to systolic pressure waves) create a non-Newtonian fluid, which force any linearized fluid mechanical analysis of microcirculation to be classified as an approximate model.

Although the effects of fluid shear stress on bone ECs has apparently not been studied, advances in this subject have been revolutionary for understanding the phenomenon in other organs, particularly coronary arteries. With all other things equal, vessels respond to increased shear stress by dilating. The resulting reduction in τ maintains strain homeostasis. A summary of biochemical events that accompany this response is presented in Table 21.1. Shear stress at the EC surface is transduced into biochemical signals by membrane-bound mechanoreceptors and strain of the underlying cytoskeleton. The mechanical component of signal transmission is known as "tensegrity" and it encompasses the extra- as well as the intra (i.e., cytoskeletal)-cellular matrices. These two structural domains are connected through integrin receptors to define a tensegrity domain. Glycoproteins on EC luminal surfaces may be considered a part of the tensegrity domain. However, the blood flowing over them is not.

By extrapolating from studies in other organs, one can expect that bone ECs are "nonexcitable."[85] Nevertheless, fluid shear between 0.08 and 8 dyn/cm^2 causes elevation of cytosolic free CA^{2+} in the presence of external ATP.[36] The Ca^{2+} does not originate externally and is associated with an increase in cytosolic inositol phosphate. Generation of this metabolite can be traced to activation of cell surface receptors which, in the presence of 2 dyn/cm^2 in veins or 20 to 60 dyn/cm^2 in arteries activates the G protein–phospholipase C pathway.[36] The pathway may be approximated (molecule names simplified and only one reaction product named at each step):

$$\text{Receptor} \rightarrow \text{G-protein} \rightarrow \text{phospholipase C} \rightarrow \text{phospatidylinositol biphosphate} \rightarrow \text{inositol phosphate} \rightarrow \text{release of sequestered } Ca^{2+}.[36]$$

The released Ca^{2+} becomes available to F-actin stress fibers, which connect integrin receptors in the cell membrane to the nuclear membrane, where signal transduction appears to result in gene expression.[85] Indeed, there is evidence that shear stresses as small as 0.5 dyn/cm^2 activate kinases for the c-jun protooncogene and 25 dyn/cm^2, considered an "arterial" magnitude, can induce c-fos activity.[85] Both of these protoonocogenes control gene expression. The mechanics of signal transmission from RGD proteins in the extracellular matrix to the receptive genes in the EC nucleus is being examined *in vitro* using tensegrity models.[86] Are these phenomena in ECs of other organs reflected in bone? Do they have counterparts in other bone cells such as osteocytes? The latter question is discussed by Burger in Chapter 28.

There is substantial evidence that cytosolic free calcium controls (1) movement of solutes across the vessel wall and secretion of (2) nitric oxide (NO), (3) PGI_2, and (4) von Willebrand factor (a carrier for clotting factor VIII, which will not be discussed further).[36] Conditions for NO and PGI_2 stimulation differ. NO secretion results from lower stimulus levels and is less dependent on precursor molecules. Also, its effect lasts longer. However, NO depends more on extracellular and less on intracellular Ca^{2+}. EC secretion of PGI_2 depends almost entirely on increases in intracellular Ca^{2+}. Release of NO and PGI_2 is typically stimulated by ATP, histamine, bradykinin, and thrombin.

Both intra- and extracellular Ca^{2+} strongly influence vascular permeability by causing ECs to contract and open pores at their cell–cell junctions.[36] Thus, permeability of vessels can be controlled directly by hydrostatic pressure and indirectly by fluid shear stress. It may seem paradoxical that NO, which was originally named EDRF (endothelium-derived relaxing factor), would be linked to a contractile process. However, actin-F stress fibers in ECs can be oriented parallel with the vessel long axis while actin in

TABLE 21.2 Duration of Shear-Stress-Induced Responses in Endothelial Cells

From Seconds to Minutes Biomechanical Transduction Stimulates:	Minutes Cytoplasmic-Nuclear Reactions	Minutes to Hours Cytokinetic Responses	Hours to Days Cellular Adaptations
Ion channels	Mitogen-activated protein (MAP) kinase expression → upregulation of transcription factors	Tensegrity amplification of cytoskeleton	Shape changes and realignment
Cytosolic Ca^{2+} release		Stimulation of endothelin-1	Reorganization of cytoskeleton
Second messenger (inositol triphosphate, diacylglycerol) transmission		Downregulation of VCAM-1	Reorganization of cell adhesion attachment pattern
		Endocytosis	Remodeling of extracellular matrix (fibronectin downregulation)
		Mitosis and protooncogene expression	

Compiled from Resnick[119] and Braddock.[85]

Note: Mechanical stimuli may be transduced rapidly, but they are often imposed for periods long enough to induce structural cellular adjustments/adaptations.

smooth muscle cells is oriented more circumferentially. Thus, the latter cells will tend to change vessel diameter while ECs affect its length, to the extent that they do not separate from one another.

One of the important differences between effects of PGI_2 and NO is length of action. Release of PGI_2 ends about 5 min after stimulation by a variety of agents. In contrast, NO release may remain as high as 50% of its initial value 30 min after stimulation. Time length of action must be factored into evaluation of *in vivo* observations of flow-mediated (shear-stress related) endothelial responses. Accordingly, examples are presented in Table 21.2.

21.2 Fluid Mechanical Aspects of Bone Blood Flow

Fluid mechanics in bone circulation has not been addressed rigorously, as an inspection of two classical biofluid dynamics works by Fung[87] and Caro et al.[88] will reveal. As with transport in any organ, there are convective and diffusive modes. Convective fluid mechanical models adhere to Newton's second law of motion in the form of the Navier–Stokes (N–S) equation. This equation states that the total force on each unit volume of fluid is the sum of the various surface (viscosity, pressure, etc.) and body (gravity, magnetism, etc.) forces acting on each element of that volume. Solving the N-S equation in its most general or analytical form is so difficult that it must be simplified to be useful for predicting biological convective flow in tubes. Two useful simplifications/linearizations are based on the Reynolds number (Re), a ratio of inertial (mass–size–velocity) to viscous force magnitudes in the fluid of interest. For higher Re values, the Bernoulli ["principle"[89]] which ignores viscosity, is applied.

$$-1/2\rho\Delta U^2 = \Delta P + \rho g \Delta h \tag{21.2}$$

where ΔU is the difference in characteristic fluid particle velocity ($U_1 - U_2$) between the ends of a tube of length L, ΔP is the hydrostatic pressure difference over L, Δh is the change in height over L, g is gravitational force, and ρ is fluid bulk density. It has been simplified by Caro et al.[88] and integrated to the third dimension to transform U to Q, giving the volumetric flow rate through L as:

$$\Delta P = 1/2\rho Q^2 (1/A_2^2 - 1/A_1^2) \tag{21.3}$$

where A_1 is the influx vessel cross-sectional area and A_2 is the average resistance vessel (or constriction) crosssectional area. At low Re, the Poiseuille equation, which ignores gravity and other body forces,

$$Q = \pi r^4 \nabla P / 8\eta \tag{21.4}$$

where r is tube inner radius, $\Delta P = \Delta P/L$, and η the bulk viscosity, is applied. The biomedical motivation for applying these equations is to predict Q and ΔP in a defined region of bone.

Although such simplifications of the equations of motion have been useful, direct measurement of their parameters in bone vessels has been difficult. Moreover, one must be aware of the simplifying assumptions that enabled such tractability. Accordingly, it is necessary to confirm their validity frequently.

Given the opaqueness of the tissue, it is not surprising that flow velocity profiles in bone vessels, which would provide verification of the assumption of steady flow, have not been reported. Such profiles would also indicate validity of the linear viscosity assumption. It is known from measurements in other tissues such as mesentery that whole-blood viscosity is Newtonian in large vessels but not in capillaries, where its density is not isotropic. As is the case in other tissues, one should expect that in bone capillaries hematocrit (RBC volume fraction) will change from point to point (a phenomenon known as the Fahraeus effect[90]) because blood cells must squeeze through tubes with diameters as small as 5 μm.

Pressure measurements are aided by the fact that blood is an incompressible fluid. However, the forces that drive blood flow originate primarily from heart muscle contraction, which introduces an element of unsteady flow. Moreover, skeletal muscle in limbs and smooth muscle surrounding noncapillary vessels provide pressure within and upon these conduits. The periodic nature of heart contractions makes their effects amenable to Fourier analysis, but the other muscles deliver an additional force with different periodic characteristics. Moreover, vessel walls are viscoelastic, with relatively large changes in properties as one moves from arteries to veins. Bone vessels have the advantage of mechanical shielding from direct compression by skeletal muscle. If sufficiently deep within a bone, they experience little longitudinal tension from stretching of tendons, fascia, or ligaments.

An additional complication in the microcirculation is the presence of transmural convective flow, which occurs through large, usually temporary, pores between ECs. Evidence suggesting that this occurs in bone has been reported from direct[91] and indirect[92] observations.

Because measurements of Q and P are so difficult to obtain in bone vasculature, a purely "blackbox" Bernoulli conservation-of-energy theorem for fluid motion was applied to bone blood supply by Brookes[2] in the 1960s, after the fashion of its use in other organs. It states:

$$\text{Total Energy} = PA + mgh + 1/2mu^2 \tag{21.5}$$

where PA is the product of hydrostatic pressure and vessel luminal surface area, m the mass of blood moved, g gravity, h the change in height between afferent and efferent vessels, and u some average RBC velocity through the bone volume of interest. The utility of this equation was that as a thermodynamic statement it provided a measure of the fraction of heart work spent moving blood through a given volume of tissue without requiring measurements within the tissue.

However, the model ignores (1) heat input, (2) work done by the wall force, and (3) kinetic energy crossing the vessel wall (the latter two because vessel wall deformation is assumed small). Friction is also ignored, although it may be, in effect, "hidden" in the kinetic energy (third) term. The model required for its application is merely measurement of (1) the pressure difference between two points, the designated afferent and efferent vessels, and (2) velocity of RBCs at those points. Masses were obtained from the specific gravity of whole blood. Brookes used the model to estimate if pressure in blood vessels of the medullary canal is higher or lower than that in adjacent extraosseous vessels.

Thermodynamic models overlook details that may confound understanding of an observation within a smaller volume of the same tissue. The remaining sections review the results of measurements that provide a more-detailed picture of bone blood supply.

21.2.1 Measurements of Convective Transport in Bone Vasculature as a Whole

21.2.1.1 Hydrostatic Pressure (P), Bone as a Starling Resistor

If one is investigating a particular bone as a fluid reservoir or changes in pressure as an indicator of its health, gross measurements are of clinical utility. None has been obtained of cortical bone or its vessels because gaining access requires drilling. Periosteal vessels would seem easy candidates for micropressure measurements using the servo-null technique of Lipowsky and Zweifach,[93] which has been available for 20 years. Yet no such study appears to have been attempted. Ficat and Arlet[94] have concluded from analysis of the literature that arteriolar capillaries fed by the nutrient artery start at about 32 mmHg, which decreases to 12 mmHg by the end of the venular capillaries in humans. If these two microcirculation pressure values were assumed for a dog, there would be a drop of about 48 mmHg between its nutrient artery and arteriolar capillaries[2] and a rise of 4 to 10 mmHg between its venular capillaries and saphenous vein.[92] Both gradient values were obtained by subtraction from intravascular (but not within the cortex) cannular probe measures. If they are assumed to characterize all vascular trees within the cortex, one might estimate local flows using three-dimensional reconstructions of cortical vasculature. Without inclusion of flow direction in each vessel segment, however, such estimates will remain global approximations.

As questionable as the accuracy would be for such a calculation, it would pale beside any attempt to apply it to the medullary canal. Because they are diagnostic of diseases such as ischemic osteonecrosis, measurements of bone medullary canals have been plentiful since first reported by Blumenthal et al. in 1952.[10] As Brookes and Revell[2] point out, it is doubtful they indicate canal pressure. They were obtained by drilling a hole through the cortex and inserting a probe consisting of a trochar (metal cannula) containing a pressure transducer that was wired to a pressure meter. Any pressure measured was filtered through the blood clot which formed in the drill wound. Reported values vary according to longitudinal location within a bone, species, and the type of bone as shown in Table 21.3, which was adapted from

TABLE 21.3 Techniques for Measuring Blood Supply of Bone

Parameter	Technique	Invasiveness	Ref.
Volumetric flow rate (Q) (all procedures are timed)	Incidence of radioactive microsphere entrapment by arterioles	Terminal; 15-μm spheres permanently block vessels	123
	Counting drops from cut vessel	Exposure and severing of vessel	26
	Clearance of non-bone-seeking radioactive isotope from blood	Terminal; bone must be harvested immediately to obtain radiographs	124
	Disappearance of injected radiopaque compound	Timed series of radiographs; noninvasive	125
	Clearance of bone-seeking radioactive isotope from blood (usually Sr^{85})	Terminal; bone must be isolated for radiography	52
	Two thermocouples measure rate of heat transfer by flowing blood	Vessels must be exposed; relatively local	126
	Rate of clearance of gas (washout of H_2 or Xe)	Probe for gas must be implanted near selected vessel	127
	Laser Doppler flowmetry	Probe must be within 3 mm of vessel	128
	Red cell velocity	Requires intravital microscopy	82
	Velocity of 1.0 μm fluorescent microspheres	Requires intravital microscopy	129
	Rate of dilution of isotope-tagged RBC hematocrit	Tissues harvested and frozen from different subjects at different times	2
Hydrostatic pressure	Trochar probe inserted in medullary canal	Hole drilled through cortical bone	95

Methods employed to measure local supply of blood to tissue near a small bed of vessels and global supply to large region of tissue. Hydrostatic pressure measurement technique has been included for comparison as most methods use variations of the trochar probe manometer.

Ficat and Arlet.[94] Nevertheless, some useful qualitative relationships can be demonstrated with this procedure. For example, rapid loading of the bone or contraction of adjacent skeletal muscle was associated with a rise in intramedullary pressure (IMP).[10] Moreover, the stress test, which consists of injecting 5 cm^3 saline through the implanted trochar and noting changes in IMP, has been useful for diagnosing ischemic osteonecrosis. In victims of the disease, the pressure rises markedly and does not return to preinjection levels for minutes. In healthy subjects the return occurs in seconds.

As indicated in Table 21.3, one can also discern a tendency for normal diaphyseal pressures to be higher than those in the metaphysis or epiphysis. Heterogeneity of IMP within the same bone reflects heterogeneity of the tissue as is evident in Fig. 21.2. Instead of a solid cylinder filled with an incompressible fluid, the medullary canal is a porous solid enclosing globular porous sinusoids, distended fat cells, gel-like extracellular matrices, and a variety of blood components from platelets to neutrophils in various stages of maturity, all of which form a viscoelastic composite. Since the dominant blood supply is retrograde, one expects an intravascular pressure drop from canal to periosteum. Porosity of vessels like sinusoids allow sufficient convective extravasation to keep available interstitial space filled with fluid, and the lack of lymphatic vessels slows release of resulting interstitial pressure. If great enough, this pressure may compress susceptible capillaries and slow blood supply. The result of these interactions is a structure that acts as a Starling resistor.[95] In a Starling resistor a rigid cylindrical chamber (cortical bone) completely encloses a flexible tube (a vessel) except for the tube ends, which receive and expel an incompressible fluid (blood). If hydrostatic pressure in the chamber exceeds that in the tube sufficiently to overcome the material resistance by the tube to deformation, the tube will collapse, stopping its flow. Wilkes and Visscher[95] based this analogy on (1) the observation that pressure in the nutrient vein reflected that in the marrow, as determined with an indwelling cannula tonometer, and (2) an approximation that the medullary canal contained an incompressible fluid. To the extent that the extravascular matrix gel is rigid and medullary canal vessels resist compression, the Starling resistor model is valid. As noted in Fig. 21.2, the nutrient vein appears to carry a minority of efferent blood, and incompressibility is a highly unlikely characteristic of medullary canal contents. It would be reasonable, nevertheless, to propose a modified version of the Starling resistor as a medullary canal model, which would be nonlinear in recognition of its extravascular matrix and porosity. Any valid model for fluid transport in bone would have to address these sources of heterogeneity.

21.2.1.2 Axial Blood Flow

21.2.1.2.1 Q in Macroscopic Volumes of Bone

Since direct viewing of circulating blood in bone has been so difficult, techniques for determination of Q that bypassed individual bone vessels were the first to be implemented. Some, such as the blood drop counting technique, were direct, acute, and quite invasive. Many of these existed before the work of Brookes in the 1960s. In the 1970s two approaches to bone Q measurement emerged, which, although acute and invasive, gave more complete information for specific regions of bone. One approach, microsphere entrapment, depended on the decreasing caliber of influx vessels to relate fraction of injected radioactive microspheres plugging arterioles or arteriolar capillaries to Q. The other approach related extravasation of injected radioactive ions or small molecules to Q. More recently, less-invasive approaches such as laser Doppler flowmetry (LDF) and positron emission tomography (PET) have been employed. On a smaller scale, bone chamber windows, which are initially invasive but can be used chronically, have obtained cortical bone Q values for one specific location and volume. Table 21.4 presents a sampling of large- and small-scale approaches to blood supply assessment in bone. The list is not complete, but it is sufficient to provide a sense of the range of approaches to this problem.

The majority of experimental measures of bone blood flow are obtained by indirect methods, and empirical formulas are used to calculate Q. They usually take the form:

$$Q = \frac{\text{experimental measure}}{\text{calibrated reference measure}} \times \text{dimensional constant} \tag{21.6}$$

TABLE 21.4 Examples of Intramedullary Pressure (in mmHg) in Adults

Date	Animal	Bone	Region	Range/Mean/Max
1952	Dog	Femur	Diaphysis	50
1955	Human	Femur	Epiphysis	30–37
1957	Dog	Femur	Diaphysis	32 (max)
1957	Dog	Femur	Inferior epiphysis	18.8 (max)
1957	Dog	Tibia	Diaphysis	51.7 (max)
1957	Dog	Tibia	Superior epiphysis	12 (max)
1959	Cat	Femur	Diaphysis	24–114
1959	Dog	Femur	Diaphysis	75–90
1960	Human	Femur	Superior metaphysis	12–15
1963	Cat	Femur	Diaphysis	37 (systole)
1964	Rabbit	Tibia	Diaphysis	4–70
1972	Dog	Femur	Diaphysis	40–120
1972	Rabbit	Tibia	Diaphysis	20–60
1972	Human	Tibia	Superior metaphysis	18[130]
1972	Human	Femur	Neck	18.7
1972	Human	Spinous process		2.2–12.9, 8.3
1972	Human	Sternum		0–8
1973	Human	Ilium		19
1984	Dog	Femur	Diaphysis	100 (max)[130]

Compiled by Ficat and Arlet[94] in 1980. A 1984 more recent measurement was added for comparison. Note that maximum diaphyseal pressures are higher than those immediately outside the bone compartment. If such pressures reflect intravascular values in the medullary canal, there can be little doubt of the general direction of the ΔP used to calculate their Q values.

TABLE 21.5 Blood Supply in Adult Dogs from Microsphere Technique

Bone	Q (ml/min/100 g)
Tibia	5 ± 3
Femur	11 ± 6
Radius + ulna	5 ± 2
Humerus	13 ± 6
Scapula	12 ± 5
Skull	14 ± 0
Mandible	1 ± 0
Spine	26 ± 10
Pelvis	14 ± 4
Ribs + sternum	24 ± 8
Skeleton as a whole	**13 ± 4**

Global values of blood supply to various bone organs. Arteriolar capture of radioactive microspheres is considered the most dependable method for evaluating bone blood flow in spite of some concerns about loss of spheres through metarterioles or larger shunts. The "skeleton as a whole" value is for the entire skeleton. Since each bone listed is of different total mass, there is no numerical relationship between the last value and those above it. Data presented are from Tothill.[96]

For example, the microsphere technique introduces a large quantity of radioactive 15-μm spheres at the heart where the aorta can provide a reference value. Experimental values are obtained from harvested bone, the arterioles of which have entrapped microspheres in proportion to their allotment of cardiac blood supply.[96] The dimensional constant in this case is ml/min. Bone yielding the experimental measure is weighed to give a Q expressed as ml/min/100 g. An example of a series of measurements using this technique is presented in Table 21.5. The "total" value represents the entire skeleton, which would include

two tibias, scapulas, etc. and one pelvis, mandible, etc. Other common measures of bone blood flow are based on extravasation of tracer solutes and will be discussed in the section on permeability below.

Extravasation techniques for measuring blood Q rely on an assumed or known permeability of a usually redioactive solute. The rate at which its concentration in the blood is "diluted" or the rate at which it is "cleared" is related to Q. Of these, the one most applied is that used by Bassingthwaighte and Kelly.[6,28,33,97–99] It utilizes for its calculation of blood flow the deceptively simple Renkin[100]–Crone[101] equation:

$$P_i S = -Q \ln(1 - E) \tag{21.7}$$

where E is a ratio representing extraction of the injected solute, P_i its diffusion coefficient through a given thickness of endothelium (i.e., the permeability coefficient of the solute), and S the endothelial surface area through which extravasation occurred. Just as the Poiseuille equation is an approximation of the N-S equation, the Renkin–Crone equation is a simplification of the Starling equation[102] (itself a simplification of the N-S equation), which states that, at any point along the pressure gradient driving blood through capillaries, there exists a transmural pressure gradient that drives fluid through the endothelial wall if it has a hydraulic conductivity > 0. This gradient is a sum of hydrostatic, osmotic, and oncotic pressures, which generate filtration. It contains no diffusion term because Starling believed diffusion was overwhelmed by convection in practice. Pappenheimer et al.[103] later showed that it was not, and developed an inclusive model. This model was too difficult to apply in experimental situations, however, and was simplified by Renkin[100] and Crone.[101]

It is evident that one does not have to know any details about microcirculation to obtain measurements for the Renkin–Crone equation. While elucidation of the local mechanisms controlling nutrient exchange in bone will be necessary before bone vascular physiology reaches the level of understanding that exists for other organs, a great deal of insight can be gained from utilizing the approach of Pappenheimer, which analyzes only gross effects of transmural transport. For example, measures of net extravasation of plasma will provide insight into effects and causes of hypervolemia or edema. The latter will require factoring in bone's lack of discrete lymphatic capillaries while allowing some role for its prelymphatic channels. Similarly, measures of extravasation of various solutes (E) ranging from Ca^{2+} to albumin serve to monitor bone metabolism and can characterize the transport behavior of osseous nonmineralized extravascular matrix (e.g., help determine if a blood–bone barrier exists).

Indicator-dilution experiments performed on bone have yielded more accurate estimates of E. They have not, however, been able to determine P_i and S individually. As a consequence their product $P_i S$, known as the "permeability-surface area product" has become accepted as one parameter in this field of study. In a typical experiment two solutes, at known concentrations, one permeative and the other not (the calibration reference), are injected in an afferent vessel at a calibrated rate and collected from an efferent vessel draining the bone volume of interest. Two outflow dilution curves characterize each solute. Comparison of the fraction of each solute appearing per unit time in the efferent vessel is used to determine E as a function of time. The maximum value of E (E_{max}) is generally used to calculate Q. Kelly[6] has reviewed indicator-dilution techniques and reported resulting measurements of Q from Eq. 21.7 for a number of fracture healing experiments.[33] However, the validity of most indicators used to estimate E_{max} has been challenged by Little and Bassingthwaighte.[104] They contended that solutes permeating by aqueous routes were not completely extracted and the remainder were too mobile after extraction to be retained. They proposed desmethylimipramine as a more suitable extraction indicator.

Determination of blood flow to a given volume of bone (V_o) under normal physiological conditions is not practical because of collateral circulation. A more practical approach is to assume that the amount of a radioactive tracer extravasated is a function of the volume of blood V that has perfused V_o. If the perfusion is measured over a given time interval (Δt) then $Q = V/\Delta t$, which can be expressed in the units ml/min/100 g if V_o and the specific gravity of the bone, $\rho = m/V_o$, are known. The shortcut to obtaining Q is by the clearance technique. The most difficult measure to obtain is V. It can be estimated from the rate at which a solute M carried by V exits blood by diffusion. The greater the value of Q, the less solute blood passing a given point loses to the surrounding bone. This loss is called "clearance" (K)

and is defined $K = Q/\lambda$. It has the units ml/s, and is the imaginary plasma volume created per unit time with $M = 0$. The term λ is the partition coefficient for the solute (fractional solubility in lipid) which indicates tendency to penetrate EC membranes. The extravascular concentration of M at a given time ($C_{M(t)}$) is set as

$$C_{M(t)} = C_{M(0)} e^{-(K/V)\Delta t} \tag{21.8}$$

If λ is known, then Q can be calculated and represents net blood flow through the bone volume measured.[6] Unfortunately, λ is only a rough approximation of the actual movement of M from plasma to the extravascular space, which in this context is termed *washout*, and clearance, its inverse, is the amount of M remaining in the plasma when it reaches the efflux vessel sampled (by withdrawing blood).

LDF is a minimally invasive technique. Its main drawback for analysis is the absence of a dependable conversion of LDF dimensions to Q.[105] PET scanning of ^{18}F is noninvasive, but the resolution of tissue with this technique is not sufficient to identify structures, and the isotope partition coefficient is not unity.[106]

21.2.1.2.2 Q in Bone Microvasculature

Brånemark[82] was the first to measure flow in bone microvasculature directly. Using RBCs as flow indicators, he measured velocities in marrow adjacent to endosteum of 1 to 1.5 mm/s in arterioles, 0.5 mm/s in sinusoids, and 0.1 to 0.3 mm/s in venules. Cortical bone showed speeds of 0.5 to 0.8 mm/s in capillaries and 0.2 to 0.5 mm/s in venules. While these measures were useful for estimating transit times for blood cells, they could not be used to calculate Q using the Poiseuille equation because their "particle" diameter of 7.5 μm carries them across too many streamlines of the flow velocity profile for it to assume a parabolic form. The nonparabolic profiles characteristic of vessels with diameters less than 40 μm are referred to as "plug flow" because the curved apex of the parabola is reduced to a flat head. Two factors that determine the exact shape of the profile are hematocrit and shear stress.[107] The latter causes migration of RBCs away from the endothelial wall, the *tubular pinch effect*, helping to form the plug.

Particles smaller than blood cells have provided a more accurate representation of fluid element velocities. Fluorescent beads are commonly used for this purpose but must be 1 μm or less in diameter to mimic a fluid particle.[108] One technique for viewing these beads that is not invasive at the time of measurement, although it requires surgical implantation, is bone chamber intravital microscopy, which employs a permanently implanted window to observe a controlled volume of cortical bone. An example of the vasculature observed by bone chamber intravital microscopy is presented in Fig. 21.4. The vessels are rendered visible by perfused fluorescein isothiocyanate conjugated with 70-kDa dextran (FITC-D70). Except for deviations from homeostasis such as inflammation, these vessels do not extravasate macromolecules as large as FITC-D70 and remain well defined for measurement of length and diameter. The bone chamber can remain implanted for long periods (e.g., 2 years), allowing chronic observations. Values of Q are obtained directly from observation of fluorescent microsphere perfusion in this model. Using 1.75-μm fluorescent microspheres injected into an aural vein of a rabbit, values of maximum particle velocity from each (kth) vessel (u_k) were obtained from videotapes of vessels in the bone chamber and q_k, its volumetric flow rate calculated[109] from

$$q_k = \pi r^2 u_k / 2 \tag{21.9}$$

Thus, $Q = \Sigma q_k$, where Σ indicates summation of all perfused input vessels, could be calculated. Since the volume of tissue in the observed bone chamber compartment was known, Q could be expressed as ml/min/100 g with the mass determined using a specific gravity of 2 for bone. A typical result is presented in Table 21.6, where it is compared with values from other sources. It will be noted that the bone chamber value is markedly higher than the others. This may be explained by the fact that at least 2 min was allowed

TABLE 21.6 Comparison of Bone Chamber Values for Microcirculatory Function with Others

Parameter	Conventional	Bone Chamber
Angiogenic rate (μm/day)	300[110]	158
Blood supply (ml/min/100 g)	4.3[131]	138
Vascularity (volume fraction)	0.062[80]	0.040

Comparison of local blood supply measures from various sources with values from bone chamber intravital microscopy. Note that conventional measurements come from global probes, which include bone regions in various metabolic states. Conventional *Q* values were obtained with microspheres, and therefore do not specifically address flow in tubes of $<$15 μm caliber. *Q* value in a bone chamber is a sum of all influx vessels perfused at any time during a 2-min observation period. Since some fraction of the vessels are unperfused at any given instant, this value is an overestimate, which would be accurate only if all patent influx vessels were perfused simultaneously. Such an apex might be achieved in an emergency. Hence, *Q* so calculated would be physiologically extraordinary and numerically maximal.

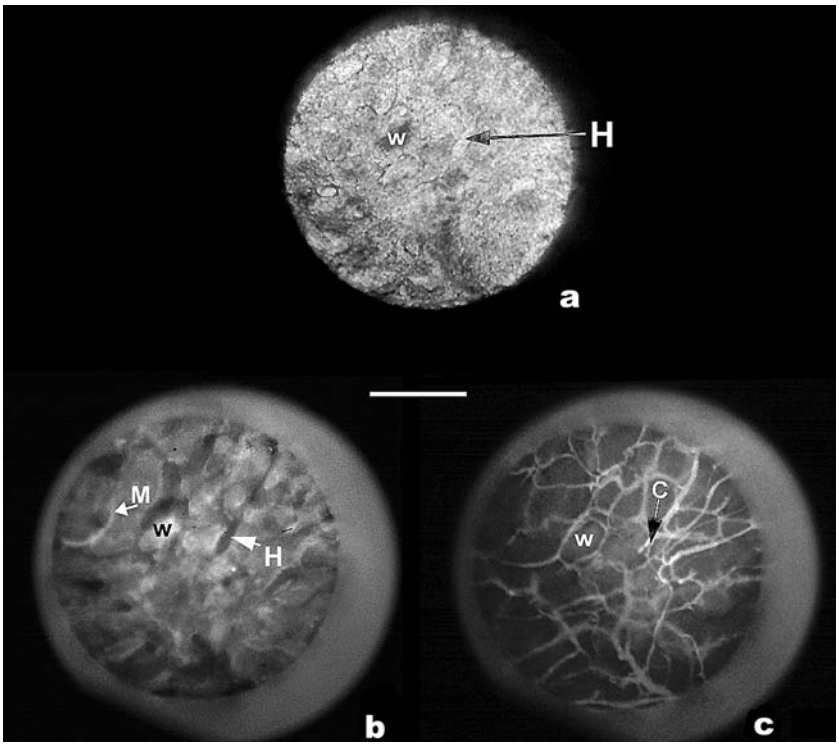

FIGURE 21.4 Bone-filled bone chamber compartment *in vivo* viewed with an intravital microscope. Scale bar in center is 480 μm. Compartment thickness is 100 μm. (a) Transmitted light illumination showing primitive woven bone (w), which appears spontaneously as the compartment fills with bone following implantation, and a Haversian canal (H), which runs parallel with the tibial long axis. The Haversian canals were formed by secondary osteons, which tend to align the canal axis with the long axis of the bone. Primary osteons, in contrast, have random direction and appear before bone becomes lamellar. In the figure the bone axis would run from about the one o'clock to the seven o'clock position of each circle. (b) Epifluorescence illumination that has excited the bone mineral label oxytetracycline. Mineralization fronts (M) appear sharp when viewed from the side and cloudy when parallel with the image plane. The primitive woven bone region (w) was actively mineralizing when label dye was injected. Haversian canal (H) appears dark, but walls show mineralization fronts laid down by osteoblasts diagrammed in Fig. 21.3. (c) Fluorescing FITC-D70 in perfused vessels under epifluorescence illumination. A capillary (c) has been identified in the Haversian canal marked in a and b. The marked vessel appears to end in the Haversian canal, suggesting that the pressure gradient that allows perfusion to occur depends on a leaky advancing tip.

for any vessel to be perfused by at least one microsphere. Since only a fraction of the vessels of a given vascular bed is perfused at any instant, the 2-min interval allows all potential vessels to be perfused and any resulting Q value must therefore be considered a maximum (a value attainable only in an emergency when all vessels were perfused simultaneously).

21.2.1.3 Transmural Transport/Nutrient Exchange

21.2.1.3.1 Convective Transmural Transport

Although local studies of bone blood supply are lacking, with exception of Brånemark's early acute observations[82] and more recent optical bone chamber studies,[109,110] the mechanical relationships found in other organs should hold for this tissue. Of course, the hydraulic conductivity of the adjacent mineralized matrix (which undergoes constant remodeling) on transport will eventually have to be accounted for in any bone fluid mechanics model.[111]

21.2.1.3.2 Diffusive Transport and Active Transport

The indicator-dilution global approaches just described reveal too little about how solutes are transported to the bone matrix from vessels and how they return. Each assumes no role for solvent drag. This assumption is apparently supported by studies that show that mineral uptake by bone is decreased with increased Q,[99,112] which is the opposite of what one would expect if transmural convection increased in response to increased intravascular hydrostatic pressure. However, vessel dilation (and/or recruitment) may occur in response to increased hydrostatic P, and the stretched walls would become more porous. A subsequent increase in extravascular hydrostatic P would enhance reabsorption and the net effect would be the same as if no filtration had occurred. This result would depend on the extravascular matrix having a very low hydraulic conductivity. In fact, there is substantial evidence that it has the opposite.[111,113–116]

However, there is also evidence that there is a blood–bone barrier that is capable of altering hydraulic conductivity.[68,111] A blood–bone barrier, presumably the osteoblast layer controlling hydraulic conductivity between the immediate extravascular matrix and the mineralized matrix-plus-canalicular system (MOD in Fig. 21.3), would create a "Windkessel"-like arrangement[87] similar to that of the aorta relative to the heart (vessel) and peripheral circulation (MOD). If there is a blood–bone barrier that can vary its hydraulic conductivity, it could exercise some control over transmural vascular convection by regulating extravascular hydrostatic P. Any contribution to extravascular matrix convection by prelymphatic channels might well be obviated. Details of this convection are discussed by Knothe Tate in more detail in Chapter 22.

Finally, other components of vessel permeability hidden by the simple P_iS term of the Renkin–Crone equation need to be addressed. The fact that normal perfusion of vessels is not constant makes one suspect that S cannot be calculated from indicator-dilution results even if a value for P_i is obtained. Any such value would be an average of pore distribution, which would conceal the distribution pattern. The question of vessel recruitment (increase/decrease in number of vessel segments perfused between any two time points) remains open. There is evidence from other organs that basement membranes mediate extravascular permeability.[48] Questions about the role of the blood–bone barrier in solute transport regulation need to be addressed. For example, are there solute pools in the extravascular space that control transmural diffusion gradients? If so, how do the compartments that result interact? Which cells in the barrier perform the transport and which nonbarrier cells control them (e.g., how do ECs and osteocytes interact)?

There is as yet no comprehensive model describing nutrient exchange in bone. The questions raised in this section suggest a need for observations as direct as possible for development of such a model. By the same token, there is need for an operational model that would relate the events of bone microcirculatory physiology as they work together to maintain bone homeostasis. The bone organ circulation is more than the sum of its microcirculatory beds, and models of how it operates as a unit, such as those suggested for other organs by Bassingthwaighte[117] and Lee,[118] are required to understand its malfunctions.

Acknowledgments

This work was supported by the Cora Kaiser Fund and the Orthopaedic Foundation of Los Angeles Orthopaedic Hospital, and by a Wright Grant to T. Thordarson of the University of Southern California.

References

1. Danckwardt-Lilliestrom, G., Reaming of the medullary cavity and its effect on diaphyseal bone, *Acta Orthop. Scand.,* 1, 1969.
2. Brookes, M. and Revell, W.J., *Blood Supply of Bone,* Springer, Santa Clara, CA, 1998, 859 pp.
3. Brookes, M. and Harrison, R.G., The vascularization of the rabbit femur and tibiofibula, *J. Anat.,* 91, 61, 1957.
4. Crock, H.V., *The Blood Supply of the Lower Limb Bones in Man,* E. & S. Livingstone, London, 1967, 103 pp.
5. Crock, H.V., *An Atlas of Vascular Anatomy of the Skeleton and Spinal Cord,* Martin Dunitz, London, 1996,
6. Kelly, P.J., Pathways of transport in bone, in *Handbook of Physiology. The Cardiovascular System. Part 1: Peripheral Circulation and Organ Blood Flow,* Geiger, S.R., Ed., American Physiological Society, Bethesda, MD, 1983, 371.
7. Rhinelander, F.W., The normal microcirculation of diaphyseal cortex and its response to fracture, *J. Bone Joint Surg.,* 50A, 784, 1968.
8. Trueta, J., *Studies of the Development and Decay of the Human Frame,* W.B. Saunders, Philadelphia, 1968, 389 pp.
9. Brookes, M., *The Blood Supply of Bone,* Butterworths, London, 1971, 338 pp.
10. Dabrowski, Z. and Tabarowski, Z., History of discoveries of bone marrow and bone vascularisation and innervation, in *Bone Circulation and Vascularization in Normal and Pathological Conditions,* Schoutens, A., Arlet, J., Gardeniers, J.W.M., and Hughes, S.P.F., Eds., Plenum Press, New York, 1993, 49.
11. Otter, M., Shoenung, J., and Williams, W.S., Evidence for different sources of stress-generated potentials in wet and dry bone, *J. Orthop. Res.,* 3, 321, 1985.
12. Thompson, D., *On Growth and Form,* Cambridge University Press, Cambridge, 1961, 346 pp.
13. Frost, H., Perspectives: bone's mechanical usage windows, *Bone Miner.,* 19, 257, 1992.
14. Knight, A.D. and Levick, J.R., Changes in the hydraulic conductivity of the blood-joint barrier with pressure, *Proc. Physiol. Soc. J. Physiol.,* 324, 47, 1981.
15. Knight, A.D. and Levick, J.R., Morphometry of the ultrastructure of the blood-joint barrier in the rabbit knee, *Q. J. Exp. Physiol.,* 69, 271, 1984.
16. Knight, A.D. and Levick, J.R., Osmotic flows and albumin reflection coeffiecients in rabbit knees, *Q. J. Exp. Physiol.,* 351, 47, 1984.
17. Levick, J.R. and Knight, A.D., Osmotic flows across the blood-joint barrier, *Ann. Rheum. Dis.,* 46, 534, 1987.
18. Levick, J. R., Flow through interstitium and other fibrous matrices, *Q. J. Exp. Physiol.,* 72, 409, 1987.
19. Levick, J.R., Microvascular architecture and exchange in synovial joints, *Microcirculation,* 2, 217, 1995.
20. Kelly, P.J., Anatomy, physiology and pathology of the blood supply of bones, *J. Bone Joint Surg.,* 50A, 766, 1968.
21. Shaw, N.E., Observations on the physiology of the circulation in bones, *Ann. Roy. Coll. Surg. Engl.,* 35, 214, 1964.
22. Nelson, G.E., Kelly, P.J., Peterson, F.A., and Janes, J.M., Blood supply of the human tibia, *J. Bone Joint Surg.,* 42A, 625, 1960.

23. Lundgaard, A., Aalkjaer, C., Holm-Nielsen, P., Mulvany, M.J., and Hansen, E.S., Method for assessment of vascular reactivity in bone: *in vitro* studies on resistance arteries isolated from porcine cancellous bone, *J. Orthop. Res.,* 14, 962, 1996.
24. Albrektsson, T., A comparison between microangiography and vital microscopic in evaluation of bone vascularization, in *Bone Circulation,* Arlet, J., Ficat, R.P., and Hungerford, D.S., Eds., Williams & Wilkins, Baltimore, MD, 1984, 162.
25. Ham, A.W. and Cormack, D.H., *Histology,* J.B. Lippincott, Philadelphia, 1979, 966 pp.
26. Drinker, C.K. and Drinker, K.R., A method for maintaining an artificial circulation through the tibia of a dog with a demonstration of the vasomotor control of the marrow, *Am. J. Physiol.,* 40, 514, 1916.
27. Heppenstall, R.B., Fracture healing, in *Fracture Treatment and Healing,* Heppenstall, R.B., Ed., W.B. Saunders, Philadelphia, 1980, 35.
28. Williams, E.A., Fitzgerald, R.H.J., and Kelly, P.J., Microcirculation of bone, in *The Physiology and Pharmacology of the Microcirculation,* Mortillaro, N.A., Ed., Academic Press, San Francisco, 1984, 267.
29. Ecoiffier, J., Prot, D., Griffié, R., and Catach, D., Étude du réseau veineux dans las os long du lapin, *Rev. Chir. Orthop.,* 43, 29, 1957.
30. Oni, O.O.A. and Gregg, P., The routes of venous escape from the marrow of the diaphysis of long bones, in *Bone Circulation and Bone Necrosis,* Arlet, J. and Mazières, B., Eds., Springer-Verlag, New York, 1988, 7.
31. McCarthy, I.D. and Hughes, S.P.F., Transport of small molecules across capillaries in bone, in *Blood Flow: Theory and Practice,* Taylor, D.E.M. and Stevens, A.L., Eds., Academic Press, New York, 1983, 313.
32. Tooke, J.E. and Smaje, L.H., The microcirculation and clinical disease, in *Clinically Applied Microcirculaton Research,* Barker, J., Anderson, G.L., and Menger, M.D., Eds., CRC Press, Boca Raton, FL, 1995, 3.
33. Kelly, P.J. and Bronk, J.T., Circulation, blood flow, and interstitial fluid flow in fracture healing, in *Bone Formation and Repair,* Brighton, C.T., Friedlaender, G., and Lane, J.M., Eds., American Academy of Orthopaedic Surgeons, Rosemont, 1994, 197.
34. De Bruyn, P.P.H., Breen, P.C., and Thomas, T.B., The microcirculation of the bone marrow, *Anat. Rec.,* 168, 55, 1970.
35. Hughes, S.P.F. and Kelly, P.J., The mechanism of ion transfer in bone, in *Bone Circulation,* Arlet, J., Ficat, R.P., and Hungerford, D.S., Eds., Williams & Wilkins, Baltimore, MD, 1984, 207.
36. Boeynaems, J.-M. and Pirotton, S., *Regulation of the Vascular Endothelium: Signals and Transduction Mechanisms,* R.G. Landes, Austin, TX, 1994, 117 pp.
37. Aschheim, E., Passage of substances across the walls of blood vessels, in *Microcirculation,* Kaley, G. and Altura, B.M., Eds., University Park Press, Baltimore, MD, 1977, 213.
38. Marshall, G.J., Geddes, A.D., and Kirchen, M.E., The sinusoidal bed of human marrows, *J. Ultrastruct. Res.,* 48, 170, 1974.
39. Burridge, K. and Chrzanowska-Wodnicka, M., Focal adhesions, contractility and signaling, *Annu. Rev. Cell Dev. Biol.,* 12, 463, 1996.
40. Chon, J.H., Netzel, R., Rock, B.M., and Chaikof, E.L., $\alpha_4\beta_1$ and $\alpha_5\beta_1$ control cell migration on fibronectin by differentially regulating cell speed and motile cell phenotype, *Ann. Biomed. Eng.* 26, 1091, 1998.
41. Ayad, S., Boot-Handford, R.P., Humphries, M.J., Kadler, K.E., and Shuttleworth, C.A., The extracellular matrix facts book, in *FactsBook Series,* Academic Press, San Diego, CA, 1994, 163 pp.
42. Craig, L.E., Spelman, J.P., Strandberg, J.D., and Zink, M.C., Endothelial cells from diverse tissues exhibit differences in growth and morphology, *Microvasc. Res.,* 1998, 55, 65.
43. Trueta, J., The role of vessels in osteogenesis, *J. Bone Joint Surg. B,* 45B, 402, 1963.

44. Jones, A.R., Clark, C.C., and Brighton, C.T., Microvessel endothelial cells and pericytes increase proliferation and repress osteoblast phenotypic markers in rat calvarial bone cell cultures, *J. Orthop. Res.,* 13, 553, 1995.
45. Oni, O.O.A., Dearing, S., and Pringle, S., Endothelial cells and bone cells, in *Bone Circulation and Vascularization in Normal and Pathological Conditions,* Schoutens, A., Arlet, A., Gardeniers, J.W.M., and Hughes, S.P., Eds., Plenum Press, New York, 1993, 43.
46. Brighton, C.T., Lorich, D.G., Kupcha, R., Reilly, T.M., Rose, R., and Woodbury, R.A.I., The pericyte as a possible osteoblast progenitor cell, *Clin. Orthop. Relat. Res.,* 275, 287, 1992.
47. Kelley, C., D'Amore, P., Hechtman, H.B., and Shepro, D., Microvascular pericyte contractility *in vitro*: comparison with other cells of the vascular wall, *J. Cell Biol.,* 104, 483, 1987.
48. Katz, M.A., Structural change in fiber matrix allows for enhanced permeability and reduced conductivity, *Microvasc. Res.,* 43, 1, 1992.
49. Wootton, R., Measurement of bone blood flow in humans, in *Bone Circulation and Vascularization in Normal and Pathological Conditions,* Schoutens, A., Arlet, J., Gardeniers, J.W.M., and Hughes, S.P.F., Eds., Plenum Press, New York, 1993, 85.
50. Winet, H., Bao, J.Y., and Thordarson, D., Collateral circulation: a confounding factor in the development of rabbit ischemic osteonecrosis models, Soc. Internat. Chir. Orthop. Traum. 21st Trien. World Congr., 1999.
51. Grundnes, O., Gjerdet, N.R., Utvåg, S.E., and Reikerås, O., Vascular and structural changes in rat femora following nailing and intramedullary occlusion, *J. Orthop. Res.,* 16, 293, 1998.
52. Shim, S.S., Copp, D.H., and Patterson, F.P., Bone blood flow in the line following sciatic nerve section, *Surg. Gynecol. Obstet.,* 123, 333, 1966.
53. Gross, P.M., Heistad, D.D., and Marcus, M.L., Neurohumeral regulation of blood flow to bones and marrow, *Am. J. Physiol.,* 237, H440, 1979.
54. Tran, M., The effect of lumbar sympathectomy on blood flow to bone, *Br. J. Pharmacol.,* 70, 363, 1980.
55. Hohmann, E.L., Elde, R.P., Rysavy, J.A., Einzig, S., and Gebhard, R.L., Innervation of periosteum and bone by sympathetic vasoactive intestinal peptide-containing nerve fibers, *Science,* 232, 868, 1986.
56. Serre, C.M., Farlay, D., Delmas, P.D., and Chenu, C., Evidence for dense and intimate innervation of the bone tissue, including glutamate-containing fibers, *Bone,* 25, 623, 1999.
57. Hughes, S.P.F., Corbett, S.A., Reichert, I.L.H., and McCarthy, I.D., The regulation of blood flow in bone, in *Osteonecrosis,* Urbaniak, J.R. and Jones, J.P., Eds., American Academy of Orthopaedic Surgeons, Rosemont, 1997, 11.
58. Luethi, U.K., Stroud, R.D., Rahn, B.A., Brown, S.A., and Merritt, K., Intracortical bone perfusion and aspirin anticoagulation or denervation, in *Bone Circulation,* Arlet, J., Ficat, P.R., and Hungerford, D.S., Eds., Williams & Wilkins, Baltimore, MD, 1984, 328.
59. Ryan, U.S., Endothelial cells, in *Clinically Applied Microcirculation Research,* Barker, J., Anderson, G.L., and Menger, M.D., Eds., CRC Press, Boca Raton, FL, 1995, 407.
60. Smith, J.J. and Kampine, J.P., *Circulatory Physiology,* Williams & Wilkins, Baltimore, MD, 1990, 345 pp.
61. Brindley, G.W., Williams, E.A., Bronk, J.T., Meadows, T.H., Montgomery, R.J., Smith, S.R., and Kelly, P.J., Parathyroid hormone effects on skeletal exchangeable calcium and bone blood flow, *Am. J. Physiol.,* 255, H94, 1988.
62. Murray, T.M., Parathyroid hormone and hyperparathyroidism, in *Metabolic Bone Disease: Cellular and Tissue Mechanisms,* Tam, C.S., Heersche, J.N.M., and Murray, J.M., Eds., CRC Press, Boca Raton, FL, 1989, 105.
63. Wang, H.H., Drugge, E.D., Yen, Y.-C., Blumenthal, M.R., and Pang, P.K.T., Effects of synthetic parathyroid hormone on hemodynamics and regional blood flows, *Eur. J. Pharmacol.,* 1984, 97, 209.
64. Driessens, M. and Vanhoutte, P.M., Effect of calcitonin hydrocortisone and parathyroid hormone on canine blood vessels, *Am. J. Physiol.,* 241, H91, 1981.

65. Reeve, J., Arlot, M., Wootton, R., Edouard, C., Tellez, M., Hesp, R., Green, J.R., and Meunier, P.J., Skeletal blood flow, iliac histomorphometry, and strontium kinetics in osteoporosis: a relationship between blood flow and corrected appositional rate, *J. Clin. Endocrinol. Metab.,* 66, 1124, 1988.
66. Pooley, J., Pooley, J.E., and Montgomery, R.J., The central venous sinus of long bones—Its role in relation to exercise, in *Bone Circulation and Bone Necrosis,* Arlet, J. and Mazières, B., Eds., Springer-Verlag, New York, 1988, 35.
67. Verhas, M., Schoutens, A., Verschaeren, A., Mone, M., Bergmann, P., and Heilporn, A., Bone demineralization and increased blone blood flow in the rat, in *Bone Circulation and Bone Necrosis,* Arlet, J. and Mazières, B., Eds., Springer-Verlag, New York, 1988, 142.
68. McCarthy, I.D. and Hughes, S.P.F., Is there a blood–bone barrier? in *Bone Circulation and Bone Necrosis,* Arlet, J. and Maziéres, B., Eds., Springer-Verlag, New York, 1988, 30.
69. Green, J.R., Reeve, J., Tellez, M., Veall, N., and Wootton, R., Skeletal blood flow in metabolic disorders of the skeleton, *Bone,* 8, 293, 1987.
70. Collin-Osdoby, P., Role of vascular endothelial cells in bone biology, *J. Cell. Biochem.,* 55, 304, 1994.
71. Davies, P.F. and Barbee, K.A., Endothelial cell surface imaging: insights into hemodynamic force transduction, *News Physiol. Sci.,* 9, 153, 1994.
72. Harrison, D.G., The endothelial cell, *Heart Dis. Stroke,* 1, 95, 1992.
73. Coessens, B.C., Adams, M.L., and Wood, M.B., Evaluation of influence of 24-hour cold preservation on endothelin production and on endothelin receptors in the bone vasculature, *J. Orthop. Res.,* 13, 725, 1995.
74. Coessens, B.C., Miller, V.M., and Wood, M.B., Endothelin induces vasoconstriction in the bone vasculature *in vitro*: an effect mediated by a single receptor population, *J. Orthop. Res.,* 14, 611, 1996.
75. Coessens, B.C., Miller, V.M., and Wood, M.B., Endothelin-A receptors mediate vascular smooth-muscle response to moderate acidosis in the canine tibial nutrient artery, *J. Orthop. Res.,* 14, 818, 1996.
76. Briggs, P.J., Moran, C.G., and Wood, M.B., Actions of endothelin-1, 2 and 3 in the microvasculature of bone, *J. Orthop. Res.,* 16, 340, 1998.
77. Davis, T.R. and Wood, M.B., The effects of ischemia on long bone vascular resistance, *J. Orthop. Res.,* 9, 883, 1991.
78. Davis, T.R.C. and Wood, M.B., Endothelial control of long bone vascular resistance, *J. Orthop. Res.,* 10, 344, 1992.
79. Davis, T.R.C. and Wood, M.B., The effects of acidosis and alkalosis on long bone vascular resistance, *J. Orthop. Res.,* 11, 834, 1993.
80. Hansen, E.S., Microvascularization, osteogenesis, and myelopoiesis in normal and pathological conditions, in *Bone Circulation and Vascularization in Normal and Pathological Conditions,* Schoutens, A., Arlet, J., Gardeniers, J.W.M., and Hughes, S.P.F., Eds., Plenum Press, New York, 1993, 29.
81. Falcone, J.C. and Meininger, G.A., Arteriolar dilation produced by venule endothelium-derived nitric oxide, *Microcirculation,* 4, 303, 1997.
82. Brånemark, P.I., Vital microscopy of bone marrow in rabbit, *Scand. J. Clin. Lab. Invest.,* 11, 1, 1959.
83. Schmid-Schönbein, G.W., The interaction between leukocytes and endothelium *in vivo, Ann. N.Y. Acad. Sci.,* 516, 348, 1988.
84. Jones, J.P., Osteonecrosis and bone marrow edema syndrome: similar etiology but a different pathogenesis, in *Osteonecrosis: Etiology, Diagnosis and Treatment,* Urbaniak, J.R. and Jones, J.P., Eds., American Academy of Orthopaedic Surgeons, Rosemont, 1997, 181.
85. Braddock, M., Schwachtgen, J.-L., Houston, P., Dickson, M.C., Lee, M.J., and Campbell, C.J., Fluid shear stress modulation of gene expression in endothelial cells, *News Physiol. Sci.,* 13, 241, 1998.
86. Ingber, D., Extracellular matrix, cellular mechanics and tissue engineering, in *Tissue Engineering,* Bell, E., Ed. Birkhäuser, Boston, 1993, 69.
87. Fung, Y.C., *Biodynamics: Circulation,* Springer-Verlag, New York, 1984, 404 pp.

88. Caro, C.G., Pedley, T.J., Schroter, R.C., and Seed, W.A., *The Mechanics of the Circulation,* Oxford University Press, New York, 1987, 527 pp.
89. Vogel, S., *Life in Moving Fluids,* Princeton University Press, Princeton, 1983, 352 pp.
90. Charm, S.E. and Kurland, G.S., *Blood Flow and Microcirculation,* John Wiley, New York, 1974, 243 pp.
91. Winet, H., Hollinger, J.O., and Albrektsson, T., Intravital microscopy-based *in vivo* observation of polymer erosion in bone, in *Encyclopedic Handbook of Biomaterials and Bioengineering,* Wise, D.L., Trantolo, D.J., Altobelli, D.E., Yaszemski, M.J., Gresser, J.D., and Schwartz, E.R., Eds., Marcel Dekker, New York, 1995, 823.
92. Bronk, J.T., Meadows, T.H., and Kelly, P.J., The relationship of increased capillary filtration and bone formation, *Clin. Orthop. Relat Res.,* 293, 338, 1993.
93. Lipowsky, H.H. and Zweifach, B.W., Methods for the simultaneous measurement of pressure differentials and flow in single unbranched vessels of the microcirculation for rheological studies, *Microvasc. Res.,* 14, 345, 1977.
94. Ficat, R.P. and Arlet, J., *Ischemia and Necrosis of Bone,* Williams & Wilkins, Baltimore, MD, 1980, 196 pp.
95. Wilkes, C.H. and Visscher, M.B., Some physiological aspects of bone marrow pressure, *J. Bone Joint Surg.,* 57A, 49, 1975.
96. Tothill, P., Measurement of bone blood flow in animals, in *Bone Circulation and Vascularization in Normal and Pathological Conditions,* Schoutens, A., Arlet, J., Gardeniers, J.W.M., and Hughes, S.P.F., Eds., Plenum Press, New York, 1993, 65.
97. Davies, D.R., Bassingthwaighte, J.B., and Kelly, P.J., Blood flow and ion exchange in bone, in *Skeletal Research,* Simmons, D.J. and Kunin, A.S., Eds., Academic Press, New York, 1979, 397.
98. Hughes, S.P.F., Lemon, G.J., Davies, D.R., Bassingthwaighte, J.B., and Kelly, B.J., Extraction of minerals after experimental fractures of the tibia in dogs, *J. Bone Joint Surg.,* 61A, 857, 1979.
99. Lemon, G.J., Davies, D.R., Hughes, S.P.F., and Bassingthwaighte, J.B., Transcapillary exchange and retention of fluoride, strontium, EDTA, sucrose and antipyrine in bone, *Calcif. Tissue Int.,* 31, 173, 1980.
100. Renkin, E.M., Transport of ^{42}potassium from blood to tissue in isolated mammalian skeletal muscle, *Am. J. Physiol.,* 197, 1205, 1959.
101. Crone, C., The permeability of capillaries in various organs as determined by use of the "indicator diffusion" method, *Acta Physiol. Scand.,* 58, 292, 1963.
102. Starling, E.M., On the absorption of fluid from the connective tissue spaces, *J. Physiol.,* 19, 312, 1896.
103. Pappenheimer, J.R., Renkin, E.M., and Borrero, L.M., Filtration, diffusion and molecular sieving through peripheral capillary membranes. A contribution to the pore theory of capillary permeability, *Am. J. Physiol.,* 167, 13, 1951.
104. Little, S.E. and Bassingthwaighte, J.B., Plasma-soluble marker for intraorgan regional flows, *Am. J. Physiol.,* 245, 4707, 1983.
105. Swiontkowski, M.F., Schlehr, F., Collins, J.C., Pou, A., and Sanders, R., Correlation of laser Doppler flowmetry with microsphere estimates for bone blood flow, in *Bone Circulation and Bone Necrosis,* Arlet, J. and Mazières, B., Eds., Springer-Verlag, New York, 1988, 121.
106. Schiepers, C., Skeletal fluoride kinetics of $^{18}F^-$ and positron emission tomography (PET): *in vivo* estimation of regional blood flow and influx rate in humans, in *Bone Circulation and Vascularization in Normal and Pathological Conditions,* Schoutens, A., Arlet, J., Gardeniers, J.W.M., and Hughes, S.P.F., Eds., Plenum Press, New York, 1993, 95.
107. Rosenblum, W.I., Viscosity: *in vitro* versus *in vivo*, in *Microcirculation,* Kaley, G. and Altura, B.M., Eds., University Park Press, Baltimore, MD, 1977, 325.
108. Rovainen, C.M., Wang, D.-B., and Woolsey, T.A., Strobe epi-illumination of fluorescent beads indicates similar velocities and wall shear rates in brain arterioles of newborn and adult mice, *Microvasc. Res.,* 43, 235, 1992.

109. Winet, H. and Bao, J.Y., Relationship between volumetric flow and blood vessel dimensions in healing cortical bone, in *Engineering Science, Fluid Mechanics,* Yates, G.T., Ed., World Scientific, New York, 161, 1990.
110. Albrektsson, T., Implantable devices for long-term vital microscopy of bone tissue, *CRC Crit. Rev. Biocompat.,* 3, 25, 1987.
111. Hillsley, M.V. and Frangos, J.A., Osteoblast hydraulic conductivity is regulated by calcitonin and parathyroid hormone, *J. Bone Miner. Res.,* 11, 114, 1996.
112. McCarthy, I.D., Mineral transport and changes in bone blood flow, *Sem. Orthop.,* 1, 147, 1986.
113. Dillaman, R.M., Movement of ferritin in the 2-day-old chick femur, *Anat. Rec.,* 209, 445, 1984.
114. Dillaman, R.M., Roer, R.D., and Gay, D.M., Fluid movement in bone: theoretical and empirical, *J. Biomech.,* 24, 163, 1991.
115. Montgomery, R.J., Sutker, B.D., Bronk, J.T., Smith, S.R., and Kelly, P.J., Interstitial fluid flow in cortical bone, *Microvasc. Res.,* 35, 295, 1988.
116. Seliger, W.G., Tissue fluid movement in compact bone, *Anat. Rec.,* 166, 247, 1970.
117. Bassingthwaighte, J.B., Through the microcirculatory maze with machete, molecule and minicomputer, *Ann. Biomed. Eng.,* 15, 503, 1987.
118. Lee, J.-S., Biomechanics of the microcirculation: an integrative and therapeutic perspective, *Ann. Biomed. Eng.,* 28, 1, 2000.
119. Resnick, N. and Gimbrone, M.A.J., Hemodynamic forces are complex regulators of endothelial gene expression, *FASEB J.,* 9, 874, 1995.
120. Hansen, E.S., Blood flow in the axial and the appendicular skeleton, in *Osteonecrosis,* Urbaniak, J.R. and Jones, J.P., Eds., American Academy of Orthopaedic Surgeons, Rosemont, 1997, 19.
121. Oni, O.O.A., Stafford, H., and Gregg, P.J., An investigation of the routes of venous drainage from the bone marrow of the human tibial diaphysis, *Clin. Orthop. Relat. Res.,* 230, 237, 1988.
122. Simmons, D.J. and Grynpas, M.D., Mechanisms of bone formation *in vivo,* in *Bone,* Hall, B.K., Ed., CRC Press, Boca Raton, FL, 1990, 193.
123. Tothill, P. and Hooper, G., Measurement of tendon blood flow in rabbits by microsphere uptake and ^{133}Xe washout, *J. Hand Surg.,* 10B, 17, 1985.
124. Petrakis, N.L., Masouredis, S.P., and Miller, P., The local blood flow in human bone marrow in leukemia and neoplastic diseases as determined by clearance rate of radionuclide (I^{131}), *J. Clin. Invest.,* 32, 952, 1953.
125. Matumoto, Y. and Mizuno, S., Rate of blood flow in the femoral head, *Med. J. Osaka Univ.,* 16, 431, 1966.
126. McPherson, A. and Juhasz, L., Symposium on Bio-mechanics and Related Bioengineering Topics, 1964, Glasgow, Scotland, Kenedi, R.M., Ed., Pergamon, Oxford, 1965, 181.
127. Whiteside, L.A., Lesker, P.A., and Simmons, D.J., Measurement of regional bone and bone marrow blood flow in the rabbit using the hydrogen washout technique, *Clin. Orthop. Relat. Res.,* 122, 340, 1977.
128. Swiontkowski, M.F., Ganz, R., Schlegel, U., and Perren, S.M., Laser doppler flowmetry for clinical evaluation of femoral head osteonecrosis, *Clin. Orthop. Relat. Res.,* 218, 181, 1987.
129. Winet, H., Bao, J.Y., and Moffat, R., A control model for tibial cortex neovascularization in the bone chamber, *J. Bone Miner. Res.,* 5, 19, 1990.
130. Bouteiller, G., Arlet, J., Blasco, A., Vigoni, F., and Elefterion, A., Is osteonecrosis of the femoral head avascular? Bone blood flow measurements after long-term treatment with corticosteroids, *Metab. Bone Dis. Relat. Res.,* 4, 313, 1983.
131. Li, G., Bronk, J.T., and Kelly, P.J., Canine blood flow estimated with microspheres, *J. Orthop. Res.,* 7, 61, 1989.

22

Interstitial Fluid Flow

Melissa L. Knothe Tate
University and Swiss Federal Institute of Technology, AO Research Institute

22.1 System Description

22.1.1 Basic Concept and Introduction

Bone represents a porous tissue containing a fluid phase, a solid matrix, and cells. The movement of the fluid phase within the pores or spaces of the solid matrix is referred to as interstitial fluid flow. Although much has been postulated on the effects of this fluid movement on cell behavior (see Section 22.5), relatively little is known about the interstitial fluid per se, the properties of the spaces and channel walls through which the fluid flows, or the nature of the flow under physiological conditions. Despite the paucity of concrete information on interstitial fluid flow in bone, much has been postulated on its role in physiological processes such as metabolism, as well as within the context of bone biology and mechanisms of growth, repair, and adaptation. This chapter reviews the "knowns" as well as the "unknowns" of interstitial fluid flow and should serve as an impetus for further research, so that the "knowns" will outweigh the "unknowns" in the future.

22.1.2 Tissue Composition

The extracellular matrix, including the solid and fluid phases but excluding the cells, comprises organic (~21% dry weight) and inorganic (~76% dry weight) components as well as water and electrolytes (0.08% wet weight). The fibrous protein collagen and inorganic bone mineral hydroxyapatite form a

0-8493-9117-2/01/$0.00+$.50

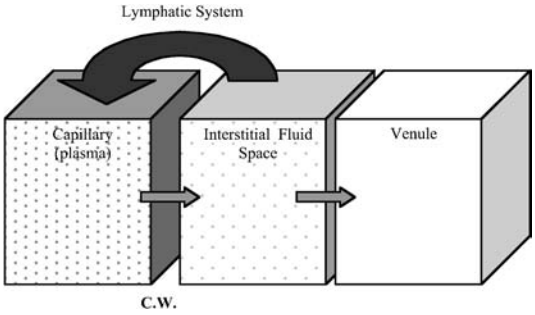

FIGURE 22.1 Schematic representation of fluid compartments; c.w., capillary wall.

composite that lends structural integrity to the tissue. Other organic constituents of the matrix ground substance include proteoglycans (0.01% dry weight), glycoproteins (0.02% dry weight), and lipids.[192] The biochemical composition of bone fluid is unknown because of the practical difficulties of obtaining a sufficiently large sample size for chemical analysis.

22.1.3 Levels of Porosity

The pores or spaces within bone can be classified into three levels including vascular spaces, spaces associated with the lacunocanalicular system, and matrix micropores. Resorption spaces may be present in the tissue as well; their size can vary from infinitely small, at the initiation of resorption, to macroscopically visible pores on the order of or larger than vascular spaces. The sizes of the spaces within bone span several orders of magnitude and correlate with other structural and molecular dimensions (Table 22.1). The permeability of bone tissue is highly dependent on the degree to which the tissue is vascularized as well as the state of mineralization within the tissue, i.e., the degree to which the matrix is mineralized and remodeled. With regard to molecular transport through bone, these varying degrees of porosity serve as a molecular sieve within the tissue (see Section 22.2).*

22.1.4 Interstitial "Tissue" Fluid as Compared with Interstitial Fluid Component of Bone

Considering the distribution of fluid between the different compartments of the body, e.g., cartilage, encapsulated organs such as the brain and kidney, interstitial fluid is that "interposed between the plasma and the cells … [with an] ionic composition similar to that of plasma."[10] The interstitial fluid is separated from the plasma by a capillary wall that serves both as a throughway as well as a barrier to transport between the plasma and interstitium (Fig. 22.1). The wall allows for passage of water and salt but is considered to be a somewhat leaky filter for proteins. The lymphatic system represents a further conduit for communication from the interstitial space to the plasma and does not serve as an obstacle to protein transport (Fig. 22.1).[10]

In contrast to cartilage, which is largely avascular, bone tissue is both vascularized and also appears to have a unique prelymphatic system (see Section 22.1.5). Furthermore, bone tissue is relatively impermeable and noncompliant compared with encapsulated organs such as the kidney or brain. Thus, the interstitial fluid in bone is expected to have a unique composition, and the flow of this fluid through bone is expected to be regulated via mechanisms other than those prevailing in cartilage or encapsulated organs. The fluid component of bone is divided into compartments, defined by the spaces or pores through which the fluid flows as well as membrane or conformational barriers that prevent free passage of fluid between compartments. At the most basic level, the vascular fluid or blood is clearly distinguished,

*For more information on bone pores and their effect on mechanical properties of the tissue, refer to Chapter 23, Bone Poroelasticity.

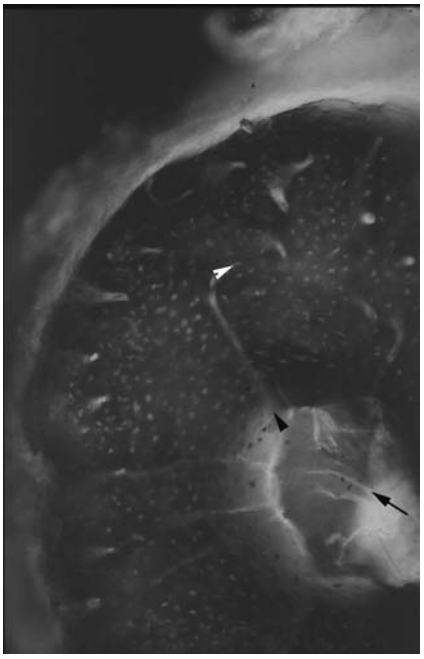

FIGURE 22.2 Portion of a cross section from the metacarpus (I) of a 180-day-old rat 10 min after procion red injection. The bone tissue shows cortical structure. Tracer appears to delineate vascular pathways from the intramedullary vessels (black arrow) to those of the endosteum (black arrowhead) and the inner cortex (white arrowhead). Numerous periosteocytic spaces show presence of tracer as well (original magnification ×120). (After Knothe Tate, M. L. et al. *Bone,* 22, 110, 1998. With permission.)

in terms of content and function, from the extravascular fluid. Furthermore, a distinction is made between intracellular and extracellular fluid, which are referred to as being compartmentalized. Extravascular, extracellular fluid includes that in which the cells bathe (filling the lacunocanalicular system), in pores between the hydroxyapatite–collagen composite, as well as "bound water" around the hydroxyapatite crystals.[31,63,84,133,154,201,211] For the purposes of this chapter, interstitial fluid comprises the fluid in bone spaces excluding the vascular and intracellular space.

22.1.5 Flow Pathways for Influx and Efflux of Interstitial Fluid to Bone Tissue

Interstitial fluid flow is essential for bone vitality. However, the pathways for inflow and effluence of interstitial fluid through bone have not yet been completely elucidated.[108] In the case of cortical bone, interstitial fluid is postulated to form via filtration from the arterial end of Haversian capillaries;[144] thus, influx is from the vascular system. Effluence is hypothesized to proceed via the venous ends of neighboring Haversian systems, by a prelymphatic system present in the matrix,[144] and/or by way of periosteal venules.[138] Prelymphatics are defined as "a system of nonendothelialized spaces that lead through interstitial tissues to the initial lymphatics;" the nearest lymphatic system to the cortex lies in the periosteum.[144] Transudance of the fluid after influx and prior to effluence occurs via the lacunocanalicular system (see Section 22.2.2.1).

In addition to bulk transport during influx of the interstitial fluid, molecules and ions move into and through the interstitial fluid from vascular, matrix and intracellular spaces.[108,144] Differences in pathways for cortical (Fig. 22.2) and trabecular bone (Fig. 22.3) reflect the unique structure of those respective tissues. The pathways of transport from the blood supply to the osteocytes in cortical bone are complex due, on the one hand, to the anastomosing vessels of the vascular system and, on the other hand, to the extensive

TABLE 22.1 Approximate Limiting Dimensions for Vascular and Extravascular Spaces within Bone, Relative to Tracer Size

Bone Space/Structure	Limiting Dimension (diameter, unless otherwise indicated)			Tracer	Diameter	M.W. (g/mol, unless otherwise indicated)
Bone		1 mm	1×10^{-3} m			
Haversian system	2.5×10^{-4} m[35,152]					
Trabeculae	$1.5–2.0 \times 10^{-4}$ m[134]					
Lamellae	$3–7 \times 10^{-6}$ m[134]					
Vascular system						
Haversian canal						
Primary	$5–7 \times 10^{-5}$ m[9,38]			^{99m}Tc-Red blood cells[145]		
Secondary	$5–12 \times 10^{-5}$ m[9]			Microspheres	15×10^{-6} m[72]	
Volkmann canal	$2.5– 5 \times 10^{-5}$ m[9]					
Epithelial fenestrae of marrow cavity vessels	1×10^{-5} m[50,117]					
		1 μm	1×10^{-6}m			
Capillaries	1×10^{-7} m[84]			Glycogens	$12–15 \times 10^{-9}$ m[189]	
				Dextrans	$7–10 \times 10^{-9}$ m[113,189]	3,000–2,000,000
Capillary wall pores	$3–4.5 \times 10^{-9}$ m[84]			Saccharated iron oxide particles	$1–10 \times 10^{-9}$ m[139]	445,000–46,000[3]
Lacunocanalicular system				Ferritin (native)	5.5×10^{-9} m[189]	440,000[189]
					11×10^{-9} m[48]	
Lacunae	$1–1.3 \times 10^{-5}$ m[9]			Fibrinogen	5.22×10^{-9} m[3]	340,000[76]
				Catalase		240,000[189]
Intralacunar distance	$3–4 \times 10^{-5}$ m[35]			IgG		180,000[76]
	$5–7 \times 10^{-6}$ m[8]					
Space between osteocyte surface and mineralized wall of lacuna	2.7×10^{-6} m[214]			LDH	4.6×10^{-9} m[3]	
Canaliculi	$1–10 \times 10^{-7}$ m[9,24,38,179a]			Myeloperoxidase	4.4×10^{-9} m[189]	160,000
				Aldolase		158,000
				Transferrin		76,000–88,000[145]
Osteocyte process	$8.5–10 \times 10^{-8}$m[38]			Serum albumin	$(4–14) \times 10^{-9}$ m[48]	64,000[145]–69,000[165]
					3.55×10^{-9} m[3]	
				Lactoperoxidase	3.6×10^{-9} m[189]	82,000[189]
					2.8×10^{-9} m[189]	68,000[165]
				Hemoglobin	3.1×10^{-9} m[3]	
					3.25×10^{-9} m[165]	
Canaliculus wall to osteocyte process surface	1×10^{-7} m[217]			Thorotrast (colloidal thorium dioxide)[57]		
	$1.42–5.0 \times 10^{-8}$ m[38]					

Space between mineralized and unmineralized zone lacunae	1–20 × 10^{-7} m[216] 3.25 × 10^{-8} m[38] 2 × 10^{-8} m[9]			Horseradish peroxidase	5–6 × 10^{-9} m[140] 3.0 × 10^{-9} m^3	40,000[140]
Postulated gap junctions between cell processes	~2 × 10^{-9} m[53]			Colloidal gold spheres	3–7 × 10^{-9} m	
Bone matrix pores, i.e.,collagen–hydroxyapatite porosity	5–12 × 10^{-9} m[80] (small fraction 12– 25 × 10^{-9} m[80]			Orosomucoid	3.0 × 10^{-9} m^3	38,000[3]
				Ovalbumin	2.76 × 10^{-9} m^3	43,000[3]
				β-Lactoglobulin	2.74 × 10^{-9} m^3	35,000[3]
				Chymotrysinogen A	2.25 × 10^{-9} m^3	25,000[3]
				Ribonuclease	2.08 × 10^{-9} m^3	13,683[3]
				Lysozyme	2.06 × 10^{-9} m^3	14,100[3]
				α-Lactalbumin	2.02 × 10^{-9} m^3	14,176[3]
				Cytochrome c	1.87 × 10^{-9} m^3	12,284[3]
					1.5 × 10^{-9} m[189]	12,800[189]
				Myoglobin	1.75 × 10^{-9} m^3	17,800[189]
				Saccharated iron oxide particles	1–10 × 10^{-9} m[217]	
				[^{14}C] Inulin	1.48 × 10^{-9} m[165]	5,000[145]
				Microperoxidase MP-11 (haem undecapeptide)	2.0 × 10^{-9} m[43] 8.9 × 10^{-10} m^3	1,800–1,900[3]
				MP-9		1630
				MP-8		1550
				Ruthenium red	1.13 × 10^{-9} m[43]	860
				Sucrose	1.08 × 10^{-9} m[48]	342[145]
				[^{14}C]Sucrose	4.0 × 10^{-8} m[84]	
		1 nm	1 × 10^{-9} m			
				Patent blue violet	6.4 × 10^{-10} m^3	566[3]
				^{51}Cr-labeled EDTA		336[145]
				Na Fluorescein	5 × 10^{-10} m^3	376[3]
				"Fluorescent dyes"		300–400[68,151]
				Azure C	4.3 × 10^{-10} m^3	277[3]
				Biotin		250[76]
				Pyrophosphate		235
				^{125}I-labeled antipyrine		188[145]
				Tritiated glycine		
				Glucose		
				Calcium ion (Ca^{2+})	1.6–2.1 × 10^{-10} m^3	139[3]
				Strontium isotope (^{85}Sr)	8.4 × 10^{-10} m	87.62

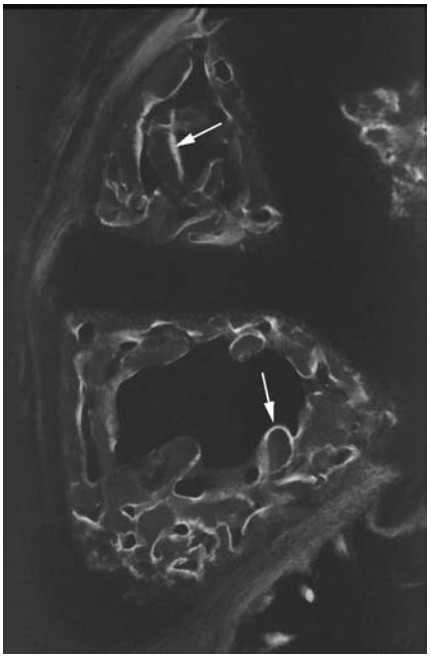

FIGURE 22.3 Bone tissue of the metacarpus in a 60-day-old rat 10 min after procion red injection. Adjacent metacarpi (III and IV), exhibiting predominantly cancellous bone structure with peripheral areas of undecalcified cartilage. Tracer appears to be concentrated in areas of calcified tissue apposing vascular areas (white arrows) (original magnification × 75). (After Knothe Tate, M. L. et al., *Bone,* 22, 110, 1998. With permission.)

extravascular fluid spaces comprising the lacunocanalicular system and matrix porosity.[108] It is believed that the blood supply entering the Haversian system is derived primarily from the vessel system of the medullary canal (Fig. 22.2). As described by Cooper, "most of the vessels involved in transmitting nourishment to the cells in compact bone arise from the medullary vessels and enter the endosteal surface of the diaphysis where they go into Haversian canals."[38] In contrast, trabecular bone is generally in close proximity to the medullary space (Fig. 22.3). Given the rapidity with which the intramedullary vascular and extravascular compartments equilibrate[138] as well as the proximity of the blood supply to the osteocytes within the bone, transport from an intramedullary vessel to a given osteocyte within a trabecula is fast compared with that from the intramedullary blood supply to a given osteocyte within the cortex of cortical bone.[62,103,104,108,111]

22.2 Molecular Transport Mechanisms in Bone

A prerequisite for metabolism in any living tissue is an adequate supply of nutrients for anabolic activity as well as a mechanism for removal of waste products resulting from catabolic activities—in short, molecular transport must be ensured. Similarly, molecular transport is necessary to ensure that adequate supply of growth factors and other osteotropic substances exist for processes associated with growth, adaptation, and repair. Within soft tissues and organs, molecular diffusion through interstitial spaces is considered the principal mechanism for movement of various physiological fluids and solutes. In contrast to the soft tissues of internal organs, approximately 85% of bone volume comprises solid material such as mineral and collagen. Thus, within the particularly dense tissue of cortical bone, osteocytes are dependent on the transport pathways comprising the lacunocanalicular system and, to a lesser degree, interconnected pores within the matrix, for maintenance of "metabolic traffic and interchange."[38,39,108,188]

22.2.1 The Diffusion–Convection Equation

Interstitial transport phenomena in bone can be described mathematically by the following partial differential equation, also referred to as the scalar form of the general diffusion-convection equation:[110]

$$\frac{\partial C}{\partial t} = \frac{\partial}{\partial x_i}\left(k_i \frac{\partial C}{\partial x_i} - u_i C\right) + Q - KC, \tag{22.1}$$

whereby the individual terms can be described as follows:

- $C(x_i,t)$ is the concentration of a given molecular species (dependent variable) (particles/volume)
- x_i is the index form for the Cartesian coordinates
- t is the time
- k_i are the diffusion coefficients (area/time)
- u_i are the components of the velocity vector (length/time)
- Q is the source, respective, sink coefficient (particles/volume • time)
- K is the reaction rate (1/time)

Eq. 22.1 is nonsymmetric and of parabolic form. This equation can be solved to determine the concentration density function ($C(x_i,t) \equiv$ location and time-dependent concentration) for molecular entities (i.e., nutrients and metabolites, growth factors, cytokines, osteotropic substances, mineral) within a defined control volume.

Eq. 22.1 is merely a mathematical description of the change in concentration of, e.g., Ca^{2+}, in a given volume of tissue, as a function of location and time. If this ion is in abundance within a given lacuna, it will distribute within the tissue over time, due to Brownian motion (diffusion), concentration gradients, and convective transport. Of course, other modes of active transport, in particular intracellular transport, may have an effect on overall distribution of the ion within the control volume; however, Eq. 22.1 describes merely transport by diffusion, convection, uptake, and reaction over time. The diffusion constant k_i depends on a number of factors including state of the tissue (affected by, e.g., composition, permeability) and temperature at which transport is taking place. Only limited information is available with regard to diffusion coefficients for bone tissue (Table 22.2). Considering physiological loading conditions in which extremely slow flow rates would be expected to prevail within the bone, it is assumed that inertial effects can be neglected. Thus, Eq. 22.1 can be written in the following form, where u and v are the time- and location-dependent components of the average velocity vector:

$$\rightarrow \frac{\partial C}{\partial t} + u\frac{\partial C}{\partial x} + v\frac{\partial C}{\partial y} - \frac{\partial}{\partial x}\left[k_x \frac{\partial C}{\partial x}\right] - \frac{\partial}{\partial y}\left[k_y \frac{\partial C}{\partial y}\right] - Q + KC = 0 \tag{22.2}$$

The validity of this assumption under physiological loading conditions including high-impact loads is not clear.

22.2.2 Diffusion or Transport in Bone Devoid of Mechanical Loading

Although several studies have shown that diffusion is a major contributing mechanism for the transport of molecules and ions across the endothelial layer of bone capillaries, diffusive mechanisms may not be sufficient to ensure adequate transport to and from osteocytes that are not in close vicinity of vascular canals.[108–110] Furthermore, due to the dynamic structure of bone, patent metabolic pathways may become blocked during remodeling processes, resulting in osteocyte starvation.[9,113b] Although vascular transport of all molecular species and intracellular transport of small molecular species is expected to be rapid, the transport rate of large molecules through the tissue is highly dependent on tissue permeability as well as membranes and conformational barriers. Thus, the concept of passive or free diffusion as the principal mechanism of exchange between the blood and interstitial fluid in bone[82] has been questioned.

TABLE 22.2 Constants Related to Bone as a Poroelastic Material

	Ref.
Diffusion Constants	
Diffusion constant: glucose through cartilage 1.4×10^{-6} to 2.3×10^{-6} cm^2/s	129–131
Free diffusion coefficient of glucose at 37° C: 8.8×10^{-6} cm^2/s	64
Diffusion constant of glucose through cortical bone, based on *in vitro* experiment: 10^{-8} cm^2/s	5
Extrapolated diffusion constant of glucose through cortical bone 3×10^{-9} cm^2/s	118
Free diffusion constant for albumin circa 9×10^{-7} cm^2/s	
Constants Related to Bone as a Poroelastic Material	
Porosity, ϕ (porosity connected to the free surface of the sample): 0.2	95
Permeability, k	
10^{-12} to 10^{-14} m^2	92
Adult canine bone: 3.32×10^{-7} cm^3/(mm minute g/cm^2)	120
Puppy bone: 20.83×10^{-7} cm^3/(mm min g/cm^2)	120
Time constant (s)	
Haversian system: 10^{-4}	92
Lacunocanalicular system (cleared of debris and filled with water): 10^{-3}	92
"Bone": order of 1 s	115
Fluid Flow Rates	
11.4–400 μl/g/h	137
600 μl/g/h, based on permeability constants	120,137

If this concept were applicable for bony tissue, nutrients would have a long transit time through the interstitial fluid compartment, resulting in large variations between the chemical environments of individual osteocytes, depending on their distance from the blood supply.[110]

22.2.2.1 Tracer Studies in "Quiescent" Bone: Elucidation of Transport Pathways and Barriers to Flow

To date, the degree to which diffusive mechanisms provide key molecules to osteocytes for maintenance of metabolic activity as well as for activation or suppression of remodeling and repair processes remains unclear. Tracer studies lend themselves to the observation of molecular transport through tissue. In general, the rate of transport for a given tracer decreases with increasing molecular weight, and for metabolically inactive species, smaller substances are transported more rapidly than larger ones. Hence, the rate of transport from the blood supply to the osteocytes is dependent on the size of the tracer molecule relative to the pathway of transport (i.e., impermeability increases and rate decreases with either decreasing dimension of the pathway for a given tracer molecule or with increasing tracer molecule size for a given pathway). To reach the osteocytes, which "bathe" in the interstitial fluid, the tracers must first pass out of the capillary blood vessels of, e.g., a Haversian capillary. The capillaries of cortical bone have a continuous epithelium lined with a basement membrane.[38,117] Thus, the fluid containing the tracer passes through the basement membrane and epithelial fenestrae of the canal vessel and then diffuses along the pathways depicted schematically in Fig. 22.4. The exact dimensions of the membrane pores and epithelial fenestrae is uncertain, although the epithelial fenestrae found in the walls of bone marrow vessels are reported to be on the order of 9 to10 μm in diameter.[50,117] Furthermore, it has been hypothesized that the bone surface of the Haversian canal is lined with cells, referred to as bone lining cells[133,143,211] or osteoblasts of the blood–bone membrane, that may play a role in maintaining bone fluids, modulating the flux of ions between compartments,[12,143] and regulating interstitial fluid pressure.[79] The tracer has to pass through this layer to reach the interstitial fluid space. Having found its way into the interstitial space, a tracer may then diffuse further via the lacunocanalicular system; the fluid space between the canaliculi walls and osteocyte processes (postulated dimension 14 to 100 nm[39,216]) provides one conduit for osteocytes

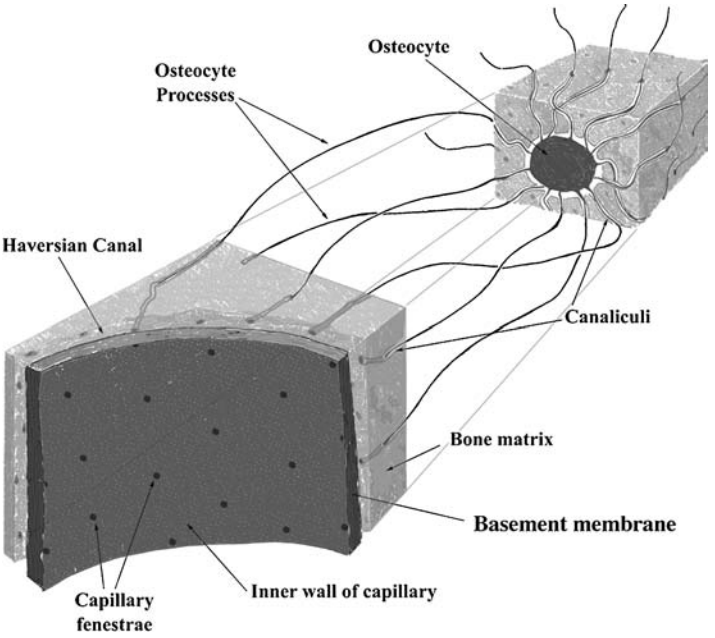

FIGURE 22.4 Schematic representation of transport pathways from the vascular system to the osteocyte. (After Knothe Tate, M. L. et al., *Bone,* 22, 114, 1998. With permission.)

to receive nourishment and to rid themselves of waste products via extracellular transport.[15,169,215] Innumerable micropores pervading the bony matrix may supply additional routes for extracellular, diffusive transport (estimated average pore size 5 to 12 nm).[80] Furthermore, intracellular transport pathways have been postulated, for example, along the cellular processes (estimated average diameter 85 to 100 nm),[38] and across gap junctions[37,59,81] (postulated size 2 nm[53]). These intracellular pathways are, by definition, not considered within the context of this chapter on interstitial fluid flow.

22.2.2.2 Limiting Dimensions of Bone Spaces Relative to Tracer Sizes

Numerous tracer studies have been conducted to investigate vascular and extravascular transport with regard to bone metabolism and physiology in general. An overview of limiting dimensions for vascular and extravascular bone spaces relative to tracer size is shown in Table 22.1. Whereas capture methods using radioactive microspheres lend themselves to measurement of blood flow through bone, they are limited to the observation of macroscopic effects due to trapping of the 15-μm spheres in microvascular channels. The outflow dilution method consists of an injection of a mixture of tracers followed by sequential sampling of the venous outflow; in bone, solutes are essentially "extracted" through the capillaries by passive diffusion. The technique has been employed to elucidate cellular, extracellular, and extravascular compartment volumes as well as residence times for tracer substances, including labeled strontium, fluoride, sucrose and phosphate compounds, red blood cells, transferrin, albumin, water, EDTA, and inulin.[46,83,84,145,154,155,176] Labeled sucrose is typically used to approximate the size of the extracellular fluid space and labeled red blood cells; transferrin and albumin serve to quantify the vascular space and its components.[176] The outflow dilution technique is efficacious for the measurement of transcapillary exchange.[84] However, it is difficult to differentiate exchange in interstitial compartments not specific for the study of interstitial transport through the lacunocanalicular system, because the tracers used are either too small to exclude transport through the micropores of the bone matrix or they are endogenous to bone, thus rendering it difficult to separate the injected tracer from naturally occurring substances within bone.

Molecular markers lend themselves particularly well to the study of extravascular transport, but the choice of a tracer is paramount. Although it has been reported that ionic charge is not a factor in the rate of transcapillary diffusion,[84] it does seem to be significant for interstitial transport.[113] Furthermore, the biochemical properties of a given tracer may affect the biology of the system and/or interstitial transport of the tracer through a given system. Molecular markers including ^{45}Ca,[23,30,70] iodinated albumin,[163,164] lead,[156] thorotrast,[188] ferritin,[49,175] and horseradish peroxidase[11,51,52,121,202,203] have been described in the literature; these tracers were utilized to follow the movement of material from the blood through the interstitial fluid space *in vivo* in healthy as well as pathological[176] bone of experimental animals, including mice, rats, chicks, rabbits, dogs, cats, and goats. In addition, interstitial fluid flow and bone perfusion have been studied using tracers including disulfine blue, procion red, microperoxidase and fluorescent-labeled dextrons of varying molecular weights in an *ex vivo* model of the skeletally mature sheep metacarpus,[62,103,106,109,111] in an *in vitro* model using small cylindrical compact bone specimens excised from sheep metacarpus,[107,109] and *in vivo* in skeletally immature as well as skeletally mature rats.[108,112,113] Whereas markers such as ^{45}Ca, albumin, and lead are exchanged with and/or incorporated within the matrix of bone tissue, thorotrast, ferritin, horseradish peroxidase, and microperoxidase, as well as water-soluble dyes such as disulfine blue, procion red, and fluorescent dextrons do not occur naturally in bone tissue. Thus, they may provide a better means for tracking and measuring the movement of material from the blood supply to the osteocytes via the interstitial space.

22.2.3 Convection and Other Modes of Transport in Bone Subject to Loading

Given the inefficiency of diffusive mechanisms for the transport of larger molecules through the relatively impermeable tissue of bone, another mechanism of transport is necessary to provide a supply of larger molecules, such as proteins, to osteocytes for the maintenance of metabolic activity, as well as for activation or suppression of modeling processes.[108,112] Early studies indicating that canaliculi are cleared 2100 times in 24 h underscore the concept that diffusion cannot be the sole mechanism of circulation within the lacunocanalicular system.[182] Based on clearance data and approximated diffusion coefficients, diffusion distances in cortical bone have been estimated to be on the order of tens of microns in an hour's time.[138] Such discrepancies in transport times would result in large variations between the chemical environments of individual osteocytes depending on their proximity to the Haversian capillary.[110] Thus, a number of biophysical mechanisms for enhancing transport, including active pumping by the osteocyte, direct effects of mechanical loading (i.e., deformation), pressure gradients, and electromechanical and biochemical mechanisms, have been proposed; these are described in more detail in the next section. In each case, the effect of fluid movement remains the same; based on the causal mechanisms, the "prime mover" may be unique.

22.3 Biophysical Mechanisms of Fluid Movement

22.3.1 Active Transport by Osteocytes

Osteocytes are described as being stellate shaped, both *in situ* and in culture. This property is innate to the osteocyte and the unique arrangement of its cytoskeleton.[1] Microtubules, which are believed to be involved in the secretion of matrix proteins such as collagen, are found in the cell body but not in the cell process. In contrast, bundles of microfilaments line the surface of the cell body and "almost completely fill the cell processes."[1,101] Although the exact function of these microfilaments is debatable, it has been proposed that they aid in the transport of small molecules from the cell body to the tip of cell processes; after passing through the gap junctions, they further aid in transport of small molecules from the next process tip to its cell body.[37,101] Given the small size of gap junctions (2 to 4 nm space), this mode of transport cannot account for movement of larger molecules through the tissue. However, in addition to aiding in active intracellular transport, these microfilaments exhibit contractile properties. Thus, it is possible that, by actively contracting and expanding their cell processes, the osteocytes send waves of

interstitial fluid through the lacunocanalicular system,[1] facilitating diffusion and promoting the mixture of solutes.

It should be noted here that the system of metabolic traffic and exchange, i.e., the lacunocanalicular system, derives from the stellate shape of the osteocytes, on the one hand, and their interconnectivity on the other hand. The extended osteocytic network (cells interconnected by connection of the multiple cell processes) forms a syncytium[146] that dictates the size and shape of the canaliculi. The "typical stellate shape of the osteocyte is not imposed on the cell by the matrix that surrounds it *in vivo*."[1]

22.3.2 Effects of Mechanical Loading

Mechanical loading of bone tissue during physiological activity results in a tissue stress state comprising cyclic dilatational and deviatoric components. The effect of dilatation or pressure imposed by cyclically loading a given volume of bone tissue is addressed below in detail (Section 22.3.3). Essentially, pressure gradients are the motor for fluid movement within tissue. In contrast, although they appear to be critical in mechanotransduction of loading signals to the cells, the role, if any, that deviatoric or shear stresses play in fluid movement is unclear (see Section 22.5.1).

22.3.3 Pressure Gradients

22.3.3.1 Biot's Theory of Poroelasticity

Biological tissues are frequently modeled as poroelastic to account for properties inherent to the fluid phase. Movement of the interstitial fluid within bone is similar to that in soft tissues, although bone is much less permeable. Thus, bone is analogous to a stiff and dense fluid-filled sponge. Biot's theory of poroelastic solids[18–20] describes the behavior of fluids in porous materials and thereby elucidates the physical basis of pressure gradients underlying load-induced fluid flow in bone. According to this theory, the solid matrix of a porous material deforms under compressive loading, thus increasing the pressure in the fluid within the pores. Disparate pressures between the interior and exterior of a porous solid cause a net flow in or out of the solid, depending on the Poisson's ratio of the material. As fluid flows out of the porous solid, the solid matrix around the pores relaxes and the fluid pressure decreases until it becomes equal to that at the surface of the solid, at which point there is no pressure gradient to drive fluid flow. Conversely, as soon as the external loading is removed, a pressure gradient results in the opposite direction and the fluid flows back into the sample until the pressure gradient reduces to zero once again. The rate of fluid pressure reduction during matrix relaxation is an exponential decay function.[18–20]

22.3.3.2 Application of Biot's Theory to Bone

A number of models based on Biot's theory of poroelasticity have been developed to examine the relationship between mechanical loading, the development of pressure gradients, and the ensuing interstitial fluid flow in bone tissue. Piekarski and Munro[168] developed a lacunocanalicular model in which they postulated that compressive loading causes an instantaneous decrease in volume of the pores (e.g., the lacunae) and the interstitial fluid contained therein, creating an instantaneous increase in fluid pressure within the lacunae. Assuming that the pressures in the lacunae and in the Haversian canal are in equilibrium prior to loading, and that the pressure of the Haversian canal is unaffected by mechanical loading, a pressure gradient develops between the lacunae and the Haversian canal, causing fluid flow through the canaliculi until the pressure equilibrates. This fluid flow from the lacunae through the canaliculi depends on both the pressure in the surrounding tissue and the resistance of the lacunae. Upon release of the compressive load, the lacunae expand and fluid is drawn back into the lacunar space, where the osteocytes reside. The postulate that mechanical loading creates pressure gradients which drive fluid flow from areas of bone in compression to those in tension, in essence the existence of load-induced fluid flow, has been proved recently using molecular tracer methods to visualize fluid displacements in cortical and trabecular bone.[62,103,107–109,111–113]

22.3.3.3 Interactions between the Medullary Canal and Capillary/Venous System

In addition to pressure gradients in the interstitial space resulting from mechanical loading during physical activities, the interaction between capillary and intramedullary pressure have been implicated as important regulators of interstitial fluid flow. In 1896, Starling formulated the law that increased capillary pressure increases transudation through tissue.[195] Given the fact that medullary pressure is influenced primarily by venous resistance in the tissue, venous and intramedullary pressure are necessarily interrelated.[220] A number of experiments have been conducted to examine these effects. In experiments designed to study the relationship of increased venous pressure to formation of periosteal bone by application of a low-pressure venous tourniquet to the tibiae of growing dogs, it was shown that an increase in venous pressure causes a concomitant increase in fluid movement from the capillaries to the interstitial space of bone tissue.[99,145] In short-term experiments (from minutes to an hour) where venous pressure was increased by ligation of the femoral vein in skeletally mature rats, no statistically significant difference in fluid movement from the capillaries to the interstitium could be observed between the control and ligated limb,[138] although the data did support the hypothesis that interstitial fluid transport proceeds from the endosteal to the periosteal surface.[138,144] In longer-term studies (weeks) it could be shown that bone marrow pressure was increased significantly by venous ligation in the hind limb of a tail-suspended rat, causing a concomitant and lasting induction of interstitial fluid flow through the ligated bone.[16] Conversely, qualitative observations of horseradish peroxidase transport through the tibia in tail-suspended (nonligated) rats showed a decrease in transport due to a reduction in venous pressure.[50]

The heartbeat causes transcortical pressure gradients that are believed to have an effect on interstitial fluid flow as well.[99,159] However, the exact role of pulsatile pressure in the capillaries on interstitial flow is poorly understood. Based on streaming potential measurements (see Section 22.3.4.2), transcortical pressure gradients caused by the heartbeat may represent another motive force for interstitial fluid flow.[159]

22.3.4 Electromechanical Effects

22.3.4.1 Piezoelectric Effects

Very early work in the electromechanical properties of bone tissue showed that bone behaves piezoelectrically when deformed.[13,14] In compression studies on cubes of dried cortical bone and tendon, a direct piezoelectric effect as well as an indirect piezoelectric effect could be proved; i.e., an electrical charge was produced by deformation, and mechanical deformation or strain was caused by the application of an electrical field, respectively.[61] At that time, collagen was implicated as being responsible for this piezoelectric behavior in bony and tendonous tissue. More recent studies have provided evidence for different sources of stress-generated potentials (SGPs) in wet and dry bone; it has been shown that the streaming potential, rather than piezoelectricity, is the dominant mechanism for creation of SGPs in wet tissue.[71,91,157]

22.3.4.2 Streaming Potentials: The Source of Strain Generated Potentials

In addition to the piezoelectrical effects observed in dried bone and tendon, unique mechanoelectrical effects have been observed in moist specimens and have been attributed to strain-generated potentials that are produced when a charged fluid, e.g., an electrolyte, flows over a charged surface.[6] Eriksson describes the "movement of the fluid in bone [as a] real, physical, electrical current and therefore … directly responsible for measured streaming potentials";[55] thus, within the limits of laminar flow, the faster the movement of the fluid, the greater the magnitude of the streaming potential through the tissue. In concurrent studies of piezoelectric and streaming potential effects in wet samples, the potentials caused by interstitial fluid flow dominate over those caused by piezoelectric effects.[71,91]

It is likely that the interstitial fluid flow underlying streaming potentials and the flow visualized by tracer distributions represent one and the same phenomenon rather than autonomous mechanisms for fluid flow within bone tissue. However, it has been postulated that streaming potentials are an effect of the anatomical structures through which the charged fluid flows and are, as such, a unique phenomenon. Whereas studies in wet bone specimens have targeted the collagen–hydroxyapatite porosity of the bone matrix as the likely milieu in which streaming potentials occur,[185,186] theoretical models of fluid flow

suggest that the location of the streaming potential may be exclusive to the bone canaliculi.[42] The crux of the issue is the state of the interstitial fluid within the tissue, i.e., whether the "bone water" is bound or unbound in its natural state *in situ,*[55] as well as the state of the walls through which the fluid flows. Unfortunately, both issues remain unresolved. Experimental studies suggest that a fraction of the water within bone exists in the free liquid state and that the remaining water is chemically bound to collagen and apatite, existing in at least three different bound states.[55] However, small-molecular-weight tracers may permeate spaces within the lacunocanalicular system as well as within matrix pores, indicating that fluid flow does occur in both spaces.[108] Recent atomic force microscope (AFM) observations indicate that the walls of the canaliculi may be sheathed with a collagen layer, acting like insulation between the wall of the canaliculus and the interstitial fluid.[74,179a] Furthermore, the arrangement of collagen fibrils along the wall may be a source of turbulence, preventing the development of laminar flow through the canaliculus.[179a] Whereas data supporting the idea of "bound" water within the matrix pores lend credence to the idea that the bone canaliculi, rather than the micropores within the matrix, are the site of streaming potentials, flow visualization and AFM observations strengthen the argument that the matrix micropores play a role in the development of streaming potentials.

22.3.5 Biochemical Mechanisms, Osmotic Pressure, Hydraulic Conductivity, and Interrelationships among Different Effects

Given the differences in composition and concentration between the extravascular, intracellular, and intravascular fluid compartments, it is assumed that osmotic pressure also plays a role in influx and exudation of fluid from one compartment to the next in bone, as is the case in cartilage and encapsulated organs. The solid phase of bone tissue has been described as acting like a molecular sieve (see Section 22.2). By controlling the flow of solutes through the tissue, local osmotic pressure gradients build up and influence the flow of fluid through the tissue. Arnold and Frost have suggested that fluid flow through bone tissue occurs by way of a "osteocyte actuated osmotic pump,"[7,59] whereby water enters and leaves the system through the lacunocanalicular system as well as the microporosity of the bone matrix. Furthermore, Arnold[7] refers to plugging action of the osteocytic processes at the junction between the canaliculus and lacuna, resulting in a valve mechanism favoring efferent over afferent flow with respect to the cell body. Finally, it has been suggested that the "hydraulic conductivity," i.e., the volumetric fluid flux per unit pressure drop, of bone tissue is modulated by the bone-lining cells or surface osteoblasts;[30,79,85,153,154,166] in cell culture experiments using osteoblasts, it could be shown that hydraulic conductivity is affected by a number of agonists including calcitonin and parathyroid hormone.[79] Similarly, tissue permeability is affected by the presence of specific osteotropic agents.[73,74,79,158] Hydraulic conductivity and the development of osmotic pressure gradients are necessarily related. Given the interrelationship among biochemical effects, osmotic pressure gradients, and hydraulic conductivity, it is not surprising that these processes are difficult to study experimentally and are thus poorly understood.

22.4 Measurement of Interstitial Fluid Flow

22.4.1 Approximations Based on Theoretical Models

Experimental study of load-induced fluid flow phenomena in bone is inherently difficult. The task of measuring the flow rate in the minute (less than 1 μm in diameter) lacunae and the canalicular systems is not trivial; mechanical probes are not feasible for flow measurements in tiny canals that are encased in hard bony tissue, and imaging techniques have not yet been developed for recording the flow in such a system. Because of these difficulties, many researchers have developed analytical and computer models to attempt to understand fluid flow phenomena in idealized model systems of bone tissue. Typically, Biot's theory of poroelasticity or some variation thereof is used as a starting point to model the interaction between the solid and fluid phase. Models have been developed to describe mechanical loading, electromechanical, and hydraulic effects in bone.

Molecular transport has been modeled at the cellular level in bone tissue. Typically, the lacunocanalicular system is the region of interest for such models. Piekarski and Munro[168] were the first to model

the previously formulated idea (Ref. 14 and others) that the lacunocanalicular system is a transport pathway operating between the blood supply and osteocytes in long bones. Using a highly idealized model of a lacunocanalicular system, they showed that stress-induced flow increases the efficiency of the transport mechanism acting between the blood supply and the osteocytes. Kufahl and Saha[115] investigated the effect of cyclic mechanical stress on fluid flow in the lacunocanalicular network. Based on their calculations, with an optimal canaliculus diameter of 0.2 μm, fluid velocity through the canaliculi would be maximized and squeeze flow could nourish four to five concentric layers of osteocytes in a given osteon. Mak et al.[127] used finite-element methods (FEM) to investigate the contribution of the bone microporosity, the canaliculi, and the Haversian canals to the overall flow of fluid through bone. Their model showed the effect of canaliculus wall permeability on development of drag forces within the canaliculi; this is significant with regard to mechanisms of mechanotransduction down to the cell membrane. Furthermore, FE modeling techniques have been used to show that diffusion alone cannot account for molecular transport in mineralized tissue.[105,110] In addition, recent models of mass transport through individual osteons as well as cortical bone tissue have elucidated the role of convective transport mechanisms in maintaining local equilibria within osteocyte lacunae.[110] Finally, models have been developed to describe effects of circulatory, non-stress-induced flow in bone, including exchange processes of tracers between blood and bone,[219] as well as the interstitial fluid flow and passive molecular species transport in porous cortical bone.[97]

At the tissue or organ level, mechanical load–induced fluid flow has been studied in model systems of osteons and whole bones (see Section 22.3.3.1). In an osteonal model, Munro and Piekarski[147–150] calculated pressure gradients in osteons under cyclic loading conditions. By depicting the structure of a single osteon as a finite number of linear, elastic, isotropic concentric cylinders separated by layers of homogeneous fluid with constant bulk modulus, cyclic axial loading was shown to cause outward radial fluid movement. Accounting for the alignment of the trabeculae in the direction of the principal stress, Piekarski postulated that fluid flow phenomena in trabecular bone are similar to those in cortical bone.[169] Finally, recent models of fluid flow in bone at a macroscopic level (where bone can be approached as an organ) provide an understanding of general processes related to functional adaptation, e.g., bone apposition patterns in response to alterations in mechanical loading patterns.[112,196–198] Using a model based on beam theory and Biot's theory of poroelasticity, the magnitude and distribution of fluid displacements in a rat tibia cross section subjected to four-point-bending loads have been determined and interpreted in light of tracer transport data from *in vitro, ex vivo,* and *in vivo* experiments.[112,196–198]

Electromechanical effects of interstitial fluid flow have been studied using cellular-, tissue-, and organ-based models as well. At a cellular and tissue level, the electromechanical effects observed experimentally in bone have been characterized using a mathematical model that accounts for the microstructure of the osteon as well as macroscopic specimen parameters.[167,172] This model was the first of its kind to explain experimental data measured in osteons and across macroscopic specimens based on electrokinetic theory and continuum mechanics. The results of this model indicate that the bone matrix microporosity represents the site through which flow associated with electromechanical effects takes place.[185,186] Johnson[92,93] modeled load-induced fluid flow in cortical bone to calculate pressure decay times in the Haversian system; based on the order of magnitude of the results, it was concluded that SGPs originate either in the lacunocanalicular system or in the Haversian system. If the lacunocanalicular system were the site of origin for the SGPs, the pressure decay times would be slower than those calculated based on this model. However, the calculated pressure times could be rationalized if one assumes that the lacunocanalicular system is filled with organic material such as proteoglycans, which would retard flow effects. Similarly, Weinbaum et al.[216] used an idealized hierarchical model of cortical bone to calculate pressure decay times to estimate the magnitude of shear stresses acting on the surface of the osteocyte process. Based on the assumption that the annulus between the osteocyte process and canalicular wall is filled with a glycocalyx-like gel such as that surrounding endothelial cells, it was concluded that the lacunocanalicular system represents the relevant level of porosity for fluid flow associated with streaming potential effects.[42,213,216] Other models have accounted for the role of streaming potentials in cellular signaling associated with remodeling processes. Harrigan and Hamilton[77] and Zhang et al.[224] developed

a mathematical model for a specific intracellular stimulus for remodeling within bone tissue, whereby SGPs are propagated between cells in a manner similar to the classical cable model for nerve cells.

Whereas theoretical models are helpful for understanding processes of fluid movement and mass transport in bone, validation of these models can be challenging. While *in vivo* and *in vitro* models often have physical limitations (see Sections 22.4.2 through 22.4.4), theoretical models are generally limited with regard to simulating bone anatomy and physiology as well as physiological loading conditions, from the organ down to the cellular level.

22.4.2 *In Vitro* Studies

As underscored in previous sections, due to the miniscule size and the difficult access to the lacunocanalicular system, fluid flow through bone is difficult to quantify. Fluid flow measured *in vitro* through intact wet bone samples is thought to be very small.[73] However, such measurements are susceptible to error due to systemic artifacts related to changes in cell vitality and fluid viscosity (a natural consequence of specimen removal from a living system) as well as methodological artifacts including debris blocking the fluid channels. Furthermore, *in vitro* measurements cannot account for the vascular influx of interstitial fluid, the naturally occurring efflux of the same fluid, or fluid flow due to the biophysical mechanisms outlined earlier in this chapter (see Section 22.3). As such, the relative volume flow of interstitial fluid present in the lacunocanalicular system and the matrix porosity at the onset of the experiment are approximated. Permeability of bone has been estimated based on experiments[73,120] and theoretical models (see Table 22.2). It has been shown that permeability increases with biochemical treatments designed to increase flow through the tissue, e.g., by alteration of the tissue ultrastructure via decalcification or deproteinization.[73,74,158] Based on these experiments and AFM data,[178,179,179a] it is suggested that the mineral phase is "shielded" from the fluid phase by organic layers. This idea appears feasible, given the great affinity of hydroxyapatite for proteins, and may lend credence to the idea that the canalicular system is insulated by an organic sheath. If proven true, this would have important implications with regard to the site of origin for SGPs, where preference would be given to the matrix microporosity over the lacunocanalicular system.

Strain-related electrical potentials have been measured *in vitro* by a number of research groups[71,119,125,126,186] and have been reviewed earlier in this chapter (see Section 22.3.4). Although *in vitro* studies by MacGinitie et al.[125] have shown that a pore size in the range of the bone microporosity or canaliculi that are occluded substantially by cellular material represents the relevant space through which interstitial fluid flows to produce streaming potentials, further studies are necessary to determine whether one or the other fluid space dominates in producing electromechanical effects.

Molecular transport studies have been conducted *in vitro* in stressed and unstressed bone using ^{45}Ca in bone samples,[193] glucose in intact canine femora,[118] horseradish peroxidase in long bones of fetal rats,[122] and procion red in cylindrical specimens explanted from cross sections of cortical bone from the sheep metacarpus.[107,109] Whereas early studies using glucose showed no effect of mechanical loading on the diffusion constant of glucose in bone,[118] loading was shown to enhance molecular transport through the relatively impermeable tissue of bone in all other *in vitro* investigations. Furthermore, a strong positive correlation could be shown between transport and number of loading cycles as well as loading rate in Knothe Tate's *in vitro* model; this model lends itself for studying the relationship among tissue heterogeneity, mechanical loading, fluid flow, and mass transport in bone.[107,109]

22.4.3 *Ex Vivo* Studies

An *ex vivo* model has been developed to study transport processes and fluid flow within bone under controlled mechanical loading and perfusion conditions.[103,111] Data from this model show that load-induced fluid flow is a powerful mechanism to enhance molecular transport within the lacunocanalicular system of cortical and cancellous bone tissue.[62,103,111] In addition to being efficacious for tracer studies under controlled transport and loading conditions, the model lends itself for concomitant studies of SGPs and load-induced fluid flow, as well as for the study of load-induced extravascular fluid flow due to pressure gradients in the intramedullary cavity or due to pulsatile blood flow.

22.4.4 *In Vivo* Studies

Although no methods are available for the direct measurement of fluid flow in bone, such measurements have been undertaken in dentine,[212] where an outward flow of 18.1 ± 15.9 pl/s/mm^2 has been recorded. Data from *in vivo* distribution inflow and outflow experiments in bone indicate that interstitial flow due to circulation through bone is rather high, comprising a volume flow rate from 11.4 to 400 μl/g/h[137] in the tibia of skeletally mature rats. By extrapolating the permeability measurements of Li et al.,[120] interstitial flows as high as 600 μl/g/h have been calculated.[138] Given that complete equilibrium is achieved within the bone marrow 3 min after injection of labeled albumin,[138] that an increase in volume of distribution due to movement into trabecular and cortical bone is observed within 30 min after injection, and that small-molecular-weight tracers are distributed through the lacunocanalicular system within short time periods after intravenous injection,[108] bulk flow and diffusive transport mechanisms may suffice to ensure an adequate supply of small molecules, such as ions and amino acids, to osteocytes in the midcortex of cortical bone within minutes.

Based on other tracer transport experiments, the apparent swift movement of interstitial fluid through bone may be indicative of the rapidity with which small molecular entities are transported through the tissue by diffusive mechanisms alone.[108] However, through the observation of different-sized tracers and their distribution under different loading conditions, it is clear that the transport of larger-molecular-weight tracers cannot be upheld by passive transport alone.[108,109,112,113] Furthermore, horseradish peroxidase uptake in the tibias of tail-suspended rats has been observed qualitatively to be reduced compared with control animals when visualized 15 min after injection with the tracer.[50] Quantitative assessment of fluid flow using fluorescent tracer techniques has shown that fluid flow *in vivo* is influenced by mechanical loading per se as well as by loading mode, i.e., whether the tissue under consideration was located within the compression or tension band with respect to the neutral axis.[112] Finally, *in vivo* studies of strain-related electrical potentials have been carried out,[119] and the effect of venous pressure on fluid flow in bone has been studied in several models, the results of which were reviewed earlier in this chapter (see Sections 22.3.3.3 and 22.3.3.4).

In vivo studies allow for interpretation of fluid flow data with respect to bone growth, adaptation, and repair. By using methods designed to visualize load-induced fluid flow in established experimental models of bone growth, adaptation, and repair, basic mechanisms underlying processes associated with bone modeling and remodeling are being elucidated.[109,112,113b]

22.5 Implications of Interstitial Fluid Flow for Bone Growth, Adaptation, and Repair

Bone, and the skeleton comprised thereof, serves three essential roles in the body, namely, as a mechanical support for the locomotor system, for the protection of the inner organs, and for metabolic function. Interdisciplinary research has shown that the microscopic and macroscopic organization of bone tissue is optimal for a dynamic balance among these functions. Bone responds to changes in its mechanical environment as well as to increased systemic demands by altering its mass and form. These adaptive phenomena are described under the rubric of Wolff's law.[221] Although a number of researchers have developed theories implicating some manifestation of mechanical forces such as stress, strain, and strain energy density for this functional adaptation,[33,34,36,65,183,222] the exact mechanism of dynamic bone growth and remodeling in response to mechanical (i.e., physiological loading as well as trauma) and systemic (i.e., healthy as well as pathological) stimuli has yet to be established.

22.5.1 Mechanotransduction Effects

In recent years, researchers have focused on the role of strain as a controlling agent in bone growth and adaptation. Strains from daily activities have been postulated to be the signals to which osteocytes respond to regulate mass and form. The "process of recognizing and responding to mechanical stimuli" is referred

to as mechanotransduction.[214] According to present knowledge, there are three possible mechanisms that may provide the biophysical basis for mechanotransduction.

22.5.1.1 Direct Mechanical Effects on Cells

A number of research groups have emphasized the mechanotransductive role of strain as a direct mechanism for microdeformation of bone cells and tissue.[26,28,29,34,60,78,86,102] Numerous *in vivo* experiments have been utilized to measure surface strain in bones exposed to controlled loading conditions, thereby establishing a relationship between mechanical loading parameters (i.e., strain magnitude, rate, number of cycles) and functional adaptation.[65,183,184] Fluid pressure[204] sensed by osteocytes and shear stresses[4,41,54,56,57,124,191,206,216] incurred on the surface of osteocytic process due to interstitial fluid movement through the canaliculi have been hypothesized to play a further role in mechanotransduction. Regardless of loading mode, the mechanisms underlying the adaptive response to mechanical loading remain unclear. Although signaling pathways are critical in effecting this response,[112] these pathways do not represent the "initial mechanoreception event" at the cell surface that triggers the chain of cell activity resulting in growth, adaptation, and repair. Rather, cell surface receptors represent the first link in the chain by transmitting mechanical forces to the cytoskeleton.[214]

22.5.1.2 Enhancement of Transport

In a broader sense, transport phenomena, as affected by mechanical loading events (locomotor as well as circulatory), represent a further possible mechanism for mechano-chemical transduction; concentration gradients can potentially affect receptor binding, osmotic pressure, membrane permeability and chemotaxis. Piekarski and Munro[168] developed theoretical models to show that mechanical loading of the poroelastic bone tissue creates transient pressure gradients that could be the motive force for deformation-induced fluid flow within bone. According to their and others' hypothesis, deformation-induced fluid flow through the lacunocanalicular system enhances molecular transport between the central blood supply and the osteocytes within a given osteon.[14,112,168] This postulate has been proved experimentally using tracer methods to visualize interstitial fluid displacements and the ensuing enhancement of mass transport.[103,108,109,111,112]

22.5.1.3 Electromechanical Effects

The literature pertaining to strain-generated potentials or streaming potentials has provided indirect evidence for the existence of fluid flow phenomena in bone.[35,71,91,92,119,157,160,170,172,173,185,186,194,199] These mechanically induced electrical signals may provide a third mechanism for strain as an indirect means for mechanotransduction, e.g., by affecting osteocyte membrane permeability or by triggering voltage-sensitive ion channels within bone.[42,77,119,224]

22.5.2 Bone Growth, Adaptation, and Repair

Studies of interstitial fluid flow in bone are quintessential for determining the stimuli to which cells are subjected when bone is loaded physiologically. Empiric proof for the important role of this fluid flow on bone growth, adaptation, and repair has been documented over the course of the last century. A whole body of literature documents the adaptive response of bone to cyclic mechanical loads (see literature from Wolff, Pauwels, Thompson, Carter, and Lanyon). Similarly, the role of venous hypertension in bone growth and repair has been the subject of a plethora of research. Bier[17] reported in 1915 that venous hypertension causes bone hypertrophy in immature animals. Recent studies have corroborated Bier's observation and have shown that venous hypertension stimulates fracture repair as well,[138] increasing the rate of bone healing in mature animals without changes in blood flow or oxygenation.[114] Experimental studies of osteomyelitic canine bone revealed pathophysiological changes in the fluid spaces within the tissue;[22] these changes are expected to have a profound effect on drug delivery, e.g., of antimicrobials, to affected areas.[104,176] Finally, changes in fluid spaces have been reported in association with growth to maturity and subsequent aging.[45,94,108,120,170] That mechanical loading and subsequent loading-induced fluid flow play a crucial role in modulating processes associated with bone growth, adaptation, and repair is clear. However, the exact mechanisms underlying these processes remain a conundrum. In the following section, a new proposal for a transport-based theory of bone (re)modeling is described.

22.5.3 Proposal for a Transport-Based Theory of Bone Remodeling

Typically, theories of bone remodeling are based on the idea that mechanical loading is crucial for modulation of cellular activities associated with functional adaptation. If an alteration in mechanical forces or some manifestation thereof (i.e., stress or strain) is the signal for bone cells to commence activities associated with adaptive processes, then every cell must be programmed at least to recognize its "normal" mechanical environment. This could be conceivable if every bone cell were to experience the same level of mechanical loading under normal conditions. However, bone is anisotropic and differences in mechanical loading occur at a local level. Thus, not only would every cell be required to be programmed, but each cell would have to be individually programmed to recognize its own baseline mechanical loading state. Only then could one explain such functional adaptation phenomena as bone resorption around orthopedic implants or disuse osteopenia. However, if each cell is truly preprogrammed to expect a certain "normal" loading environment, then functional adaptation is a misnomer for the biological processes called forth in response to environmental changes: rather than adapting to a new mechanical environment, the cells would be remodeling to recreate their original, "normal" mechanical loading state. Adaptation to new surroundings is a different strategy altogether; it requires resiliency as well as reconditioning to a new baseline state.

There are three possible strategies for osteocytes to cope in a new environment, the first two being applicable for "preprogrammed" osteocytes and the third not requiring any genetic predisposition. First, the cells can change their environment actively to recreate the milieu which they are programmed to expect. This option requires not only a "sensor" to detect the change but also an "actuator" to respond to the change. Alternatively, the cells can adapt "actively," "reprogramming" themselves to survive. This alternative requires both the potential to detect changes in loading patterns and a mechanism for "intelligent reprogramming." Another plausible possibility is that dynamic adaptation processes are a manifestation of "passive" adaptation, whereby the cell activity and ultimate cell survival are dictated by the laws of supply and demand and thus require neither special detecting nor actuating mechanisms aside from the normal cell machinery.

Taking into account the third adaptation strategy, the functional adaptation of bone can be approached as a transport problem, in which case the adaptive response reflects the need for, as well as the availability of, for example, nutrients, mineral precursors, signaling molecules, and growth factors. Transport via passive diffusion alone cannot account for movement of such molecular entities over long distances within time periods required for healthy metabolism and processes associated with bone modeling and remodeling. However, the load-bearing function of bone provides an alternative, more plausible mechanism for molecular transport in bone, i.e., convective transport via load-induced fluid flow. Piekarski and Munro's model of poroelastic behavior and load-induced fluid flow[168] provides a theoretical basis for this phenomenon.

The new remodeling theory is based on the hypothesis that mechanical load-induced fluid flow enhances the transport of substances critical for regulation of bone growth and adaptation processes.[110] Thus, convective transport via, e.g., load-induced fluid flow provides a further mechanism for the modulation of activities associated with such processes. Idealized FE models[110] provide a basis for a refined model that emulates the regulation of processes associated with bone growth and adaptation via load-induced fluid flow (Fig. 22.5). The basic idea is that cell activity and, ultimately, cell survival are dictated by the laws of supply and demand. A given change in the metabolic or mechanical loading environment of a given cell is perceived by the cell as a disturbance in the local equilibria of molecular entities. If the equilibrium is disturbed such that the local supply no longer meets demand (e.g., for cell nutrition or maintenance of mineral density), the cell intervenes actively for its survival, resorbing the inner layers of its lacuna and canaliculi. This, in turn, increases tissue permeability, resulting in increased transport and the possibility of reestablishing the local equilibria. If the cell merely "grins and bears" the disturbance (i.e., passive response), cell death, e.g., via, metabolic starvation, may ensue. All is not lost, however, since cell death is believed to trigger resorption processes as well, thus initiating the cycle of increased permeability and establishment of local equilibria once again. If a change in enviroment results in a disturbance to the

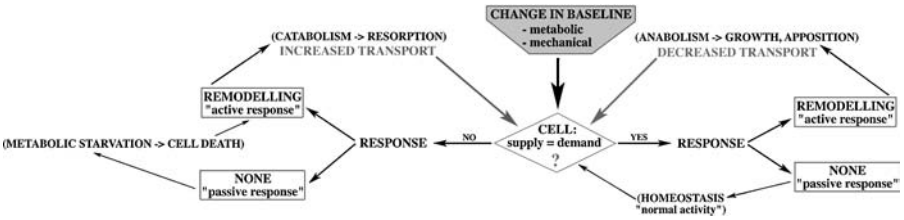

FIGURE 22.5 Algorithm for new transport-based remodeling theory. (After Knothe Tate, M. L. and Niederer, P., in *Advances in Heat and Mass Transfer in Biotechnology,* Clegg, S., Ed., American Society of Mechanical Engineers, 1998. With permission).

local equilibria such that supply meets or exceeds demand, the cell may maintain homeostasis or initiate anabolic activities such as mineral apposition and growth. Thus, tissue permeability may decrease, resulting in either reestablishment of the local equilibria or a cycle of catabolic activity.

A transport-based theory of remodeling is reasonable when one considers the regulatory role of concentration gradients for cellular differentiation in embryogenesis.[44,223] Furthermore, it is likely that the osteocytes are the principal mediators in functional adaptation based on cell biological[26,27] as well as histological observations. First, it has been shown that the relative percentage of bone tissue taken up by osteocytes in the diaphyses, metaphyses, and epiphyses corresponds to the relative rate of bone formation in those respective areas.[32,128] Second, observations of osteocytes within compact bone underscore the fact that transport processes affect the development of osteocyte morphology. Much like the development of extensive tree root systems in geographic areas experiencing little precipitation, osteocytes within lacunae farthest from the central blood supply have significantly more canaliculi than those closest to the central Haversian canal.[128] In addition, with any given lacuna, the wall nearest the blood supply exhibits more canaliculi than that facing the cement line,[128] thus maximizing the potential for transport of molecular entities from "the source." Furthermore, the osteocyte controls the size and shape of the lacuna and canaliculi in which it and its processes are encased; therefore, "in its active state," the osteocyte "is concerned with … passage of mineral ions" as well as nutrients and growth factors "into and out of the bone" (cited after Ref. 9). The interrelationship between local mineral turnover and systemic mineral metabolism has yet to be elucidated and may provide clues for an additional mechanism underlying Wolff's law. The effect of load-induced fluid flow may prove to be particularly important in this regard, as the viability of an osteocyte is a prerequisite for bone remodeling and specific osteocyte activity will define the extent of remodeling.

References

1. Aarden, E. M., Burger, E. H., and Nijweide, P. J., Function of osteocytes in bone, *J. Cell. Biochem.,* 55, 287–299, 1994.
2. Adams, P. A., Microperoxidases and iron porphyrins, in *Peroxidases in Chemistry and Biology,* Vol. II, Everse, J., Everse, K. E., and Grisham, M. B., Eds., CRC Press, Boca Raton, FL,1991, 171–200.
3. Adamson, R., unpublished data.
4. Ajubi, N. E., Klein-Nulend, J., Nijweide, P. J., Vrijheid-Lammers, T., Alblas, M. J., and Burger, E. H., Pulsating fluid flow increases prostaglandin production by cultured chicken osteocytes—a cytoskeleton-dependent process, *Biochem. Biophys. Res. Commun.,* 225, 62–68, 1996.
5. Amprino, R., *Experimentia,* 8, 380–383, 1952.
6. Anderson, J. C. and Eriksson, C., Electrical properties of wet collagen, *Nature* (London), 218, 166, 1968.
7. Arnold, J. S. and Frost, H. M., The osteocyte as a water pump, *Clin. Orthop.,* 78, 47–55, 1971.
8. Ascenzi, A., Bonucci, E., and Bocciarelli, D. S., An electron microscope study of osteon calcification, *Ultrastruct. Res.,* 12, 287–303, 1965.

9. Atkinson, P. J. and Hallsworth, A. S., The spatial structure of bone, in *Progress in Anatomy,* Vol. 2, Harrison, R. J. and Navaratman, V., Eds., Cambridge University Press, Cambridge, 1982, 179–199.
10. Aukland, K., Distribution of body fluids: local mechanisms guarding interstitial fluid volume, *J. Physiol. Paris,* 79, 395–400, 1984.
11. Ayasaka, N., Kondo, T., Goto, T., Kido, M. A., Nagata, E., and Tanaka, T., Differences in the transport systems between cementocytes and osteocytes in rats using microperoxidase as a tracer, *Arch. Oral Biol.,* 37, 363–369, 1992.
12. Baltadzhiev, G., Morphology of the Haversian canal. An electron microscopic study, *Fol. Med.* (Plovdiv), 36, 21–28, 1994.
13. Bassett, C. A. L., Electromechanical factors regulating bone architecture, in *Third European Symposium on Calcified Tissues,* Fleisch, H., Blackwood, H. J. J., and Owen, M., Eds., Springer Verlag, New York, 1966, 78–89.
14. Bassett, C. A. L., Biologic significance of piezoelectricity, *Calcif. Tissue Res.,* 1, 252–272, 1968.
15. Baud, C. A., Submicroscopic structure and functional aspects of the osteocyte, *Clin. Orthop. Relat. Res.,* 56, 227–236, 1968.
16. Bergula, A. P., Huang, W., and Frangos, J. A., Femoral vein ligation increases bone mass in the hindlimb suspended rat, *Bone,* 24, 171–177, 1999.
17. Bier, A., Production of passive hyperaemia, in *Hyperaemia as a Therapeutic Agent,* 2nd ed., Black, G. M., Ed., Hammond, Betz, 1915, 51–55.
18. Biot, M. A., General theory of three-dimensional consolidation, *J. Appl. Phys.,* 12, 155–164, 1941.
19. Biot, M. A., Theory of elasticity and consolidation for a porous anisotropic solid, *J. Appl. Phys.,* 26, 182–185, 1955.
20. Biot, M. A. and Willis, D. G., The elastic coefficients of the theory of consolidation, *Trans ASME: Appl. Mechanics Division Summer Conference*, 1957, 594–601.
21. Black, J. and Korostoff, E., Strain-related potentials in living bone, *Ann. N.Y. Acad. Sci.,* 95–120.
22. Bloom, J. D., Fitzgerald, R. H., Washington, J. A., and Kelly, P. J., The transcapillary passage and interstitial fluid concentration of penicillin in canine bone, *J. Bone Joint Surg. (Am.),* 62, 1168–1175, 1980.
23. Bosch, W. J., Plasma ^{45}Ca clearance by the tibia in the immature dog, *Am. J. Physiol.,* 216, 1150–1157, 1969.
24. Boyde, A., Scanning electron microscope studies of bone, in *The Biochemistry and Physiology of Bone,* Bourne, G. H., Ed., Academic Press, New York, 1972, 290.
25. Bronk, J. T., Meadows, T. H., and Kelly, P. J., The relationship of increased capillary filtration and bone formation, *Clin. Orthop. Relat. Res.,* 293, 338–345, 1993.
26. Burger, E. H. and Veldhuijzen, J. P., Influence of mechanical factors on bone formation, resorption, and growth *in vitro,* in *Bone,* Vol. 7, Hall, B. K., Ed., CRC Press, Boca Raton, FL, 37–56, 1993.
27. Burger, E. H. and Klein-Nulend, J., Mechanotransduction in bone—role of the lacunocanalicular network, *FASEB J.,* 13, S101–S112, 1999.
28. Burr, D. B., Schaffler, M. B., Yang, K. H., Lukoschek, M., Sivaneri, N., Blaha, J. D., and Radin, E. L., Skeletal change in response to altered strain environments: is woven bone a response to elevated strain? *Bone,* 10, 215–221, 1989.
29. Burr, D. B., Schaffler, M. B., Yang, K. H., Wu, D. D., Lukoschek, M., Kandzari, D., Sivaneri, N., Blaha, J. D., and Radin, E. L., The effects of altered strain environments on bone tissue kinetics, *Bone,* 10, 223–233, 1989.
30. Bushinsky, D. A., Chabala, J. M., and Levi-Setti, R., Ion microprobe analysis of mouse calvariae *in vitro:* evidence for a "bone membrane," *Am. J. Physiol.,* 256, E152–E158, 1989.
31. Canas, F., Terepka, A. R., and Neuman, W. F., Potassium and milieu interieur of bone, A*m. J. Physiol.,* 217, 117–120, 1969.
32. Canè, V., Marotti, G., Volpi, G., Zaffe, D., Palazzini, S., Remaggi, F., and Muglia, M. A., Size and desnity of osteocyte lacunae in different regions of long bone, *Calcif. Tissue Int.,* 34, 558–563, 1982.

33. Carter, D. R., The relationship between *in vivo* strain and cortical bone remodeling, *CRC Crit. Rev. Bioeng.,* 8, 1, 1982.
34. Carter, D. R., Mechanical loading history and skeletal biology, *J. Biomech.,* 20, 1095–1109, 1987.
35. Chakkalakal, D. A., Mechanoelectric transduction in bone, *J. Mater. Res.,* 4, 1034–1046, 1989.
36. Churches, A. E. and Howlett, C. R., The response of mature cortical bone to controlled time-varying loads, in *Mechanical Properties of Bone,* S. C. Cowin, Ed., American Society of Mechanical Engineering, New York, 1981, 69.
37. Civitelli, R., Cell-cell communication in bone, *Calcif. Tissue Int.,* 56, S29–S31, 1995.
38. Cooper, R. R., Milgram, J. W., and Robinson, R. A., Morphology of the osteon. An electron microscopic study, *J. Bone Joint Surg.,* 48A, 1239–1271, 1966.
39. Copenhaver, W. M., in *Bailey's Textbook of Histology,* Copenhaver, W. M., Bunge, R. P., and Bunge, M. B., Eds., Williams & Wilkins, Baltimore, MD, 1964, 122–123.
40. Cotran, R. S. and Karnowsky, M. J., Vascular leakage induced by horseradish peroxidase in the rat, *Proc. Soc. Exp. Biol.* (N.Y.), 126, 557–561, 1967.
41. Cowin, S. C., Moss-Salentijn, L., and Moss, M. L., Candidates for the mechanosensory system in bone, *J. Biomech. Eng.,* 113, 191–197, 1991.
42. Cowin, S. C., Weinbaum S., and Zeng Y., A case for bone canaliculi as the anatomical site of strain generated potentials, *J. Biomech.,* 28, 1281–1297, 1994.
43. Cowin, S. C., unpublished data.
44. Crick, F., Diffusion in embryogenesis, *Nature,* 225, 420–422, 1970.
45. Currey, J. D., Some effects of ageing in human Haversian systems, *J. Anat.* (London), 98, 69–75, 1964.
46. Davies, D. R. A., Bassingthwaighte, J. B., and Kelly, P. J., Transcapillary exchange of strontium and sucrose in canine tibia, *J. Appl. Physiol.,* 40, 17–22, 1976.
47. Davies, D. R., Bassingthwaighte, J. B., and Kelly, P. J., Blood flow and ion exchange in bone, in *Skeletal Research: An Experimental Approach,* Simmons, D. J. and Kunin, A. S., Eds., Academic Press, New York, 1979, 397–419.
48. De Bruyn, P. P. H., Michelson, S., and Bankston, P. W., *In vivo* endocytosis by bristle-coated pits and intracellular transport of endogenous albumin in the endothelium of the sinuses of liver and bone marrow, *Cell Tissue Res.,* 240, 1–7, 1985.
49. Dillaman, R. M., Movement of ferritin in the 2-day-old chick femur, *Anat. Rec.,* 209, 445–453, 1984.
50. Dillaman, R. M., Roer, R. D., and Gay, D. M., Fluid movement in bone: theoretical and empirical, *J. Biomech.,* 24(S1), 163–177, 1991.
51. Doty, S. B. and Schofield, B. H., Metabolic and structural changes within osteocytes of rat bone, in *Calcium, Parathyroid Hormone and the Calcitonins,* Talmage, R. V. and Munson, P. L., Eds., Elsevier, Excerpta Medica, Amsterdam, 1972, 353–364.
52. Doty, S. B., Robinson, R. A., and Schofield, B., Morphology of bone and histochemical staining characteristics of bone cells, in *Handbook of Physiology—Endocrinology,* Vol. VII, Greep, R. O. and Astwood, E. B., Eds., American Physiology Society, Bethesda, MD, 1976, 3–23.
53. Doty, S. B., Morphological evidence of gap junctions between bone cells, *Calcif. Tissue Int.,* 33, 509–512, 1981.
54. Duncan, R. L. and Turner, C. H., Mechanotransduction and the functional response of bone to mechanical strain, *Calcif. Tissue Int.,* 57, 344–358, 1995.
55. Eriksson, C., Streaming potentials and other water-dependent effects in mineralized tissues, *Ann. N.Y. Acad. Sci.,* 238, 321–328, 1974.
56. Forwood, M. R. and Turner, C. H., Response of rat tibiae to incremental loading: a quantum concept for bone formation, *Bone,* 15, 603–609, 1994.
57. Forwood, M. R. and Turner, C. H., Skeletal adaptations to mechanical usage: results from tibial loading studies in rats, *Bone,* 17, 197S–205S, 1995.
58. Frost, H. M., Measurement of osteocytes per unit volume and volume components of osteocytes and canaliculae in man, *Henry Ford Hosp. Med. Bull.,* 8, 208–211, 1960.

59. Frost, H. M., The osteocyte as a pump, in *Bone Modeling and Skeletal Modeling Errors. Orthopaedic Lectures,* Vol. 4, Charles C Thomas, Springfield, IL, 1973, 119–149.
60. Frost, H. M., A determinant of bone architecture. The minimum effective strain, *Clin. Orthop.,* 200, 198–225, 1983.
61. Fukada, E. and Yasuda, I., On the piezoelectric effect of bone, *J. Phys. Soc. Jpn.,* 12, 1158–1162, 1957.
62. Gatzka, C., Knothe, U., Niederer, P., Schneider, E., and Knothe Tate, M. L., A novel *ex vivo* model for investigation of fluid displacements in bone after endoprosthesis implantation, *J. Mater. Sci., Mater. Med.,*10, 801–806, 2000.
63. Geisler, J. Z. and Neuman, W. F., The membrane control of bone potassium, *Proc. Soc. Exp. Biol. Med.,* 130, 609–612, 1969.
64. Gladden, J. K. and Dole, M., *J. Am. Chem. Soc.,* 75, 3900, 1953.
65. Goodship, A. E., Lanyon, L. E., and McFie, H., Functional adaptation of bone to increased stress, *J. Bone Joint Surg.,* 61A, 539–546, 1979.
66. Graham, R. C., Jr. and Karnovsky, M. J., The early stages of absorption of injected horseradish peroxidase in the proximal tubules of mouse kidney: ultrastructural cytochemistry by a new technique, *J. Histochem. Cytochem.,* 14, 291–302, 1966.
67. Gray, H., *Gray's Anatomy,* 35th Br. ed., Warwick, R. and Williams, P. L., Eds., Saunders, Philadelphia, 1973.
68. Greenwald, A. S. and Haynes, D. W., A pathway for nutrients from the medullary cavity to the articular cartilage of the human femoral head, *J. Bone Joint Surg.,* 51B, 747–753, 1969.
69. Grisham, M. B. and Everse, J., Peroxidant activity of hemoglobin and myoglobin, in *Peroxidases in Chemistry and Biology,* Vol. I., Everse, J., Everse, K. E., and Grisham M. B., Eds., CRC Press, Boca Raton, FL, 1991, 335–343.
70. Groer, P. G. and Marshall, J. H., Mechanism of calcium exchange at bone surfaces, *Calcif. Tissue Res.,* 12, 175–192, 1973.
71. Gross, D. and Williams, W. S., Streaming potential and the electromechanical response of physiologically moist bone, *J. Biomech.,* 15, 277–295, 1982.
72. Gross, P. M., Marcus, M. L., and Heistad, D. D., Measurement of blood flow to bone and marrow in experimental animals by means of the microsphere technique, *J. Bone Joint Surg.,* 63A, 1028–1031, 1981.
73. Guzelsu, N. and Walsh, W. R., Streaming potential of intact wet bone, *J. Biomech.,* 23, 673–685, 1990.
74. Guzelsu, N. and Regimbal, R. L., The origin of electrokinetic potentials in bone tissue: the organic phase, *J. Biomech.,* 23, 661–672, 1990.
75. Ham, A. W., in *Histology,* 5th ed., Pitman Medical Publishing, London, 1965, 384–487.
76. Handagama, P. J., Shuman, M. A., and Bainton, D. F., Incorporation of intravenously injected albumin, immunoglobulin G and fibrinogen in guinea pig megakaryocyte granules, *J. Clin. Invest.,* 84, 73–82, 1989.
77. Harrigan, T. P. and Hamilton, J. J., Bone strain sensation via transmembrane potential changes in surface osteoblasts: loading rate and microstructural implications, *J. Biomech.,* 26, 183–200, 1993.
78. Harter, L. V., Hruska, K. A., and Duncan, R. L., Human osteoblast-like cells respond to mechanical strain with increased bone matrix production independent of hormonal regulation, *Endocrinology,* 136, 528–535, 1995.
79. Hillsley, M. V. and Frangos, J. A., Osteoblast hydraulic conductivity is regulated by calcitonin and parathyroid hormone, *J. Bone Miner. Res.,* 11, 114–124, 1996.
80. Holmes, J. M., Davies, D. H., Meath, W. J., and Beebe, R. A., Gas adsooption and surface structure of bone mineral, *Biochemistry,* 3, 2019–2024, 1964.
81. Holtrop, M. E. and Weinger, J. M., Metabolic and structural changes within osteocytes of rat bone, in *Calcium, Parathyroid Hormone and the Calcitonins,* Talmage, R. V. and Munson, P. L., Eds., Excerpta Medica, Amsterdam, 1972, 365–374.

82. Hughes, S. P. F., Davies, D. R., Bassingthwaighte, J. B., Knox, F. G., and Kelly, P. J., Bone extraction and blood clearance of disphosphonate in the dog, *Am. J. Physiol.,* 232, H341–347, 1977.
83. Hughes, S., Khan, R., Davies, R., and Lavendar, P., The uptake by the canine tibia of the bone scanning agent 99mTc-MDP before and after an osteotomy, *J. Bone Joint Surg.,* 60B, 579–582, 1978.
84. Hughes, S., Davies, R., Khan, R., and Kelly, P., Fluid spaces in bone, *Clin. Orthop. Relat. Res.,* 134, 332–341, 1978.
85. Hui, P. W., Leung, P. C., and Sher, A., Fluid conductance of cancellous bone graft as a predictor for graft–host interface healing, *J. Biomech.,* 29, 123–132, 1996.
86. Huiskes, R. and Hollister, S. J., From structure to process, from organ to cell: recent developments of FE-analysis in orthopaedic biomechanics, *J. Biomech. Eng.,* 115, 520–527, 1993.
87. Hung, C. T., Allen, F. D., Pollack, S. R., and Brighton, C. T., What is the role of the convective current density in the real-time calcium response of cultured bone cells to fluid flow? *J. Biomech.,* 29, 1403–1409, 1996.
88. Hung, C. T., Allen, F. D., Pollack, S. R., and Brighton, C. T., Intracellular Ca^{2+} stores and extracellular Ca^{2+} are required in the real-time Ca^{2+} response of bone cells experiencing fluid flow, *J. Biomech.,* 29, 1411–1417, 1996.
89. Jacobs, C. R., Yellowley, C. E., Davis, B. R., Zhou, Z., Cimbala, J. M., and Donahue, H. J., Differential effect of steady versus oscillating flow on bone cells, *J. Biomech.,* 31, 969–976, 1998.
90. Johnson, D. L., McAllister, T. N., and Frangos, J. A., Fluid flow stimulates rapid and continuous release of nitric oxide in osteoblasts, *Am. J. Physiol.,* 271, E205–E208, 1996.
91. Johnson, M. W., Chakkalakal, D. A., Harper, R. A., and Katz, J. L., Comparison of the electromechanical effects in wet and dry bone, *J. Biomech.,* 13, 437–442, 1980.
92. Johnson, M. W., Chakkalakal, D. A., Harper, R. A., and Katz J. L., Fluid flow in bone *in vitro, J. Biomech.,* 15, 881–885, 1982.
93. Johnson, M. W., Behavior of fluid in stressed bone and cellular stimulation, *Calcif. Tissue Int.,* 36S, S72–S76, 1984.
94. Jowsey, J., Studies in Haversian systems in man and some animals, *J. Anat.,* 100, 857–864, 1966.
95. Karnovsky, M. J., The ultrastructural basis of capillary permeability studied with peroxidase as a tracer, *J. Cell Biol.,* 35, 213–236, 1967.
96. Katz, J. L., Hard tissue as a composite material—I. Bounds on the elastic behavior, *J. Biomech.,* 4, 455–473, 1971.
97. Keanini, R. G., Roer, R. D., and Dillaman, R. M., A theoretical model of circulatory interstitial fluid flow and species transport within porous cortical bone, *J. Biomech.,* 28, 901–914, 1995.
98. Kelly, P. J. and Bassingthwaighte, J. B., Studies on bone ion exchanges using multiple-tracer indicator-dilution techniques, *Fed. Proc.,* 36, 2634–2639, 1977.
99. Kelly, P. J. and Bronk, J. T., Venous pressure and bone formation, *Microvasc. Res.,* 39, 364, 1990.
100. Kelly, P. J., Montgomery, R. J., and Bronk, J. T., Reaction of the circulatory system to injury and regeneration, *Clin. Orthop. Relat. Res.,* 254, 275–288, 1990.
101. King, G. J. and Holtrop, M. E., Actin-like filaments in bone cells of cultured mouse calvaria as demonstrated by binding to heavy meromyosin, *J. Cell Biol.,* 66, 445–451, 1975.
102. Klein-Nulend, J., Semeins, C. M., Ajubi, N. E., Nijweide, P. J., and Burger, E. H., Pulsating fluid flow increases nitric oxide (NO) synthesis by osteocytes but not periosteal fibroblasts—correlation with prostaglandin upregulation, *Biochem. Biophys. Res. Commun.,* 217, 640–647, 1995.
103. Knothe, U. and Knothe Tate, M. L., Microperfusion of the sheep metacarpus elucidated in an *ex vivo* model, *Clin. Orthop. Relat. Res.,* in submission, 2000.
104. Knothe, U., Gatzka, C., Niederer, P., and Knothe Tate, M. L., Clinical implications of mechanical loading on osteocyte viability, *J. Bone Joint Surg.,* in submission, 2000.
105. Knothe Tate, M. L., Niederer, P., Tepic, S., and Perren, S. M., The role of convective transport in bone physiology and functional adaptation, in *Transactions of the Combined Orthopaedic Research Societies Meeting,* San Diego, CA, 1995.

106. Knothe Tate, M. L., Niederer, P., Tepic, S., and Perren, S. M., Study of convective transport in compact bone as a modulating factor in bone structure and regeneration, presented at European Society of Biomechanics Meeting, Leuven, Belgium, 1996.
107. Knothe Tate, M. L., Niederer, P., Tepic, S., and Perren, S. M., *In vitro* investigation of deformation-induced fluid displacement in small cylindrical specimens excised from cortical sheep bone, in *Transactions of the 43rd Annual Meeting of the ORS,* San Francisco, 1997.
108. Knothe Tate, M. L., Niederer, P., and Knothe, U., *In vivo* tracer transport through the lacunocanalicular system of rat bone in an environment devoid of mechanical loading, *Bone,* 22, 107–117, 1998.
109. Knothe Tate, M. L., Knothe, U., and Niederer, P., Experimental elucidation of mechanical load-induced fluid flow and its role in bone metabolism and functional adaptation, *Am. J. Med. Sci.,* 316, 189–195, 1998.
110. Knothe Tate, M. L. and Niederer, P., A theoretical FE-based model developed to predict the relative contribution of convective and diffusive transport mechanisms for the maintenance of local equilibria within cortical bone, in *Advances in Heat and Mass Transfer in Biotechnology,* Clegg, S., Ed., The American Society of Mechanical Engineers, New York, HTD-Vol. 362, BED-Vol. 40, 133–142, 1998.
111. Knothe Tate, M. L. and Knothe, U., An *ex vivo* model to study transport processes and fluid flow in loaded bone, *J. Biomech.,* 33, 247–254, 2000.
112. Knothe Tate, M. L., Steck, R., Forwood, M. R., and Niederer, P., *In vivo* demonstration of load-induced fluid flow in the rat tibia and its potential implications for processes associated with functional adaptation, *J. Exp. Biol.,* 203, 2737–2745, 2000.
113. Knothe Tate, M. L., Tami, A., Nasser, R. R., Steck, R., and Schaffler, M. B., Permeability characteristics of different molecular tracers in loaded and unloaded bone, *Trans. Orthop. Res. Soc.* (in press, 2001).
113a. Knothe Tate, M. L. and Richards, G., unpublished data.
113b. Knothe Tate, M. L. and Schaffler, M. B., Changes in osteocyte integrity associated with bone resorption following disuse, *J. Bone Min. Res.,* 15, 5476, 2000.
114. Kruse, R. L. and Kelly, P. J., Acceleration of fracture healing distal to a venous tourniquet, *J. Bone Joint Surg.,* 56A, 730, 1974.
115. Kufahl, R. H. and Saha, S., A theoretical model for stress-generated fluid flow in the canaliculi-lacunae network in bone tissue, *J. Biomech.,* 23, 171–180, 1990.
116. Lakes, R. S. and Katz, J. L., Viscoelastic properties of wet cortical bone—II. Relaxation mechanism, *J. Biomech.,* 12, 679–687, 1979.
117. Landis, E. M. and Pappenheimer, J. R., Exchange of substances through capillary walls, in *Handbook of Physiology,* Vol. 2, Sec. 2, Hamilton, W. F. and Dow, P., Eds., American Physiological Society, Washington, D.C., 1963, 961–1034.
118. Lang, S., Stipanich, N., and Soremi, E. A., Diffusion of glucose in stressed and unstressed canine femur *in vitro, Ann. N.Y. Acad. Sci.,* 238, 139–148, 1974.
119. Lanyon, L. E. and Hartman, W., Strain related electrical potentials recorded *in vitro* and *in vivo*, *Calcif. Tissue Res.,* 22, 315–327, 1977.
120. Li, G. P., Bronk, J. T., An, K. N., and Kelly, P. J., Permeability of cortical bone of canine tibiae, *Microvasc. Res.,* 34, 302–310, 1987.
121. Lorenz, M. and Plenk, H., A perfusion method of incubation to demonstrate horseradish peroxidase in bone, *Histochemistry,* 53, 257–263, 1977.
122. Lozupone, E., Nico, B., Mancini, L., Favia, A., Lamanna, M. P., and Cagiano, R., The dynamic of the flow of the interstitial fluid into the osteocytic lacunae and canaliculi of bone cultured *in vitro, Bone,* 19(S3), 150S, 1996.
123. Lucht, U., Absorption of peroxidase by osteoclasts as studied by electron microscope histochemistry, *Histochemie,* 29, 274–286, 1972.
124. Luo, G., Cowin, S. C., Sadegh, A. M., and Arramon, Y. P., Implementation of strain rate as a bone remodeling stimulus, *J. Biomech. Eng.,* 117, 329–338, 1995.
125. MacGinitie, L. A., Seiz, K. G., Otter, M. W., and Cochran, G. V. B., Streaming potential measurements at low ionic concentrations reflect bone microstructure, *J. Biomech.,* 27, 969–978, 1994.

126. MacGinitie, L. A., Stanley, G. D., Bieber, W. A., and Wu, D. D., Bone streaming potentials and currents depend on anatomical structure and loading orientation, *J. Biomech.,* 30, 1133–1139, 1997.
127. Mak, A. F., Huang, D. T., Zhang, J. D., and Tong, P., Deformation-induced hierarchical flows and drag forces in bone canaliculi and matrix microporosity, *J. Biomech.*, 30, 11–18, 1997.
128. Marotti, G., Remaggi, F., and Zaffe, D., Quantitative investigation on osteocyte canaliculi in human compact and spongy bone, *Bone,* 6, 335–337, 1985.
129. Maroudas, A., Bullough, P. G., Swanson, S. A. V., and Freeman, M. A. R., The permeability of articular cartilage, *J. Bone Joint Surg.,* 50B, 1968.
130. Maroudas, A., Physicochemical properties of cartilage in the light of ion exchange theory, *Biophys. J.,* 8, 575–595, 1968.
131. Maroudas, A., Stockwell, R. A., Nachemson, A., and Urban, J., Factors involved in the nutrition of the human lumbar intervertebral disc: cellularity and diffusion of glucose *in vitro, J. Anat.,* 120, 113–130, 1975.
132. Matthews, B. and Andrew, D., Microvascular architecture and exchange in teeth, *Microcirculation,* 2, 305–313, 1995.
133. Matthews, J. L., Vander Weil, C., and Talmage, R. V., Bone lining cells and the bone fluid compartment, an ultrastructural study, in *Homeostasis of Phosphate and Other Minerals,* Massry, S. G., Ritz, E., and Rapado, A., Eds., Plenum Press, New York, 1978, 451–457.
134. Maximow, A. A. and Bloom, W., *A Textbook of Histology,* Saunders, Philadelphia, 1952.
135. McAllister, T. N. and Frangos, J. A., Steady and transient fluid shear stress stimulate NO release in osteoblasts through distinct biochemical pathways, *J. Bone Miner. Res.,* 14, 930–936, 1999.
136. McCarthy, I. D. and Hughes, S. P., Multiple tracer studies of bone uptake of 99mTc-MDP and 85Sr, *Am. J. Physiol.,* 256(5 Pt. 2), H1261–5, 1989.
137. McCarthy, I. D. and Lang, Y., A distributed model of exchange processes within the osteon, *J. Biomech.*, 25, 441–450, 1992.
138. McCarthy, I. D., Clearance of albumin by cortical bone and marrow, *Clin. Orthop. Relat. Res.,* 334, 24–29, 1997.
139. McDougall, W. A., Pathways of penetration and effects of horseradish peroxidase in rat molar gingiva, *Arch. Oral Biol.,* 14, 621–633, 1970.
140. McDougall, W. A., Penetration pathways of a topically applied foreign protein into rat gingiva, *J. Periodont., Res.,* 6, 89–99, 1971.
141. Meadows, T. H., Bronk, J. T., Chao, E. Y. S., and Kelly, P. J., Effect of weight-bearing on healing of cortical defects in the canine tibia, *J. Bone Joint Surg.,* 72A, 1074–1080, 1990.
142. Michel, C. C., Transport of macromolecules through microvascular walls, *Cardiovasc. Res.,* 32, 644–653, 1996.
143. Miller, S. C., de Saint-Georges, L., Bowman, B. M., and Jee, W. S., Bone lining cells: structure and function. *Scanning Microsc.,* 3, 953–960, 1989.
144. Montgomery, R. J., Sutker, B. D., Bronk, J. T., Smith, S. R., and Kelly, P. J., Interstitial fluid flow in cortical bone, *Microvasc. Res.,* 35, 295–307, 1988.
145. Morris, M. A., Lopez-Curto, J. A., Hughes, S. P. F., An, K.-N., Bassingthwaighte, J. B., and Kelly, P. J., Fluid spaces in canine bone and marrow, *Microvasc. Res.,* 23, 188–200, 1982.
146. Cowin, S. C. and Moss, M. L., Mechanosensory mechanisms in bone, in *Textbook of Tissue Engineering,* 2nd ed., Lanza, R., Langer, R., and Chick, W., Eds., Academic Press, San Diego, 723–738, 2000.
147. Munro, M. and Piekarski, K., Motion of liquids in an osteon subjected to cyclic loading, in *Advances in Bioengineering,* ASME Publication H00077, 1974, 173–176.
148. Munro, M. and Piekarski, K., A solid/liquid composite, *Composites,* 195–199, 1976.
149. Munro, M. and Piekarski, K., Stress-induced radial pressure gradients in liquid-filled multiple concentric cylinders, *J. Appl. Mech. Trans. ASME,* 218–221, 1977.

150. Munro, M. and Piekarski, K., The microstructure of cortical bone, in *1987 Biomechanics Symposium,* Vol. 84, Butler, D. I. and Torzilli, P. A., Eds., ASME, New York, 1987, 941–949.
151. Nachemson, A., Lewin, T., Maroudas, A., and Freeman, M. A. R., *In vitro* diffusion of dye through the end plates and annulus fibrosus of human lumbar intervertebral discs, *Acta Orthop. Scand.,* 41, 589–607, 1970.
152. Netter, F., *The Ciba Collection of Medical Illustrations: The Musculoskeletal System: Anatomy, Physiology and Metabolic Disorders,* Vol. 8, Part 1, Ciba-Geigy Corp., Summit, NJ, 1987.
153. Neuman, W. F., The milieu interieur of bone: Claude Bernard revisited, *Fed. Proc. Am. Soc. Exp. Biol.,* 28, 1846–1850, 1969.
154. Neuman, M. W. and Neuman, W. F., On the measurement of water compartments, pH and gradients in calvaria, *Calcif. Tissue Int.,* 31, 135–145, 1980.
155. Neuman, W. F. and Neuman, M. W., Studies of diffusion in calvaria, *Calcif. Tissue Int.,* 33, 441–444, 1981.
156. Norimatsu, H. and Talmage, R. V., Influence of calcitonin on the initial uptake of lead and mercury by bone, *Proc. Soc. Exp. Biol. Med.,* 161, 94–98, 1979.
157. Otter, M., Schoenung, J., and Williams, W. S., Evidence for different sources of stress-generated potentials in wet and dry bone, *J. Orthop. Res.,* 3, 321–324, 1985.
158. Otter, M., Goheen, S., and Williams, W. S., Streaming potentials in chemically modified bone, *J. Orthop. Res.,* 6, 346–359, 1988.
159. Otter, M., Palmieri, V. R., and Cochran, G. V. B., Transcortical streaming potentials are generated by circulatory pressure gradients in living canine tibia, *J. Orthop. Res.,* 8, 119–126, 1990.
160. Otter, M. W., Palmieri, V. R., and Wu, D. D., A comparative analysis of streaming potentials *in vivo* and *in vitro, J. Orthop. Res.,* 10, 710–719, 1992.
161. Otter, M. W., Bronk, J. T., Wu, D. D., Bieber, W. A., Kelly, P. J., and Cochran, G. V. B., Inflatable brace-related streaming potentials in living canine tibias, *Clin. Orthop. Relat. Res.,* 324, 283–291, 1996.
162. Owan, I., Burr, D. B., Turner, C. H., Qiu, J., Tu, Y., Onyia, J. E., and Duncan, R. L., Mechanotransduction in bone: osteoblasts are more responsive to fluid forces than mechanical strain, *Am. J. Physiol.,* 273, C810–815, 1997.
163. Owen, M., Triffit, J. T., and Melick, R. A., Albumin in bone, in *Hard Tissue Growth, Repair and Remineralization,* Ciba Foundation Symposium 11, Excerpta Medica, Elsevier, Amsterdam, 1973, 263–293.
164. Owen, M. and Triffit, J. T., Extravascular albumin in bone tissue, *J. Physiol.,* 257, 293–307, 1976.
165. Pappenheimer, J. R., Über die Permeabilität der Glomerulummembranen in der Niere, *Klin. Wochenschr.,* 33, 362–365, 1955.
166. Peterson, D. R., Heideger, W. J., and Beach, K. W., Calcium homeostasis: the effect of parathyroid hormone on bone membrane electrical potential difference, *Calcif. Tissue Int.,* 37, 307–311, 1985.
167. Petrov, N., Pollack, S., and Blagoeva, R., A discrete model for streaming potentials in a single osteon, *J. Biomech.,* 22, 517–521, 1989.
168. Piekarski, K. and Munro, M., Transport mechanism operating between blood supply and osteocytes in long bones, *Nature,* 269, 80–82, 1977.
169. Piekarski, K., Mechanically enhanced perfusion of bone, in *Mechanical Properties of Bone,* Joint ASME–ASCE Appl. Mech. Conf., AMD 45, 1981, 185–191.
170. Pienkowski, D. and Pollack, S. R., The origin of stress-generated potentials in fluid-saturated bone, *J. Orthop. Res.,* 1, 30–41, 1983.
171. Pinto, M. R. and Kelly P. J., Age related changes in bone in the dog: fluid spaces and their potassium content, *J. Orthop. Res.,* 2, 2–7, 1984.
172. Pollack, S., Petrov, N., Salzstein, R., Brankov, G., and Blagoeva, R., An anatomical model for streaming potentials in osteons, *J. Biomech.,* 17, 627–636, 1984.
173. Pollack, S., Salzstein, R., and Pienkowski, D., Streaming potentials in fluid-filled bone, *Ferroelectrics,* 60, 297–309, 1984.
174. Prescott, G. H., Mitchell, D. F., and Fahmy, H., Procion dyes as matrix markers in growing bone and teeth, *Am. J. Phys. Anthropol,* 29, 219–224, 1968.

175. Qin, L., Mak, A. T. F., Cheng, C. W., Hung, L. K., and Chan, K. M., Histomorphological study on pattern of fluid movement in cortical bone in goats, *Anat. Rec.,* 255, 380–387, 1999.
176. Quinlan, W. R., Hall, B. B., and Fitzgerald, R. H., Fluid spaces in normal and osteomyelitic canine bone, *J. Lab. Clin. Med.,* 102, 78–87, 1983.
177. Rahn, B. A., In vitram staining techniques, in *Handbook of Biomaterials Evaluation,* von Recum, A. F., Ed., Macmillan, New York, 1986, 471–487.
178. Reilly, G. C., Knapp, H. F., Stemmer, A. C., Niederer, P., and Knothe Tate, M. L., Using atomic force microscopy to image the lacunocanalicular system of cortical bone, American Society of Bone and Mineral Research, St. Louis, 1999.
179. Reilly, G. C., Knapp, H., Stemmer, A., Niederer, P., and Knothe Tate, M. L., An investigation of the detailed morphology of bone fluid spaces, using atomic force microscopy, *Transactions of the Orthopaedic Research Society,* Orlando, 2000.
179a. Reilly, G., Knapp, H., Stemmer, A., Niederer, P., and Knothe Tate, M. L., Investigation of the lacunocanalicular system of cortical bone using atomic force microscopy, *Ann. Biomed. Eng.* in press, 2001.
180. Rippe, B. and Haraldsson, B., Transport of macromolecules across microvascular walls: the two-pore theory, *Physiol. Rev.,* 74, 163–219, 1994.
181. Rouhana, S. W., Johnson, M. W., Chakkalakal, D. A., and Harper, R. A., Permeability of compact bone, *ASME Biomechanics Symposium,* AMD–43, 169–172, 1981.
182. Rowland, R. E., Exchangeable bone calcium, *Clin. Orthop.,* 49, 233–248, 1966.
183. Rubin, C. T. and Lanyon L. E., Regulation of bone formation by applied dynamic loads, *J. Bone Joint Surg.,* 66A, 411–417, 1984.
184. Rubin, C. T. and Lanyon, L. E., Osteoregulatory nature of mechanical stimuli: function as a determinant for adaptive remodeling in bone, *J. Orthop. Res.,* 5, 300–310, 1987.
185. Salzstein, R. A. and Pollack, S. R., Electromechanical potentials in cortical bone—I. A continuum approach, *J. Biomech.,* 20, 261–270, 1987.
186. Salzstein, R. A. and Pollack, S. R., Electromechanical potentials in cortical bone—II. Experimental analysis, *J. Biomech.*, 20, 271–280, 1987.
187. Sasaki, T., Yamaguchi, A., Higashi, S., and Yoshiki, S., Uptake of horseradish peroxidase by bone cells during endochondral bone development, *Cell Tissue Res.,* 239, 547–553, 1985.
188. Seliger, W. G., Tissue fluid movement in compact bone, *Anat. Rec.,* 166, 247–255, 1970.
189. Simionescu, M. and Simionescu, N., Ultrastructure of the microvascular wall: functional correlations, in *Handbook of Physiology*, Vol. IV, Sec. 2, Orloff, J. and Brenner, R. W., Eds., American Physiological Society, Bethesda, MD, chap. 3, 1987.
190. Skerry, T. M., Bitensky, L., Chayen, J., and Lanyon, L. E., Loading-related reorientation of bone proteoglycan *in vivo*. Strain memory in bone tissue? *J. Orthop. Res.,* 6, 547–551, 1988.
191. Smalt, R., Mitchell, F. T., Howard, R. L., and Chambers, T. J., Induction of NO and prostaglandin E_2 in osteoblasts by wall-shear stress but not mechanical strain, *Am. J. Physiol.,* 273, E751–E758, 1997.
192. Sokoloff, L. and Bland, J. H., *The Musculoskeletal System,* Williams & Wilkins, Baltimore, MD, 1975, chap. 2.
193. Solomons, C. C., Ernisse, D. J., and Roberts, R. A., *Math. Biosci.,* 9, 17, 1970.
194. Starkebaum, W. S., Pollack, S. R., and Korostoff, E., Microelectrode studies of stress generated potentials in four point bending of bone, *J. biomed. Mater. Res.,* 13, 729–751, 1979.
195. Starling, E. H., On the absorption of fluid spaces from connective tissue spaces, *J. Physiol.,* 19, 312, 1896.
196. Steck, R., Knothe Tate, M. L., Niederer, P., and Schneider, E., Theoretical modelling of load-induced fluid displacement in compact bone, in *Poromechanics,* Thimus, J. F., Abousleiman, Y., Cheng, A.-H. D., Coussy, O., and Detournay, E., Eds., A.A. Balkema, Rotterdam, 1998, 511–516.
197. Steck, R., Knothe Tate, M. L., and Niederer, P., A theoretical model of load-induced fluid displacements and its relation to interstitial fluid flow in bone, *Med. Eng. Phys.,* 22, 117–125, 2000.
198. Steck, R., Niederer, P., and Knothe Tate, M. L., *Computational Methods in Bioengineering,* Lissabon, in press, 2001.

199. Steinberg, M. E., Busenkell, G. L., Black, J., and Korostoff, E., Stress-induced potentials in moist bone *in vitro, J. Bone Joint Surg.,* 56A, 704–713, 1974.
200. Sterck, J. G. H., Klein-Nulend, J., Lips, P., and Burger, E. H., Response of normal and osteoporotic human bone cells to mechanical stress *in vitro, Am. J. Physiol.,* E1113–E1120, 1998.
201. Talmage, R. V., Calcium homeostasis—calcium transport—parathyroid action, *Clin. Orthop.,* 67, 210–224, 1969.
202. Tanaka, T., Transport pathway and uptake of microperoxidase in the junctional epithelium of healthy rat gingiva, *J. Periodont. Res.,* 19, 26–39, 1984.
203. Tanaka, T. and Sakano, A., Differences in permeability of microperoxidase and horseradish peroxidase into the alveolar bone of developing rats, *J. Dent. Res.,* 64, 870–876, 1985.
204. Thompson, D., *On Growth and Form,* Cambridge University Press, Cambridge, 1936 (reprinted 1963), 958–1025.
205. Tonna, E. A., Bone tracers: cell and tissue level techniques, in *Skeletal Research*, Academic Press, New York, 1979, 457–463.
206. Turner, C. H., Akhter, M. P., Raab, D. M., Kimmel, D. B., and Recker, R. R., A non-invasive, *in vivo* model for studying strain adaptive bone remodeling, *Bone,* 12, 73–79, 1991.
207. Turner, C. H., Forwood, M. R., and Otter, M. W., Mechanotransduction in bone: do bone cells act as sensors of fluid flow? *FASEB J.,* 8, 875–878, 1994.
208. Turner, C. H., Forwood, M. R., Rho, J.-Y., and Yoshikawa, T., Mechanical loading thresholds for lamellar and woven bone formation, *J. Bone Miner. Res.,* 9, 87–97, 1994.
209. Turner, C. H. and Forwood, M. R., What role does the osteocyte network play in bone adaptation, *Bone,* 16, 283–285, 1995.
210. Urist, M. R., Granstein, R., Nogami, H., Svenson, L., and Murphy, R., Transmembrane bone morphogenesis across multiple-walled diffusion chambers. New evidence for a diffusible bone morphogenetic property, *Arch. Surg.,* 112, 612–619, 1977.
211. Van der Weil, C. J., Grubb, S. A., and Talmage, R. V., The presence of lining on surface of human trabecular bone, *Clin. Orthop. Relat. Res.,* 134, 350–355, 1978.
212. Vongsavan, N. and Matthews, B., Fluid flow through cat dentine *in vivo, Arch. Oral Biol.,* 37, 175–185, 1992.
213. Wang, L., Fritton, S. P., Cowin, S. C., and Weinbaum, S., Fluid pressure relaxation depends upon osteonal microstructure: modelling an oscillatory bending experiment, *J. Biomech.,* 32, 663–672, 1999.
214. Wang, N., Butler, J. P., and Ingber, D. E., Mechanotransduction across the cell surface and through the cytoskeleton, *Science,* 260, 1124–1127, 1993.
215. Wasserman, F. and Yaeger, J. A., Fine structure of the osteocyte capsule and of the wall of the lacunae in bone, *Z. Zellforsch.,* 67, 636–652, 1965.
216. Weinbaum, S., Cowin, S. C., and Zeng, Y., A model for the excitation of osteocytes by mechanical loading induced bone shear stresses, *J. Biomech.,* 27, 339–360, 1994.
217. Weinstein, E., Mandel, I. D., Salkind, A., Oshrain, H. I., and Pappas, G. D., Studies of gingival *fluid, Periodontics,* 5, 161–166, 1967.
218. Wilkes, C. H. and Visscher, M. B., Some physiologic aspects of bone marrow pressure, *J. Bone Joint Surg.,* 57A, 49, 1975.
219. Willans, S. M. and McCarthy, I. D., Distributed model of blood-bone exchange, *J. Biomed. Eng.,* 8, 235–243, 1986.
220. Williams, J. L., Iannotti, J. P., Ham, A., Bleuit, J., and Chen, J. H., Effects of fluid shear stress on bone cells, *Biorheology,* 31, 163–170, 1994.
221. Wolff, J., *Das Gesertz der Transformation der Knochen,* Springer, Berlin, 1892.
222. Weinans, H., Huiskes, R., and Grootenboer, H. J., The behavior of adaptive bone-remodeling simulation models, *J. Biomech.,* 25, 1425–1441, 1992.
223. Wolpert, L., Positional information and the spatial pattern of cellular differentiation, *J. Theor. Biol.,* 25, 1–47, 1969.

224. Zhang, D., Cowin, S. C., and Weinbaum, S., Electrical signal transmission and gap junction regulation in a bone cell network: a cable model for an osteon, *Ann. Biomed. Eng.,* 25, 357–374, 1997.

23

Bone Poroelasticity

Stephen C. Cowin
The City College of New York

23.1 Introduction and Notation

23.1.1 Introduction

Poroelasticity is a well-developed theory for the interaction of fluid and solid phases of a fluid-saturated porous medium. It is widely used in geomechanics and has been applied to bone by many authors in the last 30 years. The purpose of this chapter is, first, to review the literature related to the application of poroelasticity to the interstitial bone fluid and, second, to describe the specific physical and modeling considerations that establish poroelasticity as an effective and useful model for deformation-driven bone fluid movement in bone tissue. The application of poroelasticity to bone differs from its application to soft tissues in two important ways. First, the deformations of bone are small, while those of soft tissues are generally large. Second, the bulk modulus of the mineralized bone matrix is about six times stiffer than that of the fluid in the pores, while the bulk moduli of the soft tissue matrix and the pore water are almost the same. Poroelasticity and electrokinetics can be used to explain strain-generated potentials in wet bone. It is noted that strain-generated potentials can be used as an effective tool in the experimental study of local bone fluid flow, and that the knowledge of this technique will contribute to the answers of a number of questions concerning bone mineralization, osteocyte nutrition, and the bone mechanosensory system.

Bone fluid has many functions. It transports nutrients to, and carries waste from, the bone cells (osteocytes) buried in the bony matrix. It is involved in the transport of mineral ions to the bone tissue for storage

0-8493-9117-2/01/$0.00+$.50

and retrieval of those mineral ions when they are needed by the body. Recently, bone fluid flow has been suggested to have a role in the mechanosensory system of bone. Bone deformation causes the bone fluid to flow over the bone cell membrane; the shear stress of the flowing fluid is sensed by the cell.[1–4] A full physiological understanding of this mechanosensory system will likely provide insight into the following three important clinical problems: (1) the long-term stability of bone implants, (2) the physiological mechanism underlying osteoporosis, and (3) bone maintenance in long-duration spaceflights and long-term bed rest.

Poroelasticity is a theory that models the interaction of deformation and fluid flow in a fluid-saturated porous medium. The deformation of the medium influences the flow of the fluid, and vice versa. The theory was proposed by Biot[5,6] as a theoretical extension of soil consolidation models developed to calculate the settlement of structures placed on fluid-saturated porous soils. The historical development of the theory is sketched by de Boer.[7] The theory has been widely applied to geotechnical problems beyond soil consolidation, most notably problems in rock mechanics. It will be shown below that certain porous rocks, marbles and granites, have material properties that are similar to those of bone. The application of the Biot (or effective medium) formulation of poroelasticity to bone has been suggested by several authors in the last 30 years.

The structure of this chapter is first to describe the anatomy of the bone porosity, then to summarize the development of poroelasticity and review its application to bone. Following the introduction, there is a set of three sections detailing the anatomy of the bone porosity. The first of these sections describes the local anatomy, and the two sections that follow describe the various interfaces and the different levels of porosity, respectively. The fourth section summarizes the three principal theoretical or averaging approaches to poroelasticity (effective medium, mixture theory, and homogenization). Then, after the definition of ideal poroelasticity, the constitutive and field equations for poroelasticity are briefly described, as are methods for their solution. Current knowledge of the numerical values of the bone parameters appearing in the theory are then summarized. The early (circa 1970) applications of a single-porosity poroelasticity to bone are reviewed; then the effect of the fluid compartments on wave propagation in bone is considered in a section on poroelastic waves. The center of this review is the section on a two-porosity poroelastic model for bone. In this section the material presented up to this point is drawn together to address the question of the most appropriate poroelastic model for the study of bone fluid movement and bone fluid pressures. It is followed by a review of the extension of poroelasticity to include strain-generated potentials in bone as well as a comparison of the resulting theory with experimental results. The numerical solution to an important two-porosity problem is then described. The key points of this review are summarized at the end.

23.1.2 Notation

B	compressibility coefficient, sometimes called the Skempton pore pressure coefficient
G	shear modulus of the poroelastic medium under the drained condition
G_u	shear modulus of the poroelastic medium under the undrained condition
K	bulk modulus of the poroelastic medium under the drained condition
K_f	bulk modulus of the fluid phase
K_s	bulk modulus of the solid phase
K_u	bulk modulus of the poroelastic medium under the undrained condition
u_i	components of the displacement vector of the solid
α	Biot effective stress coefficient
σ_{ij}	components of the total stress tensor
ε_{ij}	components of the strain tensor of the solid phase
p	pore fluid pressure
ζ	variation of fluid volume per unit volume of the porous material due to diffusive fluid mass transport, also called the fluid content
ϕ	pore volume fraction, the volume of pores per unit total volume, $\phi = \phi_i + \phi_m$

ϕ_i pore volume fraction (the volume of pores per unit total volume) occupied by immobile organic material
ϕ_m pore volume fraction (the volume of pores per unit total volume) occupied by mobile bone fluid
ν Poisson's ratio of the medium under the drained condition
ν_u Poisson's ratio of the medium under the undrained condition
k intrinsic Darcy law permeability constant at the lacunar–canalicular porosity; it has units of length squared and is a function of the porous bone structure only, not the fluid in the pores
t time
κ coefficient of permeability, equal to k/μ, where μ is the fluid viscosity
μ fluid viscosity

23.2 The Microstructure of the Bone Porosities

23.2.1 The Structures of Bone Associated with Bone Fluid

There are three levels of bone porosity within cortical bone and within the trabeculae of cancellous bone, all containing a fluid. In addition there are two interfaces between the three levels of bone porosity within cortical bone and within the trabeculae of cancellous bone. The purpose of the next two sections is to describe these interfaces and porosities and some related structures of bone tissue. A sketch of a partial cross section of an osteon (Fig. 23.1) shows some of the small-scale features of bone of interest. Osteons are cylindrical structures of 100 to 150 μm radii that lie very roughly along the long axes of a bone and contain at their center an osteonal canal. This canal contains blood vessel(s), a nerve, and some space

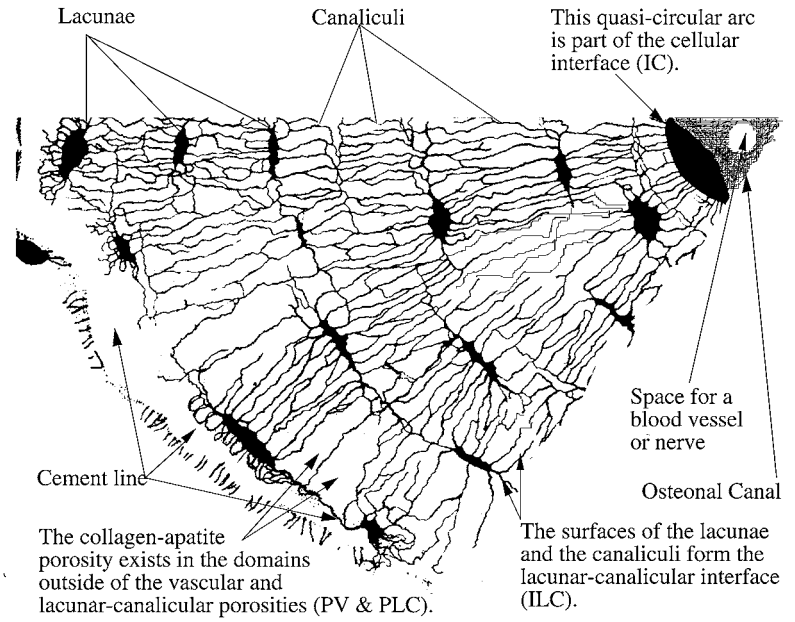

FIGURE 23.1 A pie-shaped section of an osteon. The osteonal canal is on the upper right, the cement line to the left. The osteonal canal is part of the vascular porosity (PV), the lacunae and the canaliculi are part of the lacunar-canalicular porosity (PLC), and the material in the space that is neither PV nor PLC contains the collagen-apatite porosity (PCA). The three interfaces, the cement line, the cellular interface (IC), and the lacunar-canalicular interface are each indicated. The radius of an osteon is usually about 100 to 150 μm, and the long axis of a lacuna is about 15μm. Using this information it should be possible to establish the approximate scale of the printed version of this illustration. (From Cowin, S. C., *J. Biomech.,* 32, 218–238, 1999. With permission.)

occupied by bone fluid. The walls of the osteonal canals are covered with cells and behind the cells are the entrances to the canaliculi. The canaliculi are passageways that run between lacunae or from the lacunae to the osteonal canal (Fig. 23.1). The structures described in the next section are the bone interfaces, the periosteum, the cellular interface (IC) (which includes the endosteum), the interface consisting of the walls of the lacunae and the canaliculi (ILC), and the cement lines. In the section following, the bone fluid and the bone porosities are then described. The porosities include the vascular porosity (PV), the lacunar–canalicular porosity (PLC), and the collagen-apatite porosity (PCA), as well as a porosity that does not contain bone fluid—the porosity of the intertrabecular space (PIT). These acronyms have been selected so that the first letter indicates the structure, interface (I) or porosity (P), and the subsequent letters in the acronym indicate which interface or which porosity. These may appear awkward in English, but it is a reasonable ordering in some languages (e.g., French).

23.2.2 The Interfaces between the Levels of Bone Porosity

The interfaces are structures of varying thickness and permeability between the relevant fluid compartments and structures in bone. Four of those interfaces are relevant to the bone fluid.

23.2.2.1 Periosteum

The periosteum is a specialized membrane, a layered and highly vascularized structure, covering most of the external surface of a bone. It consists of an outer dense layer of collagenous fibers and fibroblasts. This is a pretensioned, relatively impermeable fiber stocking attached to the exterior surface of bone. The inner layers are multiple layers of bone cells at various stages of differentiation. Li et al.[8] report that the periosteum acts as a barrier to bone fluid flow.

23.2.2.2 IC—The Cellular Interface, Including the Endosteum

All the surfaces of the tubular cavities of bone that contain the vasculature, the osteonal canals and the Volkmann canals, as well as the endosteum and the inner layer of the periosteum, form a single cellular interface. This interface, a small part of which is illustrated in Fig. 23.1, is a continuous confluent layer of bone-lining cells,[9] one side of which faces the vascular space and the other side of which faces the mineralized matrix. (Based on study of these surfaces at many anatomical sites in the Swiss-Webster mice, Sprague-Dawley rats, and gerbils, Chole and Tinling[10] suggest that this layer of bone-lining cells is not continuous and confluent; but their report appears to be unique.) The region interior to this interface was called the "milieu intérieur" by Bernard,[11] and Howard[12] suggested the existence of a "bone membrane" that would spatially coincide with what is called the cellular interface (IC) here. This view was endorsed by Neuman[13] and Neuman and Ramp,[14] but the endorsement was later retracted.[15] Soares et al.[16] report tight junctions occurring between the bone-lining cells on the interface, but the occurrence of these junctions does not stop fluid transport across a confluent cell layer. Neuman and Neuman[17] argued that the IC must be some sort of diffusion barrier, ion gradient, or ion pump, a view also later revised.[15] Hillsley and Frangos[18] hypothesize that the IC regulates its own hydraulic conductivity, and they present data from newborn Sprague-Dawley rats. The calvarial IC was subjected to a pressure of 7.3 mmHg and the IC transport was altered by parathyroid hormone and calcitonin. Hillsley and Frangos[18] conclude that cAMP and Ca^{2+} may mediate the changes in the IC hydraulic conductivity. Zhang et al.[19] have analytically demonstrated that there are transient pressure gradients across the interface that will transport the fluids through the interface. The bone-lining cells with tight junctions will not form a significant barrier to the transport of fluids across this interface. During each cycle of bone loading, the fluid on the vascular side of the interface (serum) will briefly mix with the fluid on the mineralized matrix side of the interface (extracellular fluid). As a first approximation it appears reasonable to assume that the hydraulic resistance of this interface is much less than the hydraulic resistance of the lacunar–canalicular porosity, which is on the bone side of the interface. It is estimated that the hydraulic resistance of this interface is on the order of the hydraulic resistance of a 0.5 μm canalicular length.[20] It is not now possible to tell if the disjoint results concerning the IC summarized in this paragraph are consistent or contradictory.

23.2.2.3 ILC—The Interface Consisting of the Walls of the Lacunae and the Canaliculi

The interface consisting of the walls of the lacunae and the canaliculi—the ILC—divides these spaces from the mineralized tissue (Fig. 23.1). All the ILC is topologically contained within the IC. It could be considered as part of the IC, but it is considered as distinct here because it is necessary to distinguish between the vascular porosity (PV) and the lacunar–canalicular porosity (PLC) and their boundaries for mechanical and physiological reasons. The evidence suggests that the ILC is relatively impermeable (at least at the level of the smallest solutes that have thus far been used). This evidence comes from various tracer studies[8,21–28] to document fluid transport in bone; see Knothe Tate et al.[28] for a summary of the tracers employed. The conclusion that the ILC is relatively impermeable is supported by the studies of Tanaka and Sakano[25] in the alveolar bone of 5-day-old rats using the small tracer microperoxidase (MP) (2 nm). These studies clearly showed that the MP only penetrated the unmineralized matrix surrounding the lacunae and the borders of the canaliculi (see Fig. 13 of that study) and was absent from the mineralized matrix. Using more mature rats, the study of Asasaka et al.[29] confirmed the failure of the small (2 nm) MP tracer to penetrate the mineralized matrix tissue from the bone fluid compartments. Further confirmation comes from Doty[27] and Knothe Tate et al,[28] who noted that the tracers ruthenium red (MW 860, 1.13 nm in largest dimension) and procion red (MW 300–400), respectively, did not penetrate the bone mineral porosity, but were present in the lacunar–canalicular porosity (PLC).

There is a caveat to the conclusion that the ILC is relatively impermeable—it does not hold for very young bones. The ILC and the associated bone porosities change rapidly after birth, being quite porous at birth and subsequently reducing their porosities as the bone tissue becomes fully mineralized.[8,16] Experimental permeability studies clearly show time-dependent changes in the interstitial pathways as bone matures. At the earliest times the unmineralized collagen–proteoglycan bone matrix is porous to large solutes. The studies with ferritin (10 nm in diameter) in 2-day-old chick embryo[24] show a continuous halo of bone fluid-stained ferritin around primary osteons 5 min after the injection of this tracer. The halo passes right through the ILC, suggesting that, before complete mineralization, pores of a larger size can exist throughout the bone matrix. Li et al.[8] report that the porosity in puppies is 3.5 times higher than that of dogs. Montgomery et al.[30] using the same tracer as Dillaman[24] in adult dogs, also found a fluorescent halo surrounding the osteonal canals; however, this halo was not continuous but formed by discrete lines suggesting that the pathways were limited to discrete pores whose spacing was similar to that observed for canaliculi. In the present work only the adult or fully mineralized situation is considered; hence the ILC is always impermeable here.

An important physiological consideration concerning the IC and the ILC arises from the fact that bone serves as a reservoir for calcium and phosphorus, and these mineral reserves should be connected to the circulation. Clearly, these minerals must cross the IC, but, must they cross the ILC? That is to say, can the necessary minerals be supplied by the bone-lining cells from the bone matrix they are situated upon, or must the osteocytes be involved in this process? It is possible that sufficient mineral can be supplied by the bone-lining cells, consistent with the suggestions above that the ILC is relatively impermeable and that the IC offers relatively small hydraulic resistance. It is also possible that the interface permeability of the ILC might be changed by physiological demands. The exact method of mineral retrieval and redeposition lies at the root of many studies.[16,28,31–33]

23.2.2.4 Cement Lines

Cement lines appear as the boundary of secondary osteons (Fig. 23.1). They represent the limit of a structural remodeling, a front where osteoclastic activity associated with the removal of bone preparatory to the construction of a new secondary osteon has ceased and osteoblastic activity associated with the new osteon begins. They are somewhat similar to osteoid in composition, but cement lines contain lipids not present in osteoid and the concentrations of some collagenous proteins and proteoglycans are different. It was thought at one time that canaliculi did not cross the cement lines, but evidence that they do is now well established.[34–36] The number density per unit area of the canaliculi crossing cement lines has not been established, nor has the anatomical distribution of their crossing been investigated. It is possible that canaliculi only cross cement lines when there is an isolated osteocyte on the other side,

perhaps residing in a small piece of a former osteon removed by remodeling. This would make the number density per unit area of canaliculi crossing cement lines dependent on anatomical site and therefore a parameter with a very inhomogeneous value. It follows that the permeability of this interface is unknown and could be very inhomogeneous. The other possibility is that bone cells in one osteon need to communicate with those in neighboring osteons to complete a whole bone cell network. If this latter case is in fact the situation, then the trespassing of the cement lines by the canaliculi will be a more homogeneous occurrence.

23.2.3 The Porosities of Bone

There are three porosities of bone associated with bone fluid; they are described below after a discussion of the composition of the bone fluid. The section closes with a discussion of the other porosity of bone, the porosity of the intertrabecular space (PIT), which contains substances more viscous than bone fluid.

23.2.3.1 Bone Fluid

Neuman and Neuman[17] called the fluid in the space outside the blood vessels and nerves in the Volkmann and osteonal canals "serum" and the fluid in the extracellular space in the lacunae and the canaliculi "extracellular fluid." Both of these fluids are called bone fluids here. Neuman and Neuman[17] noted that the "serum" and the "extracellular fluid" were nearly equivalent in composition (pH, Ca^{2+}, Na^{+}, etc.), but argued that there must be some diffusion barrier, some ion gradient or ion pump, between the two fluid compartments; a view also later revised.[15] There is no information located on the contents of the bone fluid other than that provided by Neuman and Neuman.[17]

23.2.3.2 PV—The Vascular Porosity

All the quasi-cylindrical passageways in the bone matrix—the osteonal canals and the Volkmann canals—that contain the vasculature, nerves, and bone fluid are called the vascular porosity (PV). The characteristic lineal dimension associated with this space is the radius of the Volkmann and osteonal lumens (order 20 μm); by this criterion, this porosity is the largest bone fluid porosity. The boundaries of this porosity are the IC.

Bone fluid freely exchanges with the vascular fluids because of the high permeability of the thin endothelium, the absence of a smooth-muscle layer, and the sparse basement membrane layer of the capillary walls. The bone fluid pressure in the PV cannot generally exceed the local blood pressure as the vessels would collapse. Thus, the pressure of the bone fluids is probably similar to the blood pressure in bone, on the order of 40 to 60 mmHg, which is low compared with the bone fluid pressures in the lower characteristic lineal dimension (PLC), described below.

23.2.3.3 PLC—The Lacunar–Canalicular Porosity

All the space in the lacunae and the canaliculi is called the lacunar–canalicular porosity (PLC). The characteristic lineal dimension associated with this space is the radius of the canaliculus (order 0.1 μm).

Since the bone fluid porosity with the largest lineal dimension, the PV, is always at a low pressure, the middle characteristic lineal dimension porosity—the PLC—appears to be the most important porosity for the consideration of mechanical and mechanosensory effects in bone. Calculations to be reviewed below show that the bone fluid in the PLC can sustain higher pressures for longer times due to mechanical loading. Thus, the PV functions as a low-pressure reservoir that interchanges bone fluid with the PLC. This interchange is facilitated by the fact that the lineal dimension associated with the PV is two orders of magnitude larger than that associated with the PLC, and the PV is typically at blood pressure, which is low in bone. The total volume of the bone fluid PV is, however, less than that of the PLC.[23]

Weinbaum et al.[2] and Cowin et al.[37] present a detailed theoretical model of the contents of the PLC. The PLC is the porosity associated with the slower relaxation of the excess pore pressure due to mechanical loading. It is also the porosity associated with osteocytes; the osteocyte is the prime candidate for the mechanosensory cell in bone. Weinbaum et al.[2] and Cowin et al.[37] suggest that the region between the cell membrane of the osteocyte (and the osteocytic process) on the one hand and the walls of the canaliculi

and lacunae on the other is filled with the cell glycocalyx (also called the surface matrix or capsule). The contents of this PLC, the combination of the glycocalyx and the bone fluid, is thought to function as a gel.

23.2.3.4 PCA—The Collagen–Apatite Porosity

The porosity associated with the spaces between the collagen and the crystallites of the mineral apatite (order 10-nm radius) is called the collagen–apatite porosity (PCA). This porosity is within the ILC and is the lowest characteristic lineal dimension porosity. The movement of the bone fluid in the PCA is negligible because most of the bone water in that porosity is bound by interaction with the ionic crystal.[17,38] This portion of the bone water is considered to be part of the collagen–apatite structure. The mineral in bone is referred to as apatite rather than hydroxyapatite, accepting the recent argument of Glimcher[39] that it is, in fact, the former rather than the latter.

23.2.3.5 PIT—The Porosity of the Intertrabecular Space

The bone porosity with the largest, but quite variable, characteristic lineal dimension (up to 1 mm) is associated with cancellous bone; it is referred to here as the intertrabecular porosity (PIT) of cancellous bone. It is the porosity external to, and surrounding, the trabeculae. The IC on the surface of trabeculae divides the PIT and the mineralized matrix in the trabeculae. This porosity is well connected to the medullary cavity and may contain marrow, fat, and blood vessels. These materials have a viscosity one to two orders of magnitude larger than the viscosity of the bone fluid in the PV or PLC.[40–42] The characteristic lineal dimension of the PIT varies with anatomical location; it is smaller near the load-bearing surfaces and increases to its greatest magnitude as the medullary canal is approached. The permeability associated with this porosity was surveyed by Arramon and Cowin;[43] the concentration in the present work is with the three levels of bone porosity within cortical bone and within the trabeculae of cancellous bone, not the PIT. It is mentioned here only for completeness.

23.3 Poroelasticity

23.3.1 The Approaches to Poroelasticity

There are three different major approaches to the development of the same basic equations for the theory of poroelasticity. Each approach is rigorous to its own hypotheses and stems from well-established mathematical and/or physical models for averaging material properties. The difference between the three approaches lies in the averaging processes employed.

The first approach originates in the solid mechanics tradition and the averaging process involved is the determination of effective material parameters from a representative volume element (RVE), as discussed in the work of Hashin and Shtrikman,[44] Hill,[45] and others. Standard contemporary references are the books of Christensen[46] and Nemat-Nasser and Hori.[47] The effective medium approach appears in an early form* in the early Biot work[6] and grows in sophistication with time through the work of Nur and Byerlee,[48] Rice and Cleary,[49] Carroll,[50] Rudnicki,[51] and Thompson and Willis.[52] The development of the effective medium theory over the last 35 years occurred almost in parallel with the increasing sophistication and refinement of the original Biot formulation of the effective medium approach. Applications of the Biot formulation to tissues other than bone include articular cartilage,[53,54] flow through the arterial wall,[55] and the intervertebral disk.[56]

The second approach is called the mixture theory approach; it is based on diffusion models and has a very different philosophy and a longer history than the effective medium approach. It stems from a fluid mechanics and thermodynamics tradition and goes back to the last century. Fick and Stefan

*Biot[6] (page 156) wrote, "Consider a small cubic element of soil, its sides being parallel with the coordinate axes. This element is taken to be large enough compared to the size of the pores so that it may be treated as homogeneous, and at the same time small enough, compared to the scale of the macroscopic phenomena in which we are interested, so that it may be considerd as infinitesimal in the mathematical treatment."

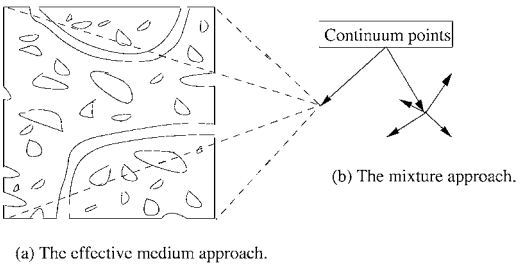

FIGURE 23.2 Illustrations of the effective medium approach and the mixture theory approach. (From Cowin, S.C., *J. Biomech.,* 32, 218–238, 1999. With permission.)

suggested (Truesdell and Toupin,[57] sect. 158) that each place in a fixed spatial frame of reference might be occupied by several different particles, one for each constituent of the mixture. This is an Eulerian approach in that the flux of the various species toward and away from a fixed spatial point is considered. Truesdell[58] assigned to each constituent of a mixture in motion a density, a body force density, a partial stress, a partial internal energy density, a partial heat flux, and a partial heat supply density. He postulated equations of balance of mass, momentum, and energy for each constituent and derived the necessary and sufficient conditions that the balance of mass, momentum, and energy for the mixture be satisfied. Bowen[59] summarized the formative years of this subject. A readable history of the subject and its applications in the period 1957 to 1975 is given by Atkin and Craine.[60,61] For subsequent developments, see Bowen[62–64] and Müller.[65,66] An advantage of mixture theory appears when a number of different fluid species are present and in relative motion. This advantage is illustrated in the theory for the swelling and deformation behavior of articular cartilage by Lai et al.[67] and Gu et al.[68] There are many other applications of the mixture theory approach to the flow through porous media in biomechanics other than bone, for example, skin,[69] the swelling of soft tissue,[70] pressure sores,[71] intervertebral disks,[72] and blood perfusion of contracting skeletal muscle.[74]

The key difference between the effective medium approach and the mixture approach to poroelastic models is the averaging process employed. The effective parameter approach illustrated in Fig. 23.2a is a schematic version of the viewpoint described in Biot.[6] A small but finite volume of the porous medium is used for the development of constitutive equations for the fluid-infiltrated solid. These constitutive equations are then assumed to be valid at a point in the continuum. This is an early form of the representative volume element (RVE) approach used in composite material theory today. The length or size of the RVE is assumed to be many times larger than the length scale of the microstructure of the material, say, the size of a pore. The length of the RVE is the length of the material structure over which the material microstructure is averaged or "homogenized" in the process of forming a continuum model. Biot's presentation is consistent with the notion of an RVE, although the RVE terminology did not exist when his theory was formulated. The homogenization approach is illustrated in Fig. 23.2a by the dashed lines from the four corners of the RVE to the continuum point. The material parameters or constants associated with the solid phase are more numerous and difficult to evaluate compared with those associated with the fluid phase. The effective medium approach provides a better understanding of the effective solid mechanical parameters like effective solid moduli than does the mixture theory approach.

The averaging process for the mixture approach is illustrated in Fig. 23.2b. This is usually an Eulerian approach in that the flux of the various species toward and away from a fixed spatial point is considered. The fixed spatial point is shown in Fig. 23.2b and the vectors represent the velocities of various species passing through the fixed spatial point. It is important to note that, for mixture theory, the averaging is density-weighted on the basis of the density of each species in the mixture, instead of being averaged over a finite volume of the porous solid as in the effective medium approach. This is a difference between the effective medium and the mixture theory approaches. In neither approach is a length scale specified, but an averaging length is implied in the effective medium approach because a finite material volume is

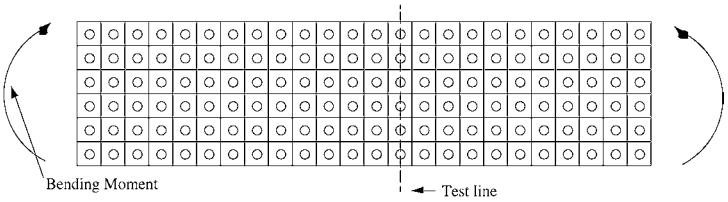

FIGURE 23.3a Schematic illustration of a model[128] for pressure/SGP generated by the bending of Haversian bone. The model has six adjacent osteons across the specimen thickness. Of course the osteons are not periodically ordered in bone tissue. The packing of osteons in real bone tends to the quasi-hexagonal rather than the idealized tetragonal packing used in this model. More noticeable is the fact that the cement lines in real bone are quasi-circular in shape and were modeled as squares for computational convenience. (From Cowin, S. C., *J. Biomech.,* 32, 218–238, 1999. With permission.)

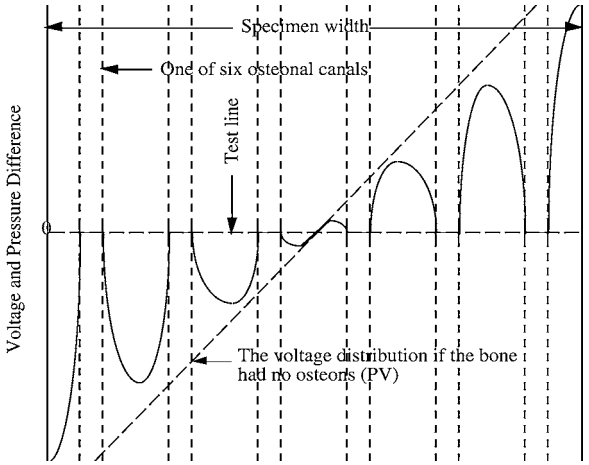

FIGURE 23.3b Schematic illustration of the results of the Wang et al., (1998) model for pressure/SGP generated by the bending of Haversian bone. The curves are voltage or pressure differences due to the low pore fluid pressure in the osteonal canals. In this model the test microelectrode is envisioned as moving along the test line of Figure 23.3a from one side of the specimen to the other. The voltage difference measured as this test line is traversed is illustrated above. The voltage difference vanishes when the osteonal lumen is crossed, giving a very inhomogeneous structure to the local pressure or voltage distribution in each osteon. If the osteons were removed, the voltage distribution would be a straight line in the central portion of the cross section and would decrease in slope as each of the boundaries is approached. The straight line portion is shown as a longer dashed above; its curved approach to the boundary is not illustrated. (From Cowin, S. C., *J. Biomech.,* 32, 218–238, 1999. With permission.)

employed as the domain over which quantities are to be averaged. On the other hand, the mixture theory approach is to consider a fixed spatial point through which different materials pass and no length scale is implied or suggested. It is difficult to imagine a length scale for the mixture theory approach other than one based on the mean free paths associated with the constituents. The significantly different averaging lengths in the two approaches reflect the difference in the averaging methods. For small strain poroelasticity, like elasticity, the difference between the Eulerian (spatial) and the Lagrangian (material) approach is a negligible higher-order term. For large deformations, this is not the case. Bowen[59,62–64] employed the Eulerian (spatial) approach for his development of mixture theories. The mixture theory development can also be accomplished from a Lagrangian approach.[73,75–78]

Bowen[64] showed that it was possible to recover the Biot constitutive equations from the mixture theory approach. In particular Bowen derived equations (his 9.23 and 9.24) that have the same form

as equations* 7 and 8 of Rice and Cleary;[49] these equations are Eq. 23.3 and 23.5 in the text below. The governing equations of the small strain, incompressible poroelastic formulation of Mow et al.[79] based on the mixture theory approach, the "biphasic theory," coincide with the governing equations of the effective medium formulation, as shown by Mow and Lai.[80]

The work of Bowen[59,62–64] employed a nontraditional thermodynamical approach suggested by Coleman and Noll[81] to restrict the form of constitutive equations. (Bowen was not alone following Coleman and Noll,[81] as Goodman and Cowin[82] and Cowin and Hegedus[83] and others followed the same path.) The method of Coleman and Noll[81] has drawn much criticism in the literature.[84–90] The main criticisms are that Coleman and Noll (1) assumed the existence of entropy as a primitive field and did not provide a method for determining (constructing) entropy and (2) used the Clausius–Duhem inequality as the mathematical statement of the second law of thermodynamics.[90] Following suggestions of Rivlin,[84,85] Casey[90] has suggested a more traditional thermodynamical path in which the entropy function is constructed in terms of other thermodynamics variables. Using this type of approach, Krishnaswamy and Batra[91] have presented a derivation of the key Bowen results that appear to address the criticisms stemming from Bowen's use of the Coleman and Noll thermodynamic approach.

The third major approach** to the development of the poroelastic equations is due to Burridge and Keller.[95] These authors rederived the dynamic form of the same basic set of equations using a two-space method of homogenization. This approach provides a systematic method for deriving macroscopic equations that govern the behavior of the medium on the microscale. Thus, at the continuum point, the three rigorous theoretical developments lead to the same set of equations, and the difference between effective medium, the mixture theory-based, and the homogenization derivations is the method of averaging. The nature of the equations is better understood because there are three approaches. The effective medium approach provides better insight into the nature of the parameters associated with the solid phase; the mixture theory approach provides the mechanism for averaging over different fluid phases; and the homogenization approach illuminates the dynamical (wave propagation) characteristics of the theory. In a summary of a technical session discussion at a 1983 geomaterials symposium on the topic of whether the mixture theory or the effective medium approach was to be favored, it was written:[96]

> There was general agreement that mixture theory had not yet demonstrated any advantage over Biot theory…the effective medium approach...for fluid saturated linearly elastic solids. However, it was pointed out that mixture theory had as its objective the formulation of a general framework for developing models of multiphase mixtures and the fact that it could not improve upon the first prototype of such a theory, namely the Biot theory, did not mean that further development of mixture theory should be abandoned. Perhaps the proper approach to the criticism of mixture theory is to evaluate and assess the axioms on which it is based.

Since that was written, the applications of mixture theory to fluid-saturated porous tissues have attractively illustrated it as a general framework for developing models of multiphase tissues, an important example being the development of the theory for the swelling and deformation behavior of articular cartilage by Lai et al.[67] However, the effective medium approach is employed in this review for the reasons stated above plus the fact that it has a longer history and the fine points have been resolved further than in the other presentations, particularly with regard to the consideration of constituent compressibility.

There are several other specialized approaches that lead to special poroelastic-type models, although not to the same set of poroelastic equations produced by the effective medium, mixture theory, and homogenization approaches. Piekarski and Munro[97] and Munro and Piekarski[98] constructed a model of an osteon from concentric hollow cylinders of progressively decreasing inner and outer radii interspersed with layers of fluid. They used this model to demonstrate effectively the convection of bone fluid caused

*Actually the second summand on the right-hand side of Bowen's equation 9.24 is missing a factor of 3; this is probably a typo or an algebraic slip.

**Huyghe[92] suggests that one could consider the averaging approach of Slattery[93] and Whitaker[94] as a fourth approach to the poroelastic equations.

by applied mechanical loading. The study by Piekarski and Munro emphasized the importance of the convective flow in the canaliculi between the lacunae as a way of enhancing the supply of nutrients between neighboring osteocytes. A similar model was employed by Kufahl and Saha.[99] Recently, Knothe Tate and Niederer[28] have employed the ideas of Piekarski and Munro to illustrate the fact that convection enhances transport within the PLC.

23.3.2 Ideal Poroelasticity

There are several bulk moduli that can be associated with a porous medium. An ideal poroelastic material is defined as a material in which two particular bulk moduli, K_s' and K_s'', are equal. The bulk modulus K_s' is defined as the change in the total medium volume per total medium volume when the entire medium is under a pressure regime in which the hydrostatic confining pressure is equal to the pore pressure,[49,100] and the bulk modulus K_s'' is defined as the change in total pore volume per total pore volume under this pressure regime.[100] For an ideal porous medium characterized by a fully connected pore space and by microscopically homogeneous and isotropic, chemically inert (solid and fluid) materials, it follows that $K_s = K_s' = K_s''$, where the notation K_s is the bulk modulus for the solid phase.[49,100] Experimentally, for many porous rocks, $K_s' = K_s''$. An *ideal poroelastic material* is defined as one for which $K_s' = K_s''$ (Ref. 100, page 123). If the matrix material is homogeneous, then it is easy to see that $K_s' = K_s''$; inhomogeneity is then the reason for $K_s' \neq K_s''$. For bone a potential source of inhomogeneity is the unmineralized or soft tissue in the PV and PLC. This tissue has a bulk compressibility approximately the same as that of the bone fluid (i.e., water). When the volumes of the pores are to be changed by the pore pressure, then all highly compressible materials, including the cells and the cell processes and any other unmineralized tissue in the lacunae and canaliculi, must be compressed as well as the mineralized matrix. Since the bulk modulus of salt water is only a sixth that of the bone matrix, much of the compressibility of the combination of the two materials will occur in the soft tissues and fluids. To consider bone tissue with its PLC as an ideal poroelastic material, the pore volume fraction ϕ of bone tissue is defined to include the immobile organic material of low compressibility, the cells and the cell processes and other unmineralized contents of the lacunae and canaliculi. In most canaliculi, there is nothing along the wall except proteoglycan, and the mineralization comes right to the edge of the lumen. The lacunae may or may not have some free unmineralized collagen fibers, depending upon age and site (trabecular osteocytes vs. cortical osteocytes).[27] Since this material is immobile and does not flow, it must be excluded from the pore volume when calculating the permeability. This special distinction for the immobile soft tissue of the PLC is recognized in two ways. First, the material with which K_s is identified does not include the soft material in the pores and the soft lining. A boundary, probably at the lamina limitans, between any unmineralized material along the canalicular wall and the fully mineralized matrix material should be identified so the volume of mineralized matrix has no unmineralized material volume and the identification of K_s' with K_s'' is justified. Second, the pore volume fraction ϕ is considered to be the sum of immobile and mobile pore volumes,

$$\phi = \phi_i + \phi_m, \tag{23.1}$$

where ϕ_i is the immobile pore volume fraction (the volume of pores per unit total volume) occupied by immobile soft material with a bulk compressibility approximately the same as that of the pore fluid, K_f, and where ϕ_m is the mobile pore volume fraction, the volume of pores per unit total volume, occupied by the (mobile) bone fluid with bulk compressibility K_f.

23.3.3 Constitutive Equations for Ideal Poroelasticity

The notation employed for poroelasticity theory in this review was selected to coincide as far as possible with the notation of Detournay and Cheng,[100] who, in turn, selected their notation to coincide with that of Rice and Cleary,[49] who, in turn, based their notation on Biot.[6] Notation is an important issue for a topic of great popularity. The notation selected here (see the list of notations after the abstract) is considered by many authors in this field to be the most appropriate. Biot himself did not, however, stay

always faithful to his own notation. Detournay and Cheng[100] provide an appendix containing equivalence relations for the various other notations (e.g., Q, R, M) used by Biot in the mid 1950s.[101] Simon[102] provides a table showing the equivalent notations for the incompressible poroelastic equations of Mow et al.[79]

The poroelastic field variables are six components of the total stress σ_{11}, σ_{22}, σ_{33}, σ_{23}, σ_{13}, and σ_{12} and the pore pressure p, the six components of the strain in the solid phase ε_{11}, ε_{22}, ε_{33}, ε_{23}, ε_{13}, and ε_{12} and the variation in (dimensionless) fluid content ζ. The variation in fluid content ζ is the variation of the fluid volume per unit volume of the porous material due to diffusive fluid mass transport. Biot viewed these variables as the conjugate pairs of stress measures (σ_{11}, σ_{22}, σ_{33}, σ_{23}, σ_{13}, σ_{12}, p) and strain measures (ε_{11}, ε_{22}, ε_{33}, ε_{23}, ε_{13}, ε_{12}, ζ) appearing in the following form in an expression for work done on the poroelastic medium: $dW = \sigma_{11}d\varepsilon_{11} + \sigma_{22}d\varepsilon_{22} + \sigma_{33}d\varepsilon_{33} + 2\sigma_{23}d\varepsilon_{23} + 2\sigma_{13}d\varepsilon_{13} + 2\sigma_{12}d\varepsilon_{12} + pd\zeta$. A fundamental idea presented by Biot[6] was that dW was an exact differential, $dW = \sigma_{11}d\varepsilon_{11} + \sigma_{22}d\varepsilon_{22} + \sigma_{33}d\varepsilon_{33} + 2\sigma_{23}d\varepsilon_{23} + 2\sigma_{13}d\varepsilon_{13} + 2\sigma_{12}d\varepsilon_{12} + pd\zeta = \varepsilon_{11}d\sigma_{11} + \varepsilon_{22}d\sigma_{22} + \varepsilon_{33}d\sigma_{33} + 2\varepsilon_{23}d\sigma_{23} + 2\varepsilon_{13}d\sigma_{13} + 2\varepsilon_{12}d\sigma_{12} + \zeta dp$. Using this argument, he showed that certain coefficients in the constitutive relations were equal, paralleling typical arguments in thermodynamics. (The poroelasticity book of Coussy[103] appropriately emphasizes the strong thermodyamical basis for the theory.) The components of the displacement vector of the solid, u_1, u_2, u_3 are related to the strain tensor by

$$\begin{aligned}
\varepsilon_{11} &= \frac{\partial u_1}{\partial x_1}, \qquad \varepsilon_{22} = \frac{\partial u_2}{\partial x_2}, \qquad \varepsilon_{33} = \frac{\partial u_3}{\partial x_3}, \\
\varepsilon_{23} &= \frac{1}{2}\left(\frac{\partial u_2}{\partial x_3} + \frac{\partial u_3}{\partial x_2}\right), \qquad \varepsilon_{13} = \frac{1}{2}\left(\frac{\partial u_1}{\partial x_3} + \frac{\partial u_3}{\partial x_1}\right), \qquad \varepsilon_{12} = \frac{1}{2}\left(\frac{\partial u_1}{\partial x_2} + \frac{\partial u_2}{\partial x_1}\right).
\end{aligned} \tag{23.2}$$

The constitutive equations will be presented for the case of isotropy even though bone is anisotropic both with respect to its stress–strain properties and its fluid flow properties, and there is a well-developed formulation of anisotropic poroelasticity.[50–52] This approach is taken for several reasons. First, it is simpler. Second, there are estimates of all the "effective" isotropic poroelastic constants for bone and the anisotropic poroelastic bone constants have not yet been evaluated. Third, in most of the situations to which the poroelastic theory has been applied to bone, the anisotropic effects were not significant. However, this situation will change, and the effects of anisotropy should be included in bone poroelasticity during the next few years. The isotropic strain–stress relations for poroelasticity are

$$\begin{aligned}
2G\varepsilon_{11} &= \sigma_{11} - \left(\frac{\nu}{1+\nu}\right)(\sigma_{11} + \sigma_{22} + \sigma_{33}) + \alpha\left(\frac{1-2\nu}{1+\nu}\right)p, \\
2G\varepsilon_{22} &= \sigma_{22} - \left(\frac{\nu}{1+\nu}\right)(\sigma_{11} + \sigma_{22} + \sigma_{33}) + \alpha\left(\frac{1-2\nu}{1+\nu}\right)p, \\
2G\varepsilon_{33} &= \sigma_{33} - \left(\frac{\nu}{1+\nu}\right)(\sigma_{11} + \sigma_{22} + \sigma_{33}) + \alpha\left(\frac{1-2\nu}{1+\nu}\right)p, \\
2G\varepsilon_{23} &= \sigma_{23}, \qquad 2G\varepsilon_{13} = \sigma_{13}, \qquad 2G\varepsilon_{12} = \sigma_{12},
\end{aligned} \tag{23.3}$$

and the stress–strain relations are

$$\begin{aligned}
\sigma_{11} + \alpha p &= 2G\varepsilon_{11} + \left(\frac{2G\nu}{1-2\nu}\right)(\varepsilon_{11} + \varepsilon_{22} + \varepsilon_{33}), \\
\sigma_{22} + \alpha p &= 2G\varepsilon_{22} + \left(\frac{2G\nu}{1-2\nu}\right)(\varepsilon_{11} + \varepsilon_{22} + \varepsilon_{33}), \\
\sigma_{33} + \alpha p &= 2G\varepsilon_{33} + \left(\frac{2G\nu}{1-2\nu}\right)(\varepsilon_{11} + \varepsilon_{22} + \varepsilon_{33}), \\
\sigma_{23} &= 2G\varepsilon_{23}, \qquad \sigma_{13} = 2G\varepsilon_{13}, \qquad \sigma_{12} = 2G\varepsilon_{12},
\end{aligned} \tag{23.4}$$

where G and ν are the drained isotropic elastic constants, the shear modulus and the Poisson's ratio, respectively, of the material, α is the ratio of the fluid volume gained (or lost) in a material element due to the volume change of that element when loaded under the drained condition (see Eq. 23.7 below), and B is called the compressibility coefficient or Skempton pore pressure coefficient (see Eq. 23.9 below). The relation between the dimensionless fluid content ζ and the stress involves the same parameters:

$$2G\zeta = \alpha\left(\frac{1-2\nu}{1+\nu}\right)\left(\sigma_{kk} + \frac{3p}{B}\right). \tag{23.5}$$

Note that Eqs. 23.3 through 23.5 are all expressed in terms of a set of four basic parameters: G, ν, B, and α. There are many other sets of these four parameters that are equivalent. In poroelasticity there is an important distinction between drained and undrained elastic moduli. The latter are the moduli associated with the situation in which fluid content ζ is not allowed to change; this means the pores are filled with fluid and the fluid does not move. On the other hand, the drained elastic moduli are the moduli associated with the situation in which pore fluid is fully drained to the environment, so that the pore fluid pressure equilibrates with the environmental pressure, usually taken to be zero. The undrained elastic constants are indicated by the subscript u and the drained elastic constants have no subscript. Thus, G and ν are the drained isotropic elastic constants, the shear modulus and the Poisson's ratio, respectively, of the material. The undrained elastic constants will be introduced below. The other two coefficients, B and α, are more complicated as they represent aspects of the structural response associated with both the solid and the fluid. Consider α first. If the pore pressure vanishes ($p = 0$), then from Eq. 23.5, $\sigma_{11} + \sigma_{22} + \sigma_{33} = 2G\,((1+\nu)/(1-2\nu))(\varepsilon_{11} + \varepsilon_{22} + \varepsilon_{33})$ and from Eq. 23.5,

$$\zeta = \alpha(\varepsilon_{11} + \varepsilon_{22} + \varepsilon_{33}); \tag{23.6}$$

thus α is the ratio of the fluid volume gained (or lost) in a material element due to the volume change of that element when loaded under the drained condition. Recall that the trace of the strain tensor, $(\varepsilon_{11} + \varepsilon_{22} + \varepsilon_{33})$, has the geometric interpretation of the change in volume per unit volume. The coefficient α is also interpreted as an effective stress coefficient because the stress–strain relations (Eq. 23.4) can be viewed as purely elastic if one lets the three quantities $\sigma_{11} + \alpha p$, $\sigma_{22} + \alpha p$, $\sigma_{33} + \alpha p$ play the role of normal "effective stresses." For an ideal isotropic poroelastic material, it may be shown[48] that

$$\alpha = 1 - \frac{K}{K_s}, \tag{23.7}$$

where K is the drained bulk modulus. Carroll[50] extended the isotropic result of Nur and Byerlee[48] to anisotropic materials; see also Thompson and Willis.[52] An interpretation of the coefficient B is obtained by considering the undrained condition ($\zeta = 0$), thus, from Eq. 23.4,

$$p = -(B/3)(\sigma_{11} + \sigma_{22} + \sigma_{33}). \tag{23.8}$$

B is called the compressibility coefficient or Skempton pore pressure coefficient[104] and is a measure of the relative compressibilities of the fluid and solid phases; it is related to the drained and undrained solid properties and the fluid properties by

$$B = \frac{\alpha K_f}{[\alpha - \phi(1-\alpha)]K_f + \phi K} = \frac{3(\nu_u - \nu)}{\alpha(1-2\nu)(1+\nu_u)}, \tag{23.9}$$

where ϕ is the pore volume fraction (the volume of pores per unit total volume). The value of B must lie between zero and one; $0 \leq B \leq 1$. B vanishes as the ratio K_f/K vanishes and B goes to one as K_f and K_s approach each other.

For an ideal poroelastic medium, the undrained elastic moduli may be expressed in terms of the set of four basic parameters, K (instead of G, $K = 2G(1 + \nu)/(3(1 - 2\nu))$), ν, B, and α, as well as the bulk moduli K_f and K_s by

$$K_u = K\left[1 + \frac{\alpha^2 K_f}{(1-\alpha)(\alpha - \phi)K_f + \phi K}\right], \tag{23.10}$$

and

$$\nu_u = \frac{3\nu + B(1-2\nu)(1-\frac{K}{K_s})}{3 - B(1-2\nu)(1-\frac{K}{K_s})}. \tag{23.11}$$

The constitutive equations of poroelasticity are completed by the addition of Darcy's law to stress–strain relations (Eq 23.3 or 23.4) and the fluid content–stress relation (Eq. 23.5) above. Darcy's law relates the fluid mass flow rate in the x_1 (x_2, x_3) direction, q_1 (q_2, q_3), to the gradient of the pore pressure p,

$$q_1 = -\kappa \frac{\partial p}{\partial x_1}, \qquad \left(q_2 = -\kappa \frac{\partial p}{\partial x_2}, \qquad q_3 = -\kappa \frac{\partial p}{\partial x_3}\right), \tag{23.12}$$

where κ is the coefficient of permeability, $\kappa = k/\mu$, where μ is the fluid viscosity and k is the intrinsic Darcy's law permeability, a constant. The intrinsic permeability k has units of length squared and is a function of the porous bone structure only, not the fluid in the pores. Darcy's law is a form of the balance of linear momentum and could include a body force term; however, such a body force would normally be a constant, and since it is only the divergence of the vector components q_1, q_2, q_3 that appears in the theory, such a body force would not appear in the final theory.

23.3.4 Field Equations for Ideal Poroelasticity

The field equations follow from the constitutive equations and the balance laws. The applicable balance laws are the conservation of linear momentum and the conservation of mass. The conservation of linear momentum is employed in the form of the stress equations of equilibrium,

$$\begin{gathered}\frac{\partial \sigma_{11}}{\partial x_1} + \frac{\partial \sigma_{12}}{\partial x_2} + \frac{\partial \sigma_{13}}{\partial x_3} + b_1 = 0, \qquad \frac{\partial \sigma_{12}}{\partial x_1} + \frac{\partial \sigma_{22}}{\partial x_2} + \frac{\partial \sigma_{23}}{\partial x_3} + b_2 = 0, \\ \frac{\partial \sigma_{13}}{\partial x_1} + \frac{\partial \sigma_{23}}{\partial x_2} + \frac{\partial \sigma_{33}}{\partial x_3} + b_3 = 0,\end{gathered} \tag{23.13}$$

where b_1, b_2, b_3 represent the components of the body force. The conservation of mass is written in the form

$$\frac{\partial \zeta}{\partial t} + \frac{\partial q_1}{\partial x_1} + \frac{\partial q_2}{\partial x_2} + \frac{\partial q_3}{\partial x_3} = \gamma, \tag{23.14}$$

where ζ is the fluid content, q_1, q_2, and q_3 are the components of the fluid mass flow rate in the x_1, x_2, and x_3 directions, respectively, and γ is the source density, that is to say, the rate of injected fluid volume per unit volume of the porous solid. In formulating the field equations, the stresses σ_{11}, σ_{22}, σ_{33}, σ_{23}, σ_{13}, σ_{12} and the pore pressure p are taken as independent variables. In elasticity theory when the stresses σ_{11}, σ_{22}, σ_{33}, σ_{23}, σ_{13}, σ_{12} are taken as the independent field variable (as opposed to the components of the displacement field u_1, u_2, and u_3), it is necessary to impose the integrability conditions on the stress to ensure that when the strain is determined from the stress, it will be possible to use the strain to integrate Eq. 23.2 to find the displacement field. By substituting the strain–stress relation (Eq. 23.3) into the strain conditions of compatibility,[105] the stress equations of compatibility are obtained:[49]

$$
\begin{aligned}
\nabla^2[\sigma_{11} - \nu(\sigma_{22} + \sigma_{33})] + \frac{\partial^2}{\partial x_1^2}(\sigma_{11} + \sigma_{22} + \sigma_{33}) + \frac{3(\nu_u - \nu)}{B(1+\nu)}\left[\nabla^2 p + \frac{\partial^2 p}{\partial x_1^2}\right] &= 0,\\
\nabla^2[\sigma_{22} - \nu(\sigma_{11} + \sigma_{33})] + \frac{\partial^2}{\partial x_2^2}(\sigma_{11} + \sigma_{22} + \sigma_{33}) + \frac{3(\nu_u - \nu)}{B(1+\nu)}\left[\nabla^2 p + \frac{\partial^2 p}{\partial x_2^2}\right] &= 0,\\
\nabla^2[\sigma_{33} - \nu(\sigma_{11} + \sigma_{22})] + \frac{\partial^2}{\partial x_3^2}(\sigma_{11} + \sigma_{22} + \sigma_{33}) + \frac{3(\nu_u - \nu)}{B(1+\nu)}\left[\nabla^2 p + \frac{\partial^2 p}{\partial x_3^2}\right] &= 0,\\
(1+\nu)\nabla^2\sigma_{12} + \frac{\partial^2}{\partial x_1 \partial x_2}(\sigma_{11} + \sigma_{22} + \sigma_{33}) + \frac{3(\nu_u - \nu)}{B(1+\nu)}\frac{\partial^2 p}{\partial x_1 \partial x_2} &= 0,\\
(1+\nu)\nabla^2\sigma_{13} + \frac{\partial^2}{\partial x_1 \partial x_3}(\sigma_{11} + \sigma_{22} + \sigma_{33}) + \frac{3(\nu_u - \nu)}{B(1+\nu)}\frac{\partial^2 p}{\partial x_1 \partial x_3} &= 0,\\
(1+\nu)\nabla^2\sigma_{23} + \frac{\partial^2}{\partial x_2 \partial x_3}(\sigma_{11} + \sigma_{22} + \sigma_{33}) + \frac{3(\nu_u - \nu)}{B(1+\nu)}\frac{\partial^2 p}{\partial x_2 \partial x_3} &= 0.
\end{aligned}
\tag{23.15}
$$

The trace of this matrix equation provides a convenient relation between $(\sigma_{11} + \sigma_{22} + \sigma_{33})$ and p:

$$
\nabla^2\left[(\sigma_{11} + \sigma_{22} + \sigma_{33}) + \frac{6(\nu_u - \nu)}{B(1-\nu)(1+\nu_u)}p\right] = 0. \tag{23.16}
$$

The expression of mass conservation (Eq. 23.14) is recast in terms of the stresses σ_{11}, σ_{22}, σ_{33}, σ_{23}, $\sigma_{13,}$ and σ_{12} and the pressure p by substituting Darcy's law (Eq 23.12) and the expression for the fluid content (Eq. 23.5) into (Eq. 23.14) and then employing (Eq 23.9), thus

$$
\kappa\nabla^2 p + \gamma = \frac{3(\nu_u - \nu)}{2GB(1+\nu)(1+\nu_u)}\frac{\partial}{\partial t}\left[(\sigma_{11} + \sigma_{22} + \sigma_{33}) + \frac{3}{B}p\right]. \tag{23.17}
$$

An alternative form of Eq. 23.17 is obtained by combining Eqs. 23.16 and Eq. 23.17, thus

$$
c\nabla^2\left[(\sigma_{11} + \sigma_{22} + \sigma_{33}) + \frac{3}{B}p\right] + q\gamma = \frac{\partial}{\partial t}\left[(\sigma_{11} + \sigma_{22} + \sigma_{33}) + \frac{3}{B}p\right], \tag{23.18}
$$

where c and q are given by

$$
c = \frac{2GB^2\kappa(1-\nu)(1+\nu_u)^2}{9(1-\nu_u)(\nu_u - \nu)}, \tag{23.19}
$$

and

$$q = \frac{2GB(1+\nu)(1+\nu_u)}{3(\nu_u - \nu)}. \tag{23.20}$$

In the formulation of the field equations in terms of the stresses σ_{11}, σ_{22}, σ_{33}, σ_{23}, σ_{13}, and σ_{12} and the pore pressure p, the governing equations are the stress equilibrium equations (Eq. 23.13), three of the compatibility equations (Eq. 23.15), and the diffusion equation (Eq. 23.18). There are many alternative formulations of these equations; see, for example, Detournay and Cheng.[100] In particular, Biot took the displacement field as an independent variable and therefore did not employ the compatibility equations.

23.3.5 Solution Methods for the Poroelastic Equations

There are both analytical and numerical methods for the solution of poroelastic boundary value problems. Detournay and Cheng[100] survey both these methods with special attention to rock mechanics. These include familiar analytical methods (displacement potentials, method of singularities) and computational methods (finite element and boundary element), and the reader is referred to Detournay and Cheng[100] for references on nonbiological tissue applications. Detournay and Cheng[100] credit Sandhu and Wilson[106] for pioneering the application of finite-element techniques to poroelasticity. Ghaboussi and Wilson[107] considered the application of poroelastic finite-element techniques in the case of a compressible fluid. Spilker et al.[108] and Simon[102] both survey the application of poroelastic finite-element models to soft tissues; however, most soft tissue applications assume incompressibility of one or more of the constituents and are not generally applicable to bone. Simon[102] cites his own work in which the various methods for the solution of transient problems are compared; his formulation of the finite-element poroelasticity follows the work of Biot. One standard finite-element program, ABAQUS,[109] is quite flexible with respect to poroelastic calculations. It is able to treat linear or nonlinear (small- or large-strain) and compressible or incompressible materials. The commercial DIANA code[110] supports compressible and incompressible finite poroelasticity.

Analytically, field equations of poroelasticity have a form similar to those for thermoelasticity and to some other continuum theories. If certain conditions are satisfied, the solution to a thermoelasticity problem coincides with that of a poroelasticity problem. Some solutions can therefore be obtained from thermoelasticity solutions. Chandrasekharaiah and Cowin[111,112] consider the unified system of field equations of thermoelasticity and poroelasticity and their solution. Most analytical poroelasticity solutions can be applied to bone if the boundary conditions match and the assumption of incompressibility has not been made. For example, the one-dimensional transient poroelastic solutions of Simon et al.[113] might be applied to bone.

There are a small number of reports addressing specific bone poroelasticity problems. Most of these reports concern strain-generated potentials (SGPs) and will be discussed below. Zhang and Cowin[114,115] studied the load-carrying capacity of the pore pressure in a poroelastic bar subject to oscillatory bending; the solution was verified by a finite-element solution of the same problem.[116]

23.4 Poroelasticity Applied to Bone

23.4.1 Bone Poroelasticity Parameter Values

The values of the poroelasticity coefficients for the PV and PLC of bone will be summarized here. In addition, the values of these coefficients of bone will be compared with those for fluid-saturated porous rocks. The bulk modulus K_f for salt water is 2.3 GPa;[117] it is assumed that bone fluid has this bulk modulus. Estimates of the values of the porosity and the permeability associated with the two distinct porosities of bone of interest, the PV and PLC, are given in Table 23.1, which was adapted from Zhang et al.[19] The total PV plus PLC is given by Li et al.[8] for canine bone as 0.094; Zhang et al.[19] use 0.09 for

TABLE 23.1 Measurements of the Porosity and Permeability for the Two Levels of Bone Porosity of Interest

Ref.	Porosity v_0	Ref.	Permeability k (m^2)
	The Vascular Porosity (PV)		
162	0.6	164	3.0×10^{-13}
23	0.015	8	5.0×10^{-15}
163	0.04	19	6.35×10^{-13}
19	0.04		
	The Lacunar–Canalicular Porosity (PLC)		
165	0.023	19	1.47×10^{-20}
23	0.042		
166	0.035		
19	0.05		

Note: The values from Zhang et al.[19] are estimates based on the data and calculations.

TABLE 23.2 Summary of Poroelastic Constants Related to the Pore Water Pressure Relaxation Times for the Two Porosities of Interest, the PV and the PLC

Porosity Level	v_0	k	μ	L	c	τ_R
PV	0.04	6.36×10^{-13} m^2	10^{-3} Pa s	1 cm	18.4 m^2/s	1.36 μs
PLC	0.05	1.47×10^{-20} m^2	10^{-3} Pa s	100 μm	5.1×10^{-7} m^2/s	4.9 ms

Here v_0 is the porosity, k is the specific permeability, μ is the fluid viscosity, L is characteristic length associated with this porosity (in the case of the lacunar–canalicular it is the radius of an osteon, 100 μm, and in the case of the PV, it is the bone cortical thickness, which would be of the order of 1 cm in a large animal, but smaller in a smaller animal), c is the pore fluid pressure diffusion coefficient and τ_R is the characteristic relaxation time of the pore fluid pressure in that porosity. The values from Zhang et al.[19] are estimates based on the data and calculations.

the sum of these two porosities. The permeability associated with the two distinct porosities of bone, the PV and PLC, is dominated by the vascular permeability. A summary of calculated (as opposed to measured) poroelastic constants related to the pore water pressure relaxation times for the two porosities of interest, the PV and PLC, is given in Table 23.2. Of particular interest is the large difference in magnitude between the values of parameters associated with the two porosities. The three orders of magnitude difference in the relaxation times of these two porosities, 1.36 μs for the PV and 4.9 ms for the PLC, indicates that a pressure peak in the PV will relax 1000 times faster than a pressure peak in the PLC. The difference in the relaxation times reflects the difference in the specific permeabilities of these two porosities or, equivalently, the difference in the pore fluid pressure diffusion coefficient c of these two porosities, as shown in Table 23.2.

A set of effective isotropic elastic constants was constructed by Cowin and Sadegh[118] from the orthotropic human femoral cortical bone data given in Cowin.[119] By using the bounds established by Hill[120] for the effective isotropic elastic constants of an anisotropic elastic material, the values $K_s = 13.92$ GPa and $G_s = 5.50$ GPa were obtained. These effective isotropic elastic moduli are equivalent to a Young's modulus of $E_s = 14.58$ GPa and a Poisson's ratio of $\nu_s = 0.325$. These and the other parameters associated with cortical bone are listed in Table 23.3 along with the values of the same parameters for certain porous rocks. It is interesting to compare the parameter values for the PLC of bone tissue with the parameter values for fluid-saturated porous rocks. The elastic properties of the bone and the fluid-saturated porous rocks are quite similar. The pore-related fluid diffusivities of the PLC of bone tissue are close to those of granite and marble, as may be seen from Table 23.3. Sandstones are much too porous to be compared with the PLC of bone. Although the material properties associated with the PLC of bone and those associated with fluid-saturated porous granite and marble are similar, significant differences in the responses of these materials can be expected because the characteristic length associated with the associated

TABLE 23.3 Summary of Poroelastic Constants for the PLC and for Various Rocks

Property (units, if any)	Bone (PLC)	Marble	Granites	Sandstones
G (GPa)—shear modulus	5	24	15–19	4.2–13
ν—drained Poisson ratio	0.32	0.25	0.25–0.27	0.12–0.20
ν_u—undrained Poisson ratio	0.33	0.27	0.30–0.34	0.28–0.33
K (GPa)—drained bulk modulus	12	40	25–35	4.6–13
K_u (GPa)—undrained bulk modulus	13	44	41–42	1.3–30
B—compressibility coefficient	0.40	0.51	0.58–0.85	0.50–0.88
K_s (GPa)—bulk modulus of the solid	14	50	45	31–42
α—effective stress coefficient	0.14	0.19	0.27–0.47	0.65–0.85
v_0—porosity	0.05	0.02	0.01–0.02	0.02–0.26
c (m^2/s) $\times$ 10^6—pore fluid pressure diffusion coefficient	0.51	13	7.0–22	5400–1.6 $\times$ 10^6
k (m^2) $\times$ 10^{20}—specific permeability	1.5	10	10–40	20,000–8.0 $\times 10^7$

The data on granites are the range for two granites and the data on sandstones indicate the range for six sandstones. The data are from Detournay and Cheng[100] and Zhang et al.[19] where the details on the specific rock data are given.

boundary value problems differ by four to seven orders of magnitude. The characteristic length associated with a bone boundary value problem is on the order of the radius of an osteon, 100 μm, or the bone cortical thickness, 1 cm, whereas that associated with porous rocks could range up to kilometers.

It is important to note the large difference between the bulk modulus K_s of the solid bone matrix (14 GPa) and the bulk modulus K_f of bone water (2.3 GPa); the solid bone matrix has a bulk modulus six times that of water. This leads to a compressibility coefficient B of 0.40 and to considerable pressure differences between the solid bone matrix and the bone pore fluid. In the case of soft tissues the bulk moduli of the soft tissue matrix and the pore water are almost the same and the compressibility coefficient B is about 1. Recall that B has a range from 0 to 1. Thus, for soft tissues, the incompressibility assumptions of the fluid and solid constituents are a reasonable approximation and $B = 1$. However, for bone, the incompressibility assumption is inconsistent with the large differences in compressibility of the constituents and, if made, could lead to large errors in the determination of the bone fluid pressures.

23.4.2 Applications of Single-Porosity Poroelasticity to Bone

Nowinski and Davis[121] considered the human skull as a poroelastic spherical shell subjected to a quasi-static load. Other contributions of these authors include the propagation of longitudinal waves in a poroelastic model of bone,[122] bone articulations as systems of poroelastic bodies in contact,[123] poroelastic models for the flexure and torsion of bones,[124] and stress concentrations around a cylindrical cavity in a poroelastic model of a bone.[125] In all of these works, Nowinski and Davis assumed a uniform porosity that included all three levels of the bone fluid porosity and the PIT. These authors also considered a uniform fluid that included all the liquids in bone from the bone fluid to the bone marrow and they acknowledged that these assumptions were "rather drastic but understandable simplifications."[121,122] It is now understood that the assumptions of Nowinski and Davis are unrealistic. Johnson et al.[126] and Johnson[127] were the first to discuss the levels of porosity outlined above in the context of Biot theory (the effective medium approach). As discussed, the porosities of bone are very nonuniform, the sizes of the pores in the different porosities differing by orders of magnitude. The PIT and PV are large-scale porosities on the basis of their characteristic pore size, and have a low pore pressure comparable with that of blood pressure. On the other hand, the smaller-scale PLC and PCA porosities sustain pore pressures many atmospheres higher. The fluids in the bone porosities are also very nonuniform; the contents (marrow, fat, blood vessels) in the PIT have a viscosity[40–42] one to two orders of magnitude larger than the viscosity of the bone fluid in the PV or PLC. Differences between the uniform porosity model for cortical bone and a multiporosity model, acknowledging the fact that the PV is several orders of magnitude larger in characteristic pore size than the PLC and has a much lower pressure, are illustrated in

the section below concerned with the experiment and the theory associated with local SGPs in bone.[128] Zhang and Cowin[114,115] and Manfredini et al.[116] consider the oscillatory bending of a single-porosity poroelastic beam, the porosity of which is taken to be the PLC. Their results correspond to the case when there are no osteons in the model. Such a model is acceptable for small trabeculae that contain no osteons, but it predicts bone fluid pore pressure fields that are seriously in error when applied to bone with osteons because of the ability of the PLC pore pressure to relax into the low-pressure PV. The results of these two models are contrasted in the next to last section on osteonal SGPs in bone.

23.4.3 Poroelastic Waves in Bone

Elastic wave propagation promises to be an important diagnostic tool for bone tissue. From measurements of the density, wave speed, and wave attenuation, the properties of the bone tissue may be evaluated. For example, the elastic constants of bone can be determined from wave speed measurements and a knowledge of the bone density. Rubin et al.[129] used elastic ultrasonic waves *in vivo* to determine acute change in the mechanical properties of runners' bones following the Boston Marathon. They found faster velocities after the race. This might be explained by the hypothesis that bone fluid had been pressed out of the bone tissue. Rubin et al.[129] reported that the measured velocity increased by 1.6%. How much bone water must be lost in order to increase the velocity by 1.6%? This question could be answered in many ways using the effective medium approach;[46,47] however, there is a simple formula given by Wyllie et al.[130] that gives an estimate directly in terms of the wave velocities in the medium. Application of that formula in this case shows that a loss of about 25% of the bone water will increase the wave velocity by 1.6%. The wave velocity returns to its normal value for the bone after a number of hours, suggesting that the water is reabsorbed by the bone tissue. McKelvie and Palmer[131] considered the frequency dependence of ultrasonic attenuation in cancellous bone in the context of Biot theory (the effective medium approach).

Biot[132–134] extended the quasi-static effective medium theory described above to include propagating waves; see also Burridge and Keller.[95] The dynamical poroelasticity theory predicts the usual elastic waves that dynamical elasticity predicts, longitudinal and shear waves. Interestingly, it predicts a second longitudinal wave in addition to the regular longitudinal wave of classical elasticity theory.[132–134] The second longitudinal wave is called the slow wave to distinguish it from the usual longitudinal wave, called the fast wave. In a limit case of the dynamical Biot theory, as the porosity tends to zero, the velocity of the slow wave goes to zero and the velocity of the fast wave coincides with the velocity of the regular elastic longitudinal wave of solid matrix material. The slow wave has been experimentally documented in ideally constituted porous media.[135,136] There is a report of measurements of the slow wave in wet human and bovine cortical bone; slow-wave velocities from 1.53 to 2.34 km/s were reported in human Haversian bone and bovine plexiform bone by Lakes et al.[137] This report is questioned by Williams[138] who points out that the slow-wave speed has an upper bound that is the velocity of sound in the fluid, 1.48 km/s; thus the wave speeds reported by Lakes et al.[137] are too fast to be slow-wave speeds. Williams[138] suggests that the wave speeds reported by Lakes et al.[137] may have been those associated with shear waves rather than the slow wave; Lakes[139] notes, however, that he did not observe the second wave when the same bone specimens were dried. Lakes[139] also notes that the anisotropy of bone might explain the inconsistency. The demonstration of the slow wave in bone remains an open question. Williams[138] outlines an experimental program for the determination of cancellous bone properties involving the measurement of the fast- and slow-wave speeds. Perhaps the program proposed will provide the impetus to have this question reopened.

23.4.4 The Two-Porosity Poroelastic Model for Bone

The material presented thus far in this review is drawn together in the present section to address the question of the most appropriate poroelastic model for the study of bone fluid movement and bone fluid pressures. The previous material has been structured to lay the groundwork for the conclusions summarized here. The main points are the following:

1. Infinitesimal strain theory is appropriate for bone. Since the normal, physiological strain that bone experiences seldom ranges above 0.4%, infinitesimal strain theory is adequate.
2. Although bone has four levels of porosity, only two of them, the PV and the PLC, are considered to be significant with respect to bone fluid movement. These two porosities have considerably different properties, particularly pore fluid pressure relaxation times.
3. Based on existing evidence, it is reasonable to conclude that the ILC is relatively impermeable and that the IC has a small hydraulic resistance compared with that in the PLC.
4. The incompressibility assumption of the fluid and solid phases, reasonable for soft tissues, is inappropriate for mineralized bone because the bulk modulus of the bone matrix is six times that of the pore fluid. The incompressibility assumption may be acceptable for embryonic or immature bone because the bulk modulus difference is not so great as it is in maturing and mature bone.

These considerations suggest the use of a two-porosity poroelastic model for bone water; such models have been employed before in geomechanics.[103,140–146] The suggested two-porosity model would consider the bone fluid pressure in the PV to be always equal to the blood pressure, and the bone fluid pressure in the PLC would be determined by the poroelastic equations using the values of parameters given above. If the domain of the poroelastic boundary value problem were taken to be the domain bounded by the IC, then the single porosity poroelastic model associated with the PLC could be employed, along with boundary conditions that set the bone fluid pressure equal to the blood pressure on the boundary. Wang et al.[128] employed a two-porosity model of this type in a work that will be described below. An alternative approach would be to apply the basic equations of poroelasticity to the two levels of porosity separately and simultaneously, connecting the two single-porosity problems by using the boundary conditions and the source density γ, that is to say, the rate of injected fluid volume per unit volume of the porous solid, that appears in the conservation of mass (Eq. 23.14) to connect the two solutions. The source density of one porosity would be the negative of the other, indicating that each would serve alternately as the source and sink of the other. The pressure in the PV would be blood pressure and the domain of the boundary value problem would be bounded by the periosteum and the endosteum.

There are a number of limitations to the validity of the proposed model. The main limitations are the following:

1. There are no measurements of the lacunar–canalicular permeability.
2. Bone is anisotropic with respect to its mechanical properties and with respect to its permeability. Only isotropic values for parameters have been given above. The theory exists to handle the anisotropy,[50–52] but all the anisotropic parameters have not been determined.
3. The viscosity and bulk compressibility of the bone fluid have never been measured. It has been assumed here that these properties of bone fluid have the same values as salt water.
4. Although, upon the basis of existing evidence, it has been concluded that the ILC is impermeable and that the IC has no additional hydraulic resistance, these claims have yet to be experimentally verified. (Mak et al.[147] consider a model in which the hydraulic resistance of the ILC is finite; that work is discussed below.)

Using the two-porosity model, Zhang et al.[19] determined the maximum pore fluid pressures due to uniaxial compression for both the PV and PLC of live cortical bone. Neglecting inertial effects, they estimated that the peak pore water pressure would be 19% of the applied axial stress in the PV and 12% of the applied axial stress in the PLC for an impulsive step loading; Jendrucko et al.[148] derive a similar estimate based on a different model. (Note that in the case of incompressibility, when $B = 1$, the peak pore water pressure would be 33.33% of the applied axial stress in both porosities, constituting an overestimate of 175% in the PV and 278% in the PLC.) The two-porosity model also predicts a slight hydraulic stiffening of the bulk modulus due to longer draining time of the PLC. The undrained bulk modulus is 6% higher than the drained bulk modulus in this case.

23.4.5 Strain-Generated Potentials in Bone

Electrodes placed on two different bone surfaces will measure a difference in voltage when wet bones are deformed quasi-statically or dynamically. These voltages are called SGPs. SGPs in wet bone are now recognized as dominantly electrokinetic phenomena explained by an extension of poroelasticity. From an experimental viewpoint, SGPs are a significant technique for the investigation of the poroelastic behavior of bone. The source of SGPs stems from the fact that the extracellular bone matrix is negatively charged due to negative fixed charges on carbohydrates and proteins; thus, a fluid electrolyte bounded by the extracellular matrix will have a diffuse double layer of positive charges. When the fluid moves, the excess positive charge is convected, thereby developing streaming currents and streaming potentials. The fluid motion is caused by the pore fluid pressure gradients induced by the deformation of the extracellular matrix as a result of whole-bone mechanical loading. Pollack and co-workers[149–151] have laid an important foundation for explaining the origin of SGPs. The foundation is based on poroelasticity and begins with the fluid movement in the bone channels convecting the charge accumulated in the diffuse double layer of positive charges. The charge distribution in the channel is determined from the linear Poisson–Boltzmann equation. The electrical potential attenuates exponentially with distance into the fluid, perpendicular to the charged surface, divided by λ, where λ is the Debye length characterizing the diffuse double layer. The typical Debye length λ for normal physiological saline is 1 nm or less; hence, the decay of the potential with respect to distance from the surface is very rapid. The total streaming current passing through all the channels of a material due to the pore pressure-driven axial flow is represented by a vector per unit area with components j_1, j_2, and j_3. This flux vector is obtained by multiplying the charge density by the local velocity field in the channel and integrating this result over the cross section of the channel. The total streaming current vector with components j_1, j_2, and j_3 is a flux vector similar to the fluid mass flow rate vector with components q_1, q_2, and q_3. Linear irreversible thermodynamics[150,152–154] provides a structure for relating these fluxes. For small departures from equilibrium in isotropic materials the components of the total streaming current vector, j_1, j_2, and j_3, and the fluid mass flow rate vector, q_1, q_2, and q_3, are related by

$$q_1 = -k^{(qp)}\frac{\partial p}{\partial x_1} + k^{(qv)}\frac{\partial V}{\partial x_1}, \qquad q_2 = -k^{(qp)}\frac{\partial p}{\partial x_2} + k^{(qv)}\frac{\partial V}{\partial x_2}, \qquad q_3 = -k^{(qp)}\frac{\partial p}{\partial x_3} + k^{(qv)}\frac{\partial V}{\partial x_3} \tag{23.21}$$

and

$$j_1 = k^{(jp)}\frac{\partial p}{\partial x_1} - k^{(jv)}\frac{\partial V}{\partial x_1}, \qquad j_2 = k^{(jp)}\frac{\partial p}{\partial x_2} - k^{(jv)}\frac{\partial V}{\partial x_2}, \qquad j_3 = k^{(jp)}\frac{\partial p}{\partial x_3} - k^{(jv)}\frac{\partial V}{\partial x_3}$$

where the superscripted k coefficients are material properties. These equations state that the components of the total streaming current vector, j_1, j_2, and j_3, and the components of the fluid mass flow rate vector, q_1, q_2, and q_3, are linearly dependent upon the voltage gradient as well as the pressure gradient. By comparing the first equation of 23.21 when the voltage gradient is zero with Darcy's law (Eq. 23.12) it can be seen that $\kappa = k^{(qp)}$. The second equation of 23.21 when the pressure gradient is zero is Ohm's law in its field version. The Onsager reciprocity theorem relates the cross-flux coefficients, $k^{(qv)} = k^{(jp)}$.

The significant and useful connection between pressure and voltage arises from the recognition that the convective and the conduction currents are equal and opposite so that there is no net current flow, $j_1 = j_2 = j_3 = 0$; then, from the second of Eqs. 23.21,

$$\frac{\partial V}{\partial x_1} = \frac{k^{(jp)}}{k^{(jv)}}\frac{\partial p}{\partial x_1}, \qquad \frac{\partial V}{\partial x_2} = \frac{k^{(jp)}}{k^{(jv)}}\frac{\partial p}{\partial x_2}, \qquad \frac{\partial V}{\partial x_3} = \frac{k^{(jp)}}{k^{(jv)}}\frac{\partial p}{\partial x_3}. \tag{23.22}$$

Integration of this system of equations yields the fact that the pressure must be proportional to the voltage:

$$p = (k^{(jv)}/k^{(jp)})V + \text{a function of time.} \tag{23.23}$$

This means that when a potential difference in bone is measured in connection with an electrokinetic event, the potential difference is proportional to a pore pressure difference between the same two points used to measure the potential difference. Since electrodes are much smaller than pore pressure probes, this theory provides a useful tool for probing the poroelastic response of bone.

Weinbaum et al.[1,2] extended the formulation of the model presented by Salzstein and Pollack[151] to the effective medium poroelastic formalism and removed the incompressibility assumption. The revised model has been applied by Weinbaum et al.,[1,2] Zeng et al.,[155] Cowin et al.,[37] and Zhang et al.[156,157] to study the mechanosensory system in bone.

23.4.6 Anatomical Site of the Strain-Generated Potentials in Bone

The anatomical site in bone tissue that contains the fluid source of the experimentally observed SGPs is not agreed upon, but Cowin et al.[37] argued that it should be the PLC. That argument is summarized here. This apparent disagreement, actually a choice between theoretical inconsistencies, is emphasized here in the hope that some researcher will resolve it in the near future. The other side of this argument is presented in Chapter 24 by Pollack. Salzstein and Pollack[151] concluded that the site of SGP creation was the PCA, because small pores of approximately 16-nm radius were consistent with their experimental data if a poroelastic–electrokinetic model with unobstructed and connected circular pores was assumed. Cowin et al.,[37] using the model of Weinbaum et al.,[2] have shown that the data of Salzstein and Pollack,[151] Scott and Korostoff,[158] and Otter et al.[159] are also consistent with the argument that the larger pore space (100 nm) of the PLC is the anatomical source site of the SGPs if the hydraulic drag and electrokinetic contribution associated with the passage of bone fluid through the space-filling surface matrix (glycocalyx) of the osteocytic process are accounted for. The mathematical models of Salzstein et al.[151] and Weinbaum et al.[2] are similar in that they combine poroelastic and electrokinetic theory to describe the phase and magnitude of the SGP. The two theories differ in the description of the interstitial fluid flow and streaming currents at the microstructural level and in the anatomical structures that determine the flow. In Weinbaum et al.[2] the resistance to fluid flow and the source of the SGP reside in the PLC, that is to say, in the fluid annulus that surrounds the osteocytic processes, i.e., the space between the cell membrane of the osteocytic process and the walls of the canaliculi—the space containing the glycocalyx or fiber matrix. In Cowin et al.[37] the negatively charged macromolecular chain mesh network of the glycocalyx is the source of the SGPs and the hydraulic resistance to the strain-driven bone fluid flow. The calculated SGP from this model matches the phase and amplitude of the measured SGPs. In the Salzstein et al.[150] model this fluid resistance and SGP are explained by assuming that an open, continuous small pore structure ($\approx$16-nm radius) exists in the mineralized collagen matrix.

Evidence indicating that the PCA is unlikely to serve as the primary source of the SGP is obtained from several sources. These include the fact that water in the PCA is strongly bound to the substrate[17] and the fact that the ILC is generally impermeable, as described in the section on interfaces above. Further, if there is significant flow through the PCA, there will be less flow in the PLC and therefore less nutrition being delivered to the osteocytes in the PLC. For these reasons it is thought that the suggestion of Mak et al.[147] that both the PLC and the PCA are sources of the experimentally observed SGPs is not plausible. Mak et al.[147] note that, since there were many assumptions associated with the physical constants in their model, their study should be considered as a parametric study of their model. For example, the authors assume a value for the ILC permeability that appears quite high in view of the tracer studies summarized in the section on the interfaces.

23.4.7 Osteonal Strain-Generated Potentials in Bone: Experiment and Theory

Recently Wang et al.[128] constructed a computational two-porosity model to illustrate an SGP effect noted in the experiments of Starkebaum et al.[160] This result will be described in greater detail because it is believed that it is the forerunner of the applications of the two-porosity bone poroelasticity model. The results of Starkebaum et al.[160] and Wang et al.[128] demonstrate that experimental SGP measurements can be used as a tool for exploring bone microstructure and permeability.

Starkebaum et al.[160] subjected a small bone specimen to 1-Hz oscillatory bending and measured the voltage distribution as one microelectrode was moved across a surface of exposed bone osteonal microstructure, while viewing through a microscope. Starkebaum et al.[160] showed that the value of the potential rose steeply from the osteonal lumen to a peak at the cement line and then descended to the lumen of the next osteon on the tension side of the specimen in bending. The potential profile is therefore a cusp. It was found that local voltage gradients surrounding the Haversian canal of an osteon were as much as 30 times the voltage gradient across the entire bone specimen. The steep cusps in the potential difference were observed around osteonal canals, with the cusps opening upward or downward depending upon whether the osteon was currently experiencing the tension or the compression phase of the bending. Because of the proportionality between the pore pressure gradient and the SGP gradient, Eq. 23.22, this means that both the variation in pore pressure and the SGP on the scale of the radius of an osteon is much greater than the variation of these fields on the specimen scale. It also illustrates the effectiveness of the microelectrode SGP measurements in documenting the local pore microstructure of bone.

In the two-porosity model of Wang et al.,[128] the osteons were arranged periodically with six adjacent osteons across the specimen thickness (Fig. 23.3a is a schematic illustration of the model). In Fig. 23.3a the PV is represented by the osteonal lumens (Haversian canals) and the other domain of the specimen is assumed to have only the PLC. The pressure in the PV is taken to be the blood pressure, which is much less than the pore pressure and is assumed to be zero; the pore pressure in the PLC is evaluated using poroelasticity theory. In this model the test microelectrode is envisioned as moving along the test line shown on Fig. 23.3a from one side of the specimen to the other. The voltage difference measured as this test line is traversed is illustrated schematically in Fig. 23.3b. The voltage difference vanishes when the osteonal lumen is reached, giving very inhomogeneous profiles of the local pressure or voltage distribution in each osteon. These results are qualitatively consistent with the measured osteonal SGP spatial profiles reported in Starkebaum et al.[160]

The importance of the two-porosity model can be easily seen from a comparison of the results of Wang et al[128] with those of Zhang and Cowin[114,115] and Manfredini et al.[116] The latter authors consider the oscillatory bending of a single-porosity poroelastic beam, the porosity of which is taken to be the PLC. Their results correspond to the case when there are no osteons in the model. Such a model is acceptable for small trabeculae that contain no osteons, but it predicts bone fluid pore pressure fields that are seriously in error when applied to bone with osteons because of the ability of bone to relax bone fluid pressure in the PLC into the low-pressure PV. When the osteons are removed, the magnitude of the voltage becomes much larger in most of the cross section and the voltage distribution changes. The voltage distribution becomes a straight line in the central portion of the cross section and, as each of the boundaries is approached, the straight line decreases its slope so that it makes a curve as it approaches the boundary. The straight line portion is shown as a long-dash line in Fig. 23.3b; its approach to the boundary is not illustrated because of the limited scale of the illustration. If there is no flow across the boundary, the slope will approach zero at the boundary.

Wang et al.[128] consider the variation of these results as a function of the frequency of the applied bending loading. Two relaxation systems are found within a two-porosity bone specimen: one associated with the PV, through which the pore pressure relaxes when the loading frequency is lower than 20 Hz, and one associated with the PLC, through which the pore pressure cannot relax when the loading frequency is higher than 1 Hz (if no flow is permitted across the external boundaries). This suggests that the PV is the dominant relaxation system for bone fluid flow during mechanical loading. This model,

which is the first to consider two distinct porosities in bone tissue, demonstrates that the consideration of the two porosities is necessary to obtain correct local bone fluid flow patterns.

23.5 Summary

This work had two objectives. The first was to review the literature related to the application of poroelasticity to bone fluid. The second was to describe the specific physical and modeling considerations that establish poroelasticity as an effective and useful model for deformation-driven bone fluid movement in bone tissue. The main points of the work are summarized as follows:

1. There are three levels of bone porosity, the vascular porosity (PV), the lacunar–canalicular porosity (PLC), and the collagen–apatite porosity (PCA), within cortical bone and within the trabeculae of cancellous bone, all containing a fluid. These porosities, their interfaces, and some related structures of bone tissue were described. The movement and interaction of the bone fluid in the PV with that in the PLC is significant for osteocyte nutrition[161] as well as, probably, mechanosensation and mineral storage and recovery.
2. There are three different major approaches to the development of the same basic equations for the theory of poroelasticity. Each approach is rigorous to its own hypotheses and stems from well-established mathematical and/or physical models for averaging material properties. The averaging processes are the difference between the three approaches. These approaches are called the effective medium, the mixture theory, and the homogenization averaging procedures. The effective medium approach is preferred here for bone fluid because it has a longer history and thus the fine points of the theory have been resolved and polished further than in the other approaches, particularly with regard to the understanding and evaluation of the physical parameters in the theory.
3. The modeling of bone as an ideal porous medium was suggested. The basic equations for linear poroelasticity were reviewed, and both analytical and numerical methods for the solution of poroelastic boundary value problems were described. The values of the poroelasticity coefficients for the PV and PLC of bone were summarized. The values of these coefficients of bone were compared with those for fluid-saturated porous rocks.
4. It was noted that the early work on the application of poroelasticity to bone in the 1970s assumed a uniform porosity that included all three levels of bone fluid porosity and the PIT as well as assuming a fluid of uniform properties that included all the liquids in bone from the bone fluid to the bone marrow.
5. Elastic wave propagation in bone is influenced by the bone fluid in its pores. Dynamical poroelasticity predicts a second longitudinal wave in addition to the regular longitudinal wave of classical elasticity theory. The second longitudinal wave is called the slow wave. It is not clear whether or not the existence of this wave in bone has been demonstrated.
6. It was suggested that a two-porosity poroelastic model is appropriate for the study of bone fluid movement and bone fluid pressures, with the two porosities the low-fluid-pressure PV and the transiently higher fluid pressure PLC.
7. Poroelasticity and electrokinetics can be used to explain SGPs in wet bone. It is noted that SGPs can be used as an effective tool in the experimental study of local bone fluid flow, and that the knowledge of this technique will contribute to the answers of a number of questions concerning bone mineralization and the bone mechanosensory system.
8. The anatomical site in bone tissue that contains the fluid source of the experimentally observed SGPs is not agreed upon, but it is argued here that it should be the PLC.
9. The application of poroelasticity to bone differs from its application to soft tissues in two important ways. First, the deformations of bone are small, whereas those of soft tissues are generally large. Second, the bulk compressibility of the mineralized bone matrix is about six times stiffer than

that of the fluid in the pores while the bulk compressibilities of the soft tissue matrix and the pore water are almost the same.

References

1. Weinbaum, S., Cowin, S. C., and Zeng, Yu, A model for the fluid shear stress excitation of membrane ion channels in osteocytic processes due to bone strain, in *1991 Advances in Bioengineering,* Vanderby, Jr., R., Ed., American Society of Mechanical Engineers, New York, 1991, 317–320.
2. Weinbaum, S., Cowin, S. C., and Zeng, Yu, A model for the excitation of osteocytes by mechanical loading-induced bone fluid shear stresses, *J. Biomech.,* 27, 339–360, 1994.
3. Moss, M. L. and Cowin, S. C., Mechanosensory mechanisms in bone, in *Textbook of Tissue Engineering,* Lanza, R., Langer, R., and Chick, W., Eds., R.G. Landes, Austin, 1997, 645–659.
4. Burger, E. L., Klein Nulend, J., and Cowin, S. C., Mechanotransduction in bone, in *Advances in Organ Biology,* Zaidi, M., Ed., JAI Press, Stamford, CT, Vol. 5a, 1998, 107–118.
5. Biot, M. A., Le problème de la consolidation des matières argileuses sous une charge, *Ann. Soc. Sci. Bruxelles,* B55, 110–113, 1935.
6. Biot, M. A., General theory of three-dimensional consolidation, *J. Appl. Phys.,* 12, 155–164, 1941.
7. de Boer, R., Highlights in the historical development of the porous media theory: toward a consistent macroscopic theory, *Appl. Mech. Rev.,* 49, 201–262, 1996.
8. Li, G., Bronk, J. T., An, K. N., and Kelly, P. J., Permeability of cortical bone of canine tibiae, *Microcirc. Res.,* 34, 302–310, 1987.
9. Miller, S. C. and Jee, W. S. S., Bone lining cells, in *Bone,* Vol. 4, *Bone Metabolism and Mineralization*, Hall, B. K., Ed., CRC Press, Boca Raton, FL, 1992, 1–19.
10. Chole, R. A. and Tinling, S. P., Incomplete coverage of mammalian bone cell matrix by lining cells, *Ann. Otol. Rhinol. Laryngol.,* 102, 543–550, 1993.
11. Bernard, C., *Leçons sur les phénomènes de la vie communs aux animaux et aux végétaux*, Vol. 1, Ballière et Fils, Paris, 1878, 113.
12. Howard, J. E., Present knowledge of parathyroid function with especial emphasis on its limitations, in *Bone Structure and Metabolism,* Wolsternholme, G. E. W. and O'Connor, C. M., Eds., Little, Brown, Boston, 1959, 206–222.
13. Neuman, W. F., *Fed. Proc. Fed. Am. Soc. Exp. Biol.,* 28, 1846, 1969.
14. Neuman, W. F. and Ramp, W. K., The concept of a bone membrane: some implications, in *Cellular Mechanisms for Calcium Transfer and Homeostasis,* Academic Press, New york, 1971, 197–209.
15. Neuman, M. W., Bone blood equilibrium, *Cal. Tissue Int.,* 34, 117–120, 1982.
16. Soares, A. M. V., Arana-Chavez, V. E., Reid, A. R., and Katchburian, B., Lanthanum tracer and freeze-fracture studies suggest that compartmentalization of early bone matrix may be related to initial mineralization, *J. Anat.,* 181, 343–356, 1992.
17. Neuman, W. F. and Neuman, M. W., *The Chemical Dynamics of Bone,* University of Chicago Press, Chicago, 1958.
18. Hillsley, M. V. and Frangos, J. A., Osteoblast hydraulic conductivity is regulated by calcitonin and parathyroid hormone, *J. Bone Miner. Res.,* 11, 114–124, 1996.
19. Zhang, D., Weinbaum, S., and Cowin, S. C., Estimates of the peak pressures in the bone pore water, *J. Biomech. Eng.,* 120, 697–703, 1998.
20. Weinbaum, S., Private communication, 1998.
21. Seliger, W. G., Tissue fluid movement in compact bone, *Anat. Rec.,* 166, 247–256, 1969.
22. Doty, S. D. and Schofield, B. H., Metabolic and structural changes within osteocytes of rat bone, in *Calcium, Parathyroid Hormone and the Calcitonins,* Talmage, B. V. and Munson, P. L., Eds, Excerpta Medica, Amsterdam, 1972, 353–364.
23. Morris, M. A., Lopez-Curato, J. A., Hughes, S. P. F., An, K. N., Bassingthwaighte, J. B. and Kelly, P. J., Fluid spaces in canine bone and marrow, *Microvasc. Res.,* 23, 188–200, 1982.

24. Dillaman, R. M., Movement of ferritin in the 2 day-old chick femur, *Anat. Rec.,* 209, 445–453, 1984.
25. Tanaka, T. and Sakano, A., Differences in permeability of microperoxidase and horseradish peroxidase into the alveolar bone of developing rats, *J. Dent. Res.,* 64, 870–876, 1985.
26. Simonet, W. T., Bronk, J. T., Pinto, M. R., Williams, E. A., Meadows, T. H., and Kelly, P. J., Cortical and cancellous bone: age-related changes in morphological features, fluid spaces, and calcium homeostasis in dogs, *Mayo Clin. Proc.,* 63, 154–160, 1988.
27. Doty, S. D., Private communication, 1997.
28. Knothe Tate, M. L., Niederer, P., and Knothe, U., *In vivo* tracer transport through the lacunocanalicular system of rat bone in an environment devoid of mechanical loading, *Bone,* 22, 107–117, 1998.
29. Asasaka, N., Kondo, T., Goto, T., Kido, M. A., Nagata, E., and Tanaka, T., Differences in the transport systems between cementocytes and osteocytes in rats using microperoxidase as a tracer, *Arch. Oral Biol.,* 37, 363–368, 1992.
30. Montgomery, R. J., Sutker, B. D., Bronk, J. T., Smith, S. R., and Kelly, P. J., Interstitial fluid flow in cortical bone, *Microvasc. Res.,* 23, 188–200, 1988.
31. Williams, S. M. and McCarthy, I. D., Distributed model of blood-bone exchange, *J. Biomed. Eng.,* 8, 235–243, 1986.
32. McCarthy, I. D. and Yang, L., A distributed model of exchange processes within the osteon, *J. Biomech.,* 25, 441–450, 1992.
33. Martin, B., Mathematical model for the mineralization of bone, *J. Orthop. Res.,* 12, 375–383, 1994.
34. Haines, R. W., Mehta, L., and Mohiuddin, A., Nutrition of interstitial lamellae of bone, *Anat. Anz.* (Jena), 154, 233–236, 1982.
35. Curtis, T. A., Ashrafti, S. H., and Weber, D. F., Canalicular communication in the cortices of human long bone, *Anat. Rec.,* 212, 336–344, 1985.
36. Qiu, S.-J., Boyce, T. M., and Schaffler, M. B., Osteocyte loss and microdamage in aging human compact bone, *Trans. Orthop. Res. Soc.,* 22, 88, 1997.
37. Cowin, S. C., Weinbaum, S., and Zeng, Yu, A case for bone canaliculi as the anatomical site of strain-generated potentials, *J. Biomech.,* 28, 1281–1296, 1995.
38. Neuman, W. F., Toribara, T. Y., and Mulrvan, B. J., The surface chemistry of bone. VII, The hydration shell, *J. Am. Chem. Soc.,* 75, 4239–4242, 1953.
39. Glimcher, M. J., The nature of the mineral phase in bone: biological and clinical implications, in *Metabolic Bone Disease,* Academic Press, New York, 23–50, 1998.
40. Bryant, J. D., The effect of impact on the marrow pressure in long bones, *J. Biomech.,* 16, 659–665, 1983.
41. Bryant, J. D., On the mechanical function of marrow in long bones, *Eng. Med.,* 17, 55–58, 1988.
42. Soboková, E., Hubrá, A., Kiefman, J., and Sobotka, Z., Rheological behavior of bone marrow, *Rheol. Acta,* 26 (Suppl.), 467–469, 1988.
43. Arramon, Y. P. and Cowin, S. C., Hydraulic stiffening of cancellous bone, *FORMA*, 12, 209–221, 1997.
44. Hashin, Z. and Shtrikman, S., Note on the variational approach to the theory of composite elastic materials, *J. Franklin Inst.,* 271, 336–341, 1961.
45. Hill, R., Elastic properties of reinforced solids: some theoretical principles, *J. Mech. Phys. Solids,* 11, 357–372, 1963.
46. Christensen, R. M., *Mechanics of Composite Materials,* Wiley, New York, 1979.
47. Nemat-Nasser, S. and Hori, M., *Micromechanics: Overall Properties of Heterogeneous Materials,* North-Holland, Amsterdam, 1993.
48. Nur, A. and Byerlee, J. D., An exact effective stress–strain law for elastic deformation of rock with fluids, *J. Geophys. Res.,* 76, 6414–6419, 1971.
49. Rice, J. R. and Cleary, M. P., Some basic stress diffusion solutions for fluid-saturated elastic porous media with compressible constituents, *Rev. Geophys. Space Phys.,* 14, 227–241, 1976.
50. Carroll, M. M., An effective stress–strain law for anisotropic elastic deformation, *J. Geophys. Res.,* 84, 7510–7512, 1979.

51. Rudnicki, J. W., Effect of pore fluid diffusion on deformation and failure of rock, in *Mechanics of Geomaterials,* Bazant, Z., Ed., Wiley, New York, 1985, 315–347.
52. Thompson, M. and Willis, J. R., A reformation of the equations of anisotropic poroelasticity, *J. Appl. Mech.,* 58, 612–616, 1991.
53. Kenyon, D. E., Consolidation in compressible mixtures, *J. Appl. Mech.,* 45, 727–732, 1978.
54. Kenyon, D. E., Consolidation in transversely isotropic solids, *J. Appl. Mech.,* 46, 65–70, 1979.
55. Kenyon, D. E., A mathematical model of water flux through aortic tissue, *Bull. Math. Biol.,* 41, 79–90, 1979.
56. Simon, B. R., Wu, J. S. S., Carlton, M. W., Kazarian, L. E., France, E. P., Evans, J. H., and Zienkiewicz, O. C., Poroelastic dynamic structural models of rhesus spinal motion segments, *Spine*, 10, 494–507, 1985.
57. Truesdell, C. A. and Toupin, R. A., The classical field theories, in *Handbuch der Physik,* Flugge, S., Ed., Springer Verlag, Berlin, 1960.
58. Truesdell, C. A., Sulle basi della termomeccania, *Rend. Lincei,* 22, 33–38, 1158–1166, 1957.
59. Bowen, R. M., Toward a thermodynamics and mechanics of mixtures, *Arch. Ration. Mech. Anal.,* 24, 370–403, 1967.
60. Atkin, R. J. and Craine, R. E., Continuum theories of mixtures: basic theory and historical development, *Q. J. Mech. Appl. Math.,* 29, 209–244, 1976.
61. Atkin, R. J. and Craine, R. E., Continuum theories of mixtures: applications, *J. Inst. Math. Appl.,* 17, 153–207, 1976.
62. Bowen, R. M., Theory of mixtures, in *Continuum Physics,* Vol. III, *Mixtures and EM Field Theories,* Academic Press, New York, 1–127, 1976.
63. Bowen, R. M., Incompressible porous media models by use of the theory of mixtures, *Int. J. Eng. Sci.,* 18, 1129–1148, 1980.
64. Bowen, R. M., Compressible porous media models by use of the theory of mixtures, *Int. J. Eng. Sci.,* 20, 697–735, 1982.
65. Müller, I., A thermodynamic theory of mixtures, *Arch. Ration. Mech. Anal.,* 28, 1–39, 1968.
66. Müller, I., *Thermodynamics,* Pitman, Boston, 1985.
67. Lai, W. M., Hou, J. S., and Mow, V. C., A triphasic theory for the swelling and deformation behaviors of articular cartilage, *J. Biomech. Eng.,* 113, 245–258, 1991.
68. Gu, W. Y., Lai, W. M., and Mow, V. C., Transport of fluid and ions through a porous-permeable charged-hydrated tissue, and streaming potential data on normal bovine articular cartilage, *J. Biomech.,* 26, 709–723, 1993.
69. Oomens, C. W. J., van Campen, D. H., and Gorrtenboer, H. J., A mixture approach to the mechanics of skin, *J. Biomech.,* 20, 877–885, 1987.
70. Lanir, Y., Biorheology and fluid flux in swelling tissues, I: Bicomponent theory for small deformations, including concentration effects, *Biorheology,* 24, 173–187, 1987.
71. Mak, A. F. T., Huang, L., and Wang, Q., A biphasic poroelastic analysis of the flow-dependent subcutaneous tissue pressure and compaction due to epidermal loadings: issues in pressure sores, *J. Biomech. Eng.,* 116, 421–429, 1994.
72. Frijns, A. J. H., Huyghe, J. M., and Jannsen, J. D., A validation of the quadriphasic mixture theory for intervertebral disc tissue, *Int. J. Eng. Sci.,* 35, 1419–1429, 1997.
73. Vankan, W. J., Huyghe, J. M., Janssen, J. D., and Huson, A., Poroelasticity of saturated solids with an application to blood perfusion, *Int. J. Eng. Sci.,* 34, 1019–1031, 1996.
74. Vankan, W. I., Huyghe, J. M., Janssen, T J. D., Huson, A., Hacking, W. J. G., and Schreiner, W., Finite element analysis of blood flow through biological tissue, *Int. J. Eng. Sci.*, 35, 375–385, 1997.
75. Huyghe, J. M., Oomens, C. W., van Campen, D. H., and Heethaar, R. M., Low Reynolds number steady state flow through a branching network of rigid vessels, *Biorheology,* 26, 55–71, 1989.
76. Huyghe, J. M. and van Campen, D. H., Finite deformation theory of hierarchically arranged porous solids: I. Balance of mass and momentum, *Int. J. Eng. Sci.,* 33, 1861–1871, 1995.

77. Huyghe, J. M. and van Campen, D. H., Finite deformation theory of hierarchically arranged porous solids: II. Constitutive behavior, *Int. J. Eng. Sci.,* 33, 1873–1886, 1995.
78. Huyghe, J. M. and Janssen, J. D., Quadriphasic mechanics of swelling incompressible porous media, *Int. J. Eng. Sci.,* 34, 793–802, 1997.
79. Mow, V. C., Kuei, S. C., Lai, W. L., and Armstrong, C., Biphasic creep and stress relaxation of articular cartilage in compression: theory and experiments, *J. Biomech. Eng.,* 102, 73–84, 1980.
80. Mow, V. C. and Lai, W. L., Recent developments in synovial joint mechanics, *SIAM Rev.,* 22, 275–317, 1980.
81. Coleman, B. D. and Noll, W., The thermodynamics of elastic materials with heat conduction, *Arch. Ration. Mech. Anal.,* 13, 167–178, 1963.
82. Goodman, M. A. and Cowin, S. C., A continuum theory for granular materials, *Arch. Ration. Mech. Anal.,* 44, 249–266, 1972.
83. Cowin, S. C. and Hegedus, D.M., Bone remodeling. I: A theory of adaptive elasticity, *J. Elasticity,* 6, 313–325, 1976.
84. Rivlin, R. S., Comments on some recent researches in thermodynamics, *Recent Adv. Eng. Sci.,* 8, 1–23, 1973.
85. Rivlin, R. S., The thermodynamics of materials with fading memory, in *Theoretical Rheology,* Hotton. J. F., Pearson, J. R. A., and K. Walters, Eds., Academic Science Publishers, New York, 1975, 83–103.
86. Lavenda, B. H., *Thermodynamics of Irreversible Processes,* Constable, London, 1978; reprinted Dover, New York, 1993.
87. Woods, L. C., Beware of axiomatics in applied mathematics, *Bull. Inst. Math. Appl.,* 9, 40–44, 1973.
88. Woods, L. C., The bogus axioms of continuum mechanics, *Bull. Inst. Math. Appl.,* 17, 98–102, 1981.
89. Biot, M. A., Generalized Lagrangian equations of non-linear reaction-diffusion, *Chem. Phys.,* 66, 11–26, 1982.
90. Casey, J., On elastic-thermo-plastic materials at finite deformations, *Int. J. Plasticity,* 14, 173–191, 1998.
91. Krishnaswamy, S. and Batra, R. C., A thermomechanical theory of solid–fluid mixtures, *Math. Mech. Solids,* 2, 143–151, 1997.
92. Huyghe, J. M., Private communication, 1998.
93. Slattery, J. C., Flow of viscoelastic fluids through porous media, *A. I. Ch. E. J.,* 13, 1066–1071, 1967.
94. Whitaker, S., Diffusion and dispersion in porous media, *A. I. Ch. E. J.,* 13, 420–427, 1967.
95. Burridge, R. and Keller, J. B., Poroelasticity equations derived from microstructure, *J. Acoust. Soc. Am.,* 70, 1140–1146, 1981.
96. Cowin, S. C., Summary of discussions on fluid infiltrated geomaterials, in *Mechanics of Geomaterials,* Z. P. Bazant, Ed., Wiley, New York, 1985, 581–582.
97. Piekarski, K. and Munro, M., Transport mechanism operating between blood supply and osteocytes in long bones, *Nature*, 269(5623), 80–82, 1977.
98. Munro, M. and Piekarski, K., Stress induced radial pressure gradients in liquid-filled multiple concentric cylinders, *J. Appl. Mech.,* 99, 218–221, 1977.
99. Kufahl, R. H. and Saha, S., A theoretical model for stress-generated fluid flow in the canaliculi-lacunae network in bone tissue, *J. Biomech.,* 23, 171–180, 1990.
100. Detournay, E. and Cheng, H.-D.A., Fundamentals of poroelasticity, in *Comprehensive Rock Engineering: Principles, Practice & Projects,* Hudson, J. A., Ed., Pergamon, New York, 1993, 113–171.
101. Biot, M. A. and Willis, D. G., The elastic coefficients of the theory of consolidation, *J. Appl. Mech.,* 24, 594–601, 1957.
102. Simon, B. R., Multiphase poroelastic finite element models for soft tissue structures, *Appl. Mech. Rev.,* 45, 191–218, 1992.
103. Coussy, O., *Mechanics of Porous Continua,* Wiley, New York, 1995.
104. Skempton, A. W., The pore pressure coefficients A and B, *Géotechnique,* 4, 143–147, 1954.

105. Gurtin, M. E., The linear theory of elasticity, in *Handbuch der Physik,* S. Flügge, Ed., Springer Verlag, Berlin, 1972, 1–296.
106. Sandhu, R. S. and Wilson, E. L., Finite element analysis of seepage in elastic media, *J. Eng. Mech. Div. Am. Soc. Civ. Eng.,* 95, 641–652, 1969.
107. Ghaboussi, J. and Wilson, E. L., Flow of compressible fluid in porous elastic media, *Int. J. Numer. Methods Eng.,* 5, 419–442, 1973.
108. Spilker, R. L., Suh, J. K., Vermilyea, M. E., and Maxian, T. A., Alternate hybrid, mixed and penalty finite formulations for the biphasic model of soft hydrated tissues, in *Biomechanics of Diarthrodial Joints,* Vol. 1, Mow, V. C., Ratcliffe, A. and Woo, S. L. Y., Eds., Springer, New York, 1990, 400–435.
109. Hibbitt, D., Karlson B., and Sorensen, P., ABAQUS Theory Manual, Version 5.5, Hibbitt, Karlson & Sorensen, Inc., 1995, pp. 2.7.1–1 to 2.7.5–2.
110. Vankan, W. J., Huyghe, J. M., Drost, M. R., Janssen J. D., and Huson A., A finite element model for hierarchical porous media, *Int. J. Numer. Methods Eng.,* 40, 1019–1031, 1997.
111. Chandrasekharaiah, D. S. and Cowin, S. C., Unified solutions for theories of thermoelasticity and poroelasticity, *J. Elasticity,* 21, 121–126, 1989.
112. Chandrasekharaiah, D. S. and Cowin, S. C., A complete solution for a unified system of field equations of thermoelasticity and poroelasticity, *Acta Mech.,* 99, 225–233, 1993.
113. Simon, B. R., Zienkiewicz, O. C., and Paul, D. K., An analytical solution for the transient response of saturated porous elastic solids, *Int. J. Numer. Anal. Methods Geomech.,* 8, 391–398, 1984.
114. Zhang, D. and Cowin, S. C., Oscillatory bending of a poroelastic beam, *J. Mech. Phys. Solids,* 42, 1575–1599, 1994.
115. Zhang, D. and Cowin, S. C., Load carrying capacity of the pore pressure in a poroelastic beam subject to oscillatory excitation, in *Mechanics of Poroelastic Media,* A. P. S. Selvaduri, Ed., Solid Mechanics and Its Application Series, Vol. 35, Wolters Kluwer Academic Publishers, Dortrecht, 1996, 273–298.
116. Manfredini, P., Cocchetti, G., Maier, G., Redaelli, A., and Montevecchi, F. M., Poroelastic finite element analysis of a bone specimen under cyclic loading, *J. Biomech.,* 32, 135–144, 1999.
117. Anderson, C. B., Mechanics of fluids, in *Marks' Standard Handbook for Mechanical Engineers,* Baumeister, T., Ed., McGraw-Hill, New York, 1967, 3.48–3.76.
118. Cowin, S. C. and Sadegh, A. M., Non-interacting modes for stress, strain and energy in hard tissue, *J. Biomech.,* 24, 859–867, 1991.
119. Cowin, S. C., The mechanical properties of cortical bone, in *Bone Mechanics,* S. C. Cowin, Ed., CRC Press, Boca Raton, FL, 1989, 97–127.
120. Hill, R., The elastic behavior of a crystalline aggregate, *Proc. Phys. Soc. London,* A65, 349–354, 1952.
121. Nowinski, J. L. and Davis, C. F., A model of the human skull as a poroelastic spherical shell subjected to a quasistatic load, *Math. Biosci.,* 8, 397–416, 1970.
122. Nowinski, J. L. and Davis, C. F., Propagation of longitudinal waves in circularly cylindrical bone elements, *J. Appl. Mech.,* 39, 578–584, 1971.
123. Nowinski, J. L., Bone articulations as systems of poroelastic bodies in contact; *AIAA J.,* 9, 62–67, 1971.
124. Nowinski, J. L. and Davis, C. F., The flexure and torsion of bones viewed as poroelastic bodies., *Int. J. Eng. Sci.,* 10, 1063–1079, 1972.
125. Nowinski, J. L., Stress concentrations around a cylindrical cavity in a bone treated as a poroelastic body, *Acta Mech.,* 13, 281–292, 1972.
126. Johnson, M. W., Chakkalakal, D. R., Harper, R. A., Katz, J. L., and Rouhana, S. W., Fluid flow in bone *in vitro, J. Biomech.,* 18, 881–885, 1982.
127. Johnson, M. W., Behavior of fluid in stressed bone and cellular stimulation, *Calcif. Tissue Int.,* 36, S72–S764, 1984.
128. Wang, L., Fritton, S., Cowin, S. C., and Weinbaum, S., Fluid pressure relaxation depends upon osteonal microstructure: modeling of an oscillatory bending experiment, *J. Biomech.,* 32, 663–672, 1999.

129. Rubin, C. T., Pratt, G. W., Porter, A. L., Lanyon, L. E., and Poss, R., The use of ultrasound *in vivo* to determine acute change in the mechanical properties of bone following intense physical activity, *J. Biomech.,* 20, 723–727, 1987.
130. Wyllie, M. R., Gregory, A. R., and Gardner, G. H. F., An experimental investigation of factors affecting elastic wave velocities in porous media, *Geophysics,* 23, 459–493, 1958.
131. McKelvie, M. L. and Palmer, S. B., The interaction of ultrasound with cancellous bone, *Phys. Med. Biol.,* 36, 1331–1340, 1991.
132. Biot, M. A., Theory of propagation of elastic waves in a fluid-saturated porous solid. I. Low frequency range, *J. Acoust. Soc. Am.,* 28, 168–178, 1956.
133. Biot, M. A., Theory of propagation of elastic waves in a fluid-saturated porous solid. II. Higher frequency range, *J. Acoust. Soc. Am.,* 28, 179–191, 1956.
134. Biot, M. A., Generalized theory of acoustic propagation in porous dissipative media, *J. Acoust. Soc. Am.,* 34, 1254–1264, 1962.
135. Plona, T. J., Observation of a second bulk compressive wave in a porous medium at ultrasonic frequencies, *Appl. Phys. Lett.,* 36, 259, 1980.
136. Berryman, J. G., Confirmation of Biot's theory, *Appl. Phys. Lett.,* 37, 382–384, 1980.
137. Lakes, R. S., Yoon, H. S., and Katz, J. L., Slow compressional wave propagation in wet human cortical bone, *Science,* 220, 513–515, 1983.
138. Williams, J. L., Ultrasonic wave propagation in cancellous and cortical bone: prediction of some experimental results by Biot's theory, *J. Acoust. Soc. Am.,* 91, 1106–1112, 1992.
139. Lakes, R. S., Private communication, 1998.
140. Barenblatt, G. I., Zheltov, I. P., and Kockina, I. N., Basic concepts in the theory of seepage of homogeneous liquids in fissured rocks (strata), *Prikl. Mat. Mekh.* (English translation), 24, 1286–1303, 1960.
141. Barenblatt, G. I. and Zheltov, I. P., On the basic equations of seepage of homogeneous liquids in fissured rock, *Akad. Nauk SSSR* (English translation), 132, 545–548, 1960.
142. Barenblatt, G. I. and Chernyi, G., On moment relations of surfaces of discontinuity in dissipative media, *Prikl. Mat. Mekh.* (English translation), 27, 1205–1218, 1963.
143. Barenblatt, G. I., On certain boundary value problems for the equations of seepage of liquid in fissured rocks, *Prikl. Mat. Mekh.* (English translation), 27, 513–518, 1963.
144. Warren, J. E. and Root, P. J., The behavior of naturally fractured reservoirs, *Soc. Petrol. Eng. J.,* 3, 245–255, 1963.
145. Wilson, R. K. and Aifantis, E. C., On the theory of consolidation with double porosity, *Int. J. Eng.,* 20, 1009–1035, 1982.
146. Barenblatt, G. I., Entov, V. M., and Ryzhik, V. M., *Theory of Fluid Flows through Natural Rocks,* Kluwer, Dordrecht, 1990.
147. Mak, A. F. T., Huang, D. T., Zhang, J. D., and Tong, P. Deformation-induced hierarchical flows and drag forces in bone canaliculi and matrix microporosity, *J. Biomech.,* 30, 11–18, 1997.
148. Jendrucko, R. J., Hyman, W. A., Newell, P. H., and Chakraborty, B. K., Theoretical evidence for the generation of high pressures in bone cells, *J. Biomech.,* 9, 87–91, 1976.
149. Pollack, S. R., Salzstein, R., and Pienkowski, D., The electric double layer in bone and its influence on stress-generated potentials, *Calcif. Tissue Int.,* 36, S77–S81, 1984.
150. Salzstein, R. A., Pollack, S. R., Mak, A. F. T., and Petrov, N., Electromechanical potentials in cortical bone—I. A continuum approach, *J. Biomech.,* 20, 261–270, 1987.
151. Salzstein, R. A. and Pollack, S. R., Electromechanical potentials in cortical bone—II. Experimental analysis, *J. Biomech.,* 20, 271–280, 1987.
152. De Groot, S. R. and Mazur, P., *Non-Equilibrium Thermodynamics,* North Holland, Amsterdam, 1969.
153. Lee, R. C., Frank, E. H., Grodzinsky, A. J., and Roylance, A. J., Oscillatory compressional behavior of articular cartilage and its associated electrochemical properties, *J. Biomech. Eng.,* 103, 280–292, 1981.

154. Coelho, D., Shapiro, M., Thovert, J. F., and Adler, P. M., Electroosmotic phenomena in porous media, *J. Colloid Interface Sci.,* 181, 169–190, 1996.
155. Zeng, Yu, Cowin, S. C., and Weinbaum, S., A fiber matrix model for fluid flow and streaming potentials in the canaliculi of an osteon, *Ann. Biomed. Eng.,* 22, 280–292, 1994.
156. Zhang, D., Cowin, S.C., and Weinbaum, S., Electrical signal transmission and gap junction regulation in bone cell network: a cable model for an osteon, *Ann. Biomed. Eng.,* 25, 357–374, 1997.
157. Zhang, D., Weinbaum, S., and Cowin, S. C., Electrical signal transmission in a bone cell network: the influence of a discrete gap junction, *Ann. Biomed. Eng.,* 26, 644–659, 1998.
158. Scott, G. C. and Korostoff, E., Oscillatory and step response electromechanical phenomena in human and bovine bone, *J. Biomech.,* 23, 127–143, 1990.
159. Otter, M. W., Palmieri, V. R., Wu, D. D., Seiz, K. G., MacGinitie, L. A., and Cochran, G. V. B., A comparative analysis of streaming potentials *in vivo* and *in vitro, J. Orthop. Res.,* 10, 710–719, 1992.
160. Starkebaum, W., Pollack, S. R., and Korostoff, E., Microelectrode studies of stress-generated potentials in four-point bending of bone, *J. Biomed. Mater. Res.*, 13, 729–751, 1979.
161. Wang, L., Cowin, S. C., Weinbaum, S., and Fritton, S., Modeling tracer transport in an osteon under cyclic loading, *Ann. Biomed. Engr.,* in press.
162. Frost, H. M., Specific surface and specific volume of normal human lamellar bone, *Henry Ford Hosp. Med. Bull.,* 10, 35–41, 1962.
163. Schaffler, M. B. and Burr, D. B., Stiffness of compact bone: effects of porosity and density, *J. Biomech.,* 21, 13–16, 1988.
164. Rouhana, S. W., Johnson, M. W., Chakkalakal, D. R., Harper, R. A., and Katz, J. L., Permeability of compact bone, *Joint ASME-ASCE Conf. Biomechanics Symp.,* AMD 43, 169–172, 1981.
165. Frost, H. M., Measurement of osteocytes per unit volume and volume components of osteocytes and canaliculae [sic] in man, *Henry Ford Hosp. Med. Bull.,* 8, 208–211, 1960.
166. Baylink, D. and Wergedal, J., Bone formation and resorption by osteocytes, in *Cellular Mechanisms for Calcium Transfer and Homeostasis,* Nichols, G., Jr., Ed., Academic Press, New York, 1971, 257–289.

24

Streaming Potentials in Bone

Solomon R. Pollack
University of Pennsylvania

24.1 Streaming Potentials in Bone: A Historical Perspective

While studying fracture repair in bone, Yasuda[1] and later with Fukada[2] identified the electrical-generating capability of bone when it is subjected to mechanical loads. The relationship between applied stress and electric charge was characterized as a classical linear piezoelectric effect. Models were elaborated to include stress gradients and spatially varying piezoelectric moduli in an attempt to explain a growing amount of data from around the world. By the mid- to late 1960s work in this field had branched into two categories. The first resulted from Yasuda's speculation and from the work of Bassett and Becker,[3] Bassett,[4] Becker et al.,[5] and Brighton[6] linking mechanoelectricity to remodeling of bone by applied forces and to fracture repair. This opened the door to the possible role of electrical effects on cellular behavior as a contributing underlying mechanism of Wolff's law.[7] This, in turn, led to the hypothesis that if, indeed, endogenous electric fields generated by mechanical stress alter cell behavior and lead to Wolff's law of bone remodeling, then electrical signals applied from exogenous sources could also alter cell behavior. Thus, the search was on for clinical devices to treat fractures, bone fusions, osteoporosis, skin wounds, and degenerative joint disease; some of these studies have led to technologies in use today.

The second category of research led investigators into the study of mechanoelectricity in wet or fluid-filled bone to explore models that approach *in vivo* bone structure and composition. Early work by Anderson and Eriksson,[8,9] Mumford and Newton,[10] and Cignitti et al.[11] clearly identified the differences in experimental results obtained when the bone was wet. These authors suggested that electrokinetics was the potential generating mechanism in wet bone rather than piezoelectricity. This inspired investigations of electrokinetics and fluid flow phenomena in other wet tissues by Grodzinsky,[12] Lee et al.,[13] Lotke et al.,[14] Mow et al.,[15] and others. In wet bone it is now generally

0-8493-9117-2/01/$0.00+$.50

recognized that electrokinetics is the underlying phenomenon that accounts for the mechanoelectric observations in bone at frequencies much less than 10^6 Hz, and it is this focus that will be the focus of this chapter.

The term *streaming potentials* relates to the fact that when mechanical forces are applied to bone, fluid moves (or "streams") through the bone giving rise to electrical potentials in accordance with electrokinetic theory. Although much has been learned from experimental and theoretical work, there remain issues yet to be resolved. These include:

1. Unequivocal proof that these endogenous streaming potentials are in fact physiologically significant in the operation of Wolff's law of bone remodeling. Such proof is difficult to obtain because one must show that streaming potentials are the cause or among the causes of the cellular-mediated remodeling response while the cells simultaneously experience shear forces and convective mass transport due to the accompanying fluid flow and matrix-related strain resulting from the applied macroscopic deformations.
2. Detailed understanding of the precise fluid flow pathways in living bone, although much progress has been made in this area.
3. The electromechanical stimuli and cellular transduction mechanisms that lead to the sequencing of cellular responses that cause the initiation of bone remodeling.

In the subsequent sections, a review of experimental findings and theory development of streaming potentials in bone will be presented. Remaining issues and future directions will be discussed.

24.2 From Piezoelectricity to Streaming Potentials in Bone

24.2.1 Introduction

When a time-dependent nonuniform mechanical load is applied to fluid-filled cortical bone, the deformation of the bone matrix produces a flow of the fluid through the pores of bone. In the presence of electrical double layers on cell and bone surfaces,[16–18] electrical charge is transported by the flow giving rise to convection or streaming currents and potentials. Steady state is rapidly achieved when reverse conduction current caused by the streaming potential balances the convection current caused by the fluid flow. The value of the electrical potential at steady state is the experimental observable. Therefore, the association of experimental data to theory requires the determination of those parameters that influence flow profiles in the pores of bone, electrical double-layer structure frequently characterized by the zeta potential, models of electrical conductivity of wet bone, and, of course, the mechanical properties of wet bone. These have been brought together in a number of theoretical models, and they will be discussed briefly in the final section as they relate to understanding of experimental results involving streaming potential.

24.2.2 Electromechanical Measurements in Transition from Dry to Wet Bone

Early experiments in electromechanical phenomena in bone involved the use of dried bone,[2] but investigators quickly realized that physiological relevance of this phenomenon required the understanding of the effect of water on observed electromechanical results. The piezoelectric coefficients of dry bovine femur bone were determined by Burr[19] by cutting specimens from the cortex and maintaining orientation of the long axis, radius, and circumferential directions. In this way the components of the piezoelectric tensor, given by Eq. 24.1, could be determined.

$$E_i(P) = \sum_{j}^{6} d_{ij}\, T_j, \tag{24.1}$$

TABLE 24.1 Piezoelectric Tensor Elements at Various Frequencies and RHs

$d''_{14}\left(\frac{pc}{N}\right)$	$d'_{14}\left(\frac{pc}{N}\right)$	log f (Hz)
	RH = 40%	
0.02	0.06	−1.75
0.015	0.055	−1
0.01	0.06	0
0.02	0.075	+1
0.03	0.125	+1.75
	RH = 55%	
0.028	0.09	−1.25
0.02	0.08	−1
0.005	0.06	0
0.02	0.068	+1
0.025	0.09	+1.75
	RH = 98%	
0.72	0.55	−0.25
0.43	0.32	0
0.28	0.15	+0.3
0.12	0.08	+0.7
0	0.08	+1.3
0	0.10	+1.7

Data from Burr.[19]

where T is the mechanical stress, $E(P)$ the generated electric polarization, and d_{ij} the piezoelectric tensor where i represents the three coordinates x, y, and z and j spans six indices corresponding to three tensile and three shear stresses. While arguments for hexagonal symmetry for cortical bone have been made, results of piezoelectric measurements in bone by Anderson and Ericsson[9] and Burr[19] failed to demonstrate this symmetry. Accordingly, all 18 d coefficients for dry bone from Eq. 24.1 are nonzero rather than the 7 that would be expected for hexagonal symmetry. Nevertheless, the shear coefficient typically represented as $d_{14} = d'_{14} - id''_{14}$, where d'_{14} and d''_{14} are the real and imaginary parts of d_{14}, is the largest of the terms and therefore represents a convenient parameter with which to explore the effect of water on electromechanical effects in bone as it goes from a dry state to a fully hydrated state in which fluid flow can occur.

Maeda et al.[20] measured both d'_{14} and d''_{14} at a frequency of 10 Hz and observed a decrease in d'_{14} of 30% when hydrating bovine cortical bone from a dry state to a hydration level of 7.4 wt % water while d''_{14} increased by a factor of 8. Hydration was achieved by equilibration of the specimens in a 25°C chamber with appropriate saturated salt solutions. The decrease in d'_{14} was attributed to increased mobility of adsorbed water in collagen and the increased value of d''_{14} was also attributed to the same mechanism in addition to a dispersion resulting from increased ionic conductivity that accompanied the water uptake by collagen.

Burr[19] studied d_{14} from 10^{-2} to 10^{2} Hz in bovine cortical bone as a function of equilibrated relative humidity (RH) up to 98% RH. Table 24.1 shows Burr's results for d'_{14} and d''_{14} as a function of frequency at approximately room temperature for three different RHs. Burr's results indicate a dramatic change in low-frequency d_{14} values with change in RH but essentially no change at higher measured frequency. He attributes this to a Maxwell Wagner dispersion with an inverse frequency dependence. Burr's results for d'_{14} are in substantial agreement with those of Reinish and Nowick[74] whose measurements were at 5.6 kHz. Reinish and Nowick measured a total decrease in d'_{14} from the dry state to the 100% RH state of 47%. In addition, they performed the inverse piezoelectric experiment in which an electric field is applied

to the bone sample and a deformation is observed and they found agreement in the d coefficients between this inverse effect and the direct effect. Neither Burr[19] nor Maeda et al.[20] correlated their results to water content in a quantitative way, and therefore the implications to the role that flowing fluid plays on mechanoelectric effects in bone is not explicit from their work.

Marino et al.[21] fully hydrated both bovine femur and Achilles tendon in saline at 24°C for 24 h and studied mechanoelectric effects at −25°C where ionic conduction in ice is reduced compared with that in water. They showed that in fully hydrated bone d_{14} decreased by a factor of two compared with dry bone when measured by the converse piezoelectric effect (tendon values decreased by a factor of 8), thereby arguing that piezoelectricity, while reduced, nevertheless existed in physiologically wet bone although it was *not* measurable at physiological temperature. In other words, even with fluid present, albeit in the ice phase, piezoelectricity was present.

Electromechanical interactions in wet bone at room temperature were considered by Petrov[22] and Johnson and colleagues,[23–25] and they both concluded that for a step deformation to bone, the measured piezoelectric potential would decrease from a peak value as an exponential with time constant given by Eq. 24.2:

$$\tau = \left[\left(\frac{4\Pi\lambda}{\varepsilon}\right)^{-1}\right], \tag{24.2}$$

where λ is the conductivity of the wet bone and ε the dielectric constant. In wet bone this value is in the microsecond range because of increased ion conductivity. Accordingly, one would expect cancellation of the dipole rotation fields that give rise to the piezoelectric effect within a microsecond, so that potentials that are characterized by persistent fields with relaxation times of the order of seconds could not be accounted for in terms of piezoelectricity. Along with studies of increased bone conductivity with increased hydration, researchers also focused on the changes in dielectric constants and piezoelectric constants with changes in temperature and hydration of bone, decalcified bone, and tendon. Maeda and Fukuda[26] found for bovine bone that d' was greater at low temperatures for all hydration levels compared with dry tissue, but then decreased below dry bone with increasing water content starting at −50°C while for dry bone, d' was constant in temperature from −150 to +50°C. The decrease they measured was consistent with values by Burr.[19] In addition they observed large increases in ε' and ε'', where the complex dielectric constant $\varepsilon = \varepsilon' + i\varepsilon''$ and the real part of ε, namely, ε' is the result of dipole rotation (or charge separation) in the presence of an applied electric field and ε'', the imaginary part of ε is the result of charge conduction in the presence of an electric field. These increases in ε occurred as temperature increased, and the increases were larger, the greater the hydration of the bone. To understand the importance of these findings one must consider the state of water in bone.

The incorporation of water into bone occurs in at least three states.[27] One is the incorporation within collagen, thereby increasing the collagen crystallinity and, as a result, increasing the piezoelectric coefficients at low temperature. The quantity of water collagen can adsorb will depend upon whether or not the collagen is mineralized. In tendon or demineralized bone, this is estimated[26,28] at 0.054 to 0.115 g water/g collagen. In bone, constriction of collagen by the apatite crystals restrict this quantity to lower values. The second phase of water is water bound to interior surfaces that lie between mineral crystallites and collagen molecules and fibers. These are water molecules that are more tightly bonded to these surfaces than to other water molecules and are therefore fixed to these surfaces. This layer of molecules is typically about 3 to 7 Å thick and is often defined by the term *slip plane* to distinguish between water that does *not* flow past a surface in the presence of a pressure gradient from the water that is mobile and, in the presence of such a gradient, does flow. The third fluid phase is the mobile water and, of course, ions dissolved in this water phase are free to move and together with mobile water do contribute to conduction as well as dielectric constant and loss mechanisms implicit in complex dielectric measurements. The hydration state that defines the transition to mobile water is referred to as h_c, the critical hydration state. In collagen, this

lies between 0.054 and 0.115 g water/g collagen, while in bone Maeda and Fukada,[26] from measurements of real and imaginary dielectric constant, measured h_c to be 0.042 g water/g dry bone. This value agrees well with previously measured h_c of 0.037 to 0.048 g water/g dry bone for human cortical bone by Marino and Becker.[21]

The amount of free water in the microporosity can be determined from the total water in the microporous compartment less the bound water component. Black and colleagues,[29,30] Morris et al.,[31] and Kelly[32] reviewed the fluid compartments in bone. Morris et al. evaluated the volume percent of fluid in various compartments of cortical canine bone. They measured total water space, extracellular space, volume due to red blood cells, and other cell volume. Their data indicate approximately 13% of the total volume of bone is water associated with the crystalline bone matrix. By using the data reported by Black et al.,[29] an average value of 8.6% by volume is water associated with the microporosity of human Haversian osteons. These volume percentages represent total water content within the microporosity and are subject to wide variation due to biological variation and the measurement methods employed. Also considered must be the amount of water that is bound to the collagen/hydroxyapatite matrix and not free to flow. Marino et al.[21] studied the dielectric properties of human cortical bone as a function of hydration and indicated that a critical hydration of 0.037 to 0.048 g water/g dry bone reflects the amount of bound water. From Black and Mattson's[29] dry bone density measurements, an average density of 1.83 g cm^{-3} is calculated. By using Marino's results, a range of 6.3 to 8.1% of the water in the microporous compartment may be bound water. By using Marino's determination of bound water volume, the results of Morris et al.[31] are that 4.9 to 6.7% would be free to flow. Black and Mattson's[29] results would indicate a range of 0.5 to 2.3% of free flow volume. Eriksson[33] indicated that 2% by wet weight, or 3.9% by volume, is free water, implicated from his studies of electrical resistance and hydration. Finally, Chakkalakal et al.[34] and Kosterich et al.[35,36] measured the electrical conductivity of cortical bone and concluded that the low-frequency conductivity of the bone–fluid system is proportional to the conductivity of the fluid and is 0.5 to 1% of the value of the conductivity of the fluid. This suggests that a lower limit of mobile water also falls in this range. As a result of the above, one can estimate that free-flowing water in (cortical) bone ranges from 0.5% to a maximum of 6.7%.

The importance of the above analysis is that to explain the dielectric constant and piezoelectric constant measurements on hydrated bone by Maeda and Fukada[26] it is necessary to identify the presence of a mobile fluid phase. The presence of such a phase then provides a sound basis for streaming potentials since, for hydration levels that are equal to or greater than h_c, water moves through the porous regions of bone when that water is subjected to appropriate pressure gradients.

Typical measurements of streaming potentials from stressed wet bone are shown in Fig. 24.1. A step load is applied to a bone specimen, for example, in four-point bending. Silver–silver chloride electrodes are placed on opposite sides of the bone such that one electrode is on the concave side during the application of the load and the other electrode is on the convex side of the bone. For cortical bone specimens approximately 1 mm thick, 30 mm long, and 10 mm wide and outer fiber strain of less than 0.2% under four-point bending, the peak amplitude of the measured voltage is typically of the order of 1 mV in amplitude for bone steeped in normal saline solutions. The relaxation time is of the order of 1 s; however, more than one relaxation time is required to characterize the data rigorously. Sinusoidal loads of varying frequency can also be applied, and amplitude and phase of the streaming potential measured.

Johnson et al.,[25] building upon the earlier work of Anderson and Ericksson,[9] Cignitti et al.,[11] and Petrov,[22] argued that the potentials generated as in Fig. 24.2 were in fact streaming potentials. He argued that the relaxation time results from the time dependence of the velocity of the flowing fluid during the application of stress and that this velocity is dependent upon the solution viscosity, not upon the conductivity of the fluid as described by Eq. 24.2. This is suggested by the Smoluchowski equation for streaming potentials,

$$\vartheta = \frac{P\varepsilon}{4\Pi\lambda\eta}, \tag{24.3}$$

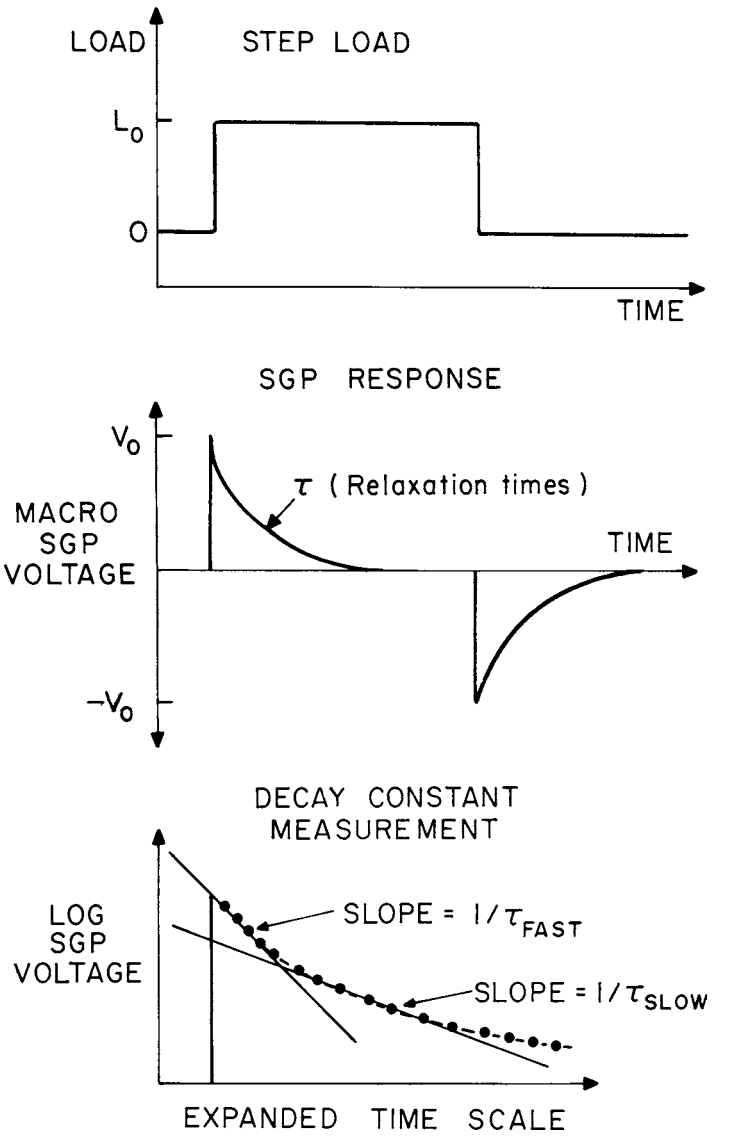

FIGURE 24.1 Streaming potential response to step loading and the decomposition of the decay constant into a fast and slow relaxation time. (From Pienkowski, D. and Pollack, S. R., *J. Orthop. Res.,* 1, 30, 1983. With permission.)

where ϑ is the streaming potential, P the driving pressure, ε the dielectric constant, λ the electrical conductivity, and η the solution viscosity. From Eq. 24.3, the amplitude of the spike in Fig. 24.1 should be inversely proportional to the product of the conductivity and viscosity even though a more-generalized theoretical expression for bone is required to explain observed relaxation times. This will be discussed later.

Gross and Williams,[16] Pienkowski and Pollack,[17] Pollack et al.,[37] and Otter et al.[38] studied the amplitude and relaxation time dependence of the mechanoelectric signals of Fig. 24.1 on solution conductivity and viscosity and also studied the effect of alterations in the zeta potential on such measurements. This body of work constitutes the evidence for the transition to streaming potentials as the underlying mechanism for mechanoelectric phenomena in wet bone at low frequencies (less than 10^{+6} Hz) and at room and body temperature.

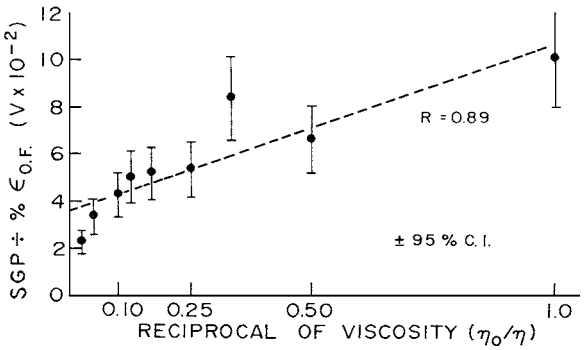

FIGURE 24.2 Streaming potential divided by the outer fiber strain as a function of the reciprocal viscosity η of the bone fluid. η_o is the viscosity of distilled water. (From Pienkowski, D. and Pollack, S. R., *J. Orthop. Res.,* 1, 30, 1983. With permission.)

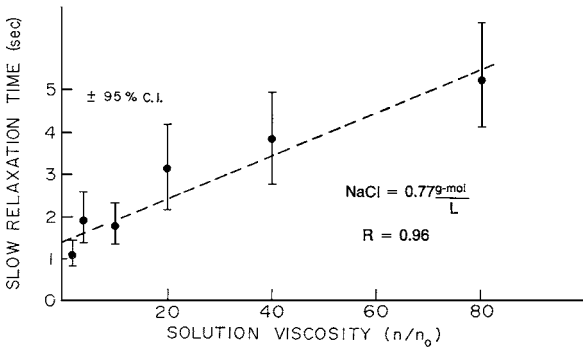

FIGURE 24.3 The slow relaxation time as a function of bone fluid viscosity; n_o is the viscosity of distilled water and the data are taken with an applied step load as shown in Fig. 24.1. (From Pienkowski, D. and Pollack, S. R., *J. Orthrop. Res.,* 1, 30, 1983. With permission.)

24.2.3 Summary of Early Streaming Potential Data

The Helmholtz Smoluchowski equation in Eq. 24.3 indicates that a streaming potential measured across a bone specimen would be proportional to the reciprocal of the product of the bone (fluid) conductivity and the fluid viscosity. In addition, the relaxation time, calculated by several authors for different bone models, is proportional to the fluid viscosity and independent of fluid conductivity. These two parameters, the amplitude and relaxation time, offer a special way to contrast piezoelectricity with electrokinetics since the piezoelectric mechanism is independent of viscosity and the relaxation time is inversely proportional to electrical conductivity.[22] Gross and Williams[16] and Pienkowski and Pollack[17] measured these relationships and typical data are shown in Figs. 24.2 through 24.4. Fig. 24.2 shows the linear relationship between the normalized amplitude of the streaming potential vs. the reciprocal of the viscosity of the fluid in the bone. In this experiment the amplitude refers to the peak amplitude at 1 Hz. Figs. 24.3 and 24.4 show the relaxation times that characterize the decay of the amplitude. These data were taken with an applied load as shown in Fig. 24.1. Fig. 24.3 shows the linear function of the relaxation time with viscosity over nearly two orders of magnitude and Fig. 24.4 shows that the relaxation times are essentially independent of solution conductivity over three orders of magnitude. These results provide a strong argument for the existence of streaming potentials in bone.

It is interesting to note that Pienkowski and Pollack[17] reported a consistent sign reversal in the streaming potential during conductivity studies using NaCl solutions with concentrations of 0.7 to 1.0 g-mol/l.

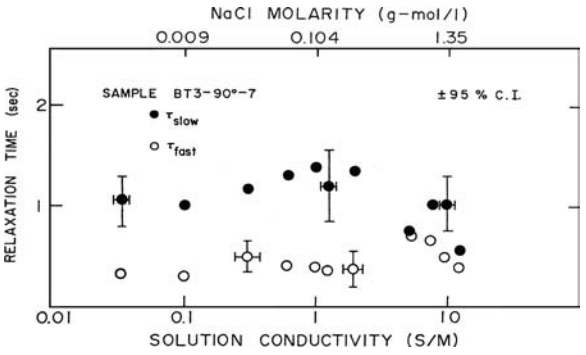

FIGURE 24.4 Stress-generated potential as a function of solution conductivity. The data are taken with an applied step load as shown in Fig. 24.1. (From Pienkowski, D. and Pollack, S. R., *J. Orthrop. Res.,* 1, 30, 1983. With permission.)

These sign reversals also occurred with KCl, NaF, and $CaCl_2$ solutions. When these salts are added to water the electrical conductivity, λ, increases and from Eq. 24.1 will decrease the amplitude of the streaming potential. However, the only parameter that can reverse the polarity of the streaming potential is the zeta potential. For example, a negative zeta potential results is a net positive charge in the Debye layer adjacent to the fluid–solid surface while the reverse is true for a positive zeta potential. When the fluid is forced to flow, charges of opposite sign accumulate on the downstream side of the bone for zeta potentials of opposite sign. The observed potential thereby reverses polarity if the zeta potential reverses polarity.[73] This was studied by Pienkowski and Pollack,[17] Berretta and Pollack,[39] and Kowalchuk and colleagues.[18,40] Berretta measured the zeta potential of wet bone as a function of NaCl concentration of the fluid. She ground the specimen into particles and measured the electrophoretic mobility from which she was able to determine the zeta potential. She found that the zeta potential of bone reversed from negative to positive at the same NaCl concentration that Pienkowski observed the polarity reversal from streaming potential measurements. From this work and the work of Kowalchuk, two important conclusions were drawn. First, support was gained for the streaming potentials in wet bone since the zeta dependence is quite specific in all models of this phenomenon. The second is that for the bone specimens studied, which were frozen, thawed, dead, machined, milled, sonicated, and steeped multiple times in various solutions, the amplitude of the zeta potential of the bone matrix, i.e., the surface of the porous region through which the fluid flows, defines the charged fluid region that gives rise to the observed streaming potentials. The presence of cells and cell substructures is not required to produce these potentials since the entire observation occurs in their absence. This point will be returned to later.

Kowalchuk et al.[40] explored the question of whether the mineral phase or collagen phase of the matrix dominated the value of zeta potential in bone. He found that calcium-deficient hydroxyapatite (CDHA) in physiological Neuman's fluid[41] has a negative zeta potential. Heretofore, the zeta potential of the mineral phase of bone had been thought to be positive, while the zeta potential of bone is negative. Because of this difference in sign, it had been suggested that the mineral phase cannot provide an electrically important surface in bone. In this study, however, the zeta potential of CDHA in Neuman's fluid was negative, countering the above argument. Since the bone mineral is actually a carbonated calcium-deficient hydroxyapatite rather than a pure stoichiometric hydroxyapatite (HA), this study of CDHA in physiological fluid approximated the *in vivo* state better than previous studies using stoichiometric HA or nonphysiological fluids. Accordingly, zeta potential measurements in Neuman's fluid do not differentiate between the protein and mineral phases with respect to their contributions to the generation of the electrically important bone surfaces solely on the basis of the sign of the zeta potential.

With increasing calcium in Neuman's fluid, the zeta potential of CDHA magnitude decreases and inverts in sign to a positive value. This result is expected for CDHA, because Ca^{2+} ions adsorb readily onto CDHA, but is opposite to that seen in bone, where the zeta potential increased in magnitude with

increasing calcium concentration at low levels in Neuman's fluid. Therefore, although the zeta potential of CDHA is negative, it does not behave the same way as bone when exposed to increasing calcium concentration in Neuman's fluid, implying that CDHA is not the predominant charge determining surface of bone. Other investigators arrived at the same conclusion using various nonphysiological steeping fluids.[42,43] It is now generally agreed that it is the collagen that plays the principal role in determining the zeta potential in machined specimens of bone.

24.3 Microelectrode Studies of Streaming Potentials in Bone

An important aspect of this field is the relationship between bone morphology and streaming potentials. In particular, the spatial relationship between fluid flow pathways and bone cells opens the door to determining the magnitude of local electrical fields experienced by bone cells when fluid moves through the porous spaces of bone. McElhaney[44] attempted to experimentally correlate measurements of electrical potentials on whole femurs with anatomical architectural features of the bone. Because quantifying the state of stress in whole-bone specimens is indeed complex at the spatial level of the cells, and because of the large size of his electrodes, he was not able to draw firm conclusions regarding the relationship between bone structure and mechanoelectric measurements.

A series of experiments was reported in which microelectrodes were used to map the electrical potentials in wet bone *during* cyclic 1-Hz deformation. Specifically, machined bone specimens were deformed in four-point bending and the electrical potentials were measured with osteons to resolution of approximately ± 5 μm. This work was reported by Starkebaum et al.,[45] Iannacone et al.,[46] and Pienkowski and Pollack.[17]

Fig. 24.5 shows typical streaming potential data as a function of position during four-point bending. Reflected and polarized light photomicrograph of the specimen surface is also shown. The open circle data points were taken between the microelectrode and the reference electrode on the compression side of the specimen. The closed circles were taken between the microelectrode and the reference electrode on the tension side of the specimen. The path of the microelectrode positions across the specimen surface is shown by a narrow dark line drawn approximately through the middle of the reflected light photograph. The specimen shown was cut at 90° to the long axis of the bone. In this particular experiment, the nearest path to a straight line was chosen to pass through the middle of a number of Haversian canals in traversing the specimen. A conventional experiment would have measured a macroscopic signal of approximately 2 mV, with the compression side negative with respect to the tension side. The highly nonlinear character of the surface microelectrode scan is apparent and is typical of such scans. The distinguishing features of the data that will be expanded upon later are the downward, cusplike shapes of the microelectrode potential approaching Haversian canals on the compression side of the specimen; the upward, cusplike shape of the potential approaching Haversian canals on the tension side of the specimen; the nearly flat potential approaching the Haversian canal at the approximate neutral axis of the specimen; and the sharp change in potential occurring near the cement line bordering two osteons, as can be seen at 900 μm in Fig. 24.5. These features were studied extensively in four-point bending.

Reproducibility of these features was studied by removing the specimen from the jig and repeating the entire experiment on the same day. This was also repeated 10 days later with the same osteons being stressed in both tension and compression. Fig. 24.6 shows a typical result of this test for an osteon under compression. The actual points at which the data were taken on the osteon are shown using small open circles on the reflected light photograph immediately above the microelectrode data.

Reversal of the specimen in the jig reverses the side of the specimen that is in tension. The same osteon can then be studied in both tension and compression. Fig. 24.7 shows the reversal in the sign of the cusplike potential when the sign of the stress changed from tension to compression.

Osteons were studied to determine both the radial and the azimuthal dependence of the electrical dependence. The results showed a logarithmic dependence on the radius and approximate symmetry with regard to azimuth in most cases. The most prominent feature of the data is the large, nonlinear electrical fields discovered at the Haversian canals during the application of stress. These fields had not

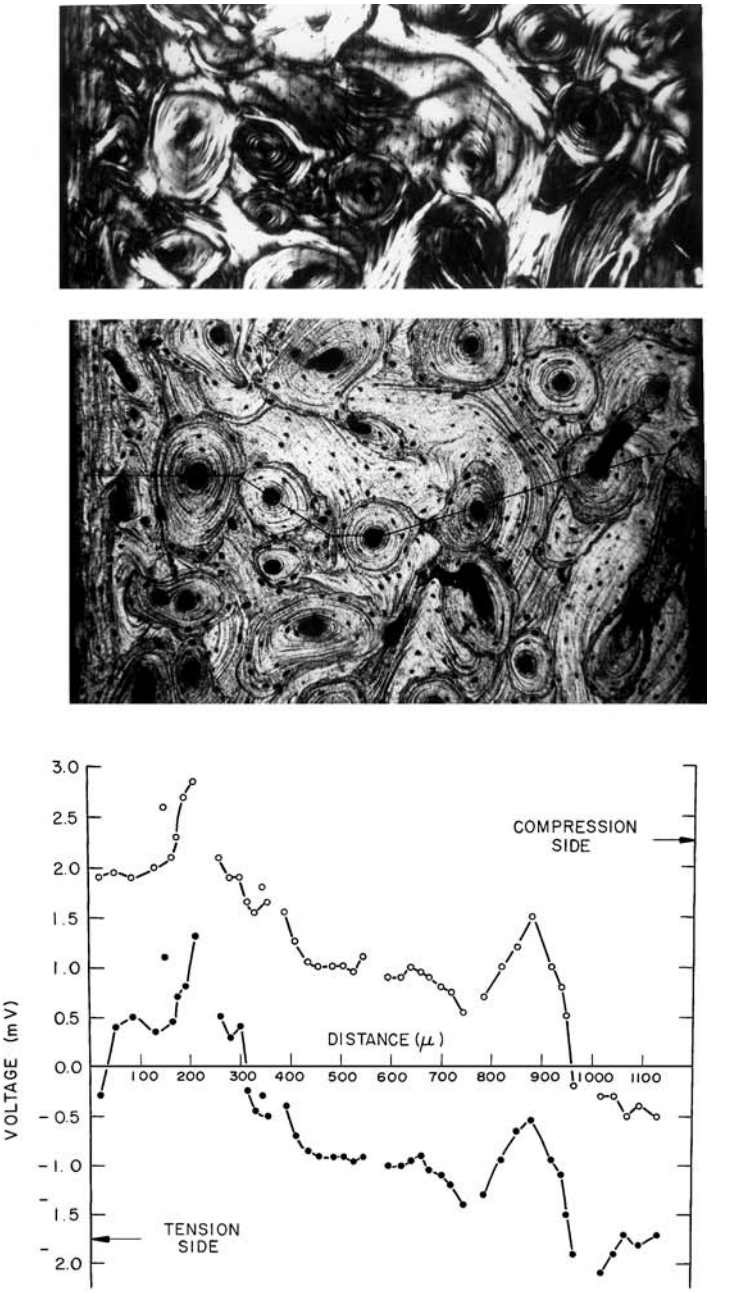

FIGURE 24.5 Microelectrode potential vs. distance across transverse sections of cortical bone deformed in four-point bending. Reflected and crossed field polarized light photograph shown in registration with data. Open circles (o) are potentials measured relative to electrode on compression side of specimen and closed circles (●) are relative to tension side. (From Starkebaum, W. et al., *J. Biomed. Mater. Res.,* 13, 729, 1979. With permission.)

been previously observed and now had to be taken into account when attempting to understand the macroscopic data, the origin of the electrical signals, and their physiological significance.

It is readily apparent from the data that there is a cusplike electrical potential around each Haversian canal, and that the potential increases (decreases) as the canal is approached for osteons on transverse tension (compression). Since the electric field, E, is the negative gradient of the potential, the local

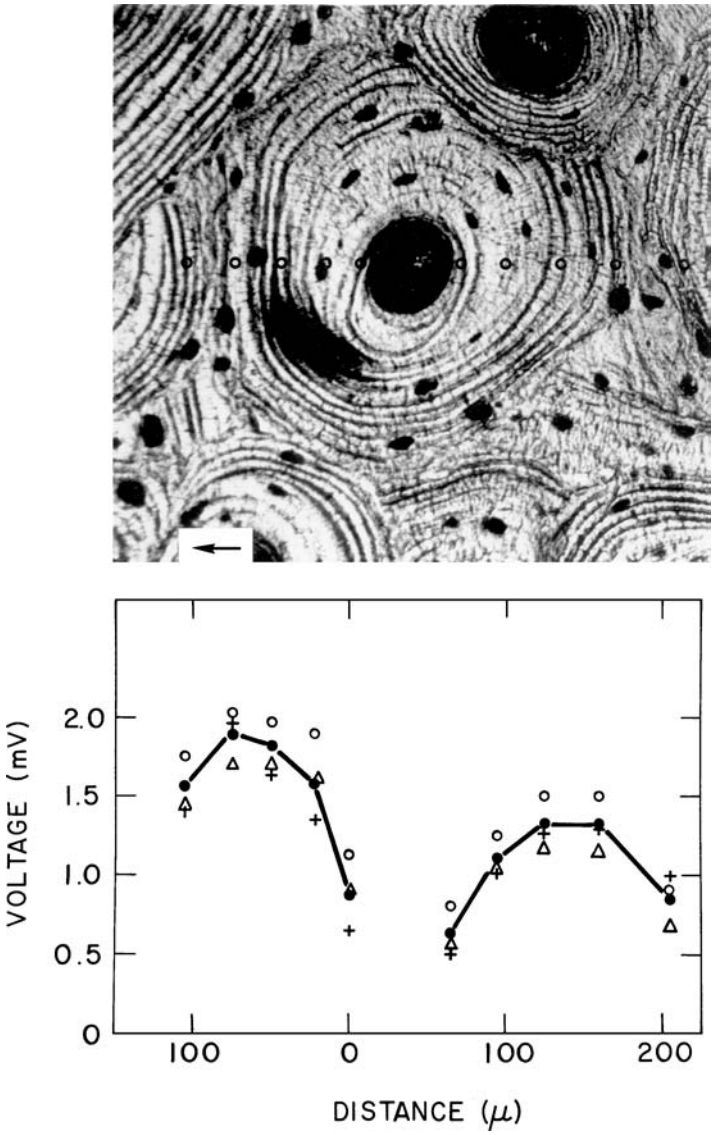

FIGURE 24.6 Reproducibility study of microelectrode streaming potential measurements for an osteon in compression. O = day 1; Δ = repeat on day 1; + = repeat data on day 10. Solid curve is the average of three sets of data. Human bone specimen No. Wh-90°. (From Starkebaum, W. et al., *J. Biomed. Mater. Res.,* 13, 729, 1979. With permission.)

electric field can be determined from plots such as shown in Fig. 24.7. This compression and tension measurement was done for all osteons studied, and Fig. 24.8 shows a plot of the electric field vs. γ_{HC}, the normalized distance of the Haversian canal from the geometric center (assumed to be the neutral axis of the specimen). This figure is for a human femoral specimen cut at 90° to the long axis of the bone. The mean value of this specimen reference voltage was 1.10 mV, which, for the specimen width of 1250 μm, gives an average macroscopic electric field of 8.8×10^{-1} V/m. This average field can be compared with the Haversian canal fields ranging to $2 \times 10^{+1}$ V/m. It is clear that local fields in the vicinity of the Haversian canal are some 20 to 30 times greater than the average macroscopic fields generated, thus suggesting their significance in the bone signaling process during adaptation and repair.

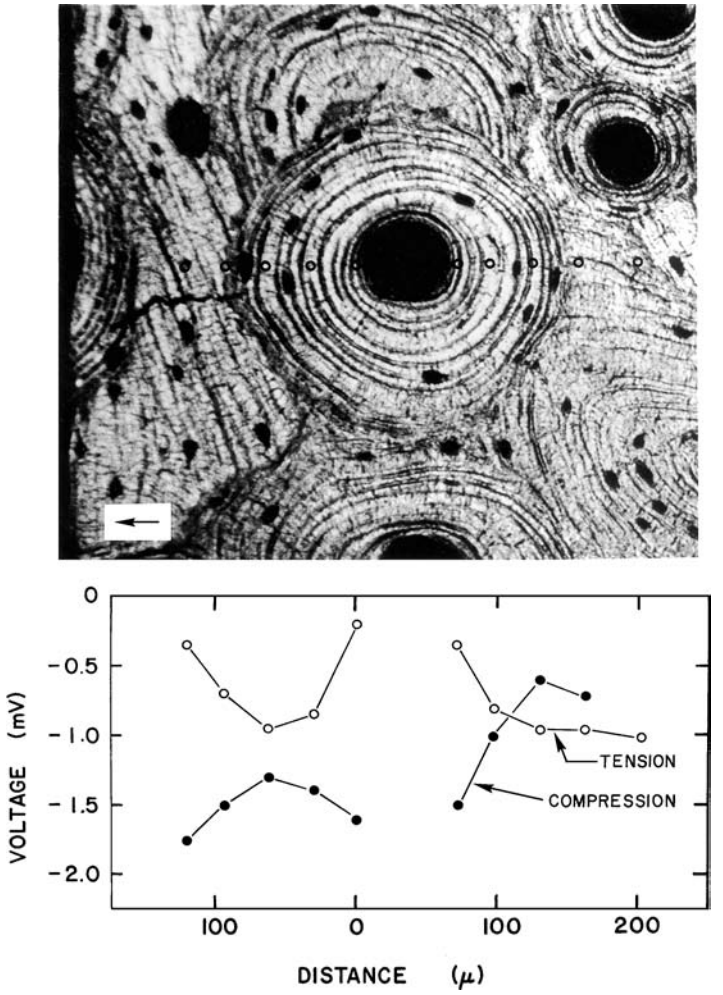

FIGURE 24.7 Microelectrode streaming potential measurements for an osteon in compression after which the specimen is reversed in the four-point jig and the same osteon is measured in tension. Osteon No. 6-12 specimen No. Wh-90°. (From Starkebaum, W. et al., *J. Biomed. Mater. Res.,* 13, 729, 1979. With permission.)

The authors note the fact that fluid motion could be observed during the experiments at 1 Hz. Oscillatory concave and convex menisci in osteocytic lacunae and in Haversian canals were observed during the loading, indicating radial flow to and from lacunae and Haversian canals. They point out that given the negative value of bone zeta potential, the flow of fluid will carry a net positive charge. Therefore, outward-directed flows will result in positive potentials in the osteon as the radius approaches the cement line and the reverse for inward directed flows toward the Haversian canal. This will give rise to radially symmetric potentials with a cylindrical symmetry and thus satisfy the logarithmic dependence on the radius, hence the observed cusps. Pienkowski and Pollack[17] also showed that if the NaCl molarity of the fluid in bone is changed and both the macroscopic and microscopic intraosteonal potentials are measured, their amplitude dependence on molarity (and hence electrical conductivity) is the same. Therefore the functional dependence on both the electrical conductivity and the zeta potential is the same for both micropotential and macropotential measurements. Therefore, while the pore system that defines the detailed pathway of fluid flow within the osteon may be different from some net macroscopic flow path, the underlying mechanism of both is electrokinetic.

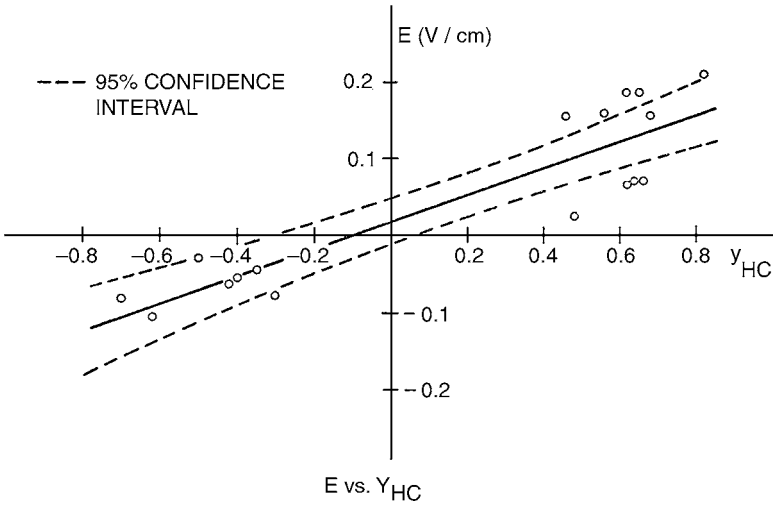

FIGURE 24.8 Haversian canal electric field vs. distance of the Haversian canal from the neutral axis during four-point bending. Positive fields and positive YHC refer to canals on the tension side of the specimen and negative values are for the compression side of the specimen. (From Starkebaum, W. et al., *J. Biomed. Mater. Res.*, 13, 729, 1979. With permission.)

24.4 Streaming Potentials in Living Bone

It is important to realize that all of the observations discussed above were made on bone specimens that were devoid of live cells and that had undergone considerable manipulation, in some cases over periods of months. Although much concern was expressed regarding reproducibility of dry bone (piezoelectric) data, considerable stability and reproducibility was observed with wet bone, as can be seen in Fig. 24.6, suggesting that bone architecture and matrix properties give rise to the detailed characteristics of observed streaming potentials. Nevertheless, the effect of cells and intact tissue structures on streaming potentials had to be quantified.

Early study of fluid transport in osteons by Piekarski and Munro,[72] Bassett and Becker,[3] Cochran et al.,[47] Black and Korostoff,[48] and Lanyon and Hartman[49] confirmed the presence of electromechanical potentials in living bone and in excised bone with viable cells. Otter et al.[52] performed the first systematic quantitative study of streaming potentials in bone specimens both *in vivo* and *in vitro*. He measured transcortical potentials in 13 canine intact tibias *in vivo* under controlled sinusoidal and step loading and then excised the specimens and studied the potentials under the same deformation routine after enough time elapsed to machine the specimens, store them overnight, and steep them for an additional 18 h to assure uniform fluid composition. His observations revealed similar results for *in vivo* and *in vitro* specimens as revealed by streaming potential amplitude normalized by the transcortical strain difference as a function of frequency, and both *in vivo* and *in vitro* data exhibited step load responses similar to those shown in Fig. 24.2. While the results appeared to be similar, Otter's detailed analysis of the functional form of the data suggested interesting and fundamental differences that have not yet been incorporated into any theory. For example, the functional description of the frequency dependence of the streaming potential showed statistically significant differences between *in vivo* and *in vitro* data when analyzed by either the Salzstein et al.[50,51] model or the stretched exponential model.[52] The reader is referred to Chapters 11 and 22 for additional discussion of the stretched exponential and the poroelastic model of Salzstein et al. In addition, analysis of the streaming potential decay time for step-loaded specimens showed statistically significant changes in the parameters that define the relaxation times with the relaxation times observed *in vitro* resulting in slower decay than those observed *in vivo*. Both of these significant differences are

sharply contrasted with the fact that the normalized (to transcortical strain) amplitude of the streaming potential was unchanged by the *in vivo* to *in vitro* measurement and by the fact that the decay times, while different, were both of the order of 1 s. Otter points out that the most logical place to search for a resolution of these results rests in an alteration of the pore system through which the fluid flows as a result of the death of the bone cells. This point will be discussed in the next section.

In another study Otter et al.[53] measured *in situ* streaming potentials in canine tibias while perfusing the femoral nutrient artery with salt solutions known to alter the zeta potentials in *in vitro* bone. He found that NaH_2PO_4 solutions increased streaming potential amplitudes while $CaCl_2$ solutions decreased streaming potential amplitude in agreement with numerous *in vitro* studies.[16,18,39,42] This change is related to the exchangeability of both calcium and phosphate with bone, leading to zeta potential changes in accordance with measured decreases and increases in streaming potentials. The perfusion changes observed by Otter strongly suggest that (calcium and phosphate) ion exchange with the bone surfaces plays a dominant role influencing the streaming potential amplitude. That is, the electrical double layer adjacent to bone matrix surfaces dominates the amplitude of the measured electrokinetic effect in bone.

Otter et al.[54] demonstrated that streaming potentials *in situ* are also modified by the protein protamine sulfate, used to reverse the anticoagulant effect of heparin with the side effect of blocking calcium efflux from bone. It is believed that protamine is specifically adsorbed on the bone surface and therefore was a candidate for perfusion studies. Using the same canine tibia model used previously, he showed a dramatic decrease in transcortical streaming potential amplitude upon injection of protamine sulfate. The decrease continued for as long as 100 min after injection. At sufficiently high concentration of the protamine he observed a reversal in the sign of the streaming potential, indicating a reversal in the sign of the bone zeta potential in an *in vivo* experiment.

Otter et al.[55] observed periodic oscillatory streaming potentials in live adult canine tibiae, which they showed were the result of heartbeat-related medullary pressure changes. These oscillations and the oscillatory streaming potentials could be removed by occluding the femoral artery and could be reduced by administering epinephrine. In addition, pressurizing the medullary canal (immediately postsacrifice) resulted in transcortical streaming potentials that were proportional to the increased pressure. The medullary canal pressurization was repeated in *in vitro* calf femurs. The amplitude of the streaming potential per mmHg pressure in the medullary canal was similar for the (dead) calf femur, the immediately sacrificed adult canine tibia, and the live, *in situ* canine tibia.

In addition, from previously described papers by this group, the knowledge is gained that *in vivo* streaming potentials exist and that detailed characteristics of the frequency response compared to *in vitro* results are statistically different although relaxation times are the same order of magnitude. Pore geometry appears to play a significant role in influencing the details of the amplitude and frequency response of *in vivo* streaming potentials, and the bone matrix, not the cells, determines the electrical double-layer parameters that influence the streaming potential amplitude and sign as it does *in vitro*.

24.5 Review of Theoretical Models of Streaming Potentials in Bone: *In Vitro* Models

In 1982, Gross and Williams[16] considered the flow of fluid from one chamber (osteocyte lacuna) to another similar chamber through a cylindrical channel of radius r (canaliculus). The nonuniform strain in the bone specimen causes a pressure difference between the two chambers, and fluid flows. This simple model was used to describe the time constants for fluid flow in terms of the dimensions of the canaliculi. The amplitude dependence of the streaming potential was determined as a function of the strain-induced pressure gradient. Johnson et al.[23–25] explored the anatomical features of the canaliculi in more detail. They argued that canaliculi devoid of cells and cell fragments would have a radius of 0.1 μm and this would lead to relaxation times of the order of 100 μs, while Haversian canal radia would result in even shorter relaxation times. Since observed relaxation times are of the order of 1.0 s, then for fluid flow through canaliculi to be the source of streaming potentials in dead bone he argued that the canaliculi

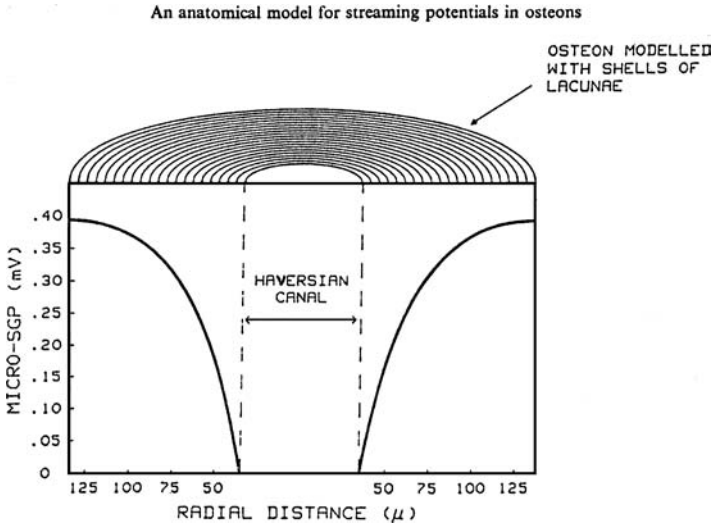

FIGURE 24.9 Predicted intraosteonal potential profile for the condition of uniaxial compressive stress. (From Pollack, S. R. et al., *J. Biomech.*, 17, 627, 1984. With permission.)

had to be partially blocked with cell debris or a smaller anatomical system of pores was involved in the flow.

Pollack et al.[56] developed an anatomical model of the osteon to explain the origin of the measured micropotential cusps (see Fig. 24.6) in terms of streaming potentials and to explore the pore system that accounts for this experimental finding. Since the data of Starkebaum et al.[45] and Iannacone et al.[46] were taken on dead bone, i.e., there were no live cells or intact cell structures due to sample preparation procedures and testing over extended periods of time, only matrix geometry was included in the model. An osteon was modeled as a cylindrical structure with spherical lacunae located uniformly on concentric lamellae shells with N_i lacunae on the ith shell. Each lacunae is drained by n cylindrical pores of radius R and length L_i, a length characteristic of the ith shell. The deformation of the spherical lacunae by the applied stress then cause the flow of fluid through the system of pores to the Haversian canal, resulting in observed streaming potentials in accordance with electrokinetic theory. The appropriate deformation, fluid flow, and electrical double-layer equations were solved and the streaming potentials calculated as a function of osteon radius under theoretical conditions that accurately replicated the experimental conditions of Starkebaum et al. Excellent agreement was found with the experiential cusplike potentials as shown in Fig. 24.9. The potential profile in Fig. 24.9 was computed for literature values of osteon and fluid parameters and fits the expression for small u values:

$$\varphi(u) = 0.014 + 0.42 \ln\left(\frac{u}{\bar{u}}\right)(\text{mV}),$$

where φ is the streaming potential, u is the radius at which the potential is computed, and $\bar{u}$ is the Haversian canal radius. This compares well with Starkebaum's result where the coefficient of the ln term was 0.62 ± 0.21 (mV). The relaxation time for decay of the streaming potential for a step load was also computed from the theory and found to be proportional to viscosity, inversely proportional to the pore radius to the fourth power times the number of pores, and proportional to the length of the pores. However, Starkebaum used 1 Hz deformation not step-loading and he did not measure the phase relationship between the streaming potential and the stress. Therefore, the relaxation times for streaming potentials *in osteons* are not known. This is unfortunate because we cannot simultaneously determine n

and R independently from this data. Several possibilities exist. For example, if $R = 0.1$ μm, i.e., the radius of an empty canaliculus, and $n = 50$ canaliculi per osteocyte, the time constant is of the order of 10^{-6} s for values of the canalicular length equal to the osteon radius minus the Haversian canal. For $R = 0.01$ μm (100 Å) and $n = 50$, the time constant computed from this model is 0.3 s. This value lies within the observed *macroscopic* time constants of 0.1 to 1.0 s measured by numerous authors.

The authors therefore conclude from this work that either partially clogged canaliculi resulting in average pore radii of the order of 100 Å are the principal flow paths that drain osteocytic lacunae under external load and give rise to the cusplike streaming potentials reported by Starkebaum et al. or, if the canaliculi are totally blocked, the flow is through the microporous spaces in the matrix or some combination of both. This theory cannot be more specific.

Finally, this single-osteon theory also explains the fact that the intraosteonal electric field is a linear function of the osteon position relative to the neutral axis in bending. This was reported by Starkebaum and is shown in Fig. 24.8. In summary, this model explained most of the features of single-osteon data reported for specimens with no live cells and confirmed the role of streaming potentials in this case.

The question of the effect of stress concentration around the Haversian canal on the symmetry of the streaming potential cusps was addressed by Petrov et al.[57] using a finite-element model to solve Biot equations from the theory of consolidation. They successfully reproduced the cusp shape of the potential observed by Starkebaum et al.[45] and Iannacone et al.[46] and computed the asymmetry as a function of the ratio of the Haversian canal radius to the radius of the cement line. They predicted an asymmetry of 20 to 30% for ratios of the above radii between 0.2 and 0.3, where the asymmetry is computed as the maximum value of the streaming potential in one direction minus the value in a direction that is 90° from the first direction normalized by the value at the original direction. This may account for the observations of asymmetry for osteons with large Haversian canals.

It was clear from the theories above, and from the data of Starkebaum and Iannacone, that the flow of fluid in deformed bone involves radial osteonal flows but must also involve flows that could be characterized as transcortical. That is, when a specimen of bone is bent, potentials are observed across the entire bone specimen even though the bone specimen may contain 10 or 20 osteons in cross section. To describe these macroscopic observations of streaming potentials, Salzstein et al.[50,51] developed a two-phase model of streaming potentials in bone based upon microporous flow within the bone matrix. The underlying hypothesis of this model is that, while radially directed flows in osteons occur involving Haversian canals, osteocyte lacunae, and canaliculi, there must be transcortical flows that may not be dependent upon this architecture and are therefore subject to analysis by considering fluid flow through the micropores in the matrix. Accordingly, they adapted the linear biphasic analysis (Armstrong et al.,[58] Mow et al.[15]) to bone and obtained the pressure in the fluid phase as a function of position for a time-dependent load. The microporous spaces are then modeled as interconnecting cylindrical pores and the electrical double layer in these pores is determined from conventional electrostatics. The permeability is taken from Scheidegger[59] in terms of φ^F, the fluid fraction, δ the pore diameter, η the fluid viscosity, and T the tortuosity of the cylindrical channels generally taken to have a value between 1 and 3. With these, the convective flow velocity is computed which then enables the determination of the streaming potential both for a sinusoidal driving load and for a step load. This formulation was successful in describing the frequency dependence of the streaming potential magnitude and the phase relative to load as shown in Fig. 24.10. In addition, the theory explained the occurrence of multiple time constants for step-loaded deformation and provided an excellent fit to the magnitude of these time constants; the fluid viscosity and conductivity dependence of streaming potential amplitude and time constants; and a fit to the volume fraction of water contained in the microporous fraction of bone. The mean value of the pore radius taken from a total of 21 equine and 14 bovine cortical bone specimens was 160 Å. It is interesting that this value falls within the range measured by Holmes et al.[60] from gas adsorption studies on bone and compares to the value of 100 Å for the fit of Starkebaum's data to the anatomical model for the osteon where the radius was assumed to be an average for either the debris-blocked canaliculi or the microporous matrix in dead bone. With hindsight, the closeness of the pore size values that contribute to the success of this model and the single-osteon model leave open the final interpretation of pathways for fluid flow

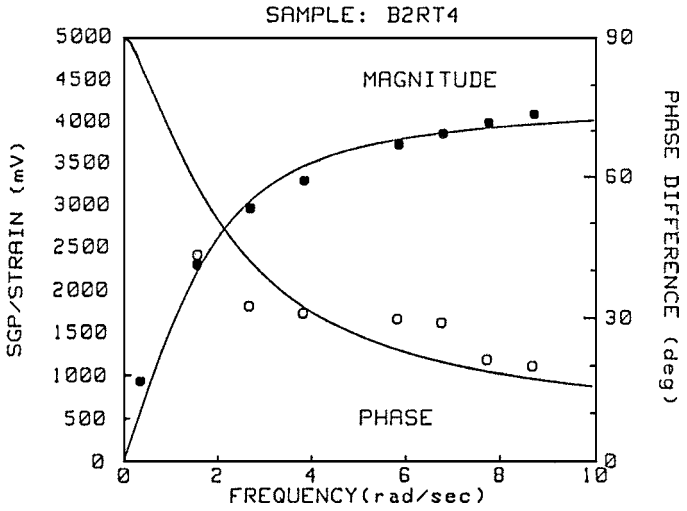

FIGURE 24.10 Dynamic characteristics of magnitude and phase from a bovine tibial specimen as a function of frequency for a sinusoidal load applied in four-point bending. Solid curve is generated from Salzstein et al. using nonlinear regression with two parameters, pore size, δ and ($\phi f/T2$) defined in text. (From Salzstein, R. A. and Pollack, S. R., *J. Biomech.,* 20(3), 271, 1987. With permission.)

when bone is deformed. This will be important in attempting to understand streaming potentials in live bone.

24.6 Theory Development in Live Bone

Theory development for live bone involves the incorporation of live intact cells and intact tissue structures into the architecture of bone. The living structure is then the basis for a theory of streaming potentials that can be validated against live bone data. The major conclusions drawn from prior work in which existing theoretical models have accounted for many of the subtleties of macroscopic and microscopic data from *dead* bone have been discussed, as well as the essential conclusions of live bone data that must be accounted for.

These conclusions include the following: macroscopic streaming potentials have the same amplitude in live bone as in dead bone when normalized by the difference in strain across the bone or by medullary pressure change; the time dependence is similar in live bone but is altered in detail in that live bone amplitude decays more rapidly than dead bone; changes in ionic content of perfusing fluid have the same effect on streaming potential amplitude in live bone as in dead bone; measurable transcortical streaming potentials in live bone result from medullary pressure oscillations caused by cardiac rhythms. It should be noted that microscopic streaming potential data in live bone osteons does not exist at this time. Therefore, the presence of the large electric fields reported in osteons by Starkebaum et al., as seen in Figs. 24.7 and 24.8 have not yet been observed for the case when cells occupy lacunae and cell processes occupy the canaliculi.

With the above thoughts in mind, consider the elegant model proposed by Weinbaum et al.,[61] Cowin et al.,[62] and Zeng et al.[71] This model adopts as its central theme the flow of fluid through the canaliculi in the space between the membrane of the osteocytic process and the canalicular wall. They model this space as a three-dimensional network of proteoglycan and other (unspecified) fibers of radius 1.0 nm with a characteristic fiber separation of approximately 7 nm. The presence of the fiber network, occupying the outer 50% of the radius of the canaliculus with the osteocytic process occupying the inner one half of the radius, results in sufficient increased drag to enable this model to predict relaxation time constants of the order of 1.0 s and physiological levels of shear stress ranging from 3 to 25 dyn/cm^2 (0.3 to 2.5 Pa).

The theory imposes an important set of linked boundary conditions that are an important part of research currently in progress. These are that the canalicular boundary allows no fluid flow from the canalicular space to the microporous space in the matrix and that the microporous space is filled with *only* a bound water layer of 10 nm thickness so that no flow occurs through this region. Therefore flow occurs only through the canalicular system. This model presents an appealing way of linking mechanically induced flow to cellular adaptation via the shear stress due to canalicular flow past osteocytes.

A careful analysis of the subject indicates that, while this theory plays an important role in the total understanding of streaming potentials, there are serious problems that are not explained. For example, a vast amount of streaming potential data described in earlier parts of this chapter were performed on dead bone with no live cells or intact cell structures. This includes bones that had been desiccated and then rehydrated repeatedly. How can the intimate model of the pericellular fibrous structure influence streaming potential data in such experiments[16,17,45,50,63] when these structures were not present when the data were observed? In fact, it was probably the case that the canalicular system was blocked by the cell debris of the decayed structures, yet model details were determined by the authors using such data. Also the difference between live and dead bone data was discussed previously in this chapter. This model cannot explain, for example, the fact that the amplitude of the streaming potential divided by the transcortical strain difference or medullary pressure was the same for live and dead bone since in dead bone the structure required to explain the live bone data is not present in the canaliculi and, if the canaliculi are blocked by cell debris, flow must occur in the microporous spaces.

The boundary condition of an impermeable canalicular wall has been questioned by a number of authors (Mak et al.,[64] Keanini et al.,[65] Cooper et al.,[66] Qin et al.[67]) as has the interpretation of bone flow experiments in adult bone using markers of various sizes.[68,69] There is no clear resolution to this issue[70] at this time because of experimental complications arising from marker transport within cells, marker binding to canalicular walls, and distortions resulting from specimen preparations, specifically demineralization. Nevertheless, flow of markers and proteins is evident within the canalicular system; however, the question of ion or water flow across canalicular walls is certainly not answered by existing data. More definitive data are required.

The argument that all the water in the microporous bone is immobile or bound water is not realistic. Earlier in this chapter the water compartments of bone were described. A bound water layer of 10 nm surrounding each mineral crystallite would define a slip plane of 100 Å with no mobile layer. Boundary layers rarely exceed a few molecular diameters so that this is at least an order of magnitude too great, given that a water molecule has a diameter of 0.28 nm. This is obviously an incorrect interpretation of Neuman's work. So now, there is a dilemma. Models based upon microporous flow are extremely successful in accounting for the details of a vast array of streaming potential data in bone with no intact cells and probably blocked or partially blocked canaliculi. But these models do not describe how the flow affects bone cells mechanically through shear or affects bone cell nutrition through convective transport. Microporous flow does create a model for endogenous electric fields in bone that can alter cell behavior.

On the other hand, the canalicular flow model with a detailed pericellular fiber structure cannot explain the vast array of streaming potential data needed to establish the fiber model parameters because the pericellular fiber structures are not present in the dead bone specimens when the data are taken. However, the model provides an excellent approach to understanding both shear and convective transport in the canaliculi of live bone.

A possible resolution of this problem is embodied in the work of Mak et al.,[64] where hierarchical flow was modeled in both the microporous space and the canalicular space as a function of ϕ_c^s, the volumetric fraction of solid in the canaliculi. Flow velocity and drag force were calculated from a finite-element model where the computational mesh represented the architecture of three Haversian canals plus canaliculi and neighboring matrix. The interfacial permeability of the canalicular wall was modeled as either equal to the total matrix permeability or to a function of both the matrix and the channel permeability. Their results, which must be viewed as a parametric study only, indicate that when $\phi_c^s \geq 0.9$, the drag forces experienced by a solid (osteocyte) in the canaliculus become comparable with those in the

microporosity. The magnitude of the drag force is strongly dependent upon the model for the canalicular permeability. Simultaneous flow fields in the microporous matrix and canaliculi are exhibited by the model and represent an interesting approach to reconciling the two types of models described in this paper.

Mak's model of simultaneous flow in the microporous and canalicular spaces can possibly be developed to describe all the data there are on streaming potentials. In the case of dead bone, the canaliculi are presumed blocked or partially blocked and the deformation-produced flow is through the microporous spaces and partially blocked canaliculi as described by Johnson et al.[24,25] and by Salzstein et al.[50] with a characteristic pore radius of approximately 16.0 nm. In live bone, simultaneous flow in both the microporous matrix and canaliculi occur such that transcortical streaming potential amplitudes are not altered while decay time constants are reduced in live bone due (presumably) to higher permeabilities for canalicular flow. Transcortical periodic streaming potentials result from flows caused by pressure oscillations from heartbeats resulting primarily in canalicular flows in live *in situ* bone as seen and proposed by Otter et al.[55] The addition of externally applied mechanical deformation results in increases in simultaneous flows in both the microporous and canalicular systems. This model also presents a method whereby the osteocyte experiences the flow in live bone, namely, by Mak's drag force, which is dependent upon the permeability of the canalicular wall and relative flow velocities in the two compartments. This dual model of fluid flow in bone requires further study and experiment to better understand and quantify the critical parameters of such a model.

References

1. Yasuda, I., Piezoelectricity of living bone, *J. Kyoto Pref. Univ. Med.,* 53, 325, 1953.
2. Fukada, E. and Yasuda, I., On the piezoelectric effect of bone, *J. Phys. Soc. Jpn.,* 10, 1158, 1957.
3. Bassett, C. A. L. and Becker, R. O., Generation of electrical potentials by bone in response to mechanical stress, *Science,* 137, 1063, 1962.
4. Bassett, C. A. L., Biologic significance of piezoelectricity, *Calcif. Tissue Int.,* 1, 252, 1968.
5. Becker, R. O., Bassett, C. A. L., and Bachman, C. H., Bioelectric factors controlling bone structure, in *Bone Biodynamics International Symposium,* Frost, H. M., Ed., Little, Brown, Boston, 1964, 209.
6. Brighton, C. T., Current concepts review: the treatment of non-unions with electricity, *J. Bone Joint Surg.,* 63A, 847, 1981.
7. Wolff, J., *Das Gesetz der Transformation der Knochen,* A. Hirschwold, Berlin, 1892.
8. Anderson, J. and Ericksson, C., Electrical properties of wet collagen, *Nature,* 218, 166, 1968.
9. Anderson, J. and Ericksson, C., Electrical properties of dry and wet bone, *Nature,* 227, 166, 1970.
10. Mumford, J. M. and Newton, A. V., Transduction of hydrostatic pressure to electric potential in human dentin, *J. Dent. Res.,* 51, 1503, 1969.
11. Cignitti, M., Figura, F., Marchetti, M., and Salleo, A., Electrokinetic effects in mechanoelectrical phenomenology of the bone, *Arch. Fisol.,* 68, 232, 1970.
12. Grodzinsky, A. J., Electromechanical and physiochemical properties of connective tissues, *CRC Crit. Rev. Biomed. Eng.,* 9, 133, 1983.
13. Lee, R. C., Frank, E. H., Grodzinsky, A. J. and Roylance, D. K., Oscillatory compressional behavior of articular cartilage and its associated electromechanical properties, *J. Biomech.,* 103, 280, 1981.
14. Lotke, P. A., Black, J., and Richardson, S., Electromechanical properties in human articular cartilage, *J. Bone Joint Surg.,* 56A, 1040, 1974.
15. Mow, V. C., Kuei, S. C., Lai, W. M., and Armstrong, C. G., Biphasic creep and stress relaxation of articular cartilage in compression: theory and experiments, *J. Biomech. Eng.,* 102, 73, 1980.
16. Gross, D. and Williams, W. S., Streaming potential and the electromechanical response of physiologically moist bone, *J. Biomech.,* 15, 227, 1982.
17. Pienkowski, D. and Pollack, S. R., The origin of stress generated potentials in fluid saturated bone, *J. Orthop. Res.,* 1, 30, 1983.

18. Kowalchuk, R. M. and Pollack, S. R., Stress generated potentials in bone: effects of bone fluid composition and kinetics, *J. Bone Joint Surg.,* 11, 874, 1983.
19. Burr, A. J., Measurement of the dynamic piezoelectric properties of bone as a function of temperature and humidity, *J. Biomech.,* 9, 495, 1976.
20. Maeda, H., Tsuda, K., and Fukada, E., The dependence on temperature and hydration of piezoelectric, dielectric and elastic constants of bone, *Jpn. J. Appl. Phys.,* 15, 2333, 1976.
21. Marino, A. A., Becker, R. O., and Bachman, C. H., Dielectric determination of bound water of bone, *Phys. Med. Biol.,* 12, 367, 1967.
22. Petrov, N., On the electromechanical interaction in physiologic wet bone, *Bulg. Acad. Sci. Biomech.,* 2, 43, 1975.
23. Johnson, M. W., Behavior of fluid in stressed bone and cellular stimulation, *Calcif. Tissue Int.,* 36, S72, 1984.
24. Johnson, M. W., Chakkalakal, D. A., Harper, R. A., and Katz, J. L., Comparison of the electromechanical effects in wet and dry bone, *J. Biomech.,* 13, 437, 1980.
25. Johnson, M. W., Chakkalakal, D. A., Harper, R. A., Katz, J. L., and Rouhana, S. W., Fluid flow in bone in vitro, *J. Biomech.,* 15, 881, 1982.
26. Maeda, H. and Fukada, E., Effect of water on piezoelectric, dielectric and elastic properties of bone, *Biopolymers,* 21, 2055, 1982.
27. Nomura, S., Hiltner, A., Lando, J. B., and Bear, E., *Biopolymers,* 16, 231, 1977.
28. Tomaselli, V. P. and Shamos, M. H., *Biopolymers,* 17, 2799, 1973.
29. Black, J. and Mattson, R. U., Relationship between porosity and mineralization in the haversian osteon, *Calcif. Tissue Int.,* 34, 332, 1982.
30. Black, J., Mattson, R. U., and Korostoff, E., Haversian osteons: size, distribution, internal structure, and orientation, *J. Biomed. Mater. Res.,* 8, 299, 1974.
31. Morris, M. A., Lopez-Curto, J. A., Hughes, S. P. F., An, K. N., Bassingthwaighte, J. B., and Kelly, P. J., Fluid spaces in canine bone and marrow, *Microvasc. Res.,* 23, 188, 1982.
32. Kelly, P. J., Pathways of transport in bone, in *Handbook of Physiology. The Cardiovascular System,* Shepherd, J. T. and Abboud, F. M., Eds., sect. 2, Vol. III, American Physiological Society, Bethesda, MD, 1983, 371.
33. Eriksson, C., Electrical properties of bone, in *Biochemistry and Physiology of Bone,* Vol. IV, Bourne, G. H., Ed., Academic Press, New York, 1976.
34. Chakkalakal, D. A., Johnson, M. W., Harper, R. A., and Katz, J. L., Dielectric properties of fluid saturated bone, *IEEE Trans. Biomed. Eng.,* BME-27, 95, 1980.
35. Kosterich, J. D., Foster, K. R., and Pollack, S. R., Dielectric permitivity and electrical conductivity of fluid saturated bone, *IEEE Trans. Biomed. Eng.,* BME-30, 81, 1983.
36. Kosterich, J. D., Foster, K. R., and Pollack, S. R., Dielectric properties of fluid saturated bone: effect of variations in conductivity of immersion fluid, *IEEE Trans. Biomed. Eng.,* BME-31, 369, 1984.
37. Pollack, S. R., Salzstein, R., and Pienkowski, D., Streaming potentials in fluid-filled bone, *Ferroelectrics,* 60, 297, 1984.
38. Otter, M. W., Dell, D. S. G., Kadaba, M. P., and Cochran, G. V. B., Quantitative comparison between streaming potentials in bone using 0.157 *M* NaCl and Hank's balanced salt solutions, *Trans BRAGS,* 7, 7, 1987.
39. Berretta, D. and Pollack, S. R., Ion concentration effects on the zeta potential of bone, *J. Orthop. Res.,* 4, 337, 1986.
40. Kowalchuk, R. M., Pollack, S. R., Ducheyne, P., and King, L. A., Particle microelectrophoresis of calcium-deficient hydroxyapatite, *J. Biomed. Mater. Res.,* 27, 783, 1993.
41. Neuman, W. F., The milieu interieur of bone: Claude Bernard revisited, *Fed. Proc.,* 28, 1846, 1969.
42. Otter, M. W., Goheen, S., and Williams, W. S., Streaming potentials in chemically modified bone, *J. Orthop. Res.,* 6, 346, 1990.
43. Guzelsu, N. and Walsh, W. R., Streaming potential of intact wet bone, *J. Biomech.,* 23(7), 673, 1990.

44. McEllaney, J. H., Charge distribution on the human femur due to load, *J. Bone Joint Surg.,* 49A, 1561, 1967.
45. Starkebaum, W., Pollack, S. R., and Korostoff, E., Microelectrode studies of stress generated potentials in four point bending of bone, *J. Biomed. Mater. Res.,* 13, 729, 1979.
46. Iannacone, W., Korostoff, E., and Pollack, S. R., Microelectrode studies of stress generated potentials obtained from uniform and non-uniform compression of human bone, *J. Biomed. Mater. Res.,* 13, 753, 1979.
47. Cochran, G. V. B., Pawluk, R., and Bassett, C. A. L., Electromechanical characteristic of bone under physiologic moisture conditions, *Clin. Orthop. Relat. Res.,* 58, 249, 1968.
48. Black, J. and Korostoff, E., Strain-related potentials in living bone, *Ann. N.Y. Acad. Sci.,* 238, 95, 1974.
49. Lanyon, L. E. and Hartman, W., Strain related electrical potentials recorded *in vitro* and *in vivo, Calcif. Tissue Res.,* 22, 315, 1977.
50. Salzstein, R. A. and Pollack, S. R., Electromechanical potentials in cortical bone, II. Experimental analysis, *J. Biomech.,* 20(3), 271, 1987.
51. Salzstein, R. A., Pollack, S. R., Mak, A. F. T., and Petrov, N., Electromechanical potentials in cortical bone. I. A continuum approach, *J. Biomech.,* 20(3), 261, 1987.
52. Otter, M. W., Palmieri, V. R., Wu, D. D., Seiz, K. G., MacGinitie, L. A., and Cochran, G. V. B., A comparative analysis of streaming potentials *in vitro* and *in vivo, J. Orthop. Res.,* 10, 710, 1992.
53. Otter, M. W., Wu, D. D., Beiber, W. A., Seiz, K. G., and Cochran, G. V. B., Alterations of streaming potentials in intact canine tibiae by vascular perfusion with specific ionic solutions: a pilot study, *Electro-Magneto Biol.,* 12(2), 85, 1993.
54. Otter, M. W., Wu, D. D., Beiber, W. A., and Cochran, G. V. B., Intraarterial protamine sulfate reduces the magnitude of streaming potentials in living canine tibia, *Calcif. Tissue Res.,* 53, 411, 1993.
55. Otter, M. W., Palmieri, V. R., and Cochran, G. V. B., Transcortical streaming potentials are generated by circulatory pressure gradients in living canine tibia, *J. Orthop. Res.,* 8, 119, 1990.
56. Pollack, S. R., Petrov, N., Salzstein, R., Brankov, G., and Blagoeva, R., An anatomical model for streaming potentials in osteons, *J. Biomech.,* 17, 627, 1984.
57. Petrov, N., Pollack, S., and Blagoeva, R., A discrete model for streaming potentials in osteons, *J. Biomech.,* 22(6/7), 517, 1989.
58. Armstrong, G., Lai, W. M., and Mow, V. C., An analysis of the unconfined compression of articular cartilage, *J. Biomech. Eng.,* 106, 165, 1984.
59. Scheidegger, A. E., *The Physics of Flow through Porous Media,* The University of Toronto Press, Toronto, 1974.
60. Holmes, J. M., Davies, D. H., Meath, W. J., and Beebe, R. A., Gas adsorption and surface structure of bone mineral, *Biochemistry,* 3, 2019, 1964.
61. Weinbaum, S., Cowin, S. C., and Zeng, Y., Excitation of osteocytes by mechanical loading-induced bone fluid shear stresses, *J. Biomech.,* 27, 339, 1994.
62. Cowin, S. C., Weinbaum, S., and Zeng, Y., A case for the bone canaliculi as the anatomical site of strain generated potentials, *J. Biomech.,* 28, 1281, 1995.
63. Scott, G. C. and Korostoff, E., Oscillatory and step response to electromechanical phenomena in human and bovine bone, *J. Biomech.,* 23, 127, 1990.
64. Mak, A. F. T., Huang, D. T., Zhang, J. D., and Tong, P., Deformation-induced hierarchical flows and drag forces in bone canaliculi and matrix microporosity, *J. Biomech.,* 30, 11, 1997.
65. Keanini, R. G., Roer, R. D., and Dillaman, R. M., A theoretical model of circulatory interstitial fluid flow and species transport within porous cortical bone, *J. Biomech.,* 28, 901, 1995.
66. Cooper, R. R., Milgram, J. W., and Robinson, R. A., Morphology of the osteon, *J. Bone Joint Surg.,* 48-A, 1239, 1966.
67. Qin, L., Mak, A. T. F., Chang, L. K., and Chan, K. M., Fluid movement in cortical bone in goats, *Anat. Rec.,* 255, 380–387, 1999.

68. Dillaman, R. M., Roer, R. D., and Gray, D. M., Fluid movement in bone: theoretical and empirical, *J. Biomech.,* 24, 163, 1991.
69. Montgomery, R. J., Sutker, B. D., Bronk, J. T., Smith, S. R., and Kelly, P. J., Interstitial fluid flow in cortical bone, *Microvasc. Res.,* 35, 295, 1988.
70. Knothe Tate, M. L., Niederer, P., and Knothe, U., In vivo tracer transport through the lacunocanalicular system of rat bone in an environment devoid of mechanical loading, *Bone,* 22, 107, 1998.
71. Zeng, Y., Cowin, S. C., and Weinbaum, S., A fiber matrix model for fluid flow and streaming potentials in the canaliculi of an osteon, *Ann. Biomed. Eng.,* 22, 280, 1994.
72. Piekarski, K. and Munro, M., Transport mechanism operating between blood supply and osteocytes in long bones, *Nature,* 269(5623), 80, 1977.
73. Pollack, S. R., Salzstein, R., and Pienkowski, D., The electric double layer in bone and its influence on stress-generated potentials, *Calcif. Tissue Res.,* 36, S77, 1984.
74. Reinish, G. B. and Nowick, A. S., Piezoelectric properties of bone as functions of moisture content, *Nature,* 253, 626, 1975.

25

The Intrinsic Permeability of Cancellous Bone

Yves P. Arramon
Parallax Medical, Inc.

Eric A. Nauman
Tulane University

25.1 Introduction

Porous media are those materials that consist of a solid matrix and interconnected void spaces through which fluid is able to flow. The *permeability* of such a material is a physical property that measures the ability of a fluid to filter through the medium. The motion of fluids through cancellous bone, in particular, is of interest for a variety of clinical and biomechanical reasons. Clinically, Hui et al. (1996) showed that the fluid conductance of cylindrical trabecular bone grafts was the best predictor of their clinical success as scaffolds in the rabbit tibial diaphysis. In addition, medical imaging techniques such as ultrasound and magnetic resonance imaging are affected by the same microstructural properties that affect the permeability (Grimm and Williams, 1993; Williams, 1992). The viscous interaction between the marrow and trabeculae of cancellous bone has been suggested as a possible mechanism by which the epiphysis may hydraulically stiffen when dynamically loaded (Kafka, 1983; Ochoa et al., 1991a,b; 1997; Simkin et al., 1985). And with respect to the design of total joint replacements, Beaudoin et al. (1991) hypothesized that the ability of polymethylmethacrylate (PMMA) to flow into the surrounding trabecular bone affects the structural integrity of the bone–prosthesis interface.

There is an abundant literature relating to fluid flow through a porous media, but most of this work caters to the soil mechanics and petrology interests. The purpose of this chapter is not to provide an exhaustive treatise on the various models of flow through porous media but rather to clarify the various terms, theories, and conventions used in the study of the permeability within the context of fluid flow through cancellous bone. Of the many theories that have been proposed to predict the permeability of porous media from other material microstructural properties, only those appropriate to this narrow context will be discussed. For a more general text on the various models of flow through porous media, the reader is advised to refer to publications dedicated to this subject such as Bear (1988), Dullien (1992), and Scheidegger (1974).

0-8493-9117-2/01/$0.00+$.50

25.2 Permeability: Darcy's Law

In the mid-19th century Henri Philibert Gaspard Darcy (1803–1858) was contracted by the city of Dijon (France) to design and oversee the construction of its water distribution network. In 1856, Darcy published a report of this work (Darcy, 1856) believing that "it would be of some use to those engaged in similar problems." As part of the study, but not its main focus, Darcy included several notes in an appendix, one of which concerns the filtration of water through sands. It is in this note (Darcy, 1856) that Darcy first states what would thereafter be known as Darcy's law of fluid flow through porous media,

$$Q = \frac{Ks}{e}[H + e + H_0], \tag{25.1}$$

where Q is the flow rate in (dimension L^3T^{-1}), s is the cross-sectional area of the sand basin in (L^2), e is the thickness of the sand layer in (L), H is the gauge pressure due to the water above the sand bed (in units of height of water, L) and H_0 is the *vacuum* (L) created by the water underneath the sand bed as it is drawn out of the apparatus (Fig. 25.1). The remaining term K is described by Darcy as "a coefficient depending on the nature of the sand," (Darcy, 1856, page 570) and would thereafter be referred to as the *permeability* of the sand (LT^{-1}).

As a unit the bracketed term in Eq. 25.1 defines the pressure differential across the filter so that the modern treatment of this equation is usually given by

$$Q_A = K\frac{\Delta H}{\Delta L}. \tag{25.2}$$

In this case $\Delta H/\Delta L$ is a measure of the average pressure gradient over the region of interest (in terms of height of water per unit length; dimension unity). Q_A is the volumetric flow rate per unit cross-sectional area (LT^{-1}) and represents the velocity of a fluid front across the porous medium and has alternately been referred to as the *seepage velocity*, *filter velocity*, or *velocity of percolation*.

When Darcy stated that the permeability depends on the nature of the sand, he did not consider any fluid but water. Clearly, however, any relationship between the flow rate of a fluid within a medium and the pressure gradient necessary to induce such a flow must include the properties of both the medium and the fluid. By the mid-1930s (Hubbert, 1940; Nutting, 1927) it had been generally accepted that a more appropriate form of Darcy's permeability constant should be

$$K = \frac{k\rho g}{\mu}, \tag{25.3}$$

where K is hereafter referred to as the *hydraulic conductivity* (LT^{-1}) to differentiate it from k, the"specific" or"intrinsic" permeability of the porous medium (L^2) and μ is the dynamic viscosity of the fluid (FTL^{-2} or $ML^{-1}T^{-1}$). Alternatively, one may write, $K = kg/\nu$, where ν is the kinematic viscosity (L^2T^{-1}).

Finally, when combining gravity and the fluid density with the nondimensional pressure gradient of Eq. 25.2, Eq. 25.2 is rewritten in the form

$$Q_A = \frac{k}{\mu}\frac{\Delta P}{\Delta L}. \tag{25.4}$$

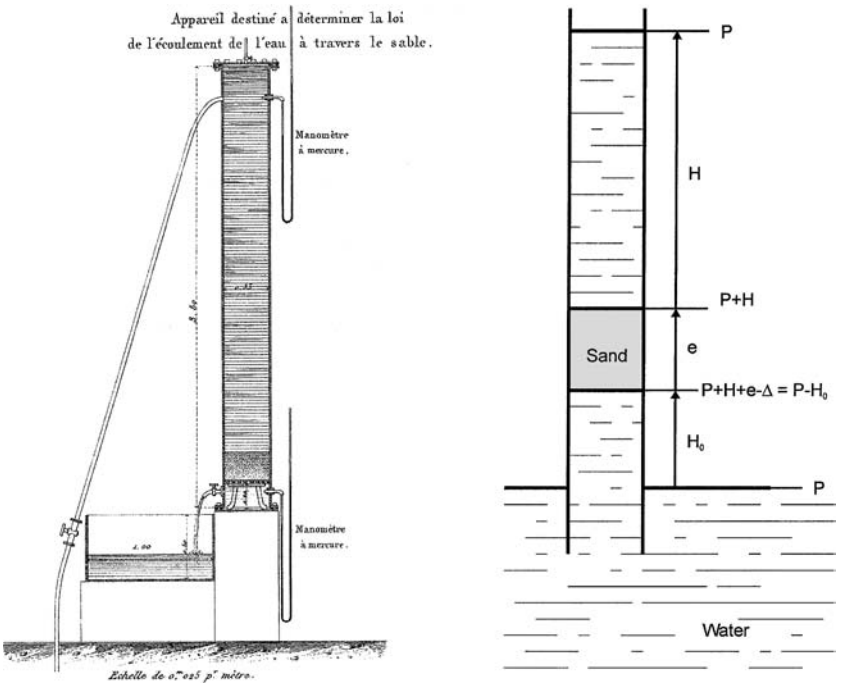

FIGURE 25.1 A reproduction of the original apparatus used by Darcy to validate his "law of flow of water through sands" along with a schematic representation of its functioning. Two mercury pressure gauges measured the pressures at the inlet and outlet of the apparatus. Water was allowed to flow from the top of the apparatus through a bed of sand of known thickness and out into a basin of known volume. The required water to fill the basin was timed to provide a measure of the flow rate. In the schema, P is the atmospheric pressure (in units of height of water), H is the pressure due to the water above the sand bed, e is the thickness of the sand bed, Δ is the pressure drop due to the sand, and H_0 is the vacuum produced by the water as it flows out of the apparatus. In Darcy's equation, $Q = (ks/e)\ [H + e + H_0]$, the bracketed term is the pressure drop Δ of the schema, s is the surface area of the sand bed, and k is the permeability of the sand. Darcy had originally discovered the same linear relationship between the pressure differential and the flow rate of water through tubes of small diameter when the water velocity did not exceed 10 to 11 cm/s (Reynolds, 1883).

In this form the pressure gradient $\Delta P/\Delta L$ has a dimension (FL^{-3}), and the significance of the intrinsic permeability k remains the same: it is a parameter independent of the fluid properties, a function of the porous medium alone. In this form the combined term k/μ is the "coefficient of permeability κ" employed in the bone poroelasticity field equation described by Cowin (1999).

Although Darcy's law was limited to unidirectional flow, the relationship can naturally be extended to three-dimensional flow and can accommodate anisotropy as well. Scheidegger (1974) and Bear (1988) offer detailed discussions on this extension. In general, Darcy's law for a three-dimensional anisotropic medium can be written as

$$Q_A = \frac{1}{\mu} k \nabla p \quad \text{or} \quad Q_{A_i} = \frac{1}{\mu} k_{ij} \frac{\partial p}{\partial x_j} \quad (i, j = 1, 2, 3), \tag{25.5}$$

where Q_A is the *area-averaged flow rate vector*, ∇p *is the vector pressure gradient*, and permeability, k, is a second-rank tensor.

25.2.1 Units of Permeability

The common unit for intrinsic permeability in a centimeter-gram-second (c.g.s.) system is the cm^2. Unfortunately, this has not been universally adopted. To provide comparisons between the various published permeabilities it is best to convert all units into c.g.s. The petroleum industry defines 1 *darcy* as the constant that relates the flow of 1 cm^3/s of a fluid of 1 centipoise viscosity through a cross-sectional area of 1 cm^2 over a distance of 1 cm with a pressure difference of 1 atm. So that the implied intrinsic permeability in (dimension L^2) is

$$k = 1 \text{ darcy} \equiv 9.8692 \times 10^{-9} \text{cm}^2.$$

In groundwater hydrology, permeability is defined as the velocity of percolation of water per unit drop in hydraulic head. So that,

$$k = 1 \text{ cm/s of water (at } 20°\text{C)} \equiv 1.02 \times 10^{-5} \text{cm}^2,$$

or occasionally also in meters per day,

$$k = 1 \text{ m/d (meters per day)} \equiv 8.814 \times 10^{-3} \text{cm}^2.$$

25.2.2 Limits of Validity

25.2.2.1 Upper Limit to Darcy's Law

In his note, Darcy mentions having found the same relationship between flow rate and pressure drop when investigating the flow of water through "tubes of small diameter" when the speed of the water was no more than "10 to 11 centimeters per second." This is the first suggestion that Darcy's law for porous media may be valid only for low flow rates. But this result was not fully appreciated until 1883 when Osborne Reynolds (1883) showed that the transition from a laminar to a turbulent flow of a fluid in a pipe depends upon the magnitude of the *Reynolds number*:

$$\text{Re} = \frac{\rho \bar{V} D}{\mu}, \tag{25.6}$$

where $\bar{V}$ is the average velocity (LT^{-1}) of the fluid, D is the diameter of the pipe, and ρ and μ are the fluid density and dynamic viscosity, respectively. In general, the transition from laminar to turbulent flow occurs for Re somewhere between 2000 and 4000.

A modified version of Eq. 25.6, which includes the porosity of the medium, has been suggested (Greenkorn, 1983).

$$\text{Re} = \frac{2D\bar{V}\rho}{3\mu(1-\phi)}, \tag{25.7}$$

where D is the effective particle diameter, $\bar{V}$ is the seepage velocity, ρ the fluid density, μ the fluid viscosity, and ϕ the specimen porosity. It should be noted that the 2/3 constant is almost always dropped from the relation. For granular material the particle is simplified to a sphere. Thus, with $D_{\text{sphere}} = 6V_{\text{sphere}}/S_{\text{sphere}}$, the characteristic dimension D for packed spheres is then

$$D = 6\frac{\text{Vol}_{\text{total}}(1-\phi)}{S_{\text{solid}}} = 6\frac{(1-\phi)}{S_v}, \tag{25.8}$$

where $\text{Vol}_{\text{total}}$ is the volume (L^3) of the sample porous medium, ϕ is its porosity, S_{solid} is the total surface (L^2) of the solid matrix, and S_v is the *specific surface* (L^{-1}) of the porous medium. By substituting the relationship for characteristic dimension D into Eq. 25.7, a relationship for Re is obtained in a form that replaces the characteristic dimension D of Eq. 25.6 by the inverse of the *specific surface*. That is to say,

$$\text{Re} = 4\frac{\rho\bar{V}}{\mu S_v}. \tag{25.9}$$

Although such a formulation of Re was developed from a packed-spheres model, it can be employed for cancellous bone. In this case only the functional form of S_v for cancellous bone needs to be determined from standard stereological measures (Underwood, 1981).

Although Darcy's law has been shown to be invalid for high flow rates, there is no"universal" critical Reynolds number for porous media. Indeed, investigators have suggested critical Re as low as 0.1 and as high as 75 (Bear, 1988; Scheidegger, 1974). Part of the uncertainty is due to the lack of definition for the characteristic length D for a porous material. For the specific case of granular material it is customary to assume that D is the average grain diameter. But this is for convenience rather than any solid geometric reasoning.

Cancellous bone has never been included in a study of critical Re, although Nauman et al. (1999) showed that for their choice of flow rates the pressure drop was a linear function of velocity. Their results suggest that the critical Re depends primarily on flow direction relative to the principal trabecular orientation. However, one must also consider variations with anatomic site, apparent density, and age, as well as differences in the experimental setup between investigators. Taken together, these variations would presumably frustrate any attempts at repeatability of the critical flow rate.

25.2.2.2 Lower Limit to Darcy's Law

It has been suggested that there may be a pressure gradient below which little or no fluid flow occurs. As such this must also be considered non-Darcian behavior. Bear (1988) offers a discussion on this lower limit and suggests that this behavior be attributed to the rheological non-Newtonian behavior of the fluid. It is clear that this condition did not exist for any of the permeability experiments reviewed for this chapter since a measurable flow must have always occurred. However, this is an important consideration if the ultimate goal is to predict the poroelastic behavior of marrow-saturated cancellous bone. If the movement of marrow is so slight that the character of the marrow (pressure gradient)/(flow) may not be Darcian, then alternatives to Darcy's law may have to be considered.

25.2.2.3 Other Non-Darcian Fluid Flows

In addition to those cases where the flow regime is outside the creeping regime, it is possible for the flow of the fluid not to satisfy laminar flow theory. Laminar flow theory requires that the fluid velocity at the fluid–solid interface be zero and the inertial effects are negligible. It is possible that the flow of marrow through the trabeculae is more akin to plug flow past an obstruction rather than the model suggested by the pipe flow analogy. For this case, alternative constitutive relations must be developed. Nevertheless, for the purpose of determining the intrinsic permeability of cancellous bone using a Darcy-type experiment, the following guidelines are offered:

1. The size of the specimen must be large enough to allow the microscopic heterogeneity of the trabeculae to be ignored, but small enough to avoid including macroscopic variation of the cancellous bone density.
2. The cancellous bone specimen must be free of any organic material that could obstruct the flow of the fluid.
3. A fluid of well-determined and consistent viscosity must be employed. If temperature affects this viscosity, then it must be controlled and/or measured.

4. The fluid flow should be varied from low to high rates until the (pressure gradient)/(flow rate) relationship significantly deviates from linear, following which only the data within the Darcian regime are considered.

25.3 Permeability Theories

That the permeability is some function of the distribution, shape, and "connectedness" of the voids is obvious but the functional relationship itself is not. Permeability theories are an attempt to characterize this material property in terms of other material and geometric properties of the medium. These theories usually involve assuming a model of a porous material for which the fluid flow and all geometric properties can be determined analytically, to measure the flow through a natural porous media and to correlate the actual and theoretical flows with the natural and artificial geometric properties. In the next sections, some of these theories will be introduced and their applications to cancellous bone discussed.

25.3.1 Hydraulic Radius-Based Theories

25.3.1.1 Assumptions

The hydraulic radius theories are based on capillaric models in which the porous medium is assumed to be "hydraulically equivalent" to a bed of thin tubes. The concept of the "hydraulic radius" is a consequence of the observation that the permeability has the dimensions of area or length squared. It is this length that is termed the hydraulic radius and a possible measure for this length might be the specific surface of the porous medium. These theories assume that the permeability relation has the basic form,

$$k = c\frac{m^2}{F(\phi)}, \tag{25.10}$$

where m is the hydraulic radius (L), $F(\phi)$ is a porosity factor, and c is a dimensionless correlation constant. The premises of hydraulic radius theories are as follows:

- None of the pores are isolated or sealed off.
- Pores are distributed randomly.
- Pores are reasonably uniform in size.
- Porosity is not too high.
- No deviation from the no-slip condition at fluid–solid interfaces.
- Fluid motion occurs like motion through a batch of capillaries.

These assumptions have been discussed by Carman (1956) and others (Bear, 1988; Dullien, 1992; Scheidegger, 1974).

25.3.1.2 Kozeny's and Related Models (Carman's Modification)

The *Kozeny* equation (Carman, 1956) and its variants are the most widely accepted of the hydraulic radius theories. Kozeny's equation is given by

$$k = \frac{c\phi^3}{S_v^2}, \tag{25.11}$$

where S_v is the specific surface of the porous medium (L^{-1}) and c is a correlation constant called the *Kozeny constant*. An extension of the Kozeny equation introduces a *tortuosity* factor, which adjusts the

straight capillary model, from which the Kozeny equation was determined, to one in which the capillaries are bent. In this case the permeability is written as

$$k = c\,\frac{\phi^3}{TS_v^2}. \tag{25.12}$$

The argument for the adjustment is that the actual flow path may be T times longer for a natural material than for the straight capillary model.

Carman (1956) later introduced a modification of the Kozeny equation, which is now known as the *Kozeny–Carman* relation

$$k = \frac{\phi^3}{5S_0^2(1-\phi)^2}, \tag{25.13}$$

where S_0 is Carman's *specific* surface (i.e., the internal surface of the pores per unit volume of the solid matrix). In his 1956 work Carman specifies the limitations of the Kozeny–Carman equation (Carman, 1956, page 13):

> It assumes that the range of pore shapes is such that k_0 [the *Kozeny constant*] is reasonably constant, and that the tortuosity is also not very susceptible to variations in pore geometry. The evidence … shows that this seems to be valid for unconsolidated media with a random pore structure, but not for flow along parallel-oriented fibers.

25.3.1.3 Anisotropic Extension of Kozeny-Carman Relation

Sullivan (Bear, 1988) introduced an orientation factor θ, which is defined as"the average value of the square of the angle between a normal to the walls forming the microscopic flow channel and the macroscopic direction of flow" (Scheidegger, 1974, page 129). The resulting formula is

$$k = \frac{c\theta\phi^3}{S_0^2(1-\phi)^2}. \tag{25.14}$$

The relationships described above characterize the permeability in terms of the porosity and the specific surface distribution. None of these relations can account for the variety of void shapes that cancellous bone displays. To what extent these variations affect the permeability is difficult to predict. But certainly porous cancellous bone does not "look" like the "packed powders" for which these relations were developed. Therefore, it is possible that the hydraulic radius models are inappropriate for cancellous bone; that other models might be more suitable.

25.3.2 Drag Theories

A different approach to the determination of permeability is that of the *drag* theories. Unlike the hydraulic radius theories for which the pressure drop is due to the friction of the fluid along the channel wall, the drag theories presume that the pressure drop is due to obstacles in the path of the fluid. Such models employ regularly arranged obstacles such as spheres and cylinders. The drag contributed by the wall of these obstacles is then estimated from the Navier–Stokes equations. The end result is a constitutive equation for the apparent permeability of a network of these regularly arranged objects. A number of these models have been investigated by Happel and Brenner (1983). Generally these models assume that:

1. The walls of the pores are treated as obstacles to an otherwise straight flow of the fluid;
2. There is no deviation from the no-slip condition at fluid–solid interfaces;
3. The seepage velocity must be in the Darcian regime.

Of particular interest to the subject of this chapter are "fiber" drag models. These models assume that the obstacles to flow are regularly arranged cylinders.

The approximate drag force per unit length of a single fiber surrounded by similar fibers all oriented in the direction of the flow is given as,

$$f = 4\pi\mu v_p, \tag{25.15}$$

where v_p is the pore velocity and equal to (Q_A/ϕ) (Scheidegger, 1974). If one lets n be the number of fibers per unit length in a unit volume of material, then, for an isotropic medium, there would be $n/3$ filaments arrayed in each of the three orthogonal directions, so that the total drag force per unit volume due to the $n/3$ filaments parallel to the flow is the pressure drop per unit length in that direction,

$$\frac{\Delta p}{L} = 4\pi \frac{n}{3} \mu v_p. \tag{25.16}$$

Similarly, the drag force f due to a cylinder perpendicular to the flow is given by

$$f = \frac{4\pi}{2 - \ln \mathrm{Re}} \mu v_p, \tag{25.17}$$

where the local Reynolds number is given by Eq. 25.6 with the characteristic dimension D defined as the fiber diameter.

The pressure drop per unit length due to *each* of the two filament sets orthogonal to the flow direction is then given by

$$f = \frac{4\pi n}{3(2 - \ln \mathrm{Re})} \mu v_p. \tag{25.18}$$

By superposition the total pressure drop per unit length due to a completely random distribution of fibers is then given by

$$\frac{\Delta p}{L} = \frac{4\pi n}{3} \frac{4 - \ln \mathrm{Re}}{2 - \ln \mathrm{Re}} \mu v_p. \tag{25.19}$$

Letting ρ_p be the apparent density of the porous (fibrous) medium, and ρ_{fiber} be the density of the fiber material, and δ be the average fiber diameter, the apparent density is then given by

$$\rho_p = \frac{\pi}{4}\delta^2 \, n\rho_{\text{fiber}}. \tag{25.20}$$

The velocity v_p can substituted by Q_A/ϕ where Q_A is the flow rate per unit area. In addition, the definition of the porosity gives $1 - \phi = \rho_p/\rho_{\text{fiber}}$. From Darcy's equation and the substitutions described above, one can then write the permeability as

$$k = \frac{3}{16} \frac{\phi\delta^2}{1 - \phi} \frac{2 - \ln\left(\frac{\delta Q_A \rho}{\mu\phi}\right)}{4 - \ln\left(\frac{\delta Q_A \rho}{\mu\phi}\right)}. \tag{25.21}$$

Unfortunately, a consequence of Iberall's drag theory is that the permeability is dependent on the flow rate Q_A. This has a profound significance since it implies that the relationship between fluid flow rate and pressure gradient is not linear.

25.4 Cancellous Bone Permeability

25.4.1 Problems Associated with the Measurement of Cancellous Bone Permeability

25.4.1.1 Range of Porosity

One problem associated with the measurement of permeability of a specimen of cancellous bone is that this tissue displays a wide range of porosity. The highly porous specimens presents a particular problem that is difficult to circumvent. As was mentioned earlier in the chapter, Darcy's law is applicable only to a range of seepage velocity called the *creeping regime* or *Darcian flow*. This range is characterized by the Reynolds number for porous medium. In the general case of a porous material, the appropriate range for Darcian flow is believed to be $\mathrm{Re} \leq 1$. Using this condition with Eq. 25.9 along with a correlation of bone specific surface with porosity (Martin, 1984), one can obtain the condition on the flow rate q for Darcian flow. When plotted against porosity and assuming water flowing through a cross-sectional area of 1 cm^2 the curve of Fig. 25.2 is obtained. The curve illustrates the reason for concern at high porosities. It can be seen that any valid measurement that uses Darcy's law to determine the permeability of a cancellous bone specimen will require that the flow rates be reduced as porosity increases. This, in

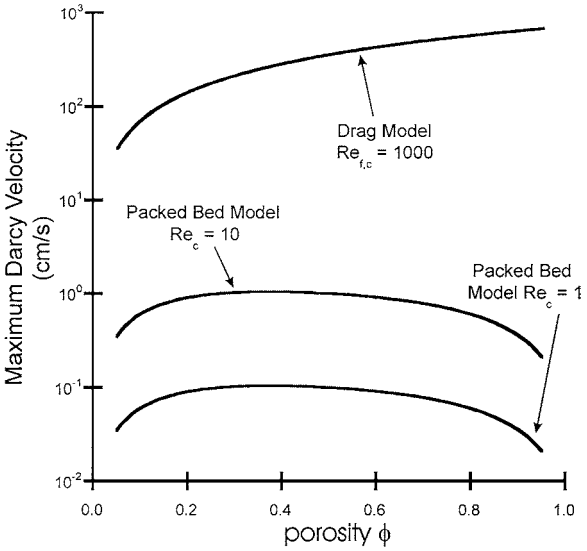

FIGURE 25.2 Darcian flow regime as a function of porosity for a packed-bed model (critical Reynolds number, $\mathrm{Re}_c = 1, 10$) and a fiber drag model ($\mathrm{Re}_c = 1000$). For the packed-bed model, the maximum allowable Darcy velocity for a given Re_c was determined by finding the flow rate of water through a specimen of cancellous bone with a cross-sectional area of 1 cm^2 is determined such that $\mathrm{Re} \leq \mathrm{Re}_c$. This condition along with Eq. 25.9 and a correlation of bone specific surface with porosity (Martin, 1984) produces a condition on the allowable flow rate through the specimen. At high porosities the flow rate must be reduced so as not to exceed Darcian flow. Unfortunately, at high porosity and low flow rates, the measured pressure gradients become exceedingly small. If transverse gradients are also desired they would become unmeasurable even for porosities as low as 60%. For the drag model, the maximum Darcy velocity was calculated so as to ensure that the Reynolds number as given by Eq. 25.6 with a characteristic dimension $D = 140$ μm was less than Re_c. (From Goulet et al., *Trans. Orthop. Res. Soc.*, 17, 159, 1992. With permission.)

turn, implies that the maximum allowable pressure gradients will also be reduced as porosity increases. If, in addition, the pressure gradients transverse to the flow direction are required to determine the anisotropy of the permeability, the magnitudes of these pressure gradients, which are already quite small under ideal conditions, would rapidly become unmeasurable even for porosities as low as 50%. It should be noted, however, that the condition that $\mathrm{Re} \leq 1$ is based on the premise of fluid flowing through packed powders and may not be applicable to cancellous bone. Indeed, for a bed of fibers the critical Re is believed to be approximately 1000 and the maximum Darcy velocity appears to increase with increasing porosity (Fig. 25.2). The nature of the microstructure of cancellous bone may therefore result in a maximum Darcy velocity that lies somewhere between these two extremes.

25.4.1.2 Specimen Size

The size of the specimen must be large enough to allow the microscopic heterogeneity of the trabeculae to be ignored, but small enough to avoid including macroscopic variation of the cancellous bone density. These measurements suggest that a cancellous bone specimen approximately 5 to 8 mm is required for testing. Unfortunately, from the soils and petrology literature, it is clear that permeability experiments were generally conducted on specimens that had a much greater sample/pore size ratio. Specimens of comparable dimensions could never be achieved with cancellous bone. Although it is unclear to what extent this limitation may affect the relevance of permeability measurements for this tissue, it may, in part, explain the wide variation of published results.

25.4.1.3 Shape of Fluid Channel

Intuitive reasoning would suggest that there should be a correlation between the porosity of a material and its permeability. However, previous attempts to correlate these two material properties have failed to produce any convincing results. It has been suggested that this failure is due to the inability of the porosity measure to describe the shape of the voids or channels through which the fluid must filter. In particular, materials that display small cracks such as those found in dried clays may display high permeabilities at very low porosities with very little change in permeability at higher porosities. Materials that display void shapes such as those found in packed powders display low permeabilities at low porosities and varying porosity/permeability relationships at higher porosities. It is reasonable to expect that a better porosity/permeability correlation may be possible with materials displaying the same void shapes.

Histological investigations indicate that cancellous bone displays no such void shape consistency when samples are excised from different species or anatomical sites. Thus, cancellous bone would not lend itself well to porosity/permeability correlation unless it were conducted on samples from the same anatomical site from the same species.

25.4.2 Results of Previous Investigations

The published values of permeability of cancellous bone range over three orders of magnitude and depend strongly on porosity and anatomical site (Fig. 25.3).

The data from each anatomical site and flow direction were fit to a Kozeny–Carman model similar to that employed by Arramon and Cowin (1997). This hydraulic radius-based relationship is of the form:

$$k = \frac{c\phi^{\alpha}}{S_v(\phi)^2}, \tag{25.22}$$

where k is the permeability, ϕ is the porosity, c and α are correlation coefficients, and $S_v(\phi)$ is the specific surface function. The functional form of the specific surface, as reported by Martin (1984), $S_v(\phi)$ is a fifth-order polynomial in porosity ϕ and was empirically determined from a wide variety of species and over a large range of porosity. Thus, Martin reports that an appropriate predictor of specific surface S_v of trabecular bone is given by

$$S_v(\phi) = 323 \cdot \phi - 939 \cdot \phi^2 + 1340 \cdot \phi^3 - 1010 \cdot \phi^4 + 288 \cdot \phi^5 \qquad (\mathrm{l/cm}) \tag{25.23}$$

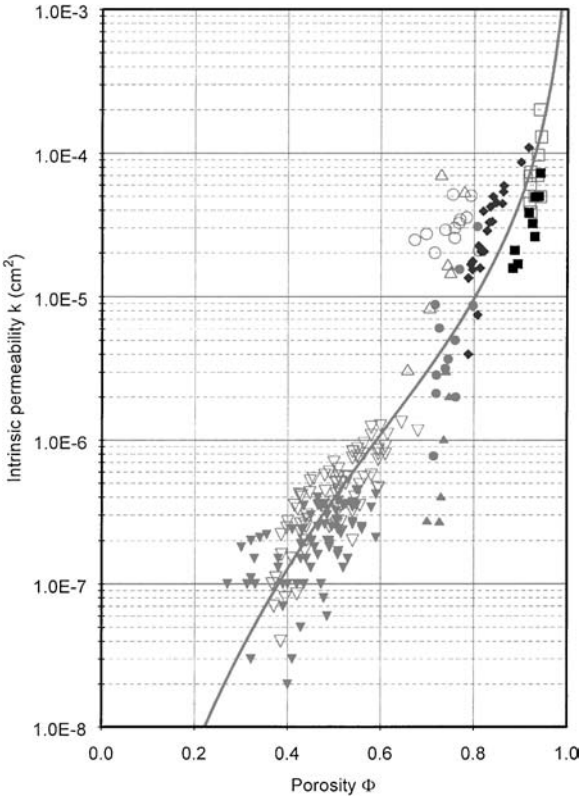

FIGURE 25.3 Intrinsic permeability of human, bovine, and porcine cancellous bone (□ longitudinal human vertebral body, ■ transverse human vertebral body, △ longitudinal human femoral neck, ▲ transverse human femoral neck, ◆ human calcaneus, ○ longitudinal bovine proximal tibia, ● transverse bovine proximal tibia, ▽ longitudinal porcine femur, ▼ transverse porcine femur) and the best fit empirical Kozeny model ($c = 2.592 \times 10^{-2}$, $\alpha = 4.668$, $R^2 = 0.847$). The Kozeny model provides a good fit to the data taken as a whole, but at any given porosity the permeability may range in value by nearly three orders of magnitude.

The Kozeny model (Eq. 25.22) provides a very good fit to the reported values of cancellous bone permeability ($c = 2.592 \times 10^{-2}$, $\alpha = 4.668$, $R^2 = 0.847$). In addition, it can be shown that this model predicts $k = 0$ for $\phi = 0$ and $k \to \infty$ as $\phi \to 1$. This characteristic is necessary for any valid permeability/porosity predictor. It should be noted, however, that this correlation does not explain all the variation in the data. For example, at a porosity of approximately 0.73, the measured permeabilities span three orders of magnitude (Fig. 25.3). This may be due to the highly anisotropic plate structure found in femoral cancellous bone. In the longitudinal direction, the permeability is quite high because the large pores are oriented primarily with the principal trabecular orientation. For flows orthogonal to the principal trabecular orientation, the fluid has to pass over a series of randomly oriented plates, and the permeability is expected to be extremely sensitive to porosity and the precise angle between the flow direction and the normal to the trabecular plates. At high porosities, Iberall's theory provides a reasonable estimate of the permeability assuming a seepage velocity of 3 cm/s, which was within the range tested by Nauman et al. (1999). The advantage of such a model is that it does not, in principle, require a correlation coefficient and can be used to predict permeability based solely on the measured architectural properties of the specimen. But the model is highly nonlinear and clearly very sensitive to the flow rate (Fig. 25.4). Consequently, it should be used with caution.

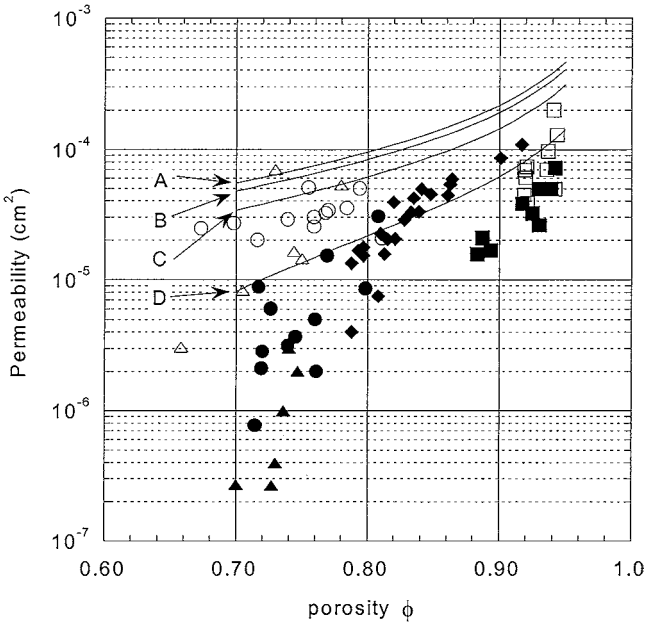

FIGURE 25.4 Comparison of Iberall's theory with an average fiber diameter of 140 μm (Goulet et al., 1992) and seepage velocities of 0.1 (A), 0.3 (B), 1.0 (C), and 3.0 cm/s (D) to experimental permeabilities for cancellous bone from the □ longitudinal human vertebral body, ■ transverse human vertebral body, △ longitudinal human femoral neck, ▲ transverse human femoral neck, ◆ human calcaneus, ○ longitudinal bovine proximal tibia, and ● transverse bovine proximal tibia. The best representation of the data is achieved for a seepage velocity of 3.0 cm/s, which is in the range of values used by Nauman et al. (1999). But the predictions exhibit a strong dependence on flow rate and should be used with caution.

The permeability measurements of Beaudoin et al. (1991) (0.3 to 1.6 $\times$ 10^{-5} cm^2) were not included in the correlation because the apparent densities reported by the authors (600 to 1200 kg/m^3) appear to be much larger than others published for the same anatomical site ($\rho \approx$ 100 to 600 kg/m^3 (Hvid et al., 1989), $\rho \approx$ 300 kg/ m^3 (Linde et al., 1992), $\rho \approx$ 310 kg/ m^3 (Carter and Hayes, 1977)). Furthermore it is not clear that the marrow was removed from the specimen. For the purpose of determining the ability of a fluid to penetrate fresh cancellous bone this experiment was appropriate. However, the differences in rheological behavior between the marrow and the silicon fluid employed in the experiment make the reported permeability inappropriate for the determination of the intrinsic permeability of this tissue.

All permeability measurements with the exception of those of Grimm et al. (1997) were conducted with water. The use of linseed oil by Grimm et al. (1997) may have provided an advantage because linseed oil has a higher viscosity than water and would allow the investigators to reduce the flow rates while maintaining large, easily measurable pressure differentials. Thus, it is easier to ensure that a Darcian flow regime exists at high porosity. Although all published reports assume that Darcian flow conditions existed for their measurements, only Nauman et al. (1999) report having verified a linear relationship between pressure gradient and flow rate.

Based on these results, porosity and architecture are the two most important variables for determining the intrinsic permeability of cancellous bone. As both vary substantially between anatomical sites and, in many cases, within a single anatomical site, there is a need for increased work in this area. The development of architecture-based mathematical models and additional experiments should provide information important to the understanding of hydraulic stiffening, tissue-engineered bone grafts, the design of total joint replacements, and improved medical imaging techniques.

TABLE 25.1 Dynamic Viscosity of Some Fluids of Interest at Near Room Temperature (20°C for nonbiological or *in vitro* for biological fluids) and Near Body Temperature (40°C for nonbiological or *in vivo* at 37°C)

	μ in (centipoise)	
Liquid	*In Vivo* Temperature	*In Vitro* Temperature
Bovine bone marrow[a]	67	—
Water[b]	0.65	1.00
Synovial fluid[c] relative	>300	—
Equine[d] relative at 25°C		(3–29)
Bovine[d] relative		
At 25°C		3.37 (2.84–4.15)
At 20°C		5(2–12)
Human[d]		
At 500/s	>300	
At 1300/s		
Leporine[d]	>300	
Blood[c]	2.3–2.8[c]	3.8–5.7
Plasma[c]	—	1.7–2.4
Serum[c]	1.1–1.2	1.6–2.2
Castor oil[b]	—	650
Ethylene glycol[b]	9.13	19.9
Methyl alcohol[b]	0.450	0.59
Ethyl alcohol[b]	0.834	1.19
Silicon fluid[b]	—	5.8×10^4
Glycerine[b]	—	950

[a] From Bryant et al. (1989) radius epiphyseal at 37°C and 42°C over shear rate range between 7 and 115/s.
[b] From various sources.
[c] Human data from Diem and Lentner (1974). (*Note*: at 20°C in fact implies *in vitro*.)
[d] From Altman and Katz (1961).

25.5 Viscosity

The *viscosity* of a fluid is the material property that determines the rate at which changes in momentum in one part of the fluid are transmitted throughout the bulk medium; see Table 25.1 for values of some fluids. Viscosity was first characterized by Newton who defined the absolute viscosity, μ, as the coefficient relating the applied shear stress $\tau(FL^{-2})$ to the spatial gradient of the velocity du/dy (T^{-1}) such that,

$$\tau = \mu \frac{du}{dy}; \tag{25.24}$$

in this form μ is the dynamic viscosity (FTL^{-2}). The c.g.s. unit of μ is the *poise* or the *centipoise*, where

$$1 \text{ poise} = 10^2 \text{ centipoise} = 1 \text{ dyn s cm}^{-2} = 1 \text{ g cm}^{-1} \text{ s}^{-1}$$
$$= 0.1 \text{ Ns m}^{-2} = 6.720 \times 10^2 \text{ lb ft}^{-1} \text{ s}^{-1}.$$

When the viscosity of a fluid appears in the form $\nu = \mu/\rho$ then ν is called the kinematic viscosity. The c.g.s units of ν are the *stoke* and the *centistoke*, where

$$1\text{stoke} = 1 \text{ cm}^2\text{s}^{-1} = 10^{-4} \text{ m}^2 \text{ s}^{-1} = 1.0764 \times 10^{-3} \text{ ft}^2 \text{ s}^{-1}.$$

The most common of experimental methods for the determination of fluid viscosity fall into three categories: *capillary* or *Ostwald* method, *rotational* or *Couette* method, and *falling ball* method.

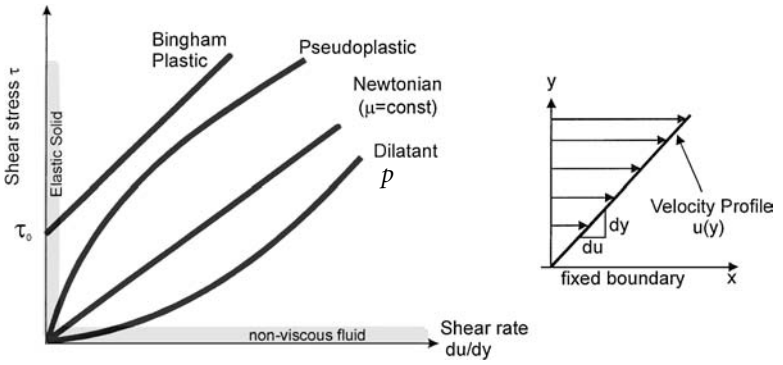

FIGURE 25.5 Illustration of some Newtonian and non-Newtonian fluid behavior. The vertical and horizontal shaded regions represent the extreme case of an elastic solid and an ideal nonviscous fluid, respectively. The shear rate is represented by the fluid velocity gradient near the fixed boundary. In the case of a permeability experiment conducted on cancellous bone, the fixed boundary is the surface of the trabeculae at which point the fluid velocity is assumed to be zero.

Appropriate for large fluid samples, the Ostwald viscometer consists of a thin tube of known diameter and length. The flow rate and pressure gradient can then be used to determine the viscosity of the fluid. The falling ball method uses the Stokes law to relate the viscosity of the fluid to the speed of a polished steel ball as it falls through a tube filled with the fluid. Although this method does not appear to have been employed on biofluids, it has been applied to oils such as linseed oil, which was used by Grimm et al. (1997), to determine the permeability human cancellous bone. For small samples sizes, the Couette viscometer is usually the best choice. This method uses two concentric cylinders, cones, or plates rotating relative to each other to relate the viscosity of the sample to the speed and torque required to overcome the fluid shear stresses. Such a method is uniquely appropriate for the determination of epiphyseal marrow viscosity since collecting large quantities of marrow from these anatomical sites would be difficult. Bryant et al. (1989) successfully used this method to determine the viscosity of epiphyseal bovine marrow (Table 25.1).

In many experimental settings it is assumed that the fluid under consideration obeys Newton's law of viscosity simply because it is a linear relationship and easier to deal with mathematically. In reality, however, many fluids, especially biological fluids such as blood and marrow, obey nonlinear stress–shear rate relations. The most common such *non-Newtonian* models include the *Bingham plastic* model, *pseudoplastic* models, *dilatant* fluids, and viscoelastic fluids (Beaudoin et al., 1991).

Bingham Plastic—A fluid that does not flow until the applied shear stress reaches a yield stress τ_0 (Fig. 25.5). Beyond the yield stress the plot of shear stress vs. velocity gradient is linear. Toothpaste is often used as an example of a Bingham plastic.

Pseudoplastic Fluids—A fluid whose apparent viscosity decreases as the velocity gradient increases (Fig. 25.5). Polymer solutions such as bone cement are common engineering examples of pseudoplastics (Krause et al., 1982). Blood and synovial fluid are also known to exhibit decreasing viscosity with increasing velocity gradients (Fung, 1993; Diem and Lentner, 1974).

Dilatant Fluids—A fluid whose apparent viscosity increases as the velocity gradient increases (Fig. 25.5). Suspensions, such as drilling muds, are typical dilatant fluids.

All of these terms describe the shear rate-dependent behavior of the viscosity. However, some fluids exhibit changes in viscosity because they have been agitated. The following terms refer to the changes the viscosity undergoes over time.

Thixotropic Fluids—Refers to a fluid whose viscosity decreases over time as the fluid flows and recovers if the fluid is left to stand. Gels that lose their consistency when shaken violently but congeal when

allowed to rest are examples of thixotropy. Occasionally the term *shear thinning* is also used to describe this behavior. Bone marrow has been reported to be thixotropic (Bryant et al., 1989; Kafka, 1983; Kafka and Jírová, 1983; Sobotkova et al., 1988).

Rheopectic—Although there is some inconsistency in this definition, it has been occasionally used to describe reverse thixotropy. *Shear thickening* is sometimes used to describe this behavior.

As a general rule the experimental determination of the viscosity of biofluids is complicated by the extraneous factors such as disease and age as well as the heterogeneity of the fluid themselves. For example, diseased synovial fluid exhibits much lower viscosity than healthy fluid (Diem and Lentner, 1974). Although plasma has been reported to behave like a Newtonian fluid, whole blood appears to behave like a pseudoplastic. The rheological behavior of blood is also different in capillaries compared with that in large blood vessels because the scale of the capillaries is nearly that of the blood cells (5 to 10 μm). For bone marrow Bryant et al. (1989) found that the bovine marrow viscosity is 10 to15 times higher in the proximal radius than in the distal and suggested that this may be due to a difference between the composition of the marrow in these two anatomical sites.

Except for synovial fluid and whole blood, there has been relatively little research on the rheological behavior of human biofluids. This is, in part, due to the experimental difficulties mentioned previously but is also due to a lack of concerted will to obtain such data. Until such data are available, the measurements of Bryant et al. (1989) will have to suffice.

25.6 Summary

The intrinsic permeability of cancellous bone plays a key role in the success of bone grafts. It is a factor that influences the effectiveness of certain medical imaging techniques and may play a role in the elastic biomechanical response of this tissue. The concept of permeability is ultimately linked to Darcy's law. This law relates the average velocity of fluid flowing through a porous medium to the pressure gradient necessary to produce such a flow. Many theoretical models have been proposed to predict the permeability from other material and microstructural properties of the porous medium. Two such models may be applicable to cancellous bone: the hydraulic radius and drag models. For the hydraulic radius models, the pressure drop is due to the viscous interaction of the fluid on the boundaries of internal fluid pathways. This approach may be suitable for low-porosity cancellous bone. However, for high-porosity cancellous bone, the concept of internal fluid channels may be irrelevant. In the hydraulic drag approach, the pressure drop is due to obstacles in the path of the fluid. Thus, this approach may be more suitable for the type of cancellous bone found in vertebral bodies. Permeability measurements for any material exhibit a great deal of scatter so it is not surprising that cancellous bone permeability for a particular porosity may differ by several orders of magnitude.

Darcy's law was originally developed for water flowing through sand. Within the context of the experimental measurements of intrinsic permeability, where either water or a light oil is the fluid, the linear relationship between pressure gradient and flow exists as long as a low seepage velocity is maintained. However, other relevant fluids do not exhibit the same Newtonian behavior. For these situations the simple linear relationship between pressure gradient and flow suggested by Darcy's law may not be applicable and a more elaborate constitutive model must employed.

References

Altman, P. L. and Katz, D. D. (1961) *Blood and Other Body Fluids,* Federation of American Societies for Experimental Biology, Washington, D.C.

Arramon, Y. P. and Cowin, S. C. (1997) Hydraulic stiffening of cancellous bone, *Forma,* 12, 209–221.

Bear, J. (1988) *Dynamics of Fluids in Porous Media,* Dover, New York.

Beaudoin, A. J., Mihalko, W. M., and Krause, W. R. (1991) Finite element modelling of polymethylmethacrylate flow through cancellous bone, *J. Biomech.,* 24, 127–136.

Bryant, J. D., David, T., Gaskell, P. H., King, S., and Lond, G. (1989) Rheology of bovine bone marrow, Proceedings of the Institution of Mechanical Engineers. Part H, *J. Eng. Med.,* 203, 71–75.

Carman, P. C. (1956) *Flow of Gases through Porous Media*, Butterworths Scientific Publications, London.

Carter, D. R. and Hayes, W. C. (1977) The compressive behavior of bone as a two-phase porous structure, *J. Bone Joint Surg.,* 59-A, 954–962.

Cowin, S. C. (1999) Bone poroelasticity, *J. Biomech.,* 32, 217–238.

Darcy, H. (1856) *Les fontaines publiques de la ville de Dijon: exposition et application des principes a suivre et des formules a employer dans les questions de distribution d'eau; ouvrage terminé par un appendice relatif aux fournitures d'eau de plusieurs villes au filtrage des eaux et a la fabrication des tuyaux de fonte, de plomb, de tole et de bitume,* Victor Dalmont Libraire des Corps imperiaux des ponts et chaussées et des mines, Paris.

Diem, K., and Lentner, C. (1974) *Scientific Tables,* 7th ed., Geigy Pharmaceuticals, Ardsley, N.Y.

Dullien, F. A. L. (1992) *Porous Media: Fluid Transport and Pore Structure*, 2nd ed., Academic Press, San Diego.

Fung, Y. C. (1993) *Biomechanics: Mechanical Properties of Living Tissues*, 2nd ed., Springer-Verlag, New York.

Goulet, R. W., Feldkamp, L. A., and Goldstein, S. A. (1992) Quantification of the architecture of cancellous bone by surface and volume orientation methods, *Trans. Orthop. Res. Soc.,* 17, 159.

Greenkorn, R. A. (1983) *Flow Phenomena in Porous Media: Fundamentals and Applications in Petroleum, Water, and Food Production,* Marcel Dekker, New York.

Grimm, M. J. and Williams, J. L. (1993) Use of ultrasound attenuation and velocity to estimate Young's modulus in trabecular bone, IEEE Nineteenth Annual Northeast Bioengineering Conf., Li, J. K. J. and Reisman, S. S., Eds., Vol. 19, 62–63.

Grimm, M. J. and Williams, J. L. (1997) Measurements of permeability in human calcaneal trabecular bone, *J. Biomech.,* 30, 743–745.

Happel, J. and Brenner, H. (1983) *Low Reynolds Number Hydrodynamics: With Special Applications to Particulate Media,* M. Nijhoff, distributed by Kluwer, Boston, MA.

Hubbert, K. (1940) The theory of ground-water motion, *J. Geol.,* 48, 785–944.

Hui, P. W., Leung, P. C., and Sher, A. (1996) Fluid conductance of cancellous bone graft as a predictor for graft-host interface healing, *J. Biomech.,* 29, 123–132.

Hvid, I., Bentzen, S. M., Linde, F., Mosekilde, L., and Pongsoipetch, B. (1989) X-ray quantitative computed tomography: the relations to physical properties of proximal tibial trabecular bone specimens, *J. Biomech.,* 22, 837–844.

Kafka, V. (1983) On hydraulic strengthening of bones, *Biorheology,* 20, 789–793.

Kafka, V. and Jírová, J. (1983) A structural mathematical model for the viscoelastic anisotropic behaviour of trabecular bone, *Biorheology,* 20, 795–805.

Krause, W. R., Miller, J., and Ng, P. (1982) The viscosity of acrylic bone cements, *J. Biomed. Mater. Res.,* 16, 219–243.

Linde, F., Hvid, I., and Madsen, F. (1992) The effect of specimen geometry on the mechanical behaviour of trabecular bone specimens, *J. Biomech.,* 25, 359–368.

Martin, R. B. (1984) Porosity and specific surface of bone, *Crit. Rev. Biomed. Eng.,* 10, 179–222.

Nauman, E. A., Fong, K. E., and Keaveny, T. M. (1999) Dependence of inter-trabecular permeability on flow direction and anatomic site, *Ann. Biomed. Eng.,* 27, 517–524.

Nutting, P. G. (1927) The movements of fluids in porous solids, *J. Franklin Inst.,* 203, 313–324.

Ochoa, J. A., Heck, D. A., Brandt, K. D., and Hillberry, B. M. (1991a) The effect of intertrabecular fluid on femoral head mechanics, *J. Rheumatol.,* 18, 580–584.

Ochoa, J. A., Sanders, A. P., Heck, D. A., and Hillberry, B. M. (1991b) Stiffening of the femoral head due to inter-trabecular fluid and intraosseous pressure, *J. Biomech. Eng.,* 113, 259–262.

Ochoa, J. A., Sanders, A. P., Kiesler, T. W., Heck, D. A., Toombs, J. P., Brandt, K. D., and Hillberry, B. M. (1997) *In vivo* observations of hydraulic stiffening in the canine femoral head, *J. Biomech. Eng.,* 119, 103–108.

Reynolds, O. (1883) An experimental investigation of the circumstances which determine whether the motion of water shall be direct or sinuous, and of the law of resistance in parallel channels, *Philos. Trans. R. Soc. London,* 174, 935–982.

Scheidegger, A. E. (1974) *The Physics of Flow through Porous Media*, 3rd ed., University of Toronto Press, Toronto.

Simkin, P. A., Pickerell, C. C., and Wallis, W. J. (1985) Hydraulic resistance in bones of the canine shoulder, *J. Biomech.,* 18, 657–663.

Sobotkova, E., Hruba, A., Keifman, J., and Sobotka, Z. (1988) Rheological behavior of bone marrow, in Progress and Trends in Rheology, *Rheologica Acta,* Vol. Suppl., 467–469.

Underwood, E. E. (1981) *Quantitative Stereology,* Addison-Wesley, Reading, MA.

Williams, J. L. (1992) Ultrasonic wave propagation in cancellous and cortical bone: prediction of some experimental results by Biot's theory, *J. Acoust. Soc. Am.,* 91, 1106–1112.

V

Bone Adaptation

26

Pathophysiology of Functional Adaptation of Bone in Remodeling and Repair *in Vivo*

Allen E. Goodship
Royal Veterinary College and Institute of Orthopaedics University College London

James L. Cunningham
University of Bristol

26.1 Introduction

Skeletal tissues in general and bone in particular are able to respond to functional influences in a manner that leads to an optimal design for the prevailing functional requirement. The architecture of bone from the tissue level to that of the organ and system arises from two major input factors. The first is the inherited genetic information that accounts for interindividual and interspecies differences. This genetic component can be considered in two ways. Evolutionary drives that determine the characteristic skeletal form found in particular species, for example, the dense long bones without a marrow cavity seen in the manatee (*Trichechus manatus*) to the large-diameter thin-walled and internally braced long bones of birds such as the large flying species, e.g., swan (Fig. 26.1). This immense biodiversity in bone architecture driven

0-8493-9117-2/01/$0.00+$.50

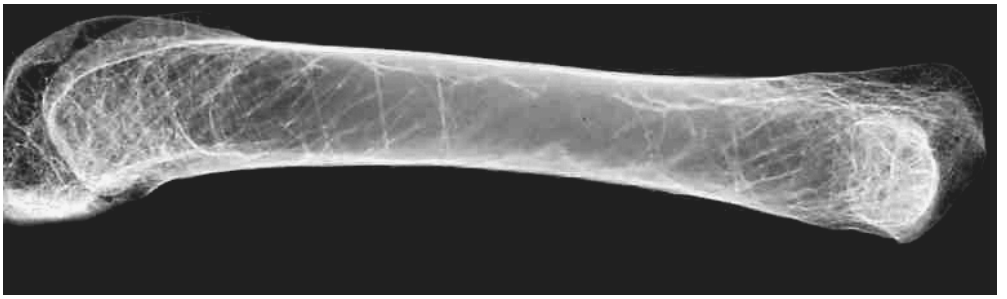

FIGURE 26.1 Radiograph of avian long bone illustrating the thin cortical wall, large-diameter medullary cavity, and internal trabecular bracing.

by evolutionary pressures is accompanied by the superimposition of functional adaptation to short-term changes in the lifestyle of the individual, the second major factor. The ability of a tissue to respond to mechanical demands is highly developed in bone.

It could be argued that the roles of the skeleton to provide structural support, protect vital organs, and act as a mineral reservoir for calcium homeostasis are inextricably linked and, without the potential for structural reorganization, all of these roles will be compromized with potentially fatal consequence for the individual. These in-built biological strategies are uniquely developed in bone. For most species the skeleton fulfills its biological role throughout the natural life of the animal. However, in humans the enhanced rate of change in lifestyle with increased longevity and decreased general functional activity contributes to the inability of the skeleton to perform its role in an increasing proportion of the aging population. In the developed world, 1 in 3 women and 1 in 12 men will suffer with clinical osteoporosis.

In addition, the crippling disease of the joints, arthritis, is also an increasing problem in which it has been suggested that one of the many factors contributing to the damage of articular cartilage is increased density of the underlying subchondral and cancellous bone. Whereas osteoporosis is predominantly a disease of the human species, arthritis is found throughout the animal kingdom.

Knowledge of the relationship between function and form in bone has increased enormously since the early observations that fascinated Galileo and Wolff. In the 1890s Wolff used his clinical and "experimental" morphological observations to develop two concepts that have become known as Wolff's law (Wolff, 1892), namely, that skeletal elements are strategically placed to optimize strength in relation to the distribution of applied loading and that the mass of the skeletal elements is directly related to the magnitude of the applied loads. At the time, these "hypotheses" could not be tested since there was no method of direct measurement of the forces acting upon the skeleton.

26.1.1 Functional Environment of the Skeleton

The advent of a technique to measure surface bone strain *in vivo* in the early 1970s provided the first direct quantification of the physiological mechanical environment of the skeleton. The result of load on a structure is deformation or strain. The development of *in vivo* strain gauging using rosette gauges around the circumference of a bone, together with morphometric data relating to second moment of area, allows calculation of the loading pattern of a particular plane of a bone.

The importance of this technique was to provide the ability to test Wolff's hypotheses and begin to elucidate the transduction pathways that control the process of functional adaptation in the skeleton. Frost (1967) initially proposed that all long bones were loaded in a manner that minimized any bending. Any increase in axial compression and any flexural deformation initiated bone formation on the concave side of the bone and resorption on the convex side to cause a drift of the bone back into axial compressive loading. However, *in vivo* instrumentation of different bones has provided evidence that some long bones, such as the ovine radius, are loaded in flexural strain during normal locomotion. Other long bones such as the tibia and femur are deformed during physiological loading

with a significant torsional component (Biewener et al., 1983). The functional patterns of deformation are significant in relation to orthopedic procedures such as fracture fixation and the integration of prostheses.

Adaptation of bone to functional demands can result in loss of bone in situations of reduced loading, or an increase in bone when functional strains are exceeded. These adaptations can occur throughout the skeleton or within one limb, one bone, or even at a specifically defined site within a bone.

The progression of understanding the factors that are important in this process together with potential applications in remodeling, repair, replacement, and regeneration of the skeleton has involved a number of different approaches. In this chapter it is the pathophysiology of mechanically related adaptation of bone in remodeling and repair that will be reviewed.

26.2 Bone Loss under Conditions of Reduced Loading

The form of adult bone is regulated by two main factors. The first is the predetermined genetic template that explains individual differences in the general size of bones between individuals. The second is the fact that bone as a tissue is able to react to changes in the level of mechanical loading and, as suggested by Wolff, will respond to both the magnitude and pattern of loading. Thus, in the absence of mechanical loading, the form of a skeletal element will revert to the basic genetically determined bone mass. Chalmers and Ray (1962) performed a classic experiment in which the cartilagenous anlage of the femur in developing mice was transplanted into the spleen, a site devoid of mechanical loading. After development, the bone was compared with that which developed under normal physiological loading (Fig. 26.2). Although the bone developed as a recognizable femur, it lacked the refinements associated with the normal functional bone. The major features induced by function were organization of the internal trabecular structure, the width of the medullary cavity and thickness of the cortical wall, the "waisting" of the femoral neck, and the curvature of the femoral diaphysis.

Thus, any reduction in the functional loading of a bone induces modeling changes that reduce the mass and revert form to that of the basic genetic template. Fell (1956) also conducted studies on cultured chick limb primordia and observed that some of the prominences on specific bones developed in culture and some did not. This was interpreted as some bony features required functional loading for development whereas others were part of the genetic template.

Wolff's early concept, that bone mass is related to the magnitude of prevailing loads, has been supported by both clinical and experimental observations. Changes in functional loading induce a cellular response

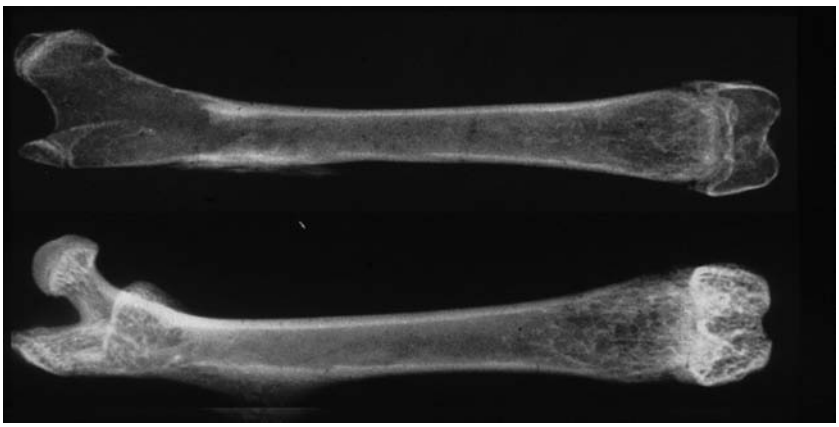

FIGURE 26.2 Two murine femora, one showing normal morphology developed within a normal functional environment (bottom), and the other developed from the cartilage anlage after transplantation to the spleen, devoid of mechanical loading (top), and showing the form associated with the genetic template alone. (From Chalmers, J. and Ray, R. D., *J. Bone Joint Surg.,* 44B, 149–164, 1962. With permission.)

to model the bone to an optimal mass to withstand the imposed load. The use of *in vivo* strain gauging to quantify the levels of deformation associated with changes in skeletal loading has now enabled the thresholds of adaptive remodeling to be determined. These values have been used to enable predictive modeling of bone in relation to implanted prostheses and degenerative skeletal disease (Weinans et al., 1993; Mullender et al., 1998).

26.2.1 Reduced Functional Loading

Reduced functional loading can occur on a generalized basis in conditions such as bed rest and long-term space flight and also in relation to particular parts of the skeleton, for example, plaster cast immobilization or neural deficits such as paraplegia. When implants are used, there are localized effects on loading within the individual bone. For example, the application of fracture fixation devices such as plate or external fixation systems act as an additional load path and reduce the strain experienced by the underlying bone.

26.2.1.1 Generalized Reduced Loading

Prolonged periods of bed rest result in a loss of bone throughout most of the skeleton. Subjects with normal bone mass become osteoporotic, with rapid loss of bone occurring in the initial period, after which the rate of loss is reduced reaching an equilibrium after about 12 weeks (Burkhart and Jowsey, 1967). At the state of equilibrium, Marotti and Marotti (1965) concluded that bone turnover was actually greater than in a mechanically functional limb. Bed-rest studies have also been used to simulate loss of functional loading that occurs in long-term space flight.

The most relevant generalized reduction in skeletal loading occurs in microgravity conditions experienced in space flight. In long-term space flight there is a considerable loss of bone mass of up to 7% of skeletal mass. Interestingly, this loss is not evenly distributed throughout the skeleton. The distal bones of the lower limb have been found to sustain the greatest loss of bone (Vogel and Whittle, 1976; Collet et al., 1997). Despite the development of countermeasures such as resistance exercises, the loss of bone mass is not prevented (Baldwin et al., 1996; Convertino, 1996). One feature of the functional environment of the lower limb bones that is lost under conditions of microgravity is the high-frequency heel strike transient. An experiment was conducted on the Euromir 1995 mission to test the hypothesis that application of a simulated heel strike transient would inhibit the bone loss expected during a long term in microgravity (Goodship et al., 1998a). The astronaut applied the mechanical stimulus to one heel and the other was used as a control, with the stimulus only applied for a short period each day (500 cycles at 0.5 Hz). Dual energy X-ray absorptiometry (DEXA) scanning was performed before and after a 6-month period on the MIR space station. The results indicated that the stimulated heel retained the preflight levels of bone mineral content, whereas the control had lost 6% of the preflight values. Thus, the use of a high-frequency, short-term, cyclical mechanical stimulus prevented the reduction in bone mass associated with reduced mechanical loading associated with reduction of gravitational forces.

Although long-term space flight and also bed-rest studies show dramatic loss of bone mass associated with disuse, it is interesting that one area of the skeleton that does not exhibit such change is the skull. Here the role of bone is to protect the most important vital organ, the brain. The observation that the recordings of bone strain in the bones of the cranial vault are significantly lower than those in the appendicular skeleton may suggest that the bones of the skull are at the genetically determined minimal mass (Hillam, 1996). There is no good evidence that the mass of the bones of the cranial vault can be increased by mechanical stimulation.

Mechanical stimulation can be provided by specific types of exercise. Studies in women with osteoporosis have shown that repeated high-impact loading achieved during jumping exercise can enhance bone mineral density in specific regions of the skeleton. Changes in the style of jumping can be used to effect bone mass enhancement either in the lumbar spine or the femoral neck (Bassey and Ramsdale, 1994). Jiang et al. (1999) also suggest that bone strain regulates bone mass and exercise protocols designed to counter the effects of osteoporosis should comprise repeated application of high peak forces, high strain rates, and high impacts. They also suggest that these exercises may condition neuromuscular control, which could play a major role

in maintaining bone mass. Others have shown a relationship between metacarpal bone mineral and grip strength, again indicating muscle forces are involved in regulation of bone mass (Osei-Hyiaman et al., 1999). It has also been shown that application of high-frequency, low-magnitude cyclical bone strain can evoke bone formation in animal models of osteoporosis (Rubin et al., 1997).

Judex et al., (2000) suggest that whereas physical activity is capable of increasing bone mass in adults, the specific mechanical stimulus is poorly defined. They determined the strain environment on the surface of the tarsometatarsus of adult roosters during high-speed running. After 3 weeks, the effect of the high-speed running was to induce periosteal bone formation in the majority of birds. However, it is the more diverse types of exercise, particulalry those involving rapid and unusual loading patterns on the skeleton, that have a greater osteogenic potential. Sports such as squash, tennis, and badminton are more effective than running, cycling, swimming, or ice hockey in providing a stimulus for increasing bone mass (Nordstrom et al., 1998). This hypothesis has also been supported in a rat model where impact loading was combined with running, and compared with running alone and with a 'sedentary' group. There was a significant additional effect of the impact loading on the bone mass of the femur (Jarvinen et al., 1998).

There are naturally occurring animal models in which disuse osteopenia has been prevented by the evolution of a different osteoregulatory mechanism. An example of this is seen in the denning bears (*Ursus americanus*). Calcium and bone metabolism were studied in black bears by Floyd et al. (1990) over summer, winter, and spring. During the winter period the bears remain in the den in a metabolically active state but recumbent and anuric for 4 months. Despite this period of skeletal inactivity, the bone mass remained unchanged from summer values. The authors did not report on muscle activity, which would be interesting in view of the specific-frequency, low-magnitude strain osteogenic stimulus reported by Huang et al. (1999).

Some species of animals do show natural changes in bone mass associated with seasonal hormone-related changes. Deer (*Cervidae*) that grow antlers (bony projections from the frontal bone) on a seasonal basis exhibit a concurrent osteopenia. Interestingly, the regions of the skeleton that are particularly influenced are non-weight-bearing bones such as the ribs. Thus, there is a cyclical seasonal osteopenia to mobilize the calcium required for the rapid bone growth associated with antler formation. The antler grows from a bud of mesenchymal tissue that differentiates into a structure very similar to a one-sided growth plate with endochondral bone formation. There is a progressive increase in size of antler with each successive year's growth. The timing and rate of growth, the shedding of the overlying modified integument (velvet), and ultimately the shedding of the antler are controlled by hormone levels. Although these structures are predominantly associated with the male and levels of testosterone, the male hormone exerts influence on antler tissues after conversion to the female hormone estrogen. Thus, in this natural model the formation may be perturbed by different levels of estrogen or its receptor distribution. During growth, the antlers are very sensitive and mechanical loading is minimal. Only after the growth ceases and the velvet is shed is the "dead" antler used in fighting for male dominance in the rut or breeding season (Fig. 26.3). Again, the mechanisms controlling bone formation and resorption in these unique natural situations may provide information to enhance understanding of mechanically related bone formation and its application to injury and disease of the skeletal system.

26.2.1.2 Localized Loss of Bone

Uhthoff and Jaworski (1978) immobilized the forelimbs of young dogs with plaster casts and showed an increase in diameter of the medullary cavity. In 1980, they repeated the study in mature dogs (Jaworski et al., 1980), again showing a disuse-related bone loss but also the ability to reverse the loss of bone with reintroduction of normal activity, demonstrating the dynamic nature of mechanically related bone modeling. The recovery of the disuse-induced deficit following remobilization was less efficient in the older dogs (40%) compared with younger dogs (70%) (Jaworski and Uhthoff, 1986). This may be because the type of postimmobilization exercise was a normal physiological activity.

Functional adaptation to mechanical conditions may be localized to a single bone or even to a specific site within a single bone. Using an external fixator, Skerry and Lanyon (1995) immobilized the tarsal joint in an ovine model. The reduction in functional loading induced a reduction in bone mineral content of the os-calcis. This bone loss was not restored by short periods of daily walking with the fixator removed.

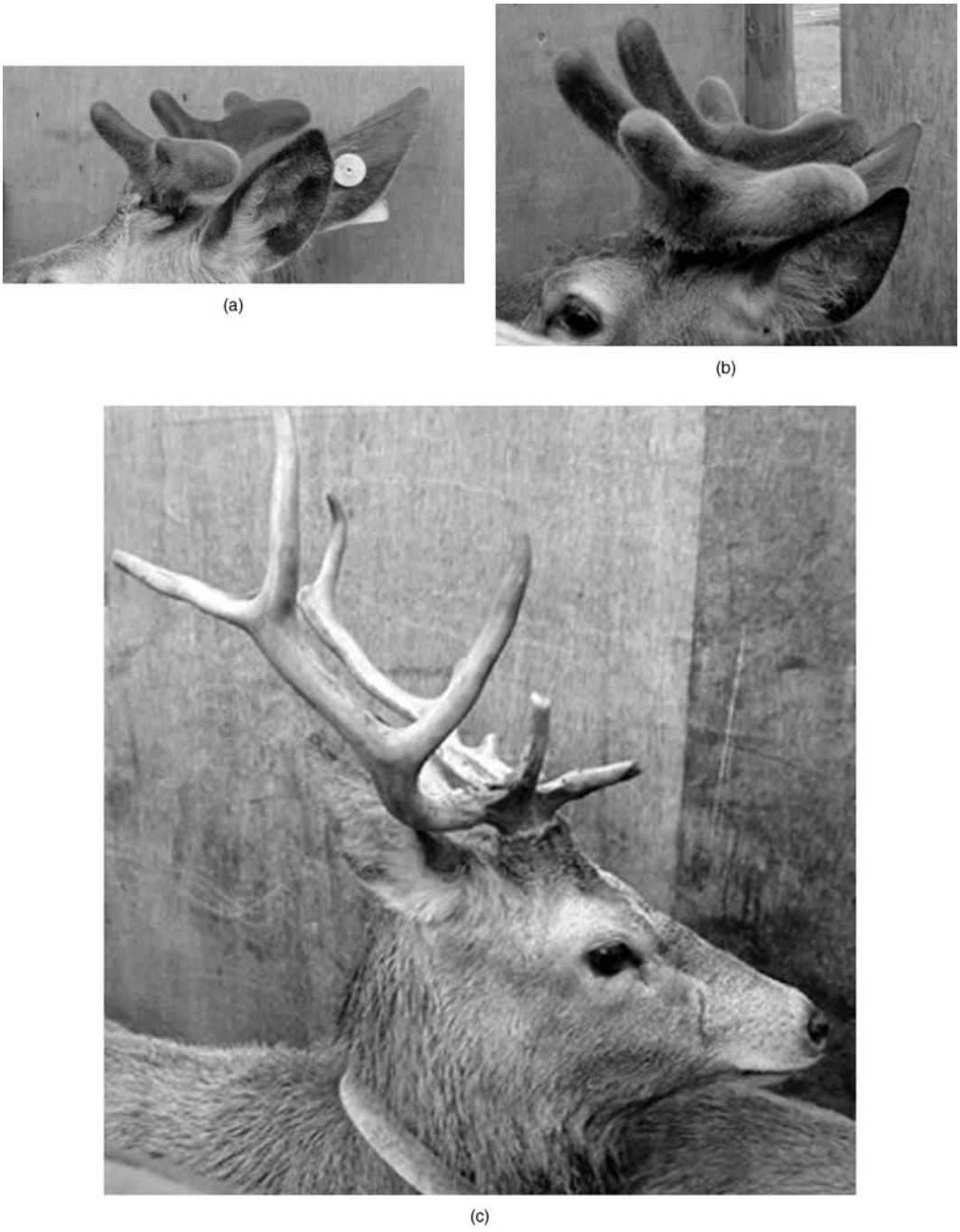

FIGURE 26.3 Deer antler early (a), mid (b), and late (c) development.

The experiment did not proceed to evaluate the effects of different types of mechanical stimulus on the bone mineral content of the bone. It appeared that normal levels of functional stimulus could not induce oseogenic activity. The strain environment was significantly reduced by the fixation method from a functional strain of -228×10^{-6} before application of the fixator, to 71×10^{-6} with the fixator in place during walking at 1.5 m/s.

O'Doherty et al. (1995) applied a rigid external fixator to the intact ovine tibial diaphysis and, using strain gauges, demonstrated a 50% reduction of normal functional strain magnitudes. A progressive time-related reduction in bone mineral content of the mid-diaphysis was shown using DEXA. In morphological terms this strain protection bone loss occurred as a result of endosteal resorption. Thus, the structure of the tubular diaphysis was modeled to optimize the material distribution in relation to structural strength, i.e., by forming a large-diameter thin-walled tube (Fig. 26.4). The imposed strain protection had no significant influence on intracortical porosity or remodeling. Unfortunately, in this experiment a reversal of the strain protection was not performed.

In other models of disuse, the application of short periods of either mechanical stimulation or electromagnetic stimulation have been shown to inhibit the reduction in bone mass expected as a result of the removal of functional stimulation. The classic avian ulnar preparation developed by Rubin (Rubin and Lanyon, 1984b) involves the isolation of the ulnar diaphysis by transverse osteotomies through the metaphyses, followed by application of stainless steel caps at each end of the isolated diaphysis to support transfixing percutaneous stainless steel pins (Fig. 26.5). The pins are clamped by an external fixator to preclude functional loading of the ulnar diaphysis. Removal of mechanical input was validated using strain gauge instrumentation. Changes in bone mass were determined by measurement of bone mineral content and also the cross-sectional area at the mid-diaphysis. This model has been used to study the effects of both mechanical and electrical stimulation. The loss of bone mass resulting from mechanical isolation has been shown to be reduced or prevented by only very short periods of applied cyclical deformation. As few as four cycles of osteogenic strain applied once per day were used to maintain the pre-isolation bone mass.

Subsequently, Rubin et al. (1990) observed a distinct strain energy component in bone in the 20 to 30 Hz frequency range. They hypothesized that this component arose directly from muscular action, as it appeared even in the absence of locomotion. By using the avian ulna model, it was demonstrated that the loss of bone mass associated with mechanical isolation was inhibited by the application of subphysiological levels of deformation applied at a specific frequency of 30 Hz (Qin et al., 1998). Analysis of *in vivo* strain data from a range of different species and anatomical sites (weight-bearing and non-weight-bearing) were subjected to a frequency analysis (Fritton et al., 2000). Strains were recorded in the frequency range 0.2 to 40 Hz, the highest strains ($>$1000 microstrain) occurring relatively few times a day while lower magnitude strains ($<$10 microstrain) occur many thousands of times per day suggesting that the predominant contribution to the strain history of a bone arises from activities not necessarily associated with vigorous locomotion.

Interestingly, specific induced electrical fields were also able to inhibit the mechanically related loss of bone mass seen in the avian ulna model. The electrical signals applied were of specific frequencies of 15, 75, and 150 Hz, the 15 Hz frequency giving the greatest osteogenic response (McLeod and Rubin, 1992).

Huang et al. (1999) has recently observed that the loss of Type II muscle fibers with increasing age altered the frequency components of muscle activity specifically in the range of 30 to 50 Hz, suggesting a possible link with age-related conditions such as osteoporosis. Application of low-magnitude, specific-frequency mechanical and electrical signals are indeed currently being used to inhibit bone loss in the avian ulna model of disuse osteopenia (Qin et al., 1998), using the aged ovariectomized ovine model of osteoporosis (Rubin et al., 1997), in preliminary clinical trials (Rubin et al., 1998) and also in the mechanical stimulation of bone repair (Goodship et al., 1997).

A mammalian model was developed by Skerry et al. (1991) to study the effects of biophysical stimuli on bone adaptation, using an isolated fibula diaphysis. As with the avian isolated ulna, bone mass decreased following isolation from the normal functional environment. Although this model was not loaded mechanically, it was used to investigate the effects of pulsed electromagnetic fields on the extent of bone loss. With the application of 1.5 Hz repetitions of 30 ms bursts of asymmetric pulses, varying from $+2.5$ to -135 mV, to the isolated fibular preparations, the authors found a significant reduction in the extent of bone loss. Interestingly, however, these electromagnetic stimuli did not elicit a hypertrophic response, but merely reduced the extent of bone loss. This difference between the mammalian and avian models could reflect differences in the characteristics of the electromagnetic signal rather than a species effect.

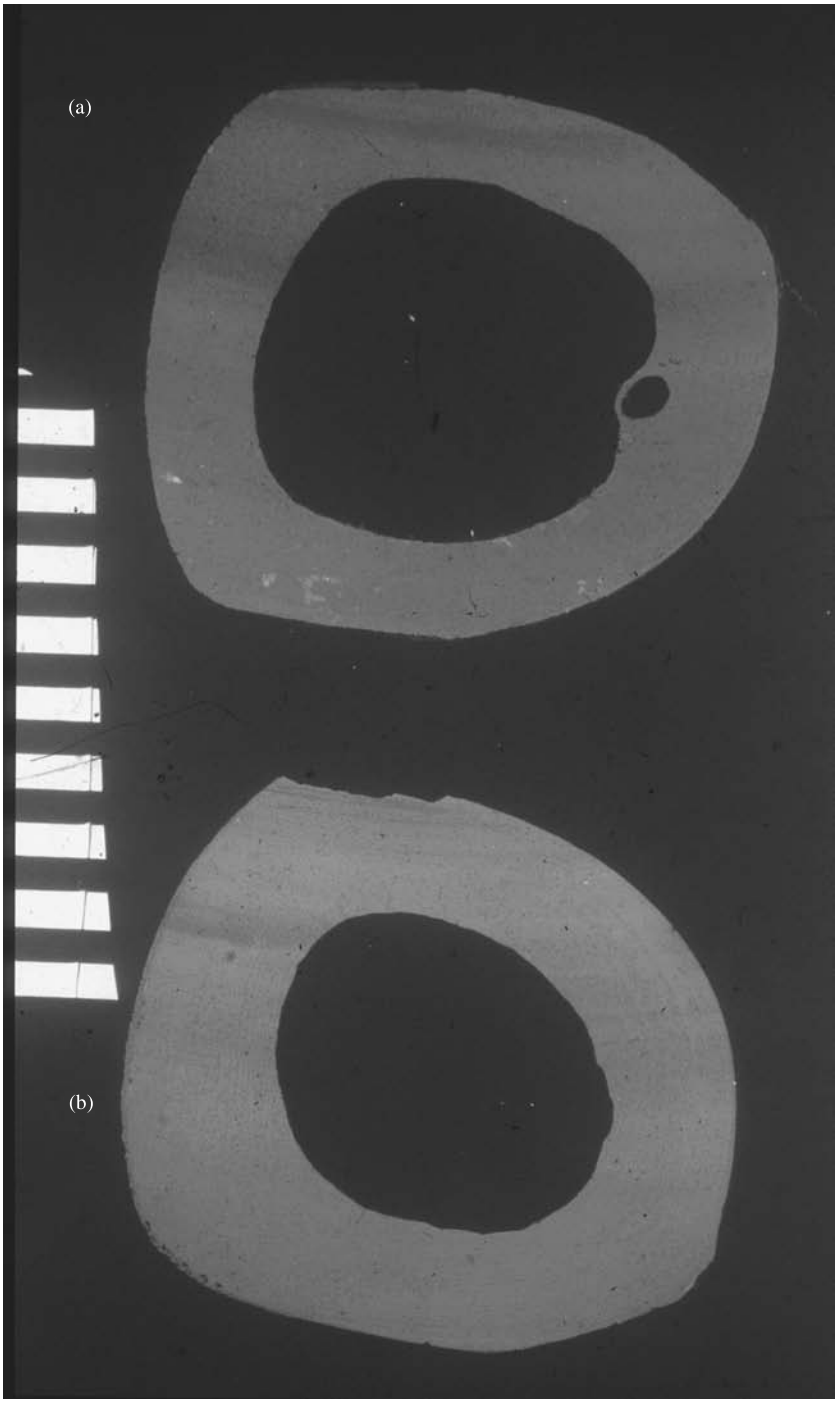

FIGURE 26.4 Microradiograph to show effect of strain protection on the morphology of the ovine tibia. (a) Transverse section of the mid-diaphysis of the control tibia. (b) Transverse section of the mid-diaphysis of the strain-protected tibia showing an increase in diameter of the medullary cavity and reduced cortical thickness but no increased intracortical porosity. (From O'Doherty, D. M. et al., *J. Biomech.*, 28, 575, 1995. With permission.)

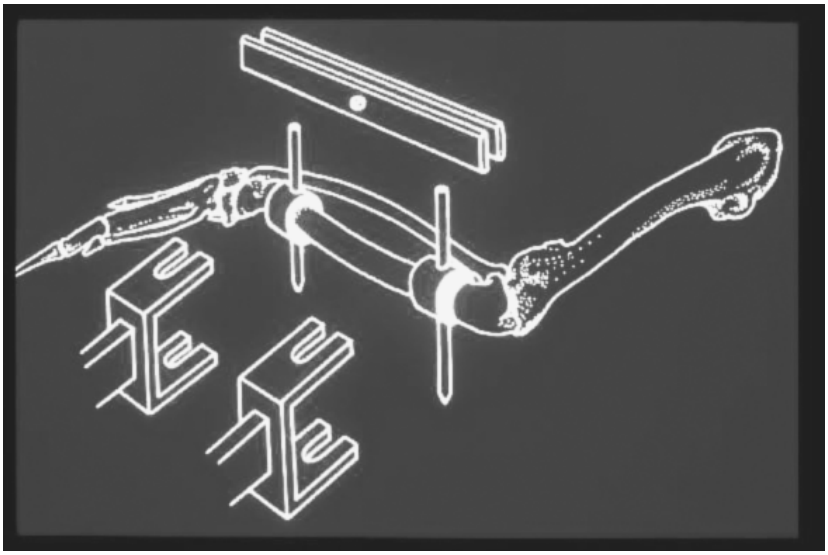

FIGURE 26.5 Avian ulna model. (From Rubin, C. T. and Lanyon, L. E., *J. Theor. Biol.,* 107, 321, 1984. With permission.)

Loss of bone in specific sites within one skeletal element is also seen in association with orthopedic implants, both in the fixation of fractures and in joint replacement.

In treatment of fractures, the limb is functionally impaired by the injury reducing the loading and consequent bone strain. Further reduction of loading close to the fracture site is imposed by the application of a fixation device to stabilize the fragments; the fixation device provides a shared load path and thus removes load from the underlying bone. Strain gauge studies in conjunction with both internal and external fixation techniques have confirmed the reduction in functional bone strain. Baggott et al. (1981) used strain gauges below an internal fixation plate on the dorsal aspect of the ovine radius to determine the level of strain protection afforded by the fixation device. The dorsal cortex of the ovine radius is an ideal site for application of the tension band principle, since normal functional strain analysis has shown the principal tensile strain is aligned to the long axis of this bone. The application of a rigid internal fixation plate, the AO DCP, resulted in a 30% strain reduction beneath the plate. Thus, application of the device induced a mechanical environment that would initiate a bone resorption response.

The use of plates in rigid internal fixation to achieve direct bone repair with osteonal remodeling across the fracture site is also associated with both modeling and remodeling changes. Matter et al. (1974) described a localized increase in porosity in the cortex underlying a compression plate together with some endosteal resorption. However, these internal fixation plates applied tightly to the periosteum compress the periosteal blood vessels. The intracortical porosity was found to be a temporary effect (Perren et al., 1988). Redesign of the underside of the plate to reduce contact (low contact dynamic compression plate (LCDCP)) reduced the intracortical porosity associated with plating (Perren et al., 1990). Thus, it appears that the intracortical effects are due to vascular compromise and the endosteal resorption results from the reduction in mechanical loading attributed to the loss of functional activity and the load sharing between the bone and the plate. In preliminary studies, it was shown that a plate incorporating a spring section applied under tension to an intact bone did not induce strain protection and intracortical porosity under the spring section compared with a standard DCP plate control (Goodship et al., 1998b).

Interestingly, in the isolated avian ulna model developed by Rubin, there is both vascular disturbance and strain reduction, the unloaded diaphyses show both endosteal resorption leading to a reduction in cortical thickness and also marked intracortical porosity (Rubin and Lanyon, 1984b). However, when

subjected to a short period of imposed cyclical loading, the intracortical porosity was not apparent. It therefore appears that there is a complex interaction between mechanical and vascular effects on bone structure.

Another important localized reduction in normal bone strain leading to bone loss is in association with skeletal prostheses, particularly the femoral component of total joint replacement. Although total hip replacement is a very successful operation in terms of pain alleviation and restoration of locomotor function, the femoral endoprosthesis results in a radical change in distribution of loads in the proximal femur. The normal anatomical load transfer from the femoral head to the diaphyseal cortices by the internal cancellous bony architecture is replaced by transfer from the endoprosthesis directly to the cortex. The proximal metaphyseal cortical bone, particularly in the region of the calcar and medial cortex, is subjected to a change in loading pattern. The presence of the loaded endoprosthesis within the medullary cavity induces a combination of reduced axial strains and increased hoop strains in the proximal metaphyseal bone (Oh and Harris, 1978; Hua and Walker, 1992). In patients with prostheses the long-term effect of the changed loading pattern is a resorption of the calcar region and reduced support for the prosthesis. This mechanically related bone loss represents one of the factors leading to an increase in aseptic loosening of prostheses beyond about the second decade postoperatively. Experimental studies in an ovine model provided evidence that the strain-related change in bone mass resulted from a change in strain distribution rather than merely a reduction in strain magnitude. In an animal with a prosthesis and sciatic paralysis, there was a generalized reduction of femoral bone mass observed as endosteal resorption and thinning of the cortex but without the typical loss of the calcar region (Lanyon et al., 1981) (Fig. 26.6).

The ovine model for both total hip replacement and hemiarthoplasty provides an accelerated loss of bone in the region of the calcar and medial cortex with functional locomotor loading occurring by 6 months postoperatively. The use of a low-modulus composite prosthesis resulted in near physiological strain distribution and magnitude on the calcar compared with an identical prosthesis made of titanium. In the titanium prosthesis group the change in strain magnitude and distribution resulted in the expected loss of bone in the calcar region. However, in the group with the composite prostheses calcar bone stock was preserved and osseo-mechanical integration occurred with trabecular bone bridging between the endosteal cortical bone and the fiber metal ingrowth regions on the prosthesis (Langkamer et al., 1992). Similar patterns of bone modeling were found using these two types of prosthesis in a canine model (Turner et al., 1997; Sumner et al., 1998).

Thus, an understanding of the strain-related adaptive response of bone is important in the design of joint replacement prostheses to maximize the functional integration of the implant with the living skeleton by avoidance of strain protection and associated loss of bone stock.

26.3 Adaptation of the Skeleton to Increased Functional Loading

26.3.1 Increased Physiological Exercise

Rubin and Lanyon (1984a) collated *in vivo* strain data from a wide range of species and anatomical locations from which they proposed the concept of "dynamic strain similarity." This concept encompasses the hypothesis that the structure and mass of the skeleton are optimized to attain a similar strain magnitude at peak physiological activity. Thus, any increase above such a strain "window" would elicit a cellular response and modeling of the structure to increase mass or alter distribution of bone tissue. At the time this rather general concept appeared to be supported by quantitative strain data obtained largely from appendicular skeletal sites. Indeed, many of the studies described later in this chapter also support this general strain control mechanism.

However, there are studies that indicated a genetic refinement and indeed a species variation. In addition, subsequent strain data also indicate a different strain environment on the axial skeleton,

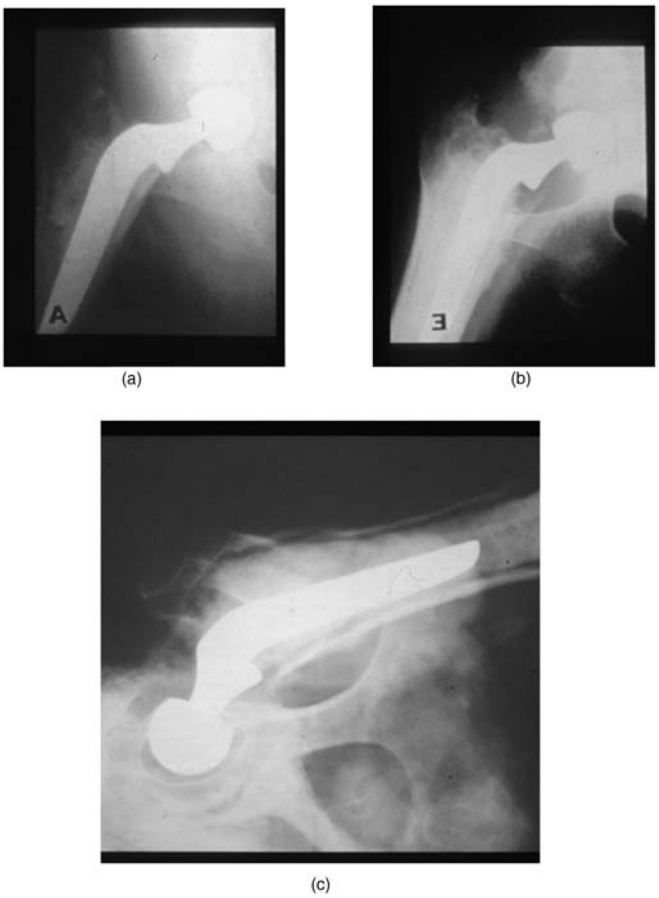

FIGURE 26.6 (a) Postoperative radiograph, (b) showing localized calcar loss 6 months after implantation of a femoral prosthesis, (c) generalized endosteal resorption but calcar preservation after implantation of a femoral prosthesis but with sciatic paralysis. (From Lanyon, L. E. et al., *J. Bone Joint Surg.,* 63-A, 989, 1981. With permission.)

particularly with respect to the calvarial bones where customary *in vivo* strains peak at values an order of magnitude lower than those in the appendicular skeleton and maximum strains appear to be elicited by muscle activity associated with facial expression and vocalization (Hillam, 1996).

Peak physiological activity may stimulate an osteogenic response; some authors report an increase in bone formation as a result of imposing high-intensity exercise resulting in a physiological strain distribution with high strain magnitudes and rates.

Judex and Zernicke (2000) studied the effects of high-speed running in roosters during skeletal development. The regimen was to run 9-week-old roosters on a treadmill for 5 min three times a day over an 8-week period. These were compared with a control group. The imposed strains were quantified using the *in vivo* strain gauge technique on the tarsometatarsus and adaptive changes evaluated in terms of bone morphology, mechanical properties, and mineral ash content. The running increased strain magnitude by 19% compared with walking strains and strain rates by 136%. No significant differences were found between exercised and control groups using this regimen. The authors concluded that an exercise regimen to induce bone adaptation must differ significantly from the habitual milieu. This conclusion is supported by many studies that will be considered later, in which imposed loading results in a nonphysiological strain distribution and a consequent osteogenic response. In addition, as indicated above, the types of exercise to reduce bone loss in osteoporosis or to increase bone mass in young adults

are generally found to be those that involve diverse and unusual loading of the skeleton, such as tennis and squash rather than running or cycling.

However, some studies do show that peak levels of normal activity can induce adaptive changes in parts of the skeleton. Firth et al. (1999) showed that galloping exercise on a treadmill induced regional changes in bone density within the third and radial carpal bones of the thoroughbred racehorse compared with a control group that only received walking exercise. Strain levels were not measured in this study. Iwamoto et al. (1999) examined the effects of treadmill exercise on cancellous bone in growing rats. They used an exercise regimen of treadmill running at 24 m/min for 1h/day, 5 days a week, for 12 weeks and compared this to "sedentary" controls. The results indicated a significant increase in bone volume with site-specific levels within the tibial metaphyses. The cancellous bone of the lumbar vertebrae, however, did not show a change with this exercise protocol. Again, the site-specific strain patterns associated with the exercise protocol were not measured.

It is difficult to compare and evaluate the exercise protocols in terms of bone strain characteristics. It could be argued that the "control" groups may be showing bone loss, rather than bone formation resulting from exercise.

26.3.2 Induced Overload of Skeletal Elements by Invasive Techniques

Early experimental studies induced increased loading by osteotomy of one of a number of bones within a limb segment followed by observations on the remaining supporting bone(s). Such studies were performed in a number of species. Murray (1936) cited a number of very early experiments showing the response of bone to increased loading conditions. Clinical observations by Bond (1913 to 1914) were made on the fibula when transplanted to replace the tibia. The transplanted fibulae increased in thickness and assumed the geometry of a tibia. In animal studies as early as 1864, Sedillot had studied the response of the canine fibula after removal of the tibia, reporting a compensatory increase in thickness. Stieve in 1927 removed two to three toes with associated metatarsal bones in dogs and observed an increase in thickness of the remaining bones but no change in their length. Wermel (in 1934) induced overloading by removal of one of the paired bones of the antebrachium in the rat, rabbit, and dog in growing animals. The general response was reported as an increase in thickness, change in cross-sectional area, and a reduction in length. Presumably, the effect on length resulted from an increased loading on the physeal plate. Tschantz and Rutihauser (1967) resected the radius in the forearm of the dog and observed changes in the smaller ulna. The early change occurring within a few hours was found to be formation of planes of plastic deformity on the compressed cortex. These comprised lamellae bent at an angle of 30° to the long axis of the bone. After 48 h signs of adaptive modeling were seen as a broad band of periostosis and bone formation from the endosteum. Initially fibrillar (woven) bone was formed but later remodeled into lamellar bone. The process was reported as rapid for the first 3 weeks, then slowing down, until at 9 months the entire cortex had remodeled into normal cortical bone. They also reported that the overloaded bone modeled to become aligned to the loading axis.

Chamay and Tschantz (1972) osteotomized the canine radius and observed hypertrophy of the ulna under different loading conditions. They reported that traction resulted in bone atrophy, and static compression only induced hypertrophy in areas where plastic lesions occurred. However, continuous intermittent compression resulted in a more widespread hypertrophy, although this was greater in regions of plastic lesions. The association of a greater response in regions associated with plastic lesions may indicate a superimposed healing response rather than pure adaptive hypertrophy.

Using strain gauges this approach was repeated in the porcine antebrachium, quantifying the surface bone strain of the normal functional radius both immediately after removal of the mid-diaphysis of the ulna and after a period of 3 months during which time the radius underwent functional adaptation. At the mid-diaphysis the cross-sectional area of the two bones was equal. Removal of the ulna diaphysis resulted in a 2.5-fold increase in surface bone strain on the dorsal surface of the radius. The response to this increase in strain was an explosive periosteal formation of bone to increase the cross-sectional area of the radius. At 3 months the adaptive hypertrophy had reduced surface bone strains to normal physiological levels. The hypertrophy of the radius resulted in the hypertrophied bone attaining the same cross-sectional area as the combined area of the radius and ulna in the contralateral limb. Thus, for the

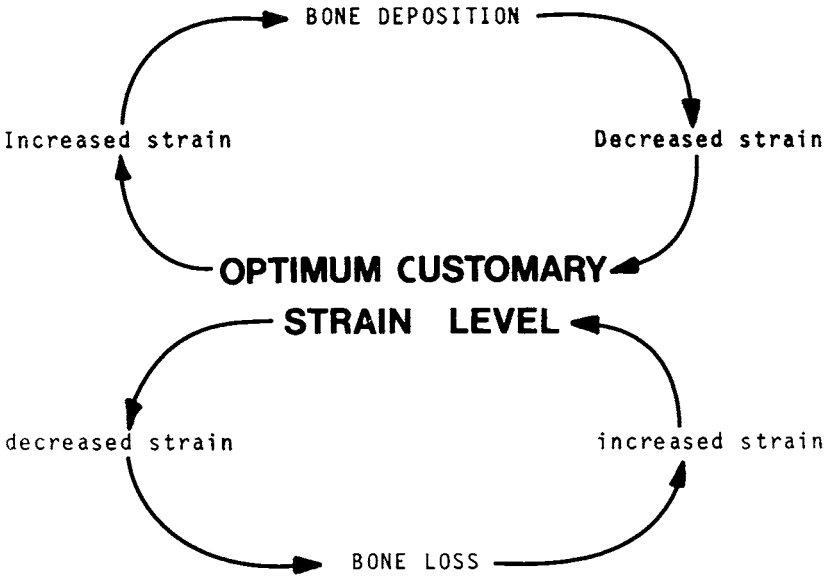

FIGURE 26.7 Strain controlled feedback loop.

first time, the response of bone to an increase in load was quantified in terms of direct mechanical measurement and associated morphometric data (Goodship et al., 1979). This experiment provided support for the hypothesis that bone mass was regulated under strain control in a feedback loop (Fig. 26.7).

The study was then repeated in the ovine antebrachium where the main load-bearing bone is the radius and the ulna is a small buttress (Lanyon et al., 1982). The increase in strain on the radius was 20% on the cranial surface but only 8% on the caudal surface. The bone was left to adapt for 1 year in adult animals. New bone was deposited largely on the caudal cortex close to the site of the resected ulna. The total area of new bone formed replaced that lost in removal of the ulna, thus equilibrating strains due to compression between osteotomized and nonosteotomized limbs. Strains due to bending and thus total strains were reduced to below functional strains on the intact bones. The authors suggested that this indicated that mechanically adaptive bone remodeling may not be related to absolute strain levels but to the relative distribution of strain. New bone formation can therefore be stimulated under conditions of subphysiological strain magnitude. Interestingly the new bone on the cranial cortex remained primary, whereas that on the caudal cortex was highly remodeled. It was suggested that remodeling may be induced under the influence of strain distributions to improve the structure and properties of the tissue.

In these types of models, the loading is related to the physical activity of the animal and is difficult to control. To attempt to define the specific osteogenic characteristics of the mechanical stimulus, it was important to develop techniques to apply defined loads to the living skeleton.

26.3.3 Induced Overload by Externally Applied Mechanical Stimuli

26.3.3.1 Application of Mechanical Stimuli by Means of Transcutaneous Implants

In the studies described so far, the imposition of loading was dependent upon the animal undertaking normal activities, predominantly locomotion, to induce loading of the bone. A further advance in understanding the response of bone to mechanical environment was the development of techniques to apply external loads to specific bones. One of the first reports of this approach was a classic series of experiments by Hert and co-workers in which the tibia of a rabbit was subjected to external loading. Transcutaneous pins were placed through the tibial diaphysis and loads applied via a system of Bowden cables. In these experiments cyclical loading was applied to the tibia. A response of the bone was

stimulated by intermittent loads but not if static loading was applied. Furthermore, in this model the response did not differ with respect to tensile or compressive deformation. From the results of this model of applied external loading it was concluded that the adaptive response was stimulated by changes in shape rather than volume (Lisková and Hert, 1971). The main criticism of this work, although pioneering for its time, was the lack of ability of methods to quantify the levels of deformation induced in the tibia.

The development of the *in vivo* strain gauge technique introduced the ability to relate loading to direct surface strain. O'Connor et al. (1982) applied external loading to the ovine radius. Tubular prostheses were inserted into the radial metaphyses from the dorsal aspect. A pneumatic actuator was used to apply bending loads to the radius. Strain gauges were used to define locomotor principal strain magnitudes and distribution. The loading was adjusted to simulate the pattern of locomotor strains but vary the strain rate and magnitude. Daily applications of cyclical strain were applied and the adaptive response assessed by measurement of cortical thickness of the radius and ulna. The results of this study indicated a significant correlation between strain rate and bone hypertrophy with a near physiological strain distribution. Interestingly, in one of the few studies measuring *in vivo* strain-related potentials with concurrent recordings from strain gauges and silver/silver chloride electrodes, Lanyon and Hartman (1977) showed that there was an increase in the regularity and magnitude of the potentials at higher speeds associated with high strain rates. This study supported the observation of O'Connor et al. (1982) that strain rate was an important component of an osteogenic mechanical stimulus. Change in strain rate was also found to be a major determinant of adaptive bone formation in a noninvasively loaded rat ulna model (Mosely and Lanyon, 1998). Churches and Howlett (1982) also used a system of applying loads via transcutaneous pins to the ovine metacarpal bone. The bone was loaded for two 1-h periods at 24 cycles/min giving a range of stress at the mid-diaphysis of 2.2 to 8.3 N/mm^2. They found the cross-sectional area of new bone to be roughly proportional to the applied stress. A significantly increased level of intracortical remodeling was seen, possibly a consequence of microcracking.

Although the hypertrophy of bone following the application of increased loads either by resection of bones or via transcutaneous implants provided valuable information on the physiology of functional adaptation of bone, these models were to some extent compromised by the animal loading the bone through normal physiological activity throughout the period of study. In addition, an intervention on one weight-bearing limb could compromise the value of the contralateral limb as a "normal" control.

The next major advance in understanding the response of bone to mechanical loading was the development of the isolated avian ulna model by Rubin and Lanyon (1984b). In this model the larger of the two bones of the antebrachium, the ulna, of the domestic fowl (*Gallus domesticus*) was isolated from functional loading by transverse osteotomies at the proximal and distal metaphyses. The level of the osteotomies was such that the blood supply to the isolated bone shaft via the nutrient artery was preserved. The diaphyseal ends were protected by stainless-steel cups transfixed by percutaneous stainless-steel pins. The functionally isolated diaphysis could then be either protected from any deformation by the application of an external fixator across the transfixing pins or loaded by application of a caliper driven by a hydraulic actuator. The applied loads were calibrated to surface bone strain using one or more rosette strain gauges. The advantage of using avian wing bones is that the contralateral wing can be used as a control without intervention on the experimental wing leading to load transfer, as would be the case if bones of weight-bearing limbs were used.

The response of the bone to different loading regimens was quantified either *in vivo,* by a noninvasive determination of bone mineral content, or postmortem by measurement of cross-sectional area. Both measurements were made at the level of the mid-diaphysis. This model provided the classic finding that a maximal hypertrophic response to an osteogenic strain regimen could be elicited by very few cycles of loading applied on a daily basis. An intermittent axial load at 0.5 Hz was applied for varying numbers of cycles per day. As few as four loading cycles per day were found to maintain the bone mass compared with strain-protected controls that lost bone as a function of time. An increase to 36 cycles of loading per day elicited an adaptive response reaching a plateau at 28 days postloading. Further increases in the

numbers of loading cycles per day did not increase the rate of hypertrophy up to 1800 cycles/day. Thus, a very short period of daily loading (72 s), will elicit a maximal modeling response. The rate of adaptation was also shown to be "dose" dependent with respect to strain magnitude (Rubin and Lanyon, 1985). The model was originally developed in the rooster (*Gallus domesticus*) and subsequently the species was changed to the male turkey (*Meleagris gallopavo*). A number of important experiments were performed using this model. In agreement with Hert, Lanyon and Rubin (1984) found no response to a static deformation of the same strain magnitude that elicited hypertrophy when applied as a cyclical stimulus.

26.3.3.2 Application of Mechanical Stimuli by Noninvasive Techniques

A number of studies have attempted to apply specific defined loading regimens to a bone without the use of implants. These techniques involve application of loads to part of a limb through the overlying soft tissues. There can be criticism of these models in terms of effects of soft tissue reaction close to the site of investigation, particularly in small rodents. Also there has been a suggestion that the mechanical properties of the soft tissues should be taken into account when applying specific mechanical regimens due to the viscoelastic properties of these tissues (Hsieh et al., 1999).

A rodent model using four-point bending of the tibia in the rat was developed by Turner et al. (1991) and was modified by Forwood et al. (1998) in terms of loading method and validated in terms of linearity of induced strain against applied loads. The distance between the fulcrum in this model was extremely small and this aspect of the technique gives rise to the influence of the local stresses around the fulcra on the bone response at the site of interest. However, this mammalian model has been used both to confirm the acute sensitivity of lining cells to a single short period of cyclical loading of a diverse distribution. Also, the model has been used to investigate the putative mediators of the mechanical signal. As in the avian ulna model, the single loading episode resulted in activation of surface osteoblasts peaking at around 3 days postloading and declining to control levels at 9 days postloading (Boppart et al., 1998).

The concept of applying a four-point bending stimulus to the tibia has also been used in mice with even smaller distances between the points of load application and the site of interest in relation to adaptive response. However, by using different strains of mice the response of bone to a standard mechanical input was found to be mouse strain dependent (Akhter et al., 1998). This study suggests a genetic modulation of the adaptive response of bone to applied loads, which may have interesting implications in relation to susceptibility of humans to degenerative conditions of the skeleton such as osteoporosis. The development of models using mice will allow investigation of the adaptive response in relation to gene knockout and transgenic strains, providing great potential to elucidate the mechanotransduction mechanisms at the gene level.

Hillam and Skerry (1995) used a similar principle but developed a model in which compressive loads were applied to the antebrachium of the rat by application of force to the elbow (olecranon) and the flexed carpal joint (Fig. 26.8). In this model the natural curvature of the radius and ulna with application of axial cyclical compressive forces induced bending strains on the rat ulna. Also, the site of investigation was remote from the area over which the external forces were applied. The bone strain was measured both during normal locomotion and when the mechanical loading was applied. This mammalian model was used to demonstrate that bone surfaces normally undergoing resorption could be conditioned by a change of mechanical environment. This model was then used by Mason et al. (1996) to investigate the effects of the mechanical stimulation on gene expression in both surface osteoblasts and intracortical osteocytes, the hypothesis being that the osteocytes were the strain-sensing cells. The model also provided the first evidence that a neural glutamate transporter was present in bone (Mason et al., 1997), located in the osteocyte, as a consequence of mechanical loading.

26.3.3.3 Mechanically Induced Matrix Microdamage

The same model was also used to study the mechanisms that are involved in secondary osteonal remodeling following mechanical impairment of the bone matrix. Cortical bone in the rat does not normally show significant levels of intracortical remodeling. Microdamage was induced by controlled cyclical loading to yield point defined as a 30% reduction in the whole-bone stiffness. This damage was confirmed

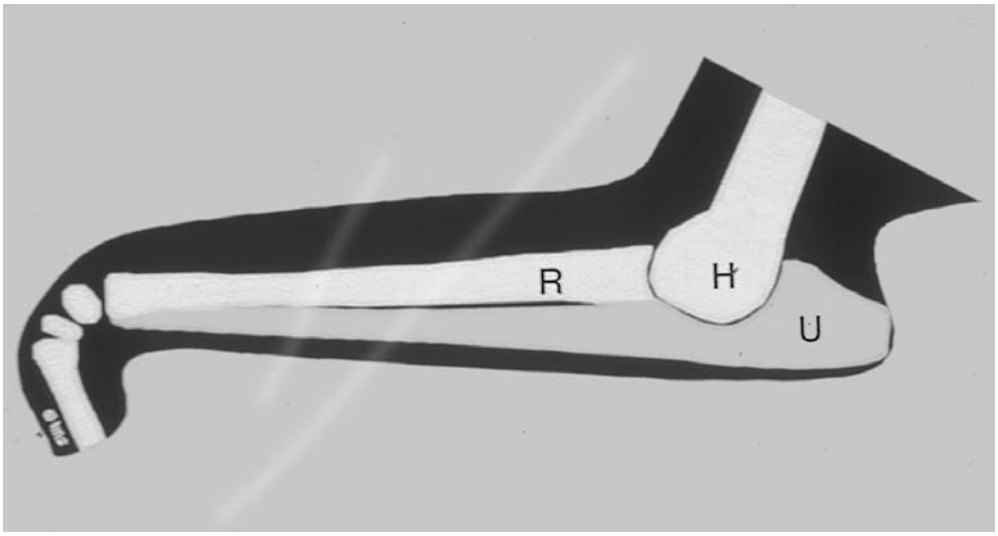

FIGURE 26.8 Model of Hillam and Skerry in which compressive loads were applied to the antebrachium of the rat by application of force to the elbow (olecranon) and flexed carpus. (From Hillam, R. A. and Skerry, T. M., *J. Bone Miner. Res.,* 10, 683, 1995. With permission.)

in some animals and others were left for a further period of time after which an increased level of osteonal remodeling was evident (Bentolila et al., 1998).

Further studies on this rat ulna model also provided evidence of an association between matrix microdamage, osteocyte integrity, indicated by apoptosis, and subsequent remodeling activity. This study suggested a hypothesis that osteocyte apoptosis was a key component of the signaling system for osteoclastic activity, targeted to remove sites of fatigue-induced matrix microdamage (Verborgt et al., 2000).

Forwood and Turner (1995) also reported that studies using the rat tibia model showed that static loads did not elicit a mechanotransduction effect in adaptive bone hypertrophy using a noninvasive four-point bending system. They concluded in this model that bone formation was threshold driven and dependent on the strain rate, amplitude, and duration of loading. From these observations they hypothesized that the strain rate determines the vigor of osteoblastic activity and the regularity of loading cycles determines osteoblast recruitment in a "quantum" fashion.

However, Meade et al. (1984) reported a study in which a continuous superimposed static load of 12 to 130 N was applied to the femur of adult mongrel dogs. The response in terms of cross-sectional area, ash weight, and mechanical stiffness indicated new bone formation had been induced by this application of static load. The induced strains were not measured, so a quantification of any increase in static or dynamic strain was not given in this study.

26.3.4 Age-Related Modulation of Mechanically Induced Bone Formation

Interestingly, the four-point-bending model in the rat tibia has also been used to show an age-related effect on adaptive bone hypertrophy: the older rats were found to be less sensitive to mechanical stimulation (Turner et al., 1995). Earlier studies by Rubin et al. (1992) had shown that whereas an adaptive response could be elicited in the young turkey, a similar mechanical stimulus using this model but in aged birds did not elicit adaptive hypertrophy. This emphasizes not only age-related changes in functional adaptation of bone but also the need to consider age as a factor when comparing data from different studies on the response of bone to mechanical stimulation.

26.3.5 Hormonal Modulation of Mechanical Adaptation of Bone

Mechanical loading effects on bone modeling and remodeling play a major role in the determination of sites of overall bone loss in conditions of hormonal and dietary drive for calcium mobilization. Interestingly, in species that show an annual osteopenia, such as deer during antler growth (Baxter et al., 1999), there is a rapid seasonal demand for calcium mobilization. The process of antler growth is complex and controlled largely by seasonally related changes in sex hormone levels. During the period of rapid growth there is an increase in bone resorption predominantly in the non-weight-bearing regions of the skeleton, such as the ribs. It may be postulated that the weight-bearing bones of the skeleton are preferentially protected from the structurally weakening effects of increased porosity by the functionally related mechanical strain stimulus (Banks et al., 1968).

26.3.6 Dietary Effects on Mechanical Adaptation of Bone

In addition to the prime role of mechanical support of the body, the skeleton also provides a reservoir of calcium. There is experimental evidence that a dietary demand for calcium mobilization, which normally results in an increase in bone remodeling with increased intracortical porosity, can be modulated by mechanical influences. In lactating female rats, the reduction of dietary calcium induces intracortical porosity and restoration of calcium levels results in secondary osteon formation. Under normal dietary conditions the bone in this species remains as primary bone. Also, in avian species calcium is normally stored in intramedullary bone prior to egg laying. This bone provides the supply of calcium without any detrimental effects on mechanical competence of the skeleton during egg laying. In domestic poultry housed intensively, the high levels of egg laying and associated calcium requirements often result in complete loss of the intramedullary bone and resorption of cortical bone. These birds have a very fragile skeleton and can sustain fractures during normal functional activity.

The application of an osteogenic mechanical stimulus in calcium-deficient laying female turkeys was found to inhibit the resorption of bone from the ulna cortex that occurred without the mechanical stimulation (Lanyon et al., 1986). This may suggest the levels of fracture in high-intensity egg production could be partly reduced by providing housing that allows greater activity to provide the osteogenic mechanical environment for the skeletons of these birds.

These studies using *in vivo* models suggest that an increased mechanical input could be used to override the osteopenic effects of some of the metabolic causes of skeletal degeneration such as osteoporosis. The nature of the downregulation of the adaptive response of the skeleton to mechanical loads must be determined before such strategies can be confirmed.

The majority of studies using *in vivo* models to investigate mechanical adaptation of bone have focused on the response of cortical bone. One of the few models developed to study the effect of imposed loads on cancellous bone utilized the tail vertebrae of rats. Chambers et al. (1993) developed a model in which the eighth caudal vertebra in the rat tail was loaded by means of pins placed in the adjacent seventh and ninth vertebrae. This model provided evidence of an adaptive bone hypertrophy in response to short periods of compressive loading in a mammalian species. As in Rubin's avian model, the daily application of cyclical loading for 36 cycles at 0.5 Hz induced a dramatic increase in trabecular bone volume resulting from deposition of lamellar bone on trabecular surfaces and also periosteal bone formation. A single application of 360 cycles of loading also induced some hypertrophy but only about 13% of that induced by daily application of 36 cycles. Unlike the avian ulna model, the actual surface bone strains were not determined in terms of magnitude and distribution of principal strains. However, this model again confirms the acute sensitivity of bone to short periods of cyclical deformation in both cortical and trabecular sites.

26.3.7 Modeling Changes in Bone Structure in Long-Term Adaptation

The osteogenic response of bone to imposed mechanical loading of a diverse strain distribution has been attributed to a need to respond to new loading patterns. To some extent these are initially an "error" signal, in that the pattern of loading is outside the physiological expectation. However, a continuation of such a stimulus does elicit a modeling response to optimize the skeletal form for the "new" loading

conditions. The initial hypertrophic bone formation could be described as "explosive" and this has been criticized as being potentially pathological. However, longer-term loading has been shown to result in a more normal histological pattern of bone tissue and a new equilibrium between mechanical environment and bone structure. The porcine radii subjected to increased loading showed an initial radial periosteal bone formation that after 3 months resumed the normal circumferential laminar bone distribution (Goodship et al., 1976). Similarly, in Rubin's avian ulna the application of the osteogenic stimulus for a period of 16 weeks resulted in a modeling outcome with cortical bone showing normal histological structure (Rubin et al., 1995). Turner et al. (1992) also found that new bone, formed in response to externally applied bending loads of the tibia, matured over a 14-week period of loading.

26.4 Transduction Pathways

Although there are numerous models for the study of functional adaptation of bone in relation to mechanical stimulation, the transduction pathways that activate cellular responses to changes in mechanical conditions are only recently being elucidated. There have been many suggestions regarding the mechanotransduction pathways.

The effect of a single train of osteogenic loading cycles in the functionally isolated avian ulna has been shown to elicit a cascade of events. This cascade comprises changes in orientation of proteoglycans in the extracellular matrix through changes in osteocyte metabolism and signaling to activation of lining cells and osteoblast matrix synthesis. The cyclical loading of bone has been shown to induce a regular orientation of proteoglycan molecules within the bone matrix. These molecules were also shown to be concentrated around the osteocyte lacunae using electron microscopy. The effect occurred after only 10 to 50 cycles and had a half-life of approximately 24 h and thus may represent a mechanism for strain memory within the matrix (Skerry et al., 1988; 1990).

Within a few minutes of loading, the osteocytes within the loaded ulna showed an increase in uptake of tritiated uridine and also increased levels of glucose 6 phosphate dehydrogenase (Pead et al., 1988; Skerry et al., 1989). These findings were suggestive of mechanical stimulation inducing synthesis of RNA within the osteocyte population. Subsequent to these early changes, the periosteal cells were activated and new bone formation occurred. This represented another pivotal finding resulting from the use of the avian ulna model. As discussed previously, this finding has also been reported subsequently in the rat tibia mammalian model.

26.4.1 Electrical and Electromagnetic Stimulation

The avian ulna model has also been used to evaluate the effects of other biophysical stimuli (McLeod and Rubin, 1992). Applied electromagnetic fields of a specific frequency were found not only to inhibit disuse osteopenia but to induce new bone formation increasing the cross-sectional area in relation to the control bone area (Fig. 26.9). Not only did the specific frequency stimulation activate osteogenesis in the ulna diaphysis but this stimulus also enhanced osseo-integration of a porous ingrowth metal implant. The specific frequency was determined by a frequency analysis of *in vivo* strain data from different sites in many species. A common frequency band was found around 20 to 30 Hz. The osteogenic effect of cyclical deformation could be induced at lower strain magnitudes as frequency was increased. This frequency-dependent effect appears to result from either direct mechanical or induced electrical stimulation of cellular activity and may involve activation of osteocytic signaling.

The use of electromagnetic stimuli to inhibit disuse osteopenia has also been validated in an isolated canine fibula model (Skerry et al., 1991). In this model a section of the fibula, a small bone without a medullary cavity, is isolated and the ends covered with caps. Specific electromagnetic waveforms were shown to inhibit the bone loss as a result of isolation from the functional environment. In this model the electromagnetic stimulus did not induce a net formation of bone.

Mechanical stimulation of living bone has been shown to be related to measured electrical potentials (Otter et al., 1990). These experiments were conducted under anesthesia in contrast to the potentials

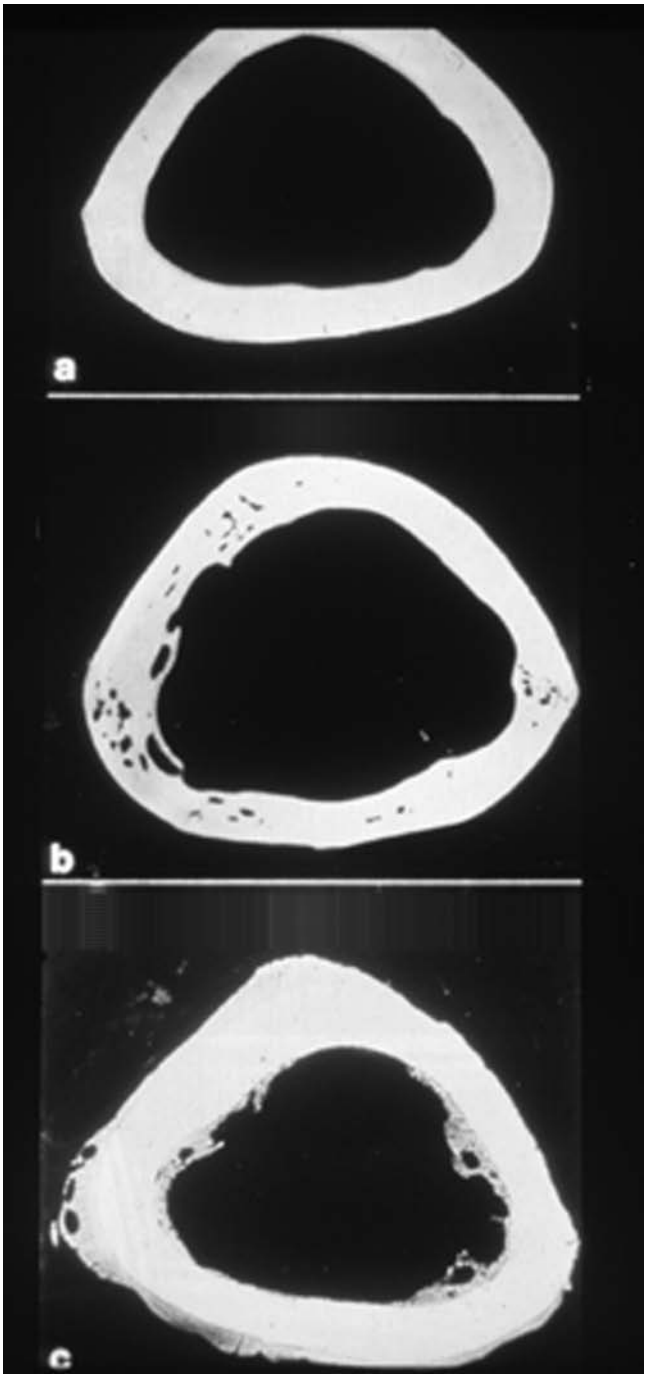

FIGURE 26.9 Induction of new bone formation with applied electromagnetic fields of a specific frequency. These can be observed to increase the cross-sectional area in relation to the control bone area. Mid-diaphyseal transverse sections of (a) nomal ulna, (b) functionally isolated ulna showing endosteal resorption and intracortical porosity, (c) stimulated ulna showing increased periosteal and endosteal bone formation. (From McLeod, K. J. and Rubin, C. T., *J. Bone Joint Surg.,* 74-A, 920, 1992. With permission.)

recorded by Lanyon and Hartman (1977) during locomotion. Understanding the functional link between mechanical deformation, streaming potentials, and activation of cellular activity to effect appropriate structural changes has been made possible by use of these models. Other aspects of the mechanoelectrical transduction pathways still require further elucidation.

26.4.2 Fluid Flow

Bone is a connective tissue with a porous extracellular matrix containing living cells with both intra- and extracellular fluid. Deformation of the tissue induces fluid movement. Flow of fluid over cell membranes may induce fluid shear stresses that could act directly on cells. The flow of ionic fluid also results in electrical streaming potentials that also have effects on the cell populations. These phenomena are being investigated by introducing tracer substances into bone to observe transport at cellular and subcellular levels (Knothe Tate et al., 1998).

26.4.3 Estrogen Mediation

In many models, the effects of estrogen have been shown to include formation of bone. In both rats and mice, high levels of exogenous estrogen induce intramedullary bone formation (Tobias et al., 1991; Samuels et al., 1999). Estrogen also reverses the loss in bone mass associated with postmenopausal osteoporosis as does diverse exercise. Recent work indicates that the adaptive response of bone to applied mechanical loading in experimental models can be amplified in the presence of estrogen (Lanyon, 1996).

26.4.4 Prostaglandins

In several of the *in vivo* models of mechanically induced bone formation there is evidence that prostaglandins are involved in mediation of the mechanical stimulus. Some of this evidence has been obtained by using prostaglandin synthetase inhibitors such as indomethacin. This agent is nonspecific and blocks the formation of both constitutive and inducible cyclo-oxygenase. The use of this agent has been shown to down-regulate mechanically induced bone formation (Pead and Lanyon, 1989; Chow and Chambers, 1994). Using a specific inducible cyclo-oxygenase (COX-2) inhibitor and indomethacin, Forwood (1996) provided evidence that COX-2 is important in the formation of lamellar bone in response to mechanical stimulation.

26.4.5 Nitric Oxide

Nitric oxide has also been shown to act as a mediator of mechanically induced bone formation. This mediator is thought to be generated independently from the prostaglandins (Chow et al., 1998). However, in this study exogenous nitric oxide donors enhanced the level of bone formation in response to mechanical loading but did not induce bone formation in the unloaded controls. This suggests that the nitric oxide pathway facilitates bone formation in response to mechanical loading but cannot be a direct component of the transduction pathway. Chambers et al. (1999) found that nitric oxide and prostaglandins are critical in the early phase of the adaptive response. Inhibitors given just before loading were effective in suppressing the response but not if given after a single short period of mechanical stimulation. They also reported the mechanical activation of gene expression in the osteocyte for c-fos and insulin-like growth factor (IGF-1) in the rat caudal vertebra model. Raab-Cullen et al. (1994) found that external loading of the tibia also induced changes in gene expression in the periosteal cells. The early response was an increase in transforming growth factor (TGF-β) and IGF-1 mRNA. Thus, the early response is an increase in cell proliferation.

26.5 Mechanical Modulation of Bone Repair

26.5.1 Direct Fracture Repair

Following fracture, bone shows a remarkable ability to mount a repair process that not only restores mechanical integrity but also restores the anatomical configuration with little or no evidence of scar tissue, as would be seen following injury in other musculoskeletal tissues. This has the advantage that

no residual stress concentration remains and the strength and stiffness of the bone returns to the prefracture values. It is said that high-energy fractures cleave the microstructural elements of bone such as secondary osteons, whereas in low-energy fractures the fracture line passes around such structures. Fracture compromises the functional use of a limb or part of the skeleton; as healing progresses function is gradually regained. The relationship between the progression of healing and increased use of the limb is poorly understood and will be considered later.

Following fracture of the bone with concomitant damage to periosteal, endosteal, and intramedullary blood vessels, a hematoma is formed at the fracture site. A repair process follows that falls into one of two types depending upon the mechanical stability at the fracture site. Under conditions of rigid stabilization with bone matrix of one fragment opposed in contact with that of the other, a process termed *direct (Primary)* fracture repair occurs. In this process intracortical remodeling occurs across the fracture site. New secondary osteons replace the damaged area and the bone heals. In this process there is little or no bone formation by the periosteum (fracture callus) or endosteum. The process takes months or years to complete.

The application of a supporting device together with the reduction in functional loading resulting from the injury reduces the very stimulus that is thought to be responsible for cellular activity involved in maintaining bone mass. This apparent paradox may be relevant to the control of the healing process. Uhthoff and Finnegan (1983) and Claes (1989) reported the observation of an increase in intracortical porosity beneath rigid fracture plates compared with less rigid plates, this being thought to be due to strain protection. Studies by the AO group suggested that this effect might also be attributed to vascular occlusion of periosteal vessels compressed by the overlying plate (Perren et al., 1988). Baggot et al. (1981) demonstrated that customary bone strain is reduced by up to 30% beneath a commercial fracture plate. This reduction in strain was accompanied by an increase in intra-cortical porosity. To differentiate between vascular and mechanical effects, a plate was modified to include a low-rate spring in the midsection. The experimental (spring) and control (standard DCP) plates were applied to the dorsal aspect (torsion surface) of the ovine radius for a period of 12 weeks. The spring plate was applied with the spring extended (under tension). Histology revealed the expected intracortical porosity and also evidence of endosteal resorption. The spring plate in which near normal loads were carried through the cortex beneath the spring showed little intracortical or endosteal bone loss. It could be argued, however, that the contact profile of the plates differed and the vascular factor may still account for remodeling differences. It is known that changes in vascular dynamics may influence bone formation. For example, bone formation distal to a venous tourniquet has been reported by Kruse and Kelly (1974).

Strain protection in the avian ulna preparation resulted in bone loss by both endosteal resorption and intracortical porosity (Rubin and Lanyon, 1985). In this model the surgical isolation inevitably causes a vascular disturbance; thus there are two potential influences on bone cell activity: first, a change in hemodynamics and, second, a reduction in customary strain. The influence of strain protection in bone modeling can be evaluated without concurrent vascular impingement by the use of external fixation. The influence of strain protection was studied by applying bilateral external fixators with identical anatomical location and frame configuration (O'Doherty et al., 1995). The experimental tibia was protected by an intact frame and in the control the fixator bar was discontinuous to allow functional loads to be carried by the tibia. Strain gauge measurements showed the functional tibial strains were reduced to 50% by the presence of the intact fixator, but with the discontinuous fixator normal strain patterns were retained. Over a period of 16 weeks bone mass decreased in the protected tibia. The loss of bone was a result of endosteal resorption and consequent thinning of the cortices. There was no evidence of intracortical porosity. Thus, these data would support a modeling change to optimize mass and structure of the bone for a decrease in functional demand. In addition, it could be postulated that intracortical resorption may be induced by changes in hemodynamics.

Direct fracture repair occurs at points of bone contact; where gaps are present these are filled by woven bone that is then remodeled. This pattern of healing is the so-called gap healing. Perren (1979) suggested that motion in areas of small fracture gaps creates high strain fields that are detrimental to bone formation. Therefore, the direct bone repair, as suggested in experimental models, may not be a common occurrence in clinical fractures.

Although there are advantages of direct repair in terms of restoration of anatomical integrity, and this is certainly required in intra-articular fractures, the process is a lengthy one taking months to years to complete with possible complications from the implant if loosening occurs and on implant removal. Rigid internal fixation is also dependent upon a knowledge of the biomechanics of the bone. In some cases an appropriate axial tension axis may not exist (e.g., tibia).

26.5.2 Indirect Fracture Repair

The second type of bone healing, indirect repair, involves the formation of a "callus" to form a biological splint that stabilizes the fracture. During this type of healing bone forms from the periosteum and endosteum to produce "hard" callus. The fracture hematoma undergoes a process of tissue differentiation through granulation tissue, fibrous tissue, fibrocartilage, and hyaline cartilage which, through the process of endochondral ossification, forms woven bone that remodels to the definitive tissue of lamellar bone. The initial repair is rapid, although the contour of the bone shows the bulge of callus for a protracted period of remodeling. There is much evidence to suggest that this process of repair produces a more rapid return to prefracture values of strength and stiffness than the slower direct healing. Sarmiento, for example, has shown that bone healing by bracing techniques results in greater torsional strength than plating (Sarmiento et al., 1980).

Indirect fracture repair is sensitive to biological and mechanical factors. The mechanical environment imposed by the fixation device, cast, brace, external fixation, or intramedullary nail influences the mass and distribution of callus. In addition to this process being seen in traumatic fracture, it also forms the basis of bone regeneration during leg lengthening and bone transport procedures. The relationship between tissue differentiation and mechanical environment is important in the scientific understanding of these procedures.

Indirect fracture healing is acutely sensitive to small changes in the mechanical environment at the fracture site. This can be easily observed at two extremes: if the fixation applied is too rigid, an atrophic nonunion will result, while if the fixation is not rigid enough, a hypertrophic nonunion occurs. Both of these are failures of the bone to unite: one through a lack of callus, the formation of which has been suppressed by overrigid fixation, the other by an overproliferation of callus, which has failed to bridge due to excessive movement. Between these two extremes, it can be hypothesized that a mechanical environment will exist at which fracture healing will proceed at an optimal rate. Clinical fractures heal under quite wide ranges of fracture site motion, as is evidenced by the relatively large motions produced in cast treatment (Lippert and Hirsch, 1974; Sarmiento et al., 1996) and the small motions produced with external fixaton (Gardner et al., 1997) and which must occur with intramedullary nailing. However, the precise influence that local fracture site mechanics has on indirect fracture has only recently been examined.

Very subtle changes in fixation construction resulting in small changes in deformation at the fracture site lead to significant changes in the biological progression of healing. An experiment (Goodship et al., 1993) in which a standard osteotomy was stabilized using a single-sided fixator with constant anatomical location and frame geometry except for one variable, namely, the offset distance between the fixator bar and the bone. A difference of only 10 mm in this one construct variable induced a significant difference in the rate of mineralization in the osteotomy gap and also the rate of increase in fracture stiffness index. The effects of fixation stiffness on bone healing have also been examined by Wu et al. (1984) and Williams et al. (1987) who found that fixators with an increased stiffness tended to give earlier union, increased rigidity, and decreased porosity compared with fixators with reduced stiffness.

White et al. (1977) applied intermittent cyclic compression to well-reduced experimental osteotomies but found no difference between those treated with constant compression and those treated with intermittent cyclical compression. Aro et al. (1990) applied nonrecoverable axial dynamization to bilateral experimental osteotomies without a significant effect compared with no dynamization. Cheal et al. (1991) applied bending deformations to a healing osteotomy to produce strains of 10% on one cortex and strains of 100% on the opposite cortex. In regions of lower strain, there was more ingrowth of vascularized soft tissue and differentiation of this tissue occurred earlier and to a greater extent. In the high-strain regions, the proliferation of callus was greatest. Claes et al. (1995) compared two experimental groups both

stabilized with external fixation. In one group the fixator was maintained rigid throughout the period of the experiment (9 weeks); in the other recoverable dynamic axial motion was produced on weight-bearing. In the rigid group, the maximum fracture gap strain was 10%, while in the group with dynamic axial motion fracture gap strains of 25 to 58% were produced on weight-bearing, strains that were found to decrease with time. The group in which dynamic axial motion was permitted was found to produce more callus and produce a stronger repair than the rigid group. In a later experiment using the same model, Claes et al. (1997) examined the influence of three sizes of osteotomy gap (1, 2, and 6 mm) and gap strain (7 and 31%) on repair. Larger gap sizes (>2 mm) were found to produce less callus and give a reduced bending stiffness of the healing bone, even when the gap strain was high. At smaller gap sizes, more callus was produced and was a maximum for the midsized gap (2 mm) and the higher strain. Bending stiffness was found to decrease with increasing gap size and reduce with increasing strain. Hence, it is possible to influence healing by manipulating the local mechanics at the fracture site, but for this to be effective the fracture gap must not be too large and the initial fracture site strains have to be of a reasonable value (approximately 10 to 50%) and repetitively applied.

In addition to the initial gap size and fracture site strain required to elicit an improved healing response, the influence of the mechanical variables (load, strain rate, loading frequency) required to produce and maintain an appropriate response to a given strain also needs to be determined. Previous work examining the response of intact bone to altered mechanical stimuli had demonstrated the positive effect of intermittent cyclic compression on the bone cell population (Lanyon and Rubin, 1984; Rubin and Lanyon, 1985). In experimental osteotomies, stabilized with external fixation, Goodship and Kenwright (1985) applied an intermittent loading regime, the characteristics of which, in terms of strain rate and number of loading cycles, were similar to that which had previously proved to be most osteogenic when stimulating intact bone. They found a significant improvement in healing when compared with the same method of fixation but without the application of intermittent loading. Further work (Goodship et al., 1987; 1998b; Kenwright and Goodship, 1989) went on to demonstrate the effect of changes in the intermittent loading regime in terms of applied load (Goodship et al., 1987), fracture gap strain (Kenwright and Goodship, 1989), and strain rate (Goodship et al., 1998b). It was also shown that the effect of the loading stimulus was maximized if it was applied in the early period postosteotomy (Goodship et al., 1998b) and that decreasing the magnitude of the stimulus with time was more effective than a stimulus of constant magnitude (Clasbrummel et al., 1997). The application of such intermittent cyclical loading to human tibial fractures also demonstrated a positive effect on the rate of healing (Kenwright et al., 1991).

26.5.3 Mechanical Variables Influencing Healing

From this and other work, the principal variable influencing healing appears to be the strain acting at the fracture site, as had been previously suggested but never demonstrated in a controlled manner. Fracture site strain is dependent on both the mode of loading of the limb and on the fracture geometry (Perren, 1979). For a similar amount of axial movement, small fracture gaps will produce higher values of strain. In clinical fracture healing, although it is likely that axial strain will predominate, there will also be significant amounts of strains produced through the action of bending and shear loads acting at the fracture site (Kenwright and Gardner, 1998). The effect of the strains produced by these loading modes has yet to be fully assessed, although it would appear that shear motion at the fracture site is not as deleterious to healing as had been previously thought; indeed, it may be as beneficial as axial motion (Park et al., 1998).

Within the fracture gap, the strains produced in the delicate healing tissues are not uniform and will depend on local geometric and material factors, and relatively small changes in strain can have marked effects on the pattern of healing observed. This is well illustrated in the experimental bone healing studies where the asymmetric nature of the fixation causes corresponding asymmetries in the callus formation observed. For example, in a previous study (Goodship et al., 1998b), a marked callus asymmetry was observed, which was closely related to the placement of the external fixator, more callus appearing on the side of the fracture adjacent to the fixator than on the side opposite it (Fig. 26.10) regardless of the nominal strain rate imposed at the osteotomy gap. This asymmetry of callus formation must result from small differences in the strains in the delicate healing tissues, and if it could be determined what level of

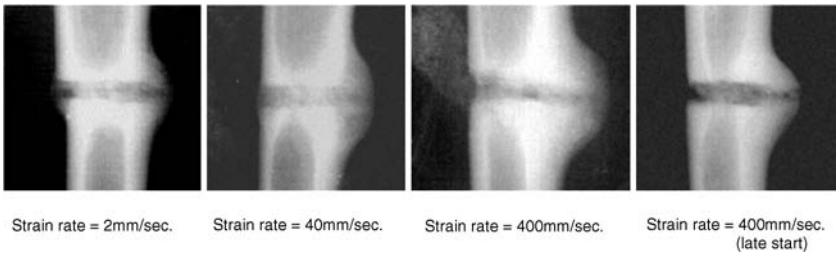

FIGURE 26.10 Callus asymmetry observed with external fixation. (From Goodship, A. E. et al., *Clin. Orthop.,* 355S, S105, 1998. With permission.)

strain particularly favored the early formation and maturation of external callus, then these data would be extremely useful in the design of new implants to optimize the healing response. It is therefore important to examine the various theories proposed regarding the influence of the prevailing stresses and strains on the tissue differentiation.

Perren introduced the concept of interfragmentary strain, i.e., the strain magnitude produced as a result of loading in the differentiating tissues at the fracture site (Perren, 1979; Perren and Cordey, 1980). He noted that tissues could not form if the strain level existing at the fracture site was greater than the failure strain for that tissue. Hence, bone could not form unless the local strain had been reduced to a level below the failure strain of bone.

Pauwels (1980) proposed that hydrostatic compression applied to mesenchymal tissue favored the formation of hyaline cartilage, while deformation favored the formation of connective tissue; a combination of deformation and hydrostatic compression led to the formation of fibrocartilage.

Carter et al. (1988; 1998) examined the importance of cyclic tissue loading and local stress and strain history on tissue formation. They hypothesized that a history of compressive hydrostatic stress was likely to produce cartilage formation while a history of tensile strain was likely to produce connective tissue. Using a finite-element (FE) model of a healing fracture, this theory predicted bone formation on bone surfaces adjacent to the fracture gap and fibrocartilage formation in the fracture gap. It also suggested cartilage formation at the endosteal side of the fracture gap, as is often observed in experimental models of bone healing.

Claes and Heigele (1999) proposed a theory of tissue differentiation relating local tissue formation to local stress and strain. They hypothesized that strain and hydrostatic pressure along the calcified surface of the callus are the determinant factors for the differentiation of the callus tissue (Fig. 26.11). It was proposed that endochondral ossification can occur under conditions of high negative hydrostatic pressures (greater than -0.15 MPa) and relatively high strains ($\pm 15\%$) while intramembraneous ossification occurs under relatively low hydrostatic pressures (± 0.15 MPa) and strains ($\pm 5\%$).

The above theories can be synthesized to give the following general theory of mesenchymal tissue differentiation in bone healing:

1. Low values of strain and hydrostatic pressure favor bone formation by intramembraneous ossification.
2. High values of compressive hydrostatic stress favor cartilage formation (if strain is low). This in turn will lead to bone formation by endochondral ossification. However, endochondral ossification can only take place (from its cartilage precursor) in conditions of relative stability (which is usually provided by the linking up of the "bridge" of callus that is provided on the periosteal surface of the bone via the process of intramembraneous ossification).
3. Connective tissue or fibrocartilage forms in areas of high strain and high hydrostatic pressure.

Further work in this area is aimed at applying such theories to the prediction of healing for a given fracture geometry and loading conditions using FE models (Gardner et al., 2000). Using such methods,

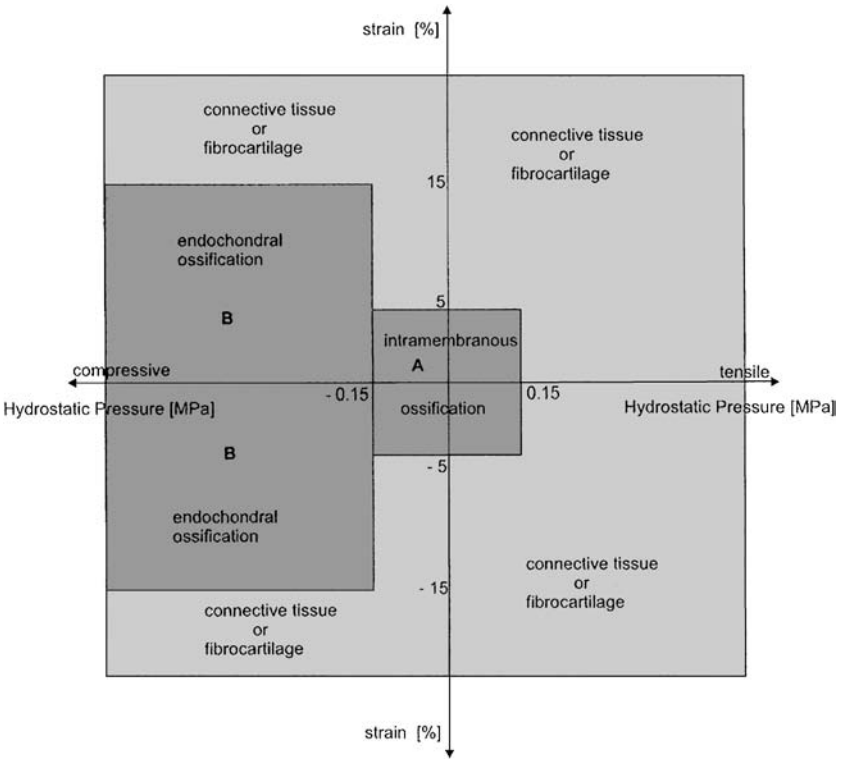

FIGURE 26.11 Effect of local stress and strain on local tissue formation during fracture healing. (From Claes, L. E. and Heigele, C. A., *J. Biomech.,* 32, 255, 1999. With permission.)

it may be possible in the future to modify the fixation as a function of time to maximize the healing of any given fracture.

26.6 Conclusions

Over the last two decades, the understanding of the interactions between mechanical environment and optimization of skeletal structure has increased dramatically. The early observations of surgeons, anatomists, and engineers have been explored using a range of techniques. Perhaps the most significant advance was that of the application of strain gauges to living bone. This allowed a direct measurement of deformation of the skeleton during functional activities. Although such techniques could also be used in cadaveric specimens and provide additional data for mathematical and computer modeling, the study of the living skeleton has enabled assumptions to be converted to actual data. Thus, strain magnitudes, rates, and distributions incurred during physiological loading could be determined in a range of species including humans. The effects of changes in loading and consequent adaptive tissue response were also made possible using *in vivo* models. The data from such studies have been applied to computer modeling and also in cell and tissue culture systems to explore the cellular and molecular mechanisms that control functional adaptation of bone.

The value of these studies has now been seen in relation to management of bone repair, improved design of skeletal prostheses, and management of degenerative conditions of the skeleton such as osteoporosis and osteoarthrosis.

In vivo studies require careful consideration and justification in relation to ethical and scientific cost vs. benefits. The continued reduction, refinement, and replacement of these studies is essential; however, there is also a need to study the response of the skeleton to mechanical stimuli in a complete

physiological environment, where hormonal and other systemic factors interact with the mechanical and mechanically related cues that normally maintain optimal skeletal form. Such studies have also made great contributions to understanding the failure of these control mechanisms in skeletal disease.

References

Akhter, M. P., Cullen, D. M., Pedersen, E. A., Kimmel, D. B., and Recker, R. R. (1998). Bone response to in vivo mechanical loading in two breeds of mice, *Calcif. Tissue Int.,* 63, 442–449.

Aro, H. T., Kelly, P. J., Lewallen, D. G., and Chao, E. Y. S. (1990). The effects of physiologic dynamic compression on bone healing under external fixation, *Clin. Orthop.,* 256, 260–273.

Baggott, D. G., Goodship, A. E., and Lanyon, L. E. (1981). A quantitative assessment of compression plate fixation in vivo: an experimental study using the sheep radius, *J. Biomech.,* 14, 701–711.

Baldwin, K. M., White, T. P., Arnaud, S. B., Edgerton, V. R., Kraemer, W. J., Kram, R., Raab-Cullen, D., and Snow, C. M. (1996). Musculoskeletal adaptations to weightlessness and development of effective countermeasures, *Med. Sci. Sports Exerc.,* 28, 1247–1253.

Banks, W. J., Jr., Epling, G. P., Kainer, R. A., and Davis, R. W. (1968). Antler growth and osteoporosis. I. Morphological and morphometric changes in the *costal compacta* during the antler growth cycle, *Anat. Rec.,* 162, 387–398.

Bassey, E. J. and Ramsdale, S. J. (1994). Increase in femoral bone density in young women following high-impact exercise, *Osteoporosis Int.,* 4, 72–75.

Baxter, B. J., Andrews, R. N., and Barrell, G. K. (1999). Bone turnover associated with antler growth in red deer (*Cervus elaphus*), *Anat. Rec.,* 256, 14–19.

Bentolila, V., Boyce, T. M., Fyhrie, D. P., Drumb, R., Skerry, T. M., and Schaffler, M. B. (1998). Intracortical remodeling in adult rat long bones after fatigue loading, *Bone,* 23, 275–281.

Biewener, A. A., Thomason, J., Goodship, A., and Lanyon, L. E. (1983). Bone stress in the horse forelimb during locomotion at different gaits: a comparison of two experimental methods, *J. Biomech.,* 16, 565–576.

Boppart, M. D., Kimmel, D. B., Yee, J. A., and Cullen, D. M. (1998). Time course of osteoblast appearance after in vivo mechanical loading, *Bone,* 23, 409–415.

Burkhart, J. M. and Jowsey, J. (1967). Parathyroid and thyroid hormones in the development of immobilisation osteoporosis, *Endocrinology,* 81, 1053–1062.

Carter, D. R., Blenman, P. R., and Beaupre, G. S. (1988). Correlations between mechanical stress history and tissue differentiation in initial fracture healing, *J. Orthop. Res.,* 6, 736–748.

Carter, D. R., Beaupre, G. S., Giori, N. J., and Helms, J. A. (1998). Mechanobiology of skeletal regeneration, *Clin. Orthop.,* 355S, S42–S55.

Chalmers, J. and Ray, R. D. (1962). The growth of transplanted foetal bones in different immunological environments, *J. Bone Joint Surg.,* 44B, 149–164.

Chamay, A. and Tschantz, P. (1972). Mechanical influences in bone remodeling. Experimental research on Wolff's law, *J. Biomech.,* 5, 173–180.

Chambers, T. J., Evans, M., Gardner, T. N., Turner-Smith, A., and Chow, J. W. (1993). Induction of bone formation in rat tail vertebrae by mechanical loading, *Bone Miner.,* 20, 167–178.

Chambers, T. J., Fox, S., Jagger, C. J., Lean, J. M., and Chow, J.W. (1999). The role of prostaglandins and nitric oxide in the response of bone to mechanical forces, *Osteoarthritis Cartilage,* 7, 422–423.

Cheal, E. J., Mansmann, K. A., DiGioia, A. M., Hayes, W. C., and Perren, S. M. (1991). Role of interfragmentary strain in fracture healing: ovine model of a healing osteotomy, *J. Orthop. Res.,* 9, 131–142.

Chow, J. W. and Chambers, T. J. (1994). Indomethacin has distinct early and late actions on bone formation induced by mechanical stimulation, *Am. J. Physiol.,* 267, E287–E292.

Chow, J. W., Fox, S. W., Lean, J. M., and Chambers, T. J. (1998). Role of nitric oxide and prostaglandins in mechanically induced bone formation, *J. Bone Miner. Res.,* 13, 1039–1044.

Churches, A. E. and Howlett, C. R. (1982). Functional adaptation of bone in response to sinusoidally varying controlled compressive loading of the ovine metacarpus, *Clin. Orthop.,* 168, 265–280.

Claes, L. (1989). The mechanical and morphological properties of bone beneath internal fixation plates of differing rigidity, *J. Orthop. Res.,* 7, 170–177.

Claes, L. E. and Heigele, C. A. (1999). Magnitudes of local stress and strain along bony surfaces predict the course and type of fracture healing, *J. Biomech.,* 32, 255–266.

Claes, L. E., Wilke, H.-J., Augat, P., Rubenacker, S., and Margevicius, K. J. (1995). Effect of dynamisation on gap healing of diaphyseal fractures under external fixation, *Clin. Biomech.,* 10, 227–234.

Claes, L., Augat, P., Suger, G., and Wilke, H.-J. (1997). Influence of size and stability of the osteotomy gap on the success of fracture healing, *J. Orthop. Res.,* 15, 577–584.

Clasbrummel, B., Muhr, G., and Goodship, A. E. (1997). Time-dependent mechanical stimulation of enchondral fracture healing in the sheep [in German], *Biomed. Tech.* (Berlin), 42 (Suppl.), 521–522.

Cochran, G. V., Wu, D. D., Lee, B. Y., Bieber, W., and Otter, M. W. (1997). Streaming potentials in gap osteotomy callus and adjacent cortex. A pilot study, *Clin. Orthop.,* 337, 291–301.

Collet, P., Uebelhart, D., Vico, L., Moro, L., Hartmann, D., Roth, M., and Alexandre, C. (1997). Effects of 1- and 6-month spaceflight on bone mass and biochemistry in two humans, *Bone,* 20, 547–551.

Convertino, V. A. (1996). Exercise as a countermeasure for physiological adaptation to prolonged spaceflight, *Med. Sci. Sports Exerc.,* 28, 999–1014

Duncan, R. L. and Turner, C. H. (1995). Mechanotransduction and the functional response of bone to mechanical strain, *Calcif. Tissue Int.,* 57, 344–358.

Einhorn, T. A. (1995). Current concepts review: enhancement of fracture healing, *J. Bone Joint Surg.,* 77-A, 940–956.

Fell, H. B. (1956) Skeletal development in tissue culture, in *The Biochemistry and Physiology of Bone,* Bourne, G. W., Ed., Academic Press, New York.

Firth, E. C., Delahunt, J., Wichtel, J. W., Birch, H. L., and Goodship, A. E. (1999). Galloping exercise induces regional changes in bone density within the third and radial carpal bones of Thoroughbred horses, *Equine Vet. J.,* 31, 111–115.

Floyd, T., Nelson, R. A., and Wynne, G. F. (1990). Calcium and bone metabolic homeostasis in active and denning black bears (*Ursus americanus*), *Clin. Orthop.,* 255, 301–309.

Forwood, M. R. (1996). Inducible cyclo-oxygenase (COX-2) mediates the induction of bone formation by mechanical loading in vivo, *J. Bone Miner. Res.,* 11, 1688–1693.

Forwood, M. R. and Turner, C. H. (1995). Skeletal adaptations to mechanical usage: results from tibial loading studies in rats, *Bone,* 17 (Suppl. 4), 197S–205S.

Forwood, M. R., Bennett, M. B., Blowers, A. R., and Nadorfi, R. L. (1998). Modification of the in vivo four-point loading model for studying mechanically induced bone adaptation, *Bone,* 23, 307–310.

Fritton, S. P., McLeod, K. J., and Rubin, C. T. (2000). Quantifying the strain history of bone: spatial uniformity and self-similarity of low-magnitude strains, *J. Biomech.,* 33, 317–325.

Frost, H. M. (1967). *An Introduction to Biomechanics,* Charles C Thomas, Springfield, IL.

Galilei, G. (1637). *Dialogues Concerning Two New Sciences,* translated by H. Crew and A. De Salvio; Macmillan, New York, 1914, 300 pp.

Gardner, T. N., Evans, M., Hardy, J., and Kenwright, J. (1997). Dynamic interfragmentary motion in fractures during routine patient activity, *Clin. Orthop.,* 336, 216–225.

Gardner, T. N., Stoll, T., Marks, L., Mishra, S., and Knothe Tate, M. (2000). The influence of mechanical stimulus on the pattern of tissue differentiation in a long bone fracture—an FEM study, *J. Biomech.,* 33, 415–425.

Goodship, A. E. and Kenwright, J. (1985). The influence of induced micromovement upon the healing of experimental tibial fractures, *J. Bone Joint Surg.,* 67-B, 650–655.

Goodship, A. E., Lanyon, L. E., and McFie, H. (1979). Functional adaptation of bone to increased stress. An experimental study, *J. Bone Joint Surg.,* 61-A, 539–546.

Goodship, A. E., Kelly, D. J., Rigby, H. S., Watkins, P. E., and Kenwright, J. (1987). The effect of different regimes of axial micromovement on the healing of experimental tibial fractures, in *Biomechanics: Basic and Applied Research,* G. Bregmann, R. Kolbel, and A. Rohlmann, Eds., Martinus Nijhoff, Dortrecht, 441–446.

Goodship, A. E., Lawes, T. J., and Harrison, L. (1998b). Biology of fracture repair, in *Sciences Basic to Orthopaedics,* S. P. F. Hughes and I. D. McCarthy, Eds., W.B. Saunders, London, 144–155.

Goodship, A. E., Watkins, P. E., Rigby, H. S., and Kenwright, J. (1993). The role of fixator frame stiffness in the control of fracture healing. An experimental study, *J. Biomech.,* 26, 1027–1035.

Goodship, A. E., Lawes, T., and Rubin, C. T. (1997). Low magnitude high frequency mechanical stimulation of endochondral bone repair, *Trans. Orthop. Res. Soc.,* 22, 234.

Goodship, A. E., Cunningham, J. L., Oganov, V., Darling, J., Miles, A. W., and Owen, G. W. (1998a). Bone loss during long term space flight is prevented by the application of a short term impulsive mechanical stimulus, *Acta Astronaut.,* 43, 65–75.

Goodship, A. E., Cunningham, J. L., and Kenwright, J. (1998c). Strain rate and timing of stimulation in mechanical modulation of fracture healing, *Clin. Orthop.,* 355S, S105–S115.

Hadjiargyrou, M., McLeod, K., Ryaby, J. P., and Rubin, C. (1998). Enhancement of fracture healing by low intensity ultrasound, *Clin. Orthop.,* 355S, S216–S229.

Hert, J., Lisková, M., and Landa, J. (1971). Reaction of bone to mechanical stimuli. 1. Continuous and intermittent loading of tibia in rabbit, *Folia Morphol.* (Prague), 19(3), 290–300.

Hillam, R. A. (1996). Response of Bone to Mechanical Load and Alterations in Circulating Hormones, Ph.D. Thesis, University of Bristol.

Hillam, R. A. and Skerry, T. M. (1995). Inhibition of bone resorption and stimulation of formation by mechanical loading of the modeling rat ulna in vivo, *J. Bone Miner. Res.,* 10, 683–689.

Hsieh, Y. F., Wang, T., and Turner, C. H. (1999). Viscoelastic response of the rat loading model: implications for studies of strain-adaptive bone formation, *Bone,* 25, 379–382.

Hua, J. and Walker, P. S. (1992). A comparison of cortical strain after cemented and press-fit proximal and distal femoral replacement, *J. Orthop. Res.,* 10, 739–744.

Huang, R. P., Rubin, C. T., and McLeod, K. J. (1999). Changes in postural muscle dynamics as a function of age, *J. Gerontol. A. Biol. Sci. Med. Sci.,* 54, B352–357.

Iwamoto, J., Yeh, J. K., and Aloia, J. F. (1999). Differential effect of treadmill exercise on three cancellous bone sites in the young growing rat, *Bone,* 24, 163–169.

Jarvinen, T. L., Kannus, P., Sievanen, H., Jolma, P., Heinonen, A., and Jarvinen, M. (1998). Randomized controlled study of effects of sudden impact loading on rat femur, *J. Bone Miner. Res.,* 13, 1475–1482.

Jaworski, Z. F. and Uhthoff, H. K. (1986). Reversibility of nontraumatic disuse osteoporosis during its active phase, *Bone,* 7, 431–439.

Jaworski, Z. F., Lisková-Kiar, M., and Uhthoff, H. K. (1980). Effect of long-term immobilisation on the pattern of bone loss in older dogs, *J. Bone Joint Surg.,* 62-B, 104–110.

Jiang, Y., Zhao, J., Rosen, C., Geusens, P., and Genant, H. K. (1999). Perspectives on bone mechanical properties and adaptive response to mechanical challenge, *J. Clin. Densitom.,* 2, 423–433.

Judex, S. and Zernicke, R. F. (2000). Does the mechanical milieu associated with high-speed running lead to adaptive changes in diaphyseal growing bone? *Bone,* 26, 153–159.

Judex, S., Gross, T. S., and Zernicke, R. F. (1997). Strain gradients correlate with sites of exercise-induced bone-forming surfaces in the adult skeleton, *J. Bone Miner. Res.,* 12, 1737–1745.

Kenwright, J. and Gardner, T. (1998). Mechanical influences on fracture healing, *Clin. Orthop.,* 355S, S179–190.

Kenwright, J. and Goodship, A. E. (1989). Controlled mechanical stimulation in the treatment of tibial fractures, *Clin. Orthop.,* 241, 36–47.

Kenwright, J., Richardson, J. B., Cunningham, J. L., White, S. H., Goodship, A. E., Adams, M. A., Magnussen, P. A., and Newman, J. H. (1991). Axial movement and tibial fractures, *J. Bone Joint Surg.,* 73-B, 654–659.

Knothe Tate, M. L., Knothe, U., and Niederer, P. (1998). Experimental elucidation of mechanical load-induced fluid flow and its potential role in bone metabolism and functional adaptation, *Am. J. Med. Sci.,* 316, 189–195.

Kruse, R. L. and Kelly, P. J. (1974). Acceleration of fracture healing distal to a venous tourniquet, *J. Bone Joint Surg.,* 56-A, 730–739.

Langkamer, V. G., O'Doherty, D. M., and Goodship, A. E. (1992). The influence of implant modulus on bone modelling and functional compatability in cementless hip arthroplasy, *Trans. Orthop. Res. Soc.,* 17, 240.

Lanyon, L. E. (1996). Using functional loading to influence bone mass and architecture: objectives, mechanisms, and relationship with estrogen of the mechanically adaptive process in bone, *Bone,* 18 (Suppl. 1), 37S–43S.

Lanyon, L. E. and Hartman, W. (1977). Strain related electrical potentials recorded in vitro and in vivo, *Calcif. Tissue Res.,* 22, 315–327.

Lanyon, L. E. and Rubin, C. T. (1984). Static vs dynamic loads as an influence on bone remodelling, *J. Biomech.,* 17, 897–905.

Lanyon, L. E., Paul, I. L., Rubin, C. T., Thrasher, E. L., DeLaura, R., Rose, R. M., and Radin, E. L. (1981). In vivo strain measurements from bone and prosthesis following total hip replacement. An experimental study in sheep, *J. Bone Joint Surg.,* 63-A, 989–1001.

Lanyon, L. E., Goodship, A. E., Pye, C. J., and McFie, J. H. (1982). Mechanically adaptive bone remodelling, *J. Biomech.,* 15, 141–154.

Lanyon, L. E., Rubin, C. T., and Baust, G. (1986). Modulation of bone loss during calcium insufficiency by controlled dynamic loading, *Calcif. Tissue Int.,* 38, 209–216.

Lippert, F. G. and Hirsch, C. (1974). The three dimensional measurement of tibia fracture motion by photogrammetry, *Clin. Orthop.,* 105, 130–143.

Lisková, M. and Hert, J. (1971). Reaction of bone to mechanical stimuli. Part 2. Periosteal and endosteal reaction of tibial diaphysis in rabbit to intermittent loading, *Folia Morphol.* (Prague), 19, 301–317.

McLeod, K. J. and Rubin, C. T. (1992). The effect of low-frequency electrical fields on osteogenesis, *J. Bone Joint Surg.,* 74-A, 920–929.

Marotti, G. and Marrotti, F. (1965). Topographic-quantitative study of bone tissue formation and reconstruction in inert bones, in *Calcified Tissues—Proceedings of the Third European Symposium in Calcified Tissues,* Fleisch, H., Blackwood, H. J. J., and Owen, M., Eds., Springer Verlag, Berlin.

Mason, D. J., Hillam, R. A., and Skerry, T. M. (1996). Constitutive in vivo mRNA expression by osteocytes of beta-actin, osteocalcin, connexin-43, IGF-I, c-fos and c-jun, but not TNF-alpha nor tartrate-resistant acid phosphatase, *J. Bone Miner. Res.,* 11, 350–357.

Mason, D. J., Suva, L. J., Genever, P. G., Patton, A. J., Steuckle, S., Hillam, R. A., and Skerry, T. M. (1997). Mechanically regulated expression of a neural glutamate transporter in bone: a role for excitatory amino acids as osteotropic agents? *Bone,* 20, 199–205.

Matter, P., Brennwald, J., and Perren, S. M. (1974). Biologische Reaktion des Knochens auf osteosyntheses Platten, *Helv. Chir. Acta* (Suppl. 12), 1–44.

Meade, J. B., Cowin, S. C., Klawitter, J. J., Van Buskirk, W. C., and Skinner, H. B. (1984). Bone remodeling due to continuously applied loads, *Calcif. Tissue Int.,* 36 (Suppl. 1), S25–30.

Mosley, J. R. and Lanyon, L. E. (1998). Strain rate as a controlling influence on adaptive modeling in response to dynamic loading of the ulna in growing male rats, *Bone,* 23, 313–318.

Mullender, M., van Rietbergen, B., Ruegsegger, P., and Huiskes, R. (1998). Effect of mechanical set point of bone cells on mechanical control of trabecular bone architecture, *Bone,* 22, 125–131.

Murray, P. D. F. (1936). *Bones,* Cambridge University Press, London.

Nordstrom, P., Pettersson, U., and Lorentzon, R. (1998). Type of physical activity, muscle strength, and pubertal stage as determinants of bone mineral density and bone area in adolescent boys, *J. Bone Miner. Res.,* 13, 1141–1148.

O'Connor, J. A., Lanyon, L. E., and MacFie, H. (1982). The influence of strain rate on adaptive bone remodelling, *J. Biomech.,* 15, 767–781.

O'Doherty, D. M., Butler, S. P., and Goodship, A. E. (1995). Stress protection due to external fixation, *J. Biomech.,* 28, 575–586.

Oh, I. and Harris, W. H. (1978). Proximal strain distribution in the loaded femur. An in vitro comparison of the distributions in the intact femur and after insertion of different hip-replacement femoral components, *J. Bone Joint Surg.,* 60-A, 75–85.

Osei-Hyiaman, D., Ueji, M., Toyokawa, S., Takahashi, H., and Kano, K. (1999). Influence of grip strength on metacarpal bone mineral density in postmenopausal Japanese women: a cross-sectional study, *Calcif. Tissue Int.,* 64, 263–266.

Otter, M. W., Palmieri, V. R., and Cochran, G. V. (1990). Transcortical streaming potentials are generated by circulatory pressure gradients in living canine tibia, *J. Orthop. Res.,* 8, 119–126.

Park, S.-H., O'Connor, K., McKellop, H., and Sarmiento, A. (1998). The influence of active shear or compression motion on fracture healing, *J. Bone Joint Surg.,* 80-A, 868–878.

Pauwels, F. (1980). *Biomechanics of the Locomotor Apparatus,* Springer-Verlag, Berlin.

Pead, M. J. and Lanyon, L. E. (1989). Indomethacin modulation of load-related stimulation of new bone formation *in vivo*; *Calcif. Tissue Int.,* 45(1), 34–40.

Pead, M. J., Suswillo, R., Skerry, T. M., Vedi, S., and Lanyon, L. E. (1988). Increased 3H-uridine levels in osteocytes following a single short period of dynamic bone loading in vivo, *Calcif. Tissue Int.,* 43, 92–96.

Perren, S. M. (1979). Physical and biological aspects of fracture healing with special reference to internal fixation, *Clin. Orthop.,* 138, 175–196.

Perren, S. M. and Cordey, J. (1980). The concept of interfragmentary strain, in *Current Concepts of Internal Fixation of Fractures,* H. K. Uhthoff, Ed., Springer-Verlag, New York, 63–77.

Perren, S. M., Cordey, J., Rahn, B. A., Gautier, E., and Schneider, E. (1988). Early temporary porosis of bone induced by internal fixation implants. A reaction to necrosis, not to stress protection? *Clin. Orthop.,* 232, 139–151.

Perren, S. M., Klaue, K., Pohler, O., Predieri, M., Steinemann, S., and Gautier, E. (1990). The limited contact dynamic compression plate (LC-DCP), *Arch. Orthop. Trauma Surg.,* 109, 304–310.

Qin, Y. X., Rubin, C. T., and McLeod, K. J. (1998). Nonlinear dependence of loading intensity and cycle number in the maintenance of bone mass and morphology, *J. Orthop. Res.,* 16, 482–489.

Raab-Cullen, D. M., Thiede, M. A., Petersen, D. N., Kimmel, D. B., and Recker, R. R. (1994). Mechanical loading stimulates rapid changes in periosteal gene expression, *Calcif. Tissue Int.,* 55, 473–478.

Rubin, C. T. and Lanyon, L. E. (1984a). Dynamic strain similarity in vertebrates; an alternative to allometric limb bone scaling, *J. Theor. Biol.,* 107, 321–327.

Rubin, C. T. and Lanyon, L. E. (1984b). Regulation of bone formation by applied dynamic loads, *J. Bone Joint Surg.,* 66-A, 397–402.

Rubin, C. T. and Lanyon, L. E. (1985). Regulation of bone mass by mechanical strain magnitude, *Calcif. Tissue Int.,* 37, 411–417.

Rubin, C. T., McLeod, K. J., and Bain, S. D. (1990). Functional strains and cortical bone adaptation: epigenetic assurance of skeletal integrity, *J. Biomech.,* 23 (Suppl. 1), 43–54.

Rubin, C. T., Bain, S. D., and McLeod, K. J. (1992). Suppression of the osteogenic response in the aging skeleton, *Calcif. Tissue Int.,* 50, 306–313.

Rubin, C. T., Gross, T. S., McLeod, K. J., and Bain, S. D. (1995). Morphologic stages in lamellar bone formation stimulated by a potent mechanical stimulus, *J. Bone Miner. Res.,* 10, 488–495.

Rubin, C., Turner, A. S., Mallinckrodt, C., Fritton, J., and McLeod, K. (1997). Site-specific increase in bone density stimulated non-invasively by extremely low magnitude thirty hertz mechanical stimulation, *Trans. Orthop. Res. Soc.,* 22, 110.

Rubin, C., Recker, R., Cullen, D., Ryaby, J., and McLeod, K. (1998). Prevention of bone loss in a postmenopausal population by low-level biomechanical intervention, *Am. Soc. Bone Miner. Res.,* 23, 1106.

Samuels, A., Perry, M. J., and Tobias, J. H. (1999). High-dose estrogen induces de novo medullary bone formation in female mice, *J. Bone Miner. Res.,* 14, 178–186

Sarmiento, A., Mullis, D. L., Latta, L. L., Tarr, R. R., and Alvarez, R. (1980). A quantitative comparative analysis of fracture healing under the influence of compression plating vs. closed weight-bearing treatment, *Clin. Orthop.,* 149, 232–239.

Sarmiento, A., McKellop, H. A., Llinas, A., Park, S. H., Lu, B., Stetson, W., and Rao, R. (1996). Effect of loading and fracture motions on diaphyseal tibial fractures, *J. Orthop. Res.,* 14, 80–84.

Skerry, T. M. and Lanyon, L. E. (1995). Interruption of disuse by short duration walking exercise does not prevent bone loss in the sheep calcaneus, *Bone,* 16, 269–274.

Skerry, T. M., Bitensky, L., Chayen, J., and Lanyon, L. E. (1988). Loading-related reorientation of bone proteoglycan in vivo. Strain memory in bone tissue? *J. Orthop. Res.,* 6, 547–551.

Skerry, T. M., Bitensky, L., Chayen, J., and Lanyon, L. E. (1989). Early strain-related changes in enzyme activity in osteocytes following bone loading in vivo, *J. Bone Miner. Res.,* 4, 783–788.

Skerry, T. M., Suswillo, R., el Haj, A. J., Ali, N. N., Dodds, R.A., and Lanyon, L. E. (1990). Load-induced proteoglycan orientation in bone tissue in vivo and in vitro, *Calcif. Tissue Int.,* 46, 318–326.

Skerry, T. M., Pead, M. J., and Lanyon, L. E. (1991). Modulation of bone loss during disuse by pulsed electromagnetic fields, *J. Orthop. Res.,* 9, 600–608.

Sumner, D. R., Turner, T. M., Igloria, R., Urban, R. M., and Galante, J. O. (1998). Functional adaptation and ingrowth of bone vary as a function of hip implant stiffness, *J. Biomech.,* 31, 909–917.

Tobias, J. H., Chow, J., Colston, K. W., and Chambers, T. J. (1991). High concentrations of 17 beta-estradiol stimulate trabecular bone formation in adult female rats, *Endocrinology,* 128, 408–412.

Tschantz, P. and Rutihauser, E. (1967). La surcharge mécanique de l'os vivant. Les déformations plastiques initiales et l'hypertrophie d'adaptation, *Ann. Anatomie Pathol.,* 12, 233–248.

Turner, C. H. and Pavalko, F. M. (1998). Mechanotransduction and functional response of the skeleton to physical stress: the mechanisms and mechanics of bone adaptation, *J. Orthop. Sci.,* 3, 346–355.

Turner, C. H., Akhter, M. P., Raab, D. M., Kimmel, D. B., and Recker, R. R. (1991). A noninvasive, in vivo model for studying strain adaptive bone modeling, *Bone,* 12, 73–79.

Turner, C. H., Woltman, T. A., and Belongia, D. A. (1992). Structural changes in rat bone subjected to long-term, in vivo mechanical loading, *Bone,* 13, 417–422.

Turner, C. H., Takano, Y., and Owan, I. (1995). Aging changes mechanical loading thresholds for bone formation in rats, *J Bone Miner. Res.,* 10, 1544–1549.

Turner, T. M., Sumner, D. R., Urban, R. M., Igloria, R., and Galante, J. O. (1997). Maintenance of proximal cortical bone with use of a less stiff femoral component in hemiarthroplasty of the hip without cement. An investigation in a canine model at six months and two years, *J. Bone Joint Surg.,* 79-A, 1381–1390.

Uhthoff, H. K. and Finnegan, M. (1983). The effects of metal plates on post-traumatic remodelling and bone mass, *J. Bone Joint Surg.,* 65-B, 66–71.

Uhthoff, H. K. and Jaworski, Z. F. (1978). Bone loss in response to long-term immobilisation, *J. Bone Joint Surg.,* 60-B, 420–429.

Verborgt, O., Gibson, G. J., and Schaffler, M. B. (2000). Loss of osteocyte integrity in association with microdamage and bone remodeling after fatigue in vivo, *J. Bone Miner. Res.,* 15, 60–67.

Vogel, J. M. and Whittle, M. W. (1976). Bone mineral changes: the second manned Skylab mission, *Aviat. Space Environ. Med.,* 47, 396–400.

Weinans, H., Huiskes, R., van Rietbergen, B., Sumner, D. R., Turner, T. M., and Galante, J. O. (1993). Adaptive bone remodeling around bonded noncemented total hip arthroplasty: a comparison between animal experiments and computer simulation, *J. Orthop. Res.,* 11, 500–513.

Williams, E. A., Rand, J. A., An, K.-N., Chao, E. Y. S., and Kelly, P. J. (1987). The early healing of tibial osteotomies stabilized by one-plane or two-plane external fixation, *J. Bone Joint Surg.,* 69-A, 355–365.

Wolff, J. (1892), *Das Gesetz der Transformation der Knocken,* Berlin. Cited by Enlow, D. H., (1963). *Principles of Bone Remodelling,* Charles C Thomas, Springfield, IL.

Wu, J.-J., Shyr, H. S., Chao, E. Y. S., and Kelly, P. J. (1984). Comparison of osteotomy healing under external fixation devices with different stiffness characteristics, *J. Bone Joint Surg.,* 66-A, 1258–1264.

27

Devices and Techniques for *in Vitro* Mechanical Stimulation of Bone Cells

Thomas D. Brown
The University of Iowa

27.1 Introduction and Historical Background

The macroscopic *in utero* development of bone, its patterns of normal growth, its architectural changes with aging, its fracture healing response, and its adaptations to functional loading alterations—among other phenomena—all depend fundamentally on mechanosensation and mechanoresponse at the cellular level. *In vitro* mechanical testing of cell culture preparations offers means by which the formidable complexity of the *in vivo* environment can be simplified, in order to isolate specific sensation and/or response mechanisms at the cellular, subcellular, or even molecular level. More so than measurements at the macroscopic level, mechanical stimulation of bone cells or bone cell cultures has required the development of novel instrumentation and specialized testing protocols. The purpose of this chapter is to review briefly the instrumentation and protocols that have evolved for *in vitro* mechanostimulus testing of bone cells. (Many of the results obtained using these devices and methods are reviewed in Chapter 28 by E. Burger.) Until fairly recently, the impetus for much of this work has come from within the biological (rather than bioengineering) research community. Hence, despite the creativity and ingenuity often marshaled to deal with the unique demands of mechanical stimulation at the cell level, it is important to appreciate that many of these preparations involve limitations (e.g., inhomogeneity, anisotropy, or uncontrolled variables) that potentially confound interpretation of experimental results. In regard to the scope of the survey, most cell culture mechanostimulus systems are nonspecific as to cell type. It is assumed that the reader's interest extends to devices potentially useful for stimulating bone and bonelike cells, even though the developers' particular focus may have happened to be on other cell types (e.g., endothelial cells, chondrocytes, fibroblasts, myocytes).

Early developments in the field of bone cell mechanostimulus were nonquantitative in nature, and date from pioneering work in the 1930s by Glucksmann.[1] He used biological structures rather than mechanical hardware to apply the loads. One preparation used to load endosteal cell cultures from chick tibiae involved substrates of explanted intercostal muscle to which pairs of adjacent ribs were left attached. Spontaneous compression of the cultured endothelial cells occurred when the ribs were drawn toward one another as a result of degeneration of the muscle tissue. A variant on this approach was to use interposed bone rudiments to serve as barriers to culture mass expansion, thus again inducing compression. Glucksmann also devised a means for biologic delivery of tension, taking advantage of surface tension effects in hanging drop cultures. Subsequently, Bassett and Hermann[2] refined the hanging-drop tensile loading technique, to study chick tibial cortex culture responses to both mechanical and electrical stimulation. In corollary studies, they modulated culture growth by stretching their culture masses over progressively larger silicone rods during periods of active growth. Compressive load delivery was achieved via autocompaction of culture masses growing between suspension clots. In related experiments,[3] this group studied *in vitro* piezoelectric responses to flexure of excised long bones with versus without cell viability. Shortly thereafter, Solomons et al.[4] undertook studies of the *in vitro* biochemical response of excised rat femora to cyclic tensile loading, using a cable-and-pulley assembly in which a small hanging weight was oscillated by means of a mechanical shaker. A dynamometer interposed in the loading train permitted estimates of the applied traction force.

The pioneering work of Rodan and colleagues[5–8] raised the standard regarding carefully quantified loading. They used several distinct preparations. For hydrostatic pressurization (quantified by mercury manometry), they worked with both suspensions of isolated cells[5,6] and with pneumatic piston compression of chick embryo long bones positioned in a syringe barrel.[7] For tensile stimulation, they configured an infusion pump to stretch collagen ribbons on which layers of rat calvarial cells were cultured.[8] In the tensile system, force and displacement transducers attached to the apparatus provided estimates of the mechanostimulus input to the ribbons. Subsequently, Somjen and colleagues[9] devised a system by means of which nonspecific (but quantified in later work[10]) distension could be input to cultures grown on standard plastic culture dishes. Their technique was to screw-distract semicircular acrylic slabs that were glued to the undersurface of the dish. At about the same time, organ culture tensile studies of newborn rabbit cranial sutures were performed by Meikle et al.,[11] using a conceptually related system involving spring-loaded partially split plastic substrates.

A wide variety of bone cell or tissue culture mechanostimulus systems have developed from this historical base. Most contemporary systems can be classified in terms of one (or more) of six distinct stimulus regimens: hydrostatic compression, platen compression, longitudinal substrate distension, substrate bending, circular substrate distension, or fluid shear.

27.2 Hydrostatic Compression

Hydrostatic compression has been frequently utilized,[12–19] owing to several attractions. The equipment involved is relatively simple (Figs. 27.1 and 27.2); the stimulus delivered is spatially and directionally homogeneous; manifolding makes it easy to study many individual sample replicates simultaneously; the waveform of transient loading inputs can be readily controlled; and the stimulus magnitude can be easily and precisely monitored. Since there is no direct contact from a load platen, artifactual local compaction of the culture is not a concern, nor is blockage of the physical pathway for metabolite transport between the culture and its nutrient medium. Additionally, the magnitude of pressure delivered does not depend on the degree of adhesion between the culture and its substrate. One disadvantage of hydrostatic loading, at least in open incubator systems at pressure levels intended to mimic quasi-physiological stress, is that the necessary gas pressures in the incubator imply very high values of pO_2 and pCO_2 in the nutrient medium, requiring compensatory treatment steps. A more fundamental issue is that the *in vivo* stress state of bone cells probably departs very appreciably from equibiaxial compression.

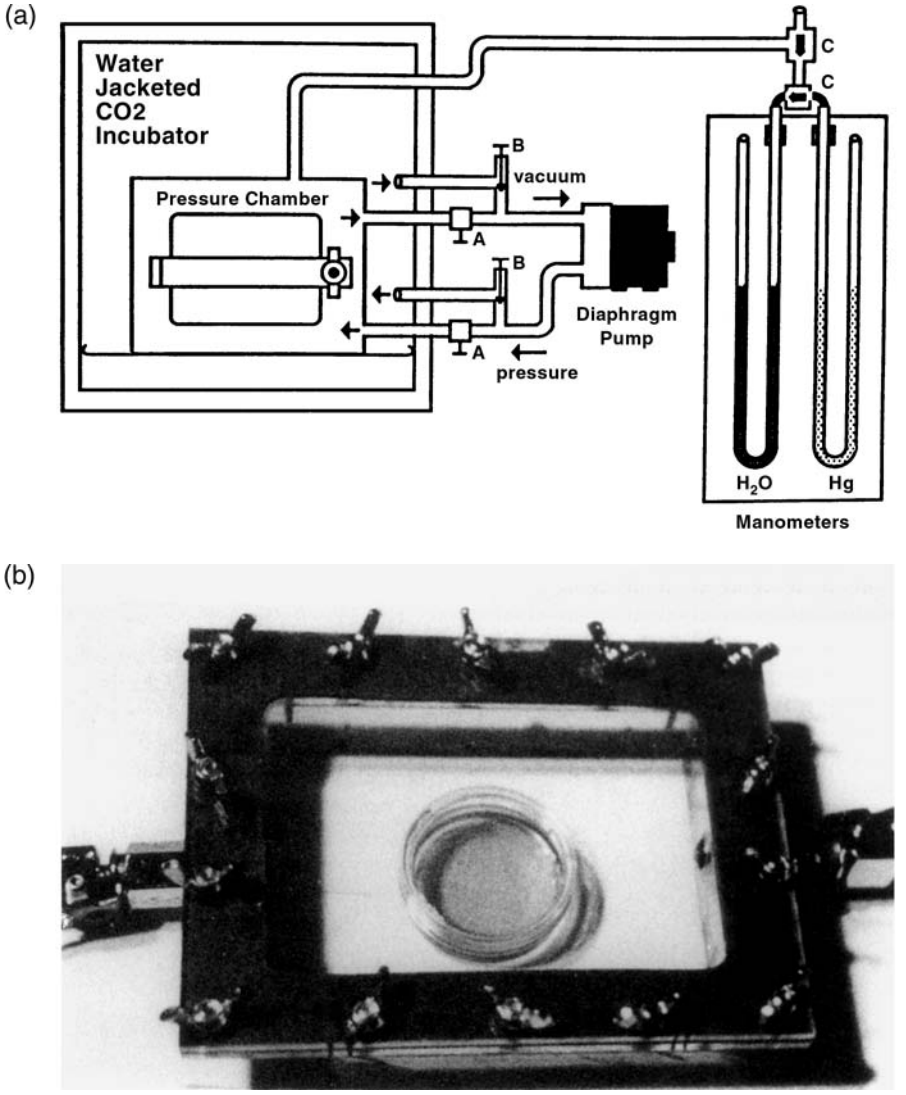

FIGURE 27.1 (a) The hydrostatic pressurization system employed by Yousefian et al.[19] Static air pressurization (or vacuum) is provided by a constant-pressure diaphragmatic pump, with needle valves (A) used to attenuate the pressure (or vacuum) delivered to the pressure chamber. Bypass trimmer valves (B) adjust the pressure (or vacuum) supplied to the incubator. Chamber pressure is monitored by simple manometry, with user selection of coarse scale (mercury column) vs. fine scale (water column) by means of a one-way valve (C). The pressure chamber itself (b) includes quick-connect fittings at its inlet and outlet covers, and plexiglass faces to allow culture visualization by inverted photomicroscopy. (From Yousefian, J. et al., *Am. J. Orthodonti. Dentofacial Orthop.,* 108, 402–409, 1995. With permission.)

Hydrostatic loading equipment, while conceptually similar for most investigations, has differed in several key implementation details. These include the pressure source (e.g., static weight, fluid head, compressed air tank, mechanical piston drive, fluid pump, or materials testing machine), the means for modulation of the pressure signal (e.g., static pressure, reciprocal piston, cam/follower, or closed-loop feedback), the type of substrate to which the bone cells are attached (e.g., culture membrane, culture dish, carrier beads, explant/matrix, or free suspension), and the presence vs. absence of a liquid/gas free surface.

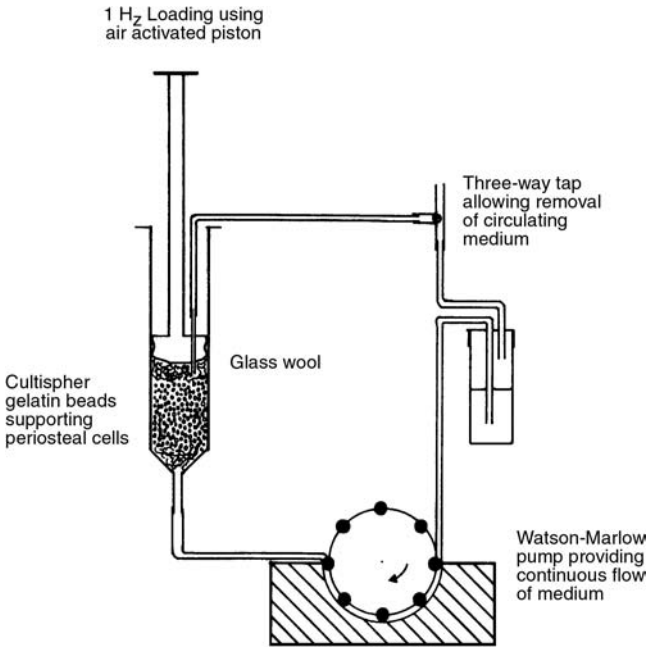

FIGURE 27.2 The hydrostatic pressurization apparatus utilized by Shelton and El Haj.[16] The culture medium is closed from incubator (not shown) atmosphere; metabolite exchange is instead achieved by active peristaltic pumping. In this system, a packed bed of gelatin beads provides the culture substrate, and hydrostatic cyclic (1 Hz) pressurization is delivered by a pneumatically driven piston, acting through a glass wool platen. (From Shelton, R.M. and El Haj, A.J., *J. Bone and Miner. Res.,* 7 (Suppl. 2), S403–S405, 1992. With permission.)

27.3 Direct Platen Contact

Direct platen loading has only occasionally been applied to bone cell or bone explant cultures, despite the frequent usage of that modality for chondrocyte cultures and for cartilage and osteochondral explants.[20–26] The key distinctions, arguably, are that bone cells *in vivo* rarely if ever experience direct counterface contact and that bone cells *in vitro* would probably experience appreciable stress shielding at even the very earliest onset of matrix mineralization. One platen loading system from which useful information has nevertheless emerged for bone (cylindrical cancellous bone biopsies) has been that of El Haj et al.,[27] a confined compression device noteworthy for its provision for continuous nutrient delivery to the test specimen by means of an auxiliary pump that circulated fluid through portals in the axial compression platens. Another platen compression instrument (Fig. 27.3), recently developed by Tanaka,[28] uses a piezoelectric actuator driven by a power amplifier, configured to develop low levels of culture strain (200 to 40,000 $\mu\varepsilon$) representative of those experienced by bone *in vivo*. This instrument was designed for arbitrary waveform inputs, at frequencies from a few tenths of a hertz up to several hundred hertz. Since the control of the system is of its power amplifier rather than of its platen displacement, the actuator excursions depend on test specimen mechanical impedance. A laser displacement transducer is therefore incorporated, to allow empirical adjustment of the power amplifier to achieve the desired specimen compression. The limiting form of platen compression is the use of localized "poke" stimuli. This has been embodied on the level of cell monolayer cultures using the side of plastic circular tubes,[29] and on the level of individual cultured cells using micropipettes.[30] Poke stimuli, unfortunately, are difficult to quantify precisely in terms of actual mechanical perturbations of the target. Platen traverse direction relative to the available target surface is necessarily variable from site to site, and the

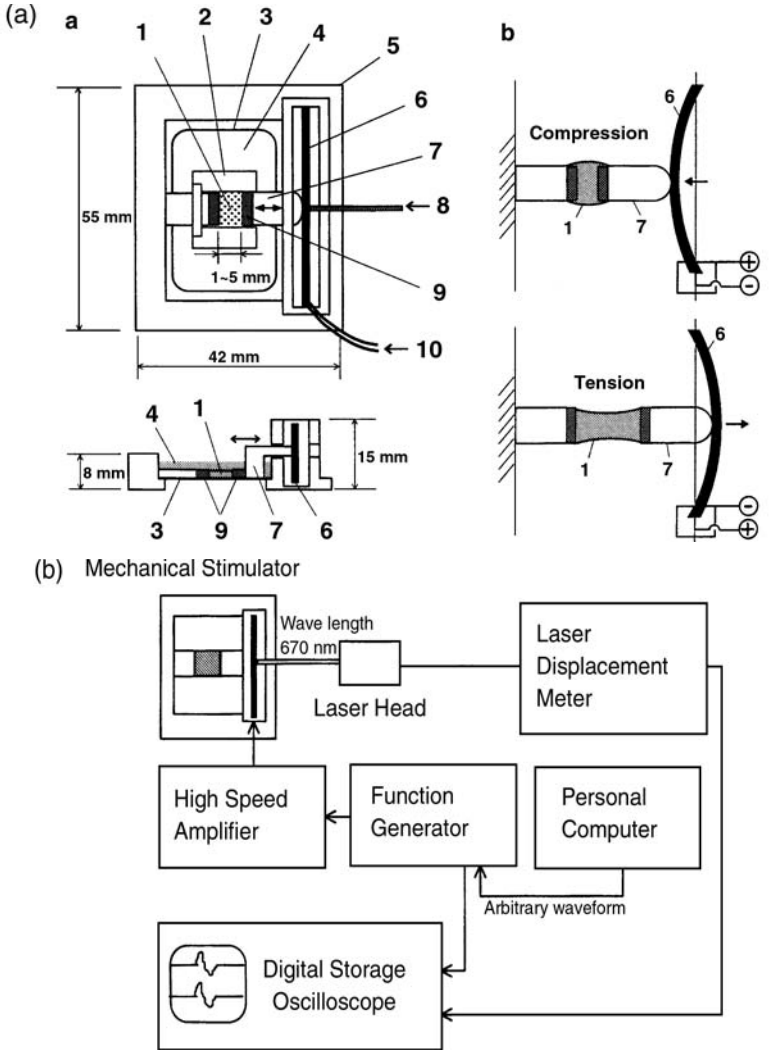

FIGURE 27.3 The platen loading system of Tanaka,[28] which is based on a piezoelectric actuator. (a) The actuator itself (6) consists of a thin brass plate, sandwiched between two piezoceramic layers having identical polarization directions. Application of a voltage difference (10) between these two layers and ground causes both layers to deflect identically, the directionality of deflection depending on voltage polarity. Cells are seeded on or in a collagen gel block (1), anchored in turn to plungers (7) by means of stainless-steel wire mesh (9). Other system components are a mold (2) for the collagen gel, a coverslip (3), the culture medium reservoir (4), and an acrylic base. Actuator displacements are monitored by a laser displacement sensor (8). (b) Control and monitoring is by means of a personal computer. Input voltage waveforms for the piezoelectric actuator are derived from a function generator, passed through a power amplifier. The function generator output, and the actuator deflection signal output from the laser displacement sensor are displayed on a digital oscilloscope. Operator intervention is necessary to adjust the gain of the power amplifier to obtain the desired actuator excursion, which depends upon the mechanical impedance of the specimen. (From Tanaka, S.M., *J. Biomech.,* 32 (4), 427–430, 1999. With permission.)

motions of even highly precise micromanipulators (e.g., 0.7-μm resolution in the case of Xia and Ferrier's system[30]) are quite coarse on the size scale of individual cells. Hence, these stimuli are semiquantitative at best, and probably are more appropriately described in qualitative terms such as "gentle pressure"[29] or "mechanical perturbation."[30]

27.4 Longitudinal Substrate Distension

Longitudinal distension of deformable substrates has been the stimulus of choice for many investigators. Systems of this class trace their lineage back to the static loading apparatus devised by Meikle et al.[11] and by Somjen et al.[9] Another early version was that of Leung et al.,[31] which achieved oscillatory substrate stretches by means of a motorized plunger/linkage arrangement. That device, which was capable of applying large strain (up to 10%) culture stimuli for multiday periods, unfortunately utilized a natural elastin substrate, and therefore likely involved appreciable heterogeneity and anisotropy of local strains. An improved system of this general type was later introduced by Ives et al.,[32] who were interested in delivering both substrate distension and fluid shear stress. Their device, which also was motor driven, was less complex mechanically (a spring-loaded pulley/cable was used instead of the cumbersome piston/linkage arrangement in the Leung et al. system), and the substrate (cast rectangular strips of 0.2-mm-thick polyetherurethane urea) was much more homogeneous and geometrically regular. Yet another motor/cam arrangement for cyclic uniaxial substrate distension was designed by Dewitt and colleagues,[33] a four-station system offering very precise control of grip-to-grip displacements. While the gripping mechanism of their device in principle could accommodate nearly arbitrary substrate geometry, these investigators chose to concentrate on a preparation that involved direct clamping of sheets of chondrocytes previously grown to confluence in nonloaded culture. Besides the issues of strain inhomogeneity and anisotropy, such an approach had obvious potential for introducing confounding mechanical stimuli, because of the need to remove the substrate from its "growth" flask for remounting in the distension apparatus.

Improvements in substrates and in culture wells have been an important component of the development of longitudinal distension devices. Murray and Rushton's system[34] involved replicate compartmentalized rectangular culture wells, fabricated by sealing parallel Permanox slabs onto a common polycarbonate base sheet. This base sheet was cyclically tensioned by means of an outrigger arm, driven by a lead screw attached to a stepper motor. Stepper motor usage held the advantage that a wide variety of input waveforms could be readily programmed. (The device developers themselves opted to concentrate on ramped square waves with a 0.01/s strain rate.) This particular design of compartmentalized rectangular wells, while advantageous from the standpoint of multiple sample replicates, probably involved appreciable culture surface strain heterogeneity, as a result of restraint from the nearby well sides. Unfortunately, no strain data were captured to document the intensity of the wall tethering effect. A conceptually related system, but one seemingly much less prone to strain heterogeneity due to wall restraint, was developed by Vandenburgh and Karlisch.[35] They too used a stepper motor for longitudinal distension of rectangular ($10 \times 25 \times 10$ mm) culture wells. In their case, however, the wells were built by meticulous silicone rubber sealing of rectangles cut from very thin (0.25-mm) silastic membrane stock. Another longitudinal stretch system (Fig. 27.4) was utilized by Neidlinger-Wilke et al.,[36] in which the culture wells were individually cast silicone rubber dishes. By means of optical measurements of the distortion of a fiducial grid ruled on the base of a calibration well, they demonstrated negligible deviation from strain homogeneity (albeit with axial vs. transverse anisotropy due to the Poisson effect) for the case of uniaxial distension induced by end-grip brackets driven by a DC motor.

Other longitudinal stretch systems have been devised to incorporate a variety of special features. Jones et al.,[37] who were interested in concurrent electrophysiological and light microscope observations of distended osteoblast-like cells, designed a symmetrical-pull system for which a small target zone of the substrate (a plastic ribbon) remained essentially fixed in space, even for imposed strains approaching 1%. Carano and Siciliani,[38] whose protocol required that cultured cells (fibroblasts, in their case) be transferred from static growth dishes to otherwise identical mechanically stimulated dishes, needed to ensure minimal distortion during the transfer process. They devised a selectively lockable substrate carriage unit for that purpose, which could be modularly inserted into their stimulus unit (a relatively simple motor-driven reciprocal linkage). Xu et al.,[39] whose application involved uniaxial distension of fully three-dimensional cultures (fetal lung cells seeded within a rectangular scaffold of blocks of Gelfoam) rather than of conventional surface-cultured monolayers, glued entire opposite faces of their scaffold blocks to distention platens. The drive mechanism of that particular system mechanism, however, involved the potentially confounding influence of electromagnetic field artifact, since it utilized solenoid

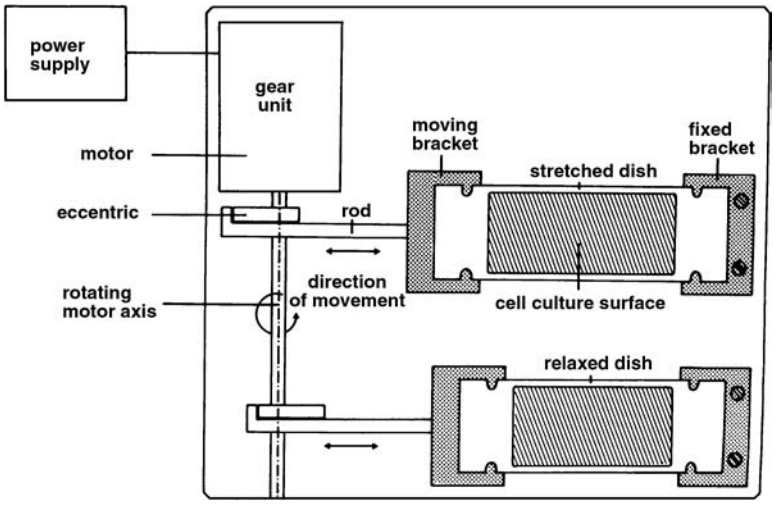

FIGURE 27.4 The longitudinal substrate distension apparatus utilized by Neidlinger-Wilke et al.[36] This is a six-station system (two stations shown), for which reciprocal motion inputs are delivered by a motor-driven cam. The culture wells are rectangular silicone elastomer dishes, molded to fit into a pair of bracket grips, one of which is fixed and the other of which moves with the cam follower. (From Neidlinger-Wilke, C. et al., *J. Orthop. Res.,* 12, 70–78, 1994. With permission.)

attraction of metal bars attached to the specimen grips. Smalt et al.,[40] who sought to distinguish osteoblast mechanostimulation due to substrate distension from that due to fluid shear, designed a grip-less longitudinal strain system aimed at minimizing coupled fluid motion. For that purpose, they used flexible silicone sealant to bond rigid cylindrical well walls very compliantly atop a horizontally distensible polystyrene film substrate, with the substrate constrained against downward deflection by means of a rigid stage support. (As with the Xu et al. system, however, their drive mechanism—again, electromagnetic attraction of a metal block—was perhaps less exemplary than their substrate tethering modality.) For applications where it suffices to perform a single static stretch to a specific strain level, discrete notches recessed in the culture well provide a simple and economical design solution.[41] Manual thumbscrews[42,43] are an almost equally simple drive mechanism, again restricted to quasi-static experiments, but offering continuous rather than discrete distension capability.

27.5 Substrate Bending

Systems that induce substrate bending provide an alternative approach to uniaxial strain of cell cultures. As a general matter, flexural systems tend to deliver a lower range of strain inputs than do distraction systems, which is often an important consideration in mechanostimulation of bone cells. Additionally, four-point-bending systems, of course, afford excellent strain homogeneity in the region between their inner pair of contacts. One of the earlier such embodiments was the system developed by Jones et al.,[37] who used 50 × 70 mm gold-coated rectangular flexure plates made of either polycarbonate or toughened glass, atop which 40 × 40 mm culture wells were fashioned using silicone rubber walls. That system was noteworthy for its incorporation of bonded resistance strain gauges, which permitted continuous readout of the strain actually developed at the culture substrate surface. A lever arm operated by a cam that was driven by an electric motor provided control of cyclic displacements input to a yoke connecting the outer contact pair (the inner supports being fixed). The system could be configured to achieve either concavity or convexity of the culture surface, thus permitting input of either compressive or tensile perturbations from strain neutrality.

A cleverly conceived albeit simply constructed four-point-bending apparatus was utilized by Owan et al.[44] to distinguish the differential sensitivity of cultured osteoblasts to substrate distension vs. to reactive fluid shear stress. Their device, fashioned primarily of acrylic, used a Vitrodyne universal materials tester to impart downward cyclic motions of the inner contact spans (prismatic triangular rods), the outer spans remaining fixed. Based on the input Vitrodyne actuator displacements, beam equations were used to calculate the culture surface strains, which were selectively verified by recordings from bonded resistance strain gauges. The essential task of independently modulating substrate strain and reactive fluid stress was approached by using substrates of parametrically varied thickness. For a given Vitrodyne stroke, essentially comparable flow fields were argued to ensue for two substrates having different thickness, whereas the peak strains developed would differ. Conversely, when the actuator stroke was adjusted to achieve parity of peak strains for two alternative substrate thicknesses, the corresponding substrate deflections (and their coupled fluid flow fields) would necessarily differ. Although this system provided no mechanism to quantify the reactive fluid stresses formally, the investigators felt that osteoblast sensitivity to reactive fluid stress variations was much more pronounced than that to substrate strain variations. Another relatively simple four-point-bending system has been used by Pitsillides et al.[45] to apply near-physiological strain duty cycles (3800 $\mu\varepsilon$, at 1 Hz) to thin plastic strips upon which embryonic chick osteocytes were cultured.

Using rectangular cast clear silicone dishes (culture area 30 $\times$ 60 mm) similar to those of Neidlinger-Wilke et al.,[36] Bottlang et al.[46] developed an elegant six-station instrument for four-point bending of cell cultures. Their system was powered by a pair of electromagnetic actuators, whose displacements were under the control of a graphical user interface computer system. Its capabilities included arbitrary waveforms, peak strains from 0 to 3000 $\mu\varepsilon$, and frequencies from 0 to 30 Hz. Homogeneity and accuracy of the input strains were characterized using holographic interferometry, laser displacement measurement, strain gauge monitoring, and finite-element analysis. Station-to-station variability was found to be less than 5%. The system was particularly intended for replicating the small strain levels experienced by bone cells *in vivo*, and could be configured to allow direct light microscope observation of the cultures.

27.6 Axisymmetric Substrate Distension

Stretching of platelike or membranelike circular substrates, either by means of prescribed kinematic inputs or by transmural pressure differentials, has to date been the single most widely used approach to cell culture mechanostimulus. An important early embodiment of the concept of distension by kinematic input was the device of Hasegawa et al.,[47] an outgrowth of an apparatus previously devised by Harrell et al.[48] In the Hasagawa system, the bottom of a standard Petriperm culture dish was pressed against a convex spherical template, and was held in place using a static weight. That system was utilized to study DNA synthesis in rat calvarial cell cultures, in both single-dish and 20-dish versions. Explicit strain levels were not reported, although the surface area of the substrate was said to be increased by 4% when held in place by two 670-g toroidal lead weights. The substrate distension was verbally described as homogeneous because of the use of uniform platen curvature, an assertion seemingly at variance with a well-established analytical contact solution for that configuration.[49] Subsequent investigators working with this type of device have based nominal strain estimates on the arc length of spherical distension of the substrate[50] or, alternatively, on changes in the visually apparent area of substrate contact.[51] Noteworthy experimental improvements on the basic Hasagawa indentation procedure have included Anderson and Norton's[52] use of an optional electrocylinder to perform dynamic or cyclic loading, and Matsuo et al.'s[53] use of a strain gauge mounted on the underside of the petri dish (the indentor being flat-ended rather than spherical) for real-time monitoring of the delivered strain waveform. A conceptually related variant is the use of small-curvature-radius indentors (prongs) to tent locally rather than broadly curve the substrate. Embodiments have included upward tenting from a motorized prong contacting the underside of the substrate,[54] or downwardly tenting by prong contact from above.[55]

The first flexible-bottomed circular cell culture plates (Fig. 27.5a) designed expressly for mechanostimulus studies were introduced in 1985 by Banes and colleagues.[56] Those plates were designed to

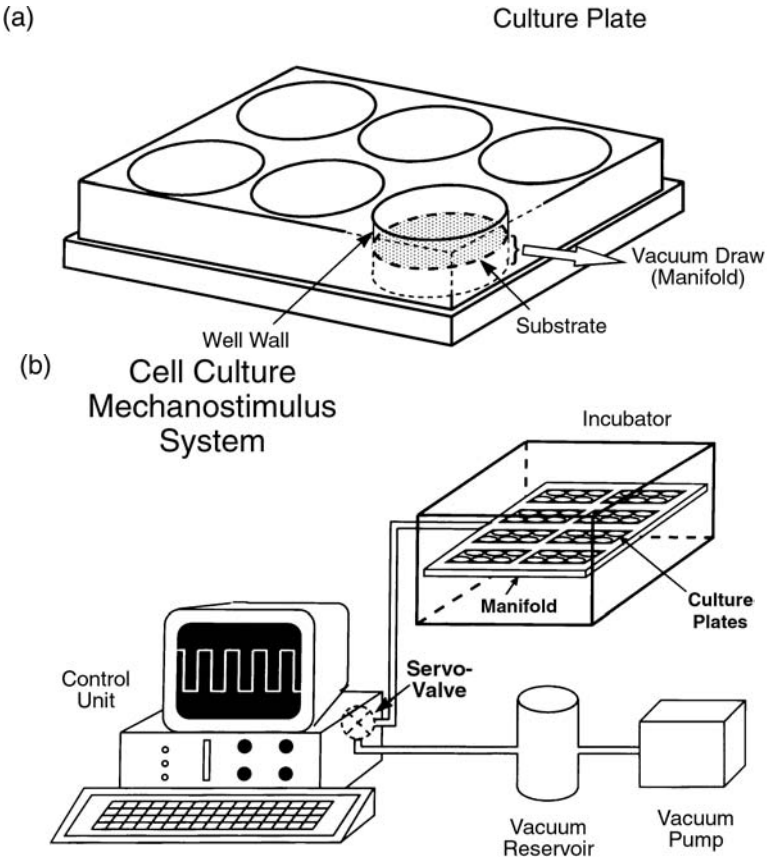

FIGURE 27.5 The substrate distension system (Flexercell) developed by Banes et al.[56] (a) Culture trays include six individual circular wells, each of which has a flexible bottom layer that sits above a manifold cavity that is subjected to cyclic vacuum. When the vacuum is applied, the substrate bulges downward, thereby developing strain on its upper surface. (b) System components include a control unit (PC based), a vacuum source (pump or house vacuum), a vacuum reservoir, one or more manifolds (eight culture trays per manifold layer for the initial Flex-I/Flex-II wells, four trays per layer for the larger BioFlex-II wells introduced subsequently), and external connection tubing. (From Brown, T.D., *Comput. Methods Biomech. Biomed. Eng.,* 3, 65–78, 1999. With permission.)

interface with a vacuum manifold system that was controlled by a PC-based programmable loading device (Fig. 27.5b). Transient vacuum applied to the flexible undersurface of the culture well caused the substrate to distend downward, thus imparting strain to the culture layer attached atop the substrate. The versatility of the system (vacuum magnitude, waveform, frequency, duty cycle) and its ease of setup and use lent it to a wide range of mechanostimulus applications. It was commercialized in 1987, under the name Flexercell®, and to date has been by far the most frequently utilized type of equipment for cell culture mechanostimulus. Literally dozens of applications papers appear each year. Unfortunately, blanket use of the term "Flexercell" has nowadays become somewhat ambiguous, because of the introduction of several key modifications of the original system. The original culture plates were supplied as six-well units, each well of which was 25 mm in diameter. There were two versions, differing only in terms of their well bottoms. The first version, designated as Flex-I®, had well bottoms consisting of a nominally 2-mm-thick slablike layer of cast siloxane rubber, whose upper surface included a proprietary amino-rich hydrophilic or collagen coating designed to facilitate cell attachment. The second version, Flex-II®, had conventional stiff well bottoms, and was intended for use as complementary (i.e., nonstretching) controls. The original PC-based vacuum control unit, designated as the FX-2000®, incorporated a

solenoid switch to toggle the substrate undersurface manifold alternately between either the vacuum source or a vent to atmosphere. Coarse and fine trim valves, whose knobs were located on the front of the control unit, allowed the user to modulate the resistance to air inflow independently during vacuum application or to air outflow during atmospheric venting, thus providing a means for (limited) control of the distension waveform. This waveform, in practice, took the form of a selectively rounded square wave. Beginning in approximately 1995, new flexible-bottomed culture plates were introduced, under the designation Bioflex-II®, for the purpose of more closely mimicking idealized membrane behavior (i.e., homogeneous radial strain) than what occurred for the relatively thick, somewhat slablike bottoms of the original Flex-I plates. Although there were also quality control and material improvements, the key distinction was geometrical: the Bioflex-II substrates were made from prefabricated rubber sheets 0.5 mm thick, and the well diameter was increased to 36 mm. Another major transition, beginning in approximately 1996, was the introduction of a new and much more elegant control unit, designated as the FX-3000. The key feature of the FX-3000 was its incorporation of a microprocessor-controlled servovalve, thus allowing user selection from a menu of waveforms, and enabling input of much more stable and more smoothly sinusoidal vacuum inputs than were possible with the FX-2000. Since both types of control unit are compatible with either type of flexible-bottomed culture plate, the term "Flexercell strain unit" can in fact refer to one of four distinct system configurations, each with very unique characteristics in terms of strain stimulus delivery. The multiplicity is further complicated by the recent introduction of a new adaptor, designated as the Stage Flexor®, designed for retrofit to Bioflex-II culture wells to constrain the central majority portion of the substrate to undergo only radial distension, thereby more closely approximating an equibiaxial strain field (see below).

Because of its widespread use within the cell mechanostimulus community, Flexercell system performance has been the subject of a number of engineering analyses. These have included experimental measurements of Flex-I surface strain distributions,[57] linearized quasi-static finite-element analysis of Flex-I strain anisotropy and inhomogeneity,[58] dynamic and geometrically nonlinear finite-element analysis of Bioflex-II strains without and with inertial nutrient coupling,[59] combined computational/experimental hyperelastic constitutive characterization of BioFlex-II substrates,[60] culture well nutrient medium flow field visualization,[61] experimental recordings of Bioflex-II harmonic oscillations,[62] fluid/structure interaction finite-element analysis of reactive stresses for Flex-I[63] and BioFlex-II[64] culture wells, and parametric finite-element analysis of strains and reactive fluid stresses for FX-2000 vs. FX-3000 vacuum waveforms.[65]

Another differential-pressure, flexible-substrate system was introduced in 1989 by Winston et al.,[66] using positive pressure rather than vacuum. Polyurethane urea diaphragms 100 μm thick, clamped peripherally by O-rings, were made to bulge upward by pressure from a central reservoir, modulated by a solenoid valve. Characterization of this system by its developers included static calibration of applied pressure vs. displacement measured at the membrane center, transient membrane center deflection measurements made using an optical probe, physical castings of the deflected membrane profile, and experimental validation of an analytically determined relationship between radial strain and centerline deflection. Brighton's group,[67] working at the same institution, soon thereafter reported a modified version of this device, incorporating polyurethane (Pellethane) membranes, polysulfone culture wells, a motor-driven reciprocating pump, and a redesigned mechanism for peripherally clamping the membranes. A special-purpose pressure-differential device was developed by Ellis et al.,[68] using silastic rubber culture substrates from Flexercell Flex-I culture plates adapted to fit into the bottom of a pneumatic cylinder. Abrupt pressure pulses (tens of milliseconds rise time) delivered by a controller connected to a tank of compressed gas engendered very high substrate strain levels (up to 72%), which were used to study the injury response of cultured neonatal rat cortical astrocytes.

A fundamental limitation to cell culture distention by diaphragmatic, transmurally pressure-driven systems is that the surface strains are heterogeneous and anisotropic. In the ideal situation of a substrate that approximates a peripherally tethered circular membrane, the radial component of strain is nearly homogeneous,[49] albeit prestrain-dependent.[69] Circumferential strain, however, varies from zero at the tethered periphery, to a maximum (in the limit, equal to the radial strain) at the membrane center.

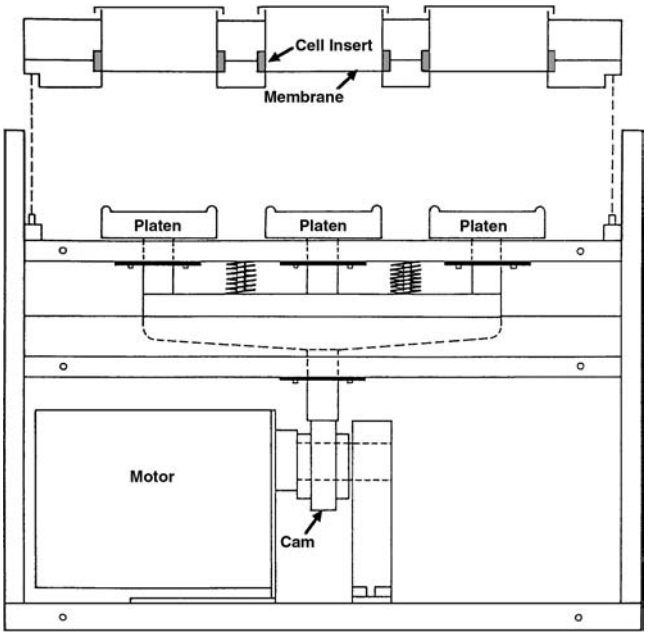

FIGURE 27.6 The equibiaxial substrate distension system developed by Schaffer et al.[70] This system has six indenter platens and six culture wells (three of each are shown in this schematic). Removable cassettes (illustrated at top) house peripherally clamped circular membranes. An alternative embodiment is the use of flexible-bottom culture dish inserts. The platen assembly is cyclically displaced vertically, by a motor-driven cam. For equibiaxial mechanostimulus, the cassette is positioned such that the distensible substrates make incipient contact with the platens when the latter are at the bottom of their stroke. The platen lips are lubricated and, with upward displacement, they permit the contacting portion of the substrate membranes to stretch freely radially outward, since the perimeters of the membranes remain constrained. (From Schaffer, J. L. et al., *J. Orthop. Res.,* 12, 709–719, 1994. With permission.)

Hence, the stimulus delivered to cells cultured atop such a substrate would be nonunique. To avoid this difficulty, several research groups have developed kinematically constrained stretch devices, using an appropriately contoured post or platen. In 1994, Schaffer et al.[70] and Hung and Williams,[71] working independently, introduced the concept of using low-friction, vertically pulsating circular ring platens (Fig. 27.6) to stretch radially the central portion of peripherally tethered culture membranes. Theoretically, at any instant during the duty cycle, all portions of the substrate remaining atop the (flat) platen experience homogeneous equibiaxial strain. Several other embodiments of this basic concept have subsequently appeared. These have included both custom devices (one using a simple manually turned screw[72] to impart axial excursion, and another using a DC gearmotor[73]), as well as an elegant commercialized system.[74] All three of these latter systems had design improvements to facilitate microscope observation, by downwardly displacing the peripheral tether of the substrate rather than upwardly displacing the central platen. For the Flexercell system, a clever retrofit (designated Stage Flexor®) has been devised to achieve kinematically equivalent motion by means of a flat central cylindrical stage positioned just below the culture substrate.[75] Because of this constraint, the imposed undersurface vacuum pulls down only the outer annular portion of the substrate, thereby radially distracting the stage-overlying circular inner portion of the substrate. (This arrangement not coincidentally preserves the focal plane position, thus also enabling microscope visualization.) Of course, all devices that utilize over-the-lip substrate distraction to achieve homogeneous equibiaxial strain necessarily assume that the substrate slides frictionlessly atop the platen. Optical tracking of surface markers in several of these systems[70,73,75] has documented that this goal is closely enough achieved in practice to allow reasonably good approximation of analytically ideal kinematic behavior. However, careful surveillance is merited regarding the

potential for localized microdamage accumulation in those portions of the substrate that undergo cyclic over-the-lip sliding. Quite apart from avoidance of frank mechanical failure, progressive development of microdamage regions with elevated compliance would alter the kinematic relationship initially prevailing between axial excursion and radial substrate distension. A very different approach to achieving homogeneous equibiaxial strains is that of Norton et al.,[76] involving a four-grip mechanism pulling a square membrane equally in two perpendicular directions. In this type of design no potential exists for artifactual friction, as there is no constraint contact. However, this approach to substrate distension is very demanding in terms of hardware implementation, and biaxial strains develop on the substrate only at sites relatively remote (in the St. Venant sense) from the grips.

Several other recent specialized embodiments of substrate distension mechanostimulus have features of potentially broader interest. Lynch and Lintilhac[77] developed a system deliberately incorporating strain heterogeneity. A Vitrodyne-driven bellows apparatus with a geometrically irregular platen was used to compress a block of cell-seeded agar. Following photoelastic mapping of the corresponding planes of block principal strain, the principal planes of mitotic division of the embedded cells were compared with those of principal passive strain. Another class of systems, reminiscent of the biologic loading regimens of Glucksmann and of Bassett and colleagues, involves selective constraint of autocontracting cultures. Essentially, metabolites from cells seeded in an acid-soluble collagen gel lattice induce the lattice to contract spontaneously. Boundary constraint(s) to free lattice contraction therefore cause a residual-like stress state to develop, leading in turn to differences in cell behavior as compared with the freely contracting situation. Geometries studied to date include peripheral constraint of circular diaphragms,[78] end-to-end constraint of unsupported rectangular strips,[79] and complete tethering of one face of the lattice against a flat substrate.[80]

27.7 Fluid Shear

Another major body of work in cell culture mechanostimulus has involved the application of fluid shear stress. It is now very well recognized that a great many cellular phenomena are influenced by fluid shear, including both mechanoreception (e.g., protein kinase signaling, integrins and focal adhesions, plasma membrane receptors, stretch-activated ion channels) and mechanoresponse (cytoskeletal remodeling, prostacyclin, intracellular calcium, nitric oxide).[81] Two principal apparatus configurations have been used to deliver fluid shear stresses: cone-and-plate systems and parallel plate flow chambers. In cone-and-plate systems (Fig. 27.7), rotation of a right circular cone is imposed about a cone axis oriented perpendicular to the surface of a flat plate.[82–85] Since the local relative velocity and the local separation between those two surfaces both vary in direct proportion to radial distance from the cone axis, this configuration achieves spatially homogeneous shear rate, and hence (for Newtonian fluid) homogeneous shear stresses on each surface. Depending on the conic taper and the imposed angular velocity, a wide range of shear stress magnitudes can be delivered, extending even into the turbulant regime.[86] By modulating the angular velocity of the cone, one can modulate the applied shear stress, although there are necessarily time lags in flow field development due to inertial effects and due to viscous diffusion effects. Disadvantages of cone-and-plate systems are that the hardware necessary for physical embodiment of this relatively simple concept tends to be fairly complex (Fig. 27.8), that secondary flow develops for finite angular velocity ω because of heterogeneity of convective acceleration, and that continuous exchange of nutrient (in the otherwise-closed culture wells) requires superposition of yet another velocity component. While it is possible to configure cone-and-plate systems for direct microscopic visualization,[87] doing so is more cumbersome than for most other mechanostimulus modalities.

In parallel plate flow chambers, a pressure differential is imposed between slit openings (manifolds) located at either end of a thin elongated rectangular chamber (Fig. 27.9a), thereby causing uniform laminar flow to develop across both faces of the chamber, the lower of which serves as the culture surface. A range of chamber sizes and aspect ratios has been used, depending on the size of the culture to be studied and the desired shear stress.[88–94] External flow loops to create the necessary pressure drop (Fig. 27.9b) have utilized either gravity heads[90,95] (steady flow) or active pumping[96] (transient flow). Among the attractions

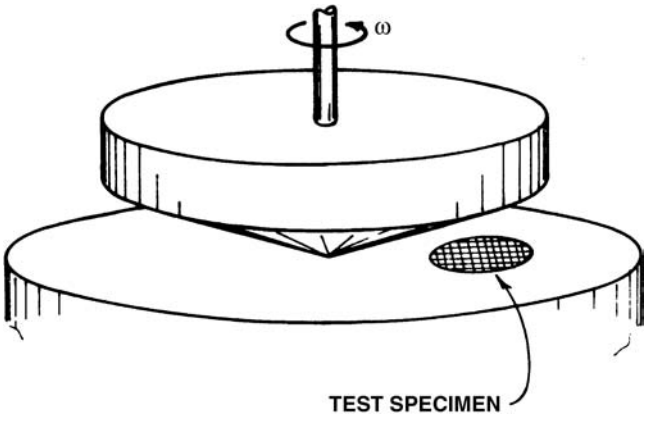

FIGURE 27.7 Conceptual schematic of cone-and-plate shear stress mechanostimulus used by Dewey.[82] Since both the absolute local velocity of the upper (i.e., conical) surface and its local separation from the lower (i.e., flat) culture surface vary linearly with radial distance from the rotation axis, the fluid shear rate at the culture surface is homogeneous. For liquid culture medium closely approximating a Newtonian fluid (as is the case for typically used media[64]), this corresponds to a culture environment of uniform shear stress. (From Dewey, C.F., *J. Biomech. Eng.,* 106, 31–35, 1984. With permission.)

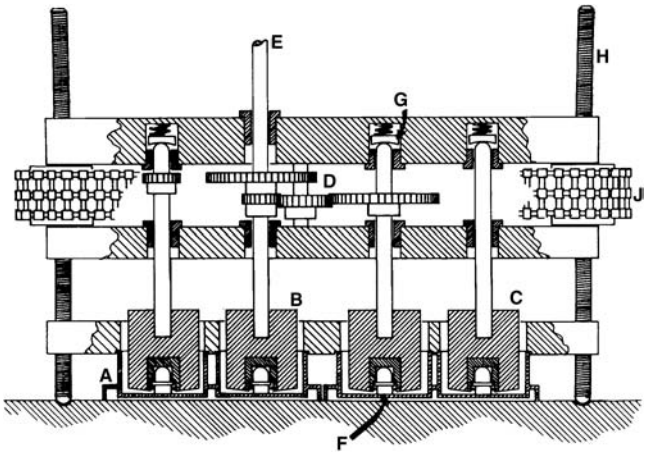

FIGURE 27.8 Physical embodiment of the multiwell cone-and-plate system operated by Van Grondelle et al.[85] This 12-well system (4 wells, A, are shown here) utilized cones (B) with a 168° included angle (i.e., a 6° opening between the cone and culture surface), and had a gear (D) and toothed belt (J) drive mechanism connected via a speed selector shaft (E) to an induction motor. Precision machining was necessary to ensure cone/rotation axis alignment relative to the culture surface. Also, it was necessary to use spring-loaded thrust pads (F, G) to maintain physical contact between the cone apex and the culture surface. (From Van Grondelle, A. et al., *J. Appl. Physiol.,* 57, 388–395, 1984. With permission.)

of the parallel plate apparatus are the homogeneity of its applied stress, the small volume of fluid required, the ease of access to the culture both physically and for microscopy, and the ease of sampling or exchange of the fluid medium. For the case of pulsatile stimulation, where the time required for flow development poses a constraint on the magnitude and/or frequency of stress application, Ruel et al.[97] have used boundary-layer theory to develop a specialized design modification utilizing a separate "settling chamber" and a curvilinearly tapered inlet, to optimize flow field development.

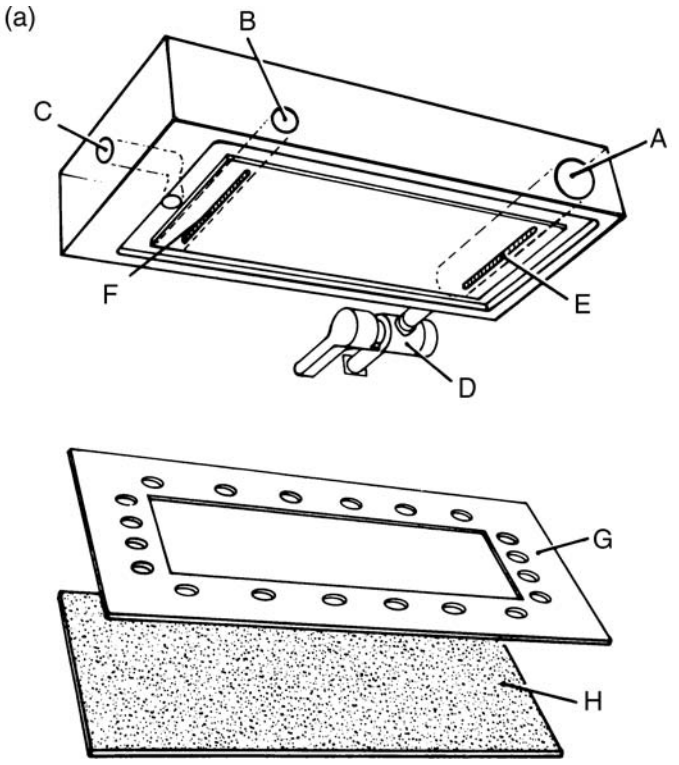

FIGURE 27.9 (a) A parallel-plate flow chamber of the type used by Frangos et al.[90] Cells are cultured on a gasketed (G) glass plate (H), held against a machined polycarbonate plate by vacuum (C). Fluid medium enters the chamber through port A and slit E, travels across the top of the culture surface, and then exits through slit F and port B. Air bubbles trapped in the entry port are removed by a manually operated valve (D). (b) The gravity-driven flow loop in the Frangos et al. system. A peristaltic pump (12) elevates medium up a tube (13) connecting a lower (2) to an upper (1) reservoir, constant filling of the latter being maintained by an overflow manifold (3). Appropriate exchange (4, 5) concentrations of air and CO_2 are maintained externally. The constant-pressure head (14) causes nutrient to circulate through the flow chamber (polycarbonate plate 6, manifold 7, glass culture plate 8, attachment vacuum 10). Monitoring capabilities include a flow meter (15), an inverted microscope (9), and a sampling port (11). (From Frangos, J. A. et al., *Biotechnol. Bioeng.,* 32, 1053–1060, 1988. With permission.)

A number of alternative approaches have been devised for fluid stress experiments targeting other specialized cell types, but which potentially have elements of applicability to studying bone and bonelike cells. Internal flow geometries (mainly involving endothelial cells, oriented toward vascular tissue engineering applications) have been utilized on lumen diameter size scales ranging from a few micrometers up to several millimeters.[98–101] LaPlaca and Thibault,[102] whose interest was in the injury response of human neurons, used angular acceleration in a parallel disk configuration to impart very high shear stress transients (up to 800 dyn/cm^2/s) to monolayer cultures. Ohata et al.[103] devised a "spritzing" protocol, wherein a jet of culture medium was made to impinge on the culture surface. No estimate was made to estimate stress levels formally in that experiment (both shear and normal stresses certainly were imparted), although the protocol was carefully controlled in terms of flow stream velocity and geometry. Tardy et al.[104] devised a system to permit systematic study of monolayer culture response to shear stress gradients, using rectangular blocks inserted into the flow stream of a parallel plate flow unit. Waters et al.[105] cultured rat mesothelial cells on microcarrier beads packed within a cylindrical column through which medium was perfused; they estimated the corresponding shear stresses (5 to 16 dyn/cm^2 in their series) by means of a packed-bed-reactor formula. Another semiquantitative approach was adopted by Pearce et al.,[106] who used orbital shakers to agitate their culture plates inertially, under conditions for which a closed-form

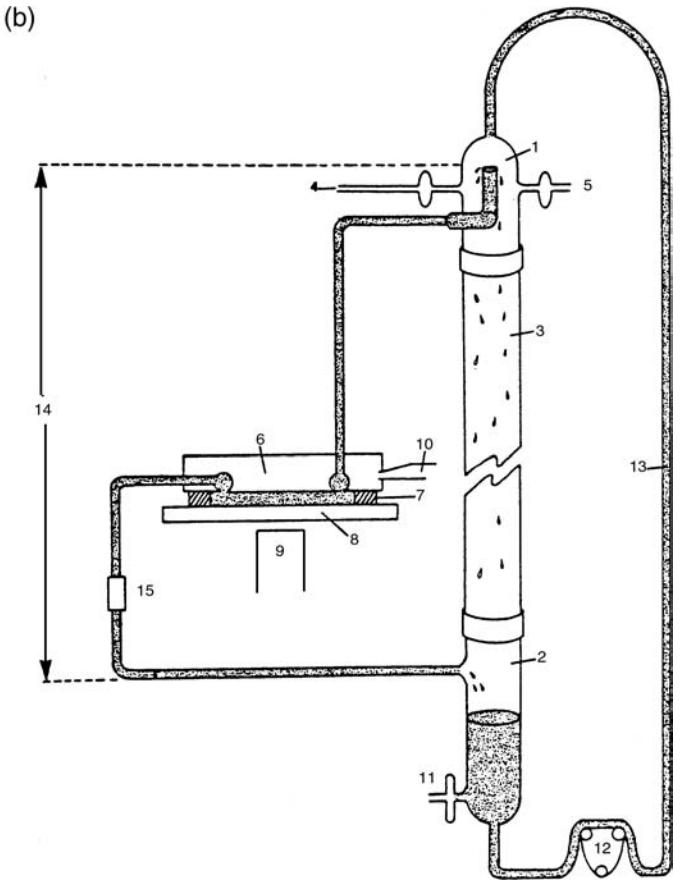

FIGURE 27.9 (Continued)

dimensionally based estimate of maximum fluid shear stress was available. One other noteworthy fluid stimulus apparatus, although involving normal stress rather than shear, was the application by Inoue et al.[107] of severe multiday inertial stimuli (up to 320 g) to osteoblasts cultured in a laboratory centrifuge.

27.8 Combined Stimuli

Fluid shear stresses and substrate distension potentially act through entirely different mechanisms, so experimental designs for cell culture mechanostimulus have occasionally addressed both modalities. Independent loading experiments for each modality, such as have been done by Smalt et al.[40] and by Wagner et al.,[108] provide perhaps the most direct distinction between the effects of these two stimuli. Studies of the interaction between these two stimulus modes, however, require a special-purpose apparatus capable of delivering both stimuli concurrently. One early approach to the problem of combining fluid stress and substrate distension was to work with cultures grown on the inner wall of highly distensible tube, through which medium was passed via a pressure gradient.[109] Independently modulating the tube pressure gradient and the pressure differential between the inner and outer walls of the tube permitted independent control of the shear stress (i.e., the flow rate) and of the nominal substrate strain, respectively. A similarly conceived paradigm was that of Moore et al.,[110] who used a four-regime test system to deliver selectively no stimulus, substrate distension only, fluid shear only, and combined distension/shear. Their apparatus involved a set of rigid outer tubes, sized to restrict pressure-induced radial expansion of inner (culture) tubes that were made from high-compliance rubber. Another variant on this basic approach is the *in situ* rabbit iliac artery stretch/shear preparation developed by Ayajiki et al.,[111] in which circumferential strain

was modulated chemically rather than by transluminal pressure differentials, and which also allowed the option for independently inputting longitudinal strain via mechanical traction. Yet another approach to simultaneous shear/distension is the four-point-bending system devised by Owan et al.,[44] which as described above independently modulated the two stimuli by utilizing different thicknesses of the substrate. This led to different culture strains for a given distance of beam displacement, although those investigators unfortunately had no means to assess the absolute fluid shear stress magnitudes for the complex fluid motions associated with specific substrate (beam) displacement histories. Another noteworthy device for concurrent stimulus is that of Wright et al.,[112] who combined substrate strain with fluid hydrostatic pressure rather than with fluid shear. Their system consisted essentially of an outer pressure vessel (connected to a regulated nitrogen cylinder), within which specimen culture dishes were positioned atop a brass cylinder that had small holes drilled in its side. Those holes served to restrict gas flow slightly into the brass cylinder, thereby setting up a small transient pressure differential across the culture plate during pressurization of the outer chamber, and causing the plate to bulge downward. By substituting a brass cylinder with much larger holes (thus permitting essentially unimpeded gas influx from the outer chamber and hence no pressure differential across the culture plate), the system could operate in a pressure-only mode.

Allowance for accurate characterization of the stimulus actually delivered is of course an important attribute of contemporary apparatus design. In the case of flow stimulus systems, shear stress determinations based on fluid velocity gradients need to be recognized as being only nominal, since irregularities in the topography of the culture layer itself can lead to appreciably nonuniform flows. Computational fluid dynamics (CFD) has come to play an increasingly important role in characterizing cell culture mechanostimulus; among the earliest applications was demonstration of local flow nonuniformity accompanying idealized[113] and then AFM-mapped[114] culture surface undulations. Also, CFD has been used by Brown and colleagues[115] to demonstrate that, even in systems designed to deliver stimulus only by substrate stretch, coupled motions of the nutrient medium can lead to appreciable levels of unintentional reactive fluid stress.

Acknowledgments

Ms. Kay L. Geguzis assisted with manuscript preparation. Financial support was provided by NIH Grant AR/DE 42845.

References

1. Glucksmann, A., Studies on bone mechanics *in vitro:* II. The role of tension and pressure in chondrogenesis, *Anat. Rec.,* 73, 39–56, 1939.
2. Bassett, C. A. L. and Hermann, L., Influence of oxygen concentration and mechanical factors on differentiation of connective tissue *in vitro, Nature,* 193, 460–461, 1961.
3. Bassett, C. A. L. and Becker. R.O., Generation of electric potentials by bone in response to mechanical stress, *Science,* 137, 1063–1064, 1962.
4. Solomons, C. C., Shuster, D., and Kwan, A., Biochemical effects of mechanical stress. I. Control of P^{32} release from rat femur *in vitro, Aerosp. Med.,* 36, 33–34, 1965.
5. Bourret, L. A. and Rodan G. A., The role of calcium in the inhibition of cAMP accumulation in epiphyseal cartilage cells exposed to physiological pressure, *J. Cell Physiol.,* 88, 353–361, 1976.
6. Rodan, G. A., Bourret L. A., Harvey, A., and Mensi, T., 3′, 5′-Cyclic AMP and 3′, 5′-cyclic GMP mediators of the mechanical effects on bone remodeling, *Science,* 189, 467–469, 1975.
7. Rodan, G. A., Mensi, T., and Harvey, A., A quantitative method for application of compressive forces to bone in tissue culture, *Calcif. Tissue Res.,* 18, 125–131, 1975.
8. Yeh, C. and Rodan, G. A., Tensile forces enhance PGE synthesis in osteoblasts grown on collagen ribbon, *Calcif. Tissue Int.,* 36(s), 67–71, 1975.

9. Somjen, D., Binderman, I., Berger, E., and Harrel, A., Bone remodeling induced by physical stress is prostaglandin E2 mediated, *Biochem. Biophys. Acta,* 627, 91–100, 1980.
10. Binderman, I., Shimshoni, Z., and Somjen, D., Biochemical pathways involved in the translation of physical stimulus into biological message, *Calcif. Tissue Int.,* 36, S82–S85, 1984.
11. Meikle, M. C., Reynolds, J. J., Sellers, A., and Dingle, J. T., Rabbit cranial sutured *in vitro*: a new method for studying the response of fibrous joints to mechanical stress, *Calcif. Tissue Int.,* 28, 137–144, 1979.
12. Bagi, C. and Burger, E. H., Mechanical stimulation by intermittent compression stimulates sulfate incorporation and matrix mineralization in fetal mouse long bone rudiments under serum-free conditions, *Calcif. Tissue Int.,* 45, 342–347, 1989.
13. Burger, E. H., Klein-Nuland, J., and Valdhuizen, J. P., Mechanical stress and osteogenesis *in vitro, J. Bone Miner., Res.,* 7(S2), S397–S401, 1992.
14. Brighton, C. T., Fisher, J. R. S., Levine, S. E., Corsetti, J. R., Reilly, T., Landsman, A. S., Williams, J. L., and Thibault, L. E., The biochemical pathway mediating the proliferative response of bone cells to a mechanical stimulus, *J. Bone Joint Surg.,* 78(A), 1337–1347, 1996.
15. Imamure, K., Ozawa, H., Hiriade, T., Takahashi, N., Shibasaki, Y., Kukahara, T., and Suda, T., Continuously applied compressive pressure induces bone resorption by a mechanism involving prostaglandin E2 synthesis, *J. Cell Physiol.,* 144, 222–228, 1990.
16. Shelton, R. M. and El Haj, A. J., A novel microcarrier bead model to investigate bone cell responses to mechanical compression *in vitro, J. Bone Miner. Res.,* 7 (Suppl. 2), S403–S405, 1992.
17. Klein-Nuland, J., Veldhuizen, J. P., and Burger, E. H., Increased calcification of growth plate cartilage as a result of compressive force *in vitro, Arthritis Rheum.,* 29, 1002–1009, 1986.
18. Ozawa, H., Imamura, K., Abe, E., Takahashi, N., Hiraide, T., Shibasaki, Y., and Fukuhara, Y., and Suda, T., Effect of continuous applied compressive pressure on mouse osteoblast-like cells (MC3T3-E1) *in vitro, J. Cell Physiol.,* 142, 177–185, 1990.
19. Yousefian, J., Firouzian, F., Shanfeld, J., Ngan, P., Lanese, R., and Davidovitch, Z., A new experimental model for studying the response of peridontal ligament cells to hydrostatic pressure, *Am. J. Orthod. Dentofacial Orthop.,* 108, 402–409, 1995.
20. Torzilli, P. A., Grigiene, R., Huang, C., Friedman, S. M., Doty, S. B., Boskey, A. L., and Lust, G., Characterization of cartilage metabolic response to static and dynamic stress using a mechanical explant test system, *J. Biomech.,* 30, 1–9, 1997.
21. Burton-Wurster, N., Vernier-Singer, M., Farquhar, T., and Lust, G., Effect of compressive loading and unloading on the synthesis of total protein, proteoglycan, and fibronectin by canine cartilage explants, *J. Orthop. Res.,* 11, 717–719, 1993.
22. Frank, E. H., Grodzinsky, A. J., Koob, T. J., and Eyre, D. R., Streaming potentials: a sensitive index of enzymatic degradation in articular cartilage, *J. Orthop. Res.,* 5, 497–508, 1987.
23. Buschmann, M. D., Gluzband, Y. A., Grodzinsky, A. J., Kimura, J. H., and Hunziker, E. B., Chondrocytes in agarose culture synthesize a mechanically functional extracellular matrix, *J. Orthop. Res.,* 10, 745–758, 1992.
24. Gray, M. L., Pizzanelli, A. M., Grodzinsky, A. J., and Lee, R. C., Mechanical and physiochemical determinants of the chondrocyte biosynthetic response, *J. Orthop. Res.,* 6, 777–792, 1988.
25. Sah, R. L., Kim, Y. J., Doong, J.-Y. H., Grodzinsky, A. J., Plaas, A. H. K., and Sandy, J. D., Biosynthetic response of cartilage explants to dynamic compression, *J. Orthop. Res.,* 7, 619–636, 1989.
26. Cheng, G. C., Libby, P., Grodzinsky, A.J., and Lee, R. T., Induction of DNA synthesis by a single transient mechanical stimulus of human vascular smooth muscle cells. Role of fibroblast factor-2, *Circulation,* 93, 99–105, 1996.
27. El Haj, A. J., Minter, S. L., Rawlinson, S. C. F., Suswillo, R., and Lanyon, L. E., Cellular responses to mechanical loading *in vitro, J. Bone Miner. Res.,* 5, 923–932, 1990.
28. Tanaka, S.M., A new mechanical stimulator for cultured bone cells using piezoelectric actuator, *J. Biomech.,* 32, 427–430, 1999.

29. Calara, F., Ameli, S., Hultgardh-Nilsson, A., Cercek, B., Kupfer, J., Hedlin, U., Forrester, J., Shah, P.K., and Nilsson, J., Autocrine induction of DNA synthesis by mechanical injury of cultured smooth muscle cells. Potential role of FGF and PDGF, *Arteriosclerosis Thrombosis Vasc. Biol.,* 16, 187–193, 1996.
30. Xia, S. L. and Ferrier, J., Calcium signal induced by mechanical perturbation of osteoclasts, *J. Cell. Physiol.,* 163, 493–501, 1995.
31. Leung, D. Y. M., Glagof, S., and Matthews, M. B., A new *in vitro* system for studying cell response to mechanical stimulation, *Exp. Cell Res.,*109, 285–298, 1977.
32. Ives, C. L., Eskin, S. G., and McIntire, L. V., Mechanical effects on endothelial cell morphology: *in vitro* assessment, *In Vitro Cell. Dev. Biol.,* 22, 500–507, 1986.
33. Dewitt, M. T., Handley, C. J., Oakes, B. W., and Lowther, D. A., *In vitro* response of chondrocytes to mechanical loading. The effects of short term mechanical tension, *Connect. Tissue Res.,* 12, 97–109, 1984.
34. Murray, D. W. and Rushton, N., The effect of strain on bone cell prostaglandin E2 release: a new experimental method, *Calcif. Tissue Int.,* 47, 35–39, 1990.
35. Vandenburgh, H. H. and Karlisch, P., Longitudinal growth of skeletal myotubes *in vitro* in a new horizontal mechanical cell stimulator, *In Vitro Cell. Dev. Biol.,* 25, 607–616, 1989.
36. Neidlinger-Wilke, C., Wilke, H.-J., and Claes, L., Dynamic stretching of human osteoblasts: an experimental model for *in vitro* stimulation of fracture gap motion, *J. Orthop. Res.,* 12, 70–78, 1994.
37. Jones, D. B., Nolte, H., Scholubbers, J. G., Turner, E., and Veltel, D., Biochemical signal transduction of mechanical strain in osteoblast-like cells, *Biomaterials,* 12, 101–110, 1991.
38. Carano, A. and Siciliani, G., Effects of continuous and intermittent forces on human fibroblasts *in vitro, Eur. J. Orthod.,* 18, 19–26, 1996.
39. Xu, J., Liu, M., Liu, J., Caniggia, I., and Post, M., Mechanical strain induces constitutive and regulated secretion of glycosaminoglycans and proteoglycans in fetal lung cells, *J. Cell Sci.,* 109, 1605–1613, 1996.
40. Smalt, R., Mitchell, F. T., Howard, R. L., and Chambers, T. J., Induction of NO and prostaglandin E2 in osteoblasts by wall-shear stress but not mechanical strain, *Am. J. Physiol.,* 273, E751–758, 1997.
41. Mitton, K. P., Tumminia, S. J., Arora, J., Zelenka, P., Epstein, D. L., and Russell, P., Transient loss of alphaB-crystallin: an early cellular response to mechanical stretch, *Biochem. Biophys. Res. Commun.,* 235, 69–73, 1997.
42. Komuru, I., Kaida, T., Shibazaki, Y., Kurabayashi, M., Takaku, F., and Yazaki, Y., Stretching cardiac myocytes stimulates proto-oncogene expression, *J. Biol. Chem.,* 265, 3595–3598, 1990.
43. Decker, M. L., Janes, D. M., Barclay, M. M., Harger, L., and Decker, R. S., Regulation of adult cardiocyte growth: effects of active and passive mechanical loading, *Am. J. Physiol.,* 272, H2902–2908, 1997.
44. Owan, I., Burr, D. B., Turner, C. H., Qiu, J., Tu, Y., Onyia, J. E., and Duncal, R. L., Mechanotransduction in bone: osteoblasts are more responsive to fluid forces than mechanical strain, *Am. J. Physiol.,* 273, C810–815, 1997.
45. Pitsillades, A. A., Rawlinson, S. C., Suswillo, R. F., Bourrin, S., Zaman, G., and Lanyon, L. E., Mechanical strain-induced NO production by bone cells: a possible role in adaptive bone (re)modeling? *FASEB J.,* 9, 1614–1622, 1995.
46. Bottlang, M., Simnacher, M., Schmitt, H., Brand, R. A., and Claes, L., A cell strain system for small homogeneous strain applications, *Biomed. Tech.,* 42, 305–309, 1997.
47. Hasagawa, S., Sato, S., Saito, S., Suzuki, Y., and Brunette, D. M., Mechanical stretching increases the number of cultured bone cells synthesizing DNA and alters their pattern of protein synthesis, *Calcif. Tissue Int.,* 37, 431–436, 1985.
48. Harrell, A., Dekel, S., and Binderman, I., Biochemical effect of mechanical stress on cultured bone cells, *Calcif. Tissue Res.* (Suppl.), 22, 202–209, 1977.

49. Williams, J. L., Chen, J. H., and Belloli, D. M., Strain fields on cell stressing devices employing clamped circular elastic diaphragms as substrates, *J. Biomech. Eng.,* 114, 377–384, 1992.
50. Basdra, E. K., Kohl, A., and Komposch, G., Mechanical stretching of peridontal ligament fibroblasts—a study on cytoskeletal involvement, *J. Orofacial Orthop.,* 57, 24–30, 1996.
51. Felix, J. A., Woodruff, M. L., and Dirksen, E. R., Stretch increases inositol 1,4,5-triphosphate concentration in airway epithelial cells, *Am. J. Respir. Cell Mol. Biol.,* 14, 296–301, 1996.
52. Anderson, K. L. and Norton, L. A., A device for the application of known simulated orthodontic forces to human cells *in vitro, J. Biomech.,* 24, 649–654, 1991.
53. Matsuo, T., Uchida, H., and Matsuo, N., Bovine and porcine trabecular cells produce F2 alpha in response to cyclic mechanical stretching, *Jpn. J. Opthalmol.,* 40, 289–296, 1996.
54. Vandenburgh, H. H., A computerized mechanical cell stimulator for tissue culture: effects on skeletal muscle organogenesis, *In Vitro Cell. Dev. Biol.,* 24, 609–619, 1988.
55. Soma, S., Matsumoto, S., and Takano-Yamamoto, T., Enhancement of conditioned medium of stretched calvarial bone cells of the osteoclast-like cell formation induced by parathyroid hormone in mouse bone marrow cultures, *Arch. Oral Biol.,* 42, 205–211, 1997.
56. Banes, A. J., Gilbert, J. L., Taylor, T., and Monbureau, O., A new vacuum-operated stress-providing instrument that applies static of variable-duration cyclic tension or compression to cells *in vitro, J. Cell Sci.,* 75, 35–42, 1985.
57. Gilbert, J. L., Banes, A. J., Link, G. W., and Jones, G. L., Video analysis of membrane strain—an application in cell stretching, *Exp. Tech.,* 14, 43–45, 1990.
58. Gilbert, J. L., Banes, A. J., Weinhold, P. S., Link, G. W., and Jones, G. L., Strain profiles for circular plates and membranes employed to mechanically deform cells *in vitro, J. Biomech.,* 27, 1169–1178, 1994.
59. Pedersen, D. R., Brown, T. D., and Banes, A. J., Mechanical behavior of a new substratum for strain-mediated cell culture experiments, *Proceedings of the 2nd North American Congress on Biomechanics,* 1992, 355–356.
60. Pedersen, D. R., Bottlang, M., Brown, T. D., and Banes, A. J., Hyperelastic constitutive properties of polydimethyl siloxane cell culture membranes, *Adv. Bioeng.,* (ASME) BED 26, 607–609, 1993.
61. Brown, T. D., Bottlang, M., Pedersen, D. R., and Banes, A. J., Flow field visualization in confirmation of a finite element model of nutrient medium reactive stress in a pressure-differential-driven cell culture mechanostimulus system, in *Transactions of the 44th Annual Meeting of the Orthopaedic Research Society,* 1998, 987.
62. Bottlang, M., Brown, T. D., and Banes, A. J., High-frequency oscillations of flexible cell culture membranes driven by cyclic vacuum pulses, in *Transactions of the 42nd Annual Meeting of the Orthopaedic Research Society,* 1996, 333.
63. Brown, T. D., Pedersen, D. R., Bottlang, M., and Banes, A. J., Fluid–structure interaction as a determinant of nutrient medium reactive stresses in mechanically stimulated cultures, in *Transactions of the 43rd Annual Meeting of the Orthopaedic Research Society,* 1997, 175.
64. Brown, T. D., Bottlang, M., Pedersen, D. R., and Banes, A. J., Development and experimental validation of a fluid/structure-interaction finite element model of a vacuum-driven cell culture mechanostimulus system, *Comput. Methods Biomech. Biomed. Eng.,* 3, 65–78, 1999.
65. Brown, T. D., Banes, A. J., Bottlang, M., and Pedersen, D. R., Nutrient depth and waveform abruptness as determinants of reactive fluid stresses in a vacuum-driven cell culture mechanostimulus system, in *Transactions of the 45th Annual Meeting of the Orthopaedic Research Society,* 1999, 633.
66. Winston, F. K., Macarak, E. J., Gorfien, F., and Thibault, L. E., A system to reproduce and quantify the biomechanical environment of the cell, *J. Appl. Physiol.,* 67, 397–405, 1989.
67. Brighton, C. T., Strafford, B., Gross, S. B., Leatherwood, D. F., Williams, J. J., and Pollack, S. R., The proliferative and synthetic response of isolated calvarial bone cells of rats to cyclic biaxial mechanical strain, *J. Bone Joint Surg.,* 73A, 320–331, 1991.

68. Ellis, E. F., McKinney, J. S., Willoughby, K. A., Liang, S., and Povlishock, J. T., A new model for rapid stretch-induced injury of cells in culture: characterization of the model using astrocytes, *J. Neurotrauma,* 12, 325–339, 1995.
69. Broadland, G. W., Dolovich, A. T., and Davies, J. E., Pretension critically affects the incremental strain field on pressure-loaded cell substrate membranes, *J. Biomech. Eng.,* 114, 418–420, 1992.
70. Schaffer, J. L., Rizen, M., L'Italien, G. J., Benbrahim, A., Megerman, J., Gerstenfeld, L. C., and Gray, M. L., Device for the application of a dynamically biaxially uniform and isotropic strain to a flexible cell culture membrane, *J. Orthop. Res.,* 12, 709–719, 1994.
71. Hung, C. T. and Williams, J. L., A method for inducing equibiaxial and uniform strains in elastomeric membranes used as cell substrates, *J. Biomech.,* 27, 227–232, 1994.
72. Lee, A. A., Delhaas, T., Waldman, L. K., MacKenna, D. A., Villarreal, F. J., and McCulloch, A. D., An equibiaxial strain system for cultured cells, *Am. J. Physiol.,* 271, C1400–1409, 1996.
73. Sotoudeh, M., Jalali S., Usami, S., Shyy, J. Y., and Chien, S., A strain device imposing dynamic and uniform equi-biaxial strain to cultured cells, *Ann. Biomed. Eng.,* 26, 181–189, 1998.
74. Ziegler, A., Introducing the Strainmaster cell stretcher. Unpublished product brochure, Z Development, Inc., 1997.
75. FX-2000 Upgrade Information Packet. Unpublished product brochure, Flexcell International Corporation, 1997.
76. Norton, L. A., Anderson, K. L., Arenholt-Bindslev, D., Anderson, L., and Melsen, B., A methodical study of shape changes in human oral cells perturbed by a simulated orthodontic strain *in vitro, Arch. Oral Biol.,* 40, 863–872, 1995.
77. Lynch, T. M. and Lintilhac, P. M., Mechanical signals in plant development: a new method for single cell studies, *Dev. Biol.,* 181, 246–256, 1997.
78. Tomasek, J. J., Haaksma, C. J., Eddy, R. J., and Vaughan, M. B., Fibroblast contraction occurs on release of tension in atached collagen lattices: dependency of an organized actinic cytoskeleton on serum, *Anat. Rec.,* 232, 359–368, 1992.
79. Chamson, A., Sudre, F., LeGuen, C., Le, J., Rattner, A., and Frey, J., Morphological alteration of fibroblasts mechanically stressed in a collagen lattice, *Arch. Dermatol. Res.,* 289, 596–599, 1997.
80. Lambert, C. A., Soudant, E. P., Nusgens, B. V., and Lapiere, C. M., Pre-translational regulation of extracellular matrix molecules and collagenase expression in fibroblasts by mechanical forces, *Lab. Invest.,* 66, 444–451, 1992.
81. Davies, P. F., Flow mediated endothelial mechanotransduction, *Physiol. Rev.,* 75, 519–560, 1995.
82. Dewey, C. F., Effects of fluid flow on living vascular cells, *J. Biomech. Eng.,* 106, 31–35, 1984.
83. Hermann, C., Zeiher, A.M., and Dimmeler, S., Shear stress inhibits H_2O_2-induced apoptosis of human endothelial cells by modulation of the glutathione redox cycle and nitric oxide synthase, *Arteriosclerosis Thrombosis Vasc. Biol.,* 17, 3588–3592, 1997.
84. Mohati, M., Gupta, M. K., Donlon, B., Ellison, B., Cooke, J., Gibbons, G., Schurman, D. J., and Smith, R. L., Expression of interleukin-6 in osteoarthritic chondrocytes and effects of fluid-induced shear on this expression in normal human chondrocytes *in vitro, J. Orthop. Res.,* 14, 67–73, 1996.
85. Van Grondelle, A., Worthen, G. S., Ellis, D., Mathias, M. M., Murphy, R. C., Strife, R. J., and Voelkel, N.F., Altering hydrodynamic variables influences PGI_2 production by isolated lungs and endothelial cells, *J. Appl. Physiol.,* 57, 388–395, 1984.
86. Topper, J. N., Cai, J., Qiu, Y., Anderson, K. R., Xu, Y. Y., Deeds, J. D., Feeley, R., Gimeno, C. J., Woolf, E. A., Tayber, O., Mays, G. G., Sampson, B. A., Shoen, F. J., Gimbrone, M. A., and Falb, D., Vascular MADs: Two novel MAD-related genes selectively inducible by flow in human vascular endothelium, *Proc. Natl. Acad. Sci. U.S.A.,* 94, 9314–9319, 1997.
87. Schnittler, H. J., Franke, R. P., Akbay, U., Mrowietz, C., and Drenckhahn, D., An improved *in vitro* rheological system for studying the effect of fluid shear stress on cultured cells, *Am. J. Physiol.,* 273, E751–758, 1997.

88. Chun, T. H., Itoh, H., Ogawa, Y., Tamura, N., Takaya, K., Igaki, T., Yamashita, J., Doi, K., Inoue, M., Masatsugu, K., Korenaga, R., Ando, J., and Nakao, K., Shear stress augments expression of C-type natriuretic peptide and adrenomedullin, *Hypertension,* 29, 1296–1302, 1997.
89. Diacovo, T. G., Roth, S. J., Morita, C. T., Rosat, J. P., Brenner, M. M., and Springer, T. A., Interactions of human alpha/beta and gamma/delta T lymphocyte subsets in shear flow with e-selectin and p-selectin, *J. Exp. Med.,* 183, 1193–1203, 1996.
90. Frangos, J. A., McIntyre, L. V., and Eskin, S. G., Shear stress induced stimulation of mammalian cell metabolism, *Biotechnol. Bioeng.,* 32, 1053–1060, 1988.
91. Hung, C. T., Pollack, S. R., Reilly, T. M., and Brighton, C. T., Real-time calcium response of cultured cells to fluid flow, *Clin. Orthop. Relat. Res.,* 313, 256–269, 1995.
92. Kuijper, P. H., Gallardo Torres, H. I., van der Linden, J. A., Lammers, J. W., Sixma, J. J., Koenderman, L., and Zwaginga, J. J., Platelet-dependent primary homeostasis promotes selectin- and integrin-mediated neutrophil adhesion to damaged endothelium under flow conditions, *Blood,* 87, 3271–3281, 1996.
93. Levesque, M. J. and Nerem, R. M., The elongation and orientation of cultured endothelial cells in response to shear stress, *J. Biomech. Eng.,* 197, 341–347, 1985.
94. Tseng, H., Peterson, T. E., and Berk, B. C., Fluid shear stress stimulates mitogen-activated protein kinase in endothelial cells, *Circ. Res.,* 77, 869–878, 1995.
95. Li, S., Piotrowicz, R. S., Levin, E. G., Shyy, Y. J., and Chien, S., Fluid shear stress induces the phosphorylation of small heat shock proteins in vascular endothelial cells, *Am. J. Physiol.,* 271, C994–C1000, 1996.
96. Jacobs, C. R., Yellowley, C. E., Davis, B. R., Zhou, Z., Cimbala, J. M., and Donohue, H. J., Differential effect of steady versus oscillating flow on bone cells, *J. Biomech.,* 31, 969–976, 1998.
97. Ruel, J., Lemay, J., Dumas, G., Doillon, C., and Charara, J., Development of a parallel plate flow chamber for studying cell behavior under pulsatile flow, *Am. Soc. Artif. Intern. Organs J.,* 41, 876–883, 1995.
98. Frame, M. D. and Sarelius, I. H., A system for culture of endothelial cells in 20-50-microns branching tubes, *Microcirculation,* 2, 377–385, 1995.
99. Redmond, E. M., Cahill, P. A., and Sitzmann, J.V., Perfused transcapillary smooth muscle and endothelial cell co-culture—a novel *in vitro* model, *In Vitro Cell. Dev. Biol.,* 31, 601–609, 1995.
100. Helmlinger, G., Berk, B. C., and Nerem, R. M., Pulsatile and steady flow-induced calcium oscillations in single cultured endothelial cells, *J. Vasc. Res.,* 33, 360–369, 1996.
101. Walluscheck, K. P., Steinhoff, G., Kelm, S., and Haverich, A., Improved endothelial cell attachment on ePTFE vascular grafts pretreated with synthetic RGD-containing peptides, *Eur. J. Vasc. Endovasc. Surg.,* 12, 321–330, 1996.
102. LaPlaca, M. C. and Thibault, L. E., An *in vitro* traumatic injury model to examine the response of neurons to a hydrodynamically-induced deformation, *Ann. Biomed. Eng.,* 25, 665–677, 1997.
103. Ohata, H., Aizawa, H., and Momose, K., Lysophosphatidic acid sentitizes mechanical stress-induced Ca^{2+} response via activation of phospholipase C and tyrosine kinase in cultured smooth muscle cells, *Life Sci.,* 60, 1287–1295, 1997.
104. Tardy, Y., Resnick, N., Nagel, T., Gimbrone, M.A., and Dewey, C. F., Shear stress gradients remodel endothelial cell monolayers *in vitro* via a cell proliferation-migration-loss cycle, *Arteriosclerosis Thrombosis Vasc. Biol.,* 17, 3102–3106, 1997.
105. Waters, C. M., Chang, J. Y., Glucksberg, M. R., DePaola, N., and Grotberg, J. B., Mechanical forces alter growth factor release by pleural mesothelial cells, *Am. J. Physiol.,* 272, L552–557, 1997.
106. Pearce, M. J., McIntyre, T. M., Prescott, S. M., Zimmerman, G. A., and Whatley, R. E., Shear stress activates cytosolic phospholipase A2 (cPLA2) and MAP kinase in human endothelial cells, *Biochem. Biophys. Res. Commun.,* 218, 500–504, 1996.
107. Inoue, H., Nakamura, O., Duan, Y., Hiraki, Y., and Sakuda, M., Effect of centrifugal force on mouse osteoblastic MC3T3-E1 cells *in vitro, J. Dent. Res.,* 72, 1351–1355, 1993.

108. Wagner, C. T., Durente, W., Christodoulides, N., Hellums, J. D., and Schafer, A. L., Hemodynamic forces induce the expression of heme oxygenase in cultured vascular smooth muscle cells, *J. Clin. Invest.,* 100, 589–596, 1997.
109. Benbrahim, A., L'Italien, G. J., Milinazzo, B. B., Warnock, D. F., Dhara, S., Gertler, J. P., Orkin, R. W., and Abbott, W. M., A compliant tubular device to study the influences of wall strain and fluid shear stress on cells of the vascular wall, *J. Vasc. Surg.,* 20, 184–190, 1994.
110. Moore, J. E., Burki, E., Suciu, A., Zhao, S., Brunier, M., Brunner, H. R., and Meister, J. J., A device for subjecting vascular endothelial cells to both fluid shear stress and circumferential cyclic stretch, *Ann. Biomed. Eng.,* 22, 416–422, 1994.
111. Ayajiki, K., Kinderman, M., Heckler, M., Fleming, I., and Busse, R., Intracellular pH and tyrosine phosphorylation but not calcium determine shear stress-induced nitric oxide production in native endothelial cells, *Circ. Res.,* 78, 750–758, 1996.
112. Wright, M., Jobanputra, P., Bavington, C., and Salter, D. M., Effect of intermittent pressure-induced strain on the electrophysiology of cultured human chondrocytes: evidence for the presence of stretch-activated membrane ion channels, *Clin. Sci.,* 90, 61–71, 1996.
113. Dewey, C. F. and DePaola, N., Exploring flow-cell interactions using computational fluid dynamics, in *Tissue Engineering,* Woo, S. L.-Y. and Seguchi, Y., Eds., ASME, New York, 1989, 31–33.
114. Davies, P. F., Mundel, T., and Barbee, K. A., A mechanism for heterogeneous endothelial responses to flow *in vivo* and *in vitro, J. Biomech.*, 28, 1553–1560, 1995.
115. Brown, T. D., Bottlang, M., Pedersen, D. R., and Banes, A. J., Loading paradigms—intentional and unintentional—for cell culture mechanostimulus, *Am. J. Med. Sci.,* 316, 162–168, 1998.

28

Experiments on Cell Mechanosensitivity: Bone Cells as Mechanical Engineers

Elisabeth H. Burger
ACTA Vrije University

Abstract—The capacity of bone tissue to adapt to changing mechanical demands is well documented, but how the cells of bone perform this task remains poorly understood. Over the last decade significant progress has been made in understanding how bone cells may sense and transduce mechanical signals derived from bone loading. These studies emphasize the role of osteocytes as the "professional" mechanosensory cells of bone, and the lacuno-canalicular porosity as the structure that mediates mechanosensing. Strain-derived flow of interstitial fluid through this porosity seems to be sensed by the osteocytes, which are thereby informed about the mechanical adequacy of the surrounding tissue. Overuse as well as disuse produce abnormal canalicular flow, which is translated into bone-forming or bone-resorbing cell signals. This concept allows one to explain local bone gain and loss during adaptation, as well as remodeling in response to fatigue damage, as processes supervised by mechanosensitive osteocytes.

28.1 Introduction

The phenomenon of bone adaptation has been known for more than a century, since the original studies of Roux (Roux, 1881) and Wolff (Wolff, 1892). Mechanical adaptation of bone is the process whereby living bone adapts its mass and structure to prevailing mechanical usage, to obtain a higher efficiency of load bearing. Adaptation will improve an individual animal's survival chance, because bone is not only hard, but also heavy. Too much of it is probably as bad as too little, leading either to uneconomic energy consumption during movement (for too high bone mass) or to an enhanced fracture risk (for too low bone mass). This readily explains the usefulness of mechanical adaptation, even if how it is performed is not understood. In the time of Roux and Wolff it also became apparent that bone is a *tissue*, made by cells and degraded by cells. The terms *osteocyte*, *osteoblast*, and *osteoclast* stem from that same time period. The mechanical function of that tissue is performed by the lifeless material between the cells, the

0-8493-9117-2/01/$0.00+$.50

extracellular mineralized matrix. The role of the cells is to make and degrade that matrix, in relation to mechanical demands.

Mechanical adaptation is an important issue for orthopedic surgeons and dentists, particularly so when therapy aims to improve or restore the mechanical performance of the skeleton, including the jaws. Unfortunately, many details of the biological process whereby bone tissue responds to loading are still obscure. However, some important progress has been made in understanding how bone tissue may sense the effect of mechanical loading, and how mechanical signals are transduced into cellular signals. This chapter aims to summarize these studies, in a manner that avoids cell-biological jargon where possible. The hope is that this approach will make the chapter useful also for non cell biologists, in particular biomechanicians and clinicians. The earlier chapters of this handbook, on basic biology, will, of course, be helpful in case the text is still unclear.

28.2 The Bone Cell Network

When discussing the cell biology of mechanical adaptation, it is useful first to consider a global scheme of the main steps that are involved (Fig. 28.1). Mechanical loading produces straining of the bone matrix, because the hard bone matrix is the load-carrying part of the tissue. The amount of strain must then somehow be sensed by bone cells. In biological systems time-variable changes are better sensed then static conditions, which is the reason strain rate is probably as important as strain magnitude (Turner et al., 1995; Mosley and Lanyon, 1998). The bone cells must translate the strain signal into a cellular signal which ensures that adaptive bone formation or resorption take place (Fig. 28.1).

Bone formation and resorption are performed by separate cells, respectively, osteoblasts and osteoclasts. They are only found at the bone surface, where the osteoblasts build a new layer of matrix on the bone surface, while the osteoclasts dig a hole in that surface. The great majority of bone cells, particularly in adult bone, are, however, neither osteoblasts nor osteoclasts, but osteocytes or lining cells (Jee, 1988; Chapters 1 and 2 in this handbook). Osteocytes are cells that lie *within* the hard bone matrix; lining cells lie *on* the bone surface and form a thin sheath that covers all bone surfaces (Fig. 28.2). Lining cells are only absent from those surfaces where osteoblasts or osteoclasts are active. Both osteocytes and lining cells are the long-lived, mature stages of osteoblasts, the cuboidal cells that produced the bone matrix (Fig. 28.3). Osteoblasts derive from proliferating immature cells in bone marrow and periosteum, the

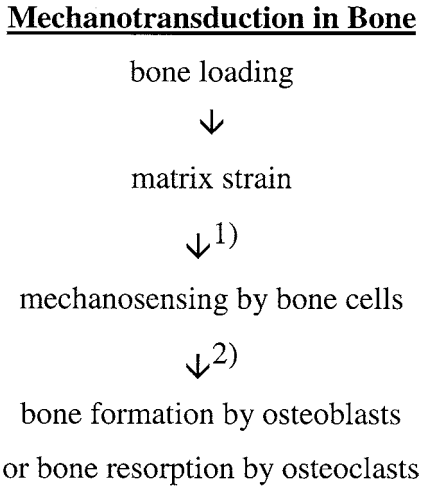

FIGURE 28.1 Scheme to show that mechanotransduction includes two important steps: (1) mechanosensing: the step where the physical signal derived from matrix strain, is sensed by the cells and translated into a biological signal; and (2) intercellular signaling: the step where biological signals are used to activate osteoblasts or osteoclasts.

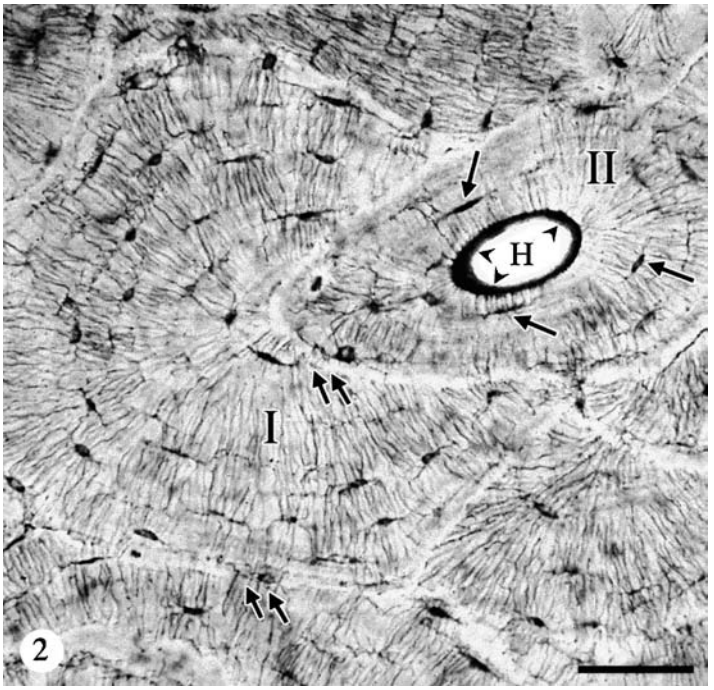

FIGURE 28.2 Histological section through compact bone, stained with Schmorl's method. The osteocytes (arrows) are lying in concentric layers around a Haversian channel (H). Lining cells lie against the wall of the Haversian channel (arrowheads). Osteocytes are connected with each other and with lining cells via many slender cell processes, which show up as thin dark lines. Osteon II was formed after osteon I, which was partly resorbed by osteoclasts before osteon II could be formed. A whitish line, the cement line, separates different osteons. Note that cement lines are sometimes crossed by osteocyte processes (double arrows). Bar = 55 μm.

so-called osteoprogenitor cells. These move toward a bone surface and start producing and secreting unmineralized matrix, or osteoid. Because they secrete matrix only at their bone-facing side, they push themselves away from that surface, leaving a new layer of osteoid behind (Fig. 28.3A). Osteocytes appear because at more or less regular intervals an osteoblast stops producing matrix. It turns off protein synthesis and becomes flat (Palumbo, 1986; Nefussi et al., 1991). As its neighboring osteoblasts continue producing matrix, this quisling osteoblast, or preosteocyte, is left behind and becomes embedded in osteoid—and is now an osteocyte. It would die of lack of nutrients as soon as the osteoid mineralizes, because mineralized bone matrix is quite impenetrable for even small molecules, if it did not keep contact with the bone surface by extending thin, fingerlike processes toward the receding osteoblast front (Palumbo et al., 1990b). When the osteoid calcifies, mineralization stops shortly before an osteocyte cell body or process is reached. As a result, osteocytes are always completely surrounded by a thin layer of nonmineralized matrix. In deproteinized preparations of bone, the small holes that contained the osteocytes show up as the osteocyte lacunae, while the tiny channels that contained the osteocyte processes are the canaliculi. Bone canaliculi are some 0.2 μm in diameter, about 250 $\times$ smaller than the Haversian and Volkmann channels, which are about 50 μm in diameter and contain blood vessels (Chapter 1). Osteocytes may have up to 80 cell processes (and therefore, 80 canaliculi) and via these processes they keep contact with other osteocytes in the deeper layers of bone as well as the surface cells.

The surface cells of bone, or bone-lining cells, also derive from osteoblasts (Fig. 28.3C). Bone-lining cells appear when for some reason bone formation stops, apparently because the amount produced is considered sufficient. The remaining osteoblasts at the bone surface become flat and quiescent, but because there are no neighboring osteoblasts that continue to make bone matrix, they are not buried in matrix.

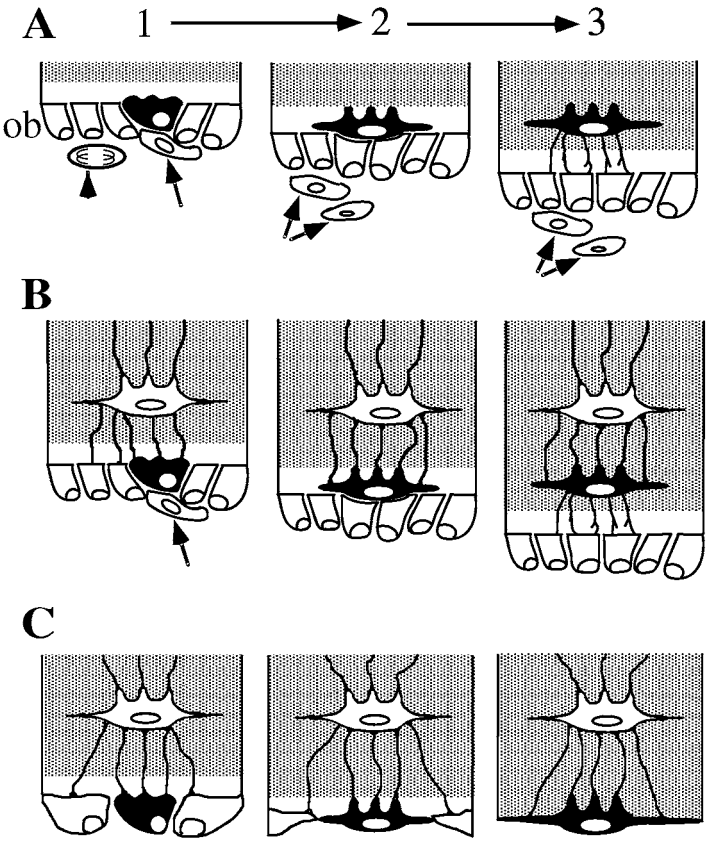

FIGURE 28.3 Schematic representation of the formation of osteocytes and lining cells from osteoblast. The stippled material is mineralized bone. A1, osteoblasts (ob) produce a layer of osteoid (white layer) against a bone surface. A2, one osteoblast (black cell) stops producing matrix, and is incorporated in osteoid. When the osteoid mineralizes (A3), the osteoblast has turned into an osteocyte. In A1–3, during rapid growth, proliferation of progenitor cells (arrowhead) ensures a plentiful supply of postmitotic preosteoblasts (arrows), which may take the place of preosteocytes. In B1–3, growth starts to diminish, because supply of proliferating progenitors has stopped, and only postmitotic preosteoblasts (arrow) remain. In C1–3, no preosteoblasts are left. All remaining osteoblasts stop producing osteoid, and the mineralization process continues until the last layer of flattening osteoblasts (C2), which become lining cells (C3). Note that in all three cases the kinetics of bone tissue growth are regulated by the rate of osteoblast progenitor cell recruitment, apart from osteoblast lifetime and osteoblast synthetic activity. (From Burger, E. H. and Klein-Nulend, J., *FASEB J.,* 13(Suppl.), S101–S112, 1999. With permission.)

Instead, they end up as a continuous layer of very thin, flat cells that cover the bone surface—the bone-lining cells. They are in contact with each other and with the superficial osteocytes via cell processes, same as osteocytes, but these are not fingerlike as osteocyte processes, but flatter and broader. The cell processes of osteocytes and lining cells are interconnected via gap junctions (Doty, 1981; Palumbo et al., 1990a; Shapiro, 1997). These gap junctions permit exchange of small signal molecules and ions between the connected cells. As a result, osteocytes and lining cells form an interconnected network of cells—and bone may be considered a three-dimensional network of cells, with hard extracellular matrix in the meshes of that network. Fig. 28.3 schematically represents the formation of osteocytes and lining cells from osteoblasts. It also shows that continued bone and osteocyte formation depends on the recruitment of new (pre-)osteoblasts from osteoprogenitor cells (Fig. 28.3A,B). Lack of new (pre-)osteoblasts leads to formation of lining cells from the remaining osteoblasts, and stopping of further (local) growth (Fig. 28.3C). In adult bone, lining cells cover the surface of the trabeculae of cancellous bone, the periosteal and endosteal envelope of cortical bone, and the Haversian and Volkmann channels of the osteons.

As will be seen in the following paragraphs, this three-dimensional cellular network, and its accompanying porous network of lacunae and canaliculi, is currently considered of fundamental importance for the process of mechanosensing in live bone. Therefore, it seemed useful to consider at some length how this network develops, and what the cellular relations are between osteoblasts, osteocytes, and lining cells. Conspicuously absent from this discussion are the osteoclasts. They derive from a different family of cells, the hemopoietic cell family, and never form part of the bone cell network (Burger et al., 1982; Scheven et al., 1986; Kurihara et al., 1989). The ordered orientation of secondary osteons, which is determined during osteoclastic excavation, strongly suggests that the direction in which osteoclasts move during bone resorption is somehow mechanically regulated. However, there is no biological explanation how osteoclasts, which operate as individual cells and not in a network, would sense the mechanical adequateness of a piece of bone. Therefore, it seems likely that mechanical regulation of bone resorption occurs in an indirect manner, via the mechanosensitive cells of the bone cell network, although experimental evidence for this concept is scarce (Bentolila et al., 1998; Smit and Burger, 2000). Evidence that osteoclast formation and activity may be controlled by cells of the osteoblast–osteocyte lineage is, however, abundant (Takahashi et al., 1988; Burger and Nijweide, 1990; Suda et al., 1995). For example, control of osteoclastic resorption by certain hormones such as parathyroid hormone and vitamin D is performed indirectly, via osteoblasts/ osteocytes. Receptors for these hormones are only found on osteoblasts and osteocytes, but not on osteoclasts. In addition, osteoblasts must be added to osteoclasts *in vitro*, before osteoclasts can be activated by these hormones (Suda et al., 1995). This has led to the concept that osteoclasts operate under control of the osteoblasts and osteocytes, that is, the cells of the bone cell network. Mechanical regulation of osteoclast activity, including the direction in which they move during resorption, by this same network, would be a logical extension of that concept. This subject is further discussed at the end of this chapter.

28.3 Mechanosensing Mechanism in Bone

In healthy, adequately adapted bone, the strains as a result of physiological loads (e.g., resulting from normal locomotion) are quite small. Quantitative studies of the strain in bones of performing animals (e.g., galloping horses, fast-flying birds, even a running human volunteer) found a maximal strain not higher than 0.2 to 0.3% (Rubin, 1984; Burr et al., 1996). This poses a problem in interpreting the results of *in vitro* studies of strained bone cells, where much higher deformations, on the order of 1 to 10% are needed to obtain a cellular response (Murray and Rushton, 1990; Burger and Veldhuijzen, 1993). In these studies isolated bone cells are usually grown on a flexible substratum, which is then strained by stretching or bending. For example, unidirectional cell stretching of 1% is required to obtain a reproducible cell proliferative response in cultures of human bone cells (Neidlinger-Wilke et al., 1995). However, in an animal study using rats, 0.15% bending strain of the intact tibia was already sufficient to activate cell proliferation and bone formation *in vivo* (Turner et al., 1994; Forwood, 1996). If one assumes that strain is somehow involved in bone cell mechanosensing, then bone tissue must possess a lever system whereby the small matrix strains are transduced into a larger signal that is sensed by bone cells. The theory of streaming potentials proposes one such lever system. Electrodes placed on the periosteal and endosteal surface of wet bone will measure a difference in voltage when the bone is bent. The work of Pollack and co-workers showed that these strain-generated potentials (SGPs) are caused by strain-induced flow of interstitial fluid within the microporosity of bone, rather then due to pressure (or piezoelectric) (Pollack et al., 1984; Salzstein and Pollack, 1987; Salzstein et al., 1987; see also Chapter 23). It was suggested that these streaming potentials would provide the physical signal for mechanical adaptation. The question of which and exactly how cells were activated was left open. Subsequent papers based on the cellular structure of bone suggested that the osteocyte network, and its accompanying lacuno-canalicular porosity, provide the best candidate for the mechanosensory system in bone (Cowin et al., 1991; 1995; see also Chapter 22). Cowin et al. (1995), using the model of Weinbaum et al. (1994), calculated that the anatomical source site of the SGPs could be the canalicular porosity and not the mineralized matrix, if the hydraulic drag and the passage of interstitial fluid through the nonmineralized matrix layer between osteocyte process

and canalicular wall are accounted for. Passage of interstitial fluid through canaliculi and along the osteocyte process as a result of bulk tissue strains had been made plausible earlier (Piekarski and Munro, 1977) and was recently demonstrated experimentally (Knothe Tate et al., 1998; see also Chapter 22). However, this strain-derived fluid flow could solely function as a means to keep osteocytes healthy, by facilitating diffusion of nutrients and waste products. In the view of Cowin and colleagues, the combination of the cellular network of osteocytes and the porous network of canaliculi act together as the mechanosensory organ of bone. It was calculated (Weinbaum et al., 1994) that bulk bone strains around 0.1% would produce a fluid shear stress in canaliculi of roughly 1 Pa. As, for example, endothelial cells, the cells lining blood vessels, can respond quite well to fluid shear stress of such magnitude, it was proposed that the canalicular fluid flow could act as the physical stimulus for mechanosensing in bone (Weinbaum et al., 1994). The flow of interstitial fluid through the bone canaliculi will have two effects, a mechanical one derived from fluid shear stress and an electrokinetic one derived from SGPs. Either of the two, or both in combination, might activate the osteocyte. For example, SGPs might modulate the movement of ions such as calcium across the cell membrane (Hung et al., 1995; 1996) while shear stress might pull at the macromolecular attachments between the cell and its surrounding matrix (Wang et al., 1994). Both ion fluxes and cellular attachment are powerful modulators of cell behavior, and therefore good conveyors of physical information (Sachs, 1989; Ingber, 1991).

Direct studies of cell responsiveness are usually performed *in vitro*, in a culture system where cells are kept alive in a medium that mimics the ionic composition of tissue interstitial fluid (Nijweide and Burger, 1990). Flow of interstitial fluid *in vivo* can then be mimicked by moving the culture medium over the cells grown as a monolayer on a substratum. The substratum is usually plastic or glass, to which most cells avidly adhere when serum is added to the culture medium. Over the last few years, several studies have tested the fluid flow responsiveness of bone cells to seek validation of the canalicular fluid flow hypothesis. Several cell preparations were used, including a preparation highly enriched in osteocytes. These studies are now briefly reviewed.

28.4 Osteocyte Mechanosensitivity

Experiments on bone cells in tissue culture are usually performed on osteoblasts or, rather, osteoblastic cells, "osteoblastic" meaning that both immature and mature stages of osteoblasts are present in the culture system. This is because many cells (10^6 to 10^8) are usually needed for biochemical analysis, and osteoblastic cells are highly proliferative in the presence of serum. Osteocytes are the least-studied cell type of bone, because they do not proliferate and are therefore difficult to maintain in tissue culture. Bone cells can be liberated from a piece of bone, using EDTA, a decalcifying agent that is not immediately toxic to cells, in combination with collagenase to degrade the organic part of bone matrix (Nijweide and Burger, 1990). Usually immature bone from neonatal rodents or chickens is used, because the matrix is not yet fully mineralized and therefore easier to degrade. This procedure will liberate osteoblasts, lining cells, and osteocytes, as well as osteoclasts. However, as the growth factors in serum, a necessary additive to keep the cells alive, also promote the rapid proliferation of osteoblastic cells in the mixture, after a week the vast majority of the cells are osteoblastic. In fact, the presence of osteocytes in such cell cultures was only detected when a monoclonal antibody had been developed that binds to a specific component in the cell membrane of osteocytes, but not osteoblasts (Nijweide and Mulder, 1986). The cell source must be chicken bone, because the antibody does not react with other animal species, unfortunately. When combined with a fluorochrome, the antibody (OB 7.3) "stains" the whole surface of the osteocyte, including its cell processes (Nijweide and Mulder, 1986; Van der Plas and Nijweide, 1992) (Fig. 28.4). This technique showed that osteocytes, when liberated from bone, round off as tiny balls when floating in liquid culture medium. However, as soon as they touch glass or plastic, they start to adhere to this substratum, a process that is strongly promoted by attachment factors in serum. They then start to send out fingerlike cell processes from the cell body, first in all directions, but soon only those "fingers" that run along and adhere to the substratum remain. If several osteocytes are seeded as a cluster, the

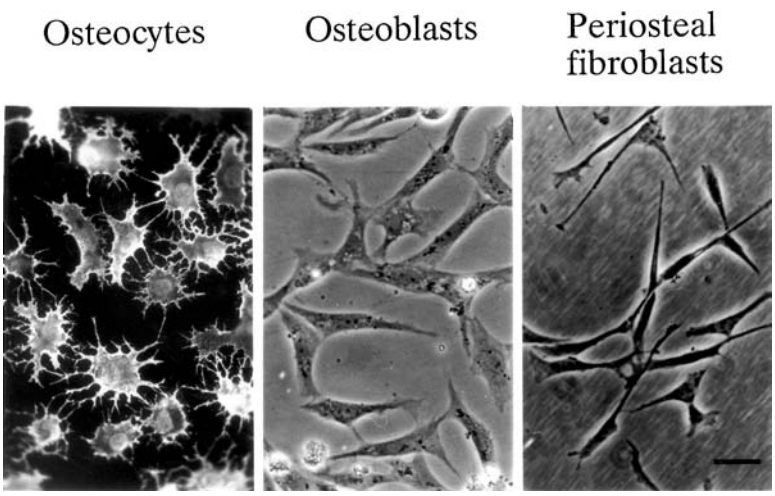

FIGURE 28.4 Morphology of osteocytes, osteoblasts, and periosteal fibroblasts isolated from embryonic chicken calvariae as observed by fluorescence or phase-contrast microscopy after 2 days of culture. Only the osteocytes stain with the osteocyte-specific antibody OB 7-3, which was linked to a fluorescent marker. The white fluoresence sharply delineates the many thin cell processes that link the osteocytes. Osteoblasts and periosteal fibroblasts do not show these cell processes and do not stain with the antibody. Magnification 1000×. (From Klein-Nulend et al., 1995a. With permission.)

cells establish contact via their fingerlike processes, which are often branched (Van der Plas et al., 1994). In this way a (two-dimensional) network of cells is again established, including gap junctions where the processes of two cells meet (P.J. Nijweide, personal communication). The cells produce all components of the organic matrix of bone, but much less so than osteoblasts (Aarden et al., 1996). Although they are rapidly overgrown by osteoblasts, cells staining with the specific osteocyte antibody could still be found in 3-week-old cultures, but only as a very small minority (Nijweide and Mulder, 1986). However, their prevalence in a cell culture can be strongly enhanced by using the technique of immunoseparation (Van der Plas and Nijweide, 1992). Cells are liberated from embryonic chicken bone, usually calvarial bones, and the osteocytes are then separated from nonosteocytes, using immunomagnetic beads. These are small polycarbonate beads with a metal nucleus, that carry the osteocyte-specific antibody on their surface. When mixed with the cell preparation, the beads only bind to osteocytes, because of the antibody. Beads plus adhering osteocytes are then drawn to a magnet, which is held against the wall of the cell container, and the other cells are removed by sucking the medium plus loose cells off with a pipette.

By using the technique of immunoseparation, three cell populations with a high (±90%) degree of homogeneity could be prepared from embryonic chicken calvariae: periosteal fibroblasts (including osteoprogenitor cells) derived from the periosteum, osteoblasts, and osteocytes (Van der Plas and Nijweide, 1992). These three populations were subsequently tested for responsiveness to stress, using prostaglandin production as parameter of cell activation (Klein-Nulend et al., 1995a). Prostaglandins, particularly PGE_2 and PGI_2, are important intercellular messenger molecules for bone cells. Experiments on whole animals have shown that they play a key role in mechanical adaptation, because inhibiting their synthesis prevents adaptation (Chow and Chambers, 1994; Forwood, 1996). Two types of mechanical stress were used; intermittent hydrostatic compressive (IHC; 0 to 13 kPa at 1 Hz) and pulsatile fluid flow (PFF; 0.7 ± 0.02 Pa at 5 Hz). As expected, hydrostatic pressure had much less effect than flow, 13,000 Pa IHC taking 6 h before a response could be measured while 0.7 Pa PFF acted after 1 h (Klein-Nulend et al., 1995a). Interestingly, however, in both cases the osteocytes were much more responsive than osteoblasts, and these more than fibroblasts (Klein-Nulend et al., 1995a). Both PGE_2 and PGI_2 were rapidly (within 5 min) released by osteocytes, and to a much larger amount than by osteoblasts and periosteal fibroblasts (Ajubi et al., 1996). These observations fitted the hypothesis that osteocytes are a

class of cells specialized in mechanosensing, better than osteoblasts, and these again better than periosteal preosteoblasts. In other words, during maturation osteoblasts develop an increasing capacity for mechanosensing, which is highest in their final differentiated stage, the osteocyte stage.

The response to fluid flow *in vitro* could be inhibited by treating the cells with cytochalasin B, a drug that disrupts actin filaments. This indicates that the actin component of the cytoskeleton was involved in the transduction of the extracellular mechanosignal to intracellular domains, such as the cell nucleus (Ajubi et al., 1996; 1999). Interestingly, a unique organization of acting bundles that span the cell body and the fingerlike processes was recently described in osteocytes (Tanaka-Kamioka et al., 1998). Actin filaments were found crucial for the maintenance of osteocyte shape *in vitro*, and an actin-bundling protein, fimbrin, was found abundantly and specifically in the osteocyte processes (Tanaka-Kamioka et al., 1998). Actin-bundling proteins such as fimbrin stabilize actin filaments through increased lateral connections between filaments, and in osteocytes this would serve to enhance the stability of osteocyte processes that is necessary for the maintenance of a communication network within bone tissue (De Arruda et al., 1990). Interestingly, fimbrin has also been found in stereo cilia of auditory hair cells, which reside in the inner ear and function as mechanosensory cells of sound (Bretcher and Weber, 1980).

Another early response of osteocyte cell cultures to fluid flow was an enhanced production of nitric oxide (NO). Osteocytes, but not periosteal fibroblasts, transiently released NO in the culture medium when exposed to pulsatile fluid flow (Klein-Nulend, 1995b). NO production was also found when whole-bone rudiments were submitted to mechanical loading in organ culture (Pitsillides et al., 1995). NO is a ubiquitous messenger molecule for intercellular communication, involved in many tissue reactions where cells must collaborate and communicate with each other (Koprowski and Maeda, 1995). Inhibition of NO production leads to inhibition of mechanically induced bone formation (Turner et al., 1996; Fox et al., 1996), in line with the *in vitro* observations that NO is involved in cell signaling after mechanical stress. Another adaptive process where NO is involved in cell signaling is the adaptation of blood vessels to changes in blood flow (Cooke et al., 1990). In blood vessels, enhanced blood flow as, for example, during exercise leads to widening of the vessel, to ensure a constant blood pressure. This response depends on the endothelial cells, thin cells that line the luminal surface of blood vessels. The endothelial cells sense the increased blood flow and produce intercellular messengers such as NO and prostaglandins, for the smooth muscle cells around the vessel, which in response relax to allow the vessel to increase in diameter (Kamiya and Ando, 1996). The capacity of endothelial cells to produce NO in response to fluid flow is related to a specific enzyme, endothelial NO synthase or ecNOS. Interestingly, this same enzyme was recently also found in bone cells derived from human bone (Klein-Nulend et al., 1998). Treatment with pulsatile fluid flow increased the level of ecNOS RNA transcripts in the bone cells, a response also described in endothelial cells (Uematsu et al., 1995; Busse and Fleming, 1998). Enhanced production of prostaglandins is also a well-described response of endothelial cells to fluid flow. It seems therefore that endothelial cells and osteocytes possess a similar sensor system for fluid flow and that both cell types are "professional" sensors of fluid flow. *Mutatis mutandis*, this is an indication that osteocytes sense bone strains via the (canalicular) fluid flow resulting from those strains.

Several recent studies have described other effects of fluid flow in osteoblastic cells. Fluid flow rapidly increased intracellular calcium in bone cells (Hung et al., 1995) an effect that was inhibited using neomycin or gadolinium, suggesting an influx of calcium via stretch-activated channels as well as release from intracellular stores (Rawlinson et al., 1996; Hung et al., 1996). Another study found evidence that fluid shear stress is more effective than mechanical stretching in activating bone cells (Owan et al., 1997). Four-point bending was applied to a cell culture substratum of variable plate thickness. The study showed unequivocally that the rate of displacement, independent of the strain magnitude, correlated with the bone cell response, measured as a change in gene expression. As the rate of displacement is proportional to the fluid force applied by the movement of fluid culture medium over the culture plate during bending, the results show that the fluid shear stress rather than the cell strain activated the bone cells (Owan et al., 1997). It is likely that this conclusion also applies to other models where bone cell monolayers are mechanically stimulated by dynamic stretching through a fluid culture medium (Burger and Veldhuijzen, 1993; Neidlinger-Wilke et al., 1995).

The increase in cellular calcium following exposure to fluid flow was recently used to study the effectiveness of steady flow, oscillating flow, and pulsating flow, of similar magnitude, in cultures of an osteoblastic human cell line (Jacobs et al., 1998). Surprisingly, this study found that oscillating flow, which likely mimics the loading-induced fluid flow in bone canaliculi better than steady or pulsatile flow, was less stimulatory to calcium influx than steady or pulsatile flow. In addition, increasing the pulse frequency and therefore the shear stress rate, *reduced* rather than increased the calcium response, both with oscillating and pulsatile flow. The authors proposed a chemotransport-dependent response mechanism, independent of shear stress but involving a factor contained in serum, to be responsible for the observed calcium responses (Jacobs et al., 1998). Unfortunately, these results are difficult to fit in other studies, where somewhat later events in the cellular response cascade were studied. For example, in the study of Owan et al. (1997) oscillating flow was in fact applied during four-point bending, leading to an impressive cellular change in mRNA expression. In another study, pulsatile flow-induced expression of COX-II, an important enzyme for prostaglandin synthesis, was independent of serum factors (Klein-Nulend et al., 1997). Several *in vivo* studies have underscored the efficacy of increased bone strain rate and pulse frequency in evoking an adaptive osteogenic response to mechanical load (Turner et al., 1994b; 1995; Mosley and Lanyon, 1998). Last, an *in vitro* study found that increasing the viscosity of the culture medium, and therefore the fluid shear stress, increased the osteoblastic response to fluid flow, measured as increased levels of cyclic AMP (Reich et al., 1990). Together, these studies advocate that fluid shear stress and/or streaming potentials, rather than chemotransport, are responsible for activating bone cells in adaptive bone remodeling. A possible explanation of the contradiction between the calcium changes and other cellular responses may be that the increase of cellular calcium does not reflect the full-blown response that bone cells produce after mechanical stimulation. It is even possible that the calcium influx represents a separate, early response that is solely the effect of mass transport. Further studies are clearly needed to sort this out. However, the sum of current evidence, including animal studies, cell culture studies, and computer simulation studies, provide strong evidence that the combination of an osteocyte network and a lacuno-canalicular porosity provides the mechanosensory system of bone.

28.5 The Lacuno-Canalicular Network and Bone Remodeling—a Hypothesis

As shown above, as well as in other chapters of this handbook, there is now evidence that strain-derived canalicular fluid flow activates osteocytes to produce anabolic factors such as prostaglandins and NO. These messenger molecules may then recruit new osteoblasts from periosteum and bone marrow stroma. To do so they must be brought to the bone surface, presumably in the same manner that waste products are removed, i.e., via the lacuno-canalicular porosity. Alternatively, an anabolic message is transported through the cellular network, via intracellular transport and gap junctions. A combination of intra- and extracellular signals is also possible. In any case, the integrity of the lacuno-canalicular network, both the cellular network and the porosity, are crucial for mechanotransduction because the porosity produces the ultimate mechanical signal for the cells. By using this concept, it is possible to explain at the cellular level, local bone gain as a result of local overuse, and local bone loss as a result of local disuse, as shown schematically in Fig. 28.5. Physiological, "normal" bone use is needed to keep osteocytes viable by enhanced displacement of nutrients and waste, but also to provide them with a basal level of mechanical stimulation by fluid shear stress (Fig. 28.5A). Under these conditions, no osteoblasts or osteoclasts are recruited. "Overuse" means overstimulation of the osteocytes by abnormally high fluid shear stress, resulting in recruitment of osteoblasts instead of lining cells to the bone surface (Fig. 28.5B). It is also possible that lining cells are activated to redifferentiate as osteoblasts (Forwood et al., 1996). The extra bone produced by the osteoblasts restores the normal level of loading and, therefore, the "use" state of osteocyte stimulation (Fig. 28.5B). "Disuse," on the other hand, reduces osteocyte shear stress stimulation as well as reducing transport of nutrients and waste products (Fig. 28.5C). The latter will

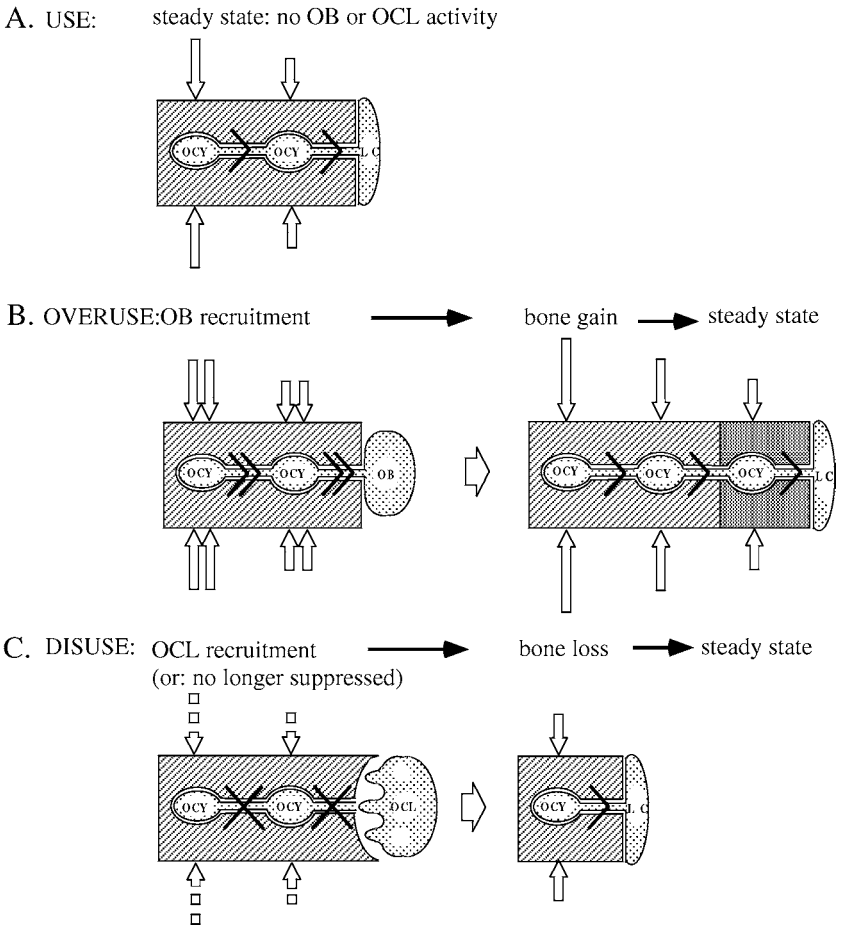

FIGURE 28.5 Schematic representation of how the osteocyte network may regulate bone modeling. (A) In the steady state, normal mechanical use ensures a basal level of fluid flow through the lacuno-canalicular porosity, indicated by an arrowhead through the canaliculi. This basal flow keeps the osteocytes viable, and also ensures basal osteocyte activation and signaling, thereby suppressing osteoblastic activity as well as osteoclastic attack. (B) During (local) overuse, the osteocytes are overactivated by enhanced fluid flow (indicated by double arrowheads), leading to release of osteoblast-recruiting signals. Subsequent osteoblastic bone formation reduces the overuse until normal mechanical strain is reestablished, thereby reestablishing the steady state of basal fluid flow. (C) During (local) disuse, the osteocytes are inactivated by lack of fluid flow (indicated by crosses through canaliculi). Inactivation leads either to release of osteoclast-recruiting signals or to lack of osteoclast-suppressing signals or both. Subsequent osteoclastic bone resorption reestablishes normal mechanical strain and basal fluid flow. OCY, osteocyte; LC, lining cell; OB, osteoblast; OCL, osteoclast; hatched area, mineralized bone matrix; dark-gray area, newly formed bone matrix; white arrows represent direction and magnitude of loading. (From Burger, E. H. and Klein-Nulend, J., *FASEB J.,* 13(Suppl.), S101–S112, 1999. With permission.)

reduce osteocyte viability, and may even lead to osteocyte death. Osteocyte death could then be the signal for recruitment of osteoclasts. Indeed, a positive correlation between osteocyte apoptosis and osteoclastic attack has been described in growing bone (Bronckers et al., 1996). It is, however, also possible that well-stimulated osteocytes *inhibit* osteoclast recruitment, and that disuse leads via under-stimulation of osteocytes to absence of osteoclast-inhibiting signals. Inhibition of bone resorption has been described in mechanically stimulated bone of experimental animals (Hillam and Skerry, 1995). Osteoclasts readily resorb slices of devitalized bone *in vitro* (Chambers et al., 1985), but in mixed cultures

of osteocytes and osteoclasts, osteocytes seemed to inhibit osteoclast activity (Tanaka et al., 1995). Recently, an osteocyte-derived protein has been described that inhibits osteoclastic bone resorption (Maejima-Ikeda et al., 1997). These findings suggest that active suppression of osteoclasts by osteocytes is feasible. In the concept of osteoclastic suppression by (well-stimulated) osteocytes, osteocyte apoptosis and osteoclastic attack are two parallel results of lack of mechanical stimulation, rather than one being the cause of the other.

The theory of osteocytic suppression of osteoclasts is useful when trying to explain the process of bone *re*modeling (Fig. 28.6). In adult bone, osteoblastic and osteoclastic activity are largely confined to bone remodeling (Jee, 1988). Remodeling is a complicated process, which starts by osteoclasts removing existing bone, by digging either a tunnel, in compact bone, or a more or less shallow groove along the surface of a trabecula. The tunnel or groove is subsequently refilled with new bone tissue by osteoblasts. Convincing evidence has accumulated over the last decade that remodeling serves to renew bone that was impaired by fatigue microdamage (Burr et al., 1985; 1997; Nunamaker et al., 1990; Burr, 1993; Burr and Martin, 1993). Fatigue microdamage results from repetitive loading in the normal physiological range, and, when accumulating over time, leads to impairment of the mechanical properties of the bone matrix. At the ultrastructural level, fatigue leads to focal patches of ultrastructural damage of the fully mineralized matrix, shown as increased permeability of the matrix for histological stain (Schaffler et al., 1994). Ultrastructural microdamage precedes the appearance of very fine cracks observable only at $> 1000 \times$ magnification, and these eventually coalesce into microcracks that can be stained with basic fuchsin and are observable at low magnification light microscopy (Burr et al., 1985). The cracks will run right through the mineralized matrix, independent of the lamellar and osteonal organization of the tissue (Schaffler et al., 1994). One may therefore assume that fatigue microdamage will interfere with the integrity of the osteocytic and lacunocanalicular network, by disrupting canaliculi and severing osteocyte processes. Finite-element analysis predicts changes in strain at the microstructural, cellular level as a result of microdamage (Prendergast and Huiskes, 1996). Increased permeability between canalicular channel and mineralized matrix will decrease the fluid drag forces in the channel (Mak et al., 1997). Fatigue damage may therefore create a situation resembling disuse at the level of the osteocyte cell body, and disrupt the communication between osteocytes and bone surface. Accumulation of fatigue damage leads to bone remodeling (Burr, 1993), starting with osteoclast recruitment. Active recruitment of osteoclasts by osteocyte signaling is, however, difficult to reconcile with disrupted communication between damaged osteocytes and the bone surface. Rather, disrupted communication should abolish active *suppression* of osteoclasts by osteocytes, thereby allowing resorption to start. Whatever the precise cellular mechanism of osteoclast recruitment, the canalicular fluid flow hypothesis predicts that fatigue microdamage will lead to bone resorption (Fig. 28.6A). Resorption of microdamaged bone will then lead to (local) overuse, and stimulation of bone formation (Fig. 28.6B). Bone formation will continue until a new steady state of normal loading ("use") is reached, where osteocytes receive again the "normal use" mechanical stimuli (Fig. 28.6C). The result is locally renewed bone tissue, formed in relation to mechanical demands.

Can the model as described above be experimentally tested? In an animal study, bending of bone proved a better stimulus for adaptive responses than vertical loading (Turner et al., 1994). As bending also produces more canalicular fluid flow than vertical loading, this result supports the canalicular fluid flow hypothesis. In addition, a recent study in rats showed reduced osteocyte and canalicular integrity around cortical resorption spaces activated by fatigue loading (Bentolila et al., 1998). This study is the first to relate experimentally osteocyte integrity to initiation of bone remodeling. Other experimental verification may come from *in vitro* studies, by submitting osteocytes to fluid shear stress and studying the production of osteoblast- and osteoclast-modulating factors. Such studies could help in further unraveling the molecular signaling cascade between bone strain and adaptive responses. The hypothesis discussed above links easily with Frost's mechanostat hypothesis (Frost, 1987). However, where Frost argues at the level of bone tissue, the current thoughts are based on the ultrastructural organization of bone tissue. It is hoped that they will help in spurring new experimental studies, leading to a better understanding of "the cell biology of Wolff's law."

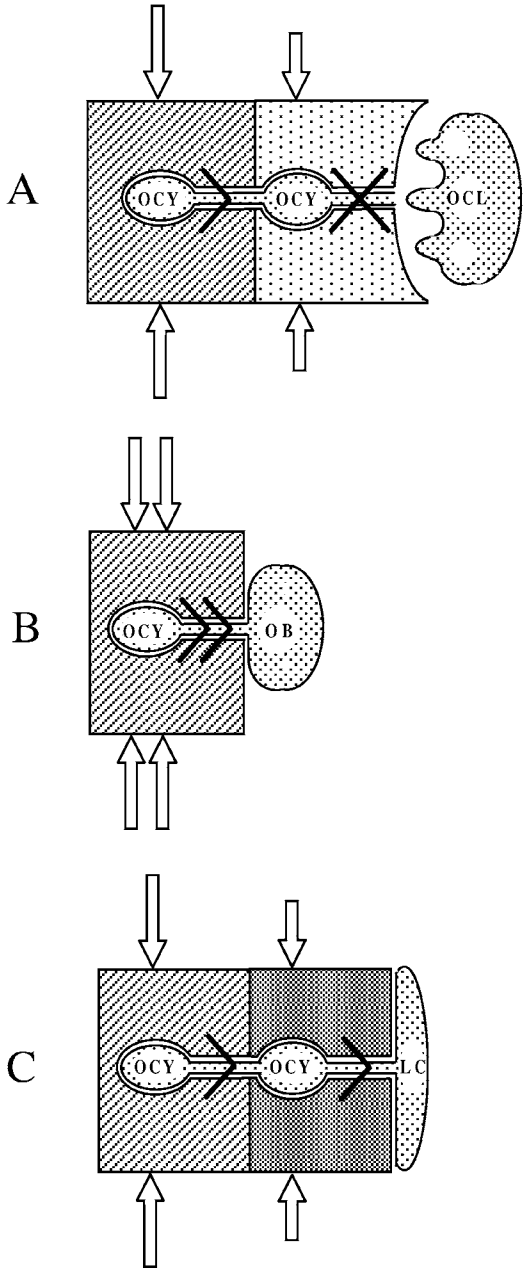

FIGURE 28.6 Schematic representation of how fatigue damage may initiate bone remodeling. (A) Accumulation of fatigue microdamage (stippled matrix) interferes with canalicular fluid flow and osteocyte signaling, by disrupting canaliculi and severing osteocyte processes. Fatigue microdamage results in osteoclast recruitment, suggesting that osteocyte signaling suppresses osteoclast recruitment rather than activating it. Osteoclasts resorb damaged bone until undamaged bone is reached, when they are again suppressed. (B) The local loss of bone after osteoclastic resorption leads to (local) overuse of the remaining undamaged bone. The resulting enhanced fluid flow through the lacuno-canalicular network leads to recruitment of osteoblasts. (C) Subsequent osteoblastic bone formation reestablishes normal mechanical use and, therefore, the steady state of basal fluid flow in the renewed bone. Stippled matrix, matrix with fatigue microdamage; for other symbols see Fig. 28.5. (From Burger, E. H. and Klein-Nulend, J., *FASEB J.*, 13(Suppl.), S101–S112, 1999. With permission.)

References

Aarden, E.M., Wassenaar, A.M.N., Alblas, M.J., and Nijweide, P.J. (1996) Immunocytochemical demonstration of extracellular matrix proteins in isolated osteocytes, *Histochem. Cell Biol.,* 106, 495–501.

Ajubi, N.E., Klein-Nulend, J., Nijweide, P.J., Vrijheid-Lammers, T., Alblas, M.J., and Burger, E.H. (1996) Pulsating fluid flow increases prostaglandin production by cultured chicken osteocytes—a cytoskeleton-dependent process, *Biochem. Biophys. Res. Commun.,* 225, 62–68.

Ajubi, N.E., Klein Nulend, J., Alblas, M.J., Burger, E.H., and Nijweide, P.J. (1999) Signal transduction pathways involved in fluid flow-induced prostaglandin E_2 production by cultured osteocytes, *Am. J. Physiol.,* 276, E171–E178.

Bentolila, V., Boyce, T.M., Fyhrie, D.P., Drumb, R., Skerry, T.M., and Schaffler, M.B. (1998) Intracortical remodeling in adult rat long bones after fatigue loading, *Bone,* 23, 275–281.

Bretcher, A. and Weber, K. (1980) Fimbrin, a new microfilament-associated protein present in microvilli and other cell surface structures, *J. Cell Biol.,* 86, 335–340.

Bronckers, A.L.J.J., Goei, S.W., Luo, G., Karsenty, G., D'Souza, R.N., Lyaruu, D.M., and Burger, E.H. (1996) DNA fragmentation during bone formation in neonatal rodents assessed by transferase-mediated en labeling, *J. Bone Miner. Res.*, 11, 1281–1291.

Burger, E.H. and Klein-Nulend, J. (1999) Mechanotransduction in bone—role of the lacuno-canalicular network, *FASEB J.,* 13 (Suppl.), S101–S112.

Burger, E.H. and Nijweide, P.J. (1991) Cellular origin and theories of osteoclast differentiation, in *Bone,* Vol. 2: *The Osteoclast*, Hall, B.K., Ed., CRC Press, Boca Raton, FL. 31–59.

Burger, E.H. and Veldhuijzen, J.P. (1993) Influence of mechanical factors on bone formation, resorption, and growth *in vitro*, in *Bone*, Vol. 7, Hall, B.K., Ed., CRC Press, Boca Raton, FL, 37–56.

Burger, E.H., Van der Meer, J.W.H., Van de Gevel, J.S., Gribnau, J.C., Thesingh, C.W., and Van Furth, R. (1982) *In vitro* formation of osteoclasts from long-term cultures of bone marrow mononuclear phagocytes, *J. Exp. Med.,* 156, 1604–1614.

Burr, D.B. (1993) Remodelling and the repair of fatigue microdamage, *Calcif. Tissue Int.,* 53, S75–S80.

Burr, D.B. and Martin, R.B. (1993) Calculating the probability that microcracks initiate resorption spaces, *J. Biomech.,* 26, 613–616.

Burr, D.B., Martin, R.B., Schaffler, M.B., and Radin, E.L. (1985) Bone remodeling in response to *in vivo* fatigue microdamage, *J. Biomech.,* 18, 189–200.

Burr, D.B., Milgrom, C., Fyhrie, D., Forwood, M., Nyska, M., Finestone, A., Hoshaw, S., Saiag, E., and Simkin, A. (1996) *In vivo* measurement of human tibial strains during rigorous activity, *Bone,* 18, 405–410.

Burr, D.B., Forwood, M.R., Fyhrie, D.P., Martin, R.B., Schaffler, M.B., and Turner, C.H. (1997) Bone microdamage and skeletal fragility in osteoporotic and stress fractures, *J. Bone Miner. Res.,* 12, 6–15.

Busse, R. and Fleming, I. (1998) Pulsatile stretch and shear stress: physical stimuli determining the production of endothelium derived relaxing factors, *J. Vasc. Res.,* 35, 73–84.

Chambers, T.J., Darby, J.A., and Fuller, K. (1985) Mammalian collagenase predisposes bone surfaces to osteoclastic resorption, *Cell Tissue Res.,* 241, 671–675.

Chow, J.W. and Chambers, T.J. (1994) Indomethacin has distinct early and late actions on bone formation induced by mechanical stimulation, *Am. J. Physiol.*, 267, E278–E292.

Cooke, J.P., Stamler, J., Andon, N., Davies P.F., McKinley, G., and Loscalzo, J. (1990) Flow stimulates endothelial cells to release a nitrovasodilator that is potentiated by reduced thiol, *Am. J. Physiol.,* 259, H804–H812.

Cowin, S.C., Moss-Salentijn, L., and Moss, M.L. (1991) Candidates for the mechanosensory system in bone, *J. Biomech. Eng.,* 113, 191–197.

Cowin, S.C., Weinbaum, S., and Zeng, Y. (1995) A case for bone canaliculi as the anatomical site of strain generated potentials, *J. Biomech.,* 28, 1281–1296.

De Arruda, M.V., Watson, S., Lin, C.S., Leavitt, J., and Matsudeira, P. (1990) Fimbrin is a homologue of the cytoplasmic phosphoprotein plastin and has domains homologous with calmodulin and actin gelatin proteins, *J. Cell Biol.,* 111, 1069–1079.

Doty, S.B. (1981) Morphological evidence of gap junctions between bone cells, *Calcif. Tissue Int.*, 33, 509–512.

Forwood, M.R. (1996) Inducible cyclooxygenase (COX-2) mediates the induction of bone formation by mechanical loading in vivo, *J. Bone Miner. Res.,* 11, 1688–1693.

Forwood, M.R., Owan, I., Takano, Y., and Turner, C.H. (1996) Increased bone formation in rat tibiae after a single short period of dynamic loading in vivo, *Am. J. Physiol.*, 270, E419–E423.

Fox, S.W., Chambers, T.J., and Chow, J.W.M. (1996) Nitric oxide is an early mediator of the increase in bone formation by mechanical stimulation, *Am. J. Physiol.,* 270, E955–E960.

Frost, H.M. (1987) Bone mass and the mechanostat: a proposal, *Anat. Rec.,* 219, 1–9.

Hillam, R.A. and Skerry, T.M. (1995) Inhibition of bone resorption and stimulation of formation by mechanical loading of the modeling rat ulna in vivo, *J. Bone Miner. Res.,* 10, 683–693.

Hung, C.T., Pollack, S.R., Reilly, T.M., and Brighton, C.T. (1995) Real-time calcium response of cultured bone cells to fluid flow, *Clin. Orthop. Relat. Res.,* 313, 256–269.

Hung, C.T., Allen, F.D., Pollack, S.R., and Brighton, C.T. (1996) Intracellular Ca^{2+} stores and extracellular Ca^{2+} are required in the real-time Ca^{2+} response of bone cells experiencing fluid flow, *J. Biomech.,* 29, 1411–1417.

Ingber, D.E. (1991) Integrins as mechanochemical transducers, *Curr. Opin. Cell Biol.,* 3, 841–848.

Jacobs, C.R., Yellowley, C.E., Davis, B.R., Zhou, Z., Cimbala, J.M., Donahue, H.J. (1998) Differential effect of steady versus oscillating flow on bone cells, *J. Biomech.,* 31, 969–976.

Jee, W.S.S. (1988) The skeletal tissues, in *Cell and Tissue Biology, A Textbook of Histology,* Weiss, L., Ed., Urban and Schwarzenberg, Munich, Germany, 213–253.

Kamiya, A. and Ando, J. (1996) Response of vascular endothelial cells to fluid shear stress: mechanism, in *Biomechanics—Functional Adaptation and Remodeling,* K. Hayashi, A. Kamiyn, K. Ono, Eds., Springer, Tokyo, 29–56.

Klein-Nulend, J., Van der Plas, A., Semeins, C.M., Ajubi, N.E., Frangos, J.A., Nijweide, P.J., and Burger, E.H. (1995a) Sensitivity of osteocytes to biomechanical stress *in vitro, FASEB J.,* 9, 441–445.

Klein-Nulend, J., Semeins, C.M., Ajubi, N.E., Nijweide, P.J., and Burger, E.H. (1995b) Pulsating fluid flow increases nitric oxide (NO) synthesis by osteocytes but not periosteal fibroblasts—correlation with prostaglandin upregulation, *Biochem. Biophys. Res. Commun.,* 217, 640–648.

Klein-Nulend, J., Burger, E.H., Semeins, C.M., Raisz, L.G., and Pilbeam, C.C. (1997) Pulsating fluid flow stimulates prostaglandin release and inducible prostaglandin G/H synthase mRNA expression in primary mouse bone cells, *J. Bone Miner. Res.,* 12, 45–51.

Klein-Nulend, J., Helfrich, M.H., Sterck, J.G.H., MacPherson, H., Joldersma, M., Ralston, S.H., Semeins, C.M., and Burger, E.H. (1998) Nitric oxide response to shear stress by human bone cell cultures is endothelial nitric oxide synthase dependent, *Biochem. Biophys. Res. Commun.,* 250, 108–114.

Knothe-Tate, M.L., Niederer, P., and Knothe, U. (1998) *In vivo* tracer transport through the lacunocanalicular system of rat bone in an environment devoid of mechanical loading, *Bone*, 22, 107–117.

Koprowski, H. and Maeda, H. (1995) *The Role of Nitric Oxide in Physiology and Pathophysiology,* Springer-Verlag, Berlin, Germany.

Kurihara, N., Suda, T., Miura, Y., Nakauchi, H., Kodama, H., Hiura, K., Hakeda, Y., and Kumegawa, M. (1989) Generation of osteoclasts from isolated hematopoietic progenitor cells, *Blood*, 74, 1295–1320.

Maejima-Ikeda, A., Aoki, M., Tsuritani, K., Kamioka, K., Hiura, K., Miyoshi, T., Hara, H., Takano-Yamamoto, T., and Kumegawa, M. (1997) Chick osteocyte-derived protein inhibits osteoclastic bone resorption, *Biochem. J.,* 322, 245–250.

Mak, A.F.T., Huang, D.T., Zhang, J.D., and Tong, P. (1997) Deformation-induced hierarchical flows and drag forces in bone canaliculi and matrix porosity, *J. Biomech.,* 30, 11–18.

Mosley, J.R. and Lanyon, L.E. (1998) Strain rate as a controlling influence on adaptive modeling in response to dynamic loading of the ulna in growing male rats, *Bone,* 23, 313–318.

Murray, D.W. and Rushton, N. (1990) The effect of strain on bone cell prostaglandin E2 release: a new experimental method, *Calcif. Tissue Int.*, 47, 35–39.

Nefussi, J.R., Sautier, J.M., Nicolas, V., and Forest, N. (1991) How osteoblasts become osteocytes: a decreasing matrix forming process, *J. Biol. Buccale,* 19, 75–82.

Neidlinger-Wilke, C., Stall, I., Claes, L., Brand, R., Hoellen, I., Rubenacker, S., Arand, M., and Kinzl, L. (1995) Human osteoblasts from younger normal and osteoporotic donors show differences in proliferation and TGF-β release in response to cyclic strain, *J. Biomech.,* 28, 1411–1418.

Nijweide, P.J. and Burger, E.H. (1990) Mechanisms of bone formation *in vitro*, in *Bone*, Vol. 1: *The Osteoblast and Osteocyte*, Hall, B.K., Ed., The Telford Press, Caldwell, NJ, 303–326.

Nijweide, P.J. and Mulder, R.J.P. (1986) Identification of osteocytes in osteoblast-like cultures using a monoclonal antibody specifically directed against osteocytes, *Histochemistry,* 84, 343–350.

Nunamaker, D.M., Butterweck, D.M., and Provost, T.M. (1990) Fatigue fractures in Thoroughbred racehorses: relationship with age, peak bone strain and training, *J. Orthop. Res.,* 8, 604–611.

Owan, I., Burr, D.B., Turner, C.H., Qui, J., Tu, Y., Onyia, J.E., and Duncan, R.L. (1997) Mechanotransduction in bone: osteoblasts are more responsive to fluid forces than mechanical strain, *Am. J. Physiol.,* 273, C810–C815.

Palumbo, C. (1986) A three-dimensional ultrastructural study of osteoid-osteocytes in the tibia of chick embryos, *Cell Tissue Res.,* 246, 125–131.

Palumbo, C., Palazzini, S., and Marotti, G. (1990a) Morphological study of intercellular junctions during osteocyte differentiation, *Bone,* 11, 401–406.

Palumbo, C., Palazzini, S., Zaffe, D., and Marotti, G. (1990b) Osteocyte differentiation in the tibia of newborn rabbit: an ultrastructural study of the formation of cytoplasmic processes, *Acta Anat.*, 137, 350–358.

Piekarski, K. and Munro, M. (1977) Transport mechanism operating between blood supply and osteocytes in long bones, *Nature,* 269, 80–82.

Pitsillides, A.A., Rawlinson, S.C.F., Suswillo, R.F.L., Bourrin, S., Zaman, G., and Lanyon, L.E. (1995) Mechanical strain-induced NO production by bone cells—a possible role in adaptive bone (re)modeling, *FASEB J.,* 9, 1614–1622.

Pollack, S.R., Salzstein, R., and Pienkowski, D. (1984) The electric double layer in bone and its influence on stress generated potentials, *Calcif. Tissue Int.,* 36, S77–S81.

Prendergast, P.J. and Huiskes, R. (1996) Microdamage and osteocyte-lacuna strain in bone: a microstructural finite element analysis, *J. Biomech. Eng.,* 118, 240–246.

Rawlinson, S.C., Pitsillides, A.A., and Lanyon, L.E. (1996) Involvement of different ion channels in osteoblasts' and osteocytes' early responses to mechanical strain, *Bone,* 19, 609–614.

Reich, K.M., Gay, C.V., and Frangos, J.A. (1990) Fluid shear stress as a mediator of osteoblast cyclic adenosine monophosphate production, *J. Cell. Physiol.,* 143, 100–104.

Roux, W. (1881) *Der Kampf der Teile im Organismus*, Engelmann, Leipzig, Germany.

Rubin, C.T. (1984) Skeletal strain and the functional significance of bone architecture, *Calcif. Tissue Int.,* 36, S11–S18.

Sachs, F. (1989) Ion channels as mechanical transducers, in *Cell Shape: Determinants, Regulation, and Regulatory Role,* Stein, W.D. and Bronner, F., Eds., Academic Press, San Diego, CA, 63–94.

Salzstein, R.A. and Pollack, S.R. (1987) Electromechanical potentials in cortical bone—experimental analysis, *J. Biomech,* 20, 271–280.

Salzstein, R.A., Pollack, S.R., Mak, A.F.T., and Petrov, N. (1987) Electromechanical potentials in cortical bone—a continuum approach, *J. Biomech.,* 20, 261–270.

Schaffler, M.B., Pitchford, W.C., Choi, K., and Riddle, J.M. (1994) Examination of compact bone microdamage using back-scattered electron microscopy, *Bone,* 15, 483–488.

Scheven, B.A.A., Visser, J.W.M., and Nijweide, P. J. (1986) *In vitro* osteoclast generation from different bone marrow fractions, including a highly enriched hematopoietic stem cell population, *Nature,* 321, 79–81.

Shapiro, F. (1997) Variable conformation of GAP junctions linking bone cells: a transmission electron microscopic study of linear, stacked linear, curvilinear, oval, and annular junctions, *Calcif. Tissue Int.,* 61, 285–293.

Smit, T.H. and Burger, E.H. (2000) Is BMU-coupling a strain-regulated phenomenon? A finite element analysis, *J. Bone Miner. Res.,* 15, 301–307.

Suda, T., Takahashi, N., and Martin, T.J. (1995) Modulation of osteoclast differentiation: update 1995, *Endocr. Rev. Monogr.,* 4, 266–270.

Takahashi, N., Akatsu, T., Udagawa, N., Sasaki, T., Yamaguchi, A., Moseley, J.M., Martin, T.J., and Suda, T. (1988) Osteoblastic cells are involved in osteoclast formation, *Endocrinology,* 123, 2600–2602.

Tanaka, K., Matsuo, T., Ohta, M., Sato, T., Tezuka, K., Nijweide, P.J., Katoh, Y., Hakeda, Y., and Kumegawa, M. (1995) Time-lapse microcinematography of osteocytes, *Miner. Electrolyte Metab.,* 21, 189–192.

Tanaka-Kamioka, K., Kamioka, H., Ris, H., and Lim, S.S. (1998) Osteocyte shape is dependent on actin filaments and osteocyte process are unique actin-rich projections, *J. Bone Miner. Res.,* 13, 1555–1568.

Turner, C.H., Forwood, M.R., Rho, J.Y., and Yoshikawa, T. (1994a) Mechanical loading thresholds for lamellar and woven bone formation, *J. Bone Miner. Res.,* 9, 87–97.

Turner, C.H., Forwood, M.R., and Otter, M.W. (1994b) Mechanotransduction in bone: do bone cells act as sensors of fluid flow? *FASEB J.,* 8, 875–878.

Turner, C.H., Owan, I., and Takano, Y. (1995) Mechanotransduction in bone: role of strain rate, *Am. J. Physiol.,* 269, E438–E442.

Turner, C.H., Takano, Y., Owan, I., and Murrell, G.A. (1996) Nitric oxide inhibitor L-NAME suppresses mechanically induced bone formation in rats, *Am. J. Physiol.,* 270, E639–E643.

Uematsu, M., Navas, J.P., Nishida, K., Ohara, Y., Murphy, T.J., Alexander, R.W., Nerem, R.M., and Harrison, D.G. (1995) Regulation of endothelial cell nitric oxide synthase mRNA expression by shear stress, *Am. J. Physiol.,* 269, C1371–1378.

Van der Plas, A. and Nijweide, P.J. (1992) Isolation and purification of osteocytes, *J. Bone Miner. Res.,* 7, 389–396.

Van der Plas, A., Aarden, E.M., Feijen, J.H., De Boer, A.H., Wiltink, A., Alblas, M.J., De Leij, L., and Nijweide, P.J. (1994) Characteristics and properties of osteocytes in culture, *J. Bone Miner. Res.,* 9, 1697–1704.

Wang, N., Butler, J.P., and Ingber, D.E. (1994) Mechanotransduction across the cell surface and through the cytoskeleton, *Science,* 260, 1124–1127.

Weinbaum, S., Cowin, S.C., and Zeng, Y. (1994) A model for the excitation of osteocytes by mechanical loading-induced bone fluid shear stresses, *J. Biomech.,* 27, 339–360.

Wolff, J. (1892) *Das Gesetz der Transformation der Knochen,* translated by Maquet, P. and Furlong, R., Springer-Verlag, Berlin, Germany, 1986.

29

Mechanosensory Mechanisms in Bone

Stephen C. Cowin
The City College of New York

Melvin L. Moss
Columbia University

29.1 Introduction

The mechanosensory mechanisms in bone include (1) the cell system that is stimulated by external mechanical loading applied to the bone; (2) the system that transduces that mechanical loading to a communicable signal; (3) the systems that transmit that signal to the effector cells for the maintenance of bone homeostasis and for strain adaptation of the bone structure. The effector cells are the osteoblasts and the osteoclasts. These systems and the mechanisms that they employ have not yet been unambiguously identified. Reviewed here are candidate systems. In particular, the current theoretical and experimental evidence that suggests that osteocytes are the principal mechanosensory cells of bone, that they are activated by shear stress from fluid flowing through the osteocyte canaliculi, and that the electrically coupled three-dimensional network of osteocytes and lining cells is a communications system for the control of bone homeostasis and structural strain adaptation is summarized.

It has long been known that living adult mammalian bone tissue adapts its material properties, and that whole bones adapt their shape, in response to altered mechanical loading.[1–8] Progress is being made in understanding the cellular mechanisms that accomplish the absorption and deposition of bone tissue. The physiological mechanism by which the mechanical loading applied to bone is sensed by the tissue and the mechanism by which the sensed signal is transmitted to the cells that accomplish the surface deposition, removal, and maintenance have not been identified. The purpose of this chapter is to review some of the background research on these mechanosensory mechanisms and to outline candidates for the mechanosensory system. (See Burger et al.[9] for an earlier review of similar literature.)

All vital cells are "irritable"; i.e., they are capable of perturbation by, and response to, alterations in their external environment.[10,11] The mechanosensing process(es) of a cell enable it to sense the presence of, and to respond to, extrinsic physical loadings. This property is widespread in uni- and multicellular animals,[12–17] plants,[18,19] and bacteria.[20] Tissue sensibility is a property of a connected set of cells and it is accomplished by the intracellular processes of mechanoreception and mechanotransduction. *Mechanoreception* is the term used to describe the process that transmits the informational content of an extracellular mechanical stimulus to a receptor cell. *Mechanotransduction* is the term used to describe the process that transforms the content of a mechanical stimulus into an *intra*cellular signal. Here, the term *mechanosensory* is employed to mean both mechanoreception and mechanotransduction. Additional processes of *inter*cellular transmission of transduced signals are required at tissue, organ, and organismal structural levels.

0-8493-9117-2/01/$0.00+$.50

29.2 The Connected Cellular Network

The bone cells that lie on all bony surfaces are osteoblasts, either active or inactive. Inactive osteoblasts are called bone-lining cells; they have the potential of becoming active osteoblasts. The bone cells that are buried in the extracellular bone matrix are the osteocytes. Each osteocyte, enclosed within its mineralized lacuna, has many (perhaps as many as 80) cytoplasmic processes. These processes are approximately 15 μm long and are arrayed three dimensionally in a manner that permits them to interconnect with similar processes of up to as many as 12 neighboring cells. These processes lie within mineralized bone matrix channels called canaliculi. The small space between the cell process plasma membrane and the canalicular wall is filled with bone fluid and macromolecular complexes of unknown composition. All bone cells except osteoclasts are extensively interconnected by the cell processes of the osteocytes, forming a *connected cellular network* (CCN).[21–23] The interconnectivity of the CCN is graphically illustrated by Fig. 29.1, which is a scanning electron micrograph showing the replicas of lacunae and canaliculi *in situ* in mandibular bone from a young subject aged 22 years. The inset shows enlarged lacunae identified by a rectangle.

The touching cell processes of two neighboring bone cells contain gap junctions.[24–31] A *gap junction* is a channel connecting two cells. The walls of the channel consist of matching rings of proteins piercing the membrane of each cell, and when the rings associated with two cells connect with each other, the cell-to-cell junction is formed. This junction allows ions and compounds of low molecular weight to pass between the two cells without passing into the extracellular space. The proteins making up a gap junction are called connexins; in bone the protein is either connexin 43 or 45, with 43 predominating (the number refers to the size of the proteins calculated in kilodaltons).[32–34] A ring of connexins in one cell membrane is generally called a connexon or hemichannel. Both mechanical strain and fluid shear stress cause increased expression of the connexin 43 in vascular tissues.[35] In cardiac tissue, the turnover rate of connexin 43 is very rapid.[36] The rapid dynamics of gap junction turnover and the plasticity of gap junction expression in response to various stimuli offer the possibility for remodeling of the intercellular circuits both within and between communication compartments in the cardiovascular system.[37] In bone, gap junctions connect superficial osteocytes to periosteal and endosteal osteoblasts. All osteoblasts are similarly interconnected laterally on

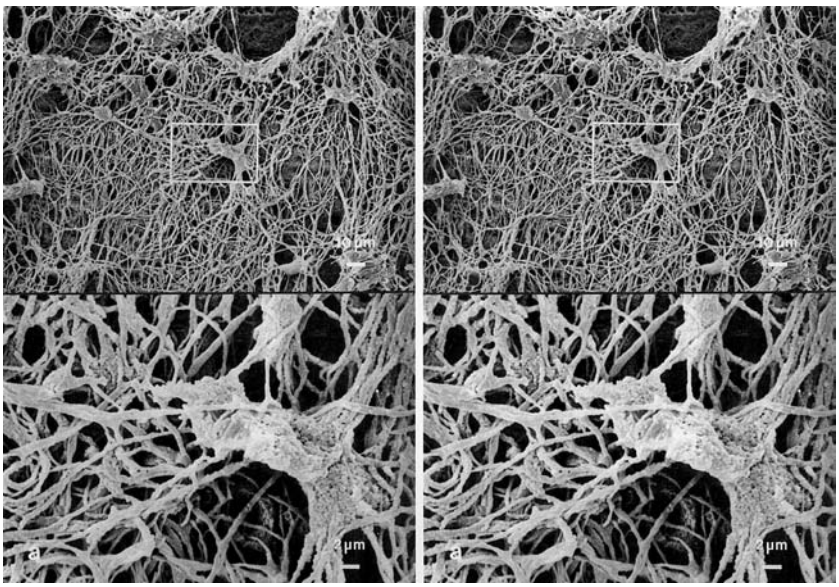

FIGURE 29.1 A scanning electron micrograph showing the replicas of lacunae and canaliculi *in situ* in mandibular bone from a young subject aged 22 years. The inset shows enlarged lacunae identified by a rectangle. This micrograph illustrates the interconnectivity of the CCN. (From Atkinson, P. J. and Hallsworth, A. S., *Gerodontology,* 2, 57, 1983. With permission.)

a bony surface; perpendicular to the bony surface, gap junctions connect periosteal osteoblasts with preosteoblastic cells, and these, in turn, are similarly interconnected. Effectively, each CCN is a true syncytium.[26,28,29,38] Gap junctions are found where the plasma membranes of a pair of markedly lapping canalicular processes meet.[38] In compact bone, canaliculi cross the cement lines that form the outer boundary of osteons. Thus, extensive communication exists between osteons and interstitial regions.[39]

Bone cells are electrically active.[40–43] In addition to permitting the intercellular transmission of ions and small molecules, gap junctions exhibit both electrical and fluorescent dye transmission.[44–47] Gap junctions are electrical synapses, in contradistinction to interneuronal, chemical synapses, and, significantly, they permit bidirectional signal traffic (e.g., biochemical, ionic, electrical, etc.). In a physical sense, the CCN represents the hard wiring[21–23,48] of bone tissue.

29.3 Mechanosensation on the CCN

29.3.1 Stimuli

The *stimulus* for bone remodeling is defined as that particular aspect of the stress or strain history of the bone that is employed by the bone to sense its mechanical load environment and to signal for the deposition, maintenance, or resorption of bone tissue. The bone tissue domain or region over which the stimulus is felt is called the *sensor* domain. When an appropriate stimulus parameter exceeds threshold values, loaded tissues respond by the triad of bone adaptation processes: deposition, resorption, and maintenance. The CCN is the site of intracellular stimulus reception, signal transduction, and intercellular signal transmission. It is thought that stimulus reception occurs in the osteocyte,[21] and that the CCN transduces and transmits the signal to the surface lining or osteoblast. The osteoblasts alone directly regulate bone deposition and maintenance, and indirectly regulate osteoclastic resorption.[49] The possible role of the osteoblast as a stimulus receptor has not yet been thoroughly investigated.[50] Although it is reasonably presumed that initial mechanosensory events occur at the plasma membrane of the osteocytic soma and/or canalicular processes, the initial receptive, and subsequent transductive, processes are not well understood.

It follows that the true biologic stimulus, although much discussed, is not precisely known. A variety of mechanical loading stimuli associated with ambulation (at a frequency of 1 to 2 Hz) have been considered for bone remodeling. The majority have followed Wolff[2,3] in suggesting that some aspect of the mechanical loading of bone is the stimulus. The mechanical stimuli suggested include strain,[51] stress,[2,3] strain energy,[52,53] strain rate,[54–60] and fatigue microdamage.[61,62] In some cases the time-averaged values of these quantities are suggested as the mechanical stimulus, and in others the amplitudes of the oscillatory components and/or peak values of these quantities are the candidates for the mechanical stimulus. Two dozen possible stimuli were compared in a combined experimental and analytic approach.[63] The data supported strain energy density, longitudinal shear stress, and tensile principal stress or strain as stimuli; no stimulus that could be described as rate dependent was among the two dozen possible stimuli considered in the study. (For a consideration of the stimulus in microgravity, see Cowin.[64])

The case for strain rate as a remodeling stimulus has been building over the last quarter century. The animal studies of Hert and co-workers[54–56] suggested the importance of strain rate. Experiments[58–60] have quantified the importance of strain rate over strain as a remodeling stimulus. The studies[65–67] directed at the understanding of the cellular mechanism for bone remodeling have suggested that the prime mover is the bone strain rate–driven motion of the bone fluid the signal of which is transduced by osteocytes. In the model of Weinbaum et al.[65,66] the shear stress from the bone fluid flow over the osteocytic processes in the canaliculi is a cellular mechanism–based model suggesting strain rate as a stimulus. The recent study of Gross et al.[68] that showed bone deposition to be related to strain gradients actually, by the model of Weinbaum et al.,[65,66]also demonstrated a dependence on strain rate.

In experiments with cultured cells it has been shown that osteocytes, but not periosteal fibroblasts, are extremely sensitive to fluid flow, resulting in increased prostaglandin as well as nitric oxide (NO) production.[69,70] Three different cell populations, namely, osteocytes, osteoblasts, and periosteal fibroblasts, were subjected to two stress regimes, pulsatile fluid flow (PFF), and intermittent hydrostatic compression (IHC).[69] IHC was

applied at 0.3 Hz with 13 kPa peak pressure. PFF was a fluid flow with a mean shear stress of 0.5 Pa with cyclic variations of 0.02 Pa at 5 Hz. The maximal hydrostatic pressure rate was 130 kPa/s and the maximal fluid shear stress rate was 12 Pa/s. Under both stress regimes, osteocytes appeared more sensitive than are osteoblasts, and osteoblasts more sensitive than periosteal fibroblasts. However, despite the large difference in peak stress and peak stress rate, PFF was more effective than IHC. Osteocytes, but not the other cell types, responded to 1-h PFF treatment with a sustained prostaglandin E_2 upregulation lasting at least 1 h after PFF was terminated. By comparison, IHC needed 6 h treatment before a response was found. These results suggested that osteocytes are more sensitive to mechanical stress than osteoblasts, which are again more sensitive than periosteal fibroblasts. Furthermore, osteocytes appeared particularly sensitive to fluid shear stress, more so than to hydrostatic stress. These conclusions are in agreement with the theory that osteocytes are the main mechanosensory cells of bone, and that they detect mechanical loading events by the canalicular flow of interstitial fluid which results from that loading event. Weinbaum et al.[66] used Biot's porous media theory to relate loads applied to a whole bone to the flow of canalicular interstitial fluid past the osteocytic processes. Their calculations predict fluid-induced shear stresses of 0.8 to 3 Pa as a result of peak physiological loading regimes. The findings that bone cells *in vitro* actually respond to fluid shear stress of 0.2 to 6 Pa[69–73] lend experimental support to the theory.

Osteocytes also rapidly release NO in response to stress[70,74] and this NO response seems to be required for the stress-related prostaglandin release.[70] Therefore, the behavior of osteocytes compares with that of endothelial cells, which regulate the flow of blood through the vascular system, and also respond to fluid flow of 0.5 Pa with increased prostaglandin and NO production.[75] The response of endothelial cells to shear stress is likely related to their role in mediating an adaptive remodeling of the vasculature, so as to maintain constant endothelial fluid shear stress throughout the arterial site of the circulation.[76]

Skeletal muscle contraction is a typical bone-loading event and has been suggested[77–79] as a stimulus. Frequency is one of the critical parameters of the muscle stimulus and it serves to differentiate this stimulus from the direct mechanical loads of ambulation that occur at a frequency of 1 to 2 Hz. The frequency of contracting muscle in tetanus is from 15 Hz to a maximum of 50 to 60 Hz in mammalian muscle.[80] It has been observed[81,82] that these higher-order frequencies, significantly related to bone adaptational responses, are[83] "present within the [muscle contraction] strain energy spectra regardless of animal or activity and implicate the dynamics of muscle contraction as the source of this energy band." The close similarity of muscle stimulus frequencies to bone tissue response frequencies is noted below.

29.3.2 Reception and Transduction

The osteocyte has been suggested as the stimulus sensor, the receptor of the stimulus signal;[21] histological and physiological data are consistent with this suggestion.[84,85] The placement and distribution of osteocytes in the CCN three-dimensional array are architecturally well suited to sense deformation of the mineralized tissue encasing them.[86] Since only a population of cells, and not an individual receptor,[87] can code unambiguously, the osteocytes in the CCN are potential mechanoreceptors by virtue of their network organization.

Osteocytic mechanotransduction may involve a number of different processes or cellular systems. These processes include stretch- and voltage-activated ion channels, cyto-matrix sensation-transduction processes, cyto-sensation by fluid shear stresses, cyto-sensation by streaming potentials, and exogenous electric field strength. Each of these processes or cellular systems is discussed below.

29.3.2.1 Stretch- and Voltage-Activated Ion Channels

The osteocytic plasma membrane contains stretch-activated ion channels,[88–91] which are also found in many other cell types.[12,92,93] When activated in strained osteocytes, they permit passage of certain ions,[94–96] including K^+, Ca^{2+}, Na^+, and Cs^+. Such ionic flow may, in turn, initiate cellular electrical events; e.g., bone cell stretch-activated channels may modulate membrane potential as well as Ca^{2+} ion flux.[12,97] Rough estimates of osteocytic mechanoreceptor strain sensitivity have been made,[21] and the calculated values cover the morphogenetically significant strain range of 0.1 to 0.3% in the literature.[58,98,99] This appears to be too low a strain to open a stretch-activated ion channel. A model involving bone fluid flow has been suggested for the amplification of the 0.1 to 0.3% strain applied to a whole bone to a value an order of

magnitude larger at the osteocytic cytoplasmic process membrane.[100] Stretch-activated ion channels also occur in osteoblastic cells.[101]

As in most cells, the osteocytic plasma membrane contains voltage-activated ion channels, and transmembrane ion flow may be a significant osseous mechanotransductive process.[41,102–104] It is also possible that such ionic flow generates osteocytic action potentials, capable of transmission through gap junctions.[45]

29.3.2.2 Cyto-Matrix Sensation-Transduction Processes

The mineralized matrix of bone tissue is strained when loaded. Macromolecular mechanical connections between the extracellular matrix and the osteocytic cell membrane exist and these connections may be capable of transmitting information from the strained extracellular matrix to the bone cell nuclear membrane. The basis of this mechanism is the physical continuity of the transmembrane integrin molecule, which is connected extracellularly with the macromolecular collagen of the organic matrix and intracellularly with the cytoskeletal actin. The latter, in turn, is connected to the nuclear membrane.[105–118] It is suggested that such a cytoskeletal lever chain, connecting to the nuclear membrane, can provide a physical stimulus able to activate the osteocytic genome,[27] possibly by first stimulating the activity of such components as the *c-fos* genes.[27,106,114,119–126]

29.3.2.3 Cyto-Sensation by Fluid Shear Stresses

A hypothesis concerning the mechanism by which the osteocytes housed in the lacunae of mechanically loaded bone sense the load applied to the bone by the detection of dynamic strains was suggested by Weinbaum et al.[65,66] It was proposed that the osteocytes are stimulated by relatively small fluid shear stresses acting on the membranes of their osteocytic processes. A hierarchical model of bone tissue structure that related the cyclic mechanical loading applied to the whole bone to the fluid shear stress at the surface of the osteocytic cell process was presented.[66] In this model the sensitivity of strain detection is a function of frequency; in the physiological frequency range (1 to 20 Hz), associated with either locomotion (1 to 2 Hz) or the maintenance of posture (15 to 30 Hz), the fluid shear stress is nearly proportional to the product of frequency and strain. Thus, if bone cells respond to strains on the order of 0.1% at frequencies of 1 or 2 Hz, they will also respond to strains on the order of 0.01% at frequencies of 20 Hz. The fluid shear stresses would also strain the macromolecular mechanical connections between the cell and the extracellular bone matrix (mentioned in the previous section); thus, fluid shear stress is also potentially capable of transmitting information from the strained matrix to the bone cell nuclear membrane, where it can effectively regulate its genomic functions.

Several investigators[127–129] have examined other aspects of the lacunar-canalicular porosity using simple circular pore models and have attempted to analyze its possible physiological importance. These studies have primarily emphasized the importance of the convective flow in the canaliculi between the lacunae as a way of enhancing the supply of nutrients between neighboring osteocytes. Previous studies on the relaxation of the excess pore pressure have been closely tied to the strain-generated potentials (SGPs) associated with bone fluid motion. The SGP studies are briefly reviewed below.

29.3.2.4 Cyto-Sensation by Streaming Potentials

The fact that the extracellular bone matrix is negatively charged due to its proteins means that a fluid electrolyte bounded by the extracellular matrix will have a diffuse double layer of positive charges. When the fluid moves, the excess positive charge is convected, thereby developing streaming currents and streaming potentials. The cause of the fluid motion is the deformation of the extracellular matrix due to whole-bone mechanical loading. Pollack and co-workers[130–132] have laid an important foundation for explaining the origin of strain generated potentials (SGP). However the anatomical site in bone tissue that is the source of the experimentally observed SGPs is not agreed upon. Salzstein and Pollack[132] concluded that this site was the collagen-hydroxyapatite porosity of the bone mineral, because small pores of approximately 16 nm radius were consistent with their experimental data if a poroelastic–electrokinetic model with unobstructed and connected circular pores was assumed.[131] Cowin et al.[67] using the model of Weinbaum et al.,[66] have shown that the data of Salzstein and Pollack,[132] Scott and

Korostoff,[133] and Otter et al.[134] are also consistent with the larger pore space (100 nm) of the lacunar-canalicular porosity being the anatomical source site of the SGPs if the hydraulic drag and electrokinetic contribution associated with the passage of bone fluid through the surface matrix (glycocalyx) of the osteocytic process are accounted for. The mathematical models of Salzstein et al.[131] and Weinbaum et al.[66] are similar in that they combine poroelastic and electrokinetic theory to describe the phase and magnitude of the SGP. The two theories differ in the description of the interstitial fluid flow and streaming currents at the microstructural level and in the anatomical structures that determine the flow. In Weinbaum et al.[66] this resistance resides in the fluid annulus that surrounds the osteocytic processes, i.e., the cell membrane of the osteocytic process, the walls of the canaliculi, and the glycocalyx (also called the surface matrix or capsule) that exists in this annular region. In Cowin et al.[67] the presence of the glycocalyx increases the SGPs and the hydraulic resistance to the strain-driven flow. The increased SGP matches the phase and amplitude of the measured SGPs. In the Salzstein et al.[131] model, this fluid resistance and SGP are achieved by assuming that an open, continuous small pore structure ($\approx$16 nm radius) exists in the mineralized matrix. The poroelastic model of Weinbaum et al.[66] for bone fluid flow has been developed further[135–139] and a review of the related poroelastic literature has appeared.[140]

Experimental evidence indicating that the collagen–hydroxyapatite porosity of the bone mineral is unlikely to serve as the primary source of the SGP is obtained from several sources, including the estimates of the pore size in the collagen–hydroxyapatite porosity and permeability studies with different-size labeled tracers in both mineralized and unmineralized bone. Such permeability studies clearly show time-dependent changes in the interstitial pathways as bone matures. At the earliest times, the unmineralized collagen–proteoglycan bone matrix is porous to large solutes. The studies with ferritin (10 nm in diameter) in 2-day-old chick embryo[141] show a continuous halo around primary osteons 5 min after the injection of this tracer. The halo passes right through the lacunar-canalicular system suggesting that, before mineralization, pores of the size predicted in Salzstein and Pollack[132] (radii $\approx$ 16 nm) can exist throughout the bone matrix. In contrast, Montgomery et al.[142] using this same tracer in adult dogs, also found a fluorescent halo surrounding the Haversian canals; however, this halo was not continuous but formed by discrete lines suggesting that the pathways were limited to discrete pores whose spacing was similar to that observed for canaliculi. This conclusion is supported by the studies of Tanaka and Sakano[143] in the alveolar bone of 5-day-old rats using the much smaller tracer, microperoxidase (MP) (2 nm). These studies clearly showed that the MP only penetrated the unmineralized matrix surrounding the lacunae and the borders of the canaliculi (see Fig. 13 of this study) and was absent from the mineralized matrix. Using more mature rats, the study of Ayasaka et al.[144] confirmed the failure of the small (2 nm) MP tracer to penetrate the mineralized matrix tissue from the bone fluid compartments.

29.3.2.5 Exogenous Electric Field Strength

Bone responds to exogenous electrical fields.[145] Although the extrinsic electrical parameters are unclear, field strength may play an important role.[145,146] A significant parallelism exists between the parameters of exogenous electrical fields and the endogenous fields produced by muscle activity. Bone responds to exogenous fields in an effective range of 1 to 10 μV/cm, strengths that are on the order of those endogenously produced in bone tissue during normal (muscle) activity.[147,148]

29.3.2.6 The Uniqueness of Osseous Mechanosensation

The difference between mechanosensation in bone tissue and mechanosensation in nonosseous processes is revealing and thought to be significant. First, most mechanosensory cells are cytologically specialized (e.g., rods and cones in the retina); bone cells are not. Second, one bone loading stimulus can evoke three adaptational responses (deposition, maintenance, or resorption) while nonosseous process stimuli evoke one (e.g., vision). Third, osseous signal transmission is aneural while all other organismal mechanosensational signals[149] utilize afferent neural pathways (e.g., the visual pathway[16]). Fourth, the evoked bone adaptational responses are confined within each "bone" independently (e.g., within a femur); there is no organismal involvement (e.g., touch is a generalized somatic sensation). However, all afferent transductive processes, osseous and nonosseous, share many common mechanisms and processes.[150,151]

29.3.3 Signal Transmission

From a communications viewpoint, the CCN is multiply noded (each osteocyte is a node) and multiply connected. Each osteocytic process is a connection between two osteocytes, and each osteocyte is multiply connected to a number of osteocytes that are near neighbors (see Fig. 29.1). Cell-to-cell communication is considered first below, then speculation on the ability of the CCN to compute as well as signal is presented. It is useful to note the possibility that bone cells, like neurons, may communicate intercellular information by volume transmission, a process that does not require direct cytological contact, but rather utilizes charges in the environment.[152–154]

29.3.3.1 Cell-to-Cell Communication

To transmit a signal over the CCN one osteocyte must be able to signal a neighboring osteocyte that will then pass the signal on until it reaches an osteoblast on the bone surface. There are a variety of chemical and electrical cell-to-cell communication methods.[155] The passage of chemical signals, such as Ca^{2+}, from cell to cell appears to occur at a rate that would be too slow to respond to the approximately 30-Hz signal associated with muscle firing. Here, the focus is on electrical cell-to-cell communication. Zhang et al.[135,136] have formulated a cable model for cell-to-cell communication in an osteon. The spatial distribution of intracellular electric potential and current from the cement line to the lumen of an osteon was estimated as the frequency of the loading and conductance of the gap junction were altered. In this model the intracellular potential and current are driven by the mechanically induced strain-generated streaming potentials produced by the cyclic mechanical loading of bone. The model differs from earlier studies[156] in that it pursues a more physiological approach in which the microanatomical dimensions of the connexon pores, osteocytic processes, and the distribution of cellular membrane area and capacitance are used to estimate quantitatively the leakage of current through the osteoblast membrane, the time delay in signal transmission along the cable, and the relative resistance of the osteocytic processes and the connexons in their open and closed states. The model predicts that the cable demonstrates a strong resonant response when the cable coupling length approaches the osteonal radius. The theory also predicts that the pore pressure relaxation time for the draining of the bone fluid into the osteonal canal is of the same order as the characteristic diffusion time for the spread of current along the membrane of the osteocytic processes. This coincidence of characteristic times produced a spectral resonance in the cable at 30 Hz. These two resonances lead to a large amplification of the intracellular potential and current in the surface osteoblasts, which could serve as the initiating signal for osteoblasts to conduct remodeling.

29.3.3.2 Signal Processing and Integration

When a physical representation of a CCN, such as Fig. 29.1, is viewed by someone familiar with communications, there is often an intuitive response that the CCN may function as a neural network for processing the mechanical loading stimulus signals being felt over the network. That idea is explored here with no justification other than shared intuition. A CCN is operationally analogous to an artificial neural network in which massively parallel, or parallel distributed, signal processing occurs.[87,157,158] (Fortunately, the bases of connectionist theory are sufficiently secure to permit a biologically realistic CCN model.[159–163])

A CCN consists of a number of relatively simple, densely interconnected, processing elements (bone cells), with many more interconnections than cells. Operationally these cells are organized into layers: an initial input, a final output, and one or more intermediate or hidden layers. However, such networks need not be numerically complex to be operationally complex.[164]

The operational processes are identical, in principle, for all bone cells in all layers. Each cell in any layer may simultaneously receive several weighted (i.e., some quantitative measure) inputs. In the initial layer these are the loading stimuli (mechanoreception). Within each cell independently, "all the weighted inputs are then summed."[165] This net sum is then compared, within the cell, against some threshold value. If this liminal value is exceeded, a signal is generated (mechanotransduction in input layer cells) that is then transmitted identically to all the hidden layer cells (adjacent osteocytes) to which each initial layer cell is connected. Similar processes of weighted signal summation, comparison, and transmission occur in these layers until final layer cells (osteoblasts) are reached. The outputs of these surface-situated

cells regulate the specific adaptation process of each group of osteoblasts.[166] All neighboring osteoblasts that carry out an identical bone adaptational process form a communication compartment, a cohort of structurally and operationally similar cells, because all these cells are interconnected by open, functional gap junctions. At the boundary between such compartments that are carrying out different adaptational processes, the intervening gap junctions are closed and are incapable of transmitting information. These boundaries are probably changing continuously as some of the cells have some downtime.[37,44]

Information is not stored discretely in a CCN, as is the case in conventional computers. Rather, it is distributed across all or part of the network, and several types of information may be stored simultaneously. The instantaneous state of a CCN is a property of all of its cells and of their connections. Accordingly, its informational representation is redundant, assuring that the network is fault, or error, tolerant; i.e., one or several inoperative cells cause little or no noticeable loss in network operations.[165]

CCNs exhibit oscillation; i.e., iterative reciprocal (feedback) signaling between layers enables them to self-organize adjustively. This is related to the fact that CCNs are not preprogrammed; rather they learn by unsupervised training,[167] a process involving the adaptation of the CCNs to the responses of the cytoskeleton to physical activity.[120] In this way, the CCN adjusts to the customary mechanical loading of the whole bone.[58] In a CCN, structurally more complex attributes and behavior gradually self-organize and emerge during operation. These are not reducible; they are neither apparent nor predictable from a prior knowledge of the behavior of individual cells.

As noted above, gap junctions as electrical synapses permit bidirectional flow of information. This is the cytological basis for the oscillatory behavior of a CCN. The presence of sharp discontinuities between groups of phenotypically different osteoblasts is related also to an associated property of gap junctions, i.e., their ability to close and so prevent the flow of information.[168,169] Significantly, informational networks can also transmit inhibitory signals, a matter beyond the present scope.[170]

It is suggested that a CCN displays the following attributes. Developmentally, it is self-organized and self-adapting and, in the sense that it is epigenetically regulated, it is untrained. Operationally, it is a stable, dynamic system, whose oscillatory behavior permits feedback; in this regard, it is noted that a CCN operates in a noisy, nonstationary environment, and that it also employs useful and necessary inhibitory inputs.

The CCN permits a triad of histological responses to a (seemingly) unitary loading event. Although in this chapter, as in almost all the related literature, the organization of bone cells is treated as if it existed only in two dimensions, and as if bone tissue loadings occurred only at certain discrete loci, and that without consideration of loading gradients, the biologic situation is otherwise. Given such a loading event, a three-dimensional bone volume, gradients of deformation must exist, and each osteocyte may sense correspondingly different strain properties. Moreover, it is probable that each osteocyte potentially is able to transmit three different signals in three different directions, some stimulatory and some inhibitory: such states have not yet been modeled.[171,172]

29.3.3.3 A Tentative Mechanotransduction Synthesis

The molecular-level mechanisms that permit muscle function to regulate directly the genomic activity of strained bone cells, including their phenotypic expression, when combined together with electric field effects and contraction frequency energetics, provide a biophysical basis for an earlier hypothesis of epigenetic regulation of skeletal tissue adaptation.[77,78,173–176]

It is probable[177,178] that electrical and mechanical transductive processes are neither exhaustive nor mutually exclusive. While utilizing differing intermediate membrane mechanisms and/or processes, they share a common final pathway;[179] i.e., both mechanical and electrical transductions result in transplasma membrane ionic flow(s), creating a signal(s) capable of intercellular transmission to neighboring bone cells via gap junctions.[66,67,135,136,180] These signals are inputs to a CCN, whose outputs regulate the bone adaptational processes.

The primacy of electrical signals is suggested here, since while bone cell transduction may also produce small biochemical molecules that can pass through gap junctions, the time course of mechanosensory processes is believed to be too rapid for the involvement of secondary messengers.[12,18,181] As was noted previously, the passage of chemical signals, such as Ca^{2+}, from cell to cell appears to occur at a rate that would be too slow to respond to the approximately 30-Hz signal associated with muscle firing.

29.4 Questions for Future Research; Socratic Questions

1. Given that several alternative plausible osseous mechanosensory modalities are postulated in the literature, is it reasonable to consider[179,182] that a possible "common pathway" exists, capable of subsuming them all?
2. Is it useful to consider[93,183] osseous mechanosensation at the quantum level?
3. Does NO play a significant role in osseous mechanosensation?[70,74,184]
4. Does the osteocytic syncytium share similar response characteristics with other cellular syncytia; i.e., are they also periodic, chaotic, and functioning at the edge of a state of chaos?[185]
5. Is bone a "smart material," organized as a "smart structure"?[186,187] Further, in this regard, is bone an "intelligent material" in the sense that this is reflected in the proposed relationship to "strain history"?
6. Is sufficient attention given to the inherent difference between *in vivo* and *in vitro* experimentation?[188]
7. Given the rapidly evolving conceptual bases for the complexity sciences, is it appropriate to consider[189–191] the extent to which bone tissue and cellular responses to mechanical loadings are evidence of a self-adapting and self-organizing biological system?
8. Given that a single osteocyte, existing in a syncytial cellular network capable of signaling back-propagation, has three-dimensional connectivity, is it possible that, in response to a unitary loading event, a unitary osteocyte is capable of simultaneously transmitting three different "signals," one in each direction, i.e., one signal for deposition, one for resorption, and one for stasis? If so, how is this accomplished? And if not, why not?
9. What factor(s) regulate the "size" (area) of a "packet" (communication compartment, cohort) of osteoblasts, all engaging simultaneously in the same activity (i.e., deposition, resorption, stasis) on a bone surface, at any one period of time?
10. What is the relationship between the electromagnetic frequencies to which bone responds, to those frequencies to which other, nonosseous cells and tissues respond?[192]
11. Is it possible to develop a comprehensive explication[193] of all aspects of bone tissue response to extrinsic "loadings" that is equally valid at all organizational levels; molecular, microscopic, cellular, tissue, and organismal?
12. What are the rules of the self-assembly process that governs the formation of structure in bone. How does this process differ in morphogenesis, growth, strain adaptation, fracture healing, and the development of secondary osteons?

References

1. Wolff, J., Uber der innere Architektur der Knochen und ihre Bedeutung fur die Frage vom Knochenwachstum, *Arch. Pathol. Anat. Physiol. Med. Virchovs Arch.,* 50, 389–453, 1870.
2. Wolff, J., *Das Gesetz der Transformation der Knochen,* Hirschwald, Berlin, 1892.
3. Wolff, J., *The Law of Bone Remodelling,* Springer, Berlin, 1986.
4. Frost, H. M., *The Laws of Bone Structure,* Charles C Thomas, Springfield, IL, 1964.
5. Frost, H. M., Tetracycline-based histological analysis of bone remodeling, *Calcif. Tissue Res.,* 3, 211–237, 1969.
6. Uhthoff, H. K. and Jaworski, Z. F. G., Bone loss in response to long term immobilization, *J. Bone Joint Surg.,* 60-B, 420–429, 1978.
7. Jaworski, Z. F. G., Liskova-Kiar, M., and Uhthoff, H. K., Effect of long term immobilization on the pattern of bone loss in older dogs, *J. Bone Joint Surg.,* 62B, 104–110, 1980.
8. Lanyon, L. E., Goodship, A. E., Pye, C. J., and MacFie, J. H., Mechanically adaptive bone remodeling, *J. Biomech.,* 15, 141–154, 1982.
9. Burger, E. L., Klein Nulend, J., and Cowin, S. C., Mechanotransduction in bone, in *Advances in Organ Biology,* Zaidi, M., Ed., Vol. 5a, JAI Press Inc., London, 1998, 107–118.
10. Jacobs, R., Ed., *Osseoperception,* Catholic University, Leuven, 1998.

11. Junge, D., *Oral Sensorimotor Function,* Medico Dental Media, International, Inc., Pacific, MO, 1998.
12. French, A. S., Mechanotransduction, *Annu. Rev. Physiol.,* 54, 135–152, 1992.
13. Kernan, M., Cowan, D., and Zuker, C., Genetic dissection of mechanoreception-defective mutations, *Drosophila Neuron,* 12, 1195–1206, 1994.
14. Fraser, D. J. and Macdonald, A. G., Crab hydrostatic pressure sensors, *Nature,* 371, 383–384, 1994.
15. Hamill, O. P. and McBride, Jr., D. W., Mechanoreceptive membrane channels, *Am. Sci.,* 83, 30–37, 1995.
16. Hackney, C. M. and Furness, D. N., Mechanotransduction in vertebrate hair cells: structure and function of the stereociliary bundle, *Am. J. Physiol.,* 268 (Cell Physiol. 37), C1–C13, 1995.
17. Cui, C., Smith, D. O., and Adler, J., Characterization of mechanosensitive channels in *Eschericia coli* cytoplasmic cell membrane by whole-cell patch clamp recording, *J. Membr. Biol.,* 144, 31–42, 1995.
18. Wildron, D. C., Thain, J. F. et al., Electrical signaling and systematic proteinase inhibitor induction in the wounded plant, *Nature,* 360, 62–65, 1992.
19. Goldsmith, P., Plant stems: a possible model system for the transduction of mechanical information in bone modeling, *Bone,* 15, 249–250, 1994.
20. Olsson, S. and Hanson, B. S., Action potential-like activity found in fungal mycelia is sensitive to stimulation, *Naturwissenschafteng,* 82, 30–31, 1995.
21. Cowin, S. C., Moss-Salentijn, L., and Moss, M. L., Candidates for the mechanosensory system in bone, *J. Biomech. Eng.,* 113, 191–197, 1991.
22. Moss, M. L., Bone as a connected cellular network: modeling and testing, in *Topics in Biomedical Engineering,* G. Ross, Ed., Pergamon Press, New York, 1991, 117–119.
23. Moss, M. L., Alternate mechanisms of bone remodeling: their representation in a connected cellular network model, *Ann. Biomed. Eng.,* 19, 636, 1991.
24. Bennett, M. V. L. and Goodenough, D. A., Gap junctions: electronic coupling and intercellular communication, *Neurosci. Res. Prog. Bull.,* 16, 373–485, 1978.
25. Doty, S. B., Morphological evidence of gap junctions between bone cells, *Calcif. Tissue Int.,* 33, 509–512, 1981.
26. Doty, S. B., Cell-to-cell communication in bone tissue, in *The Biological Mechanism of Tooth Eruption and Root Resorption,* Z. Davidovitch, Ed., EBSCO Media, Birmingham, AL, 1989, 61–69.
27. Jones, D. B. and Bingmann, D., How do osteoblasts respond to mechanical stimulation? *Cells Mater.,* 1, 329–340, 1991.
28. Schirrmacher, K., Schmitz, I., et al., Characterization of gap junctions between osteoblast-like cells in culture, *Calcif. Tissue Int.,* 51, 285–290, 1992.
29. Jones, S. J., Gray, C., and Sakamaki, H. et al., The incidence and size of gap junctions between bone cells in rat calvaria, *Anat. Embryol.,* 187, 343–352, 1993.
30. Gourdie, R. and Green, C., The incidence and size of gap junctions between bone cells in rat calvarial, *Anat. Embryol.,* 187, 343–352, 1993.
31. Civitelli, R., Cell-cell communication in bone, *Calcif. Tissue Int.,* 56 (Suppl. 1), S29–S31, 1995.
32. Minkoff, R., Rundus, V. R., and Parker, S. B. et al., Gap junction proteins exhibit early and specific expression during intramembranous bone formation in the developing chick mandible, *Anat. Embryol.,* 190, 231–241, 1994.
33. Minkoff, R. and Bales, E. S. et. al., Antisense oligonucleotide blockade of connexin expression during embryonic bone formation: evidence of functional compensation within a multigene family, *Dev. Genet.,* 24, 43–56, 1999.
34. Lecanda, F. and Towler, D. A. et.al., Gap junctional communication modulates gene expression in osteoblastic cells, *Mol. Biol. Cell,* 9, 2249–2258, 1998.
35. Cowan, D. B., Lye, S. J., and Langille, B. L., Regulation of vascular connexin 43 gene expression by mechanical loads, *Circ. Res.,* 82, 786–793, 1998.
36. Beardslee, M. A., Laing, J. G., and Beyer, E. C. et al., Rapid turnover of connexin 43 in the adult rat heart, *Circ. Res.,* 83, 629–635, 1998.

37. Spray, D. C., Gap junction proteins; where do they live and how do they die? *Circ. Res.,* 83, 679–681, 1998.
38. Rodan, G., Introduction to bone biology, *Bone,* 13, S3–S6, 1992.
39. Curtis, T. A., Ashrafi, S. H., and Weber, D. F., Canalicular communication in the cortices of human long bones, *Anat. Rec.,* 212, 336–344, 1985.
40. Bingmann, D., Tetsch, D., and Fritsch, J., Membraneigenschaften von Zellen aus Knochenexplantaten, *Z. Zahnartzl. Implantol.,* IV, 277–281, 1988.
41. Chesnoy-Marchais, D. and Fritsch, J., Voltage-gated sodium and calcium currents in rat osteoblasts, *J. Physiol.,* 398, 291–311, 1988.
42. Massass, R., Bingmann, D., Korenstein, R. et al., Membrane potential of rat calvaria bone cells: dependence on temperature, *J. Cell Physiol.,* 144, 1–11, 1990.
43. Rubinacci, A. and Villa, I. et al., Osteocyte-bone lining cell system at the origin of steady ionic current in damaged amphibian bone, *Calcif. Tissue Int.,* 63, 331–339, 1998.
44. Jeansonne, B. G., Feagin, F. F. et al., Cell-to-cell communication of osteoblasts, *J. Dent. Res.,* 58, 1415–1423, 1979.
45. Schirrmacher, K., Brummer, F. et al., Dye and electric coupling between osteoblast-like cells in culture, *Calcif. Tissue Int.,* 53, 53–60, 1993.
46. Spray, D. C., Physiological and pharmacological regulation of gap junction channels, in *Molecular Mechanisms of Epithelial Cell Junctions: From Development to Disease,* S. Chi, Ed., RG Landes, Austin, 1994, 195–215.
47. Moreno, A. P., Rook, M. B. et al., Gap junction channels: distinct voltage-sensitive and -insensitive conductance states, *Biophys. J.,* 67, 113–119, 1994.
48. Nowak, R., Cells that fire together, wire together, *J. NIH Res.,* 4, 60–64, 1992.
49. Martin, T. J. and Ng, K. W., Mechanisms by which cells of the osteoblastic lineage control osteoclast formation and activity, *J. Cell. Biochem.,* 56, 357–366, 1994.
50. Owan, I., Burr, D. B. et.al., Mechanotransduction in bone:osteoblasts are more responsive to fluid forces than mechanical strain, *Am. Physiol. Soc.,* 273, C810–815, 1997.
51. Cowin, S. C. and Hegedus, D. M., Bone remodeling I: a theory of adaptive elasticity, *J. Elasticity,* 6, 313–325, 1976.
52. Fyhrie, D. P. and Carter, D. R., A unifying principle relating stress to trabecular bone morphology, *J. Orthop. Res.,* 4, 304–317, 1986.
53. Huiskes, R., Weinans, H. J., Grootenboer, H. J. et al., Adaptive bone remodeling theory applied to prosthetic-design analysis, *J. Biomech.,* 20, 1135–1150, 1987.
54. Hert, J., Liskova, M., and Landgrot, B., Influence of the long-term continuous bending on the bone. An experimental study on the tibia of the rabbit, *Fol. Morphol.,* 17, 389–399, 1969.
55. Hert, J., Liskova, M., and Landa, J., Reaction of bone to mechanical stimuli. Part I. Continuous and intermittent loading of tibia in rabbit, *Fol. Morphol.,* 19, 290–300, 1971.
56. Hert, J., Pribylova, E., and Liskova, M., Reaction of bone to mechanical stimuli. Part 3. Microstructure of compact bone of rabbit tibia after intermittent loading, *Acta Anat.,* 82, 218–230, 1972.
57. O'Connor, J. A., Lanyon, L. E., and MacFie, H., The influence of strain rate on adaptive bone remodeling, *J. Biomech.,* 15, 767–781, 1982.
58. Lanyon, L. E., Functional strain as a determinant for bone remodeling, *Calcif. Tissue Int.,* 36, S56–S61, 1984.
59. Goldstein, S. A., Matthews, L. S., Kuhn, J. L. et al., Trabecular bone remodeling: an experimental model, *J. Biomech.,* 24 (Suppl. 1), 135–150, 1991.
60. Fritton, S. P., McLeod, K. J., and Rubin, C. T., Quantifying the strain history of bone: spatial uniformity and self-similarity of low magnitude strains, *J. Biomech.,* 33, 317–325, 2000.
61. Carter, D. R. and Hayes, W. C., Bone compressive strength: the influence of density and strain rate, *Science,* 194, 1174–1175, 1976.
62. Martin, R. B. and Burr, D. B., A hypothetical mechanism for the stimulation of osteonal remodeling by fatigue damage, *J. Biomech.,* 15, 1137–139, 1982.

63. Brown, T. D., Pedersen, D. R., and Gray, M. L. et al., Toward an identification of mechanical parameters initiating periosteal remodeling: a combined experimental and analytic approach, *J. Biomech.,* 23, 893–905, 1990.
64. Cowin, S. C., On mechanosensation in bone under microgravity, *Bone,* 22, 119S–125S, 1998.
65. Weinbaum, S., Cowin, S.C., and Zeng, Y., A model for the fluid shear stress excitation of membrane ion channels in osteocytic processes due to bone strain, in *Advances in Bioengineering,* R. Vanderby, Jr., Ed., American Society of Mechanical Engineers, New York, 1991, 317–320.
66. Weinbaum, S., Cowin, S. C., and Zeng, Y., Excitation of osteocytes by mechanical loading-induced bone fluid shear stresses, *J. Biomech.,* 27, 339–360, 1994.
67. Cowin, S. C., Weinbaum, S., and Zeng, Yu, A case for bone canaliculi as the anatomical site of strain generated potentials, *J. Biomech.,* 28, 1281–1296, 1995.
68. Gross, T. S., Edwards, J. L. et. al., Strain gradients correlate with sites of periosteal bone formation, *J. Bone Miner. Res.,* 12, 982–988, 1997.
69. Klein-Nulend, J., Van der Plas, A., Semeins, C. M., Ajubi, N. E., Frangos, J. A., Nijweide, P. J., and Burger, E. H., Sensitivity of osteocytes to biomechanical stress *in vitro, FASEB J.,* 9, 441–445, 1995.
70. Klein-Nulend, J., Semeins, C. M., Ajubi, N. E., Nijweide, P. J., and Burger, E. H., Pulsating fluid flow increases nitric oxide (NO) synthesis by osteocytes but not periosteal fibroblasts—correlation with prostaglandin upregulation, *Biochem. Biophys. Res. Commun.,* 217, 640–648, 1995.
71. Reich, K. M., Gay, C. V., and Frangos, J. A., Fluid shear stress as a mediator of osteoblast cyclic adenosine monophosphate production, *J. Cell. Physiol.,* 143, 100–104, 1990.
72. Williams, J. L., Iannotti, J. P., Ham, A., Bleuit, J., and Chen, J. H., Effects of fluid shear stress on bone cells, *Biorheology,* 31, 163–170, 1994.
73. Hung, C. T., Pollack, S. R., Reilly, T. M., and Brighton, C. T., Real-time calcium response of cultured bone cells to fluid flow, *Clin. Orthop. Relat. Res.,* 313, 256–269, 1995.
74. Pitsillides, A. A. and Rawlinson, S. C. F. et.al., Mechanical strain-induced NO production by bone cells: a possible role in adaptive bone (re)modeling? *FASEB J.,* 9, 1614–1622, 1995.
75. Hecker, M., Mülsch, A., Bassenge, E., and Busse, R., Vasoconstriction and increased flow: two principal mechanisms of shear stress-dependent endothelial autocoid release, *Am. J. Physiol.,* 265 (Heart Circ. Physiol. 34), H828-H833, 1993.
76. Kamiya, A., Bukhari, R., and Togawa, T., Adaptive regulation of wall shear stress optimizing vascular tree function, *Bull. Math. Biol.,* 46, 127–137, 1984.
77. Moss, M. L., The primacy of functional matrices in orofacial growth, *Trans. Br. Soc. Study Orthod. Dent. Pract.,* 19, 65–73, 1968.
78. Moss, M. L., A theoretical analysis of the functional matrix, *Acta Biotheor.,* 18, 195–202, 1969.
79. Moss, M. L., *The Muscle–Bone Interface: An Analysis of a Morphological Boundary.* Center for Human Growth and Development, Ann Arbor, MI, 1978.
80. McMahon, T. A., *Muscles, Reflexes, and Locomotion,* Princeton University Press, Princeton, NJ, 1984.
81. McLeod, K. J. and Rubin, C. T., The effect of low-frequency electrical fields on osteogenesis, *J. Bone Joint Surg.,* 74A, 920–929, 1992.
82. Rodrequez, A. A. and Agre, J. C. et al., Acoustic myography compared to electromyography during isometric fatigue and recovery, *Muscle Nerve.,* 16, 188–192, 1993.
83. Rubin, C. T. and Donahue, H. J. et al., Optimization of electric field parameters for the control of bone remodeling: exploitation of an indigenous mechanism for the prevention of osteopenia, *J. Bone Miner. Res.,* 8 (Suppl. 2), S573–S581, 1993.
84. Aarden, E. M., Burger, E. H., and Nijweide, P. J., Function of osteocytes in bone, *J. Cell Biochem.,* 55, 287–299, 1994.
85. Aarden, E. M., *The Third Cell—A Study of the Role of the Osteocyte in Bone,* thesis, Leiden, 1996.
86. Lanyon, L. E., Osteocytes, strain detection, bone modeling and remodeling, *Calcif. Tissue Int.,* 53 (Suppl. 1), S102–S106, 1993.
87. Edin, B. B. and Trulsson, M., Neural network analysis of the information content in population responses from human periodontal receptors, *Sci. Neural Networks,* SPIE 1710, 257–266, 1992.

88. Guggino, S. E., LaJeunesse, D., Wagner, J. A. et al., Bone remodeling signaled by a dihydropyridine- and phenylalkylamine-sensitive calcium channel, *Proc. Natl. Acad. Sci. U.S.A.,* 8, 2957–2960, 1989.
89. Duncan, R. and Misler, S., Voltage-activated and stretch activated Ba^{2+} conducting channels in an osteoblast-like cell line (URM 106), *Fed. Europ. Biochem. Soc.,* 251, 17–21, 1989.
90. Keynes, R. D., The kinetics of voltage-gated ion channels, *Q. Rev. Biophys.,* 27, 339–434, 1994.
91. Hamill, O. P. and McBride, D. W., Jr., The pharmacology of mechanogated membrane ion channels, *Pharmacol. Rev.,* 48, 231–248, 1996.
92. Morris, C. E., Mechanosensitive ion channels, *J. Membr. Biol.,* 113, 93–107, 1990.
93. Ghazi, A. and Berrier, C. et. al., Mechanosensitive ion channels and their mode of activation, *Biochimie,* 80, 357–362, 1998.
94. Sachs, F., Biophysics of mechanoreception, *Membr. Biochem.,* 6, 173–195, 1986.
95. Sachs, F., Mechanical transduction in biological systems, *CRC Rev. Biomed. Eng.,* 16, 141–169, 1988.
96. Sackin, H., Mechanosensitive channels, *Annu. Rev. Physiol.,* 57, 333–353, 1995.
97. Harter, L. V., Hruska, K. A., and Duncan, R. L., Human osteoblast-like cells respond to mechanical strain with increased bone matrix protein production independent of hormonal regulation, *Endocrinology,* 136, 528–535, 1995.
98. Rubin, C. T. and Lanyon, L. E., Regulation of bone formation by applied dynamic loads, *J. Bone Joint Surg.,* 66A, 397–415, 1984.
99. Rubin, C. T. and Lanyon, L. E., Osteoregulatory nature of mechanical stimuli: function as a determinant for adaptive bone remodeling, *J. Orthop. Res.,* 5, 300–310, 1987.
100. Cowin, S. C. and Weinbaum, S., Strain amplification in the bone mechanosensory system, *Am. J. Med. Sci.,* 316, 184–188, 1998.
101. Davidson, R. M., Tatakis, D. W., and Auerbach, A. L., Multiple forms of mechanosensitive ion channels in osteoblast-like cells, *Eur. J. Physiol.,* 416, 646–651, 1990.
102. Ravelsloot, J. H., van Houten, R. J., and Ypey, D. L. et al., High-conductance anion channels in embryonic chick osteogenic cells, *J. Bone Miner. Res.,* 6, 355–363, 1991.
103. Ferrier, J., Crygorczyk, C., Grygorczyk, R. et al., Ba^{2} -induced action potentials in osteoblastic cells, *J. Membr. Biol.,* 123, 255–259, 1991.
104. Jan, L. Y. and Jan, Y. N., Tracing the roots of ion channels, *Cell,* 69, 715–718, 1992.
105. Hughes, D. E., Salter, D. M., Dedhar, S. et al., Integrin expression in human bone, *J. Bone Miner. Res.,* 8, 527–533, 1993.
106. Watanabe, H., Miake, K., and Sasaki, J., Immunohistochemical study of the cytoskeleton of osteoblasts in the rat calvaria, *Acta Anat.,* 147, 14–23, 1993.
107. Green, P. B., Connecting gene and hormone action to form, pattern and organogenesis: biophysical transductions, *J. Exp. Bot.,* 45 (Spec. Issue), 1775–1788, 1994.
108. Richardson, A. and Parsons, J. T., Signal transduction through integrins: a central role for focal adhesion, *Bioessays,* 17, 229–236, 1995.
109. Clark, E. A. and Brugge, J. S., Integrins and signal transduction pathways: the road taken, *Science,* 268, 233–239, 1995.
110. Forgacs, G., Biological specificity and measurable physical properties of cell surface receptors and their possible role in signal transduction through the cytoskeleton, *Biochem. Cell Biol.,* 73, 317–326, 1995.
111. Shapiro, F. and Cahill, C. et al., Transmission electron microscopic demonstration of vimentin in rat osteoblast and osteocytic cell bodies and processes using the immunogold technique, *Anat. Rec.,* 241, 39–48, 1995.
112. Dolce, C., Kinniburgh, A. J., and Dziak, R., Immediate early-gene induction in rat osteoblastic cells after mechanical deformation, *Arch. Oral Biol.,* 41, 1101–1108, 1996.
113. Shyy, J. Y. and Chien, S., Role of integrins in cellular responses to mechanical stress and adhesion, *Curr. Opin. Cell Biol.,* 9, 707–713, 1997.
114. Salter, D. M., Robb, J. E., and Wright, M. O., Electrophysiological responses of human bone cells to mechanical stimulation: evidence for specific integrin function in mechanotransduction, *J. Bone Miner. Res.,* 12, 1133–1141, 1997.

115. Meazzini, M. C., Toma, C. D. et. al., Osteoblast cytoskeletal modulation in response to mechanical strain in vitro, *J. Bone Joint Surg.,* 16, 170–180, 1998.
116. Carvalho, R. S., Schaffer, J. L., and Gerstenfeld, L. C., Osteoblasts induce osteopontin expression in response to attachment on fibronectin: demonstration of a common role for integrin receptors in the signal transduction processes of cell attachment and mechanical stimulation, *J. Cell. Biochem.,* 70, 376–390, 1998.
117. Ingber, D. E., Cellular basis of mechanotransduction, *Biol. Bull.,* 194, 323–327, 1998.
118. Janmey, P. A., The cytoskeleton and cell signaling: component localization and mechanical coupling, *Physiol. Rev.,* 78, 763–774, 1998.
119. Uitto, V. J., Extracellular matrix molecules and their receptors: an overview with special emphasis on periodontal tissues, *Crit. Rev. Oral Biol. Med.,* 2, 323–354, 1991.
120. Dayhoff, J. E., Hameroff, S. R., Lahoz-Beltra, R. et al., Intracellular mechanisms in neuronal learning: adaptive models, *Int. Joint Conf. Neural Networks,* I73–I78, 1992.
121. Sadoshima, J., Takahashi, T. et al., Roles of mechano-sensitive ion channels, cytoskeleton and contractile activity in stretch-induced immediate-early gene expression and hypertrophy of cardiac myocytes, *Proc. Natl. Acad. Sci. U.S.A.,* 89, 9905–9909, 1992.
122. Yanagishita, M., Function of proteoglycans in the extracellular matrix, *Acta Pathol. Jpn.,* 4, 283–293, 1993.
123. Wang, N., Butler, J. P., and Ingber, D. E., Mechanotransduction across the cell surface and through the cytoskeleton, *Science,* 260, 1124–1127, 1993.
124. Haskin, C. and Cameron, I., Physiological levels of hydrostatic pressure alter morphology and organization of cytoskeletal and adhesion proteins in MG-63 osteosarcoma cells, *Biochem. Cell Biol.,* 71, 27–35, 1993.
125. Petrov, A. G. and Usherwood, P. N., Mechanosensitivity of cell membranes. Ion channels, lipid matrix and cytoskeleton, *Eur. Biophys. J.,* 23, 1–19, 1994.
126. Machwate, M., Jullienne, A., Moukhtar, M. et al., Temporal variation of *c-fos* protoocogene expression during osteoblasts differentiation and osteogenesis in developing rat bone, *J. Cell Biochem.,* 57, 62–70, 1995.
127. Piekarski, K. and Munro, M., Transport mechanism operating between blood supply and osteocytes in long bones, *Nature,* 269 (5623), 80–82, 1977.
128. Johnson, M. W., Chakkalakal, D. A., Harper, R. A. et al., Fluid flow in bone, *J. Biomech.,* 11, 881–885, 1982.
129. Kufahl, R. H. and Saha, S., A theoretical model for stress-generated fluid flow in the canaliculi-lacunae network in bone tissue, *J. Biomech.,* 23, 171–180, 1990.
130. Pollack, S. R., Petrov, N. et al., An anatomical model for streaming potentials in osteons, *J. Biomech.,* 17, 627–636, 1984.
131. Salzstein, R. A., Pollack, S. R. et al., Electromechanical potentials in cortical bone—I. A continuum approach, *J. Biomech.,* 20, 261–270, 1987.
132. Salzstein, R. A. and Pollack, S. R., Electromechanical potentials in cortical bone—II. Experimental analysis, *J. Biomech.,* 20, 271–280, 1987.
133. Scott, G. C. and Korostoff, E., Oscillatory and step response electromechanical phenomena in human and bovine bone, *J. Biomech.,* 23, 127–143, 1990.
134. Otter, M. W., Palmieri, V. R., Wu, D. D., et al., A comparative analysis of streaming potentials in *vivo* and *in vitro, J. Orthop. Res.,* 10, 710–719, 1992.
135. Zhang, D., Cowin, S. C., and Weinbaum, S., Electrical signal transmission and gap junction regulation in bone cell network: a cable model for an osteon, *Ann. Biomed. Eng.,* 25, 357–374, 1997.
136. Zhang, D., Cowin, S. C., and Weinbaum, S., Electrical signal transmission in a bone cell network: the influence of a discrete gap junction, *Ann. Biomed. Eng.,* 26, 644–659, 1998.
137. Zhang, D., Weinbaum, S., and Cowin, S. C., On the calculation of bone pore water pressure due to mechanical loading, *Int. J. Solids Struct.,* 35, 4981–4997, 1998.

138. Zhang, D., Weinbaum, S., and Cowin, S. C., Estimates of the peak pressures in the bone pore water, *J. Biomech. Eng.,* 120, 697–703, 1998.
139. Wang, L. and Fritton, S. P. et al., Fluid pressure relaxation depends upon osteonal microstructure: modeling of an oscillatory bending experiment, *J. Biomech.,* 32, 663–672, 1999.
140. Cowin, S. C., Bone poroelasticity, *J. Biomech.,* 32, 218–238, 1999.
141. Dillaman, R. M., Movement of ferritin in the 2-day-old chick femur, *Anat Rec.,* 209, 445–453, 1984.
142. Montgomery, R. J., Sutker, B. D. et al. Interstitial fluid flow in cortical bone, *Microvasc. Res.,* 23, 188–200, 1988.
143. Tanaka, T. and Sakano, A., Differences in permeability of microperoxidase and horseradish peroxidase into alveolar bone of developing rats, *J. Dent. Res.,* 64, 870–876, 1985.
144. Ayasaka, N., Kondo, T., Goto, T. et al., Differences in the transport systems between cementocytes and osterocytes in rats using microperoxidase as a tracer, *Arch. Oral Biol.,* 37, 363–368, 1992.
145. Otter, M. W., McLeod, K. J., and Rubin, C.T., Effects of electromagnetic fields in experimental fracture repair, *Clin. Orthop. Relat. Res.,* 355S, S90–S104, 1998.
146. Brighton, C. T., Okerehe, E., Pollack, S. et al., *In vitro* bone-cell response to a capacitively coupled electrical field. Role of field strength, pulse pattern and duty cycle, *Clin. Orthop. Rel. Res.,* 285, 255–262, 1992.
147. McLeod, K. J., Donahue, H. J. et al., Electric fields modulate bone cell function in a density-dependent manner, *J. Bone Miner. Res.,* 8, 977–984, 1993.
148. McLeod, K. J., Rubin, C. T. et.al., Skeletal cell stresses and bone adaptation, *Am. J. Med. Sci.,* 316, 176–183, 1998.
149. Moss-Salentijn, L., The human tactile system, in *Advanced Tactile Sensing for Robotics,* H. R. Nicholls, Ed., World Scientific Publishing, Singapore, 1992, chap. 4.
150. Gilbertson, T. A., Peripheral mechanisms of taste, in *The Scientific Basis of Eating,* R. W. A. Linden, Ed., Vol. 9, Karger, Basel, 1998, 1–28.
151. Wilson, D. A. and Sullivan, R. M., Peripheral mechanisms of smell, in *The Scientific Basis of Eating,* R. W. A. Linden, Ed., Vol. 9, Karger, Basel, 1998, 29–39.
152. Fuxe, J. and Agnati, L. F., Eds., *Volume Transmission in the Brain,* Raven Press, New York, 1991.
153. Marotti.G., The structure of bone tissues and the cellular control of their deposition, *Ital. J. Anat. Embryol,* 101, 25–79, 1996.
154. Schaul, N., The fundamental neural mechanisms of electroencephalography, *Electroencephalogr. Clini. Neurophysiol.,* 106, 101–107, 1998.
155. De Mello, W. C., The ways cells communicate, in *Cell-to-Cell Communication,* Plenum Press, New York, 1987, 1–20.
156. Harrigan, T. P. and Hamilton, J. J., Bone strain sensation via transmembrane potential changes in surface osteoblasts: loading rate and microstructural implications, *J. Biomech.,* 26, 183–200, 1993.
157. Denning, P. J., Neural networks, *Am. Sci.*, 80, 426–429, 1990.
158. Martino, R. L., Johnson, C. A., Suh, E. B., et al., Parallel computing in biomedical research, *Science,* 265, 902–907, 1994.
159. Dayhoff, J., *Neural Network Architecture,* Van Nostrand Reinhold, New York, 1990.
160. Grossberg, S., *Neural Networks and Artificial Intelligence,* MIT Press, Cambridge, MA, 1988.
161. Hinton, G. E. and Anderson, J. A., *Parallel Models of Associative Memory,* Lawrence Erlbaum, Hillsdale, NJ, 1989.
162. McClelland, J. L. and Rumelhart, D. E., *Parallel Distributed Processing. Psychological and Biological Models,* Vol. 2, MIT Press, Cambridge, MA, 1987.
163. Zorntzer, S. F., Davis, J., and Lau, C., *An Introduction to Neural and Electronic Networks,* Academic Press, San Diego 1990.
164. Kupfermann, I., Neural networks: they do not have to be complex to be complex, *Behav. Brain Sci.,* 15, 767–768, 1992.
165. Wasserman, P. D., *Neural Computation. Theory and Practice,* Van Nostrand Reinhold, New York, 1989.
166. Parfitt, A. M., Osteonal and hemi-osteonal remodeling: the spatial and temporal framework for signal traffic in adult human bone, *J. Cell Biochem.,* 55, 273–286, 1994.

167. Fritzke, B., Growing cell structures—a self-organizing network for unsupervised and supervised learning, *Neural Networks,* 7, 1441–1460, 1994.
168. Kam, E. and Hodgins, M. B., Communication compartments in hair follicles and their implication in differentiative control, *Development,* 114, 389–393, 1992.
169. Kodoma, R. and Eguchi, G., The loss of gap junctional cell-to-cell communication is coupled with dedifferentiation of retinal pigmented epithelial cells in the course of transdifferentiation into the lens, *Int. J. Dev. Biol.,* 38, 357–364, 1994.
170. Marotti, G., Ferretti, M., Muglia, M. A. et al., A quantitative evaluation of osteoblast-osteocyte relationships on growing endosteal surface of rabbit tibiae, *Bone,* 13, 363–368, 1992.
171. Moss, M. L., The functional matrix hypothesis revisited. l. The role of mechanotransduction, *Am. J. Orthod. Dentofac Orthop.,* 112, 8–11, 1997.
172. Moss, M. L., The functional matrix hypothesis revisited. 2. The role of an osseous connected cellular network, *Am. J. Orthod. Dentofac Orthop.,* 112, 221–226, 1997.
173. Moss, M. L. and Young, R., A functional approach to craniology, *Am. J. Phys. Anthropol.,* 18, 81–92, 1960.
174. Moss, M. L., The functional matrix, in *Vistas in Orthodontics,* B. Kraus and R. Reidel, Eds., Lea and Febiger, Philadelphia, 85–98, 1962.
175. Moss, M. L. and Salentijn, L., The primary role of the functional matrices in facial growth, *Am. J. Orthod.*, 55, 566–577, 1969.
176. Moss, M. L. and Salentijn, L., The capsular matrix, *Am. J. Orthod.,* 56, 474–490, 1969.
177. Moss, M. L., The functional matrix hypothesis revisited. 3. The genomic thesis, *Am. J. Orthod. Dentofac. Orthop.,* 112, 338–342, 1997.
178. Moss, M. L., The functional matrix hypothesis revisited. 4. The epigenetic antithesis and the resolving synthesis, *Am. J. Orthod. Dentofac. Orthop.,* 112, 410–417, 1997.
179. Bhalla, U. S. and Iyengar, R., Emergent properties of networks of biological signaling pathways, *Science,* 283, 381–383, 1999.
180. Zeng, Y., Cowin, S. C., and Weinbaum, S., A fiber matrix model for fluid flow and streaming potentials in the canaliculi of an osteon, *Ann. Biomed. Eng.,* 22, 280–292, 1994.
181. Carvalho, R. S., Scott, J. E., Suga, D. M. et al., Stimulation of signal; transduction pathways in osteoblasts by mechanical strain potentiated by parathyroid hormone, *J. Bone Miner. Res.,* 9, 999–1011, 1994.
182. Zuker, C. S. and Ranganathan, R., The path to specificity, *Science,* 283, 650–651, 1999.
183. Green, S. S. and Triffit, T., The animal brain as a quantal computer, *J. Theor. Biol.,* 184, 385–403, 1997.
184. Lee, D. H., Frean, S. P., Lees, P. et al., Dynamic mechanical compression influences nitric oxide by articular chrondrocytes, *Biochem. Biophys. Res. Comm.,* 251, 580–585, 1998.
185. Kashimori, Y., Funakubo, H., and Kambara, T., Effect of syncytium structure of receptor systems on stochastic resonance by chaotic potential fluctuation, *Biophys. J.,* 75, 1700–1711, 1998.
186. Wang, Z. L. and Kang, Z. C., *Functional and Smart Materials,* Plenum Press, New York, 1998.
187. Culshaw, P., *Smart Structures and Materials,* Artech House, Boston, 1996.
188. Brown, T. D., Bottlang, M., Pederson, D. R. et al., Loading paradigms—intentional and unintentional—for cell culture mechanostimulus, *Am. J. Med. Sci.,* 316, 162–168, 1998.
189. Heylighen. F., Publications on complex, evolving systems: a citation based survey, *Complexity,* 2, 31–36, 1997.
190. Wriggers, W., Milligan, R. A., Schulter, K. et al., Self-organized neural networks bridge the biomolecular gap, *J. Mol. Biol.,* 284, 1247–1254, 1998.
191. Cammarota, J. P., Jr. and Onaral, B., State transitions in physiologic systems: a complexity model for loss of consciousness, *IEEE Trans. Biomed. Eng.,* 45, 1017–1023, 1998.
192. Shafik, A., Electro-oophorogram: a preliminary study of the electrical activity of the ovary, *Gynecol. Obstet. Invest.,* 46, 105–110, 1998.
193. Sasaki, N. and Odajima, S., Elongation mechanism of collagen fibrils and force-strain relations of tendon at each level of structural hierarchy, *J Biomech.,* 29, 1131–1136, 1996.

194. Atkinson, P. J. and Hallsworth, A. S., The changing structure of aging human mandibular bone, *Gerodontology,* 2, 57–66, 1983.

30

The False Premise in Wolff's Law

Stephen C. Cowin
The City College of New York

30.1 Introduction

Wolff's law is generally considered to be a philosophical statement to the effect that, over time, the mechanical load applied to living bone influences the structure of bone tissue. But Wolff's claim was beyond the philosophical statement; his claim was that it was rigorous or mathematical law. From the 19th to the 20th century many argued that the rigid or "mathematical" form of Wolff's law of trabecular architecture, that promulgated by Wolff,[1,2] is not valid. That view is endorsed here. The law compares things that appear to be similar but are not, namely, stress trajectories in a homogeneous isotropic elastic material and the trabecular architecture of cancellous bone—this comparison is referred to here as the *false premise*. That is not to say that references to Wolff's law in the literature are invalid. They are not because they generally refer to his philosophical statement or to Roux's[3] concept of functional adaptation of osseous tissue, an aspect of Wolff's law that is founded in biological thought and experiment and with which Wolff did not fully agree. When the phrase "Wolff's law" appears in a paper, the author usually finds that it can be replaced with the phrase "functional adaptation." The point of this chapter is to present an argument to the effect that a clear statement of the biologically significant aspect of Wolff's "mathematical" law has not yet appeared.

There are three major points made in this chapter. First, the rigid or "mathematical" form of Wolff's law of trabecular architecture, promulgated by Wolff,[1,2] is invalid and has been identified as such almost from its publication. Second, most contemporary students of the functional adaptation of bone have implicitly rejected or ignored the rigid or "mathematical" form of Wolff's law and employ, under the name of Wolff, rules that relate average bone structure to some measure of the mechanical loading that the bone has received. There is no general agreement on the form of the rule that is to replace the "mathematical" falsity or ambiguity associated with Wolff's name, although many think that it should be Roux's[3] concept of functional adaptation of osseous tissue of which Wolff was aware, as Roux[3] was originally planned as a joint publication[4] with Wolff. Third, other laws or models of physiological phenomena that have been presented since Wolff first presented his have become established pillars of physiology, for example, the Hodgkin–Huxley theory of nerve membranes or the sliding filament model of

0-8493-9117-2/01/$0.00+$.50

muscle behavior. These physiological models relate well-defined (and generally measurable) quantities to one another by well-defined and measurable parameters. Wolff's law does not come up to the scientific standards of the Hodgkin–Huxley theory or the sliding filament model of muscle behavior. It would appear that one might profitably abandon the terminology and paradigm associated with Wolff's law and return to the study of the phenomena (phenomenon) of the functional adaptation of bone in the sense of Roux.[3]

The next part of this chapter consists of four sections. In the first, the origins of Wolff's law of trabecular architecture are sketched briefly, and, in the following section, some of the numerous previous critiques of Wolff's law are described. Stress trajectories are constructed in the third section for three objects subjected to mechanical loads. The purpose of these constructions is to highlight the general properties of stress trajectories and to emphasize features to be used in making certain points concerning the false premise. The fourth section details the false premise. The second part of this chapter consists of two sections. The first of these sections addresses the question of introducing a length restriction to separate the functional adaptation aspect of Wolff's law from the invalid assertion of the equivalence of stress trajectories with trabeculae. The final section is a summary and comment. This chapter is adapted from Cowin.[5]

30.2 The Problems with Wolff's Law

30.2.1 The Origin of Wolff's Law—The Culmann and von Meyer Drawings

In an 1867 paper,[6] entitled "Die Architektur der Spongiosa," the well-known Swiss anatomist G. H. von Meyer presented a line drawing of the cancellous or "spongy" bone structure he had observed in the proximal end of the human femur. An important Swiss structural engineer of the period, C. Culmann, was struck by the similarity between von Meyer's sketches of the cancellous bone in a frontal section of the proximal femur and the principal stress trajectories in a cranelike curved bar he was then in the process of designing. A sketch of the trabecular architecture of the type von Meyer published is shown in Fig. 30.1, along with a sketch of Culmann's crane (prepared by a student of Culmann's for the von Meyer paper); these are the *Culmann and von Meyer drawings*.

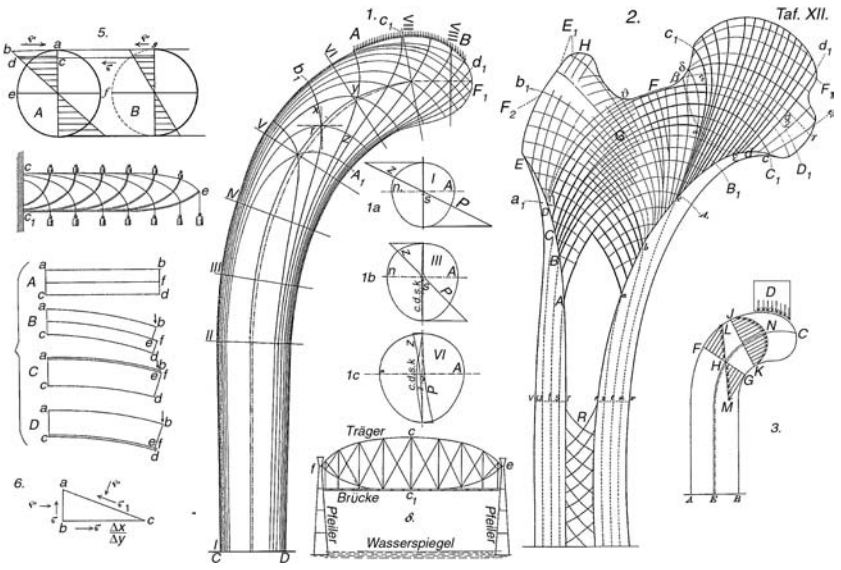

FIGURE 30.1 This is the figure created by Culmannn and von Meyter. Von Meyer's sketch is to the right of the center and Culmann's crane is left of the center. (From von Meyer, G.H., *Arch. Anat. Physiol. Wiss. Med. Reichert DuBois-Reymonds Arch.*, 34, 615–628, 1867.)

There are colorful versions of the origin of the Culmann and von Meyer drawings. Some suggest[7] that the origin of these drawings is a discussion that occurred at a meeting of the "naturforschende Gesellschaft" in Zurich, held in the late summer of 1866. In attendance were von Meyer and Culmann, who was Professor der Ingenieurwissenschaft at the newly created Eidgenössischen Polytechnikum (ETH) in Zurich. Professor Culmann was a leading structural engineering educator and his book on graphical statics,[8] the then standard procedure for structural stress analysis, appeared that year. (The finite-element method is the standard procedure for structural stress analysis today.) von Meyer made a presentation that displayed preparations and his drawings of the cancellous architecture seen in a frontal section of the proximal end of the human femur. Culmann observed that the form of the trabeculae in the proximal femur closely resembled the form of the stress trajectories of a homogeneous and continuous elastic object of the same shape as the bone and loaded in the same way. He made that observation based on his experience with a crane design that was similar in shape to the frontal section of a human femur. Fig. 30.1, taken from Wolff, [9] illustrates the relationship between trabecular architecture and the stress trajectories of Culmann's crane. The Culmann and von Meyer drawings are considered by many to be the origin of what is perceived to be Wolff's law.[4,7,10–12] Dibbets[4] points out that Roux[3] put the Culmann and von Meyer drawings in the modern context of structural adaptation. This observation of Dibbets[4] is consistent with those of other writers.[11,13–16]

In his history of structural analysis in the 19th century, Charlton[17] gives a short biographical sketch of Culmann. It appears that Culmann's involvement with the ideas of structural adaptation in bone was a minor incident in a highly successful professional career. Culmann did not publish any material on this topic, although he published a great deal on graphical statics and a very influential 1851 article on the latest advances in bridge, railway, and river-boat construction in England and the United States. Timoshenko[18] reviewed the numerous contributions of Culmann to mechanics and the theory of structures without mention of his contribution to bone mechanics.

There is no mention of J. Wolff being a party to the creation of the Culmann and von Meyer drawings, although he came on the scene very shortly thereafter. Keith[14] in the 1918 Hunterian Lecture, entitled "On Wolff's Law of Bone-Transformation," delivered before the Royal College of Surgeons (England), noted, "A rapid survey of the first decade of Wolff's professional life will place us in possession of the circumstances which led him up to his discoveries—if discoveries they can be called. He was born in West Prussia in 1836, and studied medicine in Berlin, where he graduated in 1860 at the age of 24." Keith detailed Wolff's studies of bone for the subsequent 30 years. In 1892, when he was 56 years old and had been 31 years in practice, Wolff published his book[1] in which he suggested that von Meyer's representation of the upper end of the femur is incorrect because the trabeculae cross at oblique angles. He declared that the trabeculae cross at right angles, and called himself the discoverer of "orthogonality." According to Keith, Wolff "had an uphill struggle in Berlin; recognition came late to him. In 1890 when he was 54 years of age, he was appointed professor of orthopedic surgery in the University of Berlin. He died in February, 1902, at the age of 66."

Brand and Claes,[16] echoing Keith,[14] wrote:

> With an historical perspective, it is difficult to discern a significant original concept by Wolff. Others (mentioned by Wolff) had noted the order (i.e. similarity of trabecular architecture between the same bone in different persons), had suggested the role of loading in such order, and had even implicated a key role for tension and compression stresses in ordering the trabecular architecture (i.e. the trajectorial theory). Wolff's apparently novel observation that many trabeculae are oriented at right angles under many conditions provided a related and additional (if questionable) supporting piece of evidence, and he documented the functional adaptation of bone in his many unusual specimens, but when all is said and done, Wolff synthesized more ideas from others than formulating his own.… Yet, in fairness, Wolff provided a reasonable summary of ideas at the time, and insofar as he stimulated more debate at the time than all the other researchers combined, he brilliantly succeeded.

This observation is consistent with other literature that suggests that Wolff served as a very effective publicist. Wolff wrote a number of papers[9,19–23] and a book[1] on this subject, which has been translated into English.[2]

Dibbets[4] notes that Wolff's work appeals to contemporary researchers working in the area of bone form–function relations and that some consider his views as "beyond question" or "infallible." Dibbets points out that

> Wolff's work appears to have been based on inadequate understanding of the progress made during the nineteenth century in histology and physiology. And in the (then existing) exceptional climate of swift reform (of biological thought) Wolff appears to have been a master of concealing his rigid thinking in the new nomenclature. The technical terminology he adopted had been polished to near perfection in the course of 25 years of debate. Evaluating the meaning he attached to keywords like "transformation" and "function," it becomes obvious that Wolff's account of the phenomenon of bone growth was different from our current understanding. Moreover, he was not open to advice, let alone criticism. His lectures, sometimes published as transcripts, were aggressive and belligerent toward other scientists, whom he did not hesitate to confront in person with the purpose of ridiculing their views. In his papers he showed more flexibility, and he always found a twist to connect famous names like Virchow, du Bois-Reymond, Roux or Koelliker to his work (most probably to their discomfort; none of these eminent men ever quoted Wolff other than in a rare reference to his drawings or remarkable clinical results).

Dibbets[4] outlines three of the relevant biases of Wolff. First there was Wolff's theory of interstitial growth; Wolff believed that "bone growth was identical to soft tissue growth in that it consisted solely of cell division and accumulation of intracellular material." He therefore rejected bone resorption, which was correctly described earlier as a basic remodeling activity. Wolff published a lengthy lecture "containing a fierce attack on [the man who described bone resorption as a basic remodeling activity]. Wolff was so successful in attacking his opponents that he alone may be held responsible for carrying the incorrect notion of interstitial bone growth through the latter quarter of the nineteenth century into the twentieth century. Wolff battled the concept of remodeling during his entire life."

The second bias of Wolff described by Dibbets[4] is the postulate that compacta contained condensed trabeculae, that the trabecular architecture of bone was determined from genetic rather than epigenetic information. Dibbets notes the paradox in this viewpoint: "Since heredity excludes a dynamic interaction during development, we may wonder how inheritance did relate to function in Wolff's mind." The third bias of Wolff described by Dibbets[4] is related to his use of the word *function*. Dibbets[4] argues "that by function he [Wolff] meant the restoration of the static role of bone, i.e., the support of body weight." Observing that Wolff's use of the word *function* is different from the contemporary usage of the word in this context, a usage due to Roux, Dibbets concludes that Wolff's view of the support of static load as "function" was "indeed very much contrary to Roux's dynamic notion of 'function.'" Dibbets then asks rhetorically, "How then could Wolff use a terminology he did not understand and yet apply it aptly in his book?" The answer, Dibbets suggests on the basis of a footnote in Roux,[3] is that some portions of Wolff[1] were originally planned to be a joint effort with Roux.

It might be gathered from the material cited above that all of these authors said nothing positive about Wolff's work. This is not the case, but the positive comments do not relate to the statement of Wolff's law under discussion here. Dibbets[4] points out the remarkable clinical studies of Wolff as well as the exceptional care in which the manuscript for Wolff[1] was prepared. Wolff's real contributions included experimental investigations[2] of rabbit tibiae (pp. 65 and 68), sheep tibia (p. 66), metacarpal of a calf (p. 67), and his clinical use of "remodeling force" to treat (successfully, it appears) club foot (p. 71). Dibbets[4] echoes the comment of Brand and Claes[16] that Wolff served as a very effective publicist. Dibbets'[4] conclusion regarding Wolff's lack of understanding of contemporary biological thought appears to conflict with a comment of Brand and Claes[16] that Wolff[2] provided "a reasonable summary of ideas at the time." It is likely, however, that Brand and Claes[16] are evaluating Wolff's "reasonable summary of ideas" as the ideas of contemporary orthopedic surgery while Dibbets[4] is evaluating Wolff's summary of contemporary innovative biological thought.

According to Roesler,[24] Wolferman[25] was the first to take up Wolff's ideas and he claimed that the ideas applied for higher vertebrates as well as humans. Roux[26] presented an analysis of the structure of the

cancellous tissue of an ankylosed knee. Roux's analysis was generally accepted as a proof of Wolff's law of the remodeling of bone. Koch[13] accomplished a similar study of a femur. He fully endorsed the ideas of Wolff, concluding, "The trabeculae of the upper femur, as shown in frontal sections, are arranged in two general systems, compressive and tensile, which correspond in position with the lines of maximum and minimum stresses in the femur determined by the mathematical analysis of the femur as a mechanical structure." Koch[13] also concluded, "The thickness and spacing of the trabeculae vary with the intensity of the maximum stresses at various points in the upper femur, being thickest and most closely spaced in the regions where the greatest stresses occur." Further, "the amount of bony material in the spongy bone of the upper femur varies in proportion to the intensity of the shearing force at the various sections." These conclusions echo statements made by Wolff in, for example, Wolff [2] (p. 21): "Nature used the most flexible material and met no restriction concerning the number of tension and compression trabeculae to be built. It made the number of trabeculae dependent upon the loading." Wolff suggests what many people know intuitively, namely, that the magnitude of the load influences the cross-sectional area of the structural elements, but he presented no mathematical statement for this additional suggestion. This suggestion is distinct from the idea that the trabeculae in the cancellous architecture of the real bone coincide with the stress trajectories, because (as will be illustrated below) the magnitude of the applied load can be varied without changing the stress trajectories.

Pauwels[28] reexamined the same knee that Roux studied. The knee had been preserved at the Pathological Institute of the University of Würzburg. Using two-dimensional photoelastic models to determine principal stress trajectories, Pauwels showed that Roux's analysis did not support Wolff's hypothesis. The ankylosed knee studied by Roux had a discontinuous shelf at the knee that disrupted a smooth trabecular architecture. Pauwels[29] obtained another ankylosed knee (Fig. 30.2a), one with smooth exterior surfaces, from the collection at Würzburg, and applied his methods of analyzing stress trajectories to this second knee. Fig. 30.2b shows Pauwels' sketch of the cancellous architecture of the ankylosed knee he considered and Fig. 30.2c shows the stress trajectories in his photoelastic model of the situation. Pauwels indicates that this analysis is a proof of Wolff's hypothesis. Thus, there are in the literature such reports of qualitative verification of the ideas of Wolff. These reports are of the same nature as the Culmann and von Meyer drawings, namely, a visual comparison of the trabecular architecture in a bone with the carefully selected stress trajectories of a loaded homogeneous, isotropic elastic object of similar shape.

30.2.2 Previous Critiques of Wolff's Law

In his historical sketch of bone architecture up to about 1915, Koch[13] notes that Wolff's ideas "have been vigorously assailed on various grounds by many investigators" and he mentions Zschokke,[27] among others. The critique of Keith[14] was mentioned above. However, the interested parties did not agree on a clear and concise statement of Wolff's trajectorial theory. Murray[11] is of assistance in delineating a statement of Wolff's law of trabecular architecture as it was understood by students of this subject up to the mid-1930s. He distinguishes between the "orthodox trabecular theory," which he rejects, and a less rigid theory of trabecular architecture that he accepts. Murray describes the orthodox trajectorial theory of trabecular bone structure as one that regards the trabeculae of bone as embodying the stress trajectories determined from the stress analysis of a homogeneous and continuous elastic object of the same shape as the bone and loaded in the same way. The trabeculae are thus regarded as materialized or sculptured stress trajectories. Stress trajectories are mutually orthogonal families of curves. At any point in the material the tangents to these curves represent the directions of the greatest and smallest of the normal stresses (i.e., forces per unit area in which the force is normal to the unit area). Stresses are representations of the forces acting across surfaces; thus, stress trajectories represent the direction of the action of the largest and smallest forces per unit area at a point. Since tensile stresses are taken as positive and compressive stresses as negative, the typical situation will be a small tensile stress (positive) and a larger compressive stress (negative). Wolff advanced the form of the theory that regarded each trabecula as a materialized or sculptured single stress trajectory. He based the idea on the observations of Culmann regarding von

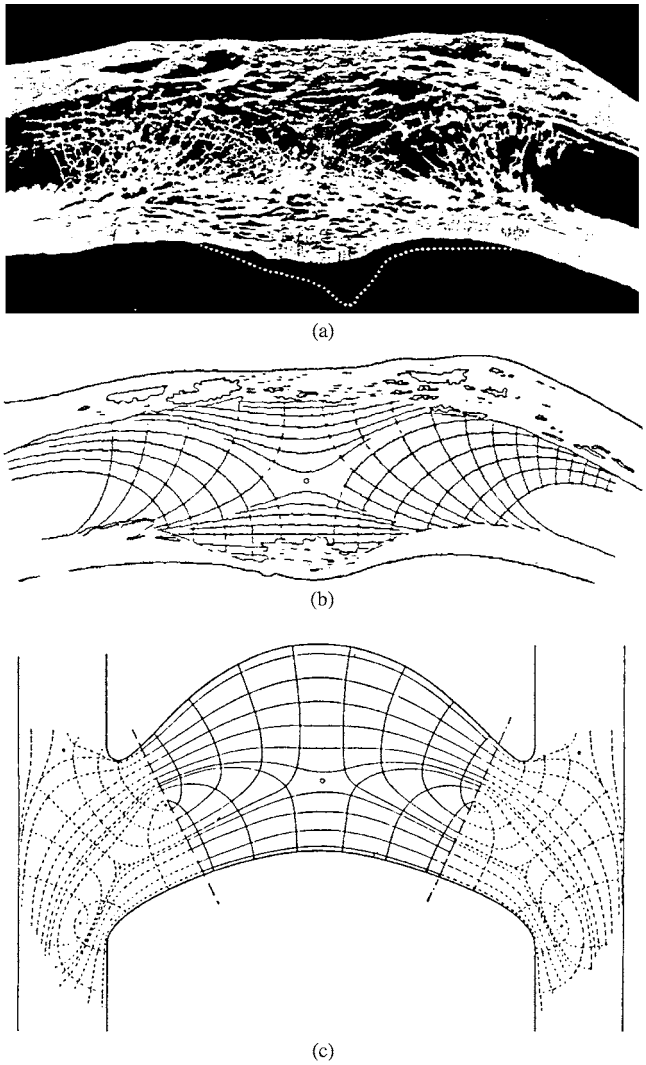

FIGURE 30.2 (a) Cross section of an ankylosed knee. (b) Pauwels' sketch of the cancellous architecture of the ankylosed knee. (c) The stress trajectories in Pauwels' photoelastic model of the situation. (From Cowin, S.C., *Forma*, 12, 247–262, 1997. With permission.)

Meyer's preparations and drawings of cancellous architecture. Murray rejected the idea. In his summary Murray states: "The position taken in this work is not that of the orthodox trajectorial theory."

Trabeculae do not cross at right angles as the orthodox trajectorial theory indicates they should. This and other criticisms of the orthodox trajectorial theory are summarized by Murray. Concerning the orthodox trajectorial theory Murray[11] wrote, "The trabeculae are thought of as drawn in such an ideal and hypothetical foundation, and the theory is intimately bound up with the existence of orthogonal structures in which all the trabeculae must cross one another at right angles, a state of affairs which … is not always found in nature." He noted that Triepel[30] was the most prominent of the trajectorial theory critics, citing twenty objections. Both Triepel and Jansen[7] objected to Wolff's assertion that trabeculae always intersect at right angles. Murray summarized the lively debate that occurred on this issue in the 1920s and 1930s.

It should be noted that Murray[11] employed the word *homogeneous* where this author uses the words *continuous* or *continuum*. Murray was correct to the extent that a discontinuous material, like a porous

sponge, is certainly inhomogeneous. However, from a physical viewpoint he was not sufficiently precise because an inhomogeneous material can be either continuous or discontinuous, and it is really the contrast between continuous and discontinuous and not between homogeneous and inhomogeneous that is the basis of his argument. The important point is that there are no restrictions on the stress concept if a material is continuous but inhomogeneous, but the stress concept is not applicable in a discontinuous material, which is necessarily inhomogeneous. In contemporary engineering terms, the difficulty is that the representative volume element (RVE), the domain that is averaged over, to form a continuum model bone, has a characteristic dimension of about 5 mm. This averaging process eliminates the details of all material structure less than 5 mm. Since all trabeculae are smaller that 5 mm, it is not possible for such a continuum model to predict trabecular orientation.

Currey[31] observes that bone biologists talk about Wolff's "law" because "Wolff, with splendid nineteenth century hubris, called his book 'Das Gesetz der Transformation der Knochen,' and 'Gesetz' means 'law' whichever way you look at it. Wolff set the nomenclatural ground rules and we have obeyed them ever since."

30.2.3 Stress Trajectories

Stress trajectories are constructed for three situations in this section. The purpose of these constructions is to highlight particular properties of stress trajectories. First, the stress trajectories for the classical problem of a cantilever beam subjected to a transverse load at its end are constructed. Then, the stress trajectories in a cruciform shape under two different mechanical loadings are considered. These latter results illustrate the crossing of stress trajectories that occur in trabeculae that cross at angles that are not right angles.

The graphical solution of the problem of a cantilever beam subjected to a transverse load at its end had been obtained by Culmann before 1866.[18] The stress trajectories associated with this problem are very close to the stress trajectories of Culmann's crane; in fact, Roesler[15] presented strong arguments in favor of the view that the illustrations associated with Culmann's name were modifications of these classical cantilever beam stress trajectories. The idea is that the graphical assistant to Culmann morphed (i.e., constructed a graphical morphological transformation of the type possible with current software) the graphical solution of the classical problem of a cantilever beam subjected to a transverse load at its end into the contribution of Culmann to the Culmann and von Meyer drawings.

Consider first a cantilever beam of length L, depth $2c$, and width w that is subjected to a transverse load P at its end (Fig. 30.3). A continuum model for the beam is assumed, a model that is linearly elastic,

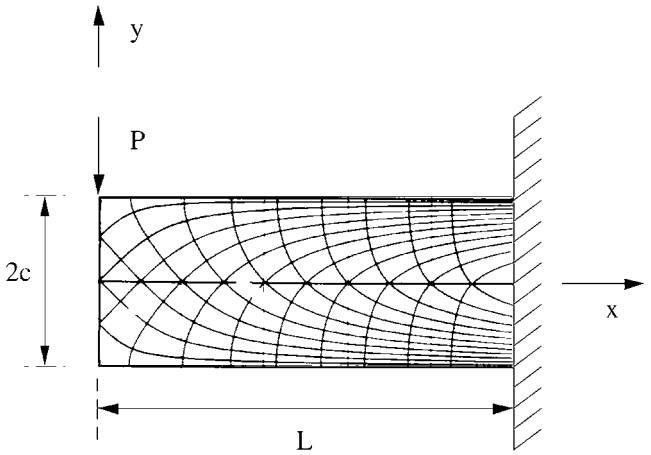

FIGURE 30.3 An illustration of the stress trajectories in a cantilever beam of length L, depth $2c$, and width w that is subjected to a transverse load P at its end. (From Cowin, S.C., *Forma*, 12, 247–262, 1997. With permission.)

homogeneous, and isotropic. The assumption of a continuum means that the properties of the beam vary smoothly from point to point and that there are no holes in the beam. The assumption of homogeneity means that the properties of the beam are the same at every point and isotropy means that the properties that have a directional character are the same in all directions. The problem is one considered in almost all books on the mechanics of materials; the presentation of Beer and Johnson[32] is followed here. The stress in the x direction, σ_x, is given at a point x,y in the beam in terms of the parameters P, c, and w as

$$\sigma_x = (3P/2wc^3)xy, \tag{30.1}$$

and the shearing stress acting in the y direction on the x plane (or vice versa), τ_{xy}, is given at a point x,y as

$$\tau_{xy} = (3P/4wc)[1 - (y^2/c^2)]. \tag{30.2}$$

Since the stress in the y direction, σ_y, is zero everywhere in the beam, the matrix representing the two-dimensional state of stress at a point in the beam is given by

$$\begin{bmatrix} \sigma_x & \tau_{xy} \\ \tau_{xy} & \sigma_y \end{bmatrix} = \frac{3P}{4wc^3} \begin{bmatrix} 2xy & c^2 - y^2 \\ c^2 - y^2 & 0 \end{bmatrix}. \tag{30.3}$$

The principal stresses, that is to say the eigenvalues of the matrix on the right hand side of Eq. 30.3, are given by

$$\begin{bmatrix} \sigma_1 & 0 \\ 0 & \sigma_2 \end{bmatrix} = \frac{3p}{4wc^3} \begin{bmatrix} xy + \sqrt{(c^2 - y^2)^2 + x^2y^2} & 0 \\ 0 & xy - \sqrt{(c^2 - y^2)^2 + x^2y^2} \end{bmatrix}, \tag{30.4}$$

and the ununitized eigenvectors are given by

$$\begin{aligned} \mathbf{e}_1 &= \left(\frac{1}{c^2}\right) (xy + \sqrt{(c^2 - y^2)^2 + x^2y^2})\mathbf{i} + (c^2 - y^2)\mathbf{j}, \\ \mathbf{e}_2 &= \left(\frac{1}{c^2}\right) (xy - \sqrt{(c^2 - y^2)^2 + x^2y^2})\mathbf{i} + (c^2 - y^2)\mathbf{j}, \end{aligned} \tag{30.5}$$

where $\mathbf{i}$ and $\mathbf{j}$ are the unit base vectors of the x, y coordinate system illustrated in Fig. 30.2. It is significant to note that the eigenvectors (Eq. 30.5) depend only on x, y, and c and are independent of the applied load P. The stress trajectories are defined as the orthogonal net of curves that are at each point tangent to the eigenvectors (Eq. 30.5), that is to say, tangent to the principal stress directions. This orthogonal family of curves is determined by the differential equations

$$\frac{dy}{dx} = \frac{xy \pm \sqrt{(c^2 - y^2)^2 + x^2y^2}}{c^2 - y^2}. \tag{30.6}$$

The solutions to the differential equations (Eq. 30.6) passing through the point x^*,y^* are given by

$$
\begin{aligned}
y(x) \;=\; & \left(\frac{x^2 y}{2(c^2 - y^2)} \pm \frac{x\sqrt{(c^2 - y^2)^2 + x^2 y^2}}{2(c^2 - y^2)} \right) \\
& + \left(\frac{2y}{(c^2 - y^2)(-4y^2 \pm \log[xy + \sqrt{(c^2 - y^2)^2 + x^2 y^2}]} \right) \\
& \times (-2y(y^*)(c^2 - y^2) \;+\; (x^*)^2 y^2 \pm (x^*)y\,\sqrt{(c^2 - y^2)^2 + (x^*)^2 y^2}] \\
& \pm \log[(x^*)y + \sqrt{(c^2 - y^2)^2 + (x^*)^2 y^2}] \pm (-2y^2)\log[(x^*)y \\
& + \sqrt{(c^2 - y^2)^2 + (x^*)^2 y^2}] \pm y^4 \log[(x^*)y + \sqrt{(c^2 - y^2)^2 + (x^*)^2 y^2}]).
\end{aligned}
\tag{30.7}
$$

The explicit forms in these results are not important. What is important is that there are two curves, one obtained by taking the plus sign and one obtained by taking the minus sign. The tangents to these two curves are orthogonal to each other at each point in the beam. Last, and most important, there are two curves passing through each point x^*,y^* of the beam. Some of these curves are illustrated in Fig. 30.3; all the curves could not be illustrated because there is a pair passing through each and every point and, if they were illustrated, the space occupied by the beam would appear black.

Consider now a lattice or trellis composed of two sets of rods or flat bars that make angles of 30° with one another. The rods or flat bars merge into one another as they cross, forming a stiff in-plane connection. If the four arms of a cruciform pair of rods or flat bars approaching an in-plane connection are loading axially, then the stress trajectories are those illustrated in Fig. 30.4. However, if the four arms of a cruciform pair of rods or flat bars approaching an in-plane connection are loading by platens that create a moment as well as an axial force, then the stress trajectories are those illustrated in Fig. 30.5. In either case it can be seen that, although the cruciform pair of rods or flat bars do not cross at right angles, the stress trajectories in the rods or flat bars maintain their right angle crossing. Note that the calculation used to determine the stress trajectories in Figs. 30.4 and 30.5 was special in that it was assumed that the RVE, the domain that is averaged over to form a continuum model, was much less than the width of a trabecula. In contemporary orthopedic biomechanics terminology, it was a "tissue level" calculation. In all other calculations of stress trajectories in this chapter, the RVE for trabecular bone has a characteristic dimension of about 5 mm. In contemporary orthopedic biomechanics terminology, these other calculations are all "apparent-level" calculations.

The exercise of constructing the stress trajectories illustrates the following points:

1. A continuum model is assumed. The model is linearly elastic, homogeneous, and isotropic.
2. The stress trajectories, by definition, are orthogonal to one another at a point.
3. Stress trajectories are everywhere dense in a stress field; between any two points there are an infinite number of trajectories.
4. Stress trajectories depend only upon the directions of the maximum and minimum stresses, not on the magnitude of these stresses. In the beam example the stress trajectories are independent of the magnitude of the applied load, that is to say that the formula 30.7 is independent of *P*. In general, the stress trajectories are independent of the magnitude of the applied load, although they can depend upon ratios of loads in the case of multiple loadings.
5. In a lattice or trellis the stress trajectories must always remain inside the elements forming the struts of the lattice or trellis.
6. Although the struts of the lattice or trellis do not cross at right angles, the stress trajectories associated with the struts will always cross at right angles. In particular, it is not necessary for the struts to cross at right angles to have the stress trajectories associated with the struts always cross at right angles.

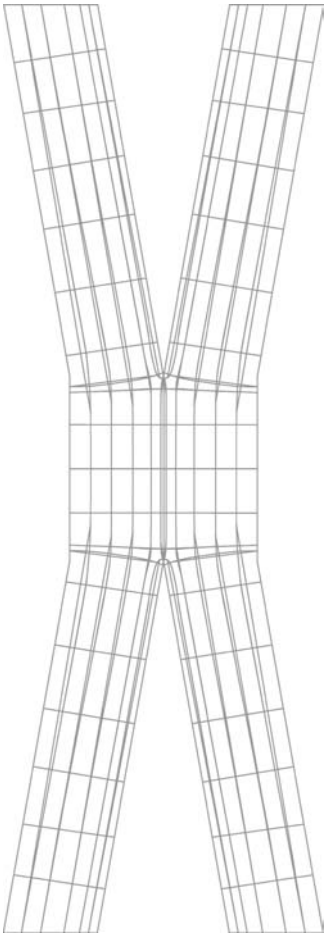

FIGURE 30.4 The stress trajectories in a cruciform pair of rods, flat bars, or trabeculae. The four arms of a cruciform shape are loaded by an axial force in the rods, flat bars, or trabeculae. (From Cowin, S.C., *Forma*, 12, 247–262, 1997. With permission.)

30.2.4 The False Premise

The false premise of Wolff's law of trabecular architecture is that there is a one-to-one correspondence between the stress trajectories of a linearly elastic, homogeneous, isotropic object in the shape of a real bone on one hand, and the trabeculae in the cancellous architecture of the real bone on the other hand, if the elastic model is statically loaded in the same way as the real bone. This premise regards the trabeculae of cancellous bone as embodying the stress trajectories determined from the stress analysis of a homogeneous and continuous elastic object of the same shape as the bone and loaded in the same way.

Stress trajectories and trabecular architecture cannot be related to one another in the manner suggested by this premise. First, for the continuum model it is assumed that bone is linearly elastic, homogeneous, and isotropic while real cancellous bone is clearly not homogeneous and not isotropic. This observation, one of the 20 objections to Wolff's law of trabecular architecture by Triepel,[30] is credited by Roesler[15] to Otto Mohr, the creator of the three-dimensional Mohr's circles representation for stress (the two-dimensional representation for stress, also called Mohr's circle, is actually due to Culmann). Second, there are an infinite number of stress trajectories between two points in the model and a finite number of trabeculae between two points in cancellous bone, so it is impossible to establish a one-to-one

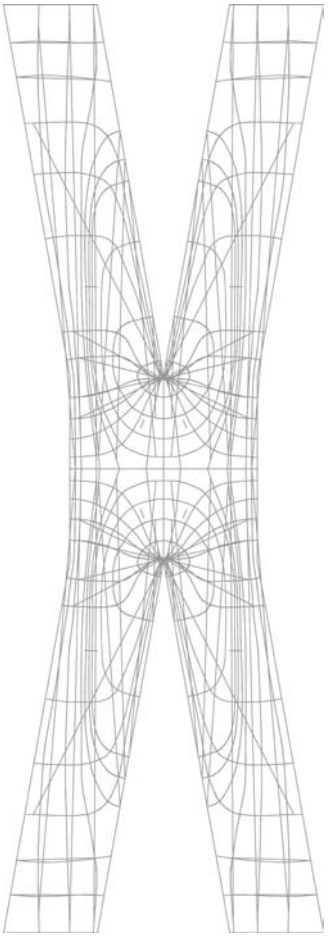

FIGURE 30.5 The stress trajectories in a cruciform pair of rods, flat bars, or trabeculae. The four arms of a cruciform shape are loaded by platens that create a moment as well as an axial force in the rods, flat bars, or trabeculae. (From Cowin, S.C., *Forma*, 12, 247–262, 1997. With permission.)

correspondence between stress trajectories and trabeculae. This is another of the objections of Triepel.[30] Third, bones are subjected to loads that vary in time, not static loads. More importantly, these loads are unknown. Thus, the loads that are to be associated with a trabecular architecture are either ambiguously specified or, if they are specified, they are specified unrealistically as static loads.

The question of trabeculae crossing at right angles has historically been a contentious one with regard to Wolff's law of trabecular architecture. Wolff[1] observed that trabeculae cross at right angles; many subsequent writers dispute this, for example, Triepel.[30] Wolff and other proponents of Wolff's law of trabecular architecture have argued that, since stress trajectories cross at right angles, trabeculae should cross at right angles, implying that trabeculae crossing at right angles is an indication of the validity of Wolff's law of trabecular architecture. To assume that the question of trabeculae crossing at right angles is of any significance for bone mechanics or bone biology assumes the basic false premise of the law of trabecular architecture. The answer to the question further exposes the false premise. From the material on stress trajectories in the previous section it is easy to see that, for a lattice, trellis, or cancellous bone, since the cross-sectional areas of the rods, struts, or trabeculae are finite, there are an infinite number of stress trajectories in each rod, strut, or trabecula. From Figs. 30.4 and 30.5 one can see that, although the struts of the lattice, trellis, or trabeculae cross at angles of 30°, for these two different loadings the stress trajectories associated with the struts will always cross at right angles. Thus, one concludes that the entire verbose and

long-lasting debate on this question was an invalid consequence of the false premise. The false premise permits only one stress trajectory per trabecula, whereas there are, in fact, infinitely many.

The reason the false premise has been accepted by so many for so long is due to the very convincing visual comparison one sees in the Culmann and von Meyer drawings (Fig. 30.1). This point was made by Murray.[11] The Culmann and von Meyer drawings and the associated story of Wolff's law of trabecular architecture make a good tale, one that people remember. In spite of much criticism since its introduction, the figure and story survive in the serious technical literature[10] as well as in current popular literature.[33] The visual comparison one makes in the Culmann and von Meyer drawings (Fig. 30.1) is something like an optical illusion. In the visual comparison, the mind's eye neglects the fact that (1) the real bone is highly porous and the model is homogeneous in density and (2) that the stress trajectories are infinite in number and only a selected few are illustrated. The overlooked contradiction is that the stress analysis assumes continuity and the visual inspection assumes discontinuity, on the same length scale.[5,34*]

30.3 Toward Resolution

30.3.1 The Resolution Length Restriction on the Trajectorial Theory

In his summary, Murray[11] wrote, "The trajectorial theory in its original and most rigid form played a useful part in calling attention to the relation which obviously does exist between bony structures and patterns of stress, but like many theories it went too far when it claimed all power for its own particular factor and neglected all others. It requires, not rejection, but dilution." Oxnard and Yang[12] suggested the dilution of the trabecular architecture theory in the following way: "The general theory thus need not be abandoned if it is supposed that the association between stress and architecture is one between an averaged orthogonal architecture that is associated with an averaged orthogonal network of stresses." Most, but not all, modern students of the functional adaptation of bone have rejected the rigid orthodox theory of Wolff and adapted suggestions along the lines of Murray[11] and Oxnard and Yang.[12] Cowin[34] suggested that the key to the dilution recommended by Murray[11] and Oxnard and Yang[12] lies in the establishment of the length scale on which bone can be considered as a continuous material. This establishes the length scale over which material properties are to be averaged. It is only at that length scale, and at no smaller length scale, that principal stress trajectories can be compared with real trabecular architecture. The minimum of this length scale should be greater than or equal to the minimum length scale for which the concept of stress is applicable when trabecular bone is considered as a continuum. This length should be at least several trabecular widths. It has been observed that the precise length is dependent on the stress gradient; specifically, Harrigan et al.[35] suggest that, if the results of a stress analysis "vary by more than 20–30% over a distance spanning three to five trabeculae, the results are suspect."

The *resolution length restriction* for the trajectorial theory suggested is that the trabecular architecture of bone follows the principal stress trajectories only for length scales equal to or larger than the length scale on which trabecular bone can be considered as a continuous material for the purpose of stress analysis. This restriction protects the trajectorial theory from the contradiction with nature embodied in the interpretations Murray called the orthodox theory, but it preserves the basic idea of the trajectorial theory.

It is not clear, however, that there exists a practical length scale on which trabecular bone can be considered as a continuous material for the purpose of stress analysis. A length scale greater than several

*The pattern of stress trajectories in beams with transverse loads (that is, not subjected to pure bending) enjoys a topological invariance of form. Note that the forms of the stress trajectories in the cantilever beam (Fig. 30.3) are independent of the magnitude of the load that creates them and that the general shape of the stress trajectories is invariant under changes in the depth and length of the beam. Thus if Fig. 30.3 were drawn on a rubber sheet, the sheet could be uniformly extended in either cardinal direction to provide a picture of the stress trajectories in a beam of the new length and new depth. It is also to be noted that beams loaded in different manners also lead to a system of stress trajectories similar to those in Fig. 30.3. For example, the stress trajectories in a simply supported and uniformly loaded beam are similar to those in Fig. 30.3, as one can see from an illustration in Koch.[13]

centimeters is impractical, and one of the order of 1 cm is of limited usefulness. If the resolution length restriction for the trajectorial theory is of the order of 1 cm, then the resulting continuum theory will be of little use in the stress analysis of cancellous bone tissue, as a contiguous volume of cancellous bone often has a dimension less than 1 cm. In effect this means that cancellous bone must be considered as a structure and not a material. An answer to this question of the appropriate length restriction for cancellous bone should come from a greater refinement of its length scales using quantitative stereology and texture analysis.[36] An important question that will be answerable soon is the following: For purposes of stress analysis, must cancellous bone be considered as a structure or as a material?

30.3.2 Abandoning the Use of Wolff's Name or the Use of the Word *Law* or Both

In a critical review, entitled "The Law of Bone Transformation: A Case of Crying Wolff," Bertram and Swartz[37] write:

> [W]e believe that future progress in the study of bone structure and function will require the removal of certain conceptual blinders associated with such a well-accepted but weakly supported paradigm [Wolff's law]; because of this, we believe that careful criticism of some currently accepted concepts is timely and appropriate. We find that the general assessment of the functional and adaptive behavior of bone that is often cited in the introductory paragraphs of new research papers is actually based in part on poorly supported presumed "facts" and the interpretation of the results of previous work that have been passed from paper to paper without receiving adequate critical appraisal. Solutions to the major problems of bone biology require a firmer foundation; a foundation that is especially important given that investigators seeking detailed answers at the cellular and molecular levels of bone physiology may be unfamiliar with the organismal phenomena they seek to explain.

The paper of Bertram and Swartz[37] is constructive in indicating that Wolff's law in its present form is a mantra and not a statement that would pass muster in either the biological sciences or the physical sciences. The use of the phrase "Wolff's law" is an inappropriate suggestion that the concept is a concrete result generally accepted by the scientific community. It implies a dignity that the concept has not achieved. In reality, the exact meaning of Wolff's law, other than that it is a synonym for the functional adaptation of osseous tissue, is uncertain. There is no generally accepted physiological model for Wolff's law.* Other laws or models of physiological phenomena that have been presented since Wolff first presented his have become established pillars of physiology, for example, the Hodgkin–Huxley theory of nerve membranes or the sliding filament model of muscle behavior. These physiological models relate well-defined (and generally measurable) quantities to one another by well-defined and measurable parameters; they unify a whole host of initially apparently disparate facts. More importantly, these physiological models are accepted by the physiology community.

Bertram and Swartz[37] suggest that the community of bone researchers may be looking at a number of different phenomena and labeling them as Wolff's law. If the builders of adaptive bone remodeling models focused on one aspect of the different phenomena labeled as Wolff's law, it would be on the computational prediction of bone remodeling about an implant. The rationale for computational modeling of the bone adaptation process stems principally from the fact that the problem of the long-term stability (10 years and longer) of structural bone implants, e.g., the total hip, has not been satisfactorily solved. To solve this problem it is possible that only a phenomenological version of Wolff's law is needed; this would appear to be a lesser standard than a physiological model. That is to say, one does

*A proposed mathematical formulation[38,39] of Wolff's law in the average or diluted sense recommended by Murray[11] and by Oxnard and Yang[12] contains many parameters that have not been measured and will be difficult to measure. It is a phenomenological model and not a physiological model. For the discussion of phenomenological models, see the following chapter by Hart. For the discussion of possible physiological models, see the preceding chapter.

not need to know how it works, one only needs to be able to predict what would happen. Many celestial movements were predictable centuries before Newton explained why. The other clinical problems that are associated with Wolff's law, namely, the search for strategies to overcome osteoporosis as well as the bone loss induced by the exposure to microgravity, will probably require a physiological model.

Any experiment to verify any form of a functional adaptation rule for bone will be difficult and expensive; it must be done *in vivo* and a knowledge of the strain, elastic constants, bone shape, and bone histology changes must be recorded as a function of time in the experiment. The elevation of a functional adaptation rule for bone to the status of the Hodgkin–Huxley theory of nerve membranes or the sliding filament model of muscle behavior is not on the horizon. This review has led the writer to see the merit in the suggestion of some that "Wolff's law" be renamed "Roux's law." It does appear that what is understood today as Wolff's law is closer to the writing of Roux than to that of Wolff. However, Currey[31] points out that "laws" in biology should be employed very sparingly, because of the contingency of life; on the other hand "theories" can be used more freely. Thus, one would speak of Roux's "theory." Another suggestion is to abandon eponyms altogether. As the term *osteon* is now used widely in place of *Haversian system* in an effort to remove eponyms from anatomy, perhaps the functional adaptation rule for bone should receive a noneponymic descriptive name like the "sliding filament model" for muscle behavior. One could speak of tissue adaptation to environmental strain, but that is too long a phrase. If the use of eponyms is avoided perhaps some other nomenclatures for this type of functional adaptation will emerge. However, the problem is not the lack of a reasonable terminology, but the lack of an acceptable theory for the functional adaptation of bone.

References

1. Wolff, J., *Das Gesetz der Transformation der Knochen,* Hirschwald, Berlin, 1892.
2. Wolff, J., *The Law of Bone Remodelling,* Springer, Berlin, 1986.
3. Roux, W., Beiträge zur Morphologie der funktionellen Anpassung, *Arch. Anat. Physiol. Anat. Abt.*, 120–185, 1885.
4. Dibbets, J. M. H., One century of Wolff's law, in *Bone Biodynamics in Orthodontic and Orthopaedic Treatment,* D. S. Carlson and S. A. Goldstein, Eds., Craniofacial Growth Series, Vol. 27, University of Michigan, Ann Arbor, 1992, 1–13.
5. Cowin, S. C. The false premise of Wolff's law of trabecular architecture, *FORMA*, 12, 247–262, 1997.
6. von Meyer, G. H., Die Architektur der Spongiosa, *Arch. Anat. Physiol. Wiss. Med. Reichert DuBois-Reymonds Arch.,* 34, 615–628, 1867.
7. Jansen, M., *On Bone Formation—Its Relation to Tension and Pressure,* Longmans, Green & Co., London, 1920.
8. Culmann, K. *Die Graphische Statik,* Verlag von von Meyer & Zeller, Zurich, 1866.
9. Wolff, J., Über die innere Architektur der Knochen und ihre Bedeutung für die Frage vom Knochenwachstum, *Arch. Pathol. Anat. Physiol. Klin. Med. (Virchov's Arch.)*, 50, 389–453, 1870.
10. D'arcy Thompson, W., *On Growth and Form,* Cambridge University Press, Cambridge, 1942.
11. Murray, P. D. F., *Bones—A Study of the Development and Structure of the Vertebrate Skeleton,* Cambridge University Press, Cambridge, 1936.
12. Oxnard, C. E. and Yang, H. C., Beyond biometrics: studies of complex biological patterns, *Symp. Zool. Soc. Lond.,* 46, 127–167, 1981.
13. Koch, J. C., Laws of bone architecture, *Am. J. Anat.,* 21, 177–298, 1917.
14. Keith, A., Hunterian lecture on Wolff's law of bone-transformation, *Lancet*, 16, 250–252, 1918.
15. Roesler, H., The history of some fundamental concepts in bone biomechanics. *J. Biomech.,* 20, 1025–1034, 1987.
16. Brand, R. and Claes, L., Review of the English translation of the book *The Law of Bone Remodelling* by J. Wolff, *J. Biomech.,* 22, 185–187, 1989.
17. Charlton, T. M., *A History of the Theory of Structures in the Nineteenth Century*, Cambridge University Press, Cambridge, 1982.

18. Timoshenko, S. P., *History of Strength of Materials*, McGraw Hill, New York, 1953.
19. Wolff, J., Über die Bedeutung der Architektur der spongiösen Substanz, *Zentralbl. Med. Wisse.,* VI. Jahrgang, 223–234, 1869.
20. Wolff, J., Beiträge zur Lehre von der Heilung der Frakturen, *Arch. Klini. Chir. (v. Langenbecks Arch.)*, 14, 270–312, 1872.
21. Wolff, J. Zur Knochenwachstumsfrage, *Arch. Pathol. Anat. Physiol. Klini. Med. (Virchovs Arch.)*, 61, 417–456, 1874.
22. Wolff, J., Das Gesetz der inneren Transformation der Knochen bei pathologischen Veränderungen der äusseren Knochenform, *Sitzungsber. Preuss. Akad. Wisse. Berlin,* 22, 475–496, 1884.
23. Wolff, J., Über die Theorie des Knochenschwundes durch vermehrten Druck und der Knochenanbildung durch Druckentlastung, *Arch. Klin. Chir. (v. Langenbecks Arch.)*, 42, 302–324, 1891.
24. Roesler, H., Some historical remarks on the theory of cancellous bone structure (Wolff's law), in Cowin, S.C., Ed., *Mechanical Properties of Bone,* American Society of Mechanical Engineers, New York, 1981.
25. Wolfermann, H., Beitrag zur Kenntnis der Architektur der Knochen, *Arch. Anat. Physiol. Wisse. Med. (Reichert DuBois-Reymonds Arch.),* 39, 312–346, 1872.
26. Roux, W., *Gesammelte Abhandlungen uber die Entwicklungsmechanik der Organismen,* W. Englemann, Leipzig, 1885.
27. Zschokke, E., *Weitere Untersuchungen über das Verhältnis der Knochenbildung zur Statik und Mechanik des Vertebraten Skelettes,* Art. Institut Orell Füssli, Zurich, 1892.
28. Pauwels, F., Kritische Überprufung der Roux'schen Abhandlung, Beschreibung und Erläuterung einer knöchernen Kniegelenksankylose, *Z. Anat. Entwgesch,* 117, 1954; *Gesammelte Abhandlungen zur funktionellen Anatomie des Bewegungsapparates,* Springer, Berlin, 1965 (translated by P. Maquet and R. Furlong, *Biomechanics of the Locomotor Apparatus,* Springer, Berlin, 1980).
29. Pauwels, F. *Biomechanics of the Locomotor Apparatus,* Springer, Berlin, 1980.
30. Triepel, H., *Die Architekturen der menschlichen Knochenspongiosa,* Verlag der J. F. Bergmann, Munich, 1922.
31. Currey, J. D., Was Wolff Correct? *FORMA,* 12, 263–266, 1997.
32. Beer, F. P. and Johnson, E. R., *Mechanics of Materials,* 2nd ed., McGraw-Hill, New York, pp. 443–445, 1992.
33. Willis, D., *The Sand Dollar and the Slide Rule,* Addison-Wesley, Reading, MA, 1995.
34. Cowin, S. C., A resolution restriction for Wolffs law of trabecular architecture, *Bull. Hosp. Joint. Dis. Orthop. Inst.*, 49, 206–213, 1989.
35. Harrigan, T. P., Jasty, M., Mann, R. W., and Harris, W. H., Limitations on the continuum assumption in cancellous bone., *J. Biomech.,* 21, 269–276, 1988.
36. Bay, B., Texture correlation: a method for the measurement of detailed strain distributions within trabecular bone, *J. Ortho. Res.*, 13, 258–267, 1995.
37. Bertram, J. E. A. and Swartz, S. M., The law of bone transformation: a case of crying Wolff *Biol. Rev.*, 66, 245–273, 1991.
38. Cowin, S. C., Wolff's law of trabecular architecture at remodeling equilibrium, *J. Biomech. Eng.,* 108, 83–88, 1986.
39. Cowin, S. C., Sadegh, A. M., and Luo, G. M., An evolutionary Wolff's law for trabecular architecture, *J. Biomech. Eng.,* 114, 129–136, 1992.

31

Bone Modeling and Remodeling: Theories and Computation

Richard T. Hart
Tulane University

31.1 Introduction

Ever since 1892, when Julius Wolff stated that "Every change in the ⋯ function of bone ⋯ is followed by certain definite changes in ⋯ internal architecture and external conformation in accordance with mathematical laws,"[1,2] investigators have sought to formulate and test mathematical rules to simulate the adaptation of bone to its various functions. Often these investigations have focused upon mechanical functions, but some also encompass "biological functions"—including mineral homeostasis, development and growth

processes, age-related changes, and hormonal influences. The common motivating factors for the theoretical and computational modeling efforts are, first, to understand and quantitatively *describe* the functional adaptation of bone, then to simulate and *predict* bone adaptation, and finally to simulate the effects of manipulations to the processes—in the hopes of testing ideas that may be therapeutically beneficial.

The study of bone—a unique living structural material—requires an interdisciplinary approach to understand and quantify its various functions and adaptations. Continued progress will depend upon approaches that blend principles and experiments in mechanics, cell biology, and biochemistry, and also incorporate clinical problems and findings. This chapter seeks to introduce and summarize the work being done to provide quantitative models of adaptive bone behavior due to mechanical function, and the computational implementation of some of these models.

This chapter is organized as follows. First, a description of important general concepts and assumptions incorporated into various adaptation models is presented, along with mechanics and computational implementation issues. Next, a series of theoretical models for describing the functional adaptation of cortical bone is presented, including example applications. A similar section for trabecular bone models and example applications follows. The chapter concludes with a general discussion and conclusions.

31.2 General Concepts and Assumptions for Adaptation Simulations

The functional adaptation of bone to mechanical usage implies the existence of a physiological control process. Essential components for the control process include sensors for detecting mechanical usage and transducers to convert the usage measures to cellular responses. The cellular responses lead to gradual changes in bone shape and/or material properties and, once the structure has adapted sufficiently, the feedback signal is diminished and further changes to shape and properties are stopped. Although this description is certainly incomplete—for example, it ignores the nonmechanical factors in the control process—the described steps must be present for the observed mechanical adaptation to occur. A schematic of this feedback control process is shown in Fig. 31.1.[3,4] Although simplified, it captures key features of the process, and raises practical questions for the development and implementation of theoretical models for bone adaptation: What is the specific nature of

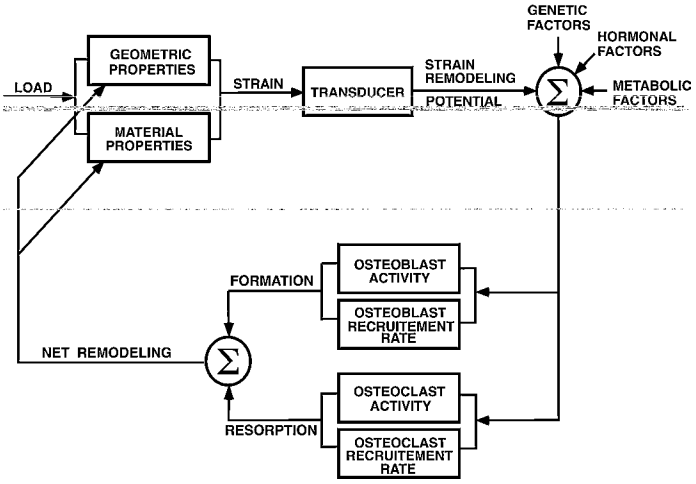

FIGURE 31.1 A schematic of the adaptive feedback process of bone. Mechanical strain, determined by loading, geometry, and material problems is transduced (e.g., streaming potentials). The mechanical function is coupled with nonmechanical factors (e.g., genetic, metabolic, hormonal) and combine to influence cell activity and number. The net formation or resorption is manifested as changes in bone geometry and/or material properties. (Redrawn from Hart, R. T., Ph.D. dissertation, Case Western Reserve University, Cleveland, 1983. With permission.)

the mechanical usage that is sensed? Is the spatial variation of the signals important? Is the temporal variation of the signals important? Is the process of adaptation—including the intermediate steps—of primary interest for the model, or is the goal of the adaptation of most interest? Is the adaptive process everywhere the same, or is there a dependence on specific bones and specific locations?

These fundamental questions are framed by the following sections that discuss *control* of the adaptive response, *mechanical signaling* to initiate adaptation—including site and time dependence, *transduction* of the mechanical signals, the *adaptive* effects, and *classification* of model types.

31.2.1 Control of the Adaptive Process

Many of the theoretical models use the concept of an error signal to drive the adaptation process. As pointed out by Roesler[5] the concept of an error-driven control of the net bone remodeling process was present as early as 1858 in the work of Roux and also in 1881 in Hunter's work. Implicit in the use of an error-driven theory is the assumption that there exists some "remodeling equilibrium" condition in which the mechanical environment of bone tissue is suitably adapted and not undergoing a process of net deposition or resorption. Only deviations in the mechanical environment from this "remodeling equilibrium" condition would initiate net remodeling activity. Some models have used a single value to represent the mechanical remodeling equilibrium state; others have used the concept of a minimum signal or a "lazy" zone to represent a range of values for which the bone would also be quiescent.[6–8]

31.2.2 Mechanical Signaling to Initiate Adaptation

To model the adaptive response, the salient features of the mechanical use that influence bone to respond must be identified. Specifically, there must be physically measurable manifestations of the changed loading that can be detected and which provide the stimuli to bone cells for modification of bone architecture. Cowin[9] argues that the stimulus is based on strain—a primary and directly measurable physical quantity representing local deformation—and not the stress, which is a well-defined but not directly measurable quantity.[9] More generally, the mechanical stimulus almost certainly depends upon some aspect of the "strain history"—a concept that incorporates all aspects of time-dependent, local deformation measures. Included under this general description would be many of the specific stimuli that have been proposed as important regulators of functional adaptation: peak strain, $E_{\max}$, strain rate, $\dot{\mathbf{E}}$, average strain, E_{avg}, spatial strain gradients, $\partial \boldsymbol{E}/\partial \boldsymbol{x}$, and strain energy density, U, defined (also see Chapter 6) as

$$U = \frac{1}{2}\lfloor \mathbf{T} \rfloor \{\mathbf{E}\} \qquad \text{or, since } \lfloor \mathbf{T} \rfloor = \lfloor \mathbf{E} \rfloor [\mathbf{C}]^T, \qquad U = \frac{1}{2}\lfloor \mathbf{E} \rfloor [\mathbf{C}]^T \{\mathbf{E}\}. \tag{31.1}$$

As seen in Eq. 31.1, the strain energy is proportional to the strain, specifically the square of the strain tensor. It has been used as the mechanical stimulus in several adaptation models, although Sadegh et al.[10] argue that it may be unnecessarily restrictive because the nature of the mechanical usage that can be detected by physiological processes is not yet well understood. In efforts to "linearize" the quadratic nature of the strain energy, two variations of the strain energy have also been proposed for the stimulus. In one, an "energy stress" is defined[11,12] as

$$\sigma_{\text{energy}} = \sqrt{2E_{\text{avg}}U}, \tag{31.2}$$

where E_{avg} is the average elastic modulus. A similar parameter has also been developed that addresses a limitation present for both the strain energy density and the "energy stress"—they are both always positive. The "mechanical intensity scalar," $\hat{E}$, is defined[13] as

$$\hat{E} \equiv \Lambda \cdot U^{1/2}, \tag{31.3}$$

where $\Lambda \equiv$ sign of $(E_{11} + E_{22} + E_{33})$ and U is the strain energy density. Thus, $\hat{E} < 0$ indicates volumetric shrinking (e.g., compression) and $\hat{E} > 0$ indicates swelling (e.g., tension), but the magnitude is a scalar that is dependent upon all components of the strain tensor.

In addition to the strain-based measures, the von Mises equivalent stress has been used as a mechanical stimulus for some bone adaptation models. The von Mises stress is a scalar measure of the stress at a point and, for isotropic materials, represents the portion of the strain energy associated with distortion. The von Mises stress, σ_0, is defined in terms of the principal stresses σ_1, σ_2, and σ_3, as

$$\sigma_0 = \sqrt{\frac{1}{2}[(\sigma_1 - \sigma_2)^2 + (\sigma_2 - \sigma_3)^2 + (\sigma_3 - \sigma_1)^2]}. \tag{31.4}$$

Unfortunately, the von Mises stress loses its physical meaning for anisotropic materials because σ_0 no longer represents the distortional portion of the strain energy for bone.[14]

Finally, as an alternative to the strain- or stress-based measures, a possible mechanical manifestation of function that leads to bone adaptation is the local damage of bone.[15] In that case, damage in the form of microcracks is repaired so that functional adaptation might be considered as a special case of the general fracture repair process of bone. This approach, however, begs the question: What is it that bone senses to signal the initiation and coordination of bone fracture repairs?

31.2.2.1 Site Dependence

Obviously, different bones provide different mechanical functions—the structural support provided by bone tissue in the femur is fundamentally different from the structural protection provided by bone tissue in the skull. Likewise, the biological environment for different sites of the same bone varies—the population of cells and nutrients at the periosteal surface of a long bone is different from the cells and nutrients at the endocortical surfaces. Frost[16] summarizes these differences by describing four different bone "envelopes"—trabecular, periosteal, endocortical, and osteonal—that represent fundamentally different biological environments. Based on these various "biological initial conditions," the adaptation response of bone within these four bone envelopes could be expected to be different, both in terms of the "remodeling equilibrium" values, and the speed of the cell-mediated adaptive responses. Given this degree of site dependence, is it reasonable to assume an even greater degree of site specificity for the adaptation response? For example, knowing that the mechanical environment at the periosteal surface on the medial side of the femur is much different than that at the lateral side, is it reasonable to assume that their adaptation to a changed mechanical environment would be the same? How about the adaptation of osteons at the midpoints of the cortical bone on opposite sides of the femur (e.g., medial and lateral)? Is it reasonable to assume that each and every site must be regarded as unique? Is it reasonable to assume that the response is completely independent of site?

Valid answers to these questions will depend upon experimental investigation of the similarities and differences between populations of like cells, e.g., osteoblasts. As more techniques from mechanics, genetics, and cell and molecular biology are refined, it may become possible to quantify the local mechanical environment, as well as the genetically determined site specificity that may be inherent in the cell functions. Nonetheless, current modeling efforts for bone adaptation require assumptions about the degree of "site dependence." As discussed by Cowin,[17] "any remodeling rate equation can be presented in site-specific form or a non-site-specific form," but choices are made in their implementation, and will be explored in subsequent sections.

31.2.2.2 Time Dependence

Another challenge in the study of functional adaptation comes from the multiple timescales needed to describe the phenomena involved. For example, shape adaptation resulting from *in vivo* ulnar osteotomy experiments shows continued adaptive responses for months.[18,19] In contrast, the individual mechanical loading cycles that the adapting radius experiences are on the orders of seconds for normal gait, and recent experimental evidence points to high-frequency (approximately 25 Hz), small strains as being important determinants of skeletal mass.[20,21] Also, as determined from experiments with the isolated turkey ulna model, Rubin and Lanyon[22] show that when large external forces are imposed, only four cycles of load a day are sufficient to prevent the loss of bone observed when no other mechanical loading cycles are applied, with only 36 cycles required to generate substantial bone addition. Modeling

these mechanical stimuli—which occur on the order of seconds or tenths of a second, including information about the loading repetitions and frequency, and accounting for changes that take place over a period of weeks or months—is a challenge. It may be that a hierarchical approach to the time dimensions will be necessary, mirroring approaches now being employed for large variations in spatial dimensions.

In addition, the concept of a "fading memory" for the mechanical strain history may be needed to model the time-dependent effects because it seems that the more recent events in the loading environment of the bone are more important than events far into the past. Presumably, those far-off past events have already stimulated the bone to initiate the appropriate functional adaptation responses. Alternatively, cells may gradually become accommodated to a changed mechanical environment.[23] If so, the accommodation implies not only a diminishing response with time, but also a possible mechanism for the existence of a "lazy zone" and a redefined "remodeling equilibrium."

31.2.3 Transduction of the Mechanical Signals

In 1981, Treharne[24] presented a comprehensive overview of the ideas that had been proposed for the mechanisms by which the bone tissue transduces the mechanical strain to adaptive responses. He summarized many references that investigated: the piezoelectric properties of collagen; changes in solubility of hydroxyapatite with load; fatigue microfracture damage and repair; hydrostatic pressure of extracellular fluid influences on bone cells; hydrostatic pressure influences on the solubility of both the mineral and collagenous components of bone; the creation of streaming potentials; and finally the direct response of cells to mechanical loading.

Since 1981, many new techniques have been developed for the study of cell mechanics, the mechanical and chemical stimuli that influence cell behavior, the adhesion of cells, and streaming potentials as reviewed by Cowin et al.[25] In particular, a strong case is made for fluid flow in the bone canaliculi as being the source of strain-generated potentials[26] that may affect the membranes of osteocytes, with the signal propagating via gap junction connections with other osteocytes, osteoblasts, and bone-lining cells.

It is not yet clear which one or combination of these mechanisms is primarily responsible for converting mechanical usage to cellular activities (see Chapter 28 for a thorough description of one mechanistic model). Despite these uncertainties, simulation models require assumptions about the mechanical stimulus and are often simply cast in terms of portions of the strain or stress history. Thus, they do not generally address the crucial steps involved in the transduction of the mechanical signals to cellular stimuli and responses although they may help guide future experimental investigations.

31.2.4 Adaptive Effects: Closing the Feedback Loop

A remaining question is how the addition or removal of bone tissue helps to achieve an adapted structure—that is, how are the stress and strain influenced by the net remodeling activity. Gjelsvik[27,28] formulated a postulate regarding the stress state of the newly deposited bone that is implicitly presumed in most models. He assumed that new and old bone would be stressed the same way. Thus, if the bone was unloaded, the stress in both the new and old bone would be zero; otherwise, both new and old bone would contribute to sharing the load. This conclusion was made based on the description by Frost[29] of the two stages in which bone is laid down: deposition of a scaffold of low-modulus, unmineralized bone followed by mineralization of the scaffold. Gjelsvik's argument about the stress state of the new bone is as follows: if the elastic modulus of the newly deposited, unmineralized material is very small (when compared with the existing bone at the surface), then the new surface layer will be strained in the same amount as the underlying bone layer, but will experience very little stress. As the material stiffness is increased during the calcification process, the stress increases so that the new and old bone are stressed in the same way. This seems most plausible when the different timescales for loading and adaptation are considered. Thus, the feedback loop is closed for the error-based control models because the adapted shape and material properties directly determine the strains and stresses—the stimuli generally considered to drive the adaptive changes.

31.2.5 Model Classification: Optimization, Phenomenological, and Mechanistic

The models that have been developed for simulating the functional adaptation of bone can be classified into three distinct groups that have different goals and modeling approaches. They are optimization, phenomenological, and mechanistic modeling. Each approach has led to new understanding of bone function and adaptation, yet each has limitations.

The application of optimization theory to study the adaptation of bones shows a variety of interesting consequences to the global starting assumptions (e.g., bone adapts to minimize mass; or bone maximizes strength; or bone eliminates notch stresses). These studies give insight into bone as a mechanical structure—and may be especially relevant for simulating evolutionary adaptation. However, when they are applied to an individual's skeletal adaptation, three major deficiencies become apparent.

First, optimization assumes that the adaptation not only seeks to achieve a stated goal (e.g., minimize mass, maximize strength) but that there are physiological processes in place that are directed toward achieving the stated goals. This assumption implies a high level of coordination and environmental awareness without a strong foundation of evidence. Second, implementation of optimization strategies focuses upon achievement of adaptive goals, but not upon the physiological process of the adaptation. Therefore, they are ill-suited to providing strategies that can develop and address questions to advance understanding or manipulation of adaptive processes. Third, by subscribing to an objective strategy to study bone adaptation, fundamental questions—including the degree of site and time dependence—cannot be critically investigated.

Consequently, the majority of bone adaptation models have been phenomenological—they seek to describe the stimulus and the response quantitatively, and are useful in developing simulations and predictions of bone adaptation. These models are particularly useful for engineering studies motivated by the desire to be able to design bone implants that will achieve interfaces with surrounding bone tissue that are initially stable and remain so. In addition, these models may provide useful clinical guidance for treatment of a variety of metabolic bone diseases such as the loss of trabecular bone tissue in postmenopausal women or to manipulate the role of tissue generation and consolidation in the fracture repair process. Thus, the development and computational implementation of phenomenological models may be sufficient for describing and predicting the adaptive bone consequences based on changed mechanical loading to improve implant design or to treat some patients.[30] However, phenomenological models do not directly contribute to understanding of the biological basis and process of functional bone adaptation. There is also a need to elucidate the interplay of genetics, hormones, drug therapy, and the mechanical environment. This level of understanding requires a mechanistic approach that goes beyond the cause-and-effect-based phenomenological models and instead seeks a detailed understanding of the steps and chemical and biological mechanisms involved in changing bone properties and architecture.[30] Further progress will depend upon close coupling of model hypotheses with quantitative experiments to test their validity.

31.3 Mechanics and Computational Issues

A number of different models and computational techniques have been proposed for simulating net bone remodeling. To organize the models so that the similarities and differences can be objectively examined and compared, it is useful first to develop general descriptions and also to describe the two different mechanical points of view for simulating functional adaptation.

A continuum point of view may consider functional adaptation as a coupled "free-boundary-value problem" (a free boundary has the potential to move, as opposed to a fixed boundary). A continuum approach includes time-dependent descriptions for both the external geometry of cortical bone surfaces (the free boundaries) and the time-dependent descriptions for changes in bone material properties. The material property changes could include changes in the cortical bone material in addition to changes in the structural (apparent) properties of cancellous bone.[31] With that point of view, differential

equations can be developed to describe changes in cortical surface locations, changes in cortical material properties, and changes in apparent trabecular bone material properties.

A micro- or tissue-level point of view acknowledges that the cells responsible for bone resorption and deposition are always on the various bone surfaces—periosteal, endocortical, trabecular, or osteonal (see Chapters 1 and 22). Thus, net remodeling can be described as a free-boundary problem in which the various external geometries—or envelopes—of cortical and cancellous bone surfaces can change over time.[32] Differential equations can be developed with this microlevel viewpoint to describe the resorption and deposition that occurs at the bone surfaces.[4] When monitored at the continuum level, the change in bone surface locations is manifested as modifications of both the shape and material properties of the bone.

31.3.1 General Assumptions and Equations: Linear Elasticity

Using an earlier description for the continuum point of view,[31] one can formulate the adaptive problem as an extension of linear elasticity theory (see Chapter 6). Although the constitutive relations could be made more complex to capture nonlinearities associated with material damage or very slow or very fast loading, the simpler linear elasticity equations are generally adequate for describing the mechanical response of bone to many loading conditions.

31.3.2 Adaptation Models

A fundamental decision for the theoretical development of adaptation models is whether to consider the *process* of the adaptation over time, or to merely consider the end point or *goals* of the adaptation. Most of the phenomenological and mechanistic modeling efforts explicitly incorporate time in their formulation so that the process of the adaptive response can be tracked, beginning from chosen starting conditions. In contrast, the optimization modeling efforts have focused upon the adaptation objectives, so they do not generally present the formulation as time dependent, even though the computational implementation may use iterative procedures that modify the starting conditions to generate the final optimized conditions.

31.3.2.1 Material Properties of Bone can Change over Time

In addition to the standard equations of linear, small-strain elasticity, the continuum point of view includes the capability for bone tissue to change its material properties over time. Most generally, this can be written as

$$[\mathbf{C}] = [\mathbf{C}(t)], \tag{31.5}$$

where $[\mathbf{C}]$ is the matrix of material properties. As will be described subsequently, a number of specific suggestions have been proposed to describe variations in material properties over time. To incorporate functional adaptation, the nature of the time dependence must be related to a mechanical stimulus. Equations of this form are used to describe changes in continuum-level cortical bone properties, sometimes called net "internal remodeling"[33] or "remodeling."[32] Additionally, this general form can be specialized to describe the continuum-level changes in trabecular properties that may be a result of either changes in the degree of trabecular porosity and/or changes in the alignment of the trabecular spicules. In the case of a continuum point of view of trabecular bone, the change in the reorientation of the primary alignment of a group of trabeculae could also be incorporated into Eq. 31.5.

31.3.2.2 Boundary Positions of Cortical Bone Surfaces Can Change over Time

The standard linear elasticity formulation may also be modified to include the capability to have bone change its shape, sometimes called "modeling,"[32] and sometimes called net "surface remodeling."[34] This feature can be written, most generally, as

$$S = S(t), \tag{31.6}$$

where S is the function describing the boundary positions. As described subsequently, several different specific forms for this equation have been proposed, relating the surface description to the mechanical stimulus. In addition to the use of the surface remodeling equations to describe changes in the external cortices, equations of this form may also be incorporated at the tissue level to describe changes in trabecular spicule size and orientation, and for the shape change of individual osteons, or even the cavities occupied by individual osteocytes.

31.3.3 Computational Implementation

The models described subsequently all consider bone adaptation to be a function of mechanical usage. Although analytical methods have been used for some idealized examples, numerical approximation methods are usually employed for quantification of the mechanical usage because of the complexity of bone geometry, material property description and distribution, and time-varying boundary conditions and mechanical loading.

The most common computational implementations for net remodeling theories are based on finite-element methods, which use computational models described by the subdivision of complex shapes into a collection of small but finite-sized elements that constitute the "mesh." Approximate solutions—in terms of displacements, strains, and stresses—can be found at any point of the structure, with the accuracy of the solution controlled by the mesh refinement. Assuming the appropriate steps are also taken for establishing the finite-element model validity, this represents a general and powerful technique for structural analysis.[35–37]

To simulate the adaptive response, the finite-element models can be incrementally updated (in terms of geometry and/or material properties) according to equations of the form generally expressed as Eq. 31.5 and/or Eq. 31.6. Because the updated geometry or material properties change the structural behavior, the updated structure must be reanalyzed to find the new displacements, strains, and stresses. The analysis-updating process may be continued until the adaptation is complete, or the user elects to terminate the simulation. The choice for controlling the incremental changes can be time dependent if the time course of the adaptation is of interest, or may be independent of time—as in the case of optimization-based simulations.

Although finite-element methods are the most powerful and general numerical technique available for solution of the spatial portion of the adaptation solution, the boundary element technique has also been used.[10] The boundary-element technique may be more computationally efficient than the finite-element method for these free-boundary-value problems because they reduce the dimensionality of the problem by one (e.g., three-dimensional geometries are described by their two-dimensional surfaces). Disadvantages of the boundary-element method include the difficulty of implementing boundary elements for analysis of anisotropic materials, and questions about their convergence behavior and the optimum degree of mesh refinement for accuracy. However, as these methods are developed and as more commercial software packages become available, they can be efficiently coupled with time-stepping methods for simulating the spatial and temporal adaptation of bone.

31.4 Theoretical Models and Simulations: Cortical Bone

This section presents a review of many of the theoretical models that have been developed and used to simulate cortical bone adaptation, and includes example applications. To motivate the need for these models, a most-striking example of cortical adaptation is first shown in Fig. 31.2. This human specimen was supplied to Wolff by Roux[1,2] and shows that a pseudoarthrosis of the tibia causes a dramatic hypertrophy of the fibula. Wolff[2] describes the specimen: "The fibula, which serves as a substitute for the tibia functionally, is enormous. Its cross section is six to eight times thicker than normal."

FIGURE 31.2 A most striking example of compensatory shape changes is the hypertrophy of the human fibula (left) following the development of a pseudoarthrosis of the tibia (right) in this lower-limb specimen supplied to Wolff by Professor Roux. (From Wolff, J., *The Law of Bone Remodeling*, Springer-Verlag, Berlin, 1986. With permission.)

31.4.1 Flexure-Neutralization Theory and the Three-Way Rule

Frost's "flexure-neutralization theory" was developed to formalize the clinical observations of the realignment of bone and could thus be classified as a phenomenological model. The theory is stated as a rule regarding the relocation of the bone surfaces: repeated nontrivial dynamic bending loads cause strains that cause bone formation drifts to build up upon concave-tending surfaces, while resorption drifts tend to erode convex-tending surfaces,[32] as shown in Fig. 31.3.

More recently, Frost[38] has introduced a "3-way rule" that symbolically represents the observations of his flexure-neutralization theory. The rule states[38] that if $f(M)$ specifies the mechanically controlled kind and rate of modeling activity on a unit area of bone surface, then

$$f(M) = \Gamma\left(\frac{\partial M}{\partial t}\right) = \alpha \cdot \beta \cdot \left(\frac{\partial M}{\partial t}\right), \tag{31.7}$$

where Γ is the drift operator, characteristic of "every small bone surface region," calculated by the product of

α, the end-load operator, which
- $= -1$ for frequent compression or zero end loads
- $= +1$ for frequent tension end loads, and

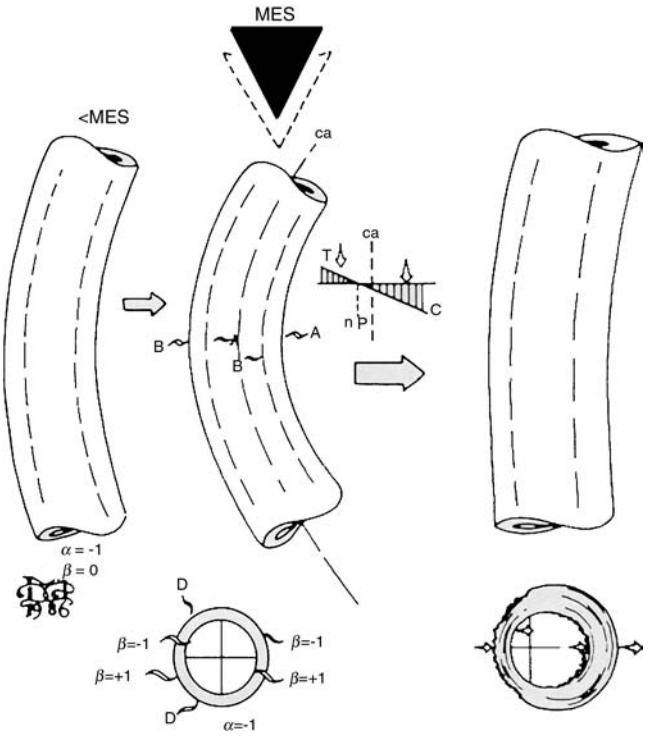

FIGURE 31.3 This example of the straightening of a long bone subjected to combined compression and bending is described by the "flexure-neutralization theory" and by the "3-way rule." Bone formation drifts add to concave-tending surfaces, while simultaneous resorption drifts erode convex-tending surfaces. (From Frost, H. M., *Introduction to a New Skeletal Physiology,* Pajaro Group, Pueblo, CO, 1995. With permission.)

β, the local strain operator, which
- $= -1$ for frequent compression or concave tending bending strains that exceed the absolute value of the "minimum effective signal," |MES|
- $= 0$ for strains below |MES|
- $= +1$ for frequent tensile or convex tending bending strains that exceed the |MES|

The quantity $\dot{M} = \left(\frac{\partial M}{\partial t}\right)$ is the drift rate function defined as:

$$\left(\frac{\partial M}{\partial t}\right) = (\varepsilon + P)\left(\frac{dk}{dt}\right), \tag{31.8}$$

where ε is the mechanical usage coefficient, P is a biologic proportioning coefficient, and dk/dt is the drift rate limit. Frost[38] suggests ranges for the values of these parameters.

The expected bone response is cataloged in the form of a "truth table" that is reproduced in Table 31.1. However, despite the fact that the "3-way rule" states the flexure-neutralization theory symbolically, it is not yet in a form that can be readily incorporated into a computational net bone remodeling program. The major difficulty that must be addressed before the ideas can be used computationally is the dependence of local information, such as the drift operator, Γ, upon global information—including the end-load operator and whether that site is a region of concave or convex bending. Based solely upon the strain at a point, the bone would have no way of "knowing" or sensing the end load or whether or not the strain is a result of concave or convex bending. But, if Frost's ideas can be reformulated in terms of components of the strain,

TABLE 31.1 Gamma Truth Table: A Catalog of the Adaptive Response of Bone to Mechanical Usage

α	β	Γ	R/O/F[a]
+1	+1	+1	F
+1	0	0	O
+1	−1	−1	R
−1	+1	−1	R
−1	0	0	O
−1	−1	+1	F

[a]R/O/F: R = resorption drift, O = no drift, F = formation drift.
Source: Frost, H. M., *Anat. Rec.,* 226(4), 403–413, 1990. With permission.

strain rate tensors, or strain gradients, rather than rules that include the loading conditions, then his observations may lead to a more fundamental understanding of the functional shapes of long bones.[32]

31.4.1.1 Example Application: Curvature Reduction

Despite the limitations for computational implementation of the three-way rule, it has been used in a series of "thought experiments." One "experiment," shown in Fig. 31.3, is described by Frost as one of the "principal structural adaptations of bone"—the diaphysis of a curved long bone that is overloaded with bending and a compression end load.[38] The *in vivo* response is described: "formation drifts arise on concave-tending surfaces, and resorbing drifts on the convex-tending surfaces. Those drifts reduce the bone's curvature, and also its subsequent bending under the same loads."[38] For this case, the parameters of the three-way rule needed to describe symbolically the adaptation on the concave-tending surfaces are $\alpha = -1, \beta = -1$, so that $\Gamma = +1$ and formation drifts should occur; the parameters on the convex-tending surfaces are: $\alpha = -1, \beta = +1$, so that $\Gamma = -1$ and resorption drifts should occur.

31.4.2 Adaptive Elasticity

Beginning in 1976, Cowin and co-workers developed and published a series of papers on "Adaptive Elasticity."[17,33,34,39–44] Adaptive elasticity is a comprehensive phenomenological theory that is based on linear elasticity theory supplemented by additional constitutive equations that allow for changes in the density—hence the stiffness—of bone and also changes in the external shapes of bone. Based on customary loadings, material properties, and boundary conditions, the mechanical condition of remodeling equilibrium could be described by the remodeling equilibrium strain state, $\mathbf{E}_0$. Then a new strain state, $\mathbf{E}$, produced by altered loading or implantation of a bone prosthesis, generates local strain differences ($\mathbf{E} - \mathbf{E}^0$). The differences are used to formulate first-order remodeling rate equations that dictate the change in bone density and/or shape.

For net surface remodeling, Cowin and Van Buskirk[34] proposed the following equation (rewritten to be consistent with the prior notation):

$$S(Q) = \lfloor \mathbf{B} \rfloor \{\mathbf{E} - \mathbf{E}^0\}, \tag{31.9}$$

where S is the speed (change in position over time) of the external bone surface at point Q, in a direction normal to the existing surface; $\lfloor \mathbf{B} \rfloor$ is the row vector of remodeling rate parameters at the point Q; $\mathbf{E}$ is the strain vector at point Q; and $\mathbf{E}^0$ is the remodeling equilibrium strain vector at point Q.

Note that the implementation of this idea could incorporate different degrees of site dependence: if both $\mathbf{E}^0$ and $\lfloor \mathbf{B} \rfloor$ were everywhere the same, then Eq. 31.9 would give results that are completely independent of site; if only $\lfloor \mathbf{B} \rfloor$ is constant, then the net remodeling rate would depend only upon the "error" between $\mathbf{E}$ and $\mathbf{E}^0$ to determine the amount of net remodeling; if $\lfloor \mathbf{B} \rfloor$ was a different constant on each of the four different bone envelopes, there would be a degree of site dependence, and if $\lfloor \mathbf{B} \rfloor$ was different at each point, that would represent absolute dependence upon site.

For describing the material property changes in cortical bone, Cowin and Hegedus[39] proposed the following rate equation:

$$\dot{e} = a(e) + \mathrm{tr}\,[A(e)\mathbf{E}], \tag{31.10}$$

where $\dot{e}$ is the rate of change in solid fraction of bone, $a(e)$ is a function of the current solid fraction, $A(e)$ is a remodeling rate parameter that is dependent upon the current solid volume fraction, and **E** is the strain tensor.

31.4.2.1 Example Applications: Ulnar Osteotomy

Eq. 31.9 has been used extensively for net surface remodeling simulations. First, an analytical example using changed axial loads demonstrated the capability of the theory to describe the eight stable solutions for changes to an idealized diaphysial cross section (involving various combinations of bone addition and removal at the endocortical and periosteal surfaces).[40] The theory was also incorporated into a beam-theory-based computer program for net surface remodeling simulations and used to estimate the remodeling rate parameters, $\lfloor \mathbf{B} \rfloor$, for five *in vivo* experiments that had previously been reported in the literature.[45] For these examples, the computational descriptions required site-specific constants to have the simulation match the experimental results, but due to limited information, estimates of the average axial strain, $E_{3\mathrm{avg}}$, were considered. Consequently, most of the remodeling rate constants, B_1, B_2, B_4, B_5, and B_6 were zero, with only B_3 nonzero. An example that simulated the results of an ulnar osteotomy in sheep is shown in Fig. 31.4. To simulate the experimentally observed adaptation in this example, a moderate degree of site specificity was required: because there were no net changes observed on the endocortical surface, B_3 on the entire endocortical surface was zero; however, because the rate of bone addition on the periosteal surface displayed differences between the tensile and compressive sites, two different values of B_3 were necessary for points on the periosteal surface to account for the observed differences.

The adaptive elasticity theory was also incorporated into a special-purpose finite-element program, RFEM3D (Remodeling Finite Element Method–3-Dimensional) that has been used to examine a variety of situations including idealized models of tubular bones showing the same eight stable solutions as previously found analytically;[31] experimental rabbit tibia subjected to superimposed bending loads;[4] idealized tubular models to study the transient effects of gradually stiffening bone added at the periosteal surface;[46] idealized models for straightening curved bone;[47] and for blind prediction of bone adaptation from *in vivo* ulnar osteotomy experiments.[48] Fig. 31.5[49] shows the same adaptation problem as illustrated in Fig. 31.4, and uses the same loading and remodeling rate parameters. However, this implementation is based on the finite-element method and is suitable for a wider range of structures than would be applicable with the beam-theory-based program described previously.

31.4.3 Cell Dynamics Model

In an attempt to build upon the phenomenological framework provided by adaptive elasticity, a more mechanistic approach, based upon the schematic of the net remodeling process illustrated in Fig. 31.1, was developed.[4,50,51] These complementary ideas are based on the concepts of geometric feedback described by Martin[52] that cast the bone adaptation process as being dependent upon cellular activity and number and the surface area available for resorption and formation. The ideas are summarized in the following where a general description is first developed and then specialized.

In general, the loads imparted to the bone will be a function of time. The resulting strain, $\mathbf{E}(\mathbf{x}, t)$, at a point **x** and time, t, is then dependent on the material properties, **C** (that may also depend on position for nonhomogeneous material models), and the applied loads.

The theory assumes that the strain remodeling potential, denoted by $p(\mathbf{x}, t)$ is a function of the strain history. The cumulative nature of the influence of the strain upon the strain remodeling potential can

FIGURE 31.4 The ulnar osteotomy experiment in mature sheep performed by Lanyon et al.[62] Each illustration represents the bone cross section in the forelimb. (Top) The contralateral control limb at 9 months showing the radius with the intact ulna. (Middle) The experimental radius at 9 months, showing marked asymmetric periosteal depostion. (Bottom) The calculated net remodeling. Solid line represents surfaces of the control bone, dashed lines represent the computational description at 9 months. The indicated length is 1 mm. (From Cowin, S. C., Hart, R. T., Balser, J. R., and Kohn, D. H., *J. Biomech.,* 18(9), 665, 1985. With permission.)

be expressed as an integral over time in the following form:

$$p(\mathbf{x}, t) = \int_{-\infty}^{t} f\{\mathbf{E}(\mathbf{x}, t)\}dt \qquad \text{or} \qquad p(\mathbf{x}, t) = \int_{0}^{\infty} f\{\mathbf{E}(\mathbf{x},(t-\tau))\}d\tau. \tag{31.11}$$

A more concise notation can be achieved by replacing the integral with a symbol denoting the history of strain as follows:

$$p(\mathbf{x}, t) = H_p\{\mathbf{E}(\mathbf{x}, (t-\tau))\} \qquad \text{for} \qquad 0 < \tau < \infty, \tag{31.12}$$

where H_p is a history functional that is dependent on the strain, the position, and time. As mentioned previously, the appropriate period over which to integrate these equations is not yet clear due to the various timescales that are important in the net remodeling processes.

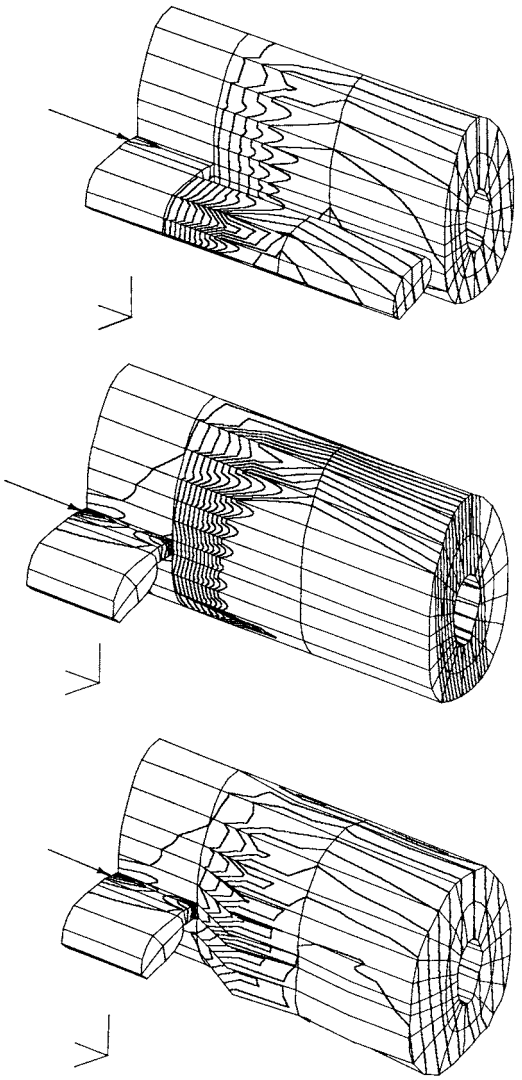

FIGURE 31.5 A finite-element simulation (RFEM3D) of the adaptation to the ulnar osteotomy shown in Fig. 31.4. (Top) the initial configuration showing the radius and intact ulna; contours map the axial strain at remodeling equilibrium, E^{o}_{zz}. (Middle) the forelimb at the start of the remodeling simulation immediately following the removal of the ulna. Contours map the axial strain distribution, E_{zz}. (Bottom) the simulated net remodeling of the ulna after 9 months, using the same remodeling rate constants as found for the simulation shown in Fig. 31.4, with the axial strain contours close to those for remodeling equilibrium, seen in the top. (From Hart, R. T., in *Science and Engineering on Supercomputers,* E. J. Pitcher, Ed., Computational Mechanics Publications, Boston, 1990. With permission.)

The relationship between remodeling and the remodeling potential comprises the effects of the potential on both the average cellular activity rate and the effect of the potential on the cellular recruitment. For the average osteoblast activity rate, $i = b$, and the average osteoclast activity rate, $i = c$,

$$a_i = H_{ai}[p(\mathbf{x}, t - \tau)] + a_{iM} + a_{iH} + a_{iG}, \qquad i = b,c, \qquad 0 < \tau < \infty, \qquad (31.13)$$

where a_i is the average volume rate of bone that is deposited per active osteoblast (or resorbed per active osteoclast), and H_{ai} is the history functional relating cellular activity to the strain remodeling potential.

Here it is assumed that the metabolic, hormonal, and genetic factors are additive, and specified by a_{iM}, a_{iH}, and a_{iG}, respectively.

A similar relationship can be written for the number of active osteoblasts (or osteoclasts) per forming area as

$$n_i = H_{ni}[p(\mathbf{x}, t - \tau)] + n_{iM} + n_{iH} + n_{iG}, \quad i = b,c, \qquad 0 < \tau < \infty. \tag{31.14}$$

Finally, since in general the entire surface area will not be available for both formation and resorption, that fraction of the entire surface area that is available for formation is denoted λ_b and the fraction available for resorption is λ_c. In general, λ_b and λ_c could be functions of time, and could depend on the current magnitude of remodeling. They are related as follows:

$$\lambda_b + \lambda_c = 1. \tag{31.15}$$

Thus, on the external surface, or the surfaces of internal voids, the velocity of the surface is written as the following rate equation:

$$\dot{d} = n_b \lambda_b a_b - n_c \lambda_c a_c. \tag{31.16}$$

where positive values for $\dot{d}$ indicate that bone is being deposited, and negative values for $\dot{d}$ indicate that bone is being actively resorbed on the surface. This equation, first proposed by Martin,[52] includes regulation of cellular number and activity by the available surface area per unit volume of bone as well as a strain-induced potential. To apply the basic concepts embodied in the above equations to specific circumstances, the functional forms must be specified. Several specific relationships have been developed.[3,51] Only the simplest type is described next, but rather than consider the cell population constant as done previously[51] the following case is for constant cellular activity.

31.4.3.1 Constant Cellular Activity: A Simple Adaptive Elasticity Model

The simplest relationship for the general equation (Eq. 31.12) relating the proposed strain-induced remodeling potential and axial strain is linear and can be written as follows:

$$p = C_p E_3, \tag{31.17}$$

where C_p is a constant coefficient. If it is assumed that the cellular population is linearly dependent on the strain-induced potential, then the number of osteoblasts (or osteoclasts) can be expressed as

$$n_i = C_{ni} p + n_{i0}. \tag{31.18}$$

The simplifying assumption of setting the activity of the cells equal to a constant (representing the original activity of the cells) results in

$$a_i = a_{i0}. \tag{31.19}$$

Then Eq 31.16 is reduced to

$$\dot{d} = C_1 E_3 + C_2, \tag{31.20}$$

where

$$C_1 = C_p(a_{b0} C_{nb} \lambda_b - a_{c0} C_{nc} \lambda_c) \qquad \text{and} \qquad C_2 = n_{b0} a_{b0} \lambda_b - n_{c0} a_{c0} \lambda_c. \tag{31.21}$$

The axial strains at which no net remodeling occurs are denoted E_3^0 and are simply

$$E_3^0 = -\frac{C_2}{C_1}. \tag{31.22}$$

This simple relationship is then equivalent to the linear relationship between surface remodeling and strain proposed by Cowin and Van Buskirk.[34] However, the present model uses constants that are not purely phenomenological, but are related to the indicated biological parameters that could be measured and possibly manipulated.

31.4.3.2 Example Application: Ulnar Osteotomy

The RFEM3D program that has been used with the theory of adaptive elasticity was written to also incorporate the adaptive mechanisms shown in Fig. 31.1. Oden[48,53] has developed and implemented the cell dynamics model into the program, and has made *a priori* predictions of the adaptation of canine radii following an ulnar osteotomy.[19,48,53] A variety of simulations were conducted to study a range of possible adaptive responses for the radius 6 months following the ulnar osteotomy. Some simulations used estimates for the remodeling rate constants from earlier studies[45] with the theory of adaptive elasticity. Other simulations were performed using the cell dynamics models with the remodeling rate constants estimated from histomorphometric measures taken 1-month postosteotomy and used with the 6-month simulations. A variety of mechanical stimuli were also used including the axial maximum strain magnitude during gait, $E_{3\max}$, and $\hat{E}$, the "mechanical intensity scalar"[13] (also calculated at the peak values during gait).

Once the blind predictions were made for the response of the radius 6 months following the ulnar osteotomy, they were compared to the experimental results,[53,54] shown in Fig. 31.6. Fig. 31.6a shows the subdivision of a radius cross section with 12 stations for measurement of cortical wall thickness.[53] Fig. 31.6b shows the comparison of experimental results with those predicted from using adaptive elasticity theory with remodeling coefficients estimated from Cowin et al.[45] and based on axial strain differences. In a qualitative sense, the prediction is quite good—the pattern of adaptation is closely predicted around the sectors, except in sector 9, which experimentally experienced resorption that was not predicted by the model. A somewhat better qualitative prediction is shown in Fig. 31.6c that incorporated the 'mechanical intensity scalar,' $\hat{E}$, with remodeling coefficients used for the 6-month prediction that were estimated from the histomorphometric quantification of cell number, activity, and distribution from a specimen 1 month after the ulnar osteotomy.

31.4.4 Site-Dependent, Strain Energy Density Model

A phenomenological approach similar to Cowin's adaptive elasticity theory for shape changes has been developed by Huiskes et al.[8] with several differences. One difference was implemented to model the observed bone behavior that shows a threshold of mechanical stimulus is required to start the process of net remodeling, sometimes referred to as a "lazy zone"[7] or a "dead zone." In addition, the mechanical stimulus is not taken to be the strain tensor, but a scalar, the strain energy density,[11,55] defined in Eq. 31.1.

The rate equation is written as

$$\frac{dX}{dt} = \begin{cases} C_x[U-(1+s)U_n]; & U > (1+s)U_n \\ 0; & U_n < U < (1+s)U_n \\ C_x[U-(1-s)U_n]; & U < (1+s)U_n \end{cases}, \tag{31.23}$$

where X is the surface growth, C_x is the remodeling rate coefficient, $2s$ is the width of the "lazy zone," and U_n is a "site-specific homeostatic equilibrium strain energy density." A two-dimensional

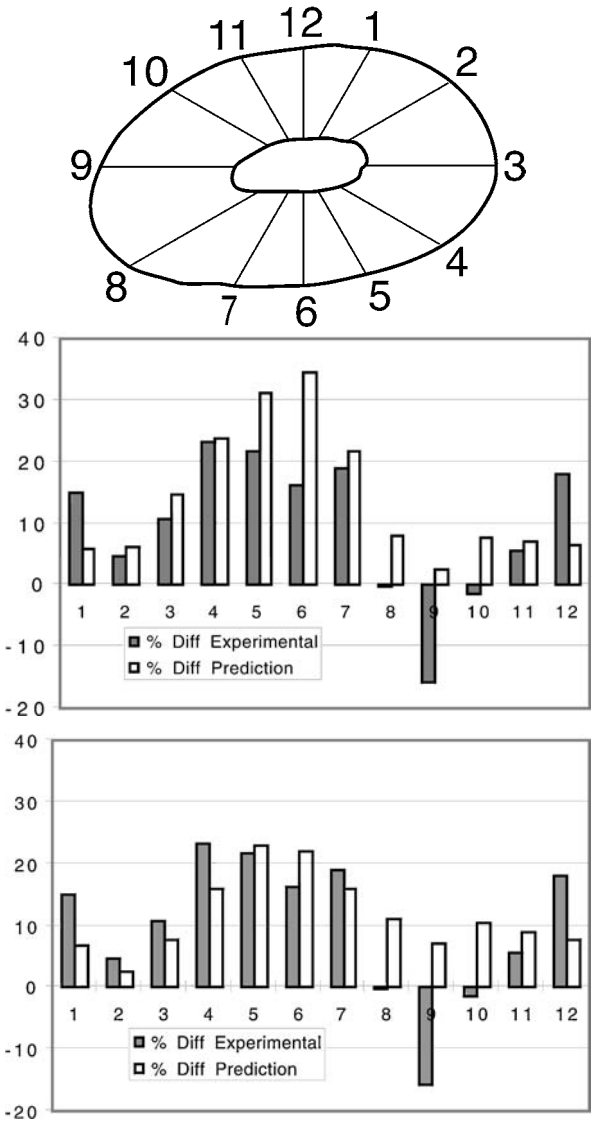

FIGURE 31.6 Comparison of experimental and predicted results for a canine ulnar osteotomy experiment. (Top) The subdivision of a canine radius cross section with 12 stations for measurement of cortical wall thickness for comparison of experimental and predicted results following a ulnar osteotomy. (Middle) Percent difference in wall thickness (comparing experimental and contralateral radii) at 6 months following an ulnar osteotomy, showing experimental and predicted results. Computed results used adaptive elasticity theory with remodeling coefficients estimated from Cowin et al.,[45] and based on axial strain differences. (Bottom) Same as above, but the predictions were made using the cell dynamics model with the mechanical intensity scalar, $\hat{E}$. Further, the remodeling coefficients used for the 6-month prediction were estimated based on the histomorphometric quantification of cell number, activity, and distribution from a specimen 1 month after the ulnar osteotomy. (From Oden, Z. M., Ph.D. dissertation, Tulane University, New Orleans, 1994. With permission.)

finite-element implementation based on the use of NONSYS and MARC (Marc Analysis Corporation, Palo Alto, CA) was developed for simulating bone adaptation for both net internal (density changes) and surface (shape changes) remodeling, using a forward Euler integration time-stepping algorithm.[8] For surface remodeling, surface points are relocated normal to the surface in each time step as

follows (with $s = 0$):[8]

$$\Delta X^j = X^j(t + \Delta t) - X^j(t) = \Delta t C_x\{U^j(t) - U_n^j\}, \qquad 1 \leq j \leq m, \tag{31.24}$$

where m is the number of surface nodal points concerned. In this implementation, the magnitude for the remodeling rate constant, C_x, was chosen arbitrarily but care was taken to ensure stability of the iteration process by choosing sufficiently small time steps, Δt. Consequently, only the final result of the remodeling process was considered. The temporal evolution was not a focus of the study.[8]

31.4.4.1 Example Application: "Stress-Shielding"

The finite-element procedures that implemented Eq. 31.23 were used by Huiskes et al.[8] to study the potential consequences for design changes of an intramedullary fixation stem. Fig. 31.7a shows the simplified two-dimensional configuration showing a cortical shell with the displacement boundary conditions, an intramedullary rod, and the applied bending moment. Side-plate elements simulated the three-dimensional nature of the problem. For net remodeling simulations, a number of parameters were varied: stem diameter, remodeling threshold, and implant–bone contact conditions. Computed results simulated resorption of the cortical shell—a phenomenon described as "stress-shielding"—that was most influenced by differences in stem rigidity. Fig. 31.7b shows the loss of bone that was simulated with the use of the most flexible stem design. In contrast, Figure 31.7c shows much more severe bone loss as a consequence of using the net remodeling simulation with the stiffest design.

31.4.5 Homogeneous Stresses at the Surface

An optimization approach has been taken by Mattheck and co-workers[56,57] in developing the "CAO," a computer-aided optimization hypothesis. Mattheck makes the observation that "a good mechanical design is characterized by a homogeneous stress distribution at its surface." As a result, a computerized implementation of CAO was developed and has been used to simulate shape change of bone (and plants). The implementation is possible with commercial finite-element codes that support swelling materials or thermal expansion (e.g., ABAQUS from Hibbitt, Karlsson, and Sorensen, Inc., Pawtucket, RI). The finite-element model is constructed with a uniformly thick surface layer. The method is based on changing the volume of the surface layer of elements as follows:

$$\dot{\varepsilon}_v = k(\sigma_M - \sigma_{\text{ref}}), \tag{31.25}$$

where $\dot{\varepsilon}_v$ is defined as the volumetric swelling rate, σ_M is the von Mises equivalent stress, σ_{ref} is a reference value of the von Mises equivalent stress, and k is a rate constant.

31.4.5.1 Example Application: Curvature Reduction

The CAO implementation has been illustrated with a number of examples, including cortical bone, trabecular bone, and—most extensively—tree adaptation.[58] The example shown in Fig. 31.8 is for the surface adaptation of a femur that is broken and then heals with a malposition.[57,58] It is very similar to the "thought experiment" application of the three-way rule, previously described and shown in Fig. 31.3. Bilinear four-noded plane strain elements were used with homogeneous and isotropic values for Young's modulus and Poisson's ratio. The initial finite-element model is intended to represent the structure shortly after fracture, and at the terminal stage of the simulation, the bone has healed and has a homogeneously distributed von Mises stress along the bone surfaces. Although the changes are applied incrementally, this optimization scheme is not intended to describe the physiological process of the adaptation.

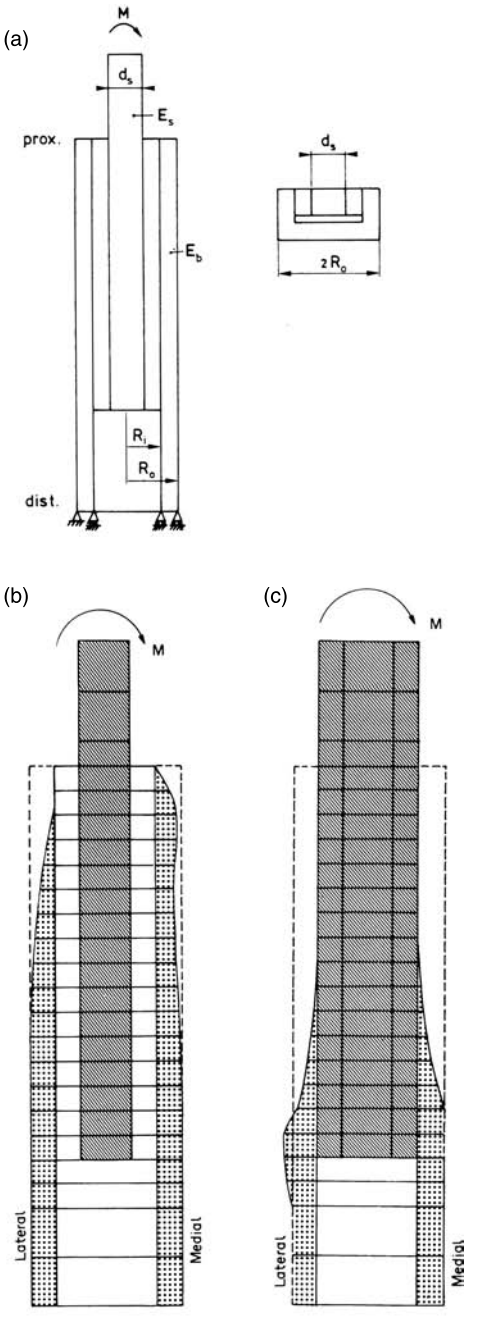

FIGURE 31.7 Example application—"stress shielding." An analysis of intramedulary fixation using the site-dependent strain energy density equations. (a) The simplified two-dimensional configuration showing a cortical shell with the displacement boundary conditions, an intramedullary rod, and the applied bending moment. (b) Shows the loss of bone that was simulated with the use of the most flexible stem design. (c) Much more severe bone loss is shown as a consequence of using the net remodeling simulation with the stiffest design, shown in (c). (From Huiskes, R. et al., *J. Biomech.,* 20(11–12), 1135, 1987. With permission.)

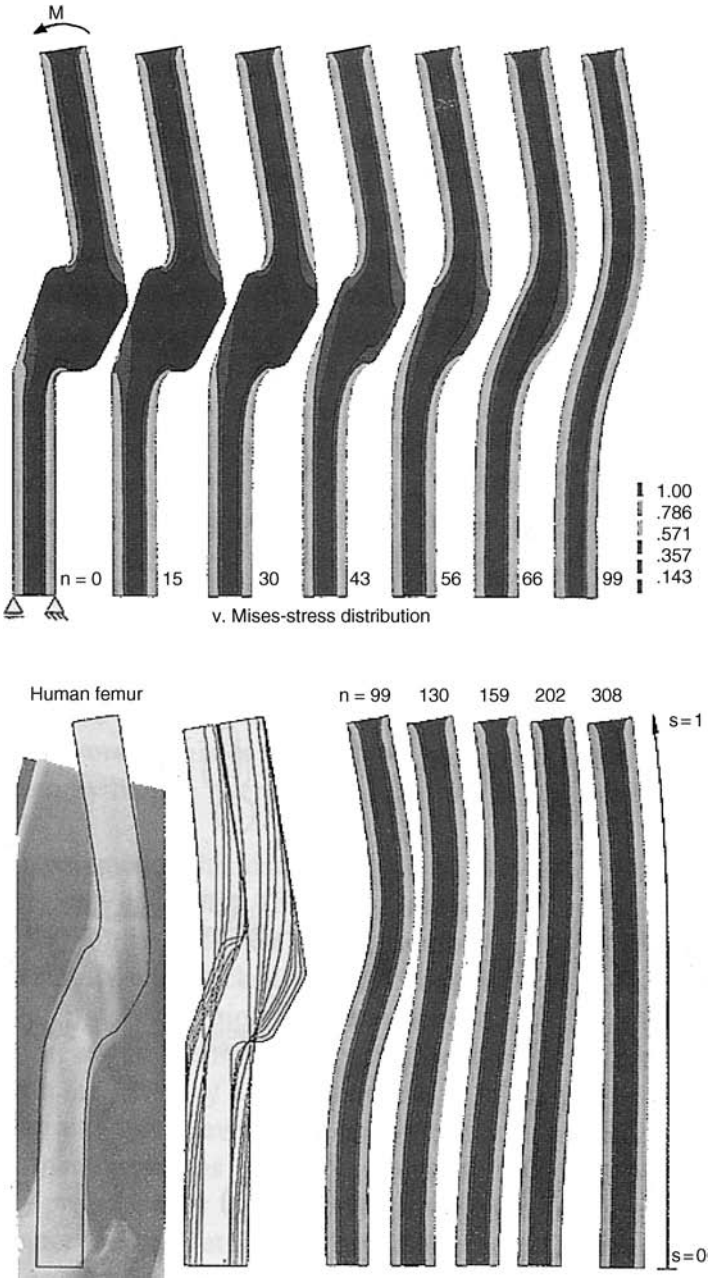

FIGURE 31.8 Simulation of the gradual straightening of a femur that is broken and heals with a malposition. The simulation, not explicitly time-dependent, shows the implementation of the "CAO" program that seeks a shape that minimizes notch stress. (From Mattheck, C., *Design in Nature,* Springer-Verlag, Berlin, 1998. With permission.)

31.4.6 Strength Optimization: Fatigue Damage and Repair

A more mechanistic method—that stops short of directly addressing the biological processes of adaptation—has been developed based on the hypothesis that "bone adapts to attain an optimal strength by regulating the damage generated in its microstructural elements."[59] Prendergast and Taylor[59] hypothesized that there is some damage at RE (remodeling equilibrium), and that the rate of repair is associated with the damage rate.

Mathematically, at RE, $\dot{\omega}_{\text{eff}} = 0$ and $\dot{\omega} = \omega_{\text{RE}}$, where ω_{eff} is the effective damage, $\dot{\omega}$ is the current rate of damage production, and ω_{RE} is the rate of damage production at RE.

Then,[59,60]

$$\frac{dX}{dt} = C \cdot \omega_{\text{eff}} = C \int_{t_0}^{t} (\dot{\omega} - \dot{\omega}_{\text{RE}}) dt, \tag{31.26}$$

where X measures the extent of the remodeling process. This expression can be implemented as a site-specific theory by variation of either the constant, C, based upon location, or by including an initial variation in the remodeling equilibrium damage. Interestingly, it has been shown that the use of the damage stimulus is equivalent to using the strain energy density,[61] although the damage stimulus may be easier to investigate experimentally.

31.4.6.1 Example Application: Ulnar Osteotomy

The same ulnar osteotomy experiment by Lanyon et al.[62] that was simulated using the theory of adaptive elasticity by Cowin et al.[45] has also been simulated using the strength optimization method.[60] A three-dimensional finite-element model of the sheep radius and ulna was developed using eight-noded linear isoparametric elements, shown in Fig. 31.9a. A finite-element analysis of the intact forelimb provided the distribution of damage at the remodeling equilibrium, calculated with a load simulating static stance. Then, following the removal of a portion of the ulna, and using a uniform constant, C, they generated a plot of the stress differences and damage distribution near the endocortical and periosteal surfaces, shown in Fig. 31.9b.

Although the analysis shows the distribution of the adaptation stimulus rather than incrementally changing the shape, the strength optimization analysis needed only one remodeling rate constant, C. This is in contrast to three different remodeling rate constants needed to produce the simulation results shown in Figs. 31.4 and 31.5. "In particular the low strains on the endosteal surface, though they generate an appreciable strain and corresponding stress difference, do not generate a significant remodelling stimulus with this approach ⋯ this suggests that a damage variable may contain more of the nonlinearity of the remodelling process than does a strain variable."[60]

31.5 Theoretical Models and Simulations: Trabecular Bone

This section provides a review of many of the theoretical models that have been developed and used to simulate trabecular bone adaptation, and closely follows a recent review of finite-element modeling for trabecular bone.[30]

Although continuum-level characterizations of the mechanical properties for trabecular bone depend primarily upon the solid volume fraction (i.e., the volume of pores is discounted), they also depend on the predominant orientation of the trabeculae. Thus, adaptation models intended to describe changes in continuum material properties have been developed to describe density changes with and without changes in anisotropy. In contrast, tissue-level descriptions are dependent only upon descriptions of trabecular shape—their size and orientation changes are manifested as volume fraction and orientation changes at the continuum level.

31.5.1 Adaptive Elasticity

The theory of adaptive elasticity discussed previously for cortical bone adaptation has been supplemented to also simulate trabecular bone adaptation at the continuum level. In addition to a description for changing material properties, Eq. 31.5, by changing the volume fraction of material, Eq. 31.10, the changing anisotropy of material is also now described.

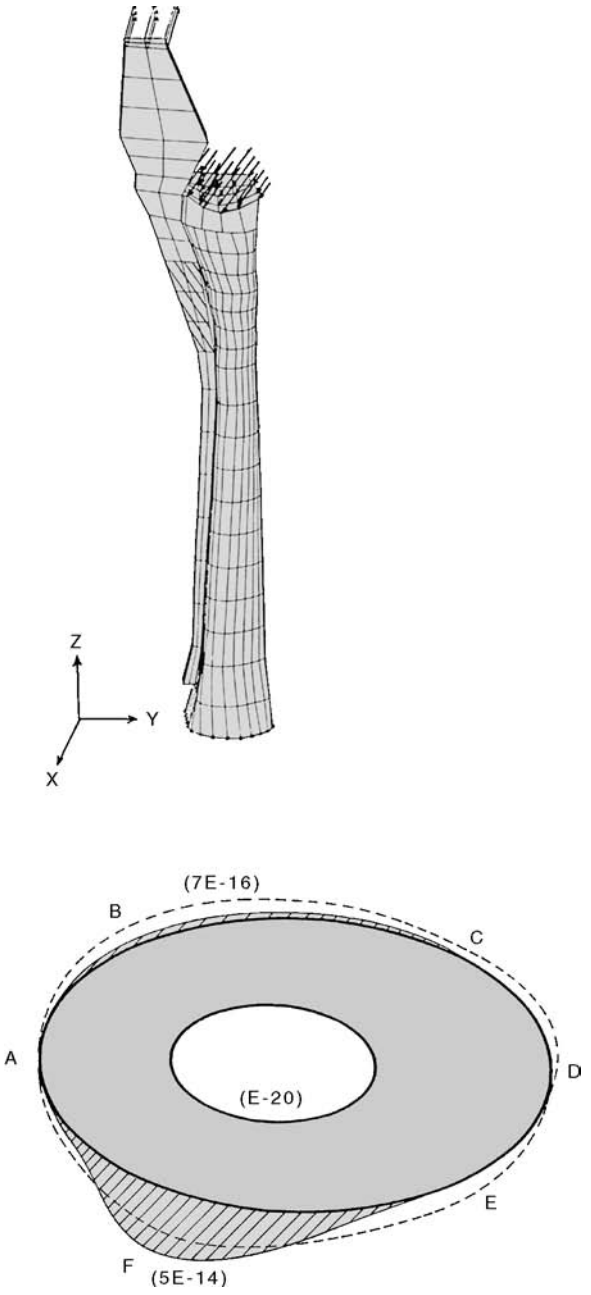

FIGURE 31.9 Another finite-element study of the adaptation to the ulnar osteotomy shown in Fig. 31.4. (a) Finite-element model of the intact sheep radius and ulna was developed using eight-noded linear isoparametric elements and analyzed to provide the distribution of damage at the remodeling equilibrium, corresponding to a load to simulate a static stance. (b) Approximate visualization of the stress difference for the intact and osteotomized conditions, and the corresponding damage-rate distribution calculated using the strength optimization equation. The dashed lines represent the stress; the crosshatched area represents the calculated damage distribution. (From McNamara, B. P. et al., *J. Biomed. Eng.,* 14(3), 209, 1992. With permission.)

Cowin defined a mathematical expression of Wolff's trajectorial theory,[41] and the mathematics also have an appealing intuitive description.[63] The basis of the mathematical expression is the use of a second-rank tensor, called the fabric tensor,[64] defined by stereological measures of predominant trabecular orientation.[65,66] (Chapter 13 has a discussion of these measures.) Mathematically, Cowin points out that at remodeling equilibrium—defined in this case as the alignment of the trabecular orientations with the principal stresses—the product of any two of the second-rank tensors that define stress, **T**, strain, **E**, and the fabric tensor, **H**, must be commutative. Then, using the notation of $\mathbf{X}^0$ to represent the equilibrium value of **X** (where **X** can be **T**, **E**, or **H**) Wolff's trajectorial theory can be expressed as

$$\mathbf{T}^0\mathbf{E}^0 = \mathbf{E}^0\mathbf{T}^0, \qquad \mathbf{T}^0\mathbf{H}^0 = \mathbf{H}^0\mathbf{T}^0, \qquad \mathbf{H}^0\mathbf{E}^0 = \mathbf{E}^0\mathbf{H}^0. \tag{31.27}$$

The intuitive description comes from using an ellipsoid to represent a second-rank tensor geometrically (strain, stress, or fabric) with the normalized length of the axes of the ellipsoid proportional to the value of the eigenvalues of the tensor, and the orientation representing the principal directions.[41,63] Then, Fig. 31.10a can be used to represent an initial situation in remodeling equilibrium, indicated by the common alignment of the three ellipsoids used to represent the stress, strain, and the fabric. A perturbation in the stress is represented in Fig. 30.10b as a new alignment of the stress ellipsoid. The strain, which responds instantaneously to the changed stress, also has a new alignment, but is not yet aligned with the stress. The trabecular bone fabric, unable to change instantaneously, retains the original alignment. After some time during which the trabecular bone has time to adapt to the new stress imposed in Fig. 31.10b, a new remodeling equilibrium is achieved, as seen in Fig. 31.10c, where the ellipsoids are once again in alignment with each other, but in the new direction dictated by the new stress imposed in Fig. 31.10b.[30]

If only the relative degree of anisotropy is of interest, then the fabric tensor **H** can be normalized by making the trace equal to one, i.e., $tr\mathbf{H} = 1$, and it becomes easier to manipulate mathematically.[44]

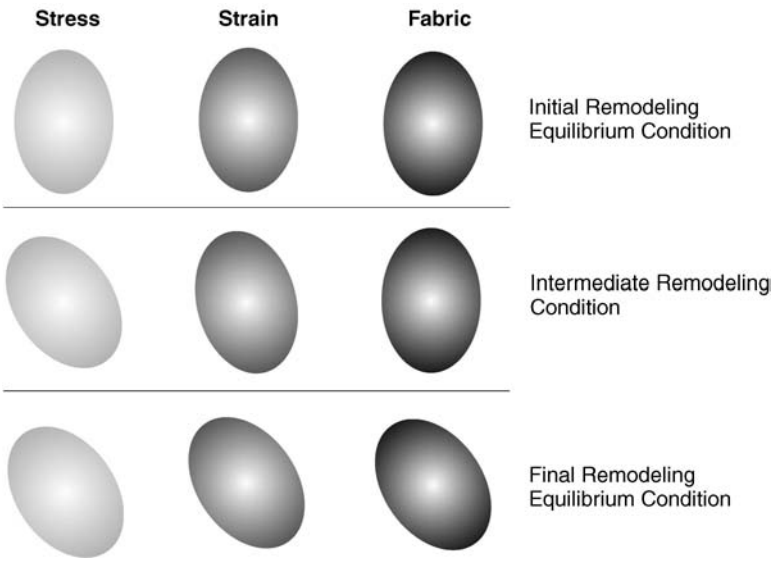

FIGURE 31.10 Intuitive description of Cowin's ideas for trabecular realignment. (Top) Representation of an initial situation in remodeling equilibrium, indicated by the common alignment of the three ellipsoids used to represent the stress, strain, and the fabric. A perturbation in the stress is shown (middle) with a new alignment of the stress ellipsoid. The strain, which responds instantaneously to the changed stress also has a new alignment, but is not yet aligned with the stress. The fabric, unable to change instantaneously, retains the original alignment. After some time during which the trabecular bone has time to adapt to the new imposed stress, a new remodeling equilibrium is achieved (bottom). The ellipsoids are once again in alignment with each other, but in a new direction. (From Hart, R. T. and Fritton, S. P., *Forma,* 12, 277, 1997. With permission.)

Then, the deviatoric part of the normalized fabric tensor is a measure of the relative degree of anisotropy denoted by **K**, and is defined as[44]

$$\mathbf{K} = \mathbf{H} - (1/3)I. \tag{31.28}$$

The stress–strain relationship can then be written as

$$\mathbf{T} = \mathbf{D}(\mathbf{K}, e)\mathbf{E}, \tag{31.29}$$

where $e = \nu - \nu_0$ is a measure of the change in solid volume fraction, ν, from a reference solid volume fraction, ν_0. This shows that the mechanical properties that express Hooke's law are explicitly expected to be functions of both the amount of material present, as measured by the solid volume fraction, ν, and the orientation of the material, as quantified by a measure of the fabric, **K**.

If it is assumed that the objective of the remodeling process is to reestablish the remodeling equilibrium strain, then a specific bone location is in RE when the eigenvalues of the strain tensor, E_1, E_2, E_3, are equal to (or within an acceptable range of) the eigenvalues of the remodeling equilibrium strain tensor, E_1^0. E_2^0, E_3^0.[44] Then two general rate equations can be written to describe the mechanically adaptive process of trabecular bone. One equation describes how the fabric changes with time,

$$\frac{d\mathbf{K}}{dt} = \frac{d\mathbf{K}(\mathbf{K}, \mathbf{E}, e)}{dt}, \tag{31.30}$$

and a second equation describes how the solid volume fraction changes with time,

$$\frac{de}{dt} = \frac{de(\mathbf{K}, \mathbf{E}, e)}{dt}. \tag{31.31}$$

The process of porosity and fabric changes would continue until the material was entirely void, entirely solid, or at remodeling equilibrium.

To specialize and implement the ideas in Eqs. 31.30 and 31.31, Cowin et al.[44] wrote them in polynomial form. Then, if higher-order terms are neglected, and if it is assumed that (1) the rate of change of the fabric depends only upon the fabric and the deviatoric strain (which measures distortion), and (2) that the rate of change of the bulk density depends only upon the bulk density and upon the dilatational strain (which measures change in volume), then Eqs. 31.29 through 31.31 can be approximated as

$$\mathbf{T} = (g_1 + g_2 e)(tr\mathbf{E})\mathbf{I} + (g_3 + g_4 e)\mathbf{E} + g_5(\mathbf{KE} + \mathbf{EK}) + g_6(\mathbf{I}(tr(\mathbf{KE}) + (tr\mathbf{E})\mathbf{K})), \tag{31.32}$$

$$\frac{d\mathbf{K}}{dt} = h_1(\hat{\mathbf{E}} - \hat{\mathbf{E}}^0) + h_2\left[\mathbf{I}(tr\mathbf{K})(\hat{\mathbf{E}} - \hat{\mathbf{E}}^0) - \frac{3}{2}(\mathbf{K}(\hat{\mathbf{E}} - \hat{\mathbf{E}}^0) + (\hat{\mathbf{E}} - \hat{\mathbf{E}}^0)\mathbf{K})\right], \tag{31.33}$$

$$\frac{de}{dt} = (f_1 + f_2 e)(tr\mathbf{E} - tr\mathbf{E}^0), \tag{31.34}$$

where the circumflex indicates the deviatoric part of the indicated tensor, and g_1 to g_6, h_1, h_2, f_1, and f_2 represent constants. Cowin et al.[44] calls this set of equations the "approximate noninteracting microstructure theory."

31.5.1.1 Example Application: Fabric Reorientation

The RFEM3D program, described previously for simulations of cortical bone adaptation, has been enhanced with the implementation of Eqs. 31.32 through 31.34.[67] Several changes were made to the program to allow for evolution of trabecular porosity and orientation in the element stiffness matrices for trabecular bone elements.[67,68] To test the implementation of the trabecular remodeling theory, an idealized finite-element

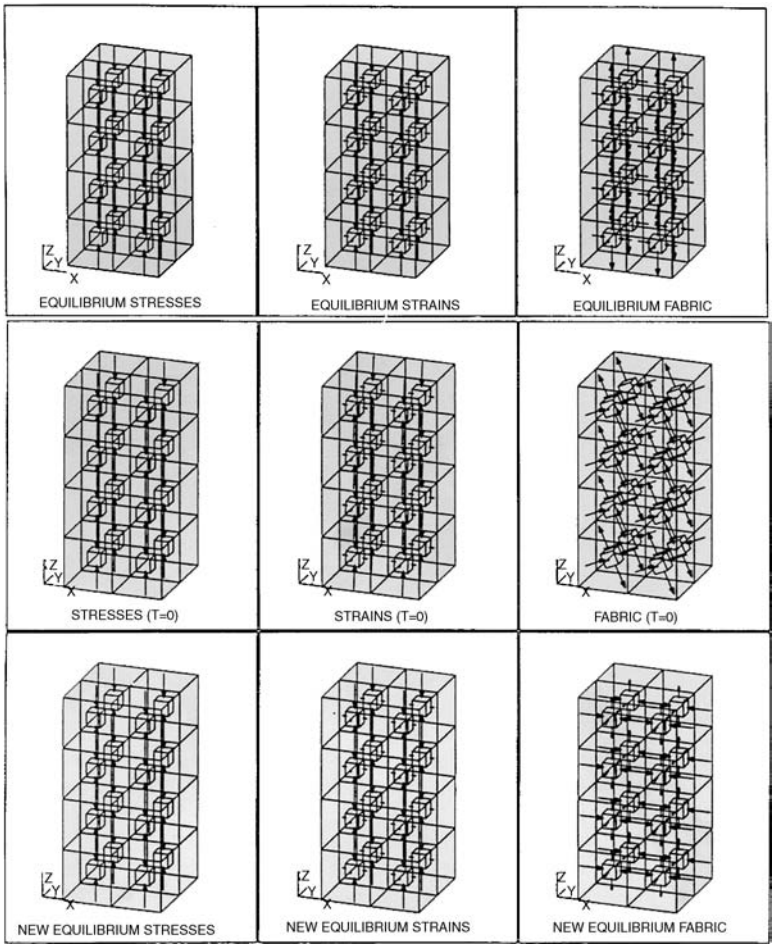

FIGURE 31.11 RFEM3D simulation of idealized trabecular bone reorientation. (Top row) The initial remodeling equilibrium stress, strain, and fabric tensors. (Middle row) The new fabric tensor applied, with altered stress and strain tensors shown. (Bottom row) The new remodeling equilibrium stress, strain, and fabric tensors. (From Hart, R. T. and Fritton, S. P., *Forma,* 12, 277, 1997. With permission.)

model of a section of trabecular bone was constructed, representing a small column ($10 \times 10 \times 20$ mm) of trabecular bone (see Fig. 31.11). To ensure accurate results, a convergence test was conducted and an appropriate model (16 elements and 141 nodes) was chosen. Each element in the model measured $5 \times 5 \times 5$ mm, the approximate minimum-length scale for valid fabric tensor measurement.[69]

For equilibrium conditions, the fabric was aligned with the global axes. Prescribed displacements in the axial direction were applied to the model, with the bottom surface constrained in the axial direction, along with the middle bottom node constrained in all three directions to prevent rigid-body motion. The initial equilibrium strains and stresses were calculated, and are shown along with the initial fabric tensors in the top row of Fig. 31.11. The tensors are illustrated with the principal components emanating from an icon placed at the centroid of each element.

To perform an idealized example of trabecular bone adaptation, the stress and strain fields were altered by changing the principal fabric directions to an off-axis angle of 30° (Fig. 31.11, middle row). RFEM3D was then run using the trabecular remodeling routines incorporating Eqs. 31.32 through 31.34 to simulate the changes in the fabric tensor and solid volume fraction for the column. The remodeling rate constants were the same as in Cowin et al.,[44] and were chosen so the net remodeling process takes approximately

160 days. After the simulated 160 days of net remodeling, results show that the stress, strain, and fabric tensor principal directions coincided once again (Fig. 31.11, bottom row). These results indicate that this computational implementation of the trabecular remodeling theory is able to simulate trabecular reorientation in response to altered stress and strain fields. The example was chosen as a convenient way to change the stress and strain fields in the bone, and the program was shown to reorient the bone correctly back to its equilibrium orientation similarly to the intuitive description of the alignment of the tensors shown in Fig. 31.10.

31.5.1.2 Trabecular Density and Orientation Models for Skeletal Morphogenesis

Using a fundamentally different approach from adaptive elasticity, Fyhrie and Carter[11] developed a theory to predict both the apparent density (or volume fraction) of bone and the trabecular orientation for a continuum description of trabecular bone material. First, they assumed that bone is an anisotropic material that tends to optimize its structural integrity while minimizing the amount of bone present. For trabecular adaptation simulations, they introduced the notion of an objective function of the form $Q(\rho,\theta,\mathbf{T})$, which is dependent upon the apparent density (or volume fraction), ρ, the orientation, θ, and the stress, **T**. Then, two special cases were examined: the case where the net bone remodeling objective is based upon the strain energy and the case where the objective is based upon the failure stress.[11]

An extension of this work to a comprehensive theory for relating local tissue stress history to skeletal biology was developed by Carter et al.[12] The theory goes beyond the usual ideas for modeling functional adaptation by relating "tissue mechanical stresses to many features of skeletal morphogenesis, growth, regeneration, maintenance, and degeneration."[12] They make a case for the consistency of the theory with many of the features of skeletal biology, and argue that the role of mechanical influence upon the biological processes is more important than has previously been recognized. This assertion brings to focus the lack of verification for the ideas about the relative importance of genetics and environment in the development, growth, and maintenance of structural tissues.

In an effort to use mechanical input as a regulator of the trabecular architecture in the proximal end of a femur, Carter et al.[70] used finite-element models with multiple loads, noting that a single loading condition cannot reasonably be expected to be the stimulus for the full trabecular architecture. The time rate of the process was not accounted for, but rather it was assumed that there was a relationship between element density and an "effective stress" written as

$$\rho = K\left(\sum_{i=1}^{c} n_i \sigma_i^M\right)^{(1/2M)}, \tag{31.35}$$

where c is the number of discrete loading conditions, K and M are constants, and n is the number of loading cycles at the "energy stress,"[11,12] defined as $\sigma_{\text{energy}} = \sqrt{2E_{\text{avg}}U}$. As described subsequently, the objective of the study was to examine the influence of mechanical factors upon the trabecular architecture, and of note is the use of a non-site-specific rule (i.e., the remodeling objective is the same for all points in the bone).

Beaupré et al.[71] modified and extended the ideas to develop a time-dependent modeling/remodeling theory. The model is based upon using a daily "stress stimulus" with a continuum level measure, ψ, defined as

$$\psi = \left(\sum_{\text{day}} n_i \bar{\sigma}_i^m\right)^{1/m}, \tag{31.36}$$

where n_i is the number of cycles of load type i, $\bar{\sigma}_i$ is the continuum level "stress" as above, and m is an empirical constant. Then, a piecewise linear approximation to an assumed bone deposition rate vs. tissue

stress stimulus is proposed that could be used for "modeling," i.e., net changes in external bone shape similar to Eq. 31.23:

$$\dot{r} = \begin{cases} c_1(\psi_b - \psi_{bAS}) + (c_1 - c_2)w_1; & (\psi_b - \psi_{bAS} < -w_1) \\ c_2(\psi_b - \psi_{bAS}); & (-w_1 \leq \psi_b - \psi_{bAS} < 0) \\ c_3(\psi_b - \psi_{bAS}); & (0 \leq \psi_b - \psi_{bAS} \leq +w_2) \\ c_4(\psi_b - \psi_{bAS}) + (c_3 - c_4)w_2; & (\psi_b - \psi_{bAS} > +w_2), \end{cases} \tag{31.37}$$

where ψ_{bAS} is the attractor state stress stimulus (for remodeling equilibrium), ψ_b is the actual stress stimulus, c_1, c_2, c_3, and c_4 are empirical rate constants, and w_1 and w_2 define the width of the normal activity region.[71] The normal activity region allows for a "window" of values for the stress stimulus in which there would be no signal for net remodeling responses.[29] In addition, by using Eq. 31.37 with histomorphometric relations and the data of Martin[72] for descriptions of bone apparent density and surface area density, Beaupré et al.[71] write a consistent equation for the rate of change of density (net internal remodeling):

$$\dot{\rho} = \dot{r} S_v \rho t, \tag{31.38}$$

where $\dot{\rho}$ is the time rate of change of the apparent density, $\dot{r}$ is the linear rate of bone apposition, S_v is the bone surface area density, and ρ_t is the "true density" of the bone tissue, assumed to be the density of fully mineralized tissue. Thus, an error between the remodeling equilibrium state (called here the attractor state) and the present mechanical state drives the signals for bone formation or resorption.

More recently, Jacobs et al.[73] have proposed a different method for simulation of net trabecular remodeling that can account for both changes in the volume fraction of material present and in the alignment of the material. Their approach does not explicitly divide the realignment and the volume fraction changes as done by Cowin et al.[44] Rather, Jacobs has chosen to operate directly upon the anisotropic stiffness tensor (with up to 21 independent constants, depending on the degree of anisotropy) that relates the stress and the strain. In that fashion, no *a priori* assumptions are needed for describing the elastic symmetry of the continuum approximation of trabecular bone behavior. This is significant because, although trabecular bone may be well characterized at the continuum level using orthotropic material properties (9 of the 21 constants are independent), there is reason to believe that during active realignment, a more general degree of anisotropy may be needed. Unfortunately, finding the 21 needed constants may not be practical, and the problem is now to assemble the *structural* stiffness matrix in its entirety. Thus, the advantage of separating out the measurable material properties (the bone matrix material properties) and the measurable structural properties (such as the fabric tensor) from the structural stiffness is lost.

With the general approach of adding evolution equations to the general anisotropic stiffness tensor, two special cases have been studied.[73] One approach was to assume that the stiffness changes in the stiffness tensor occur to maximize mechanical efficiency. The second case, more consistent with Wolff's ideas, was for stiffness changes to occur in the principal stress directions. For this second case, the time rate of change of the stiffness tensor is written as the sum of the changes in the isotropic and anisotropic portions of the tensor. If the stress, **T**, is given by the product of the stiffness tensor, **C**, and the strain tensor, **E**, then the rate equation is written as the following:[73]

$$\dot{\mathbf{C}} = \dot{\mathbf{C}}_{\text{iso}} + \dot{\mathbf{C}}_{\text{aniso}}. \tag{31.39}$$

The isotropic rate equation is the same as has been used previously, Eq. 31.37 by Beaupré et al.[71,74] For the anisotropic portion, the magnitude of each principal stress is compared to the average magnitude of the principal stresses. If a principal stress component is larger (smaller) than the average, then the

magnitude of the stiffness corresponding to the component in question is increased (decreased). Thus, stiffening of the material property tensor occurs in the direction of overloading, whereas softening occurs in the direction of underloading.[73]

31.5.1.3 Example Applications: Trabecular Bone in the Femoral Head

A 1989 paper by Carter et al.[70] is one in a series based on the use of a two-dimensional finite-element model of the proximal human femur as the basis for the application of skeletal morphogenesis theories. The basic idea is to begin with a model in which the elements all have a uniform density distribution, to then apply loads and iterate the density of each finite element based on a remodeling rule, and compare the calculated density pattern to *in vivo* patterns.

Using Eq. 31.35 with multiple loads, Carter et al.[70] calculated density distributions shown in Fig. 31.12, which are similar to those seen in the proximal femur. However, the best correspondence was observed after the third iteration of the computational implementation and in subsequent iterations, the density distribution progressed to nonphysiological distributions. (Note that because time was not specifically incorporated into the model, the iteration number has significance only within the context of the implementation the

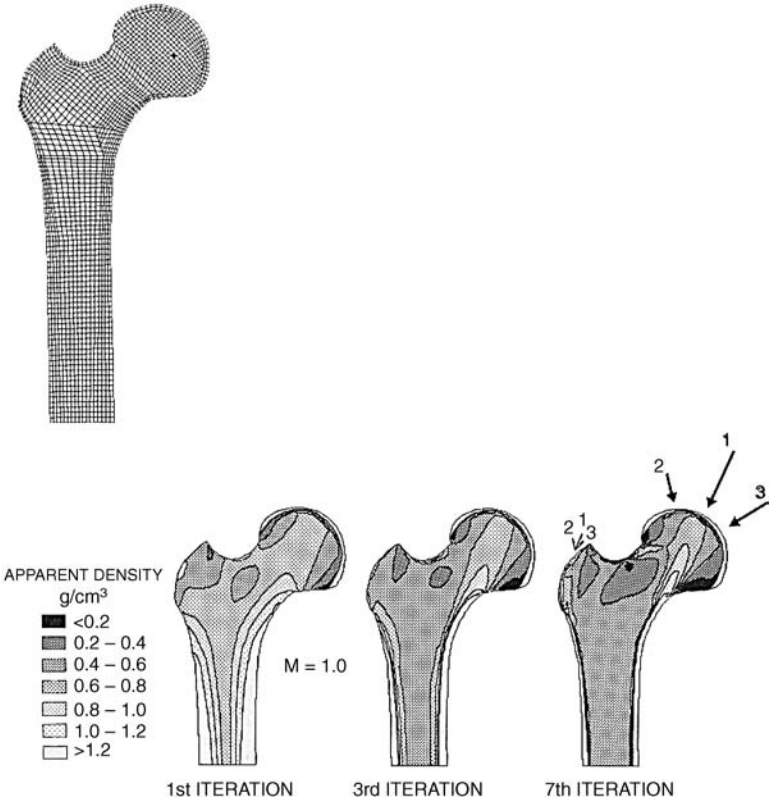

FIGURE 31.12 Examination of the distribution of trabecular bone density in the femoral head. (Top) The two-dimensional finite-element mesh. (Bottom) The predicted density distributions from Eq. 31.35 using multiple loads and a linear relationship between the density and the "effective stress." The density distribution in the third iteration is closer to the *in vivo* distribution than that found in subsequent iterations (the seventh iteration is also shown). (From Carter, D. R. et al., *J. Biomech.,* 22(3), 231, 1989. With permission.)

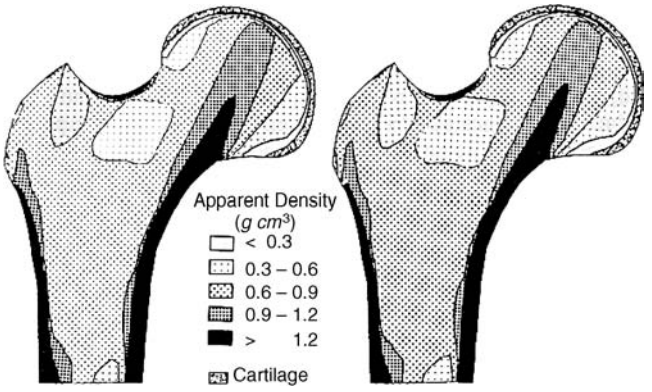

FIGURE 31.13 Another examination of the distribution of trabecular bone in the femoral head. Density distributions were calculated based upon time-dependent density equations (Eqs. 31.36 through 31.38) with a similar two-dimensional finite-element model of the proximal human femur, shown in Fig. 31.12. The results are shown for an implementation using a "lazy zone" for 330 days, left, and 412.5 days, right. In contrast to the simulation shown in Fig. 31.12, this solution was convergent with calculated density distributions remarkably similar to physiological distributions. (From Beaupré, G. S. et al., *J. Orthrop. Res.,* 8(5), 662, 1990. With permission.)

authors describe.) The authors believe that ignoring other biological influences prevented the mechanical model from converging to an equilibrium solution.[70]

Interestingly, as a consequence of the use of multiple loadings to determine the trabecular architecture, the trabecular orientations are no longer always perpendicular. This finding is at odds with Wolff's firmly held presumption, and his consequently flawed observation, that the trabeculae can *only* intersect at right angles.[75] In reality, the angles are not always at right angles (see Chapter 29).

In 1990, Beaupré et al.[74] used the time-dependent bone density equations (Eqs. 31.36 through 31.38) with a similar two-dimensional finite-element model of the proximal human femur, shown in Fig. 31.13. The implementation also used multiple load cases, but in contrast to the results obtained by Carter et al.[70] the solution was convergent with calculated density distributions remarkably similar to physiological distributions. The results are "consistent with the hypothesis that similar stress-related phenomena are responsible for both normal morphogenesis and functional adaptation in response to changes in the bone loading."[74] They also note, however, that the response to changed mechanical loading may not be unique, consistent with Weinans et al.[76]

Jacobs et al.[73] have used Eq. 31.39, which operates directly upon the full stiffness matrix with no *a priori* assumptions about the degree of anisotropy of the trabecular bone, to simulate the density distribution using a two-dimensional finite-element model of the proximal femur. The results were very similar to those obtained using an isotropic rule for density evolution,[74] and are thus also remarkably similar to physiological distributions.

31.5.2 Trabecular Density: Strain Energy Dependence

Huiskes et al.[8] presented a theory for the density distribution of bone, as well as a computational implementation and preliminary applications in prosthesis design as discussed previously. In addition to the Eq. 31.23 for shape changes, Huiskes et al.[8] proposed the following description of modulus changes:

$$\frac{dE}{dt} = \begin{cases} C_e(U - (1+s)U_n); & U > (1+s)U_n \\ 0; & (1-s)U_n \le U \le (1+s)U_n \\ C_e(U - (1-s)U_n); & U < (1-s)U_n, \end{cases} \tag{31.40}$$

where E is the elastic modulus for the point considered, U is the current strain energy density, U_n is the homeostatic value of strain energy density, C_e is a remodeling rate constant, and $2s$ is the width of the "lazy zone" representing a range of strain energy density values near the homeostatic value in which there is no net remodeling response. With no lazy zone, i.e., $s = 0$, the equation can be rewritten as

$$\frac{dE}{dt} = C_e(U - U_n). \tag{31.41}$$

In 1992, Weinans et al.[77] expanded upon computational work to simulate adaptive bone remodeling that was first presented in 1989[78] and 1990.[79] They used a time-dependent rule for regulation of density as follows:

$$\frac{d\rho}{dt} = B\left(\frac{U_a}{\rho} - k\right), \qquad 0 < \rho \leq \rho_{\text{cb}}, \tag{31.42}$$

where the apparent density is represented by $\rho = \rho(x, y, z)$, ρ_{cb} is the maximum density of cortical bone, B and k are constants, and U_a represents the sum of the apparent strain energy density for the number of loading configurations being considered. To calculate the isotropic stiffness, the apparent density was used with the power law relation between density and Young's modulus.[80]

31.5.2.1 Example Applications: Discrete Structures

In 1992, Weinans et al.[76] used Eq. 31.42 in a series of example applications using finite-element models. Rather than explicitly incorporate a new set of equations to account for the changing orientation of the trabeculae, they chose to use dense meshes of finite elements and apply Eq. 31.42 to each element. Each element in the mesh was originally given the same density and during the simulations could then reach one of three outcomes: become completely resorbed ($\rho \approx 0$); become cortical ($\rho \approx \rho_{\text{cb}}$); or remain cancellous with intermediate densities ($0 < \rho \leq \rho_{\text{cb}}$).

The simulations were performed for two-dimensional models of a proximal femur and a simple two-dimensional plate model with a linear loading distribution. The simple plate models, shown in Fig. 31.14, allowed for an investigation of the stability and uniqueness of the net remodeling equation (Eq. 31.42) and gave some surprising results. In particular, the plate model could be manipulated (by choice of the remodeling rate constants and the loading) to develop the appearance of a discrete structure, with some elements at "full" or intermediate densities, and other elements essentially "turned-off" with zero densities. In addition to creating "trabecular-like" structures, the simulations also sometimes produced "checkerboard" patterns of elements with full and zero densities.[76]

For these simulations, the solution—in terms of the discrete structures produced—was shown to be dependent upon the methods of postprocessing (averaging results gave the appearance of continuum solutions) and upon mesh refinement. The solutions prompted studies [81–83] to examine in more detail the stability and uniqueness of these solutions that give discrete structures, even though the methodology was initially dependent upon a continuum assumption. Interestingly, the checkerboard and mesh-dependent anomalies have been observed while computationally designing microstructures for new materials.[84,85] In these cases, the checkerboarding was attributed to "poor numerical modeling of the stiffness of checkerboards by lower-order finite elements" and the mesh-dependency problem—nonconvergence of the solutions—was eliminated using ideas borrowed from image processing.[85] The image-processing technique essentially allows for systematic averaging of results by "blurring" the results. The use of higher-order finite elements as an alternate means to eliminate the checkerboarding pattern has been suggested by Jacobs et al.[86] and has also been suggested in the material design literature.[84] Another computational remedy that prevents the checkerboarding was suggested by Jacobs et al.[83] with the use of a "nodal approach" (density calculated at each node) as opposed to an "element approach" (density calculated at the element centroid). Beyond the computational remedies, Mullender et al.[87] justify a "biological averaging" technique based on a spatial influence function, described next. This technique eliminates the checkerboarding by

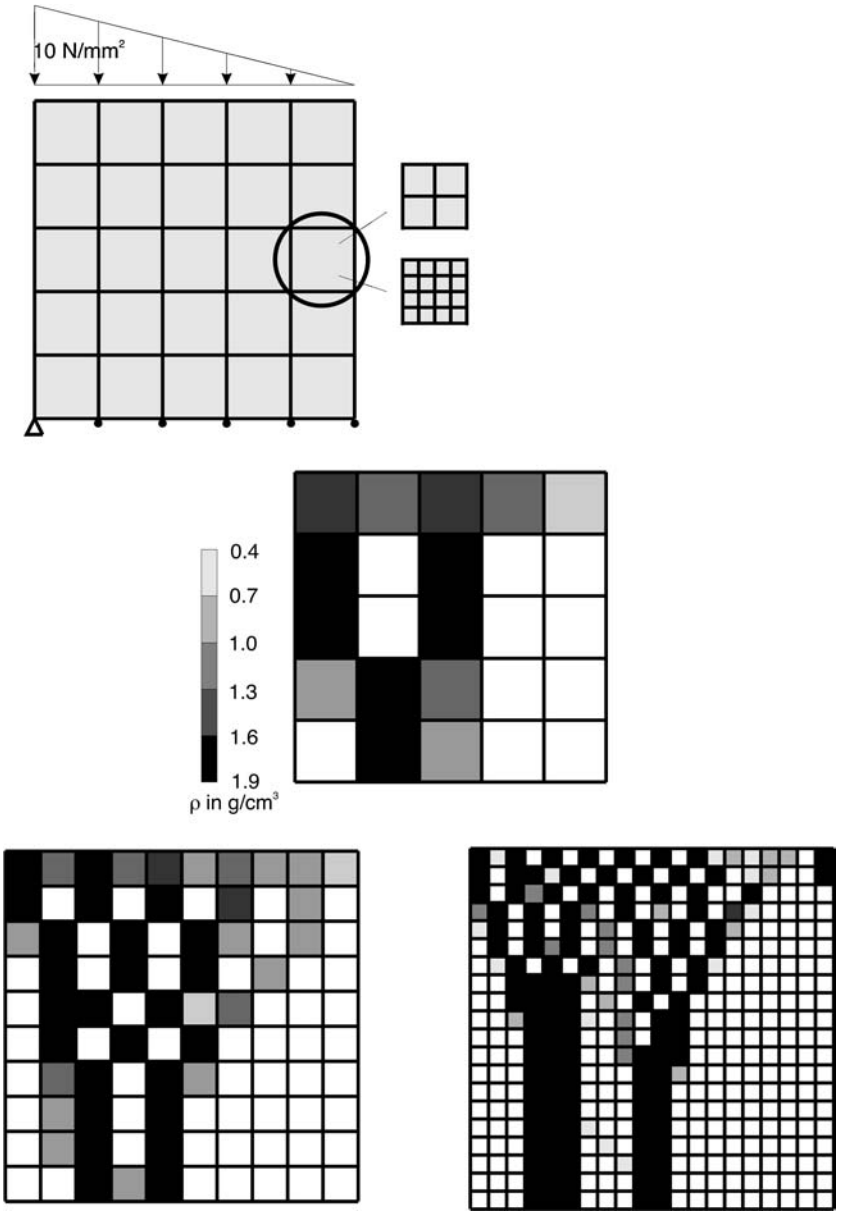

FIGURE 31.14 Analysis of the stability and uniqueness of adaptation solutions via density changes for a simple plate model. (a) Shows the plate with four-noded linear elements (5 × 5) and with additional mesh densities, including 10 × 10 and 20 × 20. The linear surface traction and boundary conditions are also shown. (b) The resultant density distributions are shown as a result of dependence of density upon strain energy density, as expressed in Eq. 31.42. The continuous structure has developed into a discrete structure with some elements at "full" or intermediate densities, and other elements essentially "turned-off" with zero densities. (Redrawn from Weinans, H. et al., *J. Biomech.,* 25(12), 1425, 1992. With permission.)

distinguishing the sensor grid (the spatial arrangement of the osteocytes) from the actor cells (the osteoblasts and osteoclasts) and the finite-element mesh.[87]

Thus, the results of Weinans et al.[76] have focused attention on some of the underlying difficulties in converting theories to computer implementations. Now it is widely recognized that the checkerboarding is simply a numerical artifact. However, the evolution of "trabecularization" in continuous structures is

a topic of continuing interest. Further research into the optimality, uniqueness, and stability of the proposed discrete structures is needed.

31.5.3 Trabecular Density and Orientation: Spatial Influence Function

Recently, a mechanistic model has been proposed for the functional adaptation of trabecular bone by Mullender and co-workers.[87,88] The basis of the model is the hypothesis that "osteocytes located within the bone sense mechanical signals and that these cells mediate osteoclasts and osteoblasts in their vicinity to adapt bone mass."[88] Each osteocyte i measures its local mechanical signal, $S_i(t)$, assumed to be the strain energy density, and influences all other "actor" cells (osteoclasts and osteoblasts) with decreasing influence based on the distance from the osteocyte. Mathematically, this is achieved by the use of a "spatial influence function" written using an exponential form as

$$f_i(\mathbf{x}) = e^{-(d_i(\mathbf{x})/D)}, \tag{31.43}$$

where $d_i(\mathbf{x})$ is the distance between osteocyte and location $\mathbf{x}$, D is the distance from an osteocyte at which its effect is e^{-1}, so that the influence of an individual osteocyte, i, decreases exponentially with distance from the cell. The use of the influence function to modify the stimulus amplitude, $S_i(t)$, summed from each osteocyte results in the stimulus value, $F(\mathbf{x},t)$:

$$F(\mathbf{x},t) = \sum_{i=1}^{N} f_i(\mathbf{x})(S_i(t) - k), \tag{31.44}$$

where k is the reference strain energy density. Then the regulation of the relative density, $m(x,t)$, is

$$\frac{dm(\mathbf{x},t)}{dt} = \tau F(\mathbf{x},t) \qquad \text{for } 0 < m(\mathbf{x},t) \leq 1, \tag{31.45}$$

where τ is a rate constant, and the elastic modulus at location $\mathbf{x}$, given by

$$E(\mathbf{x},t) = Cm(\mathbf{x},t)^{\gamma}, \tag{31.46}$$

where C and γ are constants. As described subsequently, this model has been used to investigate the "trabecularization" of bone in response to mechanical loading.

31.5.3.1 Example Applications: Tissue-Level Adaptations

The two-dimensional computational examples give striking results. First, the spatial influence function solves the computational checkerboarding artifact that had been observed with some other finite-element approaches.[87,88] Further, by using a tissue-level approach they show that initial idealized geometries with both uniform density distributions and lattice structures can give very similar "trabecularized" geometries during the computational simulations if they are loaded in the same fashion, as seen in Fig. 31.15. This computational test is a first step in showing the conditions needed for uniqueness of solutions. They also show that changing the direction of loading for the "trabecularized" geometries results in realignment of the trabeculae, and that severing a strut in the structure leads to its resorption and complete removal, as seen in Fig. 31.16. These computer simulations do a remarkably good job in mimicking a variety of the physiological behaviors of trabecular bone, and hold the real promise of providing a computational vehicle for simulation and study of the adaptive behavior of trabecular bone at the microstructural level.

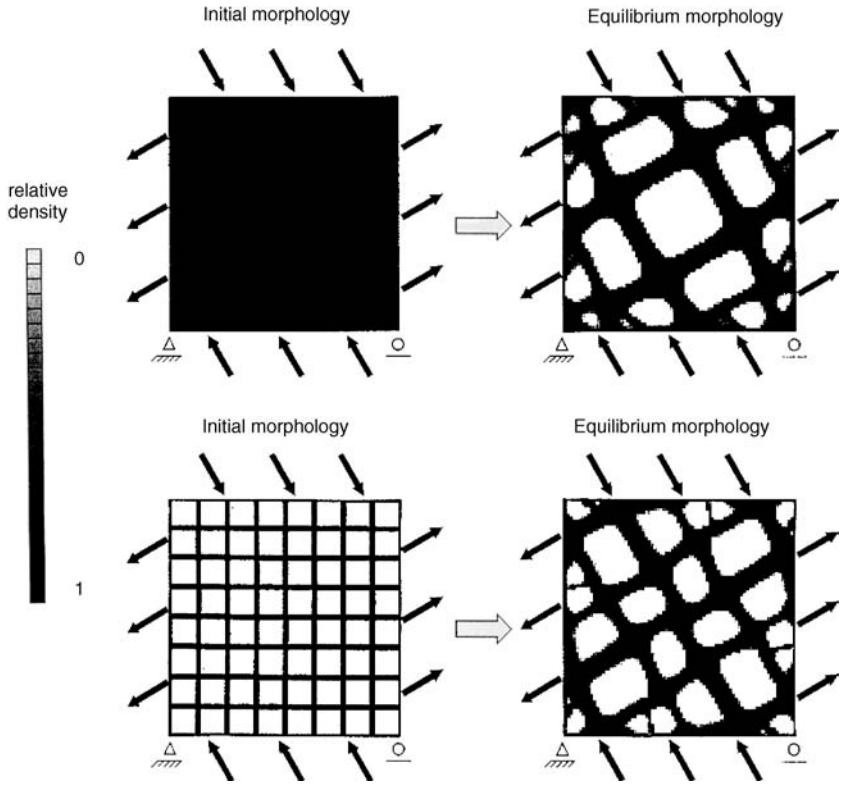

FIGURE 31.15 Trabecular bone density and orientation simulations from use of the spatial influence function. Trabecular-like patterns are formed from initial idealized goemetries with both uniform density distributions and lattice structures. The final equilibrium directions of the trabeculae match the principal stress orientation from the applied loading. (From Mullender, M. G. and Huiskes, R., *J. Orthrop. Res.,* 13(4), 503, 1995. With permission.)

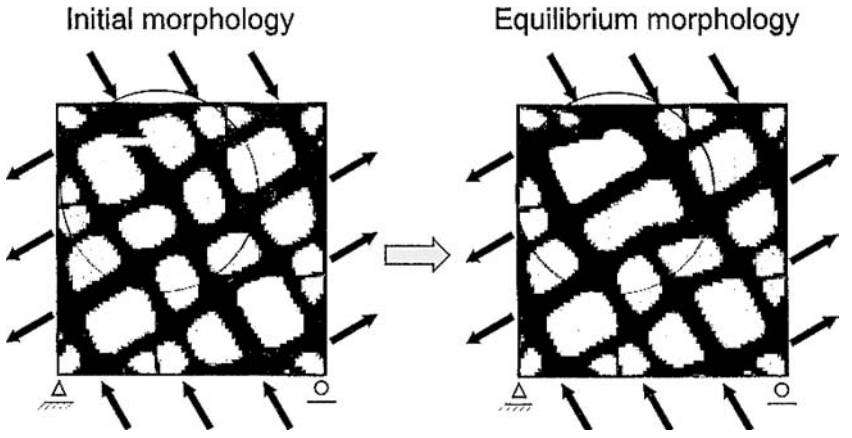

FIGURE 31.16 Simulation of the trabecular bone response due to a severed trabecular spicule. The unloaded trabecular portion is resorbed, and surrounding spicules are thickened and realigned. (From Mullender, M. G. and Huiskes, R., *J. Orthrop. Res.,* 13(4), 503, 1995. With permission.)

The notion of a spatial influence function has also been used by Smith et al.[89] with models in which the trabecular surface bone is added and removed based on the osteocytic signals. These models explore the consequences of assuming that the "set point" is located exclusively in the bone-lining cells to compare with the assumption used by Mullender and co-workers[87,88] in which the "set point" is located in the osteocytes. The simulations show trabecular reorientations similar to those in Fig. 31.15. However, an interesting consequence of having the set point located in the bone-lining cells is that—even in the equilibrium configurations—the strain energy density varies throughout the structure. This is a result of having the strain energy in the bone-lining cell dependent upon the influence function summation, and thus upon the local configuration of the trabecular architecture. The surprising consequence is that the trabecular structure shows "implicit site dependence even though each cell has the same explicit set point."[89]

31.5.4 Boundary-Element Implementation

Rather than use finite elements, Luo et al.[90] and Sadegh et al.[10] have used two-dimensional boundary elements to model idealized trabecular adaptation at the tissue level. The advantage of the boundary-element method is that due to an extra integration step in derivation of the computational implementation of the method, the dimensional order can be reduced by one. Thus, two-dimensional problems can be solved with one-dimensional elements only on the periphery of the area, and three-dimensional problems can be solved with two-dimensional elements only on the surface of the volume. There is an additional advantage for the boundary-element method when used to model free-boundary problems because boundary elements sidestep many difficulties faced when finite-element mesh distortion leads to poor numerical performance or disappearing elements.[17] Sadegh et al.[10] demonstrate the implementation and feasibility of incorporating the phenomenological surface remodeling rate equation (Eq. 31.9) into a boundary-element method.

31.5.4.1 Example Applications: Mergers and Separations; Strain and Strain Rate

For simulation of trabecular adaptation, the use of boundary-element methods is especially promising with microscale models. Sadegh et al.[10] used a series of idealized trabecular models to show that the method can be used to simulate two adjacent trabeculae that join together in a single column or the separation of one into two separate columns, as shown in Fig. 31.17. Luo et al.[90] used similar idealized boundary-element models to compare the computed differences in shape change when using dilatational strain and dilatational strain rate as the stimuli for the net remodeling response. First, they analytically demonstrated the equivalence of the stimuli in all cases except when the cyclic strain is always tensile. Consequently, in the cases when the stimuli are the same, the state of remodeling equilibrium is independent of the choice of dilatational strain or strain rate as the net remodeling stimulus. Luo et al.[90] then used models of three idealized trabecular bone patterns (cruciform, square diamond, and "brick-wall pattern") subjected to biaxial loads, and computationally demonstrated the analytical results. The computational examples (Fig. 31.18) showed that although the final shape was the same (for the cases where the two stimuli were shown to be equivalent), the two stimuli gave remarkably different evolutionary paths. The results seem to indicate this model does not suffer from some of the limitations in terms of uniqueness and stability that were observed with computational implementations of continuum-based models.

31.6 Discussion

The review provided in this chapter has described the fundamental concepts and assumptions inherent in development of models to describe the mechanical adaptation of bone. While not comprehensive, a number of adaptation models have been introduced, and example applications provided. As described recently by Currey[91] and seen in this review, many adaptation simulations have been developed and produce solutions that are qualitatively reasonable, and may fit with experimentally reported results. However, Currey points out a major problem with the approach of developing theoretical models and observing their qualitative response. Does any one particular simulation produce a better solution than

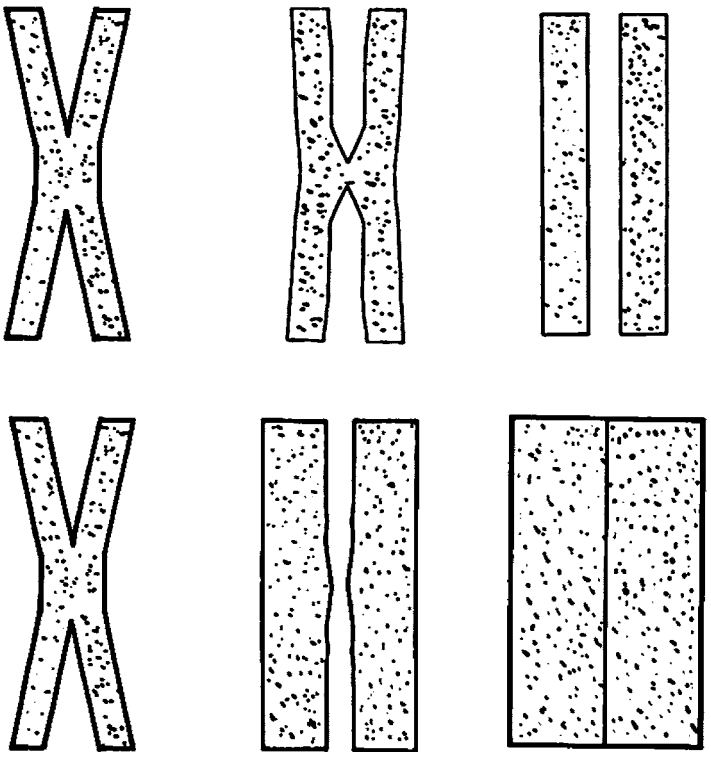

FIGURE 31.17 Boundary-element implementation of adaptation used with microscaled trabecular models. Idealized changes show that an original cruciform structure could either separate into two parallel struts (top) or join into a wide strut. (From Sadegh, A. M. et al., *J. Biomech.,* 26(2), 167, 1993. With permission.)

another approach that has already been developed? The dilemma raised by this question is evident with the examples presented in this chapter. The six models describing cortical bone adaptation illustrate examples of optimization, phenomenological, and mechanistic models. The model applications represent the consequences of osteotomy, malalignment, and intramedullary implants. For trabecular adaptation, five models have been presented, again illustrating the three model types. The applications for trabecular adaptation represent a wide range of examples and use continuum-level and tissue-level models. Although there are a variety of implementation differences—time-dependent and time-independent simulations, site-dependent and site-independent remodeling rate constants, and a variety of different strain and stress stimuli—*all the applications show qualitative agreement with some experimentally observed cortical and trabecular bone changes.* Currey[91] writes, "This is a fundamental difficulty if progress is to be made, because the literature becomes full of algorithms that predict real-life outcomes to some extent, but they are not matched against each other, there is no saying which is better than the others, so everybody can happily think that their own algorithm is satisfactory."

Certainly, a conclusion from the numerous theories and applications described in this chapter is that, at least for the simulations shown, bone models certainly seem to adapt to mechanical usage but seem not to be very picky about the specific mechanical stimuli used. It seems that any description of the mechanical situation can be successfully used to drive a satisfactory adaptation response. This apparently promiscuous response of bone to mechanical stimuli may be due to the choices used for parameters to monitor. For example, for axially loaded structures the areas of high axial strains also correlate to areas of high strain energy and to von Mises stresses. A study of 50 different mechanical parameters (six local strain components, six local stress components, three principal strains, three principal stresses, three strain invariants, three stress invariants, maximum shear strain, maximum shear stress, strain energy

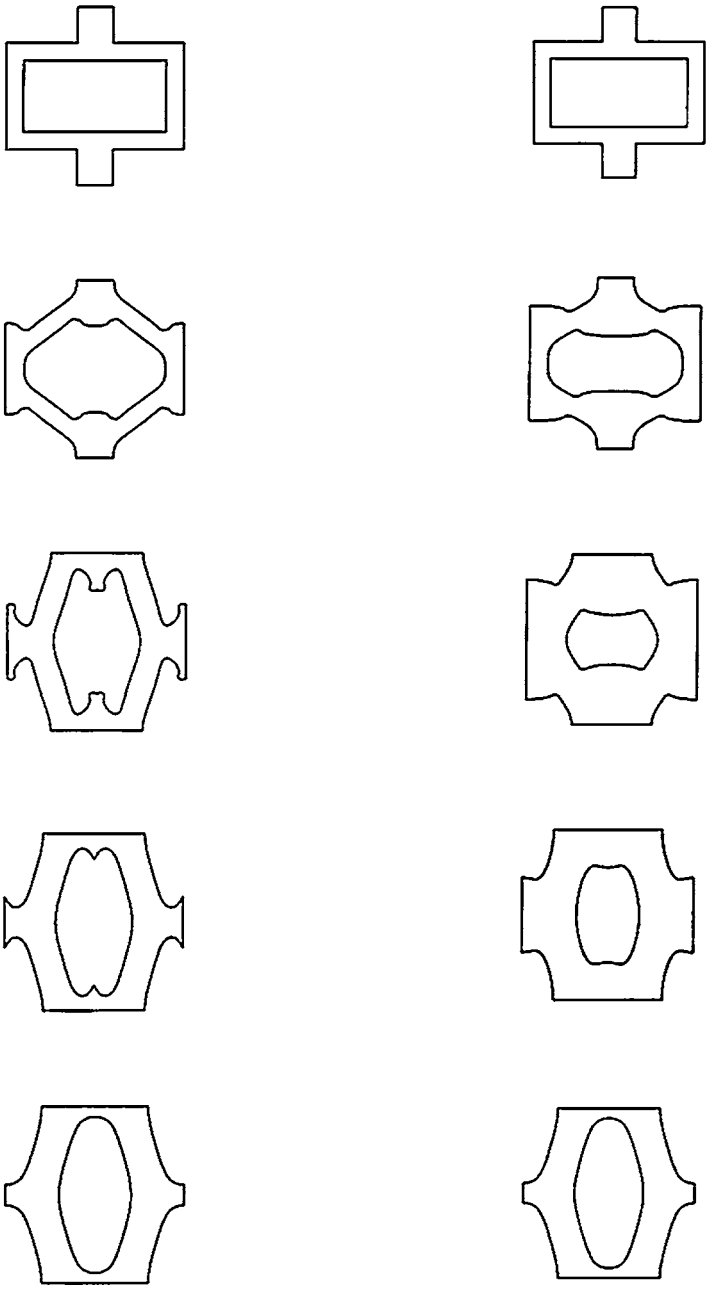

FIGURE 31.18 Boundary-element implementation of idealized periodic elements to approximate trabecular geometries. In this case, models are used to compare the computed differences in shape change when using dilatational strain and dilatational strain rate as the stimuli for net remodeling response. This example shows that although the final shape was the same when using dilatational strain (left) and dilatatational strain rate (right), the two stimuli gave remarkably different evolutionary paths. (From Luo, G. et al., *J. Biomech. Eng.,* 117(3), 329, 1995. With permission.)

density, 21 spatial strain gradients of the six strain gradients and dilatation in the three local directions, the mechanical intensity scalar, $\hat{E}$, and a signed strain energy density) shows that many of these parameters that have been used in adaptation simulations are highly correlated to one another.[92] This correlation of mechanical parameters helps mask the true regulators of the adaptation process so that distinct starting

assumptions about the nature of the mechanical parameters can result in similar simulation solutions. To be more useful, the modeling assumptions should be more tightly coupled to biological parameters that can be histologically measured and manipulated.[93]

Currey points out that a second major problem is based on the tendency for simulations to be used with a single remodeling situation, with no indication that the method is appropriate for any other one.[91] Again, which methods are best? He suggests that an algorithm be chosen as the "null hypothesis algorithm" that can satisfactorily solve a combination of idealized problems, and mirror experimental results as well. New algorithms should only be introduced to the literature if they prove superior to the "null hypothesis algorithm."[91]

A response is offered by Huiskes.[94] He points out the merit in using phenomenological models for predicting bone response even if the process is not yet well understood. He argues that the process of learning from each other as new ideas are tried and results published may be confusing, but is necessary while ideas and methods are incrementally refined and improved. Most important, he describes a specific example of how computational simulations may help in guiding experiments that can explore the mechanisms for adaptation. The specific testable hypothesis that arises from the spatial influence function[87,88] is that osteocyte density may be related to trabecular architecture. This is an exciting insight, and could be quantitatively explored.[94]

As mentioned at the outset, the merit from adaptation simulations depends upon recognizing that the different approaches have different objectives and outcomes. Optimization studies help to further understanding of bone as a mechanical structure, but do not provide useful information about the physiological process of adaptation. Phenomenological models may be useful in framing experimental questions, testing the consequences of different starting assumptions, and for the predictions of outcomes. They may even be useful for preliminary stages of implant design. However, as the focus shifts toward introducing mechanisms into the phenomenological models, the real benefits of developing and implementing a variety of different theories for bone adaptation studies begin to emerge. The models can help focus *in vivo* experiments on quantification of assumed parameters. Specifically, further advances in simulating bone adaptation will come from addressing a number of key steps, concepts, and questions: the transducers involved in converting mechanical usage into cellular responses; the degree of and physiological mechanisms for site specificity in adaptive responses; the time dependence of mechanical stimuli and physiological mechanisms responsible; and the question of a remodeling equilibrium state, how it may be initially set, and how it might be reset over time.

As inspired by Currey's[91] comments, the use of a "test suite" of example problems would prove useful as theories are developed and refined. A suite of problems could be solved using a variety of algorithms and assumptions—*especially including cases that fail to produce reasonable solutions*—and would help to improve these methods incrementally. Specific examples for the test suite may include the gradual straightening of a long bone (shown in Figs. 31.3 and 31.8). In fact, the use of strain energy density, which is always positive, did not allow the coordinated addition and removal of bone in a case where axial strains did produce the correct tendencies.[47] Similar difficulties would be expected with use of the strength optimization methods that incorporate damage as the stimulus. A test case for skeletal morphogenesis simulations might be first to determine the influence of various assumptions that are required for producing reasonable trabecular density and orientation outcomes. A test would be then to use the same values for a different region, e.g., the distal femur or proximal tibia to see the predicted patterns. Increasingly, the simulations should be cast in terms of physiological parameters that can be measured and manipulated, allowing tests of their validity as important players in functional adaptation processes. A final suggestion is the use of a "fully quantified" osteotomy experiment that includes measures of the temporal and spatial strains on the intact radius and ulna, followed by those same measures immediately following an ulnar osteotomy, and during use for several months thereafter. This level of quantification of the mechanical environment will allow a host of simulations similar to those already presented (Figs. 31.2, 31.4, 31.5, 31.6, and 31.9) but allow many more of the components of the strain history to be included as the primary stimuli.

Clearly, continued progress in the study of the functional adaptation of bone will depend upon interdisciplinary studies, and require increasingly sophisticated *in vivo*, mechanical, chemical, and cellular methods. The continuing fascination with bone—a unique and complex living structural material—will eventually yield quantitative models that allow for prediction of bone responses and for testing the consequences of therapeutic interventions.

Acknowledgments

This work was supported, in part, with a Whitaker Special Opportunity Award for Computational Tissue Engineering. The author appreciates the comments and suggestions made by M. D. Roberts, J. C. Coleman, R. B. Martin, R. Huiskes, and S. C. Cowin on an earlier draft of this chapter.

References

1. Wolff, J., *Das Gesetz der Transformation der Knochen,* Hirschwald Verlag, Berlin, 1892.
2. Wolff, J., *The Law of Bone Remodelling,* Springer-Verlag, Berlin, 1986.
3. Hart, R. T., Quantitative Response of Bone to Mechanical Stress, Ph.D. dissertation, Department of Mechanical and Aerospace Engineering, Case Western Reserve University, Cleveland, 1983.
4. Hart, R. T., D. T. Davy, and K. G. Heiple, Mathematical modeling and numerical solutions for functionally dependent bone remodeling, *Calcif. Tissue Int.,* 36(Suppl. 1), S104–109, 1984.
5. Roesler, H., Some historical remarks on the theory of cancellous bone structure (Wolff's Law), *Mechanical Properties of Bone,* S. C. Cowin, New York, American Society of Mechanical Engineers: 27–42, 1981.
6. Frost, H. M., A determinant of bone architecture. The minimum effective strain, *Clin. Orthop.,* 175, 286–292, 1983.
7. Carter, D. R., Mechanical loading histories and cortical bone remodeling, *Calcif. Tissue Int.,* 36 (Suppl. 1), S19–24, 1984.
8. Huiskes, R., H. Weinans, H. J. Grootenboer, M. Dalstra, B. Fudala, and T. J. Slooff, Adaptive bone-remodeling theory applied to prosthetic-design analysis, *J. Biomech.,* 20 (11–12), 1135–1150, 1987.
9. Cowin, S. C., Mechanical modeling of the stress adaptation process in bone, *Calcif. Tissue Int.,* 36 (Suppl. 1), S98–103, 1984.
10. Sadegh, A. M., G. M. Luo, and S. C. Cowin, Bone ingrowth: an application of the boundary element method to bone remodeling at the implant interface, *J. Biomech.,* 26(2), 167–182, 1993.
11. Fyhrie, D. P. and D. R. Carter, A unifying principle relating stress to trabecular bone morphology, *J. Orthop. Res.,* 4(3), 304–317, 1986.
12. Carter, D. R., D. P. Fyhrie, and R. T. Whalen, Trabecular bone density and loading history: regulation of connective tissue biology by mechanical energy, *J. Biomech.,* 20(8), 785–794, 1987.
13. Hart, R. T., V. V. Hennebel, N. Thongpreda, W. C. Van Buskirk, and R. C. Anderson, Modeling the biomechanics of the mandible: a three-dimensional finite element study, *J. Biomech.,* 25(3), 261–286, 1992.
14. Cowin, S. C., Deviatoric and hydrostatic mode interaction in hard and soft tissue, *J. Biomech.,* 23(1), 11–14, 1990.
15. Burr, D. B., R. B. Martin, M. B. Schaffler, and E. L. Radin, Bone remodeling in response to *in vivo* fatigue microdamage, *J. Biomech.,* 18(3), 189–200, 1985.
16. Frost, H. M., Skeletal structural adaptations to mechanical usage (SATMU): 2. Redefining Wolff's law: the remodeling problem, *Anat. Rec.,* 226(4), 414–422, 1990.
17. Cowin, S. C., Bone stress adaptation models, *J. Biomech. Eng.,* 115(4B), 528–533, 1993.
18. Lanyon, L. E., I. L. Paul, C. T. Rubin, E. L. Thrasher, R. DeLaura, R. M. Rose, and E. L. Radin, In vivo strain measurements from bone and prosthesis following total hip replacement. An experimental study in sheep, *J. Bone Joint Surg.* [Am.], 63(6), 989–1001, 1981.

19. Burr, D. B., M. B. Schaffler, K. H. Yang, M. Lukoschek, N. Sivaneri, J. D. Blaha, and E. L. Radin, Skeletal change in response to altered strain environments: is woven bone a response to elevated strain? *Bone,* 10(3), 223–233, 1989.
20. McLeod, K. J., C. T. Rubin, M. W. Otter, and Y. X. Qin, Skeletal cell stresses and bone adaptation, *Am. J. Med. Sci.,* 316(3), 176–183, 1998.
21. Qin, Y. X., C. T. Rubin, and K. J. McLeod, Nonlinear dependence of loading intensity and cycle number in the maintenance of bone mass and morphology, *J. Orthop. Res.,* 16(4), 482–489, 1998.
22. Rubin, C. T. and L. E. Lanyon, Regulation of bone formation by applied dynamic loads, *J. Bone Joint Surg.* [Am.], 66(3), 397–402, 1984.
23. Turner, C. H., Three rules for bone adaptation to mechanical stimuli, *Bone,* 23(5), 399–407, 1998.
24. Treharne, R. W., Review of Wolff's law and its proposed means of operation, *Orthop. Revi.,* X(1), 35–47, 1981.
25. Cowin, S. C., L. Moss-Salentijn, and M. L. Moss, Candidates for the mechanosensory system in bone, *J. Biomech. Eng.,* 113(2), 191–197, 1991.
26. Cowin, S. C., S. Weinbaum, and Y. Zeng, A case for bone canaliculi as the anatomical site of strain generated potentials, *J. Biomech.,* 28(11), 1281–1297, 1995.
27. Gjelsvik, A., Bone remodeling and piezoelectricity—I, *J. Biomech.,* 6, 69–77, 1973.
28. Gjelsvik, A., Bone remodeling and piezoelectricity—II, *J. Biomech.,* 6, 187–193, 1973.
29. Frost, H. A., Dynamics of bone remodeling, in *Bone Biodynamics,* H. A. Frost, Ed., Little, Brown, Boston, 315–333, 1964.
30. Hart, R. T. and S. P. Fritton, Introduction to finite element based simulation of functional adaptation of cancellous bone, *Forma,* 12, 277–299, 1997.
31. Hart, R. T., D. T. Davy, and K. G. Heiple, A computational method for stress analysis of adaptive elastic materials with a view toward applications in strain-induced bone remodeling, *J. Biomech. Eng.,* 106(4), 342–350, 1984.
32. Frost, H. M., *Intermediary Organization of the Skeleton,* CRC Press, Boca Raton, FL, 1986.
33. Cowin, S. C. and W. C. Van Buskirk, Internal bone remodeling induced by a medullary pin, *J. Biomech.,* 11(5), 269–275, 1978.
34. Cowin, S. C. and W. C. Van Buskirk, Surface bone remodeling induced by a medullary pin, *J. Biomech.,* 12(4), 269–276, 1979.
35. Huiskes, R. and E. Y. Chao, A survey of finite element analysis in orthopedic biomechanics: the first decade, *J. Biomech.,* 16(6), 385–409, 1983.
36. Cook, R. D., D. S. Malkus, and M. E. Plesha, *Concepts and Applications of Finite Element Analysis,* John Wiley & Sons, New York, 1989.
37. Hart, R. T., The finite element method, in *Bone Mechanics,* S. C. Cowin, Ed., CRC Press, Boca Raton, FL, 1989, chap. 4, 53–74.
38. Frost, H. M., Skeletal structural adaptations to mechanical usage (SATMU): 1. Redefining Wolff's law: the bone modeling problem, *Anat. Rec.,* 226(4), 403–413, 1990.
39. Cowin, S. C. and D. H. Hegedus, Bone remodeling I: Theory of adaptive elasticity, *J. Elasticity,* 6(3), 313–326, 1976.
40. Cowin, S. C. and K. Firoozbakhsh, Bone remodeling of diaphysial surfaces under constant load: theoretical predictions, *J. Biomech.,* 14(7), 471–484, 1981.
41. Cowin, S. C., Wolff's law of trabecular architecture at remodeling equilibrium, *J. Biomech. Eng.,* 108(1), 83–88, 1986.
42. Cowin, S. C. and W. C. Van Buskirk, Thermodynamic restrictions on the elastic constants of bone, *J. Biomech.,* 19(1), 85–87, 1986.
43. Cowin, S. C., Bone remodeling of diaphyseal surfaces by torsional loads: theoretical predictions, *J. Biomech.,* 20(11–12), 1111–1120, 1987.
44. Cowin, S. C., A. M. Sadegh, and G. M. Luo, An evolutionary Wolff's law for trabecular architecture, *J. Biomech. Eng.,* 114(1), 129–136, 1992.

45. Cowin, S. C., R. T. Hart, J. R. Balser, and D. H. Kohn, Functional adaptation in long bones: establishing in vivo values for surface remodeling rate coefficients, *J. Biomech.,* 18(9), 665–684, 1985.
46. Hart, R. T., A theoretical study of the influence of bone maturation rate on surface remodeling predictions: idealized models, *J. Biomech.,* 23(3), 241–257, 1990.
47. Hart, R. T. and A. M. Rust-Dawicki, Computational simulation of idealized long bone re-alignment, in *Computer Simulations in Biomedicine,* H. Power and R. T. Hart, Eds., Computational Mechanics Publications, Boston, 1995, 341–350.
48. Oden, Z. M., R. T. Hart, M. R. Forwood, and D. B. Burr, A priori prediction of functional adaptation in canine radii using a cell based mechanistic approach, *Trans. 41st Orthopaedic Research Society,* Orlando, FL, 1995.
49. Hart, R. T., V. V. Hennebel, N. Thongpreda, and D. A. Dulitz, Computer simulation of cortical bone remodeling, in *Science and Engineering on Supercomputers,* E. J. Pitcher, Ed., Computational Mechanics Publications, Boston, 1990, 57–66, 565–566.
50. Davy, D. T. and R. T. Hart, *A Theoretical Model for Mechanically Induced Bone Remodeling,* American Society of Biomechanics, Rochester, MN, 1983.
51. Hart, R. T. and D. T. Davy, Theories of bone modeling and remodeling, in *Bone Mechanics,* S. C. Cowin, Ed., CRC Press, Boca Raton, FL, 1989, chap. 11, 253–277.
52. Martin, R. B., The effects of geometric feedback in the development of osteoporosis, *J. Biomech.,* 5(5), 447–455, 1972.
53. Oden, Z. M., Computational Prediction of Functional Adaptation in Canine Radii, Ph.D. dissertation, Department of Biomedical Engineering, Tulane University, New Orleans, 1994.
54. Burr, D. B., personal communication, 1994.
55. Carter, D. R., Mechanical loading history and skeletal biology, *J. Biomech.,* 20(11–12), 1095–1109, 1987.
56. Baumgartner, A. and C. Mattheck, Computer simulation of the remodeling of trabecular bone, in *Computers in Biomedicine,* K. D. Held, C. A. Brebbia, and R. D. Ciskowski, Eds., Computational Mechanics Publications, Southampton, 1991, 291–296.
57. Mattheck, C. and H. Huber-Betzer, CAO: Computer simulation of adaptive growth in bones and trees, in *Computers in Biomedicine,* K. D. Held, C. A. Brebbia, and R. D. Ciskowski, Eds., Computational Mechanics Publications, Southampton, 1991, 243–252.
58. Mattheck, C., *Design in Nature,* Springer-Verlag, Berlin, 1998.
59. Prendergast, P. J. and D. Taylor, Prediction of bone adaptation using damage accumulation, *J. Biomech.,* 27(8), 1067–1076, 1994.
60. McNamara, B. P., P. J. Prendergast, and D. Taylor, Prediction of bone adaptation in the ulnar-osteotomized sheep's forelimb using an anatomical finite element model, *J. Biomed. Eng.,* 14(3), 209–216, 1992.
61. McNamara, B. P., Ph.D. dissertation, Department of Mechanical and Manufacturing Engineering, University of Dublin, Trinity College, Dublin, 1995.
62. Lanyon, L. E., A. E. Goodship, C. J. Pye, and J. H. MacFie, Mechanically adaptive bone remodelling, *J. Biomech.,* 15(3), 141–154, 1982.
63. Cowin, S. C., personal communication, 1986.
64. Cowin, S. C., The mechanical properties of cortical bone tissue, in *Bone Mechanics,* S. C. Cowin, Ed., CRC Press, Boca Raton, FL, 1989, 97–128.
65. Harrigan, T. P. and R. W. Mann, Characterization of microstructural anisotropy in orthopaedic materials using a second rank tensor, *J. Mater. Sci.,* 19, 761, 1984.
66. Harrigan, T. P., Bone Compliance and Its Effects in Human Hip Joint Lubrication, Sc.D. dissertation, Department of Mechanical Engineering, Massachusetts Institute of Technology, Boston, 1985.
67. Fritton, S. P., Computational Simulation of Trabecular Bone Adaptation, Ph.D. dissertation, Department of Biomedical Engineering, Tulane University, New Orleans, 1994.

68. Fritton, S. P. and R. T. Hart, Simulation of in vivo trabecular bone adaptation, *41st Annual Meeting of the Orthopaedic Research Society,* Orlando, FL, 1995.
69. Harrigan, T. P., M. Jasty, R. W. Mann, and W. H. Harris, Limitations of the continuum assumption in cancellous bone, *J. Biomech.,* 21(4), 269–275, 1988.
70. Carter, D. R., T. E. Orr, and D. P. Fyhrie, Relationships between loading history and femoral cancellous bone architecture, *J. Biomech.,* 22(3), 231–244, 1989.
71. Beaupré, G. S., T. E. Orr, and D. R. Carter, An approach for time-dependent bone modeling and remodeling—theoretical development, *J. Orthop. Res.,* 8(5), 651–661, 1990.
72. Martin, R. B., Porosity and specific surface of bone, *Crit. Rev. Biomed. Eng.,* 10(3), 179–222, 1984.
73. Jacobs, C. R., J. C. Simo, G. B. Beaupré, and D. R. Carter, Comparing an optimal efficiency assumption to a principal stress-based formulation for the simulation of anisotropic bone adaptation to mechanical loading, in *Bone Structure and Remodeling,* A. Odgaard and H. Weinans, Eds., World Scientific, Singapore, 1995, 225–237.
74. Beaupré, G. S., T. E. Orr, and D. R. Carter, An approach for time-dependent bone modeling and remodeling—application: a preliminary remodeling simulation, *J. Orthop. Res.,* 8(5), 662–670, 1990.
75. Cowin, S. C., The false premise of Wolff's law, *Forma,* 12, 247–262, 1997.
76. Weinans, H., R. Huiskes, and H. J. Grootenboer, The behavior of adaptive bone-remodeling simulation models, *J. Biomech.,* 25(12), 1425–1441, 1992.
77. Weinans, H., R. Huiskes, and H. J. Grootenboer, Effects of material properties of femoral hip components on bone remodeling, *J. Orthop. Res.,* 10(6), 845–853, 1992.
78. Weinans, H., R. Huiskes, and H. J. Grootenboer, Convergence and uniqueness of adaptive bone remodeling, *Transactions of the 35th Annual Meeting of the Orthopaedic Research Society,* Las Vegas, 1989.
79. Weinans, H., R. Huiskes, and H. J. Grootenboer, Numerical comparisons of strain-adaptive bone-remodeling theories, *Abstracts of the 1st World Congress on Biomechanics,* La Jolla, 1990.
80. Carter, D. R. and W. C. Hayes, The compressive behavior of bone as a two-phase porous structure, *J. Bone Joint Surg.* [Am.], 59(7), 954–962, 1977.
81. Harrigan, T. P. and J. J. Hamilton, An analytical and numerical study of the stability of bone remodelling theories: dependence on microstructural stimulus [published erratum appears in *J. Biomech.,* 26(3), 3656, 1993], *J. Biomech.,* 25(5), 477–488, 1992.
82. Cowin, S. C., Y. P. Arramon, G. M. Luo, and A. M. Sadegh, Chaos in the discrete-time algorithm for bone-density remodeling rate equations, *J. Biomech.,* 26(9), 1077–1089, 1993.
83. Jacobs, C. R., M. E. Levenston, G. S. Beaupré, J. C. Simo, and D. R. Carter, Numerical instabilities in bone remodeling simulations: the advantages of a node-based finite element approach, *J. Biomech.,* 28(4), 449–459, 1995.
84. Jog, C. S. and R. B. Haber, Stability of Finite Element Models for Distributed-Parameter Optimization and Topology Design, TAM Report No. 758, UIL-ENG-94-6014, University of Illinois, Urbana-Champaign, 1994.
85. Sigmund, O., Design of Material Structures Using Topology Optimization, Reports 69, Danish Center for Applied Mathematics and Mechanics, Technical University of Denmark, Lyngby, 1994.
86. Jacobs, C. R., M. E. Levenston, G. B. Beaupré, and J. C. Simo, A new implementation of finite element-based remodeling, G. N. P. J. Middleton, and K. R. Williams, Eds., in *Recent Advances in Computer Methods in Biomechanics and Biomedical Engineering,* Books and Journals International, Swansea, 1992.
87. Mullender, M. G., R. Huiskes, and H. Weinans, A physiological approach to the simulation of bone remodeling as a self-organizational control process, *J. Biomech.,* 27(11), 1389–1394, 1994.
88. Mullender, M. G. and R. Huiskes, Proposal for the regulatory mechanism of Wolff's law, *J. Orthop. Res.,* 13(4), 503–512, 1995.
89. Smith, T. S., R. B. Martin, M. Hubbard, and B. K. Bay, Surface remodeling of trabecular bone using a tissue level model, *J. Orthop. Res.,* 15(4), 593–600, 1997.

90. Luo, G., S. C. Cowin, A. M. Sadegh, and Y. P. Arramon, Implementation of strain rate as a bone remodeling stimulus, *J. Biomech. Eng.,* 117(3), 329–338, 1995.
91. Currey, J. D., The validation of algorithms used to explain adaptive remodelling in bone, in *Bone Structure and Remodelling,* A. Odgaard and H. Weinans, Eds., World Scientific, Singapore, 1995, 9–13.
92. Oden, Z. M. and R. T. Hart, 1995, Correlation between mechanical parameters that represent bone's mechanical milieu and control functional adaptation, in *Bone Structure and Remodeling: Recent Advances in Human Biology*, vol. 2, A. Odgaard and H. Weinans, Eds., World Scientific, Singapore, 1995, ix, 257.
93. Martin, R. B., The usefulness of mathematical models for bone remodeling, *Yearbook Phys. Anthropol.,* 28, 227–236, 1985.
94. Huiskes, R., The law of adaptive bone remodelling: a case for crying Newton? in *Bone Structure and Remodelling,* A. Odgaard and H. Weinans, Eds., World Scientific, Singapore, 1995, 15–24.
95. Frost, H. M., *Introduction to a New Skeletal Physiology,* Pajaro Group, Pueblo, CO, 1995.

32

Mechanics of Bone Regeneration

Patrick J. Prendergast
Trinity College Dublin

Marjolein C. H. van der Meulen
Cornell University

32.1 Introduction

Bone has the capability to regenerate, forming new osseous tissue at locations that are damaged or missing. Although this capability extends to regeneration of whole limbs in some animals,[1] in humans regeneration is on a more limited scale and occurs during defect healing, e.g., after the removal of bone screws; fracture healing; distraction osteogenesis (during limb lengthening); and integration of orthopedic implants with the host bone. During the regenerative process, bone tissue can form directly or indirectly. During indirect bone formation, also called endochondral ossification, cartilage is formed, calcified, and replaced by bone tissue. During direct bone formation, or intramembranous ossification, bone tissue forms without the intermediate cartilage stage.

The importance of the mechanical environment on tissue regeneration is evident in several ways. For example, during defect healing, when the regenerating bone is shielded from load, intramembranous, not endochondral, bone formation occurs.[2] Excessive motion during long bone fracture healing inhibits bone formation. Instead of bone, a layer of cartilage forms at the fracture ends, creating a pseudoarthrosis ("fake joint").[3] Similarly, if an implant moves excessively relative to the surrounding bone, bone formation is inhibited and a persistent fibrous tissue layer forms at the bone–implant interface.[4]

The complex nature of bone regeneration has mostly been studied during fracture healing of long bones. For this reason, experiments designed to understand long bone fracture healing will be described in Section 32.2. In Section 32.3, different theories to describe the influence of mechanics on bone regeneration will be reviewed.

32.2 Fracture Healing

Bone fracture repair occurs either by:

1. Primary (direct, osteonal) fracture healing, where the fracture gap ossifies via intramembranous bone formation without external callus, or

2. Secondary (indirect, spontaneous) fracture healing, where a multistage process of tissue regeneration stabilizes the bone with an external callus and repairs the fracture via endochondral ossification.

During primary fracture healing, the fractured cortices repair directly by osteonal remodeling across the cortex. This process is less common than secondary fracture healing because the fracture must be extremely stable and well reduced for direct healing to occur. Clinically this process is observed when fractures are stabilized by rigid fixation such as compression plating.

Secondary fracture healing occurs in a sequence of three biological phases: the inflammatory, reparative, and remodeling phases.[5] These phases involve the coordinated activity of different cell populations that proliferate, differentiate, and synthesize extracellular matrix components. This cellular activity is spatially and temporally coordinated by a variety of growth factors and other regulatory molecules, including insulin-like growth factors (IGFs), fibroblast growth factors (FGFs), platelet-derived growth factors (PDGFs), transforming growth factors (TGFs), and bone morphogenetic proteins (BMPs).[6–8]

During the inflammatory phase, the periosteum of the bone lifts, and a hematoma forms between the bone ends due to the rupture of blood vessels. This hematoma releases a large number of signaling molecules, including inflammatory cytokines such as interleukin-1 (IL-1) and interleukin-6 (IL-6), and growth factors such as PDGF and transforming growth factor-β (TGF-β).[7] These factors appear to regulate the initiation of fracture healing and the associated cellular response. For example, TGF-β has been shown to accelerate fracture healing.[9] The first cells present are pluripotent progenitor cells called mesenchymal stem cells: they originate from several possible sources (the inner cambial layer of the periosteum, the endosteum, the bone marrow, or the vascular endothelium[10–13]). These stem cells then differentiate into chondrocytes and osteocytes, which proliferate and generate the reparative callus. This differentiation of the mesenchymal cells appears to be activated by BMPs.[14]

During the reparative phase an external (periosteal) callus and an internal (medullary) callus are formed (Fig. 32.1). Intramembranous and endochondral bone formation occur simultaneously in different regions of the fracture calluses. Intramembranous ossification occurs only at the callus periphery, beneath the damaged periosteum but somewhat removed from the fracture site, and appears to be regulated by TGF-β.[8] This rapidly formed woven bone creates a mineralized *hard* callus. Endochondral ossification occurs adjacent to the fracture site and initiates with cartilage. This *soft* callus bridges across the fracture. The rapid cartilage formation of the early callus is accomplished primarily by the differentiation of mesenchymal cells into chondrocytes, and less by proliferation of existing chondrocytes.[15] TGF-β may regulate this cartilage matrix synthesis. Injection of BMP-2 into fractured rabbit tibiae increases the rate of healing, but not the size of the fracture callus.[16] Mineralization of the cartilage involves a mechanism similar to long bone growth at the growth plate[11] and requires reestablishment of the vascular and nutrient supply. Chondrocytes hypertrophy, the extracellular matrix calcifies and blood vessels penetrate the matrix. Then the calcified cartilage tissue is resorbed and replaced by woven bone formed by osteoblasts.

In the final healing phase, osteonal remodeling of the newly formed bone tissue and of the fracture ends restores the original shape and lamellar structure of the bone. White et al.[17] defined four biomechanical stages of fracture repair. At this final healing stage, the failure of a healed bone when loaded is not related to the original fracture site, while at the early stages, failure occurs through the weaker fracture.

In the reparative phase, the formation of a callus with a large cross-sectional area increases the rigidity of the bone and stabilizes the fracture ends. As ossification proceeds, the fracture becomes stiffer and the motion of the fracture fragments decreases further. Therefore, fracture stiffness may indicate successful, or unsuccessful, healing. Marsh[18] measured callus size and bending stiffness during healing of human tibiae and found no correlation between callus index (ratio of the maximum width of the callus to the diameter of the original shaft) and bending stiffness. However, a bending stiffness of less than 7 Nm/° at 20 weeks indicated a delayed union or a non-union. Similarly, Richardson et al.[19] found that patients whose tibial fractures had reached a bending stiffness of 15 Nm/° did not refracture after external fixation. This stiffness was proposed to define successful union of these fractures.

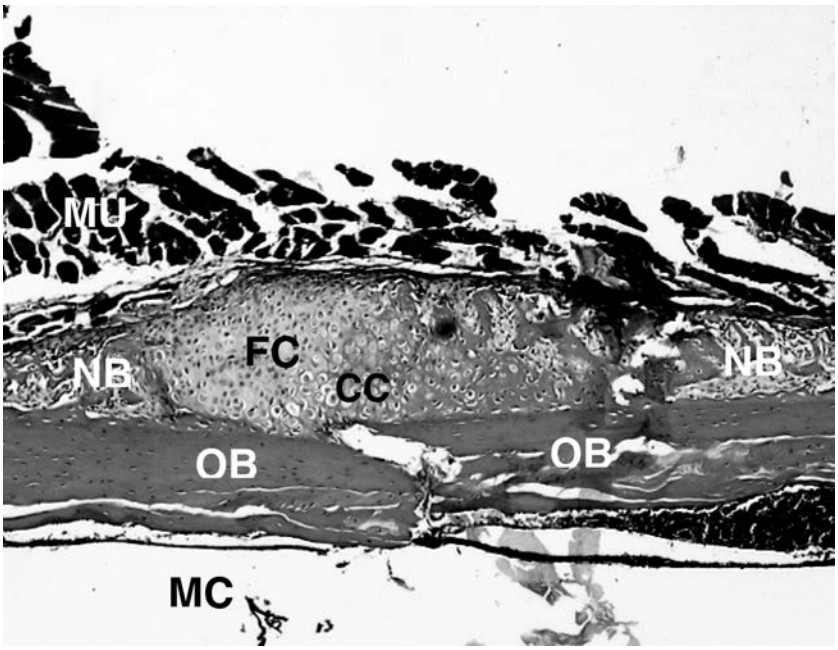

FIGURE 32.1 Histological section of a mouse fracture callus 5 days postfracture. The femur was pinned and then fractured, so no endosteal callus is present. Intramembranous bone formation is evident under the periosteum at the callus periphery; fibrous and cartilaginous callus is present adjacent to the fracture. OB = original bone, NB = new membranous bone, FC = fibrous callus, CC = cartilage callus, MC = medullary canal, MU = muscle. Trichrome staining.

The importance of the mechanical environment on fracture repair has been demonstrated experimentally and can be examined during each stage of the repair process. The type of fixation device* and the nature of the musculoskeletal loading will determine the mechanical environment within the regenerating tissue. This environment, in turn, will influence callus size, ossification rate, and healed bone strength. Based on a series of sheep experiments, Goodship et al.[20] concluded,

> More flexible fixation may lead to excessive interfragmentary motion … whereas more rigid fixation may impair callus formation contributing to … non-union.

The rates of healing, tissue ossification, and stiffness are enhanced by *cyclic* mechanical loading.[21–23] In sheep, Goodship and Kenwright[21] found that cyclic axial motion compared to rigid fixation induced earlier ossification and more rapid healing, based on increased whole-bone stiffness (Fig. 32.2). Gardner et al.[24] investigated the effect of reducing the displacement across a fracture during healing; they found more rapid healing if the displacement was reduced as healing progressed. Comparing static and cyclic compression of healing fractures, Panjabi and co-workers[22] observed a greater rate of strength increase at the middle and later healing stages in bones with cyclic loading. Delaying mechanical stimulation until after the initiation of ossification eliminates the beneficial influence of cyclic loads.[25] In the study by Goodship et al.,[20] the importance of strain rate was also demonstrated. Fractures stimulated at a moderate strain rate (40 mm/s) increased bone mineral content and stiffness faster than those stimulated at slow (2 mm/s) and fast (400 mm/s) rates. Finally, the size of the fracture gap is critical to healing. Augat et al.[26] used external fixation of metatarsus of sheep to compare healing with 1, 2, and 6 mm osteotomies, and two amounts of interfragmentary strain (7 or 31%). They showed that increasing the gap size reduced the bone stiffness and tensile strength. Because the lower interfragmentary strain adequately stimulated the callus, gap size was the more dominant of the two factors in the fracture-healing process.

*See Chapter 35 for a description of fracture fixation devices.

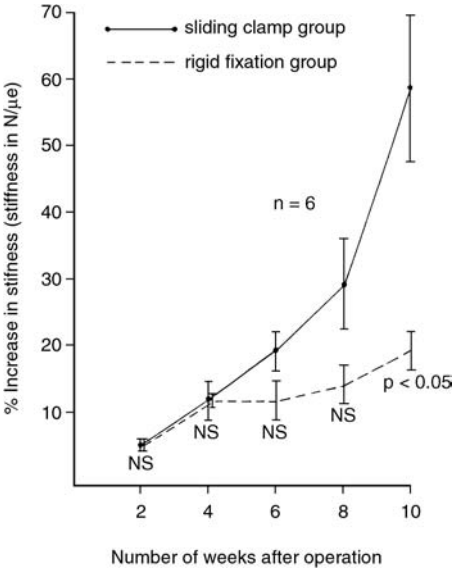

FIGURE 32.2 Mean *in vivo* increase in fracture stiffness in two groups of sheep with experimental tibial fractures. Axial movement at the fracture site different in the two groups. The difference between the two groups was significant at the 8 to 10 week period. (From Goodship, A.E. and Kenwright, J., *J. Bone Joint Surg.,* 67B, 650, 1985. With permission.)

Particularly interesting questions arise from the interaction of growth factors involved in the normal healing cascade and mechanical loading during fracture healing.[27] Growth factor expression may be regulated by mechanical stimuli, but is difficult to study in fracture healing. Distraction osteogenesis induces a bone formation response similar to fracture healing and has a better-defined spatial gradient of bone formation. Increased mechanical stimulus during distraction osteogenesis increases expression of BMP-2 and BMP-4, which may be responsible for enhanced ossification.[28] During distraction osteogenesis, BMP-4 is found at sites of proliferation and differentiation of mesenchymal cells suggesting a regulatory role in the early fracture callus.[29] The development of rodent fracture models will lead to a better understanding of these interactions.[30,31] In particular, knockout mice and other genetic manipulations offer exciting possibilities[32] and will greatly improve knowledge of fracture healing.

32.3 Mechanobiological Models

According to Carter et al.,[33] mechanobiology is the study of how mechanical or physical conditions regulate biological processes. During bone regeneration, physical forces contribute to the differentiation of the cell populations that arise over the healing period. For musculoskeletal tissues, Caplan and Boyan[34] have hypothesized that mesenchymal stem cells differentiate into one of several musculoskeletal tissues (Fig. 32.3). The mechanics of bone regeneration involves understanding how the osteogenic pathway shown in Fig. 32.3 is regulated by mechanical forces within the tissue.

32.3.1 Pauwels' Theory

Much of present-day understanding of the regulative effect of mechanical forces on tissue differentiation comes from Friedrich Pauwels. Pauwels recognized that physical factors cause stress and deformation of the mesenchymal cells, and that these stimuli could determine the cell differentiation pathway. Using simple experimental models of a fracture callus,[35] he demonstrated how shearing results in a change of *shape* of a

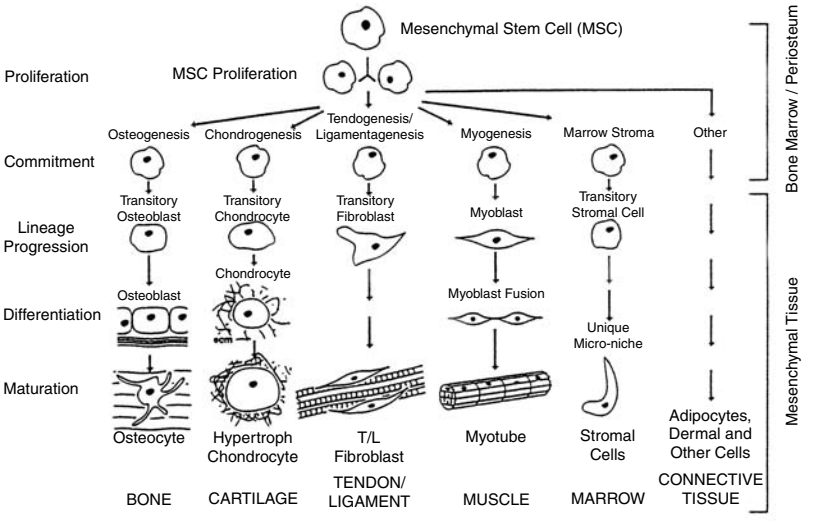

FIGURE 32.3 Mesenchymal stem cells have the potential to differentiate into a variety of tissues, such as bone, cartilage, tendon, muscle, fat, and dermis. *Commitment* to a particular pathway, as well as progression through the lineage, is dependent not just on specific growth factors and/or cytokines but also on biophysical stimuli acting on the cells. Continuous differentiation from the mesenchymal cell pool ensures that changing biophysical stimuli will elicit changing tissues. (From Caplan, A.I. and Boyan, B.D., in *Mechanism of Bone Development and Growth,* B. K. Hall, Ed., CRC Press, Boca Raton, FL, 1994. With permission.)

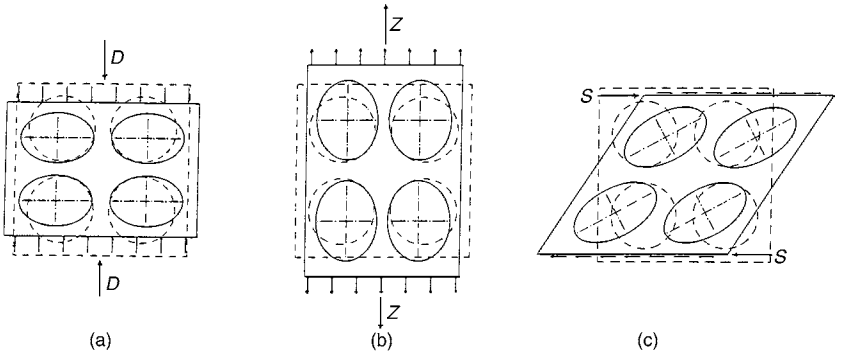

FIGURE 32.4 A direct compressive force (denoted D) "deforms the elementary particles of a cube of elastic material" into ellipsoids, as does a tensile force (denoted Z) and a shear force (denoted S). (Adapted from Pauwels, F., in *Biomechanics of the Locomotor Apparatus,* translated by Maquet, P. and Furlong, R., Springer, Berlin, 1980, 375–407.)

piece of tissue (Fig. 32.4) whereas hydrostatic pressure results in a change in *volume*. Using this concept, he proposed a quantitative hypothesis for the influence of mechanical factors on tissue differentiation as follows:

1. Shear, which causes a change in cell shape, stimulates mesenchymal cell differentiation into fibroblasts, and
2. Hydrostatic compression, which causes a change in volume without a change in shape, stimulates mesenchymal cell differentiation into chondrocytes.

By decomposing mechanical stimuli into shear and hydrostatic compression, Pauwels also predicted that a combination of shear and hydrostatic pressure would stimulate differentiation of fibrocartilage, such as occurs in the menisci of the knee or in the intervertebral disk.[36]

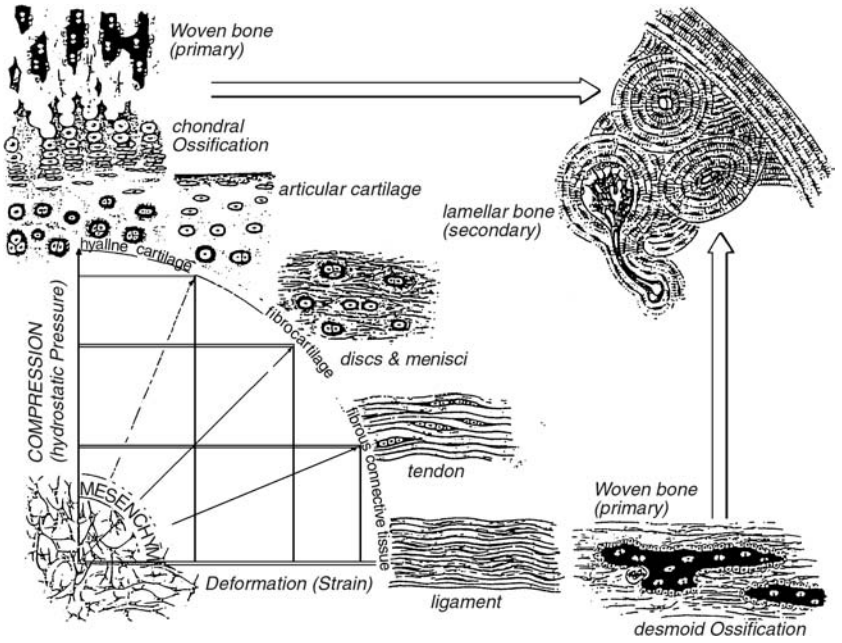

FIGURE 32.5 Pauwels' concept of tissue differentiation. Bone regeneration occurs only after stabilization of the mechanical environment by the formation of soft tissue. (From Weinans, H. and Prendergast, P.J., *Bone*, 19, 143, 1996. With permission.)

Pauwels' theory, as illustrated in Fig. 32.5, also predicted the following:

1. Primary bone formation requires a stable mechanical environment so endochondral bone formation will proceed only if the soft tissues create this low strain environment.
2. Ligamentous tissue ossifies by the process of desmoid ossification.
3. Both ossified tissues remodel and are replaced by secondary lamellar bone (indicated by arrows).

Pauwels' concept that tissue differentiation is evoked by mechanical factors drew on the ideas of earlier German biologists such as Roux and Krompecher; see Prichard.[37] Roux proposed that cells compete for a functional stimulus within the tissue.[38] Interpreting this in the context of the Pauwels theory, the functional stimulus favoring fibroblast differentiation from the mesenchymal cell pool is high shear. Endochondral bone formation, on the other hand, occurs in low strain/high compression environments.

32.3.2 Interfragmentary Strain Theory

When a fractured bone is loaded, the fracture fragments displace relative to each other. The strain produced in the fracture gap was named the "interfragmentary strain (IFS)" by Perren.[39] If the width of the fracture gap is given by L and the change in the fracture gap after loading is given by ΔL, then the strain in the longitudinal direction (IFS) is

$$\text{IFS} = \frac{\Delta L}{L}. \tag{32.1}$$

Perren's interfragmentary strain theory proposes that the fracture gap can be filled only with a tissue capable of sustaining the IFS without rupture.[40] The strain tolerance is greatest for granulation tissue, intermediate for cartilage, and least for bone (Fig. 32.6). If the IFS is high, only granulation tissue can form according to the interfragmentary strain theory. If granulation tissue does form, the callus will

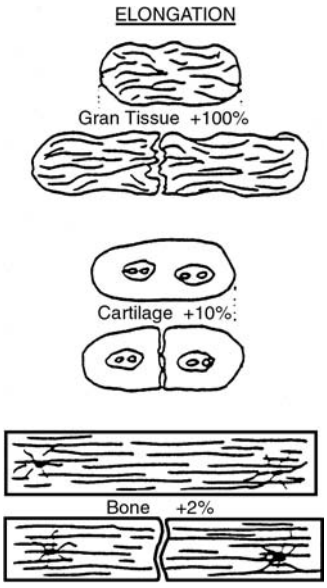

FIGURE 32.6 Strain tolerance of repair tissues. A tissue cannot exist in an environment where the interfragmentary strain exceeds the strain tolerance of the extracellular matrix of the tissue. (From Perren, S.M. and Cordey, J., in *Current Concepts of Internal Fixation of Fractures,* Springer, Berlin, 1980, 65. With permission.)

reduce the IFS. This reduction in the motion of the fracture fragments generates the environment where chondrocytes can sustain the IFS and proliferate. In this way, endochondral bone formation proceeds as the IFS is "gently and progressively limited."[40] Whether or not the presence of soft tissue will actually reduce the IFS depends on many factors, including the nature of the musculoskeletal loading on the bone, and the structural behavior of the fracture fixation device.[41]

Although the interfragmentary strain theory is useful for understanding the relationship between motion and bone healing, the theory is not a general theory of bone regeneration because

1. The strain field in the fracture gap is multiaxial,[42]
2. Mechanical stimuli vary spatially in the fracture callus.[43,44]

Furthermore, if the displacement is not very small relative to the gap size, the longitudinal strain in a fracture gap cannot be accurately calculated using Eq. 32.1 because of geometric and material nonlinearity.[45] It is noteworthy that Claes et al.,[46] who were able to determine the IFS with a telemeterized external fixation system, concluded that the IFS did not significantly influence the success of fracture healing, although inferior tissue properties were observed histologically for larger IFS.

32.3.3 Deformation/Pressure Models

Investigating the mechanics of endochondral ossification, Carter and colleagues[47,48] proposed that intermittent or cyclic mechanical loading occurring over a period of time (load history) stimulates tissue differentiation. The loading history was decomposed into discrete loading conditions, denoted *c*. Using the concepts proposed by Pauwels,[35] the stress acting on the regenerating tissue was described as a combination of two scalar quantities:

1. Hydrostatic stress (related to the dilatational strain) denoted D_i and
2. Octahedral shear stress also called the deviatoric stress (related to the distortional strain) denoted S_i,

where the subscript denotes the *i*th load case, and $i = 1, 2, 3, \ldots. c$.

There are six independent stresses in a material* written as σ_x, σ_y, σ_z, τ_{xy}, τ_{yz}, and τ_{xz}, where x, y, z is an orthogonal axis. The hydrostatic stress is given by

$$D = \frac{1}{3}(\sigma_x + \sigma_y + \sigma_z) \tag{32.2}$$

and the octahedral shear stress is given by

$$S = \frac{1}{3}\sqrt{(\sigma_x - \sigma_y)^2 + (\sigma_x - \sigma_z)^2 + (\sigma_y - \sigma_z)^2 + 6(\tau_{xy}^2 + \tau_{yz}^2 + \tau_{xz}^2)}. \tag{32.3}$$

The hydrostatic and octahedral shear stresses are *invariants* of the stress—i.e., they will have the same numeric value no matter what coordinate system is used. Carter and colleagues proposed that cyclic octahedral shear stress encourages cartilage ossification whereas the action of a cyclic hydrostatic stress inhibits ossification. The driving force for bone formation may be described by a linear combination of the stress invariants. This is termed the osteogenic index (OI), given as

$$\text{OI} = \sum_{i=1}^{c} n_i(S_i + kD_i), \tag{32.4}$$

where n_i is the number of loading cycles for the ith load case. The value of k, the empirical constant, is determined by parametric variation in computer models of fracture healing,[48,49] joint formation,[50] and endochondral ossification of the sternum.[51] High values of OI are caused by high shear stress or by tensile hydrostatic stresses—therefore, according to the osteogenic index theory, these stimuli favor endochondral bone formation. Bone formation is inhibited in the presence of large compressive hydrostatic stresses.

In a finite-element analysis of the mechanical stimuli on ossifying surfaces during fracture healing, Claes and colleagues[52,53] hypothesized that magnitudes of hydrostatic pressure and strain regulate the selection of either intramembranous or endochondral bone formation processes. By quantitative analysis of a real callus geometry, they found that if the compressive hydrostatic pressure (negative) exceeded 0.15 MPa at the regenerating bone surface then endochondral bone formation (i.e., prior formation of cartilage) occurred, whereas if the hydrostatic pressure was below this threshold then intramembranous bone formation proceeded (Fig. 32.7a).

While the osteogenic index theory refers specifically to ossification within cartilage, the concept of a stimulus combined from hydrostatic stress and shearing due to tension may be applied more generally to tissue differentiation. Tissue formation in tendons,[54] at implant interfaces,[55] and during distraction osteogenesis[56] has been analyzed using a relationship between mechanical stimuli and tissue differentiation shown in Fig. 32.7b. Stress and strain are combined on these diagrams even though these are not, in general, decoupled.[57]

32.3.4 Models Including Fluid Flow

Although models of tissues as solid elastic materials may give adequate macroscopic load/deformation responses, the cells respond to cell level deformations and fluid flows (see Chapter 27). Since tissues are composed of a solid phase (collagen, with hydroxyapatite in the case of bone) and a significant amount of fluid (mostly water), they may be analyzed as mixtures of solid and fluid constituents. When bone[58] or cartilage[59] is loaded, the fluid component may flow and cause complex mechanical stimuli within tissues at the cellular level. Several *in vitro* cell studies have demonstrated the potential regulatory role of mechanical stimulation of bone cells,[60] in the form of both fluid flow (osteocytes[61] and osteoblasts[62]) and

*See Chapter 6 for an introduction to mechanics of materials.

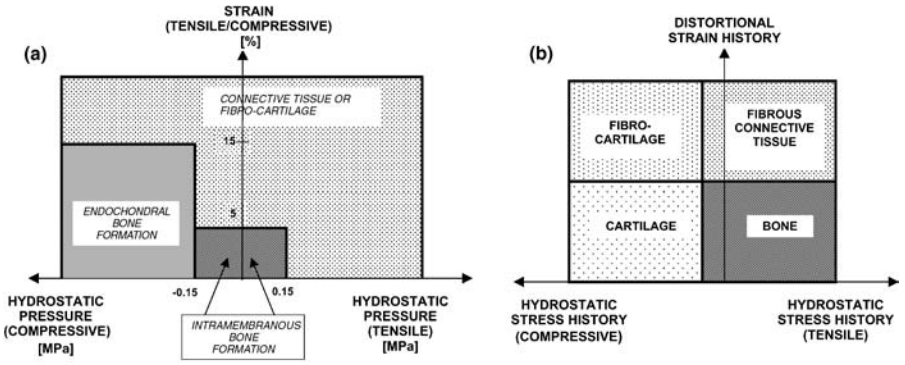

FIGURE 32.7 (a) Relationship between mechanical stimuli and bone formation. (Adapted from Claes, L.E. and Heigele, C.A., *J. Biomech.*, 32, 255, 1999.) (b) Relationship between loading history and tissue phenotype. (Adapted from Carter, D.R. et al., *Trans. Orthop. Res. Soc.*, 234, 1998.)

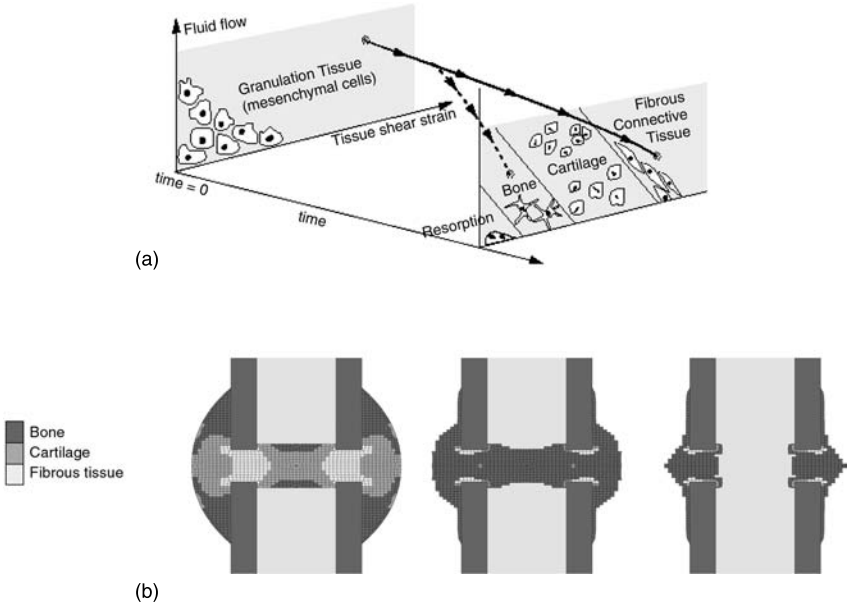

FIGURE 32.8 (a) A mechanoregulation diagram for bone formation and resorption based on mechanical strain and fluid flow; (b) application to simulation of fracture healing. (Courtesy of Damien Lacroix.)

substrate strain (osteocytes[63] and osteoblasts[64]). Owan et al.[65] have found that the responsiveness to fluid flow may dominate that of mechanical strain in bone cells.

The biomechanical stress acting on cells will be high if the fluid flow is high: therefore, deformation *and* fluid flow must be taken together to define the mechanical milieu on the cell.[66,67] Following Pauwels and the interfragmentary strain theory, high strains may be hypothesized to create the mechanical environment for fibroblast differentiation from the mesenchymal cell pool and the subsequent emergence of a fibrous connective tissue phenotype. Similarly, intermediate strains will allow cartilage formation and low strains will allow bone formation. The influence of fluid flow is to increase the deformation of the cells further. Therefore, the presence of high fluid flow will increase the biomechanical stress and thus decrease the potential for tissue differentiation in the case of each tissue phenotype. If the strain or fluid flow becomes low, then the lack of mechanical stimulation to the cells may initiate a resorptive process, as indicated by the resorption field on Fig. 32.8a.

This regulatory scheme can simulate the time course of bone regeneration around implants using a poroelastic biphasic theory to calculate the stress in the fluid and solid phases of a tissue.[68,69] For a biphasic material, the solid stress, denoted σ_s, and fluid stresses, denoted σ_f, are given by

$$\sigma_s = \phi^s pI + \lambda e^s I + 2\mu\varepsilon^s, \tag{32.5}$$

$$\sigma_f = -\phi^f pI, \tag{32.6}$$

where e and ε denote the dilatational strain and the total strain in the solid phase, p is the apparent pressure in the fluid, with ϕ denoting the volume fraction, and λ and μ being the Lamé constants. This model has been used to simulate the time-course of fracture healing[70] where the influence of loading on bone regeneration in the callus can be predicted, see Fig. 32.8b.

32.4 Future Directions

This chapter has introduced the biology of bone healing and reviewed the theories that describe the regulation of bone regeneration by mechanical forces. Fracture repair is increasingly well understood from the point of view of the molecular biologist; the influence of the mechanical factors and the interaction between biophysical and biochemical regulatory pathways have yet to be fully elucidated. Further development of models is needed to relate continuum stress to subcontinuum stimuli at the cellular level. With such models, mechanical stimuli determined from *in vitro* cell culture experiments could be used to compute how cells react within regenerating bone. These models have exciting potential not only for understanding fracture healing and tissue formation but also for designing bioreactors used to grow tissue-engineered constructs.[71]

Acknowledgments

The authors acknowledge financial support from the Wellcome Trust for a Biomedical Research Collaboration Grant between Trinity College and Cornell University. We thank Alicia Bailon-Plaza and Damien Lacroix for their contributions to this chapter.

References

1. Wolpert, L., Regeneration, in *The Triumph of the Embryo,* Oxford University Press, Oxford, 1991, chap. 13.
2. Johner, R., Zur Knochenheilung in abhängigkeit von der defektgrösse, *Helv. Chir. Acta,* 39, 409, 1972.
3. Pauwels, F., Grundriss einer biomechanik der frakturheilung, in *34th Kongress der Deutschen Orthopädischen Gesellschaft,* Ferdinand Enke, Stuttgart, 1940, 62–108. (Translated by Maquet, P, Furlong, R. as Biomechanics of fracture healing, in *Biomechanics of the Locomotor Apparatus,* Springer, Berlin, 1980, 375–407.)
4. Søballe, K., Hydroxyapatite ceramic coating for bone implant fixation. Mechanical and histological studies in dogs, *Acta Orthop. Scand.,* 64, Suppl. 255, 1993.
5. Brand, R.A. and Rubin, C.T., Fracture healing, in *Surgery of the Musculo-skeletal System;* Vol. 1, McCollister, E.C., Ed., Churchill-Livingstone, London, 1990, 93–114.
6. Bolander, M.E., Regulation of fracture repair and synthesis of matrix macromolecules, in *Bone Formation and Repair,* Brighton, C.T., Friedlander, G., and Lane, J.M., Eds., American Academy of Orthopaedic Surgeons, Rosemont, IL, 1994, chap. 11.
7. Bolander, M.E., Regulation of fracture repair by growth factors, *Proc. Soc. Exp. Biol. Med.,* 200, 165, 1992.

8. Barnes, G.L, Kostneuik, P.J., Gerstenfeld, L.C., and Einhorn, T.A., Perspective: growth factor regulation of fracture repair, *J. Bone Miner. Res.,* 14, 1805, 1999.
9. Joyce, M.E., Terek, R.M., Jingushi, S., and Bolander, M.E., Role of transforming growth factor—in fracture repair, *Ann. N.Y. Acad. Sci.,* 593, 107, 1990.
10. McKibbin, B., The biology of fracture healing in long bones, *J. Bone Joint Surg.,* 60B, 150, 1978.
11. Einhorn, T.A., The cell and molecular biology of fracture healing, *Clin. Orthop.,* 355S, 7, 1998.
12. Yoo, J.U. and Johnstone, B., The role of osteochondral progenitor cells in fracture repair, *Clin. Orthop.,* 355, 73, 1998.
13. Brighton, C.T. and Hunt, R.M., Early histological and ultrastructural changes in the medullary fracture callus, *J. Bone Joint Surg.,* 73A, 832, 1991.
14. Bostrom, M.P.G., Expression of bone morphogenetic proteins in fracture healing, *Clin. Orthop.,* 355S, S116, 1998.
15. Sandberg, M., Aro, H., Multimäka, P., Aho, H., and Vuorio, E., In situ localization of collagen production by chondrocytes and osteoblasts in fracture callus, *J. Bone Joint Surg.,* 71A, 69, 1989.
16. Bax, B.E., Wozney, J.M., and Ashurst, D.E., Bone morphogenetic protein-2 increases the rate of callus formation after fracture of rabbit tibiae, *Calcif. Tissue Int.,* 65, 83, 1999.
17. White, A.A., Panjabi, M.M., and Southwick, W.O., The four biomechanical stages of fracture repair, *J. Bone Joint Surg.,* 59A, 188, 1977.
18. Marsh, D., Concepts of fracture union, delayed union, and nonunion, *Clin. Orthop.,* 355S, 22, 1998.
19. Richardson, J.B., Cunningham, J.L., Goodship, A. E., O'Connor, B.T., and Kenwright, J., Measuring stiffness can define healing of tibial fractures, *J. Bone Joint Surg.,* 76B, 389, 1994.
20. Goodship, A.E., Watkins, P.E., Rigby, H.S., and Kenwright, J., The role of fixator frame stiffness in the control of fracture healing. An experimental study, *J. Biomech.,* 26, 1027, 1993.
21. Goodship, A.E. and Kenwright, J., The influence of induced micromovement upon the healing of tibial fractures, *J. Bone Joint Surg.,* 67B, 650, 1985.
22. Wolfe, S.W., Lorenze, M.D., Austin, G., Swigart, C.R., and Panjabi, M.M., Load-displacement behaviour in a distal radial fracture model—the effect of simulated healing on motion, *J. Bone Joint Surg.,* 81A, 53, 1999.
23. Probst, A., Janson, H., Ladas, A., and Spiegel, H.U., Callus formation and fixation rigidity: a fracture model in rats, *J. Orthop. Res.,* 17, 256, 1999.
24. Gardner, T.N., Evans, M., and Simpson, H., Temporal variation of applied inter fragmentary displacement at a bone fracture in harmony with maturation of the fracture callus, *Med. Eng. Phys.,* 20, 480, 1998.
25. Goodship, A.E., Cunningham, J.L., and Kenwright, J., Strain rate and timing of stimulation and mechanical modulation of fracture healing, *Clin. Orthop.,* 355S, S105, 1998.
26. Augat, P., Margevicius, K., Simon, J., Wolf, S., Suger, G., and Claes, L., Local tissue properties in bone healing: Influence of size and stability of the osteotomy gap, *J. Orthop. Res.,* 16, 475, 1998.
27. Cornell, C.N. and Lane, J.M., Newest factors in fracture healing, *Clin. Orthop.,* 277, 297, 1992.
28. Sato, M., Ochi, T., Nakase, T., Hirota, S., Kitamura, Y., Nomura, S., and Jasui, N., Mechanical tension-stress induces expression of bone morphogenetic protein (BMP)-2 and BMP-4, but not BMP-6, BMP-7, and GDF-5 mRNA, during distraction osteogenesis, *J. Bone Miner. Res.,* 14, 1084, 1999.
29. Li, G., Berven, S., Simpson, H., and Triffitt, J.T., Expression of BMP-4 mRNA during distraction osteogenesis in rabbits, *Acta Orthop. Scand.,* 69, 420, 1998.
30. Bonnarens, F. and Einhorn, T.A., Production of a standard closed fracture in laboratory animal bone, *J. Orthop. Res.,* 2, 97, 1984.
31. Aro, H., Eerola, E., and Aho, A.J., Determination of callus quantity in 4-week-old fractures of the rat tibia, *J. Orthop. Res.,* 3, 101, 1985.
32. van der Meulen, M.C., Bailón-Plaza, A., and Hunter, W.L., Long bone fracture healing in bone morphogenetic protein-5-deficient mice, *J. Bone Miner. Res.,* 13, S352, 1998.

33. Carter, D.R., Beaupré, G.S., Giori, N.J., and Helms, J.A., Mechanobiology of skeletal regeneration, *Clin. Orthop. Relat. Res.,* 355S, 41, 1998.
34. Caplan, A.I. and Boyan, B.D., Endochondral bone formation: the lineage cascade, in *Mechanism of Bone Development and Growth.* B. K. Hall, Ed., CRC Press, Boca Raton, FL, 1994.
35. Pauwels, F., Eine neue Theorie über den einfluss mechanischer Reize auf die Differenzierung der Stützgewebe, *Z. Anat. Entwickl.,* 121, 478, 1960. (Translated by Maquet, P., Furlong, R. as A new theory concerning the influence of mechanical stimuli in the differentiation of supporting tissues, in *Biomechanics of the Locomotor Apparatus,* Springer, Berlin, 1980, 375–407.
36. Pauwels, F., *Atlas zur Biomechanik der Gesunden und Kranken Hüfte,* Springer, Berlin, 1973.
37. Prichard, J.J., Bone, in *Tissue Repair,* McMinn, R.M.H., Ed., Academic Press, London, 1969, chap. 4.
38. Weinans, H. and Prendergast, P.J., Tissue adaptation as a dynamical process far from equilibrium, *Bone,* 19, 143, 1996.
39. Perren, S.M., Physical and biological aspects of fracture healing with special reference to internal fixation, *Clin. Orthop.,* 138, 175, 1979.
40. Perren, S.M. and Cordey, J., The concept of interfragmentary strain, in *Current Concepts of Internal Fixation of Fractures,* H. K. Uhthoff, Ed., Springer, Berlin, 1980, 63–77.
41. Tencer, A.F. and Johnson, D., *Biomechanics in Orthopaedic Trauma,* Martin Dunitz, London, 1994.
42. DiGioia III, A.M., Cheal, E.J., and Hayes, W.C., Three-dimensional strain fields in a uniform osteotomy gap, *J. Biomech. Eng.,* 108, 273, 1986.
43. Biegler, F.R. and Hart, R.T., Finite element modelling of long bone fracture healing, in *Computer Methods in Biomechanics and Biomedical Engineering,* Books and Journals International, Swansea, J. Middleton, G.N. Pande, K.R. Williams, Eds., 1992, 30–39.
44. Gardner, T.N., Stoll, T., Marks, L., and Knote-Tate, M., Mathematical modelling of stress and strain in bone fracture repair tissue, in *Computer Methods in Biomechanics and Biomedical Engineering II,* Gordon and Breach, Amsterdam, 1998, 247.
45. Meroi, E.A. and Natali, A.N., A numerical approach to the biomechanical analysis of fracture healing, *J. Biomed. Eng.,* 11, 390, 1989.
46. Claes, L., Augat, P., Suger, G., and Wilke, H.-J., Influence of size and stability of the osteotomy gap on the success of fracture healing, *J. Orthop. Res.,* 15, 577, 1997.
47. Carter, D.R., Mechanical loading history and skeletal biology, *J. Biomech.,* 20, 1095, 1987.
48. Carter, D.R., Blenman, P.R., and Beaupré, G.S., Correlations between mechanical stress history and tissue differentiation in initial fracture healing, *J. Orthop. Res.,* 6, 736, 1988.
49. Blenman, P.R., Carter, D.R., and Beaupré, G.S., Role of mechanical loading in the progressive ossification of a fracture callus, *J. Orthop. Res.,* 7, 398, 1989.
50. Carter, D.R. and Wong, M., The role of mechanical loading histories in the development of diarthrodial joints, *J. Orthop. Res.,* 6, 804, 1988.
51. Wong, M. and Carter, D.R., Mechanical stress and morphogenetic endochondral ossification of the sternum, *J. Bone Joint Surg.,* 70A, 992, 1988.
52. Claes, L.E., Heigele, C.A., Neidlinger-Wilke, C., Kaspar, D., Seidl, W., Margevicius, K.J., and Augat, P., Effects of mechanical factors on the fracture healing process, *Clin. Orthop.,* 355S, S132, 1998.
53. Claes, L.E. and Heigele, C.A., Magnitudes of local stress and strain along bony surfaces predict the course and type of fracture healing, *J. Biomech.,* 32, 255, 1999.
54. Giori, N.J., Beaupré, G. S., and Carter, D.R., Cellular shape and pressure may medicate mechanical control of tissue composition in tendons, *J. Orthop. Res.,* 11, 581, 1993.
55. Giori, N.J. Ryd, L., and Carter, D.R., Mechanical influences of tissue differentiation at bone–cement interfaces, *J. Arthroplasty,* 10, 514, 1995.
56. Carter, D.R., Helms, J.A., Tay, B.K., and Braupré, G. S., Stress and strain distributions predict tissue differentiation patterns in distraction osteogenesis, *Trans. Orthop. Res. Soc.,* 44, 234, 1998.
57. Cowin, S.C., Deviatoric and hydrostatic mode interaction in hard and soft tissue, *J. Biomech.,* 23, 11, 1990.
58. Cowin, S.C., Bone poroelasticity, *J. Biomech.,* 32, 217, 1999.

59. Mow, V.C., Ratcliffe, A., and Poole, A.R., Cartilage and diarthrodial joints as paradigms for hierarchical materials and structures, *Biomaterials,* 13, 67, 1992.
60. Brown, T.D., Techniques for mechanical stimulation of cells in vitro: a review, *J. Biomech.,* 33,3, 2000.
61. Klein-Nulend, J., van der Plas, A., Seimens, C.M., Ajubi, N.E., Frangos, J.A., Nejweide, P.J., and Burger, E.H., Sensititivity of osteocytes to biomechanical stress in vitro, *FASEB J.,* 9, 441, 1995.
62. Jacobs, C.R., Yellowley, C.E., Davis, B.R., Zhou, Z., Cimbala, J.M., and Donahue, H.J., Differential effect of steady versus oscillating flow on bone cells, *J. Biomech.,* 31, 969, 1998.
63. Pitsillides, A.A., Mechanical strain-induced NO production by bone cells: a possible role in adaptive bone (re)modelling, *FASEB J.,* 9, 1614, 1995.
64. El Haj, A.J., Mitner, S.L., Rawlinson, S.C.F., Suswillo, R., and Lanyon, L.E., Cellular responses to mechanical loading in vitro, *J. Bone Miner. Res.,* 5, 923, 1990.
65. Owan, I., Burr, D.B., Turner, C.H., Qui, J., Tu, Y., Onya, J.E., and Duncan, R.L., Mechanotransduction in bone: osteoblasts are more responsive to fluid flow than mechanical strain, *Am. J. Physiol.,* 273, C810, 1997.
66. Prendergast, P.J. and Huiskes, R., Finite element analysis of fibrous tissue morphogenesis—a study of the osteogenic index using a biphasic approach, *Mech. Composite Mater.* (Riga), 32, 209, 1996.
67. Prendergast, P.J., Huiskes, R., and Søballe, K., Biophysical stimuli on cells during tissue differentiation at implant interfaces, *J. Biomech.,* 30, 539, 1997.
68. van Driel, W.D., Huiskes, R., and Prendergast, P.J., A regulatory model for tissue differentiation using poroelastic theory, in *Poromechanics: A Tribute to Maurice A. Biot,* J.-F. Thimus, Y. Abousleiman, A.H.-D. Cheng, O. Coussy, and E. Detournay, Eds., A.A. Balkema, Rotterdam, 1998, 409–413.
69. Huiskes, R., van Driel, W.D., Prendergast, P.J., and Søballe, K., A biomechanical regulatory model for peri-prosthetic tissue formation, *J. Mater. Sci. Mater. Med.,* 8, 785, 1997.
70. Lacroix, D. and Prendergast, P.J., A model to simulate the regenerative and resporption phases of long bone fracture healing, *Trans. Orthop. Res. Soc.,* 25, 869, 2000.
71. Patrick, C.W., Mikos, A.G., and McIntire, L.V., *Frontiers in Tissue Engineering,* Pergamon, Oxford, 1998.

VI

Clinically Related Issues

33

Applications of Bone Mechanics

Marta L. Villarraga
Exponent Failure Analysis Associates

Catherine M. Ford
Exponent Failure Analysis Associates

33.1 Introduction

From youth to old age, the human skeleton is routinely exposed to mechanical environments that challenge its structural integrity. Among younger individuals, bone fractures typically occur only when the applied loads substantially exceed those associated with routine daily activities. Common events that produce fractures among younger individuals include motor vehicle accidents, falls from heights, sports-related injuries, and occupational trauma.[1] Efforts to reduce fractures associated with these types of activities often focus on designing environments and protective equipment that limit the applied loads to a level below the tolerance of the bone. In contrast, fractures among older individuals often result from events whose associated energies are substantially lower, including falls from standing height or lifting activities. In these cases, questions arise about the contribution of age-related reductions in bone strength in determining whether fracture will occur. Efforts to reduce these fractures focus on affecting the intrinsic strength of skeletal structures, for example, through pharmacological or dietary interventions, as well as on protective systems such as hip padding and energy-absorbing floors. This is in contrast to the strictly environment-oriented intervention efforts associated with higher-energy fractures in younger people. Any intervention effort to prevent bone fracture, whether aimed at the mechanical environment, bone strength, or both, must be based on a sound understanding of how the bone responds to *in vivo* mechanical loads.

Failure of skeletal structures can be described in terms of the *factor of risk,*[2] which is the ratio of the force applied to a bone during a specific activity to the force at which the bone will fracture. A factor of risk greater than 1 indicates that the bone will be overloaded and will most likely fail, whereas a factor of risk lower than 1 indicates that fracture is less likely to occur. This is the inverse of the factor of safety, traditionally used in engineering to characterize the safety of a structure. From an engineering mechanics perspective, material properties, geometry, and loading and boundary conditions are the key pieces of information needed for the design of a safe structure. All of these factors contribute to the stress distribution within the bone, and therefore influence the likelihood of bone failure (Fig. 33.1).

0-8493-9117-2/01/$0.00+$.50

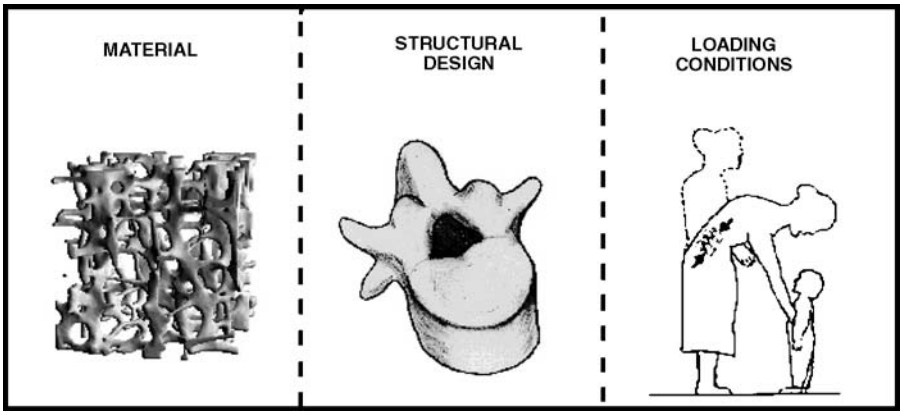

FIGURE 33.1 Characteristics of the spine that determine its capacity to carry load: material properties, structural design, and loading conditions. (From Myers, E.R. and Wilson, S.E., *Spine,* 22(24 Suppl.), 25S–31S, 1997. With permission.)

Investigators have used multiple approaches to examine the relative contributions of material properties, geometry, and loading conditions to the mechanical behavior of skeletal structures. For example, substantial knowledge has been derived from examining relationships between empirically determined structural properties of whole bones *ex vivo* and densitometric, geometric, and architectural measurements. This has been facilitated by the evolution of bone imaging technologies that allow investigators to examine the intricate details of the microstructure and material of bone. Clinical studies of factors related to *in vivo* fracture risk have complemented the understanding of whole-bone mechanics gained by examining *ex vivo* structural behavior. Issues that have emerged as important from both *ex vivo* and *in vivo* work include the relative contributions of cortical and trabecular bone, loading conditions, geometry, and age-related density variations.

A parallel approach to understanding the mechanical behavior of skeletal structures utilizes engineering models based on fundamental principles of mechanics. These models utilize the bone material properties and geometry to predict stresses under a variety of loading conditions, which is advantageous since stress cannot be directly measured in bone. Models have evolved, with ever-increasing complexity, from two-dimensional idealizations with closed-form solutions into three-dimensional, patient-specific finite-element models. While shortcomings related to these models currently limit their use in accurate prediction of whole-bone failure, such models have contributed substantially to the understanding of the factors that govern whole-bone behavior.

The aim of this chapter is to review and synthesize the research that has led to the current state of the art in the understanding of whole-bone mechanics, in particular as it relates to whole-bone fracture. Specific approaches used to study whole-bone mechanics (including experimental, clinical, and modeling work) are emphasized, using research involving the proximal femur and spine to illustrate these approaches (Fig. 33.2). The chapter begins with a review of the *in vivo* loads associated with fracture, followed by a discussion of how parameters related to applied loads affect mechanical behavior of the femur and spine. Work that has been performed to relate *ex vivo* structural properties and *in vivo* fracture risk to imaging parameters is then reviewed, followed by a discussion of the development of mathematical models of the proximal femur and spine.

33.2 Parameters Related to Applied Loads

33.2.1 Proximal Femur

The ability to predict the stress distribution within a skeletal structure is of little practical value unless the relevant *in vivo* loading conditions are known. In the same way, studies of *ex vivo* behavior are most valuable when the loading conditions employed reflect approximate *in vivo* loading conditions. Early efforts to define loads acting on the proximal femur involved the use of mathematical models and reaction

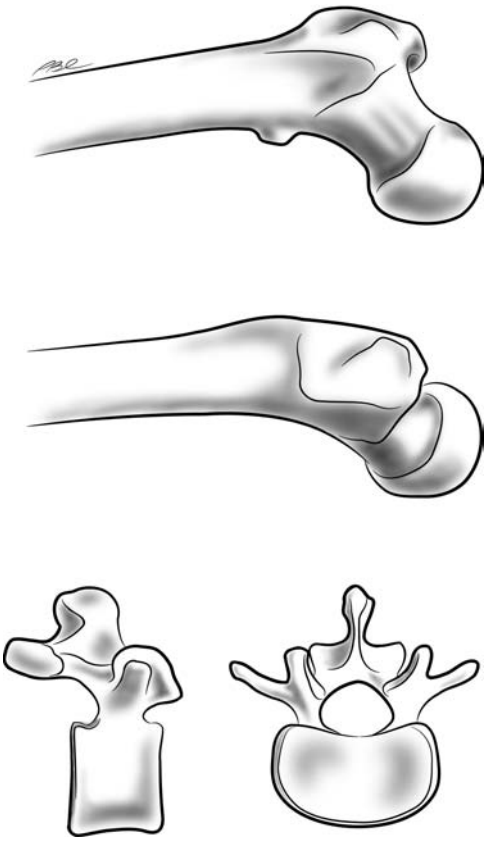

FIGURE 33.2 Femur and vertebra whole bones. (Illustration © Paul Chang. With permission.)

force measurements to estimate forces across the hip joint during stance and gait. A thorough review of the earliest work in this area is contained in Rydell.[3] Williams and Lissner[4] calculated a resultant force on the femoral head of 2.4 times body weight during single-leg stance. McLeish and Charnley[5] predicted values of 1.8 to 2.7 times body weight with the pelvis in a normal walking attitude, and found that the pelvis angle and the position of the trunk and limbs had a considerable effect on femoral forces. These predicted forces are in general agreement with those reported by Rydell,[3] whose first attempt at direct measurement of hip joint forces using an instrumented hip prosthesis yielded force magnitudes of 2.3 to 2.9 times body weight for single-leg stance and 1.6 to 3.3 times body weight for level walking. Later measurements for single-leg stance and gait using telemetered hip prostheses were generally consistent with those of Rydell for loads associated with stance and walking.[6–9] Davy et al.[7] noted that measured values for gait were often lower than previous predictions using optimization routines,[10–13] which could be explained in part by gait differences between normal subjects and those with prostheses.

The results from mathematical models and early instrumented hips have provided a fundamental understanding of the magnitude and direction of loads applied to the femur during routine (and typically noninjurious) activities of daily living. Although these data are applicable to determining stress distributions under physiological loads, the loads under which many femur fractures occur are substantially different from simple stance and gait configurations in magnitude and direction. Evidence from both clinical and experimental studies suggest that loads associated with muscular contraction can be sufficient to result in femur fracture among elderly people.[14–18] Studies using optimization methods as well as instrumented hip prostheses have demonstrated the importance of muscle forces as determinants of load transmission across the joint and therefore the stress distribution within the bone.[9,19,20] Recent investigations using instrumented hip prostheses have shown that although patients in the early postoperative

period can execute planned activities of daily living with relatively low joint contact forces, unexpected events such as stumbling or periods of instability during single-leg stance can generate resultant forces in excess of eight times body weight as a result of muscular contraction.[8,21] Forces that are within the capacity of the muscles crossing the hip joint have been shown to produce clinically realistic fracture patterns in *ex vivo* experiments,[18] consistent with retrospective clinical studies in which femur fractures were attributed to turning, stumbling, rising from a seated position, or climbing.[16,17,22] These data suggest that femur fracture can occur as a result of muscular contraction in individuals with reduced bone strength. However, attempts to rule out impact from a fall as a cause of proximal femur fracture based on either primitive stress analyses[23] or *ex vivo* fracture studies[18] should be interpreted with caution.

Despite compelling evidence that the majority of femur fractures are associated with falls,[24–27] surprisingly little is known about the magnitude and direction of loads applied to the femur during a fall. Robinovitch and colleagues[28] combined pelvis release experiments with a lumped parameter model of the body to predict peak impact forces up to approximately 8000 N or more, depending on fall height and trochanteric soft tissue thickness. By comparing their predictions to measurements of the forces required to fracture the femur under fall loading conditions, these investigators concluded that any fall from standing height with direct impact to the greater trochanter has the potential to fracture the elderly femur. van den Kroonenberg and co-workers[29] used dynamic link models of the body to predict hip impact velocities, effective mass, and peak femur impact forces during falls from standing height. Using their most-sophisticated model, which reflected experimentally determined values for impact configuration and impact velocity,[30] they predicted peak forces on the greater trochanter of 2.9 and 4.3 kN for females of 5th and 95th percentile height and weight, respectively.

The stress distribution within the femur, and therefore the likelihood of fracture, depends on the direction of the applied loads as well as their magnitude. Despite its potential importance, however, few studies have directly addressed the configuration of loads applied to the femur during a fall, and how changes in this configuration influence failure load. Courtney and co-workers[31] derived a loading configuration (Fig. 33.3) based on body positions at impact during a fall,[30] which produced clinically relevant fracture patterns. Pinilla and colleagues[32] extended this work by using cadaveric femurs to examine the

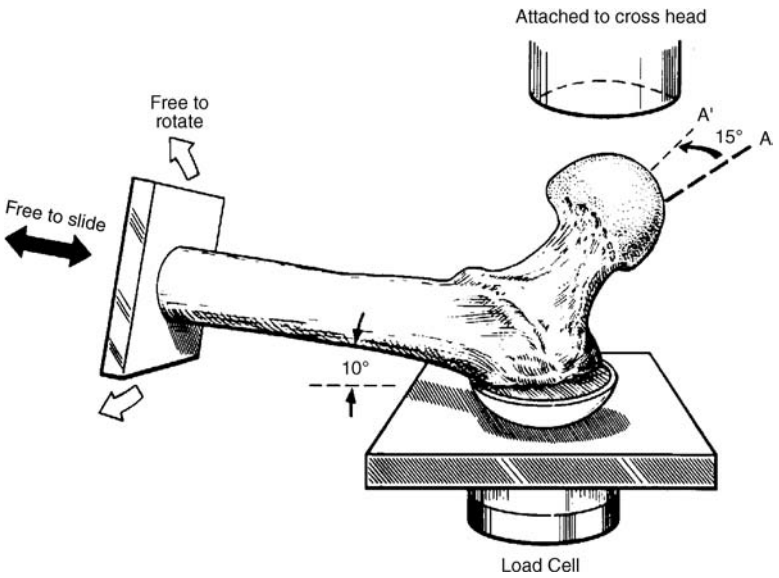

FIGURE 33.3 Diagram of the mechanical testing setup for failure tests of the proximal femur. The femoral shaft is aligned 10° from horizontal and femoral neck is internally rotated 15° relative to vertical. The femoral shaft is fixed distally but remains free to slide and rotate. (From Bouxsein, M.L. et al., *Calcif. Tissue Int.,* 56(2), 99–103, 1995. With permission.)

effect of subtle variations in impact direction from a fall. They found a significant reduction in failure load with a 30° change in the angle between the line of action of the applied force and the angle of the femoral neck, as viewed from the superior aspect of the femoral head. This reduction in failure load was noted to be comparable in magnitude to approximately 25 years of age-related bone loss after age 65. These experimental results have been confirmed by parametric finite-element analyses.[33]

Loading rate is an additional variable related to applied load that must be considered in determining the stress distribution in the femur and the likelihood of fracture. Weber et al.[34] found that, under loading conditions approximating a fall, the force required to fracture the femur increased with increasing loading rate. This general information regarding the influence of loading rate was refined by Courtney and co-workers,[31] who used a predicted loading rate based on time to peak force during a fall.[28] These authors reported that fracture forces for both younger adult and older adult femurs increase by about 20% with a 50-fold increase in applied displacement rate. Differences in both loading configuration and loading rate may partly explain why investigators have reported mean structural capacities of the proximal femur under both stance and fall loading conditions that vary by as much as a factor of four to five (Table 33.1). The wide range in failure loads reported in these *ex vivo* studies shows that failure load can be dramatically influenced by several variables; however, substantial future work is necessary to characterize precisely the contributions of these variables.

33.2.2 Spine

Every routine activity, including sitting, standing, walking, or lifting a light or heavy object, creates loads on the spine. Knowledge of relevant *in vivo* loading conditions on the spine is necessary to predict adequately the stress distribution in this structure, in both *in vivo* and *ex vivo* studies. Schultz et al.[64] predicted *in vivo* lumbar spine compressive loads ranging from 440 N (relaxed standing position) to 2350 N (forward bending with the trunk at 30° and holding an 8-kg weight at arm's length) using a combination of electromyography (EMG) and intradiscal pressure measurements on volunteers and mathematical modeling. In a later study using volunteers, Hansson et al.[65] estimated that the compressive loads on L3 during squat lifting and lifting while bent at the waist range from 5000 to 11,000 N. Using a biomechanical analysis, validated against EMG and intradiscal pressure measurements, they estimated that the compressive load on L3 during these types of exercises was about eight times greater than the shear load. Actual magnitudes of loads on an individual's lumbar vertebrae depend on the anatomy and weight of the individual, as well as on muscle forces.

Characterizing activities as specific events leading to spine fractures is the subject of current research. Complications arise in part from the fact that osteoporotic compression fractures of the spine are usually associated with minimal trauma and with loads no greater than those encountered during normal activities of daily living.[66] Another contributing factor is fatigue, which may in part explain vertebral fractures that are reported as spontaneous or are detected incidentally.[67] Loading of the spine during falls is currently under investigation, with particular emphasis on the transmission of impact forces along the spine.[67]

To understand how loads are distributed in the spine, it is important to consider the structures that form the spine and how each of these components contributes to load transmission. The majority of the compressive forces in the spine are transmitted from the intervertebral disks to the vertebral end plates, and are then distributed between the trabecular bone and cortical shell that make up the vertebral bodies. The exact percentage of contribution of the cortical shell to load sharing is still not well established and is currently under investigation. A portion of the compressive loads can also be transmitted along a parallel path, through the posterior elements and facet joints. The overall contribution of the posterior elements to vertebral body strength is currently under investigation with the help of mathematical models.[68] In evaluations of the effects of compressive loads on vertebrae, stress levels associated with end plate failure are of special concern, since the end plate has been shown to fail first under high compressive loads.[65,69] Also of concern are stress levels that exceed the strength of trabecular bone, because most of the axial compressive load on a vertebral body is carried by the trabecular bone.[67,70]

TABLE 33.1 Reported Failure Properties of the Proximal Femur and Correlations with Imaging Parameters

Author (year)	*n*	Loading Configuration	Load Rate (mm/s)	Failure Load		Imaging Method[a]	Correlated Parameter[b]	Max $r^{2(c)}$	*p* Value
				Mean (N)	Range (N)				
Smith (1953)[14]	22[d]	Stance	Gradual	9470	4310–18,700	—	—	—	—
	26[d]		Impact	371 J	170–475[e]	—	—	—	—
	21[d]	Fall	Gradual	8230	2670–15,000	—	—	—	—
	13[d]		Impact	415 J	233–624	—	—	—	—
	20[d]	Anterior bending	Gradual	4000	2270–10,700	—	—	—	—
	13[d]		Impact	49 J	24–102	—	—	—	—
Backman (1957)[35]	6	Bending, shear	Gradual	3410	—	—	—	—	—
	28	Bending, shear, compression	—	3860	1280–11,900	—	—	—	—
	22	Torsion	—	29 N−m	14–59	—	—	—	—
	17	Bending, shear, compression, torsion	—	3830	980–7850	—	—	—	—
Hirsch (1960)[36]	—	Stance	—	4900	2940–7850	—	—	—	—
Mizrahi (1984)[37]	33	Stance	0.08	—	1600–12,800	—	—	—	—
Yang (1996)[18]	14	Muscle contraction[f]	50	3040	—	—	—	—	—
Vose (1963)[38]	10[d]	Stance	37 N/s	6200	3830–10,000	X-ray	Density, Ward's triangle	0.64	0.005[g]
Phillips (1975)[39]	39	Stance	0.20	—	3070–13,300	X-ray	Average area porosity	—	—
Dalen (1976)[40]	61	Fall[h]	0.25	—	—	XRS	BMC	0.79	—
Leichter (1982)[41]	32	Stance	0.08	6100	1600–12,600	CS	Trabecular density, neck	0.66	<0.001
Sartoris (1985)[42]	19	Stance	—	—	—	DESPR	Neck density index	0.29	<0.05
Werner (1988)[43]	10	Fall[h]	0.33	—	—	DPA	BMC	NS	—
Delaere (1989)[44]	20[j]	Stance	0.03	11,000	5100–19,500	DPA	BMD, proximal diaphysis	0.55	—
Weber (1992)[34]	10	Fall	0.7	2930	1770–4940	DPA	BMD, neck	0.89	<0.0001[q]
	4		14	3510	2190–5950				
	6		4000	6020	3110–9720		BMD, intertrochanteric	0.60	0.071[q]

(continued)

Alho (1988)[45–47]	36	Stance	—	5490[k]	2750–9610	QCT	HU × CSA, neck	0.62	<0.001
Alho (1988)[47]	—	Rotation[l]	5°/min	—	—	QCT	HU × CSA, midshaft	0.50	<0.001
Husby (1989)[48]	50	Rotation[l]	15°/min	74.6(Nm)	—	QCT	HU × CSA, midshaft	0.50	<0.001
Alho (1989)[49]	26	Stance	0.08	6100	—	QCT	HU × CSA, head	0.71	<0.001
Esses (1989)[50]	8	Stance	0.88	—	—	QCT	HU, subcapital	0.64	0.02
Lotz (1990)[51]	12	Fall	0.70	2110	778–4040	QCT	HU × CSA, intertrochanteric	0.93	<0.001
Smith (1992)[52]	22	Compression[m]	0.21	—	4940–16,100	QCT	BMD, superomedial head	0.66	—
Lang (1997)[53]	13	Stance	0.5	—	—	QCT	Neck BMD (trabecular) + min CSA + FNAL	0.93	—
	13	Fall	—	—	—	QCT	Trochanter BMD (trabecular) + min CSA	0.89	—
Keyak (1998)[54]	18	Stance	—	—	—	QCT	BMD, subcapital	0.61	0.0001
							FE Model	0.75	<0.0001
	18	Fall	—	—	—		BMD × CSA, intertrochanteric	0.82	<0.0001
							FE model	0.90	<0.0001
Cody (1999)[55]	25	Stance	0.21	9920	—	QCT	FE model	0.82	—
	26			9200	—			0.84	—
Courntey (1994)[31]	19	Fall	100	—	—	DXA	CSA, neck	0.77	—
							BMD, neck	0.72	—
Courtney (1995)[56]	17	Fall	2	5430	—	DXA	BMD, neck	0.92	<0.001
							CSA, neck	0.79	—
Bouxsein (1995)[57]	16	Fall	2	3680	1730–6730	DXA	BMD, neck	0.79	<0.001
						US	BUA, calcaneus	0.51	0.002
Pinilla (1996)[32]	33	Fall, 0°[n]	100	4050	—	DXA	BMD, total	0.68	—
		Fall, 15°		3820	—			0.68	—
		Fall, 30°		3060	—			0.71	—
Cheng (1997), Nicholson (1997)[58,59]	64	Fall	14	3980	—	DXA	BMD, trochanter	0.88	<0.001
						QCT	CA, trochanter	0.83	<0.001
						US	BUA, calcaneus	0.47	<0.01

TABLE 33.1 Reported Failure Properties of the Proximal Femur and Correlations with Imaging Parameters (Continued)

Author (year)	*n*	Loading Configuration	Load Rate (mm/s)	Failure Load		Imaging Methoda	Correlated Parameterb	Max $r^{2(c)}$	*p* value
				Mean (N)	Range (N)				
Beck (1998)[60]	22	Fall	0.5	—		DXA	Failure load[p]	0.83	—
Lochmuller (1998)[61]	58[d]	Stance	1.0	3150	933–7000	DXA	BMD, trochanter and neck	0.45	<0.001
Bouxsein (1999)[62]	25	Fall	100	2640		DXA	BMD, trochanter	0.92	<0.0001
						US	BUA, calcaneus	0.70	<0.0001
Lochmuller (1999)[63]	45[d]	Stance	60	3200	933–7000	US	SOS/BUA, calcaneus[q]	0.52	<0.001

[a] XRS = X-ray spectophotometry; CS = Compton scattering; DESPR = dual-energy scanned projection radiography; DPA = dual-photon absorptiometry; QCT = quantitative computed tomography; DXA = dual-energy X-ray absorptiometry; US = sultrasound.
[b] BMC = bone mineral content; BMD = bone mineral density; HU = Hounsfield units; CSA = cross-sectional area; FNAL = femoral neck axis length; FE = finite element; CA = cortical area; BUA = broadband ultrasound attenuation; SOS = speed of sound.
[c] NS = not significant.
[d] Embalmed specimens.
[e] Seven specimens dislocated from pelvis without fracture.
[f] Simulated gluteus medius and iliopsoas contraction.
[g] *p* value calculated from raw data.
[h] Femur embedded up to neck; force applied perpendicular to shaft.
[j] Dried and defatted specimens.
[k] Median value.
[l] Femoral head cemented in polyurethane blocks and rotated about femoral neck axis.
[m] Compression applied approximately along femoral neck axis.
[n] Angle between femoral neck axis and applied load, as viewed from superior aspect of femoral head.
[p] Failure load calculated using a DXA-based curved beam model.
[q] Composite value of SOS and BUA.

Although much of the loading imposed on the spine during daily activities involves compression, many lifting activities also involve bending, which introduces a flexion component as well. Flexion has been shown to produce greater peak compressive stresses on vertebral bodies than pure compresssion.[64] To determine the effects of flexion, Granhed et al.[69] examined whether the compressive strength of thoracolumbar vertebrae varied with the direction of the applied load by comparing compressive loads applied axially to those applied in different degrees of flexion. In their study, the first components to fail were the end plates and the underlying trabecular bone. These results were similar to those of previous studies in which vertebral bodies with 3 mm of adjacent disks covering each end plate were loaded strictly axially.[71]

The intervertebral disks play an important role in the transfer of loads to the vertebral body. To examine the influence of the presence of disk material (annulus and nucleus pulposus) on load transfer and the consequent effects on the strength and stiffness of lumbar vertebral bodies, Keller et al.[72] examined the mechanical properties of trabecular bone samples from different locations with respect to the annulus or nucleus pulposus. They found regional variations in compressive properties of trabecular bone samples as a function of location with respect to the disk, with posterocentral samples having greater stiffness and strength than peripheral samples. This heterogeneous distribution of compressive mechanical properties in segments with normal disks was different from the more homogeneous distribution in segments with degenerated disks.

In addition to load magnitude and direction, loading rates and the resulting differences in strain rates must be considered when evaluating the effects of prescribed loading conditions on the spine (Table 33.2). This is of particular significance since it has been hypothesized that elderly individuals could be subjected to loads at relatively low strain rates.[73] Furthermore, strain rate has been found to increase as a result of muscular fatigue at other skeletal sites, suggesting a causal relationship with stress fractures.[74,75]

Occasional overloads may increase the risk of vertebral fracture by substantially degrading the mechanical properties of trabecular bone.[73] Examples include non-fracture-producing falls that could potentially have a deleterious effect on the mechanical competence of vertebral bodies. Keaveny et al.[73] quantified the percentage reductions in modulus and strength and the development of residual strains due to overloading. Reductions in modulus of up to 85% and reductions in strength of up to 50% occurred with overloads of as much as 3% of the total applied strain, and residual strains developed depended mainly on the magnitude of the applied strains.

Work that has been performed to characterize the magnitude and direction of loads applied to the proximal femur and spine during both daily activities and falls provides an important foundation for *ex vivo* experimental work. However, further research is necessary to characterize the loads leading to femur and spine fractures. Further consideration of boundary conditions is also warranted, including, for example, the effects of irregular end plates and compliant disks in the spine, as well as the effects of constraints at the knee joint and acetabulum on the behavior of the femur.

33.3 *Ex Vivo* Behavior and Imaging Parameters

33.3.1 Proximal Femur

Investigations of the mechanical behavior of the proximal femur *ex vivo* and the relationship to imaging parameters have provided insight into factors that are important in determining the stress distribution in the bone and resultant failure properties. Early *ex vivo* investigations of the proximal femur were primarily oriented toward determining the tolerance of the femur under different loading conditions, as well as examining the associated fracture patterns.[14,35,36,91] The results of these early investigations suggested the importance of the complex interplay between loading configuration, variations in local strength, and variations in geometry in determining the tolerance of the femur as well as the resulting fracture pattern, despite a lack of sophisticated imaging techniques.

TABLE 33.2 Correlations of Mechanical Parameters with Noninvasive Parameters for Spine Segments or Vertebral Bodies (all testing was done in compression)

Author(year)	Spine Level	*n*	Sample Type[a]	Loading Rate (mm/min)	Mechanical Parameter[b]	Mean Loads (N), Stress (MPa)	Range Loads(N), Stress (MPa)	Imaging Method[c]	Correlated Parameter[d]	Max $r^{2(e)}$	*p* Value
Mosekilde (1986)[70]	T5 T7 L2	43	VB-NE	4.5	σ_{max}		1.5–7.8		Age	0.66[f]	<0.01
Mosekilde (1990)[76]	L2	46	VB-NE	4.5	F_{max}	8260 (<50 yrs) 4590 (50–75yrs) 3110 (>75 yrs)			Age (males)	0.61[f]	<0.001
					σ_{max}	5.83 (<50 yrs.) 2.96 (50–75 yrs) 1.95 (>75 yrs)			Age (females)	0.66[f]	<0.001
		43			F_{max}	6940 (<50 yrs) 3260 (50–75 yrs) 2800 (>75 yrs)			Age (females)	0.69[f]	<0.001
					σ_{max}	5.70 (<50 yrs) 2.62 (50–75 yrs) 2.29 (>5 yrs)			Age (females)	0.71[f]	<0.001
Mosekilde (1988)[77]	L2	22	VB-NE	4.5	σ_{max}		2.00–7.04		Iliac crest TBV (%)	0.48	<0.001
					F_{max}		2400–8600			0.35	<0.01
Vesterby (1991)[78]	L2	15	VB-NE	4.5	F_{max}	6290	3940–9860		BV/TV (%) (L1)	0.49[g]	0.002
									CTh (L1)	0.56[g]	0.001
									Vm* (L1)	0.38[f, g]	0.007
									TbTh (L1)	0.52[g]	0.001
									Vtr* (L1)	0.50[g]	0.002
Korstjens (1996)[79]	L2	14	VB-NE	4.5	σ_{max}				Radiographic trabecular pattern (L3)	0.59[f]	<0.05
Hansson (1980)[71]	L1–L4	109	VB-D	5	F_{max}	3850	1520–11,000	DPA	BMC	0.74	0.01
					σ_{max}	2.27	1.02–4.95			0.48	0.01
Granhed (1989)[69]	T12–L5	52	FSU-NE	12[h]	F_{max}	5430	810–10090	DPA	BMC	positive	<0.0001
Ortoft (1993)[80]	L2–L4	46	VB-NE	4.5	F_{max}			DPA	BMC_T	0.48	<0.001
					σ_{max}				BMC_T	0.22	<0.001
					F_{max}				BMC_B	0.55	<0.001
					σ_{max}				BMC_B	0.24	<0.001

					F_{max}				BMD_T	0.41	< 0.001
					σ_{max}				BMD_T	0.23	< 0.001
Eriksson (1989)[81]	L1–L4	73	FV-D	5	σ_{max}			DPA	BMD	0.41	—
								QCT	HU	0.51	—
					F_{max}			DPA	BMC	0.64	—
								QCT	HU × SA	0.55	—
								QCT	HU	0.23	—
McBroom (1985)[82]	L1,L3	16	VB-D	6	σ_{max}				Apparent density	0.82[j]	<0.0001
					σ_{max}			QCT	HU	0.47[j]	< 0.061
Biggeman (1988)[83]	TH,L	36	FSU-NE	1kN/s	F_{max}	5300	2100–9000	QCT	BMD × EPA	0.76	< 0.001
									BMD	0.46	< 0.001
Mosekilde (1989)[84]	L2	30	VB-NE	4.5	σ_{max}			QCT	HU	0.30	< 0.001
					F_{max}				HU by QCT	0.52	< 0.001
Brinckmann (1989)[85]	TH,L	98	FSU-NE	1kN/s	F_{max}			QCT	BMD × EPA	0.64	—
Cody (1991)[86]	T11–L1	20	2 FSU-NE	12.5	F_{max}			QCT	rBMD (central region)	0.78[k]	<0.0001
									rBMD ×CSA	0.88[k]	—
McCubbrey (1995)[87]	T7–8	17	VB-D	25.4	F_{max}	1460 (n = 19)		QCT	rBMD	0.65	0.002
	T9–10	18				1690 (n = 20)				0.89	0.001
	T11–12	16				2100 (n = 17)				0.74	0.001
	L1–L2	18				1890 (n = 20)				0.74	0.001
	L3–4	18				2070 (n = 20)				0.51	0.004
	T7–8	16			Stiffness (kN/m)	1720 (n = 17)		QCT	rBMD	0.43	0.035
	T9–10	17				2000 (n = 19)				0.75	0.001
	T11–12	13				1910 (n = 15)				0.65	0.005
	L1-L2	18				1760 (n = 19)				0.35	0.029
	L3–4	15				1650 (n = 18)				0.69	0.001
Cheng (1997)[88]	L3	62	VB-D	480	F_{max}	5770		DXA	BMD	0.64	< 0.001
								QCT	BMD	0.44	< 0.001
								QCT	BMD × CSA	0.61	< 0.001
					σ_{max}	4.22		DXA	BMD	0.44	< 0.001
								QCT	BMD	0.51	< 0.001
								QCT	BMD × CSA	0.45	< 0.001

(*continued*)

TABLE 33.2 Correlations of Mechanical Parameters with Noninvasive Parameters for Spine Segments or Vertebral Bodies (all testing was done in compression) (Continued)

Author (year)	Spine Level	*n*	Sample Type[a]	Loading Rate (mm/min)	Mechanical Parameter[b]	Mean Loads (N), Stress (MPa)	Range Loads (N), Stress (MPa)	Imaging Method[c]	Correlated Parameter[d]	Max $r^{2(e)}$	*p* Value
Moro (1995)[89]	T11	11	2 FSU[l]	6	F_{max}	2080		DXA	BMD (L2) (lateral)	0.88	<0.001
									BMD(L2), (AP)	0.69	0.001
	L2	11	2 FSU[l]	6	F_{max}	2620		DXA(lateral)	BMD (L2)	0.79	<0.001
								DXA(AP)	BMD (L2)	0.52	<0.05
Edmonston (1997)[90]	T1–T4	16	VB–NE	—	F_{max}			QCT	VCD	0.50	<0.01
	T5–T8									0.36	
	T9–T12									0.38	
	L1–L5									0.45	
	T1–T4				F_{max}			DXA	BMD	0.71	<0.01
	T5–T8									0.67	
	T9–T12									0.74	
	L1–L5									0.71	

[a]VB-NE = vertebral body without endplates at both ends and sawed plano-parallel ends; VB-D = vertebral body with discs at both ends; FSU = functional spinal unit (two vertebra and intervertebral disc); FSU-NE = functional spinal unit w/o endplates; FV = full vertebra (w/posterior elements); FV-D = full vertebra with discs at both ends.

[b] σ_{max} = maximum compressive stress; F_{max} = maximum load.

[c] QCT = quantitative computed tomography; DPA = dual photon absorptiometry; DXA = dual energy x-ray absorptiometry.

[d]TBV = trabecular bone volume; BV/TV(%) = fractional volume of trabecular bone; CTh = mean thickness of cortical ring (μm); Vm* = marrow space star volume (mm^3); TbTh = mean trabecular thickness (μm); Vtr* = trabecular star volume of L1(mm^3); BMC = bone mineral content; BMC_T = BMC whole vertebrae (w/posterior elements); BMC_B = BMC vertebral body only; BMD_T = BMC_T corrected for frontal area of vertebrae; HU = Hounsfield units; SA = surface area; EPA = endplate area; rBMD = regional BMD; CSA = cross-sectional area; VCD = vertebral cancellous density.

[e] Other correlations may have been reported.

[f] Negative relationship.

[g] As reported in Figure 1.

[h] Also loaded in compression combined with flexion (<15 degrees).

[j]Log-log relationship.

[k] Multiple-regression model.

[l] Vertebral bodies above and below embedded in PMMA

—Not reported.

Imaging modalities that have been used to characterize the mechanical behavior of the proximal femur include radiography, single photon absorptiometry, dual photon absorptiometry, dual energy X-ray absorptiometry, computed tomography, and ultrasound. These techniques are discussed in Chapter 34. Correlations between femoral failure load and various measurements using these techniques are presented in Table 33.1.

Initial attempts to correlate mechanical behavior of the proximal femur with densitometric measures utilized simple radiographs.[38,39] Vose and Mack[38] found significant correlations between density measures at the Ward's triangle region and yield load of the femur; however, the loading conditions used did not reproduce clinically relevant fracture patterns. Phillips et al.[39] utilized radiographic measurements as inputs to a two-dimensional beam-bending model of the femur, achieving reasonable agreement between measured and predicted failure loads. Although this study was essentially two dimensional and limited to loading in the frontal plane, the authors did note the importance of overall neck depth, cortical thickness, neck length, neck angle, and age in predicting femoral failure load.

The difficulties associated with assessing bone mineral content via radiographs led to the use of more-sophisticated imaging techniques for this application, including X-ray spectophotometry[40] and Compton scattering.[37,41,92] Bone mineral content at the femoral neck and associated variables measured using these techniques were found to be correlated with femoral failure load,[37,40,41] as was density of the trabecular bone of the greater trochanter.[92] Correlations between densitometric measures and femoral strength have also been established using dual-energy projection radiography[42,93] and dual photon absorptiometry (DPA).[43,44] Although these investigations established a correlation between densitometric measures and failure load, the loading conditions studied were limited to the frontal plane and in some instances were highly nonphysiological. This limits extrapolation of these results to predicting *in vivo* loads likely to be associated with many hip fractures.

The relationships between densitometric parameters measured via quantitative computed tomography (QCT) and femoral structural capacity have also been widely investigated (see Table 33.1). Alho and colleagues[45–49] established correlations between QCT densities of both cortical and trabecular bone regions and femoral strength under bending and rotational loading conditions. Under the loading conditions examined, these investigators found that mass-related measurements (estimated by considering QCT density as well as cross-sectional area measurements) generally performed better than QCT density measurements alone in predicting femoral failure load. The results of these studies showed that, under axial loading conditions, trabecular parameters were better correlated with mechanical behavior than cortical parameters.[45,49] By contrast, under rotational loading conditions, cortical parameters were better correlated with failure load.[48] Esses et al.[50] also investigated QCT measurements as predictors of femoral strength *ex vivo*. These authors found that the average QCT density of trabecular bone at the subcapital region was the best predictor of strength under loads representing simplified single-leg stance. Similarly, Smith and co-workers[52] also found that trabecular QCT parameters were correlated with the compressive force required to produce impacted subcapital fractures. The importance of considering geometric factors in the mechanical behavior was reflected in the work of Cordey et al.,[94] who found that apparent femoral stiffness under stance loading conditions was better correlated with geometric than densitometric parameters measured by QCT.

The work of Lotz and Hayes[51] was the first to examine relationships between QCT parameters and femoral strength under loads associated with falls on the greater trochanter. These investigators found that the product of the average trabecular QCT number and the total cross-sectional area of the bone at the intertrochanteric region was the best predictor of failure load under fall loading conditions. Lang et al.[53] measured trabecular and integral bone mineral density (BMD) using an automated QCT technique. Their results were consistent with those of Lotz and Hayes in that trochanteric trabecular BMD was strongly correlated with femoral strength under fall loading conditions.[51] However, in contrast to the results of Lotz and Hayes[51] and Lang et al.,[53] Cheng and colleagues[58] found that trochanteric cortical area was best correlated with femoral strength under loads simulating a fall on the greater trochanter. The authors of these studies emphasized the advantages of QCT in predicting femoral failure load in that QCT allows examination of the separate contributions of cortical and trabecular bone, and also allows

for separate consideration of bone cross-sectional area. A consistent conclusion that can be drawn from this work is that incorporation of cross-sectional geometry improved predictions of femoral structural capacity, thereby demonstrating the independent contribution of geometry in determining the stress distribution within the bone.

By contrast to QCT, dual energy X-ray absorptiometry (DXA) provides a two-dimensional array of intensity profiles that are an integrated measure of bone density and geometry. Numerous investigators have reported relationships between regional BMD values measured using DXA and *ex vivo* femoral strength under both stance[54,86,95] and fall[31,32,54,56–61] loading conditions (see Table 33.1). The incorporation of DXA-based structural geometry into beam bending models of the proximal femur has resulted in improved predictions of femoral strength over DXA-based density parameters alone.[60] Courtney et al.[56] noted that once either the densitometric or geometric data were accounted for, age was not an independent predictor of fracture load. In general, DXA-based density parameters have been found to predict femoral failure load nearly as well as finite-element models.[54,55]

33.3.2 Spine

Understanding the mechanical behavior of the spine *ex vivo* and the relationship between mechanical behavior and imaging parameters has provided insight into important factors that can be useful in predicting the stress distribution and strength properties of this skeletal structure. The introduction of dual-photon absorptiometry (DPA) for *in vivo* assessment of bone mineral content (BMC) has led to its use in applications simulating *in vivo* measurements and their relationship to mechanical parameters in the spine.[69,71,72,80,96] Different specimen types have been used to determine the mechanical competence of vertebral bodies (see Table 33.2). Hansson et al.[71] noted a gender difference in vertebral strength; however, they did not note any difference between the levels tested (L1–L4) when the specimens from both sexes were combined. The studies presented in Table 33.2 suggest that density measures from DPA could be used to predict accurately the compressive properties of spinal bone.[69,71,72,80,96] The direction in which DPA measurements are performed in the spine has also been considered for its potential effect on the correlations with mechanical strength parameters. Ortoft et al.[80] found that BMC measurements from DPA performed in a lateral direction gave better correlations with vertebral compressive loads, compared with BMC measurements obtained in the anteroposterior (AP) direction. These authors noted that measurements done in the AP direction include densitometric data from the posterior elements, which do not necessarily contribute as significantly as the vertebral body to the weight-bearing capabilities of the vertebrae. In addition, this study found that using BMC measures corrected for vertebral height (BMD_T) gave a slightly improved correlation with vertebral body compressive strength.

Bone densitometric measurements in the spine determined from QCT have also been utilized to predict the mechanical properties of vertebral bone (see Table 33.2).[2,82–87,97] These studies provided positive indications of the value of using QCT as a noninvasive tool to evaluate the mechanical properties of vertebral trabecular bone. Hayes et al.[2] provided a comprehensive review up to 1991 of the efforts to relate QCT measures with directly measured density and vertebral bone strength. One of the advantages of using QCT is that this imaging modality can provide geometric dimensions in addition to density measurements. Another advantage is that densitometric data can be obtained for both cortical and cancellous bone from a single measurement.

McBroom et al.[82] conducted one of the earliest studies supporting the idea that QCT could be used as a predictor of vertebral fracture risk; they also evaluated the contribution of the cortical shell to the mechanical competence of lumbar vertebral bodies by comparing the compressive strength of vertebral bodies with and without the cortex. These investigators showed that the removal of the cortex was associated with approximately a 10% reduction in vertebral load to failure.

Efforts to relate combined QCT-derived density and geometric measurements to mechanical parameters of vertebral bone strength have also been reported (see Table 33.2).[81,83,85,86,90] Biggemann et al.[83] and Brinckman et al.[85] have pointed out that combining bone density measurements with end plate

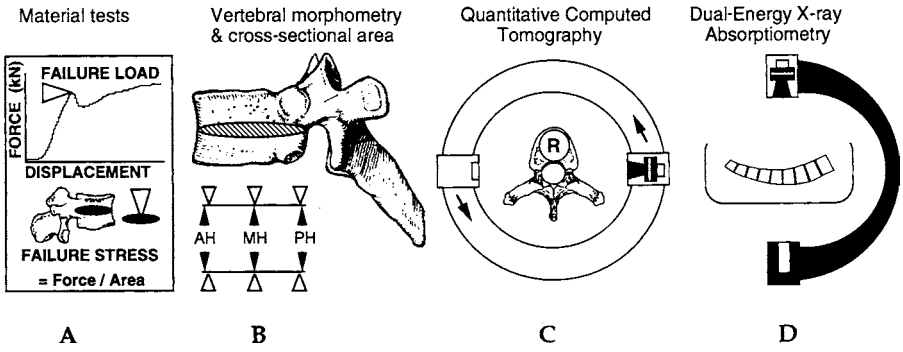

FIGURE 33.4 Methodologies used to derive input data for determining the relationship between vertebral density, geometry, and strength: (A) mechanical testing; (B) morphometric measurements; (C) QCT; (D) DXA. (From Edmondston, S.J. et al., *Osteoporosis Int.,* 7(2), 142–148, 1997. With permission.)

cross-sectional area measurements, as determined from QCT, provide a more significant correlation with thoracolumbar vertebral body compressive strength than QCT bone density measurements alone. The importance of considering the end plate cross-sectional area cannot be overlooked since cross-sectional area is inversely proportional to failure stress. Brinckmann et al. obtained a specific prediction formula for *in vivo* determination of compressive strength based on both density and end plate area with an error limit of 1 kN.[85] Cody et al.[86] combined QCT-derived regional bone density measurements (rBMD) with measurements of the minimum cross-sectional area of vertebral bodies to predict thoracolumbar vertebral fracture strength. Considering density measures from multiple regions (superior to inferior, and anterior to posterior) of the cancellous bone of the vertebral bodies is important because there are specific vertebral body locations that are more commonly selected as locations for measurement of *in vivo* BMD. In addition, McCubbrey et al.[87] showed that the distribution of cancellous BMD measures had different effects on the predictive models of static failure properties compared with models of fatigue-based failure properties. In their study, anterior density regions were more often included in the static predictive models, while posterior regions were more predictive of fatigue properties. These models indicate that different failure mechanisms may be involved in the two different mechanical test types, and, as such, care should be used when interpreting the findings from *ex vivo* testing when test protocols and loading conditions differ among studies (see Table 33.2). Edmonston et al.[90] combined morphometric measurements from QCT scans with BMD measurements from DXA to assess the relative contributions of bone densitometry and vertebral morphometry in the prediction of thoracolumbar vertebral body strength (Fig. 33.4). Contrary to previous studies, they suggested that vertebral deformity and size (as assessed by vertebral morphometry) made only a minor additional contribution to the prediction of vertebral strength compared with that provided by bone densitometry alone.

Other studies have evaluated the feasibility of using QCT to characterize the cortical shell thickness and end plate, and the dependence of these measurements on age, gender, and anatomical region within the vertebral body.[98] These geometric measurements could lead, indirectly, to a better understanding of the role of these components in vertebral mechanical properties and their relative importance in fracture etiology. The evaluation of changes in thickness of these components and the effect of such changes on overall vertebral mechanical properties are perhaps better suited for evaluation using computational models, as presented later in this chapter.

In contrast to QCT, BMD measurements obtained from DXA have been utilized much less in *ex vivo* studies for prediction of mechanical properties of vertebral bone. Investigators have used BMD measurements from DXA to predict failure properties for both thoracic and lumbar vertebrae.[67,88–100] Myers et al.[99] showed that supine lateral BMD measurements provided a better assessment than anteroposterior BMD of the fracture properties of lumbar vertebral bodies. This was in agreement with the study of Ortoft et al.,[80] which showed the effects of the presence of the posterior elements in the BMD measurements taken in the

AP direction. In a follow-up study, Moro et al.[89] used BMD measurements of cadaveric lumbar vertebrae obtained using DXA in both the lateral and AP directions and found that these provided a valid assessment for predicting compressive strength of both lumbar and thoracic vertebral bodies. The importance of this approach was that it evaluated the feasibility of using lumbar BMD to assess the mechanical competence of thoracic vertebrae, since BMD measurements at thoracic levels are limited due to shadowing of the ribs. Since BMD measured by DXA is the BMC of a region of interest divided by the projected area in the view of the DXA scan, both apparent density and geometric bone properties can influence DXA measurements.[67]

The relative structural contributions of the cortical shell, end plates, vertebral body and end plate cross-sectional area, and the trabecular bone microstructure are important in the prediction of vertebral bone strength. Consideration of these variables will allow increased understanding of how loads are distributed among different regions of the vertebrae, thereby providing better indicators of the strength of vertebral bodies. All of these factors are potentially functions of age, and can have a composite effect on the load-bearing capacity of the vertebra.

The role of the cortical ring thickness and its effects on vertebral bone strength have been evaluated.[78,101] Vesterby et al.[78] showed that the cortical ring thickness may play an important role in predicting the compressive strength of vertebral bodies. Mosekilde et al.[101] found that the thickness of the cortical ring changes with age, noting that this and changes in other aspects (internal architecture, dimensions, size) all contribute to the overall strength of vertebral bone. In a separate cadaveric lumbar vertebrae study, Mosekilde et al.[76] reported that male vertebrae had significantly greater cross-sectional area and a significant increase in vertebral body size with aging. The authors speculated that this could compensate for the un- avoidable loss of vertebral bone density and ultimate strength with age. This was in contrast to females, where no age-related increases in cross-sectional area of vertebrae have been demonstrated.

A number of investigators have examined the mechanical properties of vertebral bodies and their components (primarily trabecular bone) by evaluating the effects of applied loads on *ex vivo* specimens. Testing parameters, sample types, number of samples, and loading rates are summarized in Table 33.2. Anisotropy in thoracic and lumbar vertebral trabecular bone has been characterized by Mosekilde and Viidik.[102] Even though the relationships between whole vertebral body strength and age and trabecular bone strength and age were very similar, at any age, the maximum compressive strength for whole vertebral bodies was about 1.6 MPa higher than that of the trabecular bone specimens. In addition, in a separate study, Mosekilde et al.[70] showed that the compressive properties of whole vertebral bodies depended mainly on the compressive strength of their trabecular bone, and that there was an increase in diameter of vertebral bodies with age (4 to 5 mm from age 20 to 80 years), attributable to periosteal growth. This increase in diameter led to a significant increase in cross-sectional area, and therefore an age-related reduction in the maximum compressive stress.

Trabecular bone microstructure has long been considered for its role in vertebral bone strength and as a contributory factor to fracture risk.[77,79,103–105] In two separate studies, Mosekilde[77] and Moseklide and Danielsen[103] concluded that the strength of vertebral trabecular bone depends not only on bone mass, but also on the continuity of the trabecular bone. Furthermore, vertebral trabecular bone strength was inversely correlated with age when trabecular bone volume changes were taken into account. Both trabecular bone continuity and trabecular bone volume were an indication of the status of trabecular bone microstructure. Specific changes in trabecular morphology observed with decreasing bone density, such as number and thickness of tra- beculae and intertrabecular spacing, posed a direct threat to the strength of vertebral trabecular bone.[104]

33.4 *In Vivo* Fracture Risk and Imaging Parameters

33.4.1 Proximal Femur

Studies centered on evaluating *in vivo* fracture risk and its relationship to imaging parameters have confirmed and extended what has been learned about skeletal mechanics from *ex vivo* studies. The clinically observed increases in proximal femur fracture risk with reductions in bone density[106,107] are consistent

with *ex vivo* studies that have demonstrated strong correlations between bone density and fracture load (see Table 33.1). However, there is a substantial amount of overlap in bone density values between patients with femur fracture and controls without fractures.[108,109] Parameters associated with the mechanics of falling have been shown to be strong independent predictors of proximal femur fracture,[110–112] consistent with experimental and modeling studies that have demonstrated reductions in femoral strength associated with impact direction.[32,33]

Clinical studies have provided substantial (albeit indirect) insight into the contributions of geometric parameters to femoral strength. Using femoral radiographs, Horsman and colleagues[113] found that femoral cortical area, lateral cortical width, and calcar width were significantly lower in fracture cases compared with controls.[113] Beck et al.[114,115] evaluated changes in cross-sectional moment of inertia (CSMI) with age in men and women, noting that although the data for men suggested compensatory increases in CSMI with age, CSMI decreased with age in postmenopausal women. Using a simple beam-bending model of the femur, these authors predicted a 4 to 12% per decade increase in femoral neck stresses in women due to an apparent lack of geometric restructuring. Significant differences in hip axis length measured using DXA have been demonstrated between patients with femur fracture and controls, and differences of only a few millimeters were found to be associated with substantial differences in femoral fracture risk.[116] Despite lower bone mass, Japanese women have a lower risk of femur fracture, which could be related to the fact that they have shorter femoral necks and/or smaller neck–shaft angles.[117] It may be that femoral neck axis length and loading angle combine to determine the moment arm and the bending moment acting on the femoral neck, and therefore the likelihood of fracture.[32] Gluer et al.[118] studied pelvic radiographs, and found that reduced thickness of the femoral shaft cortex and femoral neck cortex, as well as a wider trochanteric region, were all significant and independent predictors of proximal femur fracture. Furthermore, a combination of these parameters predicted femur fracture at least as strongly as femoral neck BMD, thus emphasizing the importance of geometric parameters in femoral fracture risk.

The material and geometric properties of a bone, combined with the applied loads, determine both the load at which the bone will fracture and the resulting fracture pattern. Studies that have examined fracture patterns in the femur provide indirect but useful information with regard to stress distributions and mechanical behavior. Several investigators have found differences between populations of patients who suffer cervical vs. trochanteric femur fractures.[119–123] A consistent result from studies that have evaluated fracture patterns is that patients who suffer trochanteric fractures tend to be older,[120,123,124] and the ratio of trochanteric to cervical fractures increases with age.[123,125] Regional differences in femoral BMD may also play a role in determining whether a fracture is cervical or trochanteric. Eriksson and Widhce[120] found that, although both trochanteric and femoral neck BMD were lower in patients with trochanteric fracture, patients who suffered femoral neck fractures had lower femoral neck BMD than trochanteric BMD. Greenspan et al.[122] noted that trochanteric BMD was lower in patients with trochanteric fracture than in those with femoral neck fracture; furthermore, they found that both a decrease in trochanteric BMD and an increase in femoral neck BMD were independently associated with trochanteric fracture. These investigators also evaluated the effects of factors related to fall mechanics, but found that these parameters did not distinguish between the two types of fractures. This is consistent with the results of *ex vivo* fracture experiments, in which variations in fall loading direction did not have a statistically significant effect on fracture pattern.[32] These findings, combined with the result that differences in regional BMD predict femur fracture type, suggest that intrinsic factors (such as density distribution) may contribute more strongly to fracture pattern than differences in loading conditions. This hypothesis is further supported by the fact that most subsequent contralateral proximal femur fractures are of the same type as the first fracture.[126–128] Intrinsic factors related to geometry may also contribute to type of proximal femur fracture. For example, Ferris and colleagues[121] found that patients with trochanteric fractures had significantly shorter femoral neck lengths than patients with subcapital fractures. Further work is necessary to elucidate fully the relative contributions of density variations and loading configuration to type of femur fracture.

33.4.2 Spine

Prediction of vertebral bone strength *in vivo* is required to assess the risk of fracture or to explore potential causes of injury by relating vertebral strength to calculated spinal loads under specific circumstances. Noninvasive *in vivo* measurements of the spine have been used to predict fracture risk and to monitor the effects of interventional regimens for osteoporosis. Biggeman et al.[129] utilized QCT-based parameters, such as trabecular bone density and end plate area, to determine vertebral compressive strength *in vivo* using the relationship previously proposed by Brinckmann et al.[85] This methodology had been previously validated *ex vivo* with a standard error of less than 0.95 kN.[83] A limiting vertebral strength value of 3 kN was suggested as the minimum value below which there would be an extremely high risk of insufficiency fractures, which typically result from excessive loading of normal spines or routine loading of osteoporotic spines.[129] The use of BMD measurements at multiple sites and their relationship to a spine deformity index (SDI) have been investigated by Sogaard et al.[130] in a group of women with osteoporosis. This SDI measure was introduced as a standardized method for detecting vertebral fractures by comparing individual vertebral body heights to their original heights as predicted from measurements of T4. After performing peripheral density measurements at the distal forearm (SPA) and iliac crest (ash density), and comparing these with direct density measurements at the lumbar spine (DPA), it was concluded that lumbar BMC was the best parameter for predicting vertebral fracture risk. It was also noted that the loading history as related to microfractures, the rate of repair, and resulting changes in bone architecture must play a role in SDI as well. Gordon et al.[105] also used measurable density parameters from different noninvasive modalities to assess vertebral fracture risk *in vivo*. The use of high-resolution QCT images to assess trabecular microstructure in conjunction with BMD measurements from DXA enhanced the ability to evaluate vertebral fracture risk in a group of women, which included some who had sustained vertebral fractures. This study showed the importance of including parameters other than bone mineral density to assess vertebral fracture risk.

The trends for future assessment of *in vivo* vertebral fracture risk lie in the potential to combine measurements from noninvasive modalities with mathematical models to localize potential vertebral fracture sites and to quantify the load levels that can induce them and the resulting stresses at the tissue level. Eventually, it may be possible to monitor and quantify the effects of therapeutic interventions that are aimed at preventing osteoporosis at the microstructural level.

33.5 Development of Models of Skeletal Structures

33.5.1 Proximal Femur

Although studies of *ex vivo* mechanical behavior and *in vivo* fracture risk provide important empirical information about skeletal behavior, many questions remain regarding the contributions of various factors to whole-bone mechanics. The development of techniques for analytical modeling of skeletal structures provides a complementary approach that can aid in answering questions about bone behavior that are difficult or impossible to address experimentally or clinically. Mathematical models are particularly powerful in that they provide estimates for quantities that cannot be directly measured experimentally, such as internal stresses in whole bones. These models are intimately connected with *ex vivo* studies, in that experimental data are used as inputs to models and for validation purposes.

The earliest structural models of the proximal femur took the form of analytical expressions describing the stress distribution within the bone, derived using simple beam theory.[35,131–134] Early calculations of the principal stress distributions under loads simulating stance or gait were noted to reflect trabecular architecture within the proximal portion of the femur.[132,133] Much of the early theoretical work served to establish the fact that fundamental principles of mechanics could be used to estimate the stress distribution within a complex skeletal structure such as the femur.

Backman[35] was among the first to utilize an analytical model of the femur to address an issue in clinical orthopedics, specifically, fracture of the proximal femur. Backman developed a structural model of the

proximal femur to compare the distribution of stresses in the femoral neck under loads assumed to be associated with gait, muscular contraction, and falls on the greater trochanter. He modeled a cross section of the femoral neck using nonconcentric inner and outer ellipses to represent the cortical shell boundaries, and applied combinations of normal, shear, and bending loads at the femoral head. Although this analysis was limited to the estimation of stresses at a single cross section of the femoral neck, comparison of stresses associated with different loading conditions demonstrated the potential importance of loads that act outside of the frontal plane in producing fractures, and the results suggested that the proximal femur was weakest under these types of loads. Other investigators have incorporated geometric measurements from X-rays into beam-bending calculations to predict either the failure load of the proximal femur[39,40,93] or the ultimate stress at the femoral neck.[37]

The shortcomings associated with early closed-form solutions for determining stress distributions, along with advances in high-speed computing and the contemporaneous development of the finite-element method, led to the use of the finite-element method as a tool for estimating stresses in skeletal structures. Brekelmans et al.[135] introduced the finite-element method for use in orthopedic research because of its suitability for structures with complex geometry, material properties, and load conditions. Although early finite-element models of the femur were limited by their two-dimensional nature and simplified material property distributions,[134–136] the early work was important as an improvement over previous experimental and analytical techniques. In particular, Rybicki et al.[134] compared a two-dimensional finite-element model of the femur with an analysis based on simple beam theory, and noted that a continuum-based (i.e., finite-element) model could improve stress predictions in places where the geometry did not approximate a slender beam (e.g., the femoral neck and intertrochanteric region).

Following the introduction of the finite-element method for the analysis of whole-bone structures, investigators focused on the refinement of structural models to improve stress predictions. A natural increase in complexity was the extension of two-dimensional finite-element models to three dimensions. Valliappan et al.[137] reported results for a three-dimensional finite-element model of the proximal portion of a human femur, and compared them with results from two-dimensional finite-element analysis and simple beam theory. These comparisons demonstrated significant differences in predicted stresses, particularly in the proximal region of the femur. The work of Rohlmann et al.[138] represented further refinement of femur modeling techniques, specifically with the incorporation of limited variations in bone material properties based on density measurements from radiographs, along with increased mesh density. Both Valliappan et al. and Rohlmann et al. attempted validation of their models using surface strain measurements on human femora, with significant differences between experimental and theoretical results. Although these early three-dimensional models represented an important improvement over previous two-dimensional models and beam theory analyses, these authors also recognized the need for improvements in geometry and material property descriptions.

An important step in the evolution of structural models of the human femur was from the prediction of stress distributions to the prediction of structural failure. Vichnin and Batterman[139] developed a three-dimensional model of a human femur, using a transversely isotropic material model for the diaphyseal cortex. The primary goal of their study was to compare the behavior of a femur with and without a prosthesis. Since only diaphyseal stresses were of interest, this model had limited applicability to proximal femur fracture. However, the investigation represented an early attempt to utilize engineering failure surfaces for bone material in the prediction of failure at the whole-bone level.

The work of Lotz and colleagues[140,141] was an important step in the prediction of fracture of the proximal femur using finite-element models. These investigators developed models of the proximal femur using geometry and material properties based directly on QCT. Of critical importance in this work was the investigation of fall as well as stance loading conditions, since falls are associated with large numbers of proximal femur fractures among elderly people.[24–27] This represented an evolution beyond previous models, which had investigated only stance and gait loading conditions.[136–139] Attempts were made to model the inhomogeneity of bone material properties, and care was taken to account specifically for the contribution of the cortical shell in the proximal region. Both linear and nonlinear material models were used. Although comparisons between predicted and measured surface strains showed substantial discrepancies,

these models were reasonably effective in predicting both the onset of yielding and bone fracture for both stance and fall loading conditions. Results from these stress analyses pointed to the potential structural importance of the trochanteric and subcapital regions in fracture of the proximal femur, and demonstrated a dramatic difference in stress distributions for stance and fall loading conditions.

The desire to predict failure of the proximal femur accurately led to increased sophistication of closed-form stress analyses in parallel with refinements in finite-element models. Raftopoulos and Qassem[142] proposed a three-dimensional, composite curved beam model of the human femur for prediction of stresses; however, no numerical results were presented. An alternative approach involved the incorporation of bone mineral data into beam bending calculations. Beck and colleagues[95] introduced a computer program to estimate femoral neck cross-sectional areas and moments of inertia from DPA data, and to incorporate these cross-sectional properties into a simple beam bending model. Comparisons between predicted and measured femoral fracture loads suggested that beam bending models incorporating structural geometry from DXA could improve fracture prediction over bone mineral assessment alone. Yoshikawa and co-workers[143] proposed a similar beam bending model based on DXA, and expanded the loading conditions to include a fall on the greater trochanter. An important step in the evolution of DXA-based structural models of the proximal femur was the use of a curved beam model to estimate stresses.[144] Using a three-dimensional, QCT-derived finite-element model of the femur as a standard of comparison, these authors found that stress predictions based on the curved beam solution were better than those utilizing the conventional flexure formula. Furthermore, the curved beam analysis identified stress peaks at the femoral neck as well as at the medial intertrochanteric region under fall loading conditions, both common sites of femur fracture. Although DXA-based structural models provide information that may be useful in evaluating fracture risk, the DXA imaging technique is intrinsically limited to two dimensions. Therefore, DXA-based structural analyses cannot incorporate loads that lie outside the frontal plane, under which the femur is typically weaker,[35,140,141] and under which many proximal femur fractures occur.

A natural progression in the refinement of structural models of the proximal femur was the development of improved, QCT-based finite-element models. Substantial effort has been devoted to the development of modeling techniques that incorporate geometry and material property distributions that are unique to a particular bone. Keyak and co-workers[145–147] introduced an automated method for generating QCT-based femur models, using cube-shaped elements and density-based material properties (Fig. 33.5). Although this modeling technique produces a suboptimal representation of the bone surface, predictions of femoral stiffnesses and failure load using the technique have been reasonably well correlated with experimental measurements on the same bones.[54,55] Alternative QCT-based modeling techniques have allowed for accurate representation of the surface contours of the proximal femur (Fig. 33.6).[148–150]

Much of the effort in finite-element modeling of the proximal femur has been oriented toward refinements in model geometry and material property distribution that have led to better predictions of stress and failure load. Significant progress has been made in this regard; however, limitations related to current finite-element modeling techniques remain to be addressed. An important issue that has rarely been directly addressed in models of the femur is how to model the metaphyseal shell properly. The geometric and material properties of the cortical shell have been demonstrated to be related to femur fracture risk,[113,118] and therefore the cortical shell likely plays an important structural role in the proximal femur. Perhaps the most ambitious attempt at accurately modeling the cortical shell was contributed by Lotz et al.[140,141,151] In this series of finite-element studies, the metaphyseal shell was modeled using elements approximately 1mm thick, with material property values based on mechanical tests of metaphyseal bone from the contralateral femur. A set of "reduced" metaphyseal bone material properties was defined for portions of the femur where the cortical shell thickness was less than 1 mm. Using a generic femur geometry, these investigators found that the percentage of total load carried by the cortical shell varied substantially with location in the proximal femur. Under loads associated with both gait and falls, there was a shift in the distribution of load carried by the cortical shell from approximately 30% in the subcapital region to 96% at the base of the femoral neck. Furthermore, the percentages of load transferred by the cortical shell were not in proportion to the local tissue volume. Since differential rates of loss with age may occur between cortical and trabecular bone,[152,153] accurate prediction of femoral structural

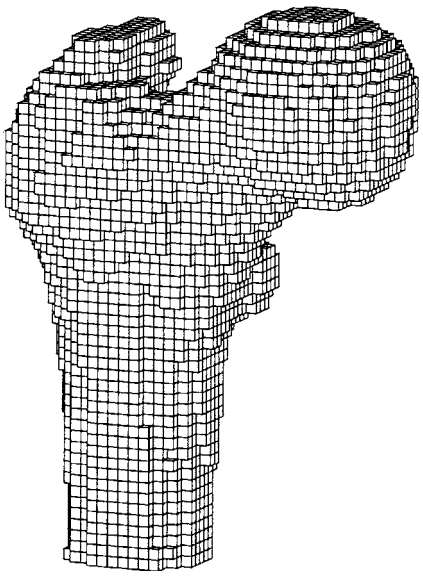

FIGURE 33.5 Voxel-based femur model with 14,534 nodes and 11,604 cube elements measuring 3 mm on a side. (From Keyak, J.H. et al., *J. Biomech.,* 31(2), 125–133, 1998. With permission.)

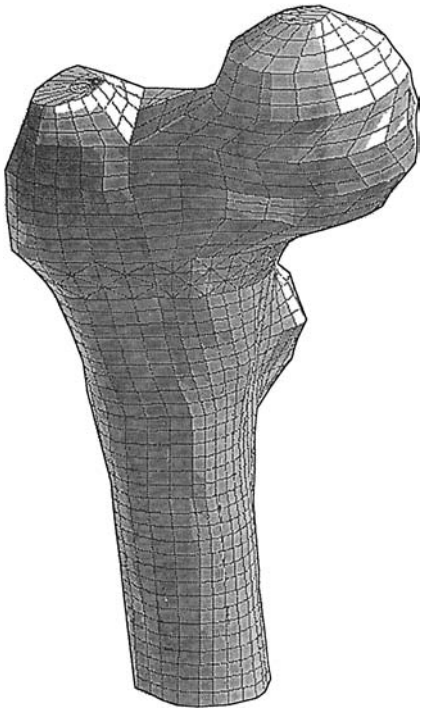

FIGURE 33.6 Smooth surface femur model of a cadaveric femur. Elements were mostly hexahedral, with tetrahedral shapes at the transition region between the shaft and epiphysis. (From Mourtada, F.A. et al., *J. Orthop. Res.,* 14(3), 483–492, 1996. With permission.)

capacity (and its changes with age) will likely require detailed modeling of the cortical shell. Current QCT-derived voxel models do not allow for effective modeling of the metaphyseal shell,[54,55] which could account in part for discrepancies between predicted and measured failure loads. Furthermore, even smooth-surface models of the femur with material properties derived from QCT data[148–150,154] are subject to volume-averaging effects, which could limit the accuracy of cortical shell properties.

Although much of the early and current work in structural modeling of the proximal femur for fracture prediction remains method oriented rather than problem oriented, as has been described previously by Huiskes and Chao,[155] finite-element models have become sufficiently sophisticated to be used as tools for addressing complex biologic problems. For example, Lotz et al.[151] developed a finite-element model to study the effects of age-related density changes on the stress distribution in the proximal femur during gait and falls, independent of variations in geometry. The results of this analysis shed light on the relative contributions of cortical and trabecular bone in load transfer in the proximal femur, and provided insight into theories related to the pathomechanics of osteoporosis. Ford and colleagues[33] used a QCT-based model to examine the effects of impact direction on structural capacity during falls, and found that reductions in strength associated with variations in impact direction were comparable to strength reductions associated with age-related bone loss.

33.5.2 Spine

Mathematical modeling of the spine, similar to that of the femur, provides a complementary approach to understanding bone behavior and, in particular, to calculating stress levels that are not possible to obtain experimentally or clinically. Comprehensive reviews related to mathematical modeling of spine structures show that early applications of the finite-element method focused primarily on understanding the behavior of intervertebral disks,[155,156] and that use of the finite-element method in the spine evolved first in the thoracolumbar region.[156–158] Only recently have these efforts shifted toward applications in the cervical spine.[156,159–161] The studies presented here focus on the use of mathematical modeling to understand what factors affect the stress distribution in vertebral bodies. Models developed to study the effects of specific clinical interventions (including spinal instrumentation) are beyond the scope of this chapter. Although spine finite-element models have evolved in complexity from two-dimensional models representing vertebral slices to complex multisegment models, this section reviews representative models of single vertebral bodies and single functional spinal units (two vertebrae and interconnecting soft tissue).

Several models of single vertebral bodies have been developed to study vertebral body stresses.[68,162–166] Ranu's[162] idealized model of a single vertebra showed that under compressive loading, the maximum stresses were at the junction of the pedicles and the vertebral body. High stresses also appeared at the anterior aspect of the vertebra, consistent with the location of wedge fractures. Mizrahi et al.[163] developed an idealized model of an isolated lumbar vertebra to examine how material properties affected end plate and cortical shell stresses. Under uniform compressive loading simulating degenerated disks, the model indicated that the peak stresses in the end plate and cortical shell were sensitive to the modulus of the underlying trabecular bone. A 50% reduction in trabecular bone modulus increased the peak stress in the end plate by 74%. In addition, disproportionate reductions in trabecular and cortical bone moduli increased peak stresses in the cortical shell and end plate. The relevance of these modulus changes is that they could reflect those typically seen in patients with osteoporosis. Although these models did not reflect the exact geometry of a vertebral body or local variations in the thickness of the cortical shell and end plate, they provide useful insight into the role of material property changes in determining the stress distribution.

The influence of geometric factors on overall strength has been examined in single vertebral body models.[68,164,166,167] A three-dimensional finite-element model of L1 with uniform compressive loading was used to examine the effect of the pedicles and posterior arch on strain distributions within the vertebral body.[68] Whyne et al.[68] found that inclusion of the posterior arch resulted in substantial decreases in maximum strain and posterior wall displacement. Improvements in the geometric and material property representation of a single vertebra were reported in a three-dimensional model of a midcervical vertebra generated from QCT data by Bozic et al.[164] The highly refined mesh of this voxel-based model incorporated

three-dimensional variation in material properties with moduli derived from QCT data. Under axial compressive loading, this model predicted the initiation of failure in the central cancellous region of the vertebral body, consistent with typical cervical burst fractures. The single lumbar vertebra model developed by Martin et al.[167] was also generated based on QCT data from cadaveric specimens and utilized the QCT data to assign material properties. This model was utilized to assess the stiffness and failure load of the vertebral body under a distributed compressive load on the superior end plate, and was successfully validated with experimental measurements. A single cervical vertebra model (C2) developed using the geometry of a cadaveric specimen was reported by Teo et al.[166] This model showed that the stress distribution within this vertebra was influenced by the direction (-45, 0, $+45°$) of the applied load on the anterior surface of the odontoid process. The regions of highest compressive stress corresponded with areas of fracture seen clinically.

A number of models have been developed to evaluate the load-carrying capacity of the cortical shell and trabecular core,[165,168,169] and the effects that these have on the overall stiffness of vertebral bodies.[170] Faulkner et al.[168] used QCT data to develop patient-specific finite-element models of lumbar vertebral bodies to examine the role of the vertebral cortex in the overall vertebral body strength under distributed compressive axial loading. These models predicted that the shell contributed 12% to the total vertebral strength in healthy individuals and 50% in ones with osteoporosis. In contrast, Burr et al.[169] had predicted from a parametric finite-element modeling study that the shell carried about 50% of the vertebral body force in a young individual, and about 90% in an individual with osteoporosis.[169] Using a geometrically simple model of a single lumbar vertebral body, Silva et al.[165] evaluated parametrically the relative load-carrying roles of the shell and the centrum. The findings from this model supported the notion that the shell accounts for only about 10% of the vertebral strength *in vivo* and that the cancellous core is the dominant structural component of the vertebral body. This is in contrast to previous studies that had reported a wider range of contribution of the cortical shell toward the overall strength of the vertebral body.[82,168,169,171] In a recent study by Liebschner et al.,[170] the effects of cortical shell and end plate material property changes on the overall vertebral body stiffness were examined in QCT-based whole vertebral body models. These models showed that vertebral body stiffness was relatively insensitive to end plate modulus variations compared with models that were evaluated with the cortical shell completely removed. Unlike previous models that varied end plate and cortical shell thickness, these models included a constant cortical shell and end plate thickness. These different approaches to examining the contribution of the cortical shell to overall vertebral strength make direct comparison of the studies difficult.

Models of single vertebral bodies provide insight into the mechanical behavior of these bones, but modeling a full functional spinal unit (FSU) has been shown to be a more accurate method for evaluating the internal stresses in the spine. With a more complete model, the effect of other spinal structures on the overall strength of vertebrae can be evaluated. In their 1995 review of the state of the finite-element method in spine mechanics, Gilbertson et al.[156] summarized pertinent contributions from single FSU models subjected to different kinds of loading. Comparison of predicted stresses and strains from various reported finite-element models with available ultimate stress and strain values indicated that the most vulnerable components under compressive loading were the cancellous bone and the end plate adjacent to the nucleus. This is consistent with findings from prior experimental studies.[65,172] Under torsional loading the posterior bony structures, including the junction of the pedicle and the vertebral body and facets, appeared to be the most vulnerable components. In addition, models showed that most of the torsional load was transmitted through the cortical shell and not the cancellous core, thereby making the cortical shell more vulnerable to shear failure under this type of loading. These findings have also been shown in *ex vivo* cadaveric work under torsional loading.[173]

One of the landmark publications of finite-element modeling of the spine is that by Shirazi-Adl et al.,[174] in which they present an L2-L3 disk-body unit model based on the geometry of a cadaveric specimen (Fig. 33.7). This model showed that under an axial compressive load of about 3000 N, the most vulnerable elements in a disk-body unit with a normal disk were the cancellous bone and the end plate adjacent to the nucleus. Shirazi-Adl et al. extended their disk-body unit to include posterior elements, facet joints, and ligamentous structures to provide a more complete representation of a spinal motion segment and loaded

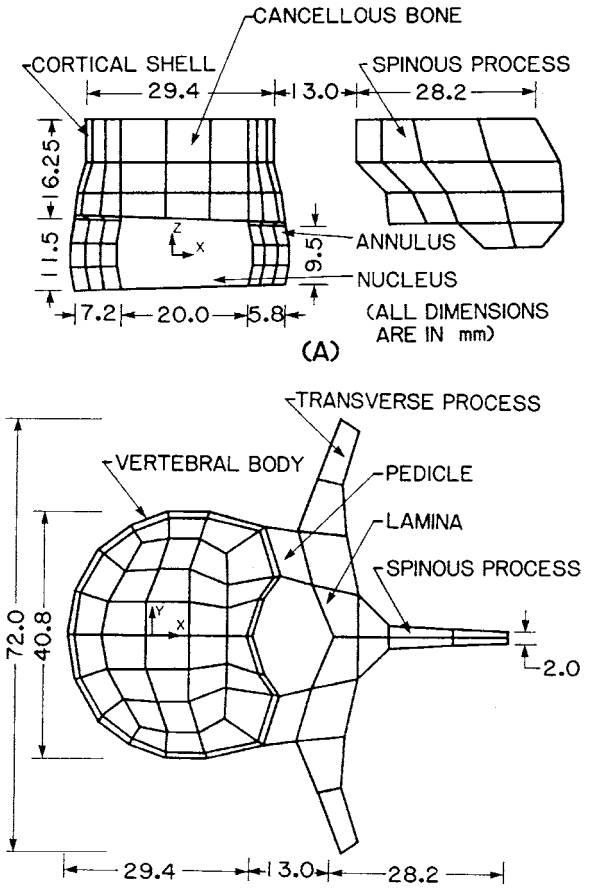

FIGURE 33.7 L2-L3 motion segment model. (From Shirazi-Adl, A. et al., *J. Biomech.,* 19(4), 331–350, 1986. With permission.)

it in the sagittal plane under flexion and extension.[175] This model was then evaluated under more complex loading conditions including axial torque and axial torque combined with compression.[176] The inclusion of the posterior elements in three-dimensional models of single motion segments of the spine had been done earlier by Hakim and King.[177] Although their model was symmetric about the sagittal plane, it included separate element representations for trabecular bone, cortex, end plate, and posterior elements. The model was experimentally validated by comparison with vertebral body surface strains. One of the earliest three-dimensional models to incorporate QCT-derived geometry for development of a finite-element model of a single lumbar motion segment, by Goel et al.,[178] incorporated all biomechanically relevant structures of the spine and was validated against experimental data.

The recent trend toward voxel-based model generation has been utilized in the spine,[164,179,180] but to a lesser extent than in femur models. The midcervical vertebral body model of Bozic et al.[164] was voxel-based, but it did not incorporate details of trabecular microstructure. Hollister et al.[179] utilized a substructure-based voxel modeling approach to determine the effect of trabecular microstructure on whole vertebral body mechanics. A three-dimensional global finite-element model of a vertebral body was generated, with geometric input from QCT, which utilized as input the effective stiffness predicted from smaller models of trabecular bone cubes. Surface strains obtained from the global finite-element model were used as input for the cube models to determine trabecular-level strains. These smaller models showed that vertical trabeculae experienced mostly axial compressive strains, whereas horizontal trabeculae were subjected to both compressive and tensile strains.

Incorporating trabecular-level detail in multisegmental spine models with properly defined material properties for all components is the next logical step in finite-element modeling of the spine. With this level of detail, it will be possible to increase understanding of the effects of localized trabecular bone loss and changes on overall spine mechanics.

33.5.3 Future Trends in Modeling Skeletal Structures

Although automated, patient-specific finite-element models may eventually be clinically useful in the assessment of both femur and spine fracture risk, an additional and potentially powerful application of finite-element models will involve parametric investigation of the factors that contribute to fracture risk. For example, well-constructed finite-element models of the femur could be used to investigate the effects of regional differences in age-related bone loss[181] under multiple loading conditions, independent of differences in femur geometry. Similar parametric studies could be performed in the spine, examining the effects of changes in material properties due to either disk degeneration or aging. Finite-element models could also be utilized to examine the structural importance of various geometric parameters that are associated with femur and spine fracture risk, while potentially controlling for the confounding effects of differences in density distribution. Future use of finite-element models for the parametric examination of factors that are difficult or impossible to examine experimentally will contribute to the evolution of the finite-element method in biomechanics from "a tool of technology to a tool of science."[182]

References

1. Melton, L. J., Epidemiology of fractures, in *Osteoporosis: Etiology, Diagnosis and Management,* Riggs, B. L. and Melton, L. J., Eds., Raven Press, New York, 1988, chap. 5.
2. Hayes, W. C., Piazza, S .J., and Zysset, P. K., Biomechanics of fracture risk prediction of the hip and spine by quantitative computed tomography, *Radiol. Clin. North Am.,* 29(1), 1, 1991.
3. Rydell, N. W., Forces acting on the femoral head-prosthesis. A study on strain gauge supplied prostheses in living persons, *Acta Orthop. Scand.,* 37(Suppl.), 1, 1966.
4. Williams, M. and Lissner, H., *Biomechanics of Human Motion.,* W. B. Saunders, Philadelphia, 1962.
5. McLeish, R. D. and Charnley, J., Abduction forces in the one-legged stance, *J. Biomech.,* 3(2), 191, 1970.
6. English, T. and Kilvington, M., *In vivo* records of hip loads using a femoral implant with telemetric output (a preliminary report), *J. Biomed. Eng.,* 1, 111, 1979.
7. Davy, D. T., Kotzar, G. M., Brown, R. H., Heiple, K. G., Goldberg, V. M., Heiple, K. G., Jr., Berilla, J., and Burstein, A. H., Telemetric force measurements across the hip after total arthroplasty, *J. Bone Joint Surg. [Am].,* 70(1), 45, 1988.
8. Kotzar, G. M., Davy, D. T., Goldberg, V. M., Heiple, K. G., Berilla, J., Heiple, K. G., Jr., Brown, R. H., and Burstein, A. H., Telemeterized *in vivo* hip joint force data: a report on two patients after total hip surgery, *J. Orthop. Res.,* 9(5), 621, 1991.
9. Brand, R. A., Pedersen, D. R., Davy, D. T., Kotzar, G. M., Heiple, K. G., and Goldberg, V. M., Comparison of hip force calculations and measurements in the same patient, *J. Arthroplasty,* 9(1), 45, 1994.
10. Crowninshield, R., Johnston, R., Andrews, J., and Brand, R., A biomechanical investigation of the human hip, *J. Biomech.,* 11, 75, 1978.
11. Crowninshield, R. and Brand, R., The prediction of forces in joint structures: distribution of intersegmental resultants, *Exercise, Sport Sci. Rev.,* 9, 159, 1981.
12. Hardt, D., Determining muscle forces in the leg during normal human walking—an application and evaluation of optimization methods, *J. Biomech. Eng.,* 100, 72, 1978.
13. Rohrle, H., Scholten, R., Sigolotto, C., Sollbach, W., and Kellner, H., Joint forces in the human pelvis-leg skeleton during walking, *J. Biomech.,* 17, 409, 1984.
14. Smith, L. D., The role of muscle contraction or intrinsic forces in the causation of fractures of the femoral neck, *J. Bone Joint Surg.,* 35-A(2), 367, 1953.

15. Kelly, J., Fractures complicating electro-convulsive therapy and chronic epilepsy, *J. Bone Joint Surg.,* 36B, 899, 1954.
16. Muckle, D. S., Iatrogenic factors in femoral neck fractures, *Injury,* 8(2), 98, 1976.
17. Sloan, J. and Holloway, G., Fractured neck of the femur: the cause of the fall? *Injury,* 13(3), 230, 1981.
18. Yang, K. H., Shen, K. L., Demetropoulos, C. K., King, A. I., Kolodziej, P., Levine, R. S., and Fitzgerald, R. H., Jr., The relationship between loading conditions and fracture patterns of the proximal femur, *J. Biomech. Eng.,* 118(4), 575, 1996.
19. Lu, T. W., Taylor, S. J., O'Connor, J. J., and Walker, P. S., Influence of muscle activity on the forces in the femur: an *in vivo* study, *J. Biomech.,* 30(11–12), 1101, 1997.
20. Lu, T. W., O'Connor, J. J., Taylor, S. J., and Walker, P. S., Validation of a lower limb model with *in vivo* femoral forces telemetered from two subjects, *J. Biomech.,* 31(1), 63, 1998.
21. Bergmann, G., Graichen, F., and Rohlmann, A., Hip joint loading during walking and running, measured in two patients, *J. Biomech.,* 26(8), 969, 1993.
22. Dias, J. J., An analysis of the nature of injury in fractures of the neck of the femur, *Age Ageing,* 16(6), 373, 1987.
23. Cotton, D. W., Whitehead, C. L., Vyas, S., Cooper, C., and Patterson, E. A., Are hip fractures caused by falling and breaking or breaking and falling? Photoelastic stress analysis, *Forens. Sci. Int.,* 65(2), 105, 1994.
24. Melton, L. and Riggs, B., Epidemiology of age-related fractures, in *The Osteoporotic Syndrome. Detection, Prevention, and Treatment,* Avioli, L., Ed., Grune and Stratton, Orlando, 1987, chap. 1.
25. Michelson, J., Myers, A., Jinnah, R., Cox, Q., and Natta, M., Epidemiology of hip fractures among the elderly, *Clin. Orthop.,* 311, 129, 1995.
26. Grisso, J., Kelsey, J., Strom, B., Chiu, G., Maislin, G., O'Brien, L., Hoffman, S., and Kaplan, F., Risk factors for falls as a cause of hip fracture in women, *N. Engl. J. Med.,* 324, 1326, 1991.
27. Cumming, R. and Klineberg, R., Fall frequency and characteristics and the risk of hip fractures, *J. Am. Geriatric Soc.,* 42, 774, 1994.
28. Robinovitch, S. N., Hayes, W. C., and McMahon, T. A., Prediction of femoral impact forces in falls on the hip, *J. Biomech. Eng.,* 113(4), 366, 1991.
29. van den Kroonenberg, A. J., Hayes, W. C., and McMahon, T. A., Dynamic models for sideways falls from standing height, *J. Biomech. Eng.,* 117(3), 309, 1995.
30. van den Kroonenberg, A. J., Hayes, W. C., and McMahon, T. A., Hip impact velocities and body configurations for voluntary falls from standing height, *J. Biomech.,* 29(6), 807, 1996.
31. Courtney, A. C., Wachtel, E. F., Myers, E. R., and Hayes, W. C., Effects of loading rate on strength of the proximal femur [published erratum appears in *Calcif. Tissue Int.,* 55(5),402, 1994], *Calcif. Tissue Int.,* 55(1), 53, 1994.
32. Pinilla, T. P., Boardman, K. C., Bouxsein, M. L., Myers, E. R., and Hayes, W. C., Impact direction from a fall influences the failure load of the proximal femur as much as age-related bone loss, *Calcif. Tissue Int.,* 58(4), 231, 1996.
33. Ford, C. M., Keaveny, T. M., and Hayes, W. C., The effect of impact direction on the structural capacity of the proximal femur during falls, *J. Bone Miner. Res.,* 11(3), 377, 1996.
34. Weber, T. G., Yang, K. H., Woo, R., and Fitzgerald, R. H., Proximal femur strength: correlation of the rate of loading and bone mineral density, *ASME Adv. Bioeng.,* 22, 111, 1992.
35. Backman, S., *The Proximal End of the Femur,* Karolinska Sjukhuset, Stockholm, 1957.
36. Hirsch, C. and Frankel, V., Analysis of forces producing fractures of the proximal end of the femur, *J. Bone Joint Surg.,* 42B(3), 633, 1960.
37. Mizrahi, J., Margulies, J. Y., Leichter, I., and Deutsch, D., Fracture of the human femoral neck: effect of density of the cancellous core, *J. Biomed. Eng.,* 6(1), 56, 1984.
38. Vose, G. P. and Mack, P. B., Roentgenologic assessment of femoral neck density as related to fracturing, *Roentgenology,* 89, 1296, 1963.
39. Phillips, J. R., Williams, J. F., and Melick, R. A., Prediction of the strength of the neck of femur from its radiological appearance, *Biomed. Eng.,* 10(10), 367, 1975.

40. Dalen, N., Hellstrom, L. G., and Jacobson, B., Bone mineral content and mechanical strength of the femoral neck, *Acta Orthop. Scand.,* 47(5), 503, 1976.
41. Leichter, I., Margulies, J. Y., Weinreb, A., Mizrahi, J., Robin, G. C., Conforty, B., Makin, M., and Bloch, B., The relationship between bone density, mineral content, and mechanical strength in the femoral neck, *Clin. Orthop.,* 163, 272, 1982.
42. Sartoris, D. J., Sommer, F. G., Kosek, J., Gies, A., and Carter, D., Dual-energy projection radiography in the evaluation of femoral neck strength, density, and mineralization, *Invest. Radiol.,* 20(5), 476, 1985.
43. Werner, C., Iversen, B. F., and Therkildsen, M. H., Contribution of the trabecular component to mechanical strength and bone mineral content of the femoral neck. An experimental study on cadaver bones, *Scand. J. Clin. Lab. Invest.,* 48(5), 457, 1988.
44. Delaere, O., Dhem, A., and Bourgois, R., Cancellous bone and mechanical strength of the femoral neck, *Arch. Orthop. Trauma Surg.,* 108(2), 72, 1989.
45. Alho, A., Hoiseth, A., and Husby, T., Bone density and bone strength—an *ex vivo* study on cadaver femora, *Rev. Chir. Orthop.,* 74(Suppl. 2), 333, 1988.
46. Alho, A., Husby, T., and Hoiseth, A., Bone mineral content and mechanical strength. An *ex vivo* study on human femora at autopsy, *Clin. Orthop.,* 227, 292, 1988.
47. Alho, A., Hoiseth, A., Husby, T., and Ekeland, A., Femoral bone density measurements by single energy computed tomography related to hip fractures, *Ann. Chir. Gynaecol.,* 77(5–6), 208, 1988.
48. Husby, T., Hoiseth, A., Alho, A., and Ronningen, H., Rotational strength of the femoral neck. Computed tomography in cadavers, *Acta Orthop. Scand.,* 60(3), 288, 1989.
49. Alho, A., Hoiseth, A., and Husby, T., Bone-mass distribution in the femur. A cadaver study on the relations of structure and strength, *Acta Orthop. Scand.,* 60(1), 101, 1989.
50. Esses, S. I., Lotz, J. C., and Hayes, W. C., Biomechanical properties of the proximal femur determined *in vitro* by single-energy quantitative computed tomography, *J. Bone Miner. Res.,* 4(5), 715, 1989.
51. Lotz, J. C. and Hayes, W. C., The use of quantitative computed tomography to estimate risk of fracture of the hip from falls, *J. Bone Joint Surg. [Am.],* 72(5), 689, 1990.
52. Smith, M. D., Cody, D. D., Goldstein, S. A., Cooperman, A. M., Matthews, L. S., and Flynn, M. J., Proximal femoral bone density and its correlation to fracture load and hip-screw penetration load, *Clin. Orthop.,* 283, 244, 1992.
53. Lang, T. F., Keyak, J. H., Heitz, M. W., Augat, P., Lu, Y., Mathur, A., and Genant, H. K., Volumetric quantitative computed tomography of the proximal femur: precision and relation to bone strength, *Bone,* 21(1), 101, 1997.
54. Keyak, J. H., Rossi, S. A., Jones, K. A., and Skinner, H. B., Prediction of femoral fracture load using automated finite element modeling, *J. Biomech.,* 31(2), 125, 1998.
55. Cody, D. D., Gross, G. J., Hou, F. J., Spencer, H. J., Goldstein, S. A., and Fyhrie, D. P., Femoral strength is better predicted by finite element models than QCT and DXA, *J. Biomech.,* 32(10), 1013, 1999.
56. Courtney, A. C., Wachtel, E. F., Myers, E. R., and Hayes, W. C., Age-related reductions in the strength of the femur tested in a fall–loading configuration, *J. Bone Joint Surg. [Am.],* 77(3), 387, 1995.
57. Bouxsein, M. L., Courtney, A. C., and Hayes, W. C., Ultrasound and densitometry of the calcaneus correlate with the failure loads of cadaveric femurs, *Calcif. Tissue Int.,* 56(2), 99, 1995.
58. Cheng, X. G., Lowet, G., Boonen, S., Nicholson, P. H., Brys, P., Nijs, J., and Dequeker, J., Assessment of the strength of proximal femur *in vitro*: relationship to femoral bone mineral density and femoral geometry, *Bone,* 20(3), 213, 1997.
59. Nicholson, P. H., Lowet, G., Cheng, X. G., Boonen, S., van der Perre, G., and Dequeker, J., Assessment of the strength of the proximal femur *in vitro*: relationship with ultrasonic measurements of the calcaneus, *Bone,* 20(3), 219, 1997.
60. Beck, T. J., Mourtada, F. A., Ruff, C. B., Scott, W. W., Jr., and Kao, G., Experimental testing of a DEXA-derived curved beam model of the proximal femur, *J. Orthop. Res.,* 16(3), 394, 1998.

61. Lochmuller, E. M., Zeller, J. B., Kaiser, D., Eckstein, F., Landgraf, J., Putz, R., and Steldinger, R., Correlation of femoral and lumbar DXA and calcaneal ultrasound, measured *in situ* with intact soft tissues, with the *in vitro* failure loads of the proximal femur, *Osteoporos. Int.,* 8(6), 591, 1998.
62. Bouxsein, M. L., Coan, B. S., and Lee, S. C., Prediction of the strength of the elderly proximal femur by bone mineral density and quantitative ultrasound measurements of the heel and tibia, *Bone,* 25(1), 49, 1999.
63. Lochmuller, E. M., Eckstein, F., Zeller, J. B., Steldinger, R., and Putz, R., Comparison of quantitative ultrasound in the human calcaneus with mechanical failure loads of the hip and spine, *Ultrasound Obstet. Gynecol.,* 14(2), 125, 1999.
64. Schultz, A., Andersson, G., Ortengren, R., Haderspeck, K., and Nachemson, A., Loads on the lumbar spine. Validation of a biomechanical analysis by measurements of intradiscal pressures and myoelectric signals, *J. Bone Joint Surg. [Am.],* 64(5), 713, 1982.
65. Hansson, T. H., Bigos, S. J., Wortley, M. K., and Spengler, D. M., The load on the lumbar spine during isometric strength testing, *Spine,* 9(7), 720, 1984.
66. Melton, L. J., Kan, S. H., Frye, M. A., Wahner, H. W., O'Fallon, W. M., and Riggs, B. L., Epidemiology of vertebral fractures in women, *Am. J. Epidemiol.,* 129(5), 1000, 1989.
67. Myers, E. R. and Wilson, S. E., Biomechanics of osteoporosis and vertebral fracture, *Spine,* 22 (24 Suppl.), 25S, 1997.
68. Whyne, C. M., Hu, S. S., Klisch, S., and Lotz, J. C., Effect of the pedicle and posterior arch on vertebral body strength predictions in finite element modeling, *Spine,* 23(8), 899, 1998.
69. Granhed, H., Jonson, R., and Hansson, T., Mineral content and strength of lumbar vertebrae. A cadaver study, *Acta Orthop. Scand.,* 60(1), 105, 1989.
70. Mosekilde, L., Normal vertebral body size and compressive strength: relations to age and to vertebral and iliac trabecular bone compressive strength, *Bone,* 7(3), 207, 1986.
71. Hansson, T., Roos, B., and Nachemson, A., The bone mineral content and ultimate compressive strength of lumbar vertebrae, *Spine,* 5(1), 46, 1980.
72. Keller, T. S., Hansson, T. H., Abram, A. C., Spengler, D. M., and Panjabi, M. M., Regional variations in the compressive properties of lumbar vertebral trabeculae. Effects of disc degeneration, *Spine,* 14(9), 1012, 1989.
73. Keaveny, T. M., Wachtel, E. F., and Kopperdahl, D. L., Mechanical behavior of human trabecular bone after overloading, *J. Orthop. Res.,* 17(3), 346, 1999.
74. Fyhrie, D. P., Milgrom, C., Hoshaw, S. J., Simkin, A., Dar, S., Drumb, D., and Burr, D. B., Effect of fatiguing exercise on longitudinal bone strain as related to stress fracture in humans, *Ann. Biomed. Eng.,* 26(4), 660, 1998.
75. Mendelson, S., Milgrom, C., Finestone, A., Lewis, J., Ronen, M., Burr, D., Fyhrie, D., Hoshaw, S., Simkin, A., and Soudry, M., Effect of cane use on tibial strain and strain rates, *Am. J. Phys. Med. Rehabil.,* 77(4), 333, 1998.
76. Mosekilde, L., Sex differences in age-related changes in vertebral body size, density and biomechanical competence in normal individuals, *Bone,* 11(2), 67, 1990.
77. Mosekilde, L., Iliac crest trabecular bone volume as predictor for vertebral compressive strength, ash density and trabecular bone volume in normal individuals, *Bone,* 9(4), 195, 1988.
78. Vesterby, A., Mosekilde, L., Gundersen, H. J., Melsen, F., Holme, K., and Sorensen, S., Biologically meaningful determinants of the *in vitro* strength of lumbar vertebrae, *Bone,* 12(3), 219, 1991.
79. Korstjens, C. M., Mosekilde, L., Spruijt, R. J., Geraets, W. G., and van der Stelt, P. F., Relations between radiographic trabecular pattern and biomechanical characteristics of human vertebrae, *Acta Radiol,* 37(5), 618, 1996.
80. Ortoft, G., Mosekilde, L., and Hasling, C., Estimation of vertebral body strength by dual photon absorptiometry in elderly individuals: comparison between measurements of total vertebral and vertebral body bone mineral, *Bone,* 14(4), 667, 1993.

81. Eriksson, S. A., Isberg, B. O., and Lindgren, J. U., Prediction of vertebral strength by dual photon absorptiometry and quantitative computed tomography, *Calcif. Tissue Int.,* 44(4), 243, 1989.
82. McBroom, R. J., Hayes, W. C., Edwards, W. T., Goldberg, R. P., and White, A. A., Prediction of vertebral body compressive fracture using quantitative computed tomography, *J. Bone Joint Surg. [Am.],* 67(8), 1206–1214, 1985.
83. Biggemann, M., Hilweg, D., and Brinckmann, P., Prediction of the compressive strength of vertebral bodies of the lumbar spine by quantitative computed tomography, *Skeletal Radiol.,* 17(4), 264, 1988.
84. Mosekilde, L., Bentzen, S. M., Ortoft, G., and Jorgensen, J., The predictive value of quantitative computed tomography for vertebral body compressive strength and ash density, *Bone,* 10(6), 465, 1989.
85. Brinckmann, P., Biggemann, M., and Hilweg, D., Prediction of the compressive strength of human lumbar vertebrae, *Spine,* 14(6), 606, 1989.
86. Cody, D. D., Goldstein, S. A., Flynn, M. J., and Brown, E. B., Correlations between vertebral regional bone mineral density (rBMD) and whole bone fracture load, *Spine,* 16(2), 146, 1991.
87. McCubbrey, D. A., Cody, D. D., Peterson, E. L., Kuhn, J. L., Flynn, M. J., and Goldstein, S. A., Static and fatigue failure properties of thoracic and lumbar vertebral bodies and their relation to regional density, *J. Biomech.,* 28(8), 891, 1995.
88. Cheng, X. G., Nicholson, P. H., Boonen, S., Lowet, G., Brys, P., Aerssens, J., Van der Perre, G., and Dequeker, J., Prediction of vertebral strength *in vitro* by spinal bone densitometry and calcaneal ultrasound, *J. Bone Miner. Res.,* 12(10), 1721, 1997.
89. Moro, M., Hecker, A. T., Bouxsein, M. L., and Myers, E. R., Failure load of thoracic vertebrae correlates with lumbar bone mineral density measured by DXA, *Calcif. Tissue Int.,* 56(3), 206, 1995.
90. Edmondston, S. J., Singer, K. P., Day, R. E., Price, R. I., and Breidahl, P. D., *Ex vivo* estimation of thoracolumbar vertebral body compressive strength: the relative contributions of bone densitometry and vertebral morphometry, *Osteoporos Int.,* 7(2), 142, 1997.
91. Mather, B. S., Variation with age and sex in strength of the femur, *Med. Biol. Eng.,* 6(2), 129, 1968.
92. Leichter, I., Simikin, A., Margulies, J. Y., Bivas, A., Roman, I., Deutsch, D., and Weinreb, A., Can the weight-bearing capacity of the femoral neck be estimated by physical measurements on the greater trochanter? *Eng. Med.,* 17(2), 59, 1988.
93. Gies, A., Carter, D., Sartoris, D., and Sommer, F., Femoral neck strength predicted from dual energy projected radiography, in *Transactions of the 31st Annual Meeting of the Orthopaedic Research Society,* 1985, 357.
94. Cordey, J., Schneider, M., Belendez, C., Ziegler, W.J., Rahn, B. A., and Perren, S. M., Effect of bone size, not density, on the stiffness of the proximal part of normal and osteoporotic human femora, *J. Bone Miner. Res.,* 7 (Suppl. 2), S437, 1992.
95. Beck, T. J., Ruff, C. B., Warden, K. E., Scott, W. W., Jr., and Rao, G. U., Predicting femoral neck strength from bone mineral data. A structural approach, *Invest. Radiol.,* 25(1), 6, 1990.
96. Hansson, T. H., Keller, T. S., and Panjabi, M. M., A study of the compressive properties of lumbar vertebral trabeculae: effects of tissue characteristics, *Spine,* 12(1), 56, 1987.
97. Lang, S. M., Moyle, D. D., Berg, E. W., Detorie, N., Gilpin, A. T., Pappas, N. J., Jr., Reynolds, J. C., Tkacik, M., and Waldron, R. L., Correlation of mechanical properties of vertebral trabecular bone with equivalent mineral density as measured by computed tomography, *J.Bone Joint Surg. [Am.],* 70(10), 1531, 1988.
98. Silva, M. J., Wang, C., Keaveny, T. M., and Hayes, W. C., Direct and computed tomography thickness measurements of the human, lumbar vertebral shell and endplate, *Bone,* 15(4), 409, 1994.
99. Myers, B. S., Arbogast, K. B., Lobaugh, B., Harper, K. D., Richardson, W. J., and Drezner, M. K., Improved assessment of lumbar vertebral body strength using supine lateral dual-energy x-ray absorptiometry, *J. Bone Miner. Res.,* 9(5), 687, 1994.

100. Tabensky, A. D., Williams, J., DeLuca, V., Briganti, E., and Seeman, E., Bone mass, area, and volumetric bone density are equally accurate, sensitive, and specific surrogates of the breaking strength of the vertebral body: an *in vitro* study, *J. Bone Miner. Res.,* 11(12), 1981, 1996.
101. Mosekilde, L., Vertebral structure and strength *in vivo* and *in vitro, Calcif. Tissue Int.,* 53(Suppl. 1), S121, 1993.
102. Mosekilde, L. and Viidik, A., Correlation between the compressive strength of iliac and vertebral trabecular bone in normal individuals, *Bone,* 6(5), 291, 1985.
103. Mosekilde, L. and Danielsen, C. C., Biomechanical competence of vertebral trabecular bone in relation to ash density and age in normal individuals, *Bone,* 8(2), 79, 1987.
104. Snyder, B. D., Piazza, S., Edwards, W. T., and Hayes, W. C., Role of trabecular morphology in the etiology of age-related vertebral fractures, *Calcif. Tissue Int.,* 53(Suppl. 1), S14, 1993.
105. Gordon, C. L., Lang, T. F., Augat, P., and Genant, H. K., Image-based assessment of spinal trabecular bone structure from high-resolution CT images, *Osteoporos Int.,* 8(4), 317, 1998.
106. Cummings, S. R., Black, D. M., Nevitt, M. C., Browner, W. S., Cauley, J. A., Genant, H. K., Mascioli, S. R., Scott, J. C., Seeley, D. G., and Steiger, P., Appendicular bone density and age predict hip fracture in women. The Study of Osteoporotic Fractures Research Group, *JAMA*, 263(5), 665, 1990.
107. Peacock, M., Turner, C. H., Liu, G., Manatunga, A. K., Timmerman, L., and Johnston, C. C., Jr., Better discrimination of hip fracture using bone density, geometry and architecture, *Osteoporos Int.,* 5(3), 167, 1995.
108. Cummings, S. R., Are patients with hip fractures more osteoporotic? Review of the evidence, *Am. J. Med.,* 78(3), 487, 1985.
109. Hoiseth, A., Alho, A., Husby, T., and Engh, V., Are patients with fractures of the femoral neck more osteoporotic? *Eur. J. Radiol.,* 13(1), 2, 1991.
110. Hayes, W. C., Myers, E. R., Morris, J. N., Gerhart, T. N., Yett, H. S., and Lipsitz, L. A., Impact near the hip dominates fracture risk in elderly nursing home residents who fall, *Calcif. Tissue Int.,* 52(3), 192, 1993.
111. Greenspan, S. L., Myers, E. R., Kiel, D. P., Parker, R. A., Hayes, W. C., and Resnick, N. M., Fall direction, bone mineral density, and function: risk factors for hip fracture in frail nursing home elderly, *Am. J. Med.,* 104(6), 539, 1998.
112. Greenspan, S. L., Myers, E. R., Maitland, L. A., Resnick, N. M., and Hayes, W. C., Fall severity and bone mineral density as risk factors for hip fracture in ambulatory elderly, *JAMA,* 271(2), 128, 1994.
113. Horsman, A., Nordin, B. E., Simpson, M., and Speed, R., Cortical and trabecular bone status in elderly women with femoral neck fracture, *Clin. Orthop.,* (166), 143, 1982.
114. Beck, T. J., Ruff, C. B., Scott, W. W., Jr., Plato, C. C., Tobin, J. D., and Quan, C. A., Sex differences in geometry of the femoral neck with aging: a structural analysis of bone mineral data, *Calcif. Tissue Int.,* 50(1), 24, 1992.
115. Beck, T. J., Ruff, C. B., and Bissessur, K., Age-related changes in female femoral neck geometry: implications for bone strength, *Calcif. Tissue Int.,* 53(Suppl. 1), S41, 1993.
116. Faulkner, K. G., Cummings, S. R., Black, D., Palermo, L., Gluer, C. C., and Genant, H. K., Simple measurement of femoral geometry predicts hip fracture: the study of osteoporotic fractures, *J. Bone Miner. Res.,* 8(10), 1211, 1993.
117. Nakamura, T., Turner, C. H., Yoshikawa, T., Slemenda, C. W., Peacock, M., Burr, D. B., Mizuno, Y., Orimo, H., Ouchi, Y., and Johnston, C. J., Do variations in hip geometry explain differences in hip fracture risk between Japanese and white Americans? *J. Bone Miner. Res.,* 9(7), 1071, 1994.
118. Gluer, C. C., Cummings, S. R., Pressman, A., Li, J., Gluer, K., Faulkner, K. G., Grampp, S., and Genant, H. K., Prediction of hip fractures from pelvic radiographs: the study of osteoporotic fractures. The Study of Osteoporotic Fractures Research Group, *J. Bone Miner. Res.,* 9(5), 671, 1994.
119. Lawton, J. O., Baker, M. R., and Dickson, R. A., Femoral neck fractures—two populations, *Lancet,* 2(8341), 70, 1983.

120. Eriksson, S. A. and Widhe, T. L., Bone mass in women with hip fracture, *Acta Orthop. Scand.,* 59(1), 19, 1988.
121. Ferris, B. D., Kennedy, C., Bhamra, M., and Muirhead-Allwood, W., Morphology of the femur in proximal femoral fractures, *J. Bone Joint Surg. [Br.],* 71(3), 475, 1989.
122. Greenspan, S. L., Myers, E. R., Maitland, L. A., Kido, T. H., Krasnow, M. B., and Hayes, W. C., Trochanteric bone mineral density is associated with type of hip fracture in the elderly, *J. Bone Miner. Res.,* 9(12), 1889, 1994.
123. Mautalen, C. A., Vega, E. M., and Einhorn, T. A., Are the etiologies of cervical and trochanteric hip fractures different? *Bone,* 18(3 Suppl.), 133S, 1996.
124. Dias, J. J., Robbins, J. A., Steingold, R. F., and Donaldson, L. J., Subcapital vs intertrochanteric fracture of the neck of the femur: are there two distinct subpopulations? *J. R. Coll. Surg. Edinb.,* 32(5), 303, 1987.
125. Hinton, R. Y. and Smith, G. S., The association of age, race, and sex with the location of proximal femoral fractures in the elderly, *J. Bone Joint Surg. [Am.],* 75(5), 752, 1993.
126. Alffram, P., An epidemiologic study of cervical and trochanteric fracture of the femur in an urban population, *Acta Orthop. Scand. Suppl.,* 65, 1964.
127. Dretakis, E., Kritsikis, N., Economou, K., and Christodoulou, N., Bilateral non-contemporary fractures of the proximal femur, *Acta Orthop. Scand.,* 52(2), 227, 1981.
128. Finsen, V. and Benum, P., The second hip fracture. An epidemiologic study, *Acta Orthop. Scand.,* 57(5), 431, 1986.
129. Biggemann, M., Hilweg, D., Seidel, S., Horst, M., and Brinckmann, P., Risk of vertebral insufficiency fractures in relation to compressive strength predicted by quantitative computed tomography, *Eur. J. Radiol.,* 13(1), 6, 1991.
130. Sogaard, C. H., Hermann, A. P., Hasling, C., and Mosekilde, L., Spine deformity index in osteoporotic women: relations to forearm and vertebral bone mineral measurements and to iliac crest ash density, *Osteoporos Int.,* 4(4), 211, 1994.
131. Wolff, J., The internal architecture of normal bone and its mathematical significance, in *The Law of Bone Remodeling,* Springer-Verlag, Berlin, 1986, chap. 2.
132. Koch, J., The laws of bone architecture, *Am. J. Anat.,* 21, 177, 1917.
133. Toridis, T., Stress analysis of the femur, *J. Biomech.,* 2, 163, 1969.
134. Rybicki, E. F., Simonen, F. A., and Weis, E. B., Jr., On the mathematical analysis of stress in the human femur, *J. Biomech.,* 5(2), 203, 1972.
135. Brekelmans, W. A., Poort, H. W., and Slooff, T. J., A new method to analyse the mechanical behaviour of skeletal parts, *Acta Orthop. Scand.,* 43(5), 301, 1972.
136. Brekelmans, W. A. and Poort, H. W., Theoretical and experimental investigation of the stress and strain situation on a femur, *Acta Orthop. Belg.,* 39(Suppl. 1), 3, 1973.
137. Valliappan, S., Svensson, N. L., and Wood, R. D., Three dimensional stress analysis of the human femur, *Comput. Biol. Med.,* 7(4), 253, 1977.
138. Rohlmann, A., Mossner, U., Bergmann, G., and Kolbel, R., Finite-element analysis and experimental investigation of stresses in a femur, *J. Biomed. Eng.,* 4(3), 241, 1982.
139. Vichnin, H. H. and Batterman, S. C., Stress analysis and failure prediction in the proximal femur before and after total hip replacement, *J. Biomech. Eng.,* 108(1), 33, 1986.
140. Lotz, J. C., Cheal, E. J., and Hayes, W. C., Fracture prediction for the proximal femur using finite element models: Part II—Nonlinear analysis, *J. Biomech. Eng.,* 113(4), 361, 1991.
141. Lotz, J. C., Cheal, E. J., and Hayes, W. C., Fracture prediction for the proximal femur using finite element models: Part I—Linear analysis, *J. Biomech. Eng.,* 113(4), 353, 1991.
142. Raftopoulos, D. D. and Qassem, W., Three-dimensional curved beam stress analysis of the human femur, *J. Biomed. Eng.,* 9(4), 356, 1987.
143. Yoshikawa, T., Turner, C. H., Peacock, M., Slemenda, C. W., Weaver, C. M., Teegarden, D., Markwardt, P., and Burr, D. B., Geometric structure of the femoral neck measured using dual-energy X-ray absorptiometry [published erratum appears in *J. Bone Miner. Res.,* 10(3), 510, 1995], *J. Bone Miner. Res.,* 9(7), 1053, 1994.

144. Mourtada, F. A., Beck, T. J., Hauser, D. L., Ruff, C. B., and Bao, G., Curved beam model of the proximal femur for estimating stress using dual-energy X-ray absorptiometry derived structural geometry, *J. Orthop. Res.,* 14(3), 483, 1996.
145. Keyak, J. H., Meagher, J. M., Skinner, H. B., and Mote, C. D., Jr., Automated three-dimensional finite element modelling of bone: a new method, *J. Biomed. Eng.,* 12(5), 389, 1990.
146. Keyak, J. H. and Skinner, H. B., Three-dimensional finite element modelling of bone: effects of element size, *J. Biomed. Eng.,* 14(6), 483, 1992.
147. Keyak, J. H., Fourkas, M. G., Meagher, J. M., and Skinner, H. B., Validation of an automated method of three-dimensional finite element modelling of bone, *J. Biomed. Eng.,* 15(6), 505, 1993.
148. McCarthy, M., Bone Geometry from CAT Scans for Finite Element Analysis—Image Processing Considerations and Modeling Effects, Ph.D. thesis, Cornell University, Ithaca, NY, 1989.
149. Edidin, A., Modeling of Bone Material Properties from CT Scans—Considerations in Biomechanical Structural Models, Ph.D. thesis, Cornell University, Ithaca, NY, 1989.
150. Merz, B., Niederer, P., Muller, R., and Ruegsegger, P., Automated finite element analysis of excised human femora based on precision—QCT, *J. Biomech. Eng.,* 118(3), 387, 1996.
151. Lotz, J. C., Cheal, E. J., and Hayes, W. C., Stress distributions within the proximal femur during gait and falls: implications for osteoporotic fracture, *Osteoporos. Int.,* 5(4), 252, 1995.
152. Riggs, B. L., Wahner, H. W., Seeman, E., Offord, K. P., Dunn, W. L., Mazess, R. B., Johnson, K. A., and Melton, L.J., Changes in bone mineral density of the proximal femur and spine with aging. Differences between the postmenopausal and senile osteoporosis syndromes, *J. Clin. Invest.,* 70(4), 716, 1982.
153. Riggs, B. L. and Melton, L.J., Involutional osteoporosis, *N. Engl. J. Med.,* 314(26), 1676, 1986.
154. Zannoni, C., Mantovani, R., and Viceconti, M., Material properties assignment to finite element models of bone structures: a new method, *Med. Eng. Phys.,* 20(10), 735, 1998.
155. Huiskes, R. and Chao, E. Y. S., A survey of finite element analysis in orthopedic biomechanics: the first decade, *J. Biomech.,* 16(6), 385, 1983.
156. Gilbertson, L. G., Goel, V. K., Kong, W. Z., and Clausen, J. D., Finite element methods in spine biomechanics research, *Crit. Rev. Biomed. Eng.,* 23(5–6), 411, 1995.
157. Goel, V. K. and Weinstein, J., *Biomechanics of the Spine: Clinical and Surgical Perspective,* CRC Press, Boca Raton, FL, 1990.
158. Yoganandan, N., Myklebust, J. B., Ray, G., and Sances, A., Mathematical and finite element analysis of spine injuries, *CRC Crit. Rev. Biomed. Eng.,* 15(1), 29, 1987.
159. Yoganandan, N., Kumaresan, S., Voo, L., and Pintar, F., Finite element applications in human cervical spine modeling, *Spine,* 21(15), 1824, 1996.
160. Yoganandan, N., Kumaresan, S. C., Voo, L., Pintar, F. A., and Larson, S. J., Finite element modeling of the C4-C6 cervical spine unit, *Med. Eng. Phys.,* 18(7), 69, 1996.
161. Yoganandan, N., Kumaresan, S., Voo, L., and Pintar, F. A., Finite element model of the human lower cervical spine: parametric analysis of the C4-C6 unit, *Spine,* 119(1), 87, 1997.
162. Ranu, H. S., A vertebral finite element model and its response to loading, *Med. Prog. Technol.,* 16(4), 189, 1990.
163. Mizrahi, J., Silva, M. J., Keaveny, T. M., Edwards, W. T., and Hayes, W. C., Finite-element stress analysis of the normal and osteoporotic lumbar vertebral body, *Spine,* 18(14), 2088, 1993.
164. Bozic, K. J., Keyak, J. H., Skinner, H. B., Bueff, H. U., and Bradford, D. S., Three-dimensional finite element modeling of a cervical vertebra: an investigation of burst fracture mechanism, *J. Spinal Disord.,* 7(2), 102, 1994.
165. Silva, M. J., Keaveny, T. M., and Hayes, W. C., Load sharing between the shell and centrum in the lumbar vertebral body, *Spine,* 22(2), 140, 1997.
166. Teo, E. C., Paul, J. P., and Evans, J. H., Finite element stress analysis of a cadaver second cervical vertebra, *Med. Biol. Eng. Comput.,* 32(2), 236, 1994.
167. Martin, H., Werner, J., Andresen, R., Schober, H. C., and Schmitz, K. P., Noninvasive assessment of stiffness and failure load of human vertebrae from CT data, *Biomed. Tech.* (Berlin), 43(4), 82, 1998.

168. Faulkner, K. G., Cann, C. E., and Hasegawa, B. H., Effect of bone distribution on vertebral strength: assessment with patient-specific nonlinear finite element analysis, *Radiology,* 179(3), 669, 1991.
169. Burr, D. B., Yang, K. H., Haley, M., and Wang, H.-C., Morphological changes and stress redistribution in the osteoporotic spine, in *Spinal Disorders in Growth and Aging,* Takahashi, H., Ed., Springer-Verlag, Tokyo, 1995, 127–147.
170. Liebschner, M. A. K., Kopperdahl, D. L., and Keaveny, T. M., Role of vertebral shell and endplate modulus on whole vertebral body stiffness, in *Proceedings of the ASME International Mechanical Engineering Congress and Exposition,* Nashville, TN, 1999, 179.
171. Rockoff, S. D., Sweet, E., and Bleustein, J., The relative contribution of trabecular and cortical bone to the strength of human lumbar vertebrae, *Calcif. Tissue Res.,* 3(2), 163, 1969.
172. Roaf, R., A study of the mechanics of spinal injuries, *J. Bone Joint Surg.,* 42B(4), 810, 1960.
173. Adams, M. A. and Hutton, W. C., The relevance of torsion to the mechanical derangement of the lumbar spine, *Spine,* 6(3), 241, 1981.
174. Shirazi-Adl, S. A., Shrivastava, A. M., and Ahmed, A. M., Stress analysis of the lumbar disc-body unit in compression: a three-dimensional nonlinear finite element study, *Spine,* 9, 120, 1984.
175. Shirazi-Adl, A., Ahmed, A. M., and Shrivastava, S. C., A finite element study of a lumbar motion segment subjected to pure sagittal plane moments, *J. Biomech.,* 19(4), 331, 1986.
176. Shirazi-Adl, S. A., Finite element evaluation of contact loads on facets of an L2-L3 lumbar segment in complex loads, *Spine,* 16(5), 533, 1991.
177. Hakim, N. S. and King, A. I., A three-dimensional finite element dynamic response analysis of a vertebra with experimental verification, *J. Biomech.,* 12, 277, 1979.
178. Goel, V. K., Kim, Y. E., Lim, T. H., and Weinstein, J. N., An analytical investigation of the mechanics of spinal instrumentation, *Spine,* 13(9), 1003, 1988.
179. Hollister, S. J., Weissman, D. E., and McCubbrey, D. A., A modeling procedure to evaluate vertebral body mechanics from trabecular microstructural properties, in *Transactions of the 39th Annual Meeting of the Orthopaedic Research Society,* San Francisco, CA, 1993, 176.
180. Fyhrie, D. P. and Hamid, M. S., The probability distribution of trabecular bone strains for vertebral cancellous bone, in *Transactions of the 39th Annual Meeting of the Orthopaedic Research Society,* San Francisco, CA, 1993, 175.
181. Greenspan, S. L., Maitland, L. A., Myers, E. R., Krasnow, M. B., and Kido, T. H., Femoral bone loss progresses with age: a longitudinal study in women over age 65, *J. Bone Miner. Res.,* 9(12), 1959, 1994.
182. Huiskes, R. and Hollister, S. J., From structure to process, from organ to cell: recent developments of FE-analysis in orthopaedic biomechanics, *J. Biomech. Eng.,* 115, 520, 1993.

34

Noninvasive Measurement of Bone Integrity

Jonathan J. Kaufman
Mount Sinai School of Medicine and CyberLogic, Inc.

Robert S. Siffert
Mount Sinai School of Medicine

34.1 Introduction

This chapter discusses methods for noninvasively measuring skeletal integrity. The skeleton, a living structure composed of bone tissue in a state of constant turnover, adapts continually to the complex and time-dependent milieu of mechanical forces to which it is subjected. As the body ages, the ability of the skeleton to perform its primary function of weight bearing is diminished, due to a loss of bone tissue. This loss of bone occurs in both the cortical and cancellous portions of the skeleton, thinning cortices and trabeculae, increasing their respective porosities, and leading to overall increases in bone fragility and risk of minimal trauma fractures.

Decreases in bone mass may arise from a host of biological, genetic, and biomechanical factors. In women, rapid bone loss occurs during the 5 years following menopause (at about 3% per year), as a result of an increase in the rate of bone remodeling and an imbalance between the activity of osteoclasts and osteoblasts, both due to estrogen deficiency.[1] Slower rates of bone loss (for example, in women more than 5 years after menopause and in men after about age 55) occur in part because of an increase in parathyroid hormone levels, which may be a result of decreased calcium absorption or reabsorption.[1] Bone loss can also result from biomechanical disuse, such as during extended bed rest or during spaceflight.

All people lose bone as they age. Identifying those individuals with excessive bone loss and fragility is important so that preventive and/or therapeutic measures can be instituted. It is also important to be able to monitor effects of treatment. At present, there are more than 28 million individuals in the United States who are at significantly increased risk of experiencing a low-trauma fracture, and the majority of these individuals have not even been identified.[2] Low bone mass leads to over 1.5 million

0-8493-9117-2/01/$0.00+$.50

minimal trauma fractures in the United States alone, with estimated annual health care costs of more than $14 billion.[2]

The risk of having a low-trauma fracture is inversely related to bone strength; thus, techniques for assessing bone integrity can be useful for identifying the at-risk population. However, the risk of fracture is not solely due to biomechanical properties. Other factors are also important, including genetic and environmental considerations, such as family history and likelihood of falling.[3] This focuses solely on the noninvasive measurement of variables that relate directly to underlying bone integrity. The current status of two leading techniques, X-ray and ultrasonic, as well as other methods, will be reviewed, and suggestions for future research will be presented.

34.2 X-Ray Densitometry

Techniques using ionizing X-ray radiation quantitate the amount of bone at a given anatomical site. This is done by measuring the attenuation (i.e., reduction in intensity) of a beam of X-ray as it passes through bone and soft tissue. For a fixed amount of soft tissue, the more attenuated the beam, the more bone mass that is present in its transmission pathway.

Bone mass is the primary factor contributing to bone strength. Quantitative relationships between bone mass and biomechanical stiffness and strength have been demonstrated.[4–9] Thus, it is not surprising that a number of X-ray densitometric techniques have been developed to assess bone integrity and are currently in clinical use. The primary ones are single and dual-energy X-ray absorptiometry, and quantitative computed tomography.[10]

34.2.1 Absorptiometric Methods

X-ray absorptiometric methods quantitate total bone mineral content (BMC) in grams (g) contained within a three-dimensional (3D) region scanned by an X-ray beam. Absorptiometric methods are *projection methods,* meaning they summate down to a plane (like a plain X ray) all the information on bone mass contained in a 3D scanned region. Often the BMC is normalized by the projected area (usually a rectangle) of the region scanned, to obtain what is referred to (in the clinical milieu) as areal bone mineral density (BMD), in grams per centimeter squared (g cm^{-2}). To avoid confusion, the acronym BMD will be used to denote this *areal* BMD only, as measured with absorptiometric techniques, to distinguish it from volumetric or apparent density—both expressed in grams per *cubic* centimeter (g cm^{-3})—which can be measured using other methods.

Of fundamental importance is the fact that clinical BMD measurements have been shown to be useful not only for estimating bone strength *in vitro*, but also for predicting the occurrence of minimal-trauma fractures.[11] For example, in a study by Cummings et al.,[12] each standard deviation decrease in femoral neck BMD increased the age-adjusted risk of hip fracture 2.6 times. They also showed that women with BMD in the lowest quartile had an 8.5-*fold* greater risk of hip fracture than those in the highest quartile.

Besides its relationship to fracture risk, present X-ray absorptiometry also has very good accuracy and precision.[11] This makes the technique a useful clinical tool for noninvasively assessing bone integrity, enabling not only detection of at-risk individuals but also monitoring of the effects of treatment.

34.2.1.1 Dual-Energy Methods

Dual-energy X-ray absorptiometry (DXA) is able to account for variations in the amount of overlying soft tissue. This is important because soft tissue affects the overall attenuation and can thus lead to errors in estimating BMD. Dual-energy methods compensate for the presence of soft tissue by measuring the attenuations of X-ray beams at two distinct energies. Let I_1 and I_2 be X-ray beam intensities at energy 1 and energy 2 after transmission through an anatomical site comprising specific but unknown amounts

of bone and soft tissue:

$$I_2 = I_{02} \exp^{-(\mu_{b2} d_b + \mu_{w2} d_w)}, \tag{34.1}$$

$$I_1 = I_{01} \exp^{-(\mu_{b1} d_b + \mu_{w1} d_w)}. \tag{34.2}$$

In Eqs. 34.1 and 34.2, I_{01} and I_{02} are the transmitted (source) X-ray beam intensities at energy 1 and energy 2, respectively, μ_{b1} and μ_{w1} are the X-ray attenuation coefficients of bone and soft tissue at energy 1, respectively, μ_{b2} and μ_{w2} are the X-ray attenuation coefficients of bone and soft tissue at energy 2, respectively, and d_b and d_w are the (integrated or total) thicknesses of bone and soft tissue, respectively, at the anatomical site of measurement. By taking the natural logarithms of both sides of the two equations and rearranging, the following matrix representation is obtained:

$$\boldsymbol{A}\boldsymbol{x} = \boldsymbol{b}, \tag{34.3}$$

where

$$b = \begin{bmatrix} \dfrac{\ln[I_{01}]}{\ln[I_1]} \\ \dfrac{\ln[I_{02}]}{\ln[I_2]} \end{bmatrix} \tag{34.4}$$

$$A = \begin{bmatrix} \mu_{b1} & \mu_{w1} \\ \mu_{b2} & \mu_{w2} \end{bmatrix} \tag{34.5}$$

and

$$x = \begin{bmatrix} d_b \\ d_w \end{bmatrix}. \tag{34.6}$$

The only unknowns are the bone and soft tissue thicknesses (represented by the x vector), which may be solved for by inverting Eq. 34.3. The inverse of $\boldsymbol{A}$ exists because the attenuation coefficients for bone and soft tissue have distinct functional dependencies ($|\boldsymbol{A}| = \mu_{b1}\,\mu_{w2} - \mu_{w1}\,\mu_{b2} \neq 0$). This fact is the basis by which dual-energy methods are able to separate out the confounding effects of soft tissue. The thickness, d_b, of bone is multiplied by a standard volumetric density, ρ_b ($\approx$1.85 g cm^{-3}) of bone, to obtain the BMD (g cm^{-2}), or multiplied by both the volumetric density and projected area of the scan to obtain the BMC (g).[13]

DXA devices have the highest accuracies and precisions of all X-ray-based methods; these range from 0.5 to 2% for precision, and from 3 to 5% for accuracy.[14] Scans may be performed at any anatomical site but are usually done at the spine, the proximal femur (hip), or the distal radius. In a typical scan, the X-ray beam is mechanically translated over a body region and detected and processed to create an integrated bone density image at the site; automatic edge detection algorithms operate to locate reproducibly a region of interest. Fig. 34.1a displays a DXA scan of the spine together with a region of interest, and Fig. 34.1b shows the associated BMD and BMC values.

34.2.1.2 Single-Energy Methods

In contrast to dual-energy methods, single-energy X-ray absorptiometric (SXA) methods measure X-ray absorption at a single energy only, and thus cannot compensate for varying amounts of soft tissue. Mathematically, this is simply a manifestation of the fact that there are two unknowns (the bone and soft tissue thicknesses, respectively) and only one equation (i.e., Eq. 34.1). Therefore, single-energy

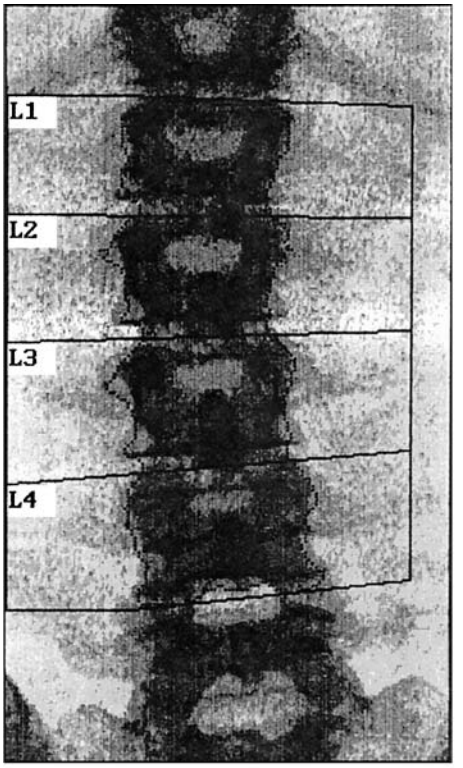

(a)

Region	Est. Area (cm^2)	Est. BMC (grams)	BMD (gms/cm^2)
L1	13.03	10.19	0.782
L2	13.39	11.64	0.869
L3	15.28	13.47	0.881
L4	16.46	14.30	0.869
TOTAL	58.16	49.60	0.853

(b)

FIGURE 34.1 (a) DXA scan of the spine, showing the regions of interest for which the areal BMD and BMC will be determined. (b) The BMD and BMC values for the scan of Fig. 34.1a.

techniques are useful at anatomical sites where the amount of soft tissue is either negligible (e.g., at the phalanges) or can be controlled, like the wrist bone (distal radius) measured in a water bath of fixed height. Single-energy methods are also utilized in *in vitro* laboratory studies, where bones may be cleaned of all soft tissue or can be placed in a fixed-height water bath.

34.2.2 Quantitative Computed Tomography

Using a technique known as quantitative computed tomography (QCT), volumetric bone density values can be measured noninvasively.[10,14] In this method, which is similar to standard computed tomography, a quantitative cross-sectional image of a bone is obtained. Similar to the absorptiometric techniques described in Section 34.2.1, QCT is also based on measurements of X-ray attenuation. However, in QCT the attenuation measurements are made not from one, but rather from a multitude of angular directions, which permits the tomographic or spatial reconstruction of the attenuation coefficient.

A QCT scan of an anatomical site (like the spine) is acquired in conjunction with a calibration phantom that is composed of a small number (usually three to seven) of materials, each material having a specific "bone-equivalent" value. A quantitative interpolation between the values of the portion of the image associated with the region of interest with the portions associated with the phantom materials allows a bone-equivalent value in g cm^{-3} to be derived. A typical QCT image of a vertebral body is shown in Fig. 34.2, which also displays a rectangular region of interest within the trabecular portion of the vertebra in which the volumetric bone mineral density was computed.

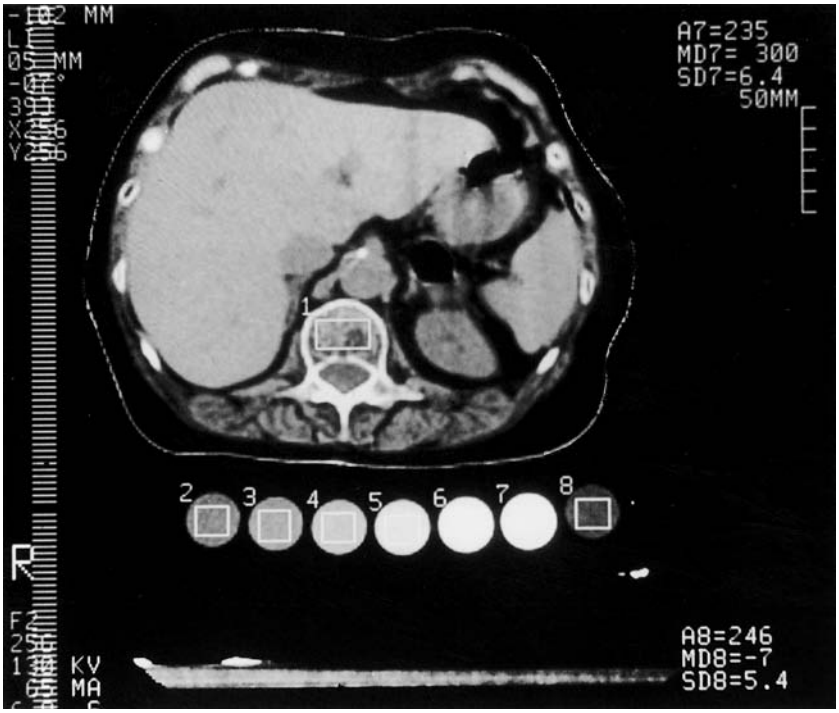

FIGURE 34.2 A QCT scan of a lumbar vertebra, showing the region of interest and the calibration phantom. (From Mirsky, E. C. and Einhorn, T. A., *J. Bone Joint Surg.*, 80-A, 1687–1698, 1998. With permission.)

34.2.3 Limitations of X-Ray Densitometry

Notwithstanding the utility of X-ray methods, there are weaknesses. Despite being the most widely used methods in practice, DXA or SXA does not discriminate between cortical and trabecular bone, "lumping together" into a single measurement the bone mass in the cortical and trabecular portions at any particular site. In addition, absorptiometry provides only areal bone mineral density, not volumetric density. Both factors can lead to decreased accuracy when estimating bone integrity and predicting fracture risk. Although QCT can estimate volumetric bone density and discriminate between cortical and trabecular bone, its high radiation dose and cost limit its practical utility. Further, QCT is difficult to use at sites which are extremely heterogeneous and geometrically complex, such as the hip.[15]

Although bone mass is the most significant component in bone strength, other factors are also important. For example, trabecular bone mass accounts for only about 65% of the observed variation in biomechanical strength *in vitro*. This can be increased up to 94% by including in the model a measure of bone architecture known as fabric, which quantifies the relative degree of architectural anisotropy.[16,17] Other studies have demonstrated the importance of considering structural and bone material properties to assess mechanical integrity.[18–21] For example, it has been shown that architecture is needed to specify the biomechanical properties of trabecular bone and that the relative degree of anisotropy is independently (of bone mass) associated with an increase of fracture incidence.[22,23] Fatigue damage is another aspect that is not measured in densitometry, but which may also play a role in low-trauma fractures.[1] X-ray densitometry does not measure *any aspect* of architecture, remodeling state, or bone material properties per se; it simply quantifies the total bone mass present at the time of measurement.

34.3 Ultrasonic Techniques

Unlike X-rays, ultrasound is a mechanical wave and, as such, has the potential to provide more information on mechanical integrity because it interacts with bone in a fundamentally distinct manner. This, combined with the fact that ultrasound involves no radiation, is relatively simple to implement and process, and can easily be used in a portable device, makes ultrasound an attractive alternative to methods based on ionizing radiation. Like bone densitometry using X-rays, ultrasound can be used to measure the attenuation of elastic energy as it passes through bone. However, ultrasound propagation through bone is a highly complex phenomenon dependent not only upon bone mass, but also on bone architecture and material properties.[24–26] Since bone strength depends on its mass, architecture, and quality, ultrasound has the unique potential for being able to more accurately assess bone integrity compared with X-ray densitometric methods.[27]

34.3.1 Review of Ultrasound Theory

Ultrasound is a mechanical wave consisting of frequencies above the range of human hearing (>20 kHz). When an ultrasound wave is propagated through a medium such as a biological tissue, it will produce regions of temporary compression and rarefaction in the tissue. Various wave modes can be propagated simultaneously, including longitudinal (when the oscillatory motion of the particles in the tissue is parallel to the wave direction), transverse or shear (particle motion is perpendicular to the wave direction), and surface or Rayleigh (propagation of the wave along an interface between two tissues, e.g., muscle and bone, and the particles of the medium execute an elliptical trajectory). In complex heterogeneous materials such as bone, ultrasound waves will generally be multimodal. These ultrasound interactions with bone and other tissues are characterized by the linear viscoelastic wave equation:[24]

$$\rho \frac{\partial^2 w}{\partial t^2} = \left(\mu + \eta \frac{\partial}{\partial t}\right)\nabla^2 w + \left(\lambda + \mu + \xi \frac{\partial}{\partial t} + \frac{\eta}{3}\frac{\partial}{\partial t}\right)\nabla(\nabla \cdot w), \tag{34.7}$$

where ρ is the volumetric density in kg m^{-3}; λ and μ are the first and second Lamé constants, respectively, in units of N m^{-2}, η and ξ are the first and second viscosities in units of N s m^{-2}; and $w = w(x, y, z, t)$ is the material displacement vector as a function of Cartesian coordinates x, y, and z and of time t. For a heterogeneous structure (such as the heel), the material parameters in Eq. 34.7 are functions of the spatial coordinates x, y, and z. For example, in the heel the bone material portions (i.e., the individual trabeculae and cortical shell) may have the following parameter values: $\rho = 1850$ kg m^{-3}, $\lambda = 9306$ MPa, $\mu = 3127$ MPa, $\eta = 40$ Pa · s, $\xi = 0.1$ Pa · s, while both the marrow spaces and overlying soft tissue within and around the heel bone may have the following values for its material parameters: $\rho = 1055$ kg m^{-3}, $\lambda = 2634$ MPa, $\mu = 0$ MPa, $\eta = 0.1$ Pa · s, $\xi \approx 0$ Pa · s.[13,25–27] Eq. 34.7 can be solved in closed form in only highly idealized problems.

The generation and reception of an ultrasound wave is usually accomplished by a piezoelectric transducer. This transducer utilizes a special material, often a ceramic, and is used to convert an electrical signal into a mechanical vibration, and vice versa.[25] For example, by placing a transducer in physical contact with the surface of the skin, an ultrasound wave can be propagated through the underlying bone. Ultrasound waves are almost totally reflected at interfaces with air, and also highly attenuated as they propagate through it. Therefore, ultrasound cannot be used in the same mode as DXA in measuring the bone mass of a thoracic or lumbar vertebra, since air in the lung or bowel would nearly eradicate the acoustic signal. This is the reason that virtually all ultrasound measurements on bone *in vivo* are carried out at such anatomically accessible sites as the calcaneus, patella, radius, and tibia, where there is minimal overlying soft tissue.

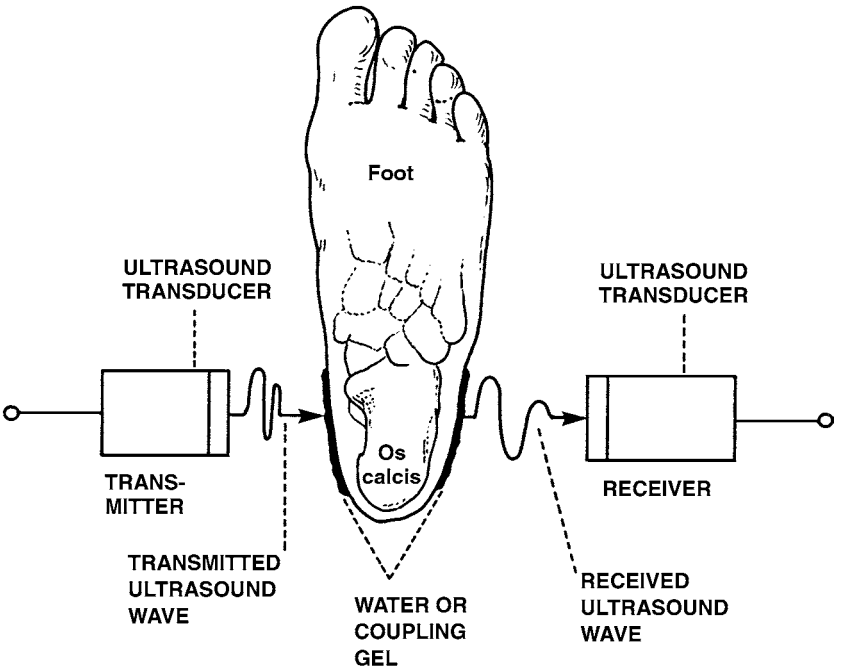

FIGURE 34.3 Most common technique used for bone assessment. In this transmission mode, two transducers are used, one for transmitting the ultrasound wave and the other for receiving the signal after it has propagated through the tissue. (From Kaufman et al., *J. Bone Miner. Res.,* 5, 517–525, 1993. With permission.)

34.3.2 Tissue Characterization

The ability of an ultrasound wave to provide information about the medium (tissue) through which it is propagating will depend on the way in which the wave is altered by the medium. The most common approach in bone assessment is to use two transducers, one as a transmitter and the other as a receiver, the latter of which measures the ultrasound signal after it has propagated through the medium.[27] A typical example is shown in schematic form in measurement of a human heel in Fig. 34.3. Other methods can also be used, such as a backscattered approach.[28] In general, two principal changes in an ultrasound signal can occur: (1) the medium can affect the velocity of the wave and (2) the medium can modify the amount of attenuation of the wave.

34.3.2.1 Influences on Ultrasound Velocity

The velocity of an ultrasound wave depends not only on the properties of the medium through which it is propagating, but also on its mode of propagation. Longitudinal waves are generally faster than shear waves, and these are faster than surface waves; thus, it is generally necessary to be able to identify not only the velocity but the mode of propagation as well. Most measurements of velocity *in vivo* have primarily longitudinal components, since soft tissue greatly attenuates other modes of propagation.[25]

Besides propagation mode, ultrasound can be measured as a phase or group velocity.[29] *Phase velocity* refers to the velocity of a wave that travels through a medium at a single frequency. *Group velocity* is a term used to describe the velocity of a wave packet or pulse that consists of a finite number of frequencies. Group velocity is the quantity most often reported since pulse measurements are easier to obtain.[29] For certain media such as water, the phase and group velocities are essentially equivalent. Media for which the phase or group velocities are not equivalent are known as *dispersive*. Bone is an example of a dispersive medium, and trabecular bone is significantly more dispersive than compact bone.[30,31] Furthermore, for dispersive materials such as bone, both the phase and group velocities are frequency dependent.

TABLE 34.1 Ultrasound Velocities for Several Common Materials and Biological Tissues[24,29,32,33,36]

Material	Velocity [m/s][a]
Water	1500
Bone, compact, human	2600–3000
Bone, cancellous, human	1530–2100
Bone, cancellous, bovine	1700–2500
Fat	1480
Lung	660
Blood	1530
Aluminum	6420
Steel	5800
Polystyrene	2350
Polymethylmethacrylate	2680
Muscle	1566

[a] All velocities are longitudinal phase velocities, measured at a nominal frequency of 1 MHz.

Therefore, different values will be obtained depending on the frequency of the ultrasound waveform. Thus, it is important that the specific experimental conditions used be recognized when comparing or analyzing reported findings. Table 34.1 displays values of ultrasound velocity for several common materials and biological tissues.

Ultrasound velocity can be analytically related to certain biomechanical properties. In the case when the ultrasound wavelength is large with respect to the cross-sectional area of the interrogated object, and for homogeneous and nondispersive media, the relationship between elastic modulus and the ultrasound longitudinal phase velocity, c, is given by the equation:

$$c = \sqrt{\frac{E}{\rho}}, \tag{34.8}$$

where E and ρ are the Young's modulus and volumetric density of the material, respectively.[32] This equation does not apply to heterogeneous, anisotropic, and dispersive materials such as bone. In this case, no general closed-form solutions exist, but the above equation may still be used to provide first-order estimates of the biomechanical properties. Since the elastic modulus of bone can be related to its density, that is,

$$E \cong k\rho^{\alpha}, \tag{34.9}$$

where k and α are constants, equations can also be derived in which E and ρ are related to the velocity, c, namely,

$$E \cong k_1 c^{2\alpha/(\alpha-1)} \tag{34.10}$$

and

$$\rho \cong k_2 c^{2/(\alpha-1)}, \tag{34.11}$$

where k_1 and k_2 are constants that depend on k and α.[4,5] Using the empirical result that the compressive strength of bone is proportional to its elastic modulus, one can relate the ultimate compressive strength, S_u, to ultrasound velocity as well:

$$S_u \cong k_3 c^{2\alpha/(\alpha-1)}, \tag{34.12}$$

where k_3 is another constant.[5]

34.3.2.2 Influences on Ultrasound Attenuation

The attenuation of an ultrasound wave occurs by a reduction of its amplitude and results in a loss of acoustic energy. Two primary mechanisms can produce this attenuation: *scattering* and *absorption*.[33] In scattering, the amplitude of the propagating wave is reduced because the energy has been redistributed in one or more directions. A simple type of scattering, backscattering, occurs when a portion of a transmitted ultrasound wave is reflected back toward the source, such as when an ultrasound wave propagates from one medium to another (e.g., from soft tissue to bone). More complex scattering can arise in a material with acoustic inhomogeneities. Bone is an excellent example of an acoustically inhomogeneous material because it is composed of a cortical shell, a trabecular framework and is filled with a liquid-like material, bone marrow.

When an ultrasound wave undergoes *absorption*, a portion of the energy of the propagating wave is converted directly into heat. This conversion is an extremely complex process and results when the density fluctuations within a medium are out of phase with the pressure fluctuations. This leads to energy loss through phase cancellation and so-called *relaxation* mechanisms.[35] In general, absorption increases with increasing ultrasound wave frequency.

In summary, the loss of ultrasound energy in a tissue will consist of the individual contributions from scattering and absorption and is expressed by the equation

$$\alpha = \alpha_s + \alpha_a, \tag{34.13}$$

where α is the attenuation coefficient and α_s and α_a are the scattering and absorption coefficients of the medium, respectively. In virtually all cases, the attenuation, α, depends on the ultrasound wavelength as well as the acoustic properties of the medium. *Attenuation* is usually expressed in the units nepers (np) or decibels (dB); 1 np is equivalent to approximately 8.65 dB. A medium that has an attenuation of 1 np will reduce the amplitude of an ultrasound wave to approximately 37% of its initial value. A medium with an attenuation of 3 np will reduce the amplitude to approximately 5%. The attenuation coefficient, α, of a medium is related to its thickness, d. This parameter can be used to derive the specific attenuation, μ, according to the equation:

$$\mu = \alpha/d. \tag{34.14}$$

Specific attenuation is usually expressed in the units npcm^{-1} or dBcm^{-1}.

As noted, ultrasound attenuation is generally a function of frequency, i.e., $\alpha = \alpha(f)$. For many materials, this relationship is approximately linear over a given frequency range. In these cases, the attenuation coefficient, α, can be characterized by its slope, α_1, and is expressed in the units nepers per megahertz (npMHz^{-1}) or decibels per megahertz (dBMHz^{-1}). In ultrasound bone assessment, the slope is a central parameter, and is known by the term *broadband ultrasound attenuation* (BUA) (i.e., $\alpha_1 \equiv$ BUA). BUA was originally suggested as a means for characterizing bone by Langton.[35] In situations where the attenuation of a material cannot be characterized by a linear dependence on frequency, polynomial functions (including nonintegral exponents) may be necessary to approximate the relationship. All materials, including bone, exhibit some degree of nonlinear behavior if the frequency range of interest is sufficiently broad. Table 34.2 displays representative values of BUA (normalized to material thickness) for several common materials and biological tissues.

BUA is computed by evaluating the Fourier transforms of a "bone signal" (the signal that has propagated through the bone tissue and overlying soft tissue if present) and a "reference signal" (a signal that has propagated through a known medium such as water), respectively, and then taking the negative logarithm of the magnitude of their quotient. A straight line is fit over a given frequency interval (nominally 300 to 800 kHz) and a least-squares (regression) estimate of BUA in dBMHz^{-1} determined. The computation typically relies on fast Fourier transformation of the signals.[36] Ultrasound velocity is usually computed in the time domain, although phase-dependent (transform) methods should more

TABLE 34.2 Differential Specific Attenuations (BUA normalized to material thickness) for Several Common Materials and Biological Tissues[24,29,32,33,36]

Material	BUA per unit length dB $MHz^{-1}\,cm^{-1}$ at 1 MHz
Water	<0.001 ($\sim f^2$)
Bone, compact, human	10 ($\sim f^{0.9 \to 2.1 \to 0.5}$)
Bone, cancellous, human	5–40($\sim f^{1 \to 2}$)
Fat	0.6
Lung	40 ($\sim f^{2 \to 1.2}$)
Blood	0.3
Aluminum	0.355 ($\sim f^2$)
Steel	0.29 ($\sim f^2$)
Polystyrene	0.35
Polymethylmethacrylate	0.4
Muscle	1.1

Note: Broadband ultrasound attenuation (BUA) is the slope of the ultrasound attenuation, measured in units of dB MHz^{-1} (see text). All attenuations are with respect to longitudinal mode of propagation. The text in parentheses indicate the approximate frequency dependence(s). Thus, for compact bone, the attenuation follows a 0.9 power at lower frequencies, increasing to a 2.1 power, and then decreasing to a 0.5 power. For additional details, consult the references. If not shown, dependence is linear around 1 MHz.

appropriately be used.[29] In the former case, times of arrival of the two (bone and reference) signals are defined relative to a leading edge or some other landmark on the signals.

Formally, the measurement of BUA and velocity can be represented as follows. Let $\boldsymbol{H}(f)$ be the complex transfer function associated with the overall path of ultrasound propagation through a tissue of interest, for example, a heel bone. Then

$$H(f) = \frac{V(f)}{V_r(f)} = e^{-\alpha(f)} e^{-j\phi(f)}, \tag{34.15}$$

where $V(f)$ and $V_r(f)$ are the Fourier transforms of the bone and reference signals, respectively, $\alpha(f)$ and $\phi(f)$ are the attenuation and phase (real) functions associated with the overall tissue pathway, and $j = (-1)^{1/2}$. The attenuation function, $\alpha(f)$, over a given frequency range, is approximated by an affine function, i.e.,

$$\alpha(f) = -\ln|H(f)| \cong \alpha_0 + \text{BUA} \cdot f/8.65\,, \tag{34.16}$$

where values for α_0 and BUA are determined by least squares. The group velocity, $v_g(f)$, can be computed from the phase function, $\phi(f)$:

$$v_g(f) \cong 2\pi d \left(\frac{d\phi(f)}{df} \right)^{-1}, \tag{34.17}$$

where d is the overall tissue thickness, and $\phi(f) = -\arg\{H(f)\}$ (radians).[29,31]

As will be seen in Section 34.3.3, less bone mass and increasing fragility are generally associated with smaller values of BUA and velocity. It is important, however, to point out that ultrasound measurements on heterogeneous materials such as bone engender a variety of practical problems that can reduce accuracy and

precision significantly. For example, irregular geometry can produce inaccurate readings of attenuation through phase cancellation effects.[37] There can also be large variations in measured attenuations and velocities depending on the specific bone region interrogated by the ultrasound wave due to associated heterogeneity of bone. Soft tissue surrounding the bone can also affect both ultrasound attenuation and velocity estimates, for example, by distorting the received waveform due to multipath interference.[31]

In summary, ultrasound assessment of bone relies primarily on the measurement of the *velocity* and *attenuation* of the ultrasound wave, which are, in general, frequency dependent. From a linear systems theoretic point of view, one may view these parameters as representations of the magnitude and phase, respectively, of a transfer function associated with the ultrasonically interrogated medium (tissue). Ultrasound characterization is based on the fundamental hypothesis that bone in different physical and biomechanical states will have different complex transfer functions. The determination of unique and quantitative relationships between these ultrasound variables and the physical properties of bone and clinical fracture risk, as well as development of reliable measurement means, constitute the critical research goals for this technology.

34.3.3 Review of Experimental and Clinical Studies

Two of the earliest attempts to relate ultrasound measurements to bone properties were reported by Lang[38] and Abdenshein and Hyatt,[39] who found high correlations between mechanically determined and ultrasonically determined elastic moduli. These findings were later reproduced by Ashman et al.[40] who studied the elastic properties of cortical bone using a more refined continuous wave technique. More recent studies on trabecular bone samples from human and bovine subjects have shown correlations of ultrasound velocity with ultimate strength ranging from 0.71 to 0.75.[41–43]

In animal studies, it has been possible to assess the interaction between a physiological event or manipulation and a physical outcome measured by ultrasound velocity assessment. Using a sheep Achilles tenotomy model to mimic biomechanical disuse, Rubin et al.[44] studied the changes in ultrasound transmission through the calcaneus over a 12-week period. They noted a 10.2% decline in ultrasound velocity in the experimental limb and this was associated with a 21% reduction in trabecular bone volume. McCarthy et al.[45] studied the relationship between ultrasound velocity and the effects of specimen orientation, density, porosity, and temperature in equine cortical bone and showed a positive linear correlation between ultrasound velocity and bone specific gravity, and an inverse relationship with porosity. To determine the ability of ultrasound to detect a therapeutic response, Lees and Hanson[46] examined the relationship between ultrasound velocity in the rabbit femora before and after sodium fluoride treatment, which was used as means for treating bone loss. They proposed that an "optimum dose" for fluoride administration could be determined based upon the ability to measure ultrasonically the elastic modulus of bone.

Two early ultrasound studies on humans were conducted by Heaney et al.[47] and Rubin et al.[48] In the study by Heaney et al., ultrasound velocity measurements made across the patella of patients with atraumatic vertebral compression fractures were 3 to 4% lower than in normal (unfractured) controls.[47] By assessing fracture incidence, these investigators were able to show that women who had ultrasound velocities below 1825 $\mathrm{m\,s^{-1}}$ were approximately six times more likely to have sustained one or more vertebral fractures than women with velocities above this level. In the study by Rubin et al., longitudinal group velocity measurements were made at the patella and tibia in individuals before and after completion of a marathon.[48] The study demonstrated the ability of ultrasound (tibial) velocity to differentiate individuals based on their performance and gender. There was also a 1.6% increase in tibial ultrasonic velocity after the race.

Other studies have used ultrasound attenuation to characterize bone tissue. *In vitro* experiments have compared BUA with X-ray densitometric findings. For example, McKelvie et al.[49] compared bone density measured with QCT to BUA in the human calcaneus and showed a correlation of $R = 0.92$. Similarly, McCloskey and co-workers[50] examined the relationship between BUA in the os calcis and both BMD determined using QCT and physical density (i.e., the volumetric density of the fluid saturated

bone sample); BUA was found to be highly correlated with both densities, $R = 0.80$, $P < 0.0001$ and $R = 0.85$, $P < 0.001$, respectively. Clinical studies using BUA have also compared ultrasound estimates to bone densitometry measurements. In one such study BUA of the calcaneus was reported to be highly correlated with QCT of the spine ($R^2 = 0.85$, $p < 0.01$).[51]

Investigators have also assessed bone density using both ultrasound attenuation and velocity measurements. One *in vitro* study examined the ability of BUA and ultrasound group velocity to detect alterations in bone mineralization on bovine bone samples.[52] Using controlled nitric acid attack to demineralize bone sequentially, BUA and velocity were shown to be highly correlated (R values between 0.84 and 0.99) with bone physical density. Another *in vitro* study determined both the attenuation and phase velocity of ultrasound over frequency ranges of 300 kHz to 3.0 MHz in cancellous bone from the human skull.[30] Besides demonstrating that the attenuation and velocity were nonlinear functions of frequency, they also concluded that the dispersion was caused principally by the scattering of ultrasound by the blood and fat-filled interstices of the bone.

Clinical investigations have reported measurements of ultrasound attenuation and group velocity in the same subjects.[53,54] Correlation coefficients between SXA (BMD) and ultrasound attenuation (BUA) and velocity in the os calcis were found to be 0.53 and 0.72, respectively. A clinical study mathematically combined BUA and velocity to derive a third parameter called "stiffness" (no relation to the biomechanical term).[55] These investigators showed that in 23 normal women and 18 women with excessive bone loss, BUA, velocity, and "stiffness" were significantly lower in the latter group of 18 subjects ($p < 0.001$).

Of greatest importance is the ability to use ultrasound measurements to predict fracture risk. In one seminal study on 60 women, Langton et al.[35] showed that patients who had experienced a hip fracture within 4 weeks of a BUA measurement had a significantly lower BUA than women who had no history of fracture. In addition, they reported a significant decrease in the BUA in relation to age. Values for BUA ranged from a low of about 25 dB MHz^{-1} to a high of almost 90 dB MHz^{-1}; the fracture patients had an average BUA of about 40 dB MHz^{-1} and the unfractured patients had an average BUA of about 75 dB MHz^{-1}, an almost twofold difference. However, this study did not correct for age, an important consideration in discriminating between fracture and nonfracture subjects, nor did it provide a statistical analysis. More recently, Miller and Porter[56] measured BUA in 840 women over the age of 65, 32 of whom had sustained a fracture of the proximal femur during the study period. The mean BUA was significantly lower in the fracture compared to the nonfracture group ($P < 0.0005$). Similar results were reported by Baran et al.,[57] who studied ultrasound attenuation of the os calcis in patients with hip fractures and those with established low bone mass (by X-ray absorptiometry), but no history of hip fracture. At ultrasound values of 50 dB MHz^{-1}, this study showed sensitivities and specificities on the order of 80% for identifying patients with hip fracture.

Most recently and significantly, three independent *prospective studies* with sample sizes of 6,500, 10,000, and 710 women, respectively, all showed that ultrasound can be used to *estimate future fracture risk* in older women.[58–60] The two ultrasound parameters, BUA and ultrasound velocity, performed about equally well. Results from these studies demonstrated an increase in fracture risk with decreasing BUA and velocity, as shown in Fig. 34.4. For example, a one standard deviation decrease in BUA led to about a *twofold* increase in risk of hip fractures.[58,59] Of special note was the fact that changes in fracture risk were similar to those as determined by X-ray absorptiometry.[58] Additionally, it has been claimed that the ability of ultrasound to predict future fractures is independent of predictions based on X-ray-based measures of bone mass (e.g., BMD), although this is a subject of controversy.[61]

The degree of reproducibility or precision in ultrasonic studies has also been reported. Given the fact that many different types of apparatuses and approaches for measuring ultrasonic attenuation and velocity are being used, there has also been a wide range of precisions reported. For example, in one recent study, an ultrasonic assessment device (Walker-Sonix, now Hologic, Bedford, MA) was used on cadaveric feet.[62] They found a precision of 6.1 and 0.8% for the attenuation and velocity, respectively. Coefficients of variation for several different devices and measurement techniques have also been published.[63] These authors reported *in vivo* precisions ranging from 0.93 to 5% for attenuation, and 0.15 to 0.64% for velocity. However, it has been suggested that the coefficients of variation reported for ultrasonic

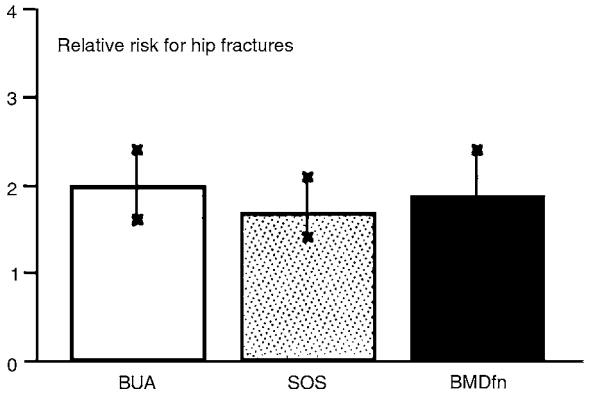

FIGURE 34.4 The relative risk for hip fractures, comparing BUA, velocity (speed of sound, SOS), and BMD of the femoral neck. The heights of the three bars on the graph indicate the increases in relative risk of hip fractures for each standard deviation decrease in BUA, SOS, or BMD, respectively. As may be seen, the relative risk increases by about a factor of two for each standard deviation reduction in BUA, SOS, or BMD. Also shown on each bar are the associated 95% confidence intervals for relative risk. (From Glüer et al., *J. Bone Miner. Res.,* 8, 1280–1288, 1997. With permission.)

velocity, as well as for attenuation, do not realistically reflect *effective* diagnostic precisions.[64] This controversy on precision and accuracy of ultrasound has also led to disagreement on its use for monitoring response due to therapy.[61] Notwithstanding, the U. S. Food and Drug Administration has approved three quantitative ultrasound devices for bone assessment in the past 2 years, and several more are likely to receive favorable consideration in the near future.

34.3.4 Computational Methods

In view of the complexity of ultrasound propagation through bone, the relative paucity of analytic results, and the practical difficulties and costs associated with experimental and clinical studies, new approaches for clarifying ultrasound interactions with bone are needed. In this regard, a computational technique for simulating propagation of ultrasound through bone has recently been reported by Luo et al.[65] Computational methods allow virtually any aspect of the bone–ultrasound interaction to be investigated. For example, it is possible to study the effects of varying viscosity of the marrow, cortical bone, and soft tissue, degree of mineralization, nonparallel surfaces, and refraction, diffraction, and scattering, to name just a few.[66–68]

In the study by Luo et al., propagation of ultrasound through 15 trabecular bone slices (similar to the one shown in Fig. 34.5) whose respective architectures (i.e., fabrics) and densities (i.e., bone volume fractions) were measured, was simulated using a computer software package (Wave2000®, CyberLogic®, Inc., New York, NY). The software provides the complete solution on a standard personal computer to a two-dimensional version of the elastic wave equation (Eq. 34.7), using a method of finite differences, modeling all the modes of propagation as well as accounting for material-dependent losses and scattering. A 1-MHz sine wave with a Gaussian envelope was used as the source waveform (Fig. 34.6), which is typical of the waveforms used in present commercial devices. A 1.4-cm source and a 1.4-cm receiver transducer pair was operated in transmission mode with the source–receiver pair in two orientations. The first was with the transducer pair aligned along the main trabecular orientation ("$\parallel$"), and the second was with the transducer pair aligned orthogonal to the main trabecular orientation ("$\perp$"). Receiver measurements were computed for each of the 15 samples in each of the two directions, for a total of 30 receiver waveforms. The ultrasound velocities (UVs) in the parallel and orthogonal directions ($UV_{\parallel}$ and $UV_{\perp}$, respectively) and *mean frequencies* (MFs) in the parallel and orthogonal directions ($MF_{\parallel}$ and $MF_{\perp}$, respectively) were computed for each of the received waveforms.[67,69] The mean frequency is

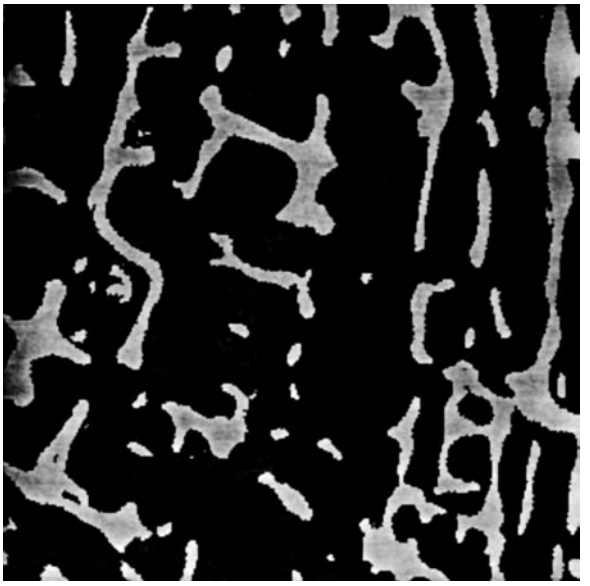

FIGURE 34.5 A single slice from a calcaneal trabecular bone sample. (From Luo, G. M. et al., *Ultrasound Med. Biol.*, 25(5), 823–830, © 1999 by World Federation of Ultrasound in Medicine & Biology. With permission of Elsevier Science.)

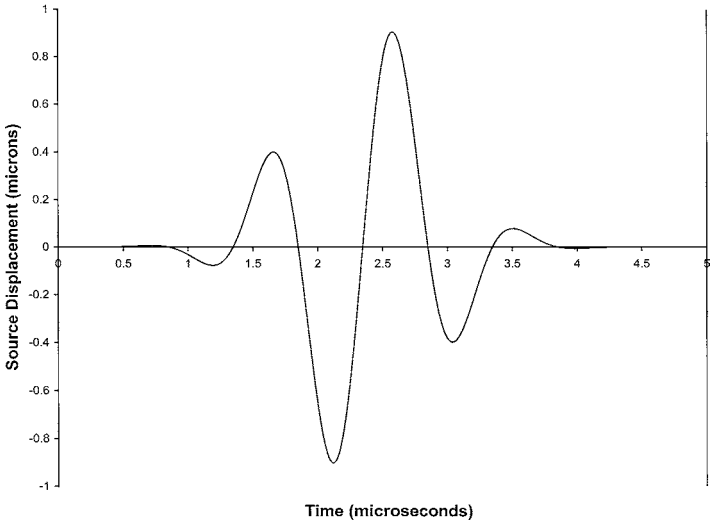

FIGURE 34.6 A 1-MHz sine wave with a Gaussian envelope, which was transmitted into the bone samples for the simulation study of Luo et al.[65] (From Luo, G. M. et al., *Ultrasound Med. Biol.*, 25(5), 823–830, © 1999 by World Federation of Ultrasound in Medicine & Biology. With permission of Elsevier Science.)

related to BUA (i.e., an increase in BUA usually implies a decrease in mean frequency), but is more robust and not as subject to artifacts as BUA.[69]

Fig. 34.7 shows an instantaneous "snapshot" of the propagating ultrasound wave within the slice of Fig. 34.5. As may be seen, there is a significant amount of scattering associated with propagation of the ultrasound wave. The simulated receiver measurements associated with the same sample along the principal direction (i.e., propagation of the ultrasound in the direction parallel to the primary orientation

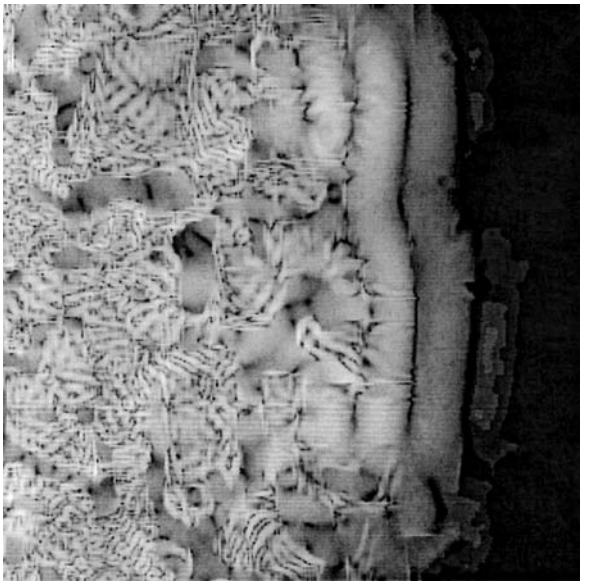

FIGURE 34.7 An instantaneous "snapshot" at $t = 7.4$ μs of an ultrasound wave propagating (from left to right) through the 2D bone slice shown in Fig. 34.5, in the direction orthogonal to the main trabecular orientation. The gray level of the image is proportional to the magnitude of the material displacement at each point in the trabecular bone slice. (From Luo, G. M. et al., *Ultrasound Med. Biol.,* 25 (5), 823–830, © 1999 by World Federation of Ultrasound in Medicine & Biology. With permission of Elsevier Science.)

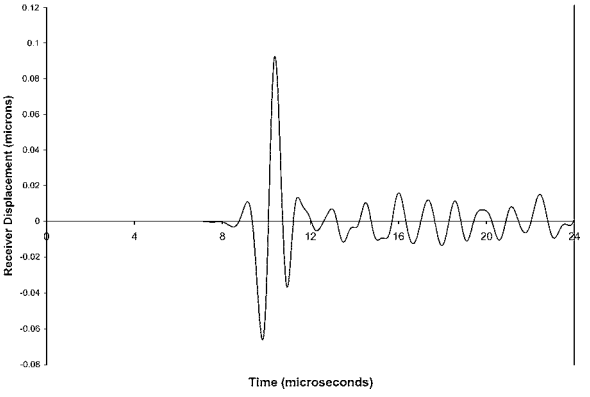

FIGURE 34.8 The simulated received waveform propagated along the principal direction of the trabeculae for the structure represented by Fig. 34.5. (From Luo, G. M. et al., *Ultrasound Med. Biol.,* 25 (5), 823–830, © 1999 by World Federation of Ultrasound in Medicine & Biology. With permission of Elsevier Science.)

of the trabeculae) and orthogonal direction (i.e., propagation of the ultrasound in the direction orthogonal to the primary orientation of the trabeculae) are shown in Figs. 34.8 and 34.9, respectively; these measurements show a remarkable similarity to experimental data.[31,67]

Plots of all the 30 UVs and MFs vs. volume fractions are shown in Figs. 34.10 and 34.11, respectively. Note that different symbols are used to denote propagation in the direction parallel (□) and orthogonal (●) to the primary orientation of the trabeculae, respectively. Linear correlation analyses with volume fraction for the two individual velocity curves of Fig. 34.10, i.e., the parallel and orthogonal data sets, resulted in R^2 values of 0.98 ($P < 0.0001$) and 0.96 ($P < 0.0001$), respectively. Linear correlation analyses with volume fraction (mass)

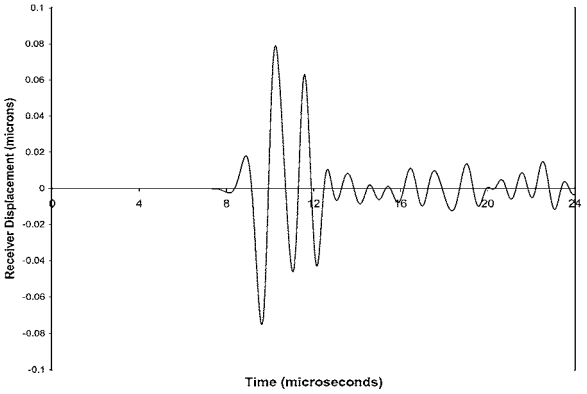

FIGURE 34.9 The simulated received waveform propagated orthogonal to the principal direction of the trabeculae for the structure represented by Fig. 34.5. (From Luo, G. M. et al., *Ultrasound Med. Biol.,* 25 (5), 823–830, © 1999 by World Federation of Ultrasound in Medicine & Biology. With permission of Elsevier Science.)

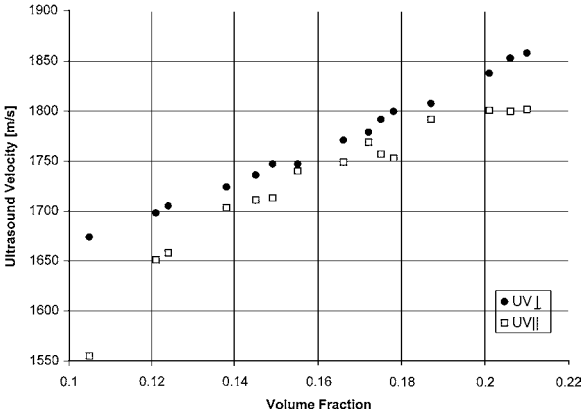

FIGURE 34.10 Plot of ultrasonic velocity (UV) vs. bone volume fraction (VF). (From Luo, G. M. et al., *Ultrasound Med. Biol.,* 25 (5), 823–830, © 1999 by World Federation of Ultrasound in Medicine & Biology. With permission of Elsevier Science.)

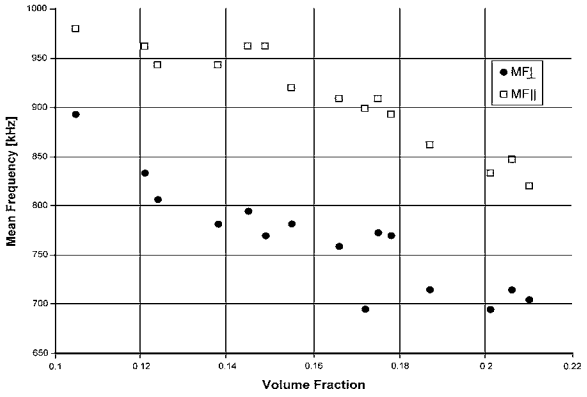

FIGURE 34.11 Plot of mean frequency (MF) vs. bone volume fraction (VF). (From Luo, G. M. et al., *Ultrasound Med. Biol.,* 25 (5), 823–830, © 1999 by World Federation of Ultrasound in Medicine & Biology. With permission of Elsevier Science.)

for the two individual mean frequency curves of Fig. 34.11, i.e., the parallel and orthogonal data sets, resulted in R^2 values of 0.91 ($P < 0.0001$) and 0.90 ($P < 0.0001$), respectively. Correlation analyses were also carried out on the ultrasound data *without regard to orientation*, that is, with the data grouped together so that there were 30 data points instead of 15 for the mean frequency and velocity linear regressions. This led to much reduced correlations as a result of the fact that the architectural orientation of the bone was not fixed, but varied from sample to sample for each of the ultrasound measurements.

The significance of these results is that it demonstrates unequivocally that ultrasound is strongly affected by the direction in which it propagates through bone. This is most readily apparent in Figs. 34.10 and 34.11, since the *only* difference in the experimental condition for each data pair, that is, for the $\parallel$ and $\perp$ ultrasound features associated with each sample, is the trabecular structure itself, as the volume fraction, transducer characteristics, and material properties are *entirely unaltered*. Previously, both theoretical and *in vitro* experimental results have demonstrated that ultrasound propagation is direction (i.e., architecturally) dependent.[70,71] The study by Chiabrera et al.[70] studied an idealized model of trabecular bone, derived the coefficients of its associated compliance matrix, and evaluated using the Christoffel relations its directionally dependent velocities. The study by Luo et al.[65] extended these results by using not idealized but realistic trabecular structures, accurately quantifying mass and architecture and relating them to ultrasound measurements.

34.3.5 Directions for Future Research

There are numerous areas to explore with respect to ultrasound assessment of bone. Ultrasound measurements, although of some utility at present, are not extremely well correlated with bone mass or strength, nor are present devices as precise as they should be. Future studies should concentrate on both basic research and developing better clinical devices.

Since ultrasound propagation depends on mass, architecture, and material properties, combining it with data related to one or more of these variables may prove useful for improving upon current capabilities. The combination of X-ray densitometric with ultrasonic measurements may provide a reasonable approach for more accurately identifying both density and architecture, and ultimately bone strength and fracture risk.[62,72–74] Since age is correlated with bone density, another alternative is to combine age with ultrasound measurements to enhance ultrasound-based density estimation.[69,72] It will also be useful to explore nonlinear combinations of ultrasound and other features (e.g., density, age, weight, height), as well as nonlinear combinations of the ultrasound features themselves, as a means to estimate bone strength and fracture risk. This can be pursued, for example, with neural networks.[72,75]

Most ultrasound measurements at present rely on large, single-element stationary transducers. More recently, imaging techniques have been proposed, both for improving reproducibility and for obtaining additional architectural information. The imaging modalities have included both the mechanical translation of the transducers, or two-dimensional (2D) array methods.[76,77] It is expected that ultrasound will become more useful as further research is pursued.

34.4 Alternative Techniques

In addition to X-ray densitometry and quantitative ultrasound, other methods have been proposed and/or studied for noninvasively assessing bone integrity. Although none seem to have the overall capability or potential that is shared by X-ray and ultrasound techniques, it is useful to mention them here.

34.4.1 Micro-CT and High-Resolution Magnetic Resonance Imaging

Two techniques that can image the microstructural aspects of trabecular bone have been reported. The first, micro-CT, is based on standard X-ray CT principles, but utilizes specialized hardware to obtain bone images at extremely high resolutions (up to ~10 μm).[78–82] Several such systems have been constructed, the most advanced one being based on extremely narrowband synchrotron radiation.[80,81] A 3D image of calcaneal trabecular bone made using such a system is shown in Fig. 34.12. The utility of

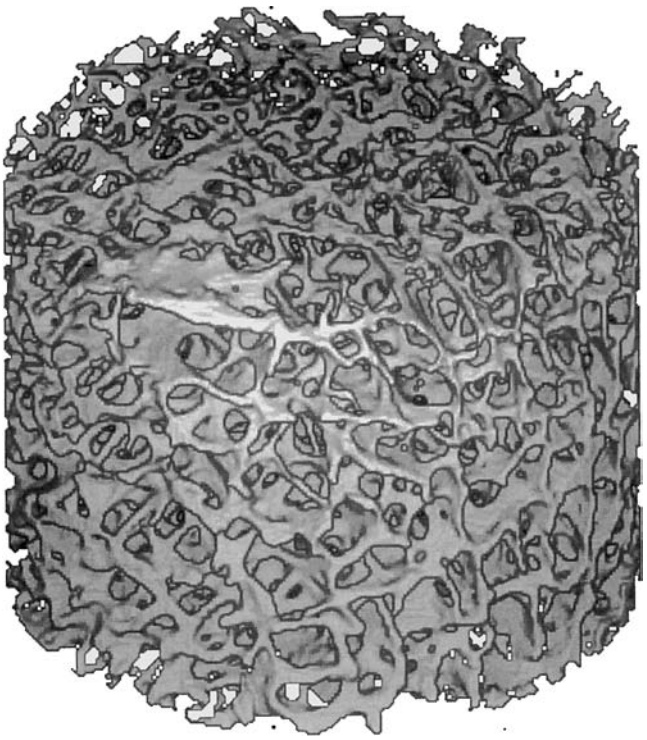

FIGURE 34.12 A 3D rendered image using micro-CT of a calcaneal trabecular bone sample. (From Luo, G. M. et al., *Ultrasound Med. Biol.,* 25 (5), 823–830, © 1999 by World Federation of Ultrasound in Medicine & Biology. With permission of Elsevier Science.)

micro-CT is that it enables the complete 3D microarchitectural distribution of trabecular bone to be measured, which can help to answer questions related to the role that architecture plays in determining bone strength. Most micro-CT systems, however, have very high radiation doses and may generally be used for small samples only, thus limiting their practical utility in the clinic.

From a conceptual point of view, high-resolution magnetic resonance imaging is similar to micro-CT. Using specialized magnetic resonance imaging hardware, namely, high magnetic field systems with small radiofrequency surface coils, 3D images of bone that depict trabecular structure can be generated.[82–84] An advantage that these systems have over micro-CT is their capability to image bone in arbitrary orientations and to be more suitable in clinical settings (no ionizing radiation and larger bodies allowed); however, their resolution (~100 μm) or contrast is not as good as micro-CT. A recent clinical study used high-resolution magnetic resonance imaging of the calcaneus and demonstrated differences in trabecular structure between patients with excessive bone loss and controls.[85] Clearly, magnetic resonance imaging is not an economically viable tool in terms of assessing integrity and fracture risk in the population at large, but its use, as with micro-CT, in research settings makes it a useful technique. Both of these imaging modalities, for example, can be used for 2D or 3D histomorphometry (e.g., measuring trabecular connectivity), to elucidate further the role that bone architecture plays in determining bone strength.[86,87]

34.4.2 Vibrational Methods

The ability of bone to conduct low-frequency vibrations (sound) was applied clinically over 50 years ago to identify the presence of fractures, although the technique has become a relatively "lost art" as more-sophisticated X-ray and other imaging techniques have been developed.[88] More recently, vibrational methods have been applied to intact bone in an attempt to assess its biomechanical properties.[89,90]

Although the subject of extensive research, no vibrational methods have yet become useful for assessing integrity in intact bone, although some success has been realized in monitoring fracture healing.[88] The basic approach in vibrational assessment is to excite the bone with a mechanical stimulus, and monitor the dynamic response(s) at a given position or set of positions. In this regard, it is not dissimilar to ultrasound methods, although the wavelengths used are much larger (in ultrasound methods, $\lambda \approx 1$ to 3 mm, while in vibrational methods $\lambda \approx 0.1$ to 1 m). However, low-frequency vibrational methods are much more subject to systematic and random errors as a result of large sensitivities with respect to transducer repositioning and skin coupling, differences in boundary conditions of the limb under test, and effects of soft tissue and muscle. These factors have prevented vibrational methods from having any significant role in assessing bone loss and integrity.

34.4.3 Plain Radiographic Textural and Pattern Analyses

Since architecture is known to play a role in bone strength, techniques that attempt to quantitate trabecular structure noninvasively have also been attempted. The most common modality used in this regard is plain radiography. One of the earliest techniques involved a subjective rating based on the qualitative appearance of trabeculation in the proximal femur.[91] The Singh index, as it was called, was developed in an attempt to evaluate those at increased risk of hip fracture, but suffered by its qualitative and subjective nature. In an effort to overcome this limitation, quantitative techniques were developed, which included objective measurements based on texture and fractal analysis.[92,93] For example, in one early study using plain radiographs of the calcaneus, textural image features were shown to be affected during periods of biomechanical disuse.[93] The features studied included fractal dimension, run length, and co-occurrence measures. Other studies have reported further on the use of fabric, fractal dimension, and Moire patterns to characterize the architectural pattern of trabecular bone.[94–97] Quantitative analysis of plain radiographs of the calcaneus *in vitro* using an architectural measure known as covariance have been reported as well.[98] Covariance is similar to fabric in that it is a measure of the anisotropy of a structure; however, it has some additional advantages in that it contains additional structural information.[99] Some researchers have also used textural and pattern analyses with other modalities (magnetic resonance imaging, for example) in an attempt to noninvasively extract architectural features from bone.[85] An important recent result has demonstrated that architecture measured directly from a 3D (micro-CT) image of calcaneal trabecular bone is directly related to summated patterns, i.e., projections of 3D volumes onto 2D surfaces, of plain radiographs.[100]

Plain radiographic-based pattern and textural analysis is very attractive because of its inherent low cost and wide availability. However, as of yet, there has been no clear clinical utility of any of the reported methods, although research is continuing.

34.4.4 Other Methods

In addition to the previously mentioned techniques, several other methods have been proposed to measure bone integrity noninvasively. One of these, biochemical markers of bone turnover, while it does not directly measure biomechanical integrity, has nevertheless been shown in some studies to provide additional information on clinical fracture risk beyond that provided by X-ray densitometry (e.g., BMD).[101] The biochemical markers, of which there are now more than ten different ones, may be measured relatively inexpensively using a subject's blood and/or urine, and provide a measure of the rate and degree of bone turnover. The markers provide a dynamic assessment of the skeleton and may be expected, in the coming years, to play an important role in assessing skeletal integrity.

Another method for bone assessment utilizes nonionizing electromagnetic measurements, similar to electrical impedance tomography or microwave imaging techniques.[102,103] In one such *in vitro* study, electrical conductances were measured on 13 human trabecular bone samples, using a plastic cylinder filled with a conducting fluid and a pair of 1-cm-diameter silver–silver chloride electrodes (Type 4560, Nikomed, Doylestown, PA) surrounding each trabecular bone sample.[104] The impedance magnitude of

each bone sample was measured (Model 1260 Impedance Analyzer, Solartron Instruments, Hampshire, UK) at 10 kHz and normalized by the length and area of the sample to obtain its electrical conductance. The bone apparent densities, ρ_a, were estimated by air-drying the samples and dividing their dry weight by their total volume. There was a high degree of correlation between the apparent density of the bone samples with measured electrical conductivity ($R = 0.94$, $P < 0.001$). Further work will be necessary to extend this work to *in vivo* applications.

Finally, two additional X-ray-based methods should be mentioned for the sake of completeness. First, measurement of *bone geometry* obtained either with plain radiographs or some other noninvasive imaging technique has been shown to provide additional information on bone integrity. This is not surprising since induced strains in bone tissue generally will depend on geometric factors. As one example, the lateral cortical thickness of the hip 2 cm distal to the calcar femorale, measured using a plain radiograph, has been shown to be an independent discriminator of hip fracture.[105] Similarly, the hip-axis length, the length along the femoral neck axis from below the lateral aspect of the greater trochanter to the caput femoris, has been shown to be an independent discriminator of hip fracture as well.[106]

Second and last, radiographic absorptiometry, the measurement of bone mineral density using a plain radiograph, is a useful technique for measuring bone mass where there is minimal soft tissue, for example, at the phalanges.[14,15] The method generally uses an aluminum calibration wedge, and expresses the BMD in aluminum-equivalent units. Radiographic absorptiometry does not perform as well when sites such as the calcaneus are used, because of its inability to account for varying amounts of overlying soft tissue. However, recent advances have attempted to address this problem, although additional research is still required.[107]

34.5 Summary

Noninvasive methods for assessing bone integrity are important for diagnosing and managing clinical bone loss, assessing fracture risk, as well as for monitoring the response to therapeutic interventions. Present-day X-ray densitometry techniques are reasonably good at making accurate and reproducible estimates of bone mineral content, and these estimates are correlated with *in vitro* measurements of bone biomechanical properties and with clinical fracture risk. Such techniques fulfill an important public health need. Quantitative ultrasound is another means for assessing bone, and is becoming an important clinical tool as well.

Because of the complexity of the human skeleton from biomechanical, geometric, and biological perspectives, the development of new methods and the improvement of existing techniques to assess bone noninvasively requires a multidisciplinary approach. The objective of obtaining accurate and precise noninvasive measurements of skeletal integrity, which are also safe, reliable, and practical, although already achieved with some degree of success, still requires significant further research and development.

References

1. Eastell, R., Pathogenesis of postmenopausal osteoporosis, in *Primer on the Metabolic Bone Diseases and Disorders of Mineral Metabolism,* Favus, M. J., Ed., Lippincott-Williams & Wilkins, Philadelphia, PA, 1999, chap. 47.
2. Barrett-Conner, E., The economics and human cost of osteoporotic fracture, *Am. J. Med.,* 98, 3, 1995.
3. Wasnich, R. D., Epidemiology of osteoporosis, in *Primer on the Metabolic Bone Diseases and Disorders of Mineral Metabolism,* Favus, M. J., Ed., Lippincott-Williams & Wilkins, Philadelphia, PA, 1999, chap. 46.
4. Carter, D. R. and Hayes, W. C., The compressive behavior of bone as a two-phase porous structure, *J. Bone Joint Surg.,* 59-A, 954, 1977.
5. Rice, J. C., Cowin, S. C., and Bowman, J. A., On the dependence of the elasticity and strength of cancellous bone on apparent density, *J. Biomech.,* 21, 155, 1988.

6. Hansson, T., Roos, B., and Nachemsom A., The bone mineral content and ultimate compressive strength of lumbar vertebrae, *Spine,* 5, 46, 1980.
7. Lang, S. M., Moyle, D. D., Berg, E. W., Detorie, N., Gilpin, A. T., Pappas, N. J., Reynolds, J. C., Tkacik, M. and Waldron, R. L., Correlation of mechanical properties of vertebral trabecular bone with equivalent mineral density as measured by computed tomography, *J. Bone Joint Surg.,* 70-A, 1531, 1988.
8. Weaver, J. K. and Chalmers, J., Cancellous bone: its strength and changes with aging and an evaluation of some methods for measuring its mineral content, *J. Bone Joint Surg.,* 48-A, 289, 1966.
9. Jensen, N. C., Madsen, L. P., and Linde, F., Topographical distribution of trabecular bone strength in the human os calcanei, *J. Biomech.,* 24, 49, 1991.
10. Ott, S. M., Kilcoyne, R. F., and Chestnut III, C., Ability of four different techniques of measuring bone mass to diagnose vertebral fractures in postmenopausal women, *J. Bone Minor. Res.,* 2, 201, 1987.
11. Miller, P. D. and Bonnick, S. L., Clinical application of bone densitometry, in *Primer on the Metabolic Bone Diseases and Disorders of Mineral Metabolism,* Favus, M. J., Ed., Lippincott-Williams & Wilkins, Philadelphia, PA, 1999, chap. 25.
12. Cummings, S. R., Black, D. M., Nevitt, M. C., Browner, W., Cauley, J., Ensrud, K., Genant, H. K., Palermo, L., Scott, J., and Vogt, T. M., Bone density at various sites for prediction of hip fracture, *Lancet,* 341, 72, 1993.
13. Attix, F. H., *Introduction to Radiological Physics and Radiation Dosimetry,* Wiley-Interscience, New York, 1986, 531.
14. Mirsky, E. C. and Einhorn, T. A., Bone densitometry in orthopaedic practice, *J. Bone Joint Surg.,* 80-A, 1687, 1998.
15. Genant, H. K., Engelke, K., Fuerst, T., Gluer, C.-C., Grampp, S., Harris, S. T., Jergas, M., Lang, T., Lu, Y., Majumdar, S., Mathur, A., and Takada, M., Review: noninvasive assessment of bone mineral and structure: state of the art, *J. Bone Miner. Res.,* 11, 707, 1996.
16. Kabel, J., van Rietbergen, B., Odgaard, A., and Huiskes, R., Bone constitutive relationships of fabric, density, and elastic properties in cancellous bone architecture, *Bone,* 25, 481, 1999.
17. Turner, C. H., and Cowin, S. C., Dependence of elastic constants of an anisotropic porous material upon porosity and fabric, *J. Mater. Sci.,* 22, 3178, 1987.
18. Feldkamp, L. A., Goldstein, S. A., Parfitt, A. M., Jesion, G., and Kleerekoper, M., The direct examination of three-dimensional bone architecture *in vitro* by computed tomography, *J. Bone Miner. Res.,* 4, 3, 1989.
19. Kleerekoper, M., Villanueva, A. R., Stanciu, J., Rao, D. S., and Parfitt, A. M., The role of three-dimensional trabecular microstructure in the pathogenesis of vertebral compression fractures, *Calcif. Tissue Int.,* 37, 594, 1985.
20. Martin, R. B. and Burr, D. B., *Structure, Function, and Adaptation of Compact Bone,* Raven Press, New York, 1989.
21. Riggs, B. L., Hodgson, S. F., O'Fallon, W. M., Chao, E. Y. S., Wahner, H. W., Muhs, J. M., Cedel, S. L., and Melton III, L. J., Effect of fluoride treatment on the fracture rate in postmenopausal women with osteoporosis, *N. Eng. J. Med.,* 322, 802, 1990.
22. Siffert, R. S., Luo, G. M., Cowin, S. C., and Kaufman, J. J., Dynamical relationships of trabecular bone density, architecture and strength in a computational model of osteopenia, *Bone,* 18, 197, 1996.
23. Wenzel, T. E., Fyhrie, D. P., Schaffler, M. B., and Goldstein, S. A., Variations in three-dimensional cancellous architecture of the proximal femur in hip fracture patients and controls. *Trans. Orthop. Res. Soc.,* 23, 86, 1998.
24. Chernov, L. A., *Wave Propagation in a Random Medium,* Dover Publications, New York, 1967.
25. Wells, P. N. T., *Biomedical Ultrasonics,* Academic Press, London, 1977.
26. Lees, S., Some properties of mineralized tissues, in *Tissue Characterization with Ultrasound,* Greenleaf, J. F., Ed., CRC Press, Boca Raton, FL, 1986, 207.

27. Kaufman, J. J. and Einhorn, T. E., Review—ultrasound assessment of bone, *J. Bone Miner. Res.,* 8, 517, 1993.
28. Zerwekh, J. E., Antich, P. P., Sakhaee, K., Gonzales, J., Gottschalk, F., and Pak, C. Y. C., Assessment by reflection ultrasound method of the effect of intermittent slow-release sodium fluoride-calcium citrate therapy on material strength of bone, *J. Bone Miner. Res.,* 6, 233, 1991.
29. Kaufman, J. J., Xu, W., Chiabrera, A. E., and Siffert, R. S., Diffraction effects in insertion mode estimation of ultrasonic group velocity, *IEEE Trans. Ultrasonics Ferroelectr. Frequency Control,* 42, 232, 1995.
30. Barger, J., Attenuation and dispersion of ultrasound in cancellous bone, in *Ultrasonic Tissue* Characterization II, Linzer, M., Ed., Spec. Publ. 525, U. S. Government Printing Office, Washington, D.C., 1979.
31. Alves, J. M., Xu, W., Lin, D., Siffert, R. S., Ryaby, J. T., and Kaufman, J. J., Ultrasonic assessment of human and bovine trabecular bone: a comparison study, *IEEE Trans. Biomed. Eng.,* 43, 249, 1996.
32. Kolsky, H., *Stress Waves in Solids,* Dover Publications, New York, 1963.
33. Goobermann, G. L., *Ultrasonics Theory and Application,* English Universities Press, London, 1968.
34. Carstensen, E. L. and Schwan, H. P., Acoustic properties of hemoglobin solutions, *J. Acoust. Soc. Am.,* 31, 305, 1959.
35. Langton, C. M., Palmer, S. B., and Porter, R. W., The measurement of broadband ultrasonic attenuation in cancellous bone, *Eng. Med.,* 13, 89, 1984.
36. Oppenheim, A. V. and Schafer, R. W., *Discrete-Time Signal Processing,* Prentice-Hall, Englewood Cliffs, NJ, 1989.
37. Hill, C. R., Ed., *Physical Principles of Medical Ultrasonics,* John Wiley & Sons, New York, 1986.
38. Lang, S. B., Ultrasonic method for measuring elastic coefficients of bone and results on fresh and dried bovine bones, *IEEE Trans. Biomed. Eng.,* 17, 101, 1970.
39. Abdenshein, W. and Hyatt, G. W., Ultrasonics and selected physical properties of bone, *Clin. Orthop. Relat. Res.,* 49, 294, 1970.
40. Ashman, B., Cowin, S. C., Van Buskirk, W. C., and Rice, J. C., A continuous wave technique for the measurement of the elastic properties of cortical bone, *J. Biomech.,* 17, 349, 1984.
41. Ashman, R. B. and Rho, J. Y., Elastic modulus of trabecular bone material, *J. Biomech.,* 21, 177, 1988.
42. Lakes, R., Yoon, H. S., and Katz, J. L., Ultrasonic wave propagation and attenuation in wet bone, *J. Biomed. Eng.,* 8, 143, 1986.
43. Turner, C. H. and Eich, M., Ultrasonic velocity as a predictor of strength in bovine cancellous bone, *Calcif. Tissue Int.,* 49, 116, 1991.
44. Rubin, C. T., Pratt, G. W., Lanyon, L. E., and Poss, R., Osteoporosis and ultrasound: non-invasive evaluation of the physical properties of bone, *Trans. Orthop. Res. Soc.,* 11, 465, 1986.
45. McCarthy, R. N., Jeffcott, L. B., and McCartney, R. N., Ultrasound speed in equine cortical bone: effects of orientation, density, porosity and temperature, *J. Biomech.,* 23, 1139, 1990.
46. Lees, S. and Hanson, D. B., Effect of fluoride dosage on bone density, sonic velocity, and longitudinal modulus of rabbit femurs, *Calcif. Tissue Int.,* 50, 92, 1992.
47. Heaney, R. P., Avioli, L. V., Chestnut, C. H., Lappe, J., Reicher, R. R., and Brandenburger, G. H., Osteoporotic bone fragility. Detection by ultrasound transmission velocity, *JAMA,* 261, 2986, 1989.
48. Rubin, C. T., Pratt, G. W., Porter, A. L., Lanyon, L. E. and Poss, R., The use of ultrasound *in vivo* to determine acute change in the mechanical properties of bone following intense physical activity, *J. Biomech.,* 20, 723, 1987.
49. McKelvie, M. L., Fordham, J., Clifford, C., and Palmer, S. B., *In vitro* comparison of quantitative computed tomography and broadband ultrasonic attenuation of trabecular bone, *Bone,* 10, 101, 1989.
50. McCloskey, E. V., Murray, S. A., and Charlesworth, D., Assessment of broadband ultrasound attenuation in the os calcis *in vitro*, *Clin. Sci.,* 78, 221, 1990.
51. Kaufman, J. J., Chiabrera, A., Fallot, S., Alves, J. M., Hermann, G., Siffert, R. S., and Grabowski, G., Ultrasonic bone tissue characterization in Gaucher disease type I, in *Acoustical Imaging,* Vol. 19, Ermet, H. and Harjes, H. P., Eds., Plenum Press, New York, 1992, 399.

52. Tavakoli, M. B. and Evans, J. A., Dependence of the velocity and attenuation in bone on the mineral content, *Phys. Med. Biol.,* 36, 1529, 1991.
53. Rossman, P., Zagzebski, J., Mesine, C., Sorenson, J., and Mazess, R. B., Comparison of speed-of-sound and ultrasound attenuation in the os calcis to bone density of the radius, femur and lumbar spine, *Clin. Phys. Physiol. Meas.,* 10, 353, 1989.
54. Zagzebski, J. A., Rossman, P. J., Mesina, C., Mazess, R. B., and Madsen, E. L., Ultrasound transmission measurements through the os calcis, *Calcif. Tissue Int.,* 49, 107, 1991.
55. Stevenson, J. and Lees, B., Precision and sensitivity of a new ultrasound bone densitometer, in *Ultrasound for Bone Measurement, Proceedings of Satellite Symposium, International Conference for Calcium Regulating Hormones,* Florence, Italy, 1992.
56. Miller, C. G. and Porter, R. W., The prediction of fracture of the proximal femur by broadband ultrasonic attenuation, in *Osteoporosis 1987,* Christiansen, C., Johansen, J. S., and Riis, B. J., Eds., Osteopress ApS, Copenhagen, Denmark, 1987, 414.
57. Baran, D. T., Kelly, A. M., and Karellas, A., Ultrasound attenuation of the os calcis in women with osteoporosis and hip fractures, *Calcif. Tissue Int.,* 43, 138, 1988.
58. Hans, D., Dargent-Molina, P., Schott, A. M., Sebert, J. L., Cormier, C., Kotzki, P. O., Delmas, P. D., Pouilles, J. M., Breat, G., and Meunier, P. J., Ultrasonographic heel measurements to predict hip fracture in elderly women: the EPIDOS prospective study, *Lancet,* 348, 511, 1996.
59. Bauer, D. C., Gluer, C. C., Cauley, J. A., Vogt, T. M., Ensrud, K. E., Genant, H. K., and Black, D. M., Bone ultrasound predicts fractures strongly and independently of densitometry in older women: a prospective study, *Arch. Intern. Med.,* 157, 629, 1997.
60. Pluijm, S. M., Graafmans, W. C., Bouter, L. M., and Lips, P., Ultrasound measurements for the prediction of osteoporotic fractures in elderly people, *Osteoporosis Int.,* 9, 550, 1999.
61. Gluer C. C. and Hans D., How to use ultrasound for risk assessment: a need for defining strategies, *Osteoporosis Int.,* 9, 193, 1999.
62. Bouxsein, M. L., Courtney, A. C., and Hayes, W. C., Ultrasound and densitometry of the calcaneus correlate with the failure loads of cadaveric femurs, *Calcif. Tissue Int.,* 56, 99, 1995.
63. Hans, D., Schott, A. M., and Meunier, P. J., Ultrasonic assessment of bone; a review, *Eur. J. Med.,* 2,157, 1993.
64. Gregg, E. W., Kriska, A. M., Salamone, L. M., Roberts, M. M., Anderson, S. J., Ferrel, R. E., Kuller, L. H., and Cauley, J. A., The epidemiology of quantitative ultrasound: a review of the relationships with bone mass, osteoporosis and fracture risk, *Osteoporosis Int.,* 7, 89, 1997.
65. Luo, G. M., Kaufman, J. J., Chiabrera, A., Bianco, B., Kinney, J. H., Haupt, D., Ryaby, J. T., and Siffert, R. S., Computational methods for ultrasonic bone assessment, *Ultrasound Med. Biol.,* 25, 823, 1999.
66. Lin, D., Xu, W., Klein, M., Einhorn, T., Kaufman, J. J., and Siffert, R. S., Effect of physical factors on ultrasound attenuation and velocity in bone, *J. Bone Miner. Res.,* 8, S319, 1993.
67. Alves, J. M., Ryaby, J. T., Siffert, R. S., Magee, F. P., and Kaufman, J. J., Influence of marrow on ultrasonic velocity and attenuation bovine trabecular bone, *Calcif. Tissue Int.,* 58, 362, 1996.
68. Xu, W. and Kaufman, J. J., Diffraction correction methods for insertion ultrasound attenuation measurement, *IEEE Trans. Biomed. Eng.,* 40, 563, 1993.
69. Kaufman, J. J., Murphy, G., Fitzpatrick, D., Liu, L., Ost, M., Alves, J. M., Magee, F. P., Ryaby, J. T., Einhorn, T. A., Siffert, R. S., and Luckey, M., A new ultrasound system for bone assessment, *J. Bone Miner. Res.,* 11, S241, 1996.
70. Chiabrera, A., Bianco, B., Siffert, R. S., and Kaufman, J. J., Ultrasound measures both bone mass and architecture: theoretical results for an idealized model of trabecular bone, *Trans. Orthop. Res. Soc.,* 21, 600, 1996.
71. Gluer, C. C., Wu, C. Y., and Genant, H. K., Broadband ultrasound attenuation signals depend on trabecular orientation: an *in vitro* study, *Osteoporosis Int.,* 3, 185, 1993.
72. Kaufman, J. J. and Chiabrera, A., Ultrasonic bone-assessment apparatus and method, U. S. Patent 5, 259, 384, issued November 9, 1993.

73. Njeh, C. F., Kuo, C. W., Langton, C. M., Atrah, H. I., and Boivin, C. M., Prediction of human femoral bone strength using ultrasound velocity and BMD: an *in vitro* study, *Osteoporosis Int.,* 7, 471, 1997.
74. Lochmuller, E. M., Zeller, J. B., Kaiser, D., Eckstein, F., Landgraf, J., Putz, R., and Steldinger, R., Correlation of femoral and lumbar DXA and calcaneal ultrasound, measured in situ with intact soft tissues, with the in vitro failure loads of the proximal femur, *Osteoporosis Int.,* 8, 591, 1998.
75. Kaufman, J. J., Alves, M., Siffert, R. S., Magee, F. P., and Ryaby, J. T., Ultrasound assessment of trabecular bone density using neural networks, *J. Bone Miner. Res.,* 9, A204, 1994.
76. Roux, C., Fournier, B., Laugier, P., Chappard, C., Kolta, S., Dougados, M., and Berger, G., Broadband ultrasound attenuation imaging: a new imaging method in osteoporosis, *J. Bone Miner. Res.,* 11, 1112, 1996.
77. Kaufman, J. J., Friess, S. H., Chiabrera, A., Sorensen, J., Ryaby, J. T., and Siffert, R. S., Two-dimensional array system for ultrasonic bone assessment, *Trans. Orthop. Res. Soc.,* 23, 966, 1998.
78. Feldkamp, L. A., Goldstein, S. A., Parfitt, A. M., Jesion, G., and Kleerekoper, M., The direct examination of three-dimensional bone architecture *in vitro* by computed tomography, *J. Bone Miner. Res.,* 4, 3, 1989.
79. Ruegsegger, P. and Koller, B., A micro-CT system for the non-destructive analysis of bone samples, in *Proc.10th International Bone Densitomety Workshop,* 25, Bomiet, Venice, Italy, 1994.
80. Kinney, J. H. and Nichold, M. C., X-ray tomographic microscopy using synchrotron radiation, *Annu. Rev. Mater. Sci.,* 22, 121, 1992.
81. Kinney, J. H., Lane, N. E., and Haupt, D. L., In vivo, three-dimensional microscopy of trabecular bone, *J. Bone Miner. Res.,* 10, 264, 1995.
82. Lang, T., Augat, P., Majumdar, S., Ouyang, X., and Genant, H. K., Noninvasive assessment of bone density and structure using computed tomography and magnetic resonance, *Bone,* 22, 149S, 1998.
83. Chung, H., Wehrli, F., Williams, J., Kugelmass, S., and Wehrli, S., Quantitative analysis of trabecular microstructure by 400 MHz nuclear magnetic resonance imaging, *J. Bone Miner. Res.,* 10, 803, 1995.
84. Muller, R., Hildebrand, T., Hauselmann, H. J., and Ruegsegger, P., *In vivo* reproducibility of three-dimensional structural properties of non-invasive bone biopsies using 3D-pQCT, *J. Bone Miner. Res.,* 11, 1745, 1996.
85. Link, T. M., Majumdar, S., Augat, P., Lin, J. C., Newitt, D., Lu, Y., Nane, N. E., and Genant, H. K., *In vivo* high resolution MRI of the calcaneus: differences in trabecular structure in osteoporosis patients, *J. Bone Miner. Res.,* 13, 1175, 1998.
86. Cortet, B., Colin, D., Dubois, P., Delcambre, B., and Marchandise, X., Methods for quantitative analysis of trabecular bone structure, *Rev. Rhum Engl. Ed.,* 62, 781, 1995.
87. Parfitt, A. M., Bone histomorphometry: proposed system for standardization of nomenclature, symbols, and units, *Calcif. Tissue Int.,* 42, 284, 1988.
88. Siffert, R. S. and Kaufman, J. J., Acoustic assessment of fracture healing: capabilities and limitations of "a lost art," *Am. J. Orthop.,* 25, 614, 1996.
89. Nokes, L. D. M. and Thorne, G. C., Vibrations in orthopaedics, in *CRC Crit. Rev. Biomed. Eng.,* 15, 1987, 309.
90. Markel, M. D. and Chao, E. Y. S., Noninvasive monitoring techniques for quantitative description of callus mineral content and mechanical properties, *Clin. Orthop. Relat. Res.,* 293, 37, 1993.
91. Singh, M., Nagrath, A. R., and Maini, P. S., Changes in trabecular pattern of the upper end of the femur as an index of osteoporosis, *J. Bone Joint Surg.* [*Am.*], 52, 457, 1970.
92. Rockoff, S. D., Scandrett, J., and Zacher, R., Quantitation of relevant image information: automated radiographic bone trabecular characterization, *Radiology,* 101, 435, 1971.
93. Kaufman, J. J., Mont, M. A., Hakim, N., Ohley, W., Lundahl, T., Soifer, T., and Siffert, R. S., Texture analysis of radiographic trabecular patterns in disuse osteopenia, *Trans. Orthop. Res. Soc.,* 12, 265, 1987.
94. Siffert, R. S., Luo, G. M., and Kaufman, J. J., Moire patterns from plain radiographs of trabecular bone, in *Proceedings 17th Annual International Conference of the IEEE Engineering in Medicine and Biology Society,* IEEE, New York, 1995.

95. Benhamou, C. L., Lespessailles, E., Jacquet, G., Harba, R., Jeannane, R., Loussot, T., Tourliere, D., and Ohley, W., Fractal organization of trabecular bone images on calcaneus radiographs, *J. Bone Miner. Res.,* 9, 1909, 1994.
96. Caliguri, P., Giger, M. L., Favus, M. J., Jia, H., Doi, K., and Dixon, L. B., Computerized radiographic analysis of osteoporosis: preliminary evaluation, *Radiology,* 186, 471, 1993.
97. Buckland-Wright, J. C., Lynch, J. A., Rymer, J., and Fogelman, I., Fractal signature analysis of macroradiographs measures trabecular organization in lumbar vertebrae of postmenopausal women, *Calcif. Tissue Int.,* 54, 106, 1994.
98. Siffert, R. S., Luo, G. M., Kaufman, J. J., and Cowin, S. C., Quantitative analysis of trabecular architecture in plain radiographs of the human os calcis, in *Transactions of the 2nd Combined Meeting of the Orthopaedic Research Societies of U.S.A., Japan, Canada and Europe,* Orthopaedic Research Society, Palatine, IL, 1995, 10.
99. Berryman, J. G., Measurement of spatial correlation functions using image processing techniques, *J. Appl. Phys.,* 57, 2374, 1985.
100. Luo, G. M., Kinney, J. H., Kaufman, J. J., Haupt, D., Chiabrera, A., and Siffert, R. S., Relationship of plain radiographic patterns to three-dimensional trabecular architecture in the human calcaneus, *Osteoporosis Int.,* 9, 339, 1999.
101. Khosla, S. and Kleerekoper, M., Biochemical markers of bone turnover, in *Primer on the Metabolic Bone Diseases and Disorders of Mineral Metabolism,* Favus, M. J., Ed., Lippincott-Williams & Wilkins, Philadelphia, PA, 1999, chap. 22.
102. Dehghani, H., Barber, D. C., and Basarab-Horwath, I., Incorporating a prior anatomical information into image reconstruction in electrical impedance tomography, *Physiol. Meas.,* 20, 87, 1999.
103. Semenov, S. Y., Svensen, R. H., Bulyshev, A. E., Souvorov, A. E., Nazarov, A. G., Sizoz, Y. E., Pavlovsky, A. V., Borisov, V. Y., Voinov, B. A., Simonova, G. I., Starostin, A. N., Posukh, V. G., Tatsis, G. P., and Baranov, V. Y., Three-dimensional microwave tomography: experimental prototype of the system and vector born reconstruction method, *IEEE Trans. Biomed. Eng.,* 46, 937, 1999.
104. Bianco, B., Chiabrera, A., Siffert, R. S., and Kaufman, J. J., Electrical assessment of trabecular bone density: theoretical and *in vitro* results, *Trans. Orthop. Res. Soc.,* 21, 716, 1996.
105. Peacock, M., Turner, C. H., Liu, G., Manatunga, A. K., Timmerman, L., and Johnston, C.C. Jr., Better discrimination of hip fracture using bone density, geometry and architecture, *Osteoporosis Int.,* 5, 167, 1995.
106. Karlsson, K. M., Sernbo, I., Obrant, K. J., Redlund-Johnell, I., and Johnell, O., Femoral neck geometry and radiographic signs of osteoporosis as predictors of hip fracture, *Bone,* 18, 327, 1996.
107. Chiabrera, A., Siffert, R. S., and Kaufman, J. J., Plain X-ray bone densitometry apparatus and method, U. S. Patent 5,917,877, issued June 29, 1999.

35

Bone Prostheses and Implants

Patrick J. Prendergast
Trinity College Dublin

35.1 Introduction

Replacing or augmenting bone with an implant can relieve the pain caused by trauma or disease. Replacement of bone occurs in joint arthroplasty or in bone grafting. Augmentation of bone with fixation devices is required for fracture healing, or for stabilization and fusion of joints, or for alignment/distraction of bones.

Bone prostheses must address several design requirements. Among these are

1. Fit a wide anatomical range of patients,
2. Maintain mechanical fixation under cyclic loading,
3. Offer a functional range of motion,
4. Provide the required kinematic stability.

The relative importance of the design requirements depends on the function of the implant. Design of surgical procedures and associated instrumentation is also an essential aspect to the development of bone prosthesis systems.

The design requirements for bone prostheses are met, first, by the selection of suitable biomaterials. These must have the required biocompatibility, i.e., perform with an appropriate host response in a specific situation.[1] Sometimes the implant must remain strictly inert to facilitate removal from the body, e.g., a fixation plate. Other implants must resorb over time, and others are designed to "osseointegrate" with the host bone—osseointegration being a process of bone ingrowth at the implant surface to create a secure bond with the bone.[2] Second, the geometry of the implant is a critical factor because it determines the stress distribution at the bone–implant interface and within the surrounding bone.[3] In the case of joint replacement prostheses, the geometry of the articulating surfaces determines the range of motion of the prosthetic joint, and the kinematic stability of the articulation.[4]

The regulatory environment for new implants plays a critical role in determining the evolution of new designs. The Food and Drug Administration (FDA) regulates medical devices in the United States[5] and in the European Union regulation is according to the Medical Device Directives.[6] Although these

0-8493-9117-2/01/$0.00+$.50

systems are fundamentally different, they do have similar implant classification systems. The lowest degree of regulation is reserved for "minimum risk," Class 1 devices. Class 2 devices require specific control tests. Class 3 devices are "maximum risk," where no comparison with an existing device can be made. Active devices, such as bone substitutes and prostheses with osseointegratative surfaces, come into Class 3.[7]

This chapter is concerned with the design and testing of Class 2 and Class 3 prostheses to replace or augment the biomechanical function of bone. In Section 35.2 a review of available biomaterials is given; then in Section 35.3 the design of specific implant systems is overviewed; and finally in Section 35.4 methods of testing implants are described.

35.2 Biomaterials

Metals, ceramics, and polymers are used to replace bone in the human body. Metals have strength and stiffness that make them suitable for many load-bearing applications. Only three metals are commonly used. In order of increasing corrosion resistance, these are stainless steel, cobalt–chromium alloys, and titanium and its alloys. Ceramics—compounds of metallic and nonmetallic elements—have a wide range of properties that make them suitable for implantation; in particular, oxide ceramics are highly wear resistant and calcium phosphate and bioactive glass ceramics have excellent osteoconductive properties. Polymers are most often used in joint replacement prostheses. In all cases, prosthesis materials must have the required biocompatibility.

35.2.1 Biocompatibility

In general, an implant will alter the mechanical and chemical environment in its immediate neighborhood (locally) and throughout the body (systemically). Williams[8] has classified the components of biocompatibility as follows:

1. *Protein absorption*. Proteins rapidly cover the surface of an implant and their interaction with the surface of the biomaterial controls the host response, including behavior of cells adjacent to the implant.
2. *Material degradation at atomic and molecular level*. Corrosion of metals,[9] resorption of ceramics,[10] and hydrolysis of polymers[11] can all occur *in vivo*. Degradation can be heavily dependent on the physiological environment.
3. *Evolution of the local host response*. The trauma of implant surgery initiates an inflammatory process in the surrounding tissues, followed by a repair process that will determine eventual stability of the implant. The time course of the repair is influenced by the chemical characteristics of the biomaterial, and by mechanical phenomena such as wear[12] and micromotion.[13]
4. *Systemic effects*. Occurring remote from the implant, these are primarily mediated by chemical and mass transport phenomena. Small particles released from the implant surface by wear or degradation may be carcinogenic, or interfere with metabolic and immunological systems.[14]

35.2.2 Metals

Surgical stainless steel of specification ASTM F138 and F139 (grades 316 and 316L) achieves corrosion resistance by forming a chromium oxide (Cr_2O_3) layer on the implant surface. Nickel further improves the corrosion resistance and improves the formability of the metal for manufacturing by stabilizing a face-centered cubic crystal structure. Molybdenum is added as it increases resistance to pitting corrosion. The other elements are added to overcome manufacturing problems (Table 35.1a). Carbon content is low to prevent chromium-carbides from depleting chromium content near the grain boundaries, which would lead to intergranular corrosion. A problem with stainless steel is its slow but finite corrosion rate. Crevice corrosion can also occur if two stainless steel components are in contact. Possibility of corrosion means that stainless steel is used mainly for temporary implants.[9]

TABLE 35.1a Composition of Stainless Steel (ASTM F138)

Element	%
Chromium	17.00–19.00
Nickel	13.00–15.50
Molybdenum	2.00–3.00
Manganese	2.00 max
Iron	Balance
P, S, Si, Cu, N	Trace amounts

TABLE 35.1b Composition of Cobalt–Chromium Alloys (ASTM F75; ASTM F90)

Element	% (F75–92) Cast	% (F90–92) Wrought (forged)
Chromium	27.0–30.00	19.00–21.00
Nickel	1.0 max	9.00–11.00
Molybdenum	5.0–7.00	—
Tungsten	—	14.00–16.00
Manganese	1.00 max	1.00–2.00
Silicon	1.00 max	0.40 max
Iron	0.75 max	3.00 max
Carbon	0.35 max	0.05–0.15
Phosphorus	—	0.040 max
Sulfur	—	0.030 max
Cobalt	Balance	Balance

TABLE 35.1c Composition of a Titanium Alloy (ASTM F136)

Element	%
Aluminium	5.5–6.5
Vanadium	3.5–4.5
Iron	0.25 max
Titanium	Balance
H, C, O, N	Trace amounts

Cobalt–chromium displays better corrosion resistance than stainless steel. It can be either cast or forged, the latter having much greater fatigue resistance. ASTM F-75 is the casting alloy and ASTM F-90 is the forging alloy, the latter containing tungsten and nickel for forgability (Table 35.1b).

Titanium and its alloys have better corrosion resistance than stainless steel or cobalt–chromium alloys.[15] This is conferred by a TiO_2 layer on the surface. However, its stiffness is lower than either stainless steel or cobalt–chromium making those materials a better choice in certain situations. There is no evidence of pitting or intergranular corrosion with titanium in biological environments. Unalloyed c.p. (commercially pure) titanium is sometimes used for sintering surface layers. The alloy used is commonly called Ti-6Al-4V, although compositions differ from this, for example, ASTM F-136 (Table 35.1c). Porous coatings of wire meshes or beads can be applied to implants to act as an anchor for bone ingrowth. Several layers of beads can be employed to improve the strength of the interface under tension (Fig. 35.1).

35.2.3 Ceramics

There are three categories of ceramics used to replace bone. The first is structural ceramics (alumina, Al_2O_3, and zirconia, ZrO_2).[16] These have higher stiffness and hardness than metals and much better wear resistance. Pure zirconia can undergo phase transitions on cooling and, to avoid this, it is alloyed with CaO, MgO, or Y_2O_3, forming partially stabilized zirconia (PSZ) or tetragonal zirconia (TZP). Both alumina and zirconia are used for heads of hip prostheses.[17]

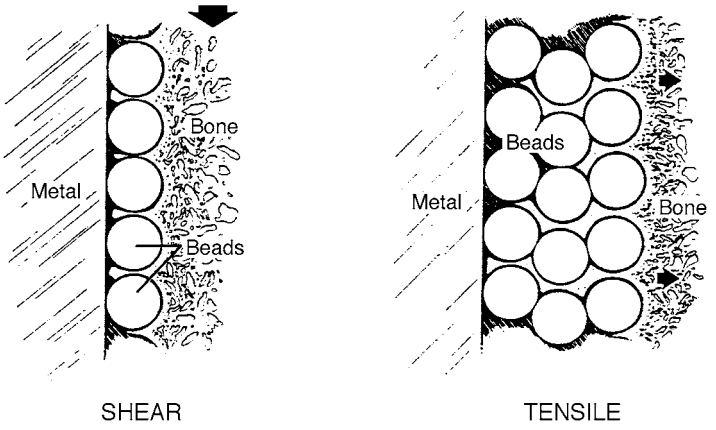

FIGURE 35.1 (a) A monolayer of beads gives adequate resistance to shear loads, and (b) a multibead layer gives superior resistance to tensile loads. (From Cameron, H. U., *Bone Implant Interface,* Mosby, St. Louis, 1994. With permisson.)

The second category of ceramic used to replace bone is calcium phosphate.[18] Hydroxyapatite (HA), $[Ca_{10}(PO_4)_6(OH)_2]$, is a calcium phosphate that is found naturally in bone. Another calcium phosphate is tricalcium phosphate (TCP), $[Ca_{10}(PO_4)_6]$. TCP biodegrades more quickly than HA, indicating that the amount of TCP should be minimized to slow the dissolution rate of an HA/TCP mix.[10] Calcium phosphates have useful osteoconductive properties and are used to coat metallic implants that aim to bond to the bone by osseointegration.[19] They are also used for synthetic bone graft materials.[20]

The third category of ceramic is bioactive glass. Ceramics in this category have excellent biocompatibility. Glasses are amorphous materials—they have no long-range atomic order. This results when the cooling from the liquid phase is sufficiently rapid to prevent crystallization. Glass bioceramics have large amounts of SiO_2, with amounts of the following compounds: P_2O_5, CaO, $Ca(PO_3)_2$, CaF_2, MgO, MgF_2, Na_2O, K_2O, Al_2O_3, B_2O_3, and Ta_2O_5/TiO_2.[21] Glass-ceramics used for implantation undergo surface dissolution in a physiological environment, resulting in the formation of a chemical bond with bone. This results in high interfacial strength. However, the toughness of the underlying glass can be low, leading to failure within the bulk material.

35.2.4 Polymers

A wide range of polymers is used for implantable devices. The first category is polymers with no cross-linking of polymer chains—called thermoplastics. Well-known examples are polyethylene (PE) and polymethylmethacrylate (PMMA). Ultrahigh-molecular-weight polyethylene (UHMWPE), so-called because it has a very long molecular chain, is very wear resistant and is used as a bearing material for the articulating surfaces of many artificial joints. Radiation sterilization and subsequent aging in storage can change the properties of PE.[22] Polyacetal, polyetheretherkeytone (PEEK), and polytetrafluroethylene (PTFE) have been used as components in hip replacement prostheses.[23] Bioresorbale polymers are used for pins and screws in treatment of musculoskeletal injuries (poly-L-lactite, PLLA),[24] and for bone plugs in modern cementing of implants.[25] The second category is polymers with heavy cross-linking of polymer chains (called thermosets), e.g., polyester (PET) is used in the augmentation of soft tissues in the musculoskeletal system.[26] Elastomers (e.g., polydimethyl siloxane, commonly called silicone) have occasional cross-linking and are characterized by the physical attribute that they can deform elastically to several hundred percent. This characteristic makes it suitable for one-piece prostheses for low-load-bearing joints such as the metacarpophalangeal,[27,28] and metatarsophalangeal[29] joints.

PMMA is used as an orthopedic bone cement for fixation of prostheses to bone. The material serves to interlock the prosthetic component to the bone. Polymerization takes place during the mixing of powder and liquid components, which is carried out in the operating theater. Mixing is critical to the

removal of pores and increasing the strength.[30] Hand-mixing has largely been superseded by vacuum mixing or centrifugation. The cement is injected into the bone using a gun while it is still in a doughy state. Formulations of "low-viscosity" cement, which delay the onset of the doughy stage thereby facilitating greater cement/bone interdigitation, have been developed.[31] As the polymerization reaction progresses, the material solidifies and the prosthesis is fixated into its final position. While PMMA cement has many advantages, there are negative attributes such as thermal necrosis of bone due to the exothermic polymerization reaction,[32] and PMMA undergoes damage accumulation as the cyclic load is applied over the lifetime of the patient.[33]

35.3 Design of Bone Prostheses

35.3.1 General Overview

Many strategies have been formulated for engineering design. The design problem may be decomposed into a series of hierarchical steps to be solved separately, e.g., Technical Systems Theory.[34] Less prescriptive approaches may include design reviews that integrate user requirements at several steps of the design process, e.g., Total Design.[35] All design strategies specify procedural rules that engineers may use as a basis for creating a new product. They may begin with a *needs analysis* leading to a *specification of objectives* for the design. Objectives may be categorized into *musts* and *wants*. Next, several different solutions are formulated, and the final step is the selection of the design solution that best meets the categorization of objectives.

This classical design process is complicated further by the requirements for quality system regulations. These specify the quality of procedures to be followed as part of the design process itself, in respect to documentation at each step, records of review meetings, and the results of implant testing procedures—including those necessary to meet industry standards.[36] Furthermore, a risk analysis may be carried out.[37] This information forms part of a *design history file* kept for each new implant design.[38]

Design issues particular to bone prostheses and implants may be enumerated as follows:

1. Magnitude and direction of the load on an implant changes in a highly complex manner, even during routine daily activities. Telemeterized implants have been used to retrieve *in vivo* data of loading on prostheses, e.g., hip,[39,40] shoulder,[41] and spine.[42] Telemetry may eventually provide daily loading data sets that can be used for standard assessment of implant performance.
2. Tissues react to the new mechanical environment created by the implant. Algorithms to predict tissue differentiation at implant interfaces[43] and fully three-dimensional (3D) predictions of bone remodeling are now available.[44]
3. Physiological joint kinematics are due to the very complex and synergistic interplay of joint surfaces, ligaments, and musculature. Precise replication of natural joints is impossible, particularly as soft tissues may have degenerated, or need to be excised to insert the implant. Designers must therefore develop new constraint mechanisms that allow functional range of motion, while maintaining kinematic stability.
4. The range of materials available for implantation is limited because of biocompatibility issues (see Section 35.2 above). These include reactivity to the bulk material and to particulate matter generated due to wear.
5. Surgical factors—the prosthesis must be implantable. New developments include surgical innovations in robotic instrumentation and minimally invasive surgery.[45,46]

35.3.2 Prosthesis and Implant Systems

In this section, the various designs of bone prostheses and implants are described. Implants may be classified as either temporary implants (those that will be removed or resorbed from the body after the bone has healed) or permanent implants (those that are intended to remain in the body indefinitely).

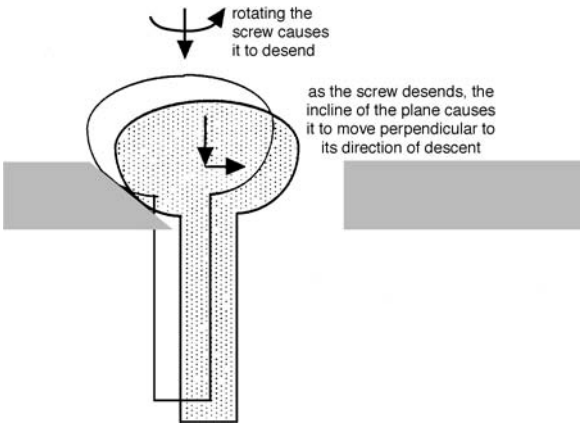

FIGURE 35.2 A longitudinal force to compress the bone fragments is created as the screw is tightened to the bone plate. (From Tencer, A. F. and Johnson, K. D., *Biomechanics in Orthopaedic Trauma,* Martin Dunitz, London, 1994. With permission.)

35.3.2.1 Temporary and Resorbable Implants

35.3.2.1.1 Bone Fixation Systems

Devices employed to fixate bone are (1) bone screws, (2) bone plates, (3) intramedullary (IM) nails, and (4) external fixators. There are a large number of these devices employed in orthopedics, reflecting the specific requirements of each bone and the variety of surgical opinion on how to treat a particular fracture. Tencer and Johnson[47] give a thorough description of the various systems.

Bone screws can be classified into cortical screws or cancellous screws. Design variables for screws are root diameter, pitch (axial motion per revolution), and thread profile.[48] Cancellous bone screws have larger threads and pitch than cortical bone screws because of the need to grip widely spaced trabeculae. The pullout strength of bone screws is also determined by the pilot drill-hole, which should not be too small (else screw breakage could occur) or too large (else screw purchase will be reduced).[47]

Bone plates are screwed directly onto the bone. Among the innovations proposed for these seemingly simple devices is the "compression plate," which achieves compression between the fracture ends by creating axial motion as the screw is tightened (Fig. 35.2).

IM nails are inserted into the intramedullary cavity of the long bones. Proximal and distal interlocking pins are used to stabilize the nail. IM nails are slightly curved to align with the natural curve of the long bone shaft—this, however, creates problems at insertion which can lead to bone splitting.[47] The cross section of the IM nail determines the rigidity and ease of insertion.[49]

External fixators stabilize a fracture by insertion of pins or wires through the skin on either side of the fracture site and connecting the pins with external sidebars. Pin diameter and thread design determine the pullout strength.[50] This method of fixation causes less surgical trauma and can facilitate better wound management than other methods.[51] Behrens[52] has classified fracture fixation devices as *uniplanar* (with sidebars in the same plane as the bone) and *multiplanar* (with sidebars surrounding the limb). Uniplanar devices are called *unilateral* if there is only one sidebar, or *bilateral* if there are two sidebars on either side of the limb. The advantage of the unilateral fixator is that there are fewer pin insertions through the skin and a correspondingly lower risk of infection—however, the mechanical stability of the bilateral fixator is greater. A multiplanar fixator, such as pioneered by the Russian orthopedic surgeon G. Ilizarov, uses tensioned wires rather than pins, thereby reducing the disturbance to the vascularity of the bone and reducing the problem of refracture at the holes when the fixator is removed.[47] Fig. 35.3 illustrates this kind of fixation system. Many experimental,[53–55] theoretical,[56,57] finite-element,[58,59] and animal studies,[60,61] have been reported on external fixation systems.

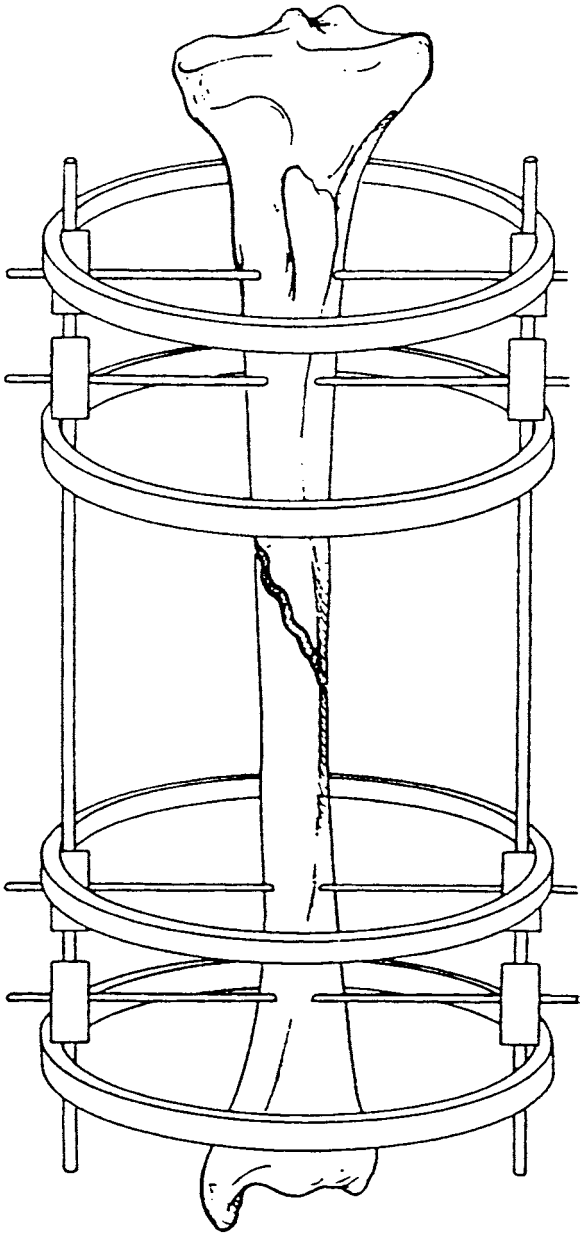

FIGURE 35.3 An external fixation system (circular configuration). (From Chao, E. Y. S. et al., *J. Biomech.,* 15, 971, 1982. With permission.)

All fixation systems alter the mechanical load transferred to bone callus. The mechanical forces transmitted to the callus influence bone regeneration during fracture healing. Beaupré et al.[62] showed that, as the callus stiffens, the fixator allows a greater proportion of the load to pass via the bone. It has been proposed[63] that the interfragmentary strain between the bone determines the tissue formed: low strains ($<2\%$) allow bone formation, higher strain causes cartilage, and excessive strains maintain granulation tissue. Pauwels[64] had earlier proposed a more complex theory implicating hydrostatic pressure in cartilage formation; recently, the influence of oxygen tension[65] and cell migration[66] have been included in biomechanical models of tissue regeneration.

35.3.2.1.2 Bone Substitute Materials

Bone graft implants are needed as a space filler in reconstructive surgery, or in spinal fusion. The available materials may be listed as follows: autograft taken from the patient, allograft taken from another human (either as chips or morselized[67]), xenograft taken from another species, or synthetic materials falling into two main categories:

1. Materials from conversion of naturally occurring materials, e.g., coralline materials,[68] which have full interconnectivity of pores and good pore distribution.
2. Entirely synthetic materials, e.g., artificially porous hydroxyapatites formed by various processing methods[69] or by replication of naturally porous cancellous bone.[70]

Bone materials have some disadvantages as grafts: autograft causes additional trauma to the patient and allograft and xenograft have risk of disease transmission. Synthetic materials have neither of these problems, but may lack appropriate porosity and pore interconnectivity,[71,72] with the exception of materials that directly replicate trabecular bone structure.[70]

Synthetic materials are made from hydroxyapatite/β-tricalcium phosphate (HA/β-TCP) composites. Since β-TCP is more resorbable than HA, the resorption rate of the implant can be designed by suitable ratio of these components. Greater porosities also favor more rapid resorption. Knowles and Bonfield[73] showed that these materials can be strengthened by addition of a glassy phase, although adding too much reduces the mechanical properties.[74] Morphogenetic proteins necessary to induce bone growth and blood vessel penetration of the graft may be added to synthetic materials,[75] and recent studies report using synthetic implants as a carrier for cells and growth factors.[76]

35.3.2.2 Permanent Implants for Total Joint Arthroplasty

A degenerated joint can be "cured" by replacing it with a prosthesis. Many attempts to design replacement implants were made over the centuries,[77] but serious problems persisted until the British orthopedic surgeon John Charnley advocated the use of PMMA as a fixation material[78] and PE as a bearing material.[79] Replacement of both sides of a joint creates a *total* joint arthroplasty, whereas replacement of one side only is called a *hemi*-arthroplasty.

The concepts of conformity and constraint are central to artificial joint design. The healthy hip joint, for example, is a ball-and-socket joint with high conformity and high constraint. The shoulder is also a ball-and-socket joint with highly conforming surfaces but, because the socket is shallow, it has low constraint.[80] Joints such as the knee are more complex with significantly different congruencies in different directions.[81] Highly constrained articulations can be designed using hinges (constant center of rotation). Hingeless joints can also be designed. Although they run the risk of dislocation, they are better able to reproduce natural joint kinematics.

35.3.2.2.1 Hip Replacement Prostheses

Many hundreds of different designs of hip joint prostheses are currently on the market.[82] They may be broadly classified into cemented or cementless devices, with fixation in the former achieved by cementing with PMMA (see Section 35.2.4) and in the latter by osseointegration (see Section 35.2.3). If cement is used for the femoral side and cementless fixation for the acetabular side, the implant is a "hybrid" design.[83] Fig. 35.4 shows a schematic of a cemented hip replacement. Stillwell et al.[84] give a description of the procedures and instrumentation involved.

Variations in prosthesis design include the size of the prosthesis head. Charnley[85] described the effect of head size: he proposed a small head because it would create a lower frictional torque than a larger head and thus reduce the potential for loosening (Fig. 35.5). However, smaller heads imply greater contact stresses on the polyethylene cup. The size of the head and the geometry of the neck determine the range of motion of the reconstruction. For a given neck geometry, a larger head size will permit a greater range of motion of the artificial joint.[86] As wear progresses, the head penetrates the acetabular cup, decreasing the range of motion. For these reasons, head diameter is a crucial design variable for which a compromise is required. Note also that the head may be removable from the tapered neck (modular prosthesis). The acetabular cup may have "metal-backing" which was introduced to create a more even stress transfer

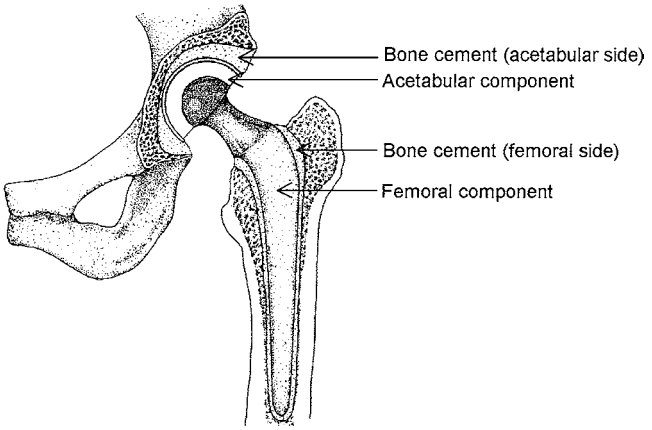

FIGURE 35.4 Total hip replacement involves replacement of both the acetabular and femoral sides. In this schematic diagram, both sides are fixated with cement. (Adapted from Hardinge, K., *Hip Replacement,* Oxford University Press, Oxford, 1983. With permission.)

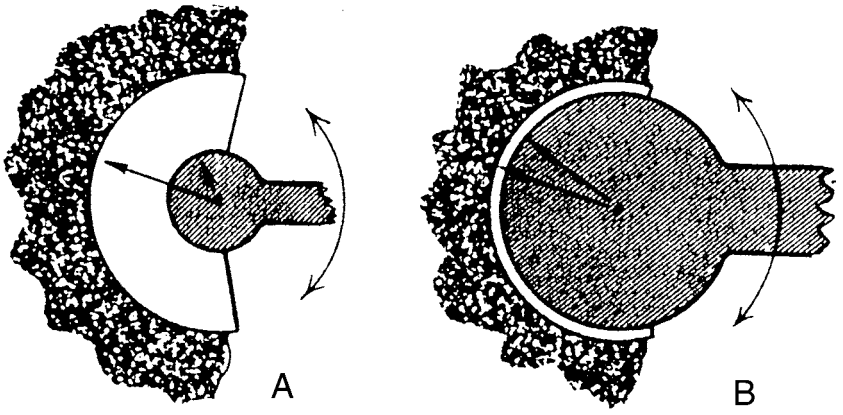

FIGURE 35.5 Illustrating how rotation of the socket against the bone is less likely with a small head and a thick socket than with a large head and a thin socket as a result of the differences in the moment of the frictional force as a result of the differences in radii of the parts. (From Charnley, J., *Lancet,* 1129, 1961. ©The Lancet Ltd. With permission.)

from the head to the acetabular bone, although this is not confirmed by stress analysis of implanted acetabuli.[87]

On the femoral side, cementless designs require a "canal-filling" stem of adequate fit with the bone to minimize interfacial micromotion and allow bone ingrowth.[88] For cemented femoral stems, the stem cross-sectional shape determines stress concentrations in the cement[89]—circular cross sections minimize stress concentrations but have the lowest resistance to slip within the cement mantle.[90] Stem shape also affects the pressure generated within the bone cement and, therefore, the interdigitation of the bone cement with the cancellous bone.[91] Another geometric difference between femoral components is the presence of a collar. The collar can either overhang the bone or just overhang the cement mantle, the latter being termed a semicollar.

The taper of the stem is also very different between prosthetic designs. The taper has at least two effects:

1. A steeper taper means that the proximal stem is more rigid than the distal stem. Huiskes and Boeklagen[92] have used stem taper as a control variable in an optimization process to minimize cement stresses; the so-called Scientific Hip prosthesis (SHP) was designed on this basis.

2. A steeper taper generates a greater wedging action of the stem within the medullary cavity.[93] The Exeter prosthesis, for example, facilitates distal movement within the bone cement. This requires a polished stem surface and the absence of a collar.[94, 95] Alternatively, if a collar is used with the objective of loading the calcar femorale (a phenomenon not confirmed by structural analyses[96,97]), it can be argued that a strong cement interface is required to prevent subsidence.[98] Chang et al.[99] found that such bonded stems have up to 60% lower cement stresses than unbonded stems.

Failure of artificial joints is a multifactorial process involving a cascade of biomechanical events. Huiskes[100] advances six *failure scenarios*, which provide a generic approach for viewing failure of all bone/prostheses systems. These failure scenarios are as follows:

1. *Accumulated Damage*: Accumulation of damage in prosthesis materials occurs during cyclic loading. Proof of damage accumulation in bone cement was provided by Jasty et al.,[101] who found partial cracking in autopsy-retrieved specimens. Experimental confirmation that the cracking process is gradual and continuous under bending loads[102] and torsional loads[103] has been provided. Damage may also accumulate within the prosthesis (leading to stem breakage) or on the interfaces.[104,105] Verdonschot and Huiskes[106] carried out a computer simulation of damage accumulation in the cement mantle of a hip replacement and found that debonding very much accelerates the damage accumulation rate. Precoating of the stem with a PMMA layer to reduce interfacial porosity may slow the rate of damage.[107]
2. *Particulate Reaction*: There are three possible sources of particles in joint replacement: wear of the articulating surfaces, abrasion of the PMMA/prosthesis/bone interfaces, and fretting between metal parts in modular prostheses.[108] For example, PE particles have been found at the cement/bone interface in acetabular cups where they initiate a macrophage inflammatory response and subsequent formation of a fibrous tissue layer.[109,110] The next event in this failure scenario is increased interfacial micromotion and mechanical loosening.
3. *Failed Ingrowth*: Failure of osseointegration to occur can be caused by large unbridgeable gaps between prosthesis and bone, or by excessive micromotion.
4. *Stress Shielding*: The implant takes load formerly transferred to the bone, thereby shielding the bone from the load and causing bone resorption. This process is most probably dependent on mechanical factors,[111] and has been observed in the proximal medial bone after hip replacement, and under the tibial component of knee replacements. While more flexible components have been proposed to prevent stress-shielding in the hip,[112] finite-element models predict that too flexible a stem creates unsustainable bone/prosthesis or bone/cement interface stresses,[113] which may lead to the failure scenario of damage accumulation (cemented implants) or failed ingrowth (cementless implants).
5. *Stress Bypass*: A prosthesis that is badly designed for a particular bone, or malsized, may transfer the loads in such a way as to bypass part of the bone entirely. Stress bypass may also result from localized osseointegration in uncemented devices—such "spot-welding" causes the load to bypass whatever bone tissue lies between the "weld" and the articulation.
6. *Destructive Wear*: Wear of the bearing surfaces may proceed to such an extent that the PE component "wears out." For example, the head may penetrate the acetabular cup in a hip replacement.

Obviously, the failure scenarios will proceed simultaneously, and the one that causes failure depends on the rate of progression of the active scenarios in a particular patient.

35.3.2.2.2 Knee Replacement Prostheses

The first total knee replacement (TKR) prostheses were hinged designs.[114] However, such high-constraint prostheses do not allow for rolling and sliding of the femoral condyles on the tibial plateau, which occurs in the healthy knee—because of this, high stresses are generated in the fixation causing premature loosening and occasional stem breakage.[115] Unconstrained designs were developed that replaced the femoral condyles with a metal component and the tibial plateau with a partially conforming PE component supported on a "tibial tray." The patella is also replaced in many designs. Walker and Sathasivam[116]

define these TKR types as one of the following:

1. Fixed-bearing condylar replacement with partially conforming surfaces, with or without the posterior cruciate ligament (PCL),
2. Mobile-bearing type, where the PE is free to slide and rotate on the tibial tray,
3. A rotating-platform type, where the PE component is allowed to rotate only about an axis, and is prevented from translating.

Knee prostheses with partially conforming surfaces require close attention to stability: the "laxity" of the healthy knee should be maintained while guarding against "dislocation."[117] Delp et al.[118] show that TKRs that "substitute" the PCL increase anterior-posterior (AP) stability with higher "tibial spines," and show also that the radius of the femoral component (posterior part) in the AP direction has a role in preventing dislocation. Knee prostheses with mobile bearings rely on the natural soft tissues and ligaments to limit and direct joint movement. Goodfellow and O'Connor[119] report that mobile-bearing prostheses that retain a functional anterior cruciate ligament (ACL) have superior survival rates. Another consideration to be borne in mind is that the moment of the muscles about the knee is determined by the tibiofemoral contact point, which is in turn determined by the radii of the femoral and tibial components in the AP plane and the functionality of the ligaments.

The conformity of the surfaces, in both AP and medial-lateral (ML) directions, influences the polyethylene stress—with the ML conformity having more effect.[120] Bartel et al.[121] substantiate this conclusion with results from a finite-element analysis of eight prosthesis designs that show that nonconforming prostheses generate the greatest polyethylene stresses 1 to 2 mm below the surface. However, Blunn et al.[122] suggest more conforming surfaces in the AP direction to reduce cyclic sliding and hence the destructive wear failure scenario. It seems that the cyclic nature of the load must be included in analyses of PE failure, and strain/damage accumulation functions have been used for this purpose.[123,124]

Fixation of knee components is achieved by intramedullary stems (which may be cemented), or posterior and/or anterior pegs, posts, or blades, often employing porous coating. Furthermore, each "compartment" of the tibia may be replaced separately (bicompartmental prostheses) or only the medial compartment may be replaced (unicompartmental knee replacement). Walker et al.[125] analyzed the stability of several configurations of tibial fixations, (Fig. 35.6). Finite-element modeling has also been employed, e.g., to identify stress-shielded regions below the tibial component.[126]

35.3.2.2.3 Shoulder Replacement Prostheses

Early designs of shoulder replacement prostheses were either constrained ball-and-socket arrangements or unconstrained prostheses with shallow glenoid sockets and large humeral heads.[127] Considering the biomechanical aspects of total shoulder arthroplasty, Walker[128] described the design conflict between the degree of containment required for stability and the need to achieve a physiological range of motion. The required degree of containment (hence, constraint) depends on the quality of the "rotator cuff" surrounding the joint. Recent designs mainly follow the unconstrained concept[129] as constrained designs gave unacceptable loosening rates. The main outstanding problem is glenoid component radiolucency, which limits the longevity to such an extent that many surgeons recommend hemi-arthroplasty of the shoulder.

Both the humeral and glenoid components may be cemented. Design variations include keeled and pegged designs of the glenoid component. A finite-element analysis by Lacroix et al.[130] has shown that pegged designs have lower cement stresses than keeled designs in normal bone, but that the reverse is true if the glenoid bone is of lower density (osteoporotic) (Fig. 35.7). Implant selection therefore depends on an assessment of bone quality.

35.3.2.2.4 Elbow Replacement Prostheses

The elbow poses some challenges for replacement because three bones meet at the joint: the humerus on one side articulating with the ulna (trochlea) and the radius (capitellum) on the other. Most often, just the humerus/ulnar articulation is replaced, although some designs replace both. Early designs of hinged (high constraint) prostheses gave high loosening rates.[131] Failures occurred due to high forces at the elbow[132] and because the range of motion needed for daily activities was not facilitated.[133] According

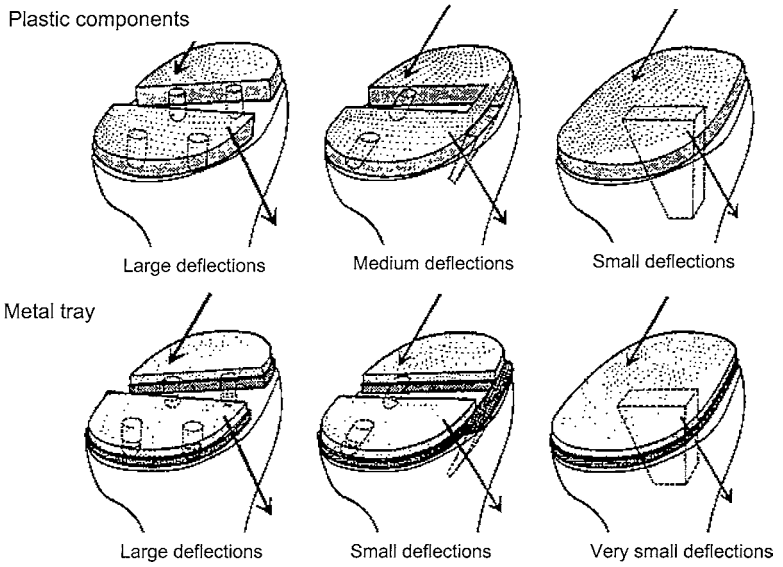

FIGURE 35.6 (Top row) From left to right, compartmental components (with two pegs each), compartmental components with an anterior cross-bridge and an anterior blade, and a one-piece component with a central peg. Loading applied by rotation of a bicondylar femoral roller. (Bottom row) Same as above but with metal backing. (From Walker, P. S. et al., *J. Bone Joint Surg.,* 63A, 258, 1981. With permission.)

to Coonrad,[134] the artificial constraints produced by the hinge caused high stresses in the cemented fixation, whereas unconstrained designs require intact carpsuloligamentous structures and run the risk of dislocation.[134] The solution of semiconstrained designs with various degrees of mediolaterial and rotary laxity has been pursued.[135–137] These hinge-type designs are sometimes termed *sloppy hinges*. Although fixations may still prove problematic,[138] the semiconstrained implants do seem to demonstrate a superior long-term performance, with Gill and Morrey[137] reporting 86% of results in the "good or excellent" category at 10 to 15 years (Coonrad–Murray design) (Fig. 35.8).

35.3.2.2.5 Ankle Replacement Prostheses

Total ankle arthroplasty replaces the joint formed by the tibia and the talus. Early designs were characterized by a rapid failure rate leading to the view that ankle arthrodesis (fusion of the joint) rather than arthroplasty should be used.[139] However, more recent studies have reported greater than 70% survivorship at 14 years using cemented fixation and congruent cylindrical surfaces.[140] Uncemented, semiconstrained prostheses have also recently reported good results.[141]

35.3.2.2.6 Wrist Replacement Prostheses

Total wrist arthroplasty (TWA) replaces the articulation formed at the radial head and the scaphoid and lunate bones of the wrist. A metacarpal component inserts distally into the intramedullary cavity of the metacarpals and a proximal component inserts into the medullary cavity of the radius. Costi et al.[142] describe the various prosthesis designs. One popular design is due to Volz,[143] whose design involves resection of the scaphoid and lunate and one half of the capitate in an attempt to maintain the center of rotation of the normal wrist. Other cemented designs (trispherical and biaxial) employ the semiconstrained option, but dislocations have been reported.[144] The uncemented design of Meuli[145] is shown in Fig. 35.9. Many authors report TWA to be technically demanding, with a high complication rate.[145,146]

35.3.2.3 Dental Implants

"Implantology," the science of dental implants, is well developed and success rates for dental implants are very high compared with orthopedic implants.[147] Implants are used to replace teeth in both the mandible and the maxilla. Most systems operate as follows: a gingival incision is made and exposure of

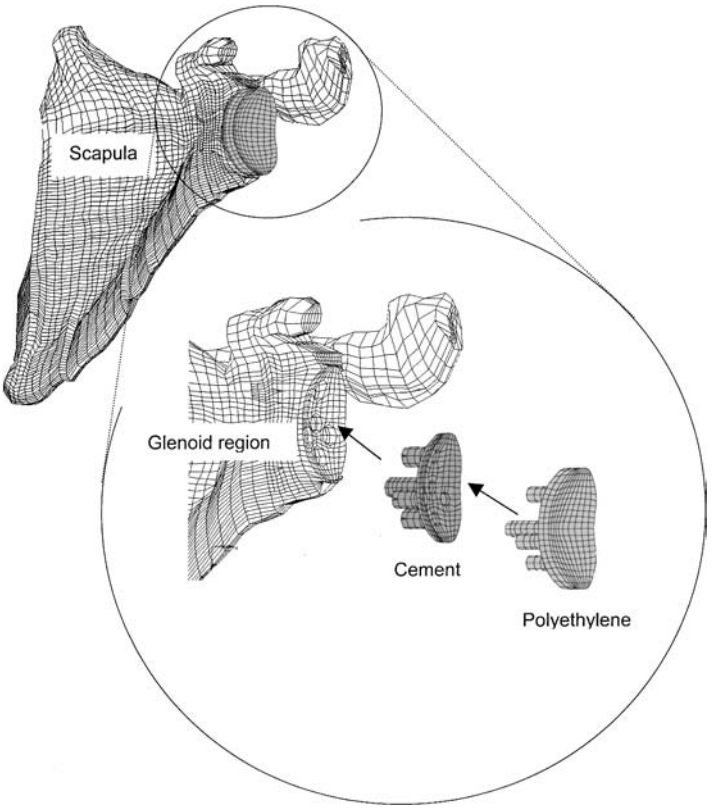

FIGURE 35.7 FE mesh of the scapula, showing a detail of a pegged glenoid prosthesis. (Courtesy of Linda Murphy, Trinity College, Dublin.)

the bone followed by a guide-drilling procedure and a series of subsequent drilling steps to prepare a cavity accurately to the required diameter and depth. The implant is then either screwed or tapped into place. The implant is filled with a temporary cover screw, and the skin sutured to cover the implant. The implant is then left in this unloaded state in the "submerged" position for a period (usually several weeks) allowing the process of ossteointegration to proceed.[148] Next the implant is exposed, the covering screw removed, and an abutment placed in position to allow soft-tissue healing before the aesthetic component is finally screwed into position. Stresses and adaptive bone remodeling around dental implants have been reported; see Vander Sloten et al.[149]

35.3.2.4 Middle-Ear Implants

The smallest bones in the body are the three ossicles. The malleus, incus, and stapes (commonly called the hammer, anvil, and stirrup) need to be replaced if they degenerate, which usually happens as a result of fluid retention in the middle ear. Prostheses come in two categories: partial ossicular replacement prostheses (PORPs) and total ossicular replacement prostheses (TORPs).[150] A PORP is used if the stapes superstructure is intact—it replaces the malleus and incus by connecting the tympanic membrane to the head of the stapes. A TORP additionally replaces the stapes superstructure and therefore connects the tympanic membrane directly to the stapes foot plate. Materials used for middle-ear implants have been reviewed by Blayney et al.[151] and include hyodroxyapatite,[152] alumina,[153] and various polymers and bioactive glasses.[150] The mechanical behavior of the middle ear was thoroughly investigated by von Békésy,[154] who identified a lever action for the ossicular chain. A recent analysis has shown that this lever action is not regained in prosthetic reconstruction.[155,156] More research is required to optimize the biofunctionality of these implants.[157]

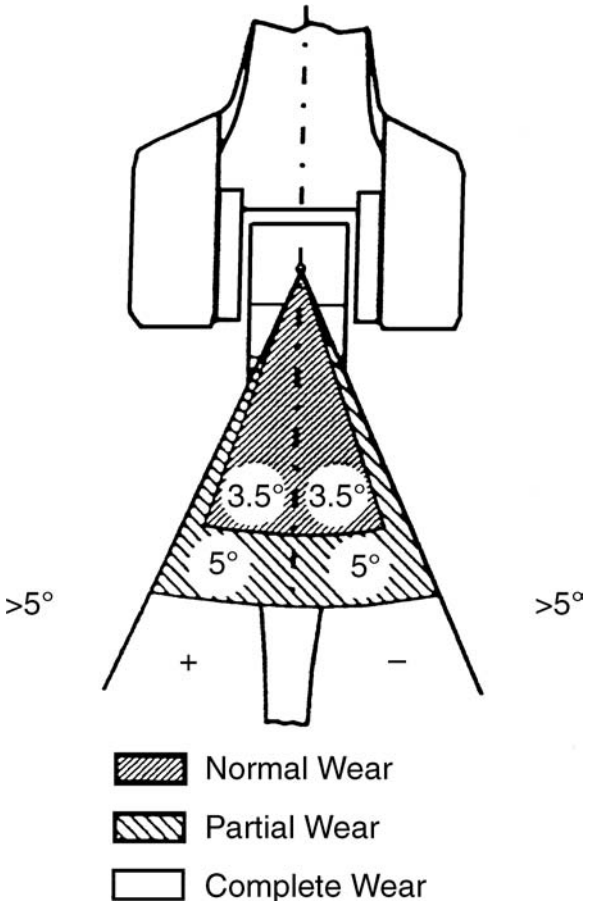

FIGURE 35.8 Coonrad–Murray elbow replacement design. It has seven degrees of varus-valgus laxity, but this increases as the wear of the polyethylene bushings progresses. (From Gill, D. R. J. and Morrey, B. F., *J. Bone Joint Surg.,* 80A, 1327, 1998. With permission.)

35.4 Analysis and Assessment of Implants

The objective of preclinical testing is to ensure the biofunctionality of new implants, to screen out inferior designs before clinical trials, and to demonstrate the superiority of new designs over competing devices at an early stage of product development. Postoperative assessment also plays a critical role in the process of implant innovation by eliminating inferior designs at the earliest possible stage.[100]

35.4.1 Preclinical Tests

35.4.1.1 Analytical Methods

Analyses of bone/implant systems using the theory of elasticity was reported by Bartel,[158] who showed that, among other things, the magnitude of the shear stresses in the cement layer of an intramedullary fixation is of similar magnitude to the normal stresses, and that the Young's modulus of the prosthesis has a significant influence on cement and bone stresses. Elasticity theory has also been used to determine contact stresses in polyethylene in hip and knee replacement.[120] Beams-on-elastic-foundations theory has been used to investigate stress transfer in intramedullary fixation. Huiskes' comprehensive analyses[32] showed that intramedullary fixation could be thought of as having a proximal region of

FIGURE 35.9 The Meuli Wrist prostheses, an uncemented design. (From Meuli, H. C., *Clin. Orthop.,* 342, 77, 1997. With permission.)

prostheses-to-bone load transfer, a midregion behaving like a composite beam, and a distal region of bone-to-prosthesis load transfer.

35.4.1.2 Finite Element Methods

Finite-element (FE) modeling techniques have advanced rapidly since they were introduced to bone mechanics in 1972.[126,159,160] FE analyses of femoral and acetabular hip components, surface hip arthroplasty, knee arthroplasty, arthroplasty of upper extremity joints, external and internal fixation, and structured implant interfaces were reviewed by Prendergast.[126] The reasons for recent rapid developments include:

1. Combined with digitized computed tomography (CT) scanning, accurate representation of complex bone geometries can be achieved. Skinner et al.[161] use the voxels of the CT image to generate a finite-element model automatically, whereas others use only the boundary definition of the bone, e.g., femur,[162] scapula,[130] acetabulum.[163]
2. The method allows parametric variation of design parameters in a way that experimental methods do not—this allows designers to compare the effects of implant geometry rapidly, e.g., hip,[99,164,165] tibial plateau,[166] and acetabular cup.[167] For example, it has been predicted that stiffer hip prostheses generate lower bone cement stresses,[168,169] that surface finish affects interface motions,[170] and that porous coating can reduce interface motion in cementless hips by more than 50%.[171]
3. FE models can be combined with bone remodeling algorithms to predict possible long-term tissue reactions around implants. Iterative computations can be used to predict the time course of periimplant tissue response, including bone remodeling and tissue differentiation. Computer simulation of bone remodeling around implants was first reported by Huiskes et al.,[172] who used strain energy density as a remodeling stimulus to compute "surface" remodeling around an intramedullary implant. They showed that higher stiffness prostheses have a greater potential for surface resorption. Further studies showed the influence of prosthesis material properties[173] and bonding characteristics[174] on bone adaptation around a hip femoral stem in terms of change in density (internal remodeling). Van Rietbergen et al.[175] compared remodeling in dogs with 3D external and internal bone remodeling simulation and found excellent correlation. Further 3D remodeling

simulations showed the effect of prosthesis stem material[162] and extent of porous coating.[176] Under certain circumstances, the postoperative stress pattern can predict the evolution of bone density without the need for a simulation.[177] Other approaches to predict peri-implant bone remodeling use

- An "effective stress" remodeling stimulus,[178]
- A damage accumulation remodeling stimulus,[179,180]
- A strain rate remodeling stimulus.[181]

35.4.1.3 Strain Measurement Methods

Strain measurement techniques are often used to determine the stress distribution in bone tissue surrounding an implant, or on the implanted material itself. Strain gauges have been used, despite the problems such as strain gauge misalignment, reinforcement effects of the gauges (e.g., on PE), and the impossibility of measuring strain at a point when the strain gradient is high.[182] Optical methods have several advantages, including the possibility of full-field results.[183,184]

Most often strain gauge analyses are performed on cadaver bone.[185–187] Strain gauge measurement of models built to several times life size have been reported, which allow use of embedded strain gauges in the cement mantle, e.g., for the knee[188] and hip.[189] Recent studies have found excellent correlation between FE and strain gauging.[190] Cristofolini[191] gives a review of the studies that address stress-shielding in the proximal femur, showing that there are great differences in the boundary conditions in the many studies. An interesting study of strain gauging of implanted femora retrieved at autopsy showed that remodeling had not succeeded in returning strain to "anywhere near normal," even 7.5 years after surgery.[192]

35.4.1.4 Simulators

Simulators are machines designed to assess the performance of prostheses under cyclic loading. Simulators must replicate the motion and loading on an implant in the biological environment. They may be divided into two classes: those concerned with wear and those concerned with loosening.

35.4.1.4.1 Wear

Wear is the progressive loss of material from surfaces due to relative movement. Mechanisms of wear are abrasion, adhesion, and fatigue wear, see Dowson.[193] Because of the sensitivity of the wear rate to many extraneous factors, experiments to determine the rate of material removal must replicate the *in vivo* loading and environmental conditions as closely as possible.

According to LaBerge et al.,[194] 11 hip joint wear simulator designs are in existence, differing in how many tests can be run simultaneously, and in how well *in vivo* kinematics are approximated. The Leeds hip simulator applies three axes of loading in a complex three-dimensional motion,[195] and has been used, for example, to show that traditional metal-on-polymer bearings have a higher wear rate than ceramic-on-polymer articulations.[193] The orientation of the articulation during the test, and the precise nature of the lubricant have been reported to be critical.[196]

Knee simulators have been reviewed by Walker and Blunn.[117] Similar considerations of *in vivo* kinematics and environmental lubricational conditions apply as with hip simulators except that the unconstrained nature of most contemporary knee prostheses poses a special challenge. Walker et al.[197] adopted a solution of controlling flexion-extension and restraining other degrees-of-freedom by simulated soft tissues.

35.4.1.4.2 Loosening

Loosening due to the damage accumulation failure scenario involves a progressive loss of mechanical integrity of the implant/bone construct. Devices to measure the 3D relative motion of the femoral stem and the bone under cyclic loading have been developed.[88,198–201] Studies which apply a form of muscle loading have also been reported.[192,202,203] However, the difficulty of applying physiological loading and the problems of reproducible prosthesis implantation[204] and of establishing a failure criterion makes quantitative simulation of loosening a difficult prospect.

35.4.2 Clinical Assessment

Ideally, a randomized clinical trial (RCT) should form part of a clinical assessment but RCT is problematic in surgery for the following reasons:[205]

1. It is difficult if not impossible to blind patients in surgical vs. nonsurgical treatments.
2. Sham surgical procedures are not considered ethically acceptable by many.
3. Patients may refuse to accept randomization.
4. There is a "learning curve" to an operative technique, which will confound the results.

Unbiased scientific assessment of implants is all the more critical to the innovation process because of the difficulties with RCT.[206]

35.4.2.1 Gait Analysis

Gait analysis has the potential to aid outcome assessment of lower-limb joint replacement.[207] For example, Andriacchi et al.[208] report a study showing a change in the stride-length/walking relationship after TKR. In a clinical study, Hilding et al.[209] reported that patients whose knee prosthesis were in the risk category for loosening had increased knee flexion moments compared with nonrisk patients; other gait parameters such as gait speed or stride length were unaffected. They advocated gait analysis to identify these patients prior to surgery.

35.4.2.2 Radiographic Assessment

Radiographic assessment of a bone prosthesis is used to identify implant "loosening," and to determine bone reactions around the implant. Radiolucent lines between the implant and the bone can be interpreted as indicating a loosening process, such as the formation of a soft fibrous tissue. Brand et al.[210] have drawn attention to the qualitative nature of this assessment. Dual-energy X-ray absorptiometry (DEXA) is more accurate, and is frequently used to assess bone remodeling around implants. For example, Ang et al.[211] compared bone remodeling around a metallic hip stem and a polymeric hip stem using DEXA and showed greater bone mineral density around the polymeric stem. Cohen and Rushton[212] describe how errors can occur during DEXA measurements. Finally, image analysis, in combination with FE modeling, has the potential for highly accurate assessment of bone reactivity, including architectural changes, *in vivo*.

35.4.2.3 Roentgen Stereophotogrammetry Analysis

Radiostereometry analysis, or RSA, is a method of measuring the relative movement of two rigid bodies. Originally used by Dr. Göran Selvik[213] to measure the relative motion of bones, it can also be applied to determination of the relative movement between prostheses and bone. Huiskes and Verdonschot[44] give a simple description of how RSA works. Two X-ray tubes are placed so as to project an image of an object onto two X-ray films. The object to be studied has tantalium pellets attached to it (because tantalium has high density) and is surrounded by a "calibration cage." This cage has markers on a control plane, which are used to determine the foci of the X-ray beams and markers on a fiducial plane used to define the laboratory coordinate system. When the foci and laboratory frame are known, the position of the object (i.e., the position of its marker pellets) can be calculated as the intersection point of the two lines joining the foci to the image point cast by the pellet on each X-ray film. Several developments have been made to optimize the procedure.[214] Kiss et al.[215] employ a method that does not have pellets on the prosthesis but instead uses prosthesis landmarks (e.g., center of the head) to define its position.

RSA has been applied to THR and TKR to determine both migration (permanent movement of the prosthesis) and inducible displacement (recoverable deflection under load). For example, Ryd et al.[216] studied a screw-fixated tibial component in TKA and found migrations and inducible displacement of the order of 0.6 and 0.3 mm, respectively. Kärrholm and co-workers report RSA of hip femoral stems for cementless[217] and cemented fixation.[218] In the latter study of 84 hips, they correlated subsidence rates of 1.2 mm or more at 2 years with a greater than 50% probability of revision. RSA has also shown the complex nature of cemented stem migration within the femur.[219]

TABLE 35.2 The Harris Hip Score

Factor	Score
Pain (seven categories with points for each)	0–40
Function (Gait, 33 points and activities, 14 points)	0–47
Range of motion	0–5
Absence of deformity	0–8
Total	*0–100*

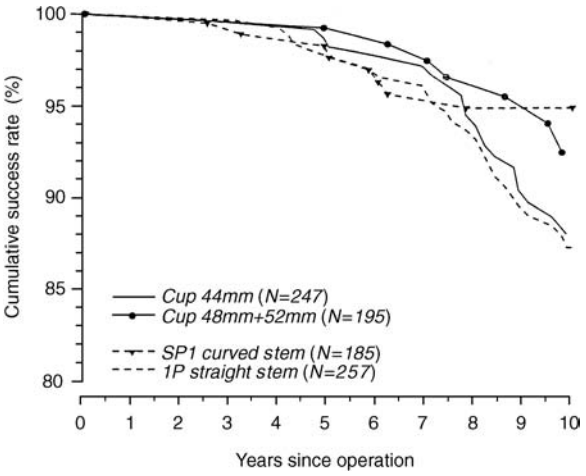

FIGURE 35.10 Survival curves for the acetabular and femoral components in 444 Lubinus arthroplasties in 398 patients. (From Partio, E. et al., *Clin. Orthop.,* 303, 140, 1994. With permission.)

35.4.2.4 Retrieval Analysis

Retrieval of prostheses at revision (e.g., knee,[220] hip[221,222]) or after death[223] allows inspection of failure phenomena such as wear.[224] Strain analysis to determine if the fixation was performing adequately can also be carried out.[112,192]

35.4.2.5 Outcome Analysis

Outcome analysis measures how well an implant is functioning by combining patient information on pain and mobility with surgical results. For example, with hip replacement there are various "hip scores." One widely used score is the Harris hip score,[225] in which the status of the hip is given a single number (Table 35.2). For example, Edidin et al.[226] report a mean Harris hip score of 91 at 51 months for a hip replacement where the femoral component was cemented in the proximal region only. Murray[227] gives a review of the Harris, Charnley, Iowa, and Mayo hip scores.

35.4.2.6 Survival Analysis

Survival analysis measures the time to some end point—usually the revision of the prosthesis. Problems encountered are loss of patients to follow-up, the small numbers of patients, and the difficulty of defining the end point. Recently published results from national hip registries in Europe, such as the Swedish registry,[228] have removed the first two problems. However, the third—the difficulty of defining an end point—can be controversial; different decisions of when to revise are possible. Fig. 35.10 shows survival curves for the Lubinus prosthesis (W. Link, Hamburg, Germany) where revision is taken as the end point.[229] In this study, different modifications to the stem and cup are compared, and failure rates associated with the femoral and acetabular sides have been differentiated. Hench and Wilson[230] present an extensive review of the performance of bone prostheses and implants in orthopedics, dentistry, and otolaryngology.

35.5 Future Directions

This chapter has shown that replacement or augmentation of bone by prostheses has led to a prolific number of devices with one common aim—to alter the load transfer in bone tissue. Bone prostheses and implants will continue to be used until the capability for growing replacement tissues outside the body by tissue engineering becomes well established. Even when that happens, implants will almost certainly be required as scaffolds in many cases, and determination of the appropriate load sharing between the scaffold and the tissue will still require a thorough understanding of the issues raised in this chapter.[231] These implants will be biomechanically "active" in the sense that they will act in synergy with the cells in the surrounding bone.[232] Modeling the performance of these implants prior to animal trials and clinical trials will become more important,[233] and attention will be further focused on preclinical testing methods.[234]

Acknowledgments

Dr. David C. Tancred and Dr. Suzanne A. Maher are thanked for their comments on the content of this chapter.

References

1. Williams, D.F., *Definitions in Biomaterials,* Elsevier, Amsterdam, 1987.
2. Skalak, R., Biomechanical considerations in osseointegrated prostheses, *J. Prosthet. Dent.,* 49, 843, 1983.
3. Huiskes, R., Principles and methods of solid biomechanics, in *Functional Behaviour of Orthopaedic Biomaterials,* Ducheyne, P. and Hastings, G.W., Eds., CRC Press, Boca Raton, FL, 1984, 51.
4. Walker, P.S., *Human Joints and Their Artificial Replacements,* Charles C Thomas: Springfield, IL, 1977.
5. Horowitz, E. and Mueller, E., Regulation of medical devices, in *An Introduction to Bioceramics,* Hench, L.L. and Wilson, J., Eds., World Scientific, Singapore, 1993, 335.
6. Crisp, S., The Medical Device Directives and their impact on the development and manufacturing of medical implants, *Proc. I. Mech. E. Part H,* 210, 233, 1996.
7. Mishra, N., Yahiro, M., and Morrey, B.F., Food and Drug Administration's regulation of orthopaedic devices, *J. Bone Joint Surg.,* 76A, 919, 1994.
8. Williams, D.F., General concepts of biocompatibility, in *Handbook of Biomaterial Properties,* Black, J. and Hastings, G., Eds., Chapman & Hall, London, 1998, 481.
9. Litsky, A.S. and Spector, M., Biomaterials, in *Orthopaedic Basic Science,* Simon, S.R., Ed., American Academy of Orthopaedic Surgeons, Rosemont, IL, 1994, 447.
10. LeGeros, R.Z., Biodegradation and bioresportion of calcium phosphate ceramics, *Clin. Mater.,* 14, 65, 1993.
11. Coury, A.J., Chemical and biochemical degradation of polymers, in *Biomaterials Science,* Ratner, B.D., Hoffman, A.S., Schoen, F.J., and Lemons, J.E., Eds., Academic Press, New York, 1996, 243.
12. Pizzoferrato, A., Ciapetti, G., Stea, S., and Toni, A., Cellular events in the mechanism of prosthesis loosening, *Clin. Mater.,* 7, 51, 1991.
13. Søballe, K., Hansen, E.S., B-Rasmussen, H., and Bünger, C., Tissue ingrowth into titanium and hydroxyapatite coated implants during stable and unstable mechanical conditions, *J. Orthop. Res.,* 10, 285, 1992.
14. Black, J., Systemic effects of biomaterials, *Biomaterials,* 5, 11, 1984.
15. Long, M. and Rack, H.J., Titanium alloys in total joint replacement—a materials science perspective, *Biomaterials,* 19, 1621, 1998.
16. Hulbert, S.F., The use of alumina and zirconia in surgical implants, in *An Introduction to Bioceramics,* Hench, L.L. and Wilson, J., Eds., World Scientific, Singapore, 1993, 25.

17. Clarke, I.C. and Willmann, G., Structural ceramics in orthopaedics, in *Bone Implant Interface,* Older, J., Ed., Springer, Berlin, 1990, 203.
18. Jarcho, M., Calcium phosphate ceramics as hard tissue prosthetics, *Clin. Orthop.,* 157, 259, 1981.
19. Willmann, G., Medical grade hydroxyapatite: state of the art, *Br. Ceram. Trans.,* 95, 212, 1996.
20. Tancred, D.C., Carr, A.J., and McCormack, B.A.O., Development of new synthetic bone graft, *J. Mater Sci. Mater. Med.,* 9, 819, 1998.
21. Hench, L.L. and Wilson, J., Properties of bioactive glasses and glass-ceramics, in *Handbook of Biomaterial Properties,* Black, J. and Hastings, G., Eds., Chapman & Hall, London, 1998, 355.
22. Kurtz, S.M., Bartel, D.L., and Rimnac, C.M., Postirradiation aging affects stress and strain in polyethylene components, *Clin. Orthop.,* 350, 209, 1998.
23. Maisrtelli, G.L., Polymers in orthopaedic surgery, in *Bone Implant Interface,* Cameron, H.U., Ed., CV Mosby, St. Louis, 1994, chap. 8.
24. Törmälä, P., Pohjonen, T., and Rokkanen, P., Bioabsorbable polymers: materials technology and surgical applications, *Proc. Inst. Mech. Eng. Part H,* 212, 101, 1998.
25. Prendergast, P.J., Birthistle, P., Waide, D.V., and Girish Kumar, N.V., An investigation of the performance of Biostop G and Hardinge bone plugs, *Proc. Inst. Mech. Eng. Part H,* 213, 361, 1999.
26. Fujikawa, K., Iseki, F., and Seedhom, B.B., Arthroscopy after anterior-cruciate reconstruction with the Leeds-Keio ligament, *J. Bone Joint Surg.,* 71B, 566, 1989.
27. Goldner, J.L. and Urbaniak, J.R., The clinical experience with silicone-Dacron metacarpophalangeal and interphalangeal joint prostheses, *J. Biomed. Mater. Res. Symp.*, 137, 1973.
28. Swanson, A.B. and Herndon, J.H., Flexible (silicone) implant arthroplasty of the metacarpophalangeal joint of the thumb, *J. Bone Joint Surg.,* 59A, 362, 1977.
29. Lewis, G. and Alva, P., Stress analysis of a flexible one-piece type first metatarsophalangeal joint implant, *J. Am. Podiatr. Med. Assoc.,* 83, 29, 1993.
30. Smith, S.W., Estok, D.M., and Harris, W.H., Total hip arthroplasty with the use of second-generation cementing techniques—an eighteen year follow-up study, *J. Bone Joint Surg.,* 80A, 1632, 1988.
31. Miller, J. and Anderson, J.A., Advances in cementing techniques in total hip arthroplasty, in *The Art of Total Hip Arthroplasty,* Stillwell, W.T., Ed., Grune & Stratton, Orlando, 1987, chap. 19.
32. Huiskes, R., Some fundamental aspects of human joint replacement, *Acta Orthop Scand.,* Suppl. 185, 1980.
33. Murphy, B.P. and Prendergast, P.J., Measurement of non-linear micro-crack accumulation rates in polymethylacrylate bone cement under cyclic loading, *J. Mater. Sci. Mater. Med.,* 10, 779, 1999.
34. Hubka, V., *Theorie Technicher Systeme,* Springer, Berlin, 1983. Translated as Hubka, V. and Eder, W.E., *Theory of Technical Systems,* Springer, New York, 1988.
35. Pugh, S. and Morley, I.E., *Total Design,* Design Division, University of Strathclyde, Glasgow, 1998.
36. Paul, J.P., Development of standards for orthopedic implants, *Proc. Inst. Mech. Eng. Part H,* 211, 119, 1997.
37. Passey, R.D.C., Foresight begins with failure mode and effect analysis, *Med. Device Technol.,* 88, 1999.
38. Slemon, D., Lecture delivered to the Institution of Engineers of Ireland, November, 1998.
39. Bergmann, G., Graichen, F., and Rohlmann, A., Hip joint loading during walking and running, measured in two patients, *J. Biomech.,* 26, 969, 1993.
40. Davy, D.T., Kotzar, G.M., Brown, R.H., Heiple, K.G., Goldberg, V.M., Heiple, K.G., Jr., Berilla, J., and Berstein, A.H., Telemetric force measurements across the hip after total arthroplasty, *J. Bone Joint Surg.,* 70A, 45, 1988.
41. Kummer, F.J., Lyon, T.R., and Zuckerman, J.D., Development of a telemetrerized shoulder prosthesis, *Clin. Orthop.,* 330, 31, 1996.
42. Rohlmann, A., Bergmann, G., Graichen, F., and Neff, G., Braces do not reduce loads on internal spinal fixation devices, *Clin. Biomech.,* 14, 97, 1999.
43. Prendergast, P.J., Huiskes, R., and Søballe, K., Biophysical stimuli on cells during tissue differentiation at implant interfaces, *J. Biomech.,* 30, 539, 1997.

44. Huiskes, R. and Verdonschot, N., Biomechanics of artificial joints: the hip, in *Basic Orthopedic Biomechanics,* Mow, V.C. and Hayes, W.C., Eds., Lippincott-Raven, New York, 1997, chap. 11.
45. Barger, W.L., Bauer, A., and Börner, M., Primary and revision total hip replacement using the Robodoc® system, *Clin. Orthop.,* 354, 82, 1998.
46. Nolte, L.P., Zamorano, L., Visarius, H., Berlemann, U., Langlotz, F., Arm, E., and Schwarzenbach, O., Clinical evaluation of a system for precision enhancement in spine surgery, *Clin. Biomech.,* 10, 293, 1995.
47. Tencer, A.F. and Johnson, K.D., *Biomechanics in Orthopaedic Trauma,* Martin Dunitz, London, 1994.
48. Perren, S.M., Cordey, J., Baumgart, Rahn, B.A., and Schatzker, J., Technical and biomechanical aspects of screws used for bone surgery, *Int. J. Orthop. Trauma,* 2, 31, 1992.
49. Johnson, K.D., Tencer, A.F., and Sherman, M.C., Biomechanical factors affecting fracture stability and femoral bursting in closed intramedullary nailing of femoral shaft fractures, with illustrative case presentations, *J. Orthop. Trauma,* 1, 1, 1987.
50. Halsey, D., Fleming, B., Pope, M.H., Krag, M., and Kristiansen, T., External fixator pin design, *Clin. Orthop.,* 278, 305, 1992.
51. Sisk, T.D., External fixation. Historic review, advantages, disadvantages, complications, and indications, *Clin. Orthop.,* 180, 15, 1983.
52. Behrens, F., A primer of fixation devices and configurations, *Clin. Orthop.,* 241, 5, 1989.
53. Churches, A.E., Tanner, K.E., and Harris, J.D., The Oxford external fixator: fixator stiffness and the effects of pin loosening, *Eng. Med.,* 14, 3, 1985.
54. McCoy, M.T., Chao, E.Y.S., and Kasman, R.A., A comparison of the mechanical performance of external fixators, *Clin. Orthop.,* 180, 23, 1983.
55. Prendergast, P.J., Toland, S.J., and Corrigan, J., Finite element analysis and mechanical testing of external fixator designs, *Proc. Inst. Mech. Eng. Part H,* 208, 103, 1994.
56. Evans, M. and Kenwright, J., The Oxford external fixation system, in *The Severely Injured Limb,* Ackroyd, C.E., O'Connor, B.T., and de Bruyn, P.F., Eds., Churchill-Livingstone, Edinburgh, 1983, chap. 10.
57. Huiskes, R. and Chao, E.Y.S., Guidelines for external fixation frame rigidity and stresses, *J. Orthop. Res.,* 4, 68, 1986.
58. Chao, E.Y.S., Kasman, R.A., and An, K.N., Rigidity and stress analysis of fracture fixation devices, *J. Biomech.,* 15, 971, 1982.
59. Juan, J.A., Prat, J., Vera, P., Hoyos, J.V., Sanchez-Lacuesta, J., Peris, J.L., Dejoz, R., and Alepuz, R., Biomechanical consequences of callus development in Hoffmann, Wagner, Orthofix, and Illizarov external fixators, *J. Biomech.,* 25, 995, 1992.
60. Goodship, A.E. and Kenwright, J., The influence of induced micromovement upon the healing of experimental tibial fractures, *J. Bone Joint Surg.,* 67B, 650, 1985.
61. Aro, H.T., Kelly, P.J., Lewallan, D.G., and Chao, E.Y.S., The effects of physiologic dynamic compression on bone healing under external fixation, *Clin. Orthop.,* 256, 260, 1990.
62. Beaupré, G.S., Hayes, W.C., Jofe, M.H., and White III, A.A., Monitoring fracture site properties with external fixation, *J. Biomech. Eng.,* 105, 120, 1983.
63. Perren, S.M., Physical and biological aspects of fracture healing with special reference to internal fixation, *Clin. Orthop.,* 138, 175, 1979.
64. Pauwels, F., *Biomechanics of the Locomotor Apparatus,* Springer, Berlin, 1980.
65. Carter D.R., Beaupré, G.S., Giori, N.J., and Helms, J.A., Mechanobiology of skeletal regeneration, *Clin. Orthop.,* 355S, 41, 1998.
66. Lacroix, D., Prendergast, P.J., Marsh, D., and Li, G., A model to simulate the regenerative and resorption phases of long bone fracture healing, *Trans. Orthop. Res. Soc.,* 25, 869, 2000.
67. Older, J., Ed., *Bone Implant Grafting,* Springer, London, 1992.
68. Roy, D.M. and Linehan, S.K., Hydroxyapatite formed from coral skeletal carbonate by hydrothermal exchange, *Nature,* 247, 220, 1974.

69. Shors, E.C. and Holmes, R.E., Porous hydroxyapatite, in *An Introduction to Bioceramics,* Hench, L. L., and Wilson, J., Eds., World Scientific, Singapore, 1993, chap. 10.
70. Tancred, D.C., McCormack, B.A.O., and Carr, A.J., A synthetic bone implant microscopically identical to cancellous bone, *Biomaterials,* 19, 2303, 1998.
71. van Blitterswijk, C.A., Grote, J.J., Kuijpers, W., Daems, W.Th., and de Groot, K., Macropore tissue ingrowth: a quantitative study on hydroxyapatite ceramic, *Biomaterials,* 7, 137, 1986.
72. Schliephake, H., Neukam, F.W., and Klosa, D., Influence of pore dimensions on bone ingrowth into porous hydroxyapatite blocks used as bone graft substitutes, *Int. J. Oral Maxillofacial Surg.,* 20, 53, 1991.
73. Knowles, J.C. and Bonfield, W., Development of glass-reinforced hydroxyapatite with enhanced mechanical poperties: the effect of glass composition and its relationship to phase changes, *J. Biomed. Mater. Res.,* 27, 1591, 1993.
74. Tancred, D.C., McCormack, B.A.O., and Carr, A.J., A quantitative study of the sintering and mechanical properties of hydroxyapatite/phosphate glass composites, *Biomaterials,* 19, 1735, 1998.
75. Habal, M.B. and Reddi, A.H., *Bone Grafts and Bone Substitutes,* Saunders, London, 1992.
76. Liebergall, M., Young, R.G., Ozawa, N., Reese, J.H., Davy, D.W., Goldberg, V.M., and Caplan, A.I., The effects of cellular manipulation and TGF-β in a composite bone graft, in *Bone Formation and Repair,* Brighton, C., Friedlaender, G., and Lane, J.M., Eds., American Academy of Orthopaedic Surgeons, Rosemont, IL, 1994, 367.
77. Walker, P.S., Historical development of artificial joints, in *Human Joints and Their Artifical Replacements,* Charles C Thomas, Springfield, 1977, 253.
78. Charnley, J., Anchorage of the femoral head prosthesis to the shaft of the femur, *J. Bone Joint Surg.,* 42B, 28, 1960.
79. Charnley, J., The long-term results of low-friction arthroplasty of the hip performed as a primary intervention, *J. Bone Joint Surg.,* 54B, 61, 1972.
80. Mow, V.C., Ratcliffe, A., and Poole, A.R., Cartilage and diarthrodial joints as paradigms for hierarchical materials and structures, *Biomaterials,* 13, 67, 1992.
81. Huiskes, R., Kremers, J., de Lange, A., Woltring, H.J., Selvik, G., and van Rens, Th.J.G., Analytical stereophotogrammetric determination of three-dimensional knee-joint geometry, *J. Biomech.,* 18, 559, 1985.
82. Murray, D.W., Carr, A.J., and Bulstrode, C.J., Which primary total hip replacement? *J. Bone Joint Surg.,* 77B, 520, 1995.
83. Harris, W.H., Hybrid total hip replacement, *Clin. Orthop.,* 333, 155, 1996.
84. Stillwell, W.T., Barber, F.S., and Mitchell, S.D., Instrumentation for total hip arthroplasty, in *The Art of Total Hip Arthroplasty,* Stillwell, W.T., Ed., Grune & Stratton, Orlando, 1987, chap. 7.
85. Charnley, J., Arthroplasty of the hip. A new operation, *Lancet,* May, 1129, 1961.
86. Keller, A., The pros and cons of heads with diameters of 32 mm or larger, in *Technical Principles, Design and Safety of Joint Implants,* Buchhorn, G.H. and Willert, H.-G., Eds., Hogrefe & Huber, Bern, 1994, 96.
87. Dalstra, M. and Huiskes, R., The influence of metal backing in cemented cups, *J. Orthop. Res.,* 16, 272, 1991.
88. Hua, J. and Walker, P.S., Relative motion of hip stems under load, *J. Bone Joint Surg.,* 76A, 95, 1994.
89. Crowninsheild, R.D., Brand, R.A., Johnston, R.C., and Milroy, J.C., The effect of femoral stem cross-sectional geometry on the cement stresses in total hip reconstruction, *Clin. Orthop.,* 146, 71, 1980.
90. Swanson, S.A.V., Mechanical aspects of fixation, in *The Scientific Basis of Joint Replacement,* Swanson, S.A.V. and Freeman, M.A.R., Eds., Pitman Medical, Turnbridge Wells, 1977, 130.
91. Maher, S.A. and McCormack, B.A.O., Quantification of interdigitation at bone cement/cancellous bone interfaces in cemented femoral reconstructions, *Proc. Inst. Mech. Eng. Part H,* 213, 347, 1999.
92. Huiskes, R. and Boeklagen, R., Mathematical shape optimization of hip prosthesis design, *J. Biomech.,* 22, 793, 1989.

93. Lee, A.J.C., Implants for fixation with and without a collar, in *Technical Principles, Design and Safety of Joint Implants,* Buchhorn, G.H. and Willert, H.-G., Eds., Hogrefe & Huber, Bern, 1994, 128.
94. Ling, R.S.M., The use of a collar and precoating on cemented femoral stems in unnecessary and detrimental, *Clin. Orthop.,* 285, 73, 1992.
95. Huiskes, R., Verdonschot, N., and Nivbrant, B., Migration, stem shape, and surface finish in cemented total hip arthroplasty, *Clin. Orthop.,* 355, 103, 1998.
96. Prendergast, P.J. and Taylor, D., Stress analysis of the proximo-medial femur after total hip replacement, *J. Biomed. Eng.,* 12, 379, 1990.
97. Fagan, M.J. and Lee, A.J.C., The role of the collar on the femoral stem of cemented hip replacements, *J. Biomed. Eng.,* 8, 295, 1986.
98. Harris, W.H., Is it advantageous to strengthen the cement-metal interface and use a collar for cemented femoral components of total hip replacements? *Clin. Orthop.,* 285, 67, 1992.
99. Chang, P.B., Mann, K.A., and Bartel, D.L., Cemented femoral stem performance—effects of proximal bonding, geometry, and neck length, *Clin. Orthop.,* 355, 57, 1998.
100. Huiskes, R., Failed innovation in total hip replacement. Diagnosis and proposals for a cure, *Acta Orthop. Scand.,* 64, 699, 1993.
101. Jasty, M., Maloney, W.J., Bragdon, C.R., O'Connor, D.O., Haire, T., and Harris, W.T., The initiation of failure in cemented femoral components of hip arthroplasties, *J. Bone Joint Surg.,* 73B, 551, 1991.
102. McCormack, B.A.O. and Prendergast, P.J., Microdamage accumulation in the cement layer of hip replacements under flexural loading, *J. Biomech.,* 32, 467, 1999.
103. McCormack, B.A.O., Prendergast, P.J., and O'Dwyer, B., Fatigue of cemented hip replacements under torsional loads, *Fatigue Fract. Eng. Mater. Struct.,* 22, 33, 1999.
104. Mann, K.A., Bartel, D.L., Wright, T.M., and Ingraffea, A.R., Mechanical characteristics of the stem-cement interface, *J. Orthop. Res.,* 9, 798, 1991.
105. McCormack, B.A.O. and Prendergast, P.J., An analysis of crack propagation paths at implant/bone-cement interfaces, *J. Biomech. Eng.,* 118, 579, 1996.
106. Verdonschot, N. and Huiskes, R., The effects of cement-stem debonding in THA on the long term failure probability of cement, *J. Biomech.,* 30, 795, 1997.
107. Stone, M.H., Wilkinson, R., and Stother, I.G., Some factors affecting the strength of the cement-metal interface, *J. Bone Joint Surg.,* 71B, 217, 1989.
108. Viceconti, M., Baleani, M., Squarzoni, S., and Toni, A., Fretting wear in a modular neck hip prostheses, *J. Biomed. Mater. Res.,* 35, 207, 1997.
109. Schmalzreid, T.P., Kwong, L.M., Jasty, M., Sedlacek, R.C., Haire, T.C., O'Connor, D., Bragdon, C. R., Kabo, J.M., Malcolm, A.J., and Harris, W.H., The mechanism of loosening in cemented acetabular components in total hip arthroplasty, *Clin. Orthop.,* 274, 60, 1992.
110. Aspenberg, P. and Van der Vis, H., Migration, particles, and fluid pressure. A discussion of causes of prosthetic loosening, *Clin. Orthop.,* 352, 75, 1998.
111. Huiskes, R., Bone remodelling around implants can be explained as an effect of mechanical adaptation, in *Total Hip Revision Surgery,* Galante, J.O., Rosenberg, A.G., and Callaghan, J.J., Eds., Raven Press, New York, 1995, chap. 15.
112. Wilke, H.-J., Seiz, R.S., Bombelli, M., Claes, L., and Dürselen, L., Biomechanical and histomorphological investigations on an isoleastic hip prosthesis after an eight month implantation period, *J. Mater. Sci. Mater. Med.,* 5, 384, 1994.
113. Huiskes, R., The various stress patterns around press-fit, ingrown, and cemented femoral stems, *Clin. Orthop.,* 261, 27, 1990.
114. Insall, J.N., Historical development, classification and characteristics of knee prostheses, in *Surgery of the Knee,* 2nd ed., Inssall, J.N., Windsor, R.E., Scott, W.N., Kelly, M.A., and Aglietti, P., Eds., Churchill-Livingstone, New York, 1993, 677.
115. Longton, E.B. and Seedhom, B.B., Total knee replacement, in *An Introduction to the Biomechanics of Joints and Joint Replacements,* Dowson, D. and Wright, V., Eds., Mechanical Engineering Publications Ltd., London, 1981, chap. 19.

116. Walker, P.S. and Sathasivam, S., The design of guide surfaces for fixed-bearing and mobile-bearing knee replacements, *J. Biomech.,* 32, 27, 1999.
117. Walker, P.S. and Blunn, G.W., Biomechanical principles of total knee replacement design, in *Basic Orthopaedic Biomechanics,* Mow, V.C. and Hayes, W.C., Eds., Lippincott-Raven, New York, 1997, chap. 12.
118. Delp, S.L., Kocmond, J.H., and Stern, S.H., Tradeoffs between motion and stability in posterior substituting knee arthroplasty design, *J. Biomech.,* 28, 1155, 1995.
119. Goodfellow, J. and O'Connor, J., The anterior cruciate ligament in knee arthroplasty. A risk-factor with unconstrained meniscal prostheses, *Clin. Orthop.,* 276, 245, 1992.
120. Bartel, D.L., Bicknell, V.L., and Wright, T.M., The effect of conformity, thickness, and material on the stresses in ultra-high molecular weight components for total joint replacement, *J. Bone Joint Surg.,* 68A, 1041, 1986.
121. Bartel, D.L., Rawlinson, J.J., Burstein, A.H., Ranawat, C.S., and Flynn, W.F., Jr., Stresses in polyethylene components of contemporary total knee replacements, *Clin. Orthop.,* 317, 76, 1995.
122. Blunn, G.W., Walker, P.S., Joshi, A., and Hardinge, K., The dominance of cyclic sliding in producing wear in total knee prostheses, *Clin. Orthop.,* 273, 253, 1991.
123. Reeves, E.A., Barton, D.C., FitzPatrick, D.P., and Fisher, J., A two-dimensional model of cyclic strain-accumulation in ultra-high molecular weight polyethylene knee replacements, *Proc. Inst. Mech. Eng. Part H,* 212, 189, 1998.
124. Sathasivam, S. and Walker, P.S., The conflicting requirements of laxity and conformity in total knee replacement, *J. Biomech.,* 32, 239, 1999.
125. Walker, P.S., Reilly, D., Thatcher, J., Ben-Dov, M., and Ewald, F.C., Fixation of tibial components of knee prostheses, *J. Bone Joint Surg.,* 63A, 258, 1981.
126. Prendergast, P.J., Finite element models in tissue mechanics and orthopaedic implant design, *Clin. Biomech.,* 12, 343, 1997.
127. Reeves, B.F., Total shoulder replacement, in *An Introduction to the Bio-mechanics of Joints and Joint Replacements,* Dowson, D. and Wright, V., Eds., Mechanical Engineering Publications, London, 1981, 207, chap. 20.
128. Walker, P.S., Some bioengineering considerations of prosthetic replacement for the gleno-humeral joint, in *Symposium on Total Joint Replacement of the Upper Extremity,* Inglis, A.E., Ed., CV Mosby, St. Louis, 1982, chap. 3.
129. McCullagh, P.J.J., Biomechanics and design of shoulder arthroplasty, *Proc. Inst. Mech. Eng.,* 209, 207, 1996.
130. Lacroix, D., Murphy, L.A., and Prendergast, P.J., Three-dimensional finite element analysis of glenoid replacement prostheses: a comparison of keeled and pegged anchorage systems, *J. Biomech. Eng.* 122, 430, 2000.
131. Lewis, G., The elbow joint and its total arthroplasty. Part I. A state-of-the-art review, *Bio-Med. Mater. Eng.,* 6, 353, 1996.
132. Amis, A.A., Dowson, D., and Wright, V., Elbow joint force predictions for some strenuous isometric actions, *J. Biomech.,* 13, 765, 1980.
133. Morrey, B.F., Askew, L.J., An, K.N., and Chao, E.Y.S., A biomechanical study of normal elbow joint motion, *J. Bone Joint Surg.,* 63A, 872, 1981.
134. Coonrad, R.W., History of total elbow arthroplasty, in *Symposium on Total Joint Replacement of the Upper Extremity,* Inglis, A.E., Ed., CV Mosby, St. Louis, 1982, chap. 8.
135. Souter, W.A., A new approach to total elbow arthroplasty, *Eng. Med.,* 10, 59, 1981.
136. King, G.W.J., Itoi, E., Risung, F., Neibur, G.L., Morrey, B.F., and An, K-N., Kinematics and stability of the Norway elbow: a cadaveric study, *Acta Orthop. Scand.,* 64, 657, 1993.
137. Gill, D.R.J. and Morrey, B.F., The Coonrad-Morrey total elbow arthroplasty in patients who have rheumatoid arthritis, *J. Bone Joint Surg.,* 80A, 1327, 1998.

138. Sjödén, G.O., Lundberg, A., and Blomgren, G.A., Late results of the Souter-Strathclyde total elbow prosthesis in rheumatoid arthritis. 6/19 implants loose after 5 years, *Acta Orthop. Scand.,* 66, 391, 1995.
139. Hamblen, D.L., Editorial: can the ankle joint be replaced? *J. Bone Joint Surg.,* 67B, 689, 1985.
140. Kofoed, H. and Sørensen, T.S., Ankle arthroplasty for rheumatoid arthritis and osteoarthritis. Perspective long term study of cemented replacements, *J. Bone Joint Surg.,* 80B, 328, 1998.
141. Pyevich, M.T., Saltzman, C.L., Callaghan, J.J., and Alvine, F.G., Total ankle arthroplasty: a unique design, *J. Bone Joint Surg.,* 80A, 1410, 1998.
142. Costi, J., Krishnan, J., and Pearcy, M., Total wrist arthroplasty: A quantitative review of the last 30 years, *J. Rheumatol.,* 25, 451, 1998.
143. Volz, R.G., Total wrist arthroplasty: a clinical and biomechanical analysis, in *Symposium on Total Joint Replacement of the Upper Extremity,* Inglis, A.E., Ed., CV Mosby, St. Louis, 1982, chap. 23.
144. O'Flynn, H.M., Rosen, A., and Weiland, A.J., Failure of the hinge mechanism of a trispherical total wrist arthroplasty. A case report and review of the literature, *J. Hand Surg.,* 24A, 156, 1999.
145. Meuli, H.C., Total wrist arthroplasty. Experience with a noncemented prosthesis, *Clin. Orthop.*, 342, 77, 1997.
146. Gellman, H., Hontas, R., Brumfield, R.H., Tozzi, J., and Conaty, J.P., Total wrist arthroplasty in rheumatoid arthritis. A long term clinical review, *Clin. Orthop.,* 342, 71, 1997.
147. Norton, M., *Dental Implants,* Quintessence Publishing, London, 1995, 33.
148. Albrektsson, T., Brånemark, P.-I., Hansson, H.A., and Lindström, J., Osseointegrated titanium implants, *Acta Orthop. Scand.,* 52, 155, 1981.
149. Van der Sloten, J., Hobatho, M.-C., and Verdonck, P., Applications of computer modelling for the design of orthopaedic, dental and cardiovascular biomaterials, *Proc. Inst. Mech. Eng. Part H,* 212, 489, 1998.
150. Kobel, K.D., Ossicular replacement prostheses, in *Clinical Performance of Skeletal Prostheses,* Hench, L.L. and Wilson, J., Eds., Chapman & Hall, London, 1996, chap. 13.
151. Blayney A.W., Williams, K.R., Erre, J.-P., Lesser, T.H.J., and Portmann, M., Problems in alloplastic middle-ear reconstruction, *Acta Otolaryngol.* (Stockholm), 112, 322, 1992.
152. Grote, J.J., Reconstruction of the middle-ear with hydroxyapatite implants.: Long term results, *Ann. Otol. Rhinol. Laryngol.,* 144, 12, 1990.
153. Yamamoto, E. and Iwanaga, M., Soft tissue reaction to ceramic ossicular replacement prostheses, *J. Laryngol. Otol.,* 101, 897, 1987.
154. von Békésy G., *Experiments on Hearing,* McGraw-Hill, New York, 1960.
155. Prendergast, P.J., Ferris, P., Rice, H.J., and Blayney, A.W., Vibroacoustic modelling of the middle ear using the finite-element method, *Audiol. Neurootol.,* 4, 185, 1999.
156. Ferris, P. and Prendergast, P.J., Middle-ear dynamics before and after ossicular replacement, *J. Biomech.,* 33, 581, 2000.
157. Hüttenbrink, K.-B., Ed., *Middle-Ear Mechanics in Research and Otosurgery,* Dresden University of Technology, Dresden, 1997.
158. Bartel, D.L., Stress analysis: effects of geometry in bone-implant systems, *Bull. Hosp. Joint Dis.,* 40, 90, 1977.
159. Huiskes, R. and Chao, E.Y.S., A survey of finite element models in biomechanics: the first decade, *J. Biomech.,* 16, 385, 1983.
160. Gilbertson, L.G., Goel, V.J., Kong, W.Z., and Clausen, J.D., Finite element models in spine biomechanics research, *Crit. Rev. Biomed. Eng.,* 23, 411, 1995.
161. Skinner, H.B., Kim, A.S., Keyak, J.H., and Mote, C.D., Jr., Femoral prosthesis implantation induces changes in bone stress that depend on the extent of porous coating, *J. Orthop. Res.,* 12, 553, 1994.
162. Husikes, R., Weinans, H., and van Rietbergen, B., The relationship between stress shielding and bone resorption around total hip stems and the effects of flexible materials, *Clin. Orthop.,* 274, 124, 1992.

163. Dalstra, M., Biomechanical Aspects of the Pelvic Bone and Design Criteria for Acetabular Prostheses., Ph.D. thesis, University of Nijmegen, 1993.
164. Huiskes, R. and Vroomen, W., A standardized finite element model for routine comparative evaluations of femoral hip prostheses, *Acta Orthop. Belg.,* 52, 258, 1986.
165. Fyhrie, D.P., Carter, D.R., and Schurman, D.J., Effects of ingrowth, geometry, and material on stress transfer under porous coated hip surface replacements, *J. Orthop. Res.,* 6, 425, 1988.
166. Cheal, E.J., Hayes, W.C., Lee, C.H., Snyder, B.D., and Miller, J., Stress analysis of a condylar knee tibial component: influence of metaphyseal shell properties and cement injection depth, *J. Orthop. Res.,* 3, 424, 1985.
167. Kurtz, S.M., Edidin, A.A., and Bartel, D.L., The role of backside polishing, cup angle, and polyethylene thickness on the contact stress in metal backed acetabular components, *J. Biomech.,* 30, 639, 1997.
168. Rohlmann, A., Mössner, U., Bergmann, G., and Köbel, R., Effects of design and material properties on stresses in hip endoprostheses, *J. Biomed. Eng.,* 9, 77, 1987.
169. Prendergast, P.J., Monaghan, J., and Taylor, D., Materials selection in the artificial hip joint using finite element analysis, *Clin. Mater.,* 4, 361,1989.
170. Kuiper, J.H. and Huiskes, R., Friction and stem stiffness affect dynamic interface motion in total hip replacement, *J. Orthop. Res.,* 14, 36–43, 1996.
171. Keaveny, T.M. and Bartel, D.L., Effects of porous coating, with and without collar support, on early relative motion for cementless hip prostheses, *J. Biomech.,* 26, 1355, 1993.
172. Huiskes, R., Weinans, H., Grootenboer, H.J., Dalstra, M., Fudala, B., and Slooff, T.J., Adaptive bone remodleling theory applied to prosthetic design analysis, *J. Biomech.,* 20, 1135, 1987.
173. Weinans, H., Huiskes, R., and Grootenboer, H.J., Effects of material properties of femoral components on bone remodelling, *J. Orthop. Res.,* 10, 845, 1990.
174. Weinans, H., Huiskes, R., and Grootenboer, H.J., Effects of fit and bonding characteristics of femoral stems on adaptive bone remodelling, *J. Biomech. Eng.,* 116, 393, 1994.
175. Van Rietbergen, B., Huiskes, R., Weinans, H., Sumner, D.R., Turner, T.M., and Galante, J.O., The mechanism of bone remodelling and resorption around press-fitted THA stems, *J. Biomech.,* 26, 369, 1993.
176. Huiskes, R. and van Rietbergen, B., Preclinical testing of total hip stems—the effects of coating placement, *Clin. Orthop.,* 319, 64, 1995.
177. Kuiper, J.H. and Huiskes, R., The predictive value of stress shielding for quantification of adaptive bone resorption around hip replacements, *J. Biomech. Eng.,* 119, 228, 1997.
178. Orr, T.E., Beaupré, G.S., Carter, D.R., and Schurman, D.J., Computer predictions of bone remodelling around porous-coated implants, *J. Arthroplasty,* 5, 191, 1990.
179. Prendergast, P.J. and Taylor, D., Design of intramedullary prostheses to prevent bone loss: predictions based on damage stimulated remodelling, *J. Biomed. Eng.,* 14, 499, 1992.
180. McNamara, B.P., Taylor, D., and Prendergast, P.J., Computer prediction of adaptive bone remodelling around noncemented femoral prostheses: the relationship between damage-based and strain-based algorithms, *Med. Eng. Phys.,* 19, 454, 1997.
181. Luo, G., Sadegh, A.M., Alexander, H., Jaffe, W., Scott, D., and Cowin, S.C., The effect of surface roughness on the stress adaptation of trabecular architecture around a cylindrical implant, *J. Biomech.,* 32, 275, 1999.
182. Little, E.G., Strain gauge measurement, in *Strain Measurement in Biomechanics,* Miles, A.W. and Tanner, K.E., Eds., Chapman & Hall, London, 1992, chap. 3.
183. Orr, J.F. and Shelton, J.C., Eds., *Optical Measurement Methods in Biomechanics,* Chapman & Hall, London, 1997.
184. Lennon, A.B., Prendergast, P.J., Whelan, M., and Forno, C., Use of grating interferometry for validation of finite element models and to investigate residual strain in polymethylacrylate, in *Computer Methods in Biomechanics and Biomedical Engineering IV,* J. Middleton, Ed., Gordon and Breach, Amsterdam (in press).

185. Oh, I. and Harris, W.H., Proximal strain distribution in the loaded femur, *J. Bone Joint Surg.,* 60A, 75, 1978.
186. Huiskes, R., Janssen, J.D., and Slooff, T.J., A detailed comparison of experimental and theoretical stress analyses of the human femur, in *Mechanical Properties of Bone,* Cowin, S.C., Ed., American Society of Mechanical Engineers, New York, 1981, 211.
187. Bourne, R.B. and Finlay, J.B., The influence of tibial component intramedullary stems and implant-cortex contact on the strain distribution of the proximal tibia following total knee arthroplasty, *Clin. Orthop.,* 208, 95, 1986.
188. Little, E.G., Kneafsey, A.G., Lynch, P., and Kennedy, M., The design of a model for a three dimensional stress analysis of the cement layer beneath a tibial plateau of a knee prosthesis, *J. Biomech.,* 18, 157, 1985.
189. Colgan, D., McTague, D., O'Donnell, P., and Little, E.G., The effect of the transverse component of the hip reaction on cement mantle stresses in a model of an implanted Exeter prosthesis, *J. Strain Anal.,* 31, 205, 1996.
190. Stolk, J., Verdonschot, N., Cristofolini, L., Firmati, L., Toni, A., and Huiskes, R., Strains in composite hip reconstructions obtained through FEA and experiments correspond closely, *Trans. Orthop. Res. Soc.,* 25, 0515, 2000.
191. Cristofolini, L., A critical analysis of stress shielding evaluation of hip prostheses, *Crit. Rev. Biomed. Eng.,* 25, 409, 1997.
192. Engh, C.A., O'Connor, D., Jasty, M., McGovern, T.F., Bobyn, J.D., and Harris, W.H., Quantification of implant micromotion, strain shielding, and bone resorption with porous-coated anatomic medullary locking femoral prostheses, *Clin. Orthop.,* 285, 13, 1992.
193. Dowson, D., A comparative study of the performance of metallic and ceramic femoral head components in total replacement hip joints, *Wear,* 190, 171, 1995.
194. LaBerge, M., Medley, J.B., and Rogers-Foy, J.M., Friction and wear, in *Handbook of Biomaterials Evaluation,* 2nd ed., van Rencum, A.F., Ed., Taylor & Francis, London, 1999, 171.
195. Bigsby, R.J. A., Hardaker, C.S., and Fisher, J., Wear of ultra-high molecular weight polyethylene acetabular cups in a physiological hip joint simulator in the anatomical position using bovine serum as a lubricant, *Proc. Inst. Mech. Eng. Part H,* 211, 265, 1997.
196. Wang, A., Essner, A., Polineni, V.K., Sun, D.C., Stark, C., and Dumbleton, J.H., Lubrication and wear of ultra-high molecular weight polyethylene in total joint replacements, in *New Directions in Tribology,* Hutchings, I.M., Ed., Mechanical Engineering Publications, London, 1997, 443.
197. Walker, P.S., Blunn, G.W., Broome, D.R., Perry, J., Watkins, A., Sathasivam, S., Dewar, M.E., and Paul, J.P., A knee simulating machine for performance evaluation of total knee replacements, *J. Biomech.,* 30, 83, 1997.
198. Schneider, E., Kinast, C., Eulenberger, J., Wyder, D., Eskilsson, G., and Perren, S.M., A comparative study of the initial stability of cementless hip prostheses, *Clin. Orthop.,* 248, 200, 1989.
199. Berzins, A., Sumner, D.R., Andriacchi, T.P., and Galante, J.O., Stem curvature and load angle influence the relative bone-implant motion of cementless femoral stems, *J. Orthop. Res.,* 11, 758, 1993.
200. Bühler, D.W., Berlemann, U., Lippuner, K., Jaeger, P., and Nolte, L.-P., Three dimensional primary stability of cementless femoral stems, *Clin. Biomech.,* 12, 75, 1997.
201. Maher, S.A., Prendergast, P.J., Waide, D.V., Reid, A.J., and Lyons, C.G., Development of an experimental procedure for pre-clinical testing of cemented hip replacements, in *Advances in Bioengineering,* American Society of Mechanical Engineers, New York, 1999, 139–140.
202. Burke, D.W., O'Connor, D.O., Zalenski, E.B., Jasty, M., and Harris, W.H., Micromotion of cemented and uncemented femoral components, *J. Bone Joint Surg.,* 73B, 33, 1991.
203. Munting, E. and Verhelpen, M., Mechanical simulator for the upper femur, *Acta Orthop. Belg.,* 59, 123, 1993.
204. Maher, S.A., Prendergast, P.J., Reid, A.J., Waide, D.V., and Toni, A., Design and validation of a machine for reproducible precision insertion of femoral prostheses for pre-clinical testing, *J. Biomech. Eng.,* 122, 203, 2000.

205. Grace, P.A., Men, medicine, and machines. The third Samuel Haughton lecture, *Ir. J. Med. Sci.,* 166, 152, 1997.
206. Prendergast, P.J. and Maher, S.A., Issues in pre-clinical testing of implants, in *Advances in Materials and Processing Technologies 99,* Hashmi, M.S.J. and Looney, L. Eds., Dublin City University, Dublin, 1999, 1195–1202.
207. Paul, J.P., *Biomechanics of Joint Replacement Implants,* Queen Margaret College, Edinburgh, 1993.
208. Andriacchi, T.P., Natarajan, R.N., and Hurwitz, D.E., Musculoskeletal dynamics, locomotion, and clinical applications, in *Basic Orthopaedic Biomechanics,* Mow, V.C. and Hayes, W.C., Eds., 2nd ed., Lippincott-Raven, New York, 1997, chap. 2.
209. Hilding, M.B., Lanshammar, H., and Ryd, L., Knee joint loading and tibial component loosening. RSA and gait analysis in 45 osteoarthritic patients before and after TKA, *J. Bone Joint Surg.,* 78B, 66, 1996.
210. Brand, R.A., Pedersen, D.R., and Yoder, S.A., How definition of "loosening" affects the incidence of loose total hip reconstructions, *Clin. Orthop.,* 210, 185, 1986.
211. Ang, K.C., Das De, S., Goh, J.C.H., Low, S.L., and Bose, K., Periprosthetic bone remodelling after cementless total hip replacement. A prospective comparison of two different implant designs, *J. Bone Joint Surg.,* 79B, 675, 1997.
212. Cohen, B. and Rushton, N., Accuracy of DEXA measurement of bone-mineral density after total hip-arthroplasty, *J. Bone Joint Surg.,* 77B, 479, 1995.
213. Selvik, G., A Roentegen Stereophotogrammetric Method for the Study of the Kinematics of the Skeletal System, Ph.D. thesis, University of Lund, 1974. Reprinted in *Acta Orthop. Scand.,* Suppl. 232, 60, 1989.
214. Kärrholm, J., Roentgen stereophotogrammetry. Review of orthopaedic applications, *Acta Orthop. Scand.,* 60, 491, 1989.
215. Kiss, J., Murray, D.W., Turner-Smith, A.R., and Bulstrode, C.J., Roentgen stereophotogrammetric analysis for assessing migration of total hip replacement femoral components, *Proc. Inst. Mech. Eng.,* 209, 169, 1995.
216. Ryd, L., Carlsson, L., and Herberts, P., Micromotion of a noncemented tibial component with screw fixation, *Clin. Orthop.,* 295, 218, 1993.
217. Kärrholm, J. and Snorrason, F., Subsidence, tip, and hump micromovements of noncoated ribbed femoral prostheses, *Clin. Orthop.,* 287, 50, 1993.
218. Kärrholm, J., Borssén, B., Löwenhielm, G., and Snorrason, F., Does early micromotion of femoral stem prostheses matter? 4–7 year stereoradiographic follow-up of 84 cemented prostheses, *J. Bone Joint Surg.,* 76B, 912, 1994.
219. Kiss, J., Murray, D.W., Turner-Smith, A.R., Bithell, J., and Bulstrode, C.J., Migration of cemented femoral components after THR—Roentgen stereophotogrammetric analysis, *J. Bone Joint Surg.,* 78B, 796, 1996.
220. Cook, S.D., Thomas, K.A., and Haddad, Jr., R.J., Histologic analysis of retrieved human porous-coated total joint components, *Clin. Orthop.,* 234, 90, 1988.
221. Culleton, T.P., Prendergast, P.J., and Taylor, D., Fatigue failure in the cement mantle of an artificial hip joint, *Clin. Mater.,*12, 95, 1993.
222. Noble, P.C., Experience with implant failures and conclusions for the future design of hip endoprostheses, in *Technical Principles, Design and Safety of Joint Implants,* Hogrefe & Huber, Berlin, 1994, 334.
223. Maloney, W.J., Jasty, M., Burke, D.W., O'Connor, D.O., Zalenski, E.B., Bragdon, C., and Harris, W.H., Biomechanical and histologic investigation of cemented total hip arthroplasties, *Clin. Orthop.,* 249, 129, 1989.
224. Wright, T.M., Rimnac, C.M., Stulberg, S.D., Mintz, L., Tsao, A.K., Klein, R.W., and McCrae, C., Wear of polyethylene in total joint replacements—observations from retrieved PCA knee implants, *Clin. Orthop.,* 276, 126, 1992.

225. Harris, W.H., Traumatic dislocation of the hip after dislocation in acetabular fractures: treatment by mould arthroplasty, an end-assessment using a new method of result evaluation, *J. Bone Joint Surg.,* 51A, 737, 1969.
226. Edidin, A.A., Merritt, P.O., Hack, B.H., and Manley, M.Y., A ported, proximally-cemented femoral stem for total hip arthroplasty, *J. Bone Joint Surg.,* 80-B, 869, 1998.
227. Murray, D.W., The hip, in *Outcome Measures in Trauma,* Carr, A., Pynsent, P.B., and Fairbank, J.C.I., Eds., Butterworth-Hinemann, London, 1993, chap. 10.
228. Malchau, H., Herberts, P., and Ahnfelt, L., Prognosis of total hip replacement in Sweden—Follow-up of 92,675 operations performed 1978–1990, *Acta Orthop. Scand.,* 64, 497, 1993.
229. Partio, E., von Bonsdorff, H., Wirta, J., and Avikainen, V., Survival of the Lubinus hip prosthesis. An eight- to 12-year follow-up evaluation of 444 cases, *Clin. Orthop.,* 303, 140, 1994.
230. Hench, L.L. and Wilson, J., Eds., *Clinical Performance of Skeletal Prostheses,* Chapman & Hall, London, 1996.
231. Huiskes, R., Biomechanics. A forceful science, *Ned. Tijdschr. Orthop.,* 5, 27, 1998.
232. van der Meulen, M.C.H. and Prendergast, P.J., Mechanics in skeletal development, adaptation and disease, *Philos. Trans. R. Soc. Lond. [Ser. A],* 358, 565, 2000.
233. Prendergast, P.J., Beverland, D., Blayney, A.W., Dunne, N.J., Gorey, T.F., Grace, P.A., McCormack, B.A.O., McGloughlin, T., O'Connell, P.R., and Orr, J.F., Modelling medical devices: the application of bioengineering in surgery, *Ir. J. Med. Sci.,* 168, 3, 1999.
234. Malchau, H., On the Importance of Stepwise Introduction of New Hip Implant Technology—Assessment of Total Hip Replacement Using Clinical Evaluation, Radiosterometry, Digitised Radiography and a National Registry, Ph.D. thesis, Göteborg University, 1995.

36

Design and Manufacture of Bone Replacement Scaffolds

Scott J. Hollister
The University of Michigan

Tien-Min Gabriel Chu
The University of Michigan

John W. Halloran
The University of Michigan

Stephen E. Feinberg
The University of Michigan

36.1 Introduction

Each year a large number of surgical cases require reconstruction of bone defects in the craniofacial and appendicular skeleton. These defects may be congenital or result from disease or trauma. The ultimate surgical goal is to replace the defect with a functioning material that will last the patient's lifetime. The two classic methods of defect reconstruction are bone grafting and synthetic material reconstruction, each having advantages and disadvantages. Bone grafting offers a biological tissue reconstruction that can undergo functional remodeling. Disadvantages of grafting include morbidity associated with a second surgical site, a limit on the amount of usable material, the need for hardware to fix the graft, and possible mismatches between graft and defect shape, requiring additional surgical time. Synthetic material reconstruction offers the advantages of not having a second surgical site, no limit on usable material, and shapes specifically manufactured for a given reconstruction. Disadvantages include the inability of synthetic materials to integrate completely with biological tissue, leading to risks of loosening between material and tissue, and the inability of the synthetic material to adapt and remodel with the host tissue to its functional environment.

Although both bone grafting and synthetic material reconstruction have been successful in many applications, their shortcomings have motivated a third approach to bone reconstruction, tissue engineering. Tissue engineering combines biologic regenerative factors, like stromal cells or growth factors, with biodegradable material scaffolds, like calcium phosphate ceramics and polylactic and polyglycolic acid polymers. The scaffold provides initial function but slowly degrades as healing bone tissue gradually takes over more function. In theory, tissue engineering provides the best of bone grafting and synthetic material reconstruction. Like synthetic reconstruction, tissue engineering requires no second surgical site and is not restricted by a limited amount of material. Like bone grafting, tissue engineering reproduces natural bone tissue that can adapt to functional demands.

0-8493-9117-2/01/$0.00+$.50

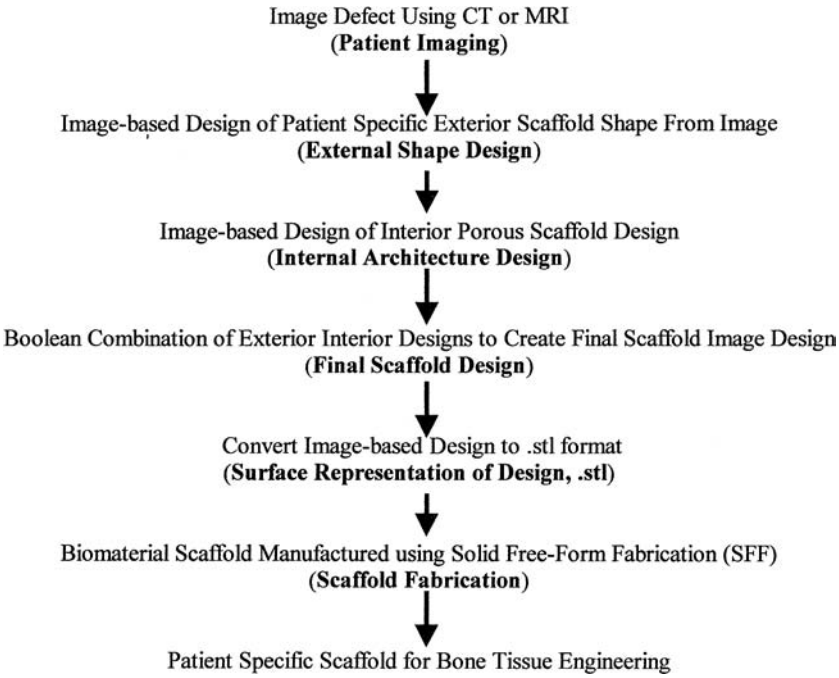

FIGURE 36.1 Overall strategy for patient specific tissue reconstruction from initial image to final manufactured scaffold.

Scaffold–biologic factor interaction is critical for successful bone tissue engineering. Many studies have noted that scaffold pore size and material can significantly influence bone vs. cartilage regeneration.[1–4] Furthermore, it is not sufficient that the scaffold have the right pore diameter for bone regeneration; those pores must have adequate connectivity and orientation so that the regenerated bone tissue can carry mechanical load. Bruder et al.[5] noted that calcium phosphate ceramics with uncontrolled pore architecture produced poor biomechanical properties, even though there was a large amount of regenerate bone tissue. In addition to internal architecture, it is necessary that the scaffold can replicate complex external shapes, especially in craniofacial reconstruction.

The need to control internal scaffold architecture and external scaffold shape depends on the ability to design and manufacture complex three-dimensional (3D) topologies. Although significant research has been performed on the biologic[6–8] and material fabrication[9,10] aspects of bone tissue engineering, controlled 3D scaffold design and fabrication have only recently received attention. The ideal goal in bone tissue engineering is to combine design and automated manufacturing techniques to create patient-specific tissue reconstruction strategies (Fig. 36.1). This chapter discusses current work on scaffold design and fabrication for bone tissue engineering, in three sections: (1) design, (2) fabrication, and (3) overall concept from design to *in vivo* testing.

36.2 Designing Bone Scaffolds

Designing bone scaffolds requires that one can design both complex, external 3D geometry to fit anatomical shapes and complex, internal 3D architecture for cell invasion and tissue regeneration. There are two computational design methodologies for creating complex 3D topology: traditional computer-aided design (CAD) and image-based design (IBD). CAD uses mathematical entities like points, lines, and surfaces to represent 3D topology. Advantages of CAD include the ability to theoretically represent topology with exact precision and the ability to represent complex structures with small amounts of data.

Disadvantages of CAD include difficulties in representing extremely complex 3D topologies, the significant amount of user time needed to create complex 3D designs, and the necessity to preprocess image data like computed tomography (CT) scans. The last point is especially relevant to bone scaffold design, since one goal is to design and fabricate patient-specific scaffolds from CT or magnetic resonance imaging (MRI) data.

IBD utilizes the idea of defining 3D topology by density distributions within voxel data sets. Advantages of IBD are the ability to represent *any* complex 3D topology and the speed with which 3D topology designs can be created. In addition, multiple 3D topologies can be combined easily using Boolean techniques. Disadvantages compared with CAD include the significantly large amounts of data needed to represent 3D topology and the fact that 3D topology can only be represented within a fraction of the smallest voxel resolution.

Weighing the relative merits of CAD and IBD, the authors have pursued IBD[11,12] based on its robustness for 3D topology representation. IBD techniques encompass any mathematical or imaging technique that can create a density distribution within a 3D voxel array. IBD can be applied to create both scaffold interior architecture and external scaffold shape. In addition, IBD allows easy combination of internal architecture and external shape designs through Boolean operations. Indeed, the use of Boolean operations provides the foundation for scaffold design using IBD. There are three basic steps to create scaffold topology by IBD: (1) creation of the exterior shape design to fit the anatomical defect including accommodation for surgical fixation, (2) creation of an internal architecture design to allow cell migration and tissue regeneration, and (3) Boolean combination of the external design with the internal architecture design to create the final scaffold.

Advantages of IBD are readily apparent when creating the exterior shape design. Using a patient's CT or MRI image, the user may outline the defect within the patient's anatomy on a slice-by-slice basis using image visualization programs such as Interactive Design Language (IDL, Research Systems, Inc., Boulder, CO), Advanced Visualization System (AVS, AVS, Inc., Waltham, MA), and PV-Wave (Visual Numerics, Inc., Boulder, CO). Combining the slices creates the exterior shape design volume. Next, holes for screw fixation are created by Boolean intersection of voxel representations of cylinders with the exterior shape outlined on a slice-by-slice basis. The purpose of having screw fixation is to allow the surgeon to attach the scaffold to the mandibular ramus that remains after surgical resection of the original degenerated mandibular condyle. An example mandibular condyle exterior design utilizing the Visible Human Female CT data set is shown in Fig. 36.2.

The next step in scaffold design is creation of the interior scaffold architecture. One way to create interconnected pore architectures is by periodic repetition of a base unit cell. If the unit cell has channels running through each side, the resulting internal architecture will have complete connectivity for tissue ingrowth. Distributing voxel density according to basic geometric shapes can create these connected cells. One of these basic shapes is an ellipsoid, represented by

$$\frac{x^2}{a^2} + \frac{y^2}{b^2} + \frac{z^2}{c^2} = 1 \tag{36.1}$$

were x is the x coordinate, y is the y coordinate, z is the z coordinate, a is the ellipsoid radius in the x direction, b is the ellipsoid radius in the y direction, and c is the ellipsoid radius in the z direction. If the voxel densities are set high when Eq. 36.1 is less than 1, connected ellipsoid shaped struts are obtained (Fig. 36.3a). Conversely, if voxel densities are set low when Eq. 36.1 is less than 1, interconnecting ellipsoidal voids are obtained (Fig. 36.3b).

Another method of creating scaffold architecture using IBD is simply to image an existing tissue microstructure, for example, porous trabecular bone. Zysset et al.[13] demonstrated the ability to design and manufacture scaffolds directly from micro-CT images of trabecular bone. This creates a naturally biomimetic scaffold architecture. The trabecular bone microstructure can be created either by micro-CT or by micro-MRI scanning.

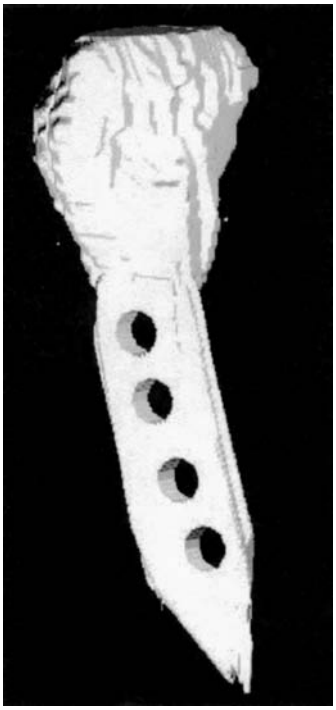

FIGURE 36.2 External shape design of a mandibular condyle scaffold generated from Visible Human data. Note holes created in exterior design to allow for screw fixation of scaffold to surrounding tissue.

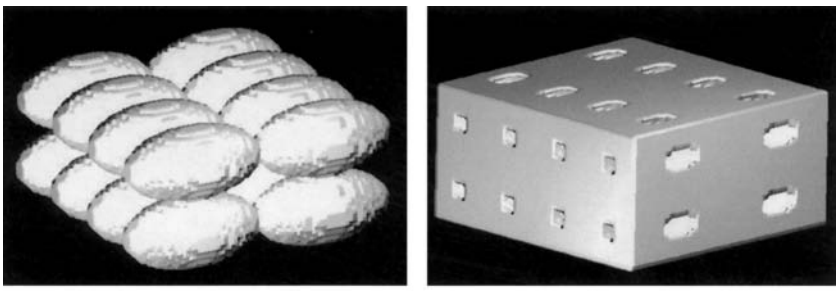

FIGURE 36.3 Sixteen combined unit cells of an ellipsoid architecture created using Eq. 36.1. (a) An ellipsoidal strut; (b) an ellipsoidal pore.

The final step in scaffold design is Boolean combination of the exterior scaffold shape and interior scaffold architecture. To do this within IBD, the voxel resolution of the exterior shape must be the same as that of the interior architecture design. In general, the exterior shape voxel resolution may be lower than the interior architecture voxel resolution. The exterior shape resolution can be made equivalent through standard trilinear or cubic interpolation schemes. Once the data resolutions are equivalent, the voxel locations are then found within the 3D interior architecture data set that represents the interior architecture scaffold topology. The corresponding voxel indices within the exterior shape design data set are then set equal to the density of the interior architecture data set. The final mandibular condyle scaffold design is shown in Fig. 36.4.

TABLE 36.1 Designed Polymer Scaffold Properties

	E_1(MPa)	E_2(MPa)	E_3(MPa)	G_{23}(MPa)	G_{13}(MPa)	G_{12}(MPa)	ν_{23}	ν_{13}	ν_{12}
Base polymer	2000	2000	2000	769	769	769	0.3	0.3	0.3
Polymer scaffold	154	154	200	17.8	17.8	18.2	0.09	0.09	0.14

Note: The first row gives the base polymer material isotropic properties. The second row gives the effective transversely isotropic properties that result from building the architecture in Fig. 36.3b from the polymer.

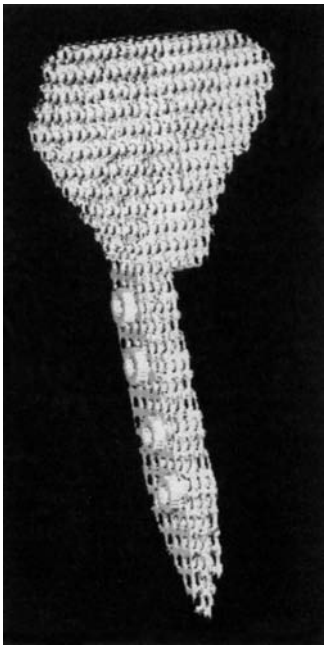

FIGURE 36.4 Final mandibular condyle scaffold design created by a Boolean intersection of external scaffold shape (Fig. 36.2) and internal ellipsoid pore (Fig. 36.3b).

Since scaffold design determines the deformation and flow environments of invading and seeded cells in addition to global mechanical function, it is desirable to analyze scaffold designs computationally before fabrication. If scaffold architecture is created by repetition of a base unit cell, homogenization analysis[14] can be used to calculate the effective scaffold properties that result from the scaffold material and architecture. Effective properties are those that would be obtained by testing a cube containing many unit cells, as opposed to the properties of the materials that make up the unit cell. For example, consider the ellipsoid void architecture in Fig. 36.3b. If it is assumed that the scaffold is made from a polyanhydride[15] that is isotropic with a Young's modulus of 2 GPa and a Poisson's ratio of 0.3, the effective engineering constants are anisotropic (Table 36.1). The polymer may be stiffened by adding hydroxyapatite (HA) particles in the mixture. This is readily accomplished using IBD by using a random number generator to set voxels to HA. If 25% of the scaffold volume is HA particles, with a Young's modulus of 100 GPa, the effective constants are obtained by homogenization (Table 36.2).

These results demonstrate that image-based methods can be readily used to assess scaffold mechanics in addition to generating scaffold design. They indicate how architecture, base material, and composite mixtures affect scaffold properties. It is also possible to apply image-based topology design methods[16] that have been used to design materials to optimize scaffold design with respect to mechanical performance. However, without extensive experiments on scaffold architecture effects on tissue regeneration, it is difficult to know the most appropriate objective function for scaffold optimization.

TABLE 36.2 Designed Hybrid Polymer/HA Scaffold Properties

	E_1(MPa)	E_2(MPa)	E_3(MPa)	G_{23}(MPa)	G_{13}(MPa)	G_{12}(MPa)	ν_{23}	ν_{13}	ν_{12}
Base polymer	2000	2000	2000	769	769	769	0.3	0.3	0.3
Base HA particles	100,000	100,000	100,000	38,491	38,491	38,491	0.3	0.3	0.3
Hybrid polymer HA scaffold	529	476	787	44	44	55	0.09	0.09	0.14

Note: The first row gives the base isotropic polymer properties. The second row gives the base isotropic properties of HA ceramic particles used to reinforce the polymer. The third row gives the effective orthotropic properties that result from building the architecture in Fig. 36.3b from the polymer/HA composite.

36.3 Fabricating Bone Scaffolds

In many studies involving fabricated bone scaffolds,[17–23] the scaffold interior architecture and external scaffold shape are not designed using computational techniques, but rather are determined by material processing and casting. In the case of corraline HA scaffolds, the internal architecture is determined by the chemical conversion of the original coral structure. For polymer or polymer–ceramic composites interior architecture is often determined by embedding a high density of salt crystals into the dissolved polymer. The dissolved polymer is then poured into a mold and treated under heat and pressure to form the external shape. Once the external shape is formed, the salt particles are leached out to leave porous interconnecting interior channels. Running the salt crystals through a sieve to obtain a specific range of crystal diameters controls the pore size.[17] These crystal diameters have been shown to correlate with scaffold pore diameters.[17] As with chemical conversion of corraline HA, there is little control over the orientation and connectivity of the internal pore architecture. Connectivity can only be assured by having a high density of salt particles.

Polymer and polymer–ceramic scaffolds fabricated using salt-leaching technique have been frequently tested both *in vitro* and *in vivo*. Ishaug et al.[18] seeded osteoblasts on poly-lactic/poly-glycolic copolymers with pore sizes in 150 to 300, 300 to 500, and 500 to 700 μm range. They found no difference in matrix deposition as measured by alkaline phosphatase activity and mineralized matrix for the three pore size ranges. Because of the high compliance of degradable biopolymers, Marra et al.[19] incorporated HA particles into blends of poly(caprolactone) and poly(D,L-lactic-co-glycolic acid) polymers. Using a sieved NaCl particle size of 150 to 250 μm and a HA granule size of $\sim$10 μm, they produced 12-mm-diameter disks that were 80% porous. They noted a five times increase in scaffold stiffness by incorporating 10% HA granules over the polymer alone. This fivefold increase is similar to the approximately fourfold increase predicted using the homogenization image-based analysis using random particle generation. Marra et al. also found that these scaffolds supported stromal cell growth and collagen matrix deposition. Laurencin et al.[20] fabricated porous scaffolds from a polyphosphazene polymer using the salt-leaching technique. They produced an average pore size of 165 μm, and stated that the scaffolds had a reconnecting porous network under scanning electron microscopy (SEM), but did not state an overall porosity. They found that osteoblasts grew and proliferated on the scaffolds, as indicated by alkaline phosphatase activity.

While *in vitro* studies typically use simple scaffold geometry, many *in vivo* studies utilizing salt-leached internal scaffold architectures have molded the scaffolds into specific shapes. Thomson et al.[21] implanted 4-cm^3 volumes of stacked porous wafers of poly(D,L-lactic-co-glycolic acid) polymer on sheep ribs. Some implanted volumes also contained bone graft particles. They noted that all implanted scaffolds supported vascularized tissue ingrowth. However, only those volumes containing bone particles showed bone tissue regeneration. The polymer alone did not generate osseous tissue. Mikos et al.[22] studied scaffold pore diameter effects on scaffold vascularization using poly(L-lactic acid) porous polymers implanted in rat mesentery. They noted that the rate of vascularized tissue ingrowth increased as the scaffold porosity and/or pore size increased. Noritaka et al.[23] used a woven mesh of polyglycolic acid fibers with 15-μm

fiber diameters and pore sizes of 75 to 100 μm to mold replicas of human phalanges. The polyglycolic acid was dissolved in a solvent and cast into vinyl polysiloxane molds. A porous woven mesh scaffold with the external shape of the phalange was obtained after solvent evaporation. These scaffolds were seeded with periosteum in the bulk of the scaffold and chondrocytes on the ends of the scaffold. The scaffolds were then implanted in athymic mice. After implantation for 20 weeks, a mineralized construct in the shape of the phalange with a cartilage cap was formed. The results of both *in vitro* and *in vivo* studies demonstrate the feasibility of fabricating functional scaffolds by dissolving polymers with embedded salt crystals into a mold, allowing the solvent to evaporate and leaching out the salt particles to form an internal porous architecture.

One difficulty with scaffold architecture fabrication by salt leaching is that there is little control over the architectural topology other than average pore diameter by controlling salt crystal size and rudimentary control over pore connectivity by high salt crystal packing density. However, studies such as those by Bruder et al.[5] and Mikos et al.[22] demonstrate that controlling internal scaffold architecture is crucial to controlling scaffold vascularization and regenerate tissue mechanical properties. Simultaneous control over external scaffold shape and internal scaffold architecture requires the use of computational design techniques such as those discussed at the beginning of this chapter. These computational techniques, however, typically generate a bone scaffold topology that presents a significant manufacturing challenge due to the complicated 3D exterior shape and interior architecture. The only feasible way to manufacture such scaffolds is using a class of techniques known as solid free-form fabrication (SFF). All SFF techniques manufacture complicated 3D structures using a layered fabrication approach. SFF techniques create components in general by material addition as opposed to traditional manufacturing techniques that create 3D structures by removing material to create the final part.

A basic premise of SFF methods is that a material in either powdered or liquid form is solidified one layer at a time in a pattern determined by a computer-generated file. Once the layer is complete, it is lowered by a specified depth and the process is repeated. In addition, supports may be generated to buttress material within the structure not supported by material from a previous layer. The mode in which material is processed depends upon the commercial system. In stereolithography (denoted as SLA, 3D Systems, Inc.) a laser is guided along the surface defined in a computer file that polymerizes a photopolymerizable material in a vat. In fused deposition modeling (FDM, Stratsys, Inc.), a viscous solution of a polymer melt is squeezed onto the layer by a guided nozzle. The nozzle path is determined by the computer-defined surface. A third method, Selective Laser Sintering (SLS, DTM Corporation, Austin, TX), uses a laser to sinter powdered material that is placed on a given layer. As with SLA, the laser is guided by a surface model defined in a computer file. A fourth method, by the Sanders Prototype, Inc. uses a thermoplastic ink-jetting technology to essentially print wax analogous to the manner in which laser printers deposit ink. A fifth method, 3D printing (3DP) prints or deposits a binder on powdered material. A sixth process, called layered object manufacturing (LOM), uses a thin sheet of paper that is rolled into the build area and laminated onto previous layers using heat and pressure. A laser is then used to cut area regions not within the surface model. The reader should consult other references for more details on SFF processes.[24,25]

Medical applications of SFF sprung up soon after the techniques were developed. The earliest uses of SFF in medicine were for surgical planning and modeling. This mimics the progression of SFF in other industrial applications, which began by using SFF to build planning prototypes before moving on to the manufacture of functional parts. Indeed, SFF techniques are commonly known as rapid prototyping, a reference to the original use of SFF for prototyping and planning purposes. A unique application of SFF procedures is the manufacture of bone tissue microstructure, as in the study of Zysset et al.[13] Since the base manufacturing material is homogeneous, in this case an epoxy resin for SLA, one may separate the effect of architecture from tissue properties on the effective stiffness of trabecular bone. Zysset et al.[13] showed that the base epoxy resin had properties in the range of those reported for trabecular tissue.[26,27] They measured orthotropic effective prototype bone properties and found those also to be within the range of reported trabecular bone effective properties.[28] This suggests manufacture of bone tissue microstructure prototypes may be another approach to help understand bone tissue structure function.

Biomedical applications of SFF have progressed from making surgical planning models and tissue prototypes to making functional parts from biomaterials that can actually be seeded with cells for tissue engineering or used as drug-delivery devices. Wu et al.[29] described the use of the 3DP technique to fabricate polymers for drug delivery. They noted that manufactured microstructures significantly influenced drug-delivery rates. An early application of SFF in tissue engineering was the work of Kim et al.[30] testing the feasibility of regenerating liver tissue using hepatocytes on SFF-manufactured scaffolds. A significant limitation to engineering critical liver tissue mass is the limited oxygen and nutrient diffusion in scaffolds that lack designed interconnected porosity. To address this issue, Kim et al.[30] used a 3DP process to create scaffolds with designed interconnected porosity from a copolymer of polylactide-coglycolide acid. The polymer powder was also packed with salt particles that were then leeched out with distilled water. The resulting 3D scaffold was 8 mm in diameter and 7 mm in height. The fabricated porosity consisted of interconnected channels 800 μm in diameter. Additional porosity with micropores ranging from 45 to 150 μm were created by the leeching process. The total porosity was 60%. Kim et al. then seeded hepatocytes on the scaffolds under both static and flow conditions, showing hepatocyte attachment to the scaffold and significantly increased partial oxygen pressure under flow conditions.

Bone replacement scaffolds can be fabricated from either biopolymers or bioceramics. Vail et al.[31] used SLS to fabricate calcium phosphate scaffolds from a mixture of monocalcium phosphates and dicalcium phosphates as raw materials. They manufactured a cylindrical test specimen 8.9 mm in height and 8.9 mm in diameter to determine effects of processing and sintering on mechanical properties. The bulk manufactured material had a stiffness of 231.0 $\pm$ 33.8 MPa and a compressive strength of 48.3 $\pm$ 7.3 MPa. Fox et al.[32] used this approach to manufacture scaffolds to replace alveolar ridge defects. The constructed an implant 3 $\times$ 6.6 $\times$ 15.3 mm with hexagonal macropores 2 mm in diameter. Porous scaffolds with hexagonal macropores were manufactured to augment alveolar ridge defects in canines. Animals sacrificed between 4 and 12 months indicated significant bone ingrowth and no adverse reaction. The amount of ingrowth was not reported. The authors' group at the University of Michigan[11,33,34] has used a process for SLA ceramic manufacturing developed by Chu, Halloran, and colleagues[35,36] to manufacture bone tissue scaffolds from HA. In this case, the HA powder is mixed in the photopolymerizable suspension. The laser then cures the polymer that binds the ceramics particles. The polymer is then burned out during the ceramic-sintering process to leave only the ceramic. This ceramics SLA process combined with IBD provides the ability to manufacture complex ceramic microstructures, including actual trabecular bone microstructure for biomimetic scaffolds (Fig. 36.5).

In addition to direct manufacturing of biomaterial scaffolds on SFF systems, one may use SFF to manufacture a mold into which a biomaterial is cast. This approach was taken by Chu et al.[34] to manufacture HA scaffolds. In this process, a 3D mold is made of the inverse of the scaffold. In other words, the scaffold pores are solid in the mold, and vice versa. A HA slurry is then pored into the mold.

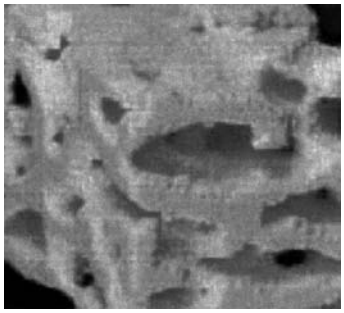

FIGURE 36.5 An 8$\times$ scale 3 $\times$ 3 $\times$ 3 mm section of human trabecular bone built from alumina oxide on a stereolithography machine.

The polymer mold is burned out at a temperature of 500°C, following which the ceramic is sintered at a temperature of 1200°C.

36.4 Bone Scaffolds: An Example from Design to Testing

Although great strides have been made in design and free-form fabrication of biomaterials, the ultimate test of these scaffolds is how they perform *in vivo*. There are a number of steps that must be taken to ensure the biological, mechanical, and material integrity of these scaffolds before they can be used for clinical applications (Fig. 36.6).

For example, the SFF procedures often use materials during processing that are not retained in the final material. However, if even trace amounts persist in the final product, they may be toxic to cells. Therefore, it is prudent to perform biocompatibility tests on the final processed material. Surgical reconstruction using manufactured bone tissue scaffolds will require standard assays to be developed in areas of biocompatibility, mechanical testing, and *in vivo* models. Only by linking a set of reproducible assays with design and material fabrication can the notion of patient-specific reconstructions via design and fabricated tissue engineering scaffolds be realized.

The authors[11,12] have recently begun work that demonstrates a potential path to bring design and manufactured scaffolds to clinical use by linking design and fabrication of HA scaffolds with an *in vivo* porcine mandibular defect model. Since this was a feasibility study focused on issues of architectural effects on bone ingrowth and compatibility, noncritical-sized defects were utilized that could be reproducibly created using a trephine. In this study, the exterior shape of the scaffold was a cylinder 8 mm in diameter and 6 mm long. Two design patterns, an orthogonal cylindrical pore design (denoted as orthogonal) and a radial pore design (denoted as radial), were constructed using IBD techniques. Since an indirect method was used, the inverse of the pore patterns was created. In other words, the scaffold channels were solid in the mold (Fig. 36.7). The voxel design representation was then converted into surface .stl format (Voxelcon, Voxel Computing, Inc., Ann Arbor, MI).

The .stl file for each scaffold design was verified and molds were built on a 3D Systems SLA 250/40 machine from Ciba-Geigy 5170 resin. Following the procedure of Chu et al.,[35] a HA slurry was prepared and pored into the resin molds. The slurry mold composite was then heated to 500°C to burn out the resin. Following burnout, the slurry was then heated to 1200°C to sinter the ceramic. X-ray diffraction confirmed that the final sintered ceramics was a form of HA known as oxy-hydroxyapatite. The final manufactured oxy-HA scaffolds closely replicated the initial designs (Fig. 36.8).

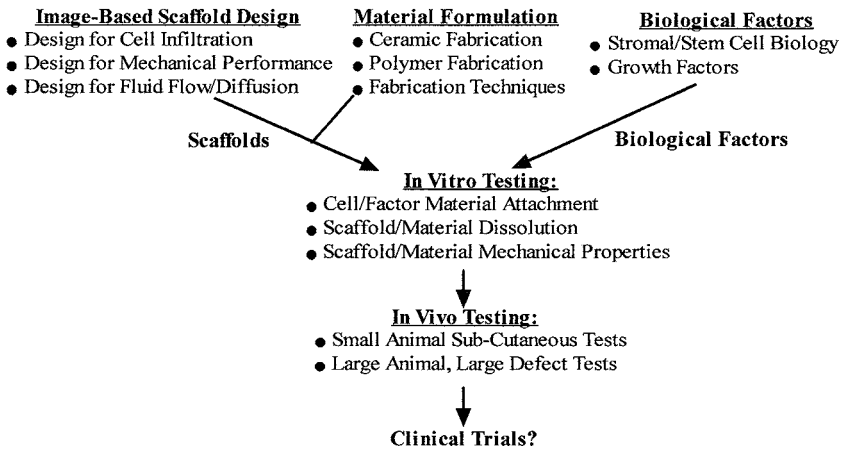

FIGURE 36.6 Research steps that must be addressed for successful scaffold-based bone tissue engineering.

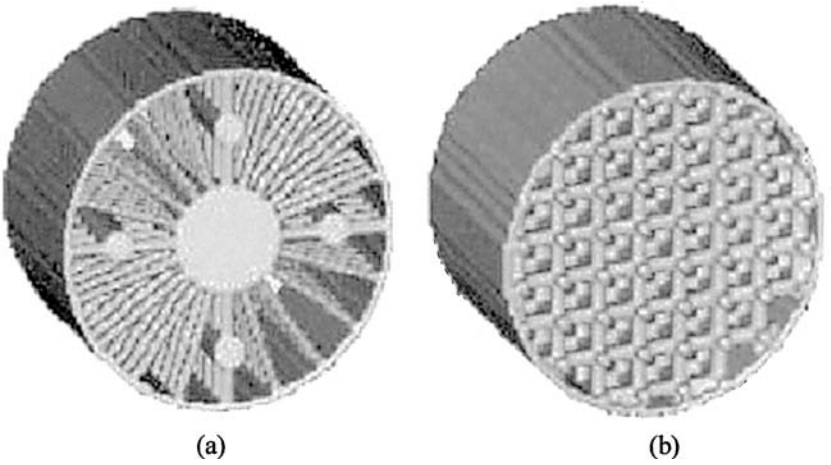

FIGURE 36.7 Image-based designs of scaffold molds. (a) Radial pore design; (b) orthogonal pore design.

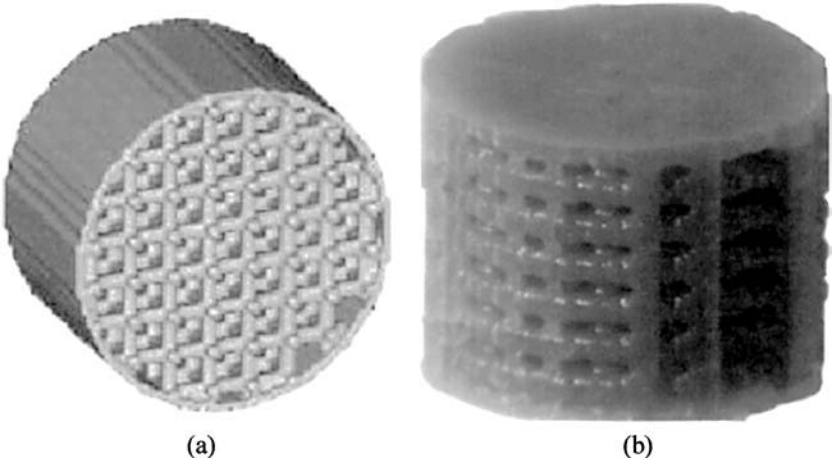

FIGURE 36.8 Comparison of scaffold mold design (a) and manufactured HA scaffold (b) (oriented at right angle to mold) shows that the manufactured scaffold replicates the design. Note that the solid beams in the mold (a) become the pores in the cast scaffold (b).

The scaffolds were implanted bilaterally in porcine mandible defects. Six animals were operated on under general anesthesia in sterile conditions at the Lone Star Veterinary Hospital in Seguin, TX. Animals were allowed unrestricted mobility on a farm and ate a normal diet 3 days following surgery. Three animals were sacrificed at 1 month and the other three at 2 months following surgery. The mandibles were retrieved following sacrifice, sectioned, and embedded in methacrylate for thick sectioning. Sections were processed for either backscattered SEM or stained with toludine blue.

Upon resection, there were no visible signs of inflammation or adverse reaction to the scaffold material. Backscattered SEM analysis confirmed these observations showing excellent integration between ingrown bone tissue and the oxy-HA scaffold (Fig. 36.9). Furthermore, bone formation closely followed the existing pore architecture, demonstrating that the designed scaffolds can guide tissue regeneration to form specific tissue architectures. Sections stained with toludine blue (Fig. 36.10) showed bone and fibrous tissue formation within the scaffold, but no cartilage. This suggests that bone formation within the scaffolds occurred by intramembranous ossification rather than by endochondral ossification. At 2 months, the orthogonal pore design had 19 $\pm$ 9% of pore volume filled with bone while the radial design had 14 $\pm$ 4% of pore volume filled with bone. This amount of bone fill is comparable with

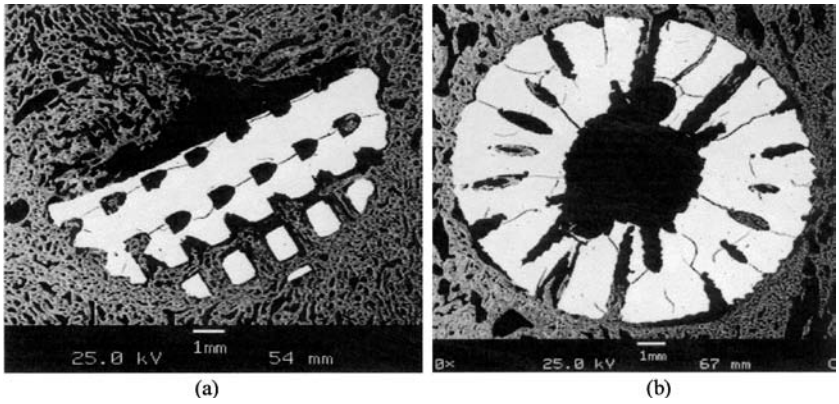

FIGURE 36.9 Bone ingrowth on manufactured scaffolds 2 months *in vivo* shown by SEM. (a) Bone ingrowth in orthogonal design; (b) bone ingrowth into radial designs. Both designs show bone integration into the scaffolds. The orthogonal design had slightly more ingrowth.

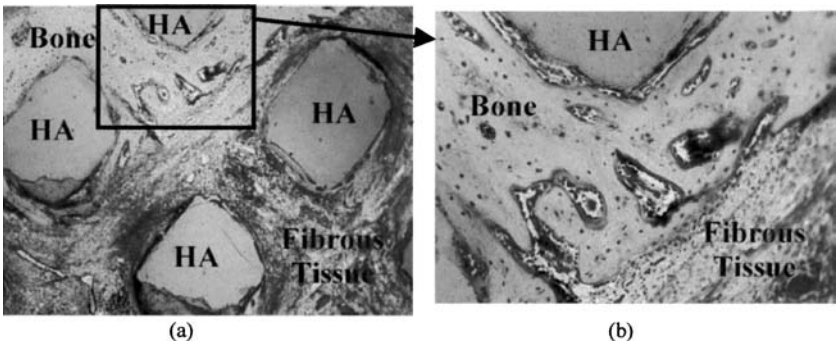

FIGURE 36.10 Toludine blue-stained sections of tissue ingrowth in manufactured scaffolds. (a) Larger section shows how scaffold channels guide the architecture of forming bone; (b) close up of the same region shows fibrous tissue formed ahead of mineralized tissue.

studies using corraline HA materials for bone reconstruction in other species in different anatomical sites. For example, Holmes and Hagler[37] found similar amounts of bone ingrowth in corraline HA implanted in canine calvaria. Although the amount of bone formed was similar in this design to conventional HA materials, it is critical to remember that, unlike the designed scaffolds, conventional HA bone replacement materials offer little control over regenerate tissue architecture.

36.5 Conclusion

Research on bone tissue engineering has shown that aspects of the scaffold material and structure can significantly affect regenerate tissue structure and function. Therefore, the ability to control scaffold architecture through design and fabrication could be a critical factor in the future clinical success of bone tissue engineering. Current fabrication techniques have primarily utilized either corraline converted phosphate ceramics or cast polymers salt-leached to develop porosity. The desire to have better control over scaffold architecture has led to the introduction of SFF techniques to manufacture scaffolds. Current work has clearly demonstrated the capability of designing and manufacturing bone tissue replacements from degradable biomaterials using SFF techniques. In addition, IBD techniques allow rapid design and analysis of complex 3D scaffold topology that can even mimic natural bone structure. The most apparent

application of this technology is surgical reconstruction of complex defects. However, two other research areas could significantly benefit from the design and manufacture of biomimetic bone structures. One application is the study of bone fragility. One can create multiple copies of the same bone structure built from materials close in property to mineralized bone. This will allow the multiple failure testing needed to define a failure surface. The second application is the study of mechanotransduction. Currently, studies of mechanotransduction occur either in *in vivo* or *in vitro* systems. *In vivo* models encapsulate all systems involved in transducing mechanical signals but are too complex to analyze completely. *In vitro* systems allow for carefully controlled experiments, but provide an environment that lacks the complexity of the *in vivo* situation. 3D culture environments could easily be manufactured using biomaterials to mimic bone structures, providing a bridge between *in vivo* and traditional *in vitro* studies.

References

1. Sampath, T.K. and Reddi, A.H., Importance of geometry of the extracellular matrix in endochondral bone differentiation, *J. Cell Biol.,* 98, 2192, 1984.
2. Kuboki, Y., Saito, T., Murata, M., Takita, H., Mizuno, M., Inoue, M., Nagai, N., and Poole, A.R., Two distinctive BMP-carriers induce zonal chondrogenesis and membranous ossification, respectively; geometrical factors of matrices for cell-differentiation, *Connect. Tissue Res.,* 32, 219, 1995.
3. Kuboki, Y., Takita, H., Kobayashi, D., Tsuruga, E., Inoue, M., Murata, M., Nagai, N., Dohi, Y., and Ohgushi, H., BMP-induces osteogenesis on the surface of hydroxyapatite with geometrically feasible and nonfeasible structures: topology of osteogenesis, *J. Biomed. Mater. Res.,* 39, 190, 1998.
4. Tsuruga, E., Takita, H., Itoh, H., Wakisaka, Y., and Kuboki, Y., Pore size of porous hydroxyapatite as the cell-substratum controls BMP-induced osteogenesis, *J. Biochem.,* 121, 1997.
5. Bruder, S.P., Kraus, K.H., Goldberg, V.M., and Kadiyala, S., Critical-sized canine segmental femoral defects are healed by autologous mesenchymal stem cell therapy, in *Transactions of the 44th Annual Meeting of the Orthopaedic Research Society,* 1998, 147.
6. Caplan, A.I. and Bruder, S.P., Cell and molecular engineering of bone regeneration, in *Principles of Tissue Engineering,* Lanza, R.P., Langer, R., and Chick W.L., Eds., Academic Press, New York, 1997.
7. Reddi, A.H., Initiation of fracture repair by bone morphogenetic proteins, *Clin. Orthop.,* 355, S66, 1998.
8. Krebsbach, P.H., Kuznetsov, S.A., Satomura, K., Emmons, R.V.B., Rowe, D.W., and Robey, P.G., Bone formation in vivo: comparison of osteogenesis by transplanted mouse and human marrow stromal fibroblasts, *Transplantation,* 63, 1059, 1997.
9. Bostrom, R.D. and Mikos, A.G., Tissue engineering of bone, in *Synthetic Biodegradable Polymer Scaffolds,* Atala, A. and Mooney, D.J., Eds., Birkhauser, Boston, 1996, chap. 12.
10. Yazemski, M.J., Payne, R.G., Hayes, W.C., Langer, R.S., and Mikos, A.G., Evolution of bone transplantation: molecular, cellular, and tissue strategies to engineer human bone, *Biomaterials,* 17, 175, 1996.
11. Hollister, S.J., Chu, T.M., Guldberg, R.E., Zysset, P.K., Levy, R.A., Halloran, J.W., and Feinberg, S.E., Image based design and manufacture of scaffolds for bone reconstruction, in *Synthesis in Bio Solid Mechanics,* Pedersen, P. and Bendsoe, M.P., Eds., Kluwer Academic Press, Dordrecht, 1999, 163.
12. Hollister, S.J., Levy, R.A., Chu, T.M., Halloran, J.W., and Feinberg, S.E., An image-based approach for designing and manufacturing craniofacial scaffolds, *Int. J. Oral Maxillofac. Surg.,* 29, 67, 2000.
13. Zysset, P.K., Marsan, A.L., Chu, T-M.G., Guldberg, R.E., Halloran, J.W., and Hollister, S.J., Rapid prototyping of trabecular bone for mechanical testing, in BED-Vol. 35, ASME Bioengineering Conference, American Society of Mechanical Engineers, New York, 1997, 387.
14. Hollister, S.J. and Kikuchi, N., Homogenization theory and digital imaging: A basis for studying the mechanics and design principles of bone tissue, *Biotechnol. Bioeng.,* 43, 586, 1994.
15. Muggli, D.S., Burkoth, A.K., and Anseth, K.S., Crosslinked polyanhydrides for use in orthopedic applications: degradation behavior and mechanics, *J. Biomed. Mater. Res.,* 46, 271, 1999.

16. Bendsoe, M.P., *Optimization of Structural Topology, Shape and Material,* Springer-Verlag, Berlin, 1995.
17. Jen, A.C., Peter, S.J., and Mikos, A.G., Preparation and use of porous poly(a-hydroester) scaffolds for bone tissue engineering, in *Tissue Engineering Methods and Protocols,* Morgan, J.R. and Yarmush, M.L., Eds., Humana Press, Totowa, NJ, 1999, chap. 11.
18. Ishaug, S.L., Crane, G.M., Miller, M.J., Yasko, A.W., Yaszemski, M.J., and Mikos, A.G., Bone formation by three-dimensional stromal osteoblast culture in biodegradable polymer scaffold, *J. Biomed. Mater. Res.,* 36, 17, 1997.
19. Marra, K.G., Szem, J.W., Kumta, P.N., DiMilla, P.A., and Weiss, L.E., In vitro analysis of biodegradable polymer blend/hydroxyapatite composites for bone tissue engineering, *J. Biomed. Mater. Res.,* 47, 324, 1999.
20. Laurencin, C.T., El-Amin, S.F., Ibim, S.E., Willoughby, D.A., Attawia, M., Allcock, H.R., and Ambrosio, A.A., A highly porous 3-dimensional polyphosphazene polymer matrix for skeletal tissue regeneration, *J. Biomed. Mater. Res.,* 30, 133, 1996.
21. Thomson, R.C., Mikos, A.G., Beahm, E., Lemon, J.C., Satterfield, W.C., Aufdemorte, T.B., and Miller, M.J., Guided tissue fabrication from periosteum using preformed biodegradable polymer scaffolds, *Biomaterials,* 20, 2007, 1999.
22. Mikos, A.G., Sarakinos, G., Lyman, M.D., Ingber, D.E., Vacanti, J.P., and Langer, R., Prevascularization of porous biodegradable polymer, *Biotechnol. Bioeng.,* 42, 716, 1993.
23. Noritaka, I., Landis, W., Kim, T.H., Gerstenfeld, L.C., Upton, J., and Vacanti, J.P., Formation of phalanges and small joints by tissue-engineering, *J. Bone Joint Surg.,* 81A, 306, 1999.
24. Jacobs, P.F., *Rapid Prototyping and Manufacturing: Fundamentals of Stereolithography,* Society for Manufacturing Engineers, Dearborn, MI, 1992.
25. Kai, C.C. and Fai, L.K., *Rapid Prototyping: Principles and Applications in Manufacturing,* John Wiley Press, New York, 1997.
26. Mente, P.L. and Lewis, J.L., Experimental method for the measurement of the elastic modulus of trabecular bone tissue, *J. Orthop. Res.,* 7, 456, 1989.
27. Choi, K., Kuhn, J.L., Ciarelli, M.J., and Goldstein, S.A., The elastic moduli of human subchondral, trabecular and cortical bone tissue and the size-dependency of cortical bone modulus, *J. Biomech.,* 23, 1103, 1990.
28. Keaveny, T.M. and Hayes, W.C., A 20-year perspective on the mechanical properties of trabecular bone, *J. Biomech. Eng.,* 115, 534, 1993.
29. Wu, B.M., Borland, S.W., Giordano, R.A., Cima, L.G., Sachs, E.M., and Cima, M.J., Solid free-form fabrication of drug delivery devices, *J. Controlled Release,* 40, 77, 1996.
30. Kim, S.S., Utsunomiya, H., Koski, J.A., Wu, B.M., Cima, M.J., Sohn, J., Mukai, K., Griffith, L., and Vacanti, J.P., Survival and function of hepatocytes on a novel three-dimensional synthetic biodegradable polymer scaffold with an intrinsic network of channel, *Ann. Surg.,* 228, 8, 1998.
31. Vail, N.K., Swain, L.D., Fox, W.C., Aufdlemorte, T.B., Lee, G., and Barlow, J.W., Materials for biomedical application, *Mater. Design,* 20, 123, 1999.
32. Fox, W.D., Swain, L.D., Aufdemorte, T.B., Lee, G., Vail, N.K., and Barlow, J.W., Custom formed synthetic bone implants in vivo, in *Transactions of the 45th Orthopaedic Research Society Meeting,* Anaheim, CA., 1999, 527.
33. Levy, R.A., Chu, T.M.G., Halloran, J.W., Feinberg, S.E., and Hollister, S.J., Computed tomography-generated porous hydroxyapatite orbital floor prosthesis as a prototype bioimplant, *Am. J. Neuroradiol.,* 18, 1522, 1997.
34. Chu, T.-M., Halloran, J.W., Hollister, S.J., and Feinberg, S.E., Hydroxyapatite with controlled internal architecture by acrylic polymerization, *J. Mater. Sci. Mater. Med.,* in press.
35. Chu, T.-M., Halloran, J.W., and Wagner, W.C., Ultraviolet curing of highly loaded hydroxyapatite suspension, in *Bioceramics: Materials and Applications,* R.P. Rusin and G.S. Fishman, Eds., Ceramic Transactions, Vol. 65, American Ceramic Society, Westerville, OH, 1995, 57.

36. Chu, T.-M. and Halloran, J.W., Hydroxyapatite for implant fabrication by stereolithography, in *Case Studies of Ceremic Product Development, Manufacturing and Commercialization,* A. Ghosh, B. Hiremath, and R. Barks, Eds., Ceramic Transactions, Vol. 75, American Ceramic Society, Westerville, OH, 1997.
37. Holmes, R.E. and Hagler, H.K., Porous hydroxyapatite as a bone graft substitute in cranial reconstruction: a histometric study, *Plast. Reconstruct. Surg.,* 81, 662, 1988.

Index

A

B

C

D

E

F

G

H

I

J

K

L

M

N

O

P

Q

R

S

T

U

V

W